AFRL-PR-WP-TP-2002-200, V3

ADVANCED LASER DIAGNOSTIC APPLICATIONS

Volume 3 of 3 (Pages 694 – 1233)

Larry P. Goss, Ph.D.

Innovative Scientific Solutions, Inc.
2766 Indian Ripple Road
Dayton, OH 45440-3638

MARCH 2001

FINAL REPORT FOR 18 SEPTEMBER 1995 – 28 SEPTEMBER 2000

Approved for public release; distribution is unlimited.

20021008 165

PROPULSION DIRECTORATE
AIR FORCE RESEARCH LABORATORY
AIR FORCE MATERIEL COMMAND
WRIGHT-PATTERSON AIR FORCE BASE, OH 45433-7251

NOTICE

USING GOVERNMENT DRAWINGS, SPECIFICATIONS, OR OTHER DATA INCLUDED IN THIS DOCUMENT FOR ANY PURPOSE OTHER THAN GOVERNMENT PROCUREMENT DOES NOT IN ANY WAY OBLIGATE THE U.S. GOVERNMENT. THE FACT THAT THE GOVERNMENT FORMULATED OR SUPPLIED THE DRAWINGS, SPECIFICATIONS, OR OTHER DATA DOES NOT LICENSE THE HOLDER OR ANY OTHER PERSON OR CORPORATION; OR CONVEY ANY RIGHTS OR PERMISSION TO MANUFACTURE, USE, OR SELL ANY PATENTED INVENTION THAT MAY RELATE TO THEM.

THIS REPORT IS RELEASABLE TO THE NATIONAL TECHNICAL INFORMATION SERVICE (NTIS). AT NTIS, IT WILL BE AVAILABLE TO THE GENERAL PUBLIC, INCLUDING FOREIGN NATIONS.

THIS TECHNICAL REPORT HAS BEEN REVIEWED AND IS APPROVED FOR PUBLICATION.

Vincent M. Belovich

VINCENT M. BELOVICH, Ph.D.
Contract Monitor
Combustion Science Branch (AFRL/PRTS)

ROBERT D. HANCOCK, Ph.D.
Chief
Combustion Science Branch, AFRL/PRTS

William E Koop

WILLIAM E. KOOP
Chief of Technology
Turbine Engine Division
Propulson Directorate

Do not return copies of this report unless contractual obligations or notice on a specific document require its return.

REPORT DOCUMENTATION PAGE

Form Approved
OMB No. 0704-0188

The public reporting burden for this collection of information is estimated to average 1 hour per response, including the time for reviewing instructions, searching existing data sources, searching existing data sources, gathering and maintaining the data needed, and completing and reviewing the collection of information. Send comments regarding this burden estimate or any other aspect of this collection of information, including suggestions for reducing this burden, to Department of Defense, Washington Headquarters Services, Directorate for information Operations and Reports (0704-0188), 1215 Jefferson Davis Highway, Suite 1204, Arlington, VA 22202-4302. Respondents should be aware that notwithstanding any other provision of law, no person shall be subject to any penalty for failing to comply with a collection of information if it does not display a currently valid OMB control number. **PLEASE DO NOT RETURN YOUR FORM TO THE ABOVE ADDRESS.**

1. REPORT DATE *(DD-MM-YY)*	2. REPORT TYPE	3. DATES COVERED *(From - To)*
March 2001	Final	09/18/1995 – 09/28/2000

4. TITLE AND SUBTITLE
ADVANCED LASER DIAGNOSTIC APPLICATIONS
Volume 3 of 3 (Pages 694 – 1233)

5a. CONTRACT NUMBER
F33615-95-C-2507

5b. GRANT NUMBER

5c. PROGRAM ELEMENT NUMBER
62203F

6. AUTHOR(S)
Larry P. Goss, Ph.D.

5d. PROJECT NUMBER
3048

5e. TASK NUMBER
04

5f. WORK UNIT NUMBER
AI

7. PERFORMING ORGANIZATION NAME(S) AND ADDRESS(ES)
Innovative Scientific Solutions, Inc.
2766 Indian Ripple Road
Dayton, OH 45440-3638

8. PERFORMING ORGANIZATION REPORT NUMBER
2507 Final

9. SPONSORING/MONITORING AGENCY NAME(S) AND ADDRESS(ES)
Propulsion Directorate
Air Force Research Laboratory
Air Force Materiel Command
Wright-Patterson Air Force Base, OH 45433-7251

10. SPONSORING/MONITORING AGENCY ACRONYM(S)
AFRL/PRTS

11. SPONSORING/MONITORING AGENCY REPORT NUMBER(S)
AFRL-PR-WP-TP-2002-200, V3

12. DISTRIBUTION/AVAILABILITY STATEMENT
Approved for public release; distribution is unlimited.

13. SUPPLEMENTARY NOTES
This is Volume 3 of 3. See also AFRL-PR-WP-TP-2002-200, V1 and AFRL-PR-WP-TP-2002-200, V2. Report contains color. Report is comprised of numerous publications, such as journal articles and conference papers.

14. ABSTRACT

Reported are results of experimental and numerical investigations on gas turbine combustion and fuel processes, including: 1) Development, evaluation, and utilization of advanced laser diagnostic and analytical techniques for studying combustion and fuel processes important to current and future military aircraft; 2) Determination of cause and investigation of schemes to eliminate combustion and thermal-stability-related problems resulting from change from JP-4 to JP-8 fuel; 3) Proposal and evaluation of advanced combustor concepts and design characteristics to optimize tradeoffs in performance, visual observables, durability, and pollutants; 4) Investigation of methods for reducing emissions of carbon monoxide, hydrocarbons, oxides of nitrogen, and smoke in current and future gas turbine combustors; 5) Design and completion of experiments for establishing a database for developing and evaluating combustor and fuel-system-component design models; 6) Development of computational-fluid-dynamics (CFD) models for gas turbine combustor and fuel-system-component design; 7) Evaluation of additive sand advanced thermally stable fuels that provide thermal stability up to 900 °F; 8) Evaluation of thermally stable and environmentally safe anti-icing additives for JP-8 and JP-900 fuels; 9) Investigation of methods of using fuel to cool hot engine components and determination of impact of fuel phase change on combustion, and 10) Investigation of new military and commercial applications for combustion and fuels technology developed in this program, including high-cycle fatigue and aging aircraft.

15. SUBJECT TERMS
Advanced laser diagnostics, fuel thermal stability, computational fluid dynamics with chemistry, vortex-flame interactions, pulse-detonation engines, trapped-vortex combustor, fuel additives, spray combustion

16. SECURITY CLASSIFICATION OF:			17. LIMITATION OF ABSTRACT:	18. NUMBER OF PAGES	19a. NAME OF RESPONSIBLE PERSON (Monitor)
a. REPORT	b. ABSTRACT	c. THIS PAGE			Vincent M. Belovich, Ph.D.
Unclassified	Unclassified	Unclassified	SAR	548	19b. TELEPHONE NUMBER *(Include Area Code)* (937) 255-4229

TABLE OF CONTENTS

Section		Page
1	INTRODUCTION	1
2	DIAGNOSTIC AND ANALYTICAL INSTRUMENTATION DEVELOPMENT	2
	2.1 COMBUSTION DIAGNOSTICS	2
	2.1.1 Overview	2
	2.1.2 Two-Dimensional Flow-Visualization Technique	2
	2.1.3 Three-Dimensional Flow-Visualization Technique	35
	2.1.4 Ultrafast-Imaging Technique	56
	2.1.5 Phase-Sensitive-Imaging Technique	71
	2.1.6 Particle-Image-Velocimetry Technique	83
	2.1.7 Pressure-Sensitive-Paint Technique	136
	2.2 FUEL DIAGNOSTICS	179
	2.2.1 Overview	179
	2.2.2 Particle-Sizing, Oxygen-Concentration, and Mass-Deposition Methods	179
	2.2.3 Picosecond Pump/Probe Diagnostics	196
	2.2.4 Spectroscopic Techniques	213
3	DIAGNOSTIC APPLICATIONS	218
	3.1 COMBUSTION STUDIES	218
	3.1.1 Overview	218
	3.1.2 Fundamental Combustion Studies	218
	3.1.2.1 Jet Diffusion Flames	218
	3.1.2.2 Counterflow Diffusion Flames	284
	3.1.3 Large-Scale Combustion Studies	369
	3.1.3.1 Trapped-Vortex Combustor	369
	3.1.3.2 Lean Blowout and Emission	416
	3.1.3.3 Combustor Design Trends	542
	3.1.3.4 Active Combustion Control	571
	3.1.3.5 Pulse Detonation Engines	623

TABLE OF CONTENTS (CONTINUED)

Section		Page
	3.2 FUEL STUDIES	644
	3.2.1 Overview	644
	3.2.2 Fuel Thermal Stability	644
	3.2.2.1 Autoxidation of Jet-A Fuels	644
	3.2.2.2 Kinetics	656
	3.2.2.3 Fuel Blends	657
	3.2.2.4 Fuel Recirculation	658
	3.2.2.5 Fuel Pyrolysis	666
	3.2.2.6 Lubricants	671
	3.2.3 Effect of Additives on Fuel Thermal Stability	676
	3.2.4 Icing Inhibitors	689
4	MODEL DEVELOPMENT	694
	4.1 COMBUSTION MODELING	694
	4.1.1 Overview	694
	4.1.2 Jet Diffusion Flames	694
	4.1.3 Opposing-Jet Diffusion Flames	913
	4.1.4 Trapped-Vortex Combustor	941
	4.1.5 Pulse Detonation Waves	981
	4.1.6 Droplet and Two-Phase Flows	986
	4.2 MODELING OF FUEL THERMAL STABILITY	1132
	4.2.1 Overview	1132
	4.2.2 Fuel Thermal Stability	1132
	APPENDIX: Presentations, Publications, and Patents	1196

4. MODEL DEVELOPMENT

4.1 COMBUSTION MODELING

4.1.1 Overview

The combustion phenomenon results from the interaction of convective and molecular diffusion of many species and from simultaneous chemical reactions among several species on small length scales. Mathematically, these interactions are described on the basis of balance equations for continuity, momentum, energy, and species mass-fraction and chemical reactions (law of mass action). Most reacting flows in practical combustors are dynamic in nature, having vortical structures ranging from Kolmogorav scale (~ 10-4 mm) through very large scales on the order of the combustor scales (~ 102 mm). Because of the enormous requirement for computer resources to simulate the turbulent motion associated with all of the length scales in a combustor, a concerted effort is being made to develop an effective turbulence model. However, such a model can be achieved only through a thorough understanding of laminar flames and the events that occur in turbulent flames. To assist the Air Force in developing a time-dependent combustor design model, ISSI has developed a series of CFDC codes. These codes have been used to aid the understanding of the fundamental processes involved in combustion and to evaluate advanced combustor concepts. The results of this effort are discussed below.

4.1.2 Jet Diffusion Flames

A study was conducted on the local extinction of a laminar, methane jet diffusion flame caused by an artificial vortex that issues radially from either the fuel-jet core or ambient air toward the flame zone. The results are reported in the paper entitled " Numerical Experiments on the Local Extinction of Jet Diffusion Flames" (see pp. 696-704). Unsteady chemical-kinetic effects on the dynamics of local flame extinction are discussed in the publication entitled "Unsteady Extinction Mechanisms of Diffusion Flames" (see pp. 705-714). In the paper entitled "A Numerical Investigation of the Stabilizing Mechanism of Methane Jet Diffusion Flames" (see pp. 715-722), a numerical study of the detailed structure of the stabilizing region of methane jet flames is discussed. An axisymmetric, time-dependent CFDC code and different detailed-chemical-kinetics models were employed for accurate prediction of the dynamics of methane laminar and transitional jet flames; the results are documented in the paper entitled "Simulation of Dynamic Methane Jet Diffusion Flame Using Finite-Rate Chemistry Model" (see pp. 723-733). The results of an experimental and numerical investigation conducted to understand the local quenching process associated with vortex-flame interactions in a methane flame are discussed in the publication entitled "Local Extinction in an Unsteady Methane-Air Jet Diffusion Flame" (see pp. 734-742). Computations employing a time-dependent, implicit, third-order-accurate numerical model, including semidetailed chemical kinetics and buoyancy effects, were used to reveal the detailed structures of vertical jet diffusion flames and flat-plate burner flames; details of this study are reported in the paper entitled, "Attachment Mechanisms of Diffusion Flames" (see pp. 743-752). In the publication entitled "Simulation of Dynamic Methane Jet Diffusion Flames Using

Finite Rate Chemistry Models" (see pp. 753-763), a comparison is made of numerical and experimental data for a steady-state flame and two dynamic flames that are dominated by buoyancy-driven instabilities. The detailed structure of the stabilizing region of an axisymmetric laminar methane jet diffusion flame was studied numerically, and the results are reported in the paper entitled "A Role of Chemical Kinetics in the Simulation of the Reaction Kernel of Methane Jet Diffusion Flames" (see pp. 764-771). A detailed numerical study was conducted to characterize the effect of buoyancy on the structure of two-dimensional, partially premixed methane-air flames, and the results are documented in the publication entitled "Gravity Effects on Steady Two-Dimensional Partially Premixed Methane-Air Flames" (see pp. 772-788). The paper entitled "Stability-Limit Predictions of Methane Jet Diffusion Flames" (see pp. 789-797) documents an attempt to predict the lifting limit of an axisymetric, laminar, methane jet diffusion flame using a time-dependent full Navier-Stokes model with buoyancy. The use of visualizations in the development and evaluation of a reacting-flow-simulation model known as UNICORN (UNsteady Ignition and COmbustion with ReactioNs) is documented in the paper entitled "Role of Flow Visualization in the Development of UNICORN" (see pp. 798-813). The detailed structure of the stabilizing region of an axisymmetric laminar methane jet diffusion flame was studied numerically by solving the time-dependent full Navier-Stokes equations with buoyancy; the paper entitled "Chemical Kinetic Structure of the Reaction Kernel of Methane Jet Diffusion Flames" (see pp. 814-850) discusses the results. Steady, two-dimensional, partially premixed slot-burner flames established by introducing a rich fuel-air mixture from the inner slot and air from the outer slots were investigated experimentally and numerically; the results are documented in the paper entitled "An Experimental and Numerical Investigation of the Structure of Steady Two-Dimensional Partially Premixed Methane-Air Flames" (see pp. 851-858). In the publication entitled "A Reaction Kernel Hypothesis for the Stability Limit of Methane Jet Diffusion Flames" (see pp. 859-882), the successful prediction of the lifting limit of an axisymmetric, laminar, co-flow, methane-air jet diffusion flame under normal earth gravity is described. The structure of a laminar methane diffusion flame formed along a porous-plate burner in a vertically upward combustion tunnel was studied numerically and experimentally, and the results are reported in the paper entitled "A Numerical and Experimental Study of the Structure of a Diffusion Flame Established in a Laminar Boundary Layer Along a Vertical Porous Plate" (see pp. 883-890). An idealized boiler that was specifically designed to facilitate experimental and numerical investigations is discussed in the paper entitled "Experimental and Numerical Investigation of Structures of Two-Dimensional Partially Premixed Methane-Air Flames" (see pp. 891-912).

AIAA 96-0521
Numerical Experiments on the Local Extinction of Jet Diffusion Flames

F. Takahashi
University of Dayton
Dayton, Ohio

V. R. Katta
Innovative Scientific Solutions, Inc.
Dayton, Ohio

34th Aerospace Sciences Meeting & Exhibit
January 15-18, 1996 / Reno, NV

For permission to copy or republish, contact the American Institute of Aeronautics and Astronautics 370 L'Enfant Promenade, S.W., Washington, D.C. 20024

NUMERICAL EXPERIMENTS ON THE LOCAL EXTINCTION OF JET DIFFUSION FLAMES

Fumiaki Takahashi*
University of Dayton, Dayton, Ohio

Viswanath R. Katta†
Innovative Scientific Solutions, Inc., Dayton, Ohio

Abstract

Local extinction of a laminar methane jet diffusion flame caused by an artificial vortex that issues radially from either fuel-jet core or ambient air toward the flame zone has been studied numerically. The simulations were motivated by experimental observations of naturally-forming internal and external shear-generated vortices. A time-dependent, axisymmetric, implicit, third-order accurate numerical model is used with variable transport properties and detailed chemical-kinetic mechanisms. A packet of jet fluid or air is ejected outward or inward, respectively, as a single-pulsed side jet at given ejection velocity and period. A vortex system with a pair of counter-rotating toroidal vortex rings is formed and penetrated into the high-temperature viscous layer. If Peclet number for mass transfer (Pe: a ratio of the characteristic diffusion time to convection time) is small, the flame zone deformed without extinction; if Pe is large, the vortex cuts through the high-temperature layer with a minimal flame movement, thus, locally extinguishing the flame. For both outward and inward vortices, the unsteady effect on the local extinction is largely attributable to an excess diffusive influx of methane, which scavenges a radical (OH, H, and O) pool on the air side of the peak temperature.

INTRODUCTION

Flame extinction phenomena have long been studied predominantly in steady laminar counterflow diffusion flames [1, 2] since a pioneering work by Tsuji and Yamaoka [3]. Stretch-induced flame extinction occurs as a result of reduced Damkhöler number (i.e., a ratio of characteristic flow [or diffusion] time to reaction time) and subsequent decrease in the flame temperature and reaction rates. Although the phenomenon has been understood well in a global sense for simple flow configurations, there exist some aspects of the subject which need further investigation. Complexities in practical turbulent flames stem from three-dimensional, transient, turbulence-flame interactions including the effects of unsteadiness, flame curvature, and chemical kinetics. The investigations of unsteadiness and curvature effects on diffusion flame extinction have received a growing attention in recent years [4-8].

In a jet diffusion flame, extinction occurs locally near the laminar-to-turbulent flame transition point as the fuel jet velocity is increased [9-13]. The vortex-flame interactions are responsible for the local extinction. A series of recent experiments [14-17] in methane jet diffusion flames using a variety of laser diagnostic techniques has revealed essential features of vortex-flame interactions, which lead to local extinction. The local extinction occurs in the near-jet region when the internal large-scale vortex rapidly reaches the flame zone location or the external vortex accelerates the entrainment flow passing through the flame zone [17].

A recent development of numerical codes for studying various aspects of transient behaviors of flames [18-20] has enabled us to simulate more challenging numerical experiments with sufficiently high accuracy. In the previous paper [21], the physical aspect of vortex-flame interactions were studied by assuming infinitely-fast one-step chemical kinetics and unity Lewis number. An attempt was made to simulate the transient response of a laminar flame zone to an artificial vortex that issues from a side jet. Although the fluid-dynamic and transport phenomena of vortex-flame interactions have been successfully simulated,

* Research Engineer, Research Institute, Senior Member AIAA
† Senior Research Engineer, Member AIAA

Copyright © 1996 by the Authors. Published by the American Institute of Aeronautics and Astronautics, Inc. with permission.

the fast chemistry model inhibited to investigate further the chemical aspect of local extinction phenomena. In this work, a detailed chemical kinetic model is incorporated in the code, and the first numerical experiments have been conducted on the local extinction of jet diffusion flames caused by an artificial vortex that issues from the fuel-jet core or ambient air. The primary objective of this study is to reveal physical and chemical aspects of the transient interactions between a laminar diffusion flame and a vortex and elucidate local extinction mechanisms.

NUMERICAL MODELS

The laminar diffusion flame considered in this paper is formed between a central methane jet and a concentric annulus air flow. Time-dependent governing equations, expressed in cylindrical coordinates, consist of mass continuity, axial and radial momentum conservation, energy conservation, and species conservation equations with the equation of state [19]. Body-force term caused by the gravitational field is included in the axial momentum equation. A detailed chemical-kinetic model [22], including 52 elementary steps for 17 species, is used to describe CH_4-O_2 combustion. Transport properties are considered to vary with temperature and species concentrations. Enthalpy of each species is calculated from polynomial curve-fits while the viscosity of the individual species is estimated from Chapman-Enskog collision theory [23]. The binary diffusion coefficient between any two species on the fuel side of the flame is assumed to be identically equal to that of the fuel and nitrogen. Similarly, on the oxidizer side of the flame, it is made identical to that of the oxygen and nitrogen. The Chapman-Enskog theory and the Lennard-Jones potentials [23] have been used to estimate these two binary diffusion coefficients.

The finite-difference form of the governing equations is constructed on a staggered grid system based on an implicit QUICKEST numerical scheme. It is third-order accurate in both space and time and has a very low numerical diffusion error. At every time-step, the pressure field is accurately calculated by solving the system of algebraic pressure Poisson equations simultaneously. An orthogonal grid system with rapidly expanding cell sizes in both axial (z) and radial (r) directions is utilized. The computational domain of 150 × 60 mm in z and r directions, respectively, is represented by a mesh system of 241 × 71. The inner diameter of the fuel tube (d = 9.6 mm) is close to that used in the experiments [14]. Grid lines are clustered near the burner lip and side jet locations. The outer boundaries of the computational domain are shifted sufficiently far enough to minimize the propagation of disturbances into the region of interest.

The initial and boundary conditions for the axial (U) and radial (V) velocities and species and energy at different flow boundaries are similar to the previous work [21] except for the increased number of species in the present calculations. The fully-developed pipe flow and boundary layer velocity profiles are used at the exits of the fuel tube and the annulus air channel, respectively. Along the burner-lip walls, no-slip boundary conditions are enforced. An extrapolation procedure with weighted zero- and first-order terms is used to estimate the flow variables on the outflow boundary. During the calculations, radial side jets are introduced from different locations in the flow field.

TEST CONDITIONS

The test cases reported in this paper are listed in Table 1. Cases 1 and 2 represents a laminar jet diffusion flame with low velocities of the primary jet (U_j), annulus air (U_a), and side jet (V_S) and a long pulse width (t_S). At the grid points within the side jet, the radial component of the local velocity is replaced by V_S and the scalar variables are maintained at the local values for a time period of t_S. The primary jet has a parabolic velocity distribution, representing the fully-developed laminar pipe flow. The radial location of the side jet ($r_S = d/2$) is nearly coincident with a dividing streamline between the jet and external fluids. The height of the side jet is chosen near the jet exit such that the flame zone interacts with the vortex intensely because of the flame proximity to the jet-fluid core. Case 3 represents a flame with higher velocities of the primary jet, annulus air, and side jet and a shorter pulse width in consideration of a naturally-forming radial mass ejection observed in turbulent flames [11, 14, 15]. In the turbulent methane jet diffusion flame stabilized on a thick burner lip, the local flame extinction occurred at the mean primary jet velocity of ~15 m/s [11]. Although the maximum radial velocity component (the mean plus three times the root mean square fluctuation) observed under such a condition was ~7 m/s [14], higher values of V_S were used for cases 2 and 3 to simulate extinction. Case 4 represents a condition where a vortex is ejected inward from outside the flame ($V_S < 0$). Although this condition is motivated by the experimental observations [17] of local extinction caused by an external vortex, the nature of the side jet in this study is different from the naturally forming vortices. For

cases 3 and 4, the velocity distribution of the primary jet is given by using the empirical equation of the 1/n-th-power law [24] for the fully-developed turbulent pipe flow with the exponent n=6 for a moderate Reynolds number (although the simulation considers laminar flows only).

A Peclet number for mass transfer defined previously [21] is

$$Pe = \tau_d / \tau_m = \delta_d V_m / D \qquad (1)$$

where τ_d: the characteristic diffusion time, τ_m: the characteristic convection time for vortex motion, δ_d: the diffusive transport layer thickness, V_m: the radial mass ejection velocity, and D: diffusion coefficient. The values of Pe determined by substituting $(r_f - r_s)$ at $t = 0$ for δ_d and V_s for V_m, for cases 1 through 4 are listed in Table 1.

RESULTS AND DISCUSSION

A steady-state solution for the diffusion flame structure without a side jet was obtained first by numerous (typically several tens of thousand times) iterative calculations using a long time step. By using the steady-state solution as the initial condition, the temporal changes in the flame structure in response to the side-jet ejection were calculated using a short time step. Figure 1 shows color-coded mappings of the calculated gas temperature (T), superimposed with locations of tracer particles (black dots) injected in front of the side jet (left-hand side), and the methane mole fraction, superimposed with velocity vectors (right-hand side) for various cases. The radial locations of the flame zone (yellow dots) determined by the temperature peak are also included in the figures.

Figures 1a is a steady-state solution under the low velocity condition for cases 1 and 2. The flame zone is formed on the air side (r = 6.8 mm at z = 20 mm) of the dividing streamline (r = 4.8 mm) which nearly coincides with a yellow band ($X_{CH4} \approx 0.4$) in the methane mole fraction mapping. Methane molecules diffuse radially in the diffusive transport layer between the dividing streamline and the flame zone. The flame zone is inclined outward downstream and the streamlines are almost parallel to the jet axis near the flame zone, and thus, the external fluid passes through the flame zone with a narrow angle into the methane diffusion layer. Oxygen diffuses inward from the external air. If the reaction rate is finite, oxygen can leak through the flame zone ($X_{O2} \neq 0$) and thus, a convective transport of oxygen contributes to the oxygen influx. The thermal layer near the flame zone (between cyan bands in the temperature mapping) is relatively thick (~6 mm at z =20 mm). For the steady-state solution for the high-velocity condition (not shown) for cases 3 and 4, the thermal layer is thinner (~ 4.4 mm at z = 20 mm).

Figures 1b through 1e show selected results of the internal side jet ejection for cases 1 through 3. The tracer particles were injected in front of the side jet (at r = 4.9 mm) over the axial distance of 4 mm at every time step. Notice that the elapse time after ejection (t) is an order of magnitude longer for cases 1 and 2 (t = 2.13 ms) than case 3 (t = 0.293 ms). Despite the difference in the magnitude of side-jet velocity and, in turn, the time scale of the process, the two cases show the following common features in the flame structures, because the vortex system formed dominates the global flow structure.

As a jet-fluid packet issues from the side jet in the jet-fluid core toward the flame surface, a sudden change in the radial-velocity distribution near the edges of the side jet induces the roll-up of fluid and the subsequent formation of a vortex system composed of a pair of counter-rotating vortex rings. The vortex system grows as it engulfs surrounding gases and penetrates into a high-temperature (highly viscous) layer toward the flame surface. The vortex structure rotates as a whole naturally because of the uneven axial-velocity distribution in the shear layer, especially for case 3 because of its higher velocity gradient. The formation of the vortex structure with counter-rotating vortex rings and the subsequent "solid-body" rotation have been observed experimentally [16].

For case 1 (Fig. 1b), the flame zone bulges out as the vortex system moves toward the flame as the whole process occurs in one order of magnitude longer time than case 3. However, the vortex loses its radial momentum without causing flame extinction and drift away downstream. By contrast, in case 2, the vortex further pushes out the flame zone (Fig. 1c) until local extinction occur at the leading edge of the bulged flame zone (Fig. 1d). For case 3 (the highest Pe), local extinction occurred as the vortex rapidly cuts through the thermal layer (Fig. 1e). Consequently, the thermal layer ahead of the vortex becomes significantly thin as the leading edge of the vortex reaches the initial flame surface location. Figure 1e shows large values of the methane mole fraction in the vortex system.

Figure 1f shows the results for the inwardly injected external vortex. Although the magnitude of the side jet velocity is small (4 m/s), local extinction occurs in a very short time (~0.2 ms). Since the calculation is axisymmetric, the vortex may accelerate as its radial location decreases. Moreover, the jet-fluid boundary would not deform as the vortex pushes

inward because of the high velocity fuel jet. Unlike the flame bulge for cases 1 and 2, the thermal layer cannot be deformed inward; thus, the diffusive layer becomes very thin as the vortex approaches the jet-fluid boundary.

Figure 2 shows the radial distributions of the axial and radial velocity components along the vortex axis with the elapse time as a parameter. Large disturbances in both components are generated by the formation and movement of the vortex. For cases 2 and 3 (Figs. 2a and 2b), the negative axial velocity region is created because of the solid-body rotation of the vortex. For case 4, the deviation from the steady-state solution is small compared to case 3.

Figure 3 shows the radial distributions of the gas temperature and species mole fractions for steady-state solutions. For both low (Fig. 3a) and high (Fig. 3b) velocity conditions, the peak temperature reached a little over 2000K. The range of the abscissa is adjusted in the figures because of the reduction in the thermal layer thickness for the high velocity case as mentioned before. The variations in the mole fractions of major and minor species show typical diffusion flame structure with X_{H2O} and X_{CO2} peaks coincide with the temperature peak, X_{CO}, X_{H2}, and X_{CH3} peaks on the fuel side, and X_{OH}, X_H, and X_O peaks on the air side. The overlapped distributions between X_{CH4} and X_{O2} as well as the fuel-side and air-side radicals are more evident for the high speed condition, indicating a more strained condition. Figure 3c is a replot of the results for both conditions using mixture fraction. The distributions of T and X_i 's are fairly coincident between the different conditions.

Figure 4 shows the results after the side jet ejection for case 3. The height is chosen to nearly coincide with the height of local extinction (z = 16 mm). At an early stage (cf. Figs. 3b and 4a), the thermo-diffusive layer near the flame zone becomes thin, the peak temperature decreased to ~1800 K, and the overlapping between X_{CH4} and X_{O2} as well as the fuel-side and air-side radicals are more evident. As a result of large methane concentration gradient (and, in turn, flux) in front of the leading edge of the vortex, a wave of methane proceed outward (compare the relative location of X_{CH4} and the temperature peak in Fig. 4b). Then, the peak temperature and the radical pool concentration (X_{OH}, X_H, and X_O) start to decrease. Methane (and methyl radical) might scavenge the radical pool important for chain-branching reactions. At the very last stage (Fig. 4c), the high-flux methane wave reached the temperature and radical pool peak locations ($X_{CH4} \approx 0.1$ at the temperature peak). Thus, the combustion process can no longer be sustained under such condition, thereby leading to extinction.

Figure 5 shows the results for the inward side jet ejection for case 4. Although the magnitude of V_s is smaller than other cases for outward ejection, the vortex-flame interaction proceeds more rapidly. Unlike ambient air, inward motion is limited by the boundary of jet fluid which is moving at high velocities. Thus, if the vortex penetrate into the thermal layer from outside, the flame zone is pushed toward the jet fluid boundary and lose its mobility. Consequently the diffusive transport layer becomes extremely thin, resulting in a high methane concentration gradient (see Fig. 5c) and the local extinction similar to outward ejection occur.

CONCLUSIONS

A unique numerical experiment, in which a packet of jet fluid or air ejected outward or inward, respectively, toward a flame zone, has illustrated essential physico-chemical processes of the vortex-flame interactions and local extinction of laminar diffusion flames. If a Peclet number is small (the order of ten or less), the vortex system pushes out the flame surface over the majority of the interaction period. If Pe is large (the order of hundred), the vortex system penetrates into the high-temperature (highly viscous) layer with a slight flame movement, leading local flame extinction. Unsteady extinction process is attributed to an excess flux of methane which purges a radical pool and halt combustion reactions.

ACKNOWLEDGMENTS

This work was supported by the U.S. Air Force, Wright Laboratory, Aero Propulsion and Power Directorate, Fuels and Lubrication Division, Wright-Patterson Air Force Base, Ohio, under Contract No. F33615-92-C-2207 (Technical Monitor: C. W. Frayne).

REFERENCES

1. Tsuji, H., *Progress in Energy and Combustion Science* 8, 93-119 (1982).
2. Law, C. K., *Progress in Energy and Combustion Science* 10, 295-318 (1984).
3. Tsuji, H., and Yamaoka, I., *Twelveth Symposium (International) on Combustion*, The Combustion Institute, Pittsburgh, 1966, pp. 979-984.
4. Tsuji, H., Yoshida, A., and Endo, N., *Twenty-Fifth Symposium (International) on Combustion*, The

Combustion Institute, Pittsburgh, 1994, pp. 1191-1197.
5. Egolfopoulos, F. N., *Twenty-Fifth Symposium (International) on Combustion*, The Combustion Institute, Pittsburgh, 1994, pp. 1375-1381.
6. Im, H. G., Bechtold, and Law, C. K., AIAA Paper 95-0128, 1995.
7. Sung, C. J., Liu, J. B., and Law, C. K., *Combustion and Flame* 102, 481-492 (1995).
8. Cuenot, B., and Poinsot, T., *Twenty-Fifth Symposium (International) on Combustion*, The Combustion Institute, 1994, pp. 1383-1390.
9. Takeno, T., and Kotani, Y., *Acta Astronaut.* 2, 999 (1975).
10. Takahashi, F., Mizomoto, M., and Ikai, S., *Combust. Flame* 48, 85 (1982).
11. Takahashi, F., and Schmoll, W. J., *Twenty-Third Symposium (International) on Combustion, The Combustion Institute*, 1991, p.677.
12. Shekarchi, S., Savas, Ö., and Gollahalli, S. R., *Combust. Flame* 73, 221 (1988).
13. Roquemore, W. M., Chen, L.-D., Goss, L. P., and Lynn, W. F., "The Structure of Jet Diffusion Flames," *Turbulent Reactive Flows* (R. Borghi and S. N. B. Murthy, Eds.), Springer-Verlag, 1993, p. 49.
14. Takahashi, F., and Goss, L. P., *Twenty-Fourth Symposium (International) on Combustion*, The Combustion Institute, Pittsburgh, 1992, pp. 351-359.
15. Takahashi, F., and Vangsness, M. D., "Near-Field CARS Measurements and the Local Extinction of Turbulent Jet Diffusion Flames," *Dynamics of Heterogeneous Combustion and Reacting Systems*, (A. L. Kuhl, J.-C. Leyer, A. A. Borisov, and W. A. Sirignano, Eds.), 1993, p. 37.
16. Hsu, K. Y., Chen, L. D., Katta, V. R., Goss, L. P., and Roquemore W.M., AIAA Paper No. 93-0455, 1993.
17. Takahashi, F., Schmoll, W. J., Trump, D. D., and Goss, L. P., AIAA Paper No. 95-0139, 1995.
18. Katta, V. R., and Roquemore, W. M., *Combust. Flame* 92, 274 (1993).
19. Katta, V. R., Goss, L. P., and Roquemore, W. M., *AIAA J.* 32, 84 (1994).
20. Katta, V. R., Goss, L. P., and Roquemore, W. M., *Combust. Flame* 96, 60 (1994).
21. Takahashi, F., and Katta, V. R., *J. Propulsion and Power* 11, 170 (1995).
22. Peters, N., "Flame Calculations with Reduced Mechanisms -- An Outline," *Reduced Kinetic Mechanisms for Applications in Combustion Systems* (N. Peters and Bernd Rogg Eds.) Springer-Verlag, Berlin, 1993, p. 3.
23. Hirschfelder, J. O., Curtis, C. F., and Bird, R. B., *The Molecular Theory of Gases and Liquids*, Wiley, New York, 1954.
24. Schlichting, H., *Boundary-Layer Theory* (Translated by J. Kestin), 7th ed., McGraw-Hill, New York, 1979, p. 599.

Table 1 Test Conditions

	Primary Jet		Annulus Air	Side Jet				
Case No.	U_j (m/s)	Velocity profile	U_a (m/s)	r_s (mm)	z_s (mm)	V_s (m/s)	t_s (ms)	Pe
1	1.5	Parabolic	1.5	4.8	14.2-16.5	7	0.5	100
2	1.5	Parabolic	1.5	4.8	14.2-16.5	14	0.5	220
3	15	1/6-th-power	3	4.8	14.2-16.5	20	0.06	260
4	15	1/6-th-power	3	9	14.2-16.5	-4	0.06	140

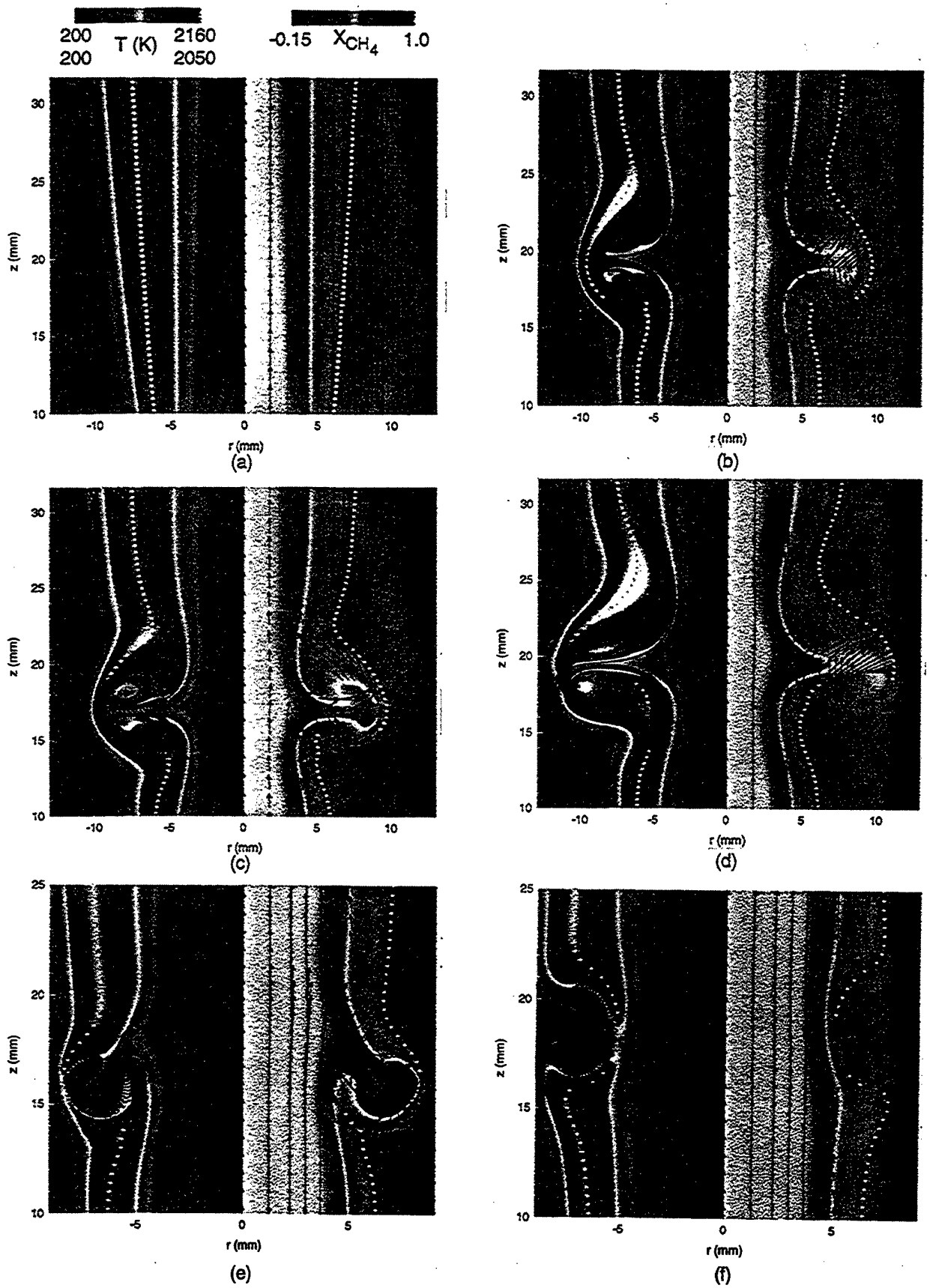

Fig. 1 Calculated temperature, methane mole fraction, and velocity vector fields with particles injected in front of the side jet. a) Steady-state solution (t = 0 s) for cases 1 and 2. b) Case 1, t = 2.13 ms. c) Case 2, t = 1.07 ms. d) Case 2, t = 2.13 ms. e) Case 3, t = 0.293 ms. f) Case 4, t = 0.293 ms.

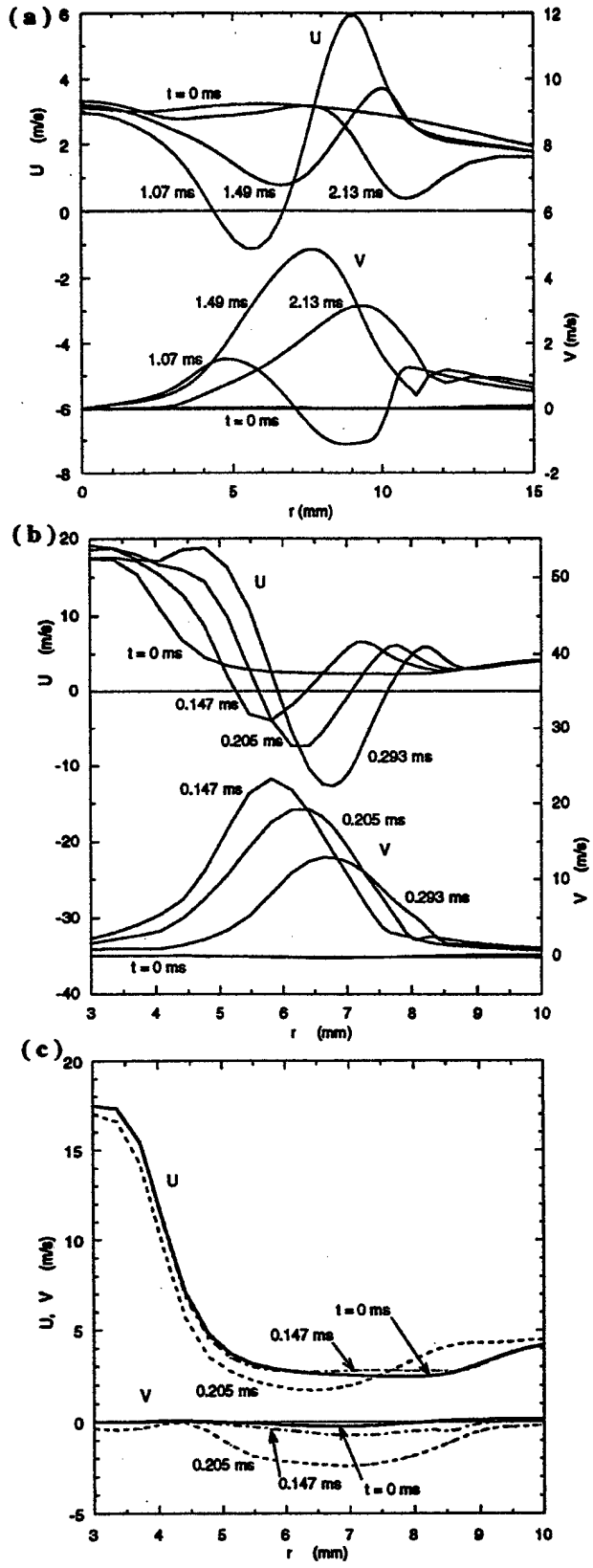

Fig. 2 Axial and radial velocity components across a methane jet flame with a side jet. a) Case 2, z = 18.5 mm. b) Case 3, z = 16 mm. c) Case 4, z = 18 mm.

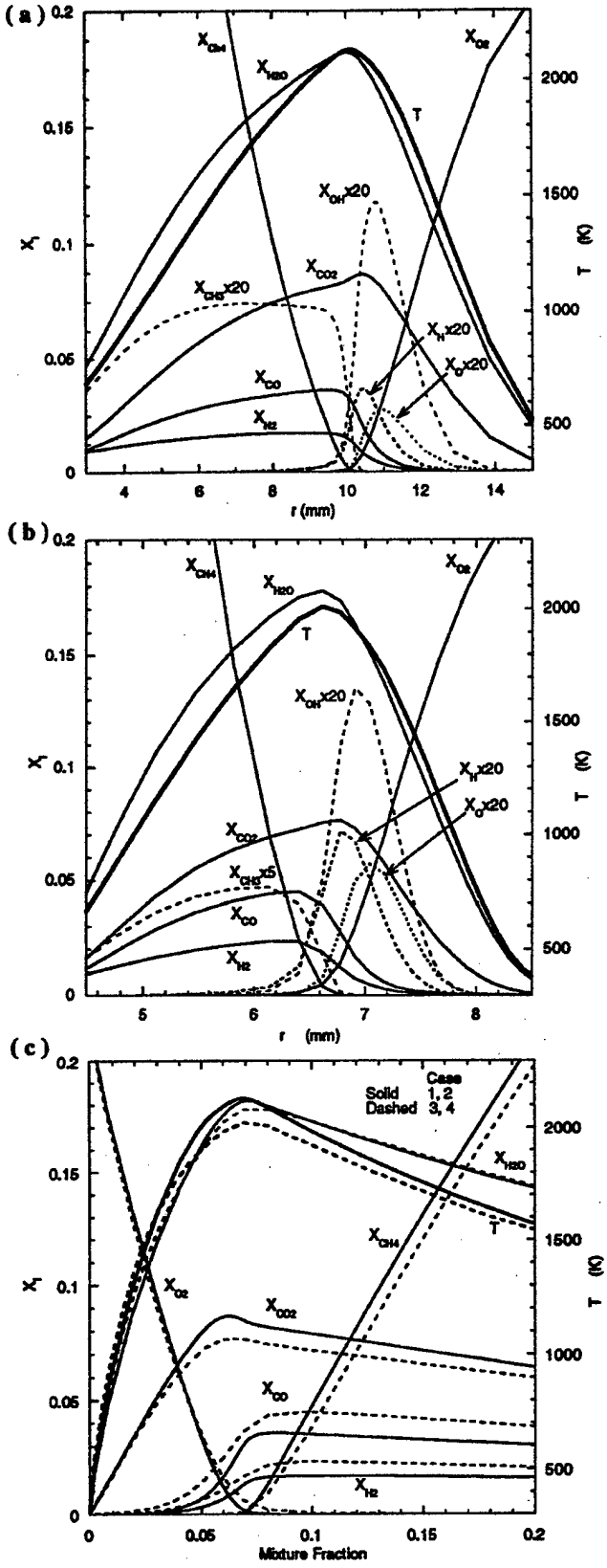

Fig. 3 Temperature and mole fractions across a methane jet flame (t = 0 s). a) Case 2, z = 18.5 mm. b) Cases 3, z = 16 mm. c) With mixture fraction.

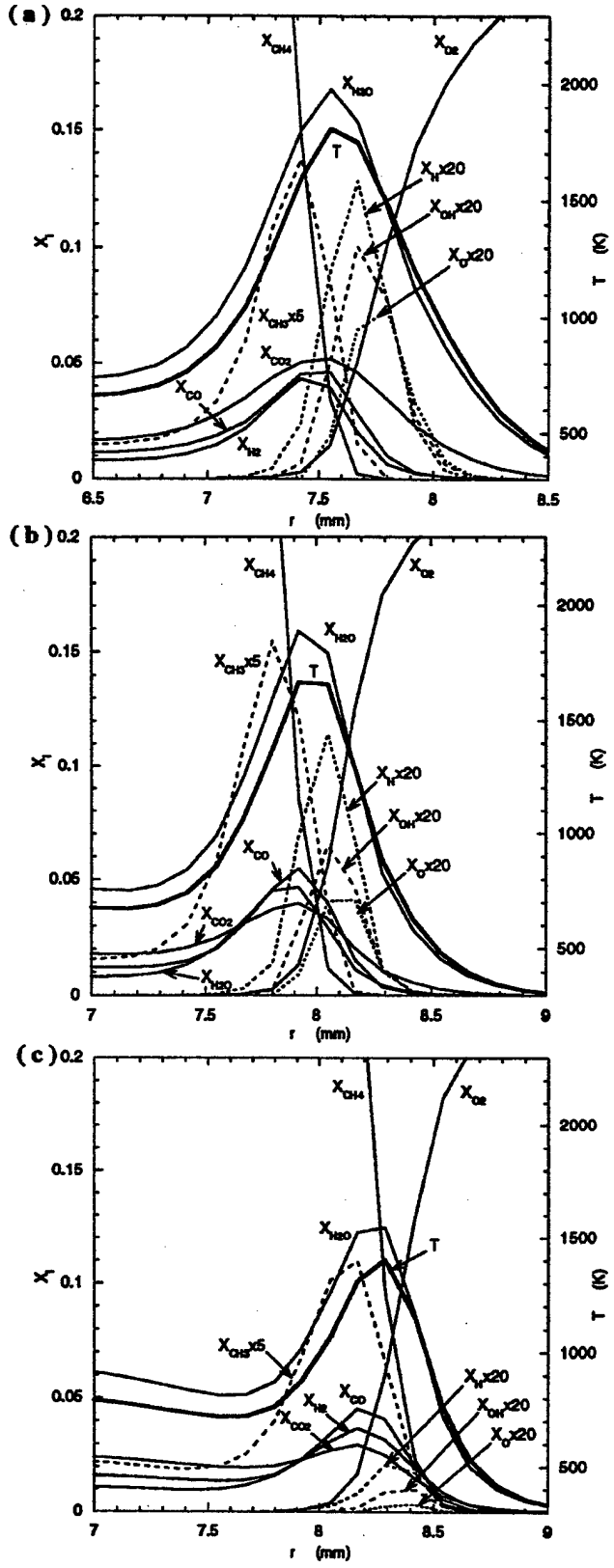

Fig. 4 Temperature and mole fractions across a methane jet flame with a side jet. Cases 3, z = 16 mm. a) t = 0.147 ms. b) t = 0.205 ms. c) t = 0.264 ms.

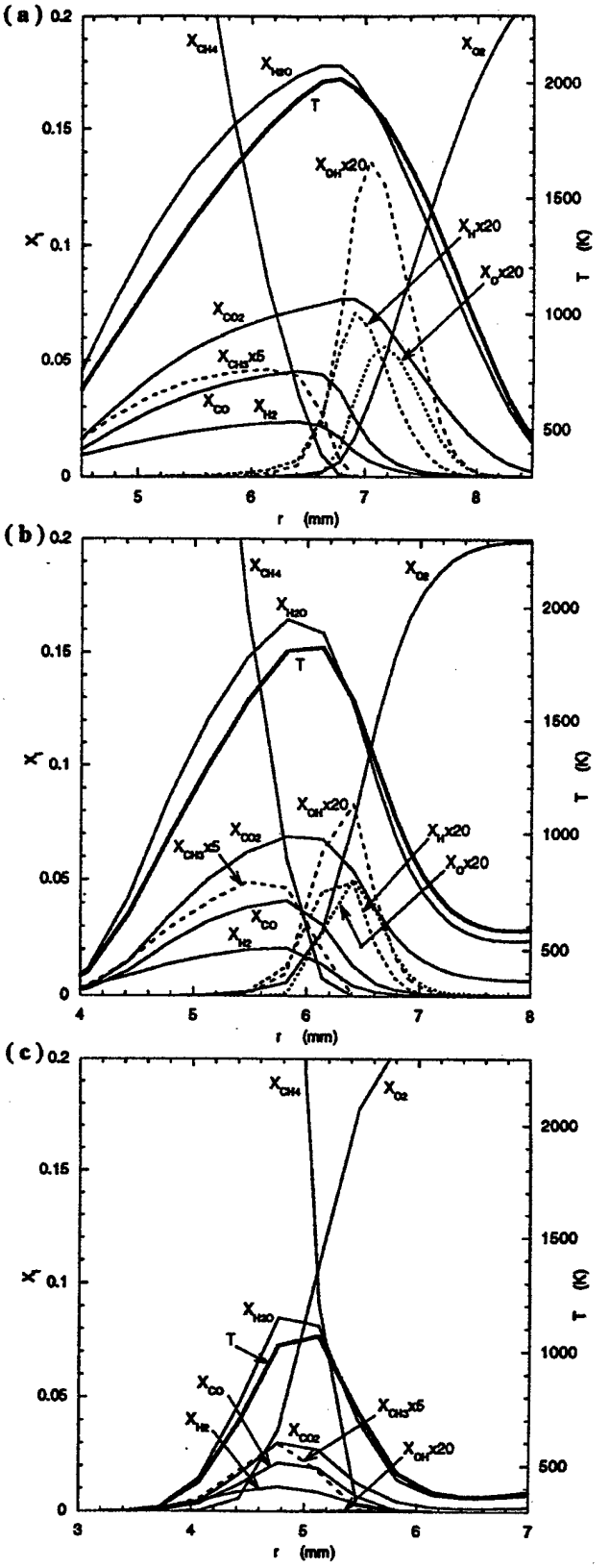

Fig. 5 Temperature and mole fractions across a methane jet flame with a side jet. Cases 4, z = 18 mm. a) t = 0.147 ms. b) t = 0.176 ms. c) t = 0.205 ms.

Twenty-Sixth Symposium (International) on Combustion/The Combustion Institute, 1996/pp. 1151–1160
PUBLISHED WITH PERMISSION

UNSTEADY EXTINCTION MECHANISMS OF DIFFUSION FLAMES

FUMIAKI TAKAHASHI
University of Dayton
Research Institute
300 College Park
Dayton, Ohio 45469, USA

VISWANATH R. KATTA
Innovative Scientific Solutions, Inc.
3845 Woodhurst Court
Dayton, Ohio 45430, USA

Unsteady chemical kinetic effects on the dynamics of local extinction of laminar methane jet diffusion flames have been studied by direct numerical simulations in which an artificial vortex issues radially from either fuel-jet core or ambient air toward the flame zone. The simulations were motivated by experimental observations of naturally forming internal and external shear-generated vortices that interfere with the flame zone. A time-dependent, axisymmetric, implicit, third-order accurate numerical model is used with variable transport properties and a semidetailed chemical kinetic model. A packet of fluid (with a local composition) is ejected outward or inward as a single-pulsed side jet at a given ejection velocity and period. A vortex system with a pair of counterrotating toroidal vortex rings is formed and penetrated into the high-temperature viscous layer. The unsteady vortex-flame interaction is divided into three sequential and overlapping regimes based on the controlling processes: diffusion, convection, and chemical kinetics. In the first two physical interaction regimes, the reaction and heat-release rates increase because of increased reactant fluxes by diffusion and convection. The detailed mechanisms of the final chemical-kinetic–controlled regime depend on whether the vortex is ejected from the fuel side or air side. The local extinction by the outward fuel-side vortex is largely attributable to excess fluxes of methane and methyl radicals, which scavenge a radical pool (OH, H, and O), thereby terminating chain reactions. The inward air-side vortex induces an excess oxygen flux primarily by convection, thereby accelerating the reactant leakage through the reaction zone and the temperature decrease.

Introduction

Extinction of diffusion flames has long been studied predominantly in steady laminar counterflow diffusion flames [1,2] since a pioneering work by Tsuji and Yamaoka [3]. Stretch-induced flame extinction occurs as a result of reduced Damkhöler number (i.e., the ratio of a characteristic flow [or diffusion] time to reaction time) and subsequent decrease in the flame temperature and reaction rates. Although the phenomenon is well understood in a global sense for its simple chemistry and flow configurations, various aspects of the subject need further investigation. The laminar flamelet model [4] assumes that turbulent diffusion flames are composed of ensembles of wrinkled, moving, laminar diffusion flame sheets and that sufficiently high strain rates (velocity gradients) cause local flamelet extinctions. Hence, questions arise as to how the structure of the laminar flamelets changes in response to local turbulent motions and whether the results obtained in steady (and stationary) counterflow diffusion flames are applicable to such flamelet extinction. Complexities in practical turbulent flames stem from three-dimensional, transient, turbulence–flame interactions including the effects of strain rate, unsteadiness, flame curvature, and chemical kinetics. Although some of these effects on diffusion flame extinction have received increased attention in recent years [5–9], little is known about unsteady chemical kinetic effects on the interactions between vortices and flame zone that eventually lead to local extinction.

As the fuel jet velocity is increased in a jet diffusion flame, local extinction occurs near the laminar-to-turbulent flame transition point as a result of vortex-flame interactions [10–14]. A series of recent experiments [15–18] in methane jet diffusion flames using a variety of laser diagnostic techniques revealed that local extinction occurred in two stages: physical and chemical interactions. The physical interaction is caused mainly by convective motions; that is, the internal large-scale vortex rapidly reaches

TABLE 1
Test conditions

Case No.	U_j (m/s)	U_a (m/s)	V_s (m/s)	t_s (ms)	Pe
1	1.5	1.5	7	0.5	100
2	1.5	1.5	14	0.5	220
3	15	3	20	0.06	260
4	15	3	−4	0.06	140

the flame zone location or the external vortex accelerates the entrainment flow passing through the flame zone [18]. The chemical interaction in the final stage is speculated [16] to be coupled with an excess fuel diffusion process but is largely unknown due to lack of knowledge of temporal variations in the concentrations of species, particularly radicals.

Recent development of numerical codes for studying various aspects of transient behaviors of flames [19–21] has enabled us to simulate more challenging numerical experiments with sufficiently high accuracy. The physical aspect of vortex-flame interactions were studied previously [22] by assuming infinitely fast one-step chemical kinetics and unity Lewis number. An attempt was made to simulate the transient response of a laminar flame zone to an artificial vortex that issues from a side jet. Although the fluid dynamic and transport phenomena of vortex-flame interactions have been simulated successfully, the fast chemistry model prohibited further investigation of the chemical aspect of local extinction phenomena. A semidetailed chemical kinetic model for methane combustion has recently been incorporated into the code and validated [23] using the experimental results of counterflow diffusion flames [8]. In this work, the first numerical experiments were conducted on the local extinction of diffusion flames caused by an artificial vortex that issues from the fuel-jet core or ambient air. The primary objectives of this study are (1) to reveal physical and chemical aspects of local extinction caused by vortex-flame interactions (particularly the effects of unsteadiness and chemical kinetics in nonstationary flames) and (2) to contribute to a better understanding and further development of laminar flamelet models for turbulent diffusion flames.

Numerical Models

Time-dependent governing equations, expressed in cylindrical coordinates, consist of mass continuity, axial and radial momentum conservation, energy conservation, and species conservation equations with the equation of state [20]. A body-force term caused by the gravitational field is included in the axial momentum equation. A semidetailed chemical kinetic model [24], including 52 elementary steps for 17 species (CH_4, O_2, CH_3, CH_2, CH, CH_2O, CHO, CO_2, CO, H_2, H, O, OH, H_2O, HO_2, H_2O_2, and N_2), is used to describe CH_4-O_2 combustion. Thermophysical and transport properties are considered to vary with temperature and species concentrations. Enthalpy of each species is calculated from polynomial curve fits, while the viscosity of the individual species is estimated from Chapman–Enskog collision theory [25]. The binary diffusion coefficient between any two species is estimated by the Chapman–Enskog theory and the Lennard–Jones potentials [25], and the effective diffusion coefficient of each species in the mixture is calculated.

The finite-difference form of the governing equations is constructed on a staggered grid system based on an implicit QUICKEST numerical scheme. It is third-order accurate in both space and time and has a very low numerical diffusion error. At every time step, the pressure field is accurately calculated by simultaneously solving the system of algebraic pressure Poisson equations. The computational domain of 150 × 60 mm in axial (z) and radial (r) directions, respectively, is represented by a mesh system of 241 × 71. The inner diameter of the fuel tube (d = 9.6 mm) is close to that used in the experiments [15]. Grid lines are clustered near the burner lip and side jet locations. The initial and boundary conditions for the axial and radial velocities and species and energy at different flow boundaries are similar to the previous work [22] except for the increased number of species in the present calculations.

The test cases reported in this paper are listed in Table 1. Cases 1 and 2 represent a laminar jet diffusion flame with low velocities of the primary jet (U_j) and annulus air (U_a). At the grid points within the side jet, the radial component of the local velocity is replaced by V_s and the scalar variables are maintained at the local values for a time period t_s. The primary jet has a parabolic velocity distribution, representing the fully developed laminar pipe flow. The radial location of the side jet ($r_s = d/2$) is nearly coincident with a dividing streamline between the jet and external fluids, and the height of the side jet is z = 14.2 ~ 16.5 mm. Case 3 represents a flame with higher jet velocities in consideration of a naturally forming radial mass ejection observed in turbulent flames [12,15,16]. Case 4 represents a condition in which a vortex is ejected inward from outside the flame ($V_s < 0$). For cases 3 and 4, the velocity distribution of the primary jet is given by using the empirical equation of the 1/nth power law [26] for the fully developed turbulent pipe flow with the exponent n = 6 for a moderate Reynolds number (although the simulation considers laminar flows only).

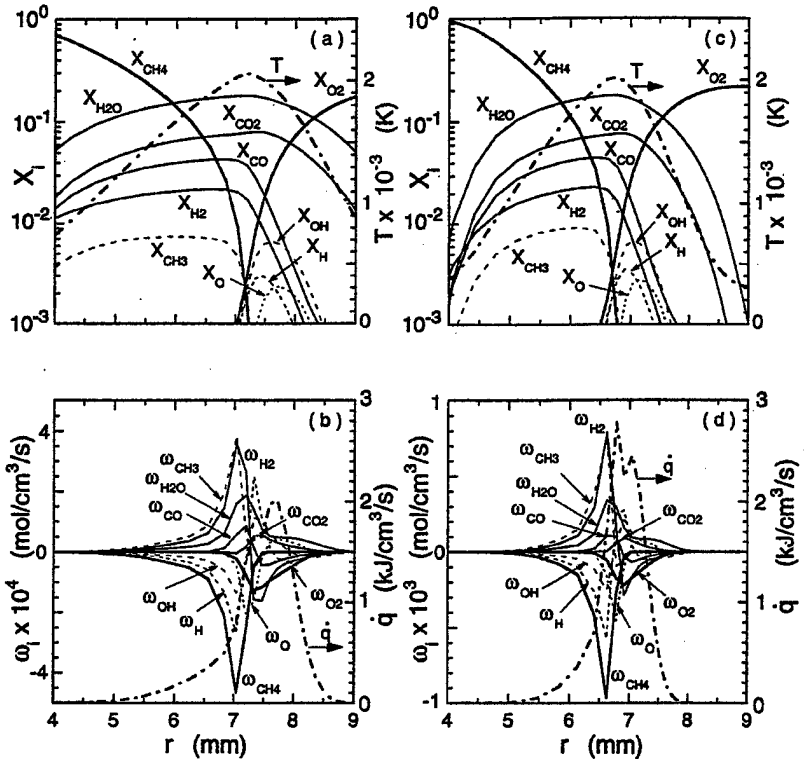

FIG. 1. Calculated temperature, mole fractions, molar production rates, and heat-release rate across a steady-state methane jet diffusion flame (t = 0 s); (a)(b) case 2, z = 18.5 mm; (c)(d) case 3, z = 16 mm.

A Peclet number for mass transfer related to the side jet ejection defined previously [22] is

$$Pe = \tau_d/\tau_m = \delta_d V_m/D \qquad (1)$$

where τ_d is the characteristic diffusion time, τ_m is the characteristic convection time for vortex motion, δ_d is the diffusive transport layer thickness, V_m is the radial mass ejection velocity, and D is the diffusion coefficient. The values of Pe determined by substituting $(r_f - r_s)$ at t = 0 for δ_d (r_f is the radial flame location) and V_s for V_m are listed in Table 1.

Results and Discussion

A steady-state solution for the diffusion flame structure without a side jet was obtained first by numerous (typically several tens of thousands) iterative calculations using a long time step. By using the steady-state solution as the initial condition, the temporal changes in the flame structure in response to the side jet ejection were calculated using a short time step. Figure 1 shows the radial distributions of the gas temperature (T), the mole fraction of species i (X_i), the net rate of molar production of species i (ω_i), and the net rate of heat release ($\dot{q}$) for steady-state solutions for the conditions of low velocities (case 2) and high velocities (case 3). In both cases, the flame structure is typical of laminar diffusion flames. The flame zone is formed on the air side of the dividing streamline ($r \approx 4.8$ mm). The variations in the mole fractions of major and minor species (see Figs. 1a and 1c) show that the temperature peak coincides with the X_{H_2O} peak in the region where X_{CH_4} and X_{O_2} vanish. The X_{CH_3}, X_{H_2}, and X_{CO} peaks are slightly on the fuel side, and the X_{CO_2}, X_H, X_{OH}, and X_O peaks are on the air side. On the fuel side, methane molecules diffuse radially based on its concentration gradient in the diffusion layer between the dividing streamline and the flame zone. In the high-temperature layer, methane decomposes to methyl radical by the fuel pyrolysis and dehydrogenation by radical species (OH and H) that produce H_2O and H_2, respectively (see Figs. 1b and 1d). On the air side, oxygen molecules diffuse inward based on its concentration gradient. Because the flame zone is inclined slightly outward downstream and the streamlines are almost parallel to the jet axis near

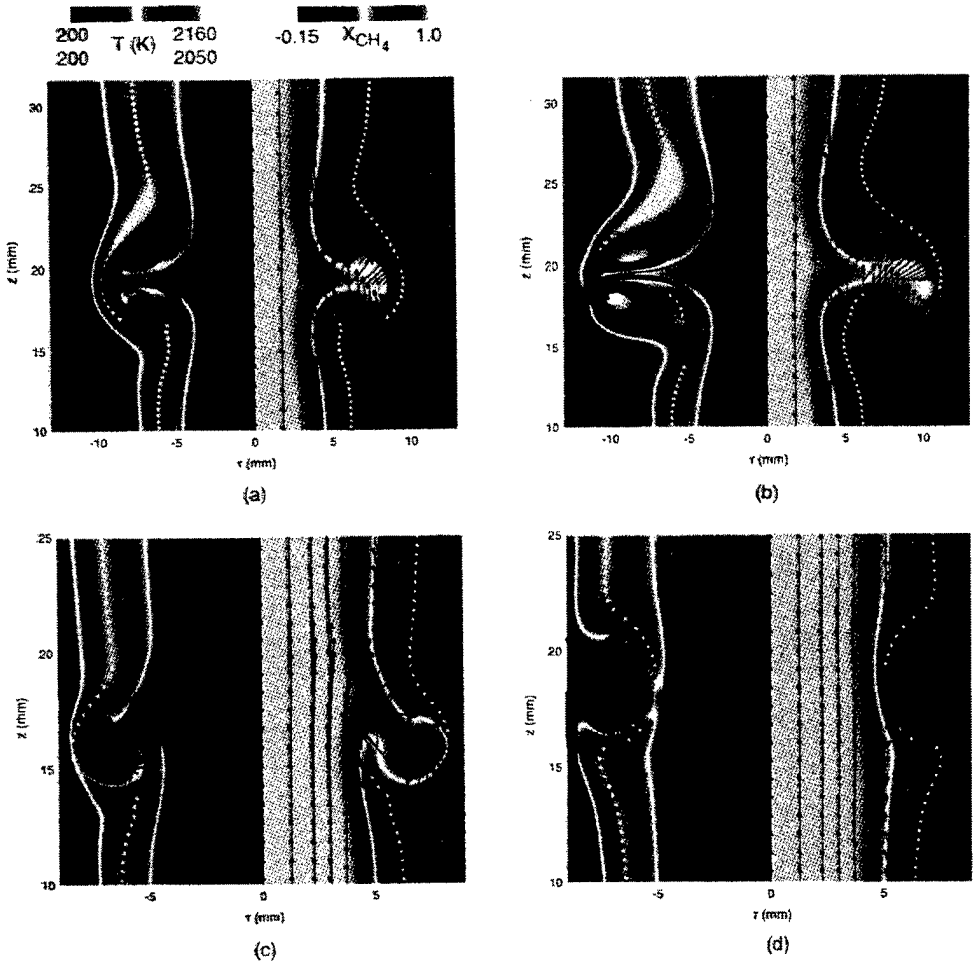

FIG. 2. Color-coded mapping of temperature field with injected particle image (left side), methane mole fraction field, and velocity vector field (right side) in a methane jet diffusion flame with a side jet; (a) case 1, t = 2.13 ms; (b) case 2, t = 2.13 ms; (c) case 3, t = 0.293 ms; (d) case 4, t = 1.17 ms. Temperature scale (maximum): (a)(b) 2160 K, (c)(d) 2050 K.

the flame zone, the external fluid passes through the flame zone with a narrow angle into the methane diffusion layer. Since the reaction rates are finite, oxygen can leak through the flame zone ($X_{O_2} \neq 0$) and, thus, a convective transport contributes to the total oxygen influx. In the high-temperature layer on the air side, radical species (OH and O) are generated from O_2 and H_2 (Figs. 1b and 1d). Since a pool of radical species (OH, H, and O) is consumed by methane and methyl radicals on the fuel side, a major heat-release step of CO oxidation by OH radicals occurs mainly on the air side.

For the high-velocity condition (Figs. 1c and 1d), the peak temperature is lower (2010 K) than that under the low-velocity condition (Figs. 1a and 1b; 2140 K), the high-temperature layer is thinner, and the leakage of reactants through the reaction zone is more evident as a result of finite-rate chemistry under a more strained condition.

Figure 2 shows color-coded mappings of the calculated gas temperature superimposed with locations of tracer particles (black dots) injected in front of the side jet (left-hand side) and the methane mole fraction superimposed with velocity vectors (right-hand side). The radial locations of the flame zone (yellow dots) determined by the temperature peak are also included in the figures. Notice that the elapsed time after ejection (t) is an order of magni-

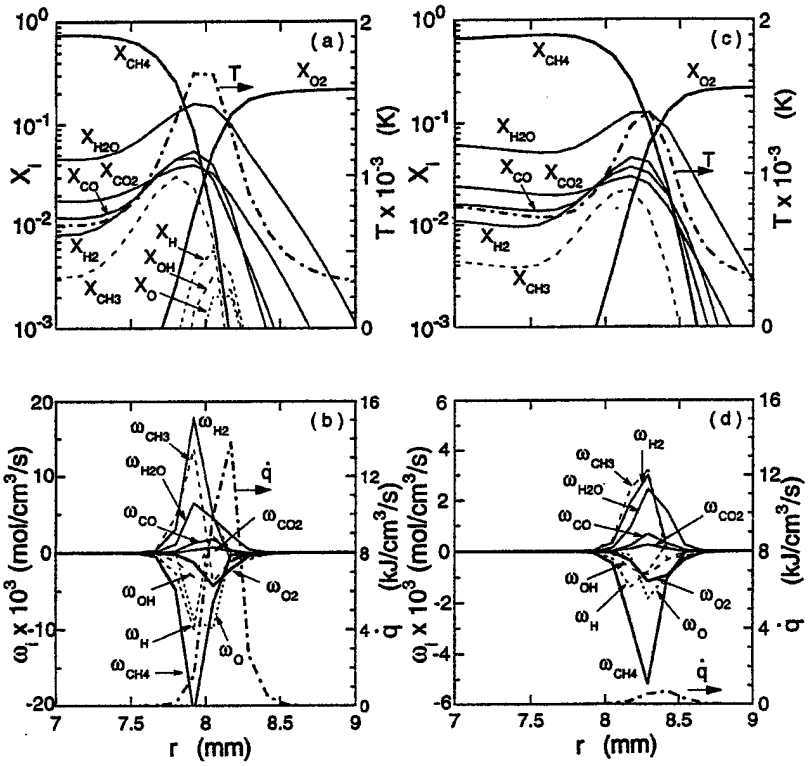

FIG. 3. Calculated temperature, mole fractions, molar production rates, and heat-release rate across a methane jet diffusion flame with a side jet; case 3, $z = 16$ mm; (a)(b) $t = 0.205$ ms; (c)(d) $t = 0.264$ ms.

tude longer for cases 1 and 2 (Figs. 2a and 2b) than for case 3 (Fig. 2c). Despite the difference in the magnitude of side jet velocity and, in turn, the time scale of the process, the low- and high-velocity cases show the following common features in the flame structures, because the large-scale vortex formed dominates the global flow structure. As the side jet issues from the jet fluid core toward the flame surface, a sudden change in the radial-velocity distribution near the edges of the side jet induces the roll-up of the neighboring fluid and the subsequent formation of a vortex system, composed of a pair of counterrotating vortex rings. The vortex system grows as it engulfs surrounding gases and penetrates into a high-temperature (highly viscous) layer toward the flame zone. The vortex structure rotates as a whole naturally because of the uneven axial-velocity distribution in the shear layer, especially for case 3 because of its higher velocity gradient. The formation of the vortex structure with counterrotating vortex rings and the subsequent rigid-body rotation have also been observed experimentally [17].

For case 1 (Fig. 2a), the flame zone bulges out as the vortex system moves toward the flame. Consequently, the thermal layer ahead of the vortex becomes significantly thin as the leading edge of the vortex (i.e., the outermost point of the injected particles) reaches the initial flame surface location. However, the vortex loses its radial momentum and drifts away downstream. By contrast, in case 2 (Fig. 2b), the vortex further pushes out the flame zone until local extinction occurs near the leading edge of the bulged flame zone. For case 3 (Fig. 2c), local extinction occurs as the vortex rapidly cuts through the thermal layer. Figure 2c shows large values of the methane mole fraction in the interior of the vortex system.

Figure 2d shows the results for the inwardly injected external vortex. Although the magnitude of the side jet velocity is small (4 m/s), local extinction occurs. Since the calculation is axisymmetric, the vortex may accelerate as its radial location decreases. Moreover, the jet fluid boundary does not deform as the vortex proceeds inward because methane flows at relatively high velocities inside the dividing streamline. Unlike the flame bulge observed in cases 1 and 2, the thermal layer cannot intrude into the

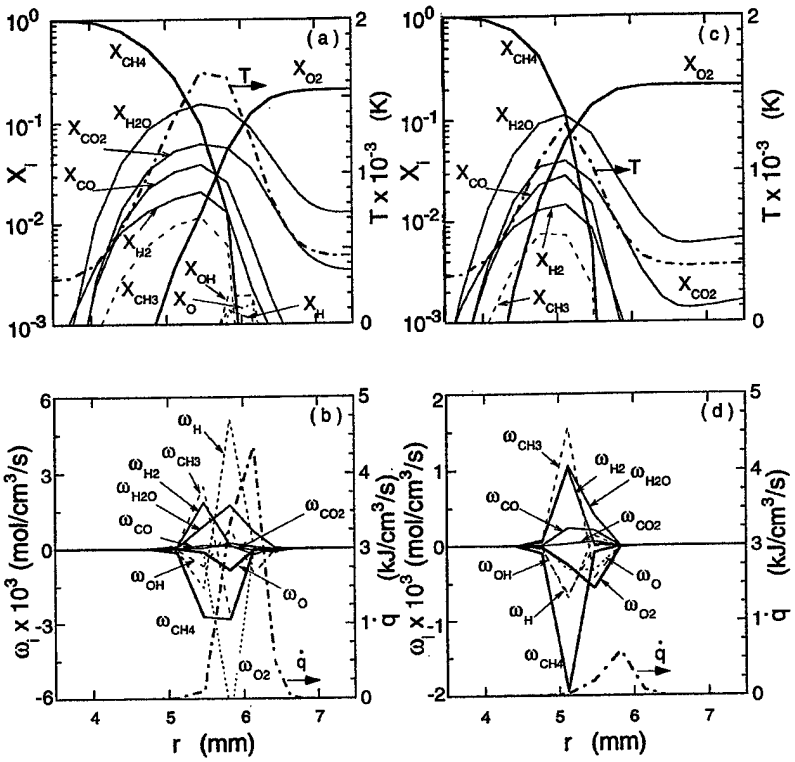

FIG. 4. Calculated temperature, mole fractions, molar production rates, and heat-release rate across a methane jet diffusion flame with a side jet; case 4, z = 18 mm; (a)(b) t = 0.733 ms; (c)(d) t = 1.026 ms.

jet core; thus, the diffusive layer becomes very thin as the vortex approaches the jet fluid boundary.

Figure 3 shows the temporal changes in the structure of a methane flame with a side jet in case 3. The height chosen for the profile plots (z = 16 mm) is nearly coincident with the height of the leading edge of the vortex near which local extinction occurs. At t = 0.205 ms (Fig. 3a), the thermodiffusive layer near the flame zone becomes thin compared to the steady-state condition (Fig. 1c), the methyl radical concentration increases significantly, the peak temperature decreases to ~1700 K, and the reactant leakage is more evident (overlapping at $X_{CH_4} = X_{O_2} \approx 0.03$). As a result of a significant increase in the methane concentration gradient and, in turn, the methane flux in front of the leading edge of the vortex, the molar production rates and heat-release rate (Fig. 3b) increase by an order of magnitude compared to those before vortex ejection (Fig. 1d). As the wave of high methane concentration front proceeds outward (Figs. 3c and 3d), methane and methyl radicals scavenge and vanish the radical pool (X_{OH}, X_H, and X_O), which is critical for H_2-O_2 chain-branching reactions. The methane and oxygen leakage increases ($X_{CH_4} = X_{O_2} \approx 0.07$), the peak temperature decreases (~1400 K), and the heat release ceases. Thus, the combustion process can no longer be sustained under such conditions, thereby leading to extinction.

Figure 4 shows the results for the inward side jet ejection for case 4. Although the magnitude of the side jet ejection velocity is significantly smaller than that in case 3, the vortex-flame interaction and local extinction processes occur more gradually. There are similarities and distinct differences in the interaction phenomena between the inward and outward ejections. As the vortex pushes the flame zone inward (Fig. 4a), the reactant leakage increases and the peak temperature decreases as seen in the outward case. However, the methyl radical concentration does not increase much and the gradients of X_{CH_4} and X_{O_2} are significantly smaller (Figs. 4a and 4c), yet the oxygen penetrates deeper onto the fuel side compared to the outward ejection (Figs. 3a and 3c). Unlike the outward vortex motion toward ambient air, the inward motion is limited by the boundary of jet fluid that is flowing at high axial velocities, and thus, the vortex nearly cuts through the flame zone (Fig. 2d). At the final stage (Figs. 4c and 4d), the radical pool disappears and exothermic reactions stop.

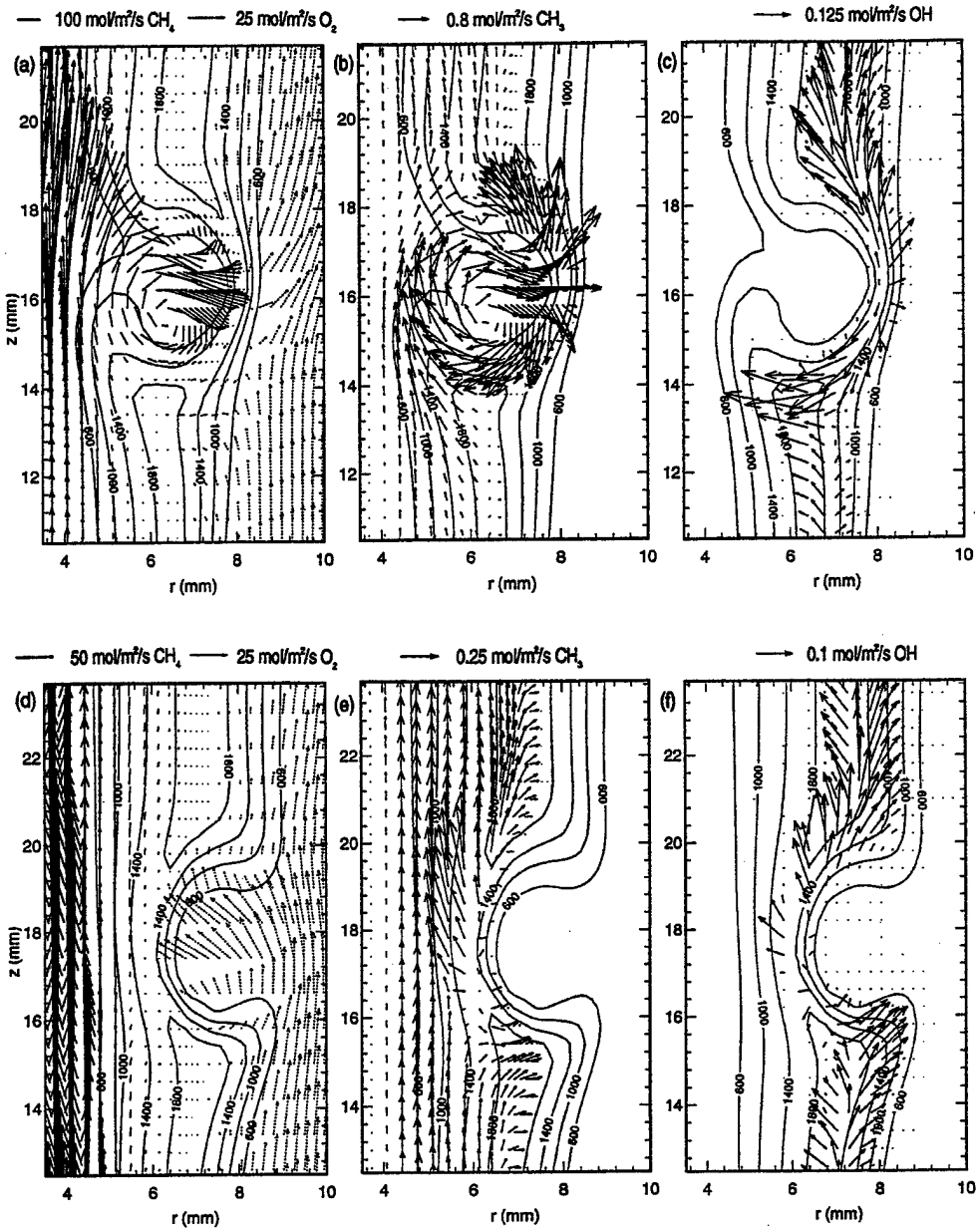

FIG. 5. Total molar flux fields of species in a methane jet diffusion flame with a side jet; (a)(d) methane and oxygen, (b)(e) methyl radical, and (c)(f) hydroxyl radical; (a)–(c) case 3, (d)–(f) case 4.

Although the plots of the mole fractions and production rates show the flame structure in a static manner, the dynamic two-dimensional transport and kinetic phenomena need to be revealed by examining the species (and heat) flux vector fields. Figure 5 shows the total (diffusion plus convection) molar flux vector fields of selected species (methane, oxygen, methyl, and hydroxyl radicals), superimposed with the isotherms. In the case of outward ejection (Figs. 5a through 5c), significant fluxes of methane

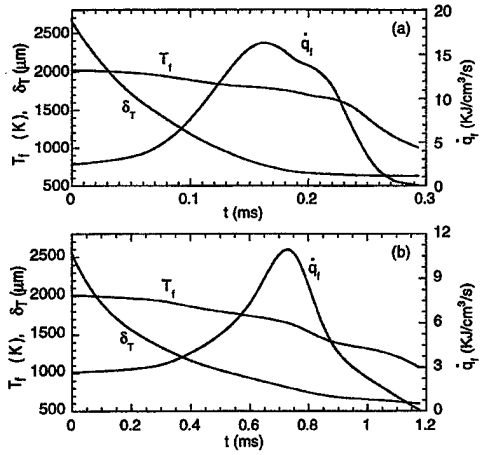

FIG. 6. Temporal variations in the peak temperature, full width at half peak temperature, and peak heat-release rate across a methane jet diffusion flame with a side jet at a height near extinction; (a) case 3, (b) case 4.

and methyl radical rush into the flame zone by both diffusion and convection. The flux of hydroxyl radicals, produced on the air side of the peak temperature and diffused both inward and outward in the steady-flame region, is small in the near-extinction flame zone as a result of scavenging by the methane and methyl radicals. In the case of inward ejection (Figs. 5d through 5f), the methane flux into the flame zone is an order of magnitude lower than that for the outward ejection, whereas the oxygen flux (mainly by convection) toward the flame zone is an order of magnitude larger. The methyl and hydroxyl radical fluxes even point inward from the near-extinction flame zone, showing distinctive differences compared to the outward ejection case. Thus, for the inward ejection, the oxygen leak through the reaction zone and the subsequent temperature decrease caused by reduced exothermic reactions play a significant role in local extinction.

Figure 6 shows the temporal variations in the peak temperature (T_f), full width at half peak temperature (δ_T), and peak heat release rate ($\dot{q}_f$) for the outward and inward ejection (cases 3 and 4). The heat-release–rate curves for both cases show two noticeable turning points ($t \approx 0.06$ ms and $t \approx 0.16$ ms for case 3; $t \approx 0.3$ ms and $t \approx 0.7$ ms for case 4). Thus, the unsteady vortex-flame interactions can be divided into three sequential and overlapping regimes based on the controlling processes: diffusion, convection, and chemical kinetics. In the early diffusion-controlled regime, the diffusion layer thickness (represented by δ_T) decreases rapidly as the vortex approaches the flame zone. The flame zone is more strained, the reactant leakage through the reaction zone increases, and the flame temperature decreases. However, the reactant concentration gradients and, in turn, fluxes into the flame zone, increase, and the reaction and heat-release rates gradually increase. As the reactant leakage increases (X_{CH_4} and $X_{O_2} \neq 0$ in the reaction zone), the convective contribution to the total reactant fluxes becomes significant. In the convection-controlled regime, the convective contribution to the reactant fluxes and, in turn, the reaction and heat-release rates increase more rapidly. However, because of the finite-rate chemistry, there is an upper limit to how much reactant can be consumed in the reaction zone. Thus, chemical kinetics begin to control the process. In the last chemical-kinetic–controlled regime, the rate of decrease in the diffusion layer thickness becomes small, while the peak temperature and the heat-release rate drop rapidly. The detailed chemical kinetic processes leading to extinction are different in the outward and inward ejection cases as described previously.

Conclusions

A unique numerical experiment, in which a packet of fluid is ejected outward or inward toward a flame zone, illustrated essential physical and chemical aspects of unsteady vortex-flame interactions and local extinction of laminar methane jet diffusion flames. The unsteady vortex-flame interactions leading to extinction can be divided into three regimes depending on the dominant process: diffusion, convection, and chemical kinetics. The first two regimes are primarily physical vortex-flame interactions. During the physical interaction stage, if a Peclet number is sufficiently large (on the order of 100), the vortex system penetrates into the high-temperature (highly viscous) layer with a slight flame movement, thus rapidly thinning the thermodiffusive layer. The reactant leakage through the reaction zone increases, the flame temperature gradually decreases, and the heat-release rate increases by enhanced diffusion in the early regime and then by convection. In the final chemical kinetic regime for the outward vortex ejection, an excess influx of methane and methyl radicals scavenge radicals (OH, H, and O) and terminate exothermic oxidation reactions of intermediate species (H_2 and CO). For the inward ejection, the convective contribution to the oxygen flux is responsible for the excessive reactant leakage, leading to extinction.

Acknowledgments

This work was supported by the U.S. Air Force, Wright Laboratory, Aero Propulsion and Power Directorate, Fuels

and Lubrication Division, Wright-Patterson Air Force Base, Ohio, under Contract No. F33615-92-C-2207 (Technical Monitor: C. W. Frayne).

REFERENCES

1. Tsuji, H., *Prog. Energy Combust. Sci.* 8:93–119 (1982).
2. Law, C. K., *Prog. Energy Combust. Sci.* 10:295–318 (1984).
3. Tsuji, H. and Yamaoka, I., *Twelfth Symposium (International) on Combustion*, The Combustion Institute, Pittsburgh, 1966, pp. 979–984.
4. Williams, F. A., *Combustion Theory*, 2d ed., The Benjamin/Cummings, Menlo Park, CA, 1985, p. 408.
5. Tsuji, H., Yoshida, A., and Endo, N., *Twenty-Fifth Symposium (International) on Combustion*, The Combustion Institute, Pittsburgh, 1994, pp. 1191–1197.
6. Egolfopoulos, F. N., *Twenty-Fifth Symposium (International) on Combustion*, The Combustion Institute, Pittsburgh, 1994, pp. 1375–1381.
7. Im, H. G., Bechtold, J. K., and Law, C. K., *Combust. Sci. Technol.* 106:345 (1995).
8. Sung, C. J., Liu, J. B., and Law, C. K., *Combust. Flame* 102:481–492 (1995).
9. Cuenot, B. and Poinsot, T., *Twenty-Fifth Symposium (International) on Combustion*, The Combustion Institute, Pittsburgh, 1994, pp. 1383–1390.
10. Takeno, T. and Kotani, Y., *Acta Astronaut.* 2:999 (1975).
11. Takahashi, F., Mizomoto, M., and Ikai, S., *Combust. Flame* 48:85 (1982).
12. Takahashi, F. and Schmoll, W. J., *Twenty-Third Symposium (International) on Combustion*, The Combustion Institute, Pittsburgh, 1991, p. 677.
13. Shekarchi, S., Savas, Ö., and Gollahalli, S. R., *Combust. Flame* 73:221 (1988).
14. Roquemore, W. M., Chen, L.-D., Goss, L. P., and Lynn, W. F., "The Structure of Jet Diffusion Flames," in *Turbulent Reactive Flows* (Borghi, R. and Murthy, S. N. B., Eds.), Springer Verlag, Berlin, 1993, p. 49.
15. Takahashi, F. and Goss, L. P., *Twenty-Fourth Symposium (International) on Combustion*, The Combustion Institute, Pittsburgh, 1992, pp. 351–359.
16. Takahashi, F. and Vangsness, M. D., "Near-Field CARS Measurements and the Local Extinction of Turbulent Jet Diffusion Flames," in *Dynamics of Heterogeneous Combustion and Reacting Systems*, (Kuhl, A. L., Leyer, J.-C., Borisov, A. A., and Sirignano, W. A., Eds.), American Institute of Aeronautics and Astronautics, Washington, D.C., 1993, p. 37.
17. Hsu, K. Y., Chen, L. D., Katta, V. R., Goss, L. P., and Roquemore W. M., AIAA Paper No. 93-0455, 1993.
18. Takahashi, F., Schmoll, W. J., Trump, D. D., and Goss, L. P., AIAA Paper No. 95-0139, 1995.
19. Katta, V. R. and Roquemore, W. M., *Combust. Flame* 92:274 (1993)
20. Katta, V. R., Goss, L. P., and Roquemore, W. M., *AIAA J.* 32:84 (1994).
21. Katta, V. R., Goss, L. P., and Roquemore, W. M., *Combust. Flame* 96:60 (1994).
22. Takahashi, F. and Katta, V. R., *J. Propulsion Power* 11:170 (1995).
23. Katta, V. R. and Roquemore, W. M., "Extinction in Methane-Air Counterflow Diffusion Flames—A Direct Numerical Study," Central States Section/The Combustion Institute Meeting, St. Louis, May 1996.
24. Peters, N., "Flame Calculations with Reduced Mechanisms—An Outline," in *Reduced Kinetic Mechanisms for Applications in Combustion Systems* (Peters, N. and Rogg, Bernd, Eds.), Springer Verlag, Berlin, 1993, p. 3.
25. Hirschfelder, J. O., Curtis, C. F., and Bird, R. B., *The Molecular Theory of Gases and Liquids*, Wiley, New York, 1954.
26. Schlichting, H., *Boundary-Layer Theory* 7th ed., (Kestin, J., Trans.), McGraw Hill, New York, 1979, p. 599.

COMMENTS

Mitchell Smooke, Yale University, USA. In your two-dimensional counterflow calculations, it was not clear what boundary conditions were employed in the radial direction. Could you comment on this?

Also, what conditions were imposed on the velocities (radial and axial) at the base of the two jets?

Author's Reply. The two-dimensional computer code used, including its chemistry model, has been validated [23] by simulating an axisymmetric counterflow diffusion flame prior to the present numerical experiment on the unsteady extinction of jet diffusion flames. In the two-dimensional counterflow flame calculations, weighted first- and second-order extrapolations were used for the outflow boundary conditions in the radial direction. In addition, to reduce the influence of errors in the boundary conditions on the flame structure, the outflow boundary was located at 50 nozzle radii in the radial direction. An identical extrapolation scheme was used for the axial outflow boundary in the present jet diffusion flame calculations.

For the boundary conditions at the fuel and air jet nozzle exits in the counterflow diffusion flame calculations, flat axial and null radial velocity profiles (plug flow) were imposed.

•

Habib N. Najm, Sandia National Laboratories, USA. The plots of concentrations and production/consumption rates

in the reported flame-vortex interaction results show a very jagged representation of the flame structure. This suggests that the flame structure is not well resolved. Even though this implicit scheme is stable under these conditions, the results seem to suffer from excessive truncation error, and are therefore questionable. A grid refinement study should help resolve this issue.

Author's Reply. In the counterflow diffusion flame calculations [23] for the model validation, the flame structures under near-extinction conditions obtained with 0.2-mm and 0.04-mm spacing were found to be identical. The grid-independent results obtained with this code with reasonably coarse grids may be attributed to the implicit procedures used. Implicit schemes not only improve stability but also allow larger time and spatial steps without loss of accuracy compared to those allowed by explicit schemes.

In the present jet flame calculations, a fixed mesh system with a varied grid spacing in the axial and radial directions was used. For the fuel-side vortex ejection, local extinction occurred when the flame zone was pushed radially outward into the grid zone where the grid spacing was 0.2 mm. Although the jagged profiles associated with the 0.2-mm grid spacing are shown in Fig. 3, we believe that the results have not suffered from any truncation error as demonstrated in the counterflow calculations. For the air-side vortex ejection, the flame zone moved into a zone where the grid spacing was 0.4 mm (Fig. 4). Although a finer grid spacing might be desirable for this case, the qualitative nature of the extinction mechanisms proposed should still be valid.

AIAA 97-0251

A Numerical Investigation of the Stabilizing Mechanism of Methane Jet Diffusion Flames

F. Takahashi
University of Dayton
Dayton, Ohio

V. R. Katta
Innovative Scientific Solutions, Inc.
Dayton, Ohio

35th Aerospace Sciences Meeting & Exhibit
January 6-10, 1997 / Reno, NV

For permission to copy or republish, contact the American Institute of Aeronautics and Astronautics 1801 Alexander Bell Drive, Suite 500, Reston, VA 22091

A NUMERICAL INVESTIGATION OF THE STABILIZING MECHANISM OF METHANE JET DIFFUSION FLAMES

Fumiaki Takahashi*
University of Dayton, Dayton, Ohio

Viswanath R. Katta†
Innovative Scientific Solutions, Inc., Dayton, Ohio

Abstract

The detailed structure of the stabilizing region of methane jet diffusion flames has been studied numerically. A time-dependent, axisymmetric, implicit, third-order accurate numerical model was used with variable properties and a semi-detailed chemical kinetic model. Stable flames under three different flow conditions along the stability curve (determined experimentally) were simulated. At the highest coflow air and lowest fuel jet velocity condition, the flame base shifted ~3 mm downstream from the burner rim, extending the dark space between the flame base and the rim, as exactly observed experimentally. The heat-release and species reaction rates exhibited sharp peaks at relatively low flame temperatures in the base region of the diffusion flame zone. This highly reactive zone provides a continuous ignition source against the incoming flow, thus holding the rest of the flame. The reactive spot is formed mainly because of the geometric configuration (end effect), which allows diffusion of radical species back into surrounding oxygen field. Partial fuel-air premixing in the extended dark space also contributes to the increased size of the reactive zone and the peak rate values.

INTRODUCTION

The flame stability phenomena are of both fundamental and practical importance because they define operational boundaries of combustion systems and they relate to the effective use of chemical energy. Unfortunately, stability mechanisms of diffusion flames are less understood than those of premixed flames largely because a characteristic parameter that reflects the reaction rates, such as the burning velocity of premixed flames, does not exist in diffusion flames. This is because the actual reaction rates in diffusion flames are limited by the transport rates of reactants, which depend on the flame structure. Furthermore, partial fuel-air premixing in the dark space between the diffusion flame base and the burner rim brings in additional complications. Consequently, the structure of the stabilizing region (flame base) must be revealed experimentally or numerically to foster a better understanding of the flame stabilization mechanisms of diffusion flames. The experimental results of the structure of stabilizing region of methane flames were reported previously [1]. This paper reports the results of numerical simulations of the stabilizing region of methane flames.

NUMERICAL MODELS

Time-dependent governing equations, expressed in cylindrical coordinates, consist of mass continuity, axial and radial momentum conservation, energy conservation, and species conservation equations with the equation of state [2]. Body-force term caused by the gravitational field is included in the axial momentum equation. A semi-detailed chemical-kinetic model [3], including 52 elementary steps for 17 species, is used to describe CH_4-O_2 combustion. The chemical kinetic parameters for the

*Research Engineer, Research Institute. Senior Member AIAA
†Senior Research Engineer, Member AIAA

Copyright © 1997 by the Authors. Published by the American Institute of Aeronautics and Astronautics, Inc. with permission.

reaction $CH_3 + H \rightarrow CH_4$ were replaced with those recommended by Warnatz [4] because they were found [5] to accurately predict the critical strain rate at extinction of counterflow diffusion flames [6]. The viscosity and binary diffusion coefficients are estimated from Chapman-Enskog collision theory [7], and enthalpy of each species is calculated from polynomial curve-fits.

The finite-difference form of the governing equations is constructed on a staggered grid system based on an implicit QUICKEST numerical scheme. The computational domain of 150 × 60 mm in axial (x) and radial (r) directions, respectively, is represented by a mesh system of 271 × 101. Grid lines are clustered near the burner lip and the entire field of interest in this study (the flame stabilizing region) is covered with a minimum grid spacing of 0.05 mm.

The initial and boundary conditions for the axial (U) and radial (V) velocities and species and energy at different flow boundaries are similar to the previous work [8]. The outer boundaries of the computational domain are shifted sufficiently far enough to minimize the propagation of disturbances into the region of interest. Along the burner-lip walls, no-slip boundary conditions are enforced. An extrapolation procedure with weighted zero- and first-order terms is used to estimate the flow variables on the outflow boundary.

The inner diameter of the fuel tube (d = 9.5 mm) is close to that used in the experiments [1]. The test cases reported in this paper are listed in Table 1. The mean jet velocity (U_j) and the mean annulus air velocity (U_a) were chosen close to the stability limit curve [1]. The fully-developed pipe flow and boundary layer velocity profiles are used inside and outside the burner tube.

TABLE 1 Test Conditions

Case No.	U_j (m/s)	U_a (m/s)
1	11.5	0.19
2	6.9	0.36
3	1.7	0.72

RESULTS AND DISCUSSION

The previous experiment [1] has revealed that the flame base is attached to the burner rim with a dark space and lifts off abruptly for flames for cases 1 and 2. For case 3, the flame base shifts a few mm downstream from the burner exit before full lifting occurs. Figure 1 shows the calculated velocity vectors, isotherms, and heat-release rate (q) contours (shaded) for cases 1 through 3. The scale of vectors is identical in all figures. An attached flame (cases 1 and 2) and a downstream-shifted (~3 mm from the burner exit) flame (case 3) were simulated accurately as observed experimentally [1]. In both cases, the coflow air was entrained through the dark space into the fuel-side of the flame zone. The high heat-release rate zone (shaded area) was formed nearly along the temperature peak, where the exothermic oxidative reactions are taking place. The heat-release rate showed a peak at the base of the flame, where temperature was relatively low (~1600 K) for all cases. The peak values are: case 1, ~210 J/cm^{3}s; case 2, ~270 J/cm^{3}s; and case 3, ~470 J/cm^{3}s. The high heat-release rate zone around its peak became wider as the flame base shifted downstream (case 3). The intervals of the isotherms below the heat-release rate peak were narrower (higher temperature gradient) for case 3 than those for cases 1 and 2. The magnitude of velocity near the peak was similar, as described later, despite a difference of more than a factor of three in the initial coflow air velocities (see Table 1).

Figure 2 shows the calculated total molar flux vectors of methane (dashed) and oxygen (solid), including both diffusion and convection terms, contours of the equivalence ratio (ϕ), and contours of the rate of formation of oxygen for cases 1 through 3. There exist striking differences between the vectors in Figs. 1 and 2 as a result of the additional contribution of molecular diffusion in Fig. 2. In the upper portion of the flame, methane diffused outwardly while the oxygen was transported by both convection and diffusion into the flame from the opposite side, typical of diffusion flames. In the dark space, particularly for case 3 (Fig. 2c), the oxygen penetrated into the fuel-side region and partially mixed with methane.

The equivalence ratio used here is defined dynamically as a ratio of the fuel and oxygen molar fluxes normalized by the stoichiometric value for methane-oxygen combustion (0.5). Thus, the equivalence ratio indicates actual fuel-air mixture strength, including the effects of both transport modes (convection or diffusion) and directions of fuel and oxygen transport. The contours of the equivalence ratio show the increase in the thickness of the mixing zone as the flame base shifts downstream for case 3.

The rate of formation of oxygen, which is an index of the global reaction rate, showed a negative peak at nearly the same location with the heat-release peak. The peak values are: case 1, -0.0006 mol/cm^{3}s; case 2, -0.0008 mol/cm^{3}s; and case 3, -0.0013 mol/cm^{3}s. The size of the high reaction-rate zone around the peak also became wider as the flame base shifted downstream (case 3). The equivalence ratio contours are narrowly spaced in the upper flame zone for all cases, typical of diffusion flames, and they spread out around the peak and the dark space. It is notable that the peak oxygen consumption area extends mostly in the fuel-lean region ($\phi \approx 0.6$ at the peak), which is consistent with the experimental observations [9, 10].

The mechanism of the formation of the peaks of the heat-release and reaction rates at the flame base is essential feature in flame stabilization. Figure 3 shows the contours of the mole fraction and rate of formation of oxygen, and the mole flux vectors of hydrogen atoms. The mole fraction of oxygen at the peak of oxygen formation rate is ~0.05, for all cases, much higher than a typical value of leakage in diffusion flames (~0.02) [11]. On the other hand, the molar flux vectors of hydrogen atoms shows its efflux from the flame in opposite directions perpendicular to the flame zone. At the edge of the flame zone, the hydrogen atom flux vectors point downward into the region of relatively high oxygen concentration. Thus, the important chain-branching reaction step $H + O_2 \rightarrow OH + O$ takes place.

Other radical species (OH and O) behave in similar manner to hydrogen atoms. Figure 4 shows the contours of the mole fraction and rate of formation of methane, and the mole flux vectors of hydroxyl radicals. The high methane consumption rate zone is slightly outside of the methane mole fraction contour of 0.02. The peak of methane consumption occurred slightly inside the peaks of heat-release and oxygen consumption rates. The hydroxyl radicals also efflux from the flame zone similar to hydrogen atoms.

Therefore, the geometric end of the flame zone creates a peculiar situation. The flame base is more exposed to air (aerated), creating relatively high oxygen concentration area. Radicals diffuse back into the high oxygen concentration area, counterflowing incoming oxygen fluxes. As a result, the reaction zone broadened, the convective contribution of the oxygen flux increased, and thus, the global reaction rate increased. For case 3, this situation was enhanced because of the partial fuel-air mixing in the extended dark space. The molar flux vectors of methane and oxygen have a common component in the direction toward the reaction peak zone (Fig. 2c).

More detailed information on the flame structure around the flame base can be extracted by examining the profiles of variables. Figure 5 shows the radial variations of the species mole fractions, temperature, and heat-release rate at the height across the peaks of the heat-release and reaction rates for cases 1 (x =0 mm) and 3 (x =3 mm). The distributions of the major species and temperature for these two cases are similar qualitatively despite the striking difference in the oxygen mole fraction contour mappings (Fig. 3) as an attached (case 1) and downstream-shifted flame (case 3). The flame structure is similar to typical diffusion flames [8] except for a secondary peak in the oxygen mole fraction on the fuel side of the peak temperature as a result of air penetration through the dark space. Although the peak temperatures were ~1600 K for both cases, the oxygen mole fractions at the peak temperature location doubled from ~0.03 to ~0.06, respectively, and the heat-release rate also doubled from ~220 to ~470 J/cm^{3}s. The secondary oxygen mole fraction peak created a reversed oxygen concentration gradient (as same as that of methane) to contribute to a portion of the oxygen flux into the flame base. More importantly, the oxygen flux

contribution in the axial direction is dominant at the edge of the flame (see Fig. 2).

The heat-release rate has a sharp peak for both cases as a result of a dominant contribution from the reaction $CH_3 + O \rightarrow CH_2O + H$, as is clearly seen in a plot of heat-release rate contributions from each elementary step (not shown).

Figure 6 shows the axial variations in the temperature, heat-release rate (q), axial and radial velocity components along the flame zone (defined as the maximum heat-release envelope) for all cases. For cases 1 and 2, the temperature variation was nearly identical, while the heat release rate slightly increased from case 1 to case 2. For case 3, the temperature gradient toward the flame base was higher than those of cases 1 and 2, and the heat release rate nearly doubled as described before. Both axial and radial velocity components are almost the same at $x = -0.3$ mm for all cases ($U \approx 0.4$ m/s and $U \approx -0.3$ m/s).

Since the flame base is held stationary, the flame base must have reaction rates high enough to sustain combustion in the flow field, providing a continuous ignition source to the incoming reactants. As the flame base secures the stable stationary combustion, the diffusion flame zone in the upper portion can be successively supported, thus keeping the flame from lifting.

CONCLUSIONS

The detailed flame structure of the stabilizing region of diffusion flames has been successfully simulated. A highly reactive zone with the peaks of the heat-release and oxygen consumption rates is formed in the flame base region. The geometric peculiarity (end effect) allowed radical influxes by back diffusion into the relatively low temperature, aerated, broadened reaction zone. Thus, the reaction zone relies on the radical supply from the flame downstream and, at the same time, it provides a continuous ignition source to the incoming reactants in the flow, thus keeping the diffusion flame from lifting.

ACKNOWLEDGMENTS

This work was supported by the U.S. Air Force. Wright Laboratory, Aero Propulsion and Power Directorate, Fuels and Lubrication Division, Wright-Patterson Air Force Base, Ohio, under Contract No. F33615-92-C-2207 (Technical Monitor: C. W. Frayne).

REFERENCES

1. Takahashi, F., Vangsness, M. D., and Schmoll, W. J., Central States/The Combustion Institute Meeting, San Antonio, TX, April 1995.
2. Katta, V. R., Goss, L. P., and Roquemore, W. M., *AIAA J.* 32, 84 (1994).
3. Peters, N., "Flame Calculations with Reduced Mechanisms--An Outline," *Reduced Kinetic Mechanisms for Applications in Combustion Systems* (N. Peters and Bernd Rogg Eds.), Springer-Verlag, Berlin, 1993, p. 3.
4. Warnatz, J., *Combustion Chemistry* (W. C. Gardiner, Ed.), Springer-Verlag, New York, 1984, p. 197.
5 Katta, V. R., and Roquemore, W. M., Central States/The Combustion Institute Meeting, St. Louis, May 1996.
6. Sung, C. J., Liu, J. B., and Law, C. K., *Combustion and Flame* 102: 481-492 (1995).
7. Hirschfelder, J. O., Curtis, C. F., and Bird, R. B., *The Molecular Theory of Gases and Liquids*, Wiley, New York, 1954.
8. Takahashi, F., and Katta, V. R., *Twenty-Sixth Symposium (International) on Combustion*, in press, 1996.
9. Robson, K., and Wilson, M. J. G., *Combust. Flame* 13, 626 (1969).
10. Takahashi, F., Mizomoto, M., and Ikai, S., *J. Heat Transfer* 110, 182 (1988).
11. Tsuji, H., and Yamaoka, I., *Twelfth Symposium (International) on Combustion*, The Combustion Institute, Pittsburgh, 1966, pp. 979-984.

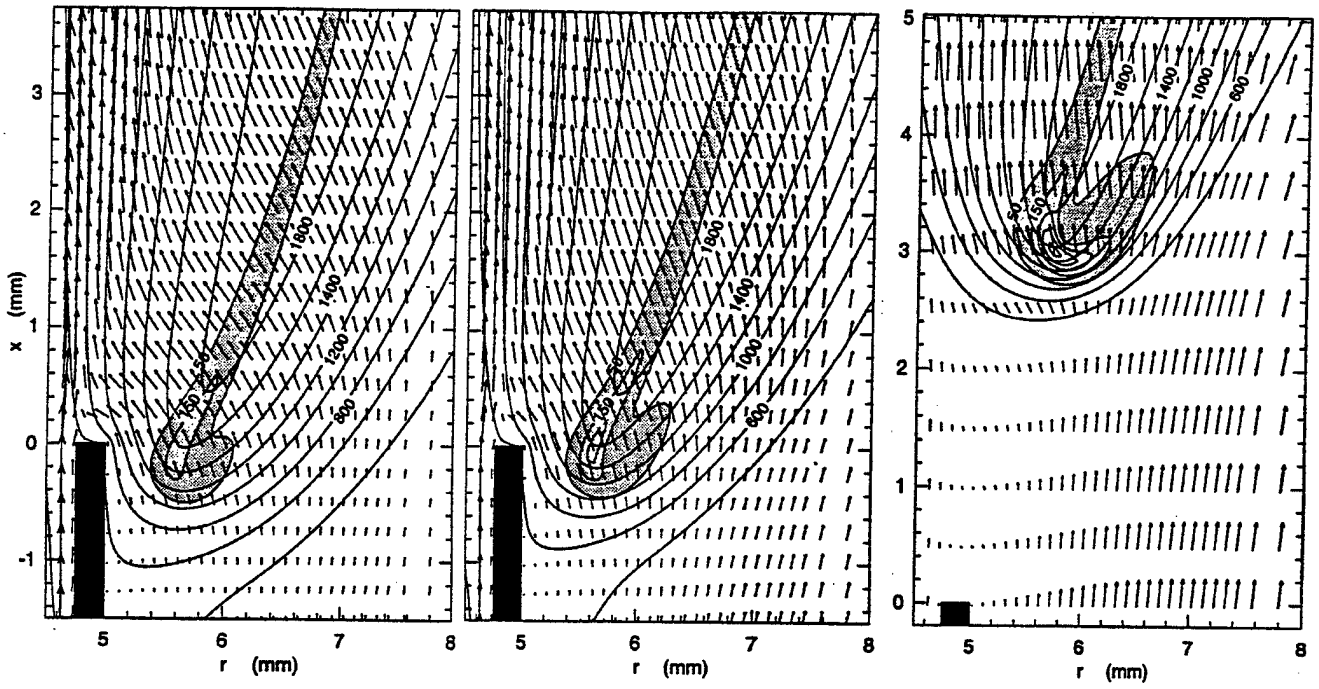

Fig. 1 Velocity vectors, isotherms (unit, K), and heat-release rate (J/cm^{3}s). (a) Case 1, (b) case 2, and (c) case 3.

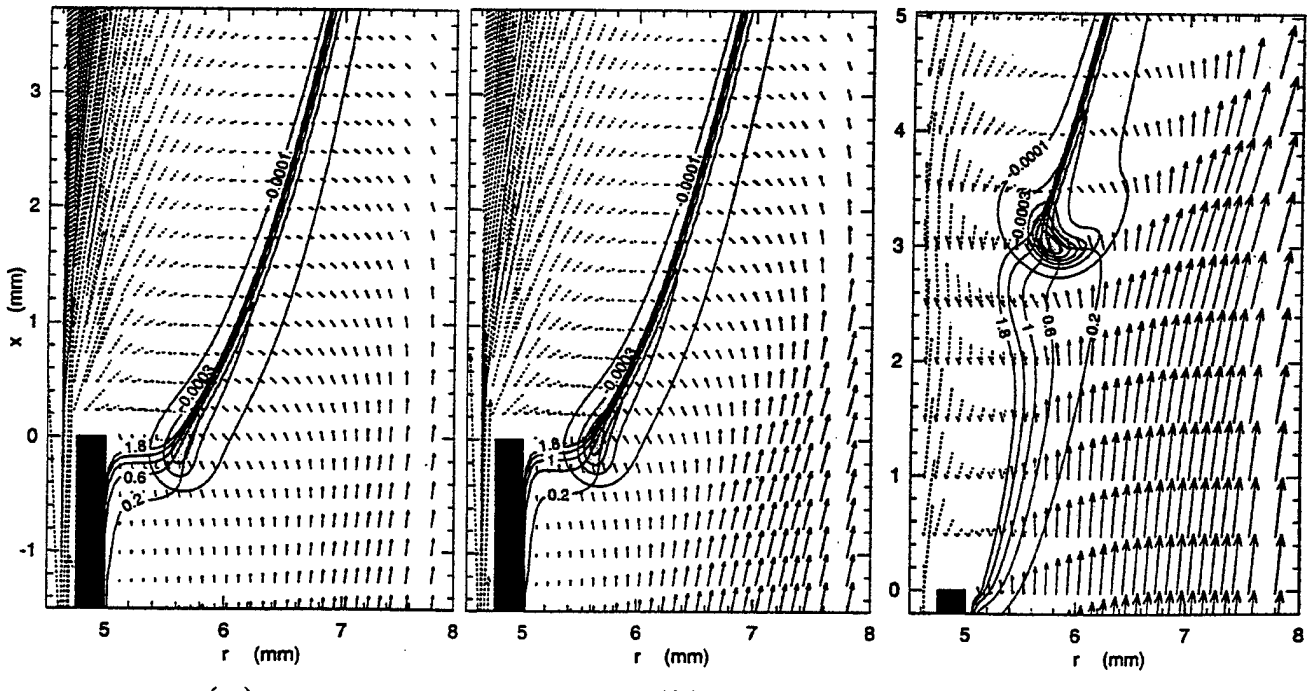

Fig. 2 Molar flux vectors of methane (dashed) and oxygen (solid), equivalence ratio, and contours of the oxygen rate of formation (mol/cm^{3}s). (a) Case 1, (b) case 2, and (c) case 3.

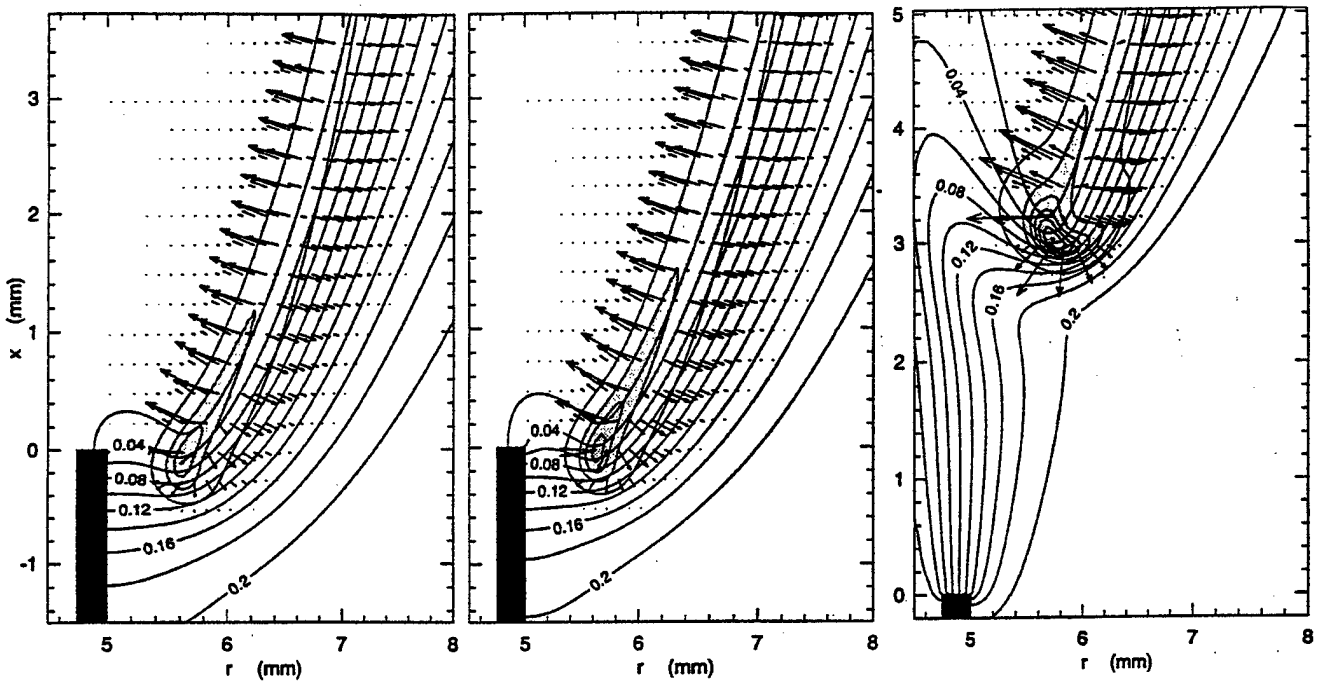

(a) (b) (c)

Fig. 3 Contours of the oxygen mole fraction, oxygen rate of formation (start, -0.0001 mol/cm^{3}s; interval, -0.0002 mol/cm^{3}s). and molar flux vectors of hydrogen atom. (a) Case 1, (b) case 2, and (c) case 3.

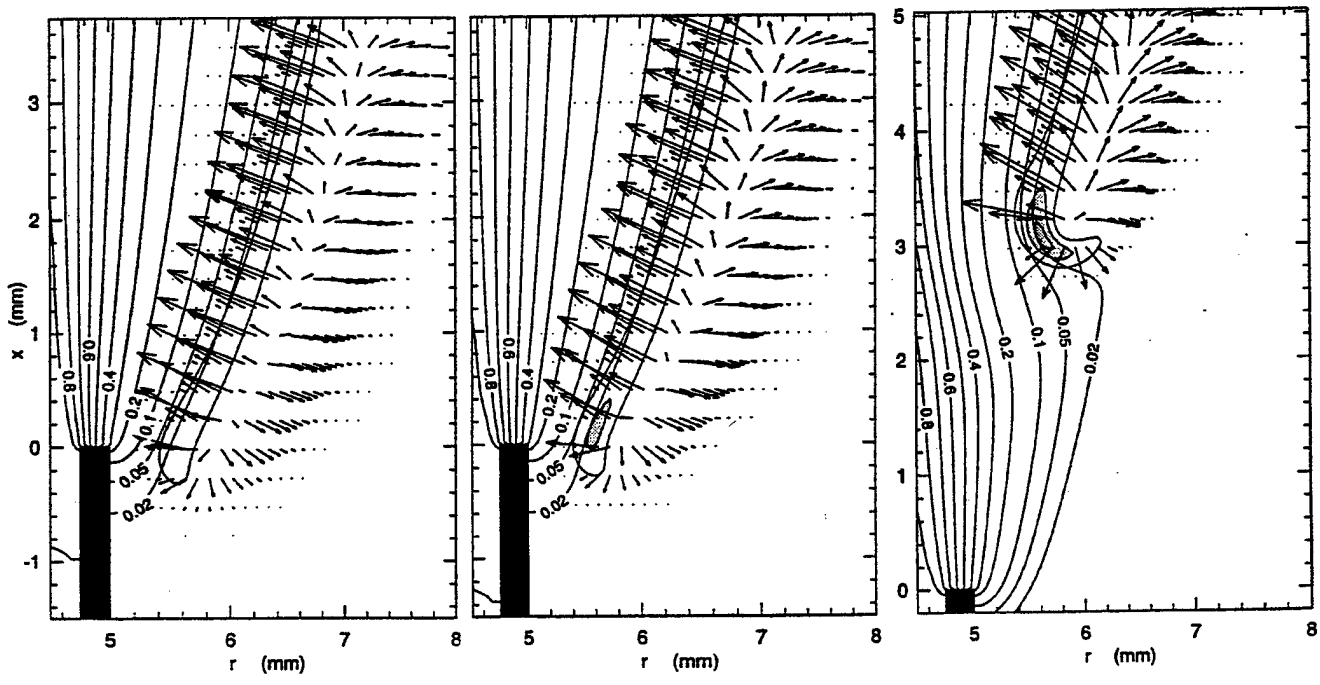

(a) (b) (c)

Fig. 4 Contours of the methane mole fraction, methane rate of formation (start, -0.0002 mol/cm^{3}s; interval, -0.0002 mol/cm^{3}s). and molar flux vectors of hydroxyl radical. (a) Case 1, (b) case 2, and (c) case 3.

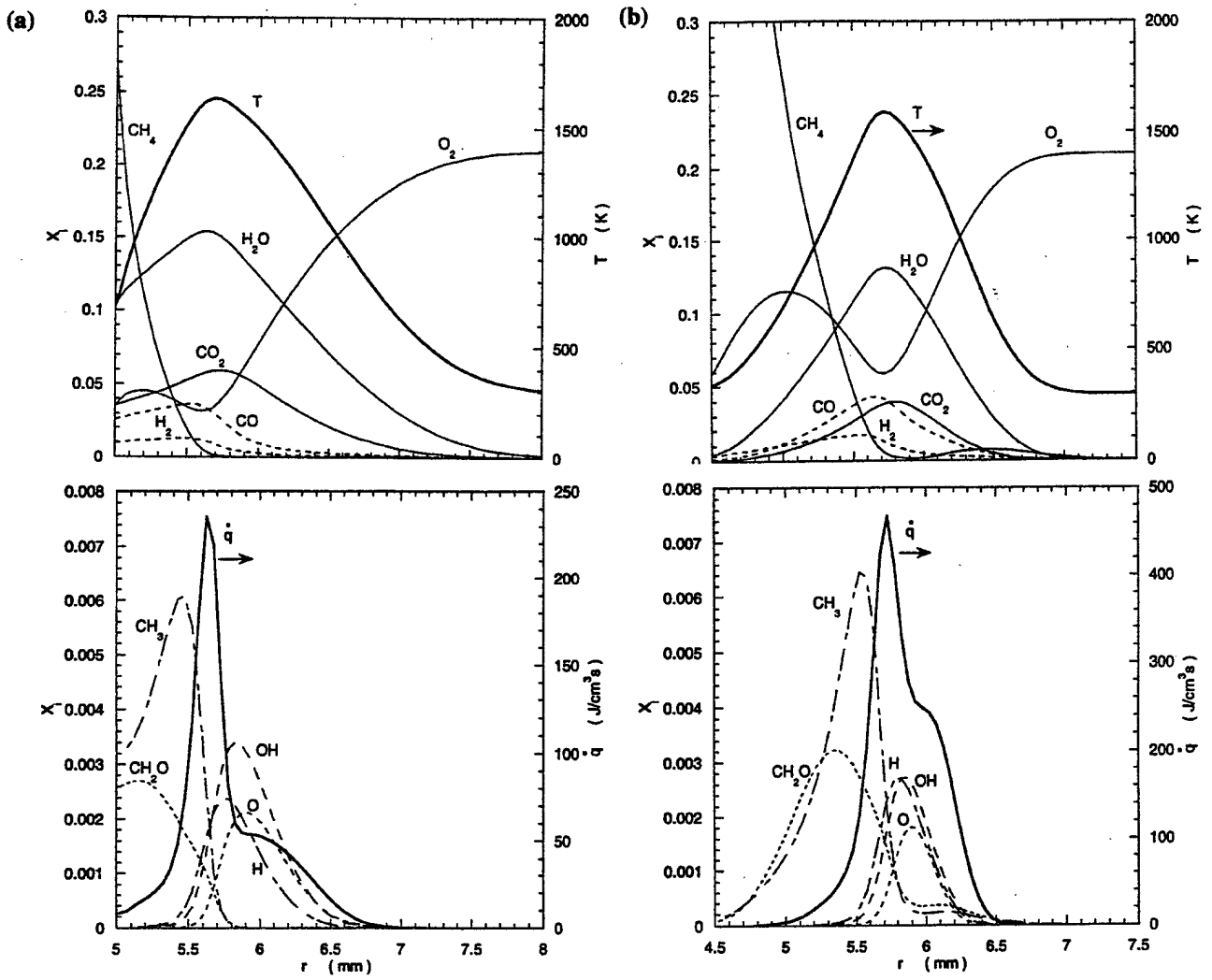

Fig. 5 Radial variations of mole fractions, temperature, and heat release rate. (a) Case 1 and (b) case 3.

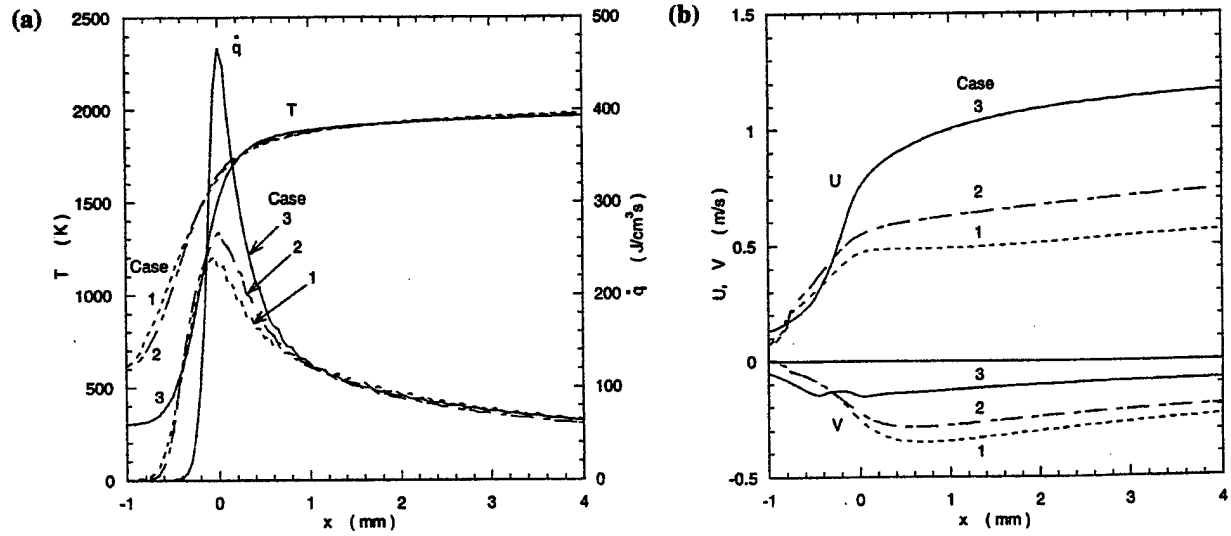

Fig. 6 Axial variations along the flame. (a) Temperature and heat-release rate, (b) axial and radial velocity components.

AIAA 97-0904

Simulation of Dynamic Methane Jet Diffusion Flame Using Finite-Rate Chemistry Model

V. R. Katta
Innovative Scientific Solutions, Inc
Dayton, OH

W. M. Roquemore
Wright Laboratory
Wright-Patterson AFB, OH

35th Aerospace Sciences Meeting & Exhibit
January 6-10, 1997 / Reno, NV

For permission to copy or republish, contact the American Institute of Aeronautics and Astronautics 1801 Alexander Bell Drive, Suite 500, Reston, VA 22091

Simulation of Dynamic Methane Jet Diffusion Flame using Finite-Rate Chemistry Model

V. R. Katta*
Innovative Scientific Solutions, Inc.
3845 Woodhurst Court
Dayton, OH 45430-1658

and

W. M. Roquemore+
Aero Propulsion Directorate
Wright Laboratory
Wright-Patterson Air Force Base, OH 45433

Abstract:

Accurate dynamic simulations for methane laminar and transitional jet flames are made using an axisymmetric, time-dependent CFDC code and different detailed-chemical-kinetics models. Comparisons are made with experimental data for a steady-state flame and for two dynamic flames that are dominated by buoyancy-driven instabilities. Ability of the three chemistry models namely; 1) modified Peters mechanism without C_2 chemistry, 2) modified Peters mechanism with C_2 chemistry and 3) GRI 1.2 mechanism in predicting coaxial jet diffusion flames under different operating conditions is investigated. It is found that the modified Peters mechanism with and without C_2 chemistry is sufficient for the simulation of jet flames for a wide range of fuel jet velocities. Both the steady-state and unsteady flame structures are compared by using scatter plots that are made from the data collected at several heights.

Introduction:

Studies of jet diffusion flames are important in understanding combustion phenomena in practical systems and for developing theories of combusting processes. Because of this, jet flames have been actively investigated since the classic works of Hotel et al[1] published in the Third Symposium on Combustion and Flame Explosion Phenomena in 1949. Considerable data on statistical quantities such as time averaged and rms values of velocity, temperature, and species concentrations have been obtained with single point measurement techniques. These data have formed the bases for understanding many of the processes occurring in jet diffusion flames. Because of the success of the statistical approach there is a tendency to think about combustion processes in terms of time-averaged parameters. For engineering applications, there is a definite value, and in many cases, a necessity of thinking in terms of mean values of parameters. However, there is a danger to this line of thinking in that the mean and fluctuating quantities can, in many cases, mask the physics and chemistry that are germane to understanding the fundamental processes that give rise to the statistical results. This is particularly true for laminar and near-transitional jet flames in which the impact of large-scale, organized, buoyancy-induced vortices on the air side of the flame and the Kelvin-Helmholtz type vortex structures on the fuel side of the flame dominate the flame characteristics. To gain an insight into these processes, it is helpful and perhaps essential to think in terms of the dynamic characteristics of jet flames.

Several numerical investigations made in the past for dynamic jet flames using conserved-scalar approach, global-chemistry and detailed chemistry models have revealed important aspects of combustion such as effect of heat-release rate,[2,3] role of buoyancy,[4,5,6] enhancement of soot formation[7] and Lewis-number effects.[8,9] However, most of these studies involving finite-rate chemistry are limited to hydrogen fuel as the kinetic models for this fuel are relatively simple. On the other hand, because of the complex nature of the reaction mechanisms, flame calculations for hydrocarbon fuels are restricted to either steady-state problems[10,11] or chemically lazy flames in which chemistry is not important.[12] Simulation of dynamic hydrocarbon flames with sufficiently accurate models for physical and chemical processes is required for understanding the processes such as flame stabilization,[13] local extinction,[14] and ignition.[15] Recently, the authors have developed a time-accurate CFDC (computational Fluid Dynamics with Chemistry) code for investigating methane diffusion flames by incorporating detailed-chemical-kinetics model.

This paper describes a numerical study conducted using the CFDC code on coaxial methane jet diffusion flames formed under different flow conditions. Accuracy of three detailed chemical-kinetics models (Peters mechanism with and without C_2 chemistry and GRI Version 1.2 mechanism) in simulating a steady methane diffusion flame is assessed. The dynamic flames predicted by the CFDC code are compared with the experimental flame images obtained using Reactive-Mie-Scattering technique. The structure of the steady-state flame is compared with those of the dynamic flames to identify the impact of vortex-flame interactions in jet flames.

* Senior Engineer, AIAA Member
\+ Senior Scientist, AIAA Member

This paper is declared a work of the U.S. Government and is not subjected to copy right protection in the United States

Modeling:

In the mathematical model,[16,17] time-dependent Navier-Stokes equations are solved along with the species- and energy-conservation equations in an uncoupled manner on a staggered-grid cylindrical coordinate system. However, the species equations are solved by coupling them through the production terms. The body-force term due to the gravitational field is included in the axial-momentum equation. A clustered mesh system is employed to trace the large gradients in flow variables near the flame surface. Three different detailed chemical-kinetics model proposed in the literature for methane-air combustion are used in this study. The first one proposed by Peters[18] consists of 17 species (CH_4, O_2, CH_3, CH_2, CH, CH_2O, CHO, CO_2, CO, H_2, H, O, OH, H_2O, HO_2, H_2O_2, and N_2) that are involving in 52 elementary reactions. This mechanism is derived from the one originally published[18] for the hydrocarbon fuels up to propane in terms of carbon content and by neglecting the species that have more than one carbon elements. The second chemistry model is an extension of the first one obtained by including the C_2 chemistry which, adds 7 additional species (C_2H, C_2H_2, C_2H_3, C_2H_4, C_2H_5, C_2H_6, and CHCO) and 29 reactions to the first reaction model. Finally, the third chemical kinetics, GRI 1.2, used in the present study is the one compiled by the Gas Research Institute (GRI). This is the most comprehensive mechanism having 31 species and 346 elementary-reaction steps and is recommended by several investigators for computing methane flames. The enthalpies of all the species are calculated from the polynomial curve fits developed for the temperature range 300 - 5000 K. The physical properties such as viscosity, thermal conductivity and binary molecular diffusion coefficients of the species are calculated using molecular dynamics. Mixture viscosity and thermal conductivity are then estimated using the Wilke and Kee expressions, respectively. Molecular diffusion is assumed to be of binary type, and the diffusion velocity of a species is calculated according to Fick's law and using the effective-diffusion coefficient of that species. The Lennard Jones potentials, effective temperatures and the coefficients for the enthalpy polynomials for each species are obtained from the CHEMKIN libraries.

While the governing equations for momentum are integrated using an implicit QUICKEST (Quadratic Upstream Interpolation for Convective Kinematics with Estimated Streaming Terms) numerical scheme which is third-order accurate in both space and time and has a low numerical diffusion error, the species and energy equations are integrated using an hybrid scheme of upwind and central differencing.[19] An orthogonal, staggered grid system with rapidly expanding cell sizes in both the z and r directions is utilized for discretizing the governing equations. After rearrangement of terms, the finite-difference form of governing equation for the variable Φ at a grid point P is written as an algebraic equation as follows:

$$A_P \Phi_P^{N+1} + A_{z^{++}} \Phi_{z^{++}}^{N+1} + A_{z^+} \Phi_{z^+}^{N+1} + A_{z^-} \Phi_{z^-}^{N+1} + A_{z^{--}} \Phi_{z^{--}}^{N+1} + A_{r^{++}} \Phi_{r^{++}}^{N+1} + A_{r^+} \Phi_{r^+}^{N+1} + A_{r^-} \Phi_{r^-}^{N+1} + A_{r^{--}} \Phi_{r^{--}}^{N+1} = S_P^{\Phi} + \Delta t . \rho_P \Phi_P^N \qquad (1)$$

Here, the time increment, Δt, is determined from the stability constraint and maintained as a constant during the entire calculation. The superscripts N and N+1 represent the known variables at the N-th time step and the unknown variables at the (N+1)-th time step, respectively; the subscripts z^+ and z^- indicate the values at the grid points immediately adjacent to a point P in the positive and negative z-directions, respectively. Similarly, the subscripts z^{++} and z^{--} represent the values at two grid points away from P in the positive and negative z directions, respectively. The coefficients A and the terms on the right hand side of the above equation are calculated from the known flow variables at the N-th time step. The N_s+2 equations represented by Eq. (1) are solved individually using an iterative ADI (Alternative Direction Implicit) technique. Here, N_s represents the total number of species considered in the model. The pressure field at every time step is accurately calculated by simultaneously solving the system of algebraic pressure Poisson equations at all grid points using the LU (Lower-Upper) decomposition technique.

The flow field considered in the present study has vortical structures of two different scales. Small-scale vortices develop on the fuel side of the flame surface along the shear layer of the fuel jet and larger-scale vortices form on the air side of the flame surface. Unsteady axisymmetric calculations are made on a physical domain of 200 x 150 mm utilizing a 201 x 71 non-uniform grid system. Generally, the computational domain is bounded by the axis of symmetry and an outflow boundary in the radial direction and by the inflow and another outflow boundary in the axial direction. Flat velocity profiles were imposed at the fuel and air inflow boundaries. The outer boundaries in the z and r directions are located sufficiently far from the nozzle exit (~ 30 nozzle diameters) and the symmetry axis (~ 20 nozzle diameters), respectively, that the propagation of boundary-induced disturbances into the region of interest is minimized. An extrapolation procedure with weighted zero- and first-order terms is used to estimate the flow variables at the outflow boundary.[17]

Results and Discussion:

Because of the complex nature of the chemical kinetics for methane combustion, several mechanisms are available in the literature with varying degree of simplification. It is important to note that most of these mechanisms are validated using well-stirred reactor data (zero-dimensional problem) and counterflow flames (one-dimensional

problem). However, as the multidimensional flames in practical geometries are subjected to varying levels of strain rate, unsteadiness, curvature etc., the question of how well these chemistry models predict when they are incorporated into multidimensional flame problems needs to be addressed. Calculations are initially made for jet diffusion flames for different jet velocities using different chemical kinetics models available in the literature. Indeed, our initial attempts for the simulation of jet diffusion flames with simpler chemistry models such as in Ref. 20 resulted in unacceptable flame stand-off distances (separation between the flame base and the nozzle exit) for different fuel jet velocities. The most recent skeletal mechanism proposed by Peters for methane combustion (24 species and 81 reactions) yielded well attached flames for lower fuel jet velocities and failed to predict the flames that are formed at higher fuel jet velocities. It is found from the trial-and-error investigation on this mechanism that the methyl-radical recombination reaction (CH_3+H=CH_4) is very sensitive to the extinction and stand-off-distance characteristics of diffusion flames. When the reaction rate proposed by Peters for this reaction is replaced by the one proposed by Warnatz[21] excellent agreement between experiment and calculation is obtained over a wide range of fuel and annular air velocities. The mechanism obtained after replacing the rate data for methyl-radical-recombination reaction is denoted as "modified Peters mechanism" in this paper and is listed in Table. 1. The reaction that is different from the original Peters mechanism is R45 in this table.

Steady-State Flame:

The mathematical model and the numerical procedure used are tested for its accuracy in simulating a confined jet diffusion flame. This flame was previously studied experimentally by Mitchell[21] and using numerical methods by Smooke.[10] The burner assembly consists of a 12.7-mm-diameter central fuel tube and a large coannular air duct of 50.8-mm diameter. The burner is enclosed in a 300-mm long Pyrex tube. Therefore, the no-slip boundary condition is used at the end of the computational domain in the radial direction. Pure methane is used as the fuel. The flow rates for the fuel and the air are such that the velocities at the exits of the central fuel tube and the annulus air duct are 0.045 m/s and 0.0988 m/s, respectively. The experimental data on this methane jet diffusion flame obtained by Mitchell[22] suggest that the flame is in steady state and hence, Smooke[10] has performed steady-state axisymmetric calculations for this flame. Gravitational force, which is quite significant in this low-speed flame, is considered in Smooke's steady-state calculations. Our previous studies on vertically mounted jet diffusion flames under similar velocity conditions indicate that buoyancy-driven vortical structures could develop and make the flame unsteady. However, the flame investigated by Mitchell et al is confined and the ambient air flow into the flame is restricted; which, could suppress the growth of the buoyancy-induced instabilities. For comparison purpose, unsteady calculations are performed for this flame using the code described previously and with the three different chemistry models. Interestingly, the computed flame established weak vortical structures outside the flame surface. As these vortices convect downstream their interaction with the flame makes the latter to flicker. However, the oscillations (or unsteadiness) up to a height of 60 mm above the burner are quite weak. Calculations performed without using the Pyrex enclosure (i.e., replacing the wall boundary with the free outflow boundary) yielded much stronger fluctuations; which, suggests that confinement reduces the flame flicker.

The iso contours of radial velocity, temperature, and mole fractions of CH_3 and OH radicals are plotted in Figs. 1-4, respectively. The flow fields computed with the three chemistry models; namely, modified Peters mechanism without C_2 chemistry [Fig. 1(a)], modified Peters mechanism with C_2 chemistry [Fig. 1(b)], and GRI 1.2 mechanism [Fig. 1(c)] are quite similar. Weak oscillations resulting from the buoyancy-induced instability are evident from the slightly squeezed iso-radial contours between z = 30 and 50 mm.

All three chemistry models have predicted same temperature distributions (Fig. 2) on the air side of the flame (r > 6.5 mm). However, on the fuel side, GRI mechanism is predicting lower temperatures compared to the other two modified Peters mechanisms. In fact, the peak temperature of 2040 K predicted by GRI chemical kinetics is 50 K less than that obtained with Peters mechanism without C_2 chemistry and ~20 K less than that obtained with C_2 chemistry. These results suggest that the formation of higher hydrocarbons effect the flame structure on the fuel side of a jet diffusion flame. This is also evident in the methyl-radical concentration plots of Fig. 4. Here, CH_3 is confined to the fuel side and inclusion of C_2 chemistry reduced its concentration [compare Figs. 4(a) and 4(b)]. The peak concentration for CH_3 radicals predicted by Peters mechanism with C_2 chemistry (~0.006) is very close to that predicted with GRI 1.2 mechanism. Interestingly, all three kinetics models yielded similar distributions for OH radical concentration (Fig. 3). As expected, the location for the peak OH concentration is found to be shifted from the peak-temperature location and is on the air side.

The model predictions are compared with the measured values of Mitchell et al[22] in Figs. 5-7. In each figure, the data collected at three heights, z = 12 mm, 24 mm, and 50 mm are compared. Figure 5 compares temperature and axial velocity while, Figs. 6 and 7 show comparisons for some species concentrations.

The experiments of Mitchell et al indicate that noticeable amount of oxygen is present in the potential core of the flame at z = 12 mm [Fig. 6(a)]. Calculations made with C_2 chemistry and GRI mechanism have well predicted this feature of the diffusion flame. The decrease in measured oxygen concentration with radial distance in the potential core suggests that the observed oxygen on the fuel side of

Table 1. Modified Peters Mechanism

Reaction	A (Mole, cm^3,s)	n	E (cal/ mole)
H_2/O2 Chain Reactions			
(R01) $H + O_2 \Rightarrow OH + O$	2.00E+14	0.0	16,800
(R02) $OH + O \Rightarrow H + O_2$	1.57E+13	0.0	840
(R03) $O + H_2 \Rightarrow OH + H$	5.06E+04	2.67	6,280
(R04) $OH + H \Rightarrow O + H_2$	2.22E+04	2.67	4,370
(R05) $H_2 + OH \Rightarrow H_2O + H$	1.00E+08	1.60	3,300
(R06) $H_2O + H \Rightarrow H_2 + OH$	4.31E+08	1.60	18,270
(R07) $OH + OH \Rightarrow O + H_2O$	1.50E+09	1.14	100
(R08) $H_2O + O \Rightarrow OH + OH$	1.47E+10	1.14	17,000
H_2O Formation and Consumption			
(R09) $O_2 + H + M \Rightarrow HO_2 + M$	2.30E+18	-0.8	0
(R10) $HO_2 + M \Rightarrow O_2 + H + M$	3.19E+18	-0.8	46,680
(R11) $HO_2 + H \Rightarrow OH + OH$	1.50E+14	0.0	1,000
(R12) $HO_2 + H \Rightarrow H_2 + O_2$	2.50E+13	0.0	692
(R13) $HO_2 + OH \Rightarrow H_2O + O_2$	6.00E+13	0.0	0
(R14) $HO_2 + H \Rightarrow H_2O + O$	3.00E+13	0.0	1,720
(R15) $HO_2 + O \Rightarrow OH + O_2$	1.80E+13	0.0	-406
H_2O_2 Formation and Consumption			
(R16) $HO_2 + HO_2 \Rightarrow H_2O_2 + O_2$	2.50E+11	0.0	-1,240
(R17) $OH + OH + M \Rightarrow H_2O_2 + M$	3.25E+22	-2.0	0
(R18) $H_2O_2 + M \Rightarrow OH + OH + M$	1.69E+24	-2.0	48,330
(R19) $H_2O_2 + H \Rightarrow H_2O + OH$	1.00E+13	0.0	3,580
(R20) $H_2O_2 + OH \Rightarrow H_2O + HO_2$	5.40E+12	0.0	1,000
(R21) $H_2O + HO_2 \Rightarrow H_2O_2 + OH$	1.80E+13	0.0	32,190
Recombination Reactions			
(R22) $H + H + M \Rightarrow H_2 + M$	1.80E+13	-1.0	0
(R23) $H + OH + M \Rightarrow H_2O + M$	2.20E+22	-2.0	0
(R24) $O + O + M \Rightarrow O_2 + M$	2.90E+17	-1.0	0
CO/CO_2 Mechanism			
(R25) $CO + OH \Rightarrow CO_2 + H$	4.40E+06	1.5	-740
(R26) $CO_2 + H \Rightarrow CO + OH$	4.96E+08	1.5	21,440
CH Consumption Reactions			
(R27) $CH + O_2 \Rightarrow CHO + O$	3.00E+13	0.0	0
(R28) $CO_2 + CH \Rightarrow CHO + CO$	3.40E+12	0.0	692
CHO Consumption Reactions			
(R29) $CHO + H \Rightarrow CO + H_2$	2.00E+14	0.0	0
(R30) $CHO + OH \Rightarrow CO + H_2O$	1.00E+14	0.0	0
(R31) $CHO + O_2 \Rightarrow CO + HO_2$	3.00E+12	0.0	0
(R32) $CHO + M \Rightarrow CO + H + M$	7.10E+14	0.0	16,800
(R33) $H + CO + M \Rightarrow CHO + M$	1.14E+15	0.0	2,380
CH_2 Consumption Reactions			
(R34) $CH_2 + H \Rightarrow CH + H_2$	8.40E+09	1.5	335
(R35) $CH + H_2 \Rightarrow CH_2 + H$	5.83E+09	1.5	3,125
(R36) $CH_2 + O \Rightarrow CO + H + H$	8.00E+13	0.0	0
(R37) $CH_2 + O_2 \Rightarrow CO + OH + H$	6.50E+12	0.0	1,500
(R38) $CH_2 + O_2 \Rightarrow CO_2 + H + H$	6.50E+12	0.0	1,500
CH_2O Consumption Reactions			
(R39) $CH_2O + H \Rightarrow CHO + H_2$	2.50E+13	0.0	3,990
(R40) $CH_2O + O \Rightarrow CHO + OH$	3.50E+13	0.0	3,490
(R41) $CH_2O + OH \Rightarrow CHO + H_2O$	3.00E+13	0.0	1,200
(R42) $CH_2O + M \Rightarrow CHO + H + M$	1.40E+17	0.0	76,500
CH_3 Consumption Reactions			
(R43) $CH_3 + H \Rightarrow CH_2 + H_2$	1.80E+14	0.0	15,050
(R44) $CH_2 + H_2 \Rightarrow CH_3 + H$	3.68E+13	0.0	10,580
(R45) $CH_3 + H \Rightarrow CH_4$ K_∞	6.00E+16	-1.0	0
K_0	6.26E+23	-1.8	0
(R46) $CH_3 + O \Rightarrow CH_2O + H$	7.00E+13	0.0	0
(R47) $CH_3 + CH_3 \Rightarrow C_2H_6$ K_∞	3.61E+13	0.0	0
K_0	1.27E+41	-7.0	2,762
(R48) $CH_3 + O_2 \Rightarrow CH_2O + OH$	3.40E+11	0.0	8,940
(R49) $CH_3 + H_2 \Rightarrow CH_4 + H$	8.39E+02	3.0	8,260
(R50) $CH_3 + H_2O \Rightarrow CH_4 + OH$	2.63E+05	2.10	16,950
CH_4 Consumption Reactions			
(R51) $CH_4 + H \Rightarrow CH_3 + H_2$	2.20E+04	3.0	8,740
(R52) $CH_4 + O \Rightarrow CH_3 + OH$	1.20E+07	2.1	7,620
(R53) $CH_4 + OH \Rightarrow CH_3 + H_2O$	1.60E+06	2.1	2,460
C_2H Consumption Reactions			
(R54) $C_2H + H_2 \Rightarrow C_2H_2 + H$	1.10E+13	0.0	2,867
(R55) $C_2H_2 + H \Rightarrow C_2H + H_2$	5.27E+13	0.0	28,656
(R56) $C_2H + O_2 \Rightarrow CHCO + O$	5.00E+13	0.0	1,505
CHCO Consumption Reactions			
(R57) $CHCO + H \Rightarrow CH_2 + CO$	3.00E+13	0.0	0
(R58) $CH_2 + CO \Rightarrow CHCO + H$	2.36E+12	0.0	-7,021
(R59) $CHCO + O \Rightarrow CO + CO + H$	1.00E+14	0.0	0
C_2H_2 Consumption Reactions			
(R60) $C_2H_2 + O \Rightarrow CH_2 + CO$	4.10E+08	1.5	1,696
(R61) $C_2H_2 + O \Rightarrow CHCO + H$	4.30E+14	0.0	12,112
(R62) $C_2H_2 + OH \Rightarrow C_2H + H_2O$	1.00E+13	0.0	7,000
(R63) $C_2H + H_2O \Rightarrow C_2H_2 + OH$	9.00E+12	0.0	-3,818
C_2H_3 Consumption Reactions			
(R64) $C_2H_3 + H \Rightarrow C_2H_2 + H_2$	3.00E+13	0.0	0
(R65) $C_2H_3 + O_2 \Rightarrow C_2H_2 + HO_2$	5.40E+11	0.0	0
(R66) $C_2H_3 \Rightarrow C_2H_2 + H$ K_∞	2.00E+14	0.0	39,717
K_0	1.19E+42	-7.5	45,486
(R67) $C_2H_2 + H \Rightarrow C_2H_3$ K_∞	1.05E+14	0.0	810
C_2H_4 Consumption Reactions			
(R68) $C_2H_4 + H \Rightarrow C_2H_3 + H_2$	1.50E+14	0.0	10,201
(R69) $C_2H_3 + H_2 \Rightarrow C_2H_4 + H$	9.61E+12	0.0	7,800
(R70) $C_2H_4 + O \Rightarrow CH_3 + CO + H$	1.60E+09	1.2	741
(R71) $C_2H_4 + OH \Rightarrow C_2H_3 + H_2O$	3.00E+13	0.0	3,010
(R72) $C_2H_3 + H_2O \Rightarrow C_2H_4 + OH$	8.29E+12	0.0	15,576
(R73) $C_2H_4 + M \Rightarrow C_2H_2 + H_2 + M$	2.50E+17	0.0	76,400
C_2H_5 Consumption Reactions			
(R74) $C_2H_5 + H \Rightarrow CH_3 + CH_3$	3.00E+13	0.0	0.0
(R75) $CH_3 + CH_3 \Rightarrow C_2H_5 + H$	3.57E+12	0.0	11,870
(R76) $C_2H_5 + O_2 \Rightarrow C_2H_4 + HO_2$	2.00E+12	0.0	4,993
(R77) $C_2H_5 \Rightarrow C_2H_4 + H$ K_∞	2.00E+13	0.0	39,657
K_0	1.00E+17	0.0	31,057
(R78) $C_2H_4 + H \Rightarrow C_2H_5$ K_∞	3.19E+13	0.0	3,013
C_2H_6 Consumption Reactions			
(R79) $C_2H_6 + H \Rightarrow C_2H_5 + H_2$	5.40E+02	3.5	5,208
(R80) $C_2H_6 + O \Rightarrow C_2H_5 + OH$	3.00E+07	2.0	5,112
(R81) $C_2H_6 + OH \Rightarrow C_2H_5 + H_2O$	6.30E+06	2.0	645

the flame should have been transported from upstream locations. However, in order this to occur the flame at the base (or burner exit) should not be completely attached to the burner such that oxygen enters the potential core through the dark space between the flame base and the burner. The computed temperature distribution (obtained with modified Peters C_1 chemistry) plotted in Fig. 2(a) indicates that the flame is closer to the nozzle compared to the other two flames in Figs. 2(b) and 2(c) which, in turn, leads to lower oxygen concentration in the potential core in Fig. 6(a). As the stand-off distance between the nozzle exit and the flame base depends on the heat transfer to the burner and the nozzle geometry; which are not modeled in the present study, one should not conclude based on the oxygen data in the fuel jet that one mechanism is better than the other.

Considering the limitations of the present CFDC model and the uncertainty in the experimental data, it may be viewed that all the three chemical mechanisms are yielding reasonably accurate flame structures. However, because of the higher number of species and reaction steps, calculations with GRI mechanism (31 species and 346 reaction) required cpu times 5 times more than that required for the calculations made with Peters mechanism (17 species and 52 reactions) and 3 times more than that required for Peters mechanism with C_2 chemistry (24 species and 81 reactions). Because of the limitations of the computer resources, calculations for the dynamic flames are made with Peters mechanism with C_2 chemistry and the results are discussed in the following sub section.

Dynamic Flames:

The experimental set-up consist of vertically mounted coannular jets and is described in Ref. 23. The central fuel jet is a 25.4 mm diameter tube which contracts to a 10 mm diameter nozzle. The nozzle is designed to provide a flat mean velocity profile with low velocity fluctuations at the nozzle exit. The annulus air jet has a diameter of 245 mm. An air velocity of 15 cm/s is used to reduce the room air disturbances in the first 15 diameters of the jet exit while not causing a significant effect on the visible flame structure. Two flames are investigated experimentally and numerically. The first one has a fuel jet velocity of 0.5 m/s and the second flame has a velocity of 4.1 m/s.

An instantaneous image of the low-speed flame obtained with the Reactive-Mie-scattering (RMS) technique[23] is shown in Fig. 8(a). With this method micron-sized TiO_2 particles, formed from the spontaneous reaction between the seeded-$TiCl_4$ vapor and the water vapor produced during combustion, are visualized by the Mie-scattered light from a laser sheet. $TiCl_4$ is seeded into both the fuel and annulus-air flows. The bright orange region in Fig. 8(a) is the luminous flame surface captured simultaneously with the Mie-scattered light.

Because of the gravity term in the axial-momentum equation and the low-speed annulus air flow, solution of the governing equations resulted in a dynamic flame, with large toroidal vortices forming naturally outside the flame surface. The computed instantaneous temperature field is shown in Fig. 8(b). The flame (or peak-temperature) surface which is identified from the temperature field is also shown in this figure using white solid circles. It is important to note that no artificial perturbation is required for the formation of the outer vortices. In the presence of gravitational force, acceleration of hot gases along the flame surface generated the outer structures as part of the solution. The frequency corresponding to the passage of these outer vortices (also known as flame flickering frequency) is close to 12 Hz. The instantaneous locations of the particles that are released along with the fuel are also shown in this figure with yellow dots. The predicted flame structure compares very well with that obtained in experiments using RMS technique. The counter-rotating toroidal vortex (at z = 140 mm in Fig. 8) that is formed due to the strong rotation of the upstream buoyancy-induced vortex is well captured by the model.

Instantaneous flame structure obtained for the higher (or transitional) fuel jet velocity case is compared with the RMS image of the experimental flame in Fig. 9. As expected, buoyancy-driven vortical structures have formed outside the flame surface in this case also and the convective frequency for these structures is found to be about 13 Hz. Interestingly, the experimental flame shows vortical structures inside the flame in addition to the outer ones. These are believed to manifest from the small perturbations that are inherent in the high-speed fuel flow and the Kelvin-Helmholz instability of the shear layer. In order to initiate and sustain the Kelvin-Helmholtz instabilities in the calculations, constant external forcing in the form of background random noise (3% of jet velocity) is used at the exit of the fuel jet. The inner vortical structures are found to grow slowly and maintain their identities over a long distance. At farther downstream locations, these vortices are dissipated with the entrainment of viscous combustion products from the flame surface.

In both the low- and transitional-speed flames (Figs. 8 and 9) it should be noted that the convective motion of the outer vortices interact with the flame surface and make it wrinkle. These interactions perturb not only the shape but also the chemical structure of the flame. For visualizing the effects of vortex-flame interactions on flame structure, scatter plots for temperature and species concentrations are shown in Fig. 10(c) and 10(d) for low-speed dynamic flame and in Figs. 10(e) and 10(f) for transitional-speed flame. For comparison purpose, the corresponding plots for the steady-state flame are shown in Figs. 10(a) and 10(b). These scatter plots represent the data collected first along the radial lines at several flame heights and then converting them into mixture fraction coordinate. Here, mixture fraction (ξ) is defined as the net mass present at any location that is originated from the fuel jet.

In general, for a steady-state flame the temperature and fuel and oxygen concentrations are yielding self similar

solutions in mixture-fraction domain. However, this is not true with respect to the intermediate species that are generated in the flame zone [c.f. Fig. 10(b)]. It is believed that the finite-rate chemistry in combination with the varying convective velocities at different flame heights is causing the species distributions depend not only on mixture fraction but also on the flame height. As expected, these deviations are more on the fuel side (ξ >0.055) for CH_3 and on the air side (ξ <0.055) for OH radicals.

Vortex-flame interactions in the two dynamic flames resulted in scattered data for every variable shown in Figs. 10(c)-10(f). Flame temperature is increased at certain phases of the interaction and decreased at the other phases. These results are similar to the ones obtained for hydrogen jet diffusion flames[8] in which, non-unity Lewis numbers are found responsible for such behavior. Since, Lewis number of methane is less than unity (similar to that of hydrogen), one might expect both the hydrogen and methane flames to behave similarly during vortex-flame interactions. As the inner vortices in transitional-speed flame are not quite close to the flame surface, their impact on the flame structure is not evident in temperature or in major species concentrations. As CH_3 is located mostly on the fuel side, these inner vortices are resulting more scatter in its concentration [Fig. 10(f)].

Conclusions:

Accurate dynamic simulations using detailed-chemical-kinetics models for hydrocarbon fuels are needed for understanding flame structure and various processes involved in laminar and transitional jet flames. An axisymmetric, time-dependent CFDC code is developed for the simulation of methane jet diffusion flames. Calculations are performed for a steady-state flame and for two dynamic flames that were investigated experimentally in the past. It is found that the modified Peters mechanism with and without C_2 chemistry are sufficient for the simulation of jet flames. Very good predictions are made using C_2 chemistry for the periodically oscillating flames that are dynamic due to the buoyancy-induced instabilities. Based on the scatter plots made from the data collected at several heights in the steady-state flame it is found that temperature and fuel and oxygen concentrations collapse on to a single curve in the mixture-fraction coordinates whereas, the intermediate-species concentrations don't follow this. It is also found that the temperature in buoyancy-dominated unsteady methane flames increases at certain phases of vortex-flame interaction which is, similar to that observed in an hydrogen flame.

Acknowledgment:

This work was supported, in part, by Air Force Contract F33615-95-C-2507 and the Air Force Office of Scientific Research.

References:

1. Hottel, H. C. and Hawthorne, W. R., "Diffusion in Laminar Flame Jets," *Third Symposium (International) on Combustion*, Flame and Explosive Phenomena, pp 254-266, 1949.

2. Ellzey, J. L., Laskey, K. J., and Oran, E. S., *Progress in Astronautics and Aeronautics*. American Institute of Aeronautics and Astronautics, Washington, D. C., 1989, Vol. 131, p. 179.

3. Yamashita, H., Kushida, G., and Takeno, T., *Proc. of Royal Soc. of London A* 431:301-314 (1990).

4. Davis, R. W., Moore, E. F., Roquemore, W. M., Chen, L.-D., Vilimpoc, V., and Goss, L. P. *Combust. Flame* , Vol. 83, 1991, p. 263.

5. Katta V. R., Goss, L. P., and Roquemore, W. M., *Combusti. Flame* 96:60-74 (1994).

6. Patnaik, G, and Kailasnath, K., Numerical Simulations of Burner-Stabilized Hydrogen-Air Flames in Microgravity, Presented at the 25th International Symposium on Combustion, Irvine, CA, July 31-August 5, 1995.

7. Kaplan, C. R., Oran, E. S., Kailasnath, K., and Ross, H. D., Gravitational Effects on Sooting Diffusion Flames, Presented at the 26th International Symposium on Combustion, Napoli, Italy, July 28-August 2, 1996.

8. Katta, V. R., Goss, L. P., and Roquemore W. M.; Effect of Nonunity Lewis number and Finite-Rate Chemistry on the Dynamics of a Hydrogen-Air Jet Diffusion Flame, *Combustion and Flame*, Vol. 96, No. 1-2, 1994, pp. 60-74.

9. Takagi T., and Xu, Z., *Combustion and Flame*, Vol. 96, Nos. 1 and 2, Jan., 1994, p.50-59

10. Smooke, M. D., "Numerical Modeling of Laminar Diffusion Flames," in *Numerical Approaches to Combustion Modeling*, Edited by E, S. Oran and J. P. Boris, Vol. 135, Progress in Aeronautics and Astronauts, AIAA, 1991, Washington, D.C.

11.Takagi, T., Yoshikawa, Y., Yoshida, K., Komiyama, and Kinoshita, S., Studies on Strained Nonpremixed Flames Affected by Flame Curvature and Preferential Diffusion, Presented at the 25th International Symposium on Combustion, Irvine, CA, July 31-August 5, 1995.

12. Katta, V. R., Goss, L. P., Roquemore, W. M., and Chen, L. D., Dynamics of Propane Jet Diffusion Flames, Submitted to Atlas of Flow Visualization, Vol. 3, The Visualization Society of Japan, 1996.

13) Takahashi, F., and Schmoll, W. J., "Lifting Criteria of Jet Diffusion Flames," *Twenty-Third Symposium (International) on Combustion*, The Combustion Institute, Pittsburgh, Pennsylvania, 1991.

14. Katta, V. R., Hsu, K. Y., and Roquemore, W. M., Simulation of Local Quenching in a Methane-Air Jet Diffusion Flame, Proceedings of the 1996 Fall Technical Meeting of the Eastern States Section of the Combustion Institute, Hilton Head, SC, Dec. 9-11, 1996, pp. 381-384.

15. Law, C. K., Heat and Mass Transfer in Combustion: Fundamental Concepts and Analytical Techniques, Progress in Energy and Combustion sciences, Vol. 10, 1984, pp. 295-318.

16. Katta, V. R., Goss, L. P., and Roquemore, W. M.; Numerical Investigations of Transitional H_2/N_2 Jet Diffusion Flames, *AIAA Journal*, Vol. 32, No. 1, 1994, pp. 84-94.

17. Katta, V. R., Goss, L. P., and Roquemore, W. M., Simulation of Vortical Structures in a Jet Diffusion Flame, International Journal of Numerical Methods for Heat and Fluid Flow, Vol. 4, No. 5, 1994, p. 413.

18. Peters, N., "Flame Calculations with Reduced Mechanisms--An Outline," in *Reduced Kinetic Mechanisms for Applications in Combustion Systems*, Lecture Notes in Physics, 1993, Springer-Verlag, New York.

19. Leonard, B. P., *Computational Methods in Applied Mechanics and Engineering* , Vol. 19, p. 59, 1979.

20. Peters, N., Lecture Notes in Physics 241, Springer, Berlin-Heidelberg, 1985, pp. 90.

21. Warnatz, J., Combustion Chemistry (W. C. Gardiner, Ed.) Springer-Verlag, New York, 1984, p. 197.

22. Mitchell, R. E., Sarofim, A. F., and Clomburg, L. A., "Experimental and Numerical Investigation of Confined Laminar Diffusion Flames," *Combustion and Flame*, Vol. 37, pp. 227-244, 1980.

23. Roquemore, W. M., Chen, L.-D., Goss, L. P., and Lynn, W. F., "Structure of Jet Diffusion Flames," *Turbulent Reactive Flows*, Lecture Notes in Engineering. Vol. 40, pp. 49-63, 1988.

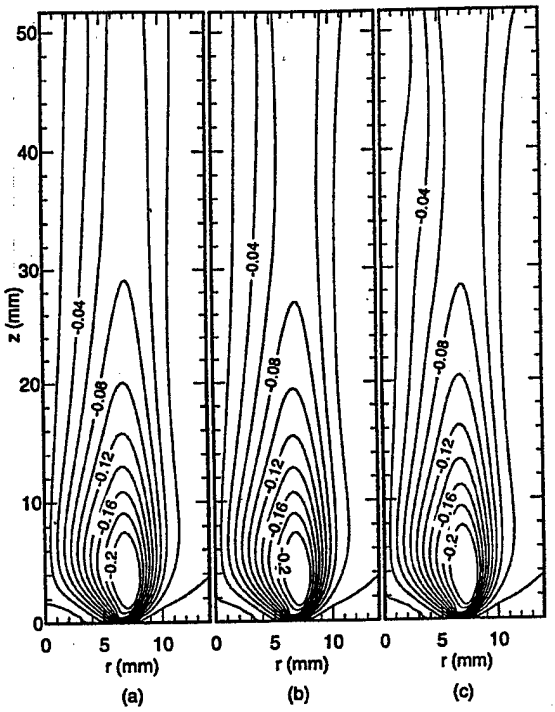

Fig. 1. Comparison of radial-velocity distributions obtained with (a) Peters mechanism with C_1 chemistry, (b) Peters mechanism with C_2 chemistry and (c) GRI 1.2 chemistry.

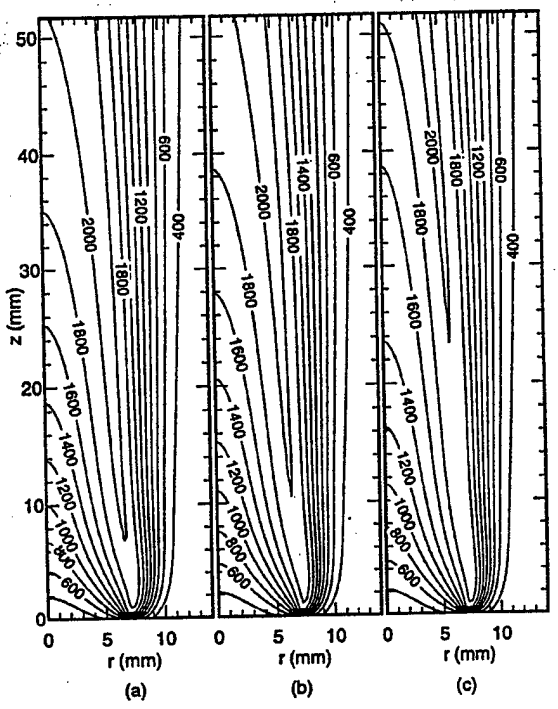

Fig. 2. Temperature distributions obtained with (a) Peter's mechanism with C_1 chemistry, (b) Peters mechanism with C_2 chemistry and (c) GRI 1.2 chemistry.

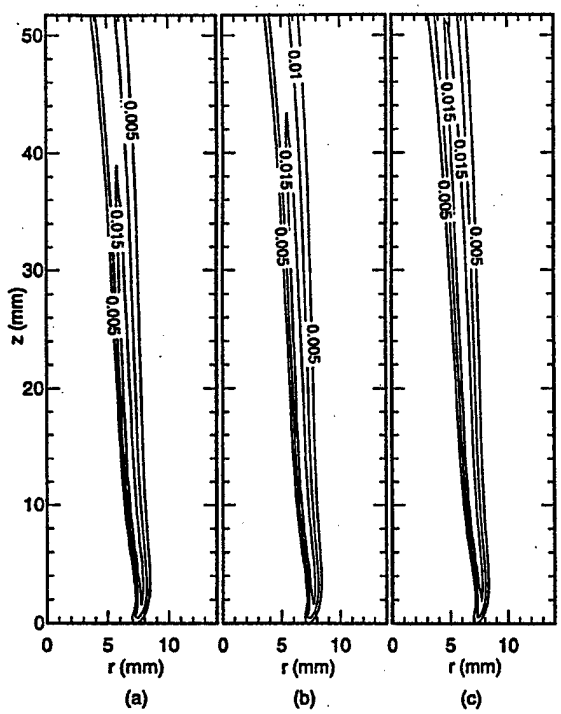

Fig. 3. OH-radical mole-fraction distributions obtained with (a) Peters mechanism with C_1 chemistry, (b) Peters mechanism with C_2 chemistry and (c) GRI 1.2 chemistry.

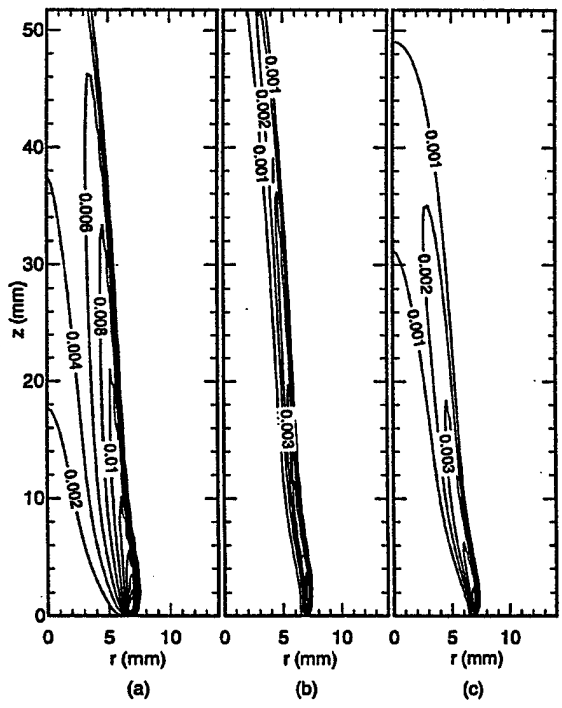

Fig. 4. Computed methyl-radical (CH_3) distributions with (a) Peters mechanism with C_1 chemistry, (b) Peters mechanism with C_2 chemistry and (c) GRI 1.2 chemistry.

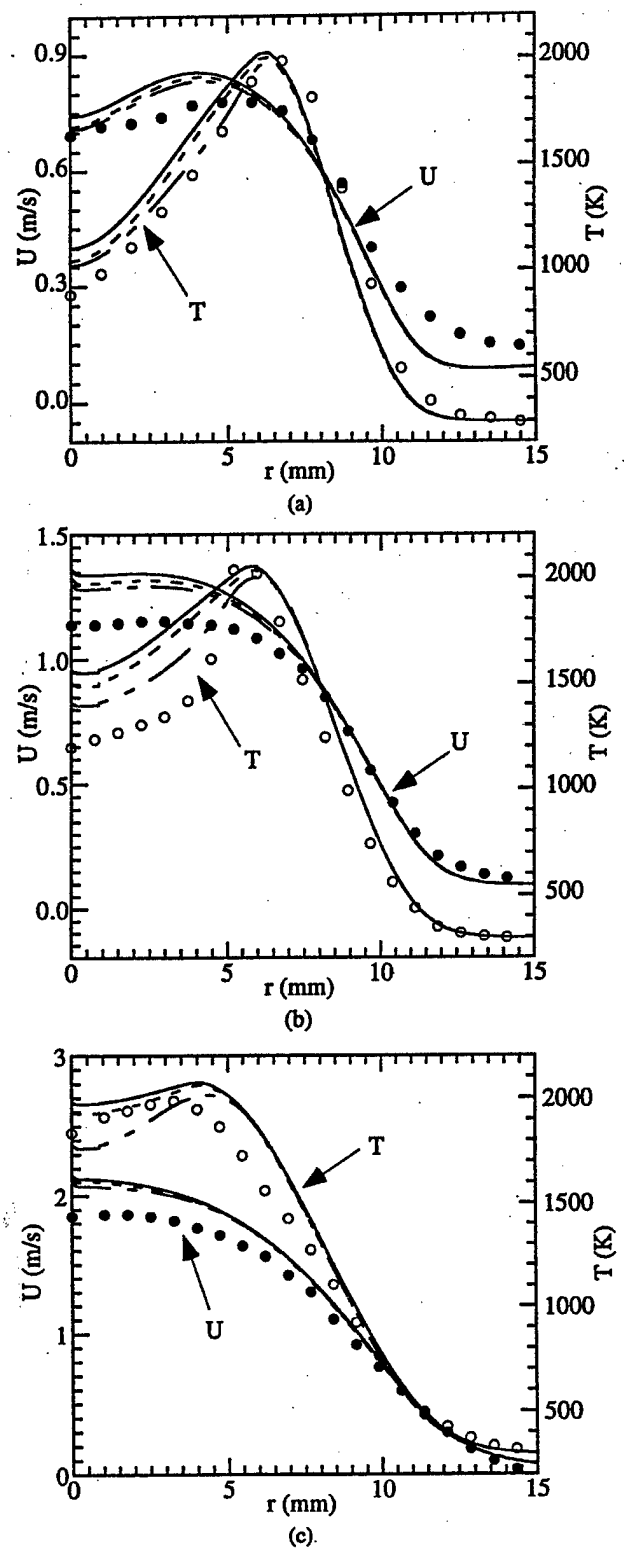

Fig. 5. Comparison of measured temperature and axial velocity with those predicted using different chemistry models at flame heights of (a) 12, (b) 24 and (c) 50 mm. Symbols represent experimental data. Solid, broken and long-broken lines represent predictions made with C_1 Peters, C_2 Peters, and GRI mechanisms, respectively.

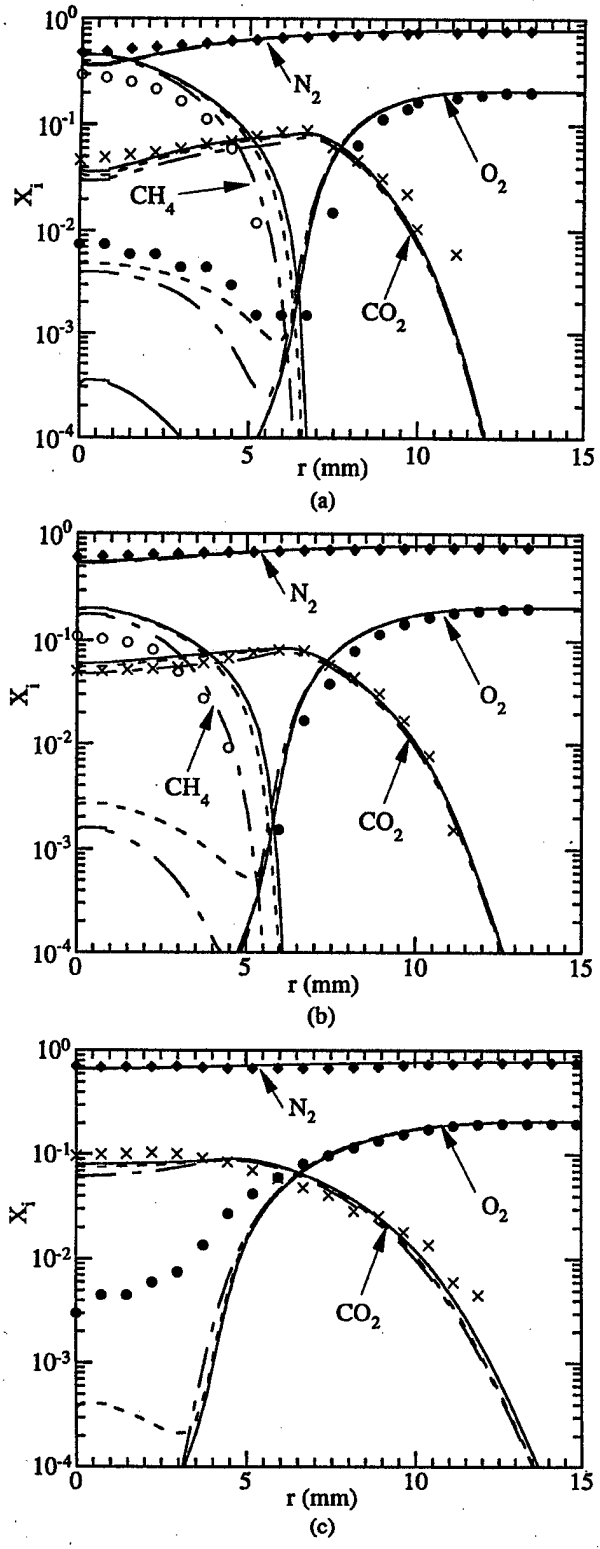

Fig. 6. Comparison of measured major species concentrations with those predicted using different chemistry models at flame heights of (a) 12, (b) 24 and (c) 50 mm. Legend is similar to that of Fig. 5.

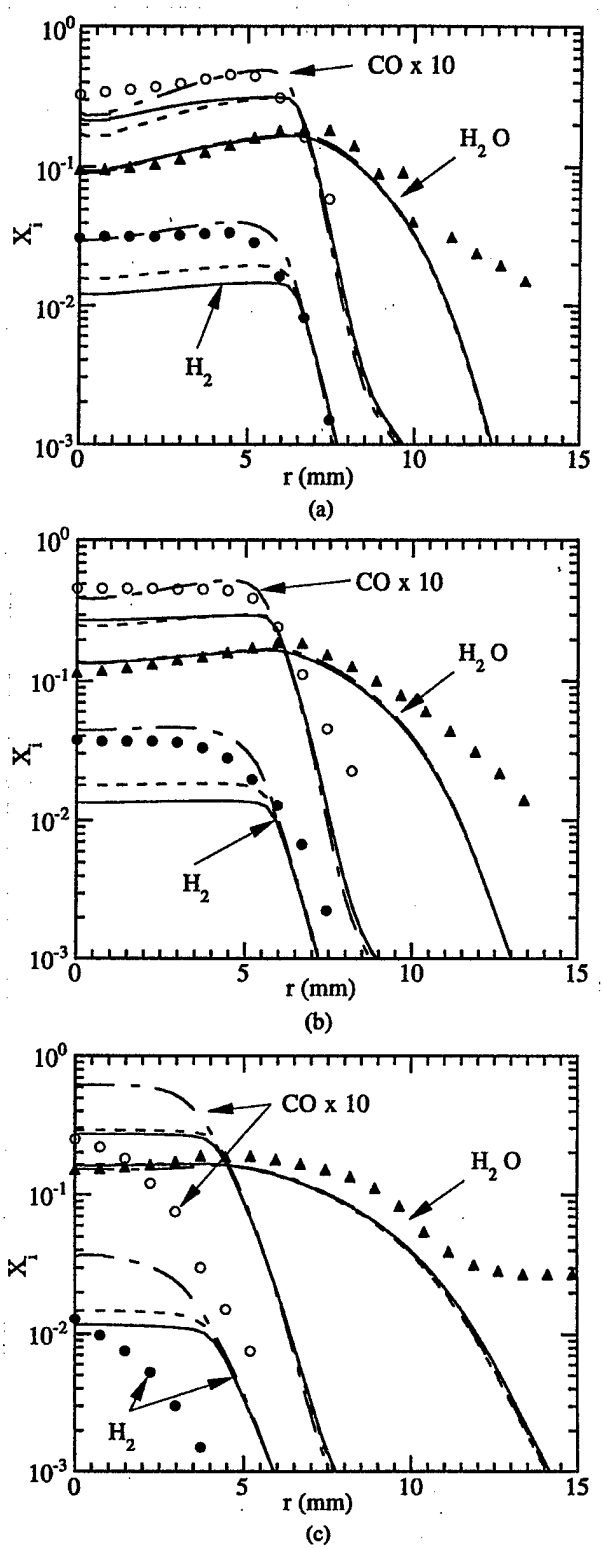

Fig. 7. Comparison of minor species concentrations predicted using different chemistry models with those measured at flame heights of (a) 12, (b) 24 and (c) 50 mm. Legend is similar to that of Fig. 5.

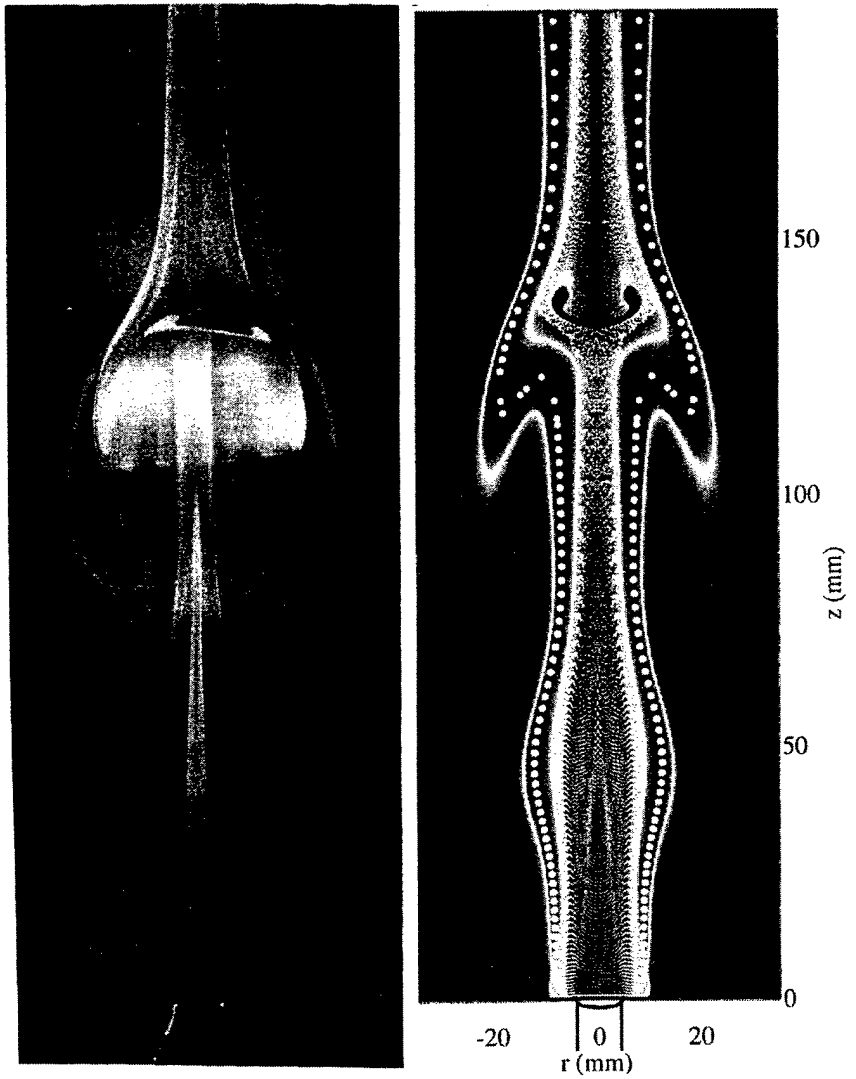

Fig. 8. Instantaneous images of experimental and computed low-speed dynamic flame. U_{jet} = 0.5 m/s, U_{air} = 0.15 m/s. (a) Reactive-Mie-Scattering image showing naturally formed vortical structures (green) and soot surface (orange) and (b) locations of particles (yellow) superimposed on computed temperature field (rainbow colors). White solid circles represent high-temperature surface.

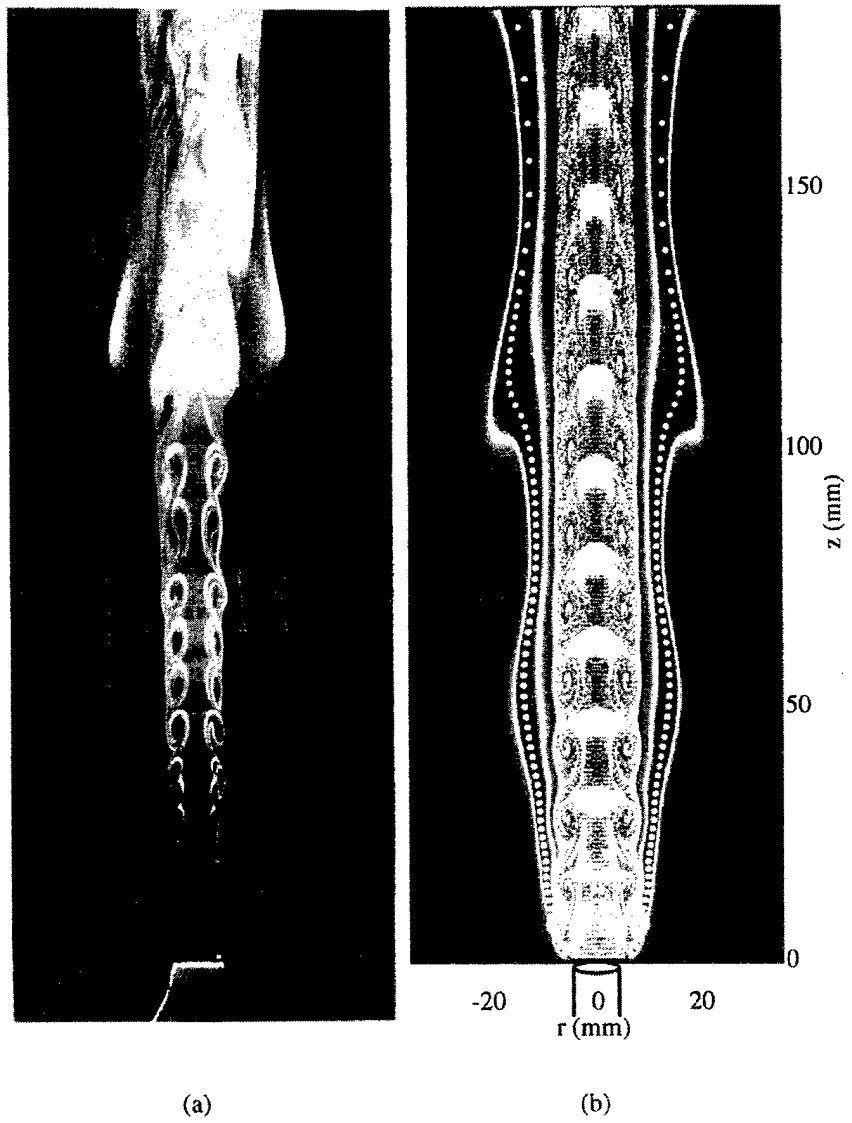

Fig. 9. Instantaneous images of experimental and computed transitional-speed dynamic flame. U_{jet} = 4.1 m/s, U_{air} = 0.15 m/s. (a) Reactive-Mie-Scattering image showing outer and inner vortices (green) and soot surface (orange) and (b) locations of particles (yellow) superimposed on the computed temperature field (rainbow colors). White solid circles represent the high-temperature surface.

Twenty-Seventh Symposium (International) on Combustion/The Combustion Institute, 1998/pp. 1121–1129
PUBLISHED WITH PERMISSION

LOCAL EXTINCTION IN AN UNSTEADY METHANE-AIR JET DIFFUSION FLAME

V. R. KATTA,[1] K. Y. HSU[1] AND W. M. ROQUEMORE[2]
[1]*Innovative Scientific Solutions, Inc.*
2766 Indian Ripple Road
Dayton, OH 45440-3638, USA
[2]*Propulsion Directorate*
Air Force Research Laboratory
Wright-Patterson Air Force Base
Dayton, OH 45433-7103, USA

Vortex–flame interactions constitute important elements of a turbulent flame and are building blocks for the development of turbulent-flame models. When a vortex originating inside the flame has sufficiently high normal velocity, it can pass through the flame, creating a localized hole in which no chemical reactions take place. An experimental and numerical investigation was conducted in an attempt to understand the local quenching process associated with the vortex–flame interaction in a methane jet diffusion flame. Axisymmetric toroidal vortices were generated periodically in a low-speed, laminar jet diffusion flame by driving the fuel jet at a frequency of 30 Hz. A time-dependent, axisymmetric computational fluid dynamics with chemistry (CFDC) model that incorporates detailed finite-rate chemistry for CH_4-O_2 combustion was developed for the simulation of this unsteady jet diffusion flame. The code was validated by direct simulation of an axisymmetric counterflow diffusion flame for different exit velocities. These calculations were found to yield more reliable predictions than those from conventional one-dimensional analyses. An accurate prediction for the quenching limit was made by replacing the rate expression of Peters for the chain termination reaction involving methyl radicals with that recommended by Warnatz. Calculations were made for the unsteady, coflowing, jet diffusion flame, and the local and temporal quenching processes observed during the vortex–flame interaction were successfully simulated. The structures of the weakly strained and near-quenching-limit flames were studied for the counterflow and coflow configurations. An order-of-magnitude increase in the production and destruction rates of methyl and oxygen radicals, respectively, was found in the flame zone of the coflowing, jet diffusion flame as it is strained to near-quenching limit—which is in contrast with that observed in a counterflow diffusion flame.

Introduction

In the design of gas-turbine combustors, characteristics of practical importance are lean blowout, high-altitude relight, emissions, and combustion efficiency. If accurate combustor design models are to be developed, a better understanding of the turbulent-chemistry interactions involved in these characteristics is required. Turbulent jet diffusion flames are often studied to gain the insight needed to develop such interaction models. The classical definition of an unconfined turbulent jet diffusion flame is provided by Hottel and Hawthorne [1]; that is, a vertically mounted jet diffusion flame is considered to be fully turbulent when its entire surface area becomes a flame brush, which means that the flame has a highly wrinkled, bumpy, or rough appearance.

Improved visualization techniques have provided additional insight into the structure of a turbulent flame and the events occurring as the flame becomes turbulent [2]. The wrinkles or bumps in the flame are observed to be localized protrusions of the flame surface that result when three-dimensional fluid elements (often associated with vortices) of different size, shape, velocity, and rotational strength interact with reaction zones of different thickness. This interaction processes is commonly referred to as the vortex–flame interaction.

An understanding of vortex–flame interactions [3] is important for several reasons. First, these interactions can increase or decrease the turbulent reaction rate. When vortex–flame interactions are moderate, they increase the surface area of the flame that leads to an overall increase in the global reaction rate and a reduction in the length of the flame. However, if a vortex retains sufficiently high normal velocity after traveling through the viscous combustion products, then it can pass through the flame by creating a localized hole in which no chemical reactions take place [4,5]. When these holes form near the jet exit, they can cause the flame to split or lift. If the holes cover a significant portion of the flame surface,

the global reaction rate can decrease, which can lead to a reduction in combustion efficiency and blowout. Second, vortex–flame interactions are considered to be building blocks for statistical theories of turbulent flames. It is conceivable that one might consider an ensemble of only a few basic types of vortex–flame interactions to gain an accurate representation of the statistical result of what might appear on first sight to be an endless number of interactions. If this idea is supported by experimental results, it may be feasible to construct a statistical turbulent-combustion model.

This paper describes a numerical and experimental study on a particular type of flame–vortex interaction that was obtained in a driven methane jet diffusion flame [6]. The computational fluid dynamics with chemistry (CFDC) code was validated by simulating the counterflow diffusion flame. The structures of weakly strained and near-quenching-limit flames were investigated for the counterflow and coflow configurations.

Mathematical Model

In the mathematical model [7], time-dependent Navier–Stokes equations are solved along with species- and energy-conservation equations in an uncoupled manner on a staggered-grid cylindrical coordinate system. However, the species equations are solved by coupling them through the production terms. The body-force term due to the gravitational field is included in the axial-momentum equation. A clustered mesh system is employed to trace the large gradients in flow variables near the flame surface. A detailed chemical-kinetics model proposed by Peters for methane-air combustion [8] is used in this formulation. It consists of 17 species (CH_4, O_2, CH_3, CH_2, CH, CH_2O, CHO, CO_2, CO, H_2, H, O, OH, H_2O, HO_2, H_2O_2, and N_2) that are involved in 52 elementary reactions. Reaction rates for these elementary reactions were obtained from Ref. [8]. The thermophysical properties such as enthalpy, viscosity, thermal conductivity, and binary molecular diffusion of all 17 species are calculated from the polynomial curve fits developed for the temperature range 300–5000 K. Mixture viscosity and thermal conductivity are then estimated using the Wilke and Kee expressions, respectively. Molecular diffusion is assumed to be of the binary-diffusion type, and the diffusion velocity of a species is calculated using Fick's law and the effective-diffusion coefficient of that species.

The finite-difference forms of the momentum equations are obtained using an implicit QUICKEST scheme [7,9], and those of the species and energy equations are obtained using a hybrid scheme of upwind and central differencing. At every time step, the pressure field is accurately calculated by solving all the pressure Poisson equations simultaneously and utilizing the LU (lower and upper diagonal) matrix-decomposition technique. The boundary conditions are treated in the same way as reported in earlier papers [7,10].

Results and Discussion

Model Validation

The CFDC model developed for the investigation of unsteady, methane jet diffusion flames was validated by direct simulation of the axisymmetric counterflow jet diffusion flame studied by Sung et al. [11]. These direct simulations for counterflow jet diffusion flames not only eliminate the concerns of the quasi-one-dimensional analyses but also provide a valuable test case for the validation of multidimensional mathematical models. The burner assembly consists of two nozzle burners with 14-mm exit diameters that are spaced 13 mm apart. The fuel and oxidizer jets emanating from the nozzles were made to impinge on each other. Outer nitrogen coflows were used to isolate and stabilize the flame. The fuel and oxidizer streams consisted of 23% methane in nitrogen and 23% oxygen in nitrogen, respectively. In addition, the mean exit velocities at the nozzles were maintained equal. Several calculations were made for different exit velocities, and the predictions were compared with the measurement results.

As described earlier, the chemical kinetics used for these simulations was adopted from the mechanism recommended by Peters [8]. Excellent agreement between the computed and measured profiles for temperature and other species was found for low-strain-rate cases (i.e., exit velocities <45.0 cm/s). However, when the exit velocity was increased beyond 50 cm/s, the computed flame quenched, although the experimental flame was extinguished at a velocity of ~77.5 cm/s. Little improvement was achieved with the inclusion of C_2 chemistry. Through a systematic sensitivity analysis of individual reactions, it was found that the chain termination reaction involving methyl radicals ($CH_3 + H = CH_4$) was responsible for the early extinction of the computed flame. Under the assumption that the values quoted by Peters have a margin of error, the calculations were made by gradually reducing the reaction rate of the foregoing chain-termination reaction. It was found that a rate that is an order of magnitude lower than that given by Peters yields extinction at a velocity of 77.5 cm/s. Interestingly, the rate of this reaction varies widely in the literature, and Warnatz [12] has recommended a different set of parameters for this reaction. The reaction rates recommended by Warnatz and Peters are quite different; at the quenching temperature (~1500 K), the rate of the former is an order of magnitude lower

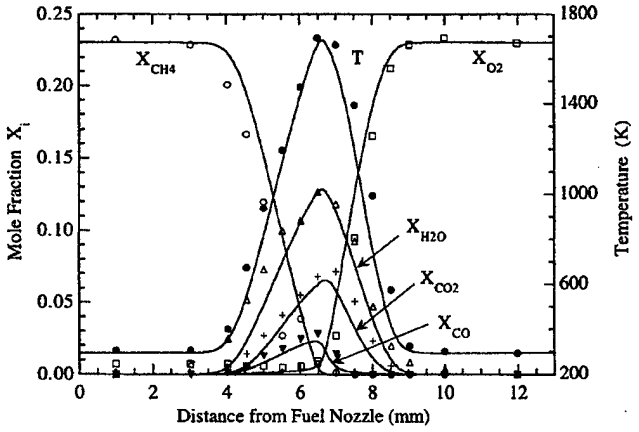

FIG. 1. Direct simulation of counterflow diffusion flame using axisymmetric CFDC code. Comparison of calculated (*lines*) and experimental (*symbols*) temperature and major-species profiles obtained along the stagnation line ($r = 0$).

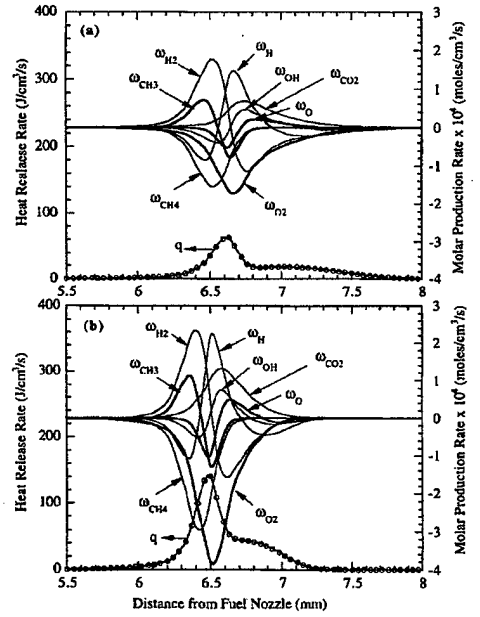

FIG. 2. Computed molar-production rates of reactants and radicals and total-heat-release rate profiles along stagnation line for (*a*) weakly strained flame with exit velocity of 25.5 cm/s and (*b*) flame at near-quenching limit with exit velocity of 77.5 cm/s.

than that of the latter. In fact, at this temperature, the reaction rate obtained from the Warnatz-recommended values matched very closely with those obtained through the trial-and-error calculations. Replacing the rate data for the $CH_3 + H = CH_4$ reaction with those given by Warnatz [12], the calculations were repeated for different exit velocities. Typical results along the stagnation line obtained for an exit velocity of 25.5 cm/s are shown in Fig. 1 and compared with the measurements of Sung et al. [11]. Excellent agreement was found between the calculated and measured values for temperature and major species concentration. It should be noted that, unlike in the one-dimensional calculations [13,14], no adjustment was made in the mass flow rates to match the predicted temperature profile with that measured—a definite advantage in using two-dimensional CFDC codes for counterflow flame problems.

Computed flame structures for the other velocity conditions (45 and 64.5 cm/s) investigated by Sung et al. [11] showed excellent agreement with the experimental data. Sung et al. [11] indicated that the counterflow diffusion flame formed between the diluted methane and oxygen jets was extinguished when the exit velocity was increased to ~77.5 cm/s. Amazingly, when the calculations were performed by increasing the exit velocity in 0.5-cm/s steps, it was found that (1) a stable flame is established for the exit velocity of 77.5 cm/s and (2) the flame is quenched when the velocity is increased to 78.0 cm/s. To characterize the differences in the structures of the weakly strained flame and the flame obtained at near-quenching limits, the total heat-release and molar-production rates for reactants, CH_3 and other radicals along the stagnation line for the 25.5- and 77.5-cm/s cases are shown in Figs. 2a and 2b, respectively. These flame structures are very similar to those computed by Sung et al. [11] for the CH_4-air counterflow diffusion flame. The peak temperature decreased from 1683 to 1518 K when the weakly strained flame (25.5 cm/s) was stretched to near-extinction limits (77.5 cm/s). Although the maximum reactant consumption rates for the latter case are nearly twice those of the former, the production and consumption rates for radicals did not change appreciably. This suggests that extinction in strained

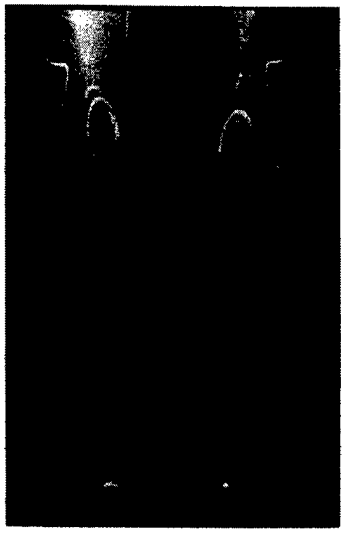

FIG. 3. Experimental image of unsteady methane jet diffusion flame obtained using reactive-Mie-scattering technique. Green emission from TiO_2 particles represents instantaneous flow field, and blue color represents time-averaged flame surface.

counterflow diffusion flames occurs as a result of the decrease in temperature.

The CFDC code used in the present study was also found to yield excellent predictions [15] for the steady coaxial jet diffusion flames studied by Mitchell et al. [16]. Also, the CFDC codes developed previously using the same methodology for H_2-O_2-N_2 combustion yielded excellent predictions for the vortex–flame interactions in hydrogen jet diffusion flames [7,17]. Consequently, the present code is being used to investigate the local quenching phenomenon that was experimentally observed in the driven methane jet diffusion flame.

Experiment on a Driven Jet Diffusion Flame

The experimental setup used to generate vortices inside a laminar jet diffusion flame is described in detail in Ref. [6]. This simple, axisymmetric unconfined burner consists of a central fuel nozzle and a coannular air duct with exit diameters of 10 and 152 mm, respectively. The fuel nozzle is connected to the speaker chamber by means of a long tapered tube. Fuel is pumped through the side ports of the speaker chamber. An audio speaker is mounted in this chamber in such a way that the hollow cone of the diaphragm is toward the nozzle exit. While a steady flow of fuel is maintained throughout the experiment, puffs of fuel are periodically ejected from the nozzle by driving the speaker with a pulse generator. The flame is shielded from room-air disturbances using a low-speed air flow in the coannular duct. This system permits precise control of the frequency, strength, and shape of the vortex that emerges from the fuel nozzle.

Several visualization and measurement techniques are used to capture the vortex–flame interaction process. An instantaneous (phase) image obtained with the reactive-Mie-scattering (RMS) technique [2] is shown in Fig. 3. With this method, micron-sized TiO_2 particles, formed from the spontaneous reaction between the seeded-$TiCl_4$ vapor and the water vapor produced during combustion, are visualized using the Mie-scattered light from a laser sheet. $TiCl_4$ is seeded into the fuel flow, and the laser firing is synchronized with the speaker driving signal. Images at different phases are obtained by changing the delay between the laser firing and the speaker driving signals. The luminous flame surface is also captured in Fig. 3; however, it represents the flame integrated over the period during which the camera shutter is open. Figure 3 illustrates that the vortices generated are quite symmetric. The vortices are introduced into the flame at a rate of 30/sec, which corresponds to the driving frequency of the speaker pulse generator. The thin lines surrounding the vortices result from the green light scattered by the TiO_2 particles. The motion of the vortices has pushed the flame surface radially outward to the point where it is locally and temporally quenched.

Vortex–Flame Interaction and Local Quenching

Typically, a methane jet diffusion flame anchors on the outer side of the fuel nozzle or tube. Simulation of this feature is very important for driven jet flames because flames simulated without the nozzle lip anchor in the shear layer and tend to lift off easily with the driving pulses. Hence, a straight tube of 1-cm height and 0.2-mm wall thickness is included in the calculation domain. Adiabatic wall boundary conditions are imposed along the tube walls.

The undriven jet flame described in the previous section is numerically simulated using the time-dependent CFDC code. Flat initial-velocity profiles with measured mass-averaged values of 1.5 and 0.4 m/s were employed at the entrance plane of the fuel tube and the exit plane of the annulus air duct, respectively. Using a mesh size of 201 × 101, calculations were first made for the unsteady flow in a 250- × 150-mm computational domain. Typical calculation on a Pentium Pro 200 MHZ PC took ~50 s per time step. The buoyancy-influenced instability resulted in a weak, low-frequency flame oscillation (~20 Hz), but no vortex roll up [5] developed outside the flame surface. This is a result of the relatively high air-flow rate (0.4 m/s) used in the annulus duct.

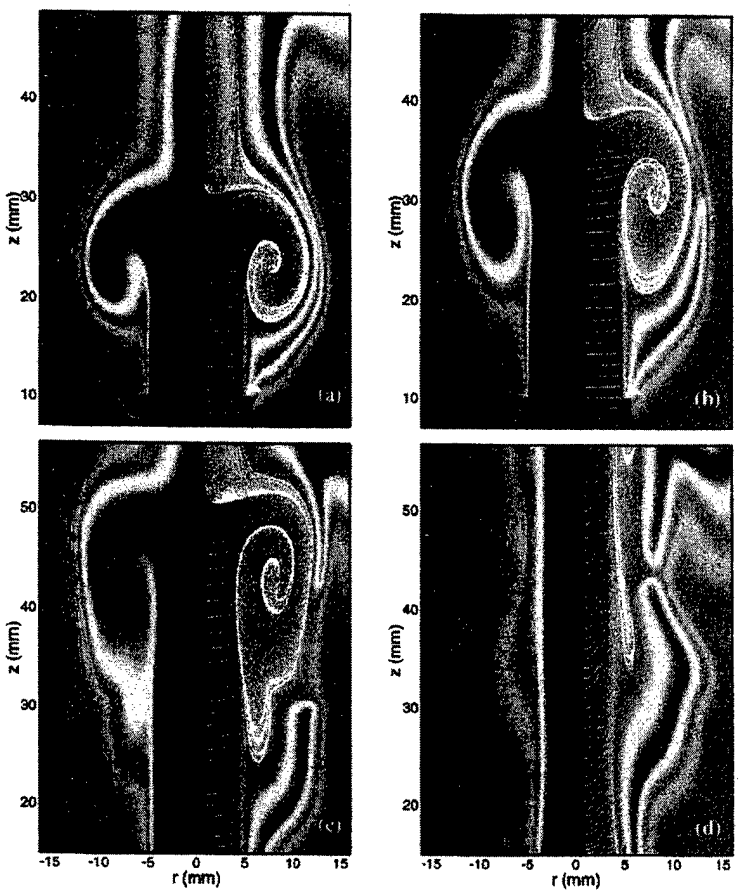

FIG. 4. Simulation of vortex–flame interaction, local quenching, and reignition in unsteady methane jet diffusion flame. Computed flames obtained at instants (*a*) t_0 + 18.5 ms, (*b*) t_0 + 19.5 ms, (c) t_0 + 21 ms, and (*d*) t_0 + 27 ms. Temperature and methane-concentration fields are shown on *left* and *right* halves, respectively. Instantaneous locations of particles (*shown in white*) are superimposed on temperature field. Iso contours of oxygen (*solid white lines*) and methyl-radical (*broken white lines*) concentrations are superimposed on methane-concentration field.

The computational flame was then driven periodically by perturbing the fuel mass-flow rate at the entrance of the fuel tube at a frequency of 30 Hz. The resulting exit velocity has a weak-suction pulse for about 13 ms, followed by a sharp mass ejection for a period of 14 ms. This velocity perturbation was obtained by modifying the experimentally measured velocities at the center of the nozzle exit under a nonreacting environment to achieve a vortex structure similar to that observed in the flame experiment.

Evolution of the computed flame is shown in Figs. 4a through 4d through instantaneous plots of temperature, species concentrations, and particle locations at t_0 + 18.5, t_0 + 19.5, t_0 + 21, and t_0 + 27 ms, respectively. Calculations were performed for several perturbation cycles prior to the results shown in these figures. The temperature field color coded between blue and red (representing 300 and 2200 K, respectively) is shown on the right half, and the fuel-concentration distribution is shown on the left half. In addition, iso contours of oxygen concentration and methyl radicals are plotted with solid and broken lines, respectively. Sets of massless particles were injected into the flow field at the exit of the fuel tube, and the instantaneous locations of all the particles are plotted in white on the right half.

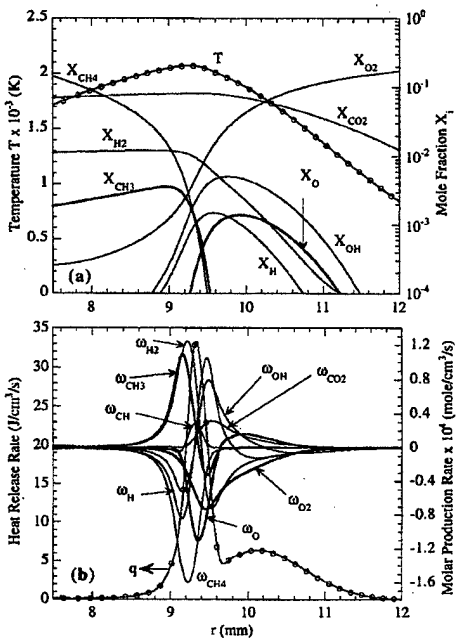

FIG. 5. Structure of steady-state (unperturbed) flame at a height of 27 mm. Radial profiles of (*a*) temperature and molar concentrations of reactants and radicals and (*b*) molar-production rates of reactants and radicals and total-heat-release rate.

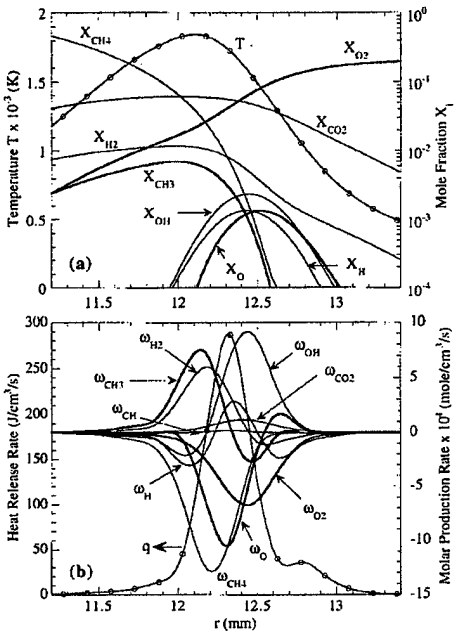

FIG. 6. Flame structure obtained at an instant when the flame is strained to near-quenching limit (t_0 + 18.5 ms). Radial profiles of (*a*) temperature and molar concentrations and (*b*) total-heat-release rate and molar-production rates. Flame height is 27 mm.

Particle-trace plots clearly identify the structure of the vortex associated with the puff of the fuel. When the fluctuating velocity was superimposed on the steady fuel flow of 1.5 m/s, the resulting velocity at the tube entrance temporarily became very low, between t_0 and t_0 + 13 ms. This near-stagnant flow condition at the nozzle entrance caused the flame surface—and, thereby, the viscous fluid—to approach the axis of symmetry. The additional fuel ejected suddenly with a velocity of 14 m/s (modified velocity of 15.5 m/s) collided with the column of viscous combustion products and then traveled radially outward (cf. Fig. 4a), forming a toroidal vortex. At this instant (t_0 + 18.5 ms), the flame surface at an axial height of z = 27 mm has moved radially outward from 7 to 12 mm. The interaction of the vortex with the flame surface caused the flame temperature to decrease; however, no local quenching was noted. At t_0 + 19.5 ms, the vortex convected downstream by about 8 mm, the flame between z = 30 and 34 mm became extinguished (Fig. 4b), and a hole in the flame surface was formed. Because the velocity in the potential core is higher than that near the flame surface, by t_0 + 21 ms, the vortex has moved farther downstream compared to the movement of the hole—leaving the tail of the vortex in the hole region (Fig. 4c). The flame and vortex shape at this time compares favorably with that of the experiment shown in Fig. 3. Note that significant amounts of oxygen and fuel are leaking through the hole and creating a premixed fuel and oxygen mixture in the neighborhood of the hole. Reignition is taking place in the hole region (Fig. 4d); as the influence of the vortex on the flame surface diminishes, the flame slowly returns to its unperturbed position, and another driving cycle follows.

The instantaneous images shown in Fig. 4 demonstrate that the present calculations have captured the important aspects of the local quenching process observed during vortex–flame interactions in a jet diffusion flame. To investigate the structural differences between the counterflow and coflow diffusion flames near extinction limits, flame structures at z = 27 mm for times t_0 ms (weakly strained flame) and t_0 + 18.5 ms (near-extinction-limit flame) are plotted in Figs. 5 and 6, respectively. The corresponding structures for the counterflow diffusion flame were shown in Figs. 2a and 2b.

As the flame is strained to near-quenching limits by the vortex, the fuel and oxidizer fluxes into the flame zone increase significantly (Figs. 5b and 6b) and result in an increase in their molar consumption rates; this, in turn, yields higher production and destruction rates for the intermediate radical species. The production rates of CH_3 and OH and the consumption rates of O and H radicals have increased by nearly an order of magnitude. However, a comparison of Figs. 5a and 6a suggests that only the methyl-radical concentration in the flame zone increases, whereas the concentrations of the other radicals such as H, O, and OH decrease. This is caused by (1) the longevity of CH_3 radicals and (2) the fact that the vortex pushes not only more fuel into the flame zone but also some preformed CH_3 radicals. Increase in the concentration of CH_3 as the vortex pushes the flame outward [18] is also evident in Fig. 4a. As discussed earlier in the context of the stability of the opposing-flow jet flame, the chain termination reaction, $CH_3 + H = CH_4$, alters the extinction characteristics of a strained flame significantly. The higher concentration of CH_3 found in the strained flame (Fig. 6) appears to be destroying the radical pool that is crucial for the stability of the flame. This flame-quenching mechanism is in contrast to that found in counterflow flames in which only a slight increase in production and consumption rates of the CH_3 and H radicals was observed when the flame was strained to the extinction limits.

Conclusion

Vortex–flame interactions are important elements of a turbulent flame and are building blocks for the development of turbulent-flame models. An experimental study was initiated recently at Wright Laboratory to establish a data base of vortex–flame interactions for the validation of time-dependent CFDC codes. Axisymmetric vortices were periodically generated inside a coflowing methane jet diffusion flame by driving the fuel jet using a speaker, and phase-locked images of interactions with the flame surface were recorded.

A time-dependent CFDC code that incorporates 17 species involved in 52 reactions was developed for simulation of the local and temporal quenching process observed during vortex–flame interactions in methane jet flames. The model was validated by directly simulating axisymmetric counterflow diffusion flames and by comparing the results with the measurement data of Sung et al. [11]. No adjustments were made in the flow rates as was done in the one-dimensional simulations of counterflow flames to match the temperature profiles for these axisymmetric calculations. It was found that although the Peters [8] mechanism yields very good predictions for the weakly strained flame structure, it fails in predicting the quenching limits. By replacing the rate expression of Peters for the $CH_3 + H = CH_4$ chain-terminating reaction with that recommended by Warnatz [12], the quenching limits were accurately obtained.

Calculations were made for the vortex–flame interactions in a coflowing jet diffusion flame. Inclusion of the fuel tube in the computational domain was found to be necessary to avoid lift-off of the flame during the driving sequence of the fuel jet. The large toroidal vortex formed from the fuel puff pushed the flame radially outward and created a hole on the flame surface. As the vortex convected downstream, reignition took place in the hole region, and the flame returned to its unperturbed position. It was found that the large increase in CH_3 radicals in the strained flame zone depleted the radical pool and, hence, quenched the flame locally. This quenching process is different from that observed in steady opposing-jet flames in which quenching occurs as a result of gradual reduction in temperature with strain rate.

Acknowledgments

This work was supported, in part, by Air Force Contract F33615-95-C-2507 and the Air Force Office of Scientific Research. The authors would like to thank Dr. Fumi Takahashi for stimulating discussions on quenching mechanisms and Mrs. Marian Whitaker for editorial comments.

REFERENCES

1. Hottel, H. C. and Hawthorne, W. R., in "Flame and Explosive Phenomena," *Third Symposium (International) on Combustion*, The Combustion Institute, Pittsburgh, 1949, pp. 254–266.
2. Roquemore, W. M., Chen, L.-D., Goss, L. P., and Lynn, W. F., in *Turbulent Reactive Flows, Lecture Notes in Engineering* (R. Borghi and S. N. B. Murthy, eds.), vol. 40, Springer-Verlag, Berlin, 1989, p. 49.
3. Takeno T., in *Twenty-Fifth Symposium (International) on Combustion*, The Combustion Institute, Pittsburgh, 1994, pp. 1061–1073.
4. Takahashi, F. and Goss, L. P., in *Twenty-Fourth Symposium (International) on Combustion*, The Combustion Institute, Pittsburgh, 1992, pp. 351–359.
5. Chen, T. H. and Goss, L. P., *Combust. Sci. Technol.* 79:311 (1991).
6. Hsu, K. Y., Chen, L.-D., Katta, V. R., Goss, L. P., and Roquemore, W. M., AIAA paper 93-0455, Reno, January.
7. Katta, V. R., Goss, L. P., and Roquemore, W. M., *AIAA J.* 32:84 (1994).
8. Peters, N., in *Reduced Kinetic Mechanisms for Applications in Combustion Systems, Lecture Notes in Physics* (N. Peters and B. Rogg, eds.), vol. m15, Springer-Verlag, Berlin, 1993, pp. 3–14.

9. Leonard, B. P., *Comput. Meth. Appl. Mech. Eng.* 19:59 (1979).
10. Katta, V. R., Goss, L. P., and Roquemore, W. M., *Int. J. Num. Meth. Heat Fluid Flow* 4:413 (1994).
11. Sung, C. J., Liu, J. B., and Law, C. K., *Combust. Flame*, 102:481 (1995).
12. Warnatz, J., in *Combustion Chemistry* (W. C. Gardiner, ed.) Springer-Verlag, New York, 1984, p. 197.
13. Kee, R. J., Miller, J. A., Evans, G. H., and Dixon-Lewis, G., in *Twenty-Second Symposium (International) on Combustion*, The Combustion Institute, Pittsburgh, 1988, pp. 1479–1494.
14. Chelliah, H. K., Law, C. K., Ueda, T., Smooke, M. D., and Williams, F. A., in *Twenty-Third Symposium (International) on Combustion*, The Combustion Institute, Pittsburgh, 1990, pp. 503–511.
15. Katta, V. R. and Roquemore, W. M., AIAA paper 97-0904, Reno, January.
16. Mitchell, R. E., Sarofim, A. F., and Clomburg, L. A., *Combust. Flame* 37:227 (1980).
17. Katta, V. R. and Roquemore, W. M., *Combust. Flame* 100:61 (1995).
18. Takahashi, F. and Katta, V. R., in *Twenty-Sixth Symposium (International) on Combustion*, The Combustion Institute, Pittsburgh, 1996, pp. 1151–1160.

COMMENTS

H. N. Najm, Sandia National Laboratories, USA. Accurate modeling of flame dynamics, especially as pertains to extinction and reignition, necessitates adequate spatial resolution of flame structure. Figure 2 suggests that the width of the heat-release rate peak, as well as the H production rate peak, is roughly 0.2–0.3 mm. How can the spatial resolution in the r direction (Δr = 0.15 mm) be adequate? Moreover, triple flames are expected to form as the flame reconnects by burning into the partially premixed hole resulting from local extinction. These are not observed in the paper, clearly due to the inadequacy of the spatial resolution for describing the thin premixed flame front in the triple flame.

Author's Reply. Figure 2 shows the structure of the opposing-flow jet flame, and the grid used for that simulation has a resolution of 0.05 mm. The coaxial jet flame shown in Figs. 5 and 6 has a reaction-zone thickness of ~1 mm, and the grid resolution of 0.15 mm is adequate for resolving its structure.

Triple or tribrachial flames are a type of edge flame that may develop in partially premixed environments. One of the fundamental criteria that must be satisfied to obtain these flames in nonpremixed flows is that adequate premixing of fuel and oxidizer must occur upstream of the flame edge. Other factors such as local velocity and preferential diffusion may also play a role in the formation of triple-flame edges. The experimental work of Chung and Lee [1] on coaxial non-premixed jet flames shows that (1) triple flames do not form near the edges of the flames that are separated from the burner by <10 mm, and (2) triple flames do not exist for methane flames that blow out once the flame-to-burner separation is >5 mm. These observations suggest that adequate premixing of fuel and oxidizer is required for the formation of triple-flame edges.

In the present calculations, the vortex–flame interaction results in local quenching, and the hole formed on the flame surface is open for ~8 ms. During this period, even in the absence of convective flow, methane will diffuse into a 0.9-mm-thickness layer, which is much thinner than the 2-mm weakly stained diffusion flame. This weak premixing probably is not sufficient to establish a triple-flame structure to the edge of the diffusion flame. Temperature and OH-concentration measurements on this flame revealed no triple-flame structure. In a related work on the structure of the flame base [2], we used a grid resolution of 0.05 mm and observed no triple-flame structure associated with a 4-mm separated flame. Based on these studies, we are convinced that triple flames do not form during the reignition process in the local hole.

REFERENCES

1. Chung, S. H. and Lee, B. J., *Combust. Flame* 86:62–72 (1991).
2. Takahasi, F., Schmoll, W. J., and Katta, V. R., in *Twenty-Seventh Symposium (International) on Combustion*, The Combustion Institute, Pittsburgh, 1998, pp. 675–684.

•

Quang-Viet Nguyen, NASA Lewis Research Center, USA.

1. Nguyen and Paul [1] observed a sudden increase in the OH field accompanying the extinction of the flame for a rich premixed methane–air flame subject to a strong vortex interaction. In your simulations of the vortex–flame interaction for non-premixed methane–air flames, do you ever observe a sudden increase in the OH concentration at the time of flame extinction?
2. In your figures, the CH field was shown to break, corresponding to your definition of extinction. Does the CH break occur suddenly (within 1 to 2 ms) or gradually over many milleseconds?
3. How were the transport properties in your simulation calculated? Recent work by Sandia National Labs [2] has found that the original transport properties theory/database (CHEMKIN) in use by many groups has problems, and a revised theory/database is now available.

REFERENCES

1. Nguyen, Q. V. and Paul, P. H., in *Twenty-Sixth Symposium (International) on Combustion*, The Combustion Institute, Pittsburgh, 1996.
2. Paul, P. H., DRFM—package for the calculation of transport properties, Sandia National Laboratories, SAND report, 1997.

Author's Reply. We do see some increase in OH concentration during the early stages of the vortex–flame interaction. This increase results from the superequilibrium concentrations that develop in weakly strained diffusion flames. During the vortex–flame interaction under consideration in the present study, the CH concentration was reduced to zero from its peak value in slightly less than 1 ms. As mentioned in the paper, we estimate the transport properties using Lennard–Jones potentials that were taken from the CHEMKIN database. It will be interesting to note the impact on our methane flames of the modifications suggested by Paul for evaluating the transport properties.

•

Robert Barlow, Sandia National Laboratories, USA.

1. To follow up on the previous question regarding the presence of triple flames, is it possible that triple-flame structure would be observed if a finer grid were used in the calculation?
2. Validation of the chemical mechanism in a steady opposed flow flame calculation does not necessarily mean that mechanism performs accurately when there is extinction and reiginition. Have you done any other testing on this mechanism, or are there plans to run the calculation using detailed chemistry, such as the GRI or Warnatz mechanisms?

Author's Reply. The grid spacing used in the present study is sufficient to capture premixed flames. Based on these calculations and the experimental data, we are convinced that the flame edges in the hole region do not exhibit triple-flame structure.

The chemical mechanism used in this paper was validated not only for the simulation of extinction in opposing-flow flames but also for the prediction of standoff distance for the coaxial jet diffusion flame [1]. Also, we have obtained reasonable predictions with this mechanism for a variety of flow conditions, and these results compare favorably with those obtained with the GRI mechanism. We are currently performing simulations using the GRI mechanism for the unsteady flame discussed in this paper.

REFERENCE

1. Takahasi, F., Schmoll, W. J., and Katta, V. R., in *Twenty-Seventh Symposium (International) on Combustion*, The Combustion Institute, Pittsburgh, 1998, pp. 675–684.

•

Charles J. Mueller, Sandia National Laboratories, USA. Did you observe any evidence of triple flames reconnection after the local extinction event?

Author's Reply. There is no triple-flame structure associated with the edges of the broken flame shown in this work.

Twenty-Seventh Symposium (International) on Combustion/The Combustion Institute, 1998/pp. 675–684
PUBLISHED WITH PERMISSION

ATTACHMENT MECHANISMS OF DIFFUSION FLAMES

FUMIAKI TAKAHASHI,[1] W. JOHN SCHMOLL[1] AND VISWANATH R. KATTA[2]
[1]*University of Dayton*
Research Institute
300 College Park
Dayton, OH 45469, USA
[2]*Innovative Scientific Solutions, Inc.*
2766 Indian Ripple Road
Dayton, OH 45440, USA

A common view of the stabilizing mechanism of methane diffusion flames, including jet and porous flat-plate burner flames, is presented. Two-color particle-imaging velocimetry measured the velocity field in the stabilizing region of jet diffusion flames under near-lifting conditions. Computations using a time-dependent, implicit, third-order accurate numerical model, including semidetailed chemical kinetics and buoyancy effects, revealed the detailed structures of the vertical jet diffusion flames and flat-plate burner flames with different orientations of the plate surface and fuel injection. The numerical results are in a good agreement with the measurements in the flame base locations and surrounding velocity fields. In the calculations of both classes of flames, the highest reactivity spot (*reaction kernel*) with peak rates of heat release, oxygen consumption, and water vapor production, was formed in the relatively low-temperature (<1600 K) flame base as a result of back diffusion of radical species against the incoming oxidizing flow. The $CH_3 + O \rightarrow CH_2O + H$ reaction predominantly contributed to the heat-release rate peak. Heuristic correlations were found between the heat-release or oxygen-consumption rate and the local velocity over a wide range. At a high coflow air velocity in a jet diffusion flame, the flame base shifted slightly downstream before lifting, resulting in a higher reactivity and thereby withstanding at a higher local velocity. On the other hand, in a long horizontal flat-plate flame with downward fuel injection, a recirculation zone was formed ahead of the flame base, resulting in an order-of-magnitude lower local velocity and reactivity. Therefore, the reaction kernel provides a stationary ignition source and sustained stable combustion for incoming reactants, thus holding the trailing diffusion flame in the oxidizing stream.

Introduction

The attachment of a diffusion flame to solid or liquid surfaces is of both fundamental and practical importance because of their relation to flame holding by bodies in combustion chambers and fire spread through condensed fuels [1]. Simple diffusion flames formed in a gaseous fuel jet [2–16] or over a flat fuel surface in a parallel oxidizing stream [1,17–19] have long been studied as model flames for practical combustion systems and fires. A common feature among these flames is the formation of flame bases, or edge flames [20], which attach to the surfaces with a small dark space in between. Therefore, there must be a common flame-holding, or standing, mechanism related to these classes of diffusion flames. If the flame attachment is properly understood, the flame detachment stability limits, that is, lifting or blow-off, can be elucidated more readily.

The base of a jet diffusion flame is often postulated [21] to possess a sort of flame velocity to propagate downward against the gas stream, thus preventing the flame from lifting. Indeed, the critical entraining velocity into the flame base at lifting correlated well with the maximum burning velocity obtainable by mixing the jet fluid and external oxidizing fluid for hydrogen flames [7,14]. Although the postulation is relevant to laminar lifted flames whose standoff distance is large enough to allow fuel-air premixing and form a triple-flame base structure [22,23], it has not been substantiated for the attached flame stabilization. Measurements in the stabilizing region of attached methane flames [4,6,9] showed a partially premixed zone in the dark space. However, at a low jet velocity, the flame structure was similar to that of a counterflow diffusion flame [24] and no evidence of premixed flame propagation was found [9]. Thus, the level of fuel-air mixing in the dark space depends on the flow conditions and fuel properties (diffusivity, reactivity, etc.), which determine the flame base location and mixing time. Moreover, the actual reaction rates in diffusion flames are controlled by the reactant transport rates. Consequently, the local flame base structure must be revealed to foster better understanding of flame stabilization.

TABLE 1
Test conditions

Case No.	Air Velocity (m/s)	Fuel Velocity (m/s)
	Jet Diffusion Flames (upward)	
J1	0.19	1.7
J2	0.19	11.5
J3	0.36	1.7
J4	0.36	6.9
J5	0.72	1.7
	Flat-Plate Burner Flames	
P0	0.65 (zero gravity)	0.02 (zero gravity)
P1	0.65 (upward)	0.02 (horizontal)
P2	0.65 (downward)	0.02 (horizontal)
P3	0.65 (horizontal)	0.02 (upward)
P4	0.65 (horizontal)	0.02 (downward)
P5	1.2 (horizontal)	0.008 (downward)

The recent development [25,26] of a numerical code enabled us to simulate accurately the structure of diffusion flames [16,27]. This paper reports the computational and experimental results of the structure of the stabilizing region of jet- and flat-plate diffusion flames to extract a common flame attachment mechanisms.

Experimental and Numerical Techniques

The burner system is similar to that described elsewhere [13–15]. The burner consists of a fuel tube (inner diameter: d = 9.45 mm, lip thickness: δ = 0.2 mm) and a concentric air tube, centered in a vertical combustion chimney. The two-color particle-imaging velocimetry (PIV) developed by Goss et al. [28] is described in a previous paper [15]. Mie scattering from the seed particles, illuminated by the time-delayed green-pulsed Nd:YAG and red dye laser sheet, is recorded on color film, digitized, and processed using a cross-correlation technique.

The numerical code developed by Katta [25,26] is the same as in previous papers [16,27]. A semidetailed chemical-kinetic model [29], including 52 elementary steps for 17 species, is used to describe CH_4-O_2 combustion. The Arrhenius parameters for the reaction $CH_3 + H \rightarrow CH_4$ (R45) are replaced with those by Warnatz [30] because they more accurately predict [26] extinction of counterflow diffusion flames [31]. The computational domain of 150 × 60 mm in axial (x) × radial (r) directions is represented by a mesh system of 271 × 101 with clustered grid lines near the jet exit with a minimum spacing of 0.05 mm. The fuel tube (d = 9.5 mm) exit plane is placed 10 mm from the inflow boundary. The fully developed pipe flow and boundary layer velocity profiles outside the burner tube are used.

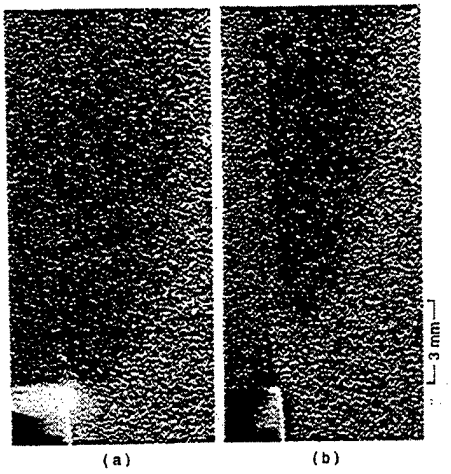

FIG. 1. Two-color particle-imaging velocimetry photographs of the stabilizing region of methane jet diffusion flames. d = 9.45 mm. Laser intensity: ~20 mJ/pulse; time delay: 70 μs; and sheet thickness: ~0.5 mm. Seed particles: zirconia (<1 μm, 97%). (a) U_a = 0.36 m/s, U_j = 6.7 m/s; (b) U_a = 0.72 m/s, U_j = 1.8 m/s.

The test conditions are listed in Table 1. The mean jet velocity (U_j) and mean annulus air velocity (U_a) for cases J2, J4, and J5 are slightly below the measured lifting limit curve [13]. The boundary conditions and results for flat-plate burner flames are described in detail elsewhere [27]. The air and fuel velocities for cases P3 and P5 are the same as thoese of the experiments [17,19].

Results and Discussion

PIV Measurements

Under the conditions of cases J1 through J4, the base of visible (blue) flame was attached to the burner rim with a dark space, which was nearly a half minimum quenching distance (2.2 mm [2]) of the methane-air mixture. As U_j was gradually increased from the conditions of cases J2 or J4, the flame lifted abruptly a few jet diameters above the burner. By contrast, for case J5, the flame base gradually shifted a few millimeters downstream just before lifting. Fig. 1 shows the PIV photographs, with the time exposure image of visible flame zone and the burner rim, under near-lifting conditions close to cases J4 and J5, respectively, revealing the distinct lifting modes. The jet Reynolds number ($Re_j = U_j d/\nu_j$ where d: jet diameter; ν_j: kinematic viscosity of methane) were ~3780 and ~1020, respectively.

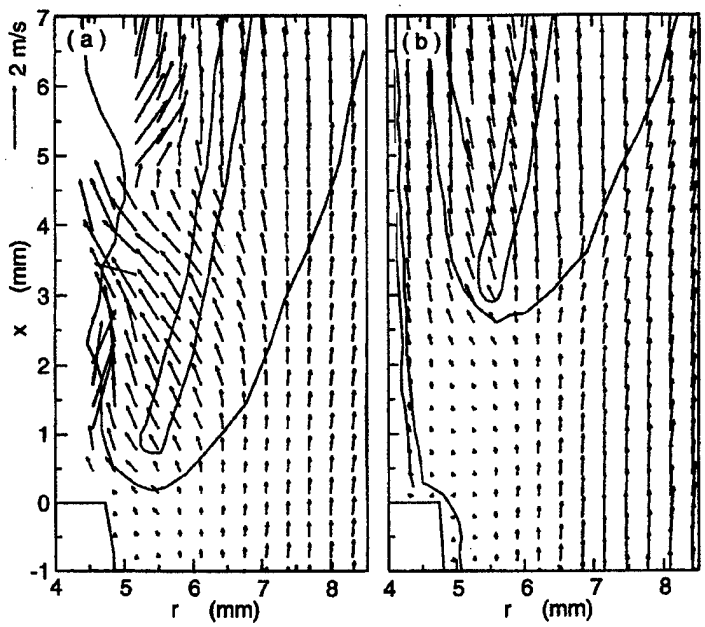

FIG. 2. Measured velocity vectors in the stabilizing region of methane jet diffusion flames, including traces of the jet-external fluid boundary, low number-density boundary, visible flame zone, and burner rim. d = 9.45 mm. (a) U_a = 0.36 m/s, U_j = 6.7 m/s; (b) U_a = 0.72 m/s, U_j 1.8 m/s.

Two-color PIV is advantageous because photographs are useful not only for velocity measurements but also for extracting qualitative flow visualization information [15]. The quality of images, including color tinge, depends on the number density of particles, particle displacement, local laser-sheet intensities, exposure period, film type, and so forth. In Fig. 1a, the pipe flow was turbulent, and the jet-external fluid boundary showed developing large-scale vortices [15]. By contrast, in Fig. 1b, the jet-external fluid boundary was smooth, showing an entirely laminar flow. The cold annulus air (high number density) was entrained through the dark space onto the fuel side of the visible flame zone. Thus, the flame base is thermally isolated from the wall effect under this condition. The outer boundary of a low number-density zone around the visible flame zone was due to thermal expansion of gases at high temperatures. The inner boundary of the low number-density zone showed an outermost streamline in the entrained high number-density flow, rather than the hot boundary, as will be described using the numerical results in the next section.

Fig. 2 shows the measured instantaneous velocity vector fields. In both cases, a low-velocity region was formed around the burner rim and wake. The annulus air slightly expanded near the flame base, accelerated in the hot zone, penetrated through the dark space, or crossed the visible flame zone. In Fig. 2a, the evolution of large-scale vortices caused a zig-zag motion on the fuel side of the visible flame zone. In Fig. 2b, the stable visible flame base shifted downstream to $x \approx 3$ mm.

Flame Base Structure

Figure 3 shows the calculated velocity vectors ($\vec{v}$), isotherms (T), and heat-release rate ($\dot{q}$) contours in the stabilizing region for cases J4 and J5. The heat-release rate showed a sharp peak at the base of the flame at relatively low temperatures (~1600 K). As will be shown later, the oxygen consumption rate ($-\omega_{O_2}$) and water vapor production rate (ω_{H_2O}) also have peaks close (typically ~0.05 mm) to the heat-release rate peak. We call this highest reactivity spot (including the peaks of $\dot{q}$, $-\omega_{O_2}$, and ω_{H_2O}) *reaction kernel* in this paper. It is notable that for cases J1 through J3 [not shown] and case J4 (Fig. 3a), the simulated flame base was attached to the burner rim, whereas for case J5 (Fig. 3b), it was slightly away (~3 mm) from the burner exit. The results are in good agreement with the experiment (Fig. 2), except that the flame base location is slightly lower than that of the experiment for case J4. In both cases J4 and J5, there was a low velocity region near the burner rim and wake. The co-flow air accelerated and

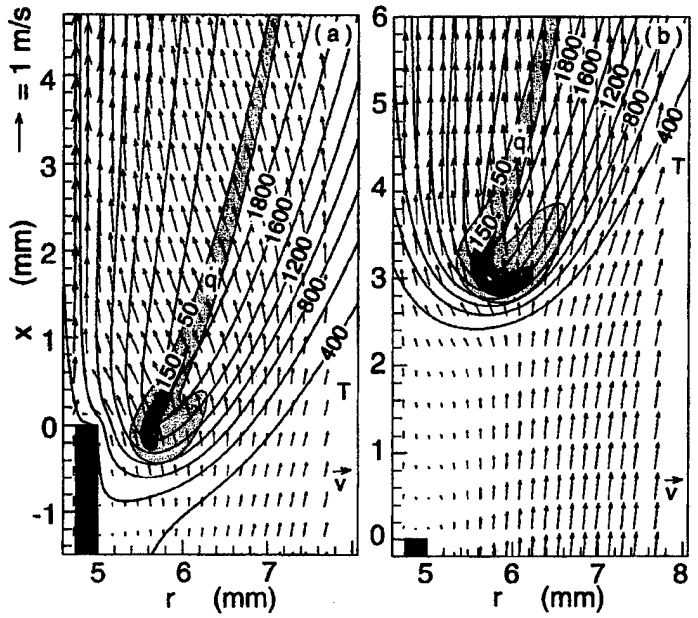

FIG. 3. Calculated velocity vectors, isotherms (unit, K), and heat-release rate (J/cm³s) in the stabilizing region of methane jet diffusion flames. (a) Case J4; (b) case J5.

stream tubes slightly expanded by approaching the flame zone, crossed the flame zone, or penetrated through the dark space onto the fuel side of the flame zone. Furthermore, in Fig. 3b, streamlines penetrating below the reaction kernel are not subjected to the flame temperatures (>1600 K), and thus, the inner boundary of the low number-density zone in the PIV photograph (Fig. 1b) was the outermost streamline of the penetrated flow rather than the isotherms. These results have demonstrated that the present numerical code, with the semidetailed kinetics, can accurately predicting the flame structure, including the standoff distance and the subtle features in the velocity field, based on the first principle without adjustable parameters.

Figure 4 shows the calculated total molar flux vectors of methane ($\vec{M}_{CH_4}$, dashed) and molecular oxygen ($\vec{M}_{O_2}$, solid), including both diffusion and convection terms, contours of the equivalence ratio (ϕ), and the oxygen consumption rate for cases J4 and J5. The equivalence ratio was determined from the fuel and oxygen molar fluxes, thus including the effects of both convection and diffusion. In the upper portion of both flames, the molar flux vectors of methane and oxygen turned toward the flame zone from the opposite sides, typical of diffusion flames. In the dark space, partial premixing occurred by interdiffusion. At the reaction kernel, there was a common component of the methane and oxygen flux vectors, an essential feature of premixed flames [9]. However, the thickness of the zone within the flammability limits ($0.5 < \phi < 1.7$ [2]) was small (<0.2 mm for J4 and <0.5 mm for J5) compared with the minimum quenching distance (2.2 mm [2]). Thus, the flames under investigation apparently did not have the triple-flame base structure [20,21]; that is, the stoichiometric flame base with fuel-rich and fuel-lean branches on the fuel and air sides, respectively. More importantly, the high reactivity zone extended more into the fuel-lean region.

Figure 5 shows the calculated total molar flux vectors of atomic hydrogen ($\vec{M}_H$), the mole fraction of molecular oxygen (X_{O_2}), and the rate of water vapor production for cases J4 and J5. In the upper portion of both flames, the molar flux vectors of atomic hydrogen pointed to opposite sides of the flame zone as a result of strong diffusion. By contrast, at the reaction kernel, hydrogen atoms diffused all around the downward directions. This trend, peculiar to the geometric edge of the flame, was also found for other radical species (OH, O, and CH_3, etc.). Hence, the flame base was more exposed to air (aerated), and the oxygen mole fraction at the reaction kernel was substantially higher than a typical oxygen leakage in diffusion flames ($X_{O_2} \approx 0.02$ [24]). The oxygen concentration gradient also became steeper around the reaction kernel. Therefore, various radical species were able to back-diffuse and interdiffuse into

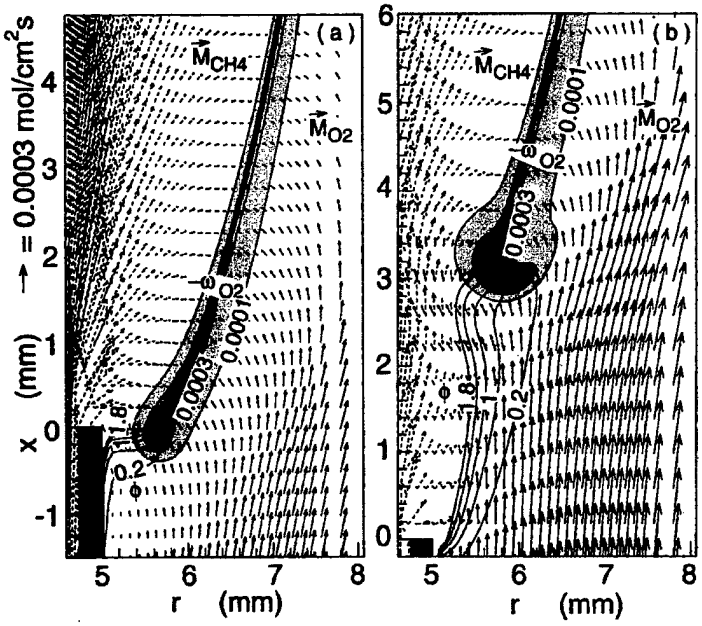

FIG. 4. Calculated molar flux vectors of methane (dashed) and molecular oxygen (solid), equivalence ratio based on the fuel and oxygen fluxes, and oxygen consumption rate (mol/cm³s) in the stabilizing region of methane jet diffusion flames. (a) Case J4; (b) case J5.

the lower-temperature, oxygen-rich zone against the convective oxidizing flow. As a result, the reaction zone broadened, convective and diffusive oxygen fluxes increased, and thus the global reaction rates increased.

More-detailed information on the flame structure, including chemical kinetic effects, can be extracted by examining the profiles of various variables. Because the deviations from pure diffusion flames were minimal in case P5 and most evident in case J5, a focus will be placed on case J5, although the general trends were similar with lesser magnitudes in other flames (cases J1 through J4). Figs. 6 and 7 show the radial variations of the temperature, species mole fractions (X_i), heat-release rate, species production rates (ω_i), and major elementary step reaction rates (ω_j) across the flame at two different heights (x = 2.98 and 6 mm) for case J5. In an upper location (Fig. 6), the distributions of the temperature and major species are typical of diffusion flames, except for the increased oxygen mole fraction on the fuel side due to the influence of the oxygen penetration through the dark space. The mole fractions and production rates of the fuel fragments (CH_3) and intermediates (H_2 and CO) peaked on the fuel side, and chain radical species (OH, H, and O) and products (H_2O and CO_2) peaked on the air side of the temperature or heat-release rate peak. The methane consumption rate peak was on the fuel side, and that of oxygen was on the air side. A prominent feature in the reaction rate plot (Fig. 6c) was paring of the forward and backward reactions. The differences indicate the deviation from partial equilibria and the net reaction rates. These reactions include: $H + O_2 \rightleftarrows OH + O$ (forward: R1/backward: R2), $O + H_2 \rightleftarrows OH + H$ (R3/R4), $H_2 + OH \rightleftarrows H_2O + H$ (R5/R6), $OH + OH \rightleftarrows O + H_2O$ (R7/R8), $CO + OH \rightleftarrows CO_2 + H$ (R25/R26), $CH_2 + H \rightleftarrows CH + H_2$ (R34/R35), $CH_3 + H_2 \rightleftarrows CH_4 + H$ (R48/R50), and $CH_3 + H_2O \rightleftarrows CH_4 + OH$ (R49/R52).

The reaction kernel structure (Fig. 7) shows striking differences and deviations from the trailing diffusion flame structure (Fig. 6). There were secondary peaks in the oxygen mole fraction ($X_{O_2} \approx 0.12$) on the fuel side of the relatively low peak temperature (~1600 K) and a small hump in the methane mole fraction ($X_{CH_4} \approx 0.007$) on the air side. These resulted from the air penetration and the methane efflux through the dark space. The minimum oxygen mole fraction at the reaction kernel was substantially higher ($X_{O_2} \approx 0.06$). The oxygen consumption rate was widely distributed over the entire reaction zone, closely following the heat-release rate and water vapor production rate. In Fig. 7c, the near-partial-equilibrium pairs disappeared, except for the reactions R7/R8. The reactions R1, R3, R5, R25, R34,

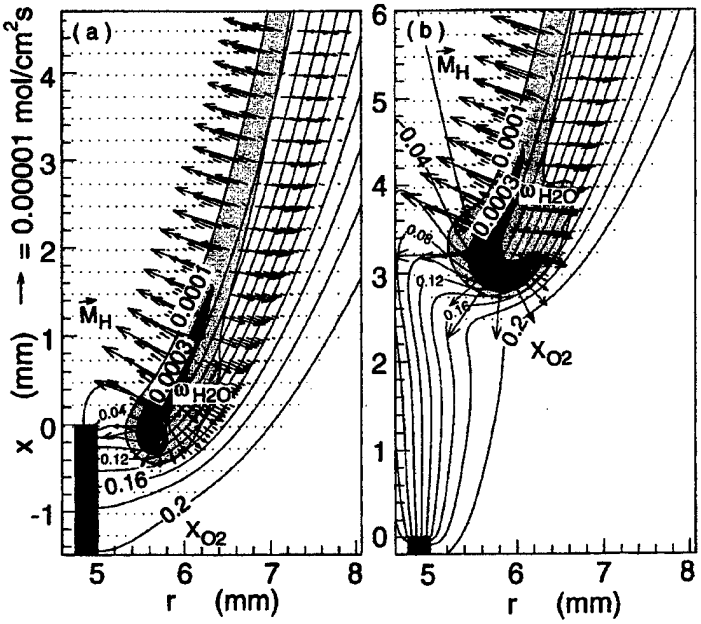

FIG. 5. Calculated molar flux vectors of atomic hydrogen, mole fraction of oxygen, and water vapor production rate (mol/cm³s) in the stabilizing region of methane jet diffusion flames. (a) Case J4; (b) case J5.

R50, and R52 are dominant compared with their counterparts, and thus their net reaction rates increased several times to an order of magnitude. Possible causes include the higher molecular oxygen concentration (for R1), the depleting radical pool at lower temperatures (R1 and R3), lower activation energy reactions favored at lower temperatures (R5, R25, R34, and R52), and reactions with larger preexponential factor (R1, R50, and R52). It is notable that the reaction rate of an important chain-branching step $H + O_2$ (R1) increased even at lower temperatures and that of $H_2 + OH$ (R5) was maintained at a high level, thus maintaining the H_2-O_2 chain reactions going. In addition, the steps $CH_4 + H$ (R50) and $CH_4 + OH$ (R52) kept producing methyl radicals. The most striking feature is a phenomenal increase in the reaction rate of $CH_3 + O \rightarrow CH_2O + H$ (R46). In fact, a plot of the heat-release rate of each chemical reaction step (not shown) revealed that this step predominantly contributed to the total heat-release rate peak at the reaction kernel. In the trailing diffusion flame zone (Fig. 7), the methyl radicals and oxygen atoms were separated on the fuel side and air side, respectively, and thus, the reaction rate of R46 and its contribution to heat release were smaller than those of R5, R7, and R2. Therefore, the back-diffusion and interdiffusion of the radical species (H, OH, O, and CH_3) directly into the oxygen-rich (fuel-lean) reaction kernel promoted chain reactions at lower temperatures and generated the heat-release and species production (or consumption) rate peaks.

Figure 8 shows the variations in the temperature, heat-release rate, and axial (U) and radial (V) velocity components along the maximum heat-release rate envelope for cases J1 through J5. The abscissa is the axial distance from the heat-release rate peak. For all cases, the temperature reached ~1600 K at the reaction kernel and asymptotically approached ~2000 K in the trailing diffusion flame zone. For case J5, the temperature gradients toward the reaction kernel and the peak heat-release rate were highest. It was noticed that the axial velocity, or total velocity ($|\vec{v}|$, not shown), at the reaction kernel was larger for a case with a higher heat-release rate peak. Because the axial (or total) velocity along the flame zone kept increasing downstream, the trailing diffusion flame might drift away downstream if not supported. Since the reactivity (peak heat-release or species production rates) at the reaction kernel is significantly larger than that in the trailing diffusion flame, the reaction kernel apparently stabilized the flame. Therefore, the reaction kernel provided a stationary ignition source to the incoming reactants and sustains stable combustion in the flow field. As the reaction kernel secures the stable combustion, the trailing diffusion flame zone can be successively supported, thus keeping the flame from lifting.

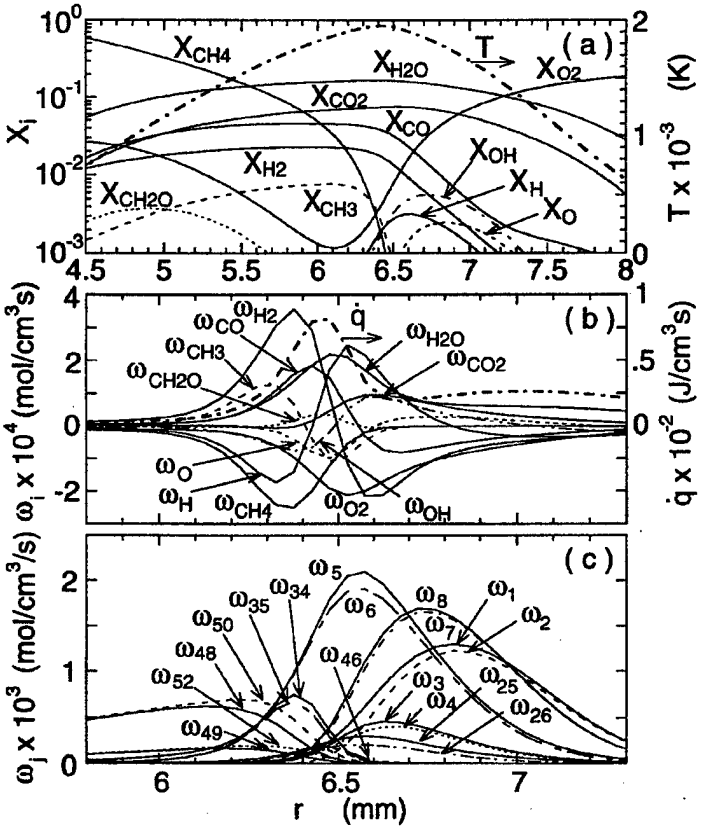

FIG. 6. Variations of the calculated (a) temperature, mole fractions; (b) heat-release rate, production rate of species i; and (c) reaction rate of step j across a methane jet diffusion flame zone. Case J5. $x = 6$ mm.

Reaction Kernel Correlations

The properties of the reaction kernel may be generalized by comparing different classes of flames, including jet diffusion flames presented here and flat-plate burner flames [27]. Because the flame base was kept stationary (or stabilized) in the flow field, reaction kernel properties were correlated with the total velocity (or axial component [not shown]) of the incoming flow. Fig. 9 shows heuristic correlations of the peak heat-release rate, or oxygen consumption rate, with the local total velocity, the temperature, and equivalence ratio at the heat-release rate or oxygen consumption rate peak. All data points of the heat-release or oxygen consumption rate for both jet- and flat-plate diffusion flames fell on single curves. These reaction kernel correlations demonstrate that the baseline mechanism responsible for flame attachment is identical for both flame systems and that the flame can be stabilized in a higher velocity flow if the reaction rates at the reaction kernel are higher. This situation is more evident as the flame base shifts downstream, becomes more aerated, and the aforementioned enhancements in reaction rates take place.

On the other hand, in case P5, the airflow along the flat plate separated and a recirculation zone was formed, thus forming the flame base in a very low velocity location upstream (~1 mm) of the fuel injection. At low flow velocities, diffusion processes dominate over convection, and, thus, the reaction rates are substantially small. The extreme case of pure diffusion flame without convection (except Stefan flow) is the small candle flame under microgravity [32], in which the highest reactivity is formed at the flame tip rather than the base. Therefore, there are two distinct regimes of diffusion flame attachment: pure diffusion and reaction kernel. In the pure diffusion regime, the diffusion flame burning at a stoichiometric fuel-oxygen flux balance might simply quench at the base. In the reaction kernel regime,

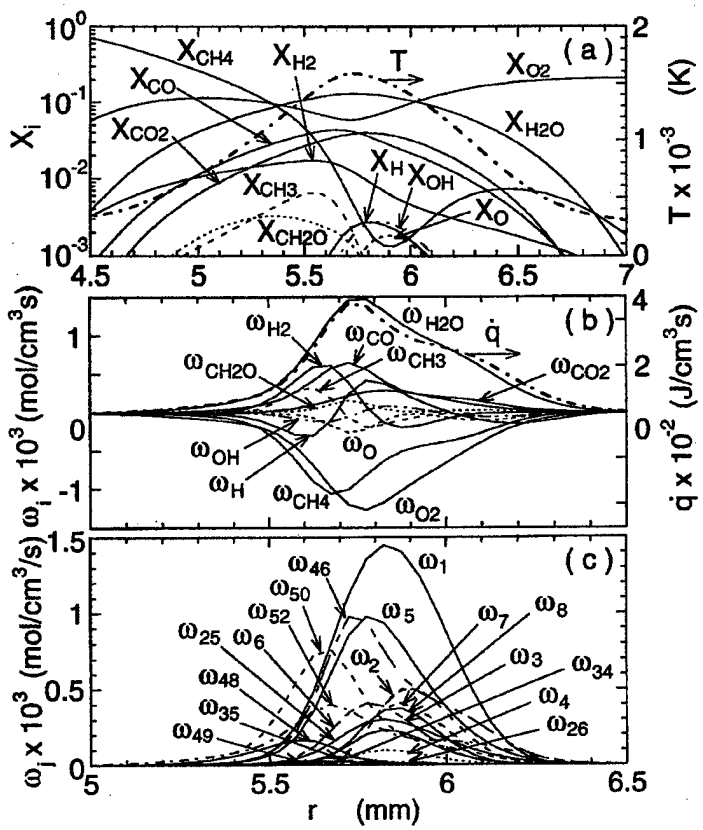

FIG. 7. Variations of the calculated (a) temperature, mole fractions; (b) heat-release rate (J/cm³s), production rate of species i; and (c) reaction rate of step j across the reaction kernel of a methane jet diffusion flame. Case J5. x = 2.98 mm.

the reactivity at the reaction kernel increases as a result of air blowing, which enhances the rates of mixed convective-diffusive, heat and reactant transport processes. Therefore, the peak reactivity is obtained under fuel-lean conditions ($0.5 < \phi < 1$) at relatively low temperatures (1500–1600 K).

Conclusions

The detailed flame structure of the stabilizing region of attached diffusion flames has been successfully simulated. A highest reactivity ($\dot{q}$ $-\omega_{O_2}$, and ω_{H_2O}) spot, that is, the reaction kernel, is formed in a relatively low-temperature (<1600 K), fuel-lean zone in the flame base. The geometric peculiarity of diffusion flame edges allows back-diffusion and interdiffusion of radical species against the incoming oxidizing stream. As a result, chain reactions, including the branching step $H + O_2 \rightarrow OH + O$, are enhanced significantly even at the lower temperatures, and the step $CH_3 + O \rightarrow CH_2O + H$ predominantly contributed to the heat-release rate peak. Heuristic correlations for $\dot{q}$ versus $|\vec{v}|$ or $-\omega_{O_2}$ versus $|\vec{v}|$ valid for both jet- and flat-plate diffusion flames were obtained at the reaction kernel. In the reaction-kernel (mixed convective-diffusive) regime, the stationary reaction kernel provides a continuous ignition source and sustained stable combustion fast enough to consume the incoming reactants, thereby successively holding the trailing diffusion flame in the flow.

Acknowledgments

This work was supported by the U. S. Air Force Research Laboratory, Propulsion Directorate, Propulsion Sciences and Advanced Concept Division, Wright-Patterson Air Force Base, Ohio, under Contract No. F33615-97-C-2719 (Technical Monitor: C. W. Frayne).

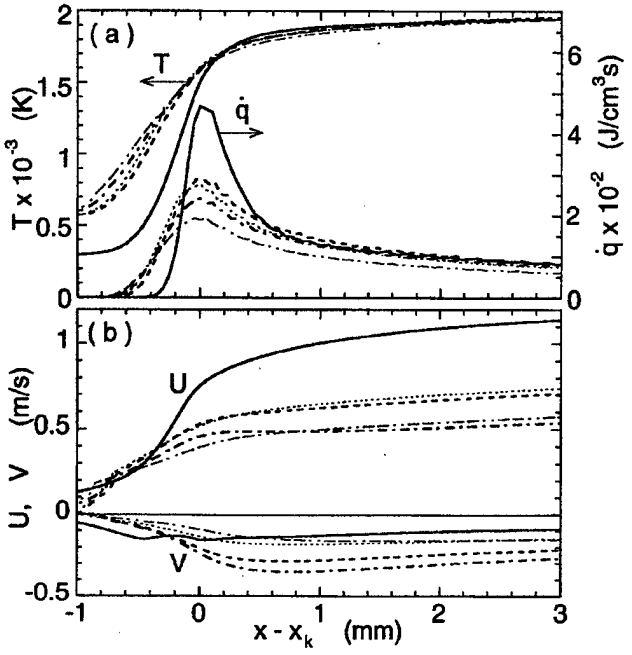

FIG. 8. Variations of the calculated (a) temperature, heat release rate, and (b) axial and radial velocity components along the maximum heat-release rate envelope in the stabilizing region of a methane jet diffusion flame. ··;——, J1; •—•—, J2; - - - - -, J3; – – – –, J4, and ———, J5.

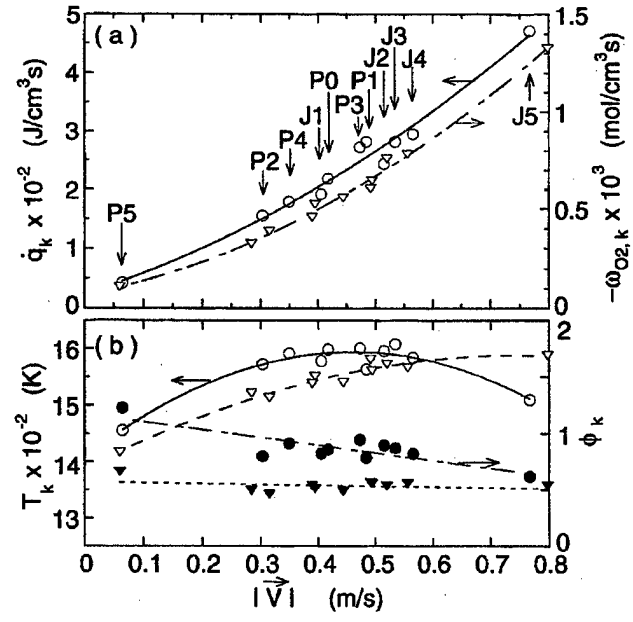

FIG. 9. (a) Correlations of the peak heat-release rate or oxygen consumption rate with the local total velocity, (b) the temperature, and equivalence ratio at the reaction kernel in the methane jet diffusion flames (cases J1–J5) and flat-plate burner diffusion flames (cases P0–P5). ○●, heat-release rate peak; ▼, oxygen consumption rate peak.

REFERENCES

1. Williams, F. A., in *Combustion Theory*, 2nd ed., Benjamin/Cummings, Menlo Park, CA, 1985, pp. 485–519.
2. Lewis, B. and von Elbe, G., in *Combustion, Flames, and Explosions of Gases*, 2nd ed., Academic Press, New York, 1961, pp. 458–510.
3. Vranos, A., Taback, E. E., and Shipman, C. W., *Combust. Flame* 12:253–260 (1968).
4. Robson, K. and Wilson, M. J. G., *Combust. Flame* 13:626–634 (1969).
5. Takeno, T. and Kotani, Y., *Acta Astronautica* 2:999–1008 (1975).
6. Kawamura, T., Asato, K., and Mazaki, T., *Combust. Sci. Technol.* 22:211–216 (1980).
7. Takahashi, F., Mizomoto, M., Ikai, S., and Futaki, N., in *Twentieth Symposium (International) on Combustion*, The Combustion Institute, 1985, pp. 295–302.
8. Eickoff, H., Lenze, B., and Leuckel, W., in *Twentieth Symposium (International) on Combustion*, The Combustion Institute, 1985, pp. 311–318.
9. Takahashi, F., Mizomoto, M., and Ikai, S., *J. Heat Transfer* 110:182–189 (1988).
10. Gollahalli, S. R., Savas, Ö., and Huang, R. F., and Rodriquez Azara, J. L., in *Twenty-First Symposium (International) on Combustion*, The Combustion Institute, 1988, pp. 1463–1471.
11. Chen, L.-D., Seaba, J. P., Roquemore, W. M., and Goss, L. P., in *Twenty-Second Symposium (International) on Combustion*, The Combustion Institute, 1989, pp. 677–684.
12. Coats, C. M. and Zhao, H., in *Twenty-Second Symposium (International) on Combustion*, The Combustion Institute, 1989, pp. 685–692.
13. Takahashi, F. and Schmoll, W. J., in *Twenty-Third Symposium (International) on Combustion*, The Combustion Institute, 1991, pp. 677–683.
14. Takahashi, F., Durbin, M. D., and Vangsness, M. D., in *Transport Phenomena in Combustion* (S. H. Chan, ed.), vol. 1, Taylor & Francis, Washington, DC, 1996, pp. 593–604.
15. Takahashi, F., Schmoll, W. J., Trump, D. D., and Goss, L., in *Twenty-Sixth Symposium (International) on Combustion*, The Combustion Institute, 1996, pp. 145–152.
16. Takahashi, F. and Katta, V. R., in *Twenty-Sixth Symposium (International) on Combustion*, The Combustion Institute, 1996, pp. 1151–1160.
17. Hirano, T. and Kanno, Y., in *Fourteenth Symposium (International) on Combustion*, The Combustion Institute, 1973, pp. 391–398.
18. Chen, C.-H. and T'ien, J. S., *Combust. Sci. Technol.* 50:283–306 (1986).
19. Ueda, T., Ooshima, A., Saito, N., and Mizomoto, M., *JSME Int. J.*, Ser. II, 34:527–532 (1991).
20. Buckmaster, J. and Weber, R., in *Twenty-Sixth Symposium (International) on Combustion*, The Combustion Institute, 1996, pp. 1143–1149.
21. Gaydon, A. G. and Wolfhard, H. G., in *Flames—Their Structure, Radiation and Temperature*, 4th ed., Chapman and Hall, London, 1979, p. 39.
22. Chung, S. H. and Lee, B. J., *Combust. Flame* 86:62–72 (1991).
23. Veynante, D., Vervisch, L., Poinsot, T., Liñán, A., and Ruetsch, G., in *Proceedings of the Summer Program, Center for Turbulence Research*, Stanford University, 1994, pp. 55–73.
24. Tsuji, H. and Yamaoka, I., in *Twelfth Symposium (International) on Combustion*, The Combustion Institute, 1966, pp. 979–984.
25. Katta, V. R., Goss, L. P., and Roquemore, W. M., *AIAA J.* 32:84–94 (1994).
26. Katta, V. R. and Roquemore, W. M., in Central States Section Technical Meeting, The Combustion Institute, St. Louis, MO, May 1996, pp. 449–454.
27. Takahashi, F. and Katta, V. R., in Central States Section Technical Meeting, The Combustion Institute Meeting, Point Clear, Alabama, April 1997, pp. 164–169.
28. Goss, L. P., Post., M. E., Trump, D. D., and Sarka, B., *J. Laser Appl.* 3:36–42 (1991).
29. Peters, N., "Flame Calculations with Reduced Mechanisms—An Outline," in *Reduced Kinetic Mechanisms for Applications in Combustion Systems* (N. Peters and Bernd Rogg, eds.), Springer-Verlag, Berlin, 1993, pp. 3–14.
30. Warnatz, J., in *Combustion Chemistry* (W. C. Gardiner, ed.), Springer-Verlag, New York, 1984, pp. 197–360.
31. Sung, C. J., Liu, J. B., and Law, C. K., *Combust. Flame* 102:481–492 (1995).
32. Dietrich, D. L., Ross, H. D., and T'ien, J. S., in *Third Microgravity Combustion Workshop*, NASA Conference Publication 10174, April 1995, pp. 31–36.

Vol. 36, No. 11, November 1998
AIAA Journal

Simulation of Dynamic Methane Jet Diffusion Flames Using Finite Rate Chemistry Models

Viswanath R. Katta*
Innovative Scientific Solutions, Inc., Dayton, Ohio 45440-3638
and
W. M. Roquemore†
U.S. Air Force Research Laboratory, Wright–Patterson Air Force Base, Ohio 45433-7103

Detailed calculations for methane jet diffusion flames under laminar and transitional conditions are made using an axisymmetric, time-dependent computational fluid dynamics code and different chemical-kinetics models. Comparisons are made with experimental data for a steady-state flame and for two dynamic flames that are dominated by buoyancy-driven instabilities. The ability of the three chemistry models—namely, 1) the modified Peters mechanism without C_2 chemistry, 2) the modified Peters mechanism with C_2 chemistry, and 3) the Gas Research Institute's Version 1.2 mechanism—in predicting the structure of coaxial jet diffusion flames under different operating conditions is investigated. It is found that the modified Peters mechanisms with and without C_2 chemistry are sufficient for the simulation of jet diffusion flames for a wide range of fuel-jet velocities. Detailed images of the vortical structures associated with the low- and transitional-speed methane jet flames are obtained using the reactive-Mie-scattering technique. These images suggest that a counter-rotating vortex is established upstream of the buoyancy-induced toroidal vortex in the low-speed-flame case and that the shear-layer vortices that develop in the transitional-speed flame are dissipated as they are convected downstream. The time-dependent calculations made using the modified Peters chemistry model have captured these unique features of the buoyancy-influenced jet flames. Finally, the unsteady flame structures obtained at a given height are compared with the steady-state flame structures.

Nomenclature

A	= coefficient used in finite difference equation
A_k	= pre-exponential in Arrhenius rate expression
c_p	= specific heat of mixture
D_{im}	= diffusion coefficient ith species in the mixture
E	= activation energy
g	= gravitational acceleration
H	= enthalpy
h	= total enthalpy
h_f^0	= heat of formation at standard state
Le	= Lewis number
M	= molecular weight
N_s	= total number of species
p	= pressure
R_0	= universal gas constant
r	= radial distance
r_f	= radius of flame surface
S^Φ	= source term in Φ equation
T	= temperature
t	= time
u	= axial-velocity component
v	= radial-velocity component
X_i	= mole fraction of ith species
Y_i	= mass fraction of ith species
z	= axial distance
α	= constant appearing in modified Arrhenius rate expression
Γ^Φ	= transport coefficient in Φ equation
λ	= thermal conductivity
μ	= viscosity
ρ	= density
ρ_0	= density of air
Φ	= flow variable
$\dot{\omega}$	= net rate of production of a species

Subscripts

i	= ith species
P	= reference grid point
z^+, r^+	= grid points adjacent to P in z and r directions, respectively
z^{++}, r^{++}	= two grid points away from P in z and r directions, respectively
z^-, r^-	= grid points adjacent to P in negative z and r directions, respectively
z^{--}, r^{--}	= two grid points away from P in negative z and r directions, respectively

Superscripts

$N, N+1$	= time-step numbers

Introduction

INVESTIGATIONS of unsteady flames are important for understanding combustion phenomena in practical systems and for developing theories of turbulent-combustion processes. For this reason dynamic jet flames have been actively studied since the classic work of Hottel and Hawthorne[1] was published in 1949. Most of the data obtained in the past were on statistical quantities such as time-averaged and rms values of velocity, temperature, and species concentration, and point and planar measurement techniques were used. These data have formed the basis for understanding many of the processes occurring in dynamic jet diffusion flames. However, such understanding has limited applications for engineering problems because of the time-averaged description of the underlying unsteady combustion processes. In many cases, the mean and fluctuating quantities can mask the physics and chemistry that are germane to an understanding of the fundamental processes that give rise to the statistical results. This is particularly true for

Presented as Paper 97-0904 at the AIAA 35th Aerospace Sciences Meeting, Reno, NV, Jan. 6–9, 1997; received Sept. 12, 1997; revision received June 30, 1998; accepted for publication July 27, 1998. This paper is declared a work of the U.S. Government and is not subject to copyright protection in the United States.

*Senior Engineer, 2766 Indian Ripple Road. E-mail: vrkatta@snake.appl.wpafb.af.mil. Member AIAA.
†Senior Scientist, Propulsion Directorate. Member AIAA.

laminar and near-transitional jet flames in which the large-scale, low-frequency (0–40 Hz), organized buoyancy-induced vortices on the air side of the flame and medium-frequency (100–1000 Hz), Kelvin–Helmholtz-type vortex structures on the fuel side of the flame dominate the flame characteristics. For example, high-speed visualizations of a buoyant jet diffusion flame have revealed that the flame surface is actually wrinkled as a result of the interaction of vortices, whereas time-averaged visualizations indicate a smooth surface. To gain insight into these low- and medium-frequency dynamic processes, it is helpful—and, perhaps, essential—to think in terms of the time-dependent characteristics of jet flames.

Several past numerical investigations on dynamic jet flames employed conserved-scalar and primitive-variable approaches. These studies revealed important aspects of combustion such as the effect of heat-release rate,[2,3] the role of buoyancy,[4–6] the enhancement of soot formation,[7] and Lewis number effects.[8,9] However, in most of these studies a simple, one-step global-chemistry model was used for representing the combustion processes. On the other hand, studies incorporating finite rate chemistry are limited to hydrogen fuel because the kinetic models for this fuel are relatively simple. Because of the complex nature of hydrocarbon reaction mechanisms, detailed flame calculations for hydrocarbon fuels are restricted to steady-state problems.[10,11] However, for understanding processes such as flame stabilization,[12] local extinction,[13] and ignition[14] in dynamic hydrocarbon flames, these flames must be simulated with sufficiently accurate models for physical and chemical processes. Over the past five years, the authors have been developing time-accurate computational fluid dynamics with chemistry (CFDC) codes by incorporating different detailed chemical-kinetics models for the investigation of unsteady jet diffusion flames.[15–17] Studies employing these codes have indicated that consideration of finite rate chemistry is essential for the simulation of localized hot spots in temperature and species concentration on the wrinkled flame surfaces.[18]

The present paper describes a numerical study conducted using the CFDC code on a coaxial methane jet diffusion flame formed under different flow conditions. The accuracy of three detailed chemical-kinetics models [Peters mechanisms with and without C_2 chemistry and the Gas Research Institute's (GRI) Version 1.2 mechanism] in simulating a steady methane diffusion flame is assessed. The dynamic flames predicted by the CFDC code are compared with experimental flame images obtained using the reactive-Mie-scattering technique. Finally, the structure of the dynamic flame is compared with that of the steady-state flame to quantify the impact of vortex–flame interactions on jet flames.

Modeling

A time-dependent, axisymmetric mathematical model that solves for axial- and radial-momentum equations, continuity, and enthalpy- and species-conservation equations is used to simulate the dynamic jet diffusion flames. The governing equations, written in the cylindrical coordinate system, are as follows:

$$\frac{\partial \rho}{\partial t} + \frac{\partial \rho u}{\partial z} + \frac{1}{r}\frac{\partial (r\rho v)}{\partial r} = 0 \tag{1}$$

$$\frac{\partial (\rho \Phi)}{\partial t} + \frac{\partial (\rho u \Phi)}{\partial z} + \frac{1}{r}\frac{\partial (r\rho v \Phi)}{\partial r} = \frac{\partial}{\partial z}\left(\Gamma^{\Phi}\frac{\partial \Phi}{\partial z}\right) + \frac{1}{r}\frac{\partial}{\partial r}\left(r\Gamma^{\Phi}\frac{\partial \Phi}{\partial r}\right) + S^{\Phi} \tag{2}$$

The general form of Eq. (2) represents the momentum, the species, or the energy-conservation equation, depending on the variable used in place of Φ. The transport coefficients Γ^{Φ} and the source terms S^{Φ} that appear in the governing equations are given in Table 1. The body-force term due to the gravitational field is included in the axial-momentum equation, where $\dot{\omega}_i$ is the mass-production rate of the ith species, and ρ_0 is the density of air. The transport property D_{im} is calculated from the binary diffusion coefficients between the ith species and the other individual species. Finally, Le_i is the Lewis number of the ith species, which is defined as

$$Le_i \equiv \frac{\lambda}{\rho D_{im} c_p} \tag{3}$$

Table 1 Transport coefficients and source terms appearing in governing equations

Φ	Γ^{Φ}	S^{Φ}
u	μ	$-\frac{\partial p}{\partial z} + (\rho_0 - \rho)g + \frac{\partial}{\partial z}\left(\mu\frac{\partial u}{\partial z}\right) + \frac{\partial}{\partial r}\left(\mu\frac{\partial v}{\partial z}\right) + \frac{\mu}{r}\frac{\partial v}{\partial z} - \frac{2}{3}\left[\frac{\partial}{\partial z}\left(\mu\frac{\partial u}{\partial z}\right) + \frac{\partial}{\partial z}\left(\mu\frac{\partial v}{\partial r}\right)\right] + \frac{\partial}{\partial z}\left(\mu\frac{v}{r}\right)$
v	μ	$-\frac{\partial p}{\partial r} + \frac{\partial}{\partial z}\left(\mu\frac{\partial u}{\partial r}\right) + \frac{\partial}{\partial r}\left(\mu\frac{\partial v}{\partial r}\right) + \frac{\mu}{r}\frac{\partial v}{\partial r} - 2\mu\frac{v}{r^2} - \frac{2}{3}\left[\frac{\partial}{\partial r}\left(\mu\frac{\partial u}{\partial z}\right) + \frac{\partial}{\partial r}\left(\mu\frac{\partial v}{\partial r}\right)\right] + \frac{\partial}{\partial r}\left(\mu\frac{v}{r}\right)$
Y_i $(i = 1 - N_s - 1)$	ρD_{im}	$\dot{\omega}_i$
H	$\frac{\lambda}{c_p}$	$\nabla\left\{\frac{\lambda}{c_p}\sum_1^{N_s}[(Le^{-1} - 1)H_i \nabla Y_i]\right\} - \sum_1^{N_s}\left(h_{fi}^0 \dot{\omega}_i\right)$

The set of expressions given by Eqs. (1) and (2) can be completed using the global-species-conservation equation

$$Y_{N_s} = 1.0 - \sum_i^{N_s - 1} Y_i \tag{4}$$

and the state equation

$$p = \rho T R_0 \sum_1^{N}\left(\frac{Y_i}{M_i}\right) \tag{5}$$

Whereas the density is obtained by solving the state equation (4), the pressure field at every time step is determined from pressure Poisson equations. Even though the governing equations are solved in an uncoupled manner, the species-conservation equations are coupled through the source terms during the solution process to improve the stability of the algorithm. Such coupling is essential in finite rate chemistry calculations because the high-reaction-rate terms make the species-conservation equations quite stiff. Temperature- and species-dependent thermodynamic and transport properties are used in this formulation.

The governing equations for u and v momentum are integrated using an implicit quadratic upstream interpolation for convective kinematics with estimated streaming terms numerical scheme,[17,19] which is third order accurate in both space and time and has a very low numerical diffusion error. On the other hand, the finite difference form of the species and enthalpy is obtained using the hybrid scheme[20] with upwind and central differencing. An orthogonal, staggered-grid system with rapidly expanding cell sizes in both the z and the r directions is utilized for discretizing the governing equations. After rearrangement of terms, the finite difference form of the governing equation for the variable Φ at a grid point P can be written as an algebraic equation as follows:

$$A_P \Phi_P^{N+1} + A_{z++}\Phi_{z++}^{N+1} + A_{z+}\Phi_{z+}^{N+1} + A_{z-}\Phi_{z-}^{N+1} + A_{z--}\Phi_{z--}^{N+1} + A_{r++}\Phi_{r++}^{N+1} + A_{r+}\Phi_{r+}^{N+1} + A_{r-}\Phi_{r-}^{N+1} + A_{r--}\Phi_{r--}^{N+1} = S_P^{\Phi} + \Delta t \cdot \rho_P \Phi_P^N \tag{6}$$

The time increment t is determined from the stability constraint and maintained as a constant during the entire calculation. The superscripts N and $N+1$ represent the known variables at the Nth time step and the unknown variables at the $(N+1)$th time step, respectively. The coefficients A and the terms on the right-hand side of the preceding equations are calculated from the known flow variables at the Nth time step. The preceding equations for $N_s + 2$ variables are solved individually using an iterative alternative direction implicit technique. The pressure field at every time step is accurately calculated by simultaneously solving the system of algebraic pressure

Poisson equations at all grid points using the lower-upper decomposition technique.

Three detailed chemical-kinetics models proposed in the literature for methane air combustion were used in this study. The first was proposed by Peters[21] and consists of 17 species (CH_4, O_2, CH_3, CH_2, CH, CH_2O, CHO, CO_2, CO, H_2, H, O, OH, H_2O, HO_2, H_2O_2, and N_2) that are involved in 52 elementary reactions. This mechanism is derived from the one originally published[21] for the hydrocarbon fuels up to propane in terms of carbon content and by neglecting the species that have more than one carbon element. The second chemistry model is an extension of the first and was obtained by including the C_2 chemistry,[21] which adds seven species (C_2H, C_2H_2, C_2H_3, C_2H_4, C_2H_5, C_2H_6, and CHCO) and 29 reactions. Finally, the third chemical-kinetics model, GRI Version 1.2, used in the present study was compiled by the Gas Research Institute. This is the most comprehensive mechanism, having 31 species and 346 elementary reaction steps, and is recommended by several investigators for computing the structures of methane flames.[22] In addition to the 24 species in the second model (Peters mechanism with C_2 chemistry), the GRI mechanism uses the following 7 species: C, $CH_2(S)$, CH_2OH, CH_3O, CH_3OH, CH_2CO, and HCCOH.

The enthalpies of all of the species are calculated from the polynomial curvefits developed for the temperature range 300–5000 K. Physical properties such as viscosity, thermal conductivity, and the binary molecular diffusion coefficients of the species are calculated using molecular dynamics. Mixture viscosity and thermal conductivity are then estimated using the Wilke and the Kee expressions,[23] respectively. Molecular diffusion is assumed to be of the binary type, and the diffusion velocity of a species is calculated according to Fick's law and using the effective-diffusion coefficient[24] of that species. The Lennard Jones potentials, the effective temperatures, and the coefficients for the enthalpy polynomials for each species are obtained from the CHEMKIN libraries.

The flowfield considered in the present study has vortical structures of two scales. Small-scale vortices develop on the fuel side of the flame surface along the shear layer of the fuel jet, and larger-scale vortices form on the air side of the flame surface. Unsteady axisymmetric calculations are made on a physical domain of 200 × 150 mm utilizing a 201 × 71 nonuniform grid system. Generally, the computational domain is bounded by the axis of symmetry and an outflow boundary in the radial direction and by the inflow and another outflow boundary in the axial direction. The outer boundaries in the z and r directions are located sufficiently far from the nozzle exit (~30 nozzle diameters) and the symmetry axis (~20 nozzle diameters), respectively, that propagation of boundary-induced disturbances into the region of interest is minimized. However, for the cases in which the flames were enclosed in a chimney, the outer boundary in the radial direction is located at a distance equal to the chimney radius, and no-slip wall conditions were imposed along this boundary.

Jet diffusion flames usually anchor to the outer edge of the burner lip, and the structure of the flame near the base depends on the boundary layer developed on the fuel tube and the heat transfer between the burner lip and the flame. However, at downstream locations (typically >1 burner diameter) the structure of the flame becomes insensitive to the flame-base conditions. Because the present study was focused on the region away from the flame base, flow in the neighborhood of the burner lip was not simulated. Flat velocity profiles were imposed at the fuel and air inflow boundaries to represent the flows exiting a contoured nozzle and a large annular duct, respectively. An extrapolation procedure with weighted zero- and first-order terms was used to estimate the flow variables at the outflow boundary.[25]

The simulations presented here were performed on a Pentium Pro 200-MHz-based personal computer with 128 MB of memory. Typical execution times using the modified Peters mechanisms without and with C_2 chemistry and the GRI Version 1.2 mechanism are ~20, ~40, and ~100 s/time step, respectively. Stably oscillating flames are usually obtained in about 3000 time steps (which corresponds to approximately four flicker cycles), starting from the solution obtained with a global-chemistry model.[15,17] It is interesting to note that, for a transitional jet diffusion flame having vortices inside and outside the flame surface, a detailed time-dependent simulation using 31 species and 346 elementary reactions (GRI Version 1.2 mechanism) can be made on a personal computer in <80 h.

Results and Discussion

Because of the complex nature of chemical kinetics for methane combustion, several mechanisms with varying degrees of simplification have been proposed in the literature.[26–28] It is important to note that most of these mechanisms have been validated using well-stirred-reactor data (zero-dimensional problem) and counterflow flames (one-dimensional problem). However, because the multidimensional flames that are encountered in practical geometries are subjected to varying levels of strain rate, unsteadiness, and curvature, for example, a question arises as to the accuracy of the predictions of these chemistry models when used for multidimensional flame problems. Initially calculations were made for jet diffusion flames for several jet velocities using different chemical-kinetics models available in the literature. Indeed, our initial attempts to simulate jet diffusion flames with simpler chemistry models (such as in Ref. 26) resulted in unacceptable flame standoff distances (separation between the flame base and the nozzle exit) for different fuel jet velocities. The most recent skeletal mechanism proposed by Peters for methane combustion (24 species and 81 reactions) yielded well-attached flames for lower fuel jet velocities but failed to predict the flames that are formed at higher velocities. A trial-and-error investigation of this mechanism revealed that the methyl-radical recombination reaction ($CH_3 + H = CH_4$) is very sensitive to the extinction and standoff distance characteristics of diffusion flames. When the reaction rate proposed by Peters for this reaction is replaced by that proposed by Warnatz,[29] excellent agreement between experiment and calculation is obtained over a wide range of fuel and annular-air velocities. The mechanism obtained after replacing the rate data for the methyl-radical-recombination reaction is referred to as the modified Peters mechanism in this paper and is listed in Table 2. The reaction that differs from the original Peters mechanism is R45 in this table. Further details about the development of the modified Peters mechanism can be found in Ref. 30.

Steady-State Flame

The mathematical model and the numerical procedure used in the present investigation were tested for their accuracy in simulating a confined jet diffusion flame. The flame chosen for this purpose was previously studied experimentally by Mitchell et al.[31] and numerically by Smooke.[10] The burner assembly consists of a 12.7-mm-diam central fuel tube and a large 50.8-mm-diam coannular-air duct. The burner is enclosed in a 300-mm-long Pyrex® tube; therefore, the no-slip boundary condition is employed at the end of the computational domain in the radial direction. Pure methane is used as the fuel. The flow rates for the fuel and air are such that the velocities at the exits of the central fuel tube and the annular-air duct are 0.045 and 0.0988 m/s, respectively. The experimental data on this methane jet diffusion flame obtained by Mitchell et al.[31] suggest that the flame is in steady state; hence, Smooke[10] performed steady-state axisymmetric calculations for this flame. Gravitational force, which is quite significant in this low-speed flame, is considered in Smooke's steady-state calculations. Our previous studies on vertically mounted jet diffusion flames under similar velocity conditions indicated that buoyancy-driven vortical structures could develop and make the flame unsteady. However, the flame investigated by Mitchell et al.[31] was confined, and the ambient airflow into the flame was restricted, which could have suppressed the growth of the buoyancy-induced instabilities. For comparison purpose, unsteady calculations were performed for this flame using the code described previously and with the three different chemistry models. Interestingly, the computed flame established weak vortical structures outside the flame surface. As these vortices are convected downstream, their interaction with the flame makes it flicker. However, the oscillations (or unsteadiness) up to a height of 60 mm above the burner are quite weak. Calculations performed without the Pyrex enclosure, i.e., replacing the wall boundary with the free outflow boundary, yielded much stronger fluctuations, which also suggests that confinement reduces the flame flicker.

Calculations were initially made using different mesh systems to obtain grid-independent results. The modified Peters mechanism without C_2 chemistry was used in these calculations, and the results obtained with 141 × 61 and 251 × 91 mesh systems are shown in Fig. 1. In each mesh system, grid points are clustered in the

Table 2 Modified Peters mechanism for methane jet diffusion flames

Reaction		A_k, mole, cm^3, s	α	E, cal/mole
H_2/O_2 chain reactions				
(R01) $H+O_2 \Rightarrow OH+O$		2.00E+14	0.0	16,800
(R02) $OH+O \Rightarrow H+O_2$		1.57E+13	0.0	840
(R03) $O+H_2 \Rightarrow OH+H$		5.06E+04	2.67	6,280
(R04) $OH+H \Rightarrow O+H_2$		2.22E+04	2.67	4,370
(R05) $H_2+OH \Rightarrow H_2O+H$		1.00E+08	1.60	3,300
(R06) $H_2O+H \Rightarrow H_2+OH$		4.31E+08	1.60	18,270
(R07) $OH+OH \Rightarrow O+H_2O$		1.50E+09	1.14	100
(R08) $H_2O+O \Rightarrow OH+OH$		1.47E+10	1.14	17,000
H_2O formation and consumption				
(R09) $O_2+H+M \Rightarrow HO_2+M$		2.30E+18	−0.8	0
(R10) $HO_2+M \Rightarrow O_2+H+M$		3.19E+18	−0.8	46,680
(R11) $HO_2+H \Rightarrow OH+OH$		1.50E+14	0.0	1,000
(R12) $HO_2+H \Rightarrow H_2+O_2$		2.50E+13	0.0	692
(R13) $HO_2+OH \Rightarrow H_2O+O_2$		6.00E+13	0.0	0
(R14) $HO_2+H \Rightarrow H_2O+O$		3.00E+13	0.0	1,720
(R15) $HO_2+O \Rightarrow OH+O_2$		1.80E+13	0.0	−406
H_2O_2 formation and consumption				
(R16) $HO_2+HO_2 \Rightarrow H_2O_2+O_2$		2.50E+11	0.0	−1,240
(R17) $OH+OH+M \Rightarrow H_2O_2+M$		3.25E+22	−2.0	0
(R18) $H_2O_2+M \Rightarrow OH+OH+M$		1.69E+24	−2.0	48,330
(R19) $H_2O_2+H \Rightarrow H_2O+OH$		1.00E+13	0.0	3,580
(R20) $H_2O_2+OH \Rightarrow H_2O+HO_2$		5.40E+12	0.0	1,000
(R21) $H_2O+HO_2 \Rightarrow H_2O_2+OH$		1.80E+13	0.0	32,190
Recombination reactions				
(R22) $H+H+M \Rightarrow H_2+M$		1.80E+13	−1.0	0
(R23) $H+OH+M \Rightarrow H_2O+M$		2.20E+22	−2.0	0
(R24) $O+O+M \Rightarrow O_2+M$		2.90E+17	−1.0	0
CO/CO_2 mechanism				
(R25) $CO+OH \Rightarrow CO_2+H$		4.40E+06	1.5	−740
(R26) $CO_2+H \Rightarrow CO+OH$		4.96E+08	1.5	21,440
CH consumption reactions				
(R27) $CH+O_2 \Rightarrow CHO+O$		3.00E+13	0.0	0
(R28) $CO_2+CH \Rightarrow CHO+CO$		3.40E+12	0.0	692
CHO consumption reactions				
(R29) $CHO+H \Rightarrow CO+H_2$		2.00E+14	0.0	0
(R30) $CHO+OH \Rightarrow CO+H_2O$		1.00E+14	0.0	0
(R31) $CHO+O_2 \Rightarrow CO+HO_2$		3.00E+12	0.0	0
(R32) $CHO+M \Rightarrow CO+H+M$		7.10E+14	0.0	16,800
(R33) $H+CO+M \Rightarrow CHO+M$		1.14E+15	0.0	2,380
CH_2 consumption reactions				
(R34) $CH_2+H \Rightarrow CH+H_2$		8.40E+09	1.5	335
(R35) $CH+H_2 \Rightarrow CH_2+H$		5.83E+09	1.5	3,125
(R36) $CH_2+O \Rightarrow CO+H+H$		8.00E+13	0.0	0
(R37) $CH_2+O_2 \Rightarrow CO+OH+H$		6.50E+12	0.0	1,500
(R38) $CH_2+O_2 \Rightarrow CO_2+H+H$		6.50E+12	0.0	1,500
CH_2O consumption reactions				
(R39) $CH_2O+H \Rightarrow CHO+H_2$		2.50E+13	0.0	3,990
(R40) $CH_2O+O \Rightarrow CHO+OH$		3.50E+13	0.0	3,490
(R41) $CH_2O+OH \Rightarrow CHO+H_2O$		3.00E+13	0.0	1,200
(R42) $CH_2O+M \Rightarrow CHO+H+M$		1.40E+17	0.0	76,500
CH_3 consumption reactions				
(R43) $CH_3+H \Rightarrow CH_2+H_2$		1.80E+14	0.0	15,050
(R44) $CH_2+H_2 \Rightarrow CH_3+H$		3.68E+13	0.0	10,580
(R45) $CH_3+H \Rightarrow CH_4$	K_∞	6.00E+16	−1.0	0
	K_0	8.00E+26	−3.0	0
(R46) $CH_3+O \Rightarrow CH_2O+H$		7.00E+13	0.0	0
(R47) $CH_3+CH_3 \Rightarrow C_2H_6$	K_∞	3.61E+13	0.0	0
	K_0	1.27E+41	−7.0	2,762
(R48) $CH_3+O_2 \Rightarrow CH_2O+OH$		3.40E+11	0.0	8,940
(R49) $CH_3+H_2 \Rightarrow CH_4+H$		8.39E+02	3.0	8,260
(R50) $CH_3+H_2O \Rightarrow CH_4+OH$		2.63E+05	2.10	16,950
CH_4 consumption reactions				
(R51) $CH_4+H \Rightarrow CH_3+H_2$		2.20E+04	3.0	8,740
(R52) $CH_4+O \Rightarrow CH_3+OH$		1.20E+07	2.1	7,620
(R53) $CH_4+OH \Rightarrow CH_3+H_2O$		1.60E+06	2.1	2,460
C_2H consumption reactions				
(R54) $C_2H+H_2 \Rightarrow C_2H_2+H$		1.10E+13	0.0	2,867
(R55) $C_2H_2+H \Rightarrow C_2H+H_2$		5.27E+13	0.0	28,656
(R56) $C_2H+O_2 \Rightarrow CHCO+O$		5.00E+13	0.0	1,505
CHCO consumption reactions				
(R57) $CHCO+H \Rightarrow CH_2+CO$		3.00E+13	0.0	0
(R58) $CH_2+CO \Rightarrow CHCO+H$		2.36E+12	0.0	−7,021
(R59) $CHCO+O \Rightarrow CO+CO+H$		1.00E+14	0.0	0
C_2H_2 consumption reactions				
(R60) $C_2H_2+O \Rightarrow CH_2+CO$		4.10E+08	1.5	1,696

Table 2 (Continued.)

Reaction		A_k, mole, cm^3, s	α	E, cal/mole
(R61) $C_2H_2+O \Rightarrow CHCO+H$		4.30E+14	0.0	12,112
(R62) $C_2H_2+OH \Rightarrow C_2H+H_2O$		1.00E+13	0.0	7,000
(R63) $C_2H+H_2O \Rightarrow C_2H_2+OH$		9.00E+12	0.0	−3,818
C_2H_3 consumption reactions				
(R64) $C_2H_3+H \Rightarrow C_2H_2+H_2$		3.00E+13	0.0	0
(R65) $C_2H_3+O_2 \Rightarrow C_2H_2+HO_2$		5.40E+11	0.0	0
(R66) $C_2H_3 \Rightarrow C_2H_2+H$	K_∞	2.00E+14	0.0	39,717
	K_0	1.19E+42	−7.5	45,486
(R67) $C_2H_2+H \Rightarrow C_2H_3$	K_∞	1.05E+14	0.0	810
C_2H_4 consumption reactions				
(R68) $C_2H_4+H \Rightarrow C_2H_3+H_2$		1.50E+14	0.0	10,201
(R69) $C_2H_3+H_2 \Rightarrow C_2H_4+H$		9.61E+12	0.0	7,800
(R70) $C_2H_4+O \Rightarrow CH_3+CO+H$		1.60E+09	1.2	741
(R71) $C_2H_4+OH \Rightarrow C_2H_3+H_2O$		3.00E+13	0.0	3,010
(R72) $C_2H_3+H_2O \Rightarrow C_2H_4+OH$		8.29E+12	0.0	15,576
(R73) $C_2H_4+M \Rightarrow C_2H_2+H_2+M$		2.50E+17	0.0	76,400
C_2H_5 consumption reactions				
(R74) $C_2H_5+H \Rightarrow CH_3+CH_3$		3.00E+13	0.0	0.0
(R75) $CH_3+CH_3 \Rightarrow C_2H_5+H$		3.57E+12	0.0	11,870
(R76) $C_2H_5+O_2 \Rightarrow C_2H_4+HO_2$		2.00E+12	0.0	4,993
(R77) $C_2H_5 \Rightarrow C_2H_4+H$	K_∞	2.00E+13	0.0	39,657
	K_0	1.00E+17	0.0	31,057
(R78) $C_2H_4+H \Rightarrow C_2H_5$	K_∞	3.19E+13	0.0	3,013
C_2H_6 consumption reactions				
(R79) $C_2H_6+H \Rightarrow C_2H_5+H_2$		5.40E+02	3.5	5,208
(R80) $C_2H_6+O \Rightarrow C_2H_5+OH$		3.00E+07	2.0	5,112
(R81) $C_2H_6+OH \Rightarrow C_2H_5+H_2O$		6.30E+06	2.0	645

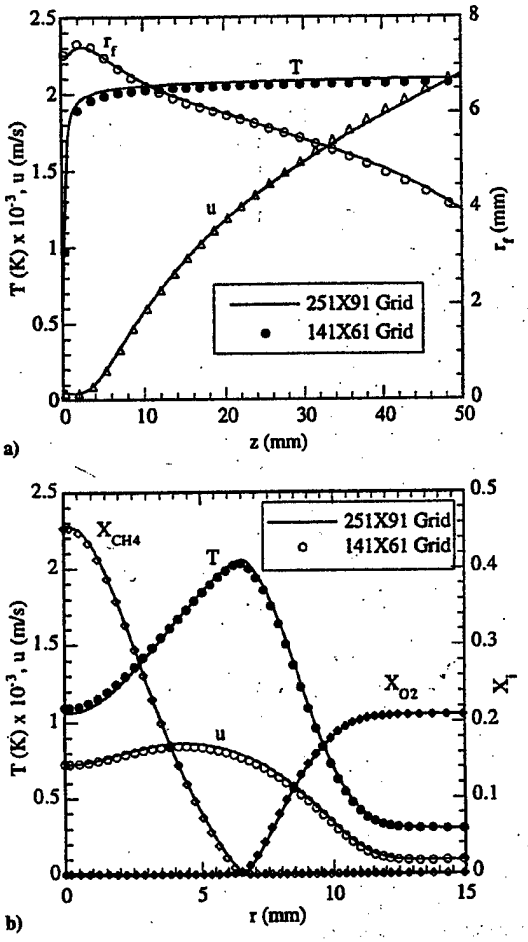

Fig. 1 Flame structures obtained with two different grids; calculations made using modified Peters mechanism without C_2 chemistry: a) axial distributions of peak temperature and its location and local axial velocity; and b) radial distributions of temperature, axial velocity, and fuel and oxygen mole fractions at $z = 12$ mm.

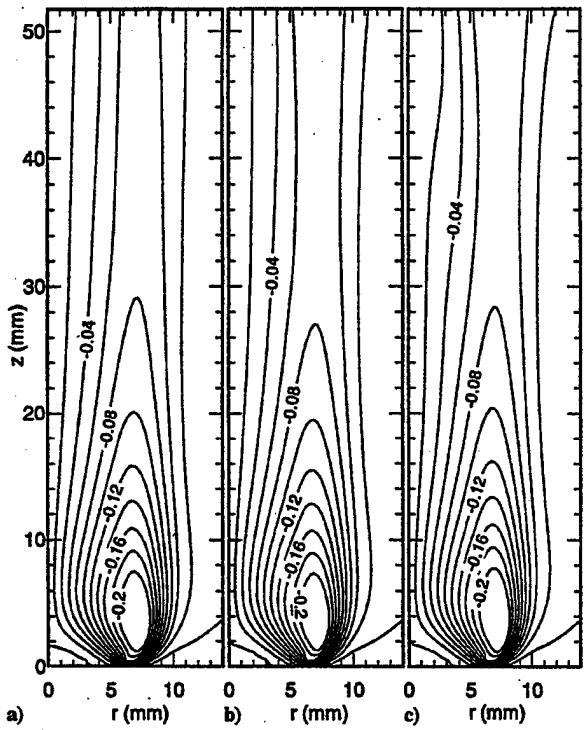

Fig. 2 Comparison of radial-velocity distributions obtained with a) modified Peters mechanism without C_2 chemistry, b) modified Peters mechanism with C_2 chemistry, and c) GRI Version 1.2 mechanism.

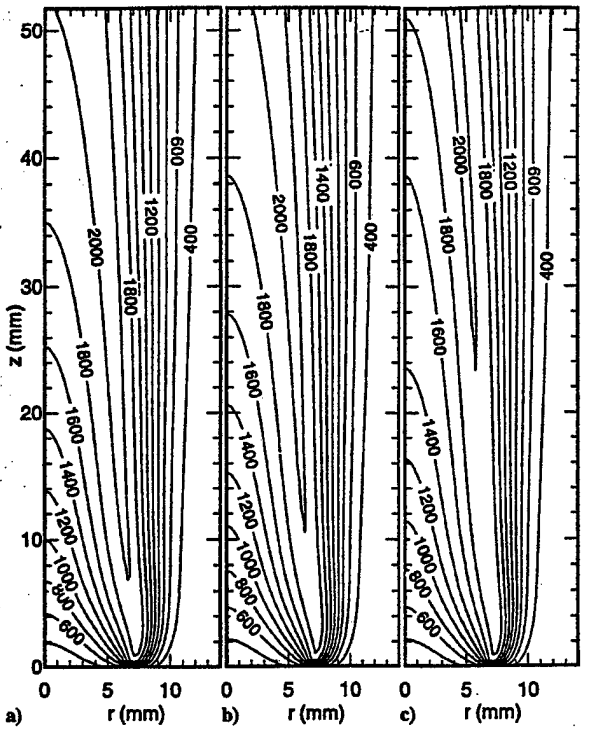

Fig. 3 Temperature distributions obtained with a) modified Peters mechanism without C_2 chemistry, b) modified Peters mechanism with C_2 chemistry, and c) GRI Version 1.2 mechanism.

neighborhood of the flame zone located between 0 and 50 mm in the axial direction. Such clustering yielded grid spacings of 0.56 and 0.28 mm in the axial and radial directions, respectively, in the neighborhood of the flame zone with the 171 × 61 mesh. The corresponding grid spacings obtained with the 251 × 91 mesh system were 0.28 and 0.14 mm in the axial and radial directions, respectively.

The variation of peak temperature location r_f with axial distance in Fig. 1a suggests that the flame near the base is bulging outwardly to accommodate a weak recirculation zone in the fuel jet. In low-speed diffusion flames, acceleration of hot combustion products due to gravitational force leads to the formation of a recirculation zone in the fuel jet,[32] as seen in the axial-velocity distribution in Fig. 1a. A comparison of results in Fig. 1 obtained with 141 × 61 and 251 × 91 mesh systems suggests that the former mesh is yielding near-grid-independent results. A maximum difference of 24 K may be noted between the peak temperatures obtained with these two mesh systems. Based on these comparisons, further calculations for this flame were made using different chemistry mechanisms on a 141 × 71 mesh system.

The results in the form of isocontours of radial velocity, temperature, and mole fractions of CH_3 and OH radicals are shown in Figs. 2–5, respectively. The flowfields computed with the three chemistry models—namely, the modified Peters mechanism without C_2 chemistry (Fig. 2a), the modified Peters mechanism with C_2 chemistry (Fig. 2b), and the GRI Version 1.2 mechanism (Fig. 2c)—are quite similar. Weak oscillations resulting from the buoyancy-induced instability are evident from the slightly squeezed isoradial contours in the region between $z = 30$ and 50 mm.

All three chemistry models predicted the same temperature distributions (Fig. 3) on the air side of the flame ($r > 6.5$ mm). However, on the fuel side, the GRI mechanism predicted lower temperatures than the two modified Peters mechanisms. In fact, the peak temperature of 2040 K predicted by GRI chemical kinetics is 50 K lower than that obtained with the Peters mechanism without C_2 chemistry and ~20 K lower than that obtained with C_2 chemistry. These results suggest that the formation of higher hydrocarbons affects the flame structure on the fuel side of a jet diffusion flame. This is also evident in the methyl-radical-concentration plots of Fig. 5. Here, CH_3 is confined to the fuel side, and inclusion of C_2 chemistry reduces its concentration (compare Figs. 5a and 5b). The peak concentration

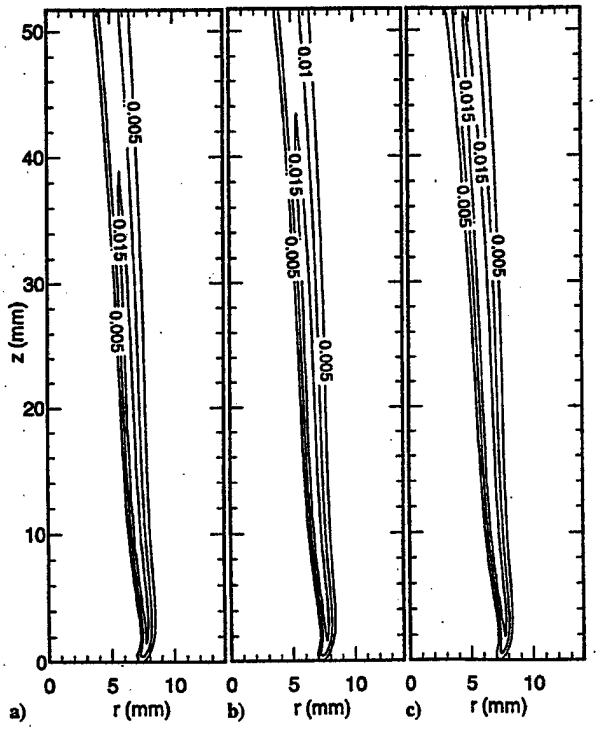

Fig. 4 OH-radical mole-fraction distributions obtained with a) modified Peters mechanism without C_2 chemistry, b) modified Peters mechanism with C_2 chemistry, and c) GRI Version 1.2 mechanism.

for CH_3 radicals predicted by the Peters mechanism with C_2 chemistry (~0.006) is very near that predicted with the GRI Version 1.2 mechanism. Interestingly, the three kinetics models yielded similar distributions for OH-radical concentration (Fig. 4). As expected, the location of the peak OH concentration is found to be shifted from the peak temperature location and is on the air side.

The model predictions are compared with the measured values of Mitchell et al.[31] in Figs. 6–9. In each figure the data collected at three

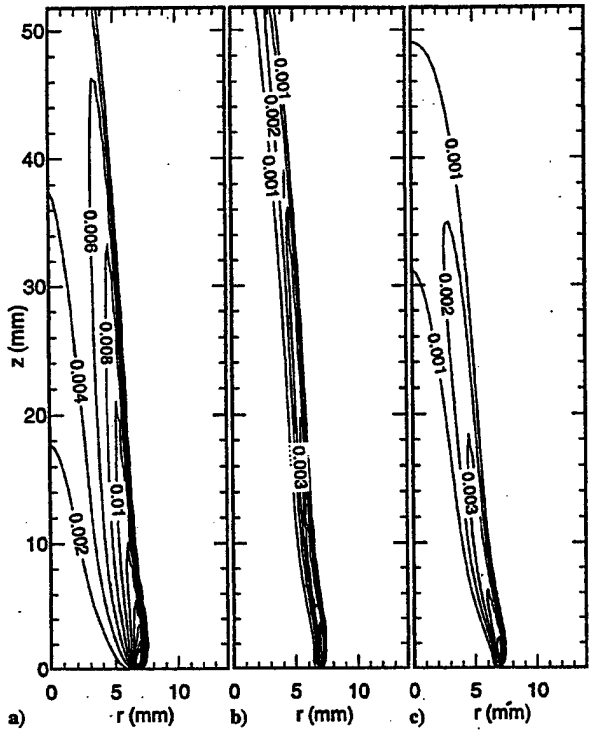

Fig. 5 Computed methyl-radical (CH_3) distributions with a) modified Peters mechanism without C_2 chemistry, b) modified Peters mechanism with C_2 chemistry, and c) GRI Version 1.2 mechanism.

heights, $z = 12$, 24, and 50 mm, are compared. Figure 6 compares temperature and axial velocity, and Figs. 7–9 show comparisons for species concentrations.

The experiments of Mitchell et al.[31] indicate that a noticeable amount of oxygen is present in the potential core of the flame at $z = 12$ mm (Fig. 7a). Calculations made with the Peters mechanism with C_2 chemistry and the GRI mechanism have reasonably predicted this feature of the diffusion flame. The decrease in measured oxygen concentration with radial distance in the potential core suggests that the observed oxygen on the fuel side of the flame was transported from upstream locations. However, for this to occur, the flame at the base (or burner exit) would not be completely attached to the burner such that oxygen would enter the potential core through the dark space between the flame base and the burner. The computed temperature distribution (obtained with the modified Peters without C_2 chemistry) plotted in Fig. 3a indicates that this flame is nearer to the nozzle than the other two flames (Figs. 3b and 3c), which, in turn, leads to lower oxygen concentration in the potential core in Fig. 7a. Because the standoff distance between the nozzle exit and the flame base depends on the heat transfer to the burner and on the nozzle geometry, which were not modeled in the present study, one should not conclude—based on the oxygen data in the fuel jet—that one mechanism is more accurate than the other.

Considering the limitations of the present CFDC model and the uncertainty in the experimental data, it may be concluded that all three chemical mechanisms are yielding reasonably accurate flame structures. However, because of the higher number of species and reaction steps, calculations with the GRI mechanism (31 species and 346 reaction) required a CPU time greater by a factor of 5 than that required for the calculations made with the Peters mechanism (17 species and 52 reactions) and greater by a factor of 3 than that required for the Peters mechanism with C_2 chemistry (24 species and 81 reactions).

Dynamic Flames

The experimental setup used for the study of these flames consists of vertically mounted coannular jets and is described in Ref. 33. The central fuel jet is a 25.4-mm-diam tube that contracts to a 10-mm-diam nozzle. The nozzle is designed to provide a flat mean velocity profile with low-velocity fluctuations at the nozzle exit. The

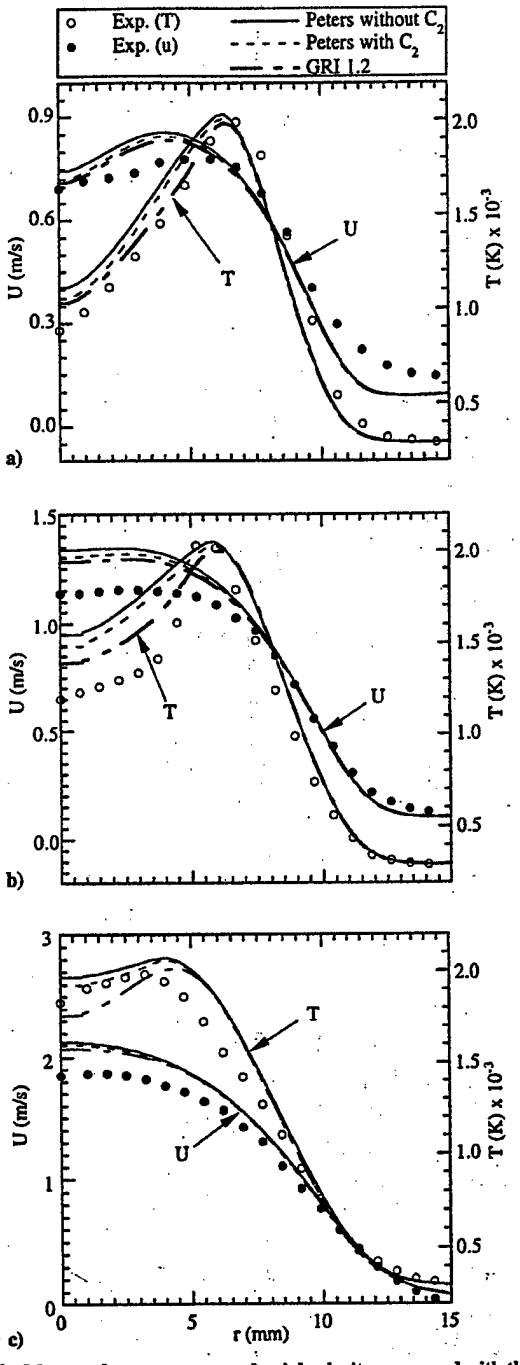

Fig. 6 Measured temperature and axial velocity compared with those predicted using different chemistry models at flame heights of a) 12, b) 24, and c) 50 mm.

annular-air jet has a diameter of 245 mm. An air velocity of 15 cm/s is used to reduce the room air disturbances in the first 15 diameters of the jet exit without significantly affecting the visible flame structure. Two flames were investigated experimentally and numerically. The first had a fuel-jet velocity of 0.5 m/s, and the second had a velocity of 4.1 m/s. Because of the buoyancy forces and the shear layer instability, these flames became dynamically oscillating ones.

Calculations for these flames were made using the three chemistry mechanisms described earlier. It was found that the global flame structures (i.e., the flame shapes, heights, and fluctuation frequencies) predicted by the three chemistry mechanisms were identical and that the chemical structures differed only on the fuel side of the flame zone where C_2 chemistry has some effect. For the sake of brevity, results obtained with the Peters mechanism with C_2 chemistry will be used in subsequent discussions of these dynamic flames.

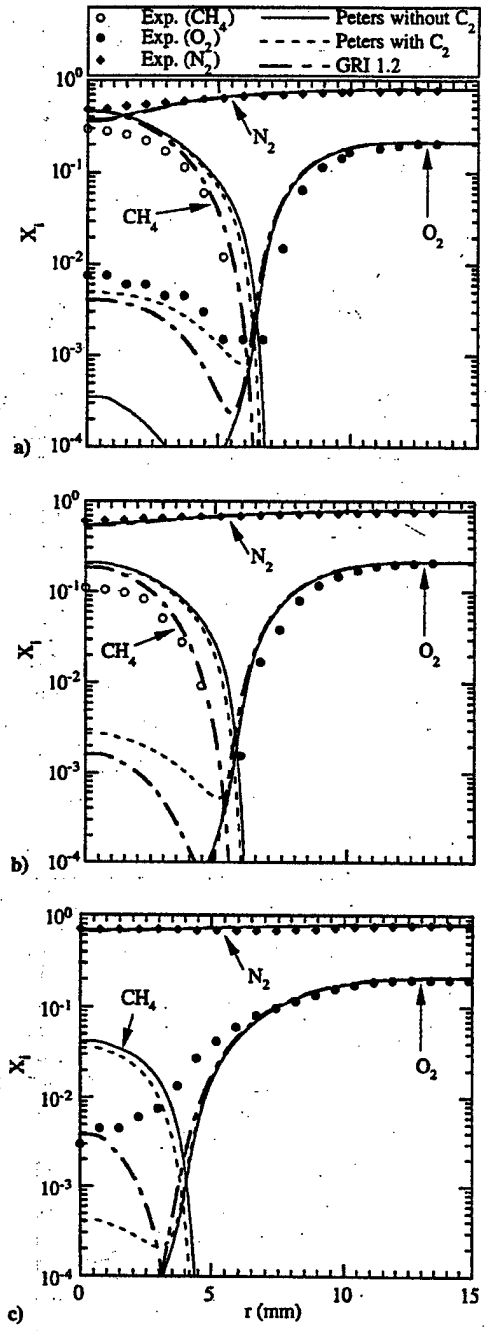

Fig. 7 CH_4, O_2, and N_2 concentrations predicted using different chemistry models compared with those measured at heights of a) 12, b) 24, and c) 50 mm.

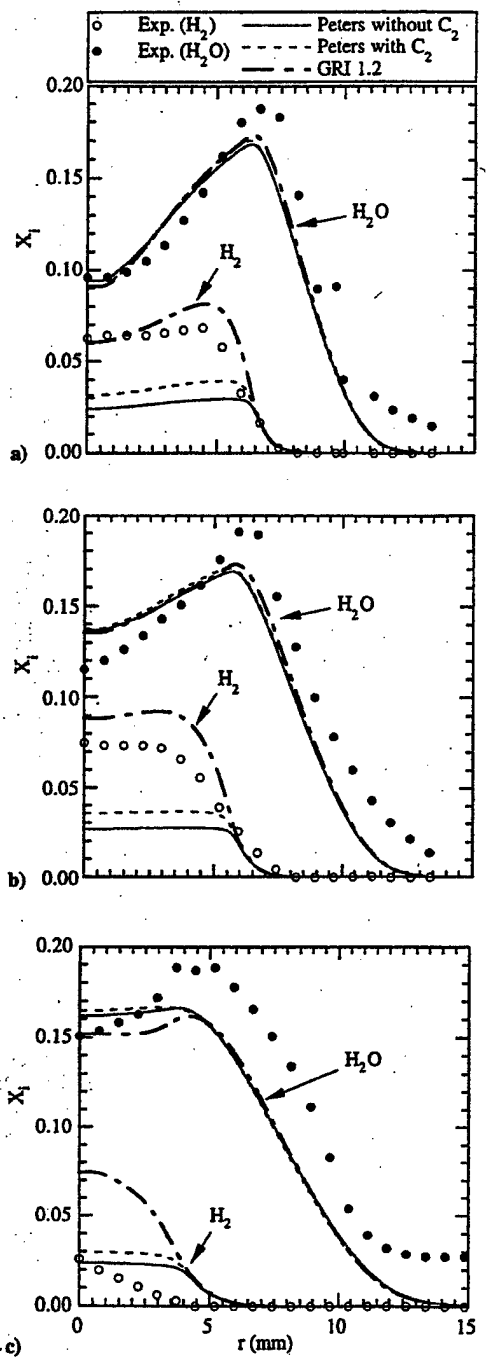

Fig. 8 H_2 and H concentrations predicted using different chemistry models compared with those measured at heights of a) 12, b) 24, and c) 50 mm.

An instantaneous image of the low-speed flame (fuel-jet velocity of 0.5 m/s) obtained with the reactive-Mie-scattering (RMS) technique[33] is shown in Fig. 10a. With this method micron-sized TiO_2 particles, formed from the spontaneous reaction between the seeded-$TiCl_4$ vapor and the water vapor produced during combustion, are visualized by the Mie-scattered light from a laser sheet. $TiCl_4$ is seeded into both the fuel and the annular-air flows. The bright region sandwiched between the inner and outer jets in Fig. 10a is the luminous flame surface captured simultaneously with the Mie-scattered light.

Because of the gravity term in the axial-momentum equation and the low-speed annular-air flow (~0.15 m/s), solution of the governing equations resulted in a dynamic flame, with large toroidal vortices forming naturally outside the flame surface. The computed instantaneous temperature field is shown in Fig. 10b. The flame (or peak temperature) surface that is identified from the temperature field is also shown (white solid circles). Note that no artificial perturbation is required for the formation of the outer vortices. In the presence of gravitational force, acceleration of hot gases along the flame surface generated the outer structures as part of the solution. As these vortices are convected downstream, they cause the flame to squeeze at certain locations ($z = 80$ and 160 mm) and bulge at others ($z = 50$ and 120 mm). The frequency corresponding to the passage of these outer vortices (also known as the flame-flickering frequency) is ~12 Hz. The instantaneous locations of the particles that are released along with the fuel are also shown (bright region in the center). The predicted flame structure compares extremely well with that obtained in experiments using the RMS technique. The counter-rotating toroidal vortex (at $z = 140$ mm in Fig. 10) that is formed as a result of the strong rotation of the upstream buoyancy-induced vortex[34] is accurately captured by the model.

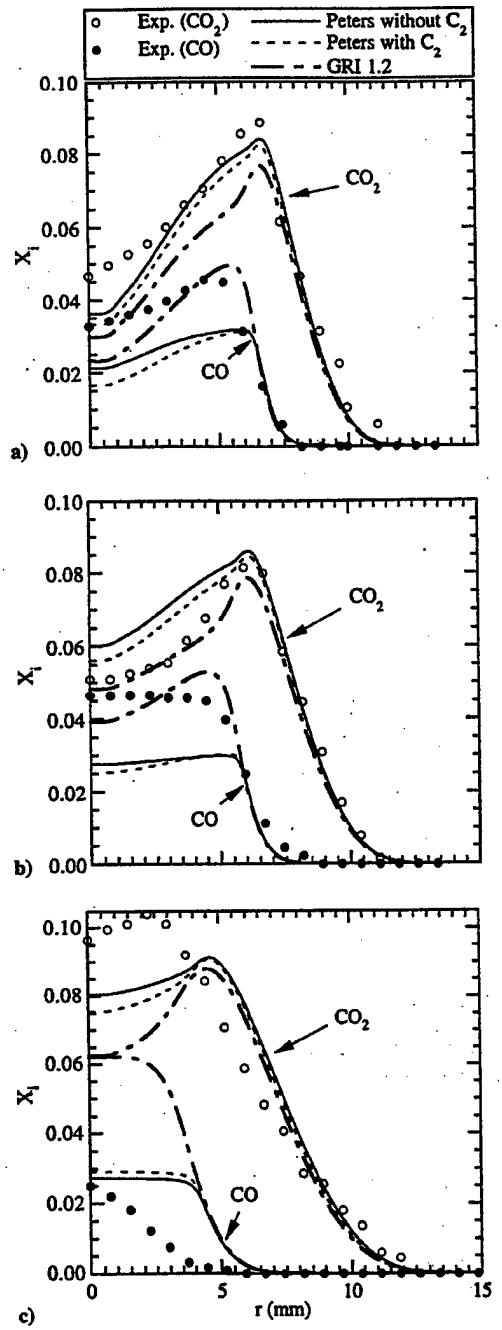

Fig. 9 CO_2 and CO concentrations predicted using different chemistry models compared with those measured at heights of a) 12, b) 24, and c) 50 mm.

The instantaneous flame structure obtained for the higher (or transitional) fuel-jet-velocity case is compared with the RMS image of the experimental flame in Fig. 11. As expected, buoyancy-driven vortical structures have formed outside the flame surface in this case also, and the convective frequency for these structures is found to be ~13 Hz. Interestingly, the experimental flame has vortical structures inside as well as outside the flame zone. Initial calculations of this flame yielded only outer structures. The inner shear layer was very laminar in nature, having no structures. The inner vortices observed in the experiments (Fig. 11a) are thought to result from the small perturbations that are inherent in the high-speed jet flow and the Kelvin–Helmholz instability of the shear layer. Although the outer vortices in the calculations caused the jet shear layer to oscillate, even at the fuel nozzle exit, this low-frequency disturbance was not amplified in the jet shear layer and, thus, did not stimulate the growth of the small-scale structures.

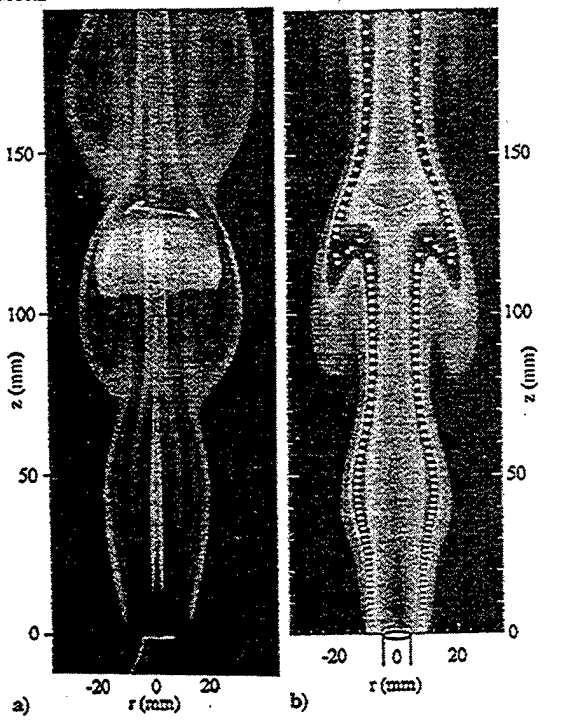

Fig. 10 Instantaneous images of experimental and computed low-speed dynamic flames. Fuel and air jet velocities are 0.5 and 0.15 m/s, respectively: a) RMS image showing naturally formed vortical structures and soot surface (bright region between the inner and outer jets); and b) locations of particles (bright central region) superimposed on computed temperature field. White solid circles represent high-temperature surface.

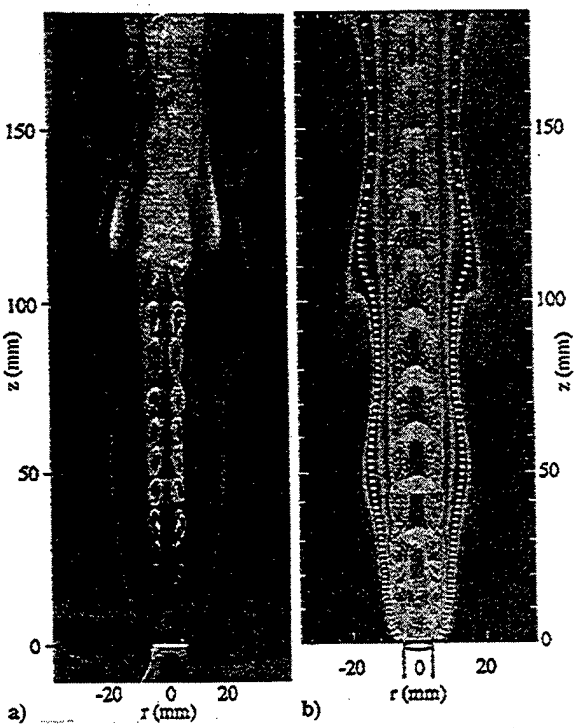

Fig. 11 Instantaneous images of experimental and computed transitional-speed dynamic flame. Fuel and air-jet velocities are 4.1 and 0.15 m/s, respectively: a) RMS image showing outer and inner vortices and soot surface (bright region between the inner and outer jets); and b) locations of particles (bright central region) superimposed on computed temperature field. White solid circles represent high-temperature surface.

To initiate and to sustain the Kelvin–Helmholtz instabilities in the calculations, constant external forcing in the form of background random noise (3% of jet velocity) was used at the exit of the fuel jet. The resulting flame is shown in Fig. 11b. The inner vortical structures are found to grow slowly and maintain their identities over a long distance. At locations farther downstream, these vortices dissipate with the entrainment of viscous combustion products from the flame surface.

In both the low- and transitional-speed flames (Figs. 10 and 11, respectively), it should be noted that the convective motion of the outer vortices interacts with the flame surface, making it wrinkle. These interactions perturb not only the shape but also the chemical structure of the flame. To illustrate the effects of vortex–flame interactions on flame structure, scatter plots of temperature and species concentration are shown in Figs. 12a and 12b for the steady-state flame, in Figs. 13a and 13b for the low-speed dynamic flame, and in Figs. 14a and 14b for the transitional-speed flame. The scatter plots for the dynamic flames (Figs. 13 and 14) were constructed by collecting 3000 instantaneous radial distributions that represent approximately four flickering cycles at a height of 80 mm above the burner. On the other hand, scatter plots for the steady-state flame (Fig. 12) were constructed from the data obtained along the radial lines at several flame heights in the region between $z = 2$ and 50 mm. Flame structures very near the burner ($z < 2$ mm) were discarded to avoid ambiguity that might result from inaccuracies in modeling the burner lip. Finally, the radial distributions were converted into mixture fraction ξ coordinates. Here, mixture fraction (ξ) is defined

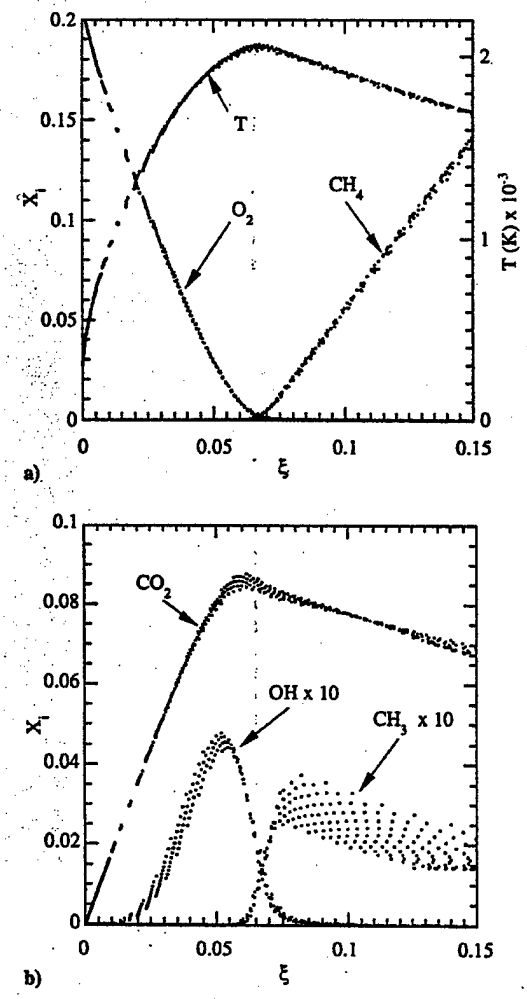

Fig. 12 Structure of steady-state flame constructed from radial distributions obtained at several heights: a) temperature and fuel and oxidizer concentrations with respect to mixture fraction; and b) variation of CO_2, CH_3, and OH concentration with respect to mixture fraction.

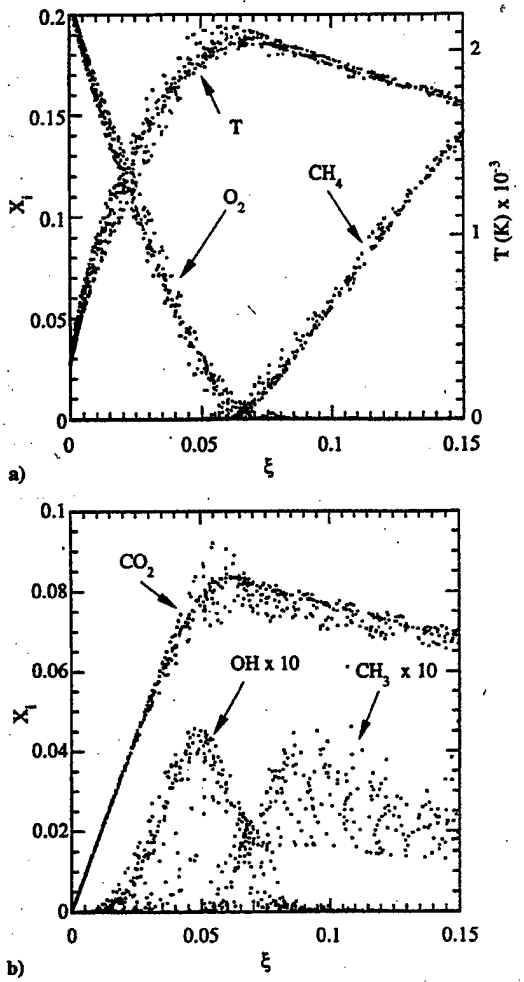

Fig. 13 Structure of low-speed buoyancy-influenced flame constructed at $z = 80$ mm from radial distributions obtained at several instants: a) temperature and fuel and oxidizer concentrations with respect to mixture fraction; and b) variation of CO_2, CH_3, and OH concentration with respect to mixture fraction.

as the fraction of the mass at any location that originated from the fuel jet and is calculated from the following expression[35]:

$$\xi = 16.0[X_{CH_4} + X_{CH_3} + X_{CH_2} + X_{CH} + X_{CH_2O} + X_{CHO} + X_{CO_2} + X_{CO} + 0.5(X_{C_2H} + X_{C_2H_2} + X_{C_2H_3} + X_{C_2H_4} + X_{C_2H_5} + X_{C_2H_6} + X_{CHCO} + X_C + X_{CH_2(S)} + X_{CH_2OH} + X_{CH_3O} + X_{CH_3OH} + X_{CH_2CO} + X_{HCCOH})]$$

where $X_i = Y_i/M_i/(Y_i/M_i)$.

In general, for a steady-state flame, the temperature, fuel concentration, and oxygen concentration yield self-similar solutions in the mixture fraction domain. However, this is not the case with respect to the intermediate species that are generated in the flame zone (cf. Fig. 12b). It is thought that the finite rate chemistry in combination with the varying convective velocities at different flame heights causes the species distributions to depend not only on mixture fraction but also on flame height. These deviations occur mainly for CH_3 on the fuel side ($\xi > 0.055$) and for OH radicals on the air side ($\xi < 0.055$) because these species are, in general, produced on the respective sides of the flame.

Vortex–flame interactions in the two dynamic flames resulted in scattered data for every variable shown in Figs. 13 and 14. Flame temperature increases at certain phases of the interaction (when the flame is compressed) and decreases at others (when the flame is stretched). These results are similar to those obtained for hydrogen

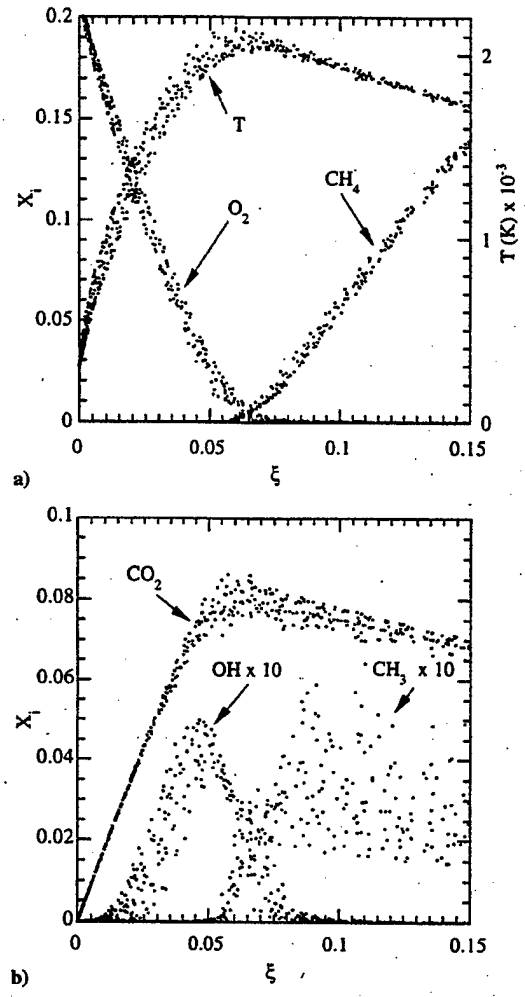

Fig. 14 Structure of a transitional-speed buoyancy-influenced flame constructed at $z = 80$ mm from radial distributions obtained at several instants: a) temperature and fuel and oxidizer concentrations with respect to mixture fraction; and b) variation of CO_2, CH_3, and OH concentration with respect to mixture fraction.

jet diffusion flames[8,18] in which nonunity Lewis numbers were found to be responsible for such behavior. Because the Lewis number of methane is less than unity (similar to that of hydrogen), one might expect hydrogen and methane flames to behave similarly during vortex–flame interactions. Because the inner vortices in transitional-speed flames are not quite near the flame surface, their impact on the flame structure is evident neither in temperature nor in major species concentration. However, because CH_3 is produced mostly on the fuel side, these inner vortices cause more scatter in its concentration (Fig. 14b).

Conclusions

Accurate dynamic simulations employing detailed chemical-kinetics models for hydrocarbon fuels are needed for understanding flame structure and various processes involved in laminar and transitional jet flames. An axisymmetric, time-dependent CFDC code was developed for the simulation of methane jet diffusion flames. Calculations were performed for a steady-state flame and for two dynamic flames that have been investigated experimentally in the past. Three chemistry models—namely, 1) the modified Peters mechanism without C_2 chemistry, 2) the modified Peters mechanism with C_2 chemistry, and 3) the GRI Version 1.2 mechanism—were used in the simulations. It was found that the modified Peters mechanisms with and without C_2 chemistry are sufficient for the simulation of these jet diffusion flames. The predicted flame shapes and flow structures of the periodically oscillating flames that are dynamic as a result of buoyancy-induced instabilities showed good correlation with the RMS images of the flames obtained in experiments. Based on the scatter plots constructed from the data collected at several heights in the steady-state flame, it was found that temperature as well as fuel and oxygen concentrations collapse onto a single curve in the mixture fraction coordinates, whereas the intermediate species concentrations do not. It was also found that the temperature in buoyancy-dominated unsteady methane flames increases at certain phases of the vortex–flame interaction—behavior that is similar to that observed in a hydrogen flame.

Acknowledgments

This work was supported, in part, by Air Force Contract F33615-95-C-2507 and the U.S. Air Force Office of Scientific Research.

References

[1]Hottel, H. C., and Hawthorne, W. R., "Diffusion in Laminar Flame Jets," *Proceedings of Third Symposium (International) on Combustion, Flame and Explosive Phenomena*, Combustion Inst., Pittsburgh, PA, 1949, pp. 254–266.

[2]Ellzey, J. L., Laskey, K. J., and Oran, E. S., "Dynamics of an Unsteady Diffusion Flame: Effects of Heat Release Rate and Viscosity," *Dynamics of Deflagrations and Reactive Systems: Flames*, edited by A. L. Kahl, J. C. Leyer, A. A. Borisov, and W. A. Sirgnano, Vol. 131, Progress in Astronautics and Aeronautics, AIAA, Washington, DC, 1989, p. 179.

[3]Yamashita, H., Kushida, G., and Takeno, T., "A Numerical Study of the Transition of Jet Diffusion Flames," *Proceedings of the Royal Society of London A*, Vol. 431, No. 1882, 1990, pp. 301–314.

[4]Davis, R. W., Moore, E. F., Roquemore, W. M., Chen, L.-D., Vilimpoc, V., and Goss, L. P., "Preliminary Results of a Numerical-Experimental Study of the Dynamic Structure of a Buoyant Jet Diffusion Flame," *Combustion and Flame*, Vol. 83, No. 3/4, 1991, pp. 263–270.

[5]Katta, V. R., Goss, L. P., and Roquemore, W. M., "Effect of Nonunity Lewis Number and Finite-Rate Chemistry on the Dynamics of a Hydrogen-Air Jet Diffusion Flame," *Combustion and Flame*, Vol. 96, No. 1/2, 1994, pp. 60–74.

[6]Patnaik, G., and Kailasanath, K., "Numerical Simulations of Burner-Stabilized Hydrogen-Air Flames in Microgravity," *Combustion and Flame*, Vol. 99, No. 10, 1994, pp. 247–253.

[7]Kaplan, C. R., Oran, E. S., Kailasanath, K., and Ross, H. D., "Gravitational Effects on Sooting Diffusion Flames," *26th Symposium (International) on Combustion*, Combustion Inst., Pittsburgh, PA, 1996, pp. 1301–1309.

[8]Katta, V. R., Goss, L. P., and Roquemore, W. M., "Effect of Nonunity Lewis Number and Finite-Rate Chemistry on the Dynamics of a Hydrogen-Air Jet Diffusion Flame," *Combustion and Flame*, Vol. 96, Nos. 1, 2, 1994, pp. 60–74.

[9]Takagi, T., and Xu, Z., "Numerical Analysis of Laminar Diffusion Flames—Effects of Preferential Diffusion of Heat and Species," *Combustion and Flame*, Vol. 96, Nos. 1, 2, 1994, pp. 50–59.

[10]Smooke, M. D., "Numerical Modeling of Laminar Diffusion Flames," *Numerical Approaches to Combustion Modeling*, edited by E. S. Oran and J. P. Boris, Vol. 135, Progress in Astronautics and Aeronautics, AIAA, Washington, DC, 1991, pp. 183–223.

[11]Takagi, T., Yoshikawa, Y., Yoshida, K., Komiyama, M., and Kinoshita, S., "Studies on Strained Nonpremixed Flames Affected by Flame Curvature and Preferential Diffusion," *26th Symposium (International) on Combustion*, Combustion Inst., Pittsburgh, PA, 1996, pp. 1103–1110.

[12]Takahashi, F., and Schmoll, W. J., "Lifting Criteria of Jet Diffusion Flames," *Twenty-Third Symposium (International) on Combustion*, Combustion Inst., Pittsburgh, PA, 1991, p. 677.

[13]Hsu, K. Y., Chen, L.-D., Katta, V. R., Goss, L. P., and Roquemore, W. M., "Experimental and Numerical Investigations of the Vortex-Flame Interactions in a Driven Jet Diffusion Flame," AIAA Paper 93-0455, Jan. 1993.

[14]Law, C. K., "Heat and Mass Transfer in Combustion: Fundamental Concepts and Analytical Techniques," *Progress in Energy and Combustion Sciences*, Vol. 10, No. 3, 1984, pp. 295–318.

[15]Katta, V. R., Goss, L. P., Roquemore, W. M., and Chen, L. D., "Dynamics of Propane Jet Diffusion Flames," *Atlas of Flow Visualization*, Vol. 3, CRC Press, New York, 1997, pp. 181–198.

[16]Takahashi, F., and Katta, V. R., "Unsteady Extinction Mechanisms of Diffusion Flames," *26th Symposium (International) on Combustion*, Combustion Inst., Pittsburgh, PA, 1996, pp. 1151–1160.

[17]Katta, V. R., Goss, L. P., and Roquemore, W. M., "Numerical Investigations of Transitional H_2/N_2 Jet Diffusion Flames," *AIAA Journal*, Vol. 32, No. 1, 1994, pp. 84–94.

[18]Katta, V. R., and Roquemore, W. M., "On the Structure of Stretched/Compressed Laminar Flamelet—Influence of Preferential Diffusion," *Combustion and Flame*, Vol. 100, No. 1, 1995, p. 61.

[19]Leonard, B. P., "A Stable and Accurate Convective Modeling Procedure Based on Quadratic Upstream Interpolation," *Computer Methods in Applied Mechanics and Engineering*, Vol. 19, No. 1, 1979, pp. 59–98.

[20]Spalding, D. B., "A Novel Finite Difference Formulation for Difference Expressions Involving Both First and Second Derivatives," *International Journal of Numerical Methods in Engineering*, Vol. 4, 1972, p. 551.

[21]Peters, N., "Flame Calculations with Reduced Mechanisms—An Outline," *Reduced Kinetic Mechanisms for Applications in Combustion Systems*, Lecture Notes in Physics, Springer–Verlag, New York, 1993, pp. 3–14.

[22]Frenklach, M., Wang, H., Goldenberg, M., Smith, G. P., Golden, D. M., Bowman, C. T., Hanson, R. K., Gardiner, W. C., and Lissianski, V., "GRI-Mech—An Optimized Detailed Chemical Reaction Mechanism for Methane Combustion," Gas Research Inst., TR GRI-95/0058, Chicago, IL, Nov. 1995.

[23]Hirschfelder, J. O., Curtiss, C. F., and Bird, R. B., *Molecular Theory of Gases and Liquids*, Wiley, New York, 1954, Chaps. 8, 9.

[24]Williams, F. A., *Combustion Theory—The Fundamentals of Chemically Reacting Flow Systems*, Addison–Wesley, Reading, MA, 1985, Appendix E.

[25]Katta, V. R., Goss, L. P., and Roquemore, W. M., "Simulation of Vortical Structures in a Jet Diffusion Flame," *International Journal of Numerical Methods for Heat and Fluid Flow*, Vol. 4, No. 5, 1994, p. 413.

[26]Peters, N., "Numerical and Asymptotic Analysis of Systematically Reduced Reaction Schemes for Hydrocarbon Flames," *Numerical Simulation of Combustion Phenomena*, edited by R. Glowinski, B. Larrouturou, and R. Temam, Vol. 241, Lecture Notes in Physics, Springer–Verlag, Berlin, 1985, p. 90.

[27]Smooke, M. D. (ed.), *Reduced Kinetic Mechanisms and Asymptotic Approximations for Methane–Air Flames*, Springer–Verlag, Berlin, 1991.

[28]Kee, R. J., Miller, J. A., Evans, G. H., and Dixon-Lewis, G., "A Computational Model of the Structure and Extinction of Strained Opposed Flow Premixed Methane-Air Flames," *22nd Symposium (International) on Combustion*, Combustion Inst., Pittsburgh, PA, 1988, pp. 1479–1494.

[29]Warnatz, J., *Combustion Chemistry*, edited by W. C. Gardiner, Springer–Verlag, New York, 1984, p. 197.

[30]Katta, V. R., and Roquemore, W. M., "Extinction in Methane-Air Counterflow Diffusion Flame—A Direct Numerical Study," *Combustion Fundamentals and Applications*, Combustion Inst., Pittsburgh, PA, 1996, pp. 449–454.

[31]Mitchell, R. E., Sarofim, A. F., and Clomburg, L. A., "Experimental and Numerical Investigation of Confined Laminar Diffusion Flames," *Combustion and Flame*, Vol. 37, No. 3, 1980, pp. 227–244.

[32]Davis, R. W., Moore, E. F., Roquemore, W. M., Chen, L.-D., Vilimpoc, V., and Goss, L. P., "Preliminary Results of a Numerical-Experimental Study of the Dynamic Structure of a Buoyant Jet Diffusion Flame," *Combustion and Flame*, Vol. 83, No. 3/4, 1991, pp. 263–270.

[33]Roquemore, W. M., Chen, L.-D., Goss, L. P., and Lynn, W. F., "Structure of Jet Diffusion Flames," *Turbulent Reactive Flows*, Vol. 40, Lecture Notes in Engineering, Springer–Verlag, Berlin, 1988, pp. 49–63.

[34]Eickhoff, H., and Winandy, A., "Visualization of Vortex Formation in Jet Diffusion Flames," *Combustion and Flame*, Vol. 60, No. 1, 1985, pp. 99–101.

[35]Nandula, S. P., Brown, T. M., and Pitz, R. W., "Measurements of Scalar Dissipation in the Reaction Zones of Turbulent Nonpremixed H_2-Air Flames," *Combustion and Flame*, Vol. 99, No. 3/4, 1994, p. 445.

K. Kailasanath
Associate Editor

Proceedings of the
5th ASME/JSME Joint Thermal Engineering Conference
March 15-19, 1999, San Diego, California

AJTE99-6190

A ROLE OF CHEMICAL KINETICS IN THE SIMULATION OF THE REACTION KERNEL OF METHANE JET DIFFUSION FLAMES

Fumiaki Takahashi
University of Dayton Research Institute
300 College Park
Dayton, Ohio, 45469
Telephone: 937-252-8138
FAX: 937-252-9917
E-mail: ftakahas@engr.udayton.edu

Viswanath R. Katta
Innovative Scientific Solutions, Inc.
2766 Indian Ripple Road
Dayton, Ohio, 45440
Telephone: 937-255-8781
FAX: 937-255-3139
E-mail: vrkatta@snake.appl.wpafb.af.mil

Keywords: diffusion flame, flame structure, flame stabilization, chemical kinetics, numerical simulation

ABSTRACT

The detailed structure of the stabilizing region of an axisymmetric laminar methane jet diffusion flame has been studied numerically. Computations using a time-dependent, implicit, third-order accurate numerical scheme with buoyancy effects were performed using two different C_2-chemistry models and compared with the previous results using a C_1-chemistry model. The results were nearly identical for all kinetic models except that the C_1-chemistry model over-predicted the methyl-radical and formaldehyde concentrations on the fuel side of the flame and that the standoff distance of the flame base from the burner rim varied. The standoff distance was sensitive to the $CH_3 + H + (M) \rightarrow CH_4 + (M)$ reaction. The highest reactivity spot (reaction kernel) was formed in the relatively low-temperature (<1600 K) flame base, where the $CH_3 + O \rightarrow CH_2O + H$ reaction predominantly contributed to the heat release, providing a stationary ignition source to incoming reactants and thereby stabilizing the trailing diffusion flame.

INTRODUCTION

The interaction between a flame and surfaces plays an important role in flame holding in combustors and flame spread through condensed fuels (Williams, 1985). Flame-flow phenomena, including transport and chemical reactions around the flame base near the surfaces, control flame stabilization and spreading mechanisms. Experimental efforts have been made (Robson and Wilson, 1969; Kawamura et al., 1980; Takahashi et al., 1985, 1988, 1996) to measure the structure of a small (~a few mm^2) stabilizing region of jet diffusion flames. Theoretical works (Buckmaster and Weber, 1996; Wichman and Varatharajan, 1997) have been directed toward modeling of the flame behavior in the vicinity of a fuel-oxidizer divider. Unfortunately, previous results generally suffer from the lack of detailed structure information, particularly on the radical-species concentration fields and their chemical reactions.

The authors have recently (Takahashi et al., 1998) proposed a unified view of the stabilizing mechanism of methane diffusion flames, formed in a jet or over a flat-plate burner, based on numerical analyses. A semi-detailed C_1-chemistry model (Peters, 1993) for 17 species and 52 reactions was used. The highest reactivity spot (reaction kernel) was formed in the flame base as a result of radical back-diffusion and reactions. Heuristic correlations were found between the heat release, or oxygen consumption rate, and the local velocity at the reaction kernel over a wide range of flow conditions for the two types of flames. Thus, the reaction kernel was responsible for stabilizing the flame.

Since the C_1-chemistry model was used to obtain the reaction kernel correlations, it is important to validate and differentiate the results using more comprehensive models, including C_2 chemistry and from different sources. Because the fate of methyl radical plays a key role in the methane combustion (Warnatz, 1984), the inclusion of C_2 species may alter the flame structure. In this paper, two different C_2-chemistry models (Peters, 1993; Frenklach et al, 1995) are used to reveal the effects of chemical kinetics on the simulation of the reaction kernel structure and to further understand the stabilization mechanisms of diffusion flames.

Copyright © 1999 by ASME
PUBLISHED WITH PERMISSION

NUMERICAL METHODS

The numerical code developed (Katta et al., 1994) is essentially the same as in previous papers (Takahashi and Katta, 1995, 1996, 1997; Takahashi et al., 1998) except for the chemical kinetic model used. Time-dependent governing equations, expressed in cylindrical coordinates, consist of mass continuity, axial and radial momentum conservation, energy conservation, and species conservation equations with the equation of state. Body-force term caused by the gravitational field is included in the axial momentum equation. The viscosity and binary diffusion coefficients are estimated from Chapman-Enskog collision theory (Hirschfelder, 1954), and the enthalpy of each species is calculated from polynomial curve-fits.

In the current calculations, the semi-detailed chemistry model (Table 1; Peters, 1993) for 24 species and 81 elementary steps is used. The reactions for C_2 species (R47 and R54 through R81) are added to the C_1-chemistry model (Peters, 1993) used previously (Takahashi and Katta, 1996, 1997; Takahashi et al., 1998). A comprehensive C_2-chemistry model (GRI-Mech Version 1.2; Frenklach et al., 1995) for 31 species and 346 reactions, excluding nitrogen chemistry, was also used for comparison. For all kinetic models, the Arrhenius parameters for the reaction $CH_3 + H \rightarrow CH_4$ (R45) are replaced with those by Warnatz (1984). Otherwise the extinction limit of counterflow diffusion flames were predicted at a significantly lower strain rate (Katta and Roquemore, 1996) compared to that determined experimentally by Sung et al. (1995), and the jet diffusion flames under consideration prematurely lifted off under conditions below the stability limit obtained experimentally (Takahashi and Schmoll, 1991).

The finite-difference form of the governing equations is constructed on a staggered grid system based on an implicit QUICKEST numerical scheme. The computational domain of 150 × 60 mm in axial (x) × radial (r) directions is represented by a mesh system of 271 × 101 with clustered grid lines near the jet exit with a minimum spacing of 0.05 mm. The inner diameter (d = 9.5 mm) and lip thickness (0.25 mm) of the fuel tube are close to those used in the previous experiments (Takahashi and Schmoll, 1991). The fuel tube exit plane is placed 10 mm from the inflow boundary. The fully developed pipe flow and boundary layer velocity profiles outside the burner tube are used. The test conditions are listed in Table 2. The mean jet velocity (U_j) and mean coflowing air velocity (U_a) are the same as case J5 in the previous work (Takahashi et al., 1998) and slightly below the measured lifting-limit curve (Takahashi and Schmoll, 1991).

The initial and boundary conditions for the axial (U) and radial (V) velocities and species and energy at different flow boundaries are the same as the previous work (Takahashi et al., 1998). The outer boundaries of the computational domain are shifted sufficiently far enough to minimize the propagation of disturbances into the region of interest. No-slip boundary conditions are enforced along the burner walls. An extrapolation procedure with weighted zero- and first-order terms is used to estimate the flow variables on the outflow boundary.

RESULTS AND DISCUSSION

Near-Jet-Exit Field

Figure 1a shows the calculated velocity vectors ($\vec{v}$), isotherms (T), and heat-release rate ($\dot{q}$) contours in the stabilizing region for case 2 (see Table 2). The heat-release rate showed a sharp peak at the base of the flame at relatively low temperatures (~1600 K) as was obtained for case 1 shown in previous paper (Takahashi et al., 1998). As will be shown later, the oxygen consumption rate ($-\omega_{O_2}$) and water vapor production rate (ω_{H_2O}) also have peaks close (typically ~0.05 mm) to the heat-release rate peak. The authors (Takahashi et al., 1998) named this highest reactivity spot (including the peaks of $\dot{q}$, $-\omega_{O_2}$, and ω_{H_2O}) a *reaction kernel.*

It is notable that the standoff distance of the simulated flame base depends on the chemistry model: case 1, x_k = 2.98 mm; case 2, x_k = 3.98 mm; and case 3, x_k = 2.38 mm. In fact, if the original kinetic parameters for reaction R45 were used, the flame base drifted away downstream, thus prematurely resulting in lifting. Therefore, with some variations in the standoff distance, these computational results effectively predicted the flame base shifting just before full-fledged lifting to the height of a few jet diameters. Because the flame base location is also sensitive to the boundary conditions, particularly the boundary layer velocity profile of the air flow outside the burner wall, the predicted values are in reasonable agreement with the observed standoff distance of $x \approx 3$ mm (Takahashi et al., 1998). There was a low velocity region near the burner rim and wake. The co-flow air accelerated and stream tubes slightly expanded by approaching the flame zone, crossing the flame zone, or penetrating through the dark space onto the fuel-side of the flame zone. Despite the differences in the standoff distance for the three different cases (1, Takahashi et al., 1998; 2, Fig. 1a; 3, not shown), the velocity vectors and temperature fields around the flame base are extremely similar.

Figure 1b shows the calculated total molar flux vectors of methane ($\vec{M}_{CH_4}$, dashed) and molecular oxygen ($\vec{M}_{O_2}$, solid), including both diffusion and convection terms, contours of the equivalence ratio (ϕ), and the oxygen consumption rate for case 2. The equivalence ratio was determined from the fuel and oxygen molar fluxes, thus including the dynamic effects of both convection and diffusion. In the upper portion of the flame, the molar flux vectors of methane and oxygen turned toward the flame zone from the opposite sides, typical of diffusion flames. Although partial premixing occurred in the dark space, the flame under investigation did not have the triple-flame structure (Chung and Lee, 1991; Veynante et al., 1994; Wichman and Varatharajan, 1997); i.e., the stoichiometric flame base with fuel-rich and fuel-lean branches on the fuel and air sides,

Copyright © 1999 by ASME

Table 1 CH4 Mechanism[a]

		A	n	E
H_2/O_2 Chain Reactions				
(R01)	$H + O_2 \rightarrow OH + O$	2.00E+14	0.0	16,800
(R02)	$OH + O \rightarrow H + O_2$	1.57E+13	0.0	840
(R03)	$O + H_2 \rightarrow OH + H$	5.06E+04	2.67	6,280
(R04)	$OH + H \rightarrow O + H_2$	2.22E+04	2.67	4,370
(R05)	$H_2 + OH \rightarrow H_2O + H$	1.00E+08	1.60	3,300
(R06)	$H_2O + H \rightarrow H_2 + OH$	4.31E+08	1.60	18,270
(R07)	$OH + OH \rightarrow O + H_2O$	1.50E+09	1.14	100
(R08)	$H_2O + O \rightarrow OH + OH$	1.47E+10	1.14	17,000
H_2O Formation and Consumption				
(R09)	$O_2 + H + M \rightarrow HO_2 + M$	2.30E+18	-0.8	0
(R10)	$HO_2 + M \rightarrow O_2 + H + M$	3.19E+18	-0.8	46,680
(R11)	$HO_2 + H \rightarrow OH + OH$	1.50E+14	0.0	1,000
(R12)	$HO_2 + H \rightarrow H_2 + O_2$	2.50E+13	0.0	692
(R13)	$HO_2 + OH \rightarrow H_2O + O_2$	6.00E+13	0.0	0
(R14)	$HO_2 + H \rightarrow H_2O + O$	3.00E+13	0.0	1,720
(R15)	$HO_2 + O \rightarrow OH + O_2$	1.80E+13	0.0	-406
H_2O_2 Formation and Consumption				
(R16)	$HO_2 + HO_2 \rightarrow H_2O_2 + O_2$	2.50E+11	0.0	-1,240
(R17)	$OH + OH + M \rightarrow H_2O_2 + M$	3.25E+22	-2.0	0
(R18)	$H_2O_2 + M \rightarrow OH + OH + M$	1.69E+24	-2.0	48,330
(R19)	$H_2O_2 + H \rightarrow H_2O + OH$	1.00E+13	0.0	3,580
(R20)	$H_2O_2 + OH \rightarrow H_2O + HO_2$	5.40E+12	0.0	1,000
(R21)	$H_2O + HO_2 \rightarrow H_2O_2 + OH$	1.80E+13	0.0	32,190
Recombination Reactions				
(R22)	$H + H + M \rightarrow H_2 + M$	1.80E+13	-1.0	0
(R23)	$H + OH + M \rightarrow H_2O + M$	2.20E+22	-2.0	0
(R24)	$O + O + M \rightarrow O_2 + M$	2.90E+17	-1.0	0
CO/CO_2 Mechanism				
(R25)	$CO + OH \rightarrow CO_2 + H$	4.40E+06	1.5	-740
(R26)	$CO_2 + H \rightarrow CO + OH$	4.96E+08	1.5	21,440
CH Consumption Reactions				
(R27)	$CH + O_2 \rightarrow CHO + O$	3.00E+13	0.0	0
(R28)	$CO_2 + CH \rightarrow CHO + CO$	3.40E+12	0.0	692
CHO Consumption Reactions				
(R29)	$CHO + H \rightarrow CO + H_2$	2.00E+14	0.0	0
(R30)	$CHO + OH \rightarrow CO + H_2O$	1.00E+14	0.0	0
(R31)	$CHO + O_2 \rightarrow CO + HO_2$	3.00E+12	0.0	0
(R32)	$CHO + M \rightarrow CO + H + M$	7.10E+14	0.0	16,800
(R33)	$H + CO + M \rightarrow CHO + M$	1.14E+15	0.0	2,380
CH_2 Consumption Reactions				
(R34)	$CH_2 + H \rightarrow CH + H_2$	8.40E+09	1.5	335
(R35)	$CH + H_2 \rightarrow CH_2 + H$	5.83E+09	1.5	3,125
(R36)	$CH_2 + O \rightarrow CO + H + H$	8.00E+13	0.0	0
(R37)	$CH_2 + O_2 \rightarrow CO + OH + H$	6.50E+12	0.0	1,500
(R38)	$CH_2 + O_2 \rightarrow CO_2 + H + H$	6.50E+12	0.0	1,500
CH_2O Consumption Reactions				
(R39)	$CH_2O + H \rightarrow CHO + H_2$	2.50E+13	0.0	3,990
(R40)	$CH_2O + O \rightarrow CHO + OH$	3.50E+13	0.0	3,490
(R41)	$CH_2O + OH \rightarrow CHO + H_2O$	3.00E+13	0.0	1,200
(R42)	$CH_2O + M \rightarrow CHO + H + M$	1.40E+17	0.0	76,500

(continues)

Table 1 (*continued*)

			A	n	E
CH_3 Consumption Reactions					
(R43)	$CH_3 + H \rightarrow CH_2 + H_2$		1.80E+14	0.0	15,050
(R44)	$CH_2 + H_2 \rightarrow CH_3 + H$		3.68E+13	0.0	10,580
(R45)	$CH_3 + H \rightarrow CH_4$	K_∞	6.00E+16	-1.0	0
		K_0	8.00E+26	-3.0	0
(R46)	$CH_3 + O \rightarrow CH_2O + H$		7.00E+13	0.0	0
(R47)	$CH_3 + CH_3 \rightarrow C_2H_6$	K_∞	3.61E+13	0.0	0
		K_0	1.27E+41	-7.0	2,762
(R48)	$CH_3 + O_2 \rightarrow CH_2O + OH$		3.40E+11	0.0	8,940
(R49)	$CH_3 + H_2 \rightarrow CH_4 + H$		8.39E+02	3.0	8,260
(R50)	$CH_3 + H_2O \rightarrow CH_4 + OH$		2.63E+05	2.10	16,950
CH_4 Consumption Reactions					
(R51)	$CH_4 + H \rightarrow CH_3 + H_2$		2.20E+04	3.0	8,740
(R52)	$CH_4 + O \rightarrow CH_3 + OH$		1.20E+07	2.1	7,620
(R53)	$CH_4 + OH \rightarrow CH_3 + H_2O$		1.60E+06	2.1	2,460
C_2H Consumption Reactions					
(R54)	$C_2H + H_2 \rightarrow C_2H_2 + H$		1.10E+13	0.0	2,867
(R55)	$C_2H_2 + H \rightarrow C_2H + H_2$		5.27E+13	0.0	28,656
(R56)	$C_2H + O_2 \rightarrow CHCO + O$		5.00E+13	0.0	1,505
CHCO Consumption Reactions					
(R57)	$CHCO + H \rightarrow CH_2 + CO$		3.00E+13	0.0	0
(R58)	$CH_2 + CO \rightarrow CHCO + H$		2.36E+12	0.0	-7,021
(R59)	$CHCO + O \rightarrow CO + CO + H$		1.00E+14	0.0	0
C_2H_2 Consumption Reactions					
(R60)	$C_2H_2 + O \rightarrow CH_2 + CO$		4.10E+08	1.5	1,696
(R61)	$C_2H_2 + O \rightarrow CHCO + H$		4.30E+14	0.0	12,112
(R62)	$C_2H_2 + OH \rightarrow C_2H + H_2O$		1.00E+13	0.0	7,000
(R63)	$C_2H + H_2O \rightarrow C_2H_2 + OH$		9.00E+12	0.0	-3,818
C_2H_3 Consumption Reactions					
(R64)	$C_2H_3 + H \rightarrow C_2H_2 + H_2$		3.00E+13	0.0	0
(R65)	$C_2H_3 + O_2 \rightarrow C_2H_2 + HO_2$		5.40E+11	0.0	0
(R66)	$C_2H_3 \rightarrow C_2H_2 + H$	K_∞	2.00E+14	0.0	39,717
		K_0	1.19E+42	-7.5	45,486
(R67)	$C_2H_2 + H \rightarrow C_2H_3$	K_∞	1.05E+14	0.0	810
C_2H_4 Consumption Reactions					
(R68)	$C_2H_4 + H \rightarrow C_2H_3 + H_2$		1.50E+14	0.0	10,201
(R69)	$C_2H_3 + H_2 \rightarrow C_2H_4 + H$		9.61E+12	0.0	7,800
(R70)	$C_2H_4 + O \rightarrow CH_3 + CO + H$		1.60E+09	1.2	741
(R71)	$C_2H_4 + OH \rightarrow C_2H_3 + H_2O$		3.00E+13	0.0	3,010
(R72)	$C_2H_3 + H_2O \rightarrow C_2H_4 + OH$		8.29E+12	0.0	15,576
(R73)	$C_2H_4 + M \rightarrow C_2H_2 + H_2 + M$		2.50E+17	0.0	76,400
C_2H_5 Consumption Reactions					
(R74)	$C_2H_5 + H \rightarrow CH_3 + CH_3$		3.00E+13	0.0	0.0
(R75)	$CH_3 + CH_3 \rightarrow C_2H_5 + H$		3.57E+12	0.0	11,870
(R76)	$C_2H_5 + O_2 \rightarrow C_2H_4 + HO_2$		2.00E+12	0.0	4,993
(R77)	$C_2H_5 \rightarrow C_2H_4 + H$	K_∞	2.00E+13	0.0	39,657
		K_0	1.00E+17	0.0	31,057
(R78)	$C_2H_4 + H \rightarrow C_2H_5$	K_∞	3.19E+13	0.0	3,013
C_2H_6 Consumption Reactions					
(R79)	$C_2H_6 + H \rightarrow C_2H_5 + H_2$		5.40E+02	3.5	5,208
(R80)	$C_2H_6 + O \rightarrow C_2H_5 + OH$		3.00E+07	2.0	5,112
(R81)	$C_2H_6 + OH \rightarrow C_2H_5 + H_2O$		6.30E+06	2.0	645

[a] Reaction rates in cm^3 mol s cal units, $k = AT^n \exp(-E/RT)$.
Source: Peters (1995), Warnatz (1984) [(R45)].

Copyright © 1999 by ASME

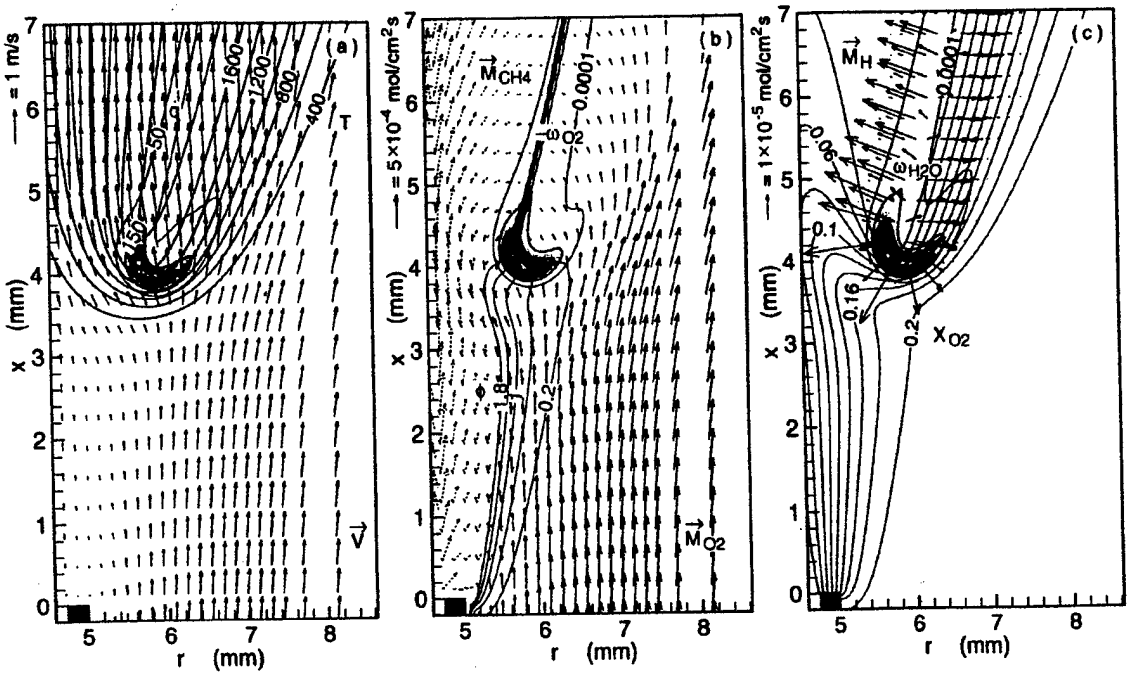

Fig. 1 Calculated (a) velocity vectors, isotherms (unit, K), heat-release rate (J/cm^{3}s), (b) molar flux vectors of methane (dashed) and molecular oxygen (solid), equivalence ratio based on the fuel and oxygen fluxes, and oxygen consumption rate (mol/cm^{3}s), (c) molar flux vectors of atomic hydrogen, mole fraction of oxygen, and water vapor production rate (mol/cm^{3}s) in the stabilizing region of methane jet diffusion flames. Case 2.

Table 2 Test Conditions

Case	U_j (m/s)	U_a (m/s)	Chemistry Model
1	1.7	0.72	Peters/Warnatz C_1/17 species/52 reactions
2	1.7	0.72	Peters/Warnatz C_2/24 species/81 reactions
3	1.7	0.72	GRI-Mech/Warnatz C_2/31 species/346 reactions

respectively. Chung and Lee (1991) observed axisymmetric, lifted, laminar diffusion flames with the triple-flame structure with a long (approximately several cm to 10+ cm) lift-off distance for n-butane and propane, but methane flame blew off without lifting.

Figure 1c shows the calculated total molar flux vectors of atomic hydrogen ($\vec{M}_H$), the mole fraction of molecular oxygen (X_{O_2}), and the rate of water vapor production for case 2. In the upper portion, the molar flux vectors of atomic hydrogen pointed to the opposite sides of the flame zone as a result of strong diffusion. By contrast, at the reaction kernel, hydrogen atoms diffused downward in every directions. This trend, peculiar to the geometric edge of the flame, was also found for other radical species (OH, O, and CH_3, etc.). Hence, the flame base was more exposed to air (aerated) under relatively high oxygen mole fraction. The oxygen concentration gradient also became steeper around the reaction kernel. Therefore, various radical species were able to back-diffuse and interdiffuse into the lower-temperature, oxygen-rich zone against the convective oxidizing flow. As a result, the reaction zone broadened, convective and diffusive oxygen fluxes increased, and thus the global reaction rates increased.

Trailing Flame Structure

To compare the detailed flame structure using different chemistry models, the profiles of various variables are examined at two different heights: the trailing flame and reaction kernel. Figures 2 and 3 show the radial variations of the temperature, species mole fractions (X_i), heat release rate, and species production rates (ω_i), across the trailing flame at a height of 3 mm from the reaction kernel for the three cases. As will be shown later (Figs. 6 and 7), the variations along the flame zone are similar if the axial distance from the reaction kernel is used and asymptotically approach constant values downstream. Thus, 3 mm from the reaction kernel is arbitrarily chosen to represent the trailing flame structure.

The distributions of the temperature and major species are typical of diffusion flames, except for the increased oxygen mole fraction on the fuel side and residual methane on the air side due to the oxygen penetration and methane efflux through the dark space below the flame base. The variations of the temperature, mole fractions, and production rates are very

Copyright © 1999 by ASME

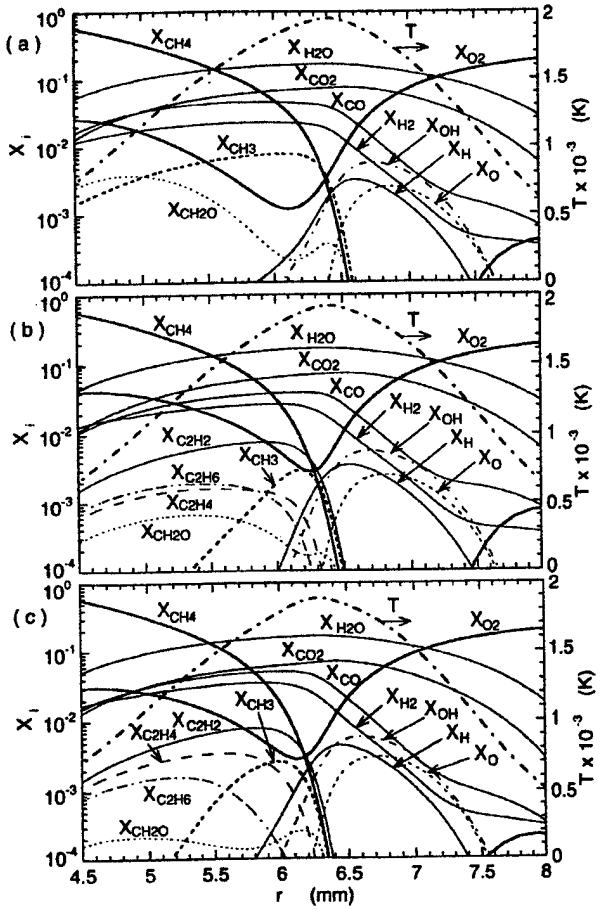

Fig. 2 Variations of the calculated temperature and mole fractions across the trailing flame zone at $x \approx x_k + 3$ mm. (a) Case 1, x = 6 mm; (b) Case 2, x = 7 mm; and (c) case 3, x = 5.38 mm.

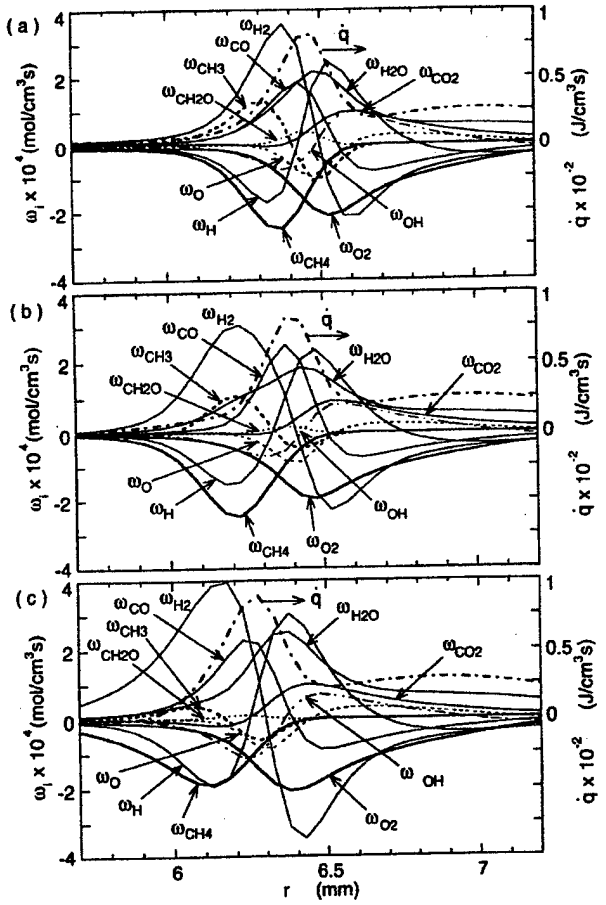

Fig. 3 Variations of the calculated species formation rate across the trailing flame zone at $x \approx x_k + 3$ mm. (a) Case 1, x = 6 mm; (b) Case 2, x = 7 mm; and (c) case 3, x = 5.38 mm.

similar for the three cases, except for those of the fuel fragments—methyl radical (CH_3) and C_2 species, and an oxidated intermediate—formaldehyde (CH_2O), on the fuel-side of the temperature peak. The mole fractions and production rates of the fuel fragments (CH_3 and C_2 species) and intermediates (H_2, CO, and CH_2O) peaked on the fuel-side, and those of the chain radical species (OH, H, and O) and products (H_2O and CO_2) peaked on the air-side of the temperature or heat-release rate peak. The methane consumption rate peak was on the fuel-side and that of oxygen was on the air side.

The fate of methyl radical plays a key role in the methane combustion (Warnatz, 1984). The methyl radical is formed by dehydrogenation of methane by radical attack (R51 through R53), oxidized by atomic and molecular oxygen attack to form formaldehyde (R46 and R48), further decomposed (R43), or recombined with hydrogen atom or another methyl radical to form methane (R45) or ethane (R47). The lack of the C_2 route in case 1 led to overprediction of the methyl radical and formaldehyde (Fig. 2a). The secondary peak of the formaldehyde mole fraction on the fuel side (r ≈ 5 mm) is due to the high-concentration formaldehyde formed near the reaction kernel (to be shown) and transported by convection (see the velocity vectors in Fig. 1a) because the rate of formation vanished in this region at this height (Fig. 3a). For cases 2 and 3 (Figs. 2b and 2c), the formation of ethane (R47) significantly reduced the methyl radical mole fraction on the fuel side (r <6 mm). The difference between the Peters (1993) and GRI (Frenklach, 1995) mechanisms in the reaction rate of the methyl-methyl recombination step made an appreciable difference in the variation of the ethane mole fraction, particularly at higher temperatures.

Reaction Kernel Structure

Figures 4 and 5 show the radial variations of calculated variables across the reaction kernel. The reaction kernel structure shows striking differences from the trailing diffusion

Copyright © 1999 by ASME

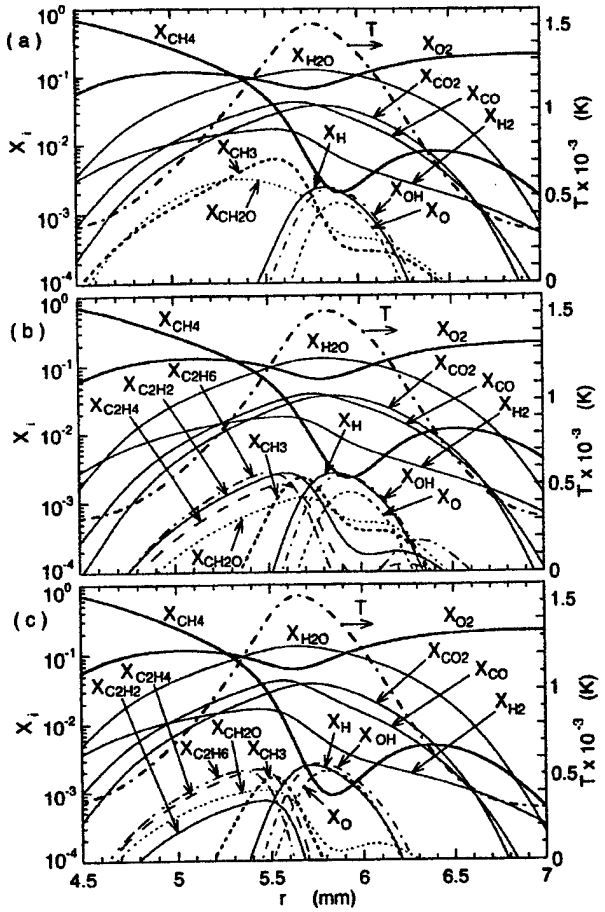

Fig. 4 Variations of the calculated temperature and mole fractions across the reaction kernel (x_k). (a) Case 1, x = 2.98 mm; (b) Case 2, x = 3.98 mm; and (c) case 3, x = 2.38 mm.

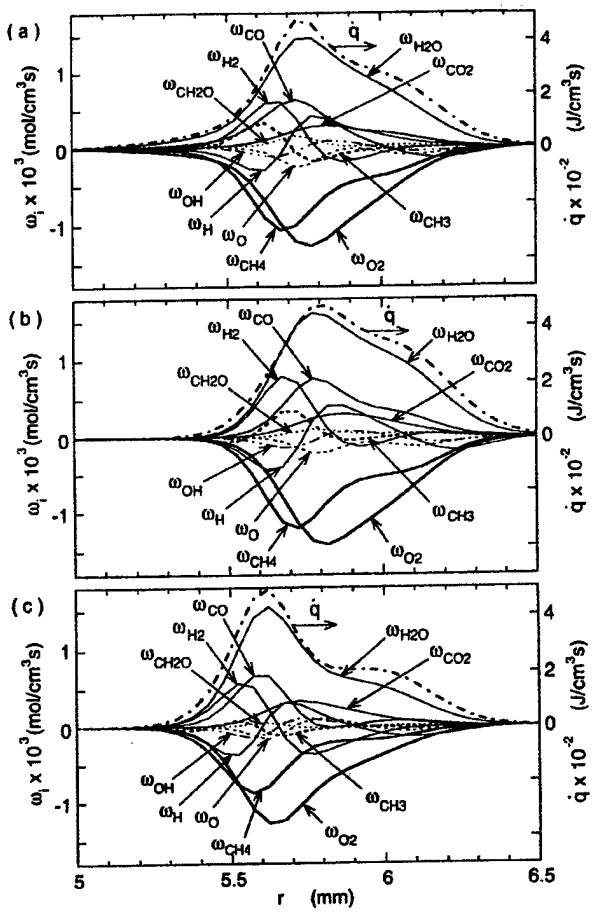

Fig. 5 Variations of the calculated species formation rate across the reaction kernel (x_k). (a) Case 1, x = 2.98 mm; (b) Case 2, x = 3.98 mm; and (c) case 3, x = 2.38 mm.

flame structure. However, despite the differences in the dark space standoff distance, the variations are very similar among the three cases, again except for the minor species on the fuel side. In all cases, there were secondary peaks in the oxygen mole fraction ($X_{O2} \approx 0.12$) on the fuel-side of the relatively low peak temperature (~1500 K) and a small hump in the methane mole fraction (X_{CH4}: 0.005-0.011) on the air side. These resulted from the air penetration and the methane efflux through the dark space. The minimum oxygen mole fraction at the reaction kernel was substantially higher ($X_{O2} \approx 0.06$) than that in the trailing flame (X_{O2}: 0.001-0.004) and even in moderately strained counterflow diffusion flames ($X_{O2} \approx 0.02$ [Tsuji and Yamaoka, 1971]).. The oxygen consumption rate was widely distributed over the entire reaction zone, closely following the heat-release rate and water vapor production rate. The C_1 chemistry in case 1 again overpredicted the methyl radical and formaldehyde mole fractions on the fuel side (Fig. 4a).

In the trailing diffusion flame zone (Fig. 2), the methyl radicals and oxygen atoms were separated on the fuel-side and air-side, respectively, and thus, the reaction rate of R46 and its contribution to heat release were small. By contrast, in the reaction kernel, the back-diffusion of the radical species (H, OH, O, and CH_3) directly into the oxygen-rich (fuel-lean) reaction kernel. As a result, chain reactions, particularly the chain branching reaction $H + O_2 \rightarrow OH + O$ (R01), the product forming reaction $H_2 + OH \rightarrow H_2O + H$ (R05), and another branching reaction $O + H_2 \rightarrow OH + H$ (R03) are promoted compared to their reverse reactions at relatively low flame temperatures. More importantly, as reported in a previous paper (Takahashi et al., 1998), the reaction step $CH_3 + O \rightarrow CH_2O + H$ (R46) predominantly contributed to the total heat-release rate peak at the reaction kernel. Therefore, the methane oxidation path through $CH_4 \rightarrow CH_3 \rightarrow CH_2O \rightarrow CHO \rightarrow CO$ must be the dominant route compared to that through the C_2 species or methyl decomposition to CH_2.

Copyright © 1999 by ASME

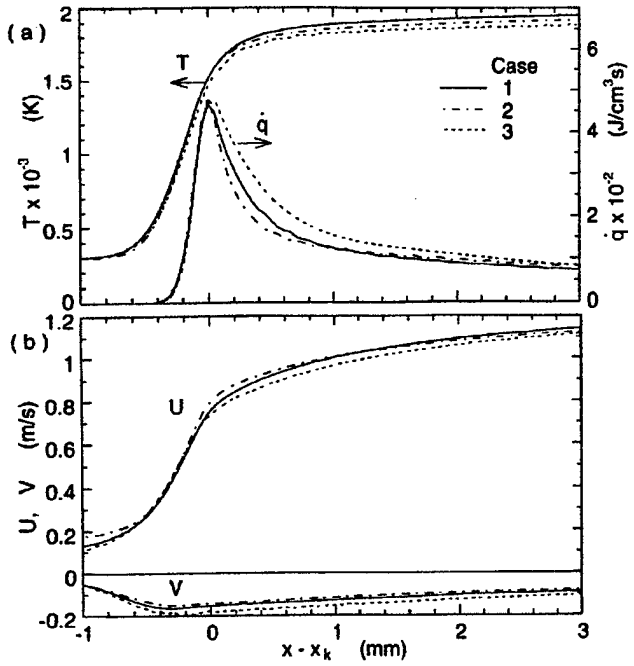

Fig. 6 Variations of the calculated (a) temperature, heat release rate, (b) axial, and radial velocity components along the maximum temperature envelope in the stabilizing region of a methane jet diffusion flame.

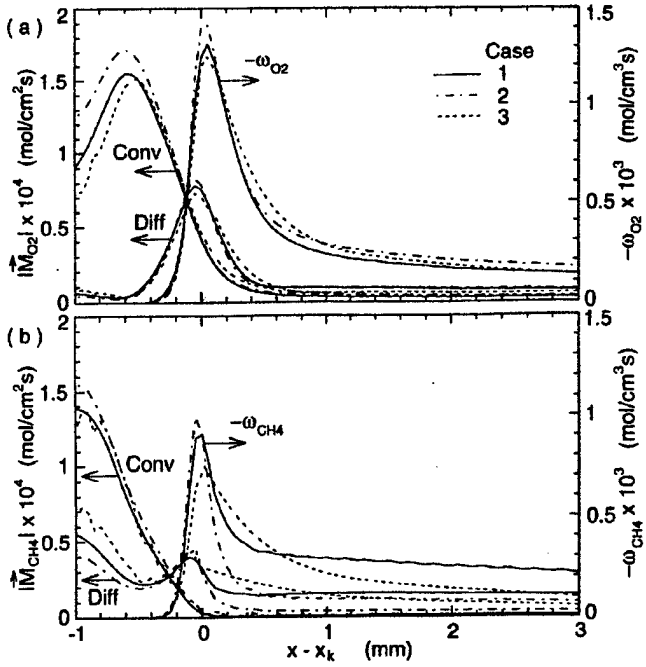

Fig. 7 Variations of the calculated convective, diffusive molar fluxes, and consumption rate of (a) methane and (b) oxygen along the maximum temperature envelope in the stabilizing region of a methane jet diffusion flame.

The axial location of the reaction kernel shifted as the C_2 chemistry was added: case 1, x_k = ~3 mm, case 2, x_k = ~4 mm. Apparently, the fate of methyl radical plays a key role in the flame stabilization. As a result of the additional methyl radical destruction step to form ethane, the methyl concentration dropped significantly on the fuel side. The additional reactions for C_2 species might compete with other species for radicals and might delay the methane decomposition and oxidation processes, thereby expanding the standoff distance.

Flame Stabilization

Figure 6 shows the variations in (a) the temperature, heat-release rate, (b) axial, and radial velocity components along the flame zone (maximum temperature envelope) for cases 1 through 3. The results using the maximum heat-release rate envelope (not shown) are similar. The abscissa is the axial distance from the reaction kernel (heat-release rate peak). For all cases, the variations are similar; the temperature reached ~1500 K at the reaction kernel and asymptotically approached in the trailing flame constant values (1900-2000 K), which are slightly lower for C_2-chemistry models. Because the axial (or total) velocity along the flame zone kept increasing downstream, the trailing diffusion flame might drift away downstream if not supported by upstream portions.

Figure 7 shows the variations in the convective and diffusive molar fluxes and consumption rates of (a) oxygen and (b) methane along the flame zone (maximum temperature envelope) for cases 1 through 3. Again the results along the maximum heat-release rate envelope (not shown) are similar. The diffusive molar fluxes and consumption rates of oxygen and fuel peaked near the reaction kernel ($x \approx x_k$), a sink of the reactants. In addition, the convective contribution to the total oxygen flux was also several times larger than those in the trailing flame because of the high concentration of leaked oxygen in the broadened reaction zone. Thus, the reactivity (peak heat-release rate, oxygen and methane consumption rates, or water vapor production rate) at the reaction kernel is several times larger than that in the trailing diffusion flame, and the reaction kernel apparently stabilized the flame. Therefore, the reaction kernel provided a stationary ignition source to the incoming reactants and sustains stable combustion in the flow field. As the reaction kernel secures the stable combustion, the trailing diffusion flame zone can be successively supported, thus keeping the flame from lifting.

CONCLUSIONS

The detailed flame structure of the stabilizing region of jet diffusion flames was revealed numerically using three different chemistry models. A highest reactivity ($\dot{q}$, $-\omega_{O_2}$, and ω_{H_2O}) spot, i.e., reaction kernel, is formed in a relatively low-temperature (<1600 K), fuel-lean, broadened reaction zone in

Copyright © 1999 by ASME

the flame base as a result of radical back-diffusion and reactions. The $CH_3 + O \rightarrow CH_2O + H$ reaction predominantly contributed to the heat-release rate peak. The standoff distance was sensitive to the $CH_3 + H + (M) \rightarrow CH_4 + (M)$ reaction. As C_2-chemistry was added (case 1 to 2), the overall methane decomposition and oxidation processes were delayed and the reaction kernel farther shifted downstream, whereas the completely different GRI/Warnatz mechanism (case 3) resulted in a shorter standoff distance. Despite the variation in the standoff distance, the calculated reaction kernel structures were nearly identical for different chemistry models, except that the C_1 chemistry model overpredicted methyl radical and formaldehyde mole fractions on the fuel-side of the flame zone. The reaction kernel is responsible for stabilizing the trailing diffusion flame zone.

ACKNOWLEDGMENTS

This work was supported by the U. S. Air Force Research Laboratory, Propulsion Directorate, Propulsion Sciences and Advanced Concept Division, Wright-Patterson Air Force Base, Ohio, under Contract No. F33615-97-C-2719 (Technical Monitor: C. W. Frayne).

REFERENCES

Buckmaster, J., and Weber, R., 1996, "Edge-Flame Holding," *Twenty-Sixth Symposium (International) on Combustion,* The Combustion Institute, pp. 1143-1149.

Chung, S. H., and Lee, B. J., 1991, "On the Characteristics of Laminar Lifted Flames in a Nonpremixed Jet," *Combustion and Flame,* Vol. 86, pp. 62-72.

Frenklach, M., Wang, H., Goldenberg, M., Smith, G. P., Golden, D. M., Bowman, C. T., Hanson, R. K., Gardiner, W. C., Lissianski, V., 1995 "GRI-Mech—An Optimized Detailed Chemical Reaction Mechanism for Methane Combustion," Gas Research Institute Technical Report No. GRI-95/0058.

Hirschfelder, J. O., Curtis, C. F., and Bird, R. B., 1954, *The Molecular Theory of Gases and Liquids,* Wiley, New York.

Katta, V. R., Goss, L. P., and Roquemore, W. M., 1994, "Numerical Investigations of Transitional H_2/N_2 Jet Diffusion Flames," *AIAA Journal,* Vol. 32, pp. 84-94.

Katta, V. R., and Roquemore, W. M., 1996, "Extinction in Methane-Air Counterflow Diffusion Flame—A Direct Numerical Study," Central States/The Combustion Institute Meeting, St. Louis.

Kawamura, T., Asato, K., and Mazaki, T., 1980, "Structure Analysis of the Stabilizing Region of Plane, Laminar Fuel-Jet Flames," *Combustion Science and Technology,* Vol. 22, pp. 211-216.

Peters, N., 1993, "Flame Calculations with Reduced Mechanisms--An Outline," *Reduced Kinetic Mechanisms for Applications in Combustion Systems* (N. Peters and B. Rogg Eds.), Springer-Verlag, Berlin, pp. 3-14.

Robson, K., and Wilson, M. J. G., 1969, "The Stability of Laminar Diffusion Flames of Methane," *Combustion and Flame,* Vol. 13, pp. 626-634.

Sung, C. J., Liu, J. B., and Law, C. K., 1995, "Structural Response of Counterflow Diffusion Flames to Strain Rate Variations," *Combustion and Flame,* Vol. 102, pp. 481-492.

Takahashi, F., and Katta, V. R., 1995, "Numerical Experiments on the Vortex-Flame Interactions in a Jet Diffusion Flames," *Journal of Propulsion and Power,* Vol. 11, pp. 170-177.

Takahashi, F., and Katta, V. R., 1996, "Unsteady Extinction Mechanisms of Diffusion Flames," *Twenty-Sixth Symposium (International) on Combustion,* The Combustion Institute, The Combustion Institute, pp. 1151-1160.

Takahashi, F., and Katta, V. R., 1997, "A Numerical Study of a Methane Diffusion Flame over a Flat Surface," *Proceedings of the Second International Symposium on Scale Modeling,* Lexington, Kentucky.

Takahashi, F., and Schmoll, W. J., 1991, "Lifting Criteria of Jet Diffusion Flames," *Twenty-Third Symposium (International) on Combustion,* The Combustion Institute, pp. 677-683.

Takahashi, F., Mizomoto, M., Ikai, S., Futaki, N., 1985, "Lifting Mechanism of Free Jet Diffusion Flames," *Twentieth Symposium (International) on Combustion,* The Combustion Institute, pp. 295-302.

Takahashi, F., Mizomoto, M., and Ikai, S., 1988, "Structure of the Stabilizing Region of a Laminar Jet Diffusion Flame," ASME *Journal of Heat Transfer,* Vol. 110, pp. 182-189.

Takahashi, F., Durbin, M. D., and Vangsness, M. D., 1996, "Stabilization of Hydrogen Jet Diffusion Flames With or Without Swirl," *Transport Phenomena in Combustion* (S. H. Chan, ed.), Vol. 1, Taylor & Francis, Washington, D. C., pp. 593-604.

Takahashi, F., Schmoll, W. J., and Katta, V. R., 1998, "Attachment Mechanisms of Diffusion Flames," *Twenty-Seventh Symposium (International) on Combustion,* The Combustion Institute, The Combustion Institute, in press.

Tsuji, H., and Yamaoka, I., 1971, "Structure Analysis of Counterflow Diffusion Flames in the Forward Stagnation Region of a Porous Cylinder," *Thirteenth Symposium (International) on Combustion,* The Combustion Institute, The Combustion Institute, pp. 979-984.

Veynante, D., Vervisch, L., Poinsot, T., Liñán, A., and Ruetsch, G., 1994, "Triple Flame Structure and Diffusion Flame Stabilization," Proceedings of the Summer Program, Center for Turbulence Research, Stanford University, pp. 55-73.

Warnatz, J., 1984, "Rate Coefficients in the C/H/O system," *Combustion Chemistry* (W. C. Gardiner, Ed.), Springer-Verlag, New York, p. 197-360.

Wichman, I. S., and Varatharajan, B., 1997, "Generic Features of Diffusion Flame Behavior near Cold Chemically Inert Surfaces," Central States Section/The Combustion Institute Meeting, Point Clear, Alabama.

Williams, F. A., 1985, *Combustion Theory,* 2nd ed., The Benjamin/Cummings, p.485.

Copyright © 1999 by ASME

Gravity Effects on Steady Two-Dimensional Partially Premixed Methane–Air Flames

ZHUANG SHU, CHUN W. CHOI, SURESH K. AGGARWAL, VISWANATH R. KATTA,† and ISHWAR K. PURI*

Department of Mechanical Engineering, University of Illinois at Chicago, Chicago, IL 60607-7022

Under normal-gravity conditions the flame heat release produces both flow dilatation and buoyancy effects. While it may be possible to minimize gravitational effects in a fully premixed flame by isolating buoyancy effects to the lower-density postflame region or plume, this cannot be accomplished in nonpremixed flames. It is known that partially premixed flames can contain two reaction zones, one with a premixed-like structure and the other consisting of a transport-limited nonpremixed zone (in which mixing and entrainment effects are significant). For these reasons it is important to understand the fundamental interaction between flow dilatation and buoyancy effects in partially premixed flames. A detailed numerical study is conducted to characterize the effect of buoyancy on the structure of two-dimensional partially premixed methane–air flames. The computational model is validated by comparison with the experimentally obtained chemiluminescent emission from excited-C_2^* free radical species as well as with velocity vectors obtained using particle image velocimetry. Both the experiments and simulations indicate the presence of two reaction zones that are synergistically coupled, with each region providing heat and/or chemical species for the other. While the inner premixed flame is only weakly affected by gravity, the outer flame shows significant spatial differences for the two cases due to buoyancy-induced entrainment, since advection of air into the outer reaction zone increases in the presence of gravity. The presence of gravity induces more compact flames, influences the velocity profiles in the post–inner flame region, and increases the normal strain rate. Although the spatial differences between the 0- and 1-g flames are more significant on the lean side, the state relationships in that region are relatively unaffected by gravity. On the other hand, the inner (rich-side) reaction zone shifts toward less-rich locations in the presence of gravity, possibly due to the enhanced buoyant mixing. The 1-g flames exhibit a larger energy loss in the form of CO and H_2 emissions. © 1999 by The Combustion Institute

INTRODUCTION

Partially premixed flames may be established by design by placing a fuel-rich mixture in contact with a fuel-lean mixture, but these flames also occur otherwise in many practical systems. For instance, initially nonpremixed combustion may involve regions of local extinction followed by partial premixing and reignition [1]. Likewise, partial premixing is an important process in nonpremixed flame liftoff phenomena, since the reactants can mix slightly prior to ignition [2, 3]. Nonuniform evaporation in spray flames can also result in local fuel-rich regions in which burning occurs in the partially premixed mode and the technique of lean direct injection used to achieve stable combustion and reduced pollutant levels involves regions of partially premixed combustion. In addition, unwanted fires can originate in a partially premixed mode when a pyrolyzed or evaporated fuel forms an initial fuel-rich mixture with the ambient air.

Under normal-gravity conditions the flame heat release produces both flow dilatation and buoyancy effects in partially premixed flames. Gas expansion due to the heating causes downstream motion normal to the flamefront. The buoyant gases accelerate the flow in an opposite direction to the gravity vector, causing air entrainment that enhances the fuel–air mixing and, consequently, influences the upstream region. While it is possible to minimize gravitational effects in a premixed flame by isolating buoyancy effects to the lower-density postflame region or plume, it is not so straightforward to do so in nonpremixed flames. Several investigations have established that partially premixed flames can contain two reaction zones [4–11], one with a premixed-like structure and the other consisting of a transport-limited nonpremixed zone (in which mixing and entrainment effects are significant). The thickness of the preheat zone associated with the premixed flame can be decreased by increasing the fuel–air equivalence ratio [12].

*Corresponding author. E-mail: ikpuri@uic.edu
†Innovative Scientific Solutions, Inc. Dayton, OH 45430.

COMBUSTION AND FLAME 118:91–107 (1999)
© 1999 by The Combustion Institute
Published by Elsevier Science Inc. PUBLISHED WITH PERMISSION
0010-2180/99/$–see front matter
PII S0010-2180(98)00149-7

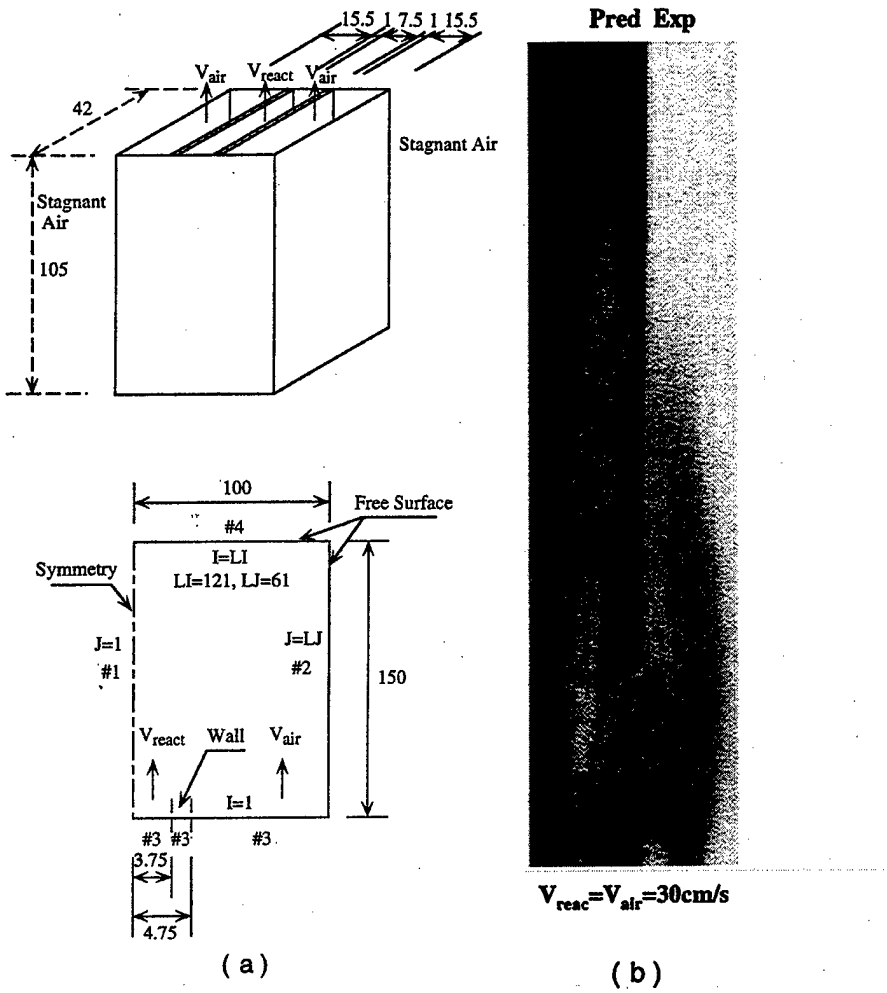

Fig. 1. (a) Schematic diagram of the 100 mm × 150 mm (or 61 × 121 gridline) computational domain. The symbols I and J, respectively, represent the axial and transverse gridlines. The boundary conditions are also specified. The simulated burner consists of an inner 7.5-mm slot with two 15.5-mm outer slots on either side of it. The wall thickness separating the slots is 1 mm. (b) Comparison of the simulated heat release rates with an experimentally obtained C_2-chemiluminescence image for a 1-g flame established at $\phi = 2$, and $V_{reac} = V_{air} = 30$ cm s^{-1}.

For these reasons it is important to understand the interaction between flow dilatation and buoyancy effects in partially premixed flames. This investigation compares the results obtained from numerical computations of two-dimensional, partially premixed methane–air flames established under both normal and zero-gravity conditions.

PROCEDURE

The computational study employs a flow configuration based on a rectangular Wolfhard-Parker slot burner that is schematically depicted in Fig. 1a and described elsewhere [13]. A fuel-rich mixture is introduced from the inner slot, and air from either side of it. Identical two-dimensional flames are established on either side of the centerline. The numerical simulations are conducted on one side of the symmetry plane (plane 1). The other three planes bounding the domain are the free surface (plane 2), the inflow boundary (plane 3), and the outflow boundary (plane 4).

The combustion process is simulated by em-

ploying a detailed numerical model based on the solution of time-dependent governing equations for a two-dimensional reacting flow. Using Cartesian coordinates (x, y), these equations can be written in the form

$$\frac{\partial(\rho\phi)}{\partial t} + \frac{\partial(\rho u\phi)}{\partial x} + \frac{\partial(\rho v\phi)}{\partial y} = \frac{\partial}{\partial x}\left(\Gamma^{\phi}\frac{\partial\phi}{\partial x}\right) + \frac{\partial}{\partial y}\left(\Gamma^{\phi}\frac{\partial\phi}{\partial y}\right) + S^{\phi}$$

where ρ denotes density, and u and v the transverse (x) and axial (y) velocity components, respectively. The general form of the equation represents either of the mass, momentum, species, or energy conservation equations, depending on the variable used for ϕ. The transport coefficient Γ^{ϕ} and the source terms S^{ϕ} appearing in the governing equations are provided in Table 1 of Ref. 10. The set of governing equations is completed by using the overall species conservation equation and the equation of state $p = \rho R_u T \Sigma_i Y_i/M_i$, where R_u is the universal gas constant, T the temperature, and M_i the molecular weight of the ith species. The thermodynamic and transport properties appearing in the above equations are considered to be temperature- and species-dependent. First, the viscosity and thermal conductivity of the individual species are estimated based on Chapman-Enskog collision theory, following which those of the mixture are determined using the Wilke semi-empirical formulae. Chapman-Enskog theory and the Lennard-Jones potentials are used to estimate the binary-diffusion coefficient between each species and nitrogen D_{i-N_2}. The enthalpy h and specific heat are calculated for each species using the polynomial curve fits from Ref. 14.

An implicit algorithm is employed to solve the unsteady gas-phase equations. The governing equations are integrated by using a finite control volume approach with a staggered, nonuniform grid system. The finite-difference forms of the momentum equations are obtained using an implicit scheme [15], whereas those of the species and energy equations are obtained using a hybrid scheme [16]. Grid lines are clustered near the flame surfaces to resolve the steep gradients of the dependent variables. Boundaries of the computational domain are shifted sufficiently to minimize the propagation of disturbances. An iterative Alternating Direction Implicit (ADI) technique is used for solving the resulting $(N_S + 3)$ sets of algebraic equations. A stable numerical-integration procedure is achieved by coupling the species and energy equations through the chemical-reaction source terms. At each time step the pressure field is calculated by solving the pressure Poisson equations at all grid points simultaneously and utilizing the Lower and Upper (LU) matrix-decomposition technique. Further details about the numerical procedure and the treatment of boundary conditions are provided in earlier publications [10, 11, 17–20]. Numerical validation studies employing different grids as well as comparison with experimental results are contained in Refs. 10, 11, and 13. A relatively detailed 17-species, 52-step C_1-mechanism is used to represent the CH_4–air chemistry [21].

The simulations are validated by comparing the predicted heat release profile with the experimentally obtained chemiluminescent emission due to excited-C_2^* free radical species from a representative flame established under normal-gravity conditions (cf. Fig. 1b). Images of the (1, 0) C_2 Swan band (at a wavelength of 473 nm [22]) are obtained using an ITT F4577 intensified 513 × 480 pixel camera through a narrow wavelength interference filter (470 ± 10 nm), and transferred to a frame grabber and processed by subtracting a representative background image. The emission can be interpreted as a signature of chemical reaction and heat release [23–26], since the excited C_2^* free radical species is short-lived, a good indicator of the reaction zone [25], and its light intensity is known to vary linearly with the volumetric heat release [13, 26]. The chemiluminescence images are directly proportional to the C_2^* formation rate and, thus, serve as a qualitative rate measure of the flame chemistry [27].

The computed velocity field is compared with velocity vectors obtained using particle image velocimetry (PIV) (cf. Fig. 2). The flow is seeded with TiO_2 particles and the particle illumination source consists of a double-pulsed Continuum Nd:YAG laser. Particle images are captured two times (due to the double pulse) using a TI RS-170 CCD camera. The digitized

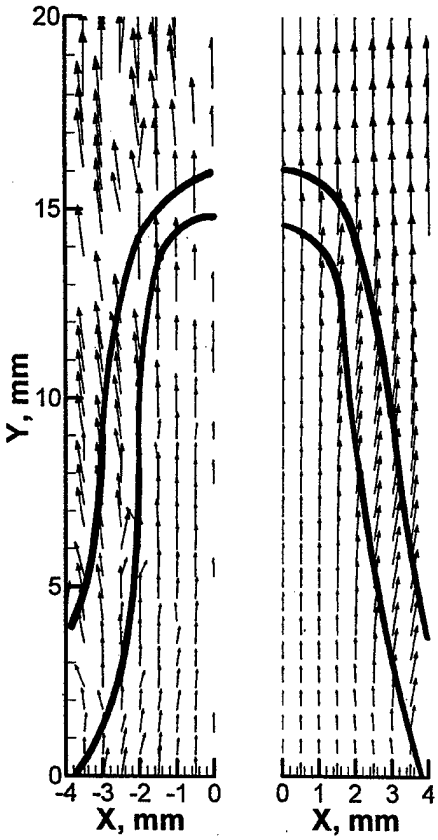

Fig. 2. Comparison of the measured ($-4 \leq x \leq 0$ mm) and predicted velocity vectors ($0 \leq x \leq 4$ mm) for a flame established at $\phi = 2$, $V_{air} = 30$ cm s^{-1}, and $V_{reac} = 30$ cm s^{-1}. The corresponding flame interface (chemiluminescent image and simulated heat release) is superimposed on the two plots.

image is fed to an array processor and analyzed using commercial autocorrelation software (TSI). Several precautions are taken to ensure reliability. Each interrogation spot contains more than 10 particle image pairs. Through extensive trial and error, the interrogation spot size is made small enough for a single vector to describe the flow at that location, and the laser sheet thick enough for out-of-plane particle motion to not be problematic and for sufficient particle pairs to be present. The particle displacement is kept greater than two particle image diameters, but not more than one-quarter of the interrogation spot size. The overlap between spots is adjusted to increase the vector density. In order to obtain accurate data for the range of flow velocities, the PIV measurement window was set at 7.5 × 5.5 mm, respectively, in the x- and y-wise directions. This choice restricted the lowest possible velocity measurement for the acquired particle displacements to 30 cm s^{-1}. Further details of the PIV system are contained in Ref. 13.

RESULTS AND DISCUSSION

Figure 1b contains a comparison between the predicted heat release rate and the experimentally obtained emission image for a representative 1-g methane–air flame established at an equivalence ratio $\phi = 2$, and air and reactant velocities (respectively, V_{air} and V_{reac}) of 30 cm s^{-1}. Both the simulated heat release and the C_2^* emission signal are confined to two relatively thin sheet-like reaction zones, one each on the rich and lean sides of the flow. The simulation and experiment show excellent agreement with respect to the spatial location of the reaction zones.

Combustion proceeds in two distinct separated reaction zones, one an inner premixed flame and the other an outer nonpremixed flame. The two reaction zones in analogous counterflow flames are "merged" due to higher strain rate effects [28]. This is due to flowfield differences between one- and two-dimensional flames, since merged partially premixed flames can be retracted into double flames provided the flowfield stretch rates are low enough [29]. The highest temperatures occur in the outer flame. The chemistry is frozen in the region between the inner and outer reaction zones despite the high temperatures there due to a local scarcity of hydroxyl radicals that are required to oxidize the intermediate species CO and H_2, which are formed in the inner (premixed-like) reaction zone. Based on the heat release rate profiles, the inner and outer flame lengths are, respectively, 16 and 48 mm. Both these heights agree with the measured values obtained from the emission images of Fig. 1b. The reaction and heat release rates are much weaker at the tip of the outer flame than at its base, whereas the inner premixed flame has comparable reaction and heat release rates at both its tip and base.

Figure 2 compares the experimentally obtained and computed velocity vectors in the 1-g flame discussed in the context of Fig. 1b. The flame interface separates smaller velocity magnitudes on the reactant side from larger values on the partially burned side in both sets of data. The measured and predicted results are in excellent agreement. Flow dilatation due to the inner flame heat release causes the velocity vectors to move away from the centerline. The experimental data are sparse in some postflame regions, since dilatation reduces the particle seed densities in those areas considerably. Consequently, there is some discrepancy in the comparison in the postflame region due to experimental uncertainties.

Figure 3 depicts the normal- and zero-gravity flame structures for different values of V_{reac} and ϕ. For both the 1-g and 0-g flames, the inner and outer reaction zone heights increase as either or both of the reactant velocity and the equivalence ratio are increased. The dependence of the inner flame height on the reactant velocity is attributable to the residence time, since the chemical reaction time essentially depends only on the equivalence ratio. Consequently, the premixed reaction zone moves to increasingly higher axial locations as V_{reac} is raised. On the other hand, the chemical reaction time also increases as ϕ is increased and, consequently, the inner flame height increases. The increase in the outer flame height with larger reactant velocities is attributed to two factors: (1) Due to the strong synergistic interactions between the two flames, the outer flame height increases with the inner flame height. (2) Larger values of V_{reac} enhance the advection fluxes of CO and H_2 (that are provided by the inner reaction zone and serve as intermediate fuels) that move the outer flame farther downstream in the axial direction.

We have found that the heights of both the inner and outer reaction zones at 1-g are well-correlated with the function $F = V_{reac}(1 + V_{reac}/V_{air})(\phi - 1)$, where V_{reac} denotes the velocity of the flow issuing from the inner slot, and V_{air} represents the velocity of the air introduced from the outer slot [13]. A linear best fit provides relations for the inner reaction zone height $L_i = (0.3F + 2)$ mm, and the outer height $L_O = (0.6F + 20)$ mm in the ranges $25 \leq F \leq 280$ mm, $5 \leq L_i \leq 85$ mm, and $20 \leq L_i \leq 145$ mm.

Another important observation from Fig. 3 is that the presence of gravity reduces the spatial separation between the inner and outer reaction zones and, thereby, enhances the interaction between these regions. In addition, while the inner flame characteristics are essentially unaffected by gravity, the outer flame shows a strong sensitivity to gravity. For all the cases considered, the presence of gravity makes the outer flame more compact, taller, and closer to the inner flame. In addition, the outer flames exhibit weaker reaction rates at their tips at zero-gravity as compared to their 1-g counterparts. This is apparently caused by the relatively enhanced diffusive fluxes downstream of the inner premixed zone compared to the reduced advection fluxes in the outer region for the 0-g flames. This may have important implications with regard to the overall pollutant formation in partially premixed flames, especially with respect to CO leakage from the zero-gravity flames.

The iso-temperature contours for two flames, one established at 1 g and the other at 0 g at $\phi = 2$ and $V_{reac} = V_{air} = 30$ cm s^{-1}, are presented in Fig. 4. The corresponding heat release rate profiles are contained in Fig. 3b. In the 1-g case the reactants flow out of the burner in an opposite direction to the gravitational vector. The Froude number $Fr(=V_{reac}^2/gL = 1.22)$ for the 1-g flame is of order unity so that the inertial and gravitational effects are of similar magnitude. The air entrainment that occurs at 1 g is illustrated by the direction of the velocity vectors in the outer flow that turn toward the centerline. Flow dilatation due to the inner flame heat release causes the velocity vectors to move away from the centerline. The temperature of the outer reaction zones is higher than in the respective inner zones. The heat release rates associated with the two inner (rich-side) reaction zones are similar for the two flames. However, the outer reaction zone heat release rates are different for the two flames, since buoyancy effects elongate the outer nonpremixed flame in the presence of gravity. Consequently, the inner reaction zones exhibit like temperature profiles for the two cases, whereas the outer reaction zone temperatures are dissimilar. Buoyancy effects cause the outer reac-

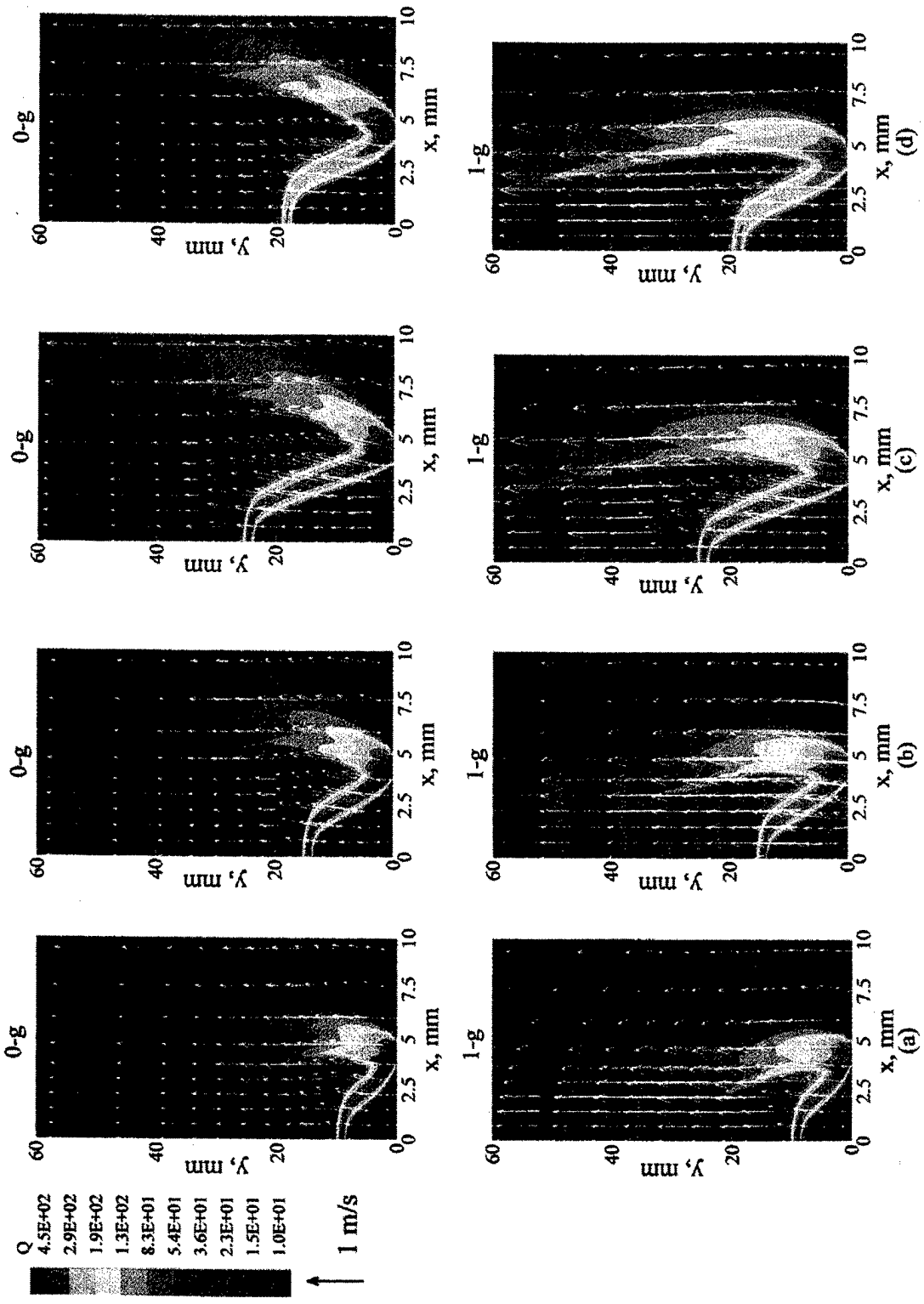
0-g
1-g
y, mm
x, mm
(a)
(b)
(c)
(d)
Q
4.5E+02
2.9E+02
1.9E+02
1.3E+02
8.3E+01
5.4E+01
3.6E+01
2.3E+01
1.5E+01
1.0E+01
1 m/s

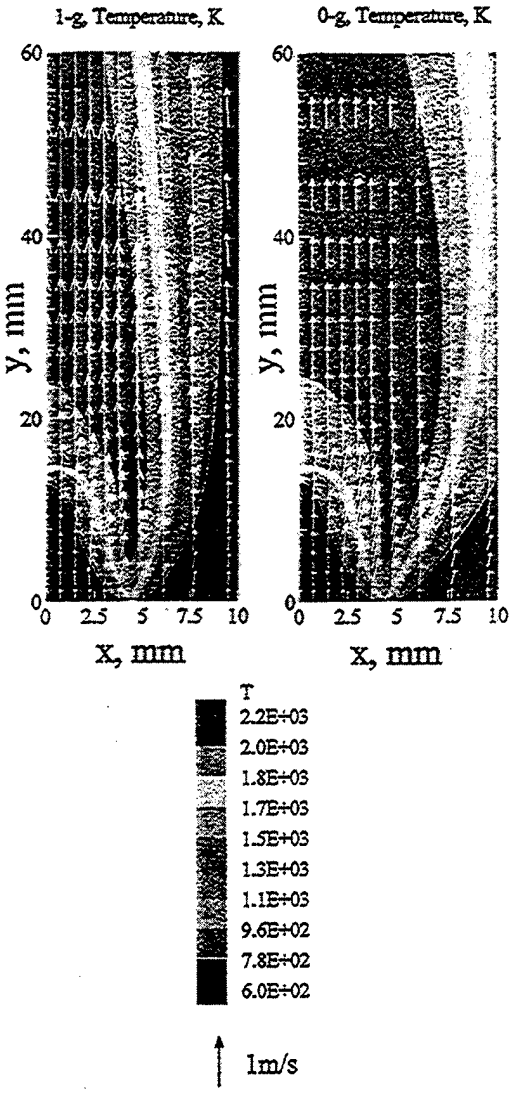

Fig. 4. Temperature profiles for (a) 1-g and (b) 0-g flames, both established at $\phi = 2$ and $V_{reac} = V_{air} = 30$ cm s^{-1}.

tion zone to become slender and more compact than in the corresponding 0-g case.

The effects of flow dilatation are apparent along the premixed flame both in the presence and absence of gravity, and gas expansion turns the velocity vectors away from the centerline. In the presence of gravity, buoyancy effects accelerate the products and, consequently, direct the velocity vectors toward the centerline. Therefore, the advection of the (outer) air flow into the outer reaction zone increases in the presence of gravity. While the inner reaction zone height based on the heat release profile is unaffected by gravitational effects, the topography of the outer reaction zone is significantly different. The 1-g flame exhibits much steeper temperature gradients in its outer reaction zone as the enhanced air advection both increases the local reaction rate and cools that region.

The spatial changes in the outer flame chemistry are illustrated in Fig. 5 which compares the reaction rate contours of the major fuel decomposition reaction $CH_4 + H \Leftrightarrow CH_3 + H_2$ and the product-formation reaction $H_2 + OH \Leftrightarrow H_2O + H$ for the two flames. Whereas the outer reaction zone tip is closed at 1 g (based on the methane-consumption reaction), that for the 0-g flame is open. Likewise, water formation occurs in a broader spatial region at zero gravity. This is due to the relatively limited transport of air into the outer reaction zone under 0-g conditions so that the fuel must diffuse farther into the air stream in order to meet its oxidizer demand. The corresponding inner reaction zones exhibit much smaller topographical differences. The inner zone reaction rate intensity at 0 g is slightly lower. The methane consumption rate is higher in the inner premixed flame due to its higher concentrations in that region. Since oxygen is deficient in the premixed reaction zone, methane leaks through it and is also consumed in the nonpremixed flame, although at lower rates. The outer reaction zone is transport-limited and is, therefore, spatially thicker than the inner premixed flame.

A detailed examination of the reaction rates previously reported by us [11, 13] indicated that: (1) The major pathway for methane consumption proceeds through the reactions $CH_4 + H \Leftrightarrow CH_3 + H_2$, $CH_3 + O \Leftrightarrow CH_2O + H$, $CH_2O + H \Leftrightarrow CHO + H_2$, and $CHO + M \Leftrightarrow$

Fig. 3. Heat release rate contours and velocity vector plots for several normal- and zero-gravity flames (for all of the cases $V_{air} = 30$ cm/s): (a) $V_{reac} = 20$ cm/s, $\phi = 2.0$; (b) $V_{reac} = 30$ cm/s, $\phi = 2.0$; (c) $V_{reac} = 50$ cm/s, $\phi = 2.0$; (d) $V_{reac} = 30$ cm/s, $\phi = 2.5$.

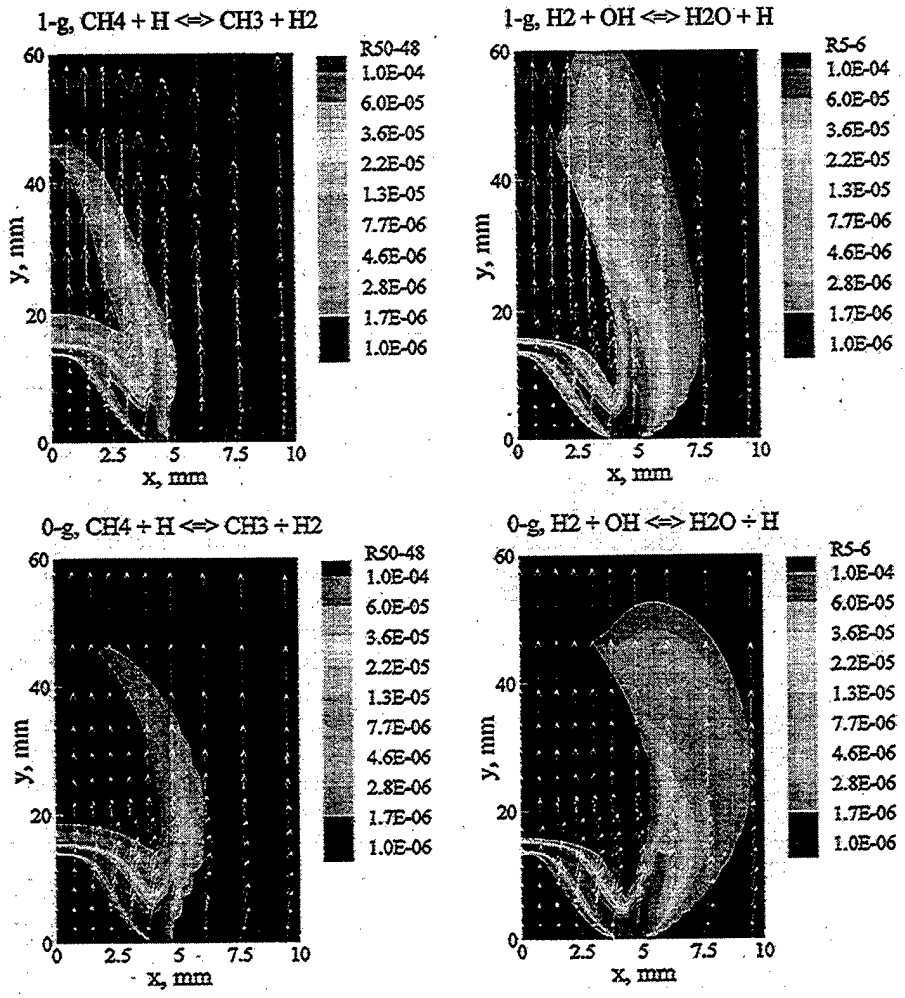

Fig. 5. Contours of two major chemical reaction rates $CH_4 + H \Leftrightarrow CH_3 + H_2$ and $H_2 + OH \Leftrightarrow H_2O + H$ for the (a) 1-g and (b) 0-g flame established at $\phi = 2$ and $V_{reac} = V_{air} = 30$ cm s^{-1}.

CO + H + M; (2) Carbon monoxide and hydrogen are oxidized in the outer nonpremixed flame, respectively, through the reactions CO + $OH \Leftrightarrow CO_2 + H$ and $H_2 + OH \Leftrightarrow H_2O + H$; and (3) O_2 is converted into hydroxyl radicals in this flame through the sequential reactions O_2+H + M $\Leftrightarrow HO_2$ + M and HO_2 + H $\Leftrightarrow$ OH + OH. In those investigations we reported that the two reaction zones are synergistically coupled and each provides heat and/or chemical species for the other. The premixed flame requires H-atoms for the reactions that initiate CH_4 and O_2 consumption and produces the partial oxidation products CO and H_2 (which provide the fuel for the nonpremixed flame). The nonpremixed flame consumes the premixed flame products and, in turn, produces H-atoms that are, in part, transported back into the inner region [11, 13]. Our results show that the heat release rate profile strongly correlates with CO- and H_2-oxidation [13]. Therefore, the region between the inner and outer flames is characterized by heat and mass transport by both advection and diffusion, but where negligible chemical reaction occurs due to the relative paucity of hydroxyl radicals that are required to oxidize CO and H_2.

The advection of O_2, CH_4, and H-atoms in

both the 1- and 0-g flames is illustrated in Fig. 6. The advection term is $\rho u Y_i \vec{i} + \rho u Y_j \vec{j}$, where $\vec{i}$ and $\vec{j}$ denote the directional vectors. The advection of methane and oxygen into the inner reaction zone is very similar for the two flames. Under normal gravity conditions methane is advected toward the centerline at higher axial and radial locations ($y > 20$ mm, $x > 2.5$ mm), while at 0 g this CH_4-transport in this manner is roughly parallel to the centerline. The difference between the two flames is clearer in the context of O_2 advection, since buoyancy both accelerates the flow and greatly enhances oxidizer transport toward the centerline. While the advection of H-atoms in the region of the inner reaction zone is similar for both the 1- and 0-g flames, it is markedly dissimilar in the region of the outer reaction zone. Therefore, buoyant transport enhances radical advection into the outer reaction zone. In contrast, the flux of radical species into the outer reaction zone of the zero-gravity flame is smaller and, consequently, the reactant residence times are larger in the outer zone of that flame. The advective flux of the various species in the region contained between the inner and outer reaction zones is much larger at normal gravity and, consequently, the separation between the inner and outer reaction zones is smaller at 1-g. In general, buoyancy effects increase the advection of all species. The consequence of this is that the 1-g flames exhibit larger emission of unburned intermediates, such as CO and H_2 (as discussed later in context of Figs. 11a and b).

In summary, the zero-gravity flame is spatially broader than the normal gravity flame. While the inner premixed spatial region appears to be relatively unaffected by gravitational effects, the outer flame is significantly dissimilar for the two cases. The gravitational effects that occur in the postflame zone of the inner flame do not significantly influence its upstream region in accord with previous results for premixed flames [30]. The reactions along the carbon-consumption chain are weaker in the outer nonpremixed region at zero-gravity and occur in a larger reaction volume. The outer flame is thicker in the absence of gravity, since buoyant mixing is absent, suggesting that its structure will be more sensitive to any flow or stoichiometry perturbations.

The diffusive flux, which has the form $-(\rho D_{i-N_2})(\partial Y_i/\partial x)\vec{i} + (\rho D_{i-N_2})(\partial Y_i/\partial y)_i\vec{j}$, of O_2, CO, and OH radicals for the two flames is compared in Fig. 7. Buoyancy effects have a negligible impact on the diffusion of species into and out of the inner reaction zone. The diffusive fluxes associated with the outer reaction zone are, however, influenced by gravity, since that reaction zone topography, and, therefore, the species concentration gradients are different in the two flames. The enhanced mixing in the outer reaction zone at 1 g causes the reactions to proceed faster and the oxygen gradients to be steeper. This also increases oxygen diffusion into that region under normal gravity. The slower oxygen transport at 0 g induces the carbon monoxide to diffuse further away from the centerline before its conversion into CO_2 by hydroxyl radicals. Overall, gravity does not impact the diffusive fluxes as strongly as it does advection, in particular, in the outer reaction zone. However, the relative influence of the diffusive fluxes in comparison to advection is significantly enhanced in the absence of gravity.

Flame stretch occurs due to both flow nonuniformities along the flame surface and curvature [31]. The outer flame exhibits a larger curvature (based on either the heat release or various reaction rates) in the absence of gravity (cf. Fig. 3). The normal gravity outer flame is curved at its base and virtually planar elsewhere. The tips of both the inner and outer reaction zones appear to be locally planar (based on the local advection) so that the local stretch rate there is essentially due to aerodynamic straining alone. While the flow is oblique to the inner reaction zone surface everywhere, it is virtually normal to the outer flame surface in the vicinity of the centerline. Therefore, the inner reaction zone is stretched at the centerline, whereas the outer flame experiences negligible stretch. The fuel-side strain rate (in this case that associated with the inner flame) has been previously interpreted as a sensitive indicator of partially premixed flame structure in one-dimensional counterflow flames [28]. Figure 8a presents the centerline velocity profiles for several flames, which show large differences due to gravitational effects. The velocity profiles prior to the inner flame are nearly identical in the presence and absence of gravity, but exhibit significant

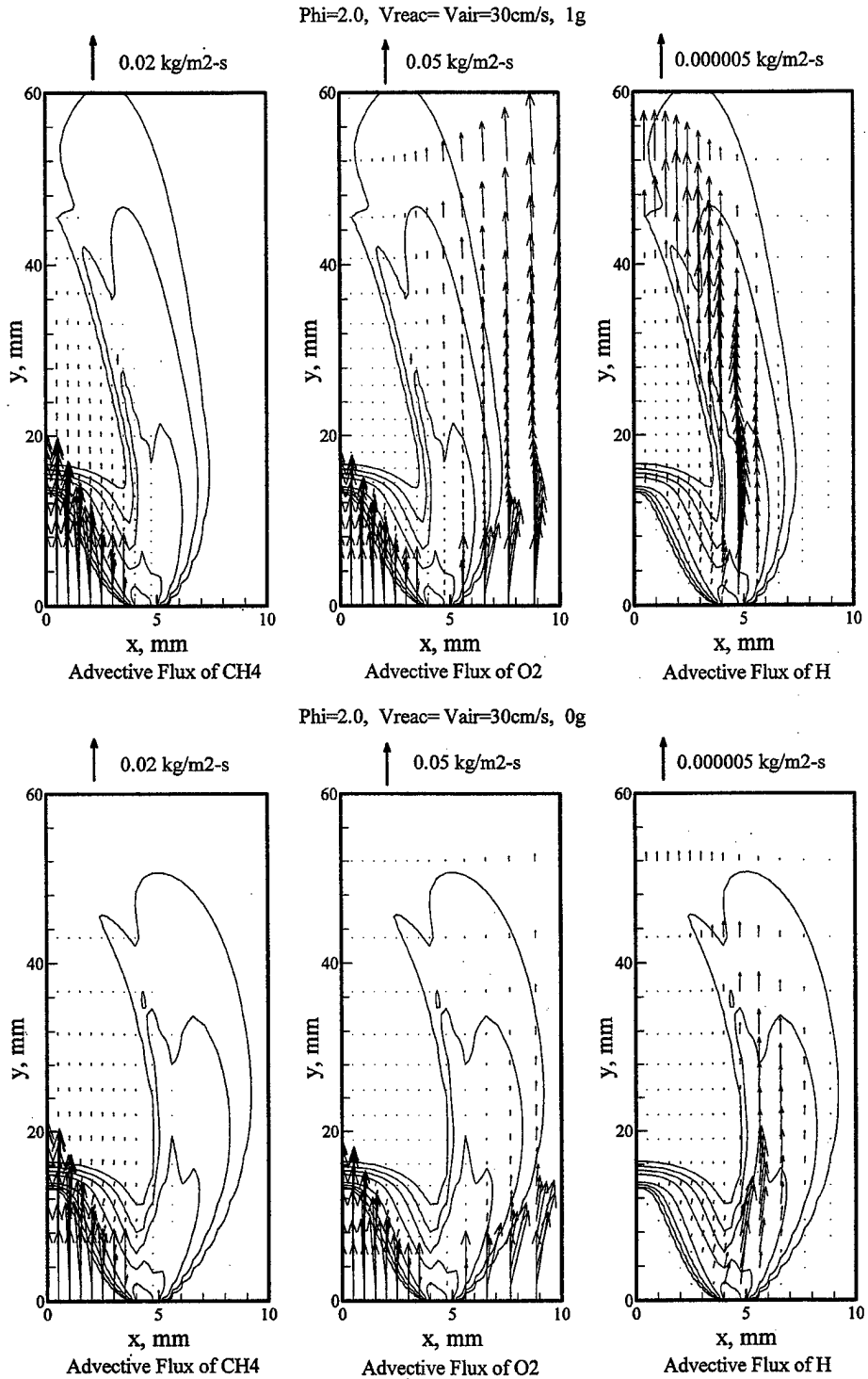

Fig. 6. Advection flux of CH_4, O_2, and H-atoms under (a) normal-gravity and (b) zero-gravity conditions. A scale for the magnitude of the vectors is provided at the top of the figures.

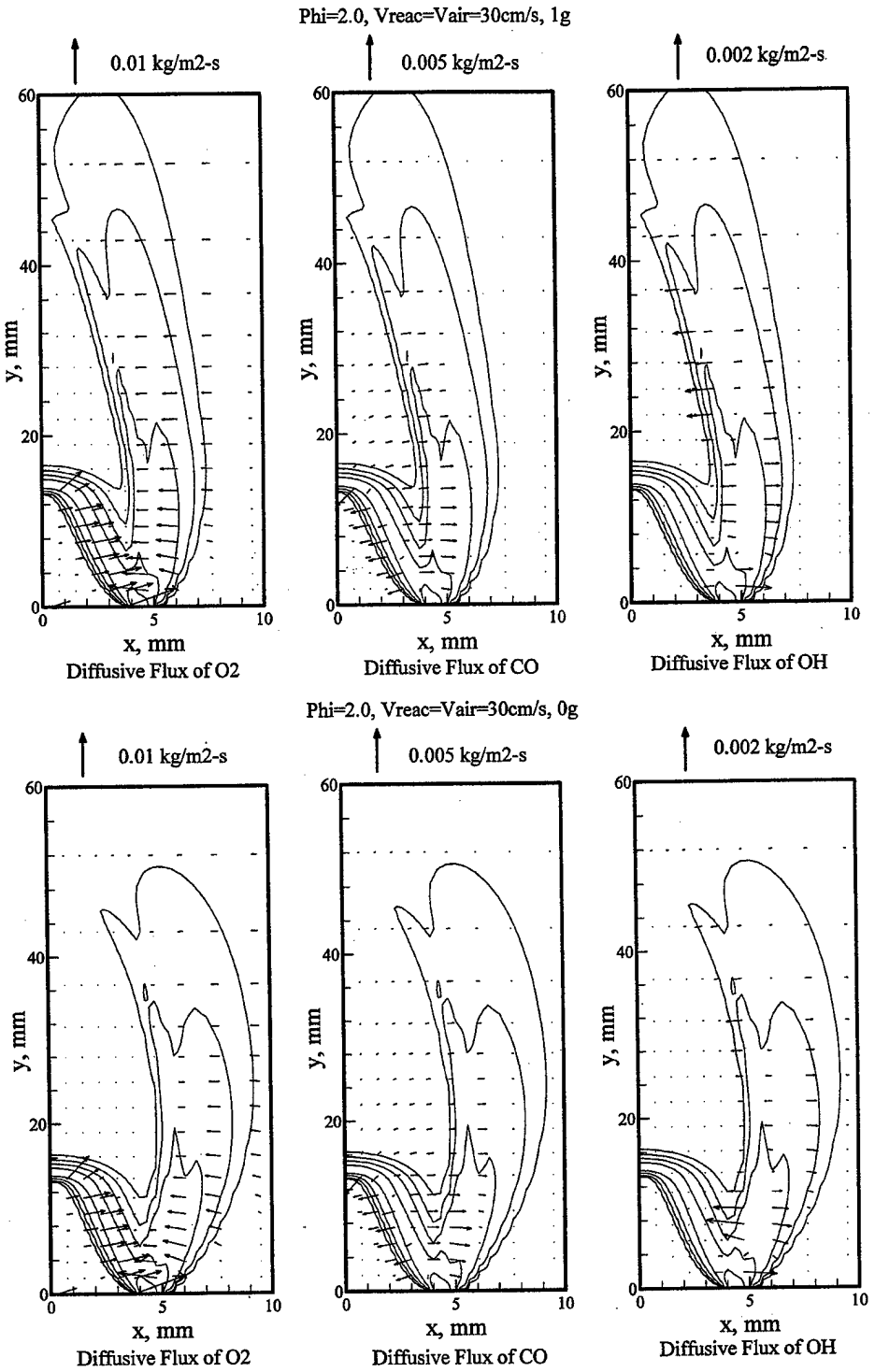

Fig. 7. Diffusion flux of O_2, CO, and OH radicals under (a) normal-gravity and (b) zero-gravity conditions. A scale for the magnitude of the vectors is provided at the top of the figures.

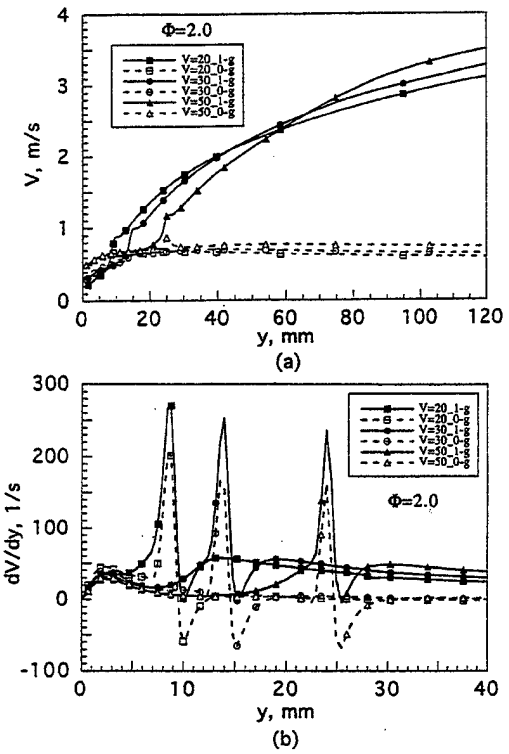

Fig. 8. Profiles of centerline (a) velocity, and (b) strain rate for normal- and zero-gravity flames established at $\phi = 2$, $V_{air} = 30$ cm s^{-1}, and $V_{reac} = 20$, 30, and 50 cm s^{-1}.

differences in the postflame region. The zero-gravity flames exhibit a small velocity increase due to dilatation, whereas the velocity in the normal-gravity flames increases severalfold due to buoyancy effects.

Since there are no transverse gradients or transverse velocity components along the centerline, the strain rate tensor there contains a single component, i.e., the normal axial strain rate. The corresponding centerline normal strain rates for the flames discussed in Fig. 8a are presented in Fig. 8b. These rates vary, having their largest and smallest values, respectively, in the preheat and the heat release regions of the inner reaction zone. The normal strain rate in the initial cold flow is unaffected by gravity. Just prior to the preheat zone, the normal strain rate is negligible when $V_{reac} = 30$ and 50 cm s^{-1}. Therefore, the double flame structure (that is not apparent at this stoichiometry in higher shear strain rate counterflow flames [28]) is due to the lower strain rates in the two-dimensional configuration. Increasing the initial reactant velocity decreases the maximum values of the normal strain rate. Further downstream, the rates relax to moderate values under normal-gravity conditions, and are negligible in the absence of gravity. In general, the absence of gravity decreases the local strain rate allowing for further spatial separation of the two reaction zones.

The spatial broadening of the reaction zone due to gravity is illustrated in Figs. 9a–c which present various spatially integrated (in the axial direction) reaction rate profiles with respect to transverse position. Figure 9a presents the transverse profile of the spatially integrated methane consumption reaction for the two flames. While the reaction is concentrated around one axial location at 1 g, since the outer flame is wider at 0 g, the reaction proceeds at two distinct axial locations at that condition. This is also true of the CO- and H_2-oxidation reactions as illustrated in Figs. 9b and c. The reactions peak in the vicinity of the axial location of the flame base at both normal- and zero-gravity. At 0 g, the reaction rates also exhibit peaks at transverse locations that are further displaced from the centerline. The increased spatial separation between the inner and outer reaction zones at 0 g is also evident from Figs. 9a–c.

In contrast, if the reaction rates are spatially integrated in the transverse direction, their normal- and zero-gravity profiles are similar for the two flames. This is illustrated in Fig. 9d through the profile of the reaction $H_2 + OH \Leftrightarrow H_2O + H$. Although the transversely integrated reaction rate is slightly higher at higher axial locations for the 1-g flame, the (axial) differences between the two flames are not as pronounced as in the transverse direction (cf. Figs. 9a–c). These figures again illustrate how the outer nonpremixed-type reaction zone must move outward into the air stream to meet the oxidizer demand of the unburned methane and the intermediate species CO and H_2.

The effects of varying strain rates, and multi-dimensional transport of heat and radicals on the flame structure can be investigated by examining the state relationships of the various scalars. Previous investigations have found that

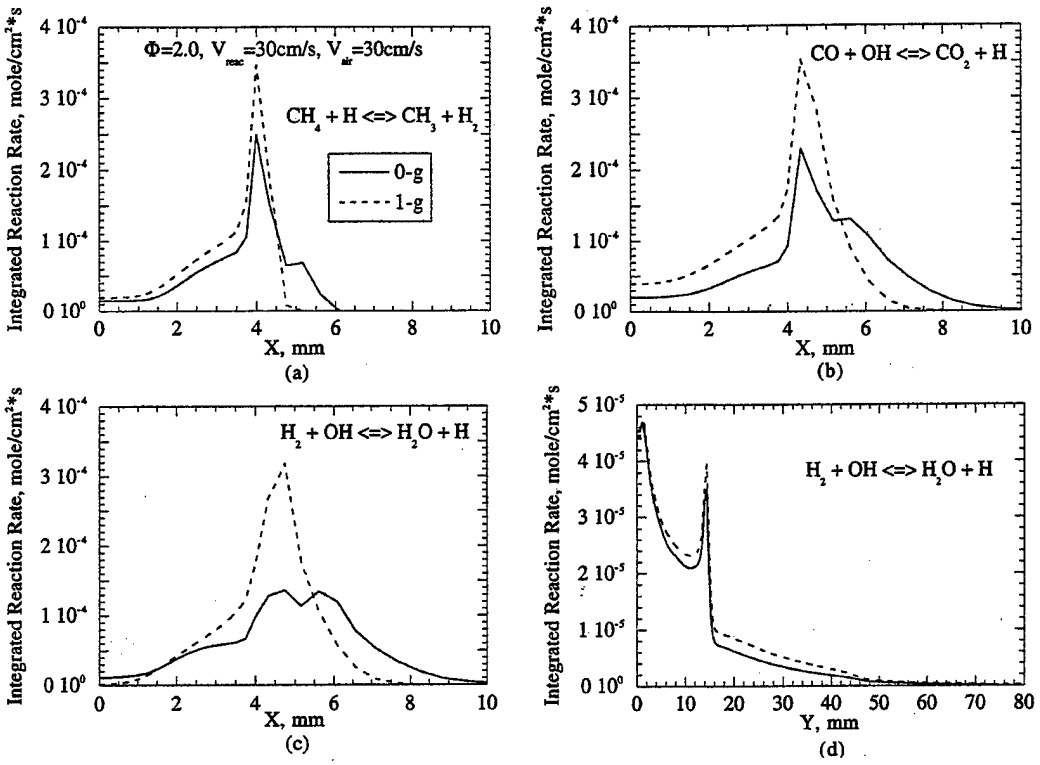

Fig. 9. Integrated rate profiles with respect to the transverse direction for the reactions (a) $CH_4 + H \Leftrightarrow CH_3 + H_2$; (b) $CO + OH \Leftrightarrow CO_2 + H$; (c) $H_2 + OH \Leftrightarrow H_2O + H$; and (d) (with respect to the axial direction) for the reaction $H_2 + OH \Leftrightarrow H_2O + H$.

state relationships (in terms of the mixture fraction) for the major species are generally applicable to nonpremixed hydrocarbon–air flames established in various configurations over a range of strain rates [32]. It is known that partially premixed flames can also be characterized with respect to a modified mixture fraction $\xi = (Z - Z_l)/(Z_r - Z_l)$, where Z denotes the relative local mass fraction originating in the fuel, and the subscripts r and l are conditions relevant at the boundaries of the rich and lean regions, respectively [1, 3, 8, 11].

State relationships for the temperature and H_2 mass fraction are presented in Fig. 10 along three sets of transverse locations with respect to ξ (defined in terms of the local nitrogen mass fraction) for two flames established under similar flow and stoichiometric conditions, but under normal- and zero-gravity. The temperature and H_2 profiles clearly show the two rich- and lean-side reaction zones. The lean-side temperature is higher, as has been previously noted [28, 29]. The locations of both the rich and lean reaction zones differ with respect to ξ, depending on their transverse positions. Due to the spatial differences between the 0- and 1-g flames on the lean side we expect the state relationships to differ in that region. The peak temperature on the lean side is 2181 K for the 0-g flame and 2164 K for the 1-g flame. This small reduction in the peak temperature can be explained by the enhanced mixing of fuel and air in the presence of gravity and the buoyancy-induced convective heat transfer.

The inner (rich-side) reaction zone shifts towards less-rich locations in the presence of gravity as seen from the profiles contained in Fig. 10. It is clear from Fig. 6 that the flow divergence is larger as one moves transversely outward from the centerline, and consequently, the local strain rate also increases. The two-dimensional slot flame is characterized by a

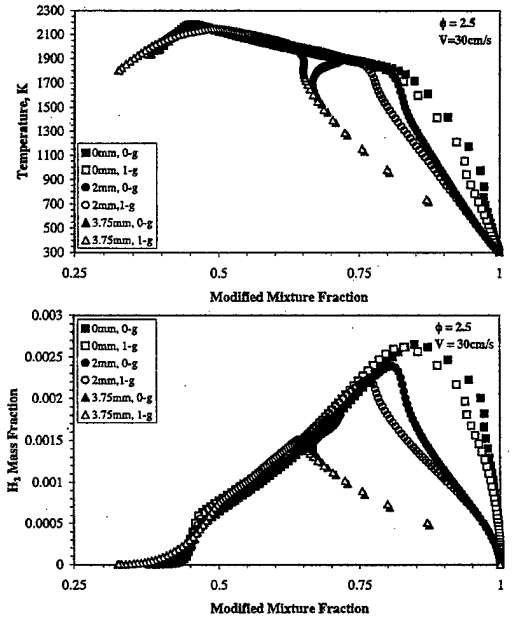

Fig. 10. Profiles of axial (a) temperature, and (b) H_2 mass fraction with respect to the modified mixture fraction for normal- and zero-gravity flames established at $\phi = 2.5$, $V_{air} = V_{reac} = 30$ cm s^{-1} along three transverse locations: $x = 0$, 2, and 3.75 mm.

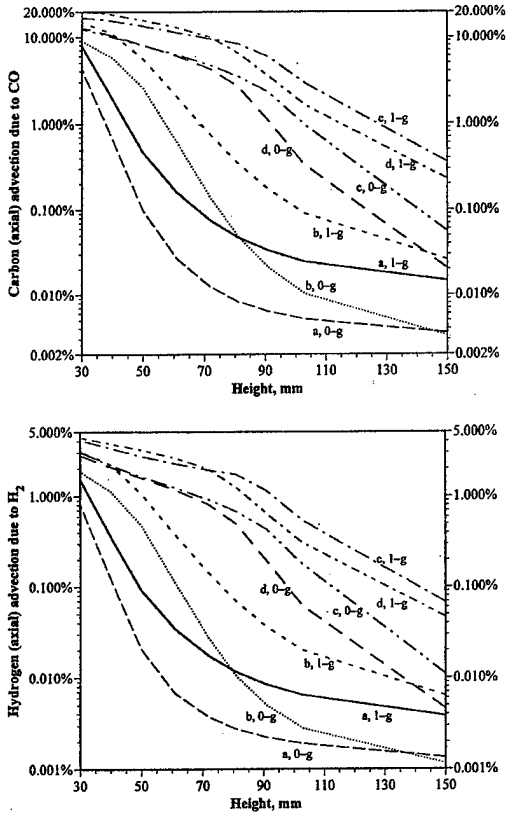

Fig. 11. The axial advection of (a) carbon contained in CO, and (b) hydrogen contained in H_2 as a weight percentage of both species introduced into the domain in the form of CH_4. The conditions a, b, c, and d are the same as for the normal- and zero-gravity flames discussed in the context of Fig. 3.

multiplicity of local aerodynamic strain rates. The results contained in Fig. 10 show that as the local strain rate increases, the inner rich-side reaction zone moves closer in mixture fraction space to the lean outer reaction zone. Consequently, while gravity affects the outer lean reaction zone, strain rate effects are more pronounced on the inner reaction zone. Since the presence of gravity slightly increases the strain rate experienced by the rich inner reaction zone, its location in the 1-g flame moves relatively closer to the lean side in mixture fraction space as compared to the 0-g flame. In accord with a residence time criterion, the H_2 mass fraction in the outer reaction zone decreases with increasing flame straining.

Figures 11a and b, respectively, present the fractional axial advection of carbon atoms (contained in CO) and hydrogen atoms (contained in H_2) in comparison to their flux in the form of fuel. The fractional axial advection of either elemental species is calculated through the expression $(a_{k,i}/a_{k,CH_4})(W_{CH_4} \int_0^L Y_i \rho v_y \, dx)/(W_i \int_0^L (Y_{CH_4} \rho v_y)_0 \, dx)$, where W denotes the molecular weight, Y the mass fraction, ρ the density, v_y the axial velocity, L the width of the computational half domain, the subscript i refers to either CO or H_2, while the subscript 0 refers to conditions at the influx plane into the domain, i.e., at $y = 0$ which is the burner exit. The ratio $(a_{k,i}/a_{k,CH_4})$ refers to the relative number of atoms of element k (either C or H) contained in species i (respectively, CO or H_2) compared to the corresponding number in CH_4. The carbon and hydrogen fractional advection is presented in Figs. 11a and b for the eight flames that are discussed in the context of Fig. 3. In general, the fractional advection of these elemental species is always greater at 1 g, confirming the relatively enhanced role of molecular transport in the absence of gravity. The simulations show that the value of the fractional

advection rises when either V_{react} or the inner equivalence ratio is increased.

The introduction of buoyancy increases the unburned carbon and hydrogen loss from the domain, since the higher advection under normal gravity reduces the residence time available for complete combustion of the intermediate fuels CO and H_2. Therefore, at 1 g the percentage of carbon advection at a 150 mm height approximately varies between 0.01% (for the V_{air} = 30 cm/s, V_{reac} = 20 cm/s, ϕ = 2.0 flame) to 0.4% (for the V_{air} = 30 cm/s, V_{reac} = 50 cm/s, ϕ = 2.0 flame). The corresponding range for the zero-gravity flames is lower by almost one order of magnitude, lying between 0.003–0.06%. The analogous bounds for the fractional unburned H-atom loss lies between approximately 0.004–0.07% for the 1-g flames, and between 0.001–0.01% for the 0-g flames. The 1-g flames have more vigorous reaction at the tips of the outer nonpremixed reaction zone which tends to decrease the unburned C- and H-atom losses. However, the enhanced advection in the presence of gravity dominates and, consequently, leads to higher CO and H_2 emissions than at 0 g.

Finally, we address the issue of thermal radiation. The radiative cooling time τ_r for a gaseous volume initially at the adiabatic flame temperature T_f can be estimated as $\tau_r = T_f/(dT/dt) \approx T_f/(q/\rho c_p)$, where q denotes the heat loss rate, ρ the density, and c_p the constant pressure specific heat [33]. Using the optically thin gas assumption, $q = [4\sigma a_p(T_f^4 - T_O^4)]$ (where σ represents the Stefan-Boltzmann constant, a_p the Planck mean absorption coefficient, and T_O the ambient temperature) and the ideal gas state relationship, τ_r can be expressed in the form $\tau_r \approx \{\gamma/(\gamma - 1)\}P/\{4\sigma a_p(T_f^4 - T_O^4)\}$, where γ denotes the specific heat ratio, and P the ambient pressure. Assuming atmospheric conditions, a_p = 56 cm^{-1}, γ = 1.35, T_O = 298 K, and the "flame" temperatures in typical methane–air partially premixed flames to vary from 1650 K in the inner premixed reaction zone to 2200 K in the outer nonpremixed region, the corresponding τ_r values lie in the range 0.3–0.09 s.

The diffusive time scale $\tau_d = \delta^2/\alpha$ represents the molecular transport of species or thermal energy across a region of thickness δ, with α denoting a temperature-averaged (mass or thermal) diffusivity. The buoyant transport time scale $\tau_b \approx L/U_b$. Here, L represents a characteristic length, and $U_b \approx [gL(\Delta\rho/\rho)]^{1/2}$ is the buoyancy-induced velocity, with g denoting the gravitational acceleration, ρ density, and $\Delta\rho$ the density change across the flamefront. For flames $\Delta\rho/\rho \approx 1$ with the result that $\tau_b \approx (L/g)^{1/2}$ [33].

We assume representative values for α and g, respectively equal to 1.5 cm^2 s^{-1} and 980 cm s^{-2} [33]. For typical characteristic length scales in the range 1–10 cm, τ_b varies from 0.03–0.1 s. For τ_d to lie within these bounds, the transport region must be 2 to 4 mm thick. This thickness depends on the level of partial premixing and the velocities of the reactant streams. Therefore, if the transport zone thickness exceeds 4 mm (as is the norm in the slot burner flames that we have investigated), gravitational effects overwhelm transport effects, since $\tau_b < \tau_d$. This is clearly illustrated in the comparisons between 1- and 0-g flames contained in Figs. 3–7.

For typical characteristic length scales in the range 1–10 cm, τ_b varies from 0.03–0.1 s. Hence, radiation effects may be relatively unimportant at normal gravity, since buoyant convection is a faster process. On the contrary, under microgravity conditions at which τ_b is sufficiently large, radiation effects are expected to be more significant. Therefore, future studies should address the issue of thermal radiation from these flames, particularly since heat losses should further weaken the 0-g outer reaction zone tip.

CONCLUSIONS

We have presented the results of a numerical investigation of two-dimensional partially premixed methane–air flames established under both normal- and zero-gravity. The computational model has been previously validated. Further validation is obtained by comparing the experimentally obtained chemiluminescent emission due to excited-C_2^* free radical species with the simulated heat release for a representative flame.

1. The structure of a near-unity Froude number flame is discussed. Combustion occurs in two reaction zones, one an inner premixed flame

and the other an outer nonpremixed flame. The reaction and heat release rates are much weaker at the tip of the outer flame than at its base. The inner premixed flame has comparable reaction and heat release rates at both its tip and base.

2. The premixed flame requires H-atoms for CH_4 and O_2 consumption, and produces CO and H_2 (which provide the "fuel" for the nonpremixed flame). The nonpremixed flame consumes these products and, in turn, produces H-atoms that are transported back into the inner region.
3. The zero-gravity flame is spatially larger than the corresponding normal-gravity flame. While the spatial characteristics of the inner premixed region are relatively unaffected by gravitational effects, the outer nonpremixed zones exhibit significant differences. More air is advected into the outer reaction zone in the presence of gravity. Consequently, the outer flame is thicker for the 0-g case, since the role of radial diffusive transport is relatively enhanced. While buoyancy effects significantly influence advection, gravity has a small effect on the absolute values of the species' diffusive fluxes.
4. The inner reaction zone is strained at the centerline, whereas the outer zone experiences negligible strain and this lower strain rate allows a double-flame structure to exist. The absence of gravity decreases the local value of the normal strain rate allowing for further spatial separation of the two reaction zones.
5. The presence of gravity reduces the spatial separation (and thereby enhances the interactions) between the inner and outer reaction zones. The outer reaction zones are more compact, taller, and exhibit more vigorous reaction at their tips at 1-g than at zero-gravity.
6. The presence of buoyancy significantly influences the region downstream of the inner reaction zone. Consequently, the inner (rich-side) reaction zone shifts slightly toward less-rich locations in the presence of gravity. The two-dimensional flame is characterized by a multiplicity of local aerodynamic strain rates. As this rate increases, the inner rich-side reaction zone moves closer in mixture fraction space to the lean outer reaction zone.
7. Buoyancy effects increase the advection, thereby reducing the residence time available for the oxidation of CO and H_2. Consequently, there is a larger loss of unburned C- and H-atoms from the 1-g flames than in the absence of gravity. Although the 1-g flames involve more vigorous reaction at their tips (which would decrease the unburned C- and H-atom losses), the enhanced advection dominates and leads to higher CO and H_2 emissions than at zero-gravity.

This research was supported by the National Science Foundation Combustion and Plasma Systems Program through Grant No. CTS-9707000 for which Dr. Farley Fisher is the program director.

REFERENCES

1. Peters, N., *Twentieth Symposium (International) on Combustion*, The Combustion Institute, Pittsburgh, 1984, pp. 353–360.
2. Smooke, M. D., Seshadri, K., and Puri, I. K., *Twenty-Second Symposium (International) on Combustion*, The Combustion Institute, Pittsburgh, 1988, pp. 1555–1563.
3. Rogg, B., Behrendt, F., and Warnatz, J., *Twenty-First Symposium (International) on Combustion*, The Combustion Institute, Pittsburgh, 1986, p. 1533.
4. Yamaoka, I., and Tsuji, H. *Fifteenth Symposium (International) on Combustion*, The Combustion Institute, Pittsburgh, 1974, p. 737.
5. Yamaoka, I., and Tsuji, H. *Sixteenth Symposium (International) on Combustion*, The Combustion Institute, Pittsburgh, 1976, p. 1145.
6. Yamaoka, I., and Tsuji, H. *Seventeenth Symposium (International) on Combustion*, The Combustion Institute, Pittsburgh, 1978, p. 843.
7. Hamins, A., Thridandam, H., and Seshadri, K., *Chem. Eng. Sci.* 40:2027–2038 (1985).
8. Seshadri, K., Puri, I., and Peters, N., *Combust. Flame* 61:237–249 (1985).
9. Law. C. K., Li, T. X., Chung, S. H., Kim, J. S., and Zhu, D. L., *Combust. Sci. Technol.* 64:199–232 (1989).
10. Shu, Z., Aggarwal, S. K., Katta, V. R., and Puri, I. K., *Combust. Flame* 111:276–295 (1997).
11. Shu, Z., Aggarwal, S. K., Katta, V. R., and Puri, I. K., *Combust. Flame* 111:296–311 (1997).
12. Yule. A. J., Chigier, N. A., Ralph, S., Boulderstone, R., and Ventura, J., *AIAA J.* 19:752–760 (1981).
13. Shu, Z., Krass, B. J., Choi, C. W., Aggarwal, S. K., Katta, V. R., and Puri, I. K., *Twenty-Seventh Symposium (International) on Combustion*, Boulder, Colorado, August 2–7, 1998, Paper No. 049 (accepted).
14. Kee. R. J., Miller, J. A., and Warnatz, J. (1983). *A Fortran Program Package for the Evaluation of Gas-phase Viscosities, Conductivities, and Diffusion Coeffi-*

cients. Rept. SAND83-8209, Sandia National Laboratories.
15. Leonard, B. P., *Comput. Methods Appl. Mechanics Eng.* 19:59–98 (1979).
16. Spalding, D. B., *Int. J. Num. Meth. Mech. Eng.* 4:551 (1972).
17. Katta, V. R., Goss, L. P., and Roquemore, W. M., *Combust. Flame* 96:60–74 (1994).
18. Takahashi, F., and Katta, V. R., *AIAA J. Propulsion Power* 11 (1995).
19. Aggarwal, S. K., Park, T. W., and Katta, V. R., *Combust. Sci. Technol.* 113:429–438 (1996).
20. Patadia, H. (1995). M.S. thesis, University of Illinois at Chicago.
21. Peters, N., in *Reduced Kinetic Mechanisms for Applications in Combustion Systems, Lecture Notes in Physics* (N. Peters and B. Rogg, Eds.), Springer-Verlag, Vol. 15, 1993, pp. 3–14.
22. Pearse, R. W. B., and Gaydon, A. G., *The Identification of Molecular Spectra*, 4th ed., Chapman and Hall, London, 1976, p. 83.
23. Beyler, C. L., and Gouldin, F. C., *Eighteenth Symposium (International) on Combustion*, The Combustion Institute, Pittsburgh, 1981, pp. 1011–1019.
24. Dibble, R. W., Long, M. B., and Masri, A., *Prog. Astronaut. Aeronaut.* 105:99–109 (1986).
25. Brandon, Y., and Samaniego, J.-M., *Combust. Sci. Technol.* 84:81–89 (1992).
26. McManus, K., Yip, B., and Candel, S., *Exptl. Thermal Fluid Sci.* 10:486–502 (1995).
27. Najm, H. N., Paul, P. H., Mueller, C. J., and Wyckoff, P. S., *Combust. Flame* 113:312–332 (1998).
28. Tanoff, M., Smooke, M. D., Osborne, R. J., Brown, T. M., and Pitz, R. W., *Twenty-Sixth Symposium (International) on Combustion*, The Combustion Institute, Pittsburgh, 1996, pp. 1121–1128.
29. Nishioka, M., Nakagawa, S., Ishikawa, Y., and Takeno, T., *Combust. Flame* 98:127–138 (1994).
30. Durox, D., Yuan, T., Baillot, F., and Most, J. M., *Combust. Flame* 102:501–511 (1995).
31. Law, C. K., *Twenty-Second Symposium (International) on Combustion*, The Combustion Institute, Pittsburgh, 1988, pp. 1381–1402.
32. Sivathanu, Y. R., and Faeth, G. M., *Combust. Flame* 82:211–230 (1990).
33. Ronney, P. D., "Combustion Experiments in Space," paper presented at 36th Israel Annual Conference on Aerosciences, Feb. 1996.

Received 23 June 1998; revised 8 October 1998; accepted 26 October 1998

AIAA 99-2781

Stability-Limit Predictions of Methane Jet Diffusion Flames

F. Takahashi
University of Dayton
Dayton, OH

V. R. Katta
Innovative Scientific Solutions, Inc.
2766 Indian Ripple Road
Dayton, OH

35th AIAA/ASME/SAE/ASEE Joint Propulsion Conference and Exhibit
20–24 June 1999
Los Angeles, California

For permission to copy or to republish, contact the American Institute of Aeronautics and Astronautics, 1801 Alexander Bell Drive, Suite 500, Reston, VA, 20191-4344.

AIAA-99-2781

STABILITY-LIMIT PREDICTIONS OF METHANE JET DIFFUSION FLAMES

Fumiaki Takahashi*
University of Dayton Research Institute
300 College Park
Dayton, Ohio 45469

Viswanath R. Katta†
Innovative Scientific Solutions, Inc.
2766 Indian Ripple Road
Dayton, Ohio, 45440

ABSTRACT

An attempt is made to predict the lifting limit of an axisymmetric laminar methane jet diffusion flame. Computations for solving the time-dependent full Navier-Stokes equations with buoyancy were performed using an implicit, third-order accurate numerical scheme and a semi-detailed C_2-chemistry model. The calculated standoff distance of the flame base prior to lifting was comparable to that experimentally observed. As the mean co-flow air velocity was increased at a fixed fuel jet velocity toward a lifting limit, the *reaction kernel* (peak reactivity spot) in the flame base broadened and shifted to a new stabilizing point downstream, where a higher reactivity could be obtained to sustain combustion against a higher incoming flow velocity. The reactivity augmentation is due to a "blowing effect," which caused enhanced convective and diffusive fluxes of oxygen into the reaction kernel, while maintaining the reaction kernel temperature (~1550 K) and equivalence ratio (~0.5) at nearly constant levels. A novel hypothesis for the flame stabilizing mechanism is proposed: that a flame lifts or blows off if the total oxygen flux feeding into the reaction kernel exceeds a limit that the reaction kernel can consume by oxidation reactions.

INTRODUCTION

The stability of diffusion flames has long been a fundamental and practical research subject in combustion [1-13]. Local flame-flow phenomena, including transport processes and chemical reactions around the flame base, control the flame stabilizing mechanism. Therefore, to gain in-depth understanding of the subject, detailed flame-base structure resulting from the transport and reaction processes must be revealed. Unfortunately, previous investigations of the flame-base structure and behavior, including experiments [3, 5, 8] and theories [14-16], generally suffered from the lack of detailed information, particularly on radicals. Diagnostic techniques available to measure various species in a small flame-stabilizing region are limited, and theories generally ignore radical species. As a result of recent advances in computational capabilities and chemistry models, a numerical approach seems most promising to obtain comprehensive information on the flame structure.

In previous papers [17, 18], the chemical kinetic structure of the flame stabilizing region of methane diffusion flames and the role of chemistry models were reported. In this paper, the effect of co-flow air velocity on a near-lifting-limit flame was investigated to reveal the flame stabilizing mechanism.

NUMERICAL METHODS

The numerical code (UNICORN) used in this study was developed by Katta et al. [19] and validated against measurements and flow visualization of various diffusion and premixed flame phenomena; i.e., unsteady characteristics, extinction, and ignition [20, 21]. The code has also been used in numerical experiments on vortex-flame interactions and attachment mechanisms of methane jet diffusion flames [17, 18, 22, 23]. Time-dependent governing equations, expressed in cylindrical coordinates, consist of mass continuity, axial and radial full Navier-Stokes momentum conservation, energy conservation, and species conservation equations with the ideal-gas equation of state. A body-force term caused by the gravitational field is included in the axial momentum equation. The momentum equations are integrated using an implicit QUICKEST numerical scheme [19], which is third-order accurate in both space and time and has a very low numerical-diffusion error. The finite-difference form of the species and enthalpy is obtained using the hybrid scheme with upwind and central differencing. The coefficients of viscosity, thermal conductivity, and

* Research Engineer, Research Institute, Senior Member AIAA
† Senior Research Engineer, Member AIAA
Copyright © 1999 by the authors. Published by the American Institute of Aeronautics and Astronautics, Inc. with permission.

diffusion are estimated using molecular dynamics and mixture rules [24]. The enthalpy of each species is calculated from polynomial curve-fits using the CHEMKIN libraries.

The semi-detailed chemistry model [25] for 24 species and 81 elementary steps is used. The Arrhenius parameters for the reaction $CH_3 + H \rightarrow CH_4$ are replaced with those by Warnatz [26]. Otherwise, the extinction limit of counterflow diffusion flames was predicted at a significantly lower strain rate [27] compared to that determined experimentally by Sung et al. [28], and the jet diffusion flames under consideration prematurely lifted off under conditions below the stability limit obtained experimentally [12].

The computational domain of 150 × 60 mm in the axial (x) × radial (r) directions is represented by a mesh system of up to 371 × 101 with clustered grid lines near the jet exit and a minimum spacing of 0.05 mm. The inner diameter (d = 9.5 mm) and lip thickness (0.25 mm) of the fuel tube are close to those used in the previous experiments [12]. The fuel tube exit plane is placed 10 mm from the inflow boundary. The fully developed pipe flow in the fuel tube and boundary layer velocity profiles outside the burner tube are used. Several cases with various mean co-flow air velocities (U_a) at a constant mean jet velocity (U_j) are simulated to approach the lifting limit [12]. The initial and boundary conditions for the axial (U) and radial (V) velocities and species and energy at different flow boundaries are the same as the previous work [17]. The outer boundaries of the computational domain are shifted sufficiently far enough to minimize the propagation of disturbances into the region of interest. No-slip boundary conditions are enforced along the burner walls. An extrapolation procedure with weighted zero- and first-order terms is used to estimate the flow variables on the outflow boundary.

RESULTS AND DISCUSSION

Figure 1 shows the two-color particle image velocimetry (PIV) photographs of the stabilizing region of near-lifting and lifted methane jet diffusion flames. The burner system and the PIV technique used is described elsewhere [12, 17]. Submicron particles were illuminated by a sheet of green and red pulsed (10 ns) lasers with a known time delay. The high number-density cold airflow, a low number-density hot zone around the flame, and the jet-external dividing streamline were visualized. A time-exposure (1/30 s) image of the blue flame zone was also recorded in the photographs. As the lifting condition approached (Figs. 1a to 1b), the flame base shifted gradually away from the burner rim a few millimeters. The outer cold air was entrained into the fuel jet through the dark space between the flame base and the rim. Thus, the flame base (Fig. 1b) was thermally disconnected from the burner wall, and the effect of heat losses to the burner wall vanished before lifting. After lifting, the flame base was stabilized a few jet diameters downstream. No sign of wings of the triple flame structure [11, 14, 16, 29] was observed at the base of methane diffusion flames as reported by Chung [11].

Figure 2 shows the experimental result [12] of a stability-limit curve and the lift-off height (h_L) at the lifting limit. The critical mean jet velocity at the stability limit decreased monotonously as the mean co-flow air velocity increased, except for low air velocity conditions (U_a < 0.1 m/s) under which the outer air tube (26.9 mm i.d.) blocked free air entrainment. The minimum lift-off height was in the range of 0.2 < U_a < 0.4 m/s.

Figure 3 shows the computational results of the structure of the flame base under a near-lifting condition (U_a = 0.8 m/s and U_j = 1.7 m/s). Figure 3a shows the calculated velocity vectors ($\vec{v}$), isotherms (T), and oxygen mole fraction (X_{O_2}) contours. The flame base resided farther downstream (~10 mm) from the jet exit, compared to the case previously reported (~4 mm) for U_a = 0.72 m/s at the same U_j using the same C_2-chemistry model [18]. The flame base is anchored in a relatively low-velocity wake region formed by the boundary layers along the burner walls. The velocity vectors and the oxygen mole fraction contours show air penetration onto the fuel side of the flame. As a result, a relatively high oxygen concentration zone surrounds the flame base.

Figure 3b shows a close-up view of the flame stabilizing region, including the velocity vectors, isotherms, and heat-release rate ($\dot{q}$) contours. The heat-release rate contours show that the *reaction kernel* (highest reactivity spot) at the flame base was farther broadened outwardly, compared to the lower air velocity case previously studied [18]. The velocity vectors show the lateral expansion of stream tubes as well as the longitudinal acceleration as the flow approached the hot zone around the flame base due to thermal expansion of gases and the pressure field deformation.

Figure 3c shows the calculated total molar flux vectors of methane ($\vec{M}_{CH_4}$) and molecular oxygen ($\vec{M}_{O_2}$), including both diffusion and convection terms, contours of the equivalence ratio (ϕ), and the oxygen consumption rate ($-\omega_{O_2}$). The equivalence ratio was determined from the fuel and oxygen molar fluxes, thus including the dynamic effects of both convection and diffusion. The equivalence ratio based on the fluxes differed from that based on the mole fractions, particularly in the region near the reaction kernel, which is a strong sink of the reactants.

Although the partial premixing of the fuel and oxygen in the dark space progressed further compared to the lower air velocity case [18], the thickness of the mixing layer within the flammability limits (0.5 < ϕ <1.7)

was ~0.8 mm, just below the reaction kernel, which was still less than half the minimum quenching distance of 2.2 mm [1]. Thus, the mixing layer was too narrow for an ordinary premixed flame to propagate through at the laminar burning velocity. More importantly, the reaction kernel was more under fuel-lean conditions and the peak reactivity was obtained at $\phi \approx 0.5$, unlike the ordinary premixed flames that have the maximum burning velocity at $\phi \approx 1$. Therefore, the reaction kernel structure is different from the ordinary premixed flame or the fuel-lean branch of the triple-flame structure [11, 14, 16, 29].

Figure 3d shows the calculated total molar flux vectors of atomic hydrogen ($\bar{M}_H$), the mole fraction of molecular oxygen, and the rate of water vapor production (ω_{H_2O}). Hydrogen atoms diffused downward in every direction into high oxygen concentration region around the reaction kernel, inducing the most important chain branching reaction $H + O_2 \rightarrow OH + O$. Other radical species (OH, O, and CH_3, etc.) also back-diffused against the convective oxidizing flow, reacted with each other and with oxygen, broadened the reaction zone, and increased the global reaction rates even at relatively low temperatures (<1600 K).

Figure 4 shows the effects of the mean air velocity on the reaction kernel coordinates (x_k, y_k) at the heat-release rate peak and axial and radial velocity components (U_k, V_k), including the previous results (C_1-chemistry) [17] as well as the current results (C_2-chemistry). As the mean air velocity was increased, the axial coordinate (standoff distance) of the reaction kernel increased dramatically, while the radial distance maintained nearly constant (Fig. 4a). The C_2-chemistry model resulted in a longer standoff distance as previously reported [18]. The computational results matched very well with the experimental observation of the (visible) flame base location and the lifting limit data (U_a = 0.76 m/s and U_j = 1.7 m/s [12], see Fig. 1). The axial velocity component of the incoming flow into the reaction kernel also increased rapidly, while the magnitude of the radial velocity component approached zero (vertical flow direction) (Fig. 4b). The current C_2-chemistry model results almost perfectly matched the previous C_1-chemistry results.

In the previous paper [17], heuristic correlations valid for both jet- and flat-plate diffusion flames were obtained between the peak heat-release rate, or oxygen consumption rate, and the total velocity at the reaction kernel. The reaction kernel correlations demonstrated that the baseline mechanism responsible for flame stabilization and attachment was identical for both types of diffusion flames. Figure 5 shows the reaction kernel correlation plot, temperature and equivalence ratio, including the points for various U_a at U_j = 1.7 m/s only. Both peak heat-release rate and the oxygen consumption rate increased almost linearly with the magnitude of the velocity at each peak location in the reaction kernel (Fig. 5a). Thus, the reaction kernel shifted to a new stabilizing point downstream, where a higher reactivity could be obtained and withstood a higher incoming flow velocity. The reactivity augmentation was due to increased diffusive and convective oxygen fluxes into the reaction kernel caused by "blowing." As the incoming velocity was increased, the slopes ($\dot{q}/|\vec{v}|$ or $-\omega_{O_2}/|\vec{v}|$) of the curves became somewhat smaller, while the reaction kernel temperatures and equivalence ratios at both $\dot{q}$ and $-\omega_{O_2}$ peaks remained nearly constant in the ranges of 1500-1600 K and 0.5-0.6, respectively (Fig. 5b). Thus, the incoming velocity tended to increase faster than the reactivity increase toward lifting.

CONCLUSIONS

Computations of laminar methane jet diffusion flames revealed the flame structure and behavior of the reaction kernel (highest reactivity [$\dot{q}$, $-\omega_{O_2}$, and ω_{H_2O}] spot) in response to an increase in the co-flow air velocity. The simulated reaction kernel shifted away from the jet exit, matching qualitative and quantitative experimental observations under conditions toward the lifting limit. At a downstream location, the reaction kernel sustained combustion under a higher incoming flow velocity as a result of a higher reactivity, while the reaction kernel temperature (1500– 1600 K) and equivalence ratio (0.5-0.6) remained nearly constant during the shifting. The correlations between the heat-release rate or oxygen consumption rate vs. the total velocity at the reaction kernel indicated that the increasing rate of the incoming flow velocity exceeded that of the reactivity. This new finding leads to a hypothesis that lifting occurs if the fluxes of reactants exceed a limit beyond which the reaction kernel cannot consume them. Consequently, the reaction kernel can no longer find a new stationary stabilizing location downstream, and the trailing flame drifts away downstream, eventually leading to lift or blow-off.

ACKNOWLEDGMENT

This work was supported by the U. S. Air Force Research Laboratory, Propulsion Directorate, Propulsion Sciences and Advanced Concept Division, Wright-Patterson Air Force Base, Ohio, under Contract No. F33615-97-C-2719 (Technical Monitor: C. W. Frayne).

REFERENCES

1. Lewis, B., and von Elbe, G., *Combustion, Flames, and Explosions of Gases,* 2nd ed., Academic Press, New York, 1961.
2. Vranos, A., Taback, E. E., and Shipman, C. W., "An Experimental Study of the Stability of Hydrogen-Air Diffusion Flames," *Combust. Flame* 12: 253 (1968).

3. Robson, K., and Wilson, M. J. G., "The Stability of Laminar Diffusion Flames of Methane," *Combust. Flame* 13: 626 (1969).
4. Takeno, T., and Kotani, Y., "An Experimental Study on the Stability of Jet Diffusion Flames," *Acta Astronaut.* 2: 999 (1975).
5. Kawamura, T., Asato, K., and Mazaki, T., "Structure Analysis of the Stabilizing Region of Plane, Laminar Fuel-jet Flames," *Combust. Sci. Technol.* 22: 211 (1980).
6. Takahashi, F., Mizomoto, M., Ikai, S., Futaki, N., "Lifting Mechanism of Free Jet Diffusion Flames," *Twentieth Symposium (International) on Combustion*, The Combustion Institute, 1985, pp. 295-302.
7. Eickoff, H., Lenze, B., and Leuckel, W., "Experimental Investigation on the Stabilization Mechanism of Jet Diffusion Flames," *Twentieth Symposium (International) on Combustion*, The Combustion Institute, 1985, pp. 311-318.
8. Takahashi, F., Mizomoto, M., and Ikai, S., "Structure of the Stabilizing Region of a Laminar Jet Diffusion Flame," *J. Heat Transfer* 110: 182 (1988).
9. Gollahalli, S. R., Savas, Ö., and Huang, R. F., and Rodriquez Azara, J. L., "Structure of Attached and Lifted Gas Jet Flames, in Hysteresis Region," *Twenty-First Symposium (International) on Combustion*, The Combustion Institute, 1988, pp. 1463-1471.
10. Coats, C. M., and Zhao, H., "Transition and Stability of Turbulent Jet Diffusion Flames," *Twenty-Second Symposium (International) on Combustion*, The Combustion Institute, 1989, pp. 685-692.
11. Chung, S. H. and Lee, B. J., "On the Characteristics of Laminar Lifted Flames in a Nonpremixed Jet," *Combust. Flame* 86: 62, (1991).
12. Takahashi, F., and Schmoll, W. J., "Lifting Criteria of Jet Diffusion Flames," *Twenty-Third Symposium (International) on Combustion*, The Combustion Institute, 1991, pp. 677-683.
13. Takahashi, F., Durbin, M. D., and Vangsness, M. D., "Stabilization of Hydrogen Jet Diffusion Flames With or Without Swirl," *Transport Phenomena in Combustion* (S. H. Chan, ed.), Vol. 1, Taylor & Francis, Washington, D. C., 1996, pp. 593-604.
14. Veynante, D., Vervisch, L., Poinsot, T., Liñán, A., and Ruetsch, G., "Triple Flame Structure and Diffusion Flame Stabilization," Proceedings of the Summer Program, Center for Turbulence Research, Stanford University, Palo Alto, California, 1994, pp. 55-73.
15. Buckmaster, J. and Weber, R., "Edge-flame Holding," *Twenty-Sixth Symposium (International) on Combustion*, The Combustion Institute, Pittsburgh, 1996, pp. 1143-1149.
16. Wichman, I. S. and Ramadan, B., "Theory of Attached and Lifted Diffusion Flames," *Physics of Fluids* 10: 3145-3154 (1998).
17. Takahashi, F. and Katta, V. R., "Attachment Mechanisms of Diffusion Flames," *Twenty-Seventh Symposium (International) on Combustion*, The Combustion Institute, Pittsburgh, 1998, pp. 675-684.
18. Takahashi, F. and Katta, V. R., "A Role of Chemical Kinetics in the Simulation of the Reaction Kernel of Methane Jet Diffusion Flames," Proc. 5th ASME/JSME Joint Thermal Engineering Conference, San Diego, Paper No. AJTE99-6190, 1999.
19. Katta, V. R., Goss, L. P., and Roquemore, W. M., "Numerical Investigations of Transitional H_2/N_2 Jet Diffusion Flames," *AIAA J.* 32: 84 (1994).
20. Katta, V. R. and Roquemore, W. M., "Simulation of Dynamic Methane Jet Diffusion Flames Using Finite Rate Chemistry Models," *AIAA J.* 36: 2044 (1996).
21. Roquemore, W. M., and Katta, V. R., "Role of Flow Visualization in the Development of UNICORN," *Proceedings of VSJ-SPIE98*, Yokohama, Japan, Paper No. KL310, 1998.
22. Takahashi, F. and Katta, V. R., "Numerical Experiments on the Vortex-flame Interactions in Jet Diffusion Flames," *J. Propulsion Power* 11: 170 (1995).
23. Takahashi, F. and Katta, V. R., "Unsteady Extinction Mechanisms of Diffusion Flames," *Twenty-Sixth Symposium (International) on Combustion*, The Combustion Institute, Pittsburgh, 1996, pp. 1151-1160.
24. Hirschfelder, J. O., Curtis, C. F., and Bird, R. B., *The Molecular Theory of Gases and Liquids*, Wiley, New York, 1954.
25. Peters, N., "Flame Calculations With Reduced Mechanisms—An Outline," *Reduced Kinetic Mechanisms for Applications in Combustion Systems* (N. Peters and B. Rogg, Eds.), Springer-Verlag, Berlin, 1993, pp. 3-14.
26. Warnatz, J., "Rate Coefficients in the C/H/O System," *Combustion Chemistry* (W. C. Gardiner, Ed.), Springer-Verlag, New York, 1984, p. 197-360.
27. Katta, V. R. and Roquemore, W. M., "Extinction in Methane-Air Counterflow Diffusion Flame—a Direct Numerical Study," Central States/The Combustion Institute Meeting, St. Louis, Paper No. 80, 1996, pp. 449-454.
28. Sung, C. J., Liu, J. B., and Law, C. K., "Structural Response of Counterflow Diffusion Flames to Strain Rate Variations," *Combust. Flame* 102: 481 (1995).
29. Plessing, T., Terhoeven, P., Peters, N., and Mansour, M. S., "An Experimental and Numerical Study on a Laminar Triple Flame," *Combust. Flame* 115: 335 (1998).

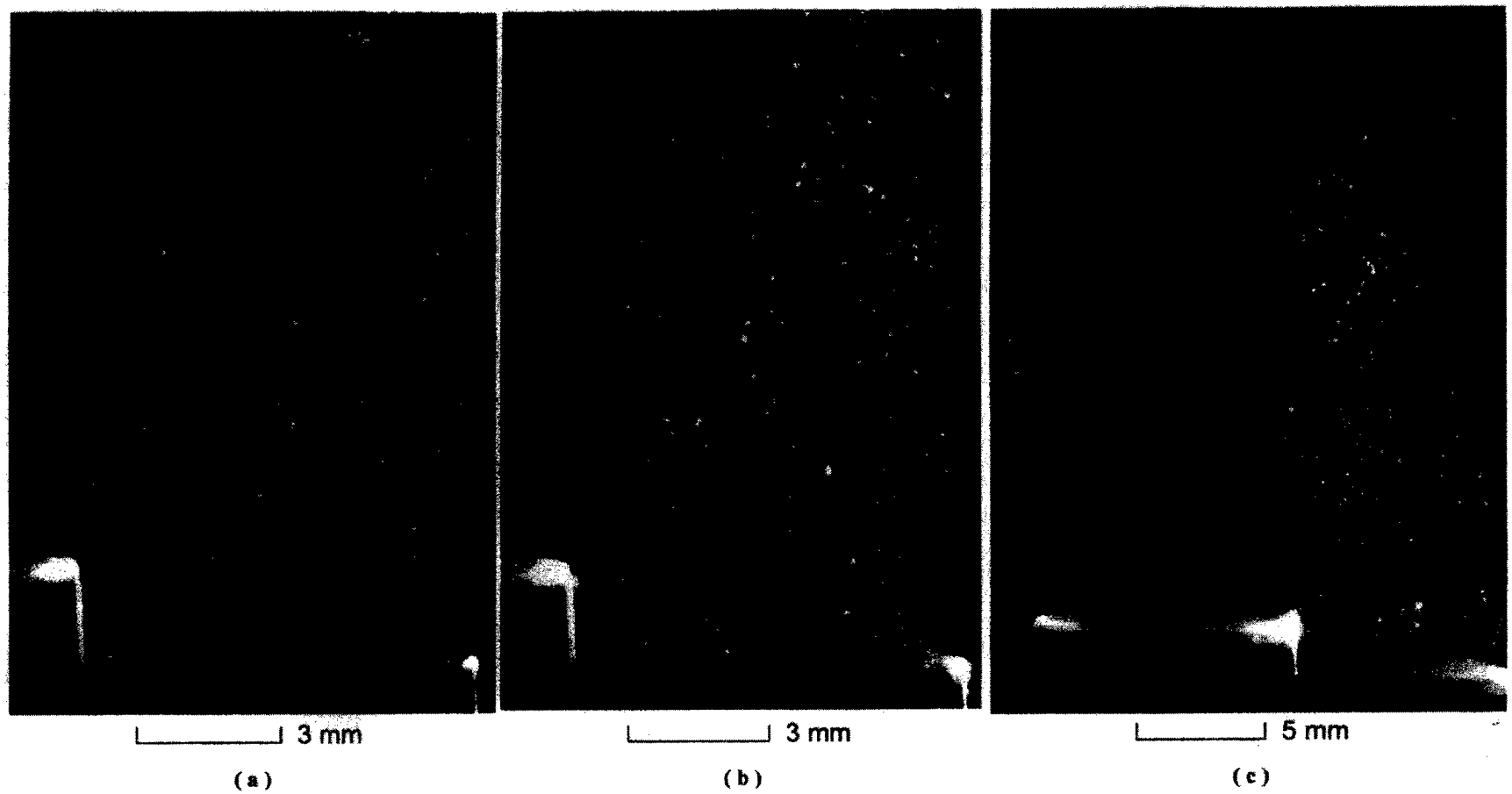

Fig. 1 Two-color particle image velocimetry photographs of the stabilizing region of methane jet diffusion flames. d = 9.45 mm. Laser intensity: ~20 mJ/pulse; pulse width: 10 ns; time delay: 70 μs; and sheet thickness: ~0.5 mm. Exposure time: 1/30 s. Seed particles: zirconia (<1 μm, 97 %). U_a = 0.36 m/s. (a) U_j = 6.7 m/s, (b) U_j = 7.5 m/s, (c) U_j = 7.6 m/s.

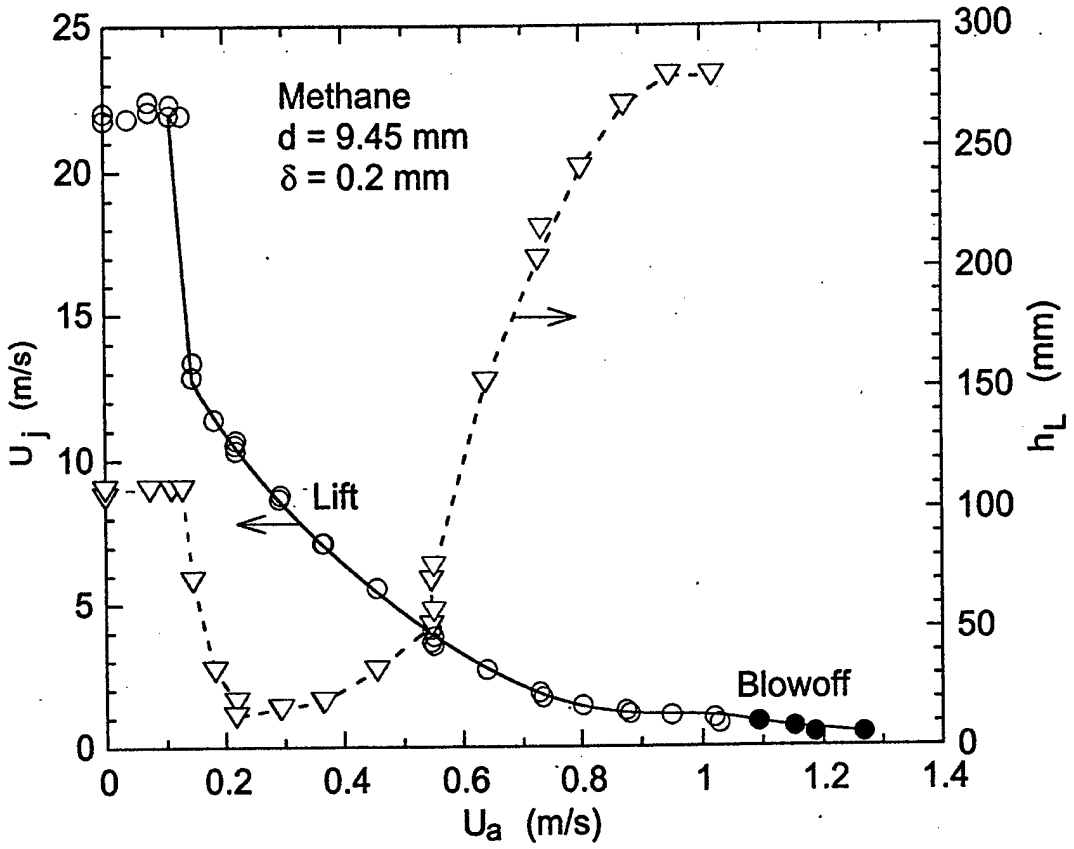

Fig. 2 Experimental stability limit and lift-off height [12].

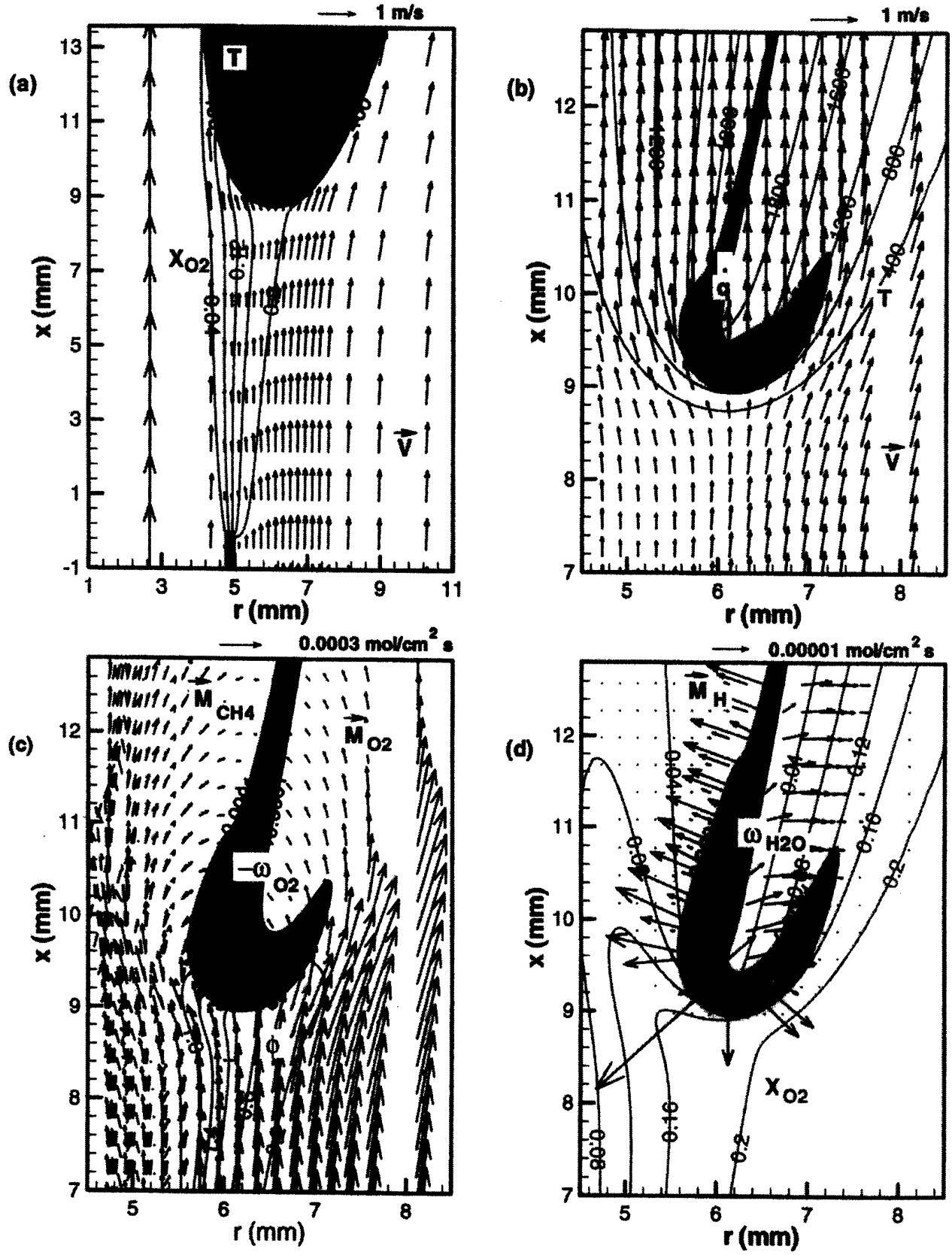

Fig. 3. Distributions of several computed variables in the stabilizing region of a near-lift-off methane jet diffusion flame. (a) Temperature, oxygen concentration and velocity field, (b) temperature, heat release rate and velocity field, (c) molar flux vectors of methane and oxygen, oxygen consumption rate and equivalence ratio based on fuel and oxygen fluxes, and (d) production rate of water vapor, oxygen concentration and molar flux vectors of atomic hydrogen

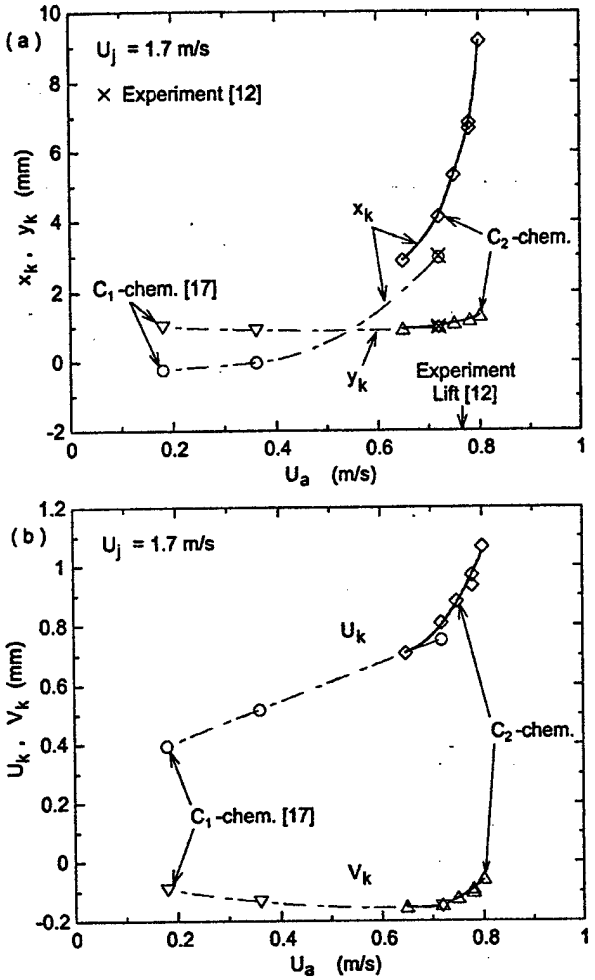

Fig. 4 Effects of the mean co-flow air velocity on (a) the reaction kernel coordinates (q_k peak) and (b) axial and radial velocity components.

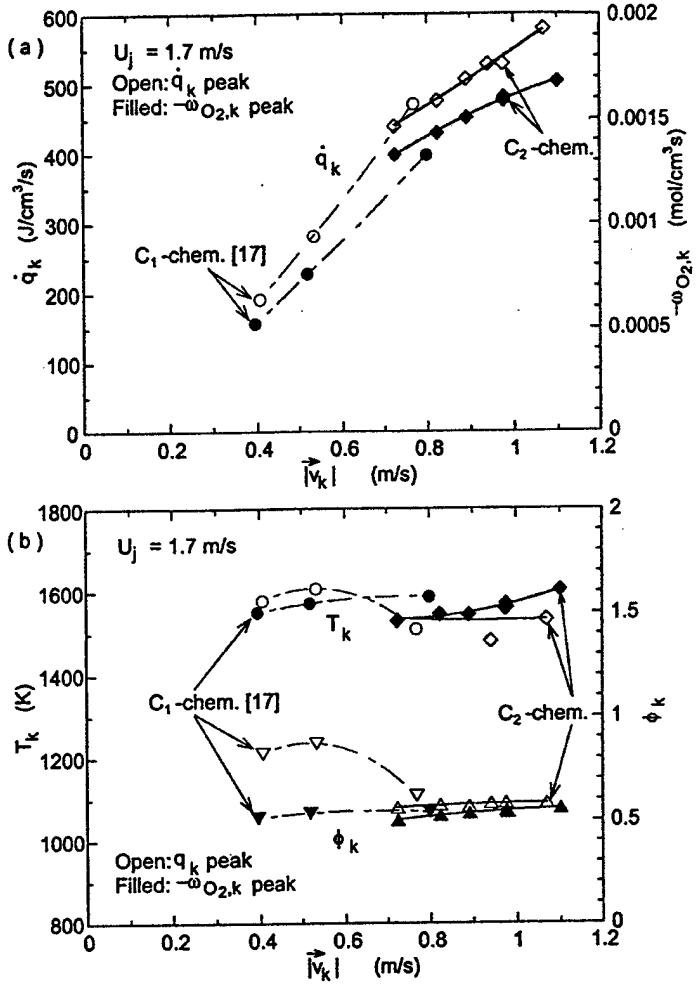

Fig. 5 (a) Reaction kernel correlations between the heat-release rate or oxygen consumption rate and the incoming velocity, (b) the reaction kernel temperature and equivalence ratio.

©2000 The Visualization Society of Japan and Ohmsha, Ltd.
Journal of Visualization, Vol. 2, Nos. 3/4 (2000) 257-272
PUBLISHED WITH PERMISSION

Role of Flow Visualization in the Development of UNICORN

Roquemore, W. M.*[1] and Katta, V. R.*[2]

*[1] Air Force Research Laboratory, Wright-Patterson Air Force Base, OH 45433-7103, USA.
*[2] Innovative Scientific Solutions, Inc., 2766 Indian Ripple Road, Dayton, OH 45440-3638, USA.

Received 6 April 1999.
Revised 20 September 1999.

Abstract: This paper describes how visualizations have been used in the development and evaluation of a reacting-flow-simulation model known as UNICORN (UNsteady Ignition and COmbustion with ReactioNs). UNICORN, which solves full Navier-Stokes equations, has evolved over a 6-year period and is perhaps one of the most thoroughly evaluated codes of its kind. It evolved hand-in-hand with experiments that have been conducted to test its ability to predict ignition, extinction, and the dynamic characteristics of diffusion and premixed flames of hydrogen, methane, and propane fuels and that are stabilized in different ways. This paper also describes how UNICORN has been used, in conjunction with experiments, to provide new insights into combusting flows. Also, predictions of unobserved phenomena that were later confirmed by experiments are described. This paper demonstrates that the judicious use of a well-validated simulation in conjunction with laser based diagnostics is an effective way of understanding complex combusting flows.

Keywords: vortices, visualization, flames, combustion, laser diagnostics, turbulence.

1. Introduction

Studies of jet diffusion flames are important in understanding combustion phenomena, developing theories of combusting processes, and developing and evaluating design codes for practical combustion systems. Because of this, jet flames have been actively investigated since the classic works of Hottel et al. (1949). Considerable data on statistical quantities such as time-averaged and root mean squared (rms) values of velocity, temperature, and species concentrations have been obtained with single point measurement techniques. These data have formed the bases for understanding many of the processes occurring in jet diffusion flames. However, such understanding has limited applications for engineering problems because of the time-averaged description of the underlying unsteady combustion processes. In many cases, the mean and fluctuating quantities can mask the physics and chemistry that are germane to an understanding of the fundamental processes that give rise to the statistical results. This is particularly true for laminar and near-transitional jet flames in which the large-scale, low-frequency (0-40 Hz), organized, and absolutely unstable buoyancy-induced vortices on the air side of the flame and medium-frequency (100-1000 Hz), Kelvin-Helmholtz-type vortex structures on the fuel side of the flame dominate the flame characteristics. For example, high-speed visualizations of a buoyant jet diffusion flame have revealed that the flame surface is actually wrinkled as a result of the interaction of vortices, while time-averaged visualizations indicate a smooth surface. To gain insight into these low- and medium-frequency dynamic processes, it is helpful – and, perhaps, essential – to think in terms of the time-dependent characteristics of jet flames.

Several numerical investigations made in the past for dynamic jet flames using conserved-scalar approach, global-chemistry and detailed chemistry models have revealed important aspects of combustion such as effect of

heat-release rate (Ellzey et al., 1989; Yamashita et al., 1990), role of buoyancy (Davis et al., 1991; Katta and Roquemore, 1993; Patnaik and Kailasanath, 1994), enhancement of soot formation (Kaplan et al., 1996), and Lewis-number effects (Katta et al., 1994a; Takagi and Xu, 1994 ; Takagi et al., 1996). However, most of these studies, involving finite-rate chemistry, are limited to hydrogen fuel as the kinetic models for this fuel are relatively simple. Because of the complex nature of the reaction mechanisms, flame calculations for hydrocarbon fuels are restricted to either steady-state problems or chemically lazy flames in which chemistry is not important. Simulation of dynamic hydrocarbon flames with sufficiently accurate models for physical and chemical processes is required for understanding ignition, blow-out, instabilities, and emissions.

The authors have been developing a time-accurate CFDC (computational Fluid Dynamics with Chemistry) code (Katta et al., 1994a, 1994b, 1994c) known as UNICORN (UNsteady Ignition and COmbustion with ReactioNs) for the past six years. UNICORN is continuing to be developed as a research tool to better understand the dynamic characteristics of flames and as a future design tool for combustion systems. From its conception, the development of UNICORN has been strongly coupled with experiments that are designed: to evaluate the chemistry and transport models used in the code and to challenge its ability to predict complex dynamic characteristics of combusting flows. Because of the strong coupling with experiments, UNICORN is perhaps one of the most thoroughly evaluated Navier-Stokes based codes that have been developed. Visualizations have been used extensively in the development of UNICORN and in providing insights into the different combusting flows that have been studied. A simple view of the approach used to develop UNICORN is illustrated by the flame visualization in Fig. 1. The idea was to start the development of UNICORN by trying to predict the steady and dynamic characteristics of simple laminar like flames such as illustrated in Fig. 1(a), and then progress in a methodical way to the more complex flames illustrated in Figs. 1(b) and 1(c). This approach has proven to be extremely useful in systematically identifying and correcting deficiencies in the models used in UNICORN. It has also been demonstrated the power of using computations and experiments in concert to better understand both diffusion and premixed combustion flows. Indeed, UNICORN has evolved to the point where it has correctly predicted unknown combustion phenomena that were later confirmed experimentally. This paper illustrates the role of visualizations in the development of UNICORN and describes some of the insights into combustion processes that have resulted from the combined use of experimental and computational visualization methods.

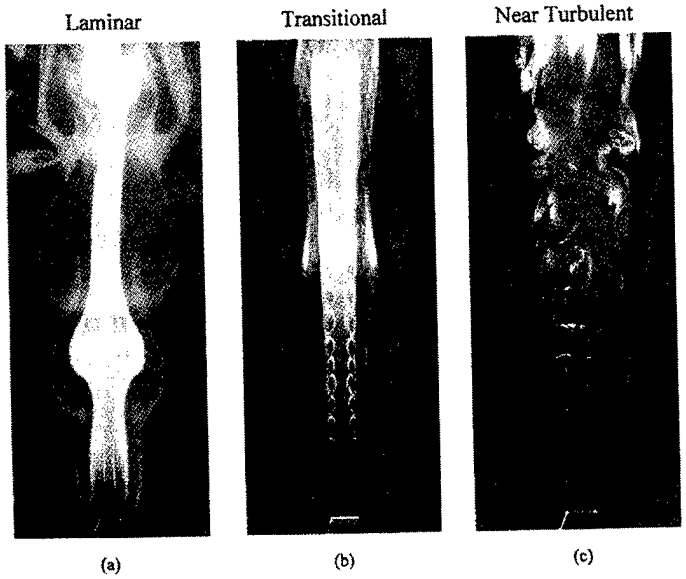

Fig. 1. Vertically mounted jet diffusion flame for different jet velocity conditions: (a) low-speed, laminar flame; (b) medium-speed, transitional flame; (c) high-speed, turbulent flame.

2. Model Description

UNICORN is a time-dependent, axisymmetric mathematical model that solves for axial- and radial-momentum equations, continuity, and enthalpy- and species-conservation equations to simulate a variety of dynamic jet flames. The governing equations, written in the cylindrical-coordinate system, are as follows:

$$\frac{\partial \rho}{\partial t}+\frac{\partial \rho u}{\partial z}+\frac{1}{r}\frac{\partial (r\rho v)}{\partial r}=0 \tag{1}$$

and

$$\frac{\partial (\rho \Phi)}{\partial t}+\frac{\partial (\rho u \Phi)}{\partial z}+\frac{1}{r}\frac{\partial (r\rho v \Phi)}{\partial r}=\frac{\partial}{\partial z}\left[\Gamma^{\Phi}\frac{\partial \Phi}{\partial z}\right]+\frac{1}{r}\frac{\partial}{\partial r}\left[r\Gamma^{\Phi}\frac{\partial \Phi}{\partial r}\right]+S^{\Phi} \tag{2}$$

Table 1. Transport coefficients and source terms appearing in governing equations.

Φ	Γ^{Φ}	S^{Φ}
u	μ	$-\frac{\partial p}{\partial z}+(\rho_0-\rho)g+\frac{\partial}{\partial z}\left(\mu\frac{\partial u}{\partial z}\right)+\frac{\partial}{\partial r}\left(\mu\frac{\partial v}{\partial z}\right)+\frac{\mu}{r}\frac{\partial v}{\partial z}$ $-\frac{2}{3}\left\{\frac{\partial}{\partial z}\left(\mu\frac{\partial u}{\partial z}\right)+\frac{\partial}{\partial z}\left(\mu\frac{\partial v}{\partial r}\right)\right\}+\frac{\partial}{\partial z}\left(\mu\frac{v}{r}\right)$
v	μ	$-\frac{\partial p}{\partial r}+\frac{\partial}{\partial z}\left(\mu\frac{\partial u}{\partial r}\right)+\frac{\partial}{\partial r}\left(\mu\frac{\partial v}{\partial r}\right)+\frac{\mu}{r}\frac{\partial v}{\partial r}-2\mu\frac{v}{r^2}$ $-\frac{2}{3}\left\{\frac{\partial}{\partial z}\left(\mu\frac{\partial u}{\partial z}\right)+\frac{\partial}{\partial z}\left(\mu\frac{\partial v}{\partial r}\right)\right\}+\frac{\partial}{\partial r}\left(\mu\frac{v}{r}\right)$
Y_i $(i=1\sim N_s-1)$	ρD_{im}	$\dot{\omega}_i$
H	$\frac{\lambda}{c_p}$	$\nabla\left[\frac{\lambda}{C_p}\sum_1^{N_s}\left\{\left(Le^{-1}-1\right)H_i\nabla Y_i\right\}\right]-\sum_1^{N_s}\left(h_{fi}^0\dot{\omega}_i\right)$

Here ρ represents density; u and v are the axial and radial components of the velocity vector, respectively; and p is pressure. The general form of Eq. 2 represents the momentum, the species, or the energy-conservation equation, depending on the variable used in place of Φ. In Table 1, the transport coefficients Γ^{Φ} and the source terms S^{Φ} that appear in the governing equations are given. The body-force term due to the gravitational field is included in the axial-momentum equation. Here μ, λ, and c_p are the viscosity, thermal conductivity, and specific heat of the mixture, respectively; Y_i is the mass fraction; H_i is the enthalpy; h_{fi}^0 is the heat of formation at standard state (temperature T_0); and ω_i is the mass-production rate of the i^{th} species; ρ_0 is the density of air; and g is the gravitational acceleration. The transport property D_{im} is the effective diffusion coefficient of the i^{th} species, which is calculated from the binary diffusion coefficients between that species and the other individual species. Finally, Le_i is the Lewis number of the i^{th} species, which is defined as

$$Le_i \equiv \frac{\lambda}{\rho D_{im} c_p}. \tag{3}$$

The set of expressions given by Eqs. 1 and 2 can be completed using the global-species-conservation equation

$$Y_{N_s}=1.0-\sum_i^{N_s-1} Y_i \tag{4}$$

and the state equation

$$p=\rho T R_0 \sum_1^N \left(\frac{Y_i}{M_i}\right) \tag{5}$$

where R_0 is the universal gas constant; T is the temperature; and Y_i and M_i are the mass fraction and molecular weight of the i^{th} species, respectively. While density is obtained by solving the state Eq. 5, the pressure field at every time step is determined from pressure Poisson equations. Even though the governing equations are solved in an uncoupled manner, the species-conservation equations are coupled through the source terms during the solution process to improve the stability of the algorithm. Such coupling is essential in finite-rate-chemistry calculations since the high-reaction-rate terms make the species-conservation equations quite stiff. Temperature- and species-dependent thermodynamic and transport properties are used in this formulation.

The governing equations for u and v momentum are integrated using an implicit QUICKEST (Quadratic Upstream Interpolation for Convective Kinematics with Estimated Streaming Terms) numerical scheme (Katta et al., 1994b; Leonard, 1979), which is third-order accurate in both space and time and has a very low numerical-diffusion error. On the other hand, the finite-difference forms of the species and enthalpy equations are obtained using the hybrid scheme (Spalding, 1972) with upwind and central differencing. An orthogonal, staggered-grid system with rapidly expanding cell sizes in both the z and the r directions is utilized for discretizing the governing equations. After rearrangement of terms, the finite-difference form of the governing equation for the variable Φ at a grid point P can be written as an algebraic equation as follows:

$$A_P\Phi_P^{N+1} + A_{z^{++}}\Phi_{z^{++}}^{N+1} + A_{z^+}\Phi_{z^+}^{N+1} + A_{z^-}\Phi_{z^-}^{N+1} + A_{z^{--}}\Phi_{z^{--}}^{N+1} + A_{r^{++}}\Phi_{r^{++}}^{N+1} + A_{r^+}\Phi_{r^+}^{N+1} + A_{r^-}\Phi_{r^-}^{N+1} + A_{r^{--}}\Phi_{r^{--}}^{N+1} = S_P^{\Phi} + \Delta t.\rho_P\Phi_P^N \quad (6)$$

The time increment, Δt, is determined from the stability constraint and maintained as a constant during the entire calculation. The superscripts N and N+1 represent the known variables at the N^{th} time step and the unknown variables at the $(N+1)^{th}$ time step, respectively; the subscripts z^+ and z^- indicate the values at the grid points immediately adjacent to point P in the positive and negative z-directions, respectively. Similarly, the subscripts z^{++} and z^{--} represent the values at two grid points from P in the respective directions. The coefficients A and the terms on the right-hand side of the above equations are calculated from the known flow variables at the N^{th} time step. The above equations for N+2 variables are solved individually using an iterative ADI (Alternative Direction Implicit) technique. The pressure field, at every time step, is accurately calculated by simultaneously solving the system of algebraic pressure Poisson equations at all grid points using the LU (Lower-Upper) decomposition technique.

The enthalpies of all the species are calculated from the polynomial curve fits developed for the temperature range 300-5000K. Physical properties such as viscosity, thermal conductivity, and the binary molecular diffusion coefficients of the species are calculated using molecular dynamics. Mixture viscosity and thermal conductivity are then estimated using the Wilke and the Kee expressions (Hirschfelder, 1954), respectively. Molecular diffusion is assumed to be of the binary type, and the diffusion velocity of a species is calculated according to Fick's law and using the effective-diffusion coefficient (Williams, 1985) of that species. The Lennard Jones potentials, the effective temperatures, and the coefficients for the enthalpy polynomials for each species are obtained from the CHEMKIN libraries.

3. Results and Discussion

Many chemistry models have been used in the evolution of UNICORN, starting with a one step global model for hydrocarbon fuels and progressing to complete chemistry for hydrogen to near complete chemistry for propane. These models were used in studying different aspects of steady and unsteady flames. Some of these results are discussed in the following sections.

3.1 Flame-base Structure

Predictions of the attachment region of jet flames are a significant challenge for CFD based codes. The reason is that near the stability limit of these flames, the calculations are strongly dependent on the accuracy of various mathematical models incorporated into the code. Even though, the exact mechanisms that govern the stability of a diffusion flame are less understood, it is generally believed that flow field, chemistry and heat and mass transfer are important for the simulation of flames near the stability limit. UNICORN has been used to investigate the stability phenomenon by simulating three methane jet diffusion flames that were experimentally found to be near the stability limits (Takahashi and Schmoll, 1991). The photographs of the three flames taken by seeding the flow with PIV particles are shown in left halves of Figs. 2(a), 2(b), and 2(c), respectively. The blue region in these

photographs represents the luminous flame, which, in general, will be located within the high-temperature region. The inner diameter and wall thickness of the fuel tube are 9.5 and 0.45 mm, respectively. The flow conditions and the stability statuses for the three flames are listed in Table 2.

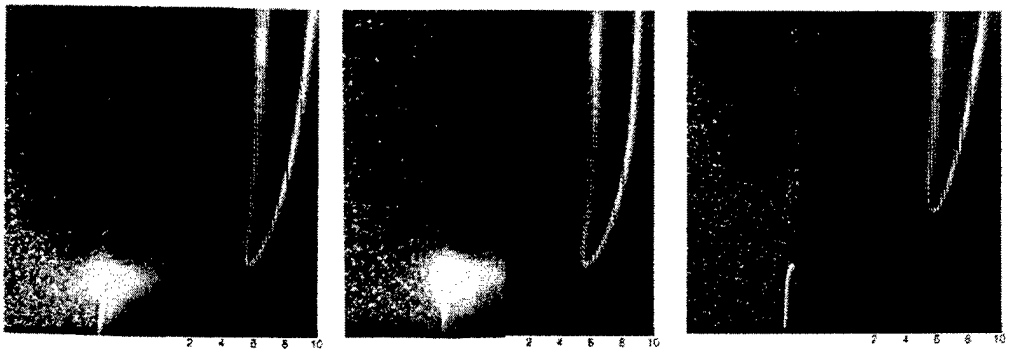

(a) (b) (c)

Fig. 2. Methane jet diffusion flames operating close to stability limits: (a) higher fuel jet and lower annular air velocities—attached flame; (b) medium fuel and air jets—attached flame; (c) lower fuel jet and higher annular air velocities—separated flame.

Table 2. Flow conditions used for the flame stability studies.

Flame No.	U_j (m/s)	U_a (m/s)	Stability
1	11.5	0.19	attached
2	6.9	0.36	attached
3	1.7	0.72	separated

Calculations for the three methane flames in Table 1 were made using Peters 17-species and 52-reaction model (Peters, 1993). The fully developed pipe flow and boundary-layer velocity profiles were used inside and outside the fuel tube, respectively. Results in the form of velocity vectors superimposed over the temperature field are shown on the right halves of the quantitative visualizations in Figs. 2(a), 2(b), and 2(c). A comparison of experimental and simulated flame visualizations in Fig. 2 suggest that the code is able to reproduce the stability phenomenon of diffusion flames. Calculations have resulted in attached flames for the cases 1 and 2 and a 3-mm separated flame for case 3. After obtaining this general agreement between experiments and calculations, the flow and chemistry data associated with the simulations is further analyzed to understand the mechanisms responsible for stabilizing diffusion flames and the results are published recently (Takahashi and Katta, 1997; Takahashi et al., 1998).

3.2 Unsteady Laminar Flames

UNICORN was developed for the purpose of accurately predicting the dynamics characteristic of unsteady combustion flows. The ability of UNICORN to predict unsteady combustion processes has been tested by conducting experimental/numerical investigations on various dynamic flames. Extensive experimental studies have been performed on buoyant, laminar jet flames that tend to oscillate at a stable frequency. An example of such flames is the hydrogen/air buoyant jet diffusion flame studied by Vilimpoc and Goss (1988). The time-accuracy of results obtained with UNICORN was investigated by simulating this flame. The fuel used was a mixture of hydrogen and nitrogen in a volumetric ratio of 3.5 to 1. The flame was stabilized on a contoured nozzle having an exit diameter of 10 mm. The fuel jet was mounted vertically and had a mass averaged exit velocity of 3.55 m/s. The flame was surrounded by a 150-mm-diameter co-annular air jet having a velocity of 35 cm/s which helped to shield the central jet flame from room-air disturbances. An instantaneous image of the experimental flame visualized by the Reactive-Mie-Scattering technique (Roquemore et al., 1989) is shown in Fig. 3(a). At this low jet velocity, the shear layer is laminar in nature, and no shear-layer instabilities have developed. Three outside large-scale structures are clearly visible, even though the third one at the top is somewhat smeared by the room air.

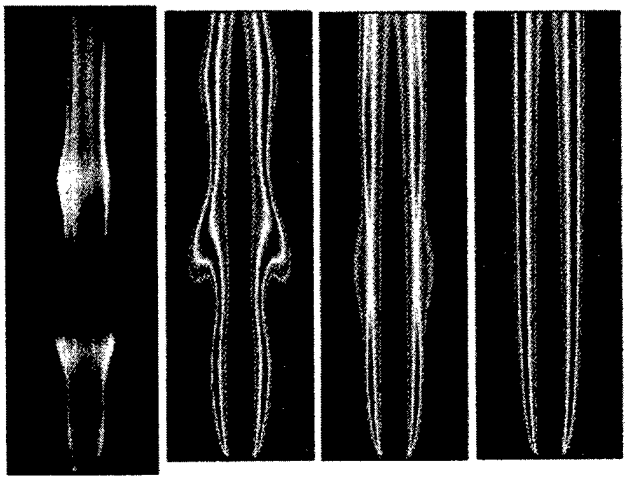

Fig. 3. Comparison of experimental and computed hydrogen/air flames for fuel-jet velocity of 3.26 m/s: (a) Reactive-Mie-Scattering image of experimental flame; (b) instantaneous temperature contours of computed flame; (c) iso-temperature contours obtained from time-averaged flame; (d) iso-temperature contours of steady-state flame.

Calculations were performed using a chemical-kinetics model consists of 8 species and 26 reactions (Katta et al., 1994a). An instantaneous iso-temperature color visualization of the computed flame is shown in Fig. 3(b) at a phase very near that of the experimental image in Fig. 3(a). It should be pointed out that no artificial perturbations were introduced to generate these buoyancy-driven structures. Once a vortex is developed it rolls along the flame surface while it is convected downstream. During this process, the vortex interacts strongly with the flame, making the flame surface bulge and squeeze. This motion is simulated by the time-dependent calculations, as observed in animations of the dynamic characteristics of the flame. Freezing of the flame motion, as in Figs. 3(a) and 3(b), shows that the bulging and squeezing of the experimental and computed flame surfaces occur at about the same heights. Excellent agreement was obtained between the calculated and measured flame-flicker frequency. At 80 mm above the nozzle, a 14.8-Hz frequency was obtained from the computed temperature fluctuations, while the frequency was observed to be ~15 Hz in the experiments.

Time averaged data and steady state calculations can provide misleading information about unsteady flames. This is illustrated in the time-average visualization of several instantaneous temperature contours shown in Fig. 3(c). In the averaged view, the second and third buoyant structures have disappeared, but the first structure is still evident as a locally diffused flame. Since the mean temperature reflects the time the flame spends at a given location, the presence of the first bulge indicates that the flame spends considerable time in the bulged position at an axial location between 50 and 100 mm. The isotherms in the interior of the jet ($r < 10$ mm) are only moderately affected by the dynamic motion of the outer structures, as evidenced by the similarity of the instantaneous [Fig. 3(b)] and averaged [Fig. 3(c)] isotherms. To illustrate the importance of simulating the dynamic flames using unsteady CFD code, calculations were also performed for the same flame using the steady-state option of UNICORN. Solution for this case converged to a flame having perfectly smooth surface. The iso-temperature visualization of the resulted flame is shown in Fig. 3(d); which does not resemble either the instantaneous flame [Fig. 3(b)] or time-averaged flame [Fig. 3(c)].

The computed time evolution of temperature as the large outer structures are convected past a fixed radial line 80 mm above the nozzle tip is visualized in Fig. 4. The data shown at $\tau = 150$ ms represent the temperature recorded 150 ms prior to that shown at 0 ms. Bulging and squeezing of the flame due to the convective motion of the outer vortices cause the periodic oscillation in the flame surface and create the elliptical-shaped islands of relatively cold fuel (< 1500K) near the centerline of the jet. The temperature evolution of the experimental flame at the same height ($z = 80$ mm) obtained using Thin-Filament-Pyrometry technique (Goss et al., 1989) compares well with the predictions. The period of oscillation measured from this plot (~65 ms) matches that obtained from the frequency data obtained from experiments.

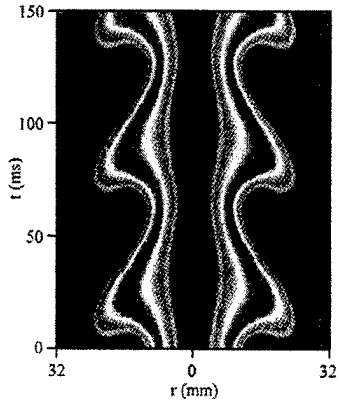

Fig. 4. Predicted temperature evolution of the flame in Fig. 3 at 80 mm above nozzle.

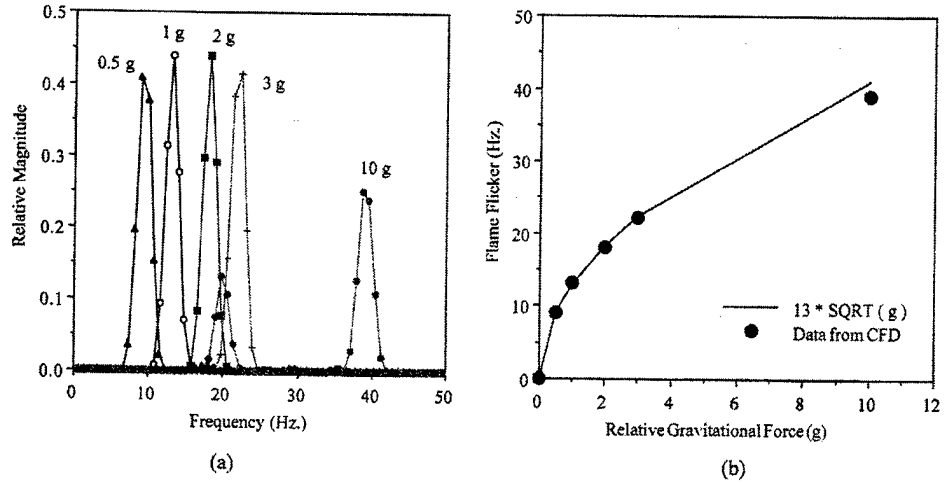

Fig. 5. (a) Frequency spectra obtained from temperature for different gravitational forces; (b) correlation between flicker frequency and gravitational force.

One of the powerful features of simulations is that one can systematically vary parameters that cannot be easily varied in experiments. This is illustrated by a study of the flame similar to that in Fig. 3. A lower air flow of 0.2 m/s is used in this numerical experiment. The gravitational force was varied to determine the effects of buoyancy on the outer structures. Calculations were made with $1/2g^*$, $1g^*$, $2g^*$, $3g^*$ and $10g^*$, where g^* is the earth's gravitational acceleration. As expected, the diameter of the flame decreases and the frequency of oscillation increases with g. The flame oscillation is found to be very periodic up to $3g^*$. At $10g^*$ the oscillations appear to be a combination of two oscillations having different frequencies and magnitudes. Frequency spectra from the temperature fluctuations are obtained using FFT (Fast Fourier Transform) and are shown in Fig. 5(a). The peaks are somewhat broad because of the limited number of samples stored. Nevertheless, each spectrum except that of $10g^*$ case has a single peak, indicating the periodicity of the flow. For the normal-gravity ($1g^*$) case, the frequency for the outer structures is 12.8 Hz. The frequency spectrum for the $10g^*$ case has two distinct peaks. The one at 38 Hz corresponds to the fundamental frequency, and the subharmonic of this (19 Hz.) appears as the second peak. The variation of the flame-flickering frequency with respect to gravitational force is plotted in Fig. 5(b). The data points are well fitted with the following equation:

$$\text{Flickering Frequency} = f^* \sqrt{\frac{g}{g^*}}$$

where f^* represents the flickering frequency for the gravitational acceleration g^* of the earth. Additional calculations at a very low g (= $0.05g^*$) also yielded a frequency that is falling right on top of the curve-fit given by

the above equation. The predicted square-root dependence of the frequency on gravitational acceleration is supported by the recent microgravity experiments of Bahadori et al. (1996).

3.3 Unsteady Transitional Flames

Calculations were made for a transitional hydrogen flame having a fuel jet velocity of 7.64 m/s. The volumetric ratio between the hydrogen and nitrogen in this case was 3.44 to 1. A Reactive-Mie-Scattering image of an instantaneous flame is shown in Fig. 6(a). This flame is highly symmetric, even up to a height of 250 mm (25 diameters) and has well-organized structures both outside and inside the flame surface. As the inner vortices move downstream, they are squeezed radially and elongated axially but still retain their symmetry.

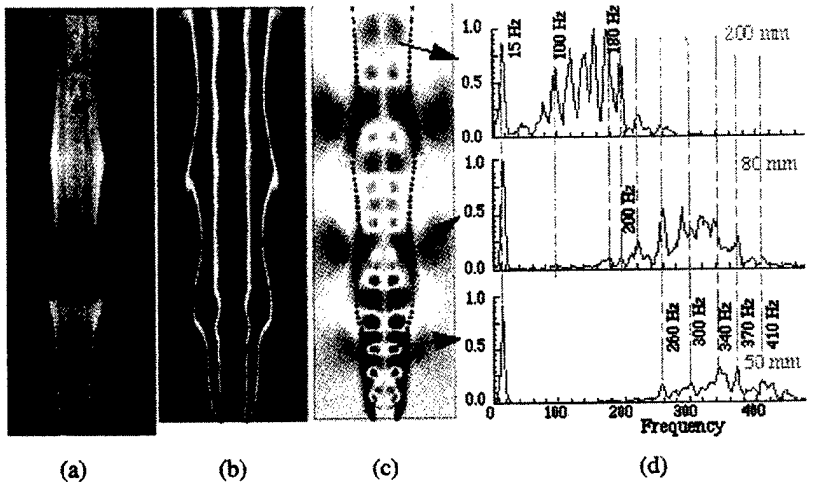

Fig. 6. Visualization of large-scale outer and small-scale inner vortices of 7.64-m/s hydrogen/air flame: (a) experimental flame obtained with Reactive-Mie-Scattering technique; (b) instantaneous iso-temperature contours of computed flame; (c) instantaneous iso-radial velocity map; (d) frequency spectra obtained from temperature data recorded within shear layer at different axial locations.

The computed results in the form of iso-temperature and iso-radial-velocity plots are shown in Figs. 6(b) and 6(c), respectively. In order to generate and sustain the shear-layer instabilities in the calculated flame, random disturbances were introduced at the exit of the fuel-jet. First, a few millimeters above the nozzle, but within the shear layer, a circular zone having a radius of three grid spacings was chosen. At all grid points within this zone, random disturbances of 1% magnitude were introduced to the local axial-velocity component. In the isotherms plot [Fig. 6(b)] and iso-axial velocity plots, the inner vortices appear as wavy lines. On the other hand, these vortices are more evident in the iso-radial-velocity contours of Fig. 6(c). Here, red and blue colors represent positive (outward) and negative (inward) radial velocities, respectively.

A comparison of the calculated flame in Figs. 6(b) and 6(c) with the experimental flame in Fig. 6(a) shows that the simulation provides a good prediction of the structural features of the inner vortices. The numerical model was able to predict the flame-surface location with reasonable accuracy up to a height of ~200 mm above the nozzle. For example, the computed flame diameters at the first three flame bulges from the nozzle are 37, 41, and 42 mm, respectively, as compared to 32, 41, and 41 mm measured from the experimental image. Also, the frequency of the computed inner vortices, as noted by the number of vortices per unit length, is about the same as that in the experiments. The simulation also correctly predicts the unusual spatial development of the vortices as they are convected downstream. Note that in the experiment, Fig. 6(a), the vortices in the shear layer of the jet do not grow radially as they do in cold jets. Instead, the vortices grow axially and become elongated as they are convected downstream. The computed inner vortices in Figs. 6(c) exhibit these same characteristics.

Figure 6(d) shows frequency spectra obtained from temperature data collected at a radial location of 5 mm within the shear-layer at different axial distances from the nozzle exit. The data, stored from 10,000 time-steps, covered a real time of 0.75 s. The calculated spectra compare favorably with those measured by Lee (1992) in a 10-mm-diameter jet diffusion flame. The fuel was hydrogen and nitrogen with a mixture ratio of 3.5 to 1. The exit

velocity at the jet was 7.8 m/s (Lee, 1992). Lee used Fourier transforms to obtain the spectrum from time and spatially resolved temperature measurements using Thin Filament Pyrometry at several heights in the flame. The spectral peaks at a height of 50 mm were compared with those shown in Fig. 6(d) at a height of 50 mm. The measured peak frequency was ~340 Hz, with smaller peaks at ~380, 480, 300, 240, and 15.6 Hz. This compares favorably with the calculated peak frequency of 340 Hz and smaller peaks at ~370, 410, 300, 260, and 15 Hz. Spectra measured at downstream locations showed the same trends as those in Fig. 6(d). That is, the peak frequencies decreased with height. A similar shift from high to low frequency with height in the flame was also observed by Yule et al. (1981) for a 6-m/s methane flame having well-organized inner vortices. From this limited analysis, the simulation appears to predict the spectrum reasonably well, which suggests that it has captured the essential physics of the problem.

Both the inner and outer vortices of the flame shown in Fig. 6 seem to interact with the flame surface by locally squeezing or expanding. During this process the flame temperature could change. However, the degree to which the vortex-flame interaction alters the flame temperature is dependent on the local Lewis number. Similarly, this interaction may also modify the species concentration as a result of the variations in species diffusion coefficients. The interaction of the inner and outer vortices with the flame was studied by plotting radial distribution of temperature at an axial location of 120 mm (Fig. 7). Scattered instantaneous values were obtained over a period of 0.4 s. The average profile is shown by solid line. From the visualization of the temperature-evolution in Fig. 7(a) at this axial location, it was observed that the flame surface oscillates radially between r = 13 and 17 mm. As mentioned previously, the outer vortices are mainly responsible for this oscillation.

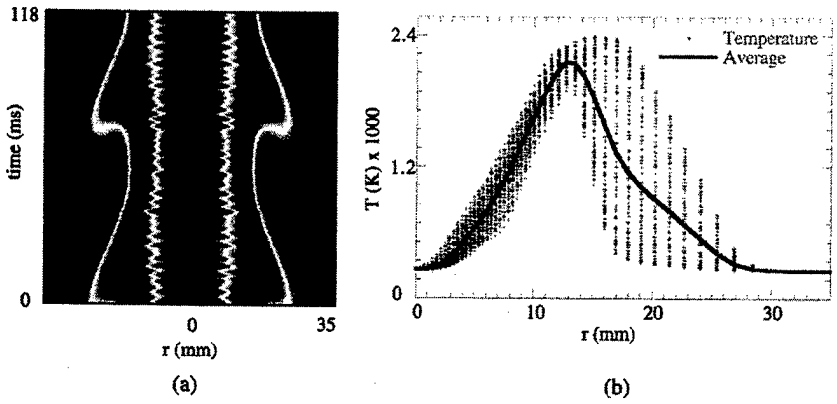

Fig. 7. (a) Predicted temperature evolution; (b) scatter plot of temperature fluctuations of the flame in Fig. 6 at a height of 80 mm above nozzle.

The scatter plot of instantaneous temperatures [Fig. 7(b)] indicates that the flame temperature reaches a maximum value when it is pushed outward radially, i.e., at r = 17 mm. As the flame moves radially inward, the peak temperature gradually decreases; however, a maximum in average temperature occurs near the radially most inward location of the flame. With reference to Fig. 7(a) and the scatter plot in Fig. 7(a), it should be noted that the outer vortices cause more temperature fluctuations outside the flame surface than inside; therefore, the average temperature is lower at r > 13 mm.

3.4 Vortex-flame Interactions

At this point, UNICORN has been thoroughly evaluated using steady, unsteady, and transitional flames. The logical next step in its development is to proceed to turbulent combusting flows. This means adding a subgrid model and three-dimensionality to UNICORN. This is relatively simple process as far as code development goes, however; the price comes from extremely long computational times. We viewed the long computational times as more of an impediment instead of an advancement in the development process. Thus, we started thinking about how we could approach the turbulent problem without making a large sacrifice in computational time. Our approach is to eliminate the statistical nature of turbulence that makes it difficult to study and investigate individual turbulent events that could be created repetitively in the laboratory and studied with a two-dimensional code.

A turbulent flame can be thought of as an ensemble of different individual vortex-flame interactions. A

flame is considered to be fully turbulent, according to Hottel and Hawthorne (1949), when its entire surface area becomes a flame brush, i.e., highly wrinkled, bumpy, and rough. The wrinkles and bumps in the flame are the localized protrusions of the flame surface that result from the interaction of the three-dimensional fluid elements with the reaction zone. Photographs (Fig. 8) taken with high-speed cameras indicate that these interacting fluid elements (insert in Fig. 8) in a turbulent flame are often associated with vortices of different sizes, shapes, and strengths. As seen in the last section there are many interesting, yet not well understood, processes associated with vortex-flame interactions. In this section, we describe the results of computational and experimental studies of vortex-flame interactions starting with naturally developing vortices in buoyant diffusion flames and progressing to driven vortices.

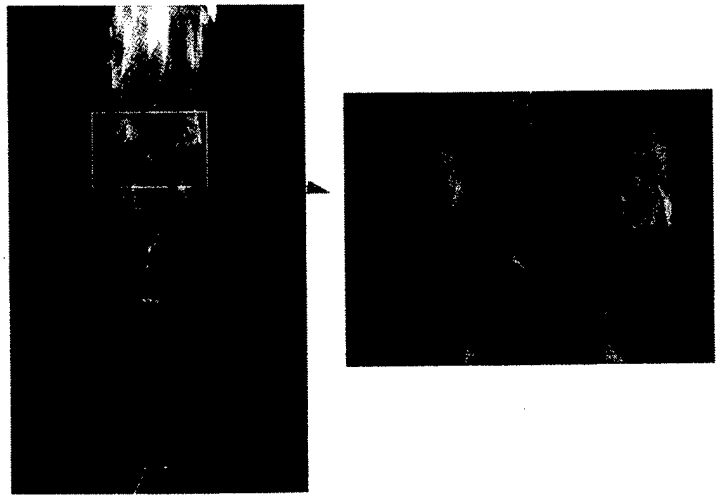

Fig. 8. Near-turbulent jet diffusion flame showing the random vortex-flame-interaction events. Blowup of such an event is shown in the insert.

(1) Naturally Developing Vortices

Studies on various low-speed jet diffusion flames show that the buoyancy generated large-scale vortical structures interact with the flame surface as they are convected downstream. These highly periodic flames provide data for understanding chemical and fluid-dynamic aspects of the vortex interactions with a laminar flame. Recent numerical studies (Katta et al., 1994a; Katta and Roquemore, 1995) on a low-speed buoyant H_2/air jet diffusion flame using UNICORN and finite-rate chemistry with NO-formation reactions have predicted that the local temperature and concentration of NO increase in the compressed regions and decrease in the stretched regions of the flame. Laminar-flamelet theory (Peters and Williams, 1983) suggests that when a diffusion flame is stretched (as in a vortex-flame interaction) the flame temperature decreases due to the increased reactant fluxes. Furthermore, the reduced Damkohler number (ratio of residence time to reaction time), might explain the predicted changes in the stretched regions of the flame, however, it could not explain the temperature changes in the compressed regions of the vortex-flame interaction. The explanation of the change in temperature in the stretched and compressed regions of a flame, as described in detail in Katta and Roquemore (1995), is based on the non-unity value of the local Lewis number and curvature effects. This explanation is qualitatively consistent with the studies of Law (1984). To verify these predictions, two experimental studies have been undertaken, one conducted by Carter et al. (1995) and a second conducted by Grisch et al. (1996). In both experiments, phase-locked measurements of temperature and NO concentrations were made as an outer vortex interacted with a low-speed hydrogen/air jet diffusion flame.

Measured and computed variations in temperature and molar concentration of OH and NO across the flame with time at an axial distance of 80 mm are plotted in Figs. 9(a), 9(b), and 9(c), respectively. Data at elapsed time τ represent the flame as observed at τ ms prior to zero. Measurements are visualized on the left side of each figure and computed results are visualized on the right side. Temperatures were measured using the Thin-Filament-Pyrometry technique (Goss et al., 1989) and OH and NO concentrations were obtained using Laser Induced Fluorescence (Carter et al., 1995). Measurements shown in Fig. 9(a) confirm the predicted increase in temperature

in the compressed region and decrease in temperature in the stretched region. The species OH is confined to a narrow zone and is mostly on the air-side of the flame. Its concentration decreases as the flame is pulled radially outward. Measurements shown in Fig. 9(c) also confirm that a large fraction of the NO is produced during the vortex-flame interaction and on the air-side of the high-temperature surface. Entrainment of NO into the air-side vortex indicates the longevity of the NO molecules. In contrast to the behavior of OH, NO production becomes maximum when the flame is bulging outward (compressed).

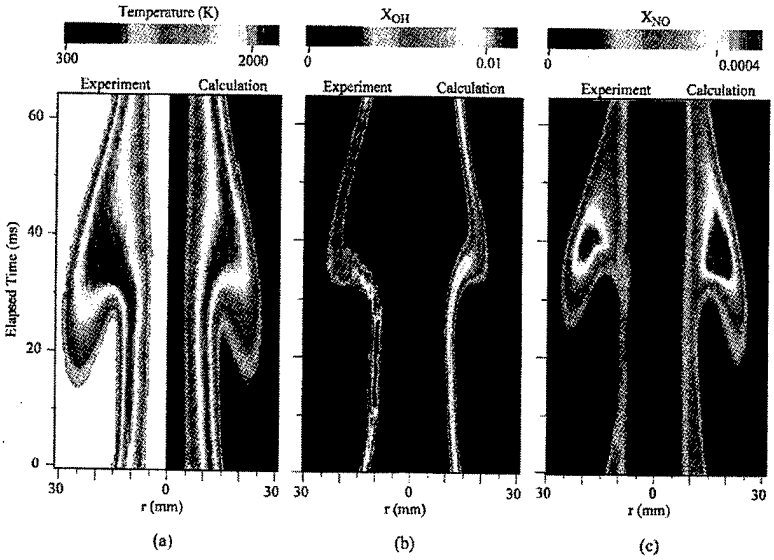

Fig. 9. Evolution of (a) temperature, (b) OH concentration, and (c) NO concentration of dynamic flame shown in Fig. 3 at axial location of 80 mm from nozzle exit. Data at any given elapsed time, *t*, represents that the observer might have seen *t* ms prior to 0. Contour table for each plot is given at the top. In each figure measurements are shown on the left and predictions on the right.

In the second experiment, Grisch et al. (1996) have measured temperatures and NO-concentrations using CARS and Degenerative-Four-Wave-Mixing techniques, respectively. Measurements were made on a similar flame that had a slightly smaller fuel flow rate than that shown in Fig. 9. Measurements were made at the fixed axial (z = 135 mm) and radial locations (r = 6.5 and 16.5 mm) and the data are plotted (symbols) along with the corresponding computed values (solid lines) in Fig 10. In this plot, the molar concentration of NO in the experimental and computed flames are compared using relative units. Both the calculations and experiments show that at radial locations away from the flame surface [Fig. 10(a)] the periodic variations in NO concentration follow closely that of temperature. However, near the flame surface [Fig. 10(b)] the concentration of NO is much higher in the compressed region compared to that in the stretched region. The two peaks in the temperature profile at times 77 and 92 ms represent the stretched and compressed flamelets, respectively. As observed in the previous experimental (Vilimpoc and Goss, 1988) and numerical (Katta and Roquemore, 1995) studies, the temperature of the compressed flamelet is higher than that of the stretched flamelet and it was attributed by Katta et al. (1994a) to the non-unity Lewis number of the local gas mixture. Measurements seem to exhibit larger variation in temperatures of the stretched and compressed flamelets than was predicted. However, calculated data at a radial location slightly different from that used in Fig. 10(b) show a temperature difference of ~100 K. Thus, the agreement between the measured and computed data at both radial locations [Figs. 10(a) and 10(b)] for both temperature and NO concentration is considered to be very good. This comparison confirms the fact that temperature and NO concentration indeed increase with the flame compression; with the NO concentration being affected more significantly.

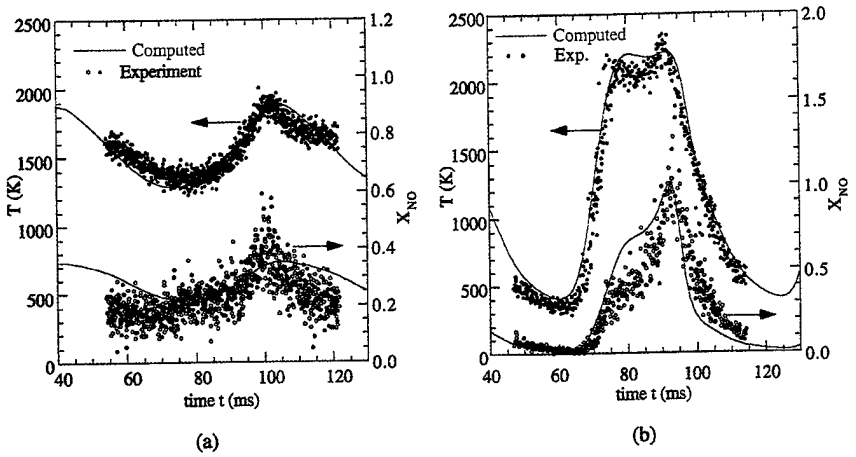

Fig. 10. Predicted and measured temperature and NO-concentration fluctuations obtained at axial distance of 135 mm and at radial locations of (a) 6.5 and (b) 26.5 mm in a buoyant hydrogen/air jet diffusion flame.

(2) Driven Vortices

Studies involving vortices that are formed and interact naturally with the flame surface provide valuable insights into vortex-flame interactions, however, there are also some major limitations associated with such studies as the size and strength of the vortices cannot be readily changed. Typically, the vortices, that develop in buoyant jet flames, range in size of several centimeters for laboratory flame to several meters in large fires. Only the larger vortices produce sufficient stretch to cause local extinction. On the other hand, turbulent flames involve strong interactions between flames and vortices having sizes ranging from mm to several meters. Therefore, to understand vortex-flame interactions that could simulate those in turbulent flames, studies must be performed with various sizes of vortices. This can be achieved by externally driving a vortex and forcing it to interact with a flame in a controlled way.

Hsu et al. (1993) established a vortex inside a laminar jet diffusion flame fueled with methane by driving the fuel jet. The experimental setup consists of a central fuel nozzle and a coannular air duct with exit diameters of 10 and 152 mm, respectively. The fuel nozzle is connected to the speaker chamber by means of a long tapered tube. Fuel is pumped through the side ports of the speaker chamber. An audio speaker is mounted in this chamber in such a way that the hollow cone of the diaphragm is toward the nozzle exit. While a steady flow of fuel is maintained throughout the experiment, puffs of fuel are periodically ejected from the nozzle by driving the speaker with a pulse generator. The flame is shielded from room-air disturbances using a low-speed air flow in the coannular duct. This system permits precise control of the frequency, strength, and shape of the vortex that emerges from the fuel nozzle.

Phase-Locked RMS visualizations at 8, 10, 12 and 14 ms after firing the vortex are shown from left to right in upper half of Fig. 11. The vortex structures captured by the RMS visualizations can be recognized by their dark green-yellow appearance. These images are frozen by the 10-ns flash of the laser sheet passing through the center of the flame and thus, accurately represent the time and spatial evolution of the vortices. However, the flame image is the result of averaging by the film during the time the camera shutter is open, which is about 1 ms in this case. The apparent flame locations in Fig. 11 are marked by the yellow and blue colors in the photograph.

The vortex-flame interactions are evident in Fig. 11. At the 8-ms instant, a large vortex that rotates downward is observed. There is also a counter rotating "secondary" vortex on top of the large "primary" vortex but it is too small to be clearly observed. Two milliseconds later, however, the size of the "secondary" vortex became comparable to that of the "primary" vortex. It is clear that they form a pair of counter rotating vortex rings. Almost all of the outward radial motion of the vortices occurs between 0 and 10 ms. The vortex interaction with the flame produces a hole that occurs between 8 and 10 ms. Once the hole is formed and the vortex pair reaches its maximum radial location, it appears to rotate inward. This is observed for time-delays of 12 and 14 ms. The hole–which is clearly a ring, as noted by the dark band across the flame–remains open for a long period of time.

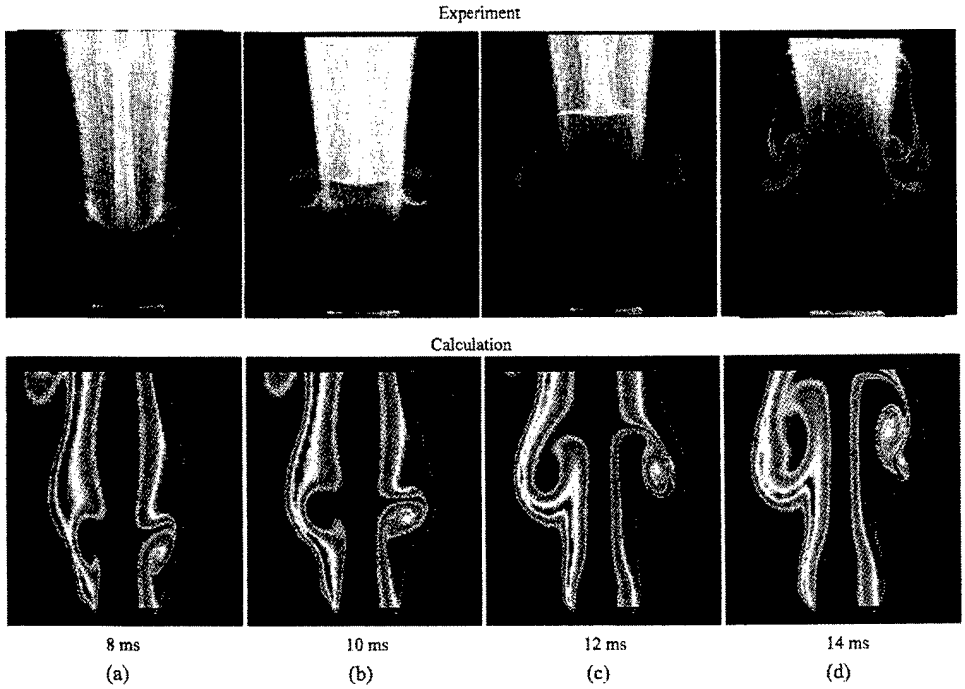

Fig. 11. Vortex-flame interaction in driven methane/air jet diffusion flame. Experimental images obtained using Reactive-Mie-Scattering technique are shown in the upper half. Green emission from TiO_2 particles represents instantaneous flowfield, and blue color represents time-averaged flame surface. Predictions made using global-chemistry model are shown in the lower half. Temperature is plotted on left and particle locations are plotted on right.

The results of the numerical simulations at approximately the same time-delays as those of the experiments of Fig. 11 are shown in the lower half of Fig. 11. Composite visualizations of isotherms (left) and color-coded particle tracings (right) are presented at each instant. Also shown in the figure are the predicted instantaneous stoichiometric mixture fraction locations, marked by the white dots outside the particle tracings. The numerical simulation reproduces the evolution of the primary vortex of the experiments using the particle tracking technique. The counter-rotating vortex ring is also evident in the simulation. The isotherm representation did not identify the vortex pair that is shown by particle tracings. In fact, the temperature field prediction seems to suggest the existence of a single vortex region. The numerical simulation appears to produce nearly the same time and spatial evolution of the ring vortex as observed in the experimental visualizations.

Note that the computed visualizations in Fig. 11 appear to capture the quenching process during the vortex-flame interaction just as observed in the experiments. However, the flame is not completely quenched since there is still a high temperature zone. It appears that the high temperature is thinned out by the vortex-flame interaction. Quenching normally results from a reduction in chemical reaction rate and hence a reduction in heat release rate. However, chemical quenching is not possible because infinitely fast global reaction chemistry was used in the calculations. The thinning of the flame zone with infinitely fast chemistry is an interesting phenomenon. A better understanding of the processes causing it could give additional insights into the quenching process. It is useful to examine how the flame thinning comes about in the calculations. The insights will come form visualizing the vortex-flame interaction in several different ways.

Figure 12 is a visualization of the computed vortex-flame interaction at a time when the flame is stretched thin. The left side of the visualization contains an iso-temperature color plot and the right side contains iso-concentration plots of fuel and oxygen fields separated by the peak-temperature surface (solid white dots). The instantaneous particle field is superimposed on the right-hand side image and the velocity field is superimposed on the left-hand side. Note that particle tracking provides a visualization that is very similar to the RMS visualizations shown in Fig. 11. The particle track and velocity vector visualizations in Fig. 12 show that the primary counter-rotating ring vortex has a high radial velocity in the region where the flame is being stretched. This is due to the

fuel being deflected as it approaches the flame zone. The fuel is deflected away from the flame zone because of the high viscosity barrier caused by the high temperature around the flame surface and the large density ratio between the entrained fluid and the flame. Since the deflected fuel is not transported into the flame, the flame thickness momentarily decrease even though infinitely fast chemistry is used in the simulation. The decrease in flame temperature is resulting from the coarseness of the mesh used. It should be noted that different ways of visualizing the flame thinning process provided the insights into the transport processes causing it. However, the question as to whether the real quenching process observed in Fig. 11 is due to the deflection of fuel from the flame or from finite rate chemistry has not been answered. To address the effects of finite rate chemistry calculations were performed using Peters' chemical kinetics (Peters, 1993). Details of these investigations are published else where (Katta et al., 1998b).

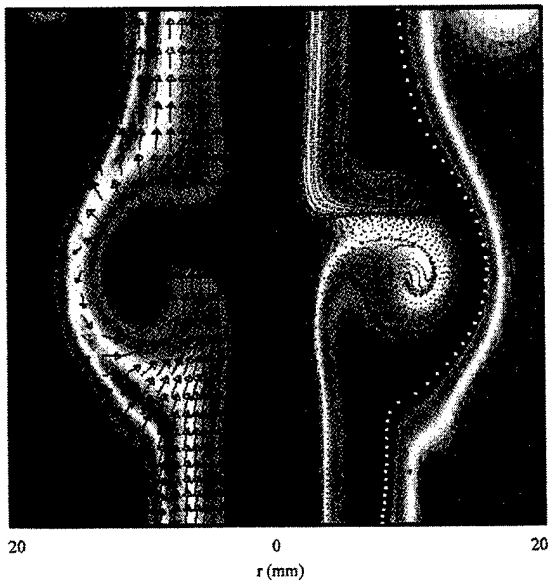

Fig. 12. Blowup of the vortex-flame interaction at an instant corresponding to Fig. 11(b). Temperature and velocity field are shown on the left-hand side. Fuel and oxygen concentrations and particle locations are shown on the right-hand side.

In previous sections, the results of combined numerical/experimental investigations have demonstrated the value of visualization in evaluating UNICORN and using it as a research tool to understand simple, dynamic flames. A long-range goal for UNICORN is that it will be used as a tool to aid in the design of practical combustion systems such as gas turbine combustors. Recently, UNICORN has been used for the prediction of complex flowfields in research combustors (Durbin et al., 1996; Katta and Roquemore, 1998a) and demonstrated the need for dynamic simulations in those combustors.

4. Summary

Accurate simulations employing detailed-chemical-kinetics models for different fuels are needed for understanding flame structure and various processes involved in unsteady flames. An axisymmetric, time-dependent CFDC (Computational Fluid Dynamics with Chemistry) code known as UNICORN has been developed over the past 6 years for the simulation of dynamic flames. During its development, experimental/numerical investigations have been performed on various flames to validate and establish the accuracy of the predictions. Both qualitative and quantitative visualizations have been used extensively for comparing the predictions with experimental data and in exploring the physics associated with the problems. Parametric studies have also been conducted to identify the factors that are important in these dynamic flames.

Calculations using UNICORN have been performed for unsteady laminar and transitional jet diffusion flames of hydrogen, methane and propane fuels. The predicted flame shapes and flow structures of periodically

oscillating flames, that result from an absolute buoyancy-induced instability, showed good correlation with the Reactive-Mie-Scattering images of the flames obtained in experiments. UNICORN predicted and it was later found experimentally that the temperature and hence, nitric oxide, in these buoyancy-dominated unsteady flames increase at certain phases of the vortex-flame interaction; a characteristic behavior of hydrogen and methane flames. Simulations for transitional flames having inner and outer vortices reveled that viscosity, volumetric expansion and body force due to buoyancy are responsible for the slower growth and longer coherence lengths for the inner vortices.

A combined experimental/numerical study was made for the vortex-flame interactions in a coflowing methane jet diffusion flame. A large toroidal vortex formed from the fuel puff and pushed the flame radially outward and created a hole on the flame surface. As the vortex convected downstream, re-ignition took place in the region of the hole and the flame returned to its unperturbed position. UNICORN has been used to investigate the vortex evolution, quenching and ignition processes associated with this vortex-flame interaction.

Acknowledgments

This work was supported, in part, by Air Force Contracts F33615-90-C-2033 and F33615-95-C-2507 and the Air Force Office of Scientific Research. The authors would like to acknowledge Drs. L.-D. Chen, F. Takahashi, L. P. Goss, K.-Y. Hsu, J. R. Gord, C. D. Carter, G. J. Fiechtner, S. P. Gogineni, R. D. Hancock and F. R. Schauer for the support given in developing advanced-measurement techniques. The authors would also like to thank Professor J. C. Rolon, for stimulating discussions and Mrs. M. M. Whitaker for her excellent editorial help.

References

Bahadori, M. Y., Zhou, L., Stocker, D. P. and Hegde, U., "Measurements of Flame Flicker Under Different Gravitational Levels," Proceedings of the 1996 Fall Technical Meeting of the Eastern States Section of The Combustion Institute, Pittsburgh, PA, (1996), 451-454.

Carter, C. D., Goss, L. P., Hsu, K. Y., Katta, V. R. and Trump, D. D., Paper No. 080, Proceedings of the Combined Central States/Western States/Mexican National Sections Meeting of the Combustion Institute, April 23-26 (1995).

Davis, R. W., Moore, E. F., Roquemore, W. M., Chen, L.-D., Vilimpoc, V. and Goss, L. P., "Preliminary Results of a Numerical-Experimental Study of the Dynamic Structure of a Buoyant Jet Diffusion Flame," Combustion and Flame, 83, 3/4, (1991), 263-270.

Durbin, M. D., Vangsness, D., Ballal, D. and Katta, V. R., "Study of Flame Stability in a Step Swirl Combustor," Transactions of the ASME: Journal of Engineering for Gas Turbine and Power, 118, (1996), 308.

Ellzey, J. L., Laskey, K. J. and Oran, E. S., "Dynamics of an Unsteady Diffusion Flame: Effects of Heat Release Rate and Viscosity," in Dynamics of Deflagrations and Reactive Systems: Flames, A. L. Kahl, J. C. Leyer, A. A. Borisov, and W. A. Sirgnano, Eds., Vol. 131, Progress in Astronautics and Aeronautics, (1989), 179, American Institute of Aeronautics and Astronautics, Washington, D. C..

Goss, L. P., Vilimpoc, V., Sarka, B. and Lynn, W. F., "Thin-Filament Pyrometry: A Novel Thermometric Technique for Combusting Flows," ASME Trans., J. Eng. Gas Turbines Power, 111, (1989), 46.

Grisch, F., Attal-Tretout, B., Bouchardy, P., Katta, V. R. and Roquemore, W. M., "A Vortex-Flame Interaction Study Using Four-Wave Mixing Techniques," J. Nonlinear Opt. Phys. Mater., 5(3), (1996), 505.

Hirschfelder, J. O., Curtiss, C. F. and Bird, R. B., Molecular Theory of Gases and Liquids, (1954), Chapters 8 and 9, John Wiley & Sons, Inc., New York.

Hottel, H. C. and Hawthorne, W. R., "Diffusion in Laminar Flame Jets," Third Symposium (International) on Combustion, Flame and Explosive Phenomena, The Combustion Institute, Pittsburgh, PA, (1949), 254-266 .

Hsu, K. Y., Chen, L.-D., Katta, V. R., Goss, L. P. and Roquemore, W. M., "Experimental and Numerical Investigations of the Vortex-Flame Interactions in a Driven Jet Diffusion Flame," AIAA Paper 93-0455, Reno, Jan., 11-16 (1993).

Kaplan, C. R., Oran, E. S., Kailasanath, K. and Ross, H. D., "Gravitational Effects on Sooting Diffusion Flames," 26th Symposium (International) on Combustion, The combustion Institute, Pittsburgh, PA, (1996), 1301-1309 .

Katta, V. R. and Roquemore, W. M., "Role of Inner and Outer Structures in a Transitional Diffusion Flame," Combustion and Flame, 92, 2, (1993), 274-282.

Katta, V. R., Goss, L. P. and Roquemore W. M., "Effect of Nonunity Lewis number and Finite-Rate Chemistry on the Dynamics of a Hydrogen-Air Jet Diffusion Flame," Combustion and Flame, 96, 1-2, (1994a), 60-74.

Katta, V. R., Goss, L. P. and Roquemore, W. M., "Numerical Investigations of Transitional H_2/N_2 Jet Diffusion Flames," AIAA Journal, 32, 1, (1994b), 84-94.

Katta, V. R., Goss, L. P. and Roquemore, W. M., "Simulation of Vortical Structures in a Jet Diffusion Flame," International Journal of Numerical Methods for Heat and Fluid Flow, 4, 5, (1994c), 413.

Katta, V. R. and Roquemore, W. M., "On the Structure of Stretched/Compressed Laminar Flamelet – Influence of Preferential Diffusion," Combustion and Flame, 100, 1, (1995), 61.

Katta, V. R. and Roquemore, W. M., "Numerical Studies on Trapped-Vortex Concepts for Stable Combustion," Trans. ASME: J. Eng. Gas Turb. Power 120, (April, 1998a), 60.

Katta, V. R. Hsu, K. Y. and Roquemore, W. M., "Local Extinction in an Unsteady Methane-Air Jet Diffusion Flame," 27th Symposium (International) on Combustion, The Combustion Institute, Boulder, CO, Aug (1998b). 2-7.

Law, C. K., "Heat and Mass Transfer in Combustion: Fundamental Concepts and Analytical Techniques," Progress in Energy and Combustion Sciences, 10, 3, (1984), 295-318.

Lee, S., Flow-Flame Interactions of Transitional Nitrogen Diluted Hydrogen Jet Diffusion Flames, Ph. D. Thesis, University of Iowa, Iowa City, IA, December (1992).

Leonard, B. P., "A Stable and Accurate Convective Modeling Procedure Based on Quadratic Upstream Interpolation," Computer Methods in

Applied Mechanics and Engineering , 19, 1, (1979), 59-98.
Patnaik, G. and Kailasanath, K., "Numerical Simulations of Burner-Stabilized Hydrogen-Air Flames in Microgravity," Combustion and Flame, 99, 10, (1994), 247-253.
Peters, N. and Williams, F. A., AIAA J. 21:423 (1983).
Peters, N., "Flame Calculations with Reduced Mechanisms – An Outline," in Reduced Kinetic Mechanisms for Applications in Combustion Systems, Lecture Notes in Physics, Vol. 15, (1993), 3-14, Springer-Verlag, New York.
Roquemore, W. M., Chen, L-D., Goss, L. P. and Lynn, W. F., "Structure of Jet Diffusion Flames," Turbulent Reactive Flows, edited by R. Borghi and S. N. B. Murthy, Lecture Notes in Engineering, Vol. 40, (1989), 49-63, Springer-Verlag, Berlin.
Spalding, D. B., "A Novel Finite Difference Formulation for Difference Expressions Involving Both First and Second Derivatives," International Journal of Numerical Methods in Engineering , 4, (1972), 551.
Takagi, T. and Xu, Z., "Numerical Analysis of Laminar Diffusion Flames – Effects of Preferential Diffusion of Heat and Species," Combustion and Flame, 96, 1 and 2, (1994), 50-59.
Takagi, T., Yoshikawa, Y., Yoshida, K., Komiyama, M. and Kinoshita, S., "Studies on Strained Nonpremixed Flames Affected by Flame Curvature and Preferential Diffusion," 26th Symposium (International) on Combustion, The combustion Institute, Pittsburgh, PA, (1996), 1103-1110.
Takahashi, F. and Schmoll, W. J., "Lifting Criteria of Jet Diffusion Flames," Twenty-Third Symposium (International) on Combustion, The Combustion Institute, Pennsylvania, PA, (1991), 677.
Takahashi, F. and Katta, V. R., "A Numerical Investigation of the Stabilizing Mechanism of Methane Jet Diffusion Flames," AIAA Paper 97-0251, 35th Aerospace Sciences Meeting and Exhibit, January 6-10, Reno, NV, (1997).
Takahashi, F., Schmoll, W. J. and Katta, V. R., "Attachment Mechanisms of Diffusion Flames," 27th Symposium (International) on Combustion, The Combustion Institute, Boulder, CO, Aug. 2-7 (1998).
Vilimpoc, V. and Goss, L. P., "SiC-Based Thin-Filament Pyrometry: Theory and Thermal Properties," Twenty-Second Symposium (International) on Combustion, The Combustion Institute, Pittsburgh, PA, (1988), 1907-1914.
Williams, F. A., Combustion Theory - The Fundamentals of Chemically Reacting Flow Systems, (1985), Appendix E, Addison-Wesley Publishing Co., Reading, MA.
Yamashita, H., Kushida, G. and Takeno, T., "A Numerical Study of the Transition of Jet Diffusion Flames," Proceedings of the Royal Society of London A, 431, 1882, (1990), 301-314.
Yule, A. J., Chigier, N. A., Ralph, S., Boulderstone, R. and Ventura, J., "Combustion-Transition Interaction in a Jet Flame," AIAA Journal, 19, 6, (1981), 752-760.

Author Profile

William Melvyn "Mel" Roquemore: He received BS degree in Physics in 1963 from Auburn University. After graduation, employed at the Air Force Aero Propulsion Laboratory. Received MS degree in Physics in 1969 from the University of Dayton and Ph.D. degree in Physics from the University of Cincinnati as part of an Air Force Long Term Training Program. Is currently Senior Scientist at the Propulsion Directorate of the Air Force Research Laboratory. Directs experimental and computational research involving fundamental combustion processes and advanced combustor concepts. Is an Air Force Research Laboratory Fellow and has authored 150 publications in combustion and combustion diagnostics.

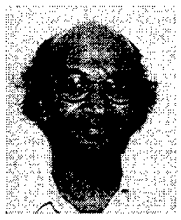

Viswanath Reddy Katta: He received B.Tech. degree in Electrical Engineering in 1979 from Jawaharlal Nehru Technological University and M.Tech. and Ph.D. degrees in Aerospace Engineering from Indian Institute of Technology, Madras, in 1981 and 1986, respectively. Worked at Nagoya University, Japan, before moving to U.S. in 1989. NRC Post Doctoral Fellow and then employed by SRL before taking current position. Cofounder and Vice-President of Innovative Scientific Solutions Inc. Current interests include simulation of reacting flows, droplet combustion, detonations, vortex dynamics, and fuel thermal stability. Authored more than 150 technical papers in these areas. Associate Fellow of AIAA and member of APS, ASME, and Combustion Institute.

Copyright Ownership -
Taylor & Francis Ltd

Combust. Sci. and Tech., 2000, Vol. 155, pp. 243-279
Reprints available directly from the publisher
Photocopying permitted by license only

PUBLISHED WITH PERMISSION

© 2000 OPA (Overseas Publishers Association) N.V.
Published by license under the
Gordon and Breach Science Publishers imprint.
Printed in Malaysia

Chemical Kinetic Structure of the Reaction Kernel of Methane Jet Diffusion Flames

FUMIAKI TAKAHASHI[a*] and VISWANATH R. KATTA[b]

[a]*University of Dayton Research Institute, 300 College Park Dayton, Ohio 45469–0140 and* [b]*Innovative Scientific Solutions, Inc., 2766 Indian Ripple Road, Dayton, Ohio 45440*

(Received March 03, 1999; Revised August 23, 1999)

The detailed structure of the stabilizing region of an axisymmetric laminar methane jet diffusion flame has been studied numerically by solving the time-dependent full Navier-Stokes equations with buoyancy using an implicit, third-order accurate numerical scheme and two detailed C_2-chemistry models. The calculated standoff distance of the flame base was comparable to that experimentally observed but chemistry-model dependent. Nevertheless, local flame structure around the base was nearly identical, except that the C_1-chemistry previously used overpredicted the methyl and formaldehyde concentrations. The fuel-lean, highest-reactivity spot (*reaction kernel*) responsible for flame stabilization was formed as a result of back-diffusion of radicals into the oxygen-abundant flame base, thereby dramatically enhancing the H_2-O_2 chain reactions, the CH_3 formation and oxidation via formaldehyde, the C_2-reaction path, and the HO_2 reactions at relatively low temperatures (<1600 K). In particular, the $H + O_2 \rightarrow OH + O$ and $CH_3 + O \rightarrow CH_2O + H$ reactions played a decisive role in the reaction kernel.

Keywords: Diffusion flame; flame structure; flame stabilization; chemical kinetics

INTRODUCTION

The interaction between a flame and surfaces plays an important role in flame holding in combustors and fire spread through condensed fuels (Williams, 1985). Flame-flow phenomena, including transport processes and chemical reactions around the flame base near the surfaces, control flame stability and spreading mechanisms. Understanding of the flame stabilization of laminar diffusion flames is weak compared to that of laminar premixed flames, primarily due to

* Correspondence author: E-mail: ftakahas@engr.udayton.edu

the lack of a global parameter reflecting the reaction rates of diffusion flames (cf. the burning velocity of premixed flames). In diffusion flames, transport processes are in general rate determining. However, in the flame stabilizing region (flame base), partial premixing of fuel and air occurs in the quenched (dark) space near the surfaces and accelerates coupled transport and reaction processes. An early postulation (Gaydon and Wolfhard, 1979) that "there must be a sort of flame velocity in this premixed zone at the base which causes the combustion processes to propagate downwards along the flame front against the gas stream, thus preventing the flame from lifting" has long prevailed among researchers without experimental proof.

A correlation was obtained (Takahashi et al., 1985, 1996) between the velocity of the flow entrained into the flame base at lifting and the maximum burning velocity for hydrogen diffusion flames. However, the flame structure measurements (Robson and Wilson, 1969; Kawamura et al., 1980; Takahashi et al., 1988) in a small (~a few mm square) stabilizing region of rim-attached, laminar diffusion flames of methane revealed a premixed zone which was too narrow for a premixed flame to propagate. A much longer axial distance, or residence time, from the burner rim to the flame base is required for the fuel-air interdiffusion process to form a thick premixing layer. Near the flame base of lifted laminar flames with a liftoff height of several to 10+ cm, Chung and Lee (1991) observed a tribrachial structure composed of a lean premixed flame, a rich premixed flame, and a diffusion flame extending downstream from the same point for propane and n-butane, but not for methane and ethane. Chung and Lee attributed the different behavior to the Schmidt number ($Sc > 1$ for propane and butane; $0.5 < Sc < 1$ for methane and ethane). The tribrachial (or triple) flame structure could be formed by artificially increasing the thickness of the premixing layer in a lifted laminar axisymmetric flame of a diluted methane jet surrounded by a lean methane-air coflow and an outer coflow air (Plessing et al., 1998). Furthermore, theoretical works have been directed toward modeling of the flame behavior in the vicinity of a fuel-oxidizer divider using the triple-flame (Veynante et al., 1994; Wichman and Varatharajan, 1997) or edge-flame (Buckmaster and Weber, 1996) concept.

Unfortunately, previous results generally suffered from the lack of detailed flame structure information, particularly on radical concentrations and reactions. Diagnostic techniques available to measure various species in a small flame-stabilizing region are limited. As a result of recent advances in computational capabilities and chemistry models, a numerical approach seems most promising to obtain comprehensive chemical kinetic structure. In this paper, the new results of numerical analyses using two different C_2-chemistry models, in addition to C_1-chemistry model previously used (Takahashi et al., 1998), are reported to

reveal the chemical kinetic structure of the stabilizing region of methane diffusion flames and to expand the knowledge of flame stabilization mechanisms. Because the reaction mechanisms available are typically "calibrated" for 1D premixed flame systems, the current work is a pioneering attempt to see if these mechanisms accurately predict the two-dimensionally distributed variables around the diffusion flame base and the subtly balanced standoff distance. A novel approach is employed here to reveal the influence of the variation of individual rate coefficients on the flame-base standoff distance in consideration of the 2D flame structure.

NUMERICAL METHODS

The numerical code (UNICORN) used in this study was developed by Katta et al. (1994) and validated against measurements and flow visualization of various diffusion and premixed flame phenomena; i.e., unsteady characteristics, extinction, ignition, vortex-flame interactions, and flame attachment mechanisms (Roquemore and Katta, 1998; Katta and Roquemore, 1998; Takahashi and Katta, 1995, 1996, 1997; Takahashi et al., 1998).

The time-dependent, axisymmetric mathematical model of UNICORN, which solves for axial- and radial-momentum equations, continuity, and enthalpy- and species-conservation equations is used to simulate the near-base regions of jet diffusion flames. The governing equations, written in the cylindrical-coordinate system, are as follow:

$$\frac{\partial \rho}{\partial t} + \frac{\partial \rho u}{\partial z} + \frac{1}{r}\frac{\partial (r\rho v)}{\partial r} = 0 \tag{1}$$

and

$$\frac{\partial (\rho \Phi)}{\partial t} + \frac{\partial (\rho u \Phi)}{\partial z} + \frac{1}{r}\frac{\partial (r\rho v \Phi)}{\partial r} = \frac{\partial}{\partial z}\left[\Gamma^{\Phi}\frac{\partial \Phi}{\partial z}\right] + \frac{1}{r}\frac{\partial}{\partial r}\left[r\Gamma^{\Phi}\frac{\partial \Phi}{\partial r}\right] + S^{\Phi} \tag{2}$$

Here ρ represents density; u and v are the axial and radial components of the velocity vector, respectively; and p is pressure. The general form of Eq. 2 represents the momentum, the species, or the energy-conservation equation, depending on the variable used in place of Φ. In Table I, the transport coefficients Γ^{Φ} and the source term S^{Φ} that appear in the governing equations are given. The body-force term due to the gravitational field is included in the axial-momentum equation. Here μ, λ, and c_p are the viscosity, thermal conductivity, and specific heat of the mixture, respectively; Y_i is the mass fraction; H_i is the enthalpy; $h^{\circ}_{f,i}$ is the heat of formation at standard state (temperature T_0); and $\dot{\omega}_i$ is the mass-production rate of species i; ρ_0 is the density of air; and g is the gravita-

tional acceleration. The transport property D_{im} is the effective diffusion coefficient for species i (Williams, 1985), which is calculated from the binary diffusion coefficients between that species and the other individual species. Finally, Le_i is the Lewis number for species i, which is defined as

$$Le_i \equiv \frac{\lambda}{\rho D_{im} c_p}. \tag{3}$$

TABLE I Transport Coefficients and Source Terms Appearing in the Governing Equations

Φ	Γ^Φ	S^Φ
u	μ	$-\frac{\partial p}{\partial z} + (\varrho_0 - \varrho)g + \frac{\partial}{\partial z}\left(\mu\frac{\partial u}{\partial z}\right) + \frac{\partial}{\partial r}\left(\mu\frac{\partial v}{\partial z}\right) + \frac{\mu}{r}\frac{\partial v}{\partial z}$ $-\frac{2}{3}\left\{\frac{\partial}{\partial z}\left(\mu\frac{\partial u}{\partial z}\right) + \frac{\partial}{\partial z}\left(\mu\frac{\partial v}{\partial r}\right)\right\} + \frac{\partial}{\partial z}\left(\mu\frac{v}{r}\right)$
v	μ	$-\frac{\partial p}{\partial r} + \frac{\partial}{\partial z}\left(\mu\frac{\partial u}{\partial r}\right) + \frac{\partial}{\partial r}\left(\mu\frac{\partial v}{\partial r}\right) + \frac{\mu}{r}\frac{\partial v}{\partial r} - 2\mu\frac{v}{r^2}$ $-\frac{2}{3}\left\{\frac{\partial}{\partial r}\left(\mu\frac{\partial u}{\partial z}\right) + \frac{\partial}{\partial r}\left(\mu\frac{\partial v}{\partial r}\right)\right\} + \frac{\partial}{\partial r}\left(\mu\frac{v}{r}\right)$
$Y_i\,(i = 1, \ldots, N_s - 1)$	ρD_{im}	$\dot{\omega}_i$
H	$\frac{\lambda}{c_p}$	$\nabla\left[\frac{\lambda}{c_p}\sum_{i=1}^{N_s}\left\{\left(Le^{-1} - 1\right) H_i \nabla Y_i\right\}\right] - \sum_{i=1}^{N_s}\left(h^\circ_{f,i}\,\dot{\omega}_i\right)$

The set of expressions given by Eqs. 1 and 2 can be completed using the global-species-conservation equation

$$Y_{N_2} = 1 - \sum_{i=1}^{N_s - 1} Y_i \tag{4}$$

and the state equation

$$p = \rho R_0 T \sum_{i=1}^{N_s}\left(\frac{Y_i}{M_i}\right) \tag{5}$$

where R_0 is the universal gas constant; T is the temperature; and Y_i and M_i are the mass fraction and molecular weight of species i, respectively. While density is obtained by solving the state equation (5), the pressure field at every time step is determined from pressure Poisson equations. Even though the governing equations are solved in an uncoupled manner, the species-conservation equations are coupled through the source terms during the solution process to improve the sta-

bility of the algorithm. Such coupling is essential in finite-rate-chemistry calculations since the high-reaction-rate terms make the species-conservation equations quite stiff. Temperature- and species-dependent thermodynamic and transport properties are used in this formulation.

The governing equations for u and v momentum are integrated using an implicit QUICKEST (Quadratic Upstream Interpolation for Convective Kinematics with Estimated Streaming Terms) numerical scheme (Katta et al., 1994; Leonard, 1979), which is third-order accurate in both space and time and has a very low numerical-diffusion error. On the other hand, the finite-difference form of the species and enthalpy is obtained using the hybrid scheme (Spalding, 1972) with upwind and central differencing. An orthogonal, staggered-grid system with rapidly expanding cell sizes in both the z and the r directions is utilized for discretizing the governing equations. After rearrangement of terms, the finite-difference form of the governing equation for the variable Φ at a grid point P can be written as an algebraic equation as follows:

$$A_P\Phi_P^{N+1} + A_{z++}\Phi_{z++}^{N+1} + A_{z+}\Phi_{z+}^{N+1} + A_{z-}\Phi_{z-}^{N+1} + A_{z--}\Phi_{z--}^{N+1} + A_{r++}\Phi_{r++}^{N+1} + A_{r+}\Phi_{r+}^{N+1} + A_{r-}\Phi_{r-}^{N+1} + A_{r--}\Phi_{r--}^{N+1} = S_P^{\Phi} + \Delta t \cdot \rho_P\Phi_P^N \qquad (6)$$

The time increment (Δt) is determined from the stability constraint and maintained as a constant during the entire calculation. The superscripts N and N+1 represent the known variables at the time step N and the unknown variables at the time step N+1, respectively; the subscripts z^+ and z^- indicate the values at the grid points immediately adjacent to point P in the positive and negative z-directions, respectively. Similarly, the subscripts z^{++} and z^{--} represent the values at two grid points from P in the respective directions. The coefficients A and the terms on the right-hand side of the above equations are calculated from the known flow variables at the time step N. The above equations for N_s+2 variables are solved individually using an iterative ADI (Alternative Direction Implicit) technique. The pressure field at every time step is accurately calculated by simultaneously solving the system of algebraic pressure Poisson equations at all grid points using the LU (Lower-Upper) decomposition technique.

Three detailed chemical-kinetic models proposed in the literature for methane-air combustion were used in this study. The first was proposed by Peters (1993) and consists of 17 species (CH_4, O_2, CH_3, CH_2, CH, CH_2O, CHO, CO_2, CO, H_2, H, O, OH, H_2O, HO_2, H_2O_2, and N_2 [inert]) that are involved in 52 elementary reactions as shown in Table II (R1 through R53, except R47). This mechanism is derived from the one originally published (Peters, 1993) for the hydrocarbon fuels up to propane in terms of carbon content and by neglecting the species that have more than one carbon element. This C_1-chemistry model was used in the previous studies (Takahashi and Katta, 1996, 1997; Takahashi et al.,

1998). The second chemistry model (R1 through R81 in Table II) is an extension of the first and was obtained by including the C_2-chemistry (Peters, 1993) which adds seven additional species (C_2H, C_2H_2, C_2H_3, C_2H_4, C_2H_5, C_2H_6, and CHCO) and 29 reactions. Finally, the third chemistry model used in the present study was compiled by the Gas Research Institute (GRI-Mech, version 1.2). This is the most comprehensive mechanism, having 31 species and 346 elementary-reaction steps, and is recommended by several investigators for computing the structures of methane flames (Frenklach et al., 1995). In addition to the 24 species in the second model (Peters mechanism with C_2 chemistry), the GRI mechanism uses the following seven additional species: C, $CH_2(S)$, CH_2OH, CH_3O, CH_3OH, CH_2CO, and HCCOH, but the Arrhenius parameters have been collected independently.

TABLE II CH_4 Mechanism[a]

		A	n	E
H_2/O_2 Chain Reactions				
(R1)	$H + O_2 \rightarrow OH + O$	2.00E+14	0.0	16,800
(R2)	$OH + O \rightarrow H + O_2$	1.57E+13	0.0	840
(R3)	$O + H_2 \rightarrow OH + H$	5.06E+04	2.67	6,280
(R4)	$OH + H \rightarrow O + H_2$	2.22E+04	2.67	4,370
(R5)	$H_2 + OH \rightarrow H_2O + H$	1.00E+08	1.60	3,300
(R6)	$H_2O + H \rightarrow H_2 + OH$	4.31E+08	1.60	18,270
(R7)	$OH + OH \rightarrow O + H_2O$	1.50E+09	1.14	100
(R8)	$H_2O + O \rightarrow OH + OH$	1.47E+10	1.14	17,000
HO_2 Formation and Consumption				
(R9)	$O_2 + H + M \rightarrow HO_2 + M$	2.30E+18	−0.8	0
(R10)	$HO_2 + M \rightarrow O_2 + H + M$	3.19E+18	−0.8	46,680
(R11)	$HO_2 + H \rightarrow OH + OH$	1.50E+14	0.0	1,000
(R12)	$HO_2 + H \rightarrow H_2 + O_2$	2.50E+13	0.0	692
(R13)	$HO_2 + OH \rightarrow H_2O + O_2$	6.00E+13	0.0	0
(R14)	$HO_2 + H \rightarrow H_2O + O$	3.00E+13	0.0	1,720
(R15)	$HO_2 + O \rightarrow OH + O_2$	1.80E+13	0.0	−406
H_2O_2 Formation and Consumption				
(R16)	$HO_2 + HO_2 \rightarrow H_2O_2 + O_2$	2.50E+11	0.0	−1,240
(R17)	$OH + OH + M \rightarrow H_2O_2 + M$	3.25E+22	−2.0	0
(R18)	$H_2O_2 + M \rightarrow OH + OH + M$	1.69E+24	−2.0	48,330
(R19)	$H_2O_2 + H \rightarrow H_2O + OH$	1.00E+13	0.0	3,580
(R20)	$H_2O_2 + OH \rightarrow H_2O + HO_2$	5.40E+12	0.0	1,000
(R21)	$H_2O + HO_2 \rightarrow H_2O_2 + OH$	1.80E+13	0.0	32,190

			A	n	E
Recombination Reactions					
(R22)	$H + H + M \rightarrow H_2 + M$		1.80E+18	−1.0	0
(R23)	$H + OH + M \rightarrow H_2O + M$		2.20E+22	−2.0	0
(R24)	$O + O + M \rightarrow O_2 + M$		2.90E+17	−1.0	0
CO/CO_2 Mechanism					
(R25)	$CO + OH \rightarrow CO_2 + H$		4.40E+06	1.5	−740
(R26)	$CO_2 + H \rightarrow CO + OH$		4.96E+08	1.5	21,440
CH Consumption Reactions					
(R27)	$CH + O_2 \rightarrow CHO + O$		3.00E+13	0.0	0
(R28)	$CO_2 + CH \rightarrow CHO + CO$		3.40E+12	0.0	692
CHO Consumption Reactions					
(R29)	$CHO + H \rightarrow CO + H_2$		2.00E+14	0.0	0
(R30)	$CHO + OH \rightarrow CO + H_2O$		1.00E+14	0.0	0
(R31)	$CHO + O_2 \rightarrow CO + HO_2$		3.00E+12	0.0	0
(R32)	$CHO + M \rightarrow CO + H + M$		7.10E+14	0.0	16,800
(R33)	$H + CO + M \rightarrow CHO + M$		1.14E+15	0.0	2,380
CH_2 Consumption Reactions					
(R34)	$CH_2 + H \rightarrow CH + H_2$		8.40E+09	1.5	335
(R35)	$CH + H_2 \rightarrow CH_2 + H$		5.83E+09	1.5	3,125
(R36)	$CH_2 + O \rightarrow CO + H + H$		8.00E+13	0.0	0
(R37)	$CH_2 + O_2 \rightarrow CO + OH + H$		6.50E+12	0.0	1,500
(R38)	$CH_2 + O_2 \rightarrow CO_2 + H + H$		6.50E+12	0.0	1,500
CH_2O Consumption Reactions					
(R39)	$CH_2O + H \rightarrow CHO + H_2$		2.50E+13	0.0	3,990
(R40)	$CH_2O + O \rightarrow CHO + OH$		3.50E+13	0.0	3,490
(R41)	$CH_2O + OH \rightarrow CHO + H_2O$		3.00E+13	0.0	1,200
(R42)	$CH_2O + M \rightarrow CHO + H + M$		1.40E+17	0.0	76,500
CH_3 Consumption Reactions					
(R43)	$CH_3 + H \rightarrow CH_2 + H_2$		1.80E+14	0.0	15,050
(R44)	$CH_2 + H_2 \rightarrow CH_3 + H$		3.68E+13	0.0	10,580
(R45)	$CH_3 + H \rightarrow CH_4$	K_∞	6.00E+16	−1.0	0
		K_0	8.00E+26	−3.0	0
(R46)	$CH_3 + O \rightarrow CH_2O + H$		7.00E+13	0.0	0
(R47)	$CH_3 + CH_3 \rightarrow C_2H_6$	K_∞	3.61E+13	0.0	0
		K_0	1.27E+41	−7.0	2,762
(R48)	$CH_3 + O_2 \rightarrow CH_2O + OH$		3.40E+11	0.0	8,940

			A	n	E
(R49)	$CH_3 + H_2 \rightarrow CH_4 + H$		8.39E+02	3.0	8,260
(R50)	$CH_3 + H_2O \rightarrow CH_4 + OH$		2.63E+05	2.10	16,950
CH_4 Consumption Reactions					
(R51)	$CH_4 + H \rightarrow CH_3 + H_2$		2.20E+04	3.0	8,740
(R52)	$CH_4 + O \rightarrow CH_3 + OH$		1.20E+07	2.1	7,620
(R53)	$CH_4 + OH \rightarrow CH_3 + H_2O$		1.60E+06	2.1	2,460
C_2H Consumption Reactions					
(R54)	$C_2H + H_2 \rightarrow C_2H_2 + H$		1.10E+13	0.0	2,867
(R55)	$C_2H_2 + H \rightarrow C_2H + H_2$		5.27E+13	0.0	28,656
(R56)	$C_2H + O_2 \rightarrow CHCO + O$		5.00E+13	0.0	1,505
CHCO Consumption Reactions					
(R57)	$CHCO + H \rightarrow CH_2 + CO$		3.00E+13	0.0	0
(R58)	$CH_2 + CO \rightarrow CHCO + H$		2.36E+12	0.0	−7,021
(R59)	$CHCO + O \rightarrow CO + CO + H$		1.00E+14	0.0	0
C_2H_2 Consumption Reactions					
(R60)	$C_2H_2 + O \rightarrow CH_2 + CO$		4.10E+08	1.5	1,696
(R61)	$C_2H_2 + O \rightarrow CHCO + H$		4.30E+14	0.0	12,112
(R62)	$C_2H_2 + OH \rightarrow C_2H + H_2O$		1.00E+13	0.0	7,000
(R63)	$C_2H + H_2O \rightarrow C_2H_2 + OH$		9.00E+12	0.0	−3,818
C_2H_3 Consumption Reactions					
(R64)	$C_2H_3 + H \rightarrow C_2H_2 + H_2$		3.00E+13	0.0	0
(R65)	$C_2H_3 + O_2 \rightarrow C_2H_2 + HO_2$		5.40E+11	0.0	0
(R66)	$C_2H_3 \rightarrow C_2H_2 + H$	K_∞	2.00E+14	0.0	39,717
		K_0	1.19E+42	−7.5	45,486
(R67)	$C_2H_2 + H \rightarrow C_2H_3$	K_∞	1.05E+14	0.0	810
C_2H_4 Consumption Reactions					
(R68)	$C_2H_4 + H \rightarrow C_2H_3 + H_2$		1.50E+14	0.0	10,201
(R69)	$C_2H_3 + H_2 \rightarrow C_2H_4 + H$		9.61E+12	0.0	7,800
(R70)	$C_2H_4 + O \rightarrow CH_3 + CO + H$		1.60E+09	1.2	741
(R71)	$C_2H_4 + OH \rightarrow C_2H_3 + H_2O$		3.00E+13	0.0	3,010
(R72)	$C_2H_3 + H_2O \rightarrow C_2H_4 + OH$		8.28E+12	0.0	15,576
(R73)	$C_2H_4 + M \rightarrow C_2H_2 + H_2 + M$		2.50E+17	0.0	76,400
C_2H_5 Consumption Reactions					
(R74)	$C_2H_5 + H \rightarrow CH_3 + CH_3$		3.00E+13	0.0	0.0
(R75)	$CH_3 + CH_3 \rightarrow C_2H_5 + H$		3.57E+12	0.0	11,870
(R76)	$C_2H_5 + O_2 \rightarrow C_2H_4 + HO_2$		2.00E+12	0.0	4,993

			A	*n*	*E*
(R77)	$C_2H_5 \rightarrow C_2H_4 + H$	K_∞	2.00E+13	0.0	39,657
		K_0	1.00E+17	0.0	31,057
(R78)	$C_2H_4 + H \rightarrow C_2H_5$	K_∞	3.19E+13	0.0	3,013
C_2H_6 Consumption Reactions					
(R79)	$C_2H_6 + H \rightarrow C_2H_5 + H_2$		5.40E+02	3.5	5,208
(R80)	$C_2H_6 + O \rightarrow C_2H_5 + OH$		3.00E+07	2.0	5,112
(R81)	$C_2H_6 + OH \rightarrow C_2H_5 + H_2O$		6.30E+06	2.0	645

[a] Reaction rates in cm^3 mol s cal units, $k = AT^n\exp(-E/RT)$.

Source: Peters (1995), Warnatz (1984) (R45).

Although it is beyond the scope of this study to "tune" the kinetic mechanisms to the current application, the Arrhenius parameters for the reaction $CH_3 + H \rightarrow CH_4$ (R45) are replaced with those by Warnatz (1984) for all kinetic models. Otherwise, the extinction limit of counterflow diffusion flames was predicted at a significantly lower strain rate (Katta and Roquemore, 1996) compared to that determined experimentally by Sung et al. (1995), and the jet diffusion flames under consideration prematurely lifted off under conditions below the stability limit obtained experimentally (Takahashi and Schmoll, 1991).

The enthalpies of individual species are calculated from the polynomial curve fits developed for the temperature range 300 – 5000 K. Physical properties such as viscosity, thermal conductivity, and the binary molecular diffusion coefficients of the species are calculated using molecular dynamics. Mixture viscosity and thermal conductivity are then estimated using the Wilke and Kee expressions (Hirschfelder et al., 1954), respectively. Molecular diffusion is assumed to be of the binary type, and the diffusion velocity of a species is calculated according to Fick's law and the effective diffusion coefficient (Williams, 1985) of that species. The Lennard-Jones potentials, the effective temperatures, and the coefficients for the enthalpy polynomials for each species are obtained from the CHEMKIN libraries.

The computational domain and the boundary conditions employed are shown in Fig. 1. The computational domain is bounded by (I) the inflow and (II) outflow boundaries in the axial direction, (III) the axis of symmetry, and (IV) the outer uniform-flow boundary in the radial direction. The outflow and outer uniform-flow boundaries (II and IV, respectively) of the computational domain are located sufficiently far from the jet exit and the centerline, respectively, to minimize the propagation of disturbances into the region of interest. Unsteady axisymmetric calculations are made on a physical domain of 80×50 mm using a 271×101 nonuniform grid system with clustered grid lines near the jet exit with

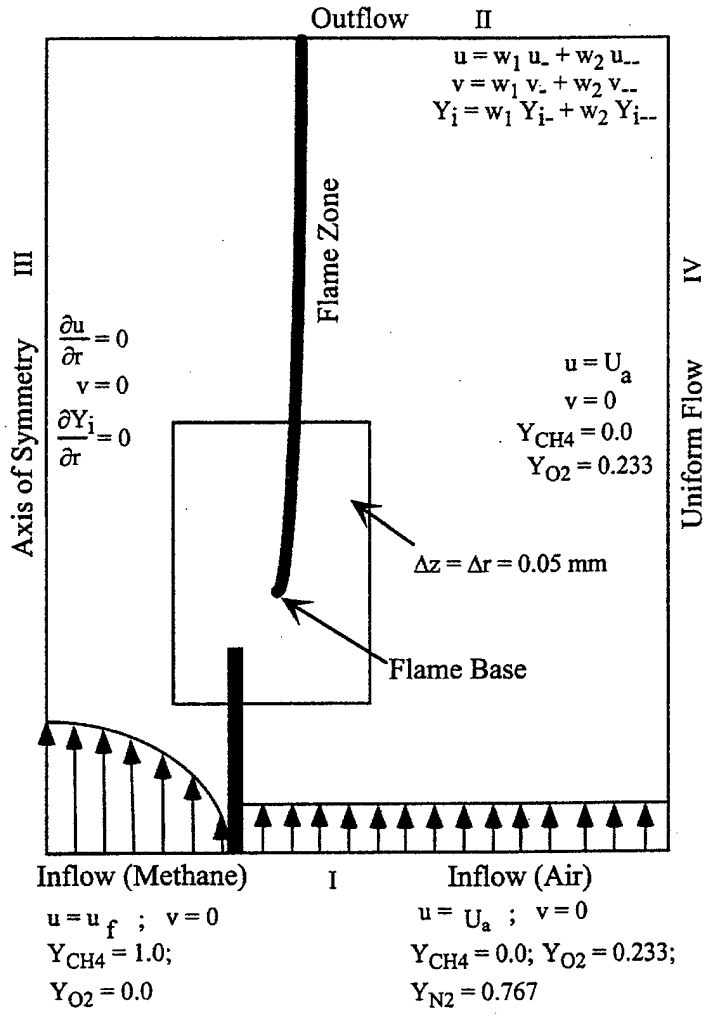

FIGURE 1 Computational domain and boundary conditions

a minimum spacing of 0.05 mm. The previous work (Katta and Roquemore, 1996, 1998) on counterflow and co-axial jet diffusion flames suggests that 0.05-mm grid spacing is sufficient for resolving the flame structure even with the GRI mechanism for methane combustion. The reaction zone thickness for the

flames considered in this paper based on short-lived species such as CH is about 0.6 mm; which is resolved by 12 grid points with the present grid system. In addition, the semi-implicit numerical scheme employed yields more accurate results on a coarse mesh compared to those obtained with an explicit numerical scheme.

The inner diameter (9.5 mm) and lip thickness (0.25 mm) of the fuel tube are close to those used in the previous experiments (Takahashi and Schmoll, 1991). The fuel tube exit plane is placed 10 mm from the inflow boundary I. A developed fuel-jet velocity profile and a uniform air velocity profile are used at the inflow boundary I. No-slip boundary conditions are enforced along the burner walls. Although the outflow boundary II is more difficult to treat if vortices develop (Katta and Roquemore, 1998) because the flow leaving this boundary continuously evolves in time as the vortices cross the boundary, the results presented in this paper are obtained under entirely laminar, vortex-free steady-state conditions. A simple extrapolation procedure with weighted zero- and first-order terms is used to estimate the flow variables on the boundary. The weighting factors, w_1 and w_2 (see Fig. 1), are selected by the trial-and-error approach; the main criterion used is that the disturbances crossing the outflow boundary should leave smoothly without generating unwanted reflections.

In this study, three different calculations have been performed using the three different chemistry models described above under the same flow conditions listed in Table III. The mean jet velocity (U_j = 1.7 m/s, the jet Reynolds number: ~1025) and the mean coflowing air velocity (U_a = 0.72 m/s) are the same as Case J5 in the previous work (Takahashi et al., 1998) and is slightly below the measured critical lifting-limit condition (U_{jc}= 2 m/s at U_a = 0.72 m/s [Takahashi and Schmoll, 1991]). Typically, a steady-state solution is obtained in approximately 30,000 time steps with Δt= 10 μs. This number comes down for the calculations that are started with a close initial solution.

TABLE III Test Conditions

Case	U_j *(m/s)*	U_a *(m/s)*	*Chemistry Model*
1	1.7	0.72	Peters/Warnatz C_1-chemistry, 17 species, 52 reactions
2	1.7	0.72	Peters/Warnatz C_2-chemistry, 24 species, 81 reactions
3	1.7	0.72	GRI-Mech/Warnatz C_2-chemistry, 31 species, 346 reactions

Finally, the mixture fraction (ζ) defined as the fraction of the mass at any location that originated from the fuel jet is determined from the calculated species mole fractions using the following expression (Nandula et al., 1994):

$$\zeta = 16.0[X_{CH_4} + X_{CH_3} + X_{CH_2} + X_{CH} + X_{CH_2O} + X_{CHO} + X_{CO_2} + X_{CO} + 0.5(X_{C_2H} + X_{C_2H_2} + X_{C_2H_3} + X_{C_2H_4} + X_{C_2H_5} + X_{C_2H_6} + X_{CHCO} + X_C + X_{CH_2(S)} + X_{CH_2OH} + X_{CH_3O} + X_{CH_3OH} + X_{CH_2CO} + X_{HCCOH})]$$

where

$$X_i = \frac{Y_i/M_i}{\sum_{j=1}^{N_s}(Y_j/M_j)}$$

RESULTS AND DISCUSSION

Flame-Flow Visualization

Figure 2 shows the two-color particle image velocimetry photographs of the stabilizing region of near-lifting methane jet diffusion flames at two different mean jet velocities (U_j = 1.7 and 1.8 m/s) at a fixed mean air velocity (U_a = 0.72 m/s). The technique used is described elsewhere (Takahashi et al., 1998). Submicron particles were illuminated by a sheet of green and red pulsed (10 ns) lasers with a known time delay; the high number-density cold outer airflow, a low number density hot zone around the flame, and the jet-external fluid dividing streamline were visualized. A time-exposure (1/30 s) image of the blue flame zone was also recorded in the photographs. Under the flow conditions approaching lifting, the flame base gradually shifted upward a few millimeters away from the burner rim (Fig. 2). The outer cold air was entrained into the fuel jet through the dark space between the flame base and the rim, thus thermally disconnecting the flame base from the burner rim. At the lifting condition (U_{jc} = 2 m/s), the flame base abruptly lifted off ~20 cm above the jet exit and became a turbulent flame. Thus, the standoff distance was extremely sensitive to a small variation in the mean jet velocity just before the lifting limit. It should be noted that the numerical simulations presented in this paper were performed for the above-mentioned *shifted* laminar flame conditions, not the lifted flame.

Near-Jet-Exit Field

Figure 3a shows the calculated velocity vectors (**v**), isotherms (T), and total heat-release rate ($\dot{q}$) contours in the stabilizing region for Case 2 (see Table III). The total heat-release rate is a sum of contributions of individual elementary

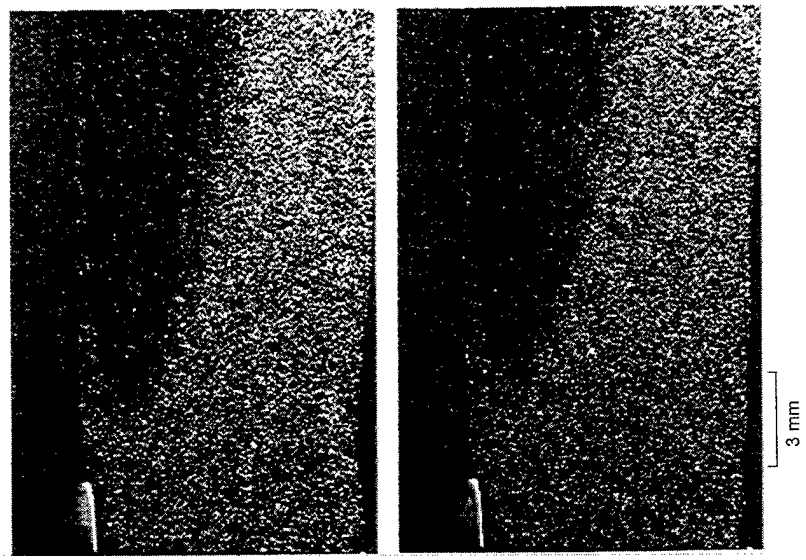

FIGURE 2 Two-color particle image velocimetry photographs of the stabilizing region of methane jet diffusion flames. $d = 9.45$ mm. Laser intensity: ~20 mJ/pulse; pulse width: 10 ns; time delay: 70 μs; and sheet thickness: ~0.5 mm. Exposure time: 1/30 s. Seed particles: zirconia (<1 μm, 97 %). $U_a = 0.72$ m/s. (a) $U_j = 1.7$ m/s, (b) $U_j = 1.8$ m/s (See Color Plate I at the back of this issue)

reaction steps. The heat-release rate showed a sharp peak at the base of the flame at relatively low temperatures (<1600 K) as was obtained for Case 1 shown in a previous paper (Takahashi et al., 1998). As shown in Figs. 3b and 3c, respectively, the molar oxygen consumption rate $(-\hat{\omega}_{O_2})$ and water vapor production rate $(\hat{\omega}_{H_2O})$ also have peaks close (typically ~0.05 mm) to the heat-release rate peak. The authors (Takahashi et al., 1998) named this highest reactivity spot (including the peaks of $\dot{q}$, $-\hat{\omega}_{O_2}$, and $\hat{\omega}_{H_2O}$) a *reaction kernel.*

It is notable that the calculated standoff distance (z_k) from the burner rim to the reaction kernel in the simulated flame depends on the chemistry model: Case 1, $z_k = 2.98$ mm; Case 2, $z_k = 4.13$ mm; and Case 3, $z_k = 2.38$ mm. Nevertheless, considering the extreme sensitivity of the standoff distance just before full-fledged lifting as described in the preceding section, it is remarkable that the simulated standoff distances of the shifted flames were in fair agreement with the experimental observation (~3 mm) in all cases. This point is particularly important because the flame base would drift away downstream and prematurely lift off if the kinetic parameters for reaction R45 by Peters (1993) were not replaced with those of Warnatz (1984). The influence of individual rates of elementary

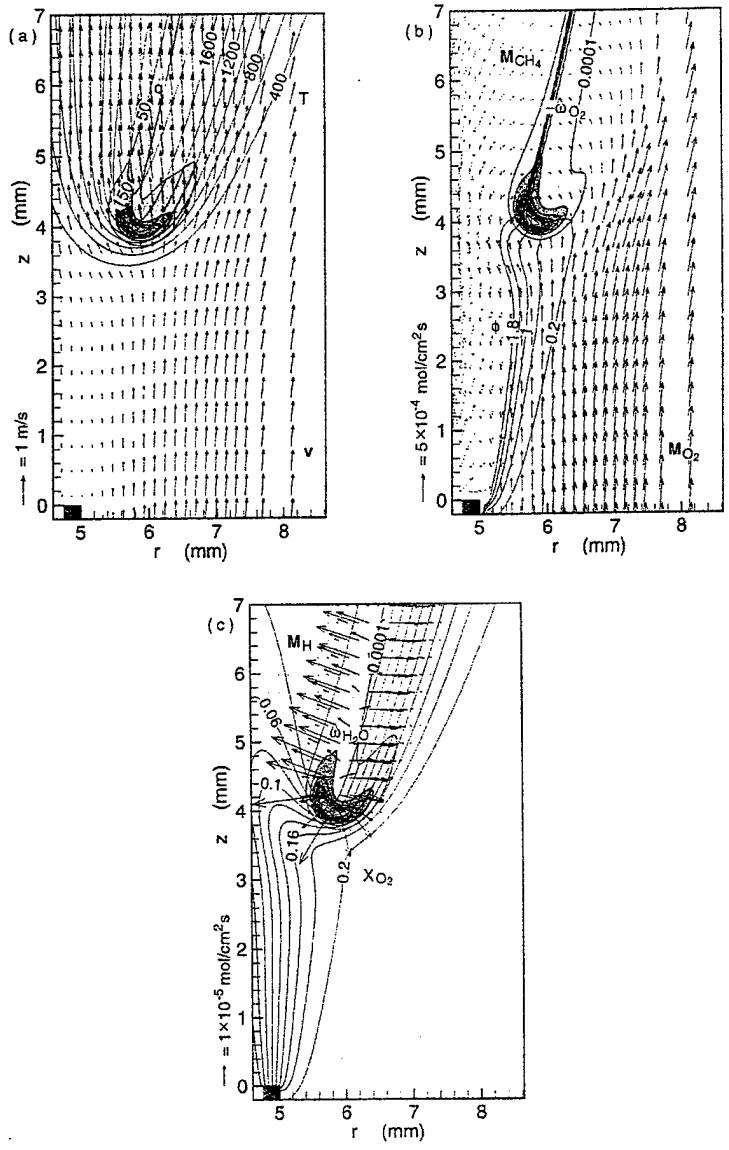

FIGURE 3 Calculated (a) velocity vectors, isotherms (unit, K), total heat-release rate (J/cm^3s); (b) molar flux vectors of methane (dashed) and molecular oxygen (solid), equivalence ratio based on the fuel and oxygen fluxes, and oxygen consumption rate (mol/cm^3s); (c) molar flux vectors of atomic hydrogen, mole fraction of oxygen, and water vapor production rate (mol/cm^3s) in the stabilizing region of methane jet diffusion flames. Case 2 (See Color Plate II at the back of this issue)

reactions on the standoff distance will be discussed later. The calculated standoff distance is also sensitive to the boundary layer velocity profile of the airflow developed outside the burner wall. Because the base of the shifted flame, unlike the rim-attached flame, is thermally disconnected from the burner wall (Fig. 3a) as observed experimentally (Fig. 2), the heat loss to the burner is insignificant in the flame stabilization although the flame base is aerodynamically cooled.

In Fig. 3a, there was a low velocity region near the burner rim and wake in the "dark" space between the flame base and the rim. The external fluid crossed the flame zone or penetrated through the dark space onto the fuel-side of the flame zone. In the hot zone around the flame, the external fluid accelerated and its stream tubes slightly expanded due to the longitudinal and lateral thermal expansion of gases, respectively. Despite the differences in the standoff distance for the three different cases (Case 1, Takahashi et al., 1998; Case 2, Fig. 3a; Case 3, not shown), the velocity vectors and temperature fields around the flame base are extremely similar.

Figure 3b shows the calculated total molar flux vectors of methane (M_{CH_4}, dashed) and molecular oxygen (M_{O_2}, solid), including both diffusion and convection terms, contours of the equivalence ratio (ϕ), and the oxygen consumption rate for Case 2. The equivalence ratio was determined from the fuel and oxygen molar fluxes, thus including the dynamic effects of both convection and diffusion. In the upper portion of the flame, the molar flux vectors of methane and oxygen turned toward the flame zone from the opposite sides, typical of diffusion flames. Partial premixing occurred in the dark space and the reaction zone was broadened around the fuel-lean ($\phi_k \approx 0.6$) reaction kernel. It should be noted that the leading edge (base) of the flame stabilizes at the fuel-lean side ($\phi < 1$), although one might speculate that the flame stabilizes at the fuel-rich side since the laminar burning velocity of methane-air premixed flames peaks around $\phi \approx 1.1$ (Lewis and von Elbe, 1961). However, the current result is consistent with the experimental measurements (Robson and Wilson, 1969; Takahashi et al., 1988) that revealed that the visible flame base was in the fuel-lean condition ($\phi \approx 0.6$). Robson and Wilson (1969) argued by quoting the results of the burning velocity measurements with heat losses by Kaskan (1957), who found that lean flames burn considerably faster than stoichiometric flames that are cooled to the same final temperature.

The present result shows that although the flame stabilizes in a partially premixed region, the stabilization of laminar diffusion flames is different from the characteristics of premixed flames as postulated by Gaydon and Wolfhard (1979). The thickness of the mixing layer within the flammability limits ($0.5 < \phi < 1.7$) just below the reaction kernel (approximately 0.6 mm) was much less than the minimum quenching distance of methane-air mixtures (2.2 mm [Lewis and

von Elbe, 1961]). Thus, the flame base cannot propagate through the mixing layer as a premixed flame. In other words, the flame base under investigation did not have the premixed-flame or triple-flame structure (Chung and Lee, 1991; Veynante et al., 1994; Wichman and Varatharajan, 1997; Plessing et al., 1998). This computed result is consistent with the experimental observation (Fig. 2) that the flame base has no premixed-flame wings.

Figure 3c shows the calculated total molar flux vectors of atomic hydrogen ($\mathbf{M}_H$), the mole fraction of molecular oxygen (X_{O_2}), and the rate of water vapor production for Case 2. In the upper portion, the molar flux vectors of atomic hydrogen pointed to the opposite sides of the flame zone as a result of strong diffusion. By contrast, hydrogen atoms diffused downward in every direction at the reaction kernel. This trend, peculiar to the geometric edge of the flame, was also found for other radical species (OH, O, and CH_3, etc.) generated in the high-temperature reaction zone. The flame base was more exposed to air (aerated); the oxygen mole fraction reached up to 10+ % and the oxygen concentration gradient also became steeper around the reaction kernel, thus increasing both convective and diffusive contributions to the oxygen flux. Therefore, as will be discussed in detail, various radical species back-diffused against the convective oxidizing flow, reacted with each other and with molecular oxygen, broadened the reaction zone, and increased the global reaction rates even at relatively low temperatures.

Trailing Flame Structure

To examine the detailed flame structure and compare the results for different chemistry models, the profiles of various variables are plotted at two different heights: the trailing flame zone and reaction kernel. Figures 4 and 5 show the radial variations of the temperature, species mole fractions (X_i), total heat release rate, and species production rates ($\hat{\omega}_i$) across the trailing flame zone at a height of 3 mm from the reaction kernel for the three cases. As discussed in a latter section, if the axial distance from the reaction kernel is used, the variations of the variables along the flame zone are similar and asymptotically approach constant values downstream. Thus, 3 mm from the reaction kernel is arbitrarily chosen, rather than a fixed height, to represent the trailing flame structure.

The distributions of the temperature and the mole fractions of major species (Fig. 4) are typical of diffusion flames, except for the increased oxygen mole fraction on the fuel side and residual methane on the air side due to the oxygen penetration and methane efflux through the dark space below the flame base. The variations of the temperature and mole fractions are very similar for the three cases, except for those of the fuel fragments (methyl radical CH_3 and C_2 species)

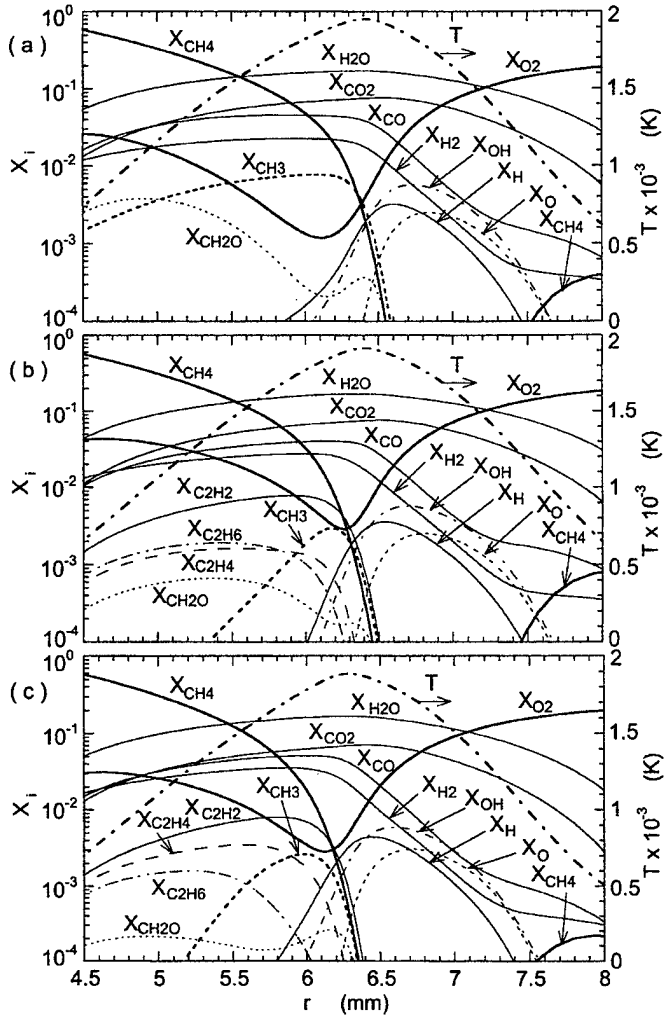

FIGURE 4 Variations of the calculated temperature and species mole fractions across the trailing flame zone ($z = z_k + 3$ mm). (a) Case 1, z= 6 mm; (b) Case 2, $z = 7.13$ mm; and (c) Case 3, $z = 5.38$ mm

and an oxidated hydrocarbon intermediate (formaldehyde CH_2O) on the fuel-side of the temperature peak. The production rates (Fig. 5) show that the hydrocarbon fragments, H_2, and CO were primarily formed on the fuel side and

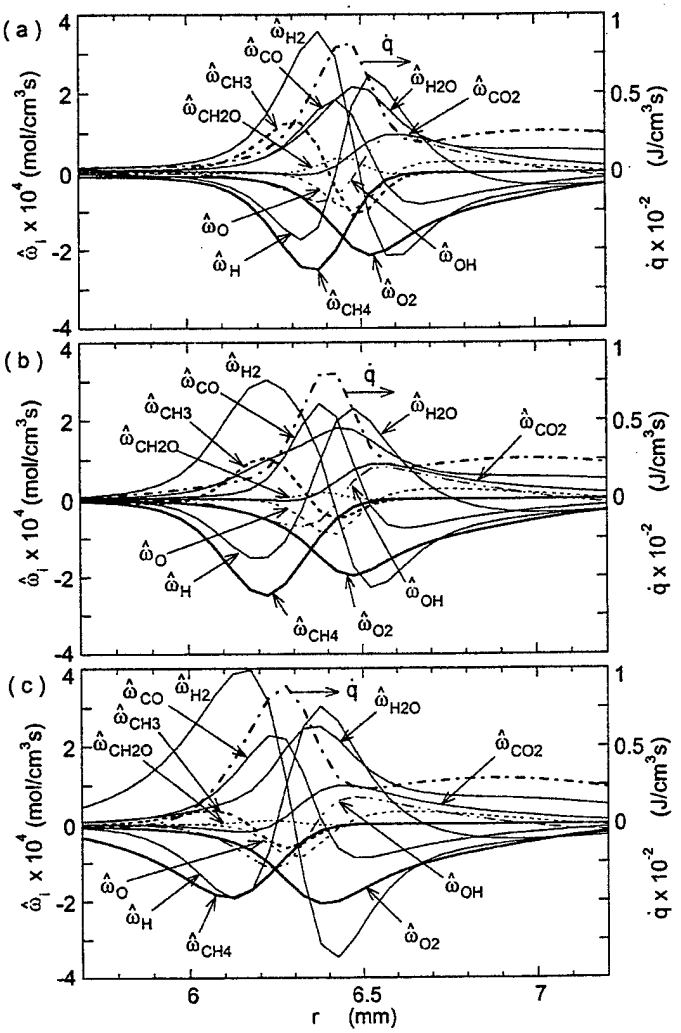

FIGURE 5 Variations of the calculated species formation rate across the trailing flame zone ($z = z_k + 3$ mm). (a) Case 1, $z = 6$ mm; (b) Case 2, $z = 7.13$ mm; and (c) Case 3, $z = 5.38$ mm

consumed on the air side of the peak temperature or heat-release rate; and the chain radical species (H, OH, and O) were produced on the air side and consumed on the fuel side. The methane consumption rate peak was on the fuel-side and that of oxygen and the production rates of the final products (H_2O, CO_2) were on the air side.

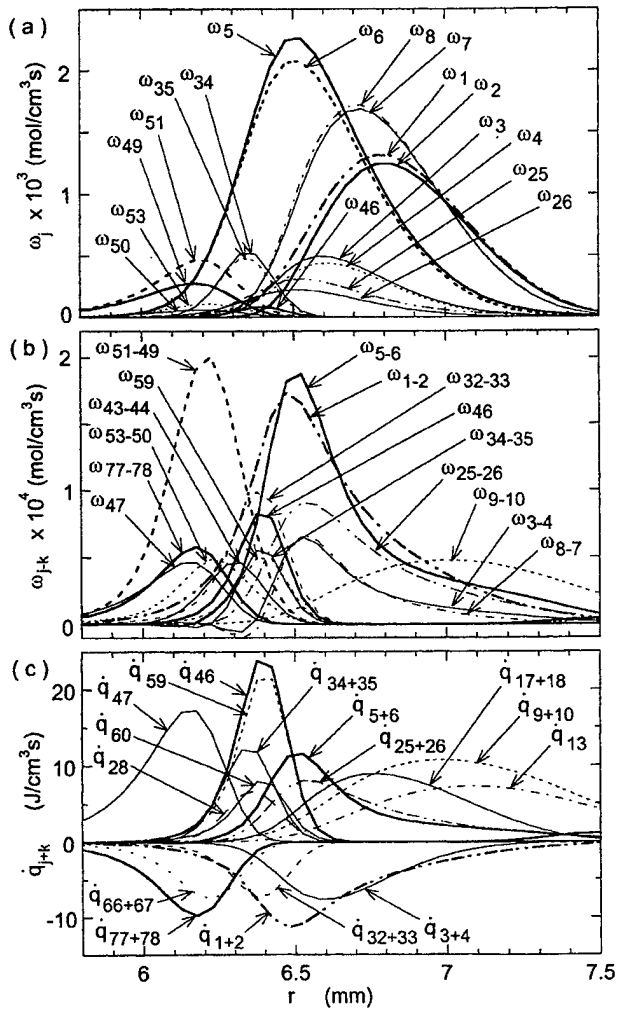

FIGURE 6 Variations of the calculated (a) individual reaction rates, (b) net reaction rates, and (c) net heat-release rates of major elementary steps across the trailing flame zone ($z = z_k + 3$ mm). Case 2, $z = 7.13$ mm

To investigate contributions of individual reaction steps to the flame structure, the results for Case 2 are presented here in more detail. Figure 6a shows the molar reaction rates of selected individual elementary reaction steps (ω_j). The

absolute magnitudes of ω_5, ω_6, ω_8, ω_7, ω_1, ω_2 were particularly large. As was reported previously (Takahahshi et al., 1998) for Case 1, pairing of forward and backward reactions was obvious; the differences indicate the deviation from partial equilibria. Fig. 6b shows the net reaction rates ($\omega_{j\text{-}k} = \omega_j - \omega_k$ or ω_j if the backward reaction was not included in the model). The reaction rate peaks revealed four distinct zones: fuel decomposition (see peaks of $\omega_{51\text{–}49}$, ω_{47}, $\omega_{77\text{–}78}$, $\omega_{53\text{–}50}$, and $\omega_{43\text{–}44}$) on the fuel side, hydrocarbon fragment oxidation/decomposition ($\omega_{32\text{–}33}$, ω_{46}, $\omega_{34\text{–}35}$, ω_{59}) around the peak temperature or heat-release rate ($r = 6.4$ mm), H_2-O_2 chain/product formation ($\omega_{5\text{–}6}$, $\omega_{1\text{–}2}$, $\omega_{25\text{–}26}$, $\omega_{3\text{–}4}$, $\omega_{8\text{–}7}$), and HO_2/H_2O reactions ($\omega_{9\text{–}10}$) on the air side. Figure 6c shows the net heat-release rates of the paired or non-paired reactions ($\dot{q}_{j+k} = \dot{q}_j + \dot{q}_k$ or $\dot{q}_j$). The major contributors to positive heat release are $\dot{q}_{46}, \dot{q}_{59}, \dot{q}_{34+35}, \dot{q}_{60}$, and $\dot{q}_{28}$ with their peak locations coincident with that of the total heat-release rate, ethane formation ($\dot{q}_{47}$) on the fuel side, the H_2/CO oxidation ($\dot{q}_{5+6}, \dot{q}_{25+26}$), and the HO_2/H_2O reactions ($\dot{q}_{9+10}, \dot{q}_{13}$) on the air side. The negative contributors are the C_2 hydrocarbon decomposition ($\dot{q}_{77+78}, \dot{q}_{66+67}$) on the fuel side, the chain branching reactions ($\dot{q}_{1+2}, \dot{q}_{3+4}$), and the CHO decomposition reaction ($\dot{q}_{32+33}$) on the air side.

The results illustrate a typical picture of methane oxidation processes in diffusion flames as summarized in Fig. 7. Here, the individual species are shown based on the approximate radial locations of the species formation rate peaks relative to the heat-release or temperature peak. The H attack on O_2 induces the chain branching (R1) to form a radical pool of H, OH, and O. The dehydrogenation of methane primarily by the H attack produces the CH_3 and H_2 (R51) and the OH attack on H_2 (R5) forms the product H_2O and further contributes to the radical-pool build-up. The fate of methyl radical plays a key role in the methane combustion (Warnatz, 1984). The methyl radical is oxidized by the O attack to form formaldehyde (R46), decompose to CH_2 (R43), or recombined with another methyl radical to form ethane (R47). The peak values of the reaction rates of these reactions were in the same order ($\omega_{46} \approx 8 \times 10^{-5}$mol/cm^{3}s, $\omega_{43\text{–}44} \approx 4.5 \times 10^{-5}$ mol/cm^{3}s, $\omega_{47} \approx 4.6 \times 10^{-5}$ mol/cm^{3}s). In the trailing flame zone, the concentration peaks of CH_3 and O were separated by the flame zone on the fuel and air sides, respectively (Fig. 4), and thus, R46 was limited in a narrow zone where the heat release peaks. The secondary peak of the formaldehyde mole fraction on the fuel side ($r \approx 5.4$ mm) in Fig. 4b is due to the high-concentration formaldehyde formed near the reaction kernel (to be shown) and transported by convection (see the velocity vectors in Fig. 3a) because the rate of formation vanished in this region at this height ($\hat{\omega}_{CH_2O}$ in Fig. 5b or ω_{46} in Fig. 6b). The lack of the C_2 route in Case 1 led to overprediction of the methyl radical and formaldehyde concentrations (Fig. 4a). For Cases 2 and 3 (Figs. 4b and 4c), the formation of

ethane (R47) significantly reduced the methyl radical mole fraction on the fuel side ($r < 6$ mm).

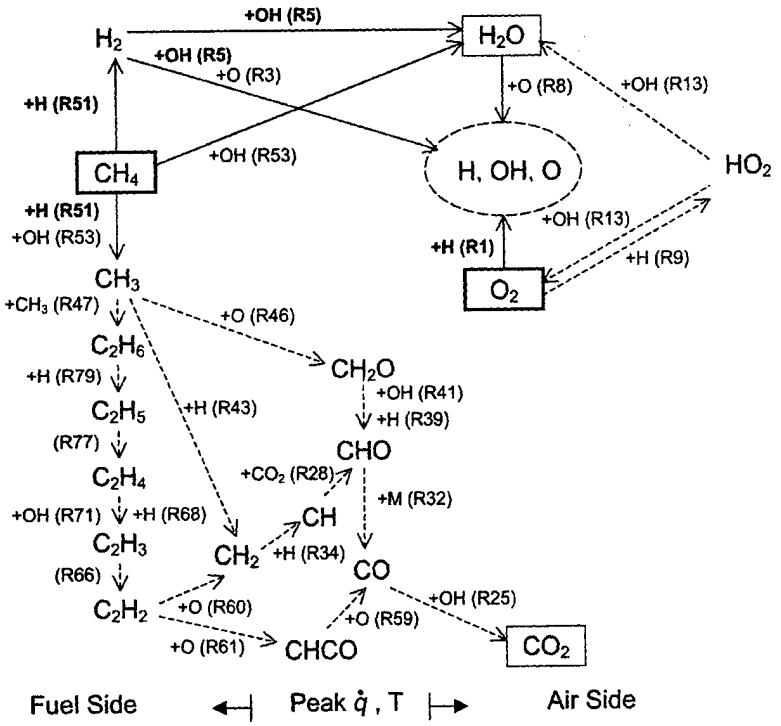

FIGURE 7 Flow diagram for the oxidation of CH_4 in the trailing flame zone. Peak net reaction rate: --> 0.00003 – 0.0001 mol/cm^{3}s; → >0.0001 mol/cm^{3}s. Case 2

Because Figs. 4 and 5 show the variations at different heights, depending on the standoff distances, the radial locations of the peak temperature, or heat-release rate, are slightly different among Cases 1 through 3. To correct for the level of jet fluid mixing in the radial direction and to examine the changes in the flame structure due to chemical kinetic effects, the selected variables are replotted against the mixture fraction in Fig. 8. Both the temperature and total heat-release rate peaks for Cases 1 – 3 were nearly at the same mixture fraction (~0.063), which was greater than the stoichiometric value for methane-air combustion (0.055). Unlike the simple fuel-oxygen stoichiometry, the current comprehensive computations, including multi-component multi-step chemistry and transport processes, simulated the non-equilibrium chemistry and preferential

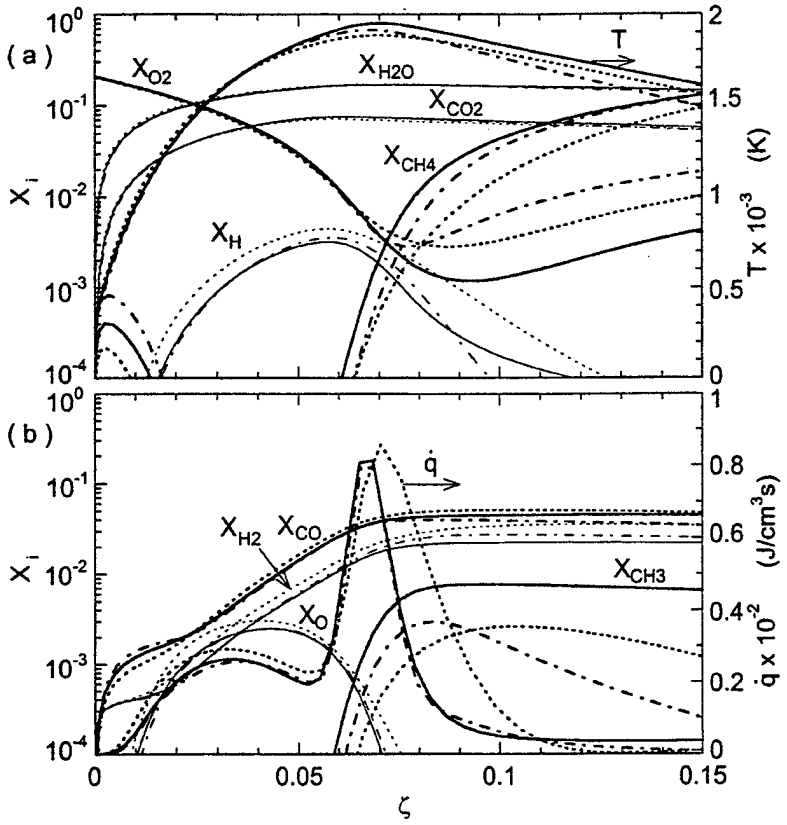

FIGURE 8 (a)(b) Variations of the calculated species mole fractions, temperature, and total heat-release rate as a function of the mixture fraction across the trailing flame zone ($z = z_k + 3$ mm). ——, Case 1, $z = 6$ mm; —·—, Case 2, $z = 7.13$ mm; ------, Case 3, $z = 5.38$ mm

diffusion effects. The variables on the air-side of the flame zone had similar values for all cases, while the kinetic effects were more evident on the fuel side. The chain radical species (H, OH, and O) formed on the air side diffused into the fuel side and attacked the initial fuel and its fragments. In general, Cases 2 and 3 resulted in lower temperature, lower X_{CH_4} and X_{CH_3}, and higher X_{O_2} than those of Case 1 on the fuel side. The differences between Cases 2 and 3 were more complicated because of the differences in the Peters (1993) and GRI (Frenklach, 1995) mechanisms in the reaction rates of the methyl formation/oxidation/recombination steps and the radical pool formation. In particular, Case 3

showed larger X_H and X_O, and deeper penetration of H and O into the fuel side, resulting in smaller X_{CH_4} and a wider $\dot{q}$ peak shifted toward the fuel side.

Reaction Kernel Structure

Figures 9 and 10 show the radial variations of calculated variables across the reaction kernel. The reaction kernel structure shows striking differences from the trailing diffusion flame structure. However, despite the differences in the stand-off distance, the variations are very similar among the three cases, except for the minor species on the fuel side. In all cases, there were secondary peaks in the oxygen mole fraction ($X_{O2} \approx 0.12$) on the fuel side of the relatively low peak temperature (1510–1545 K) and a small hump in the methane mole fraction (X_{CH4}: 0.005–0.011) on the air side. These resulted from the air penetration and the methane efflux through the dark space. The minimum oxygen mole fraction at the reaction kernel was substantially higher ($X_{O2} \approx 0.06$) than that in the trailing flame (X_{O2}: 0.001–0.004) and the measurement in moderately strained counterflow diffusion flames ($X_{O2} \approx 0.02$ [Tsuji and Yamaoka, 1971]). Furthermore, the distributions of the chain radicals (H, OH, and O) and CH_3 widely overlapped compared to the trailing flame (Fig. 4). The C_1 chemistry in Case 1 (Fig. 9a) again overpredicted the methyl radical and formaldehyde mole fractions on the fuel side. In all cases (Fig. 10), the oxygen consumption rate was widely distributed over the entire reaction zone, closely following the heat-release rate and water vapor production rate.

The results for Case 2 are presented in more detail in Fig. 11. Figure 11a shows the molar reaction rates of individual elementary reaction steps. Unlike the results for the trailing diffusion flame zone (Fig. 6a), the paring of forward and backward reactions is no longer obvious (except for R7/R8), thus departing farther away from the partial equilibrium. As a result, the net reaction rates (Fig. 11b) generally increased several times; particularly, those of the chain branching reaction $H + O_2 \rightarrow OH + O$ (ω_{1-2}) and methyl oxidation $CH_3 + O \rightarrow CH_2O + H$ (ω_{46}) were enhanced nearly an order of magnitude. It is also noticed that the clear separation in four zones in the radial direction observed in the trailing flame does not exist and that reactions involving HO_2 (ω_{9-10} and ω_{11}) are still evident on the air side. Fig. 11c shows the net heat-release rates of individual reaction steps. The most striking feature is a ten-fold increase in $\dot{q}_{46}$ compared to that in the trailing flame (Fig. 6c). Other positive contributions besides the product formation ($\dot{q}_{5+6}$ and $\dot{q}_{25+26}$) include the oxidation reactions ($\dot{q}_{29}, \dot{q}_{41}$, and $\dot{q}_{59}$) and HO_2 reactions ($\dot{q}_{9+10}, \dot{q}_{11}$, and $\dot{q}_{13}$). The negative

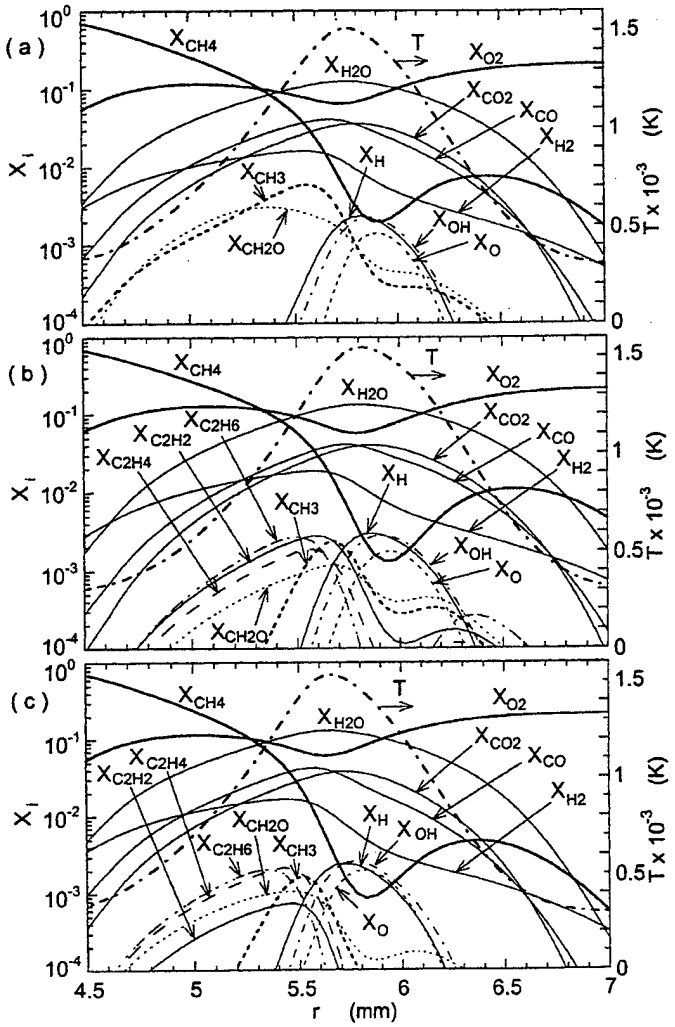

FIGURE 9 Variations of the calculated temperature and species mole fractions across the reaction kernel ($z = z_k$). (a) Case 1, $z = 2.98$ mm; (b) Case 2, $z = 4.13$ mm; and (c) Case 3, $z = 2.38$ mm

contributors are the chain-branching reaction ($\dot{q}_{1+2}$) and hydrocarbon decomposition reactions ($\dot{q}_{32+33}$, $\dot{q}_{77+78}$, and $\dot{q}_{66+67}$).

The reaction paths in the reaction kernel are summarized in Fig. 12. In the reaction kernel, the chain radical species (H, OH, O) and the fuel fragments (CH_3

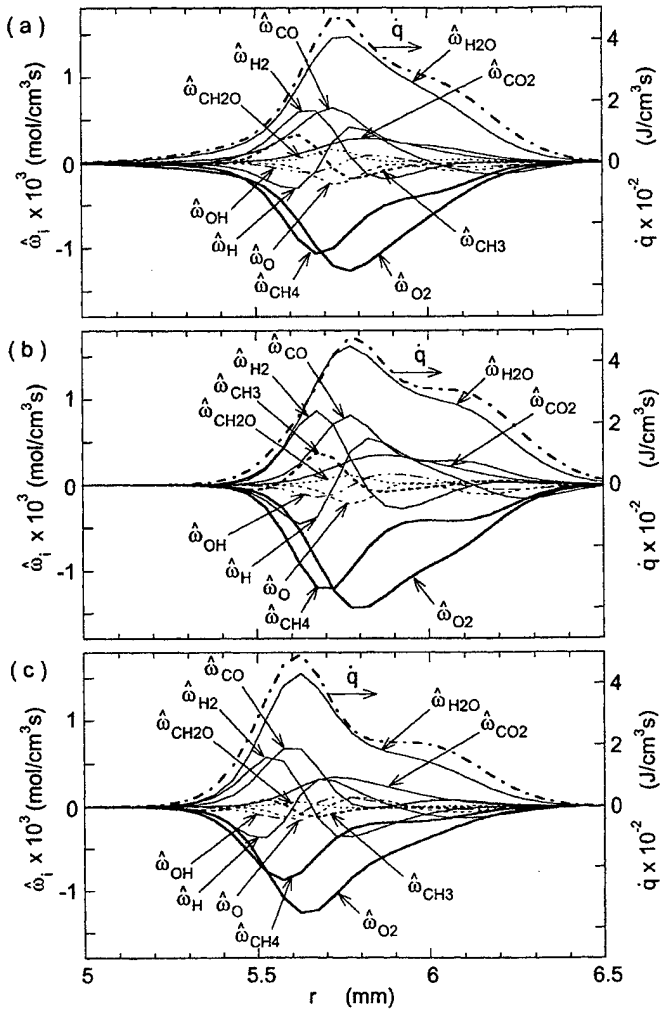

FIGURE 10 Variations of the calculated species formation rate across the reaction kernel ($z = z_k$). (a) Case 1, $z = 2.98$ mm; (b) Case 2, $z = 4.13$ mm; and (c) Case 3, $z = 2.38$ mm

and H_2) formed in the high temperature reaction zone downstream could diffuse back downward directly into the oxygen-rich (fuel-lean) reaction kernel against the upward oxidizing flow. As a result, the H attack on O_2 promoted the chain branching reaction $H + O_2 \rightarrow OH + O$ (R1) and subsequent chain reactions, thus

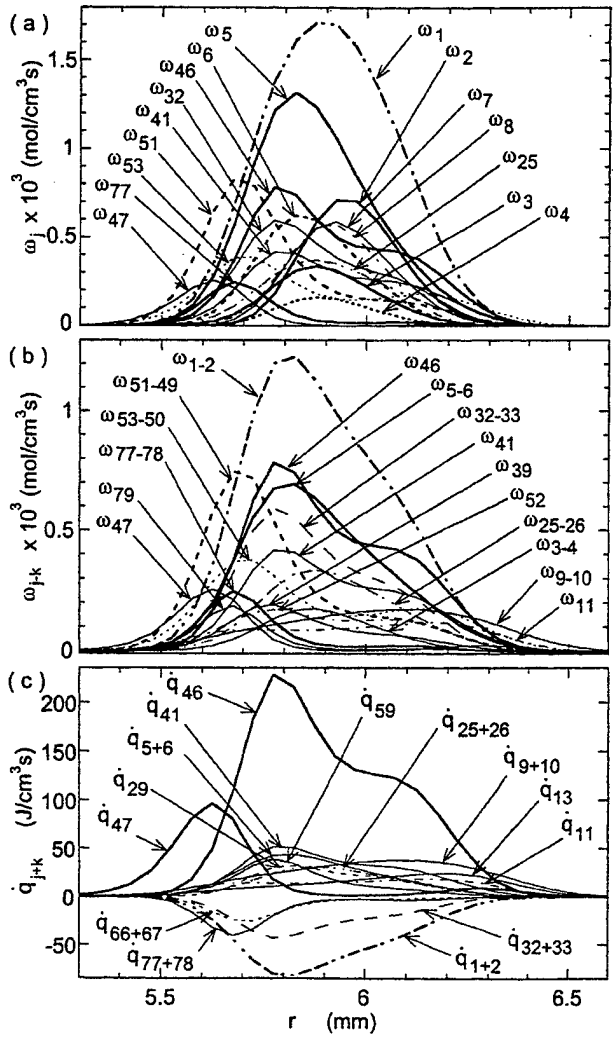

FIGURE 11 Variations of the calculated (a) individual reaction rates, (b) net reaction rates, and (c) net heat-release rates of major elementary steps across the reaction kernel ($z = z_k$). Case 2, $z = 4.13$ mm

building up the radical pool at high reaction rates. In addition to the H attack on CH_4 (R51), the OH radical also participated to the CH_4 dehydrogenation (R53). More importantly, the O attack on CH_3(R46) (peak $\omega_{46} \approx 8 \times 10^{-4}$ mol/cm^{3}s) significantly surpassed the other pathways ($\omega_{43-44} \approx 6 \times 10^{-5}$ mol/cm^{3}s, $\omega_{47} \approx$

2.5×10^{-4} mol/cm^{3}s) and predominantly contributed (peak $\dot{q}_{46} \approx 230\,\mathrm{J/cm^3s}$) to the total heat-release rate peak at the reaction kernel ($\dot{q}_k \approx 480\,\mathrm{J/cm^3s}$).

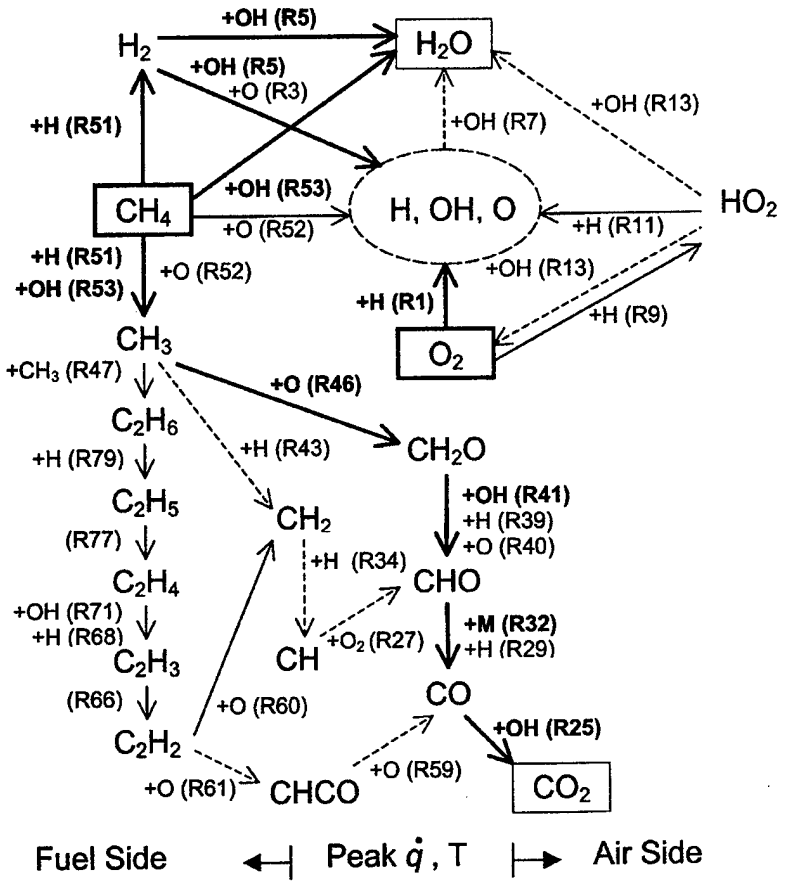

FIGURE 12 Flow diagram for the oxidation of CH_4 in the reaction kernel. Peak net reaction rate: --> 0.00006 – 0.0001 mol/cm^{3}s; → 0.0001–0.0003 mol/cm^{3}s; ← >0.0003 mol/cm^{3}s. Case 2

Figure 13 shows the variations of the selected variables as a function of the mixture fraction across the reaction kernel. The mixture fractions at both temperature and total heat-release rate peaks for Cases 1 – 3 were approximately 0.05, which was smaller than the stoichiometric value for methane-air combustion (0.055) in contrast to the greater value in the trailing flame (Fig. 8). The high

concentration of oxygen in a wide range and the fuel efflux onto the air side enabled the CH_4 decomposition and oxidation even on the fuel side. Consequently, a wide overlapping zone of high X_{CH_3} and X_O was created on the air side and, thus, the heat-release rate peak widened and shifted toward the air side.

Reaction Kernel Standoff Distance

The axial location of the reaction kernel shifted downstream as the C_2 chemistry was added: Case 1, $z_k \approx 3$ mm, Case 2, $z_k \approx 4$ mm. As a result of the additional methyl radical destruction step to form ethane, the methyl concentration dropped significantly on the fuel side (peak X_{CH3}: ~0.0006 for Case 1 [Fig. 9a], ~0.0002 for Case 2 [Fig. 9b]). The additional reactions for the C_2 path through R47 consumed CH_3 in the fuel side and competed with the formaldehyde formation (R46). Furthermore, the C_2 path might compete with other species for radicals. Thus, the overall methane decomposition and oxidation processes slowed down, thereby shifting the reaction kernel downstream (upward) to a new stabilizing point and gaining a longer fuel-air mixing time.

Because the standoff distance directly relates to the mechanism for flame stabilization, the influence of individual rate coefficients of methane and methyl consumption reaction steps (R43-R53) was investigated by a unique approach; the reaction rates were artificially decreased 1/10 or increased 10 times for Case 2. Although the procedure resembles the conventional sensitivity analysis, in which the effect of a small change in the reaction rate on the rate-related quantity is examined, here the reaction rate was varied rather substantially to see the effect on a global property; i.e., the standoff distance. In this manner, important reactions in flame stabilization can be identified and their relations to the two-dimensionally distributed flame structure can be revealed. Case 2 was used to include C_2 chemistry effect, and the number of time steps was limited to 3000 to obtain reasonable results within acceptable computation times. Figure 14 shows the changes in the standoff distance of the reaction kernel (Δz_k), in which positive values indicate the flame-base movement away from the burner rim and negative is vice versa. In a global sense, higher rates of fuel oxidation move the flame base toward the rim (stabilizing) and vice versa (destabilizing). More precisely from the chemical kinetics standpoint, there are several influential factors; i.e., whether the initial magnitudes of ω_j and reactants' X_i are large or small among others, whether a radical species is formed or destroyed, whether the direction of the reaction is for or against the general oxidation pathways, and whether it is exothermic (positive $\dot{q}_j$) or endothermic (negative $\dot{q}_j$).

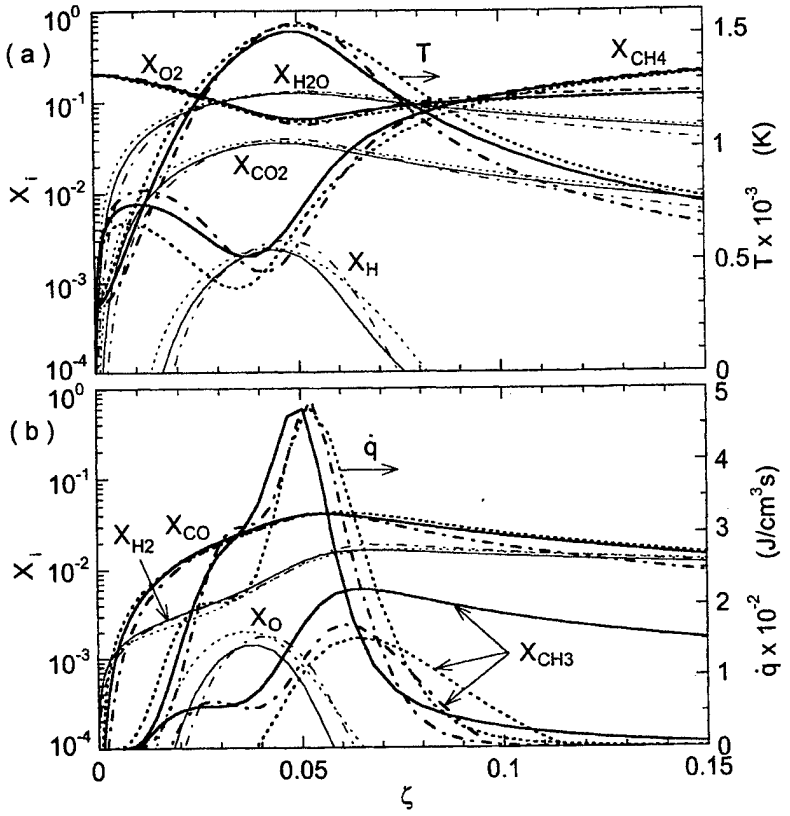

FIGURE 13 (a)(b) Variations of the calculated species mole fractions, temperature, and total heat-release rate as a function of the mixture fraction across the reaction kernel ($z = z_k$). ——, Case 1, $z = 2.98$ mm; ——·——, Case 2, $z = 4.13$ mm; -------, Case 3, $z = 2.38$ mm

The most significant influence was observed for both increased and decreased rates of the $CH_4 + H \rightarrow CH_3 + H_2$ reaction (R51) (flame destabilizing and stabilizing, respectively) and the increased rate of the reverse reaction (R49) (stabilizing). Although this reaction was a major fuel decomposition step in the CH_4 oxidation (Fig. 12), X_{CH4} was an order of magnitude larger than other hydrocarbon fragments (Fig. 8) and the initial ω_{51} was large ($\approx 8\times10^{-4}$ mol/cm^{3}s at the peak, see Fig. 11a) on the fuel side of the reaction kernel. As a result, R51 with $10\times\omega_{51}$ efficiently removed the H atoms, which were needed for the chain-branching reaction (R1) to establish the radical pool, thus causing the

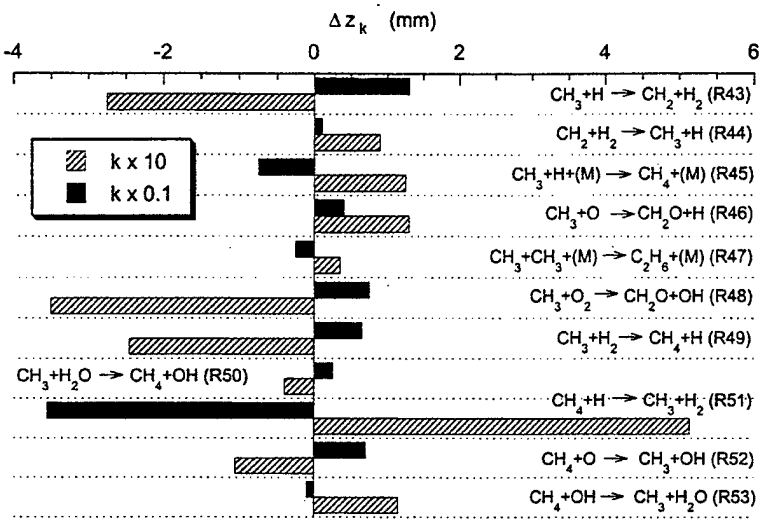

FIGURE 14 Influence of the variation of individual rate coefficients by a factor of 1/10 or 10 on the calculated standoff distance of the reaction kernel of a methane jet diffusion flame. Case 2

flame destabilizing effect. Because ω_{49} was an order of magnitude smaller ($\approx 8\times10^{-5}$ mol/cm^{3}s at the peak) than ω_{51}, the ten-fold increase of ω_{49} resulted in a flame stabilizing effect similar to that of a 1/10 decrease in ω_{51}, but a 1/10 decrease of already-small ω_{49} exerted a much smaller destabilizing impact compared to $10\times\omega_{51}$. An increase in the rate of the $CH_3 + O_2 \rightarrow CH_2O + OH$ reaction (R48) also moved the flame base close to the rim (stabilizing). Because of the partial premixing and the abundance of molecular oxygen around the reaction kernel, the oxidation processes via formaldehyde are considered to be the major route similar to premixed combustion (Warnatz, 1984). Thus, because the initial ω_{48} was small ($\approx 3\times10^{-5}$ mol/cm^{3}s at the peak), its 10× increase contributed to accelerate the oxidation in addition to the major contributor CH_3+ O → CH_2O + H (R46) (see Fig. 12). The effect of the 1/10 decrease of already-small ω_{48} was as small as that for R49. The effect of the major CH_3 oxidation reaction (R46) was more complicated (10× and 1/10 changes were both flame destabilizing). Because the initial ω_{46} was large ($\approx 8\times10^{-4}$ mol/cm^{3}s at the peak), its 10× increase effectively removed the O atoms and 1/10 decrease cut off the main oxidation path, thus both experiencing the destabilization effect. The $CH_3 + H \rightarrow CH_2$+ H_2 reaction (R43) also influenced significantly the standoff distance by affecting another oxidation path $CH_4 \rightarrow CH_3 \rightarrow CH_2 \rightarrow CH \rightarrow CHO \rightarrow CO$ (Fig. 12). Because the initial ω_{43} was small ($\approx 6\times10^{-5}$ mol/cm^{3}s at the peak),

increasing ω_{43}ten times promoted the oxidation route in parallel to the formaldehyde route through R46 (Fig. 12) without significantly removing the H atoms, thus exerting the flame stabilizing effect. Since ω_{44} was small ($\approx 2\times10^{-6}$ mol/cm^{3}s), its 1/10 effect was negligible. Although R45 was similar to R43, R45's direction was opposite that of R43 with respect to the fuel decomposition/oxidation pathways, resulting in the reverse effect. The R53/R50 reactions had similar effects with R51/49 in removing radical species, but with a much smaller magnitude because the OH radical reaction (R5) played a lesser role than the chain-branching reaction by the H atom (R1) in the radical pool buildup (Fig. 12). Since R52 was chain carrying and ω_{52} was moderate ($\approx 2\times10^{-4}$ mol/cm^{3}s), its 10× increase helped the fuel decomposition without having much impact on the radical pool, thus resulting in the flame stabilizing effect; the 1/10 effect is vice versa. The increase in ω_{47} for the C_2 pathway was flame destabilizing because of the competition with R46 for CH_3 and delayed the global fuel oxidation processes, but its impact was relatively small probably because no chain radicals were involved in the reaction.

Therefore, the fate of hydrogen atom; i.e., the competition between the rates of H removal by methane (R51) and the chain-branching reaction with molecular oxygen (R1), and the fate of methyl radical; i.e., the competition between the rates of the major methyl oxidation step (R46) and others (R48, R43), played key roles in determining the location of the base of the shifted diffusion flames. Thus, in diffusion flames, the rates of individual reactions are coupled with the flame structure (i.e., the 2D distributions of species concentrations, fluxes, production rates, temperature, and velocity) around the reaction kernel and are indeed important in flame stabilization.

Flame Stabilization

Figure 15 shows the variations in (a) the temperature and heat-release rate; (b) axial and radial velocity components; (c) convective, diffusive molar fluxes, and consumption rates of oxygen; and (d) methane along the flame zone for Cases 1 through 3. The abscissa is the axial distance from the reaction kernel ($z - z_k$) with the radial location following the maximum temperature envelope. The results using the maximum heat-release rate envelope (not shown) are similar. For all cases, the variations are similar; the temperature reached 1510–1545 K at the reaction kernel and asymptotically approached 1900–2000 K, with Case 1 highest and Case 3 lowest (Fig. 15a). Because the axial (or total) velocity along the flame zone kept increasing downstream (Fig. 15b), the trailing diffusion flame might drift away downstream if not supported by upstream portions. The diffusive molar fluxes and consumption rates of oxygen (Fig. 15c) and fuel (Fig. 15d)

peaked near the reaction kernel ($z \approx z_k$), a sink of the reactants. In addition, the convective contribution to the total oxygen flux was also several times larger at the reaction kernel than that in the trailing flame because of the high concentration of oxygen (Fig. 9b) in the broadened reaction zone (Fig. 15c). Thus, the reactivity (peak $\dot{q}$, $-\hat{\omega}_{O_2}$, $-\hat{\omega}_{CH_4}$, and $\hat{\omega}_{H_2O}$) at the reaction kernel is several times larger than that in the trailing diffusion flame. Therefore, the reaction kernel apparently stabilized the trailing flame; the reaction kernel provided a stationary ignition source to the incoming reactants and sustains stable combustion in the flow field. As the reaction kernel secures the stable combustion, the trailing diffusion flame zone can be successively supported, thus keeping the flame from lifting.

CONCLUSIONS

The current comprehensive numerical simulations revealed the detailed flame structure, including the chemical kinetic nature, of the stabilizing region of laminar methane jet diffusion flames. A unique geometric configuration of the flame edge (base) allowed fuel fragments and radical species formed in the high-temperature reaction zone (mainly CH_3 and H_2 on the fuel side and H, OH, and O on the air side) to diffuse back downward against the upward oxidizing flow and react each other and with molecular oxygen. Consequently, the reaction kernel with the highest reactivity ($\dot{q}, -\hat{\omega}_{O_2}$, and $\hat{\omega}_{H_2O}$) was formed in a relatively low-temperature (<1600 K), oxygen-abundant ($X_{O_2} > 0.06$), broadened reaction zone at the flame base. In the reaction kernel, the net rate of the chain-branching reaction $H + O_2 \rightarrow OH + O$ (R1) was augmented by an order of magnitude compared to that in the trailing flame, and the major CH_3 oxidation reaction $CH_3 + O \rightarrow CH_2O + H$ (R46) predominantly contributed to the heat-release rate peak. The calculated standoff distance of the reaction kernel was comparable to that observed experimentally with some variations due to the chemical kinetic model used. Nevertheless, the calculated reaction kernel structure was nearly identical for all chemistry models, except that the C_1-chemistry model overpredicted methyl and formaldehyde mole fractions on the fuel-side of the flame zone. As C_2-chemistry was added in the Peters/Warnatz mechanism (Case 1 to 2), the overall methane decomposition and oxidation processes were delayed by additional radical removal by hydrocarbons, thus shifting the reaction kernel farther downstream. The standoff distance was sensitive to methane and methyl consumption reactions, particularly the $CH_4 + H \Leftrightarrow CH_3 + H_2$ reactions (R51/R49), which compete for the H atoms with R1, and the $CH_3 + O_2 \rightarrow CH_2O + OH$ reaction (R48), which augment the CH_3 oxidation in addition to

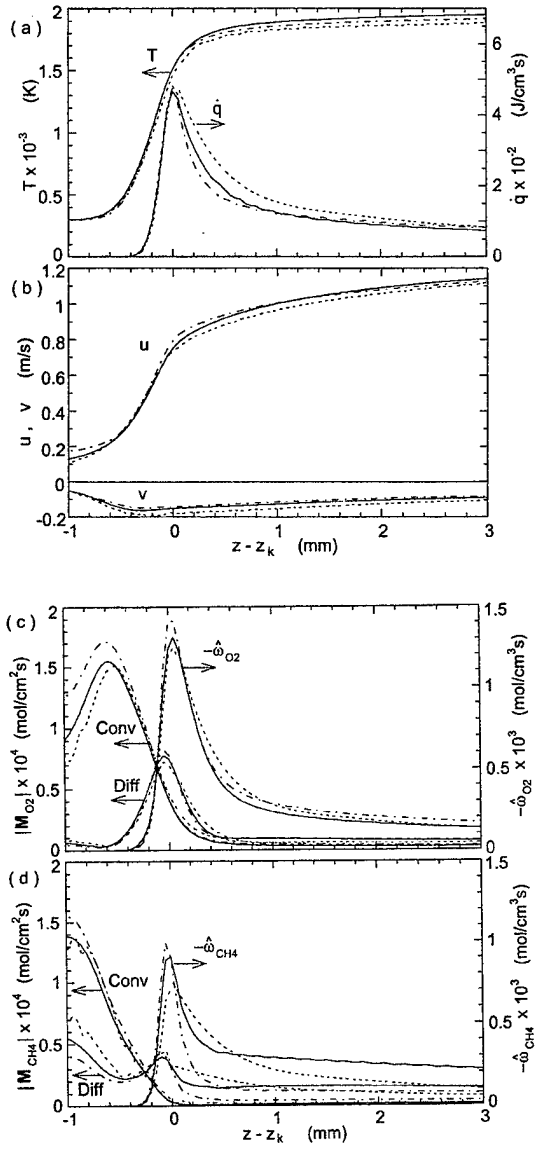

FIGURE 15 Variations of the calculated (a) temperature and heat release rate; (b) axial and radial velocity components; (c) convective, diffusive molar fluxes, and consumption rate of oxygen; and (d) methane along the maximum temperature envelope in the stabilizing region of a methane jet diffusion flame. ——, Case 1, $z_k = 2.98$ mm; ——, Case 2, $z_k = 4.13$ mm; ------, Case 3, $z_k = 2.38$ mm

R46. Therefore, in a global sense, the rates of these reactions (R1, R46, R51, and R48) are critical to determining how fast the reactants can be consumed and whether or not the stationary reaction kernel can be formed in the incoming oxidizing flow with a certain velocity. If the reactions cannot be completed within the residence time available, the stationary reaction kernel cannot be sustained, the trailing flame drifts away downstream, and the flame eventually lifts or blows off. The knowledge of the detailed chemical kinetic structure of the reaction kernel – an essential part of the flame stabilization mechanism – may lead to a means to augment flame holding or retard fire spread.

NOMENCLATURE

A	A coefficient used in the finite-difference equation
A_k	Pre-exponential factor in the Arrhenius rate expression
c_p	Specific heat at constant pressure
D_{im}	Diffusion coefficient for species i in the mixture
E	Activation energy
g	Gravitational acceleration
H	Enthalpy
h	Total enthalpy
$h^{\circ}_{f,i}$	Standard heat of formation for species i
Le	Lewis number
M	Molecular weight
$\mathbf{M}$	Molar flux vector
N_s	Total number of species
p	Pressure
$\dot{q}$	Heat-release rate
R_0	Universal gas constant
r	Radial distance
S^{Φ}	Source term in the Φ-equation
T	Temperature
t	Time
u	Axial-velocity component

U	Mean velocity
v	Radial-velocity component
$\mathbf{v}$	Velocity vector
X_i	Mole fraction of species i
Y_i	Mass fraction of species i
z	Axial distance
α	A constant appearing in the modified Arrhenius rate expression
ϕ	Equivalence ratio
Φ	A flow variable
Γ^{Φ}	Transport coefficient in the Φ-equation
λ	Thermal conductivity
μ	Viscosity
ρ	Density
ρ_0	Density of air
$\dot{\omega}_i$	Mass rate of production of species i
$\hat{\omega}_i$	Molar rate of production of species i
ω_j, ω_k	Molar reaction rates for the reaction step j and k, respectively
ζ	Mixture fraction

Subscripts

a	Co-flowing air
i	Species i
j	Jet fluid
j, k	Reaction steps j and k, respectively
k	Reaction kernel
P	Reference grid point
z^+, r^+	Grid points adjacent to P in the positive z and r directions, respectively
z^{++}, r^{++}	Two grid points away from P in the positive z and r directions, respectively
z^-, r^-	Grid points adjacent to P in the negative z and r directions, respectively
z^{--}, r^{--}	Two grid points away from P in the negative z and r directions, respectively

Superscripts

$N, N+1$ Time-step numbers

Acknowledgements

This work was supported by the U. S. Air Force Research Laboratory, Propulsion Directorate, Propulsion Sciences and Advanced Concept Division, Wright-Patterson Air Force Base, Ohio, under Contract No. F33615–97-C-2719 (Technical Monitor: C. W. Frayne). An initial version of this paper was published as "A Role of Chemical Kinetics in the Simulation of the Reaction Kernel of Methane Jet Diffusion Flames," F. Takahashi and V. R. Katta, in the Proceedings of the 5th ASME/JSME Joint Thermal Engineering Conference (AJTE99–6190) by The American Society of Mechanical Engineers.

References

Buckmaster, J. and Weber, R. (1996). Edge-flame holding. *Twenty-Sixth Symposium (International) on Combustion*, The Combustion Institute, Pittsburgh, Pennsylvania, pp. 1143–1149.

Chung, S. H. and Lee, B. J. (1991). On the characteristics of laminar lifted flames in a nonpremixed jet. *Combust. Flame* **86**, 62.

Frenklach, M., Wang, H., Goldenberg, M., Smith, G. P., Golden, D. M., Bowman, C. T., Hanson, R. K., Gardiner, W. C., Lissianski, V. (1995). GRI-Mech – an optimized detailed chemical reaction mechanism for methane combustion. Technical Report No. GRI-95/0058, Gas Research Institute, Chicago, Illinois.

Gaydon, A. G. and Wolfhard, H. G. (1979). *Flames-Their structure, radiation and temperature*, 4th Ed., Champman and Hall, London, p. 39.

Hirschfelder, J. O., Curtis, C. F., and Bird, R. B. (1954). *The Molecular Theory of Gases and Liquids*, Chaps. 8 and 9, Wiley, New York.

Kaskan, W. E. (1957). The dependence of flame temperature on mass burning velocity. *Sixth Symposium (International) on Combustion*, Reinhold, New York, pp. 134–143.

Katta, V. R., Goss, L. P., and Roquemore, W. M. (1994). Numerical investigations of transitional H_2/N_2 jet diffusion flames. *AIAA J.* **32**, 84.

Katta, V. R. and Roquemore, W. M. (1996). Extinction in methane-air counterflow diffusion flame-a direct numerical study. Central States/The Combustion Institute Meeting, St. Louis. Paper No. 80, pp. 449–454.

Katta, V. R. and Roquemore, W. M. (1998). Simulation of dynamic methane jet diffusion flames using finite rate chemistry models. *AIAA J.* **36**, 2044.

Kawamura, T., Asato, K., and Mazaki, T. (1980). Structure analysis of the stabilizing region of plane, laminar fuel-jet flames. *Combust. Sci. Technol.* **2**, 211.

Leonard, B. P. (1979). A stable and accurate convective modeling procedure based on quadratic upstream interpolation. *Computer Methods in Appl. Mech. and Engrg.* **19**, 59–98.

Lewis, B. and von Elbe, G. (1961). *Combustion, Flames and Explosions of Gases*, 2nd Ed., Academic Press, New York, 1961, p. 458.

Nandula, S. P., Brown, T. M., and Pitz, R. W. (1994). Measurements of scalar dissipation in the reaction zones of turbulent nonpremixed H_2-air flames. *Combust. Flame* **99**, 445.

Peters, N. (1993). Flame calculations with reduced mechanisms – an outline. In N. Peters and B. Rogg (Eds.) *Reduced Kinetic Mechanisms for Applications in Combustion Systems*, Springer-Verlag, Berlin, pp. 3–14.

Plessing, T., Terhoeven, P., Peters, N., and Mansour, M. S. (1998). An experimental and numerical study on a laminar triple flame. *Combust. Flame* **115**, 335.

Robson, K. and Wilson, M. J. G. (1969). The stability of laminar diffusion flames of methane, *Combust. Flame* **13**, 626.

Roquemore, W. M., and Katta, V. R. (1998). Role of flow visualization in the development of UNICORN. *Proceedings of VSJ-SPIE98*, Yokohama, Japan, Paper No. KL310.

Spalding, D. B. (1972). A novel finite difference formulation for difference expressions involving both first and second derivatives. *Int. J. Numerical Methods in Engng.* **4**, 551.

Sung, C. J., Liu, J. B., and Law, C. K. (1995). Structural response of counterflow diffusion flames to strain rate variations. *Combust. Flame* **102**, 481.

Takahashi, F. and Katta, V. R. (1995). Numerical experiments on the vortex-flame interactions in a jet diffusion flames. *J. Propulsion Power* **11**, 170.

Takahashi, F. and Katta, V. R. (1996). Unsteady extinction mechanisms of diffusion flames. *Twenty-Sixth Symposium (International) on Combustion*, The Combustion Institute, Pittsburgh, Pennsylvania, pp. 1151–1160.

Takahashi, F. and Katta, V. R. (1997). A numerical study of a methane diffusion flame over a flat surface. *Proceedings of the Second International Symposium on Scale Modeling*, Lexington, Kentucky, pp. 271–282.

Takahashi, F. and Schmoll, W. J. (1991). Lifting criteria of jet diffusion flames. *Twenty-Third Symposium (International) on Combustion*, The Combustion Institute, Pittsburgh, Pennsylvania, pp. 677–683.

Takahashi, F., Mizomoto, M., Ikai, S., Futaki, N. (1985). Lifting mechanism of free jet diffusion flames. *Twentieth Symposium (International) on Combustion*, The Combustion Institute, Pittsburgh, pp. 295–302.

Takahashi, F., Mizomoto, M., and Ikai, S. (1988). Structure of the stabilizing region of a laminar jet diffusion flame. *J. Heat Transfer* **110**, 182.

Takahashi, F., Durbin, M. D., and Vangsness, M. D. (1996). Stabilization of hydrogen jet diffusion flames with or without swirl. In S. H. Chan (Ed.) *Transport Phenomena in Combustion*, Taylor & Francis, Washington, D. C., Vol. 1, pp. 593–604.

Takahashi, F., Schmoll, W. J., and Katta, V. R. (1998). Attachment mechanisms of diffusion flames. *Twenty-Seventh Symposium (International) on Combustion*, The Combustion Institute, Pittsburgh, Pennsylvania, pp. 675–684.

Tsuji, H. and Yamaoka, I. (1971). Structure analysis of counterflow diffusion flames in the forward stagnation region of a porous cylinder. *Thirteenth Symposium (International) on Combustion*, The Combustion Institute, Pittsburgh, Pennsylvania, pp. 979–984.

Veynante, D., Vervisch, L., Poinsot, T., Liñán, A., and Ruetsch, G. (1994). Triple flame structure and diffusion flame stabilization. Proceedings of the Summer Program, Center for Turbulence Research, Stanford University, Palo Alto, California, pp. 55–73.

Warnatz, J. (1984). Rate coefficients in the C/H/O system. In W. C. Gardiner, (Ed.) *Combustion Chemistry*, Springer-Verlag, New York, pp. 197–360.

Wichman, I.S., Lakkaraju, N., and Ramadan, B. (1997). The structure of guenched triple flames near cold walls in convective flows. *Combust. Sci. Technol.* 127, p. 141.

Williams, F. A. (1985). *Combustion Theory*, 2nd ed.. The Benjamin/Cummings, Menlo Park, California.

Twenty-Seventh Symposium (International) on Combustion/The Combustion Institute, 1998/pp. 625–632

PUBLISHED WITH PERMISSION

AN EXPERIMENTAL AND NUMERICAL INVESTIGATION OF THE STRUCTURE OF STEADY TWO-DIMENSIONAL PARTIALLY PREMIXED METHANE-AIR FLAMES

ZHUANG SHU, BRADY J. KRASS, CHUN W. CHOI, SURESH K. AGGARWAL, VISWANATH R. KATTA* AND ISHWAR K. PURI

Department of Mechanical Engineering (M/C 251)
University of Illinois at Chicago
842 W. Taylor St., RM 2039
Chicago, IL 60607-7022, USA

Steady two-dimensional partially premixed slot-burner flames established by introducing a rich fuel-air mixture from the inner slot and air from the two outer slots are investigated. Numerical simulations are conducted using detailed chemistry, velocity measurements are made using particle image velocimetry, and images of the chemiluminescent reaction zones are obtained. Two reaction zones are evident; one in an inner rich-side premixedlike flame and the other in an outer lean-side non-premixed flame. Validation of the predictions involves a comparison of the (1) premixed and non-premixed flame heights, (2) the double-flame structure, and (3) velocity vectors. The measured and predicted velocity vectors are in good agreement and show that the flame interface separates smaller velocity magnitudes on the reactant side from larger values on the (partially) burned side. The outer flame temperature is higher than that of the inner premixed flame. A substantial amount of methane leaks past the inner flame and reacts in the outer non-premixed zone. The inner flame produces partially oxidized products such as H_2 and CO, which provide the fuel for the non-premixed flame. The initiation reaction $CH_4 + H \Leftrightarrow CH_3 + H_2$ proceeds strongly at the base of the flame where both the inner and outer flames are connected and at the tip of the inner flame, and it is weak along the sides of both inner and outer flames in accord with the chemiluminescent images. Carbon dioxide formation through the reaction $CO + OH \Leftrightarrow CO_2 + H$ is more diffuse than methane consumption in the outer flame, because the availability of hydroxyl radicals in that region is limited through oxidizer transport.

Introduction

Partially premixed flames are established when a fuel-rich mixture is separated from a fuel-lean mixture by the flame, and both fuel and oxidizer are simultaneously present on at least one side of the flame interface. A generic partially premixed flame consists of two streams with, respectively, rich and lean side equivalence ratios ϕ_r and ϕ_l, where $1 < \phi_r \leq \infty$ and $0 \leq \phi_l < 1$ [1]. Partially premixed flames may also occur in those regions of non-premixed flames where fuel-air mixing ensues as a consequence of local quenching (e.g., during flame liftoff) and in premixed applications due to poor initial mixing. For instance, Rogg et al. [2] have observed that partial premixing of laminar flamelets is essential for the prediction of non-premixed turbulent flame structure. In spray flames, nonuniform evaporation can result in locally fuel-rich regions in which burning occurs in the partially premixed mode.

Previous investigations of partially premixed flames have employed counterflow and coflow flame configurations [2–11]. Yamaoka and Tsuji [3–5] have investigated partially premixed flames established in the forward stagnation region of a porous cylinder that was immersed in a uniform air stream and observed that, depending on the stoichiometry of the premixed mixture, two separate reaction zones could be established. Opposed-jet counterflow flame studies have shown partial premixing to make the flames less resistant to stretch under certain circumstances and for these flames to exhibit both a diffusion and premixedlike structure [6–8]. More recent investigations have focused on unsteady flames [9–11]. The objective of this investigation is to (1) investigate the flame structure of two-dimensional partially premixed flames in greater detail and (2) provide experimental validation for our numerical model.

Procedure

Numerical Method

A time-dependent two-dimensional model based on a direct numerical simulation methodology is

*Present address: Innovative Scientific Solutions, Inc. Dayton, OH 45430.

employed, and a relatively detailed 17-species, 52-step mechanism proposed by Peters [12] is used to represent the CH_4-air chemistry. The governing equations can be written in Cartesian coordinates (x, y) in the form

$$\frac{\partial(\rho\phi)}{\partial t} + \frac{\partial(\rho u\phi)}{\partial x} + \frac{\partial(\rho v\phi)}{\partial y} = \frac{\partial}{\partial x}\left(\Gamma^{\phi}\frac{\partial\phi}{\partial x}\right) + \frac{\partial}{\partial y}\left(\Gamma^{\phi}\frac{\partial\phi}{\partial y}\right) + S^{\phi}$$

where ρ represents the density and u and v the transverse (x) and axial (y) velocity components, respectively. The general form of the foregoing equation represents either of the mass, momentum, species, or energy conservation equations. The transport coefficient Γ^{ϕ} and the source terms S^{ϕ} appearing in the governing equations are provided in Ref. [10]. Using the overall species conservation equation and the equation of state completes the set of governing equations. A detailed algorithm, similar to that in CHEMKIN [13], is employed to calculate the thermodynamic and transport properties. The equations are integrated by using a finite-control volume approach with a staggered, nonuniform grid system. The finite-difference forms of the momentum equations are obtained using an implicit scheme [14], while those of the species and energy equations are obtained using a hybrid scheme [15]. Further details about the numerical procedure, validation, and the treatment of boundary conditions are provided in earlier publications [10,11,16–19].

Experimental Method

Instantaneous measurements of the velocity vectors and the flame heat release are made. We have used instruments that can be readily used to characterize analogous unsteady flames that are to be the focus of a subsequent investigation.

Particle image velocimetry

Particle image velocimetry (PIV) is a useful method to gain quantitative instantaneous information about an unsteady flow field. Using this technique, a portion of the flow field is illuminated, and the Lorenz–Mie scattering from seed particles is imaged. Although the technique is valuable, implementing it in reacting flows presents challenges due to the large range of particle seeding densities that are required due to flow dilatation [20] so that only a few applications to combustion systems have been reported [21–28], none for partially premixed flames.

The particle illumination source consists of a double-pulsed Continuum Nd:YAG laser, and the flow is seeded with TiO_2 particles. Particle images are captured two times (due to the double pulse) using a TI RS-170 CCD camera. The digitized image is fed to an array processor and analyzed using commercial autocorrelation software obtained from TSI. The analysis involves dividing the image into a grid and taking a two-dimensional fast Fourier transform (FFT) of the sections to determine the peak intensity locations. The distances between those locations are measured, and a velocity vector is predicted. Several precautions are taken to ensure reliability. Each interrogation spot contains more than 10 particle image pairs. Through extensive trial and error, the interrogation spot size is made small enough for a single vector to describe the flow at that location, and the laser sheet is made thick enough for out-of-plane particle motion to not be problematic and for sufficient particle pairs to be present. The particle displacement is kept greater than two particle image diameters but not more than one-quarter of the interrogation spot size. The overlap between spots is adjusted to increase the vector density. Further details of the PIV system are contained in Ref. [29].

C_2-radical imaging

In general, the chemiluminescent emission from flames may be interpreted as a signature of chemical reaction and heat release from which the flame geometry can be determined [30–33]. The excited states of CH and OH have been, respectively, suggested as the major emitters from the premixed and non-premixed reaction zones of partially premixed flames [34]. The excited C_2^* free radical species is short-lived and is also a good indicator of the reaction zone [32], and its light intensity is known to vary linearly with the volumetric heat release [33]. Spectral emission images are obtained at the 473-nm wavelength (1,0) C_2 Swan band [35]. We have used an ITT F4577 513 × 480 pixel intensified camera and a narrow wavelength interference filter (470 ± 10 nm). The spectral response of the CCD camera is relatively flat in the range between 420 and 900 nm and is ≈0.02 amps/W at 470 nm. The images are transferred to a frame grabber (P360F, Dipix) and processed after subtracting a representative background image to obtain a histogram that consists of a matrix in which each pixel gray level is represented by an integer N in the range $0 \leq N \leq 256$.

Configuration

The flames are established on a rectangular Wolfhard–Parker slot burner, a schematic diagram of which is shown in Fig. 1. A rich fuel-air mixture is introduced from the inner slot and air from the two outer slots. The aspect ratio of the inner slot is 5.6, and the three-slot burner establishes a flame with two identical two-dimensional flame sheets [36]. In such a rectangular geometry, where cross-stream line-of-sight integration may be acceptable, emission measurements provide an inexpensive alternative to more sophisticated laser-based methods. The

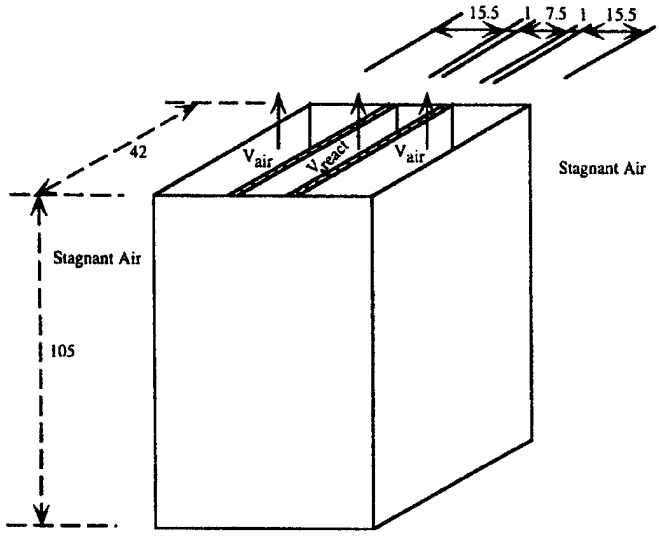

FIG. 1. Schematic diagram of the burner that consists of an inner 7.5-mm slot with two 15.5-mm outer slots on either side of it. The wall thickness separating the slots is 1 mm. Ceramic flow straighteners are placed in all three slots.

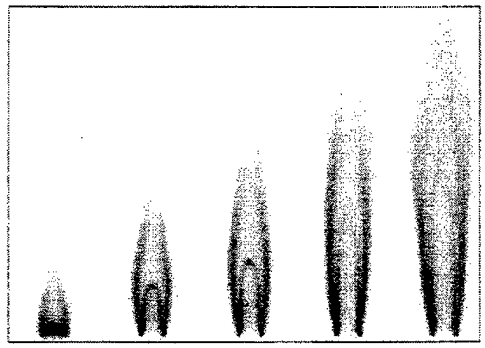

FIG. 2. C_2-emission images from flames established at $\phi = 2$, $V_{air} = 30$ cm s^{-1}, and (successively from left to right) $V_{reac} = 20$, 30, 40, 50, and 70 cm s^{-1}.

numerical simulations are conducted on one side of the symmetry plane of a two-dimensional domain. The other planes bounding the domain consist of two free surfaces and the inlet plane.

Results and Discussion

In the experiments, methane-air mixtures are introduced through the inner slot at fuel-rich equivalence ratios $\phi = 2$, 2.5, and 3. For each of these conditions, the inner and outer slot velocities (respectively, V_{reac} and V_{air}) are varied such that $V_{reac} = 20$, 30, 40, 50, and 70 cm s^{-1}, and $V_{air} = 30$, 50, and 70 cm s^{-1}. Figure 2 contains a representative set of C_2^*-emission images for flames established at fixed values of ϕ and V_{air} but at the five reactant flow velocities. Two distinct reaction zones are evident, one each on the rich and lean sides of the flow. The flames exhibit a double-flame structure over the range of flow rates investigated. In analogous counterflow flames established at this stoichiometry, the two flames were found to be merged [37], although it is known that the double-flame structure exists at low-enough flame stretch rates [34]. This indicates that the slot burner flame adjusts to locations where the fuel-side stretch rates are low and exhibits a double-flame structure.

Both the inner and outer flame heights grow as the reactant velocity (and, thereby, reactant flux) increases. The two flame heights also increase as the equivalence ratio is raised, because the stoichiometry moves from a premixedlike mode ($\phi \to 1$) to a non-premixed condition ($\phi \to \infty$) so that the flame

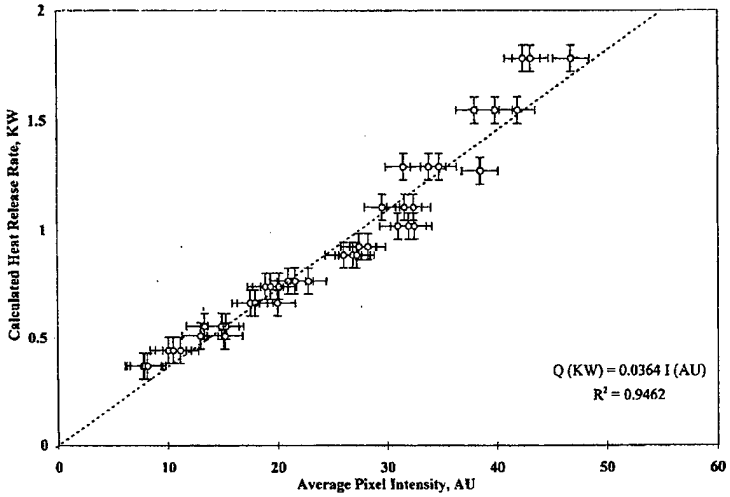

FIG. 3. Correlation of the predicted heat-release rate Q based on the measured flow rates with the average pixel C_2-chemiluminescence intensity I. The linear relationship is of the form $Q = 0.036I$. Bars represent the standard error.

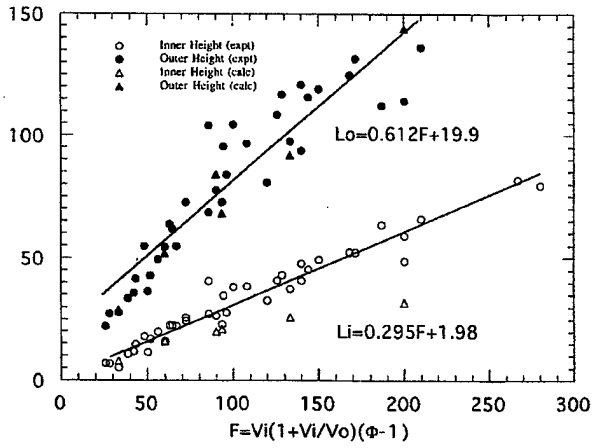

FIG. 4. Correlation of the inner (L_i) and outer (L_0) flame heights with the function $V_{reac}(1 + V_{reac}/V_{air})(\phi - 1)$. The closed and open symbols, respectively, denote the outer and inner flame heights. The circles and triangles (● and ▲), respectively, represent the measured and predicted values. Six flame heights are predicted for the conditions $\phi = 2$, $V_{reac} = 20$, 30, 40, and 50 cm s^{-1}, $V_{air} = 30$ cm s^{-1}; and $\phi = 2.5$, $V_{reac} = 30$ and 50 cm s^{-1}, $V_{air} = 30$ cm s^{-1}.

becomes mixing limited. Increasing the outer velocity decreases both flame heights because the higher air-side flux reduces the outer (non-premixed-type) flame height, which, in turn, interacts with the inner (premixedlike) flame whose height also declines.

The C_2^* emission signal is confined to relatively thin sheetlike reaction zones. For that reason, the total signal is directly proportional to the flame surface area and is well correlated with the reactant flow rate in accord with previously reported results [33,38]. Figure 3 contains a plot of the average pixel intensity I with respect to the predicted heat-release rate Q based on the reactant flow rate in the form of a linear relationship $Q = \alpha I$. The chemiluminescence images are directly proportional to the C_2^* formation rate and, thus, serve as a qualitative rate measure of the flame chemistry [39].

Figure 4 contains a correlation of both flame heights with the function $F = V_{reac}(1 + V_{reac}/V_{air})(\phi - 1)$. The measured outer flame height L_0 data show greater scatter than the corresponding inner flame heights L_i. While measurements of L_i are straightforward, the outer flame emission provides images consisting of two unclosed interfaces on either side of the inner slot. Geometric tangents must be superimposed upon these interfaces in order to

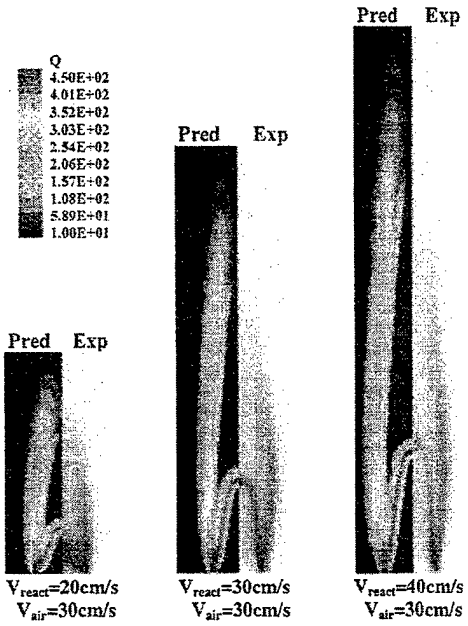

FIG. 5. Comparison of the simulated heat-release rates with the experimentally obtained C_2-chemiluminescence images for three flames established at $\phi = 2$ and $V_{air} = 30$ cm s^{-1}, and with $V_{reac} = 20$, 30, and 40 cm s^{-1}.

evaluate L_0, leaving its exact value open to some interpretation. Furthermore, at higher V_{reac} values, the outer flames become unsteady and begin to slowly flicker. Consequently, the outer images become somewhat thicker and more diffuse, introducing additional error into the tangent measurements, particularly as ϕ increases. Therefore, some L_0 values are not reported. Regardless of these uncertainties, the inner and outer flame heights are well correlated with F. A linear best fit provides relations for the inner flame height $L_i = (0.3F + 2)$ mm, and the outer height $L_0 = (0.6F + 20)$ mm in the ranges $25 \leq F \leq 280$ mm, $5 \leq L_i \leq 85$ mm, and $20 \leq L_i \leq 145$ mm.

While there is excellent agreement between the measured and predicted values of L_0, a comparison of the corresponding inner flame heights shows a progressively larger disagreement as F increases. Najm et al. [39] have suggested that the largest share of the carbon flow in methane-air flames is carried by the path $CH_3 \rightarrow CH_2O \rightarrow CHO \rightarrow CO$ (initiated by the reaction $CH_3 + O \Leftrightarrow CH_2O + H$), and only a minor amount by reactions involving the methyl radical that finally produce excited-state C_2. The predicted flame heights contained in Fig. 4 are based on the two peak axial centerline values of the initiation reaction $CH_4 + H \Leftrightarrow CH_3 + H_2$, corresponding to the inner and outer flames. Our analysis has shown that the simulated flame heights based on this criteria are virtually identical to those based on the peak heat-release rates; the peak rates of $CH_3 + O \Leftrightarrow CH_2O + H$; the peak CO-formation rates through the reaction $CHO + M \Leftrightarrow CO + H + M$; and either the peak formyl radical mole fractions or the peak CHO formation rates (as CHO has been reported to be an excellent marker of flame heat release [39]). Therefore, the discrepancy between the predicted and measured values of L_i is not due to a spatial difference between the predicted heat release and measured C_2^*-emission regions and must be attributed to the rich-side flame chemistry. This will be the focus of a subsequent investigation.

Figure 5 presents a comparison of the predicted heat-release rates with the experimentally obtained emission images for four flames. The comparison is less satisfactory when V_{reac} is smaller. This may be attributed to the proportionally larger heat losses (which are not simulated) from the smaller flame to the burner during the experiments. These losses influence the inner premixedlike reaction zone more than the outer transport-limited non-premixed reaction region. There is good agreement when the air and reactant velocities are identical, and the comparison again exhibits some discrepancies when V_{reac} exceeds V_{air}. Some differences are to be expected (particularly on the rich side and, consequently, related to the inner flame heights), because C_2 chemistry is neglected in the simulations. However, even when a quantitative comparison fails, it is possible to accurately simulate the qualitative shape and structure of the reaction zone.

The emission signal is strongest at the base of the

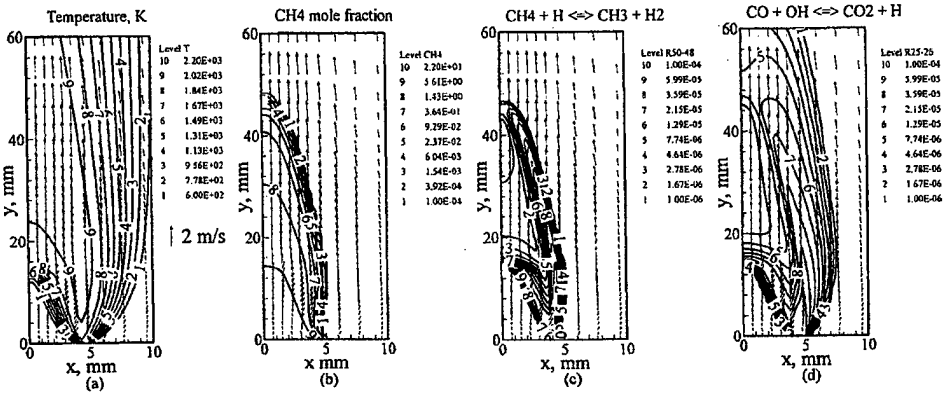

FIG. 6. (a) Comparison of the measured ($-4 \leq x \leq 0$ mm) and predicted velocity vectors ($0 \leq x \leq 4$ mm) for a flame established at $\phi = 2$, $V_{afr} = 30$ cm s^{-1}, and $V_{reac} = 30$ cm s^{-1}. The corresponding flame interface (chemiluminescent image and simulated heat release) are superimposed on the two plots. (b) Comparison of the measured (●) and predicted (○) centerline velocities for a flame established at $\phi = 2$, $V_{air} = 30$ cm s^{-1}, and $V_{reac} = 30$ cm s^{-1}.

inner and outer flames, that is, where the two flames are connected. Both the simulated heat-release rates and the chemiluminescence along the sides of the inner (premixed) flame decrease due to stretch effects as V_{reac} increases, with higher levels being associated with the flame tip and base. Therefore, it appears that the reaction zone is more vigorous at the tip and base of the inner flame than along its sides. The heat-release rate progressively decreases along the outer (non-premixed) flame at downstream locations. The non-premixed reaction zone has a weak tip, and reaction rates are stronger in upstream regions of that flame.

The measured and predicted velocity vectors are compared in Fig. 6a. The measurements mirror the simulations, and the flame interface separates smaller velocity magnitudes on the reactant side from larger values on the (partially) burned side. Both sets capture the air entrainment in the region between $3 \leq x \leq 1.5$ mm and $0 \leq y \leq 4$ mm where the velocity vectors turn toward the centerline. The gas expansion due to heat release causes the velocity vectors to move outward with respect to the centerline along the inner flame.

In order to obtain accurate data for the range of flow velocities, the PIV measurement window was set at 7.5 × 5.5 mm, respectively, in the x- and y-wise directions. This choice restricted the lowest possible velocity measurement for the acquired particle displacements to 30 cm s^{-1} (which equals the reactant and air inlet velocities). The experimental data are sparse in some postflame regions, because flow dilatation greatly reduces the particle seed densities in those areas. Although the measured velocities were obtained after averaging the vectors acquired from 10 PIV images, they are representative of each of those images. The measured and predicted velocities along the flame centerline (which, being in the symmetry plane, contain only an axial component) are compared in Fig. 6b. There is good agreement between the two sets in the preflame zone, but there is some discrepancy in the postflame region that is probably due to experimental uncertainties. The centerline velocity profile is representative of a preflame preheat zone, the inner (premixed) flame zone, and a postflame zone that is heated due to heat transfer from the outer flame.

These zones can be differentiated in the flame structure presented in Fig. 7 (for a flame exhibiting excellent agreement between the experiments and predictions). The region between the inner and outer flames is the hottest as seen from the temperature contours of Fig. 7a. The outer reaction zone temperature is higher than that of the inner premixed flame. A substantial amount of methane leaks past the inner flame and reacts in the outer non-premixed zone, as presented in Fig. 7b. Likewise, oxygen is consumed in both the inner and outer flames. Oxygen is entrained into the outer non-premixed flame, as can be seen by examining the air-side velocity vectors, which advect air to the centerline. The inner flame produces partially oxidized products, such as H_2 and CO that provide the "fuel" for the non-premixed flame. The velocity vectors turn toward the outer slots in the post-inner flame region, thereby advecting these species into the non-premixed flame.

The initiation reaction $CH_4 + H \Leftrightarrow CH_3 + H_2$ proceeds strongly at the base of the flame, where both the inner and outer flames are connected, and at the tip of the inner flame. On the other hand, it is weak along the sides of the inner and outer flames.

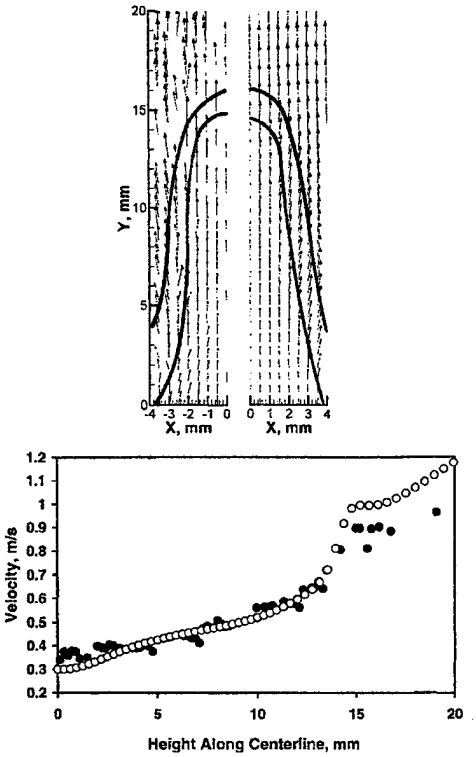

FIG. 7. Predicted flame structure of a flame established at $\phi = 2$, $V_{air} = 30$ cm s^{-1}, and $V_{reac} = 30$ cm s^{-1}. (a) Temperature, (b) CH_4 mole fraction, (c) the rate of the reaction $CH_4 + H \Leftrightarrow CH_3 + H_2$, and (d) the rate of the reaction $CO + OH \Leftrightarrow CO_2 + H$.

This is in accord with the chemiluminescent images contained in Fig. 2 that show that while the outer flame tip is open, the inner flame is always closed for the investigated range of conditions. The CO-oxidation reaction $CO + OH \Leftrightarrow CO_2 + H$ shown in Fig. 7d exhibits a similar distribution. Carbon dioxide formation through this reaction is more diffuse in the outer flame, because the availability of hydroxyl radicals in that region (through the initiation step $O_2 + H \Leftrightarrow OH + O$) is limited by oxidizer transport.

Conclusions

The results of an experimental and numerical investigation of two-dimensional partially premixed methane-air flames are presented. A detailed validation of the predictions involves a comparison of the (1) inner and outer flame heights over a wide range of conditions, (2) flame reaction zones, and (3) velocity vectors. Overall, the comparison is excellent, but some discrepancies remain. Some are likely due to the absence of C_2 chemistry in the simulations. This aspect will be explored in future work.

1. For the range of conditions considered, sheetlike inner (premixed) and outer (non-premixed) reaction zones are formed. The inner (premixed) flame zone has a closed tip, and reactions proceed stronger at its base and tip than along its sides. The flames exhibit a double-flame structure over the range of investigated flow rates, indicating that the flame location self-adjusts itself to locations where the fuel-side stretch rates are low.
2. The measured and predicted values of L_0 are in good agreement. Comparisons of the corresponding values of L_i show a progressively larger disagreement as F increases, which is attributed to the rich-side flame chemistry, because C_2 chemistry is neglected in the simulations. Both flame heights correlate well with the function $F = V_{reac}(1 + V_{reac}/V_{air})(\phi - 1)$.
3. The flame has four zones: an inner preflame preheat zone, the inner (premixed) flame zone in which CO and H_2 are formed, a post-inner flame zone situated between the inner and outer flames containing hot products, and a non-premixed outer region in which CO and H_2 oxidation occur.

Acknowledgments

This research was supported by the National Science Foundation Combustion and Plasma Systems Program through Grant Number CTS-9707000 for which Dr. Farley Fisher is the Program Director. We are grateful to Dr. Anthony Hamins (NIST) for sharing a slot burner design.

REFERENCES

1. Seshadri, K., Puri, I., and Peters, N., *Combust. Flame* 61:237–249 (1985).
2. Rogg, B., Behrendt, F., and Warnatz, J., in *Twenty-First Symposium (International) on Combustion*, The Combustion Institute, Pittsburgh, 1986, p. 1533.
3. Yamaoka, I. and Tsuji, H., in *Fifteenth Symposium (International) on Combustion*, The Combustion Institute, Pittsburgh, 1974, p. 737.
4. Yamaoka, I. and Tsuji, H., in *Sixteenth Symposium (International) on Combustion*, The Combustion Institute, Pittsburgh, 1976, p. 1145.
5. Yamaoka, I. and Tsuji, H., in *Seventeenth Symposium (International) on Combustion*, The Combustion Institute, Pittsburgh, 1978, p. 843.
6. Hamins, A., Thridandam, H., and Seshadri, K., *Chem. Eng. Sci.* 40:2027–2038 (1985).
7. Smooke, M. D., Seshadri, K., and Puri, I. K., in *Twenty-Second Symposium (International) on Combustion*, The Combustion Institute, Pittsburgh, 1988, pp. 1555–1563.

8. Law, C. K., Li, T. X., Chung, S. H., Kim, J. S., and Zhu, D. L., *Combust. Sci. Technol.* 64:199–232 (1989).
9. Brown, T. M., Pitz, R. J., and Sung, S. J., Paper no. AIAA 97-0903 presented at the AIAA 35th Aerospace Sciences Meeting and Exhibit, Reno, Nevada, January 6–10, 1997.
10. Shu, Z., Aggarwal, S. K., Katta, V. R., and Puri, I. K., *Combust. Flame* 111:276–295 (1997).
11. Shu, Z., Aggarwal, S. K., Katta, V. R., and Puri, I. K., *Combust. Flame* 111:296–311 (1997).
12. Peters, N., in *Reduced Kinetic Mechanisms for Applications in Combustion Systems, Lecture Notes in Physics* (N. Peters and B. Rogg, eds.), Springer-Verlag, New York, 1996, vol. m15, pp. 3–14.
13. Kee, R. J., Miller, J. A., and Warnatz, J., "A Fortran Program Package for the Evaluation of Gas-phase Viscosities, Conductivities, and Diffusion Coefficients," Sandia National Laboratories report SAND83-8209.
14. Leonard, B. P., *Comput: Meth. Appl. Mech. Eng.* 19:59–98 (1979).
15. Spalding, D. B., *Int. J. Num. Meth. Mech. Eng.* 4:551 (1972).
16. Katta, V. R., Goss, L. P., and Roquemore, W. M., *Combust. Flame* 96:60–74 (1994).
17. Takahashi, F. and Katta, V. R., *AIAA J. Propul. Power* 11 (1995).
18. Aggarwal, S. K., Park, T. W., and Katta, V. R., *Combust. Sci. Technol.* 113:429–438 (1996).
19. Patadia, H., "Transient Structure of Methane-Air and Methanol-Air Diffusion Flames," Master's thesis, The University of Illinois at Chicago, 1995.
20. Frank, J. H., Lyons, K. M., and Long, M. B., *Combust. Flame* 107:1–12 (1996).
21. Reuss, D. L., Bardsley, M., Felton, P. G., Landreth, C. C., and Adrian, R. J., SAE paper 90-0053.
22. Armstrong, N. W. H., Ph.D. thesis, University of Cambridge, 1992.
23. Goss, L. P., Post, M. E., Trump, D. D., and Sarka, B., *J. Laser Appl.* 3:36–42 (1991).
24. Reuss, D. L., Landreth, C. C., and Adrian, R. J., *Combust. Sci. Technol.* 67:73–83 (1989).
25. Armstrong, N. W. H. and Bray, K. N. C., SAE paper 92-2322.
26. Lecordier, B., Mouquallid, S., Vottier, S., Rouland, E., Allano, D., and Trinite, M., *Exp. Fluids* 17:205–208 (1994).
27. Driscoll, J. F., Stukus, D. J., Roberts, W. L., Post, M. E., and Goss, L. P., *Combust. Sci. Technol.* 96:213–229 (1994).
28. Ereaut, P. R., *J. Inst. Energy* 62:14–20 (1989).
29. Bunnell, R. K., "A Theoretical and Experimental Investigation of Well-Mixed Combustion in a Rapid-Mixing Burner," Master's thesis, The University of Illinois at Chicago, 1996.
30. Beyler, C. L. and Gouldin, F. C., in *Eighteenth Symposium (International) on Combustion*, The Combustion Institute, Pittsburgh, 1981, pp. 1011–1019.
31. Dibble, R. W., Long, M. B., and Masri, A., *Prog. Astronaut. Aeronaut.* 105:99–109 (1986).
32. Brandon, Y. and Samaniego, J.-M., *Combust. Sci. Technol.* 84:81–89 (1992).
33. McManus, K., Yip, B., and Candel, S., *Exptl. Thermal Fluid Sci.* 10:486–502 (1995).
34. Nishioka, M., Nakagawa, S., Ishikawa, Y., and Takeno, T., *Combust. Flame* 98:127–138 (1994).
35. Pearse, R. W. B. and Gaydon, A. G., in *The Identification of Molecular Spectra*, 4th ed., Chapman and Hall, London, 1976, p. 83.
36. Smyth, K. C. and Tjossem, P. J. H., in *Twenty-Third Symposium (International) on Combustion*, The Combustion Institute, Pittsburgh, 1990, pp. 1829–1837.
37. Tanoff, M., Smooke, M. D., Osborne, R. J., Brown, T. M., and Pitz, R. W., in *Twenty-Sixth Symposium (International) on Combustion*, The Combustion Institute, Pittsburgh, 1996, pp. 1121–1128.
38. Hurle, I. R., Price, R. B., Sugden, T. M., Thomas, R. R. S., and Thomas, A., *Proc. R. Soc. London A* 303:409–427 (1968).
39. Najm, H. N., Paul, P. H., Mueller, C. J., and Wyckoff, P. S., *Combust. Flame* 113:312–332 (1998).

Presented at the Twenty-Eighth International Symposium on Combustion, Edinburgh, Scotland, 30 July - 4 August 2000; published in Proceedings of the Combustion Institute, Vol. 28, 2000.
PUBLISHED WITH PERMISSION

A Reaction Kernel Hypothesis for the Stability Limit of Methane Jet Diffusion Flames

Fumiaki Takahashi*
University of Dayton Research Institute
Dayton, Ohio, U.S.A.

Viswanath R. Katta
Innovative Scientific Solutions, Inc.
Dayton, Ohio, U.S.A.

Abstract

The lifting limit of an axisymmetric, laminar, co-flow methane-air jet diffusion flame under normal earth gravity has been successfully predicted. Computations of the time-dependent full Navier-Stokes equations with buoyancy were performed using an implicit, third-order accurate numerical scheme and a detailed C_2-chemistry model. A one-step global chemistry model was also used to reveal its deficiencies and to demonstrate the need for "tuning" its kinetic parameters for the studies on flame lifting. The detailed chemistry model resulted in the standoff distance of the flame from the burner rim in good agreement with that measured previously. As the mean co-flow air velocity was increased, at a fixed fuel jet velocity under the near-limit condition, the calculated *reaction kernel* (peak reactivity spot) in the flame base broadened and rapidly shifted away downstream. As a result, a higher reactivity (heat-release rate, oxygen consumption rate, etc.) at the reaction kernel could be obtained to sustain combustion against a higher incoming flow velocity, or a shorter residence time. The reactivity augmentation is due to a "blowing" effect, which caused enhanced convective and diffusive fluxes of oxygen into the relatively low-temperature (~1550 K) fuel-lean (equivalence ratio ≈ 0.55) reaction kernel. Based on these new findings, a reaction kernel hypothesis is proposed for the diffusion flame stability; i.e., a subtle balance between the residence time and reaction time in the reaction kernel is maintained by its continuous movement in the downstream direction in response to the destabilizing effect caused by an increase in the co-flow air velocity and the overall reaction time eventually exceeds the available residence time at the stability limit. If a secondary stabilizing point is obtained as a result of the transition to a turbulent flame base downstream, the flame lifts off, otherwise it blows off.

* Current address: National Center for Microgravity Research, NASA Glenn Research Center, Cleveland, Ohio, U.S.A.

INTRODUCTION

Diffusion flames have been used widely in practical combustion systems, and most fires spreading through condensed fuels are of the diffusion type. Thus, the blow-off stability of diffusion flames has long been a fundamental and practical research subject in combustion [1-11]. Local flame-flow phenomena, including heat and mass transport processes and chemical reactions around the flame base, which is often located in the vicinity of condensed surfaces, control the flame stabilizing and spreading mechanisms. Under the earth gravity, the transport processes are characterized by a mixed convective-diffusive regime, whereas, in microgravity, a pure diffusive regime may occur if forced convection is absent. Therefore, the flame stabilizing and spreading mechanisms may differ accordingly. To gain an in-depth understanding of the subject, the detailed flame-base structure resulting from the transport and reaction processes must be revealed. Unfortunately, previous investigations of the flame-base structure and behavior, including experiments [2, 4, 7], theories, and numerical studies with global chemistry [12-14], generally suffered from the lack of detailed information, particularly on the role of radical species. Experimental techniques for measuring radical species are limited in spatial and temporal resolutions, and theories generally ignore radicals. As a result of recent advances in computational capabilities and detailed chemistry models, a numerical approach has become a powerful tool to obtain precise information on the flame-base structure.

The authors [15, 16] have used a comprehensive computational fluid dynamics code [17, 18] with detailed chemistry models to reveal the complex structure of the stabilizing region of diffusion flames, including jet flames and flat-plate burner flames. In previous papers [15, 16], the attachment mechanism and the chemical kinetic structure of the flame-stabilizing region of methane jet diffusion flames were reported. This paper extends the previous effort to a more challenging

task, i.e., numerical prediction of the stability limit of a diffusion flame without using adjustable variables. As far as the authors know, no such attempt has been reported thus far in the literature. The effect of co-flow air velocity on the structure of the flame base and its subtly balanced standoff distance under the near-lifting-limit condition was investigated to simulate the lifting phenomenon. The emphasis in this paper is placed on the flame stability mechanism in the mixed convective-diffusive regime under the normal earth gravity. Computations were also performed using a one-step global chemistry model to find the kinetic parameters, for which the standoff distance was the same as that of the detailed chemistry. The incorrect flame-base structure obtained as a result of the simple chemistry model relates to the formation of a triple flame reported in the literature.

NUMERICAL METHODS

The numerical code (UNICORN) used in this study, developed by Katta et al. [17, 18], is described in more detail elsewhere [16]. Time-dependent governing equations, expressed in cylindrical coordinates, consist of continuity, axial and radial full Navier-Stokes momentum conservation, energy conservation, and species conservation equations with the ideal-gas equation of state. A body-force term caused by the gravitational field is included in the axial momentum equation. The momentum equations are integrated using an implicit QUICKEST numerical scheme [17] for the convection terms, which is third-order accurate in both space and time and has a very low numerical-diffusion error. The finite-difference form of the species and enthalpy is obtained using the hybrid scheme with upwind and central differences. The coefficients of viscosity, thermal conductivity, and diffusion are estimated using molecular dynamics and mixture rules. The enthalpy of each species is calculated from polynomial curve-fits using the CHEMKIN libraries.

The detailed C_2-chemistry model [19] for 24 species and 81 elementary steps is used. The Arrhenius parameters for the reaction $CH_3 + H \rightarrow CH_4$ are replaced with those by Warnatz [20]. Otherwise, the extinction limit of counterflow diffusion flames was predicted at a significantly lower strain rate than that determined experimentally, and the jet diffusion flames under consideration prematurely lifted off under conditions below the stability limit obtained experimentally [11]. The one-step global chemistry for the methane-oxygen combustion is also used with the Arrhenius-type reaction rate expression

$$\hat{\omega}_{CH_4} = -A\exp(-E/RT)[CH_4][O_2]$$

where $\hat{\omega}_{CH_4}$ is the molar rate of production of methane, A is the pre-exponential factor, E is the overall activation energy, R is the universal gas constant, T is the temperature, and $[CH_4]$ and $[O_2]$ are the molar concentrations of methane and oxygen, respectively. For a constant overall activation energy (E = 40 kcal/mol), the pre-exponential factor was widely varied to obtain a flame-base standoff distance comparable to that of the detailed chemistry.

The computational domain of 150 × 60 mm in the axial (z) × radial (r) directions is represented by a mesh of up to 371 × 101 with clustered grid lines near the jet exit and a minimum spacing of 0.05 mm. The inner diameter (d = 9.6 mm) and lip thickness (δ = 0.2 mm) of the fuel tube are close to those used in previous experiments [11]. The fuel tube exit plane is placed 10 mm downstream from the inflow boundary in the open computational domain. Fully developed pipe flow in the fuel tube and boundary layer velocity profiles outside the burner tube are used. Several computations were performed for various mean co-flow air velocities ($0.36 < U_a < 0.8$ m/s) to simulate the experimentally determined lifting limit (U_a = 0.76 m/s [11]) at a constant mean jet velocity (U_j = 1.7 m/s). The initial and boundary conditions for the axial (U) and radial (V) velocities and species and energy at different flow boundaries are the same as in

previous work [16]. The outer boundaries of the computational domain are placed sufficiently far away to minimize the reflection of disturbances on the region of interest. No-slip boundary conditions are enforced along the burner walls. To estimate the flow variables on the outflow boundary, the values at two upstream grids are extrapolated with zeroth- and first-order terms with weighting coefficients.

RESULTS AND DISCUSSION

Figure 1 shows a previously measured stability-limit curve [11] and the newly reported lift-off height (h_L) of the visible flame base from the jet exit for lifted co-flow methane-air jet diffusion flames. In general, the critical mean fuel jet velocity at the stability limit (U_{jc}) decreased monotonically as the mean co-flow air velocity increased, except for $U_a < 0.1$ m/s, for which the outer air tube (26.9 mm i.d.), used only in the experiment, acted like a bluff body, thus blocking free entrainment of surrounding air. The lift-off height decreased rapidly as the mean air velocity was increased up to $U_a \approx 0.2$ m/s, because U_{jc} of the turbulent fuel jet decreased and thus the fuel-air mixing time at a fixed height increased, thereby forming a turbulent flame base closer to the jet exit. On the other hand, the lift-off height rapidly increased for $U_a > 0.5$ m/s because the jet Reynolds number (Re_j) fell below 2300 and the fuel jet became laminar, thus significantly decreasing the fuel-air mixing until the transition to turbulent flame base occurred downstream. The flame blew off without lifting for $U_a > 1.03$ m/s because no secondary stabilization point was found due to excess dilution of the fuel by surrounding air.

Fig. 1

Figure 2 shows the unpublished [21] two-color particle image velocimetry photographs of the stabilizing region of near-lifting and lifted methane jet diffusion flames using the same burner system [11]. Submicron zirconia particles were illuminated by a sheet of green and red pulsed

Fig. 2

(10 ns) lasers with a known time delay (70 μs). Only qualitative visualization characteristics are described here. The high number-density cold airflow, a low number-density hot zone around the flame, and the dividing streamline between jet and external fluids were visualized. A time-exposure (1/30 s) image of the blue flame zone revealed no sign of the triple flame structure [10, 12, 14, 22] at the base of both near-lifting-limit and lifted methane jet diffusion flames. At a near-lifting condition (Fig. 2a), the flame base shifted downstream a few millimeters away from the burner rim. The outer cold air was entrained into the fuel jet through the dark space between the flame base and the rim, thus, thermally disconnecting the flame base from the burner wall and vanishing the heat losses to the burner wall before lifting. After lifting (Fig. 2b), the flame base was stabilized a few jet diameters downstream. The large-scale vortical structure, evolved in the shear layer (Fig. 2b), entrained the co-flow air and enhanced molecular mixing, thus resulting in a short lift-off height under this condition (see Fig. 1).

In a previous paper [16], the detailed chemical kinetic structure of the reaction kernel of a methane flame was calculated under one flow condition using three different kinetic models, including the C_2-chemistry used here. In this study, simulations of the shifted laminar flame base (similar to the one shown in Fig. 2a) were performed for various mean air velocities for the same mean fuel jet velocity (U_j = 1.7 m/s [$Re_j \approx 1025$]) to reveal the processes leading to flame lifting. Note that for this condition the experimentally observed lift-off height was over 20 cm (see Fig. 1). Figure 3 shows the calculated structure of the flame base under a near-limit condition (U_a = 0.8 m/s). Figure 3a shows the calculated velocity vectors (**v**), isotherms (T), total heat-release rate ($\dot{q}$), and equivalence ratio (ϕ) determined from the fuel and oxygen fluxes. The heat-release rate contours show the *reaction kernel*, or highest reactivity spot, at the flame base. As compared to the previous result using the same chemistry model for a lower air velocity (U_a =

Fig. 3

0.72 m/s) for the same jet velocity (Fig. 3a in [16]), the reaction kernel drifted farther downstream from the jet exit (~4 → ~9 mm) and somewhat broadened on the air side. The flame base is still anchored in a relatively low-velocity region that extendes from the wake of the burner rim. The velocity vectors show the lateral expansion of stream tubes as well as the longitudinal acceleration as the flow approaches the hot zone around the flame base due to thermal expansion of gases and the pressure field deformation. The partial premixing of the fuel and oxygen over the standoff distance progressed further compared to the lower co-flow air velocity case [16]; thus, the thickness of the mixing layer within the flammability limits ($0.5 < \phi < 1.7$ [1]) somewhat increased (~0.6 → ~0.8 mm) just below the reaction kernel. However, the flammable layer thickness was still less than half the minimum quenching distance of 2.2 mm [1] and too narrow to form an ordinary premixed flame or triple flame [10, 12, 14, 22] to propagate through it. More importantly, the reaction kernel expanded mostly over the fuel-lean region and the peak reactivity was obtained at $\phi \approx 0.5$, unlike ordinary premixed flames that have the maximum burning velocity at an equivalence ratio slightly greater than unity. Therefore, the reaction kernel structure is different from the ordinary premixed flame or the fuel-lean branch of the triple-flame structure.

Figure 3b shows the calculated total molar flux vectors of methane ($\mathbf{M}_{CH_4}$), oxygen ($\mathbf{M}_{O_2}$), and atomic hydrogen ($\mathbf{M}_H$), the mole fractions of methane (X_{CH_4}) and oxygen (X_{O_2}), and the molar oxygen consumption rate ($-\hat{\omega}_{O_2}$). The molar flux vectors of methane and oxygen overlap in the mixing layer. Because the flame base was formed on the air side of the dividing streamline for a pure hydrocarbon diffusion flame in air, the convective contribution to the oxygen flux dominated and the methane was rapidly diluted with airby diverging radial diffusion. Consequently, the oxygen penetrated onto the fuel side of the flame base more than the methane

(see X_{O_2} and X_{CH_4} contours in Fig. 3b). As discussed in more detail previously [16], hydrogen atoms diffused in every downward direction against the incoming flow into the high oxygen concentration region around the reaction kernel, inducing the most important chain branching reaction $H + O_2 \rightarrow OH + O$. Other radical species (OH, O, and CH_3, etc.) also back-diffused, reacted with each other and with molecules, including oxygen and hydrogen, broadened the reaction zone, and increased the global reaction rates even at relatively low temperatures (<1600 K). The $CH_3 + O \rightarrow CH_2O + H$ reaction was identified [16] as a dominant contributor to the total heat-release rate in the reaction kernel. Furthermore, the HO_2 reactions also contributed to the heat-release rate and extended the reaction kernel on the fuel-lean air side.

The results of computations using the one-step global chemistry model with $U_a = 0.72$ m/s and $U_j = 1.7$ m/s were significantly different from those obtained using the detailed chemistry [16] under the same flow conditions. For a fixed global activation energy (40 kcal/mol), the flame base was attached to the burner rim for the pre-exponential factor $A > 2.3 \times 10^{15}$ cm^3/mol·s, and the flame blew off prematurely for $A < 2.1 \times 10^{15}$ cm^3/mol·s. Figure 4 shows the result for $A = 2.15 \times 10^{15}$ cm^3/mol·s, for which the standoff distance was comparable to the value (~4 mm) obtained previously [16] using the C_2-chemistry model. For the global chemistry model, the peak heat-release rate (424 J/cm^{3}s) at the flame base was somewhat smaller than that (476 J/cm^{3}s) of the C_2-chemistry [16], whereas the temperature at the peak heat-release rate (~1800 K) was much higher than that (~1550 K) in the previous work [16] because of the steep dependence of the heat release, or the reaction rate, on the temperature.

Fig. 4

Furthermore, the heat-release rate contour shows a peculiar wing extending from the flame base onto the fuel side as a result of the oxygen penetration and the global reaction between methane and oxygen. Because there is no such elementary reaction in reality, the

detailed-chemistry computation [16] did not create the fuel-side wing. By contrast, the detailed chemistry resulted in the reaction zone broadening onto the air side due to radical reactions (CH_3 + O $\rightarrow$ CH_2O + H and HO_2 reactions), yet the one-step chemistry failed to simulate such structure because of the lack of radical reactions. Therefore, it may be argued that the one-step global chemistry and the symmetric penetration of fuel and oxygen onto opposite sides of the flame (resulting from the identical fuel and air velocity conditions in the two-dimensional system) chosen in the previous studies [12, 14] might have contributed for the prediction of nearly symmetric triple flames.

Figure 5a shows the effects of the mean air velocity on the calculated reaction kernel coordinates (z_k, $y_k = r_k - d/2$) at the heat-release rate peak and the axial and radial velocity components (U_k, V_k), including the previous (C_1-chemistry) [15] and current results (C_2-chemistry). Although the C_2-chemistry model resulted in a somewhat longer standoff distance ($z_k \approx 4$ mm) than that of C_1-chemistry (~3 mm) for $U_a = 0.72$ m/s, the computational results are in good agreement with the experimental observation, considering their steep variation with the air velocity. As the mean air velocity was increased, the standoff distance of the reaction kernel increased dramatically, while the radial distance was nearly constant, eventually leading to lifting at $U_a \approx 0.8$ m/s, which was nearly identical to that determined experimentally ($U_a = 0.76$ m/s for $U_j = 1.7$ m/s [11], see Fig. 1). Although the current transient model has the capability of predicting the details of the transition from a stabilized to a lifted flame if the processes are laminar, the results for $U_a > 0.8$ m/s are not reported here, because the flame base entered into the coaser-mesh region downstream. Moreover, the actual lifted flame observed was turbulent as a result of the transition to turbulent jet induced by cold-air entrainment. Neverthless, the essential features of the dynamics of the lifting process has been captured in the current simulations. The

Fig. 5

axial velocity component of the incoming flow into the reaction kernel also increased rapidly toward the lifting condition, while the magnitude of the radial velocity component approached zero. The magnitudes of the velocity components are similar for the C_1- and C_2-chemistry models. Furthermore, Fig. 5b shows temperatures and equivalence ratios at the reaction kernel (at both $\dot{q}$ and $-\hat{\omega}_{O_2}$ peaks), revealing nearly constant values in the ranges of 1500-1600 K and 0.5-0.6, respectively, except for the equivalence ratio ($\phi_k \approx 0.8$) at the $\dot{q}$ peak for nearly rim-attached flames ($U_a < 0.5$ m/s).

In a previous paper [15], heuristic correlations valid for both jet- and flat-plate diffusion flames were obtained between the peak heat-release rate, or oxygen consumption rate, and the total velocity at the reaction kernel. The reaction kernel correlations demonstrated that the baseline mechanism responsible for flame stabilization and attachment was identical for both types of diffusion flames. Figure 6a shows the reaction kernel correlation plot, including points for U_j = 1.7 m/s and various U_a near lifting. Both the peak heat-release rate and oxygen consumption rate increased almost proportionally with the magnitude of the velocity in the reaction kernel. Thus, the reaction kernel shifted to a new stabilizing point downstream, where a higher reactivity could be obtained, and withstood a higher incoming flow velocity. The reactivity augmentation was due to a so-called "blowing" effect, which caused increased convective and diffusive contributions to the oxygen fluxes into the reaction kernel.

Here, we consider the reaction kernel with a volume of (width, w_k) × (longitudinal length, l_k)× (unit depth) for simplicity. The residence time of a fluid element to cross the reaction kernel length would then be $\tau_{res} \propto l_k/|v_k|$, and the overall chemical reaction time in the reaction kernel would be represented as $\tau_{chem} \propto 1/(\dot{q}_k w_k l_k)$ or $1/(-\hat{\omega}_{O_2,k} w_k l_k)$. Then the ratio of the residence time and chemical time (local Damköhler numbers of the first kind) in the reaction kernel would

be $D_k \equiv \tau_{res}/\tau_{chem} \propto \dot{q}_k w_k l_k^2/|v_k|$ or $-\hat{\omega}_{O_2,k} w_k l_k^2/|v_k|$. Therefore, the slopes of the curves in Fig. 6a ($\dot{q}_k/|v_k|$ or $-\hat{\omega}_{O_2,k}/|v_k|$) plotted in Fig. 6b are related to the local Damköhler number. As U_a was increased, the slopes slightly increased first and then decreased as the reaction kernel shifted downstream toward lifting, but the variations are moderate (<18%) (see the C_2-chemistry results in Fig. 6b). Because the reaction kernel broadened (larger w_k) toward lifting, the variations in the local Damköhler number must be even smaller. Thus, this result indicates that lifting occurs as a result of continuous downstream shift of the location of the reaction kernel, which sustained combustion at a comparable level as a result of a subtle balance between the residence time and chemical time, which are determined by convection, (multi-component) diffusion, and (multi-step) reactions.

CONCLUSIONS

Computations of laminar methane jet diffusion flames using a detailed C_2-chemistry model revealed the flame structure and behavior of the reaction kernel and accurately predicted the flame lifting limit in response to an increase in the co-flow air velocity. At a downstream location, the reaction kernel sustained fuel-lean combustion under a higher incoming flow velocity as a result of an augmented reactivity caused by the "blowing" effect, which increased the convective and diffusive contributions to the oxygen flux. The local Damköhler numbers, deduced from the ratios of the heat-release rate, or oxygen consumption rate, and the total velocity at the reaction kernel, maintained same levels toward lifting. These new findings lead to a novel hypothesis that flame lifting or blow-off occurs if the reaction kernel, in which a subtle balance between the residence time and reaction times is maintained, continuously shifts downstream in response to the destabilizing effect (i.e., increasing the co-flow velocity) and that the reaction time eventually

exceeds the residence time at the stability limit. If a secondary stabilizing point is obtained by forming a turbulent flame base further downstream, the flame lifts off, otherwise, it blows off due to excess dilution of the fuel by surrounding air. In addition, the one-step global chemistry model resulted in an incorrect flame-base structure due to the unrealistic global methane-oxygen reaction, which lead to a fuel-side flame wing, and the lack of radical reactions, which otherwise creates the air-side reaction broadening.

ACKNOWLEDGMENT

This work was, in part, supported under the Cooperative Agreement No. NCC3-675 (Technical Officer: Dr. Kurt R. Sacksteder) by the Office of Life and Microgravity Sciences and Applications, Human Exploration and Development of Space Enterprise, National Aeronautics and Space Administration, Washington, DC, and, in part, by the US Air Force Office of Scientific Research.

REFERENCES

1. Lewis, B., and von Elbe, G., *Combustion, Flames, and Explosions of Gases,* 2nd ed., Academic Press, New York, 1961.
2. Robson, K., and Wilson, M. J. G., *Combust. Flame* 13: 626 (1969).
3. Takeno, T., and Kotani, Y., *Acta Astronaut.* 2: 999 (1975).
4. Kawamura, T., Asato, K., and Mazaki, T., *Combust. Sci. Technol.* 22: 211 (1980).
5. Takahashi, F., Mizomoto, M., Ikai, S., Futaki, N., *Proc. Combust. Inst.* 20: 295-302 (1985).
6. Eickoff, H., Lenze, B., and Leuckel, W., *Proc. Combust. Inst.* 20: 311-318 (1985).
7. Takahashi, F., Mizomoto, M., and Ikai, S., *J. Heat Transfer* 110: 182 (1988).
8. Gollahalli, S. R., Savas, Ö., Huang, R. F., and Rodriquez Azara, J. L., *Proc. Combust. Inst.* 21: 1463-1471 (1988).
9. Chen, L.-D., Seaba, J. P., Roquemore, W. M., and Goss, L. P., *Proc. Combust. Inst.* 22: 677-683 (1989).
10. Chung, S. H. and Lee, B. J., *Combust. Flame* 86: 62, (1991).
11. Takahashi, F., and Schmoll, W. J., *Proc. Combust. Inst.* 23: 677-683 (1991).
12. Veynante, D., Vervisch, L., Poinsot, T., Liñán, A., and Ruetsch, G., Proceedings of the Summer Program, Center for Turbulence Research, Stanford University, Palo Alto, California, 1994, pp. 55-73.
13. Buckmaster, J. and Weber, R., *Proc. Combust. Inst.* 26: 1143-1149 (1996).
14. Wichman, I. S. and Ramadan, B., *Physics of Fluids* 10: 3145-3154 (1998).
15. Takahashi, F. and Katta, V. R., *Proc. Combust. Inst.* 27: 675-684 (1998).
16. Takahashi, F. and Katta, V. R., *Combust. Sci. Technol.*, in press, 1999.
17. Katta, V. R., Goss, L. P., and Roquemore, W. M., *AIAA J.* 32: 84 (1994).

18. Roquemore, W. M., and Katta, V. R., *Proceedings of VSJ-SPIE98,* Yokohama, Japan, Paper No. KL310, 1998.

19. Peters, N., "Flame Calculations With Reduced Mechanisms—An Outline," in *Reduced Kinetic Mechanisms for Applications in Combustion Systems* (N. Peters and B. Rogg, Eds.), Springer-Verlag, Berlin, 1993, pp. 3-14.

20. Warnatz, J., "Rate Coefficients in the C/H/O System," in *Combustion Chemistry* (W. C. Gardiner, Ed.), Springer-Verlag, New York, 1984, p. 197-360.

21. Takahashi, F., Vangsness, M. D., and Schmoll, W. J., "Structure of the Stabilizing Region of Methane Jet Diffusion Flames," Joint Central/Western States Sections/The Combustion Institute Meeting, San Antonio, Texas, April 1995.

22. Plessing, T., Terhoeven, P., Peters, N., and Mansour, M. S., *Combust. Flame* 115: 335 (1998).

Figure Captions

Figure 1 Measured stability limits [11] and lift-off height of methane-air co-flow jet diffusion flames. $d = 9.45$ mm, $\delta = 0.2$ mm.

Figure 2 Two-color particle image velocimetry photographs of the stabilizing region of methane jet diffusion flames [21]. Laser intensity: ~20 mJ/pulse; pulse width: 10 ns; time delay: 70 μs; and sheet thickness: ~0.5 mm. Exposure time: 1/30 s. Seed particles: zirconia (<1 μm, 97 %). $d = 9.45$ mm. $U_a = 0.36$ m/s. (a) $U_j = 7.5$ m/s, seeded both fuel and air; (b) $U_j = 7.6$ m/s, seeded air only.

Figure 3 (a) Calculated velocity vectors, isotherms (unit K), heat-release rate (start at 50 J/cm^{3}s with a 100-J/cm^{3}s interval), equivalence ratio; (b) molar flux vectors of methane, oxygen, and atomic hydrogen, mole fractions of methane and oxygen, and oxygen consumption rate (start at 0.0001 mol/cm^{3}s with a 0.0004-mol/cm^{3}s interval) in the stabilizing region of a near-limit methane jet diffusion flame. $U_j = 1.7$ m/s, $U_a = 0.8$ m/s. C_2-chemistry model.

Figure 4 Flame-base structure with the one-step global chemistry model ($E = 40$ kcal/mol, $A = 2.15 \times 10^{15}$ cm^3/mol·s): calculated velocity vectors, isotherms (unit K), heat-release rate (start at 50 J/cm^{3}s with a 100-J/cm^{3}s interval), and mole fractions of methane and oxygen in the stabilizing region of a near-limit methane jet diffusion flame. $U_j = 1.7$ m/s, $U_a = 0.72$ m/s.

Figure 5 Effects of the mean co-flow air velocity on the reaction kernel properties. (a) Calculated reaction kernel coordinates and axial and radial velocity components at the heat-release rate peak. ○●, z_k; ∇▼, y_k; ◇ ◆ U_k; ΔA, V_k; + ×, Measured axial and radial visible flame base locations, respectively [16]. (b) Calculated reaction kernel

temperatures and equivalence ratios. ○●, T_k; ◇◆, ϕ_k at the heat-release rate peak; ∇▼, T_k; ΔΔ, ϕ_k at the oxygen consumption rate peak. Open, C_2-chemistry; filled, C_1-chemistry [15].

Figure 6 (a) Reaction kernel correlations between the heat-release rate, or oxygen consumption rate, and the incoming velocity. ○●, $\dot{q}_k$; ∇▼, $-\hat{\omega}_{O_2,k}$. (b) The ratios of the heat-release rate, or oxygen consumption rate, and the reaction kernel velocity. ○●, $\dot{q}_k/|v_k|$; ∇▼, $-\hat{\omega}_{O_2,k}/|v_k|$. Open, C_2-chemistry; filled, C_1-chemistry [15].

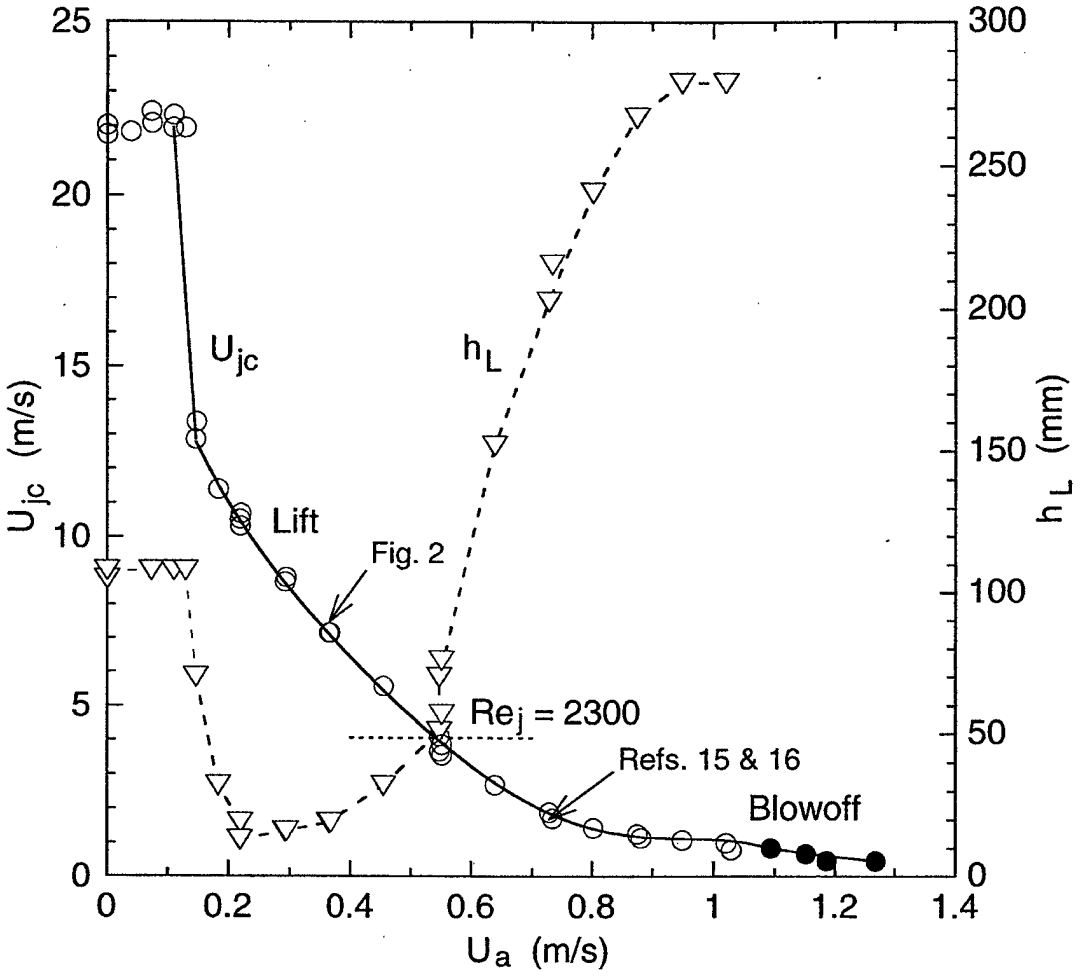
25
20
15
10
5
0
300
250
200
150
100
50
0
0
0.2
0.4
0.6
0.8
1
1.2
1.4
U_{jc} (m/s)
h_L (mm)
U_a (m/s)
U_{jc}
h_L
Lift
Fig. 2
$Re_j = 2300$
Refs. 15 & 16
Blowoff

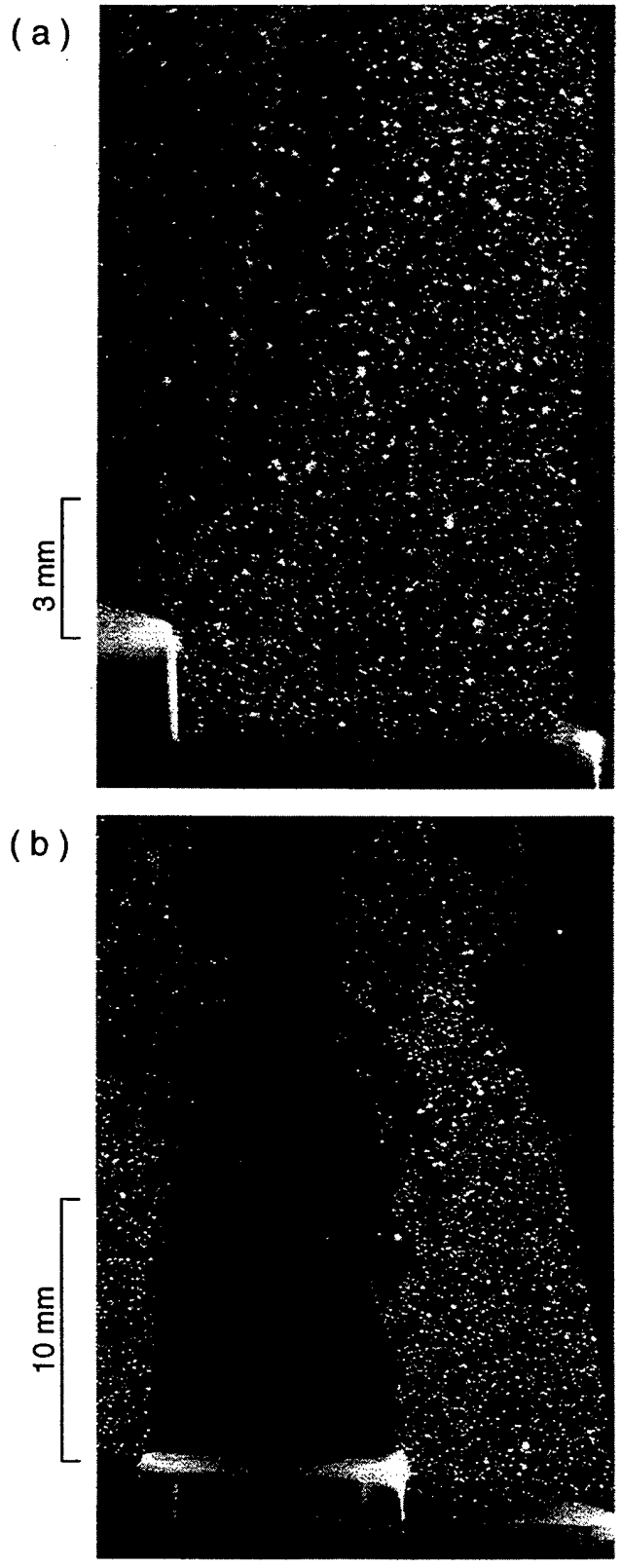
(a)
3 mm
(b)
10 mm

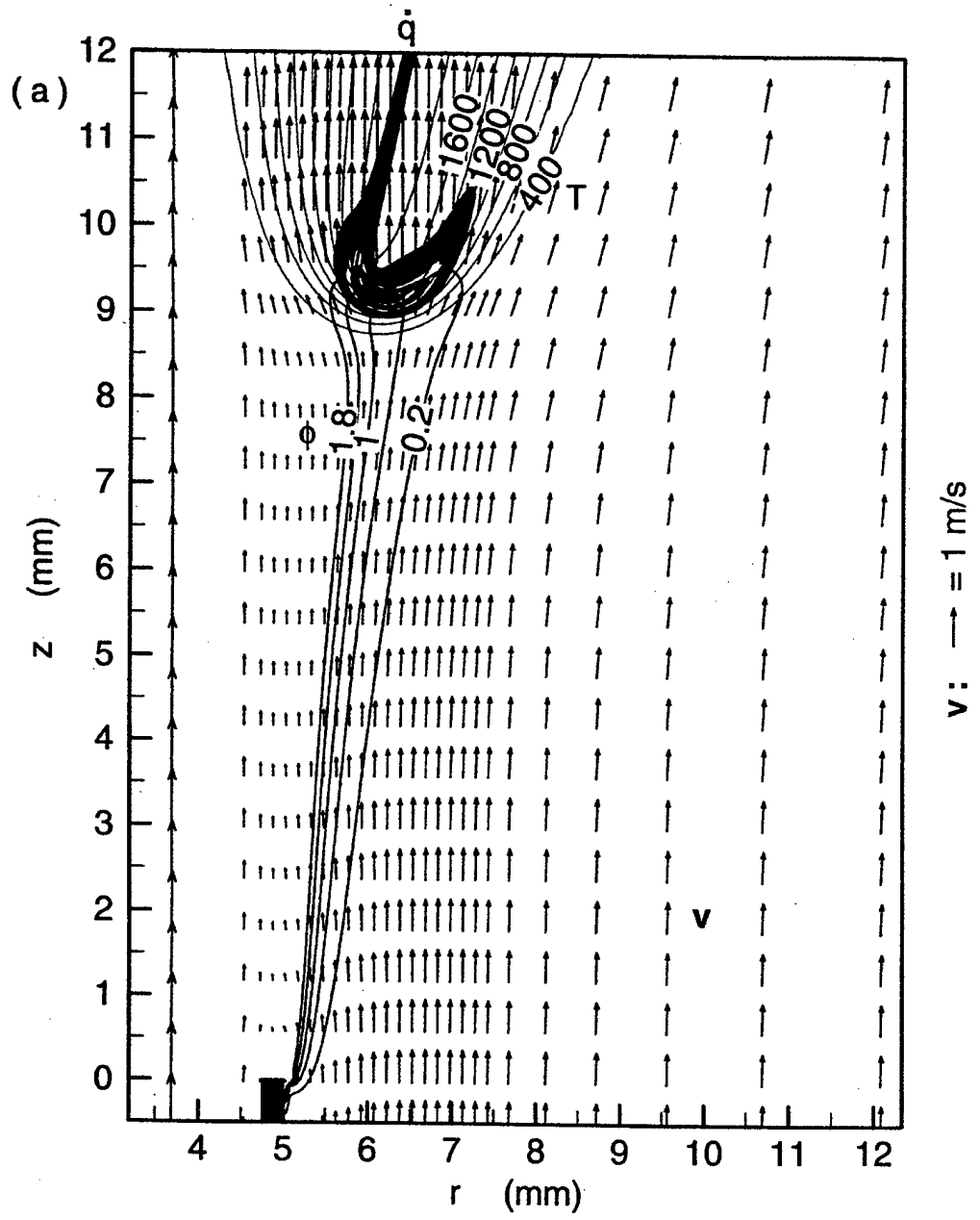
(a)
q̇
1600
1200
800
400
T
1.8
1.1
0.2
φ
v
z (mm)
r (mm)
v : ⟶ = 1 m/s

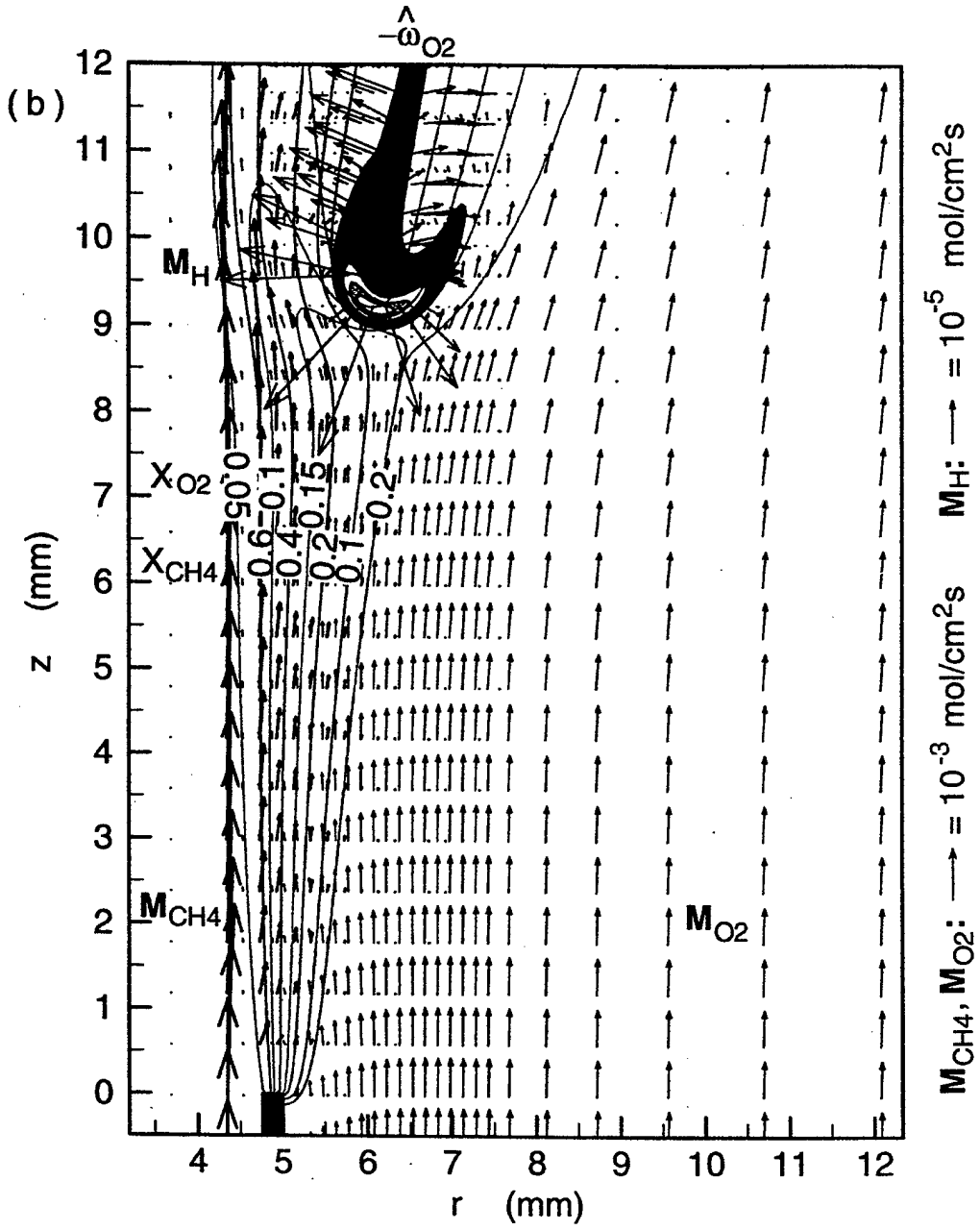
(b)
$-\hat{\omega}_{O2}$
M_H
X_{O2}
X_{CH4}
M_{CH4}
M_{O2}
0.05
0.1
0.15
0.2
0.6
0.4
0.2
0.1
z (mm)
r (mm)
M_{CH4}, M_{O2}: ⟶ = 10^{-3} mol/cm^{2}s
M_H: ⟶ = 10^{-5} mol/cm^{2}s

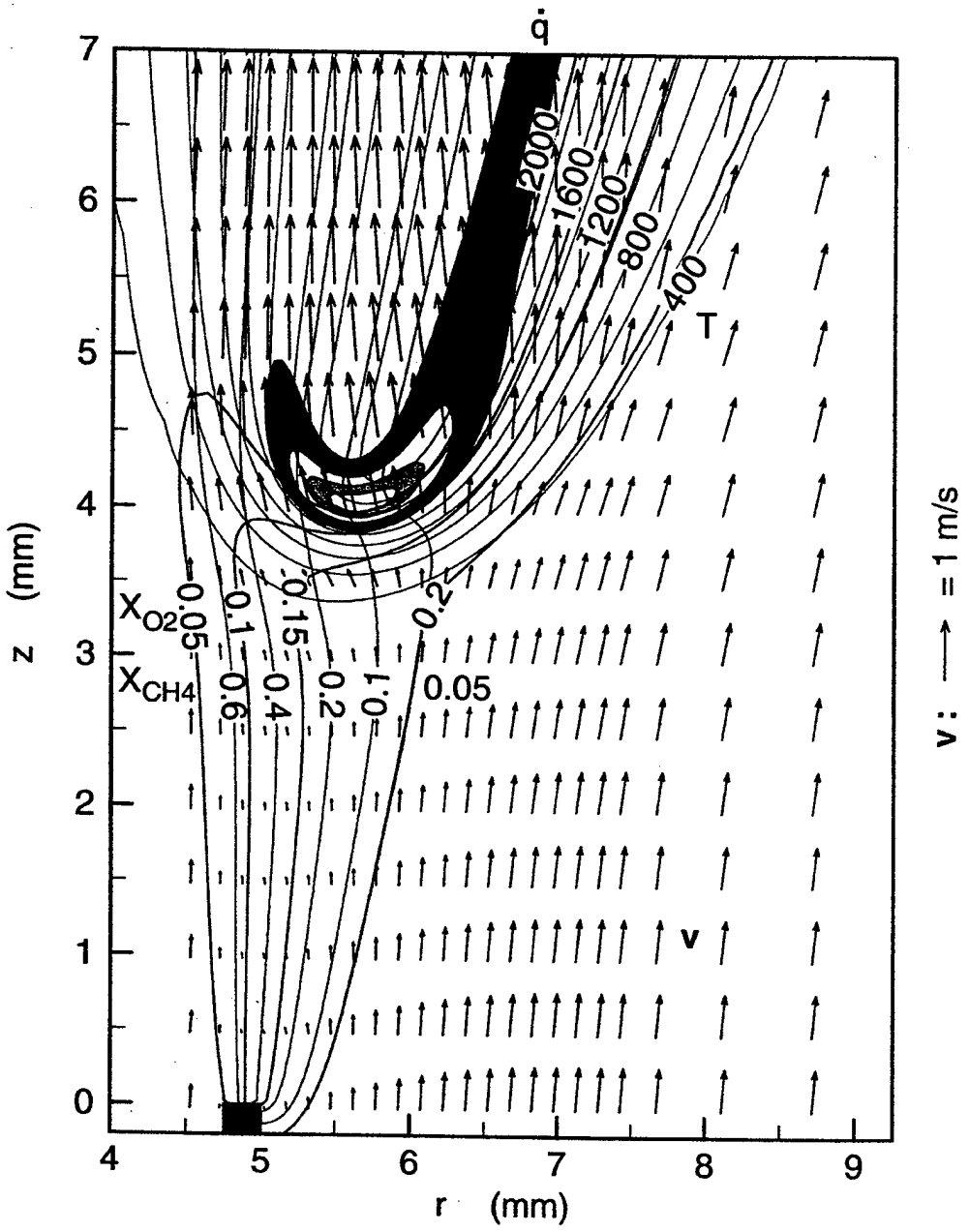
q̇
2000
1600
1200
800
400
T
0.05
0.1
0.15
0.2
X_{O2}
X_{CH4}
0.6
0.4
0.2
0.1
0.05
v
z (mm)
r (mm)
v : ⟶ = 1 m/s
0
1
2
3
4
5
6
7
4
5
6
7
8
9

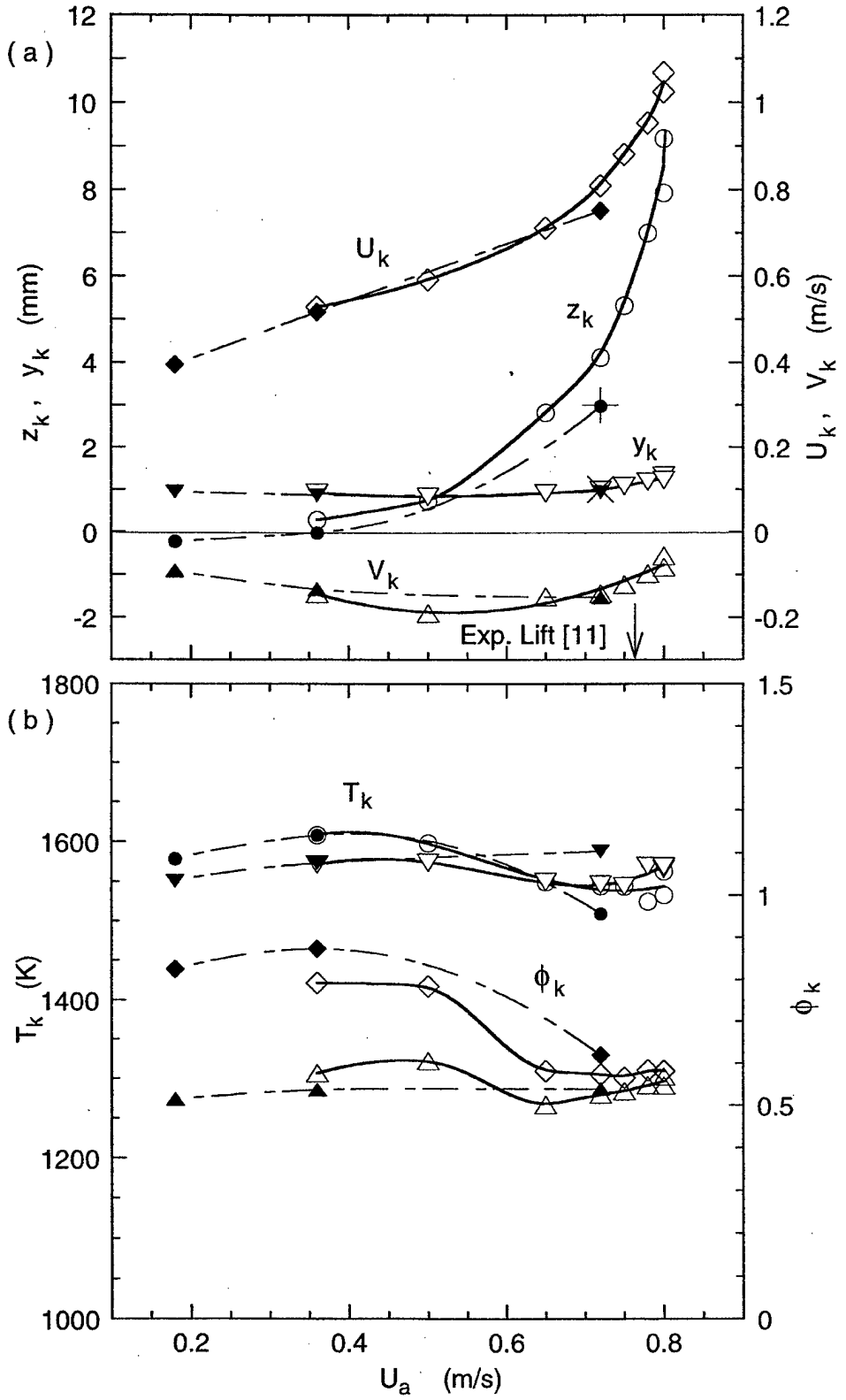
(a)
(b)
U_k
z_k
y_k
V_k
Exp. Lift [11]
T_k
ϕ_k
z_k, y_k (mm)
U_k, V_k (m/s)
T_k (K)
ϕ_k
U_a (m/s)
12
10
8
6
4
2
0
-2
1.2
1
0.8
0.6
0.4
0.2
0
-0.2
1800
1600
1400
1200
1000
1.5
1
0.5
0
0.2
0.4
0.6
0.8

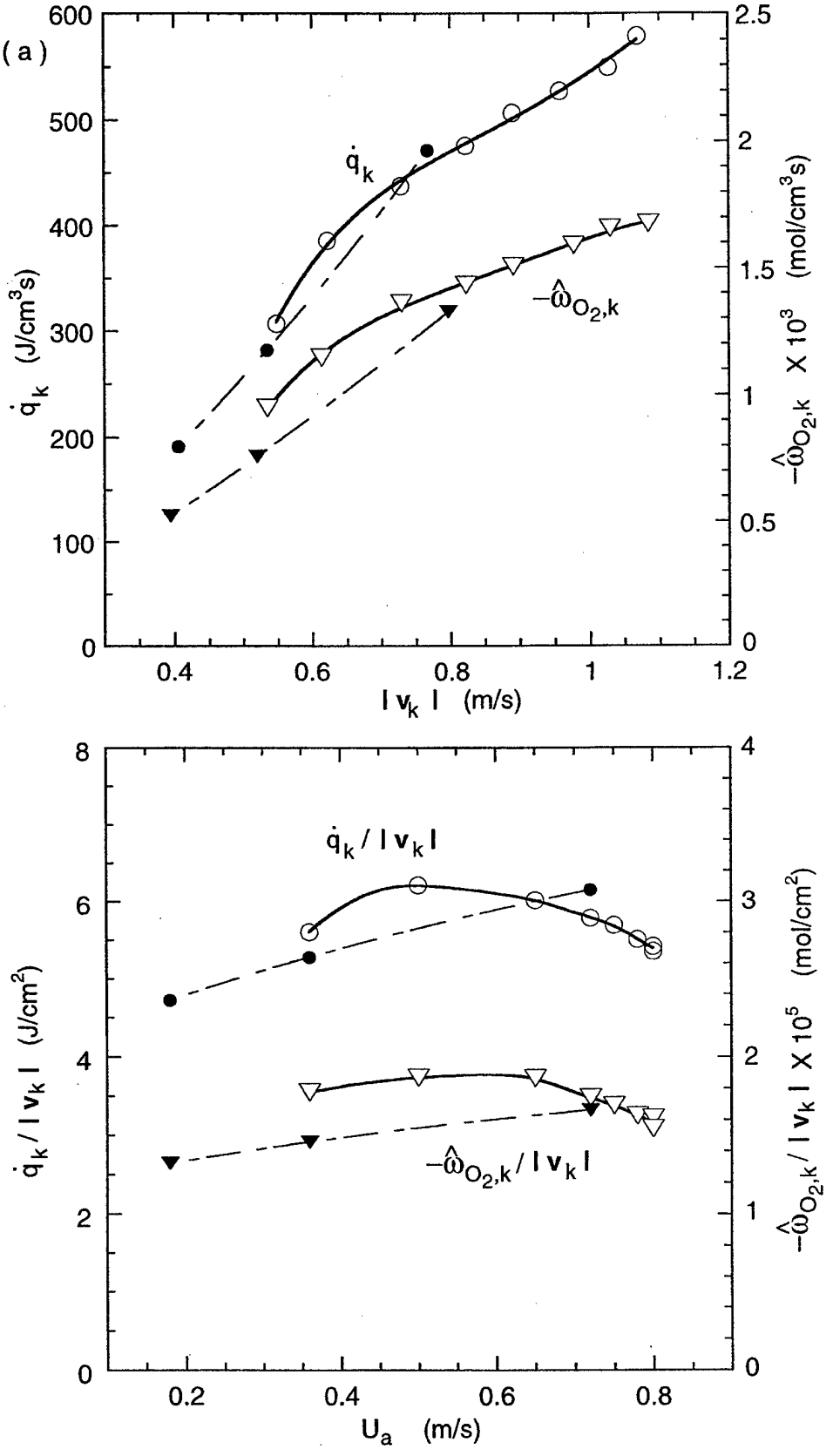
(a)
$\dot{q}_k$
$-\hat{\omega}_{O_2,k}$
$\dot{q}_k$ (J/cm^{3}s)
$-\hat{\omega}_{O_2,k}$ X 10^3 (mol/cm^{3}s)
| v_k | (m/s)
$\dot{q}_k$ / | v_k | (J/cm^2)
$-\hat{\omega}_{O_2,k}$ / | v_k | X 10^5 (mol/cm^2)
U_a (m/s)

Proceedings of the
Third International Symposium on Scale Modeling
September 10-13, 2000, Nagoya, Japan

ORIGINALLY PRESENTED AT **ISSM3**
REPUBLISHED WITH PERMISSION

A NUMERICAL AND EXPERIMENTAL STUDY OF THE STRUCTURE OF A DIFFUSION FLAME ESTABLISHED IN A LAMINAR BOUNDARY LAYER ALONG A VERTICAL POROUS PLATE

Fumiaki TAKAHASHI*, Viswanath R. KATTA, Masashi NAGAMORI†, Toshihisa UEDA†, and Masao TAKEUCHI§**
* National Center for Microgravity Research on Fluids and Combustion
NASA Glenn Research Center, MS 500-115
Cleveland, Ohio 44135, USA
** Innovative Scientific Solutions, Inc.
Dayton, Ohio, USA
† Department of Mechanical Engineering, Keio University
Yokohama, Japan
§ National Institute for Resources and Environment
Tsukuba, Japan

Key words: Diffusion flame structure, Flame stabilization, Fire spread, Boundary layer

ABSTRACT

The structure of a laminar methane diffusion flame formed along a porous-plate burner in a vertically upward combustion tunnel has been studied numerically and experimentally in normal earth gravity. Computations were performed by solving time-dependent Navier-Stokes equations including gravity along with energy- and species-conservation equations with a detailed C_2-chemistry model. The OH radical concentration field was observed qualitatively using planar laser-induced fluorescence (PLIF). As the air velocity was increased or the fuel injection velocity was decreased, the OH fluorescence appeared weaker and the flame eventually became unstable. The calculated flame structure was essentially similar to that of burner-rim-attached jet diffusion flames previously studied; a peak reactivity spot (reaction kernel) was formed in the flame base, thus anchoring the flame in the boundary layer of the incoming oxidizing stream. The calculated concentration and rate of formation of the OH radical peaked along the airside of the peak temperature, heat-release, or oxygen consumption rate, whereas the rate of destruction of the OH radical peaked on the fuel-side. The OH radicals diffused onto both sides of the flame and dehydrogenated CH_4 and H_2 on the fuel-side and HO_2 on the airside. In the flame base, radical species diffused back into an oxygen-rich reaction kernel, thus enhancing the chain-branching $H + O_2 \rightarrow OH + O$ and heat-releasing $CH_3 + O \rightarrow CH_2O + H$ reactions. Therefore, the chain radicals (H, OH, and O) played a key role in the combustion chemistry, transport phenomena, and, in turn, flame stabilization.

INTRODUCTION

As the construction of the International Space Station and the plan for the human exploration and development of space progress, various fire safety concerns in both terrestrial and extraterrestrial environments have become more realistic issues. Such issues include material flammability, fire spread rates, flame extinction, stabilization, and fire suppression.

A flame formed in a boundary layer of gaseous oxidizing stream along condensed fuel surfaces has long been studied because it relates to various combustion phenomena, including propellant combustion, abrasive burning, flame holding in combustion systems, and fire spread. In particular, the aerodynamic and thermal structures of a laminar diffusion flame over a liquid fuel pool or a flat porous plate issuing gaseous fuel have been studied as a simplified model flame by numerous investigators theoretically, numerically, and experimentally (Chen and Toong, 1964; Penner and Libby, 1967; Nakagawa et al., 1971; Kim et al., 1971; Kikkawa and Yoshikawa, 1973; Hirano and Kanno, 1973; Lavid and Berlad, 1977; Shin and Pagni, 1978; Liu et al., 1981; Mori et al., 1982; Ramachandra and Raghunandan, 1983; Ramachandra and Raghunandan, 1984; Mao et al., 1984; Raju and Law, 1985; Chen and T'ien, 1986; Ueda and Mizomoto, 1986; Ueda et al., 1991; Yashima and Hirano, 1995; Takahashi and Katta, 1997; Rohmat et al., 1998;). In fire spreading processes, complex interactions between the flame and the condensed fuel—heat transfer, fuel pyrolysis, vaporization, mass transfer, chemical reactions—take place in a small region around a flame leading edge. The chemical reaction rates are generally limited by the reactant transport rates in diffusion flames, yet partial fuel-air premixing around the leading flame edge may bring in additional complications. Thus, the structure of the flame leading edge (base) must be revealed experimentally or numerically to foster a better understanding of the diffusion flame holding and spreading mechanisms. Unfortunately, the detailed flame structure data are extremely limited. Because of apparent difficulties in measuring variables, including radical species concentrations, in the small flame-stabilizing region near the surface, a computational approach along with experimental validations appears to be particularly beneficial.

In this paper, the detailed structure of a laminar diffusion flame of methane established along a porous plate burner placed vertically in an airstream has been investigated numerically and experimentally, in normal earth gravity as a baseline case, to elucidate the flame structure and stabilizing mechanisms, which constitute building blocks of more complex fire spreading phenomena in various environments.

EXPERIMENTAL APPARATUS AND PROCEDURE

Figure 1 shows a schematic of a flow field in a vertical combustion tunnel. Air flows upward along the solid wall and a laminar boundary layer is formed. The test section is a rectangular channel with a 50mm × 210mm cross-section. A flat porous plate with 46mm × 100mm surface area is set flush with one of the vertical walls to supply fuel (CH_4). The fuel is injected from the porous plate and a flame is formed in the laminar boundary layer.

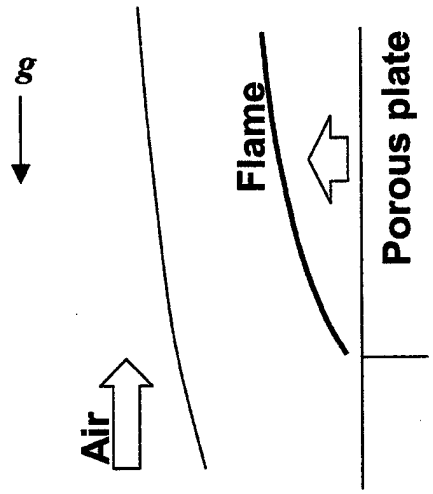

Figure 1 Schematic of the flow field

Two-dimensional images of OH-PLIF intensity are taken by a PLIF measurement system shown in Fig.2. A pulsed KrF Exima laser (248 nm, Lambda Phisik COMPex 150) is used as a light source. A-X(3,0), $P_2(8)$ line beam (248.46nm) is used as an induced light. A vertical laser sheet with 30-mm height and 1-mm thickness is formed by a lens unit and is introduced into the test section through a vertical slit opening in the vertical wall opposite to the porous plate.

Since the wave length of fluorescent light from OH radical is around 310 nm, the image is taken by a CCD camera with an image intensifier (LaVision: Flamestar II 383 × 575 pixels) through a quartz glass at the side wall of the test section and a band pass filter (UG11). To reduce the effect of the variation of the induced laser intensity and statistical noises, 200images are accumulated.

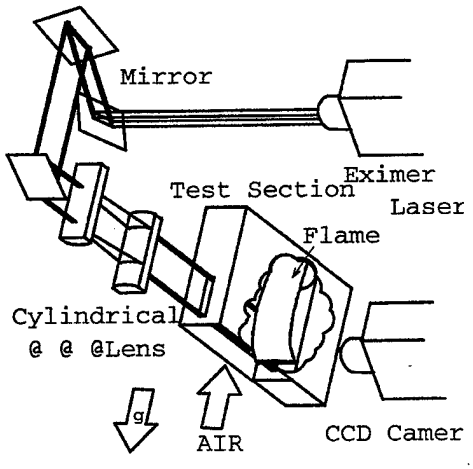

Figure 2 PLIF measurement system

In the present study, the reflection from the wall surfaces is not negligibly weak. Thus, the reflective light is eliminated as follows: at the beginning of the experiments, the image without flame is taken in which only a reflective light is recorded. In this case, 200 images are accumulated as well. This image of a reflective light is subtracted from the image with a flame using image analysis software (Lavision: SC 3.1). Experiments have been done by varying the free-stream air velocity (U_∞) and the fuel injection velocity (v).

NUMERICAL METHODS

In the mathematical model (Katta et al., 1994a), time-dependent Navier-Stokes equations are solved along with species- and energy-conservation equations in an uncoupled manner on a staggered-grid coordinate system. However, the species equations are solved by coupling them through the production terms. A clustered mesh system is employed to trace the large gradients in flow variables near the flame surface. A detailed chemical-kinetics model proposed by Peters (1993) for methane-air combustion is used in this formulation. It consists of 24 species (CH_4, O_2, CH_3, CH_2, CH, CH_2O, CHO, CO_2, CO, C_2H, C_2H_2, C_2H_3, C_2H_4, C_2H_5, C_2H_6, CHCO, H_2, H, O, OH, H_2O, HO_2, H_2O_2, and N_2) that are involved in 81 elementary reactions. Reaction rates for these elementary reactions have been obtained from Peters (1993) and Warnatz (1984) as listed elsewhere (Takahashi and Katta, 2000a).

The thermo-physical properties such as enthalpy, viscosity, thermal conductivity and binary molecular diffusion coefficients of all individual species are calculated from the polynomial curve fits developed for the temperature range 300 - 5000 K. Mixture viscosity and thermal conductivity are then estimated using the Wilke and Kee expressions, respectively. Molecular diffusion is assumed to be of the binary-diffusion type, and the diffusion velocity of a species is calculated according to Fick's law and using the effective-diffusion coefficient of that species.

The finite-difference forms of the momentum equations are obtained using an implicit QUICKEST scheme (Katta et al., 1994a) and those of the species and energy equations are obtained using a hybrid scheme of upwind and central differencing. At every time-step, the pressure field is accurately calculated by solving all the pressure Poisson equations simultaneously and utilizing the LU (Lower and Upper diagonal) matrix-decomposition technique. Treatment of the boundary conditions is identical to that reported in earlier papers (Katta et al., 1994a, 1994b; Takahashi et al., 1998; Takahashi and Katta, 2000a, 2000b). Simulations presented in this paper are performed on a Pentium II 400-MHz-based Personal Computer with 1.0 GB of memory. Typical execution time using the Peters 24-species mechanism is ~40 s/time-step, respectively on a 451x151 grid system. Using a time step of 25 μs, a complete solution is obtained in ~ 5000 time steps—which corresponds to ~50 h.

Calculations for the boundary-layer flame were performed for different flow conditions and wall and porous plate configurations. The computational domain and boundary conditions are shown in Fig. 3. As in the experiment, a flat plate having a length of 26.9 mm was placed ahead of a 33.1-mm long porous plate. Another flat plate of 40-mm long was placed behind the porous plate. In order to get a good match between the measured and computed velocity profiles at the beginning of the porous plate, a profile that represents boundary-layer-velocity profile over a 10-mm long flat plate was used at the inflow boundary. As the wall plates adjacent to the porous plate were water cooled in the experiment, room temperature (297 K) was forced for the wall and porous plates in the calculations.

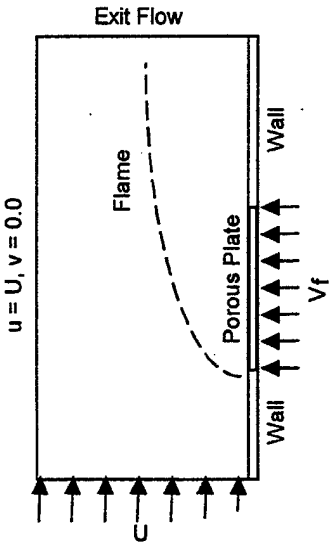

Fig. 3 Computational domain

RESULTS AND DISCUSSION

Experiment

Figure 4 shows the measured stability-limit diagram expressed in v vs. U_∞. The value of v at the stability limit increases with increasing U_∞. In Fig. 4, the conditions for the PLIF measurements are also shown as (1)-(5).

Figure 5 shows the two-dimensional OH-PLIF intensity images. High OH-PLIF intensity was observed along the visible flame. Since the air flow was upward and crossing the flame zone from the air side to fuel side, the diffusive region of OH

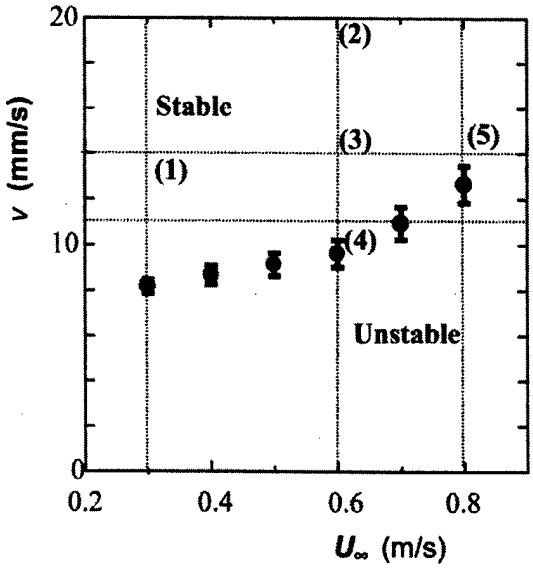

Figure 4 Stability limits

was very narrow in the air side, while OH was observed in a wide region in the fuel side at low levels. In the flame leading-edge region, no branches corresponding to the fuel-rich and fuel-lean premixed flame branches of a triple flame were observed visibly or in the OH-PLIF intensity. The result of the present study supports the following computational results showing that the leading edge essentially is the edge of a diffusion flame with peak reactivity as a result of enhanced transport phenomena.

For the stable flame conditions (Figs. 5[1] and 5[3]), the flame leading edge was located close to the upstream end of the porous plate and the OH-PLIF intensity was high. As the flame conditions approached the stability limit with increasing U_∞ or decreasing v, the flame leading edge moved downstream and the OH-PLIF intensity decreased (Figs. 5[4] and 5[5]). This result suggests that the flame leading edge became weaker in reactivity. As was shown in Fig. 4, the flame became unstable with a further increase in U_∞ or decrease in v. These results indicated that the flame leading edge became unstable as a result of the limited chemical reaction rates, leading to extinction.

Radical species, including OH, are necessary to continue the combustion. Thus, high radical pool concentrations near the flame leading edge are necessary for flame stabilization. As U_∞ was increased, convective transport of radicals from the reaction

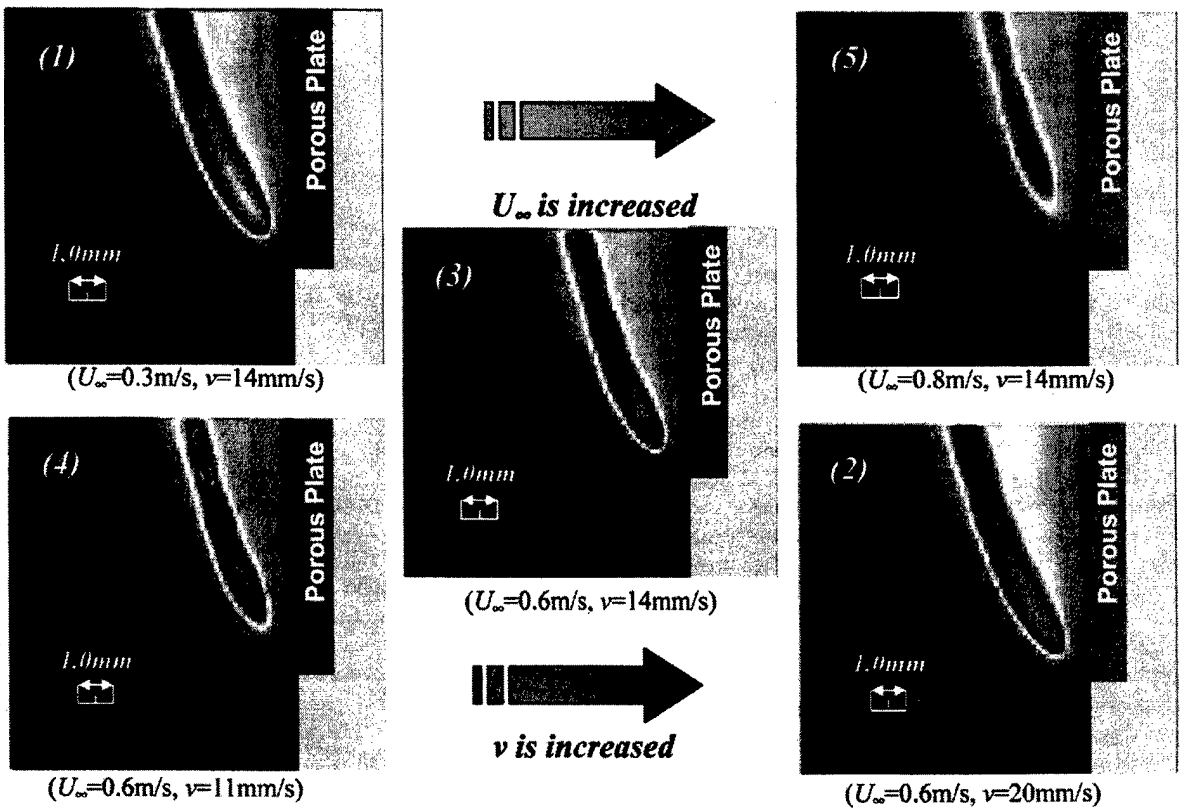

Figure 5 Two-dimensional OH concentration images

zone to the downstream direction increased, thereby resulted in an decrease in the radical concentration around the flame leading edge. As v wais decreased, the supply of CH_4 which was the original source of radicals decreased and then the radical concentration around the leading flame edge decreased.

Computation

Before simulating the flame structure, the calculated velocity profile in a cold flow was compared with the measurement by hot-wire anemometry and the equivalent Blasius profile at the leading edge of the porous plate (Fig. 6). In this calculation, the flow through the porous plate was set to zero. Here, U_∞ is the free stream air flow velocity and η is defined as $\eta = y(U_\infty/\nu x')^{1/2}$, where ν is the viscosity of air and x' is the axial distance from the virtual origin. x' was determined as 26.9 mm from the comparison between the measurement and the Blasius solution.

Reacting-flow calculations for the boundary-layer flame were performed by introducing high-temperature region along the initial mixing layer between the fuel and air. Injection of fuel through the porous plate and the flame established over the flat plate act as obstruction to the incoming airflow. As a result, the velocity profile at the leading edge of the porous plate was distorted as shown in Fig. 7. Here, the results *were* also compared to those obtained using a coarse-grid system. The close match obtained between the results computed with the 451 × 151 and 261 × 91 grid systems adequacy of the 0.05-mm grid spacing used with the finer mesh system

Figure 8 shows the calculated velocity vectors (v), isotherms (T), total heat-release rate ($\dot{q}$), and equivalence ratio

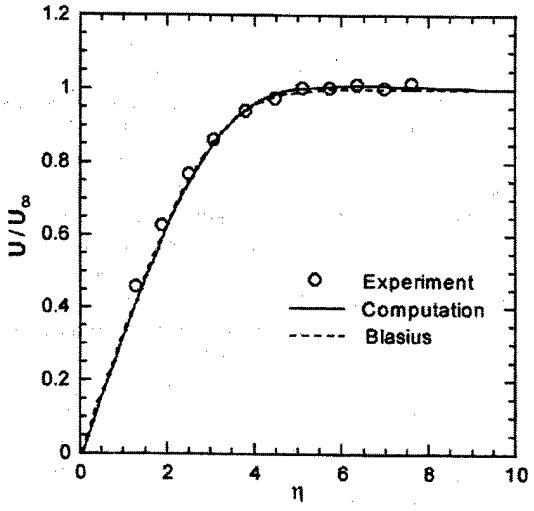

Fig. 6 Calculated and measured velocity distributions compared with the Blasius solution. U_∞ = 0.6 m/s, x = 0.

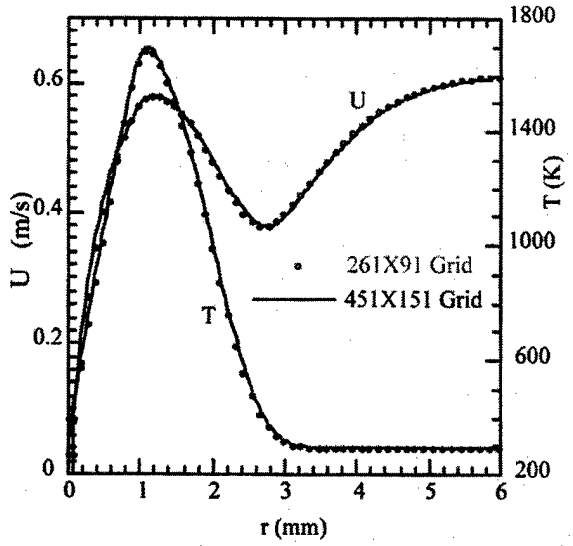

Fig. 7 Calculated axial velocity component and temperature. U∞ = 0.6 m/s, v = 14 mm/s, x = 0.

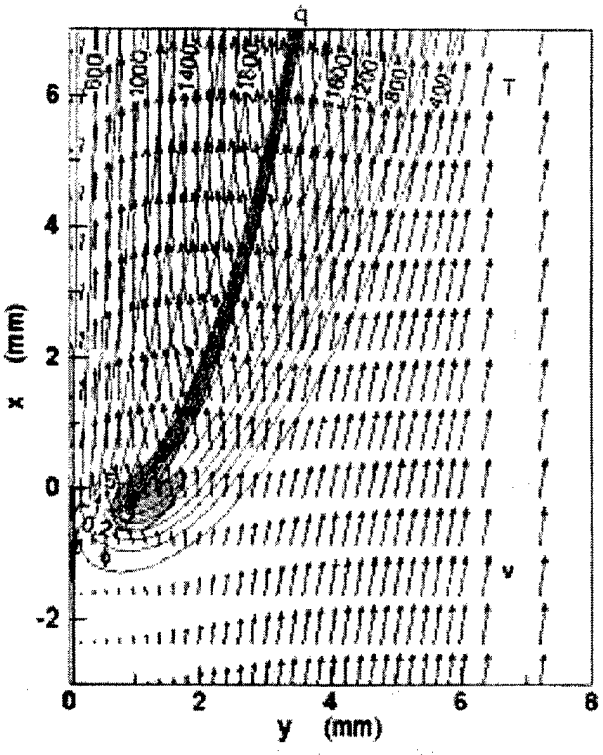

Fig. 8 Calculated velocity vectors, isotherms, total heat-release rate, and equivalence ratio in the stabilizing region. U_∞= 0.6 m/s, v = 14 mm/s.

(ϕ) in the stabilizing region. The total heat-release rate is a sum of contributions of individual elementary reaction steps. The peak reactivity spot (reaction kernel) was formed at the base of the flame at relatively low temperatures (<1600 K) as was obtained for jet diffusion flames (Takahashi et al., 1998; Takahashi and Katta, 2000a, 2000b). The flame base resided in the boundary layer of the approaching air flow, which was locally accelerated in the hot zone (velocity overshoot) due to the thermal expansion of gases and gravity. The external fluid crossed the flame zone or penetrated through the quenching space between the flame base and the surface onto the fuel-side of the flame zone. The velocity vectors and temperature fields around the flame base are extremely similar to those of burner-rim-attached jet diffusion flames (Takahashi et al., 1998).

Figure 9 shows the calculated mole fractions of methane (X_{CH_4}) and oxygen (X_{O_2}), and the molar oxygen consumption rate ($-\hat{\omega}_{O_2}$). As the air flows through the quenching zone between the flame base and the surface, the oxygen penetrated onto the fuel side of the flame more than the methane efflux onto the air side by diffusion. As a result, the partially premixed zone within the flammability limits ($0.5 < \phi < 1.7$) was formed in a narrow region in the quenching zone (see Fig. 8). As was in the jet diffusion flames, the reaction kernel was formed in the relatively low-temperature (~1600 K) fuel-lean ($\phi \approx 0.6$) conditions.

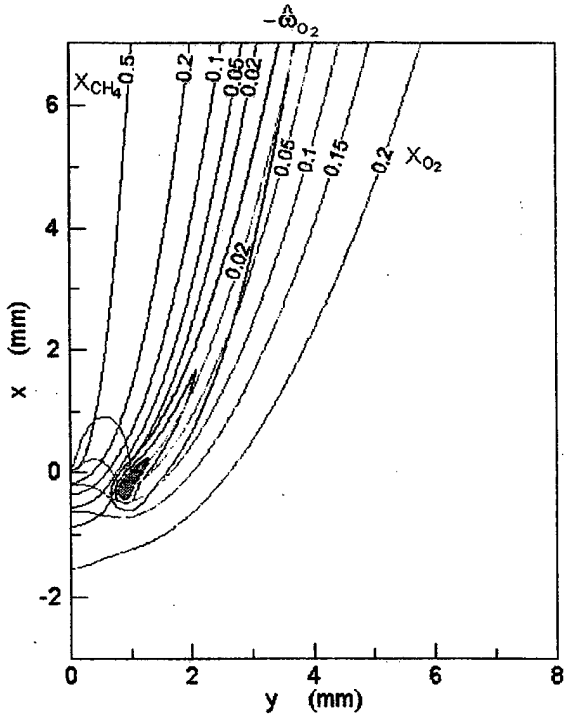

Fig. 9 Calculated mole fractions of methane and oxygen, and molar oxygen consumption rate (0.0001, 0.0003, and 0.0005 mol/cm^{3}s). U_∞= 0.6 m/s, v = 14. mm/s.

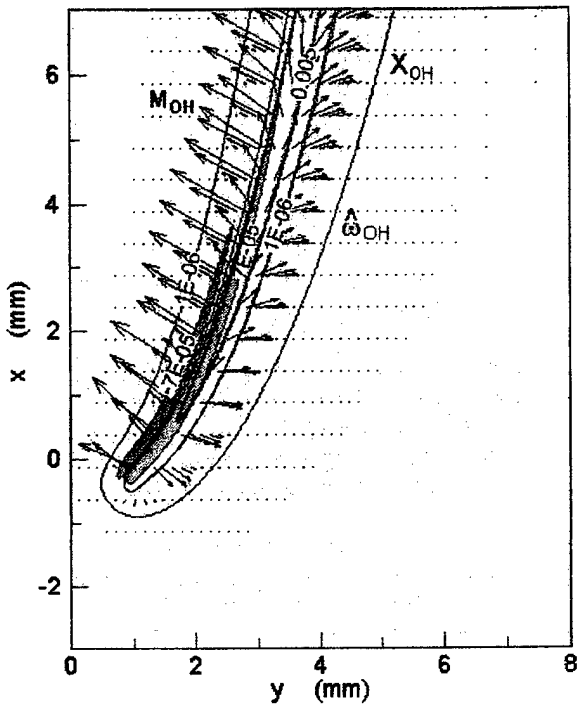

Fig. 10 Calculated mole fraction, molar flux vector, and formation rate of OH. U_∞= 0.6 m/s, v = 14.

Figure 10 shows the calculated OH mole fraction (X_{OH}), total molar flux vectors (M_{OH}), and molar rate of formation ($\hat{\omega}_{OH}$). The peak OH mole fraction and rate of formation resided along and slightly outside (air side) of the peak temperature, heat-release rate (Fig. 8), or oxygen consumption rate (Fig. 9). The radical pool was built as a result of H_2-O_2 chain reactions (R1-R8) (Takahashi and Katta, 2000a), including the most important chain-branching reaction: $H + O_2 \rightarrow OH + O$ (R1), particularly in the reaction kernel, where H atom diffused back against the incoming O_2-rich flow. The OH radical diffused on both sides of the flame and destructed mainly by dehydrogenation of CH_4 and H_2 ($CH_4 + OH \rightarrow CH_3 + H_2O$ [R53]), $H_2 + OH \rightarrow H_2O + H$ [R5]) on the fuel side and HO_2 ($HO_2 + OH \rightarrow H_2O + O_2$ [R13]) on the air side. In the reaction kernel, the heat-releasing $CH_3 + O \rightarrow CH_2O + H$ reaction was the major contribution to the heat-release rate peak (Fig. 9) as described in more detail elsewhere (Takahashi and Katta, 2000a).

CONCLUSIONS

The two-dimensional computations and OH-PLIF observations have revealed the structure of the flame stabilizing (leading edge) region of a diffusion flame formed in a boundary layer of a vertically upward air stream along a flat porous plate burner. As the flow conditions approached the stability limit, by either increasing the free stream velocity or decreasing the fuel injection velocity, the observed OH-PLIF intensity (and thus reactivity) around the leading flame edge weakened, and the flame became unstable and eventually blew off. The calculated peak OH zone and the observed OH-PLIF intensity were slightly outside (air side) of the flame zone. The computations revealed the chemical kinetic structure; the OH radical was formed by chain-branching reaction: $H + O_2 \rightarrow OH + O$ (R1), diffused on both sides of the flame, and destructed mainly by dehydrogenation of CH_4 and H_2 ($CH_4 + OH \rightarrow CH_3 + H_2O$ [R53]), $H_2 + OH \rightarrow H_2O + H$ [R5]) on the fuel side and HO_2 ($HO_2 + OH \rightarrow H_2O + O_2$ [R13]) on the air side. Both computation and experiment showed no sign of branches of rich and lean premixed flames, perceived by previous researchers as part of a triple flame structure.

ACKNOWLEDGMENTS

This work was supported under the Cooperative Agreement No. NCC3-675 (Technical Officer: Dr. Kurt R. Sacksteder) by the Office of Life and Microgravity Sciences and Applications, Human Exploration and Development of Space Enterprise, National Aeronautics and Space Administration, Washington, DC.

REFERENCES

Chen, C.-H. and T'ien, J. S., 1986 "Diffusion Flame Stabilization at the Leading Edge of a Fuel Plate," Combust. Science and Technology, Vol. 50, pp. 283-306.

Chen, T.-N. and Toong, T.-Y., 1964, "Laminar Boundary-Layer Wedge Flows with Evaporation and Combustion," Heterogeneous Combustion, Academic Press, New York, pp. 643-664.

Hirano, T. and Kanno, Y., 1973, "Aerodynamic and Thermal Structures of the Laminar Boundary Layer over a Flat Plate With a Diffusion Flame," Fourteenth Symposium (International) on Combustion, The Combustion Institute, Pittsburgh, PA, pp. 391-398.

Katta, V. R., Goss, L. P., and Roquemore, W. M., 1994a, AIAA Journal, Vol. 32, p. 84.

Katta, V. R., Goss, L. P., and Roquemore, W. M., 1994b, International Journal of Numerical Meth. Heat Fluid Flow, Vol. 4, p. 413.

Kikkawa, S. and Yoshikawa, K., 1973 "Theoretical Investigation on Laminar Boundary Layer with Combustion on a Flat Plate," International Journal of Heat and Mass Transfer, Vol. 16, pp. 1215-1229.

Kim, J. S., de Ris, J., and Kroesser, F. W., 1971, "Laminar Free-Convective Burning of Fuel Surfaces," Thirteenth Symposium (International) on Combustion, The Combustion Institute, Pittsburgh, PA, p. 949-961.

Lavid, M. and Berlad, A. L., 1977, "Gravitational Effects on Chemically Reacting Laminar Boundary Layer Flows Over a Horizontal Flat Plate," Sixteenth Symposium (International) on Combustion, The Combustion Institute, Pittsburgh, PA, pp. 1557-1568.

Liu, K. V., Lloyd, J. R. and Yang, K. T., 1981, "An Investigation of a Laminar Diffusion Flame Adjacent to a Vertical Flat Plate Burner," International Journal of Heat and Mass Transfer, Vol. 24, pp. 1959-1970.

Mao, C.-P., Kodama, H., and Fernandez-Pello, A. C., 1984, "Convective Structure of a Diffusion Flame over a Flat Combustible Surface," Combustion and Flame, Vol. 57, pp. 209-236.

Mori, Y., Hijikata, K., Miyauchi, T., and Ikeda, H., 1982, "Fundamental Study of the Laminar Boundary Layer Combustion of Liquid Fuels," Proc. JSME, Vol 48, pp. 1174-1181.

Nakagawa, Y., Nishiwaki, N., and Hirata, M., 1971, "Effect of Combustion on a Laminar Boundary Layer," Thirteenth Symposium (International) on Combustion, The Combustion Institute, Pittsburgh, PA, pp. 813-819.

Penner, S. S. and Libby, P. A., 1967, "Convective Laminar Heat Transfer with Combustion for a Lewis Number of Unity," Astronautica Acta, Vol. 13, pp. 75-91.

Peters, N., 1993, "Flame calculations with reduced mechanisms—an outline," Reduced Kinetic Mechanisms for Applications in Combustion Systems, Lecture notes in Physics, N. Peters and B. Rogg, Eds., Spriger-Verlag, Berlin, Vol. 15, pp. 3-14.

Raju, M. S. and Law, C. K., 1985, "Mixed Convective Burning of a Horizontal Flat Plate," AIAA Journal, Vol. 23, pp. 612-617.

Ramachandra, A. and Raghunandan, B. N., 1983, "On the Velocity Overshoot in a Laminar Boundary Layer Diffusion Flames," Combustion Science and Technology, Vol. 33, pp. 309-313.

Rohmat, T. A., Katoh, H., Obara, T., Yoshihashi, T., and Ohyagi, S., 1998, "Diffusion Flame Stabilized on a Porous Plate in a Parallel Airstream," AIAA Journal, Vol. 36, pp. 1945-1952.

Shin, T. M. and Pagni, P. J., 1978, "Laminar Mixed-Mode, Forced and Free, Diffusion Flames," Journal of Heat Transfer, Vol. 100, pp. 253-259.

Ramachandra, A. and Raghunandan, B. N., 1984 "Investigations on the Stability and Extinction of a Laminar

Diffusion Flame over a Porous Flat Plate," *Combustion Science and Technology* 36: 109-121.

Takahashi, F., and Katta, V. R., 1997, "A Numerical Study of a Methane Diffusion Flame Over a Flat Surface," Proceedings of the Second International Symposium on Scale Modeling, Lexington, KY.

Takahashi, F., Schmoll, W. J., and Katta, V. R., 1998, "Attachment Mechanisms of Diffusion Flames," Twenty-Seventh Symposium (International) on Combustion, The Combustion Institute, Pittsburgh, PA, pp. 675-684.

Takahashi, F., and Katta, V. R., 2000a, "Chemical Kinetic Structure of the Reaction Kernel of Methane Jet Diffusion Flames," Combustion Science and Technology, Vol. 155, pp. 243-279.

Takahashi, F., and Katta, V. R., 2000b, "A Reaction Kernel Hypothesis for the Stability Limit of Methane Jet Diffusion Flames," Twenty-Eighth Symposium (International) on Combustion, The Combustion Institute, Pittsburgh, PA, to appear.

Ueda, T. and Mizomoto, M., 1986, "Aerodynamic Structure of a Laminar Boundary Layer Diffusion Flame over a Horizontal Flat Plate," Transaction of JSME, Vol. 52, pp. 3787-3793.

Ueda, T., Ooshima, A., Saito, N., and Mizomoto, M., 1991 "Aerodynamic Structure of a Laminar Boundary Layer Diffusion Flame over a Horizontal Flat Plate (Experimental Analysis)," JSME International Journal, Series II, 34, pp. 527-532.

Warnatz, J., 1984, "Rate Coefficients in the C/H/O System," in Combustion Chemistry, W. C. Gardiner, Ed., Springer-Verlag, New York, pp. 197-360.

Yashima, M., and Hirano, T., 1995, "Characteristics of Leading Flame Edge on a Moving Combustible Solid Surface," Combustion Science and Technology, Vol. 129, pp. 371-391.

Presented at the Twenty-Eighth International Symposium on Combustion, Edinburgh, Scotland, 30 July - 4 August 2000; published in Proceedings of the Combustion Institute, Vol. 28, 2000.
PUBLISHED WITH PERMISSION

Experimental and Numerical Investigation of Structures of Two-Dimensional Partially Premixed Methane-Air Flames

V. R. Katta
Innovative Scientific Solutions, Inc.
2766 Indian Ripple Road
Dayton, OH 45440

and

L. Brenez and J. C. Rolon
Laboratoire E.M2.C
Ecole Centrale Paris and CNRS
F-92295 Châtenay-Malabry Cedex, FRANCE

Abstract:

Studies on laminar partially premixed flames are essential for the design of efficient household boilers. An idealized boiler has been designed recently to facilitate experimental and numerical investigations using various non-intrusive measurement techniques and two-dimensional Computational Fluid Dynamics (CFD) codes. This boiler mimics a commercial one in terms of power density and performance. Three test cases are selected in the present study to asses the accuracy of predictions made using a recently developed CFD code. The global equivalence ratio (primary air + secondary air) for all three cases is the same; however, the local equivalence ratio of the fuel is varied to obtain different partially premixed flame configurations. While two cases result in Bunsen-type flames, the third one yields a V-shaped flame. Spontaneous emissions from CH and OH radicals in these partially premixed flames are measured using CCD cameras and the results compared with the predictions. Calculations are performed using 24-species modified Peters chemical kinetics and a 31-species GRI-V1.2 mechanism. The weak-inner premixed and outer diffusion flames in Case 2, the Bunsen-type flame in Case 4, and the V-type flame in Case 5 are accurately simulated by the modified Peters mechanism. The predicted flame shapes and heights match well with those obtained in the experiments. On the other hand, even though GRI-V1.2 chemistry seems to predict stable flames well, it is found to fail in predicting flame structures for the conditions that are near the blowout limits. This observation on the GRI mechanism in simulating partially premixed flames is consistent with the longer standoff distances found in our earlier studies on the diffusion flame base.

Introduction:

Laminar premixed combustion has been widely studied by several researchers [1-4] since these flames are most commonly used in practical devices. On the other hand, partially premixed flames offer the advantages of both diffusion and premixed flames with regard to safety, lower pollutant levels, and flame stability. Because of these advantages, partially premixed flames may play a significant role in the development of next-generation combustion devices. To date, only a few studies have been devoted to laminar partially premixed flames employing natural gas and operating conditions similar to those used in practical devices [5,6]. It is apparent that the lack of basic knowledge in partially premixed flames is restricting the understanding of stabilization and pollutant-emission mechanisms in household boilers. Thus, fundamental studies on partially premixed flames are essential in meeting the increasingly stringent regulations concerning NOx emission limits. For example, although NOx emissions for most of the natural-gas-powered household boilers are currently around 120 mg/kWh [7], the standards are moving toward lower limits, i. e., 50 mg/kWh.

Over the years, burner manufacturers have developed rules of thumb for choosing combination design parameters such as primary fuel-air ratio, port loading, and port spacing to meet the required specifications; accordingly, most past measurements were made at the input and output of the device. This global approach often results in unwanted effects such as increase an in CO emissions or a decrease in flame stability while NOx emissions are reduced. Since the formation of pollutants in combustion devices depends on the details of the combustion process itself, insight into these fundamental processes is required for proper design of the device.

Recently, an idealized boiler was developed by Gaz de France and Worgas under a project supported by the European Community which aimed at developing tools for the design of clean, efficient household boilers. This idealized boiler mimics a commercial one in terms of power density and performance but has a simplified two-dimensional geometry. The present paper describes an experimental/numerical study conducted on this idealized boiler using non-intrusive measurement techniques and a Computational Fluid Dynamics with Chemistry (CFDC) code

developed recently for the simulation of methane flames. Several partially premixed Bunsen-type flames were obtained by varying the primary equivalence ratio while maintaining the overall equivalence ratio. V-type flames were also studied by inserting a plate in the fuel jet. The accuracies of different detailed chemical-kinetics models in simulating steady, partially premixed methane/air flames were assessed. Finally, the structures of the Bunsen- and V-type flames obtained under the same flow conditions were compared.

Experimental Setup:

Various experiments were carried out on an idealized boiler developed by Gaz de France and Worgas to mimic the key features of practical boilers while simplifying the problem to a two-dimensional one. This simplified burner consists of seven identical fuel slots (also called primary channels) having dimensions of 3 mm in width and 150 mm in length. The fuel slots are sandwiched symmetrically between 12-mm-wide air slots (also called secondary channels). Before the fuel (a mixture of methane and air) and air are passed through the respective primary and secondary channels, they flow through honeycomb filters, glass beads, and then a laminarization grid to ensure that the flows exiting the burner assembly will be highly laminar. The methane/air mixture is homogenized in a plenum chamber before entering the primary channels.

The combustion chamber (150 x 115 x 150 mm) is protected from entrainment of surrounding air by glass windows. A heat exchanger and then a chimney are placed above the combustion chamber. Five test cases were established to gain an understanding of the partially premixed flame structures associated with this idealized boiler. In all of these cases, total air and methane flowrates were set to 13.504 and 1.013 m^3/h, respectively. These flow rates correspond to a global equivalence ratio of 0.71. The primary and secondary air flow rates were independently adjusted to yield the five test conditions tabulated in Table 1. Cases 1 and 2 have the same primary and secondary flow rates and differ only in the composition of the fuel. While natural gas was used in Case 1, pure methane was used in Case 2. Test cases 4 and 5 differ only in the fact that a plate was

inserted in the fuel slots in the latter case. These plates modify the fluid dynamics and, thus, the shape of the flame for the same local equivalence ratio used in these cases.

To study the combustion mechanisms in the idealized boiler, two levels of measurements were performed: 1) global ones in the exhaust gasses and 2) detailed ones in the combustion chamber. To obtain the flame geometry and information on the chemical activity and heat-release rate [8] chemiluminescence of CH, OH, and C_2 radicals was measured. While several other measurements [9] such as OH PLIF, and thermocouple and gas analyzers were also used for characterizing the burner, they are not discussed in this paper for the sake of brevity.

In the present investigation 12-bit images of CH, OH, and C_2 global spontaneous emission were recorded using a Princeton-Instruments ICCD camera (576 x 384 pixel array) that is thermally stabilized at a low temperature using the Peltier system. Interference filters with a narrow bandwidth were used to select the emission from the radical species of interest. The camera was connected to the ST138 controller that stored the images before they were processed on a PC with Winview software. A TTL signal was provided by a HAMEG programmable function generator and delivered to a DG535 digital delay that allowed modification of the delay and exposure times of the ICCD matrix. The spatial resolution obtained by the camera was 0.2 mm per pixel. Since the emission intensities of various radical species are dramatically different, the exposure time was the only parameter adjusted during the measurements (from a few microseconds for global and OH emission to 10 ms for C_2 radical emission). Only those measurements obtained for the central slot of the burner are presented here. Also, only results obtained for Test Cases 2, 4, and 5 are presented.

Numerical Model:

A time-dependent, two-dimensional mathematical model known as UNICORN (Unsteady Ignition and Combustion using ReactioNs) [10] was used to simulate the partially premixed flames considered in this study. It solves for u- and v-momentum equations, continuity, and enthalpy- and species-conservation equations on a staggered grid system. The body-force term due to the

gravitational field is included in one of the momentum (u) equations for simulating vertically mounted flames. A clustered mesh system is employed to trace the large gradients in flow variables near the flame surface. A detailed chemical-kinetics model--originally proposed by Peters for methane-air combustion [11] and then modified by Katta and Roquemore [12] for better predictive capabilities--is used in this formulation. It consists of 24 species (CH_4, O_2, CH_3, CH_2, CH, CH_2O, CHO, CO_2, CO, H_2, H, O, OH, H_2O, HO_2, H_2O_2, C_2H, C_2H_2, C_2H_3, C_2H_4, C_2H_5, C_2H_6, CHCO and N_2) that are involved in 81 elementary reactions. Reaction rates for these elementary reactions were obtained from Ref. 11. A more comprehensive chemistry model GRI-V1.2 [13] developed by the Gas Research Institute was also used for comparison purpose. Thermo-physical properties such as enthalpy, viscosity, thermal conductivity, and binary molecular diffusion of all the species were calculated from the polynomial curve fits developed for the temperature range 300 - 5000 K. Mixture viscosity and thermal conductivity were estimated using the Wilke and Kee expressions, respectively. Molecular diffusion was assumed to be of the binary-diffusion type, and the diffusion velocity of a species was calculated using Fick's law and the effective-diffusion coefficient of that species in the mixture. Finally, the Lennard Jones potentials, the effective temperatures, and the coefficients for the enthalpy polynomials for each species are obtained from the CHEMKIN libraries.

The finite-difference forms of the momentum equations were obtained using an implicit QUICKEST scheme [14,15], and those of the species and energy equations were obtained using a hybrid scheme of upwind and central differencing. At every time-step, the pressure field was accurately calculated by solving all the pressure Poisson equations simultaneously and utilizing the LU (Lower and Upper diagonal) matrix-decomposition technique. The boundary conditions were treated as reported in earlier papers [16].

Since the idealized burner described in the previous section represents seven identical premixed flames, calculations were made for only one flame, utilizing the symmetricity in the burner configuration. The burner geometry and the boundary conditions used for the simulations are shown in Fig. 1. The tapered walls of the actual burner (shown with broken lines) are approximated as straight wall (solid lines) in the present calculations. Since the calculations were

started 15 mm upstream and the step changes in the wall geometries occurred 7.5 mm ahead of the burner tip, the low-speed laminar flow in the passages provided a stable boundary-layer flow over the corners. As a result, the approximations made for the burner geometry caused only minimal discrepancy between the simulated and actual flowfields.

Accuracy of the Simulations:

Calculations were made using a 171x71 grid system that gives a uniform grid spacing of 0.1 mm in the flame zone. To evaluate the sufficiency of the grid spacing in simulating the partially premixed flames considered, calculations for Case 2 were also made using a 251x111 grid system having a 0.05-mm spacing. Results obtained for Case 2 at a height of 4 mm above the burner tip are shown in Fig. 2. Here, the symbols represent results obtained with 171x71 grid system, while the solid lines indicate those obtained with fine mesh. As will be discussed later, the flame in this case had an inner premixed flame, and an outer diffusion flame and calculations made with coarse and fine grids captured them accurately. Overall, the heat-release rate and temperature predicted by both mesh systems were nearly identical. The slightly lower temperature at the center predicted by the fine mesh resulted from the slightly longer (by ~0.4 mm) inner flame obtained with this mesh. Figure 2 further demonstrates that even the heats of production of radical species such as OH and CH_3 are well predicted by the coarse mesh. Overall, the comparisons made for Case 2 suggest that the 171x71 mesh yields sufficiently accurate results for the partially premixed flames considered here.

To assess the accuracy of the chemical kinetics (modified Peters mechanism) used in the model, calculations were also performed for this case using GRI-V1.2 chemical kinetics. Results in the form of temperature and OH-concentration distribution at a distance of 4 mm above the burner tip are shown in Fig. 2 by broken lines. Even though the temperature and OH-concentration profiles agree well with the predictions made using the modified Peters mechanism, a careful examination of the data in Fig. 2 reveals that results obtained with the GRI-V1.2 mechanism did not predict the weak inner flame between Y = 1 and 2 mm. As a result, the profiles for heat-release rate and

species-production rates predicted by the GRI-V1.2 deviate significantly from those shown in Fig. 2.

The simulations presented here were performed on a Pentium II 400-MHz-based Personal Computer with 512 MB of memory. Typical execution times using the modified Peters mechanisms without and with C_2 chemistry and the GRI Version 1.2 mechanism are ~8, ~17, and ~42 s/time step, respectively. Converged solutions for different cases were obtained in about 1000 time steps.

Results and Discussion:

Predictions made for the Case-2 flame are presented in Fig. 3 along with the experimental results. By plotting the predictions and measurement results on the right and left halves, respectively, the molar-concentration distributions of CH and OH radicals can be compared in Figs. 3(a) and 3(b), respectively. Figure 3 suggests that the flame heights and shapes for both the inner premixed and outer diffusion flames are very well predicted. In fact, the inner flame for this fuel-rich case is quite weak and is supported by the outer diffusion flame. The predicted concentration distribution of the CH radical matches well with the measurements. Calculations have even predicted the subtle variations such as thinning of the CH concentration in the region near the tip of the inner flame (X ~ 5 mm). However, the calculations indicate that much more OH is formed in the outer diffusion flame than in the inner flame, which is in contrast to the distributions obtained using OH-emission measurements. To further investigate this discrepancy, additional calculations for this flame were made using two other reaction mechanisms: 1) the modified Peters mechanism without C_2 chemistry [12], and 2) the Gas Research Institute GRI-V1.2 [13]. Both these mechanisms yielded flames similar to the one predicted using the 24-species modified Peters mechanism, and the maximum deviation among the predictions of peak OH concentrations was found to be less than 5%. Interestingly, the GRI-V1.2 mechanism did not predict the weak inner flame (OH concentration between X = 1 and 2 mm in Fig. 2), while both the modified Peters mechanisms with and without C_2 chemistry predicted that accurately. This is

consistent with our earlier calculations for the diffusion-flame stability limits. GRI-V1.2 tends to predict longer standoff distances [17] and earlier quenching with respect to strain rate. The thicker OH distribution in the experiments was also observed by Plessing et al. [18] while investigating triple-flame structures in partially premixed gases.

The inner flame in Figs. 2 and 3 is formed with a fuel/air mixture having an equivalence ratio of 1.67. It is known that such a fuel-rich premixed flame yields OH concentrations that are much lower than those obtained with the corresponding diffusion flames. Even though the calculations made with different chemistry mechanisms predicted this behavior (i.e., that the OH concentration in the premixed-flame region is much lower than that in the diffusion-flame region), the OH-emission image obtained in the experiment did not exhibit this behavior. It is important to note here that the images of CH and OH obtained in the experiments were raw ones and required some correction for temperature and nitrogen concentrations.

Cases 4 and 5 represent fuel-lean flames. Predictions made for these cases are compared with the measurement results in Figs. 4 and 5, respectively. It is known that the premixed flames are stabilized at the burner lip, partly due to the balance between the heat loss to the surrounding media and heat generated at the flame base. The fuel-lean flame of Case 4 represents a flame that is very near the lean-blowout limit. Both the calculations and the experiment showed a dark space of ~1 mm between the flame base and the burner in which the temperature was below the ignition value and radical concentrations decreased rapidly toward the burner lip. For this case also the flame heights and shapes were well predicted by the present model. On the other hand, calculations using the GRI-V1.2 mechanism did not produce a stable flame. In those simulations, the flame moved slowly downstream until it cleared the computational domain.

The flow boundary conditions for Case 5 are identical to those used for Case 4, the only difference being that a thin plate was inserted in the fuel jet, as shown in Fig. 1, in the latter case. The insertion of the bluff body modifies the flow field and yields a different flame structure. The predicted and measured flame structures for this case are shown in Fig. 5. Calculations for this case were made using the flame data of Case 4 as initial conditions. The plate inserted in the fuel jet created a low-velocity zone behind the bluff body; at the same time the average fuel velocity within

the slot has increased by 33% due to blockage. While this higher velocity destabilized the flame anchored to the burner lip, the lower velocity behind the bluff body provided stabilizing conditions for anchoring the premixed flame there. As a result, the Bunsen-type flame structure in Case 4 slowly transformed into a V-type one in Case 5. As seen in Fig. 5, calculations correctly predicted the flame response to changes in the flowfield. The computed flame is slightly (~ 1 mm) closer to the plate and has spread about 1 mm less than that observed in the experiment. This discrepancy resulted from the approximations made to the wedge-like plate inserted in the experiment. The wedge-like body in the fuel stream was expected to cause the fuel to flow away from the center, creating a less-intense but more widely spread region of low-velocity flow. On the other hand, calculations made with GRI-V1.2 chemistry for this case resulted in a flat flame stationed ~10 mm above the burner--which is quite different from that observed in the experiment.

Detailed structures of the flames near the tips for Cases 4 and 5 are shown in Figs. 6 and 7, respectively. Temperature, u-velocity, and some major-species concentrations at X = 4 mm for the outer-lip-stabilized flame in Case 4 are plotted in Fig. 6(a), while heat-release rate and molar-production rate for each of the major species are plotted in Fig. 6(b). Similar plots for the inner-plate-stabilized flame in Case 5 are shown in Fig. 7 at X = 2 mm. A comparison of these structures reveals that the reaction zone of the inner-plate-stabilized flame (~1.8 mm) is nearly three times that (~ 0.6 mm) of the outer-lip-stabilized flame. Because of this spread combustion in Case 5, the peak heat-release rate, temperature, and species-production rates are lower than those in Case 4. Especially the production rate and concentration of H_2 are significantly reduced in Case 5. As a result of the spread combustion the reactions in the post-combustion region are completed quickly in Case 5 (X < 12 mm in Fig. 5), whereas, because of the concentrated combustion, the post-combustion reactions are extended to heights > 20 mm (Fig. 4) in Case 4. This type of spread combustion with rapid termination of post-combustion reactions produces more homogeneous hot gases and a lower pollutant region between the burner and the heat exchanger, which will be studied in the future.

Conclusions:

An idealized boiler was designed to aid the understanding of the combustion process in a commercial household boiler. Several experimental and numerical studies were performed for this idealized boiler under different flow conditions. For developing a mathematical model that can produce accurate results even under limiting conditions, three cases were selected in the present study. While the same global equivalence ratio (based on primary and secondary air) was utilized for all the three cases, the local equivalence ratio of the primary fuel was varied to obtain different partially premixed flame configurations. While Bunsen-type flames were obtained for Cases 2 and 4, a bluff body (plate) was introduced in Case 5 to form a V-shaped flame. Spontaneous emissions from CH and OH radicals were compared with the predicted concentrations of the respective species.

A two-dimensional, time-dependent CFDC code was developed for the simulation of methane/air partially premixed flames. Calculations were performed using modified Peters and GRI-V1.2 chemical mechanisms. The weak inner premixed and outer diffusion flames in Case 2 were captured accurately by the modified Peters mechanism, while the GRI-V1.2 mechanism predicted only the latter flame. Calculations for Case 5 were made using the Bunsen-type flame obtained in Case 4 as initial conditions. The plate inserted in Case 5 destabilized the flame on the outer lip and provided a stabilization region in the center to form a V-shaped flame. The modified Peters mechanism predicted this transition accurately, while the GRI-V1.2 mechanism failed to yield stabilized flames for Cases 4 and 5. The spread combustion associated with the V-shaped flame in Case 5 was found to complete the post combustion reactions quickly in a short distance.

Overall, calculations performed for the three cases using the modified Peters mechanism yielded results that are in good agreement with the measurement results and the GRI-V1.2 seemed to fail in providing a reasonable flame structure for the conditions that are near the blowout limits.

Acknowledgments:

This work was supported, in part, by Air Force Contract F33615-95-C-2507 and the Air Force Office of Scientific Research. The results of this project are published with the kind permission of the companies, universities, and organizations involved in TOPDEC and of the European Commission whose financial contribution to this project is also greatly appreciated. Finally, the authors would like to thank Mrs. M. M. Whitaker for excellent editorial help.

References:

1. Nguyen, Q. V., Dibble, R., Carter, C. D., Fiechtner, G. J., and Barlow, R. S., *Combust. Flame* 105:499-510 (1996).
2. Van Oostendorp, D. L., Borghols, W. T. A., and Levinsky, H. B., *Combust. Sci. Technol.* 79:195-206 (1991).
3. Arrigotti, S., Bernstein, S., Levinsky, H. B., Van Oostendorp, D. L., and van der Meij, C. E., *Proc. of 1992 International Gas Research Conference*, Orlando, 1992, p. 1753.
4. Hasko, S. M., Fairweather, M., Bachman, J. S., Imbach, J., van der Meij, C. E., Mokhov, A. V., Jacobs, R. A. A. M., and Levinsky, H. B., *Proc. of 1995 International Gas Research Conference*, Orlando, 1995, p. 33.
5. Van der Meij, C. E., Mokhov, A. V., Jacobs, R. A. A. M., and Levinsky, H. B., *Proc. Combust. Inst.* 25: 243-250 (1994).
6. Levinsky, H. B., Van Oostendorp, D. L., Van der Meij, C. E., Jacobs, R. A. A. M., and Mokhov, A. V., *Proc. of 1992 International Gas Research Conference*, Orlando, 1992, p. 1578.
7. Joos, L., *Proc. of the 6th International Gas Congress (IRGUC)*, Prague, 1995, p.111.
8. Shu, Z., Krass, J., Choi, C. W., Aggarwal, S. K., Katta, V. R. and Puri, I. K., *Proc. Combust. Inst.* 27:625-640 (1998).
9. Miquel, P., Larass, N., Lasagni, F., Perrin, M., F., Beghi, M., Hasko, S., Fairweather, M., Hargrave, G., Sherwood, G., Levinsky, H., Mokhov, A., DeVries, H., Martin, J.-P., Rolon, J.-C., Brenez, L., Scouflaire, P., Shin, D., Peiter, G., Dreier, T., and Volpp H., *Proc. of International Gas Research Conference*, San Diego, 1998, p. 461.
10. Roquemore, W. M., and Katta, V. R., *J. Visualization*, 2:257-272 (2000).
11. Peters, N., in *Reduced Kinetic Mechanisms for Applications in Combustion Systems, Lecture Notes in Physics*, (Springer-Verlag, New York, 1993), Vol. m15, p. 3.
12. Katta, V. R., and Roquemore, W. M., *AIAA J* 36:2044-2054 (1998).

13. Frenklach, M., Wang, H., Goldenberg, M., Smith, G. P., Golden, D. M., Bowman, C. T., Hanson, R. K., Gardiner, W. C., V. Lissianski, V., Gas Research InstituteTechnical Report No. GRI-95/0058.

14. Leonard, B. P., *Comput. Meth. Appl. Mech. Eng.*, 19:59-98 (1979).

15. Katta, V. R., Goss, L. P., and Roquemore, W. M., *AIAA J.* 32:84-94 (1994).

16. Katta, V. R., Goss, L. P., and Roquemore, W. M., *Int. J. of Numer. Meth. Heat Fluid Flow*, 4:413-424 (1994).

17. Takahashi, F., and Katta, V. R., *Combust. Sci. Technol* 155:243-279 (2000).

18. Plessing, T., Terhoeven, P., Peters, N., and Mansor, M., *Combust. Flame* 115:335-353 (1998)

Table 1: Test Cases and Conditions

Case No.	Fuel	Fuel Flow Rate m^3/h	Primary Air Flow Rate m^3/h	Secondary Air Flow Rate m^3/h	Local ϕ_{mix}
1	Natural gas blend	1.013	5.788	7.717	1.67
2	Methane	1.013	5.788	7.717	1.67
3	Methane	1.013	13.504	0	0.71
4 & 5	Methane	1.013	11.575	1.929	0.83

List of Figures:

Figure 1. Schematic diagram of burner used for simulation of partially premixed flames in idealized boiler.

Figure 2. Comparison of temperature, OH concentration, heat-release rate, and heat of production due to individual species obtained using different grid systems and chemistry models for Case 2 at X = 4 mm.

Figure 3. Measured and computed iso-molar-concentration plots of (a) CH and (b) OH radicals in Case 2. Measured data (left) obtained from spontaneous emission, and computed data (right) obtained using modified Peters mechanism.

Figure 4. Measured and computed iso-molar-concentration plots of (a) CH and (b) OH radicals in Case 4. Measured data (left) obtained from spontaneous emission, and computed data (right) obtained using modified Peters mechanism.

Figure 5. Measured and computed iso-molar-concentration plots of (a) CH and (b) OH radicals in Case 5. Measured data (left) obtained from spontaneous emission, and computed data (right) obtained using modified Peters mechanism.

Figure 6. Structure of the Bunsen-type flame in Case 4 at X = 4 mm. (a) Temperature, u velocity, and major-species concentrations. (b) Heat-release and molar-production rates for major species.

Figure 7. Structure of V-type flame in Case 5 at X = 2 mm. (a) Temperature, u velocity, and major-species concentrations. (b) Heat-release and molar-production rates for major species.

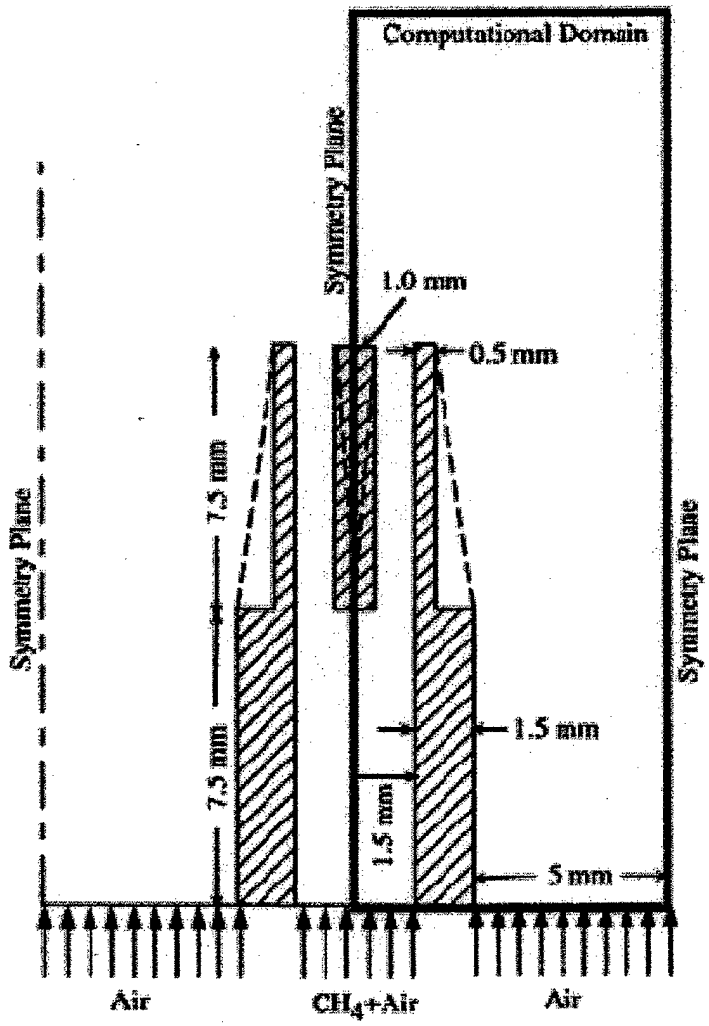
Computational Domain
Symmetry Plane
Symmetry Plane
Symmetry Plane
1.0 mm
0.5 mm
7.5 mm
7.5 mm
1.5 mm
1.5 mm
5 mm
Air
CH4+Air
Air

Figure 1

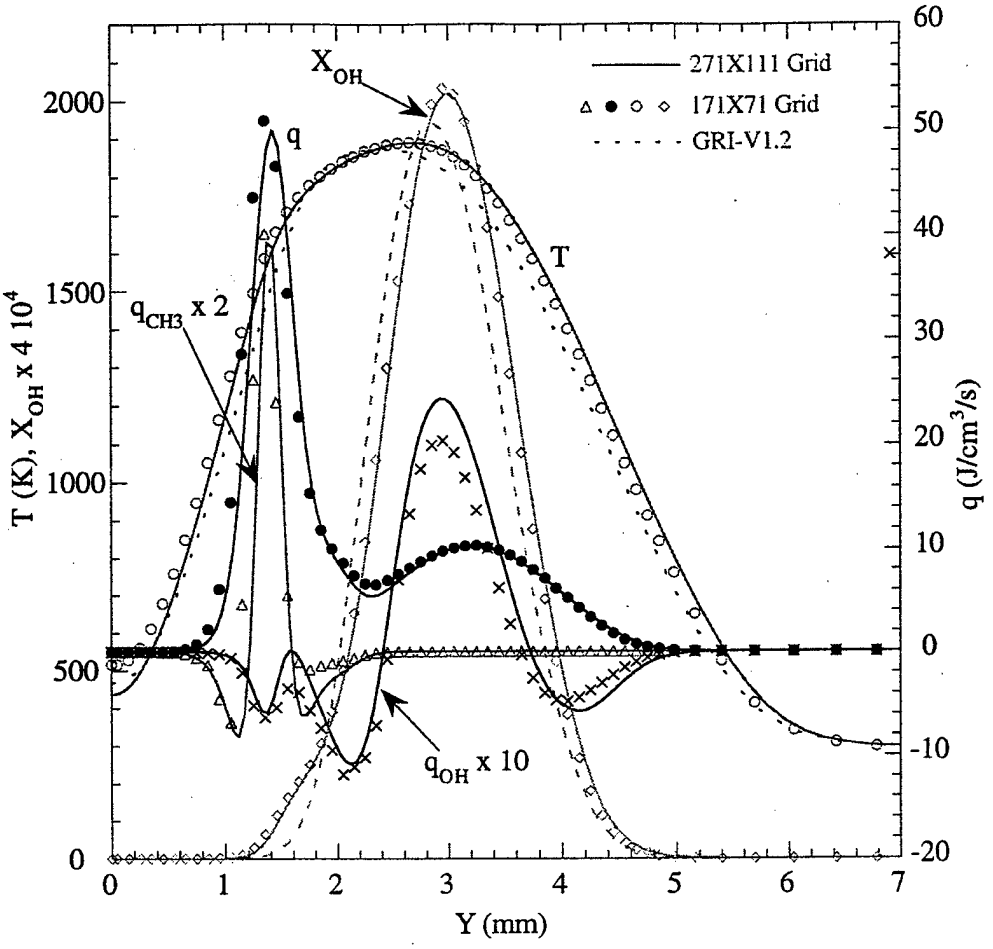
271X111 Grid
171X71 Grid
GRI-V1.2
X_{OH}
q
T
q_{CH3} x 2
q_{OH} x 10
T (K), X_{OH} x 4 10^4
q ($J/cm^3/s$)
Y (mm)
0
500
1000
1500
2000
-20
-10
0
10
20
30
40
50
60
1
2
3
4
5
6
7

Figure 2

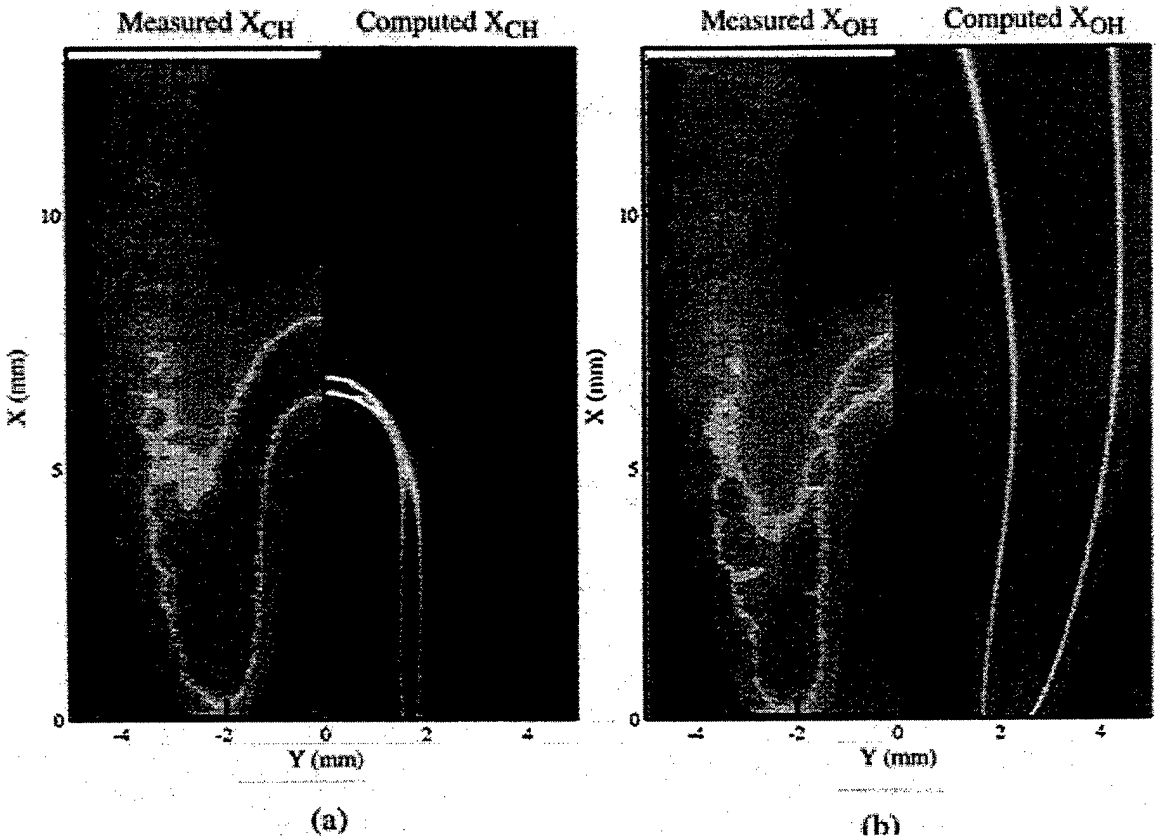
Measured X_{CH}
Computed X_{CH}
Measured X_{OH}
Computed X_{OH}
X (mm)
Y (mm)
10
5
0
-4
-2
0
2
4
(a)
(b)

Figure 3

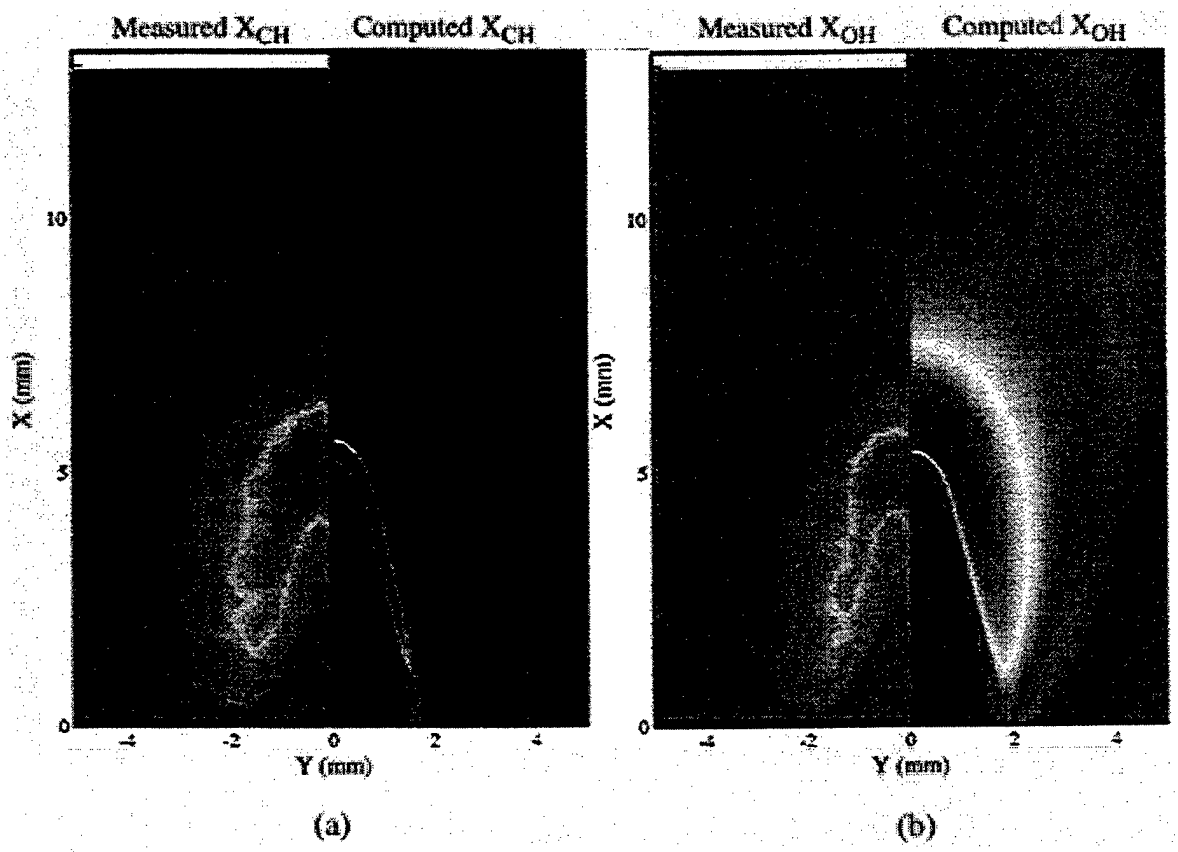
Measured X_{CH}
Computed X_{CH}
Measured X_{OH}
Computed X_{OH}
X (mm)
Y (mm)
(a)
(b)

Figure 4

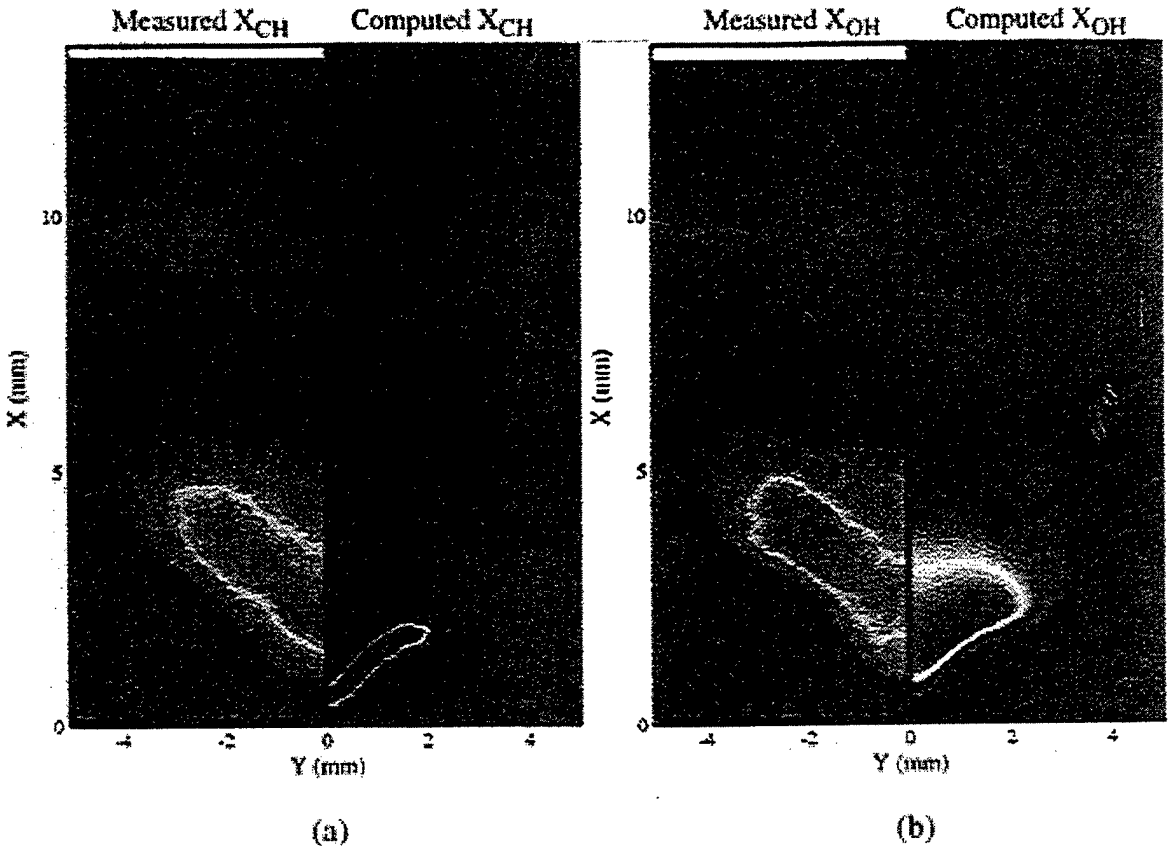
Measured X_{CH}
Computed X_{CH}
Measured X_{OH}
Computed X_{OH}
X (mm)
Y (mm)
10
5
0
-4
-2
0
2
4
(a)
(b)

Figure 5

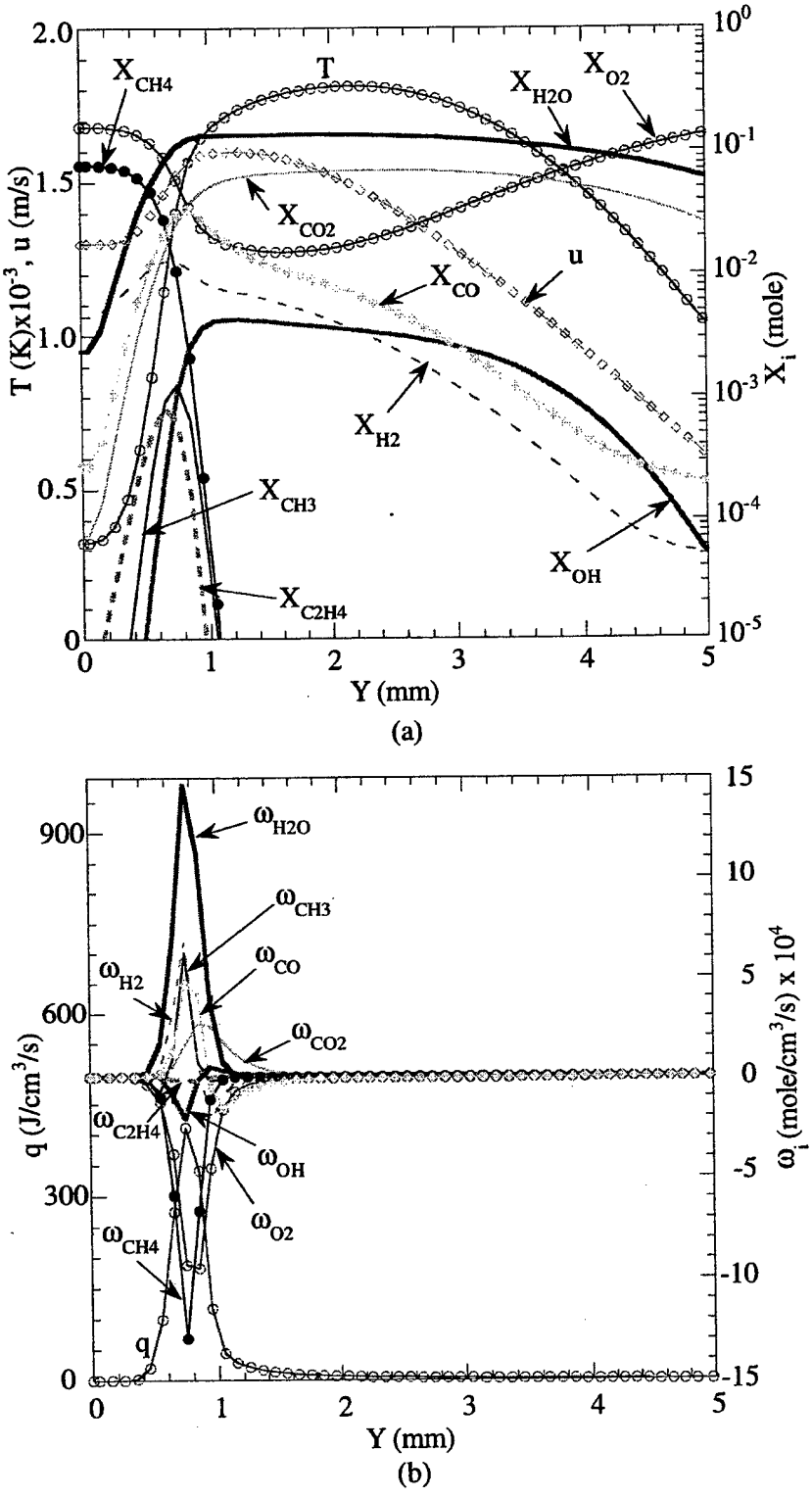
2.0
1.5
1.0
0.5
0
T (K)x10^{-3}, u (m/s)
10^0
10^{-1}
10^{-2}
10^{-3}
10^{-4}
10^{-5}
X_i (mole)
X_{CH4}
T
X_{H2O}
X_{O2}
X_{CO2}
X_{CO}
u
X_{H2}
X_{CH3}
X_{OH}
X_{C2H4}
0
1
2
3
4
5
Y (mm)
(a)
900
600
300
0
q (J/cm^3/s)
15
10
5
0
-5
-10
-15
ω_i (mole/cm^3/s) x 10^4
ω_{H2O}
ω_{CH3}
ω_{CO}
ω_{H2}
ω_{CO2}
ω_{C2H4}
ω_{OH}
ω_{O2}
ω_{CH4}
q
0
1
2
3
4
5
Y (mm)
(b)

Figure 6

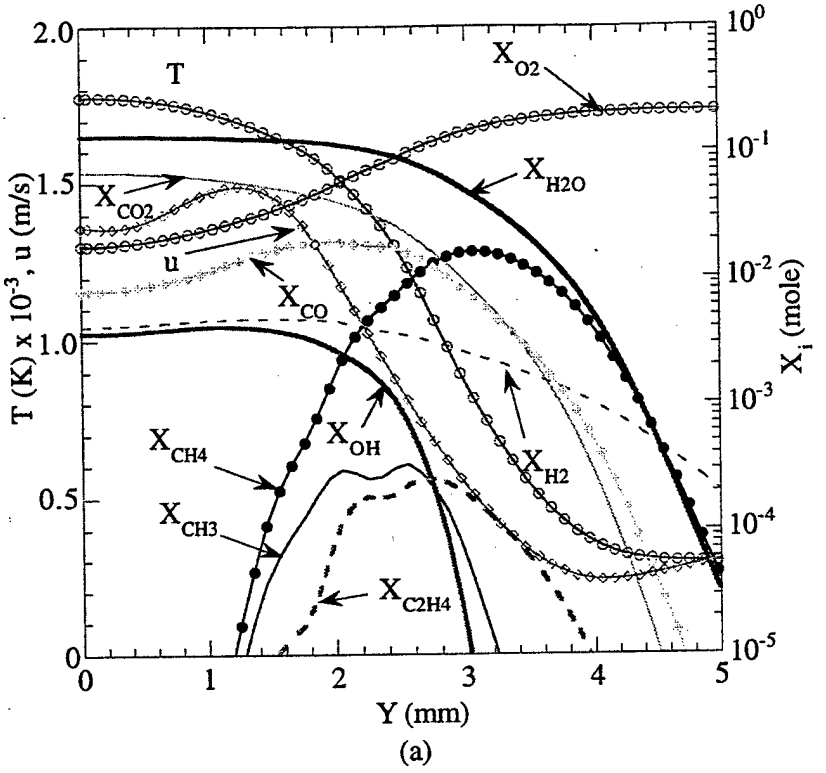
T
X_{O2}
X_{H2O}
X_{CO2}
u
X_{CO}
X_{OH}
X_{CH4}
X_{CH3}
X_{H2}
X_{C2H4}
T (K) x 10^{-3}, u (m/s)
X_i (mole)
Y (mm)
(a)

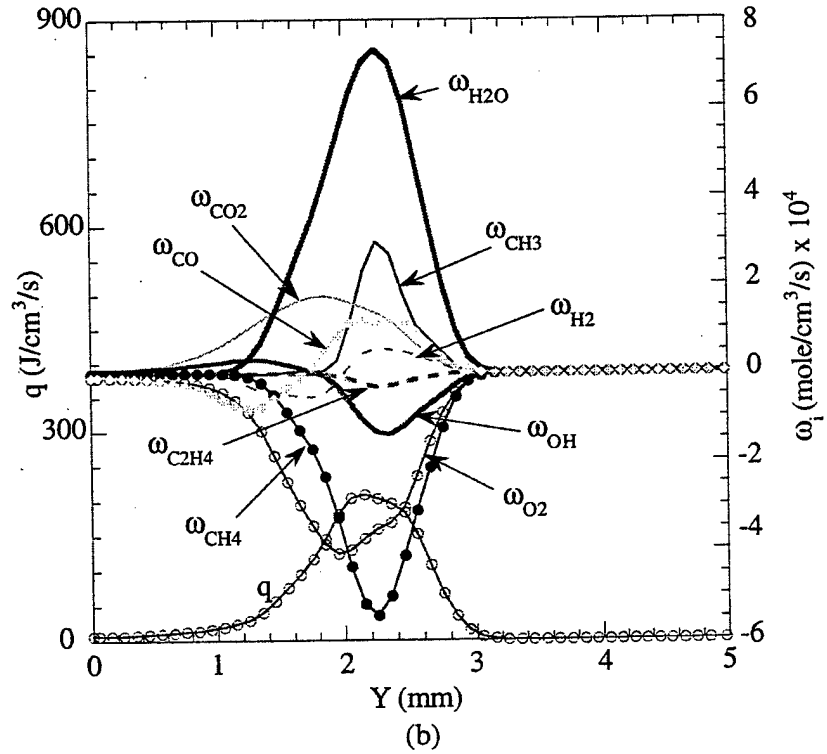
ω_{H2O}
ω_{CO2}
ω_{CO}
ω_{CH3}
ω_{H2}
ω_{OH}
ω_{C2H4}
ω_{O2}
ω_{CH4}
q
q (J/cm^3/s)
ω_i (mole/cm^3/s) x 10^4
Y (mm)
(b)

Figure 7

4.1.3 Opposing-Jet Diffusion Flames

A flame formed between opposing fuel and air jets represents a simple system for simulating and understanding laminar flame structure. The paper entitled "Response of Hydrogen-Air Opposing-Jet Diffusion Flame to Different Types of Perturbations" (see pp. 914-934) documents the results of a numerical investigation to explore the similarities and differences in unsteady flame structures that are established through various modes of perturbation in an opposed-jet diffusion flame. A time-dependent, axisymmetric CFDC code that incorporates finite-rate chemical kinetics was developed for the direct simulation of counterflow jet flames; using this code, the extinction process in strained flames was investigated, and the results are reported in the paper entitled "Extinction in Methane-Air Counterflow Diffusion Flame – A Direct Numerical Study" (see pp. 935-940).

Presented at the Twenty-Eighth International Symposium on Combustion, Edinburgh, Scotland, 30 July - 4 August 2000; published in Proceedings of the Combustion Institute, Vol. 28, 2000.
PUBLISHED WITH PERMISSION

Response of Hydrogen-Air Opposing-Jet Diffusion Flame to Different Types of Perturbations

V. R. Katta
Innovative Scientific Solutions, Inc.
2766 Indian Ripple Road
Dayton, OH 45440

and

W. M. Roquemore
Air Force Research Laboratory
Propulsion Directorate
Wright-Patterson Air Force Base, OH 45433

Abstract:

Studies on the structure of a strained flame in a steady or unsteady state are important to the understanding of turbulent-flame behavior. A numerical investigation is performed to explore the similarities and differences in unsteady flame structures that are established through various modes of perturbation in an opposed-jet diffusion flame. A diluted hydrogen-nitrogen mixture is used as the fuel. Vortices are driven toward the flame surface with different velocities from the air side, fuel side, or both sides. Changes in the structure of the flame during its interaction with the incoming vortex/vortices are investigated using a time-dependent CFDC code that incorporates 13 species and 74 reactions. Calculations have identified two types of unsteady flames--traveling and stationary. It is found that when a vortex is issued from either the air or the fuel side, the flame not only becomes strained but also moves with the vortex head, creating a traveling unsteady flame. On the other hand, if two vortices are issued--one from each side of the flame--then the flame is subjected to an unsteady strain rate; however, it is locked in a spatial location, leading to a stationary unsteady flame. The structures of theses two types of unsteady flames near the extinction limits are studied. Stationary unsteady flames are also established by fluctuating the fuel and air jets simultaneously, and sinusoidally, and their structures are compared with those obtained during the vortex/flame interactions. It is found that in comparison with stationary unsteady flames, traveling unsteady flames can be subjected to higher strain rates without extinction.

Introduction:

Studies on the structure of dynamic flames are important to the understanding of fundamental combustion processes; they provide insights into turbulent combustion phenomena and help developing and evaluating simplified models that can be used in design codes for practical combustion systems. Unsteady flames are subjected to stretching that varies in time; typically, the time scale for the changes in strain rate is comparable to the chemical response time of the system. Numerous investigations (experimental and numerical)[1-3] have been performed to quantify the scalar structure of steady-state, aerodynamically strained, planar diffusion flames. Such studies on counterflow diffusion flames have not only provided benchmark experimental data but also yielded valuable insight into the flame behavior in response to strain rate. However, in practical combustion devices, flames are subjected to severe unsteadiness that results from the random motion of vortices;[4,5] this led to studies of unsteady counterflow flames. To retain the simplicity offered by planar diffusion flames, unsteadiness is imposed on counterflow flames by fluctuating the fuel and air jets simultaneously and sinusoidally.[6,7] These studies have demonstrated that the unsteady flames can be stretched beyond the steady-state extinction limit.

During vortex-flame interactions, which are often considered to be the building blocks for statistical theories of turbulence, the flame surface is subjected not only to unsteadiness but also to deformation. To investigate the effects of curvature on unsteady flames, both theoretical and experimental studies have been initiated.[8,9] In particular, experiments designed by Roberts et al.[10] and by Rolon[11] have created great interest, especially because of their unique ability to inject a well-characterized vortex toward the flame surface.

Unsteady flames may be treated into two categories separated into two types--namely, traveling and stationary. In the first type not only the strain rate on the flame but also its location changes with time. On the other hand, in the second type, only the strain rate on the flame varies with time, while the flame itself is locked spatially. In an opposing-jet flame, when a vortex is issued from either the air or the fuel side, the flame not only becomes strained but also moves with the vortex head, creating a traveling unsteady flame. However, if two vortices are issued--one from each side

of the flame--then the flame becomes locked to a spatial location, even though it is subjected to an unsteady strain rate. This leads to a stationary unsteady flame. Structures of theses two types of unsteady flames must be understood if mathematical models for turbulent flames are to be developed.

Several investigators have developed models[12-14] for the study of vortex-flame interactions in opposing-jet flames. In all of these models, it is assumed that an artificially created (by specifying the vorticity field) vortex pair interacts with a flat flame formed in a parallel flow. Although such an assumption has advantages in exploring interesting aspects of vortex-flame interactions, investigations employing this assumption do not represent actual interactions in opposing-jet flames and hence, they could not facilitate direct comparisons between predictions and measurement results and make verification of the predictions difficult.

Recent advances in computer-hardware technology and the need to improve the understanding of combustion phenomena under complex practical situations have led to the development of two- and three-dimensional Computational Fluid Dynamics models that incorporate detailed chemical kinetics (CFDC).[15,16] Complete simulation of the counterflow diffusion flame using multi-dimensional models would not only eliminate the concerns regarding the simplified analyses but also provide a valuable tool for studies of vortex-flame interactions in counterflow premixed[10] and diffusion[11] flames. This paper describes a numerical study of traveling and stationary unsteady flames generated through various vortex/flame interactions in a hydrogen opposing-jet diffusion flame.

Numerical Model:

Time-dependent, axisymmetric Navier-Stokes equations written in the cylindrical-coordinate (z-r) system are solved along with species- and energy-conservation equations.[17] A detailed-chemical-kinetics model has been used to describe hydrogen-air combustion. This model consists of thirteen species--namely, H_2, O_2, H, O, OH, H_2O, HO_2, H_2O_2, N, NO, NO_2, N_2O, and N_2. A

detailed-chemical-kinetics model having 74 reactions among the constituent species is used, and the rate constants for this H_2-O_2-N_2 reaction system were obtained from Ref. 18.

Temperature- and species-dependent property calculations are incorporated in the model. The governing equations are integrated on a nonuniform staggered-grid system. An orthogonal grid having rapidly expanding cell sizes in both the axial and radial directions is employed. The finite-difference forms of the momentum equations are obtained using an implicit QUICKEST scheme,[19,20] and those of the species and energy equations are obtained using a hybrid scheme of upwind and central differencing. At every time step, the pressure field is calculated by solving the pressure Poisson equations simultaneously and utilizing the LU (Lower and Upper diagonal) matrix-decomposition technique. This model has been validated previously by simulating various steady and unsteady counterflow[21] and coflow[17,22] jet diffusion flames.

Results:

The opposing-jet-flame burner used for the studies of unsteady flame structures was designed by Rolon[11] and is shown in Fig. 1(a) and is described in Ref. 11. A flat flame is formed between the fuel and air jets having velocities of 0.69 and 0.5 m/s, respectively. The hydrogen-to-nitrogen ratio used for the fuel jet is 0.38. Calculations for this axisymmetric flame were made using a non-uniform 301 x 121 mesh system distributed over a physical domain of 40 x 40 mm, which yielded a mesh spacing of 0.1 mm in both the axial (z) and the radial (r) directions in the region of interest.

Steady-State Flame Structure:

The computed steady-state flame structure along the stagnation line is shown in Fig. 1(b). The 48-s^{-1} air-side strain rate of this flame represents a weakly strained one. The flame (peak-temperature region) is located at z = 19.2 mm, and its temperature of 1560 K is only slightly lower than the corresponding adiabatic temperature of 1614 K. In general, the peak strain rate on the fuel side ($K_f = 60\ s^{-1}$) will be greater than that on the air side as a result of the difference in the density

of the two jets. Even at this low strain rate, the fuel and oxidizer are not completely consumed simultaneously in the flame zone. In a overlap region of ~1 mm, both H_2 and O_2 are present.

The steady-state strain rate of the opposing-jet flame can be increased by gradually increasing the velocities of the fuel and air jets. Calculations were repeated by varying the jet velocities, and it was found that a stable steady-state flame can be obtained for fuel and air jet velocities of 16 and 14 m/s, respectively. These velocities yielded an air-side strain rate (K_a) and flame temperature of 1410 s^{-1} and 1130 K, respectively; these values agree favorably with calculations made by Gutheil et al.[23]

Air-Side Vortex:

As described earlier, vortices are shot toward the flame surface from the air side by injecting a specified amount of air (2.2 cm^3) through the syringe tube. Vortex evolution and its interaction with the flame surface depend on the injection time. In general, with the shorter injection times, the generated vortices travel faster toward the flame surface and affect its structure as the local flow time scales approach the chemical time scales. In the present study, the unsteady flame simulations were performed by injecting air through the syringe tube in such a way that the velocity at the exit increased linearly at a rate of 10^3 m/s/s.

The axial velocities recorded at four locations along the stagnation line (z = 0, 12.5, 20, and 27.5 mm) are plotted with respect to time in Fig. 2(a). The profile at z = 0 represents the one used to represent the transient boundary conditions for the unsteady-flame simulation. In the opposing-flow configuration, the linearly increasing velocity profile transformed into a wave-like profile as the injected mass approached the stagnation point. The oscillations in the axial velocity that appear after the vortex has passed result from the secondary instabilities established on the injected-air-jet column. These instabilities were also observed in the experiments of Fiechtner.[24]

The vortex and flame structures at t = 12.1 ms are shown in Fig. 2(b). While the vortex structure is shown through plots of the instantaneous locations of the particles that were continuously injected from both the air and fuel nozzles, the flame structure is shown through plots

of the iso-contour lines of temperature (on the right side) and OH concentration (on the left side). Since a diffusion flame is always established on the air side of the stagnation plane, the vortex head crossed the high-temperature contour in this case. At 12 ms, the flame is quenched annularly, as observed from the break in the OH contours. This annular-quenching phenomenon was also observed in the experiments of Fiechtner et al.[21,24] for the same conditions.

Fuel-Side Vortex:

The unsteady traveling flame established by a fuel-side vortex is shown in Fig. 3. In this case also the amount of fluid (fuel) injected from the fuel-side syringe nozzle is equal to that employed for the air-side vortex generation. However, as evident from the slopes of the velocities in Fig. 3(a), the vortex generated on the fuel side is traveling slower than that generated on the air side. This is due to the lower momentum associated with the light fuel injected at the same velocity. The secondary oscillations developed on the injected-fuel-jet column are also weaker in this case.

The vortex and flame structures at t = 12.1 ms are shown in Fig. 3(b). Since the diffusion flame is always established on the air side of the stagnation plane, the vortex head originated on the fuel side never crosses the high-temperature contour. The continuous OH and temperature contours around the vortex head indicate that the flame has not been quenched in this case.

Vortices from Both Sides:

An unsteady stationary flame was established by injecting the same amount of fluid from each of the fuel- and air-side nozzles. The axial velocities recorded at the four locations (z = 0, 12.5, 20, and 27.5 mm) are plotted with respect to time in Fig. 4(a), and the vortex and flame structures at t = 9.5 ms are shown in Fig. 4(b). In this case also, the amount of fluid injected from each of the syringe nozzles was the same as that used in the previous two cases. However, because of the differences in density, the vortex generated on the air side traveled slightly faster than that

generated on the fuel side. As a result, the flame surface drifted about 0.5 mm toward the fuel nozzle from the steady-state flame location of 19.2 mm in 9.5 ms.

The interaction of the two vortices with the flame surface [Fig. 4(b)] resulted in a point extinction. In this case, extinction first occurred at the stagnation line and then extended radially outward. This is in contrast to the annular extinction observed in the case of the air-side-vortex/flame interaction [Fig. 2(b)].

Vibrating Flame:

Another method of creating a stationary unsteady flame in an opposing-jet-flame configuration involves vibrating the flame using sinusoidal velocity modulation for the fuel and air jets. Typical results for this case are shown in Fig. 5. Here, the air and fuel jet velocities are modulated with imposed velocities of 10 and 12.1 m/s, respectively. To avoid high negative velocities at the nozzle exits, which result in significant suction of the surrounding fluid into the nozzles, the steady-state velocities are increased to 5 and 6.9 m/s for the air and fuel flows, respectively. The frequency of oscillation is 150 Hz. As evident in Fig. 5(a), the velocity modulations on two sides of the flame are in phase with each other.

The flowfields obtained in the minimum- and maximum-velocity phases are shown in the left and right halves of Fig. 5(b), respectively. In this figure, iso-temperature contours are superimposed on the velocity fields. Because of the fluctuating strain rate applied to the flame, its thickness varies between 3.1 mm (in minimum-velocity phase) and 1.0 mm (in maximum-velocity phase), and the flame has not been extinguished. Note that the steady-state flame thickness for this increased-velocity case is ~1.5 mm.

Discussion

The air-side and fuel-side vortex/flame interactions resulted in traveling unsteady flames. However, a detailed analysis of the simulations revealed that the traveling unsteady flames associated with these moderate-speed vortices transform into traveling steady-state flames near the end of the interaction process. For demonstrating the effects of such transformation on flame behavior, traces of the flame location and the changes in the flame temperature are shown in Fig. 6 as functions of time for all four cases considered in this study. To elucidate the extinction process, the flame structures along the stagnation line for these four cases are plotted in Fig. 7. The times is Figs. 7(a)-7(d) and those in Figs. 2-5, respectively, are matched

With both the air-side- and the fuel-side-injection cases, the flame velocity increased with time initially and then approached a constant value (flame velocity is aparent from the slope in the flame position in Fig. 6). In the case of the air-side vortex, the flame reached a steady velocity of 4.05 m/s in about 11 ms after the start of the vortex injection. Between 11 and 13 ms, the flame represents a traveling steady-state flame. Interestingly, the flame temperature decreased quickly to 1230 K from 1560 K while the flame was accelerating and then slowly to ~1150 K while the flame was moving at a constant velocity of 4.05 m/s. When the temperature of the flame was reduced to 1150 K, quenching occurred and then the temperature was decreased again rapidly to room temperature, even though the vortex was traveling at the same velocity of 4.05 m/s. This suggests that the diffusion flame responds more to acceleration than to translational velocity. In fact, the flame temperature decreased only by 10 K in the case of the fuel-side-vortex/flame interaction during this constant-velocity phase. This means that the flame chemistry in this case adjusted to the new velocity conditions, and quenching did not occur even when the interaction was advanced for a long period of time. Of course, other factors such as flame curvature might become significant in extended-period interactions and could affect the flame chemistry. Indeed, in the case of the air-side-vortex/flame interaction that is what occurred to yield annular extinction. Extinction in this case occurred in an annular ring away from the stagnation line, even though the local air-side strain rate was lower than that at the stagnation line.

The air-side strain rate at the stagnation line during the air-side-vortex/flame interaction increased to 340 s^{-1} at t = 9.1 ms and to 1770 s^{-1} at t = 12.1 ms [Fig. 7(a)]. The flame at this instant is near to its extinction limit. In contrast, the steady-state flame was extinguished for a strain rate of only 1410 s^{-1}. This is in agreement with previous studies[25] which suggest that unsteady flames withstand much higher stain rates than the steady-state ones.

In the case of the fuel-side-vortex/flame interaction, the flame reached a steady velocity of 3.5 m/s in about 10 ms after the start of fuel injection, resulting in a traveling stationary flame between 10 and 13 ms. The air-side strain rate increased to only 180 s^{-1} at t = 9.1 ms and to 820 s^{-1} at t = 12.1 ms. Even though the flame in this case was not extinguished, its temperature was reduced to 1260 K--just 110 K above the extinction value. Further calculations with slightly higher acceleration ($1.1x10^3$ m/s^2) for fuel injection yielded extinction. Interestingly, even in this case the air-side strain rate increased to 912 s^{-1} only--which is much lower than that required to extinguish the flame with the air-side vortex. On the other hand, the fuel-side strain rate (K_f) increased to a value well above 1800 s^{-1}. This suggests that even though the air-side stain rate is used to characterize a steady-state flame, it is not sufficient to describe the extinction behavior of an unsteady flame, especially when the flame is perturbed with fuel-side vortices. Similarly, when the air- and fuel-side vortices were used simultaneously to perturb the flame, the respective side strain rates reached values of 1690 and 2300 s^{-1} just after extinction [Fig. 7(c)]. As seen in Fig. 6, the flame did not move appreciably from its steady-state location during the vortex/flame/vortex-interaction process. However, the temperature decreased more rapidly than in the single-vortex/flame-interaction cases.

When the flame was periodically perturbed by modulating the fuel and air flows, it did not become quenched but reached near-extinction limits. As seen in Fig. 6, the flame temperature oscillated between 1450 and 1150 K, and its location moved within a 1-mm space. The structure of the flame when its temperature is lowest is shown in Fig. 7(d). Interestingly, the air- and fuel-side strain rates increased to only 1400 and 1650 s-1, respectively; these rates were significantly lower than those required for extinguishing the flame using a single vortex or double vortices. This is understandable since the flame in the vibrating case was subjected to periodic perturbation for a

long period of time (four cycles prior to t = 0) and since the flame chemistry does not respond similarly to increasing and decreasing strain rates. This was confirmed in our further studies with different frequencies, which indicated that the maximum strain rates required for extinguishing the flame increase with frequency. Such observation is consistent with the other numerical and experimental studies such as in References 6, 7, and 25. It is important to note that perturbation of the same magnitude but at a lower frequency developed higher strain rates on the flame.

Conclusions:

Unsteady flames are often studied to gain a better understanding of turbulent-flame structures and, hence, facilitate the development of accurate turbulence-chemistry interaction models. A time-dependent CFDC code that incorporates 13 species and 74 reactions among the constituent species has been developed for simulation of unsteady flames resulting from different vortex-flame interactions in opposing-flow hydrogen jet diffusion flames. The model has been validated by direct simulation of several steady-state and unsteady axisymmetric counterflow and coflow jet diffusion flames.

A steady-state opposing-flow jet flame was established using the Rolon-burner geometry. Several unsteady flames were then obtained by injecting vortices into the flow by ramping the velocity at the center portion of the air-jet exit, fuel-jet exit, or both. Calculations performed for different injection schemes have identified two types of unsteady flames--namely, traveling and stationary. It was found that when a vortex is issued either from the air or the fuel side, the flame is not only strained but also moves with the vortex head, creating a traveling unsteady flame. On the other hand, if two vortices are issued--one from each side of the flame--then the flame is subjected to an unsteady strain rate; however, it is locked to a spatial location, leading to a stationary unsteady flame. A stationary-unsteady flame is also obtained by fluctuating the fuel and air jet velocities sinusoidally. It was found that the air-side strain rate is not sufficient for characterizing unsteady flames, especially those perturbed from the fuel side. In general, unsteady flames were found to withstand higher strain rates than the steady-state ones; in particular, traveling unsteady flames can withstand higher strain rates than stationary unsteady flames.

Acknowledgments:

This work was supported, in part, by Air Force Contract F33615-95-C-2507 and the Air Force Office of Scientific Research. The authors would like to thank Mrs. M. M. Whitaker for excellent editorial help.

References:

1. Kee, R. J., Miller, J. A., Evans, G. H., and Dixon-Lewis, G., *Proc. Combust. Inst.* 22: 1479-1486 (1988).
2. Dixon-Lewis, G., *Proc. Combust. Inst.* 23: 305-324 (1990).
3. Chelliah, H. K., Law, C. K., Ueda, T., Smooke, M. D., and Williams, F. A., *Proc. Combust. Inst.* 23: 503-510 (1990).
4. Hottel, H. C., and Hawthorne, W. R. *Proc. Combust. Inst.* 3: 254-266 (1949).
5. Roquemore, W. M., Chen, L.-D., Goss, L. P., and Lynn, W. F. in *Turbulent Reactive Flows*, Lecture Notes in Engineering (R. Borghi and S. N. B. Murthy, Eds.) (Springer-Verlag, Berlin, 1989), Vol. 40, p. 49.
6. Darabiha, N., *Comb. Sci. Technol.*, 86: 163 (1992).
7. Egolfopoulos, F. N., and C. S. Campbell, *J. Fluid Mech.*, 318: 1 (1996).
8. Paul, P. H., and Najm, H. N., *Proc. Combust. Inst.* 27: 43-50 (1998).
9. Patnaik, G., and Kailasanath, K., *Proc. Combust. Inst.* 27: 711-717 (1998).
10. Roberts, W. L., Driscoll, J. F., Drake, M. C., Ratcliffe, J. W., *Proc. Combust. Inst.* 24: 169-176 (1992).
11. Rolon, J. C., Aguerre, F., and Candel, S., *Combust. Flame* 100:422 (1995)
12. Ashurst, W. T., *Combust. Sci. Technol.* 92:87 (1993).
13. Poinsot, T., Trouve, A., Veynante, D., Candel, S., and Esposito, E., *J. Fluid Mech.* 177:265 (1987).
14. Rutland, C. J., and Ferziger, J. H., *Combust. Flame* 84:343 (1991).
15. Smooke, M. D., Ern, A., Tanoff, M. A., Valdati, B. A., Mohammed, R. K., Marran, D. F., Long, M. B., *Proc. Combust. Inst.* 26: 2161-2168 (1996).
16. Katta, V. R., and Roquemore, W. M., AIAA Paper 97-0904, Jan., 1997.
17. Katta, V. R., and Roquemore, W. M., *Combust. Flame* 100:61 (1995).

18. Frenklach, M., Wang, H., Goldenberg, M., Smith, G. P., Golden, D. M., Bowman, C. T., Hanson, R. K., Gardiner, W. C., V. Lissianski, V., Gas Research Institute Technical Report No. GRI-95/0058, November 1, 1995.

19. Leonard, B. P., *Comput. Meth. Appl. Mech. Eng.*, 19:59 (1979).

20. Katta, V. R., Goss, L. P., and Roquemore, W. M., *AIAA J.*, 32:84 (1994).

21. Katta, V. R., Carter, C. D., Fiechtner, G. J., Roquemore, W. M., Gord, J. R., and Rolon, J. C., *Proc. Combust. Inst.* 27: 587-594 (1998).

22. Grisch, F., Attal-Tretout, B., Bouchardy, P., Katta, V. R., and Roquemore, W. M., *J. Nonlin. Opt. Phys. Mater.*, 5:505 (1996)

23. Gutheil, E., Balakrishnan, G., and Williams, F. A., in *Lecture Notes in Physics* (N. Peters and B. Rogg, Eds.) (Springer-Verlag, New York, 1993), pp. 177-195.

24. Fiechtner, G. J., Renard, P.-H, Carter, C. D., Gord, J. R., and Rolon, J. C., 1998, *J Visualization* 2: 331-342 (2000)

25. Brown, T. M., Pitz, R. W., and Sung C. J., *Proc. Combust. Inst.* 27: 703-710 (1998).

List of Figures:

Figure 1. (a) Opposing-jet flame burner designed by Rolon, (b) steady-state flame structure obtained for air and fuel jet velocities of 0.5 and 0.69 m/s, respectively.

Figure 2. Traveling unsteady flame created by forcing vortex from air side. (a) Variation of velocity with time at different locations, (b) at t = 12.1 ms, iso-contours of temperature on right side and OH concentration on left side, superimposed on instantaneous locations of particles injected from fuel and air sides.

Figure 3. Traveling unsteady flame created by forcing vortex from fuel side. (a) Variation of velocity with time at different locations, (b) at t = 12.1 ms, iso-contours of temperature on right side and OH concentration on left side, superimposed on instantaneous locations of particles injected from fuel and air sides.

Figure 4. Stationary unsteady flame created by forcing vortices from air and fuel sides. (a) Variation of velocity with time at different locations, (b) at t = 9.5 ms, iso-contours of temperature on right side and OH concentration on left side, superimposed on instantaneous locations of particles injected from fuel and air sides.

Figure 5. Stationary unsteady flame created by pulsating both air and fuel jets simultaneously and sinusoidally. (a) Variation of velocity with time at different locations, (b) iso-temperature contours superimposed on velocity vectors at minimum-velocity instant on left side and at maximum-velocity instant on right side.

Figure 6. Variations of flame location and temperature with time obtained for different unsteady flames.

Figure 7. Flame structure along stagnation line (a) at 12.1 ms during air-side-vortex/flame interaction, (b) at 12.1 ms during fuel-side-vortex/flame interaction, (c) at 9.5 ms during double-vortex/flame interaction, and (d) at maximum-stretch phase on vibrating flame.

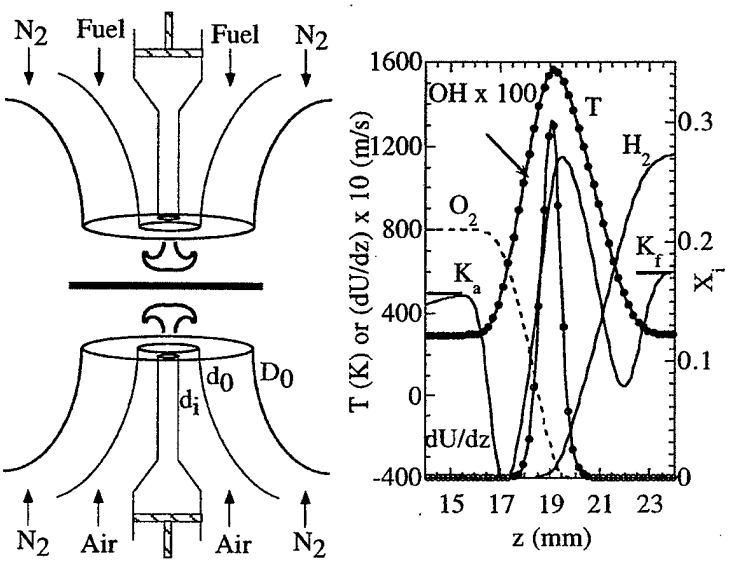
N2
Fuel
Fuel
N2
D0
d0
di
N2
Air
Air
N2
1600
1200
800
400
0
-400
OH x 100
T
H2
O2
Kf
Ka
dU/dz
T (K) or (dU/dz) x 10 (m/s)
Xi
0.3
0.2
0.1
0
15
17
19
21
23
z (mm)

(a) (b)

Figure 1

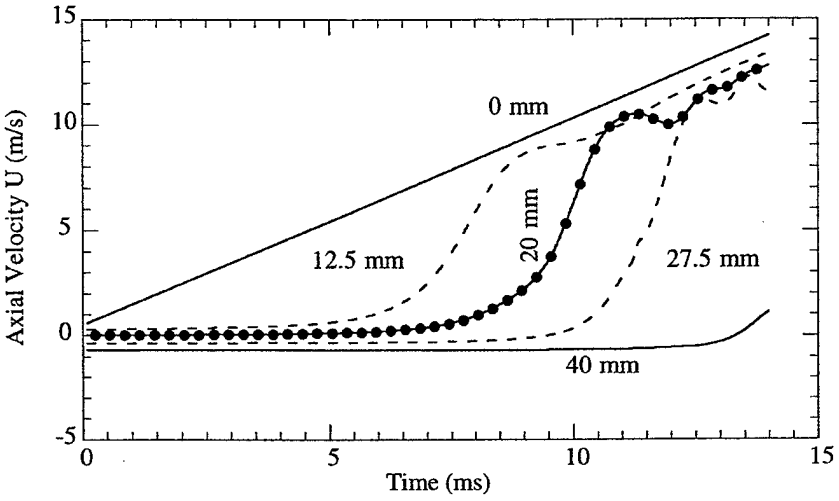

(a)

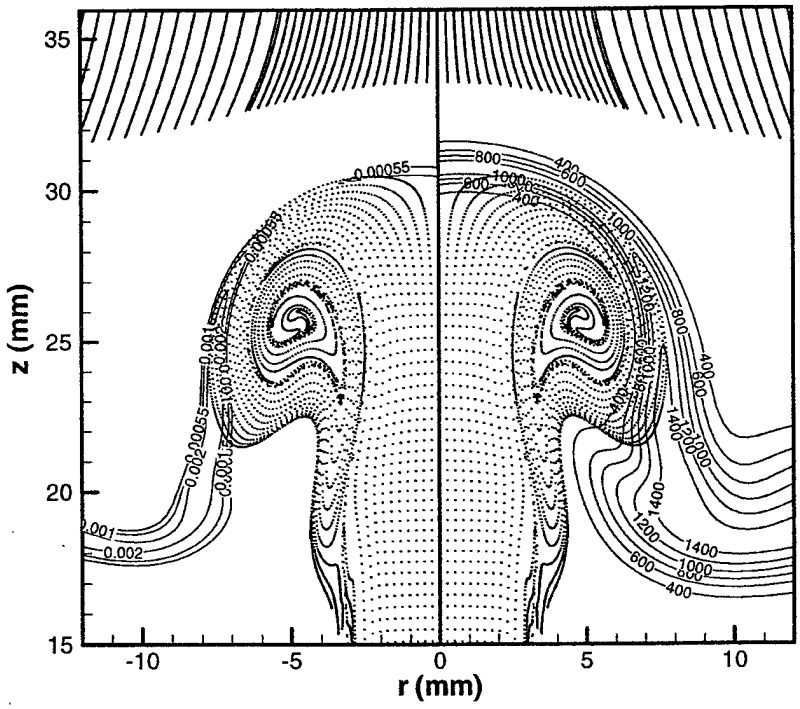

(b)

Figure 2

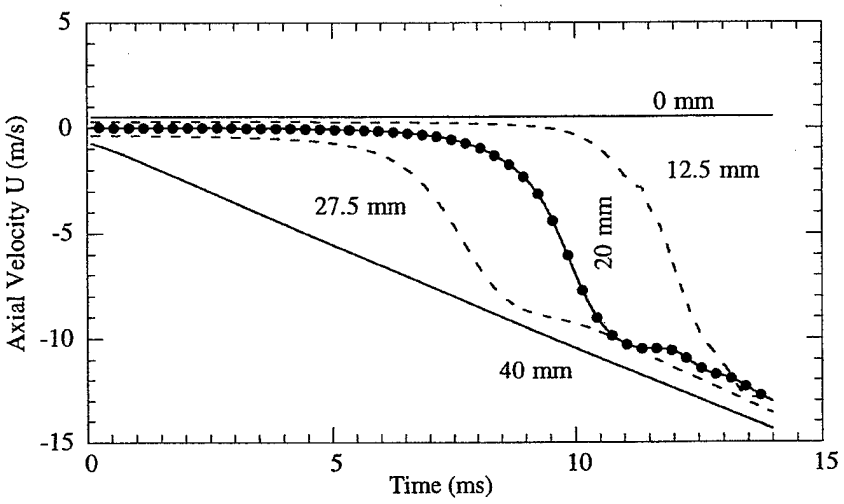

(a)

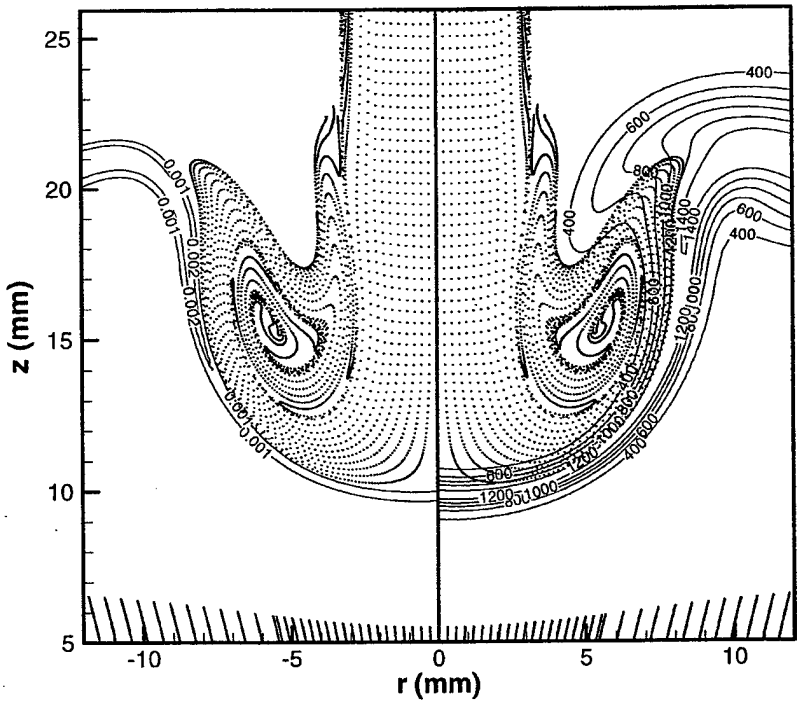

(b)

Figure 3

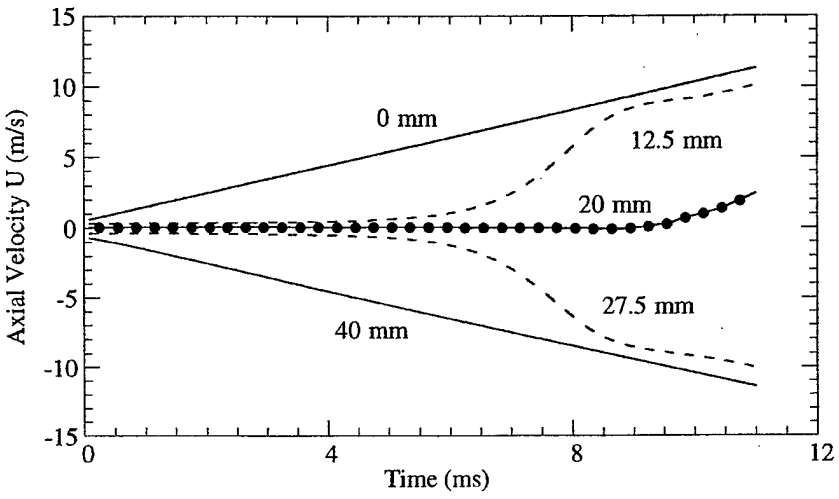
Axial Velocity U (m/s)
Time (ms)
0 mm
12.5 mm
20 mm
27.5 mm
40 mm

(a)

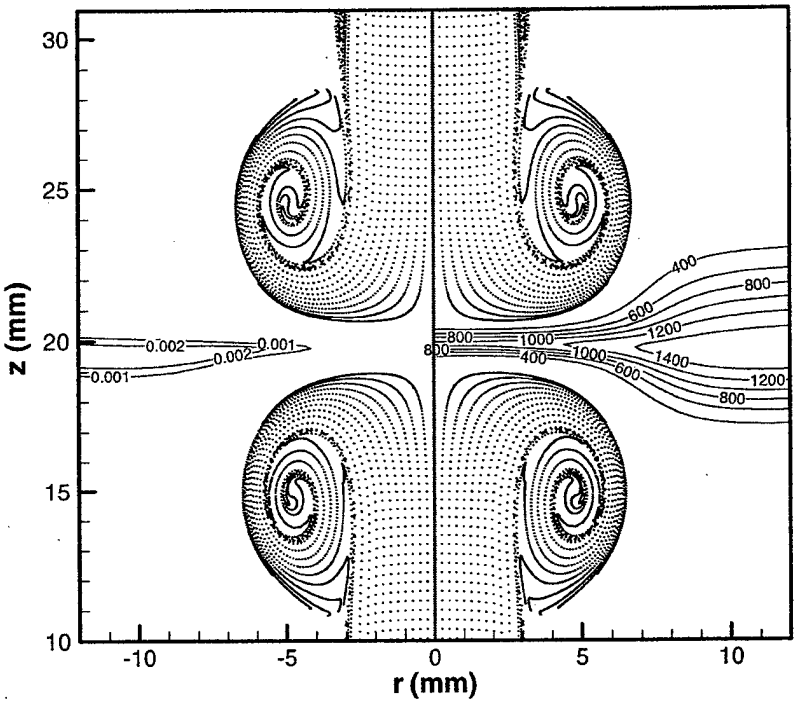
z (mm)
r (mm)
0.001
0.002
400
600
800
1000
1200
1400

(b)

Figure 4

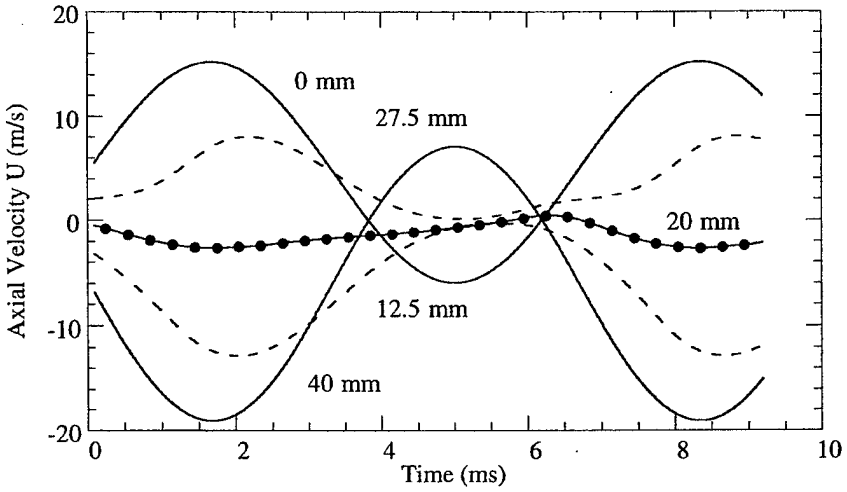
0 mm
27.5 mm
20 mm
12.5 mm
40 mm
Axial Velocity U (m/s)
Time (ms)

(a)

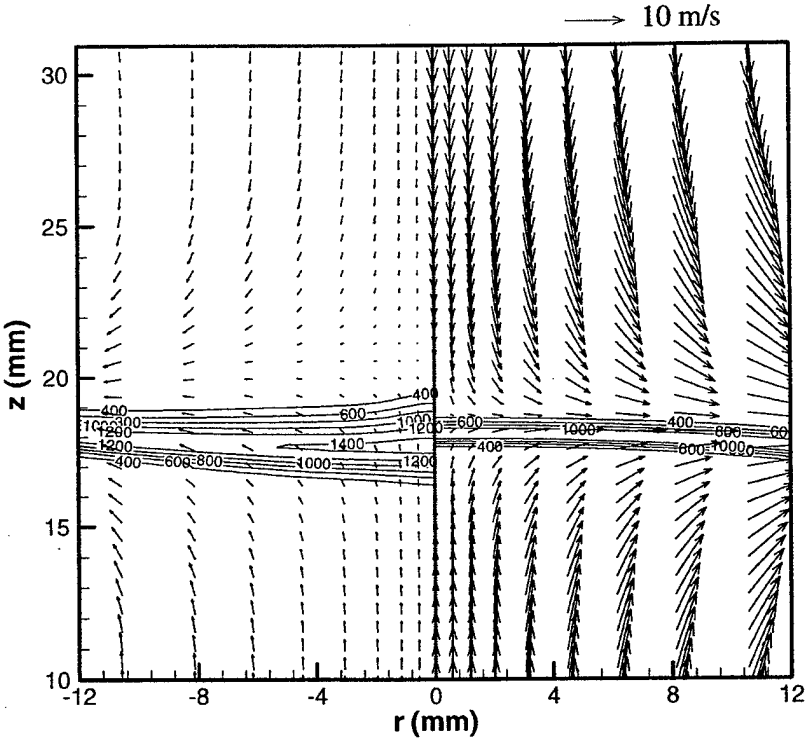
10 m/s
z (mm)
r (mm)

(b)

Figure 5

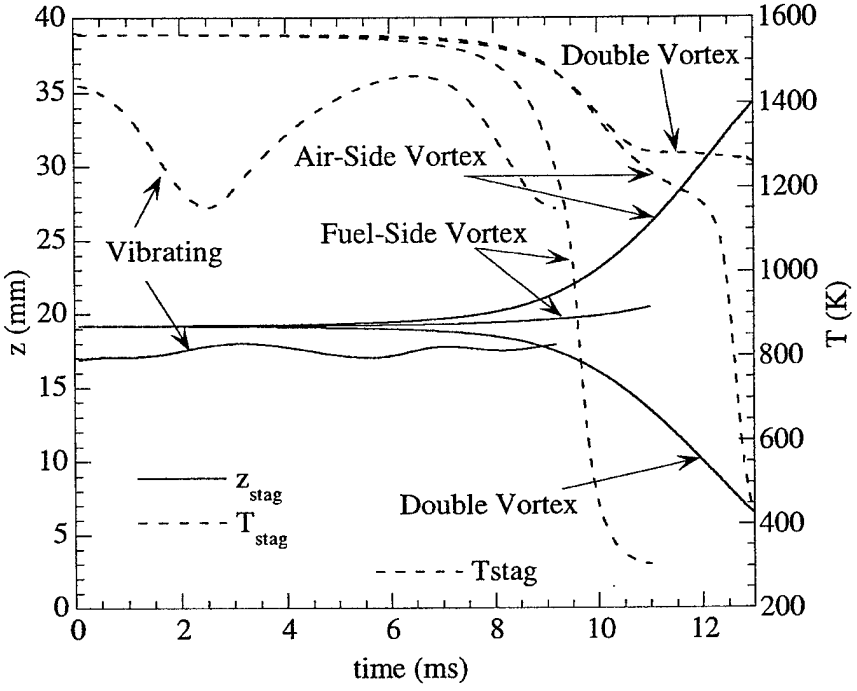
Double Vortex
Air-Side Vortex
Fuel-Side Vortex
Vibrating
Double Vortex
Tstag
z_{stag}
T_{stag}
z (mm)
T (K)
time (ms)
0
5
10
15
20
25
30
35
40
200
400
600
800
1000
1200
1400
1600
0
2
4
6
8
10
12

Figure 6

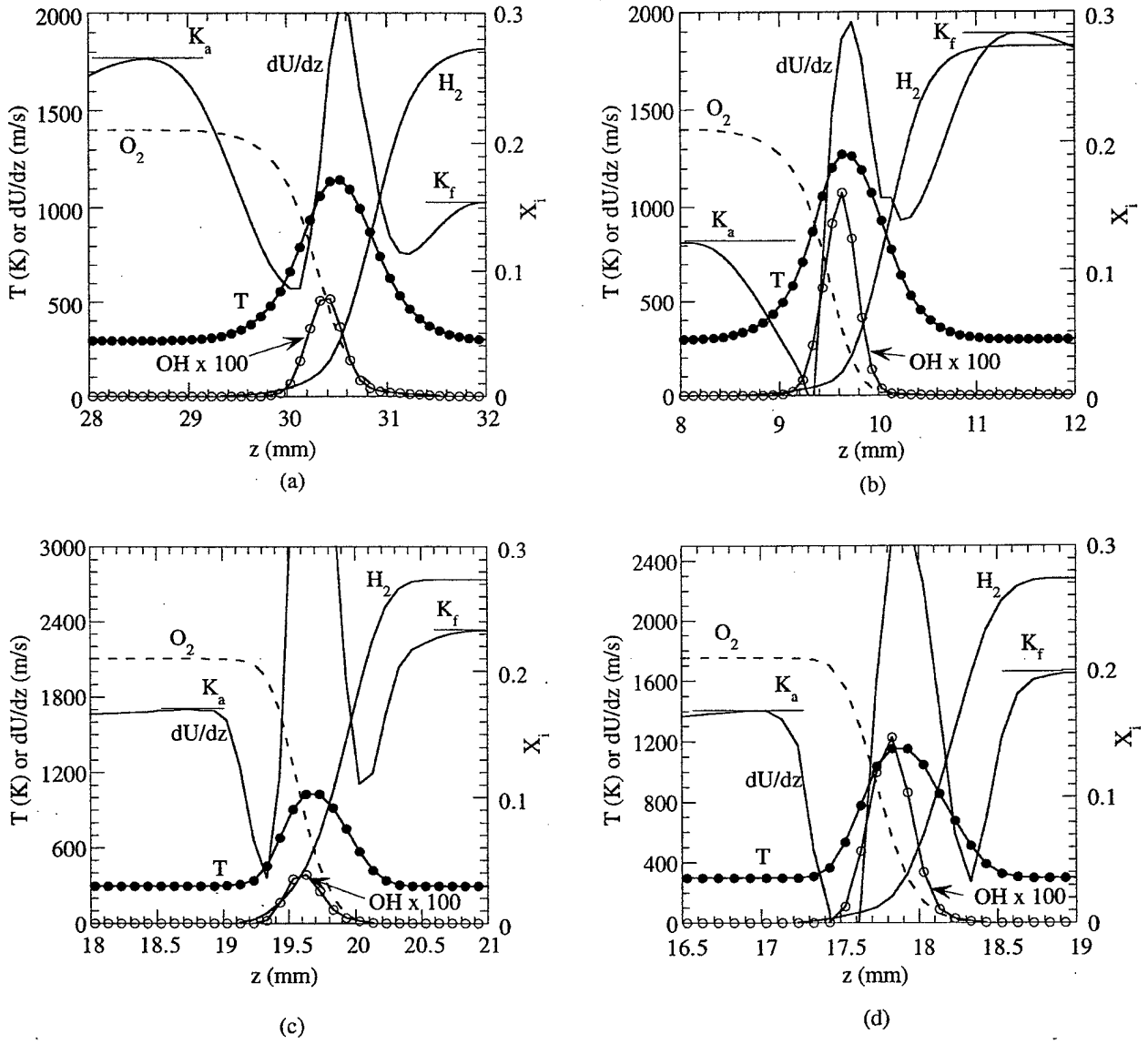

Figure 7

In *Combustion Fundamentals and Applications* (Proceedings, Spring Technical Meeting, Central States Section, The Combustion Institute, 5-7 May 1996, St. Louis, MO) (The Combustion Institute, Pittsburgh, PA, 1996), pp. 449-454.

Extinction in Methane-Air Counterflow Diffusion Flame--A Direct Numerical Study

V. R. Katta
Innovative Scientific Solutions, Inc.
3845 Woodhurst Court
Dayton, OH 45430

W. M. Roquemore
Aero Propulsion Directorate
Wright Laboratory
Wright-Patterson Air Force Base, OH 45433

In numerical calculations of counterflow-diffusion-flame structures, a similarity transformation is usually introduced to treat the problem as quasi-one dimensional. Despite the apparent successful comparisons with experiments, some concern has been expressed regarding the quasi-one-dimensional simplification for the problem. A time-dependent, axisymmetric CFDC code that incorporates finite-rate chemical kinetics is developed for the direct simulation of counterflow jet flames and using this the extinction process in strained flames is investigated. The model was validated by comparing the flame structure at different strain rates and the extinction limits with those obtained from experiments. Accuracy of different chemical kinetics in predicting the flame structure and the extinction limits is also investigated.

Introduction

A thorough understanding of the flame structure, ignition and extinction of laminar flames is essential for the development and application of laminar flamelet concepts to turbulent flames. A flame formed in between the opposing fuel and air jets represent a simple system for simulating and understanding laminar flame structure. Recently a numerous investigations (experimental and numerical) [1,2] have been performed to quantify the scalar structure of steady-state, aerodynamically strained, planar diffusion flames. Such studies on counterflow diffusion flames not only provided benchmark experimental data but also yielded insight into the flame behavior in response to strain rate. In numerical calculations of counterflow diffusion-flame structures, a similarity transformation is usually introduced to treat the problem as quasi-one dimensional. In addition, it is further assumed that the outer inviscid flow is either 1) irrotational, enabling a velocity potential to be introduced--which leads to potential flow-boundary conditions or 2) rotational by imposing zero radial velocity at the nozzle exits--which leads to plug-flow boundary conditions. However, studies of Chelliah et al [3] suggest that the experimental outer flow is neither a plug flow nor a potential flow. Therefore, in order to reconcile the differences in the adopted boundary condition in the calculation and the mixed flow in the experiment--and recognizing that there is one degree of freedom in specifying the boundary condition of the flow at each boundary because the radial velocity profile at the inlet is not precisely described--the mass fluxes at both nozzle exits are adjusted such that the calculated and measured temperature profiles are aligned. Despite apparent successful comparisons with experiments, some concern has been expressed regarding the quasi-one-dimensional simplification for the counterflow diffusion flames.

Recent advances in computer-hardware technology and the need to improve the understanding of combustion phenomena under complex situations have led to the development of two- and three-dimensional Computational Fluid Dynamics models that incorporate detailed chemical kinetics [4,5]. However, to the knowledge of the authors, no complete simulation of the counterflow diffusion flame has been reported. Such simulations not only eliminate the concerns of the quasi-one-dimensional analyses but also provide a valuable test case for the validation of mathematical models. Also recent experimental studies on vortex-flame interactions in counterflow diffusion [6] and premixed [7] flames demand two/three-dimensional simulations of counterflow flames.

This paper describes a direct numerical study conducted on a counterflow methane jet diffusion flame. The CFDC code is validated by simulating several flames that were experimentally investigated. The structures of weakly strained and near-quenching-limit flames are studied and the results are focused on the near-extinction-limit flames. Accuracy of different detailed chemical-kinetics models proposed in the literature in simulating a counterflow diffusion flame is assessed.

Mathematical Model

In the mathematical model [8,9], time-dependent Navier-Stokes equations are solved along with species- and energy-conservation equations in an uncoupled manner on a staggered-grid cylindrical coordinate system. However, the species equations are solved by coupling them through the production terms. A clustered mesh system is employed to trace the large gradients in flow

variables near the flame surface. Different detailed chemical-kinetics models proposed in the literature for the simulation of methane-air combustion are used in this study. These models consist of either 17 species (CH_4, O_2, CH_3, CH_2, CH, CH_2O, CHO, CO_2, CO, H_2, H, O, OH, H_2O, HO_2, H_2O_2, and N_2) or 24 species (C_2H, C_2H_2, C_2H_3, C_2H_4, C_2H_5, C_2H_6, CHCO in addition to the previous 17 species). The total number of elementary reactions involving these reactive species is 52, 81 or 86 depending on the reaction mechanism used. The reaction rates for these elementary reactions have been obtained from various sources [10,11,12]. The thermo-physical properties such as enthalpy, viscosity, thermal conductivity and binary molecular diffusion coefficients of all the species are calculated from the polynomial curve fits developed for the temperature range 300 - 5000 K. Mixture viscosity and thermal conductivity are then estimated using the Wilke and Kee expressions, respectively. Molecular diffusion is assumed to be of the binary-diffusion type, and the diffusion velocity of a species is initially calculated according to Fick's law and then modified for the effective-diffusion coefficient of that species.

The finite-difference forms of the momentum equations are obtained using an implicit QUICKEST scheme[8], and those of the species and energy equations are obtained using a hybrid scheme of upwind and central differencing. At every time-step, the pressure field is accurately calculated by solving all the pressure Poisson equations simultaneously and utilizing the LU (Lower and Upper diagonal) matrix-decomposition technique. Treatment of the boundary conditions is identical to that reported in earlier papers [8,9].

Results And Discussion

The CFDC model developed for the simulation of a time-dependent methane jet flames was used for the analysis of counterflow jet diffusion flames. The flame system investigated in the present study was previously studied experimentally by Sung et al [13]. The burner assembly consists of two nozzle burners with 14-mm exit diameters spaced 13 mm apart. The fuel and oxidizer jets emanating from the nozzles were made to impinge on each other. Outer nitrogen co-flows were used to isolate and stabilize the flame. The fuel and oxidizer streams consisted of 23% methane in nitrogen and 23% oxygen in nitrogen, respectively. In addition, the mean exit velocities at the nozzles were kept equal. Several calculations were made for different exit velocities, and the results were compared to the measurements. A typical flame computed using the axisymmetric code for an exit velocity of 25.5 cm/s is shown in Fig. 1 in the form of streamlines superimposed over the iso-temperature contours. Fuel flowing from the bottom nozzle (z = 0) reacts with the oxidizer flowing from the top (z = 13 mm) and yields a steady laminar flame on the oxidizer side of the stagnation plane (zero axial velocity plane, z ~ 5.8 mm). The flame surface may be identified from the 1680-K contours passing through z ~ 6.7-mm plane in Fig. 1.

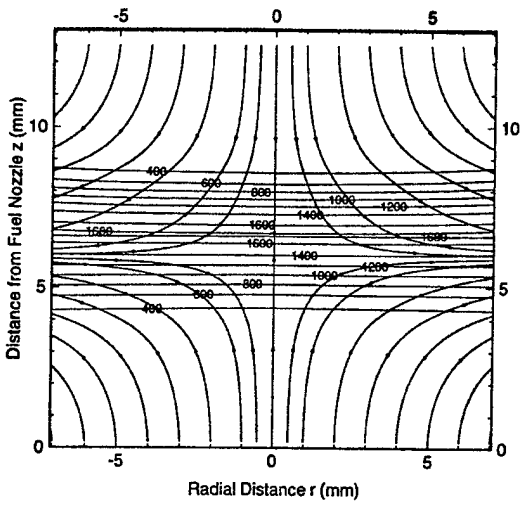

Fig. 1. Axi-symmetric counterflow diffusion flame directly simulated for an exit velocity of 25.5 cm/s using Computational Fluid Dynamics with Chemistry (CFDC) model. Streamlines originating from fuel side (bottom) and oxidizer side (top) are superimposed over iso-temperature contours.

The 17-species, 52-reaction chemical kinetics used for the above simulations was adopted from the mechanism recommended by Peters [10]. The computed and measured profiles for temperature and for some major species shown in Fig. 2 compare very well. In fact, excellent agreement was obtained between the calculations and measurements for low-strain-rate flames with exit velocities < 40.0 cm/s. When the strain rate on the flame was further increased, calculations predicted flame extinction for an exit velocity of 45.5 cm/s. On the other hand, Sung et al found that the experimental flame was extinguished at a velocity of ~ 77.5 cm/s. In fact, when the same CFDC code was used for the prediction of coflowing jet diffusion flames it was noted that flame at the base separates from the nozzle at velocities for which experiments have shown well attached flames.

In order to obtain better predictions for the flames that are subjected to higher strain rate, different chemical kinetics were incorporated into the CFDC code. Results in the form of centerline flame temperature Vs strain rate obtained using selected mechanisms are shown in Fig. 3. Here, strain rate is defined based on the exit velocities at the fuel and air nozzles and the separation between those nozzles. As expected flame temperature decreases with strain rate and extinction occurs when it falls bellow ~1500 K. The data obtained using Peters mechanism which was used for the simulations in Figs. 1 and 2 is shown with solid circles in Fig. 3. Small improvement was obtained in the prediction of extinction conditions with the inclusion of C_2 chemistry [10]. This version of Peters mechanism has 24 species and 81 elementary reactions. C_2 chemistry impact the flame structure

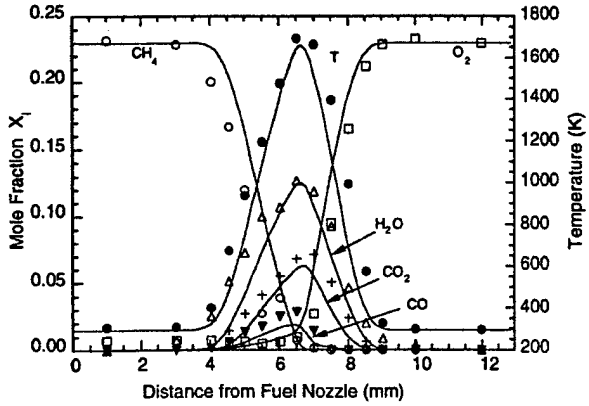

Fig. 2. Comparison of calculated (lines) using Peters Mechanism and experimental (symbols) temperature and major species profiles obtained along the centerline (z = 0) for a weakly strained flame with exit velocity of 25.5 cm/s.

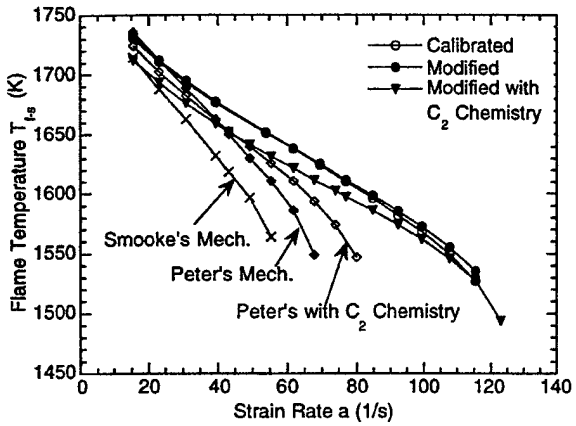

Fig. 3. Variation of flame temperature at centerline with strain rate obtained using different reaction mechanisms. Calculations were extended to extinction limits.

negligibly small at lower strain-rate conditions by decreasing the flame temperature by less than 10 degrees and improved the extinction strain-rate limit to 80 s^{-1} (corresponding to 52 cm/s exit velocity). The predicted extinction strain rate using C_2 chemistry is still well below the experimentally obtained one of 119 s^{-1} (corresponding to 77.5 cm/s exit velocity) [13].

The next chemical-kinetics mechanism incorporated into the CFDC code is that used by Smooke et al. [12]. Only C_1 chemistry was first used in the present study and the results are plotted in Fig. 3 using cross symbols. This mechanism consists of 17 species and 86 reactions yielded counterflow flames only up to a strain rate of 55 s^{-1} (or 35.7 cm/s velocity). Adding C_2 chemistry may result in slightly better results; however, one should not expect any better performance than that obtained with Peters mechanism with C_2 chemistry. In order to improve the CFDC models in predicting the highly strained flame, a sensitivity analysis was performed on Peters mechanism by modifying the individual reaction rates. Through this systematic sensitivity analysis, it was found that the chain termination reaction involving methyl radicals ($CH_3 + H = CH_4$) was responsible for the early extinguishment of the computed flames. Peters mechanism uses Lindemann form for the rate coefficient of the $CH_3 + H = CH_4$ reaction. Assuming that the values quoted by Peters have a degree of error margin, the calculations were made by gradually reducing the reaction rate of the above chain-termination reaction. It was found that an order of magnitude lower rate than the value given by Peters yields flame extinguishment at a velocity of 77.5 cm/s--which matches with the experiment very well.

The strain rate Vs flame temperature plot obtained with this calibrated mechanism is shown in Fig. 3 using open circles. Interestingly, there is a wide variation in the literature for the rate of the $CH_3 + H = CH_4$ reaction, and Warnatz [11] has recommended a different set of parameters for this reaction. A modified Peters mechanism is obtained by replacing the rate expression of $CH_3 + H = CH_4$ reaction with that recommended by Warnatz and the results obtained are plotted in Fig. 3 using solid circles and solid triangles for chemical mechanisms with and without C_2 chemistry, respectively. Results obtained with the modified and calibrated chemistry models followed each other closely and gave excellent prediction for the extinction strain rate.

The rate coefficients obtained from different rate expressions for $CH_3 + H = CH_4$ reaction are plotted in Fig. 4 at several temperatures and the rate expressions are listed in Table 1. As evident in Fig. 4, Smooke et al used a modified Arrhenius form and Peter and Warnatz used Lindemann form for the rate expression. The rate coefficients used by Smooke et al, recommended by Peters and Warnatz are quite different; and at the quenching temperature (~ 1500 K), the latter is an order of magnitude lower than the former two. In fact, at this temperature the

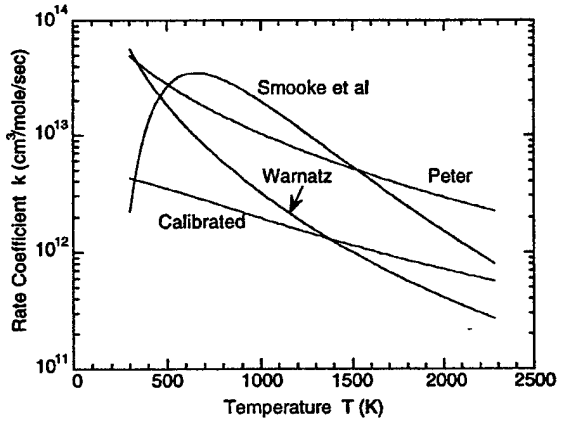

Fig. 4. Specific reaction rate for $CH_3 + H = CH_4$ reaction calculated at several temperatures using different rate expressions found in the literature.

Table 1 Rate Expressions for $CH_3 + H = CH_4$ reaction

Source		A (cm^3/mole/s)	n	E (cal/mole)
Peter [10]	k_∞	2.108 E+14	0.0	0.0
	k_0	6.257 E+23	-1.8	0.0
warnatz [11]	k_∞	6.000 E+16	-1.0	0.0
	k_0	8.000 E+26	-3.0	0.0
Smooke [12]		6.000 E+16	-7.0	9050.0
Calibrated	k_∞	5.610 E+12	0.0	0.0
	k_0	6.257 E+23	-1.8	0.0

reaction rate obtained from the Warnatz-recommended values matched very closely with those obtained through the trial-and-error sensitivity calculations. This indeed suggests the accuracy of the present counterflow-flame calculations using the two-dimensional model. By using the modified chemistry mechanism, calculations are performed for different exit velocities and the results are compared with those obtained experimentally by Sung et al. for a weakly strained, moderately strained, and highly strained flame in Figs. 5, 6, and 7, respectively. Excellent agreement was found between the calculations and measurements for temperature and major species for all the three cases. It should be noted that, unlike in the one-dimensional calculations, no adjustment was made to the mass flow rates to match the temperature profile--a definite advantage in using two-dimensional CFDC codes for counterflow flame problems. The flame structure and the axial velocity profiles along the centerline are shown in Fig. 8 for different strain rates. As expected, the flame thickness and temperature decrease with strain rate and the velocity profiles show peaks that resulted from the thermal expansion in the flame zone on both sides of the stagnation point. These axi-symmetric calculations indicate that even though the velocity profiles are not symmetric with respect to the zero-velocity (stagnation) point they all pass through the stagnation point at the same location from the fuel nozzle exit. As the flame is strained the peak-temperature location moves closer to this stagnation point. The flame and flow structures of the flame at near-extinction limit (77.5 cm/s) are shown in Fig. 9. The flame temperature at the centerline is lower than those at other radial locations. This variation in temperature along the flame surface was not observed in the weakly strained flame (Fig. 1) and is believed to be resulting from the non-unity Lewis numbers of the species in the flame zone.

Sung et al. [13] indicated that the counterflow diffusion flame formed between the diluted methane and oxygen jets was extinguished when the exit velocity was increased to ~ 77.5 cm/s. Amazingly, when the calculations were performed (using the modified chemical kinetics) by increasing the exit velocity in steps of 0.5

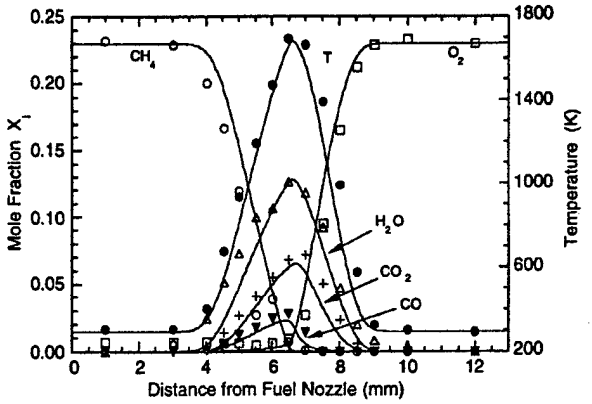

Fig. 5. Comparison of calculated (lines) using Modified Mechanism and experimental (symbols) temperature and major species profiles obtained along centerline (z = 0) for weakly strained flame with exit velocity of 25.5 cm/s.

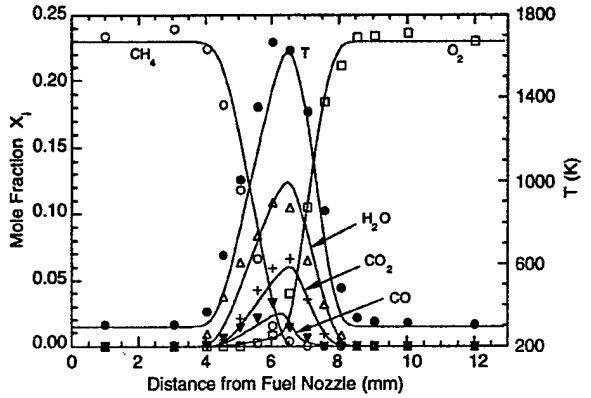

Fig. 6. Comparison of calculated (lines) using Modified Mechanism and experimental (symbols) temperature and major species profiles obtained along centerline (z = 0) for moderately strained flame with exit velocity of 45.0 cm/s.

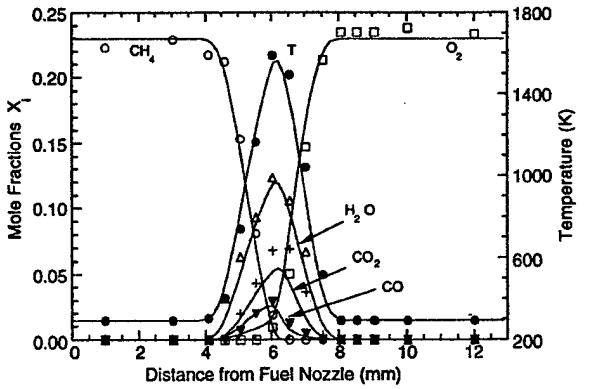

Fig. 7. Comparison of calculated (lines) using Modified Mechanism and experimental (symbols) temperature and major species profiles obtained along centerline (z = 0) for highly strained flame with exit velocity of 65.0 cm/s.

cm/s, it was found that 1) a stable flame is established for the exit velocity of 77.5 cm/s and 2) the flame is quenched when the velocity is increased to 78.0 cm/s. A fundamental concern with the numerical simulations is that dependency of the results on grid spacing and especially in the simulations for reactive flows it is believed that one should use extremely fine mesh system to resolve all the reaction time scales. This may be true with an explicit-type calculations. The numerical procedure used in the present CFDC code is based on semi-implicit formulation and it is found that one can obtain grid independent results without going for extremely fine grid system. Calculations presented in Figs. 1 through 9 were obtained using a 101x41 grid system. The 101 grid points were uniformly distributed in the axial direction between the fuel and oxidizer nozzles

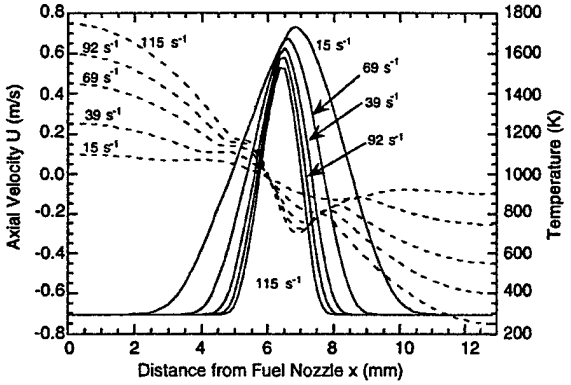

Fig. 8. Computed axial velocity and temperature profiles along centerlines of counterflow diffusion flames under different strain rates.

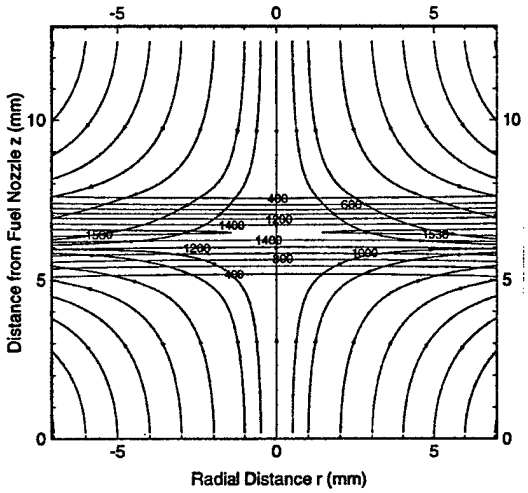

Fig. 9. Highly strained axi-symmetric counterflow diffusion flame simulated for an exit velocity of 75.5 cm/s. Streamlines originating from fuel (bottom) and oxidizer (top) side are superimposed over iso-temperature contours.

that were separated by 13 mm. Calculations were performed using a 301x41 grid system for different velocities and found negligible differences between these results and those obtained with 101x41 grid system. The extinction limit obtained with the finer mesh system did not change from 77.5 cm/s. The temperature, axial velocity distributions along the centerline obtained with the two grid systems are compared in Fig. 10 and the profiles for reactants and radical concentrations in Fig. 11 for the near-extinction limit flame (77.5 cm/s).

In order to investigate the differences in the structures of the weakly strained flame and the flame obtained at near quenching limits, the total heat-release and molar-production rates for reactants, CH_3 and other radicals along the stagnation line for the 25.5 and 77.5-cm/s cases are shown in Figs. 12(a) and 12(b), respectively. These flame structures are very similar to those computed by Sung et al. [13] for the pure methane-air counterflow

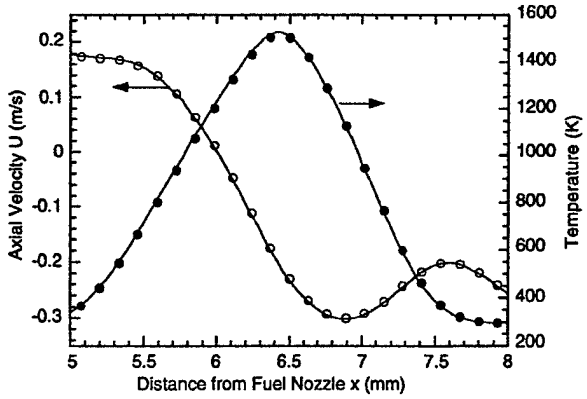

Fig. 10. Comparison of axial velocity and temperature profiles along centerline of counterflow diffusion flames at near extinction condition (77.5 cm/s) obtained using 101x41 (symbols) and 301x41 (lines) grid systems.

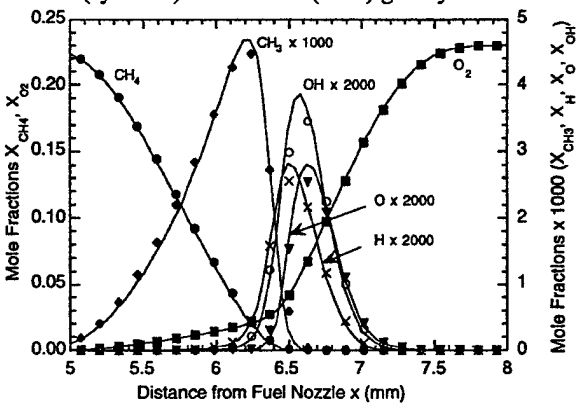

Fig. 11. Comparison of different species profiles along centerline of counterflow diffusion flames at near extinction condition (77.5 cm/s) obtained using 101x41 (symbols) and 301x41 (lines) grid systems.

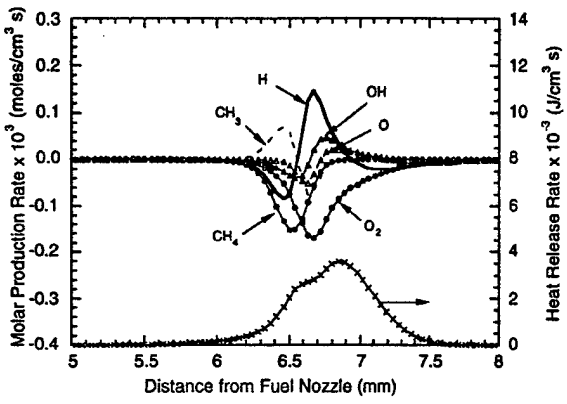

(a)

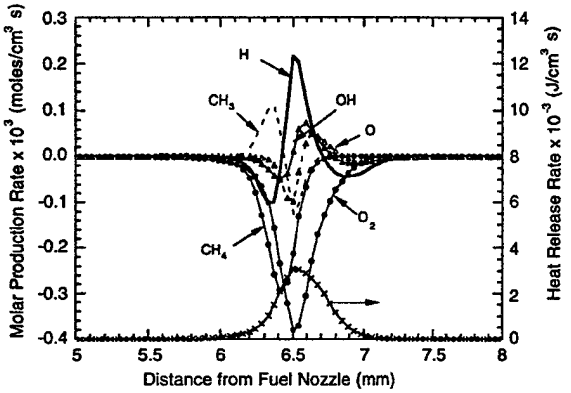

(b)

Fig. 12. Computed molar-production rates of reactants and radicals and total-heat-release rate profiles along stagnation line for (a) weakly strained flame with exit velocity of 25.5 cm/s and (b) flame at near quenching limit with exit velocity of 77.5 cm/s.

diffusion flame. The peak temperature decreased from 1683 to 1518 K when the weakly strained flame (25.5 cm/s) was stretched to near extinction limits (77.5 cm/s). However, the maximum reactant consumption rates for the latter case are nearly twice those of the former and the rates for radicals did not change much. This suggests that extinction in strained counterflow diffusion flame primarily occurs due to the decrease in temperature.

Conclusions

A time-dependent, axisymmetric CFDC code that uses finite-rate chemistry models was developed for the direct simulation of counterflow jet diffusion flames formed between diluted methane and air jets. The results were compared with the measurements of Sung et al. Unlike in the one-dimensional simulations of counterflow flames, no adjustments were made for the flow rates in these axisymmetric calculations to match the computed and measured temperature profiles. It was found that although Peters mechanism yields very good predictions for the weakly strained flame structure, it fails in predicting the quenching limits. In fact, several mechanisms reported in the literature seem to give good predictions only for weakly strained flames and they tend to fail as the flames are strained to the extinction limits. Through trial-and-error analysis it is found that the radical destruction reaction ($CH_3 + H = CH_4$) is the most sensitive reaction in governing the extinction limits. By replacing the rate expression of Peters for the $CH_3 + H = CH_4$ chain-terminating reaction by the one recommended by Warnatz, the quenching limits were accurately obtained. It is also found that use of implicit-type procedures eliminates the need of using very fine grid system for the calculation of reactive flows.

References

1. Kee, R. J., Miller, J. A., Evans, G. H., and Dixon-Lewis, G., in Twenty-Second Symposium (International) on Combustion, The Combustion Institute, Pittsburgh, 1988, p. 1479.
2. Dixon-Lewis, G., in Twenty-Third Symposium (International) on Combustion, The Combustion Institute, Pittsburgh, 1990, p. 305.
3. Chelliah, H. K., Law, C. K., Ueda, T., Smooke, M. D., and Williams, F. A., in Twenty-Third Symposium (International) on Combustion, The Combustion Institute, Pittsburgh, 1990, p. 503.
4. Katta, V. R., Goss, L. P., and Roquemore, W. M., Combustion and Flame 96:60 (1994).
5. Rutland, C., and Ferziger, J., AIAA Paper 89-0127, Reno, 1989.
6. Rolon, J. C., Aguerre, F., and Candel, S., Combustion and Flame 100:422 (1995)
7. Roberts, W. L., Driscoll, J. F., Drake, M. C., Ratcliffe, J. W., Twenty-Fourth Symposium (International) on Combustion, The Combustion Institute, Pittsburgh, 1992.
8. Katta, V. R., Goss, L. P., and Roquemore, W. M., AIAA J. 32:84 (1994).
9. Katta, V. R., Goss, L. P., and Roquemore, W. M., Int. J. Num. Meth. Heat Fluid Flow, 4:413 (1994)
10. Peters, N., in Reduced Kinetic Mechanisms for Applications in Combustion Systems, Lecture notes in Physics (N. Peters and B. Rogg, Eds.), Spriger-Verlag, Berlin, 1993, Vol. m15, p. 3-14.
11. Warnatz, J., Combustion Chemistry (W. C. Gardiner, Ed.) Springer-Verlag, New York, 1984, p. 197.
12. Smooke, M. D., in Numerical Approaches to Combustion Modeling, (S. Oran and J. Boris, Eds.), Progress in Astronautics and Aeronautics, Vol. 135, 1991, p. 183.
13. Sung, C. J., Liu, J. B., and Law, C. K., Combustion and Flame, 102:481 (1995).

4.1.4 Trapped-Vortex Combustor

Spatially locked vortices in the cavities of a combustor can aid in stabilizing the flame but restrict the entrainment of the main air into the cavity. Through proper cavity design it is possible to lock (trap) the vortices spatially, thereby stabilizing the flame. In an attempt to understand the dynamics in these different-sized cavities under cold and combusting environments, a numerical investigation was performed; and the results are reported in the paper entitled "Numerical Studies on Trapped-Vortex Combustor" (see pp. 942-952). In the study reported in the paper entitled "Direct Numerical Simulation of Unsteady Non-Reacting Flows in a Trapped-Vortex Combustor," it was found that mass injection increases the optimum size of the cavity, providing more efficient mixing and longer residence time for the fuel/air mixture. This paper, by V. R. Katta with W. M. Roquemore (AFRL), was presented at the Seventh International Symposium on Computational Fluid Dynamics, 15-19 September 1997, Beijing, China, and published in the Conference Proceedings [(F. G. Zhuang, Ed.) (International Academic Publishers, Beijing, China, 1997), pp. 791-796]. A numerical investigation was performed to aid the understanding of the entrainment and residence-time characteristics of cavity flows for different cavity and spindle sizes; the results are documented in the paper entitled "Numerical Studies on Trapped-Vortex Concepts for Stable Combustion" (see pp. 953-961). An investigation of the vortex dynamics of a cavity into which fluid mass is directly injected through jets is discussed in the paper entitled "Study on Trapped-Vortex Combustor – Effect of Injection on Flow Dynamics" (see pp. 962-970). A numerical study of a trapped-vortex combustor was conducted utilizing a detailed chemistry model with 33 species and 92 reversible reactions incorporated to simulate propane combustion; the results are discussed in a publication entitled "Simulation of Unsteady Flows in an Axisymmetric Research Combustor Using Detailed-Chemical Kinetics" (see pp. 971-980).

AIAA 96-2660

Numerical Studies on Trapped-Vortex Combustor

V. R. Katta
Innovative Scientific Solutions, Inc.
Dayton, OH

W. M. Roquemore
Wright Laboratory
Wright-Patterson AFB, OH

32nd AIAA/ASME/SAE/ASEE
Joint Propulsion Conference
July 1-3, 1996 / Lake Buena Vista, FL

For permission to copy or republish, contact the American Institute of Aeronautics and Astronautics
1801 Alexander Bell Drive, Suite 500, Reston, VA 22091

NUMERICAL STUDIES ON TRAPPED-VORTEX COMBUSTOR

V. R. Katta*
Innovative Scientific Solutions, Inc.
Dayton, OH

and

W. M. Roquemore**
Wright Laboratory
Wright-Patterson Air Force Base, OH

Abstract:

Spatially locked vortices in the cavities of a combustor aid in stabilizing the flames. On the other hand, these stationary vortices also restrict the entrainment of the main air into the cavity. For obtaining good performance characteristics in a trapped-vortex combustor, a sufficient amount of fuel and air must be injected directly into the cavity. This paper describes a numerical investigation performed for understanding the vortex dynamics in cavities having different sizes under cold and combusting environments. A third-order-accurate time-dependent Computational Fluid Dynamics with Chemistry (CFDC) code was used for simulating the dynamic flows associated with forebody-spindle-disk geometry. It was found from the non-reacting flow simulations that at the optimum disk location, the vortices inside the cavity and behind the disk are spatially locked. It was also found that for cavity sizes smaller than the optimum, multiple vortices develop within the cavity and are associated with vortex shedding. The preliminary reacting-flow calculations indicated that the dynamic vortices developed inside the cavity with the injection of fuel and air do not shed, even though the cavity size was determined based on cold-flow conditions.

Introduction:

A revolutionary advancement in the development of a simple, compact, and efficient method of combustion was recently proposed by Hsu et al.[1] This new combustor concept employs a vortex that is trapped in a cavity to stabilize the flame--hence, is referred as Trapped-Vortex (TV) concept. Even though the idea of trapping a vortex for flame stabilization purposes is novel one, interest in the utilization of vortex motion to aerodynamic advantage has intrigued aerodynamicists for many years. Experiments of Rohsenow et al.[2] have shown that when two circular orifices are placed in series in a pipe, a large recovery of pressure occurs across the second orifice in certain circumstances; hence, the overall pressure drop is considerably less for the two orifices than for a single one having the same flow. In ribbed diffusers, Migay[3] found that balancing the fluid removed by entrainment and the fluid entering the cavity by reversed flow ensures that the flow outside the cavities will follow the ribs fairly closely, and a good pressure recovery will be obtained. Mair[4] showed that on mounting a disk behind the base of a blunt body the drag of the blunt object can be reduced. Using similar concepts, Roshko and Koenig[5] reported a reduction in drag of blunt forebodies when disks are placed on spindles ahead of the body.

In order to understand the aerodynamics associated with minimum-drag conditions, Little and Whipkey[6] conducted extensive investigations on the dynamic nature of flows over bluff bodies using smoke-flow-visualization and laser-velocimetry techniques. Because of the limitations of the smoke tunnel, they used reduced flow conditions (~ 0.3 m/s) and half-scaled geometries for the flow-visualization studies and full-scale geometries and turbulent flows (~ 30 m/s) for the time-averaged drag measurements. Based on these reduced and full-scale experiments, they correlated the afterbody drag and the motion of the vortex in the wake region and postulated that a minimum-drag condition established when the wake vortices are locked between two disks mounted in series on a spindle. They also suggested that the cavity formed between the disk and the bluff body should be of such dimensions that the locked vortex effectively fills the cavity. Since these dynamic flow results were obtained for velocities lower by nearly two orders of magnitude than those used in the full-size wind-tunnel experiments, these conclusions are open to question. And also, in practical combustors, partial burning takes place in the recirculation zones and in the cavity vortices which could alter the vortex dynamics. As a result, it might be expected that the criterion for trapping a vortex in a combustor would be different from that observed in cold flows.

Performing experimental studies on vortex dynamics inside the cavities in a combusting environment is extremely difficult mainly because of 1) limited access to the bright, hot cavity flow and 2) problems arising from the use of moving parts. On the other hand, recent progress in Direct-Numerical-Simulation (DNS) techniques[7,8] has led to a growing interest in the investigation of dynamic flows computationally which, provides an alternative means of addressing issues concerning minimum drag and locked vortices under high-speed and combusting conditions.

In the present paper numerical studies were made on the flowfields in a research trapped-vortex combustor[1] using a third-order-accurate time-dependent Computational Fluid Dynamics with Chemistry (CFDC) code and a large number of grid points. Cold-flow simulations for a forebody-spindle-disk geometry that is similar to the one used in the trapped-vortex combustor were made to gain an understanding of the dynamic nature of the cavity flow.

* Senior Engineer, Member AIAA

** Senior Scientist, Member AIAA

This paper is declared a work of the U.S. Government and is not subjected to copyright protection in the United States.

Calculations for the cold and reacting flows were also performed using k-ε turbulence model and the results are compared with the instantaneous and time-averaged DNS data.

Modeling:

A time-dependent, axisymmetric mathematical model that solves for axial- and radial-momentum equations, continuity, and enthalpy- and species-conservation equations is used to simulate the flowfields in the trapped-vortex combustor. Density is obtained by solving the state equation, while the pressure field at every time step is determined from pressure Poisson equations. For the cases in which turbulent-flow characteristics were modeled, the time-dependent equations for turbulent energy (k) and turbulent-energy dissipation (ε) are also solved, along with the other governing equations. The standard isotropic k-ε turbulence model is incorporated in those cases. Even though all the governing equations are solved in an uncoupled manner, the turbulence and species-conservation equations are coupled through the source terms during the solution process to improve the stability of the algorithm.

In the present analysis of reacting flows, the simple global-chemical-kinetics model involving propane, oxygen, water, carbon dioxide, and nitrogen used is expressed as follows;

$$C_3H_8 + 5\ O_2 + N_2 ==> 3\ CO_2 + 4\ H_2O + N_2.$$

The specific reaction rate for the above equation is written in Arrhenius form, with an activation energy of 1000 cal/mole and pre-exponential of 1.0×10^{16} $m^6/mole^2/s$ to yield very high reaction rates at all temperatures.

An orthogonal, staggered-grid system with varying cell sizes in both the x and r directions is utilized. The momentum equations are integrated using an implicit QUICKEST (Quadratic Upstream Interpolation for Convective Kinematics with Estimated Streaming Terms) numerical scheme[9,10] which is third-order accurate in both space and time and has a very low numerical diffusion error. On the other hand, the species, enthalpy, and turbulence-energy conservation equations, which have relatively large source terms, are integrated using the hybrid scheme of Spalding.[11] By rearrangement of the terms, the finite-difference form of each governing equation at all grid points is written as a system of algebraic equations which is then solved using the Alternative-Direction-Implicit (ADI) technique. The time increment, Δt, is determined from the stability constraint and maintained as a constant during the entire calculation. The pressure field at every time step is accurately calculated by simultaneously solving the system of algebraic pressure Poisson equations at all grid points using the LU (Lower-Upper) decomposition technique.

Temperature- and species-dependent thermodynamic and transport properties are used in this formulation. The enthalpy of each species is calculated from polynomial curve-fits, while the viscosity, thermal conductivity, and diffusion coefficients of the species are estimated from the Lennard-Jones potentials.

Flat velocity profiles are used at the fuel and air inflow boundaries. A simple extrapolation procedure[12] with weighted zero- and first-order terms was used to estimate the flow variables at the out-flow boundary. The usual no-slip, adiabatic, and chemically inert boundary conditions were applied at the walls. Wall functions were used for determining the gradients of the flow variables near the walls in the cases where turbulence was modeled.

Results and Discussion:

The geometry chosen for the study of fluid-dynamics effects on a bluff forebody is very similar to that used by Little and Whipkey[6] in their experimental investigations on locked vortices and by Hsu et al.[1] in the trapped-vortex combustor. It consists of a 100-mm-diameter flat cylindrical forebody enclosed in an annular cylindrical tube having a 200-mm inner diameter. An afterbody disk having diameter and thickness of 75 and 2 mm, respectively, is attached to the forebody using a spindle of 9-mm diameter. The size of the cavity formed between the forebody and the disk is varied by moving the disk toward or away from the forebody. Airflow over this body develops vortices inside the cavity and behind the disk; normally these vortices shed, and the flow becomes dynamic in nature. The velocity of the air used in the annular gap between the forebody and the surrounding tube is 30 m/s. Axisymmetric calculations are made for different cavity sizes using a 301 X 91 grid system. The geometry and the grid system used are shown in Fig. 1. Variation of the grid spacing was adopted in both the axial (x) and radial (r) directions to cluster the grid points in the cavity and near the walls.

Starting from a uniform initial flowfield around the forebody-spindle-afterbody combination, direct numerical simulations (DNS) are made for different cavity sizes using the model described earlier. Turbulence modeling was not used in these direct simulations. In order to obtain results not biased by the initial uniform flowfield, initial calculations for 25,000 time steps (corresponding to 0.675 s of real time) were discarded prior to recording of the

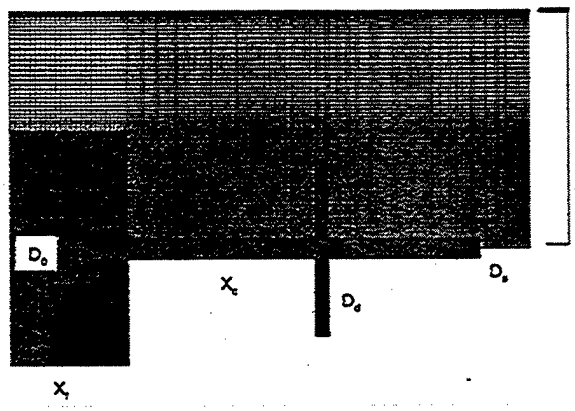

Fig. 1. Geometry of the forebody-spindle-disk combination used for the study of trapped-vortex concepts in cold and combustion environments. Grid system employed for the direct simulation of large-scale structures is also shown.

dynamic solutions. Calculations were then continued for another 5,000 time steps for data-analysis purposes.

Cold Flow in Cavity:

Calculations were performed on the afterbody-spindle-forebody combination described previously for different cavity sizes and for an annular airflow velocity of 30 m/s. The direct simulation using 301 X 91 grid points resulted in dynamic flows with a degree of unsteadiness related to the cavity size.

The instantaneous solution obtained for the forebody-spindle combination (without the disk) is shown in Fig. 2 in the form of velocity vectors in the upper half and particle traces in the lower half. This solution represents data obtained at the end of the 30,000-time-step calculation. The flowfield is nearly at steady state, with a large recirculation zone being created downstream of the forebody and extending up to z = 160 mm. A small vortex has also developed in the corner of the forebody and spindle. For visualizing the dynamic nature of the flow, the instantaneous positions of the particles that were continuously released from locations near the entrance region are shown in Fig. 2. The solid triangles represent the locations of the particles that were released in the freestream and close to the forebody, whereas the open circles represent the locations of the particles that were released away (r > 60 mm) from the forebody. The steady nature of the flowfield in the absence of the afterbody disk (Fig. 2) is evident from the separate streaks of particles. Note that none of the particles injected into the freestream entered the recirculation region formed behind the forebody. On the other hand, the particles that were injected into the recirculation zone (not shown in the figure for clarity) remained within the recirculation region.

Perturbation to the steady flow that developed over the forebody-spindle geometry is studied by placing a disk on the spindle. The instantaneous flowfields obtained with the disk located at different distances from the forebody are shown in Figs. 3(a)-3(d). The plotting scheme used for these figures is identical to that used in Fig. 2. In general, vortices are formed in the cavity and downstream of the disk in all cases. When the cavity formed between the forebody and disk is small [Fig. 3(a)], several vortices are

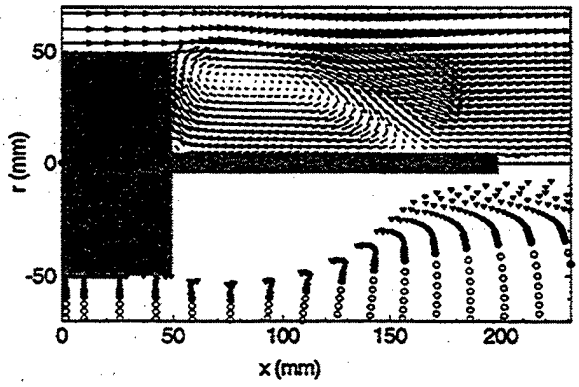

Fig. 2. Non-reacting flow around the geometry formed with 100-mm-diameter forebody and a spindle of D_s/D_0 = 0.0938. Velocity vectors and particle distributions are shown in the upper and lower halves, respectively.

developed within the cavity, and the flow is dominated by two counter-rotating vortices. Note that the largest vortex in the cavity is rotating in the direction opposite that of the recirculating vortex seen in Fig. 2. The unsteady nature of these cavity vortices triggers shedding of the large recirculating vortex formed behind the disk. The dynamics of the flow may be visualized readily from the particle traces (or streak-lines) shown on the lower half of each plot in Fig. 3. A significant number of particles represented by solid triangles has entered the cavity and the vortex behind the disk in the case of X_c/D_0 = 0.4; which, indicates the intense mixing resulting from the dynamic flow structures.

When the disk was located at X_c/D_0 = 0.6, the cavity flow became steady; as a result, the flow behind the disk also became nearly steady [Fig. 3(b)]. The total drag under this condition reached a minimum value. Well-defined corner vortices have formed in this case. Interestingly, the direction of rotation of the fluid in the cavity follows that observed for the no-disk case (Fig. 2). The steady vortices in the cavity and behind the disk in this optimum case seem to be the split parts of the steady vortex computed without the disk, and the velocity vectors at the tip of the disk show that the fluid is passing around the disk smoothly. However, the location of the main-flow re-attachment point on the spindle has shifted from 110 to 125 mm from the forebody with the addition of the disk. This increase in the re-attachment distance was also observed in the flow-visualization experiments of Little and Whipkey.[6] Simulations made for X_c/D_0 = 0.7 [Fig. 3(c)] yielded perfectly steady vortices within the cavity and behind the disk. The flow structure is similar to that observed for the X_c/D_0 = 0.6 case.

For cavity sizes greater than $X_c/D_0 > 0.7$, flow in the cavity and behind the disk became unsteady [Fig. 3(d)], resulting an increase in the drag coefficient. Unlike in the smaller-than-optimum-cavity case [Fig. 3(a)], only one dominating vortex was formed in the cavity and a multiple-vortex structure was established behind the disk. Neither the vortices from the cavity nor the ones behind the disk in this larger-than-optimum-cavity case seem to shed. However, since the size of the cavity in these cases is larger than the optimum one, the trapped vortex rotates within the cavity. This is evident from the particle traces plotted in the bottom half of Fig. 3(d). At this instant the solid-triangle particles are pulled into the cavity since the vortex is closer to the disk; at other instants these particles pass over the disk when the vortex is pushed toward the forebody. Close examination of the cavity-flow structure in Fig. 3(d) suggests that vortices are not shedding from the cavity. The particle distribution in this figure also indicates that particles lump together while moving around the center of the cavity; when that lump approaches the edge of the afterbody, a fraction of particles leaves the cavity. This implies that particles are entrained into the cavity vortex during a certain phase and then exit the cavity during a different phase, leading to periodic accumulation of particles in the cavity.

Calculations for the forebody-spindle-afterbody geometries are also made using the k-ε turbulence model. For these calculations grid, time-step, and flow conditions utilized are the same as those used for the direct

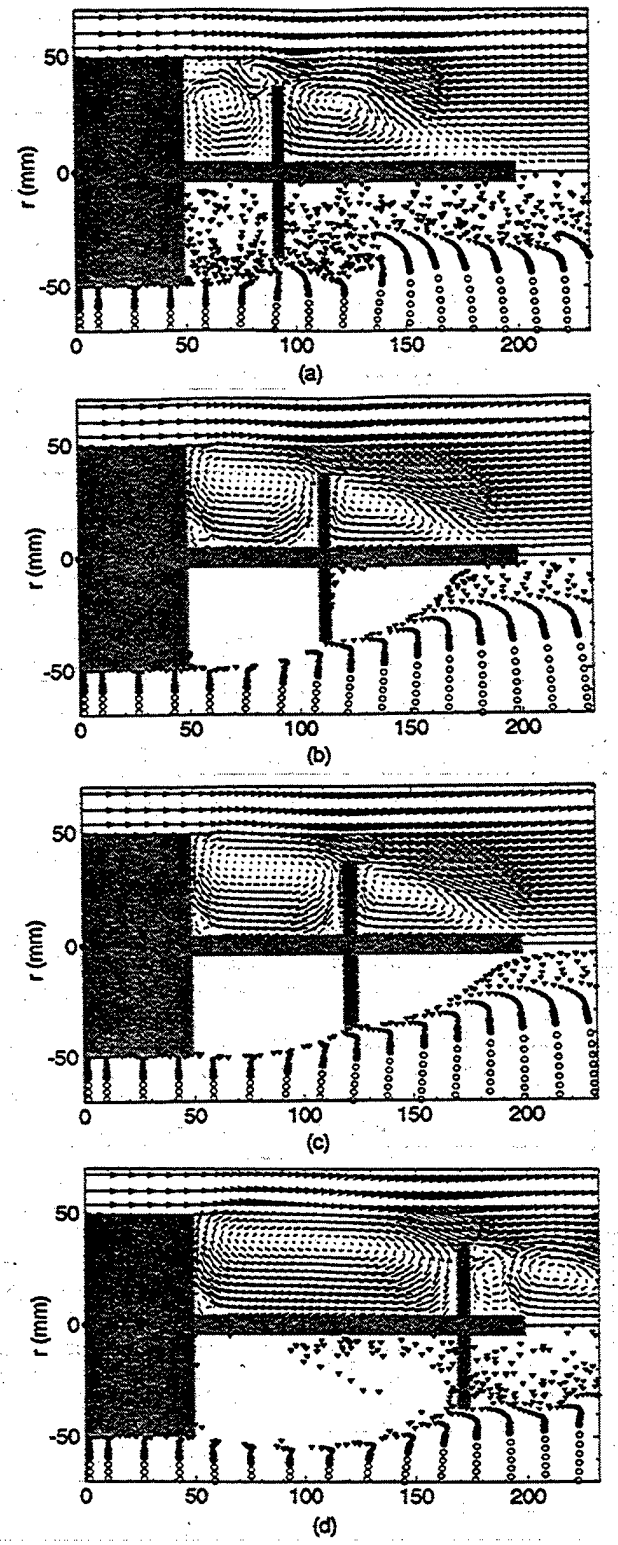

Fig. 3. Instantaneous flowfields obtained using direct numerical simulations for the forebody-spindle-disk combination for various disk locations. X_c/D_0 = a) 0.4, b) 0.6, c) 0.7, and d) 1.2. Velocity vectors and particle distributions are shown in the upper and lower halves, respectively.

simulations. Interestingly, for every cavity size, the simulation with the turbulence model quickly converged to steady-state flowfield. Results obtained for cavity sizes X_c/D_0 = 0.4, 0.6, 0.7, and 1.2 are shown in Figs. 4(a), 4(b), 4(c), and 4(d), respectively. Since each of these solutions represents a steady-state flowfield, streamlines are plotted rather than particle traces.

In general, the turbulent-flow calculations yielded a single vortex in the cavity region and another behind the disk. In the case of X_c/D_0 = 0.4, the direction of rotation of the cavity vortex is normal (clockwise). On the other hand, as shown in Fig. 3(a), the direct simulations resulted in a multiple-vortex structure with the largest one rotating in the counterclockwise direction. The flow structure downstream of the disk captured by k-ε turbulence calculations is also quite different from that captured by direct simulations. The vortex in the former is squeezed toward the spindle, whereas that in the latter is pushed away from the spindle. For the near optimum-size-cavity cases where the flow is in steady state, turbulent and direct calculations yielded similar solutions. The turbulent calculations predicted flow reattachment on the spindle at x = 175 and 192 mm for the X_c/D_0 = 0.6 and 0.7 cases, respectively, while the direct simulations predicted reattachment at x = 175 and 186 mm, respectively. However, some minor differences exists in the solutions obtained by the turbulent and direct calculations for these cases. The turbulence model seems to dissipate the corner vortices that are observed in the direct simulations.

The cavity flow structures predicted by the turbulent and direct simulations for the X_c/D_0 = 1.2 case [Figs. 4(d) and 3(d), respectively] are similar in nature, even though the latter is dynamically oscillating within the cavity. Interestingly, the streamline drawn from the edge of the forebody in Fig. 4(d) shows that flow dips slightly into the cavity near the disk and then flows back around the tip of the disk. This dividing streamline also suggests that no flow is entering the recirculation region. The dynamic flow structure downstream of the disk predicted by the direct simulations is quite different from the single-vortex structure obtained with the k-ε turbulence model.

Figures 3 and 4 provide only qualitative comparisons between the direct and turbulent simulations since the former represents an instantaneous solution of a dynamic flow. For making quantitative comparisons, the total drag coefficients of these geometries are computed and compared with the experimental data and the results are given in Ref. 13. Both the time-averaged DNS and k-ε model results gave good predictions for the total drag coefficient for different cavity sizes even though the latter did not capture the dynamic motion of large-scale vortices.

Combusting Flow:

Considering the advantages of locked vortices for stable combustion, Hsu et al.[1] have developed a laboratory combustor that can be operated over a wide range of flow-rate conditions. The geometry of the center-body combustor designed by Hsu et al.[1] is similar to that studied by Little and Whipkey[6] for non-reacting flows. For investigating the vortex characteristics in the cavity under combusting-flow environment, calculations were made for

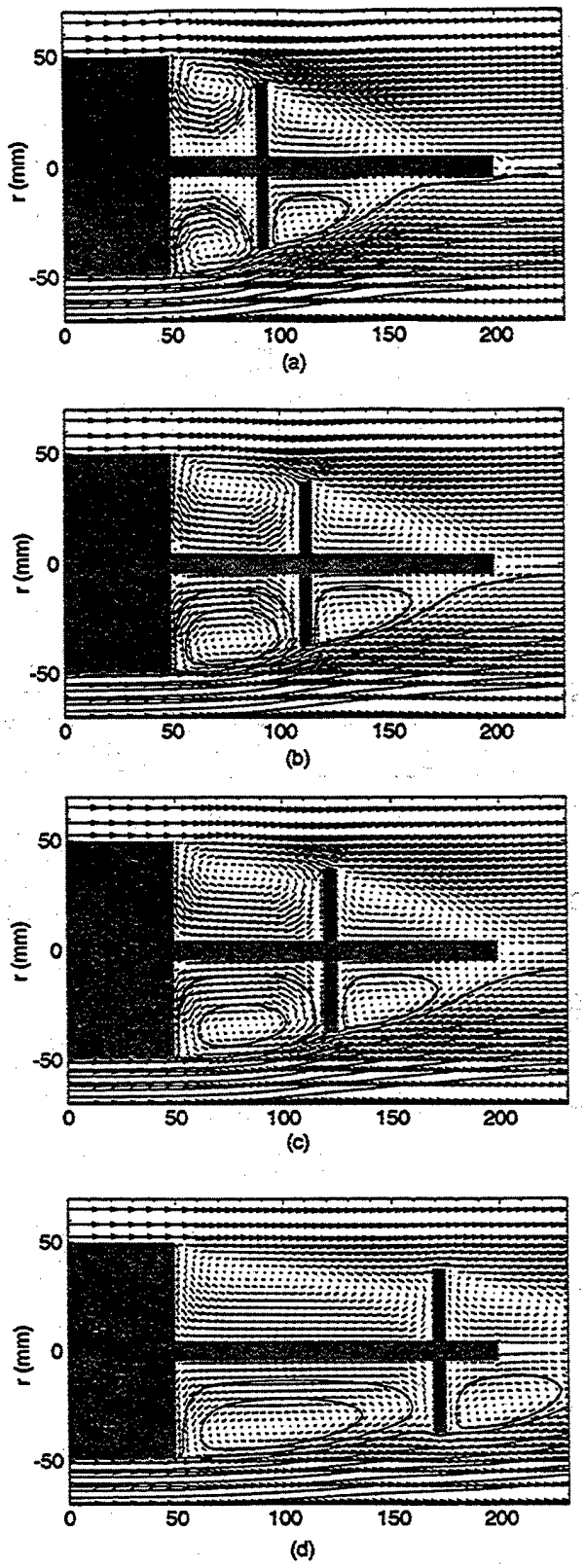

Fig. 4. Steady-state flowfields obtained using k-ε turbulence model for the forebody-spindle-disk combination. X_c/D_0 = a) 0.4, b) 0.6, c) 0.7, and d) 1.2.

the reacting flow in the combustor of Hsu et al.[1] This combustor consists of a forebody and an afterbody of diameters 70 and 50.8 mm, respectively. The combustor is enclosed in a 80-mm-diameter Pyrex annular tube. Main air is delivered through the annular gap between the Pyrex tube and the forebody at a velocity of 42 m/s. Primary air and fuel (propane) are injected into the cavity from the afterbody. Fuel and air are carried to the afterbody through a central tube that connects the afterbody to the forebody. Figure 5(a), obtained using a normal photographic camera with long exposure time, shows the flame and the combustor geometry for operation under primary equivalence ratio (defined as fuel-to-air ratio injected into the cavity relative to the ratio required for stoichiometric combustion) of 4.4.

Calculations were made for the above fuel-rich condition using a 251 X 101 grid system. Fuel and air in the experiment were injected into the cavity through three coannular rows of holes drilled on the face of the afterbody. The fuel holes were sandwiched between the air holes. The symmetric distribution of holes is assumed to provide only weak three-dimensional effects. For performing axisymmetric calculations on this near-symmetric combusting flow, the fuel and air holes were replaced with annular slots of 1-mm width in the model. The flat velocities of 12.4 and 5 m/s at the exits of air and fuel slots gave the measured flow rates of 56 and 25 slpm, respectively.

The instantaneous flow computed with a fast-chemistry assumption is shown in Fig. 5(b) by plotting iso-temperature contours and velocity vectors plotted in the upper and lower halves, respectively. Computed flow in the cavity has a large vortex generated by the high-speed annulus air flow and several small vortices that are primarily developed from the interaction of fuel and air jets injected into the cavity. Fig. 5(b) also indicates that the flow of combustion products from the cavity over the disk is associated with only weak shedding. To visualize the dynamic characteristics of this combusting flow, results obtained at different instants (time steps) are shown in Fig. 6. The time interval between two consecutive images is 2 ms. The important observations made from these instantaneous images are 1) the cavity flow seems dynamic and the injection jets into the cavity flap radially, 2) the fairly steady vortex formed in the wake region of the disk indicates that the vortex shedding from the cavity is not sufficiently strong to disturb the wake vortex, and 3) the high-temperature contours (Nos. 9 and A) are always located close to the spindle and the forebody. The weak vortex shedding from the cavity suggests that the global vortex structure in the cavity represents a locked vortex. Note that the design strategy used by Hsu et al.[1] for determining the cavity size was based on the conditions for obtaining locked vortices in cold flows without primary injection. For this cavity size, cold-flow calculations also showed locked vortices within the cavity and behind the afterbody. Absence of strong vortex shedding from the cavity, noted from the reacting flow calculations made with primary injection (Fig. 6), suggests that the locked-vortex criterion obtained using cold annular flow yields locked vortices (overall) in the reacting flow case also. Additional calculations must be

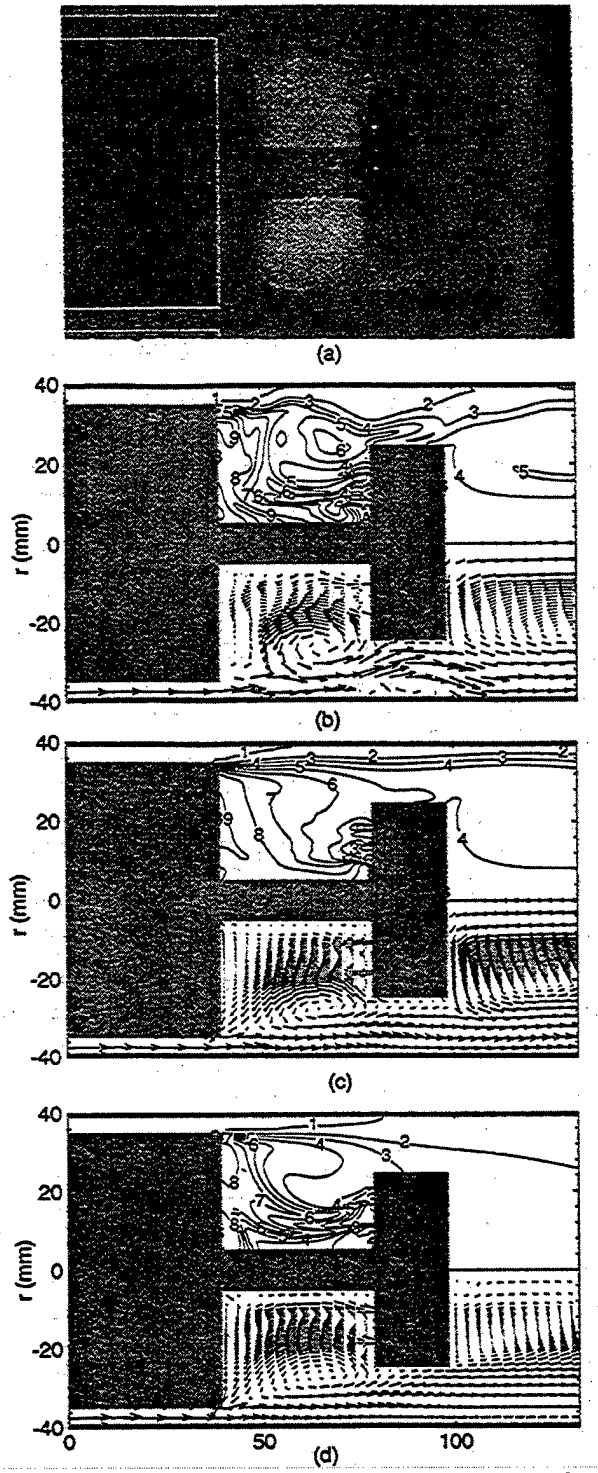

Fig. 5. Reacting flow inside trapped-vortex combustor for primary equivalence ratio of 4.4. a) Direct photograph of the flame inside the trapped-vortex combustor, b) an instantaneous flowfield obtained with direct numerical simulation, c) flame obtained by averaging several instantaneous solutions and d) steady-state flame simulated using k-ε turbulence model. Iso-temperature contours are plotted with an interval of 150 K starting from 300 K.

performed with different cavity sizes before a general conclusion can be reached regarding locked vortices in cold and reacting flows.

The overall flow structure and the temperature field are obtained from DNS by time averaging the 8000 instantaneous solutions over a period of 40 ms and the results are shown in Fig. 5(c). The dominating cavity vortex and the near steady-state wake vortex noted in the instantaneous solutions (Fig. 6) have appeared in the time-averaged data as stable recirculation regions. A small recirculation region in the corner of the spindle and disk may also be noted in Fig. 5(c). Time averaging has also eliminated the temperatures that are greater than 1600 K [absence of Contour No. A in Fig. 5(c)].

The computed peak temperature (time-averaged) of 1600 K is lower than that measured (~ 1900 K) in the experiment. In fact, even the instantaneous temperature never exceeded 1750 K in the direct numerical simulations. Since a fast-chemistry model was used in the present simulations, the lower computed temperature could be resulting from the mixing-limited environment in the cavity. It is known that even though large-scale flow structures play a major role in the mixing of fuel and air, small scales are important for mixing on a local level. The present simulations predict only the large-scale vortical structures in the cavity. The lower predicted temperature could then be due to the absence of small-scale vortices in the calculations. For verifying this, calculations were made by including the k-ε model for turbulence. Computations resulted in a steady flow and the predicted temperature field is shown in Fig. 5(d). Note that the same 251 X 101 grid system utilized in DNS was employed for these simulations also. Surprisingly, the peak temperature obtained in Fig. 5(d) was only 1500 K– lower than that obtained without the turbulence model. This suggests that the combustion in the cavity is not limited by the small-scale mixing.

In experiments, primary fuel and air are passed through the central tube and afterbody before being injected into the cavity. Since both the center tube and afterbody are surrounded by the hot combustion products, their wall temperatures are expected to be higher than the temperature of the incoming fuel and air which, in turn, heats the fuel and air. On the other hand, even though the walls of the afterbody and center tube were treated as adiabatic walls in the present simulations, fuel and air were injected into the cavity at room temperature since flow inside the tubes was not considered. It is believed that the hotter fuel and air injected into the cavity leads to the higher temperatures in the experiment.

A comparison between the time-averaged flow field [Fig. 5(c)] and the steady-state solution resulted from k-ε model [Fig. 5(d)] reveals significant similarities. Mainly, the recirculation zone observed in the time-averaged data matches well with that obtained with k-ε model. On the other hand, the wake vortex behind the disk and the corner vortex of the spindle and disk predicted with k-ε turbulence model are weaker than those obtained from the time-averaged DNS data. Temperature distributions in Figs. 5(c) and 5(d) are also quite different. Simulations with k-ε model yielded jet-flame structures in the cavity

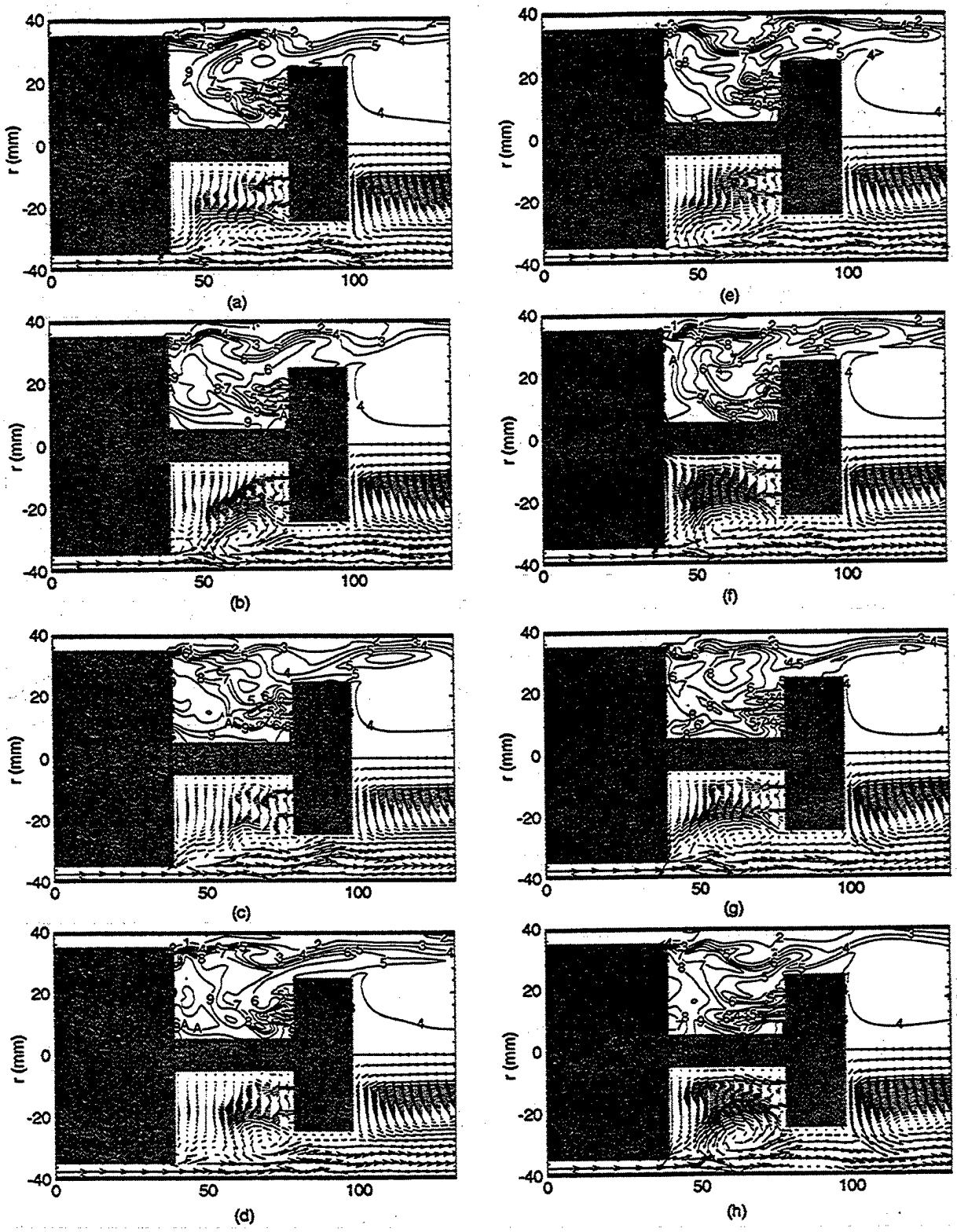

Fig. 6. Reacting flow in trapped-vortex combustor at different instants. a) t_0, b) t_0+2, c) t_0+4, d) t_0+6, e) t_0+8, f) t_0+10, g) t_0+12 and h) t_0+16 ms. Iso-temperature contours are plotted with an interval of 150 K starting from 300 K.

following the fuel and air injections where as, more uniform temperature distributions are obtained with DNS.

Radial temperature distributions obtained from the experiments and the ones predicted with DNS (time-averaged) and k-ε model are compared at axial distances of 45, 65, and 80 mm in Figs. 7(a), 7(b), and 7(c), respectively. Overall, only a qualitative comparison may be noticed between the calculations and the experiment. Interestingly, the DNS results are closer to the experiment than the results obtained with k-ε model. Especially, near the spindle DNS has correctly predicted the higher temperatures. The higher measured temperatures at x = 80 mm (close to the disk) indicate that the fuel and air are preheated before being injected into the cavity--which needs to be considered in the future calculations.

Ability of the incorporated k-ε model in predicting combusting flows is tested by simulating two vertically mounted turbulent jet flames that were studied experimentally[14,15] and numerically[16] earlier. The burner used in these studies was a 7.74-mm diameter straight tube and the fuel was issued into stagnant air at a Reynolds number of 15,000. Results obtained for the pure-methane flame are compared with the experimental data and the k-ε simulations of Lockwood and Stolakis[16] in Fig. 8 and those for a 42% diluted flame are compared in Fig. 9. The exit velocities of the fuel in these two cases were 55 and 43 m/s. In both the flames, k-ε models predicted temperatures greater than the measured values and Lockwood and Stolakis found that inclusion of radiation model brought the predicted temperatures closer to the experiment. Nevertheless, the present k-ε model results are in reasonably good agreement with the results obtained by Lockwood and Stolakis. Based on these results and the disagreement observed between the k-ε predictions and the measurements in the case of trapped-vortex combustor it is speculated that k-ε model is inadequate for the prediction of reacting flowfields in trapped-vortex combustor which are dominated by the motion of large-scale vortices.

Calculations are also made for a lower equivalence ratio (2.2) case. Direct photograph of the flame, instantaneous and time-averaged results obtained with DNS, and the steady-state results obtained with k-ε model are shown in Figs. 10(a), 10(b), 10(c), and 10(d), respectively. The lower equivalence ratio in this case is achieved by increasing the air injection velocity to 24.8 m/s. All other inflow boundary conditions used in this case are identical to those used in the 4.4-equivalence-ratio

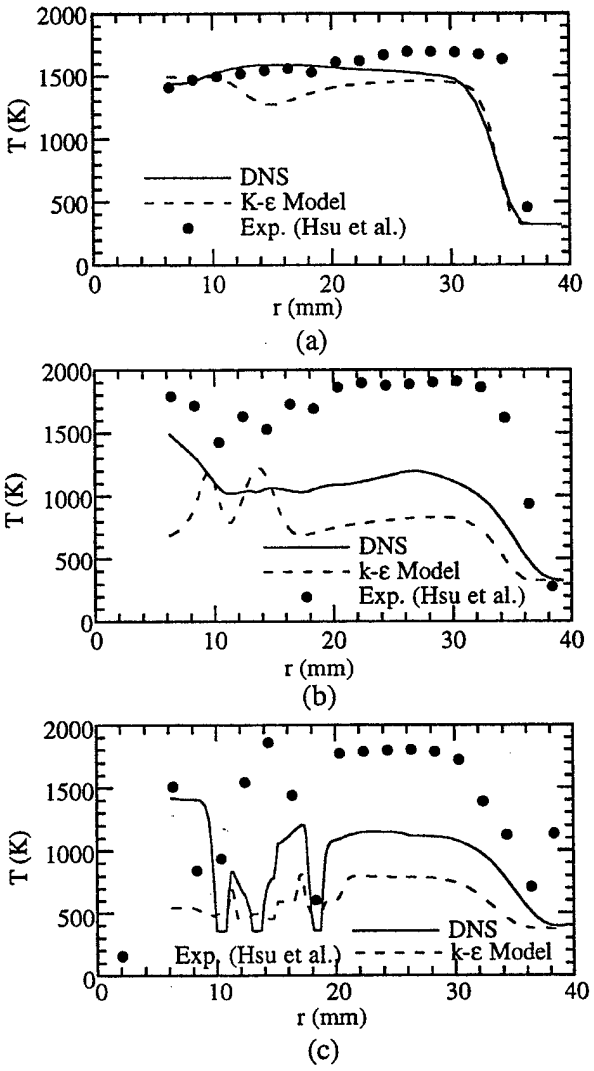

Fig. 7. Radial temperature distributions inside trapped-vortex combustor at heights a) 45 mm, b) 65 mm, and c) 80 mm for primary equivalence ratio of 4.4.

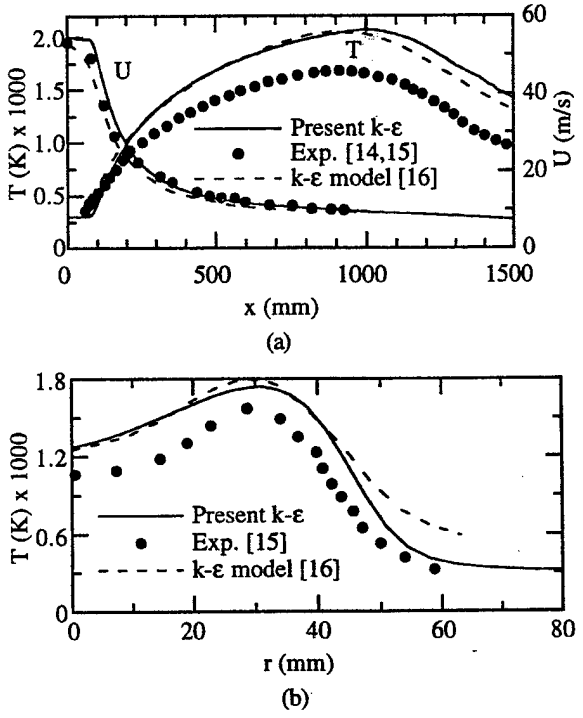

Fig. 8. Comparison between experiment and k-ε model calculations for a vertically mounted turbulent jet flame. a) Temperature and axial velocity along symmetry axis, and b) radial temperature distribution at x = 280 mm.

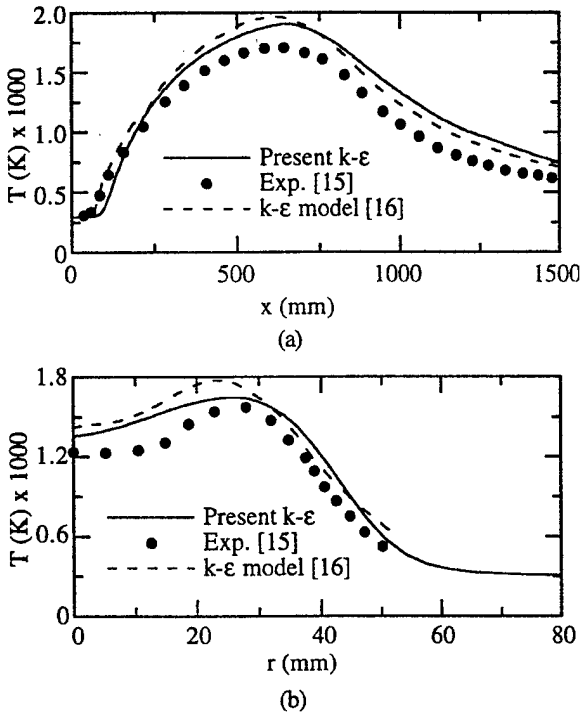

Fig. 9. Comparison between experiment and k-ε model calculations for a vertically mounted turbulent jet flame. a) Temperature and axial velocity along symmetry axis, and b) radial temperature distribution at x = 280 mm.

case. Because of the higher injection velocity, air jets are penetrating well into the cavity and a stronger recirculation zone is established between the spindle and the neighboring air jet. Interestingly, the wake vortex in this case also is nearly steady and overall dynamics of the cavity flow has not changed much with the increase in air injection. These calculations suggest that the cavity flow is dominated by the high momentum annulus air flow and the injection into the cavity has only secondary effects on the cavity flow. Further calculations should be made with different cavity sizes to understand the role of injection on cavity flow.

Conclusions:

Vortex shedding behind a bluff forebody leads to a higher drag coefficient and in combustors leads to blowout and poor combustion efficiency. It is known that the drag coefficient of the bluff body can be decreased by trapping the wake vortices using disks. The dynamics of the vortices formed inside the cavity and behind the disk are studied using a time-dependent, axisymmetric Computational Fluid Dynamics with Chemistry (CFDC) code. A large number of grid points with ΔX and $\Delta r \sim 0.9$ mm was used to capture the large-scale structures whose physical size is up to an order of magnitude smaller than the cavity height. It is found that when the cavity has optimum length the vortices within the cavity and behind the disk are spatially locked. More than one dominant vortex developed in smaller-than-optimum cavities and vortex shedding always observed from these cavities. On

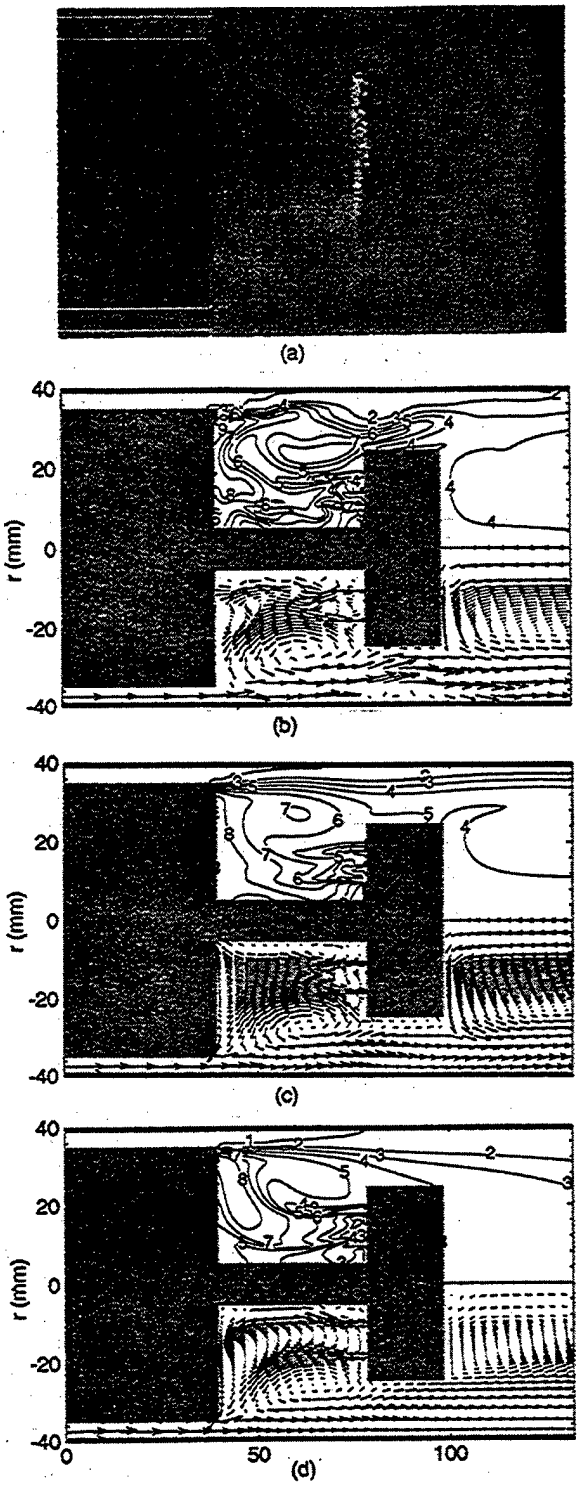

Fig. 10. Reacting flow inside trapped-vortex combustor for primary equivalence ratio of 2.2. a) Direct photograph of the flame inside the trapped-vortex combustor, b) an instantaneous solution obtained with direct numerical simulation, c) flame obtained by averaging several instantaneous solutions and d) steady-state flame simulated using k-ε turbulence model. Iso-temperature contours are plotted with an interval of 150 K starting from 300 K.

the other hand, a single dominating vortex formed and moved within a larger-than-optimum cavity and shedding was not observed from the cavity. Calculations made with k-ε turbulence model yielded steady flows for all cavity sizes.

Axisymmetric calculations were also performed for the reacting flow in the trapped-vortex combustor designed by Hsu et al. using the fast-chemistry model. Injection of air and fuel into the cavity led to the development of several unsteady vortices in the direct numerical simulations. Time-averaged results constructed from DNS data and the steady-state results obtained with k-ε turbulence model are compared with the experimental data. The qualitative agreement between the measurements and the predictions was found to be better for direct numerical simulation. Preliminary results suggest that the optimum cavity length determined from the non-reacting annular flow seems to yield non-shedding cavity flows, even with combustion and fluid injections into the cavities. Additional calculations must be performed to verify this conclusion for different-geometry combustors. The time-averaged flow structures obtained for this cavity size are found to be similar to the steady-state flow structures obtained with k-ε model.

Acknowledgment:

This work was supported, in part, by Air Force Contract F33615-95-C-2507 and the Air Force Office of Scientific Research. The authors would like to thank Dr. Mark Hsu for stimulating discussions and allowing us to use Figs. 5(a) and 10(a) and Mrs. Marian Whitaker for the Editorial help.

References:

1. Hsu, K. Y., Goss, L. P., Trump, D. D., and Roquemore, W. M., "Performance of a Trapped-Vortex Combustor," AIAA Paper 95-0810, Washington, D. C., Jan. 9-12, 1995.
2. Rohsenow, W. M., Fink, C. H., and Pollis, S. R., "Flow Through Two Orifices in Series," American Society of Mechanical Engineers Paper No. 51-A-87, 1951.
3. Migay, V. K., "Study of Ribbed Diffusers" (in Russian), Toploenergetika, No. 10, 1962, English translation issued as A.R.C. Paper 25, p. 382, 1963.
4. Mair, W. A., "The Effect of a Rear-Mounted Disc on the Drag of a Blunt-Based Body of Revolution," The Aeronautical Quarterly, Nov., pp. 350-360, 1965.
5. Roshko, A. and Koenig, K., "Interaction Effects on the Drag of Bluff Bodies in Tandem," Presented at the Symposium on Aerodynamic Drag Mechanisms of Bluff Bodies and Road Vehicles, General Motors Research Laboratories, Sept. 27-28, 1976.
6. Little, B. H., and Whipkey, R. R., "Locked Vortex Afterbodies," Journal of Aircraft, Vol. 16, No. 5, 1979.
7. Grinstein, F. F., and Kailasanath K., "Three-Dimensional Numerical Simulations of Unsteady Reactive Square Jets", 25th International Symposium on Combustion, Combustion Institute, Pittsburgh, PA, 1995.
8. Veynante, D., Vervisch, L., Poinsot, T., Linan, A., and Ruetsch, G., "Triple Flame Structure and Diffusion Flame Stabilization", Proceedings of the Summer Program 1994, Center for Turbulent Research, NASA Ames/Stanford University, CA pp. 55-73, 1994.
9. Katta, V. R., Goss, L. P., and Roquemore, W. M., "Numerical Investigations of Transitional H2/N2 Jet Diffusion Flames", AIAA Journal , Vol. 32, 1994, pp. 84-94, 1994.
10. Leonard, B. P., "A Stable and Accurate Convective Modeling Procedure Based on Quadratic Upstream Interpolation," Computer Methods in Applied Mech. and Engineer., Vol. 19, p. 59, 1979.
11. Spalding, D. B., "A Novel Finite Difference Formulation for Difference Expressions Involving Both First and Second Derivatives," International Journal for Numerical Methods in Engineering, Vol. 4 , pp. 551-559, 1972.
12. Katta, V. R., Goss, L. P., and Roquemore, W. M., "Simulation of Vortical Structures in a Jet Diffusion Flame," Int. J. Num. Meth. Heat Fluid Flow, Vol. 4, p. 413, 1994.
13. Katta, V. R., and Roquemore, W. M., "Study of Trapped-Vortex Concepts for Aerodynamic Drag Reduction," Presented at the First AFOSR Conference on Dynamic Motion CFD, Rutgers University, NJ, June 3-5, 1996.
14. El-Banhawy, Y., Hassan, M. A., Lockwood, F. C., and Moneib, H. A., "Velocity and Unburned Hydrocarbon Measurements in a Vertical Turbulent-Free Jet Diffusion Flame", Combustion and Flame, Vol. 53, 1983, pp. 145-148.
15. Lockwood, F. C., and Moneib, H. A., "Fluctuating Temperature Measurements in Turbulent Jet Diffusion Flames", Combustion and Flame, Vol. 47, 1982, p. 291.
16. Lockwood, F. C., and Stolakis, P., "Assessment of Two Turbulence Models for Turbulent Round Diffusion Jets with Combustion", in Turbulent Shear Flows, Vol. 4, Ed. L. J. S. Bradbury, F. Durst, B. E. Launder, F. W. Schmidt and J. H. Whitelaw, Spriger-Verlag, Berlin, 1985, pp. 228-344.

Numerical Studies on Trapped-Vortex Concepts for Stable Combustion

V. R. Katta
Innovative Scientific Solutions, Inc.,
Dayton, OH 45430

W. M. Roquemore
Wright Laboratory,
Wright-Patterson Air Force Base, OH 45433

Spatially locked vortices in the cavities of a combustor aid in stabilizing the flames. On the other hand, these stationary vortices also restrict the entrainment of the main air into the cavity. For obtaining good performance characteristics in a trapped-vortex combustor, a sufficient amount of fuel and air must be injected directly into the cavity. This paper describes a numerical investigation performed to understand better the entrainment and residence-time characteristics of cavity flows for different cavity and spindle sizes. A third-order-accurate time-dependent Computational Fluid Dynamics with Chemistry (CFDC) code was used for simulating the dynamic flows associated with forebody-spindle-disk geometry. It was found from the nonreacting flow simulations that the drag coefficient decreases with cavity length and that an optimum size exists for achieving a minimum value. These observations support the earlier experimental findings of Little and Whipkey (1979). At the optimum disk location, the vortices inside the cavity and behind the disk are spatially locked. It was also found that for cavity sizes slightly larger than the optimum, even though the vortices are spatially locked, the drag coefficient increases significantly. Entrainment of the main flow was observed to be greater into the smaller-than-optimum cavities. The reacting-flow calculations indicate that the dynamic vortices developed inside the cavity with the injection of fuel and air do not shed, even though the cavity size was determined based on cold-flow conditions.

Introduction

A revolutionary advancement in the development of a simple, compact, and efficient method of combustion was recently proposed by Hsu et al. (1995). This new combustor concept employs a vortex that is trapped in a cavity to stabilize the flame, and hence, is referred as the Trapped-Vortex (TV) concept. Even though the idea of trapping a vortex for flame stabilization purposes is a novel one, interest in the utilization of vortex motion to aerodynamic advantage has intrigued aerodynamicists for many years. The experiments of Rohsenow et al. (1951) have shown that when two circular orifices are placed in series in a pipe, in certain circumstances, a large recovery of pressure may occur across the second orifice; hence, the overall pressure drop is considerably less for the two orifices than for a single one having the same flow. In ribbed diffusers, Migay (1963) found that balancing the fluid removed by entrainment and the fluid entering the cavity by reversed flow ensures that the flow outside the cavities will follow the ribs fairly closely and a good pressure recovery will be obtained. By mounting a disk behind the base of a blunt body, Mair (1965) has shown that the afterbody drag of the blunt object will be reduced. Using similar concepts, Roshko and Koenig (1976) have reported a reduction in drag of blunt forebodies when disks are placed on spindles ahead of the body.

In order to understand the aerodynamics associated with minimum-drag conditions, Little and Whipkey (1979) conducted extensive investigations on the dynamic nature of flows over bluff bodies using smoke-flow-visualization and laser-velocimetry techniques. Because of the limitations of the smoke tunnel, they used reduced flow conditions (~0.3 m/s) and half-scaled geometries for the flow-visualization studies and full-scale geometries and turbulent flows (~30 m/s) for the time-averaged drag measurements. Based on these reduced and full-scale experiments, they correlated the afterbody drag and the motion of the vortex in the wake region and postulated that a minimum-drag condition was established when the wake vortices are locked between two disks mounted in series on a spindle. They also suggested that the cavity formed between the disk and the bluff body should be of such dimensions that the locked vortex effectively fills the cavity. Since these dynamic flow results were obtained for velocities lower by nearly two orders of magnitude than those used in the full-size wind-tunnel experiments, these conclusions are open to question. And also, in practical combustors, partial burning takes place in the recirculation zones and in the cavity vortices, which could alter the vortex dynamics. As a result, it might be expected that the criterion for trapping a vortex in a combustor would be different from that observed in cold flows.

Performing experimental studies on vortex dynamics inside the cavities in a combusting environment is extremely difficult mainly because of (1) limited access to the bright, hot cavity flow and (2) problems arising from the use of moving parts. On the other hand, recent progress in Direct-Numerical-Simulation techniques (Grinstein and Kailasanath, 1995; Veynante et al., 1994) has led to a growing interest in investigating dynamic flows computationally.

In the present investigation the trapped-vortex concepts were studied numerically using a third-order-accurate time-dependent Computational Fluid Dynamics with Chemistry (CFDC) code. Results obtained for cold flows with different cavity sizes were analyzed to gain an understanding of the dynamic nature, entrainment, and residence-time characteristics of the cavity flow. Calculations were also performed for the reacting flow in the center-body trapped-vortex combustor using a fast-chemistry assumption.

Modeling

A time-dependent, axisymmetric mathematical model that solves for axial- and radial-momentum equations, continuity,

Contributed by the International Gas Turbine Institute and presented at Turbo Asia '96, Jakarta, Indonesia, November 5–7, 1996. Manuscript received at ASME Headquarters July 1996. Paper No. 96-TA-19. Associate Technical Editor: J. W. Shinn.

Copyright © 1998 by ASME
PUBLISHED WITH PERMISSION

and enthalpy- and species-conservation equations is used to simulate the flowfields in the trapped-vortex combustor. Density is obtained by solving the state equation, while the pressure field at every time step is determined from pressure Poisson equations. For the cases in which turbulent-flow characteristics were modeled, the time-dependent equations for turbulent energy (k) and turbulent-energy dissipation (ϵ) are also solved, along with the other governing equations. The standard isotropic $k-\epsilon$ turbulence model is incorporated in those cases. Even though all the governing equations are solved in an uncoupled manner, the turbulence and species-conservation equations are coupled through the source terms during the solution process to improve the stability of the algorithm.

In the present analysis of reacting flows, the simple global-chemical-kinetics model involving propane, oxygen, water, carbon dioxide, and nitrogen used is expressed as follows:

$$C_3H_8 + 5\ O_2 + N_2 \Rightarrow 3\ CO_2 + 4\ H_2O + N_2.$$

The specific reaction rate for this equation is written in Arrhenius form, with an activation energy of 1000 cal/mole and pre-exponential of 1.0×10^{16} m^6/mole^2/s to yield very high reaction rates at all temperatures. These numbers for reaction rate are obtained from a trial-and-error calculations on turbulent free jets (Katta and Roquemore, 1996).

An orthogonal, staggered-grid system with varying cell sizes in both the x and r directions is utilized. The momentum equations are integrated using an implicit QUICKEST (Quadratic Upstream Interpolation for Convective Kinematics with Estimated Streaming Terms) numerical scheme (Katta et al., 1994a; Leonard, 1979) which is third-order accurate in both space and time and has a very low numerical diffusion error. On the other hand, the species, enthalpy, and turbulence-energy conservation equations, which have relatively large source terms, are integrated using the hybrid scheme of Spalding (1972). By rearrangement of the terms, the finite-difference form of each governing equation at all grid points is written as a system of algebraic equations which is then solved using the Alternative-Direction-Implicit (ADI) technique. The time increment, Δt, is determined from the stability constraint and maintained as a constant during the entire calculation. The pressure field at every time step is accurately calculated by simultaneously solving the system of algebraic pressure Poisson equations at all grid points using the LU (Lower–Upper) decomposition technique.

Temperature- and species-dependent thermodynamic and transport properties are used in this formulation. The enthalpy of each species is calculated from polynomial curve fits, while the viscosity, thermal conductivity, and diffusion coefficients of the species are estimated from the Lennard–Jones potentials.

Flat velocity profiles are used at the fuel and air inflow boundaries. A simple extrapolation procedure (Katta et al., 1994b) with weighted zero- and first-order terms was used to estimate the flow variables at the out-flow boundary. The usual no-slip, adiabatic, and chemically inert boundary conditions were applied at the walls. Wall functions were used for determining the gradients of the flow variables near the walls in the cases where turbulence was modeled.

Results and Discussion

The geometry chosen for the study of fluid-dynamics effects on a bluff forebody is very similar to that used by Little and Whipkey (1979) in their experimental investigations on locked vortices. It consists of a 100-mm-dia flat cylindrical forebody enclosed in an annular cylindrical tube having a 200-mm I.D. An afterbody disk having a diameter and thickness of 75 and 2 mm, respectively, is attached to the forebody using spindles. Two sizes of spindle (9- and 28-mm diameter) are used. The size of the cavity formed between the forebody and the disk is varied by moving the disk toward or away from the forebody. Airflow over this body develops vortices inside the cavity and

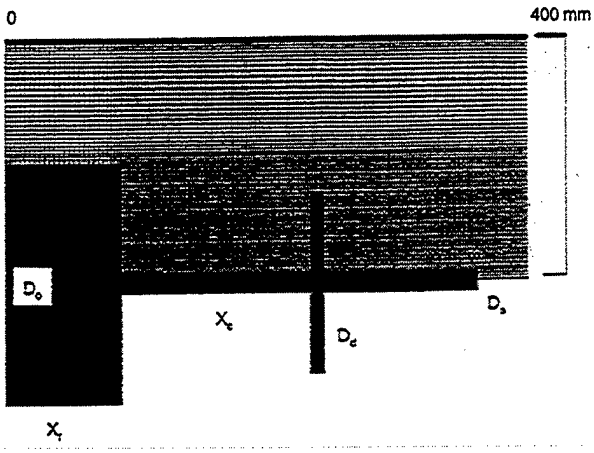

Fig. 1 Geometry of the forebody-spindle-disk combination used for the study of trapped-vortex concepts in cold and combustion environments. Grid system employed for the direct simulation of large-scale structures is also shown.

behind the disk; normally these vortices shed, and the flow becomes dynamic in nature. The velocity of the air used in the annular gap between the forebody and the surrounding tube is 30 m/s. Axisymmetric calculations are made for different cavity sizes using a 301 × 91 grid system. The geometry and the grid system used are shown in Fig. 1. Varying grid spacing was adopted in both the axial (x) and radial (r) directions to cluster the grid points in the cavity and near the walls.

Starting from an uniform initial flowfield around the forebody-spindle-afterbody combination, direct numerical simulations are made for different cavity sizes using the model described earlier. Turbulence modeling was not used for these cold-flow cases. In order to obtain results that are not biased by the initial uniform flowfield, initial calculations for 25,000 time steps (corresponding to 0.675 s of real time) were discarded prior to the recording of the dynamic solutions. Calculations were then continued for another 5000 time steps for data-analysis purposes.

Drag on Forebody-Spindle-Afterbody Combination. The total time-averaged drag coefficient (C_D) on the forebody-spindle-disk combination for each case is computed from the unsteady data using the expression

$$C_D = \int_0^{t_c} (c_p + c_w)dt$$

$$= \frac{1}{\rho_\infty V_\infty^2} \int_0^{t_c} \left[\int (p_w - p_0)dA + \int \tau_w dA \right] dt$$

Here, p_w and p_0 correspond to wall and inlet pressures, respectively; τ_w is the wall shear stress; and c_p and c_w are the pressure-drag and skin-friction coefficients, respectively. Time t_c corresponds to the calculated time. For investigating the drag increase or decrease resulting from the cavity formed between the forebody and the disk, calculations are first made for the forebody-spindle combination alone. These calculations are made without the use of a turbulence model. The total drag coefficients (C_D) obtained for the large (28-mm) and small (9-mm) spindles are 0.125 and 0.151, respectively. The corresponding values measured by Little and Whipkey are 0.179 and 0.186, respectively. Considering the fact that surface roughness and small-scale turbulence near the walls may contribute additional drag in the experiments, the values predicted by the model that neglected these effects seem to be reasonably good.

Calculations were performed on an afterbody-spindle-forebody combination for different cavity sizes and for the annular

airflow velocity of 30 m/s. The direct simulation using 301 × 91 grid points resulted in dynamic flows with a degree of unsteadiness related to the cavity size. Time-averaged quantities from these calculations were obtained by averaging the data over a period of 135 ms (5000 time steps). Calculations were also made incorporating $k-\epsilon$ turbulence model. Even though the same fine grid having 301 × 91 points was used in these simulations, use of the $k-\epsilon$ turbulence model yielded steady flowfields for all the cavity sizes. The drag coefficient obtained from the direct simulations and from the calculations made using the $k-\epsilon$ turbulence model for different cavity sizes indicate that the drag coefficient decreases initially with the separation between the forebody and disk and increases for large separations—which is similar to the behavior observed in the experiments. Quantitative comparisons with the experimental data are made for changes in drag coefficient (ΔC_D) for different cavity sizes which are obtained by subtracting the base drag coefficient (without disk) from that obtained with the disk.

Computed results in the form of drag reduction obtained for different cavity sizes are compared with the experimentally measured ones in Fig. 2(a) and 2(b) for small- and large-spindle cases, respectively. Both the calculations and the experimental data show that drag reduction is maximum when the disk is placed 50 to 60 mm downstream of the forebody. Interestingly, even though the simulations with the $k-\epsilon$ turbulence model did not result in the dynamic flows observed in the experiments, the drag coefficients compare favorably with those from the experiment. On the other hand, the direct simulations obtained by solving Navier–Stokes equations without incorporating any turbulence models yielded dynamic flows similar to those observed in the experiment. It is known that the 30-m/s airflow would result in turbulent flow in the channel created by the annular tube and the forebody-spindle-disk combination. However, the higher-order-accurate algorithms used for solving the momentum and pressure Poisson equations are expected to simulate flow structures that are comparable to the grid system utilized. In the present study, the grid spacing in the cavity region varies from 0.8 to 0.92 mm, and a time step equal to 0.027 ms was chosen. With the use of this model, flow structures of 6-mm size (an order of magnitude smaller than the cavity height) can be resolved. The reasonably good agreement seen in Fig. 2 suggests that the drag force associated with this geometry is dominated by the large-scale motion of the fluid and that the small scales (turbulent scales) are playing a secondary role. For both spindle sizes, a maximum drop in drag coefficient occurs for approximately the same cavity length.

The calculated drag-coefficient profile for the small-spindle (D_s/D_0 = 0.0938) case [Fig. 2(a)] indicates that the drag coefficient decreases monotonically to a minimum value and then increases for cavity lengths greater than 60 mm. On the other hand, for a larger spindle (D_s/D_0 = 0.281), it should be noted that the drag coefficient increases significantly for cavity lengths between 40 and 60 mm before reaching the minimum value [Fig. 2(b)]. Turbulent-flow calculations with the $k-\epsilon$ model yielded no spikes in drag coefficient for either spindle size. Detailed analysis of the time-dependent data obtained for a cavity length of 50 mm indicated that the vortices inside the cavity became quite unsteady, resulting in more shedding of vortices from the cavity and, hence, a higher drag coefficient. Experiments showed no such spikes for the large-spindle case; however, interestingly, a large spike in the drag-coefficient profile was observed for the small-spindle case, indicating that for some smaller-than-optimum size cavities, the drag coefficient could increase drastically. Calculations have captured this phenomenon, but for a different spindle size. The discrepancy noted between the calculations and the experimental results regarding the occurrence of drag spike is believed to result from geometric parameters such as rounded corners and surface roughness and flow quantities such as inlet profiles and fluctuations that are inherent in the experiments. Additional work is needed in the modeling and experimental aspects to allow better comparisons; however, since the present model is reasonably predicting the drag-coefficient Vs cavity-length profile and spikes in the drag coefficient for certain cavity sizes, the model results could be used with confidence to obtain a qualitative understanding of the physical process that result in such effects.

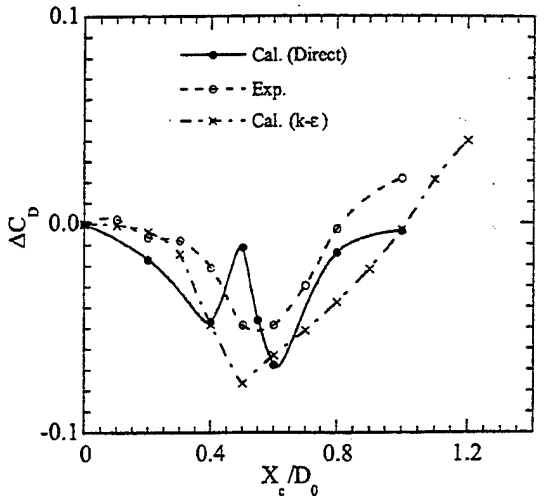

(a)

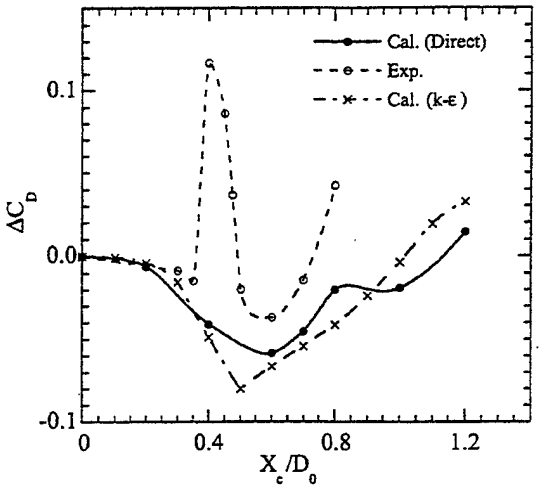

(b)

Fig. 2 Change in drag coefficient resulting from the addition of disk to forebody-spindle geometry obtained for different cavity lengths: (a) small-spindle (D_s/D_0 = 0.281) case

Flow Structures. The instantaneous solution obtained for the forebody-spindle combination (without the disk) is shown in Fig. 3 in the form of velocity vectors in the upper half and particle traces in the lower half. This solution represents data obtained at the end of the 30,000-time-step calculation. The flowfield is nearly at steady state, with a large recirculation zone being created downstream of the forebody and extending up to z = 160 mm. A small vortex has also developed in the corner of the forebody and spindle. For visualizing the dynamic nature of the flow, the instantaneous positions of the particles that were continuously released from locations near the entrance region are shown in Fig. 3. The solid triangles represent the locations of the particles that were released in the free stream and close

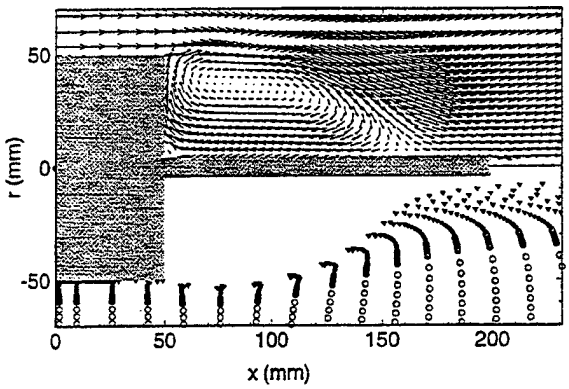

Fig. 3 Nonreacting flow around the geometry formed with 100-mm-dia forebody and a spindle of $D_s/D_0 = 0.0938$. Velocity vectors and particle distributions are shown in the upper and lower halves, respectively.

to the forebody, whereas the open circles represent the locations of the particles that were released away ($r > 60$ mm) from the forebody. The steady nature of the flowfield in the absence of the afterbody disk (Fig. 3) is evident from the separate streaks of particles. Note that none of the particles injected into the free stream entered the recirculation region formed behind the forebody. On the other hand, the particles that were injected into the recirculation zone (not shown in the figure for clarity) remained within the recirculation region.

Perturbation to the steady flow that developed over the forebody-spindle geometry is studied by placing a disk on the spindle. The instantaneous flowfields obtained with the disk located at different distances from the forebody are shown in Figs. 4(*a*)–4(*d*). The plotting scheme used for these figures is identical to that used in Fig. 3. In general, vortices are formed in the cavity and downstream of the disk in all cases. When the cavity formed between the forebody and disk is small [Fig. 4(*a*)], several vortices are developed within the cavity, and the flow is dominated by two counterrotating vortices. Note that the largest vortex in the cavity is rotating in the direction opposite that of the recirculating vortex seen in Fig. 3. The unsteady nature of these cavity vortices triggers shedding of the large recirculating vortex formed behind the disk. The dynamics of the flow may be visualized readily from the particle traces (or streak-lines) shown on the lower half of each plot in Fig. 4. A significant number of particles represented by solid triangles has entered the cavity and the vortex behind the disk in the case of $X_c/D_0 = 0.4$, which indicates the intense mixing resulting from the dynamic flow structures.

When the disk was located at $X_c/D_0 = 0.6$, the cavity flow became steady; as a result, the flow behind the disk also became nearly steady [Fig. 4(*b*)]. The total drag under this condition reached a minimum value. Well-defined corner vortices have formed in this case. Interestingly, the direction of rotation of the fluid in the cavity follows that observed for the no-disk case (Fig. 3). The steady vortices in the cavity and behind the disk in this optimum case seem to be the split parts of the steady vortex computed without the disk, and the velocity vectors at the tip of the disk show that the fluid is passing around the disk smoothly. However, the location of the main-flow re-attachment point on the spindle has shifted from 110 to 125 mm from the forebody with the addition of the disk. This increase in the re-attachment distance was also observed in the flow-visualization experiments of Little and Whipkey (1979). Simulations made for $X_c/D_0 = 0.7$ [Fig. 4(*c*)] yielded perfectly steady vortices within the cavity and behind the disk. The flow structure is similar to that observed for the $X_c/D_0 = 0.6$ case.

For cavity sizes greater than $X_c/D_0 > 0.7$, flow in the cavity and behind the disk became unsteady [Fig. 4(*d*)], resulting an increase in the drag coefficient. Unlike in the smaller-than-optimum-cavity case [Fig. 4(*a*)], only one dominating vortex was formed in the cavity and a multiple-vortex structure was established behind the disk. The vortex in this larger-than-optimum-cavity case is not shedding. However, since the size of the cavity in this case is larger than the optimum one, the trapped vortex rotates within the cavity. This is evident from the particle traces plotted in the bottom half of Fig. 4(*d*). At this instant the solid-triangle particles are pulled into the cavity

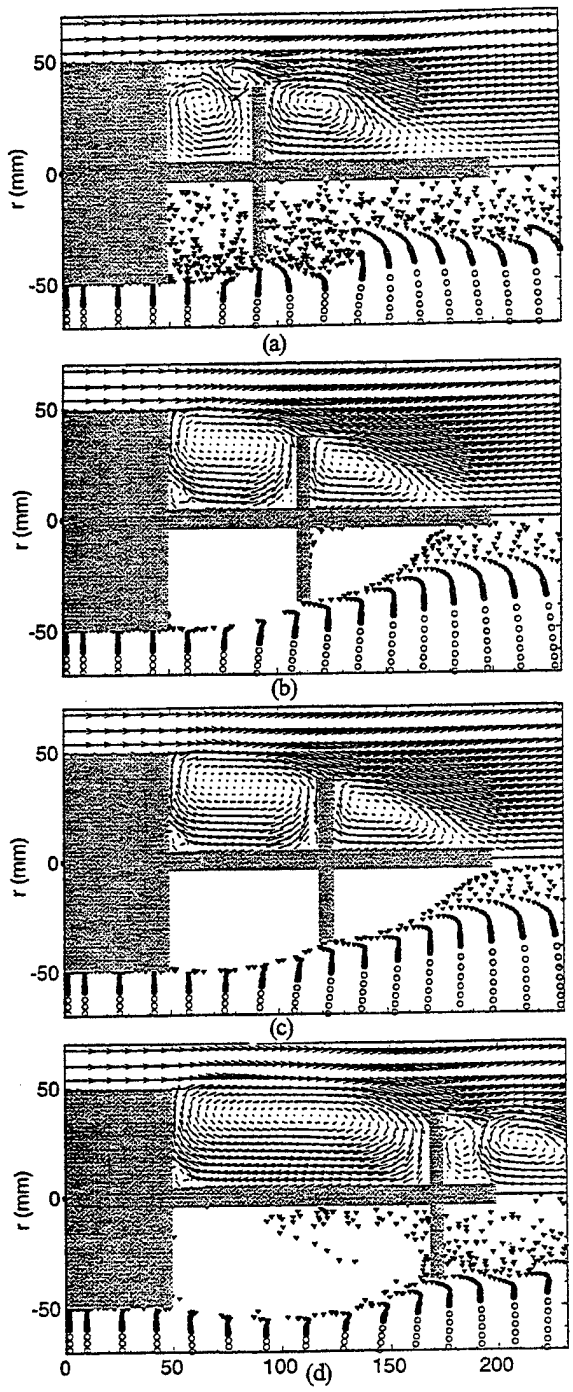

Fig. 4 Instantaneous flowfields obtained using direct numerical simulations for forebody-spindle-disk combination for various disk locations. X_c/D_0 = (*a*) 0.4, (*b*) 0.6, (*c*) 0.7, and (*d*) 1.2. Velocity vectors and particle distributions are shown in upper and lower halves, respectively.

since the vortex is closer to the disk; at other instants these particles pass over the disk when the vortex is pushed toward the forebody. The distribution of particles in this figure also indicates that particles lump together while moving around the center of the cavity; when that lump approaches the edge of the afterbody, a fraction of particles leaves the cavity. This implies that particles are entrained into the cavity vortex during a certain phase and then exit the cavity during a different phase, leading to periodic accumulation of particles in the cavity.

Calculations for the forebody-spindle-afterbody geometries are also made using the $k-\epsilon$ turbulence model. For these calculations grid, time-step, and flow conditions utilized are the same as those used for the direct simulations. Interestingly, for every cavity size, the simulation with the turbulence model quickly converged to steady-state flowfield. Results obtained for cavity sizes $X_c/D_0 = 0.4$, 0.6, 0.7, and 1.2 are shown in Figs. 5(*a*), 5(*b*), 5(*c*), and 5(*d*), respectively. Since each of these solutions represents a steady-state flowfield, streamlines are plotted rather than particle traces.

In general, the turbulent-flow calculations yielded a single vortex in the cavity region and another behind the disk. In the case of $X_c/D_0 = 0.4$, the direction of rotation of the cavity vortex is normal (clockwise). On the other hand, as shown in Fig. 4(*a*), the direct simulations resulted in a multiple-vortex structure with the largest one rotating in the counterclockwise direction, which compares well with the experimental data obtained by Little and Whipkey (1979). The flow structure downstream of the disk captured by $k-\epsilon$ turbulence calculations is also quite different from that captured by direct simulations. The vortex in the former is squeezed toward the spindle, whereas that in the latter is pushed away from the spindle. For the near optimum-size-cavity cases where the flow is at steady state, turbulent and direct calculations yielded similar solutions. The turbulent calculations predicted flow reattachment on the spindle at $x = 175$ and 192 mm for the $X_c/D_0 = 0.6$ and 0.7 cases, respectively, while the direct simulations predicted reattachment at $x = 175$ and 186 mm, respectively. However, some minor differences exist in the solutions obtained by the turbulent and direct calculations for these cases. The turbulence model seems to dissipate the corner vortices that are observed in the direct simulations.

The cavity flow structures predicted by the turbulent and direct simulations for the $X_c/D_0 = 1.2$ case [Figs. 5(*d*) and 4(*d*), respectively] are similar in nature, even though the latter is dynamically oscillating within the cavity. Interestingly, the streamline drawn from the edge of the forebody in Fig. 5(*d*) shows that flow dips slightly into the cavity near the disk and then flows back around the tip of the disk. This dividing streamline also suggests that no flow is entering the recirculation region. The dynamic flow structure downstream of the disk predicted by the direct simulations is quite different from the single-vortex structure obtained with the $k-\epsilon$ turbulence model.

In general, results obtained for the larger-spindle case are similar to those shown in Figs. 4 and 5. Calculations were also made for different disk sizes, and similar dynamic flow structures were found. These calculations suggest that the minimum-drag-coefficient condition seems to be coupled to the steadiness of the vortex trapped in the cavity formed between the forebody and disk. Multiple vortices form in the smaller cavities and periodically shed, which, in turn, makes the vortex behind the disk shed also. The single dominating vortex established in larger cavities rotates within the cavity, which, in turn, develops multiple vortex structures behind the disk.

The drag coefficient computed as a function of time for different disk locations for smaller and larger spindles is shown in Figs. 6(*a*) and 6(*b*), respectively. The time-averaged data shown in Fig. 2 correspond to the instantaneous data given in Fig. 6(*a*). Data for the optimum cavity sizes are shown with solid circles. Overall, the frequency for fluctuations in ΔC_D is found to be inversely related to the cavity size. For cavities

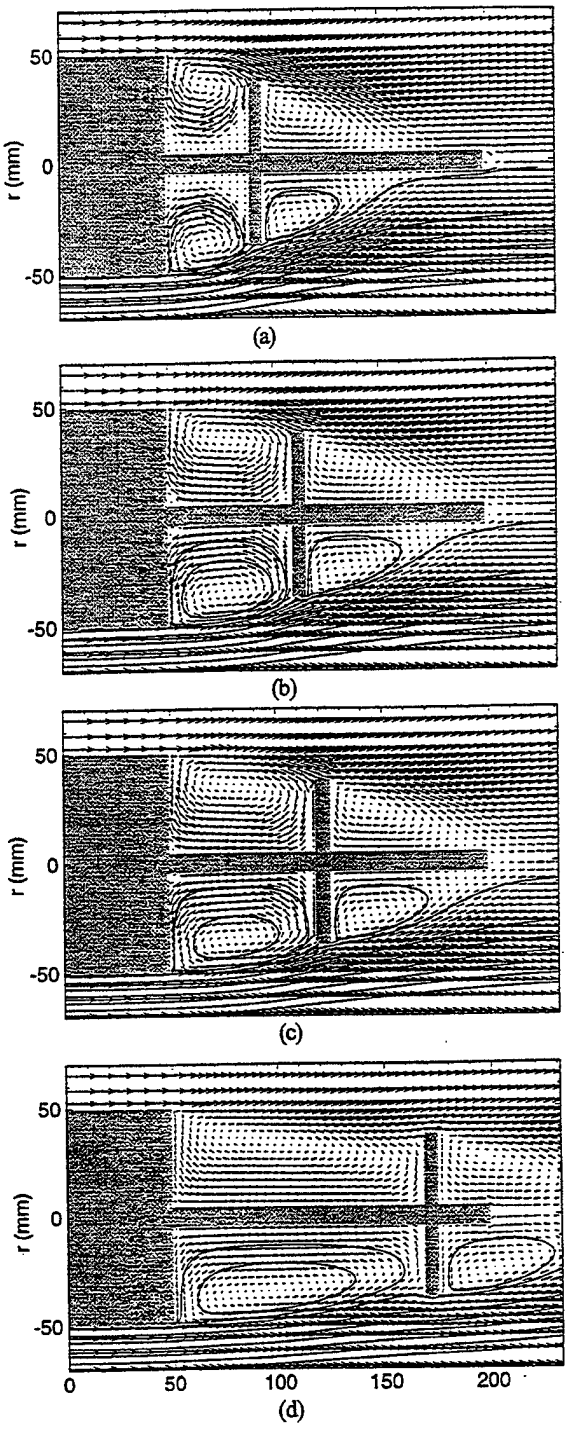

Fig. 5 Steady-state flowfields obtained using $k-\epsilon$ turbulence model for the forebody-spindle-disk combination. X_c/D_0 = (*a*) 0.4, (*b*) 0.6, (*c*) 0.7, and (*d*) 1.2.

smaller than the optimum size, calculations have always yielded fluctuating drag coefficients. On the other hand, for larger-than-optimum cavities, fluctuations in the drag coefficient are observed only for significantly larger cavities. Interestingly, the near-steady drag coefficient for $X_c/D_0 = 0.7$ in the case of the smaller spindle [Fig. 6(*a*)] and for $X_c/D_0 = 0.8$ in the case of the larger spindle [Fig. 6(*b*)] is significantly higher than the respective values obtained with the optimum cavity sizes. This

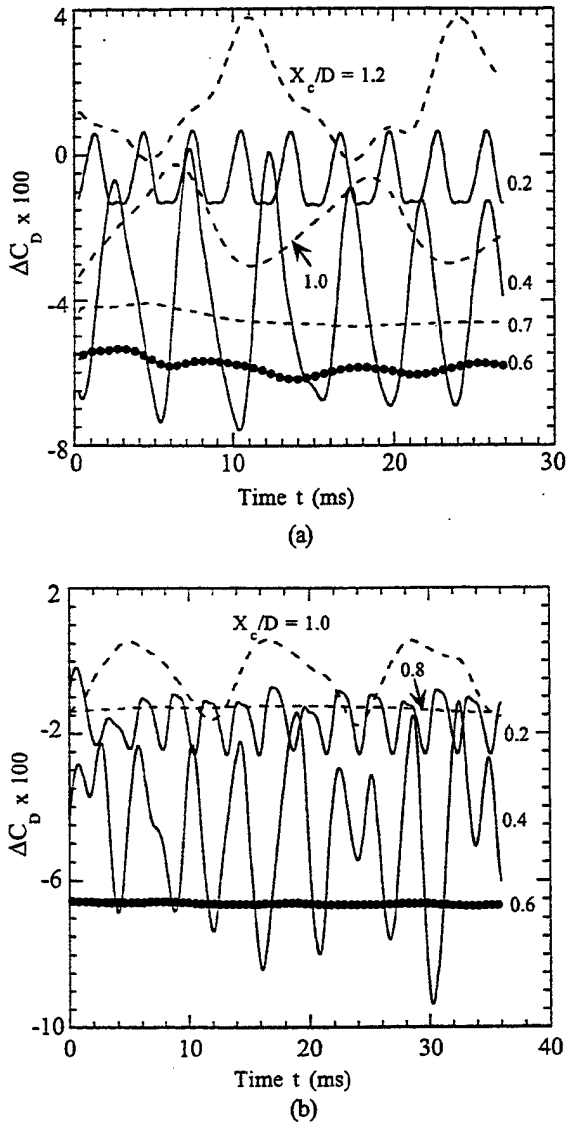

Fig. 6 Change in drag coefficient with time resulting from the addition of the disk to the forebody-spindle geometry obtained for different cavity lengths: (*a*) small-spindle case; (*b*) large-spindle case

indicates that even though under minimum-drag conditions the vortices in the cavity and behind the disk are locked spatially, the converse—locked vortices yielding minimum drag—is not always true.

Residence Time and Entrainment in the Cavity. With the proper choice of cavity dimensions such as length and height, the vortex/vortices in the cavity can be made stationary. On the other hand, a stationary vortex yields minimum mass exchange between the vortex and the main flow (flow in the annular gap). In a combustor, this implies that the transport of the oxidizer from the main flow into the cavity will be minimum when the vortices in the cavity are locked. Since locked vortices help to stabilize the flames in the combustor, for accommodating the decrease in the oxidizer entrainment into the cavity, additional air must be fed into the cavity directly to obtain better performance from the trapped-vortex combustor. Therefore, it is important to understand the residence time and entrainment characteristics of cavity flows for different cavity sizes.

A quantitative estimation of entrainment is difficult in a dynamic-flow system since entrainment resulting from vortex motion and fluid transported from the molecular and/or turbulent diffusion are tightly coupled. The concentration of tracer fluid, which represents the net transport from entrainment and diffusion, cannot yield the entrainment characteristics of a dynamic flow. Therefore, in the present study, estimations for the residence time and entrainment resulting from the dynamic motion of vortices in the cavity are made by following a unique approach based on particle distribution. Two sets of massless particles were injected into the combustor—one set in the cavity region close to the forebody (Location A) and the other into the air flow at the entrance (Location B). Both sets of particles were injected into the flowfield with a time interval of 0.27 ms. The fraction of the mass that originated in the cavity and remained in the cavity after t ms is obtained by summing the particles that were released from Location A at a time t ms prior and are still laying within the cavity. The decay of injected fluid in the cavity at different times for different cavity sizes is shown in Fig. 7(a). Since the residence time for the fluid that is injected into the cavity is inversely proportional to the decay time, Fig. 7(a) also represents the residence-time characteristics

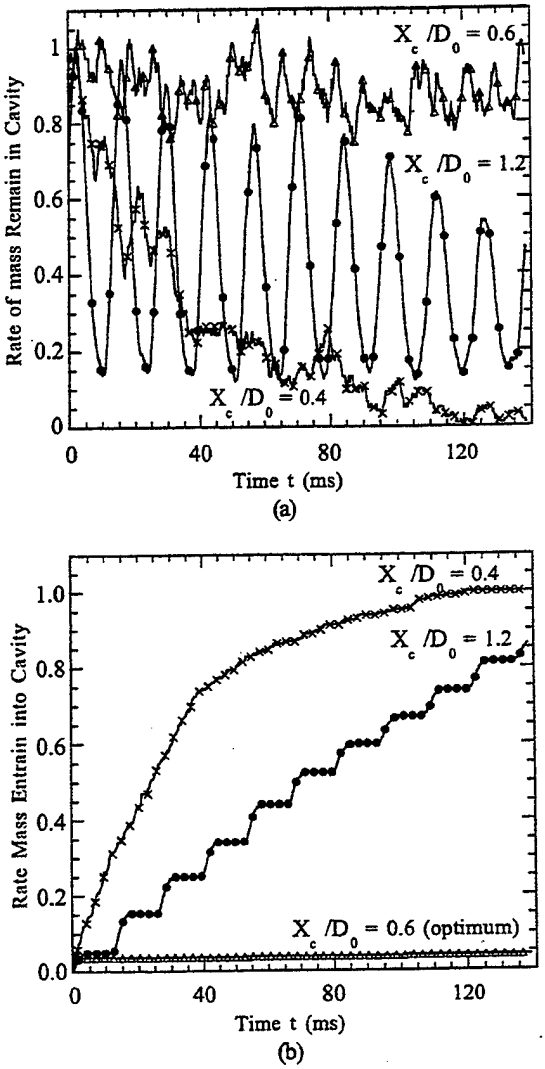

Fig. 7 Residence-time and entrainment characteristics obtained from particle distributions for different cavity lengths: (*a*) ratio of rate of decrease in cavity mass and rate of injection of mass into cavity; (*b*) ratio of rate of increase in cavity mass and rate of injection of mass outside cavity

for different cavity sizes. The observations made from Fig. 7(*a*) are as follows: (1) When the vortices in the cavity become stable (0.6 case), the injected fluid remains in the cavity. The small fluctuations obviously indicate that the vortices in the cavity are not perfectly locked. (2) For the case of X_c/D_0 = 0.4, the injected fluid leaves the cavity with time. Interestingly, the fluid decay in this case is not a linear function of time. Figure 7(*a*) indicates that the initial 80 percent of the fluid left the cavity in about 40 ms, whereas the remaining 20 percent fluid required ~80 ms to leave the cavity. This variation in residence time results from the differences in the dynamic characteristic of the vortices in the cavity. The vortices in the upper half seem to shed from the cavity, whereas the ones in the lower half move within the cavity itself. Therefore, the particles (or mass) injected into the vortices in the upper half have less residence time, and the particles injected into the lower-half vortices remain in the cavity for longer periods of time. Because of the difference in the residence times of the mass injected from different locations within the cavity, evenly distributed combustion within the cavity can be achieved by injecting fuel and air into the cavity at multiple locations with varying flow rates.

Flow within the cavity becomes dynamic also for the cases where the length of cavity is greater than that of the optimum one. As a result, the mass of the fluid remaining in the cavity decreases with time [Fig. 7(*a*)]. However, unlike in the case of the shorter-than-optimum cavity, fluid fluctuates at a near-constant frequency (72 Hz). These fluctuations result either from entrainment of particles into the cavity that had left earlier or from accumulation of particles resulting from a phase lag between the injection and ejection times. A close look at the cavity-flow structure in Fig. 5(*d*) suggests that vortices are *not* shedding from the cavity; hence, entrainment of cavity particles back into the cavity may be ruled out. The particle distribution in this figure also indicates that particles lump together while moving around the center of the cavity and when that lump comes closer to the edge of the afterbody, a fraction of particles leaves the cavity. This implies that the particles injected into the cavity vortex at a certain phase leave the cavity quickly [corresponds to the maxima in the X_c/D_0 = 1.2 curve in Fig. 7(*a*)]; on the other hand, those injected at other phases tend to remain in the cavity for longer periods of time (corresponds to the minima). This scenario can be confirmed by considering the relationship between the time period for one cycle (~14 ms) and the distance traveled by the particle lump (~340 mm, obtained from the cavity dimensions), which yields a velocity of 24 m/s—close to the jet velocity or the recirculating flow velocity in the cavity. These insights into the vortex dynamics and particle accumulation in the cavity aid in determining the injection pattern for providing longer or shorter residence times for the fuel–air mixture to obtain better combustion and pollutant management.

For bringing the main air/fuel into the cavity, it is important to know the entrainment characteristics of the vortices for different cavity sizes. Such characteristics for three cavity sizes were obtained by calculating the number of particles injected in the main flow and entrained into the cavity. Entrainment rates from the particle count are shown in Fig. 7(*b*). As expected, when the vortex is trapped in the optimally designed cavity, very little main flow is entrained into the cavity. This emphasizes the important aspect of the trapped-vortex combustor—that under optimum design conditions, the fuel and air necessary for efficient combustion in the cavity should be directly injected into the cavity without relying on entrainment from the main flow. On the other hand, when the cavity is smaller than the optimum one, as in the case of X_c/D_0 = 0.4, the entrainment rate initially increased linearly up to t = 40 ms and later slowly reached a saturated value. The balance between entrainment into and shedding from the cavity resulted in a saturated level for the main-flow particles in the cavity. In the case of the larger-than-optimum cavity [X_c/D_0 = 1.2 case in Fig. 7(*b*)], particles that were injected into the main flow entered the cavity in a stepwise fashion. As discussed earlier, a maximum number of particles enters the cavity during a certain period of the vortex evolution. The gradual decrease in the step height with time indicates that the entrainment rate is approaching a saturated value.

Combusting Flow. Considering the advantages of locked vortices for stable combustion, Hsu et al. (1995) have developed a laboratory combustor that can operate over a wide range of flow-rate conditions. The geometry of the center-body combustor designed by Hsu et al. (1995) is similar to that studied by Little and Whipkey (1979) for nonreacting flows. For investigating the vortex characteristics in the cavity under combusting-flow environment, calculations were made for the simulation of reacting flow for the combustor of Hsu et al. (1995). This combustor consists of a forebody and an afterbody of diameters 70 and 50.8 mm, respectively. The combustor is enclosed in a 80-mm-dia Pyrex annular tube. Main air is delivered through the annular gap between the Pyrex tube and the forebody at a velocity of 42 m/s. Primary air and fuel (propane) are injected into the cavity from the afterbody. Fuel and air are carried to the afterbody through a central tube that connects the afterbody to the forebody. Figure 8(*a*), obtained using a normal photographic camera with long exposure time, shows the flame and the combustor geometry for operation under a primary equivalence ratio (defined as fuel-to-air ratio injected into the cavity relative to the ratio required for stoichiometric combustion) of 4.4.

Calculations were made for this fuel-rich condition using a 251 × 101 grid system. Fuel and air in the experiment were injected into the cavity through three coannular rows of holes drilled on the face of the afterbody. The fuel holes were sandwiched between the air holes. The symmetric distribution of holes is assumed to provide only weak three-dimensional effects. For performing axisymmetric calculations on this near-symmetric combusting flow, the fuel and air holes were replaced with annular slots of 1-mm width in the model. The flat velocities of 12.4 and 5 m/s at the exits of air and fuel slots gave the measured flow rates of 56 and 25 slpm, respectively.

The instantaneous flow computed with a fast-chemistry assumption is shown in Fig. 8(*b*) by plotting iso-temperature contours and velocity vectors in the upper and lower halves, respectively. Computed flow in the cavity has a large vortex generated by the high-speed annulus air flow and several small vortices that are primarily developed from the interaction of fuel and air jets injected into the cavity. Figure 8(*b*) also indicates that the flow of combustion products from the cavity over the disk is associated with only weak shedding. This was confirmed by making an animation of the time-dependent solution. The weak vortex shedding from the cavity suggests that the global vortex structure in the cavity represents a locked vortex. Note that the design strategy used by Hsu et al. (1995) for determining the cavity size was based on the conditions for obtaining locked vortices in cold flows without primary injection. For this cavity size, cold-flow calculations also showed locked vortices within the cavity and behind the afterbody. Absence of strong vortex shedding from the cavity, noted from the reacting flow calculations made with primary injection (Fig. 8), suggests that the locked-vortex criterion obtained using cold annular flow yields locked vortices (overall) in the reacting flow case also. Additional calculations must be performed with different cavity sizes before a general conclusion can be reached regarding locked vortices in cold and reacting flows.

The overall flow structure and the temperature field are obtained from direct numerical simulations by time averaging the 8000 instantaneous solutions over a period of 40 ms. The results are shown in Fig. 8(*c*). The dominating cavity vortex and the near steady-state wake vortex noted in the instantaneous solutions [e.g., Fig. 8(*b*)] have appeared in the time-averaged data

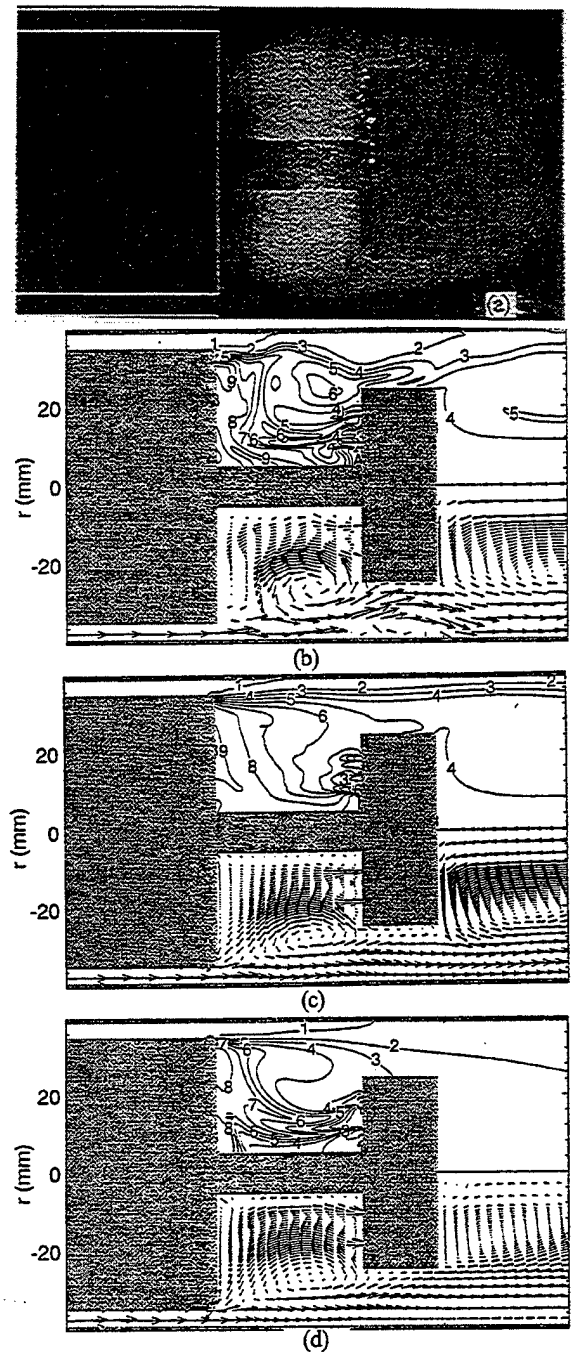

Fig. 8 Reacting flow inside trapped-vortex combustor for primary equivalence ratio of 4.4: (*a*) direct photograph of flame, (*b*) instantaneous flowfield obtained with direct numerical simulation, (*c*) flame obtained by averaging several instantaneous solutions, and (*d*) steady-state flame simulated using $k-\epsilon$ turbulence model. Iso-temperature contours are plotted with 150-K interval from 300 K.

as stable recirculation regions. A small recirculation region in the corner of the spindle and disk may also be noted in Fig. 8(*c*). Time averaging has also eliminated the temperatures that are greater than 1600 K [absence of Contour No. A in Fig. 8(*c*)].

The computed peak temperature (time-averaged) of 1600 K is lower than that measured (~1900 K) in the experiment. In fact, even the instantaneous temperature never exceeded 1750 K in the direct numerical simulations. Since a fast-chemistry model was used in the present simulations, the lower computed temperature could be resulting from the mixing-limited environment in the cavity. It is known that even though large-scale flow structures play a major role in the mixing of fuel and air, small scales are important for mixing on a local level. The present simulations predict only the large-scale vortical structures in the cavity. The lower predicted temperature could then be due to the absence of small-scale vortices in the calculations. For verifying this, calculations were made by including the $k-\epsilon$ model for turbulence. Computations resulted in a steady flow and the predicted temperature field is shown in Fig. 8(*d*). Note that the same 251 × 101 grid system utilized in direct numerical simulations was employed for these calculations also. Surprisingly, the peak temperature obtained in Fig. 8(*d*) was only 1500 K—lower than that obtained without the turbulence model. This suggests that the combustion in the cavity is not limited by the small-scale mixing.

In experiments, primary fuel and air are passed through the central tube and afterbody before being injected into the cavity. Since both the center tube and afterbody are surrounded by the hot combustion products, their wall temperatures are expected to be higher than the temperature of the incoming fuel and air, which, in turn, heats the fuel and air. On the other hand, even though the walls of the afterbody and center tube were treated as adiabatic walls in the present simulations, fuel and air were injected in the cavity at room temperature since flow inside the tubes was not considered. It is believed that the hotter fuel and air injected into the cavity leads to the higher temperatures in the experiment.

A comparison between the time-averaged flow field [Fig. 8(*c*)] and the steady-state solution resulted from $k-\epsilon$ model [Fig. 8(*d*)] reveals significant similarities. Mainly, the recirculation zone observed in the time-averaged data matches well with that obtained with $k-\epsilon$ model. On the other hand, the wake vortex behind the disk and the corner vortex of the spindle and disk predicted with $k-\epsilon$ turbulence model are weaker than those obtained from the time-averaged direct-numerical-simulations data. The temperature distributions in Figs. 8(*c*) and 8(*d*) are also quite different. Simulations with the $k-\epsilon$ model yielded jet-flame structures in the cavity following the fuel and air injections, whereas, more uniform temperature distributions are obtained with direct numerical simulations.

Summary

Vortex shedding behind a bluff forebody leads to a higher drag coefficient. It is known that by trapping these wake vortices using disks, the drag coefficient of the forebody-spindle-disk combination can be decreased. The dynamics of the vortices formed inside the cavity and behind the forebody were studied using a time-dependent, axisymmetric Computational Fluid Dynamics with Chemistry (CFDC) code. A large number of grid points with ΔX and $\Delta r \sim 0.9$ mm was used to capture the large-scale structures whose physical size is up to an order of magnitude smaller than the cavity height. The important conclusions reached from the calculations made with different cavity sizes, spindle diameters, and disks are that (1) changes in drag coefficient can be predicted from the simulation of large-scale structures alone, (2) for the optimum cavity length at which the drag coefficient becomes minimum, the vortices in the cavity and behind the disk are locked spatially; however, the converse—locked vortices correspond to a minimum-drag condition—is not always true, (3) more than one dominant vortex is developed in smaller-than-optimum cavities and vortex shedding always occurs from these cavities, (4) a single dominating vortex formed within a larger-than-optimum cavity moves within the cavity and shedding is not associated, and (5) because of the cavity-vortex shedding, entrainment into the cavity is greater and residence time is lower in the smaller-

than-optimum cases compared to those in the larger-than-optimum ones. These findings are useful in determining the locations for injecting primary air and fuel into the cavities for trapped-vortex-combustor applications.

Calculations were also performed for the reacting flow in the trapped-vortex combustor designed by Hsu et al. (1995) using the fast-chemistry model. Preliminary results suggest that the optimum cavity length determined from the nonreacting annular flow seems to yield nonshedding cavity flows, even with combustion and primary injection into the cavities. Additional calculations must be performed to verify this conclusion for different-geometry combustors.

Acknowledgments

This work was supported, in part, by Air Force Contract No. F33615-95-C-2507 and the Air Force Office of Scientific Research. The authors would like to thank Dr. Mark Hsu for stimulating discussions and allowing us to use Fig. 8(*a*) and Mrs. Marian Whitaker for the editorial help.

References

Grinstein, F. F., and Kailasanath K., 1995, "Three-Dimensional Numerical Simulations of Unsteady Reactive Square Jets," *Proc. 25th International Symposium on Combustion*, Combustion Institute, Pittsburgh, PA.

Hsu, K. Y., Goss, L. P., Trump, D. D., and Roquemore, W. M., 1995, "Performance of a Trapped-Vortex Combustor," AIAA Paper No. 95-0810.

Katta, V. R., Goss, L. P., and Roquemore, W. M., 1994a, "Numerical Investigations of Transitional H2/N2 Jet Diffusion Flames," *AIAA Journal*, Vol. 32, pp. 84–94.

Katta, V. R., Goss, L. P., and Roquemore, W. M., 1994b, "Simulation of Vortical Structures in a Jet Diffusion Flame," *Int. J. Num. Meth. Heat Fluid Flow*, Vol. 4, p. 413.

Katta, V. R., and Roquemore, W. M., 1996, "Numerical Studies on Trapped-Vortex Combustor," AIAA Paper No. 96-2660.

Leonard, B. P., 1979, "A Stable and Accurate Convective Modeling Procedure Based on Quadratic Upstream Interpolation," *Computer Methods in Applied Mech. and Engineer.*, Vol. 19, p. 59.

Little, B. H., and Whipkey, R. R., 1979, "Locked Vortex Afterbodies," *Journal of Aircraft*, Vol. 16, No. 5.

Mair, W. A., 1965, "The Effect of a Rear-Mounted Disc on the Drag of a Blunt-Based Body of Revolution," *The Aeronautical Quarterly*, Nov., pp. 350–360.

Migay, V. K., 1963, "Study of Ribbed Diffusers" [in Russian], *Toploenergetika*, No. 10, 1962, English translation issued as A.R.C. Paper 25,382.

Rohsenow, W. M., Fink, C. H., and Pollis, S. R., 1951, "Flow Through Two Orifices in Series," ASME Paper No. 51-A-87.

Roshko, A., and Koenig, K., 1976, "Interaction Effects on the Drag of Bluff Bodies in Tandem," presented at the symposium on Aerodynamic Drag Mechanisms of Bluff Bodies and Road Vehicles, General Motors Research Laboratories, Sept. 27–28.

Spalding, D. B., 1972, "A Novel Finite Difference Formulation for Difference Expressions Involving Both First and Second Derivatives," *International Journal for Numerical Methods in Engineering*, Vol. 4, pp. 551–559.

Veynante, D., Vervisch, L., Poinsot, T., Linan, A., and Ruetsch, G., 1994, "Triple Flame Structure and Diffusion Flame Stabilization," *Proc. Summer Program 1994*, Center for Turbulent Research, NASA Ames/Stanford University, CA, pp. 55–73.

JOURNAL OF PROPULSION AND POWER
Vol. 14, No. 3, May–June 1998

PUBLISHED WITH PERMISSION

Study on Trapped-Vortex Combustor—Effect of Injection on Flow Dynamics

Viswanath R. Katta*
Innovative Scientific Solutions, Inc., Dayton, Ohio 45440-3638
and
W. M. Roquemore†
U.S. Air Force Research Laboratory, Wright–Patterson Air Force Base, Ohio 45433-7103

Low-velocity flows in the cavities of a combustor can aid in establishing stable flames. However, unsteady flows in and around cavities may destabilize these flames. By proper cavity design it is possible to lock (trap) the vortices spatially and, thereby, stabilize the flames. The spatially locked vortices restrict the entrainment of main air into the cavity. For obtaining good performance characteristics with a trapped-vortex combustor, a sufficient amount of fuel and air must be injected directly into the cavity. This mass injection can alter the dynamic characteristics of the flow inside and around the cavity. The present study employed a numerical simulation to investigate the vortex dynamics of a cavity into which fluid mass is directly injected through jets. A third-order-accurate, time-dependent, computational fluid dynamics with chemistry code was used for simulating the dynamic flows associated with an axisymmetric, centerbody trapped-vortex combustor under nonreacting and reacting conditions. It was found that mass injection increases the optimum size (width-to-diameter ratio) of the cavity. Injection of small amounts of fluid into a nonoptimum cavity increases the unsteadiness of the flow. Fluid injected into the optimum-size cavity is transported along the outer core of the vortex, providing more efficient mixing and a longer residence time for the fuel/air mixture. It was also found that use of thinner afterbodies results in the cavity flow being more dynamic. Calculations made with a global-chemistry model revealed that at higher annulus air velocities, combustion is limited to the cavity region. As in the case of cold flows, the injection jets in reacting flows are pushed outward from the center when the cavity size is small.

Nomenclature

A = coefficient used in finite difference equation
C_p = pressure coefficient
c_p = specific heat of the mixture
D = diffusion coefficient
D_0 = forebody diameter
dA = incremental area
H = enthalpy
h = total enthalpy
h_f^0 = heat of formation at standard state
Le = Lewis number
M = molecular weight
N_s = total number of species
p = pressure
R_0 = universal gas constant
r = radial distance
S_n = number of wall surfaces
S^Φ = source term in Φ equation
T = temperature
t = time
u = axial velocity component
V = velocity
v = radial velocity component
X_c = cavity length
Y = mass fraction
z = axial distance
Γ^Φ = transport coefficient in Φ equation
ΔH = disk thickness
λ = thermal conductivity
μ = viscosity
ρ = density
Φ = represents a flow variable
$\dot{\omega}$ = net rate of production of a species

Subscripts
i = ith species
j = jth reaction
P = reference grid point
w = wall
z^+, r^+ = grid points adjacent to P in z and r directions, respectively
z^{++}, r^{++} = two grid points away from P in z and r directions, respectively
z^-, r^- = grid points adjacent to P in negative z and r directions, respectively
z^{--}, r^{--} = two grid points away from P in negative z and r directions, respectively
∞ = freestream

Superscript
N = time-step number

Presented as Paper 97-3256 at the AIAA/ASME/SAE/ASEE 33rd Joint Propulsion Conference and Exhibit, Seattle, WA, July 6–9, 1997; received Aug. 25, 1997; revision received Jan. 30, 1998; accepted for publication Jan. 30, 1998. This paper is declared a work of the U.S. Government and is not subject to copyright protection in the United States.

*Senior Engineer, 2786 Indian Ripple Road.
†Senior Scientist, Propulsion Directorate.

Introduction

UNSTEADY flow in and around cavity-type geometries occurs in a variety of applications such as slotted wind tunnels, slotted flumes, bellow-type configurations, and aircraft engine and airframe components. In particular, the unsteady flow in aircraft combustors limits fuel-lean operation and degrades flame-stability characteristics. Recently, a simple, compact, and efficient method of using cavities to stabilize combustion was proposed by Hsu et al.[1] Because this concept uses

a vortex that is trapped in a cavity to stabilize the flame, it is referred as the trapped-vortex (TV) concept. Several investigators have recognized the aerodynamic advantages of locking the vortices inside and around the cavity in a nonreacting flow.[2–4] Experiments of Rohsenow et al.[2] have shown that when two circular orifices are placed in series in a pipe, a large recovery of pressure occurs across the second orifice in certain circumstances; hence, the overall pressure drop is considerably less for the two orifices than for a single one having the same flow. In ribbed diffusers, Migay[3] found that balancing the fluid removed by entrainment and the fluid entering the cavity by reversed flow ensures that the flow outside the cavities will follow the ribs fairly closely, and a good pressure recovery will be achieved. Mair[4] showed that by mounting a disk behind the base of a blunt body, the drag of the blunt object can be reduced. Using similar concepts, Roshko and Koenig[5] reported a reduction in drag of blunt forebodies when disks were placed on spindles ahead of the bodies.

Little and Whipkey[6] conducted extensive investigations on the dynamic nature of flows over bluff bodies using smoke-flow visualization and laser–velocimetry (LV) techniques. Because of the limitations of the smoke tunnel, they employed reduced-flow conditions (~0.3 m/s) and half-scale geometries for the flow-visualization studies and full-scale geometries and turbulent flows (~30 m/s) for the time-averaged drag measurements. Based on these reduced and full-scale experiments, they correlated the afterbody drag and the motion of the vortex in the wake region and postulated that a minimum-drag condition is established when the wake vortices are locked between two disks mounted in series on a spindle. They also suggested that the cavity formed between the disk and the bluff body should be of such dimensions that the locked vortex would effectively fill the cavity. Based on reduced-scale, flow-visualization experiments on cavities formed between a forebody and an afterbody, Little and Whipkey correlated the drag and motion of the vortex in the cavity region and postulated that a minimum-drag condition is established when the cavity vortices are locked between the two bodies. Katta and Roquemore[7,8] used direct numerical simulations to investigate the Little and Whipkey experiments under turbulent-flow conditions. The simulations successfully predicted that a cavity having a length-to-diameter ratio of 0.45 becomes stationary and that the pressure-drag coefficient is reduced to a minimum value when the vortices are locked inside and around the cavity. This suggests that the relationship between the minimum drag coefficient and the vortex motion is also valid in the case of turbulent flows. These simulations demonstrated the capability of numerical simulations in the study of the dynamic processes associated with cavities.

Two major differences exist between flows associated with airframe cavities and those associated with the combustor cavities. First, the heat release and higher viscosity of the combustion products associated with the partial burning that takes place in the cavities could alter the vortex dynamics. As a result, the criterion for trapping a vortex in a heated flow would differ from that for trapping a vortex in a cold flow. Secondly, it is known that a locked vortex entrains a minimum amount of fluid from the main flow; hence, to achieve continuous combustion in trapped-vortex combustors, fuel and air must be directly fed into the cavity. Experimental investigations of Hsu et al.[1] also indicate that a TV combustor operates most efficiently when fuel and air are injected directly into the cavity. However, direct injection of mass (air and/or fuel) into the cavity could alter the geometrical criterion derived for locking vortices inside passive cavities, i.e., without injection.

The purpose of this study was to investigate the dynamics of cavity flows as jets are directly injected into the cavity. A third-order-accurate, time-dependent, computational fluid dynamics with chemistry (CFDC) code and a large number of grid points were used to investigate the flowfields in a research TV combustor[1] under nonreacting and reacting flow conditions.

Modeling

A time-dependent, axisymmetric mathematical model that solves for axial- and radial-momentum, continuity, and enthalpy- and species-conservation equations is used to simulate the flowfields in the TV combustor. The governing equations, written in a cylindrical-coordinate system, are as follows:

$$\frac{\partial \rho}{\partial t} + \frac{\partial \rho u}{\partial z} + \frac{1}{r}\frac{\partial (r\rho v)}{\partial r} = 0 \tag{1}$$

$$\frac{\partial (\rho\Phi)}{\partial t} + \frac{\partial (\rho u\Phi)}{\partial z} + \frac{1}{r}\frac{\partial (r\rho v\Phi)}{\partial r} = \frac{\partial}{\partial z}\left[\Gamma^{\Phi}\frac{\partial \Phi}{\partial z}\right] + \frac{\partial}{\partial r}\left[r\Gamma^{\Phi}\frac{\partial \Phi}{\partial r}\right] + S^{\Phi} \tag{2}$$

Here u and v are the axial and radial components of the velocity vector, respectively. The general form of Eq. (2) represents the momentum, the species, or the energy-conservation equation, depending on the variable used in place of Φ. In Table 1 the transport coefficients Γ^{Φ} and the source terms S^{Φ} that appear in the governing equations are given.

The partial set of equations represented by Eqs. (1) and (2) can be completed using the global-species-conservation equation

$$Y_{N_s} = 1.0 - \sum_{i}^{N_s-1} Y_i \tag{3}$$

and the state equation

$$p = \rho T R_0 \sum_{i}^{N_s} \left(\frac{Y_i}{M_i}\right) \tag{4}$$

where Y_i and M_i are the mass fraction and molecular weight of the ith species, respectively. While density is obtained by solving the state equation [Eq. (4)], the pressure field at every

Table 1 Transport coefficients and source terms in governing equations

Φ	Γ^{Φ}	S^{Φ}
u	μ	$\frac{\partial p}{\partial z} + \frac{\partial}{\partial z}\left(\mu\frac{\partial u}{\partial z}\right) + \frac{\partial}{\partial r}\left(\mu\frac{\partial v}{\partial z}\right) + \frac{\mu}{r}\frac{\partial v}{\partial z} - \frac{2}{3}\left\{\frac{\partial}{\partial z}\left(\mu\frac{\partial u}{\partial z}\right) + \frac{\partial}{\partial z}\left(\mu\frac{\partial v}{\partial r}\right)\right\} + \frac{\partial}{\partial z}\left(\mu\frac{v}{r}\right)$
v	μ	$\frac{\partial p}{\partial r} + \frac{\partial}{\partial z}\left(\mu\frac{\partial u}{\partial r}\right) + \frac{\partial}{\partial r}\left(\mu\frac{\partial v}{\partial r}\right) + \frac{\mu}{r}\frac{\partial v}{\partial r} - 2\mu\frac{v}{r^2} - \frac{2}{3}\left\{\frac{\partial}{\partial r}\left(\mu\frac{\partial u}{\partial z}\right) + \frac{\partial}{\partial r}\left(\mu\frac{\partial v}{\partial r}\right)\right\} + \frac{\partial}{\partial r}\left(\mu\frac{v}{r}\right)$
H	λ/c_p	$\nabla\left[\frac{\lambda}{c_p}\sum_{1}^{N_s}\{(Le^{-1}-1)H_i\nabla Y_i\}\right] - \sum_{1}^{N_s}(h_{f_i}^{0}\dot{\omega}_i)$
$Y\ (i = 1 \sim N_s - 1)$	ρD_{i-N_s}	$\dot{\omega}_i$

time step is determined from pressure Poisson equations. Even though governing equations are solved in an uncoupled manner, species-conservation equations are coupled through the source terms during the solution process to improve the stability of the algorithm. Temperature- and species-dependent thermodynamic and transport properties are used in this formulation. The enthalpy of each species is calculated from polynomial curve fits; the viscosity, thermal conductivity, and diffusion coefficients of the species are estimated from the Lennard–Jones potentials.

In the present work reacting flows were simulated using the following global-chemical-kinetics model involving propane, oxygen, water, carbon dioxide, and nitrogen:

$$C_3H_8 + 5O_2 + 17.73N_2 \Rightarrow 3CO_2 + 4H_2O + 17.73N_2 \quad (5)$$

The specific reaction rate for Eq. (5) is written in Arrhenius form with a very large pre-exponential factor.

The governing equations are integrated using an implicit QUICKEST (quadratic upstream interpolation for convective kinematics with estimated streaming terms) numerical scheme,[9,10] which is third-order accurate in both space and time and has a very low numerical-diffusion error. An orthogonal, staggered-grid system with rapidly expanding cell sizes in both the z and r directions is utilized for discretizing the governing equations. After rearrangement of terms, the finite difference form of the governing equation for the variable Φ at a grid point P can be written as an algebraic equation as follows:

$$A_P\Phi_P^{N+1} + A_{z^{++}}\Phi_{z^{++}}^{N+1} + A_{z^+}\Phi_{z^+}^{N+1} + A_{z^-}\Phi_{z^-}^{N+1} + A_{z^{--}}\Phi_{z^{--}}^{N+1} + A_{r^{++}}\Phi_{r^{++}}^{N+1} + A_{r^+}\Phi_{r^+}^{N+1} + A_{r^-}\Phi_{r^-}^{N+1} + A_{r^{--}}\Phi_{r^{--}}^{N+1} = S_P^{\Phi} + \Delta t \cdot \rho_P\Phi_P^N \quad (6)$$

The time increment t is determined from the stability constraint and maintained as a constant during the entire calculation. The superscripts N and $N + 1$ represent the known variables at the Nth time step and the unknown variables at the $(N + 1)$th time step, respectively; the subscripts z^+ and z^- indicate the values at the grid points immediately adjacent to point P in the positive and negative z directions, respectively. Similarly, the subscripts z^{++} and z^{--} represent the values at two grid points from P in the respective directions. The coefficients A and the terms on the right-hand side of the previous equation are calculated from the known flow variables at the Nth time step. The preceding equations for $N_s + 2$ variables are solved individually using an iterative alternative direction implicit technique. The pressure field at every time step is accurately calculated by simultaneously solving the system of algebraic pressure Poisson equations at all grid points using the lower–upper (LU) decomposition technique.

Flat-velocity profiles are used at the main and primary inflow boundaries. A simple extrapolation procedure[11] with weighted zero- and first-order terms is employed to estimate the flow variables at the outflow boundary. The usual no-slip, adiabatic, and chemically inert boundary conditions are applied at the walls.

Model Validation

The CFDC code developed on the basis of the methodology described in the previous section was used previously to investigate various dynamic flows in both reacting and nonreacting environments. In conjunction with global-chemistry[10] and finite rate chemistry[12] models, the code was successfully used to predict the dynamic characteristics of jet diffusion and premixed flames. After incorporation of a finite rate global chemistry model, it was also used to investigate the attached and lifted flames in a swirl-stabilized step combustor,[13] and a reasonable correlation between experimental results and calculations was obtained.

Nonreacting flow calculations for geometries similar to the one employed in the present investigation showed that the vortex shedding behind a bluff body can lead to a higher drag coefficient.[7] Those simulations also demonstrated that by proper choice of cavity size, the vortices within the cavity and behind the afterbody can be locked and, thereby, the drag coefficient of the forebody–spindle–disk combination decreased. For different cavity sizes the predicted dynamics of the vortices formed inside the cavity and behind the forebody compared well with the results of smoke visualizations and LV measurements of Little and Whipkey.[6]

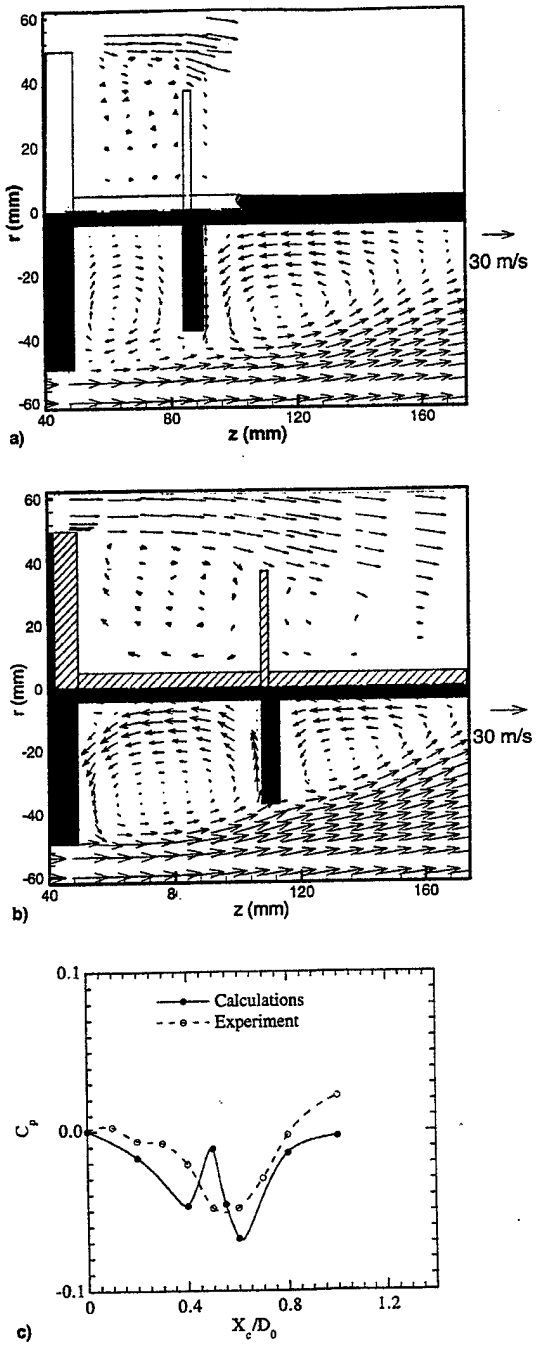

Fig. 1 Computed and measured velocity fields around forebody–spindle–disk geometry for a) smaller-than-optimum and b) optimum size cavities. c) Change in pressure coefficient for different cavity sizes. Experimental data are taken from Ref. 6.

Typical results obtained for the forebody–spindle–disk geometry of Little and Whipkey are shown in Fig. 1 along with the corresponding experimental data. An annular air velocity of 30 m/s was used in both the calculations and the experiment. As discussed previously, flow within the cavity and behind the disk became dynamic for cavity sizes other than the optimum one. The flowfield obtained for a smaller-than-optimum ($X_c/D_0 = 0.35$) size cavity is shown in Fig. 1a, and that for the optimum ($X_c/D_0 = 0.6$) one is shown in Fig. 1b. Here, the computed velocities (shown in the lower half) are obtained by time-averaging over 8000 instantaneous solutions, and the measured velocities (upper half) represent the time-averaged LV data. Figures 1a and 1b suggest that calculations have captured the key features of these dynamic flows; namely, a steady flow in the optimum-size cavity, an unsteady flow in the smaller-than-optimum size cavity, multiple-vortex structure within the cavities, and the direction of rotation of the vortices. Note that in the smaller-than-optimum size cavity, the larger vortex is rotating in the direction opposite that in the optimum-size cavity. Interestingly, time-averaged calculations using the k-ε model failed to predict these features. Details of these calculations were given in Ref. 7.

Changes in the pressure drag coefficient resulting from the addition of different size cavities to the forebody are shown in Fig. 1c. Both the calculations and the experimental results indicate that the drag coefficient becomes minimum for $X_c/D_0 \sim 0.6$. In addition, calculations predicted a sudden increase in the drag coefficient for $X_c/D_0 \sim 0.5$. Even though the experimental data did not show such a spike in the drag-coefficient curve, additional measurements[6] made with a slightly thicker spindle yielded similar spikes. Overall, the dynamic calculations performed on forebody-spindle-disk geometries using the CFDC code described earlier have yielded satisfactory results. The grid spacing of ~0.9 mm in the z and r directions used in these simulations was found to be sufficient to capture the large-scale structures whose physical size is greater than the length scales that are an order of magnitude smaller than the cavity height. Because the code and the calculation methodology adopted in the present investigations of injection effects on cavity flows are essentially the same as those used for the forebody-spindle-disk cases, the accuracy of the results presented in this paper is expected to be comparable to that obtained in the earlier work.[7] In addition, a grid spacing of ~0.5 mm (nearly half of that used in the previous studies on locked vortices) in the z and r directions was used in the present simulations primarily to resolve the injection jets.

Results and Discussion

The geometry chosen for the present study is similar to that of the TV combustor designed by Hsu et al.,[1] and to that used by Little and Whipkey[6] in their cold-flow experimental investigations on locked vortices. It consists of a 70-mm-diam flat cylindrical forebody enclosed in an annular cylindrical tube having an 80-mm i.d. An afterbody disk having a diameter and thickness of 50.8 and 20 mm, respectively, is attached to the forebody using a 9-mm-diam centerbody. The size of the cavity formed between the forebody and the afterbody is varied by moving the latter toward or away from the former. Airflow over this body develops vortices inside the cavity and behind the afterbody; normally these vortices shed, and the flow becomes dynamic in nature. The velocity of the air used in the annular gap between the forebody and the surrounding tube is 40 m/s. Primary air and fuel (propane) are injected into the cavity from the afterbody. Fuel and air are carried to the afterbody through a central tube that connects the afterbody to the forebody. The geometry and the grid system used are shown in Fig. 2. Variation of the grid spacing was adopted in both the axial z and radial r directions to cluster the grid points in the cavity and near the walls.

In the experiments of Hsu et al.,[1] fuel and air were introduced into the cavity from concentric holes on the afterbody. However, in the present axisymmetric simulations, these injection holes are grouped into three annular ring jets with the fuel jet sandwiched between the airjets. Based on the hole size and mean distance from the centerline, the reconstructed annular jets of 1-mm thickness are located in the afterbody, as shown in Fig. 2. The centers of these three annular jets (A, B, and C) are located 11, 14, and 19 mm from the axis of symmetry, respectively. Jets A and C represent air, and jet B represents fuel (propane) in the experiment and in the combusting-flow calculations; however, for simplification, all three jets are assumed to be airjets in the nonreacting calculations. Exit velocities for jets A, B, and C are 12.4, 5.0, and 12.4 m/s, respectively. This fuel and air injection results in a global (or overall) equivalence ratio of 0.2 in the combustor and a primary equivalence ratio (defined as the fuel-to-air ratio injected

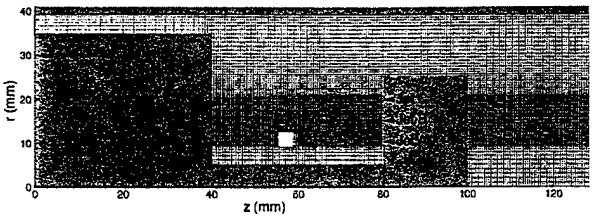

Fig. 2 Geometry and grid system used for studying effects of injection on dynamic characteristics of flows in cavity formed between the forebody and afterbody of an axisymmetric trapped-vortex combustor.

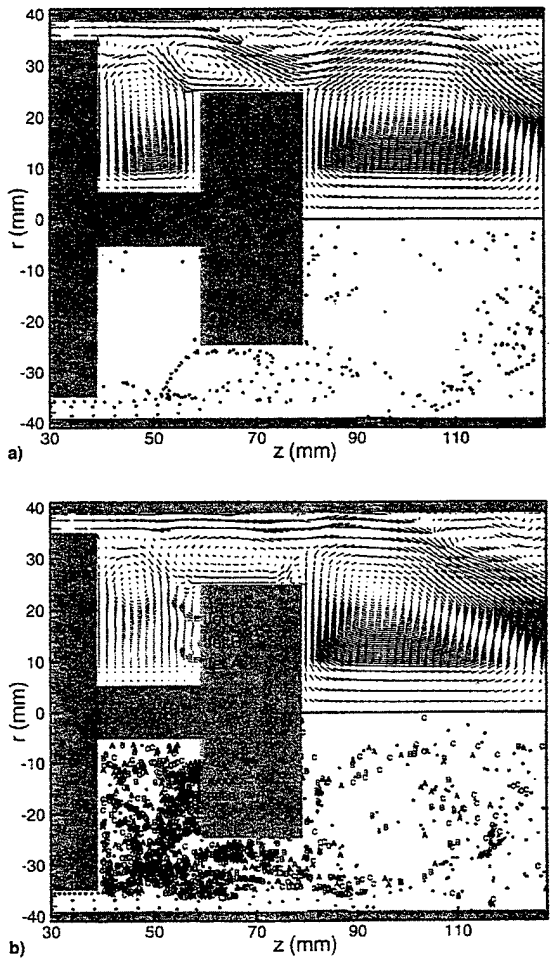

Fig. 3 Instantaneous nonreacting flowfields obtained for small-size cavity a) without and b) with cavity injection.

into the cavity relative to the ratio required for stoichiometric combustion) of 4.4 in the cavity.

Starting from a uniform initial flowfield in the combustor, direct numerical simulations are made for different cavity sizes and injection conditions. For obtaining results not biased by the initial uniform flowfield, initial calculations for 25,000 time steps (corresponding to 0.600 s of real time) were discarded prior to recording the dynamic solutions. Calculations were then continued for another 5000 time steps for data-analysis purposes.

For understanding the influence of fluid injection on flow dynamics, calculations were made for different injection conditions and afterbody locations. A 341 × 101 grid system was used in the calculations. Instantaneous flowfields obtained for three cavity sizes are shown in Figs. 3, 4, and 5. Hsu et al.[1] found that the cavity size given in Fig. 4 yielded optimum performance under combustion conditions. The width-to-diameter (forebody) ratio of this cavity is 0.57. The smaller and larger cavities shown in Figs. 3 and 5 have width-to-diameter ratios of 0.285 and 0.855, respectively. The flowfields obtained for small-, medium-, and large-size cavities with cavity injection are shown in Figs. 3b, 4b, and 5b, respectively. In these figures instantaneous velocity fields are shown on one side of the combustor, and traces of the particles injected from different locations are shown on the other side.

Passive Flows in Cavity

It is known that passive-cavity flows (without injection or combustion) become unsteady for cavity sizes that are smaller

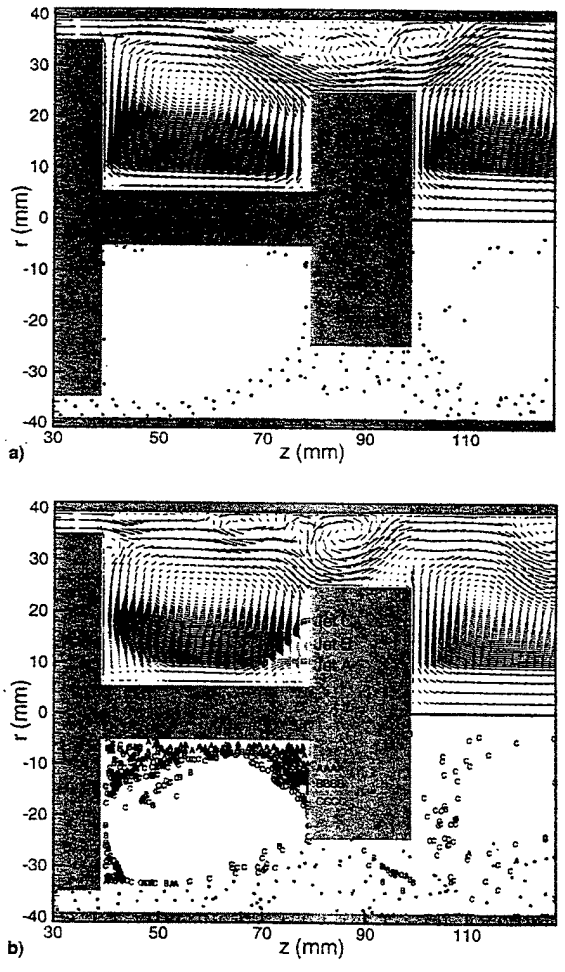

Fig. 4 Instantaneous nonreacting flowfields obtained for medium (optimum)-size cavity a) without and b) with cavity injection.

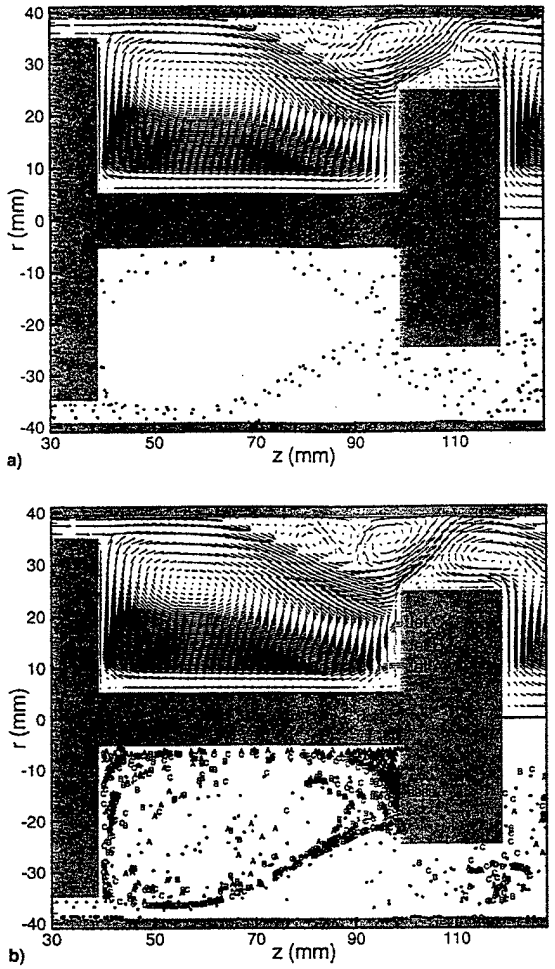

Fig. 5 Instantaneous nonreacting flowfields obtained for large-size cavity a) without and b) with cavity injection.

or larger than the optimum. Instantaneous results obtained for the smaller-size cavity (Fig. 3a) indicate that the flowfield is quite complex as a result of the formation of several vortices. Because of the presence of the cavity, the main flow is expanded toward the centerbody which, in turn, results in flow separation on the outer wall. Interestingly, fluid in the cavity is rotating counterclockwise and is separated from the main flow by two other vortices that are rotating naturally in the clockwise direction. Several instantaneous solutions of this flow revealed that the vortices in the cavity are not shedding but moving back and forth within the cavity. This is expected because the expanding main flow confines the cavity vortices by impinging on the thick afterbody (20 mm). Further calculations made with a thinner afterbody resulted in significant vortex shedding from the cavity. Because of the lack of vortex shedding from the cavity, only a few particles that are injected into the main flow enter the cavity. However, the widely distributed particles behind the afterbody suggest that the flow is quite dynamic.

For the medium- and large-size cavities, only one major vortex is formed within the cavity. The flow is unsteady because this vortex is moving inside the cavity. The particle traces suggest that the flow around the large-size cavity (Fig. 5a) is more dynamic than that around the medium-size cavity (Fig. 4a). In the latter case, the main flow is expanding and entering the cavity slightly upstream of the forebody. The particles injected into the main flow are directly entering the cavity. This means that the size (width) of the cavity might be larger than the optimum size for trapping the vortices. This cavity size was

determined experimentally to be optimum in a combustion environment. However, it may not represent the optimum size for a nonreacting flow environment. The major differences between cold and combusting flows from a cavity-flow dynamics viewpoint are 1) the damping effect of heat release on flow instabilities, and 2) the addition of mass into the cavity from primary-fuel and air injections.

Effect of Injection on Cold Flows in a Cavity

For understanding the mass-addition effects of jets on cavity-flow dynamics, calculations were made with air injections for the cavity sizes shown in Figs. 3a, 4a, and 5a; the resulting instantaneous flowfields are plotted in Figs. 3b, 4b, and 5b, respectively. The convective transport of the injected fluids is visualized by representing the particles that are released from jets A, B, and C by symbols A, B, and C, respectively. Note that the particles released from the main flow are represented by open circles.

The addition of mass into the cavity increased the unsteadiness of the flow in the cases of small- and large-size cavities (Figs. 3b and 5b, respectively). This is evident from the increase in the number of main-flow particles (open circles) in the cavity. Very few main-flow particles enter the medium-size cavity (Fig. 4b) when injection is introduced. This suggests that mass addition has a stabilizing effect on the flow in the medium-size cavity and a destabilizing effect in the other two cases. The particle trajectories also reveal that the mass injected from the three jets is distributed more in the small- and large-size cavities than in the medium-size one. In fact, the three jets are confined to the outer core of the trapped vortex (Fig. 4b), and only particles released from jet C are entrained into the wake behind the afterbody. Based on these calculations, one might intuitively predict the scenario for the combusting cases. For an overall equivalence ratio of 0.2, the increased mixing between the primary jets and the cavity flow in the nonoptimum cavities could locally make the mixture fuel-lean. When the cavity becomes unsteady, one might expect significant intermittent burning, which, in turn, leads to poor combustion efficiency. In the medium-size-cavity case, all three jets are transported stably around the cavity vortex, which enhances the mixing of jets. As the fuel and air are injected at a primary equivalence ratio of 4.4, the mixture is

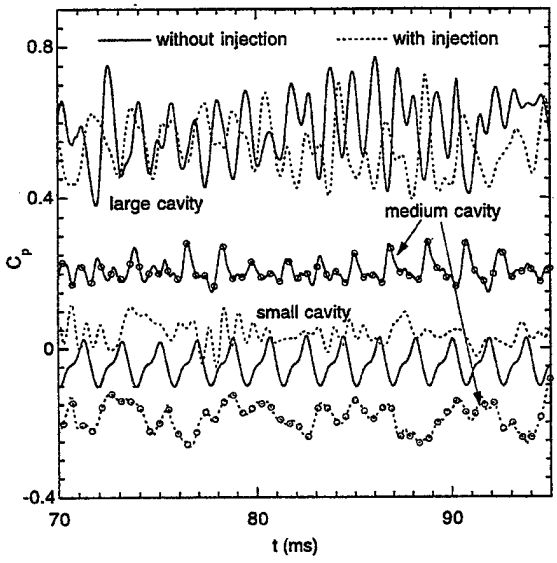

Fig. 6 Variation of pressure coefficient for different cavity sizes without and with injection.

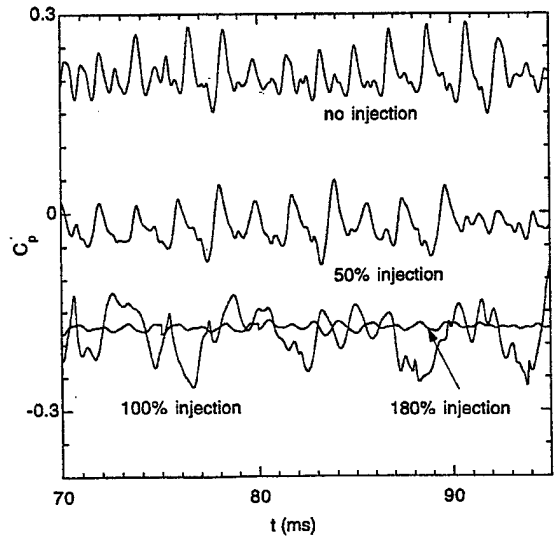

Fig. 7 Effect of injection mass on pressure coefficient.

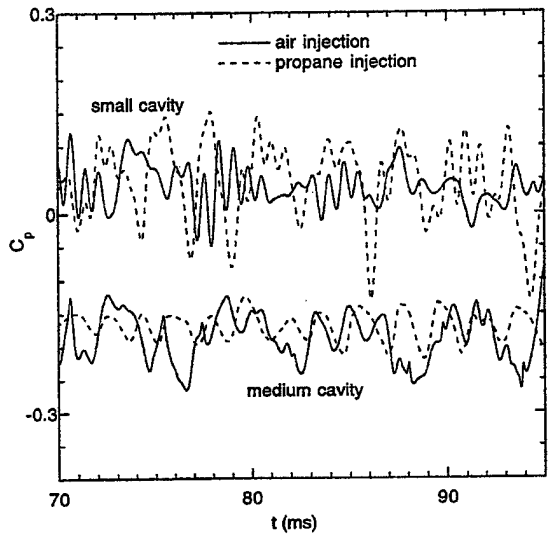

Fig. 8 Comparison of pressure coefficients predicted with air and propane injections for two different cavity sizes.

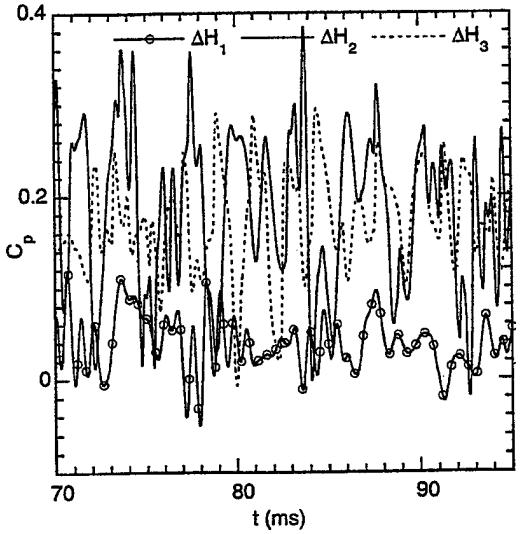

Fig. 9 Effect of afterbody thickness on pressure coefficient. H_1, H_2, and H_3 represent 20-, 10-, and 5-mm thicknesses, respectively.

expected to burn steadily in the outer core of the cavity vortex, and combustion would occur at the maximum extent, depending on the physical dimensions of the cavity or the residence time. The experiments of Hsu et al.[1] clearly demonstrated these features of the TV combustor. They obtained stable and intense burning when fuel and air were injected into the medium-sized cavity at a primary equivalence ratio of 4.4.

Flow unsteadiness in combustors not only causes the flames to burn inefficiently but also increases the pressure force across the combustor. The pressure coefficient C_p is calculated using the expression

$$Cp = \sum_{1}^{Sn} \frac{1}{\rho_\infty V_\infty^2} \int (p_w - p_\infty)\, dA \qquad (7)$$

Here, p_w and p correspond to wall and freestream pressures, respectively, and S_n represents the number of wall surfaces in the computational domain. The calculated C_p as a function of time is shown in Fig. 6 for the six cases discussed earlier. The solid curves of this figure represent the pressure coefficient in the absence of cavity injection. It should be noted from the plot that the small cavity has the lowest C_p. However, when injection is included, the pressure coefficient of the small cavity increases slightly, remains at the same higher level for the large cavity, and decreases significantly in the medium-size cavity. In fact, the medium cavity with injection has the lowest pressure coefficient among the six cases considered.

Even though the medium-size cavity with injection yielded the lowest C_p, it still does not exhibit a perfectly steady flow pattern. This could be caused by either insufficient or excess mass injection into the cavity. For understanding the effect of mass injection on flow dynamics, two additional calculations were made for the medium-size cavity with injections of 50 and 180% of the mass used in the calculations shown in Fig. 6. The pressure coefficients for different injection cases are plotted in Fig. 7. These calculations suggest that 1) the frequency of the oscillations decreases with injection mass, 2) the pressure coefficient for 180% injection becomes nearly steady, and 3) the pressure coefficient decreases with injection mass.

Figure 8 shows the differences in pressure-coefficient fluctuations with air and propane injections. Here, the middle jet (jet B) is replaced with propane fuel, and injection mass is the

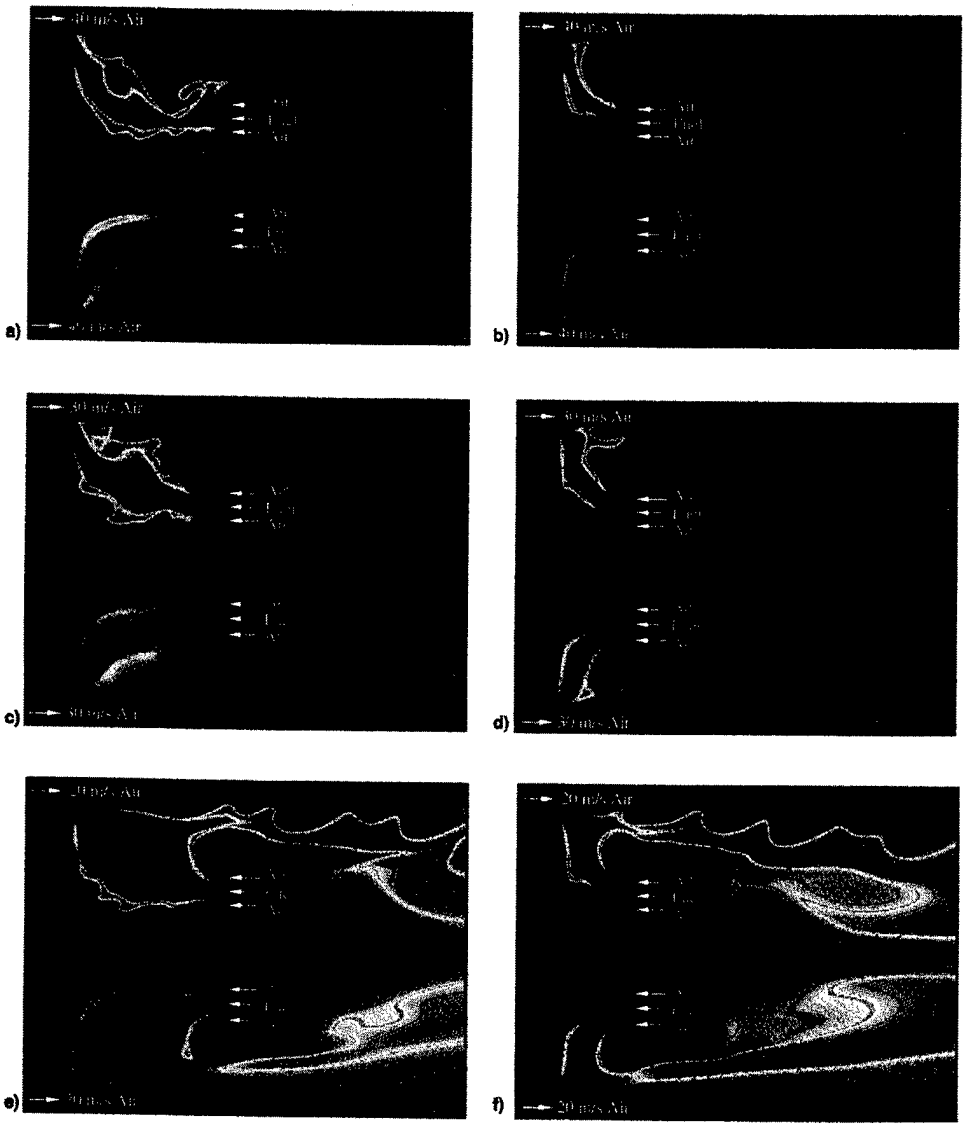

Fig. 10 Reacting flowfields obtained for different main-flow velocities. In each plot temperature variation between 300 K (blue) and 2000 K (red) is shown with rainbow color palette. Instantaneous and time-averaged data are shown in upper and lower halves, respectively. a) Medium- and b) small-size cavity flows for a main-flow velocity of 40 m/s. c) Medium- and d) small-size cavity flows for a main-flow velocity of 30 m/s. e) Medium- and f) small-size cavity flows for a main-flow velocity of 20 m/s.

same as that in Fig. 6. The density variation appears to have no impact on the medium-size cavity; in the small-size-cavity case, however, propane injection generates slightly higher amplitude pressure fluctuations. The effect of afterbody thickness on the unsteady flow inside and around the cavity was studied by simulating the flow over three afterbody thicknesses. These calculations were performed for the small-size cavity with normal (100%) air injection. Fluctuating pressure coefficients as functions of time are plotted in Fig. 9. While H_1 represents the thickness of the standard afterbody (20 mm), H_2 and H_3 represent 50 and 25% of the thickness of the standard afterbody, respectively. As expected, the thinner afterbodies provided better communication between the cavity and the afterbody-wake flows. This resulted in increased pressure coefficients. The larger-amplitude fluctuations for the thinner afterbodies suggest increased vortex shedding from the cavity.

Effect of Combustion on Cavity Flows

For investigating the vortex characteristics in the cavity under combusting-flow conditions, calculations were made for the simulation of reacting flow in the combustor described previously. Hsu et al.[1] found that this combustor operates most stably when the cavity size is at the optimum value (Fig. 4) and when the primary air and fuel (propane) are injected into the cavity at an equivalence ratio of 4.4. Calculations were made for this fuel-rich condition using the 341 × 101 grid system.

The instantaneous and time-averaged temperature fields computed with a fast-chemistry assumption are shown in the upper and lower halves of Fig. 10a, respectively. In general, the center fuel jet is mixing with the neighboring airjets and burning as two distinct flames. The instantaneous-temperature field suggests that the flow in the cavity has a large vortex generated by the high-speed annulus airflow and several small vortices that have developed primarily from the interaction of fuel and air jets injected into the cavity. Small puffs of fuel are penetrating through the outer airjet periodically. The existence of jet-like flame structures in the time-averaged temperature field in Fig. 10a indicates that the large cavity vortex is nearly stable. Note that for this cavity size, cold-flow calculations with injection also yielded a nearly stable vortex within the cavity (Fig. 4b).

The effect of cavity size on combustion was studied by simulating the reacting flow in a 50% smaller cavity and by maintaining the same injection velocities for the fuel and airjets as those used for the optimum-size-cavity calculations. The instantaneous and time-averaged temperature fields are shown in Fig. 10b. Interestingly, the combustion is still confined within the cavity, even though the lengths of the jet-like flames have been reduced by nearly one-half. A significant amount of fuel is escaping from the cavity, mixing with the annulus air, and burning without raising the local temperature significantly as the mixture becomes very fuel-lean. As the cavity vortex becomes weaker in the case of the smaller-size cavity (Fig. 10b), the flames are pushed away from the center tube. This behavior is also seen in the cold-flow simulations made with injection (Figs. 3b).

Reacting-flow calculations were also made for different annulus-airflow velocities on the optimum-size and smaller-size cavities. Results obtained for a 30-m/s annulus flow are shown in Figs. 10c and 10d for the two cavity sizes, and those obtained for a 20-m/s annulus flow are shown in Figs. 10e and 10f. As expected, the strength of the cavity vortex is decreasing with reduction in annulus airflow. Because of this the outer airjet is turning back around the afterbody and the separation between the two flame jets has increased. The lower annulus airflow is also increasing the local equivalence ratio outside the cavity which, in turn, results in higher temperatures downstream of the afterbody. This behavior was also experimentally observed by Hsu et al.[1] In addition, for lower annulus flows, the shear-layer vortices are becoming more organized.

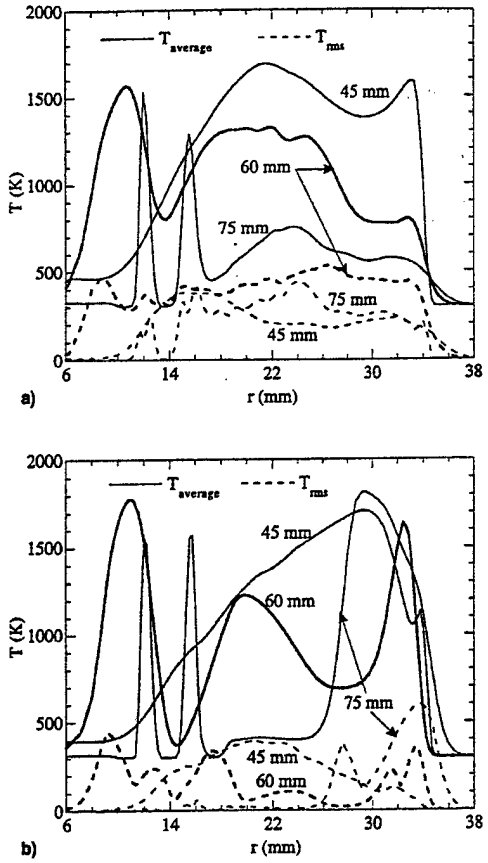

Fig. 11 Radial distributions of mean and rms temperature at different axial locations in the cavity for annular air velocities of a) 40 and b) 20 m/s.

For quantifying the unsteadiness associated with the combusting flows shown in Fig. 10, the mean and rms temperatures are obtained from 20,000 instantaneous solutions over a period of 120 ms. Figures 11a and 11b show the radial distributions of these temperatures at different axial locations in the medium-sized cavity operating at annular-air velocities of 40 and 20 m/s, respectively. The three axial distances in the cavity z = 45, 60, and 75 mm correspond to locations 1) near the forebody, 2) at the center of the cavity, and 3) near the disk, respectively. As expected, the rms temperatures in the 20-m/s case are smaller than those obtained with the 40-m/s air velocity. Overall, the low level of rms (<500 K) values for the temperature fluctuations noted in the cavity region is very similar to that observed in the experiments.[1]

Summary and Conclusions

Unsteady flow inside and around the cavity, in general, leads to a higher drag coefficient, and in combustors it creates further problems related to blowout and poor combustion efficiency. It is known that the unsteadiness of the flow can be reduced by proper cavity design. The dynamics of the vortices formed inside and around the cavity was studied using a time-dependent, axisymmetric CFDC code. The geometry used in this study was an axisymmetric, centerbody trapped-vortex combustor employed by Hsu et al.[1] A large number of grid points with z and $r \sim 0.5$ mm was used to capture the vortical structures having length scales that are an order of magnitude smaller than the height of the cavity. Fluid was injected into the cavity from three locations at different flow rates to investigate the effects of fluid injection on vortex dynamics. It was found that the optimum cavity size for obtaining steady flow inside and around the cavity should be larger in the case of

fluid injection than for passive cavities (with no injection). The flow becomes more unsteady when the fluid is injected into nonoptimum (larger or smaller than the optimum) cavities. Calculations made with air and propane injections yielded very similar flow patterns and pressure coefficients. On the other hand, the thickness of the afterbody seems to have a strong influence on the flow pattern. Thinner afterbodies resulted in higher pressure coefficients, with fluctuations larger than those observed with the thicker afterbodies.

Calculations made using a single-step global-chemistry model revealed that the fuel injected into the cavity mixes with the injected air and burns like a jet flame. It was found that a lesser amount of fuel is burned in the smaller-size cavity than in the optimum-size one. The spilled-over fuel from the cavity mixes with the annulus airflow and results in fuel-lean mixtures. As the local mixture becomes less fuel-lean with the reduced annulus flow, the temperature downstream of the forebody increases. Future calculations will be made for these flows employing a detailed-chemical-kinetics model for propane combustion to investigate the flame-stability characteristics in the trapped-vortex combustor.

Acknowledgment

This work was supported, in part, by U.S. Air Force Contract F33615-95-C-2507 and the U.S. Air Force Office of Scientific Research.

References

[1]Hsu, K.-Y., Goss, L. P., and Roquemore, W. M., "Characteristics of a Trapped-Vortex Combustor," *Journal of Propulsion and Power*, Vol. 14, No. 1, 1998, pp. 57–65.

[2]Rohsenow, W. M., Fink, C. H., and Pollis, S. R., "Flow Through Two Orifices in Series," American Society of Mechanical Engineers, Paper 51-A-87, 1951.

[3]Migay, V. K., "Study of Ribbed Diffusers," (in Russian), *Toploenergetika*, No. 10, 1962; English Translation, A.R.C. Paper 25, 1963, p. 382.

[4]Mair, W. A., "The Effect of a Rear-Mounted Disc on the Drag of a Blunt-Based Body of Revolution," *The Aeronautical Quarterly*, Vol. 10, Pt. 4, Nov. 1965, pp. 350–360.

[5]Roshko, A., and Koenig, K., "Interaction Effects on the Drag of Bluff Bodies in Tandem," Symposium on Aerodynamic Drag Mechanisms of Bluff Bodies and Road Vehicles, General Motors Research Lab., Sept. 1976.

[6]Little, B. H., and Whipkey, R. R., "Locked Vortex Afterbodies," *Journal of Aircraft*, Vol. 16, No. 5, 1979, pp. 296–302.

[7]Katta, V. R., and Roquemore, W. M., "Numerical Studies on Trapped-Vortex Concepts for Stable Combustion," *Journal of Engineering for Gas Turbines and Power* (to be published).

[8]Katta, V. R., and Roquemore, W. M., "Numerical Studies on Trapped-Vortex Combustor," AIAA Paper 96-2660, July 1996.

[9]Leonard, B. P., "A Stable and Accurate Convective Modeling Procedure Based on Quadratic Upstream Interpolation," *Computer Methods in Applied Mechanics and Engineering*, Vol. 19, 1979, p. 59.

[10]Katta, V. R., Goss, L. P., and Roquemore, W. M., "Numerical Investigations of Transitional H_2/N_2 Jet Diffusion Flames," *AIAA Journal*, Vol. 32, No. 1, 1994, pp. 84–94.

[11]Katta, V. R., Goss, L. P., and Roquemore, W. M., "Simulation of Vortical Structures in a Jet Diffusion Flame," *International Journal of Numerical Methods in Heat and Fluid Flow*, Vol. 4, 1994, pp. 413–424.

[12]Katta, V. R., and Roquemore, W. M., "Numerical Studies on the Structure of Two-Dimensional H_2/Air Premixed Jet Flame," *Combustion and Flame*, Vol. 102, Nos. 1 and 2, 1995, pp. 21–40.

[13]Durbin, M. D., Vangsness, D., Ballal, D., and Katta, V. R., "Study of Flame Stability in a Step Swirl Combustor," *Journal of Engineering for Gas Turbine and Power*, Vol. 118, No. 2, 1996, pp. 308–315.

Color reproductions courtesy of Innovative Scientific Solutions, Inc.

AIAA 98-3766

Simulation of Unsteady Flows in an Axisymmetric Research Combustor Using Detailed-Chemical Kinetics

V. R. Katta
Innovative Scientific Solutions, Inc
Dayton, OH

W. M. Roquemore
Air Force Research Laboratory
Wright-Patterson AFB, OH

34th AIAA/ASME/SAE/ASEE
Joint Propulsion Conference & Exhibit
July 13-15, 1998 / Cleveland, OH

For permission to copy or republish, contact the American Institute of Aeronautics and Astronautics
1801 Alexander Bell Drive, Suite 500, Reston, VA 20191

Simulation of Unsteady Flows in an Axisymmetric Research Combustor Using Detailed-Chemical Kinetics

Viswanath R. Katta*
Innovative Scientific Solutions, Inc.
2766 Indian Ripple Road
Dayton, OH 45440-3638

W. M. Roquemore+
Propulsion Directorate
Air Force Research Laboratory
Wright-Patterson Air Force Base, OH 45433-7103

Abstract

Low-velocity flows in the cavities of a combustor can aid in establishing stable flames. However, unsteady flows in and around cavities may destabilize these flames. By proper cavity design it is possible to lock (trap) the vortices spatially and, thereby, stabilize the flames. The spatially locked vortices restrict the entrainment of main air into the cavity. For obtaining good performance characteristics with a trapped-vortex combustor, a sufficient amount of fuel and air must be injected directly into the cavity. This mass injection can alter the dynamic characteristics of the flow inside and around the cavity. The present numerical study investigates the vortex dynamics of a cavity in to which fuel and air are directly injected through jets. A third-order-accurate, time-dependent, Computational-Fluid-Dynamics-with-Chemistry (CFDC) code was used for simulating the dynamic reacting flows associated with an axisymmetric, center-body trapped-vortex combustor. A detailed chemistry model with 33 species and 92 reversible reactions was incorporated into the code to simulate propane combustion. An opposing-jet diffusion flame is simulated under different strain rates for validating the CFDC code. It is found that the incorporated chemistry mechanism; even though, yielding sufficiently accurate results at lower strain rates, is predicting flame extinction at strain rates much lower than those obtained in the experiments. Reacting flows simulated in trapped-vortex combustor for an annular velocity of 10 m/s suggest that flame extinguishes first in the region near the forebody corner.

Introduction

Unsteady flow in and around cavity-type geometries occurs in a variety of applications such as slotted wind tunnels, slotted flumes, bellows-type configurations, and aircraft-engine and airframe components. In particular, the unsteady flow in aircraft combustors restricts fuel-lean operation and degrades flame-stability characteristics. Recently, a simple, compact, and efficient method of using cavities to stabilize combustion was proposed by Hsu et al.[1] Since this concept uses a vortex that is trapped in a cavity to stabilize the flame, it is referred as the Trapped-Vortex (TV) concept. Several investigators have recognized the aerodynamic advantages of locking the vortices inside and around the cavity[2-4] in a nonreacting flow. Experiments of Rohsenow et al.[2] have shown that when two circular orifices are placed in series in a pipe, a large recovery of pressure occurs across the second orifice in certain circumstances; hence, the overall pressure drop is considerably less for the two orifices than for a single one having the same flow. In ribbed diffusers, Migay[3] found that balancing the fluid removed by entrainment and the fluid entering the cavity by reversed flow ensures that the flow outside the cavities will follow the ribs fairly closely, and a good pressure recovery will be achieved. Mair[4] showed that by mounting a disk behind the base of a blunt body, the drag of the blunt object can be reduced. Using similar concepts, Roshko and Koenig[5] reported a reduction in drag of blunt forebodies when disks were placed on spindles ahead of the bodies.

Little and Whipkey[6] conducted extensive investigations on the dynamic nature of flows over bluff bodies using smoke-flow-visualization and laser-velocimetry techniques. Because of the limitations of the smoke tunnel, they employed reduced flow conditions (~ 0.3 m/s) and half-scale geometries for the flow-visualization studies and full-scale geometries and turbulent flows (~ 30 m/s) for the time-averaged drag measurements. Based on these reduced and full-scale experiments, they correlated the afterbody drag and the motion of the vortex in the wake region and postulated that a minimum-drag condition is established when the wake vortices are locked between two disks mounted in series on a spindle. They also suggested that the cavity formed between

*Senior Engineer, Member AIAA
+Senior Scientist, Member AIAA
This paper is declared a work of the U. S. Government and is not subjected to copyright protection in the United States.

the disk and the bluff body should be of such dimensions that the locked vortex would effectively fill the cavity. Based on reduced-scale flow-visualization experiments on cavities formed between a forebody and an afterbody, Little and Whipkey[6] correlated the drag and motion of the vortex in the cavity region and postulated that a minimum-drag condition is established when the cavity vortices are locked between the two bodies. Recently, Katta and Roquemore[7,8] used direct numerical simulations to investigate the Little and Whipkey experiments under turbulent-flow conditions. The simulations successfully predicted that a cavity having a length-to-diameter ratio of 0.45 becomes stationary and that the pressure-drag coefficient is reduced to a minimum value when the vortices are locked inside and around the cavity. This suggests that the relationship between the minimum drag coefficient and the vortex motion is also valid in the case of turbulent flows. These simulations demonstrated the capability of numerical simulations in the study of the dynamic processes associated with cavities.

Two major differences exist between flows associated with airframe cavities and those associated with the combustor cavities. First, the heat release and higher viscosity of the combustion products associated with the partial burning that takes place in the cavities could alter the vortex dynamics. As a result, the criterion for trapping a vortex in a heated flow would differ from that for trapping a vortex in a cold flow. Secondly, it is known that a locked vortex entrains a minimum amount of fluid from the main flow; hence, to achieve continuous combustion in trapped-vortex combustors, fuel and air must be directly fed into the cavity. Experimental investigations of Hsu et al.[1] also indicate that a trapped-vortex combustor operates most efficiently when fuel and air are injected directly into the cavity. However, direct injection of mass (air and/or fuel) into the cavity could alter the geometrical criterion derived for locking vortices inside passive cavities (i.e., without injection).

The purpose of this study was to investigate the dynamics of reacting flows in the trapped-vortex combustor as fuel and air jets are directly injected into the cavity. A third-order-accurate, time-dependent, Computational Fluid Dynamics with Chemistry (CFDC) code and a large number of grid points were used to investigate the these flowfields.

Modeling

A time-dependent, axisymmetric mathematical model that solves for axial- and radial-momentum equations, continuity, and enthalpy- and species-conservation equations in cylindrical-coordinate system is used to simulate the unsteady flows inside a trapped-vortex combustor. The pressure field at every time step is determined from pressure Poisson equations. Even though the governing equations are solved in an uncoupled manner, the species-conservation equations are coupled through the source terms during the solution process to improve the stability of the algorithm. Such coupling is essential in finite-rate-chemistry calculations since the high-reaction-rate terms make the species-conservation equations quite stiff. Temperature- and species-dependent thermodynamic and transport properties are used in this formulation.

The governing equations for axial and radial momentum are integrated using an implicit QUICKEST (Quadratic Upstream Interpolation for Convective Kinematics with Estimated Streaming Terms) numerical scheme,[9,10] which is third-order accurate in both space and time and has a very low numerical-diffusion error. On the other hand, the finite-difference form of the species and enthalpy is obtained using the hybrid scheme[11] with upwind and central differencing. An orthogonal, staggered-grid system with rapidly varying cell sizes in both the axial (z) and the radial (r) directions is utilized for discretizing the governing equations. The algebraic equations for N_s+2 variables (N_s -1 species, u and v) are solved individually using an iterative ADI (Alternative Direction Implicit) technique. The pressure-field at every time step is accurately calculated by solving the algebraic-pressure-Poisson equations at all grid points simultaneously using the LU (Lower-Upper) decomposition technique.

A detailed chemical-kinetics model[12] that consists of 33 species (C_3H_8, O_2, CH_4, CH_3, CH_2, CH, CH_2O, CHO, CO_2, CO, H_2, H, O, OH, H_2O, HO_2, H_2O_2, C_2H, C_2H_2, C_2H_3, C_2H_4, C_2H_5, C_2H_6, CHCO, C_3H_3, C_3H_4, C_3H_5, C_3H_6, iC_3H_7, nC_3H_7, CH_2OH, CH_3OH, and N_2) and 92 reversible elementary reactions is used. The details of the reactions are given in Table 1. This mechanism is obtained by extending the one recommended of Peters' by 1) including all the backward reactions and 2) including the last five reactions (R88-R92) to improve the ignition characteristics at lower temperatures.

The enthalpies of all the species are calculated from the polynomial curve fits developed for the temperature range 300 - 5000 K. Physical properties such as viscosity, thermal conductivity, and the binary molecular diffusion coefficients of the species are calculated using molecular dynamics. Mixture viscosity and thermal conductivity are then estimated using the Wilke and the Kee expressions,[13] respectively.

Table 1. Modified Peters Mechanism for Propane Combustion

Reaction	A_k (Mole, cm^3,s)	α	E (cal/ mole)
R01 $H + O_2 <=> OH + O$	2.00E+14	0.0	16,800
R02 $O + H_2 <=> OH + H$	5.06E+04	2.67	6,280
R03 $H_2 + OH <=> H_2O + H$	1.00E+08	1.60	3,300
R04 $OH + OH <=> O + H_2O$	1.50E+09	1.14	100
R05 $O_2 + H + M <=> HO_2 + M$	2.30E+18	-0.8	0
R06 $HO_2 + H <=> OH + OH$	1.50E+14	0.0	1,000
R07 $HO_2 + H <=> H_2 + O_2$	2.50E+13	0.0	692
R08 $HO_2 + OH <=> H_2O + O_2$	6.00E+13	0.0	0
R09 $HO_2 + H <=> H_2O + O$	3.00E+13	0.0	1,720
R10 $HO_2 + O <=> OH + O_2$	1.80E+13	0.0	-406
R11 $HO_2 + HO_2 <=> H_2O_2 + O_2$	2.50E+11	0.0	-1,240
R12 $OH + OH + M <=> H_2O_2 + M$	3.25E+22	-2.0	0
R13 $H_2O_2 + H <=> H_2O + OH$	1.00E+13	0.0	3,580
R14 $H_2O_2 + OH <=> H_2O + HO_2$	5.40E+12	0.0	1,000
R15 $H + H + M <=> H_2 + M$	1.80E+13	-1.0	0
R16 $H + OH + M <=> H_2O + M$	2.20E+22	-2.0	0
R17 $O + O + M <=> O_2 + M$	2.90E+17	-1.0	0
R18 $CO + OH <=> CO_2 + H$	4.40E+06	1.5	-740
R19 $CH + O_2 <=> CHO + O$	3.00E+13	0.0	0
R20 $CO_2 + CH <=> CHO + CO$	3.40E+12	0.0	692
R21 $CHO + H <=> CO + H_2$	2.00E+14	0.0	0
R22 $CHO + OH <=> CO + H_2O$	1.00E+14	0.0	0
R23 $CHO + O_2 <=> CO + HO_2$	3.00E+12	0.0	0
R24 $CHO + M <=> CO + H + M$	7.10E+14	0.0	16,800
R25 $CH_2 + H <=> CH + H_2$	8.40E+09	1.5	335
R26 $CH_2 + O <=> CO + H + H$	8.00E+13	0.0	0
R27 $CH_2 + O_2 <=> CO + OH + H$	6.50E+12	0.0	1,500
R28 $CH_2 + O_2 <=> CO_2 + H + H$	6.50E+12	0.0	1,500
R29 $CH_2O + H <=> CHO + H_2$	2.50E+13	0.0	3,990
R30 $CH_2O + O <=> CHO + OH$	3.50E+13	0.0	3,490
R31 $CH_2O + OH <=> CHO + H_2O$	3.00E+13	0.0	1,200
R32 $CH_2O + M <=> CHO + H + M$	1.40E+17	0.0	76,500
R33 $CH_3 + H <=> CH_2 + H_2$	1.80E+14	0.0	15,050
R34 $CH_3 + H <=> CH_4$ K_∞	6.00E+16	-1.0	0
K_0	6.26E+23	-1.8	0
R35 $CH_3 + O <=> CH_2O + H$	7.00E+13	0.0	0
R36 $CH_3 + CH_3 <=> C_2H_6$ K_∞	3.61E+13	0.0	0
K_0	1.27E+41	-7.0	2,762
R37 $CH_3 + O_2 <=> CH_2O + OH$	3.40E+11	0.0	8,940
R38 $CH_4 + H <=> CH_3 + H_2$	2.20E+04	3.0	8,740
R39 $CH_4 + O <=> CH_3 + OH$	1.20E+07	2.1	7,620
R40 $CH_4 + OH <=> CH_3 + H_2O$	1.60E+06	2.1	2,460
R41 $C_2H + H_2 <=> C_2H_2 + H$	1.10E+13	0.0	2,867
R42 $C_2H + O_2 <=> CHCO + O$	5.00E+13	0.0	1,505
R43 $CHCO + H <=> CH_2 + CO$	3.00E+13	0.0	0
R44 $CHCO + O <=> CO + CO + H$	1.00E+14	0.0	0
R45 $C_2H_2 + O <=> CH_2 + CO$	4.10E+08	1.5	1,696
R46 $C_2H_2 + O <=> CHCO + H$	4.30E+14	0.0	12,112
R47 $C_2H_2 + OH <=> C_2H + H_2O$	1.00E+13	0.0	7,000
R48 $C_2H_2 + CH <=> C_3H_3$	2.10E+14	0.0	-120
R49 $C_2H_3 + H <=> C_2H_2 + H_2$	3.00E+13	0.0	0
R50 $C_2H_3 + O_2 <=> C_2H_2 + HO_2$	5.40E+11	0.0	0
R51 $C_2H_3 <=> C_2H_2 + H$ K_∞	2.00E+14	0.0	39,717
K_0	1.19E+42	-7.5	45,486
R52 $C_2H_4 + H <=> C_2H_3 + H_2$	1.50E+14	0.0	10,201
R53 $C_2H_4 + O <=> CH_3 + CO + H$	1.60E+09	1.2	741
R54 $C_2H_4 + OH <=> C_2H_3 + H_2O$	3.00E+13	0.0	3,010
R55 $C_2H_4 + M <=> C_2H_2 + H_2 + M$	2.50E+17	0.0	76,400
R56 $C_2H_5 + H <=> CH_3 + CH_3$	3.00E+13	0.0	0.0
R57 $C_2H_5 + O_2 <=> C_2H_4 + HO_2$	2.00E+12	0.0	4,993
R58 $C_2H_5 <=> C_2H_4 + H$ K_∞	2.00E+13	0.0	39,657
K_0	1.00E+17	0.0	31,057
R59 $C_2H_6 + H <=> C_2H_5 + H_2$	5.40E+02	3.5	5,208
R60 $C_2H_6 + O <=> C_2H_5 + OH$	3.00E+07	2.0	5,112
R61 $C_2H_6 + OH <=> C_2H_5 + H_2O$	6.30E+06	2.0	645
R62 $C_3H_3 + O_2 <=> CHCO + CH_2O$	6.00E+12	0.0	0
R63 $C_3H_3 + O <=> C_2H_3 + CO$	3.80E+13	0.0	0
R64 $C_3H_4 <=> C_3H_3 + H$ K_∞	5.00E+14	0.0	88,393
R65 $C_3H_4 + O <=> C_2H_2 + CH_2O$	1.00E+12	0.0	0
R66 $C_3H_4 + O <=> C_2H_3 + CHO$	1.00E+12	0.0	0
R67 $C_3H_4 + OH <=> C_2H_3 + CH_2O$	1.00E+12	0.0	0
R68 $C_3H_4 + OH <=> C_2H_4 + CHO$	1.00E+12	0.0	0
R69 $C_3H_5 <=> C_3H_4 + H$	3.98E+13	0.0	70,022
R70 $C_3H_5 + H <=> C_3H_4 + H_2$	1.00E+13	0.0	0
R71 $C_3H_6 <=> C_2H_3 + CH_3$	3.15E+15	0.0	85,837
R72 $C_3H_6 + H <=> C_3H_5 + H_2$	5.00E+12	0.0	1,505
R73 $nC_3H_7 <=> C_2H_4 + CH_3$	9.60E+13	0.0	31,009
R74 $nC_3H_7 <=> C_3H_6 + H$	1.25E+14	0.0	37,006
R75 $iC_3H_7 <=> C_2H_4 + CH_3$	6.30E+13	0.0	36,910
R76 $iC_3H_7 + O_2 <=> C_3H_6 + HO_2$	1.00E+12	0.0	4,993
R77 $C_3H_8 + H <=> nC_3H_7 + H_2$	1.30E+14	0.0	9,699
R78 $C_3H_8 + H <=> iC_3H_7 + H_2$	1.00E+14	0.0	8,338
R79 $C_3H_8 + O <=> nC_3H_7 + OH$	3.00E+13	0.0	5,758
R80 $C_3H_8 + O <=> iC_3H_7 + OH$	2.60E+13	0.0	4,467
R81 $C_3H_8 + OH <=> nC_3H_7 + H_2O$	3.70E+12	0.0	1,648
R82 $C_3H_8 + OH <=> iC_3H_7 + H_2O$	2.80E+12	0.0	860
R83 $CH_2OH + H <=> CH_2O + H_2$	3.00E+13	0.0	0
R84 $CH_2OH + O_2 <=> CH_2O + HO_2$	1.00E+13	0.0	7,191
R85 $CH_2OH + M <=> CH_2O + H + M$	1.00E+14	0.0	25,108
R86 $CH_3OH + H <=> CH_2OH + H_2$	4.00E+13	0.0	6,092
R87 $CH_3OH + OH <=> CH_2OH + H_2O$	1.00E+13	0.0	1,696
R88 $nC_3H_7 + H + M <=> C_3H_8 + M$	3.60E+13	0.0	0
R89 $iC_3H_7 + H + M <=> C_3H_8 + M$	2.40E+13	0.0	0
R90 $C_3H_8 + O_2 <=> nC_3H_7 + HO_2$	3.98E+13	0.0	50,910
R91 $C_3H_8 + O_2 <=> iC_3H_7 + HO_2$	3.98E+13	0.0	47,565
R92 $C_3H_8 <=> C_2H_5 + CH_3$	7.90E+22	-1.8	88,632

Molecular diffusion is assumed to be of the binary type, and the diffusion velocity of a species is calculated according to Fick's law and using the effective-diffusion coefficient of that species. The Lennard Jones potentials, the effective temperatures, and the coefficients for the enthalpy polynomials for each species are obtained from the CHEMKIN libraries.

Flat velocity profiles are used at the main and primary inflow boundaries. A simple extrapolation procedure[14] with weighted zero- and first-order terms is employed to estimate the flow variables at the outflow boundary. The usual no-slip, adiabatic, and chemically inert boundary conditions are applied at the walls.

The simulations presented here were performed on a Pentium Pro 300-MHz-based Personal Computer with 128 MB of memory. Typical execution times using a grid system of 301x121 is ~170 s/time step. Stable flames are usually obtained in about 5000 time steps (which corresponds to approximately 60-ms real time), starting from the solution obtained with a global-chemistry model.[7,8] It is interesting to note that a detailed time-dependent simulation using 33 species and 184 elementary reactions (finite-rate chemistry model for propane fuel) for dynamic flows in a research combustor can be made on a personal computer in < 240 h.

Results and Discussion

Simulation of Opposing-Jet Diffusion Flames

The CFDC model developed for the simulation of a time-dependent propane flames in a combustor was first tested for the prediction of a counterflow jet diffusion flame. The burner assembly used for this study consists of two nozzles with 14-mm exit diameters spaced 13 mm apart. The fuel and oxidizer jets emanating from the nozzles were made to impinge on each other. Outer nitrogen co-flows were used to isolate and stabilize the flame. The fuel and oxidizer streams consisted of pure propane and air, respectively. Several calculations were made for different exit velocities, and the results were compared to the measurements. A typical flame computed using the axisymmetric code for an exit velocity of 1.5 m/s is shown in Fig. 1 in the form of velocity vectors superimposed over the iso-OH contours on the left side and over the iso-temperature contours on the right side. Fuel flowing from the bottom nozzle (z = 0) reacts with the oxidizer flowing from the top (z = 13 mm) and yields a steady laminar flame on the oxidizer side of the stagnation plane (zero axial velocity plane, z ~ 7.3 mm). The flame surface may be identified from the maximum-temperature (1600 K) contour passing through z ~ 7.8-mm plane in Fig. 1. Note that the flame is slightly curved toward the air jet.

The flame structure at the stagnation line is shown in the form of distributions of velocity, velocity gradient and temperature in Fig. 2. While the distributions of major species are shown in Fig. 3, those of some minor species are shown in Figs. 4 and 5. The flame structure shown in Figs. 2 - 5 is not compared with the experimental one because of the lack of quantitative data published with respect to jet velocities. Traditionally, experimental data on one-dimensional flames are reported in terms of strain rate to facilitate validation of results obtained with asymptotic-models which use strain rate as a parameter. As the actual local strain rate along the stagnation line varies significantly within the flame zone, such data could not be used to compare with the results obtained from the direct simulation of opposing-jet flames. Nevertheless, the flame structure shown in Figs. 2-5 is qualitatively similar to that of a typical opposing-jet diffusion flame.[15]

An opposing-jet flame is usually characterized by the air-side strain rate (a), which may be obtained by calculating the maximum velocity gradient on the air side of the flame.[16] The 400-s^{-1} strain rate of the steady-state flame in Fig. 1 represents that of a highly strained flame. Figure 3 indicates that oxygen is not completely burned in the flame zone and small amount of oxygen is leaking through the flame surface.

Results in the form of centerline flame temperature Vs air-side strain rate obtained using different jet velocities are shown in Fig. 6. As expected flame temperature decreases with strain rate and extinction occurs when strain rate increases above 400 s^{-1}. This extinction strain rate seems to be much lower than that obtained in the experiments (~ 880 s^{-1}) and it could be related to the limitations of the chemistry model (Table 1) used in the present study.

Simulation of Reacting Flows in Trapped-Vortex Combustor

The geometry chosen for the present study is similar to that of the trapped-vortex combustor designed by Hsu et al.[1] and to that used by Little and Whipkey[6] in their cold-flow experimental investigations on locked vortices. It consists of a 70-mm-diameter flat cylindrical forebody enclosed in an annular cylindrical tube having an 80-mm inner diameter. An afterbody disk having diameter and thickness of 50.8 and 20 mm, respectively, is attached to the forebody using a 9-mm-diameter center body. The size of the cavity formed between the forebody and the afterbody is

varied by moving the latter toward or away from the former. Airflow over this body develops vortices inside the cavity and behind the afterbody; normally these vortices shed, and the flow becomes dynamic in nature. The velocity of the air in the annular gap between the forebody and the surrounding tube is varied between 10 and 40 m/s. Primary air and fuel (propane) are injected into the cavity from the afterbody. Fuel and air are carried to the afterbody through a central tube that connects the afterbody to the forebody. The geometry and the 301X121 grid system used are shown in Fig. 7. Variation of the grid spacing was adopted in both the axial (z) and radial (r) directions to cluster the grid points in the cavity and near the walls.

In the experiments of Hsu et al.,[1] fuel and air were introduced into the cavity from concentric holes on the afterbody. However, in the present axisymmetric simulations, these injection holes are grouped into three annular ring jets with the fuel jet sandwiched between the air jets. Based on the hole size and mean distance from the centerline, the reconstructed annular jets of 1.5-mm thickness are located in the afterbody, as shown in Fig. 7. The centers of these three annular jets (A, B, and C) are located 11, 14, and 19 mm from the axis of symmetry, respectively. While Jets A and C represent that of air, Jet B represents that of propane fuel. Exit velocities for Jets A, B, and C are 5.0, 2.5, and 5.0 m/s, respectively. This injection of fuel and air results in global (or overall) equivalence ratios of 0.57 and 0.3 in the combustor for the annular-air velocities of 10 and 20 m/s, respectively. The primary equivalence ratio in the cavity (defined as the fuel-to-air ratio injected into the cavity relative to the ratio required for stoichiometric combustion) is ~ 5.4.

The instantaneous results obtained with a global-chemistry (one-step reaction model[7,8]) are shown in Figs. 8 and 9 for annular air velocities of 10 and 20 m/s, respectively. Velocity field and temperature are shown in Figs. 8(a) and 9(a) in the upper and lower halves, respectively. In general, the center fuel jet is mixing with the neighboring air jets and burning as two distinct flames. The instantaneous-temperature field suggests that the flow in the cavity has a large vortex generated by the high-speed annulus air flow and several small vortices that have developed primarily from the interaction of fuel and air jets injected into the cavity.

The scalar dissipation rate (χ) associated with these flows is calculated using the following expression;

$$\chi = 2D_{eff}\left[\left(\frac{d\xi}{dz}\right)^2 + \left(\frac{d\xi}{dr}\right)^2\right]$$

Here, mixture fraction (ξ) is defined as the fraction of the mass at any location that is originated from the fuel jet and is calculated from the following expression

$$\xi = X_{C_3H_8} + X_{iC_3H_7} + X_{nC_3H_7} + X_{C_3H_6} + X_{C_3H_5} + X_{C_3H_4} + X_{C_3H_3} + \tfrac{2}{3}(X_{C_2H} + X_{C_2H_2} + X_{C_2H_3} + X_{C_2H_4} + X_{C_2H_5} + X_{C_2H_6} + X_{CHCO}) + \tfrac{1}{3}(X_{CH_4} + X_{CH_3} + X_{CH_2} + X_{CH} + X_{CH_2O} + X_{CHO} + X_{CO_2} + X_{CO} + X_{CH_2OH} + X_{CH_3OH})$$

Here, X_i represents the mole fraction of i^{th} species. The mixture fraction (ξ) used in the above equation is a conserved scalar describing the state of mixing between the fuel and oxidizer. One might notice a great variation in the choice of conserved scalars in the literature.

The distributions of mixture fraction and scalar dissipation rate for the 10-m/s and 20-m/s cases are shown in Figs. 8(b) and 9(b), respectively. The higher annuls velocity in the latter case is generating more fluctuations in the cavity flow as noted from the scalar-dissipation-rate plots. The concentrations of fuel and oxygen are shown in Figs. 8(c) for 10-m/s case and those for 20-m/s case are shown in Fig. 9(c).

Using the solutions shown in Figs. 8 and 9 as initial flows, calculations with finite-rate chemistry are made for the 10 m/s and 20 m/s annular-air-flow cases. Surprisingly, calculations made for the latter case initiated flame extinction in the neighborhood of the injection-jet bases and quickly the entire flame got extinguished. Results obtained for the 10-m/s case at two instants are shown in Figs. 10 and 11. In general, the flame predicted by the global-chemistry model in the shear layer between the annular and cavity flows near the forebody is extinguished in the finite-rate-chemistry calculations. The OH seems to form in thin regions in the cavity.

Summary

Unsteady flow inside and around the cavity, in general, leads to a higher drag coefficient and in combustors creates further problems related to blowout and poor combustion efficiency. It is known that the unsteadiness of the flow can be reduced by proper cavity design. The dynamics of the vortices formed inside and around the cavity was studied using a time-dependent, axisymmetric CFDC code. The geometry used in this study was an axisymmetric, center-body trapped-vortex combustor employed by Hsu et al. A large number of grid points with z and r ~ 0.25 mm was used to capture the vortical structures having length scales that are an order of magnitude smaller than the height of the cavity. Fuel and air were

injected into the cavity from three locations. A detailed-chemical-kinetics model involving 33 species and 92 reversible reactions for propane combustion is used to investigate the flame-stability characteristics. It was found that this chemistry model was not sufficient to yield stable combustion for the velocity conditions at which experiments have provided stable combustion. However, at a lower annular velocity (i. e., at 10 m/s) the detailed-chemistry calculations resulted in stable flames similar to those observed in the experiments and are also similar to the ones obtained using a global-chemistry model.

Acknowledgments

This work was supported, in part, by Air Force Contract F33615-95-C-2507 and the Air Force Office of Scientific Research.

References

1. Hsu, K. Y., Goss, L. P., Trump, D. D., and Roquemore, W. M., "Characteristics of a Trapped-Vortex Combustor," Journal of Propulsion and Power, Vol. 14, No. 1, 1998.
2. Rohsenow, W. M., Fink, C. H., and Pollis, S. R., "Flow Through Two Orifices in Series," ASME Paper No. 51-A-87, 1951.
3. Migay, V. K., "Study of Ribbed Diffusers," (in Russian), *Toploenergetika*, No. 10, 1962, English Translation issued as A.R.C. Paper 25, p. 382, 1963.
4. Mair, W. A., "The Effect of a Rear-Mounted Disc on the Drag of a Blunt-Based Body of Revolution," The Aeronautical Quarterly, Vol. 10, Pt. 4, Nov., 1965, pp. 350-360.
5. Roshko, A. and Koenig, K., "Interaction Effects on the Drag of Bluff Bodies in Tandem," Symposium on Aerodynamic Drag Mechanisms of Bluff Bodies and Road Vehicles, General Motors Research Laboratories, Sept. 27-28, 1976.
6. Little, B. H., and Whipkey, R. R., "Locked Vortex Afterbodies," Journal of Aircraft, Vol. 16, No. 5, 1979, pp. 296-302.
7. Katta, V. R., and Roquemore, W. M., "Numerical Studies on Trapped-Vortex Concepts for Stable Combustion," Journal of Engineering for Gas Turbines and Power, Vol. 120, No. 1, Jan. 1998, p. 60.
8. Katta, V. R., and Roquemore, W. M., "Numerical Studies on Trapped-Vortex Combustor," AIAA Paper No. 96-2660, 32nd AIAA Joint Propulsion Meeting, Lake Buena Vista, FL, July 1-3, 1996.
9. Leonard, B. P., "A Stable and Accurate Convective Modeling Procedure Based on Quadratic Upstream Interpolation," Computer Methods in Applied Mech. and Engineering, Vol. 19, 1979, p. 59.
10. Katta, V. R., Goss, L. P., and Roquemore, W. M., "Numerical Investigations of Transitional H_2/N_2 Jet Diffusion Flames", AIAA Journal , Vol. 32, 1994, pp. 84-94.
11. Spalding, D. B., "A Novel Finite Difference Formulation for Difference Expressions Involving Both First and Second Derivatives," International Journal of Numerical Methods in Engineering , Vol. 4, 1972, p. 551.
12. Peters, N., "Flame Calculations with Reduced Mechanisms--An Outline," in Reduced Kinetic Mechanisms for Applications in Combustion Systems, Lecture Notes in Physics, Springer-Verlag, New York, 1993.
13. Hirschfelder, J. O., Curtiss, C. F., and Bird, R. B., Molecular Theory of Gases and Liquids, John Wiley & Sons, Inc., New York, 1954.
14. Katta, V. R., Goss, L. P., and Roquemore, W. M., "Simulation of Vortical Structures in a Jet Diffusion Flame," International Journal of Numerical Methods in Heat and Fluid Flow, Vol. 4, 1994, p. 413.
15. Leung, K. M., Lindstedt, R. P., and Jones, W. P., "reduced Kinetic Mechanisms for Propane Diffusion Flames," in Reduced Kinetic Mechanisms for Applications in Combustion Systems, Lecture Notes in Physics, Springer-Verlag, New York, 1993.
16. Chelliah, H. K., Law, C. K., Ueda, T., Smooke, M. D., and Williams, F. A., in Twenty-Third Symposium (International) on Combustion, The Combustion Institute, Pittsburgh, PA, 1990, p. 503.

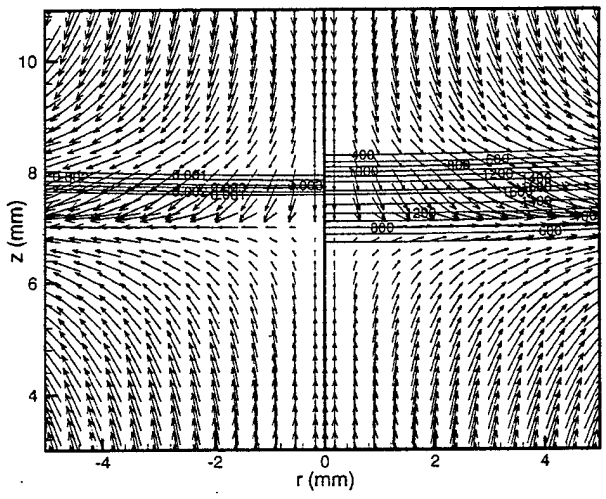

Fig. 1. Opposing-jet diffusion flame. OH (left) and T (right) are superimposed over velocity field.

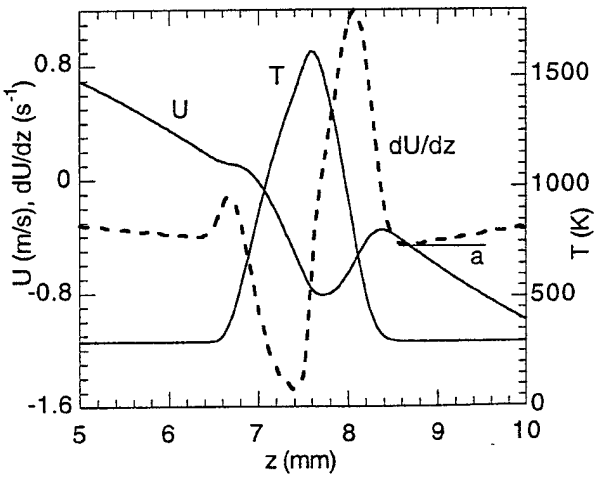

Fig. 2. Temperature and velocity along stagnation line.

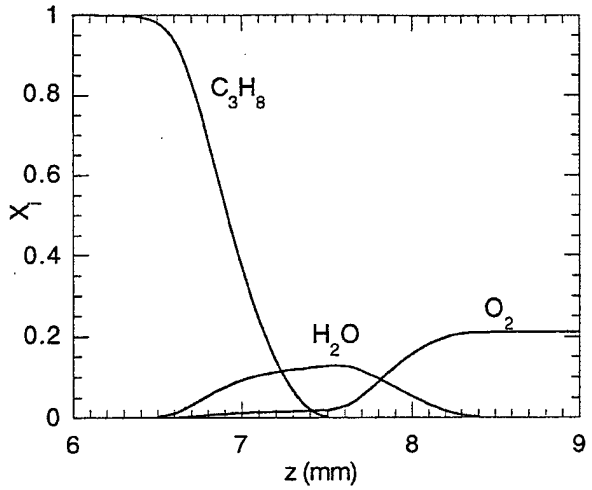

Fig. 3. Major species distributions along stagnation line.

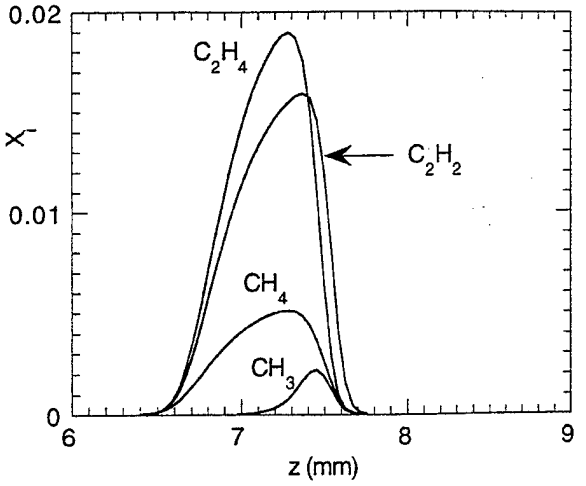

Fig. 5. Other species distributions along stagnation line.

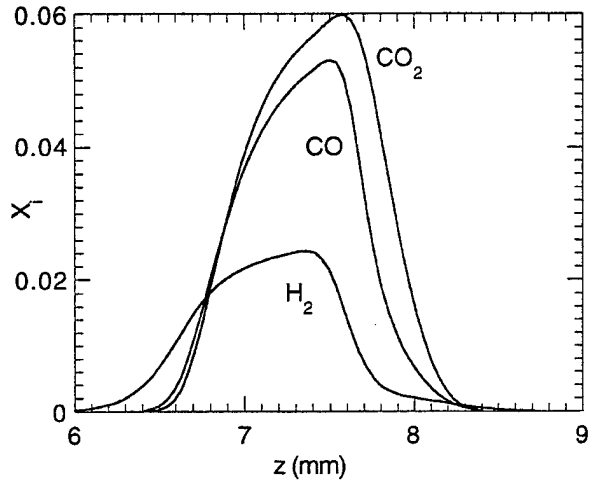

Fig. 4. Minor species distributions along stagnation line.

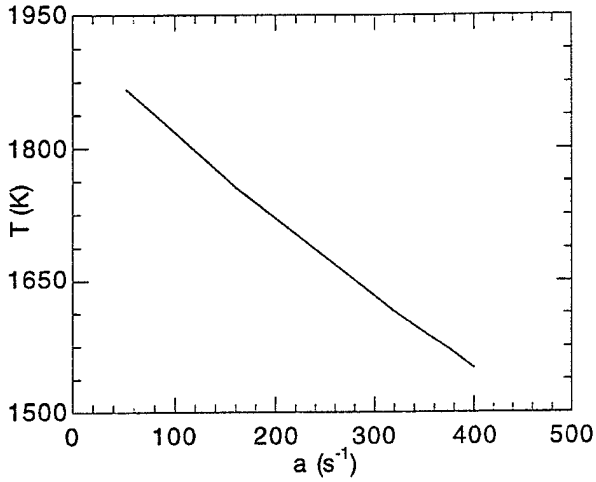

Fig. 6. Flame temperature at different strain Rates.

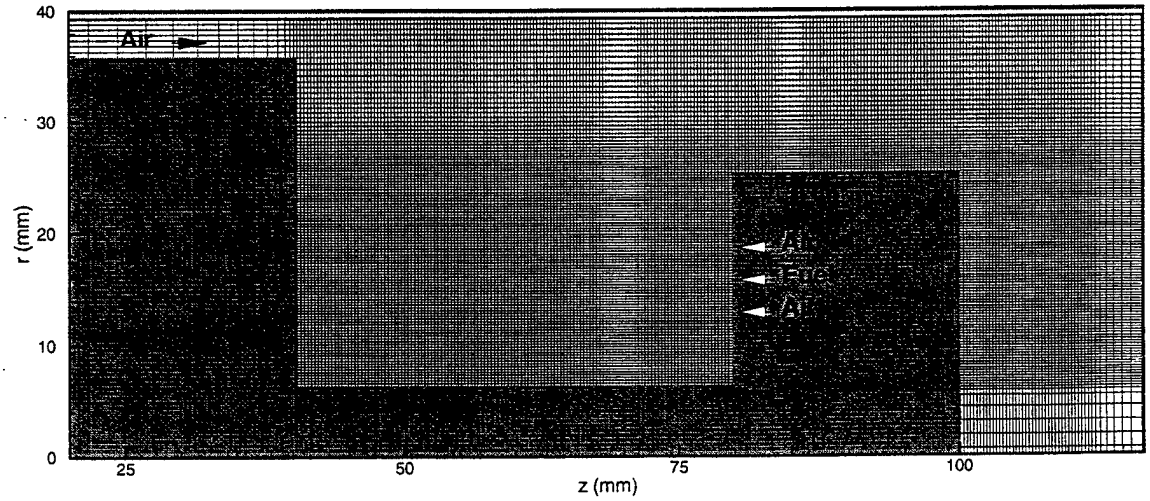

Fig. 7. Geometry and grid system used for the simulation of reacting flows inside trapped-vortex combustor.

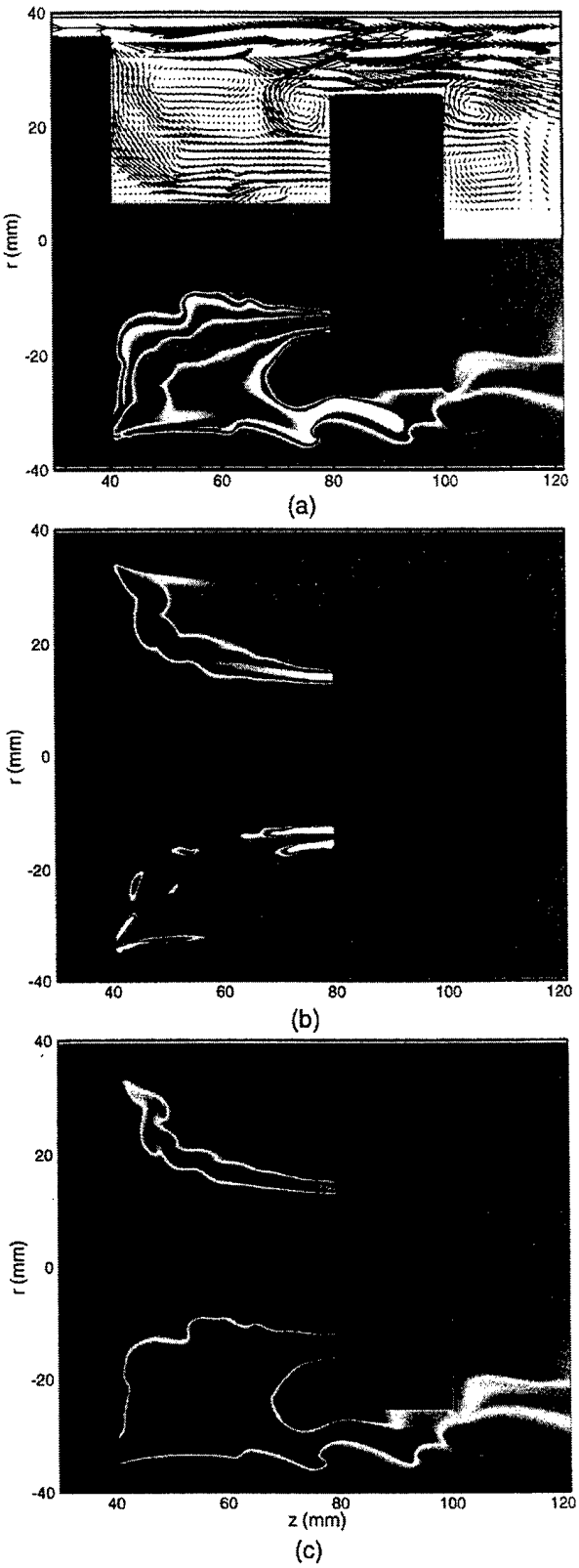

Fig. 8. Prediction using global-chemistry model. (a) Velocity and temperature; (b) Mixture fraction and scalar dissipation rate; (c) Fuel and oxygen. V_a = 10 m/s.

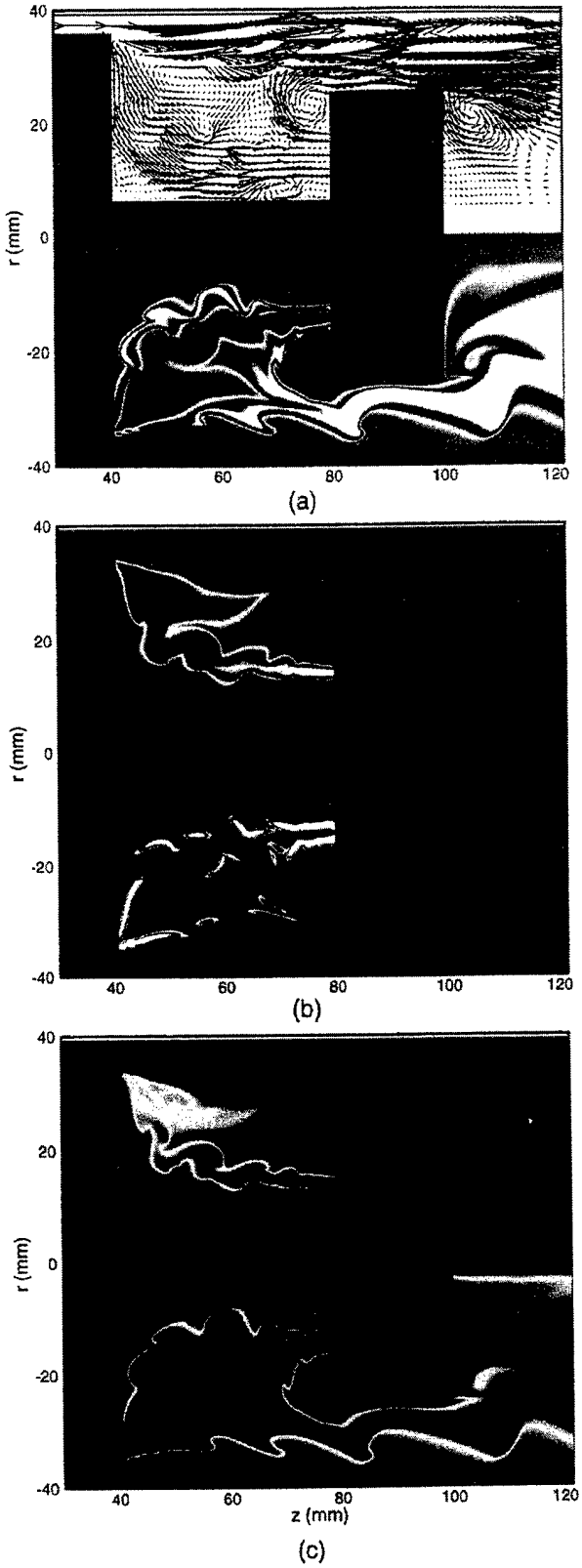

Fig. 9. Prediction using global-chemistry model. (a) Velocity and temperature; (b) Mixture fraction and scalar dissipation rate; (c) Fuel and oxygen. V_a = 10 m/s.

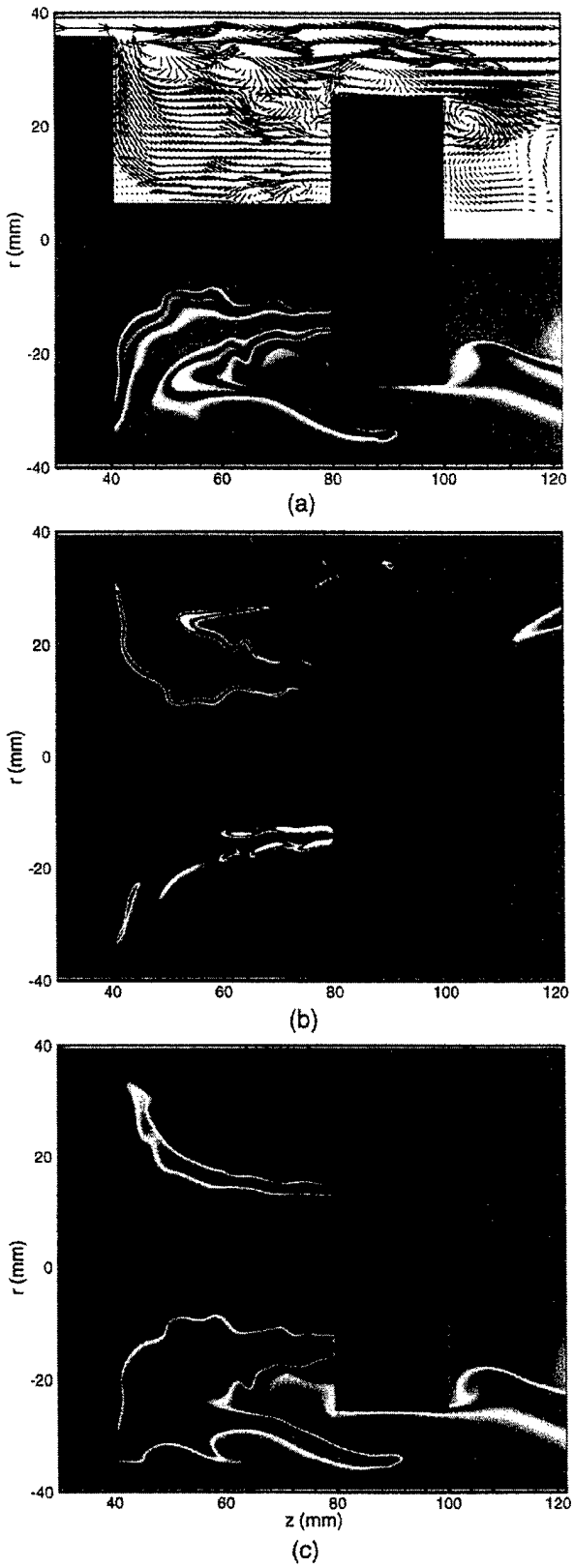

Fig. 10. Prediction using detailed-chemistry model. Flowfield at $t = t_0$. (a) Velocity and temperature; (b) OH and scalar dissipation rate; (c) Fuel and oxygen.

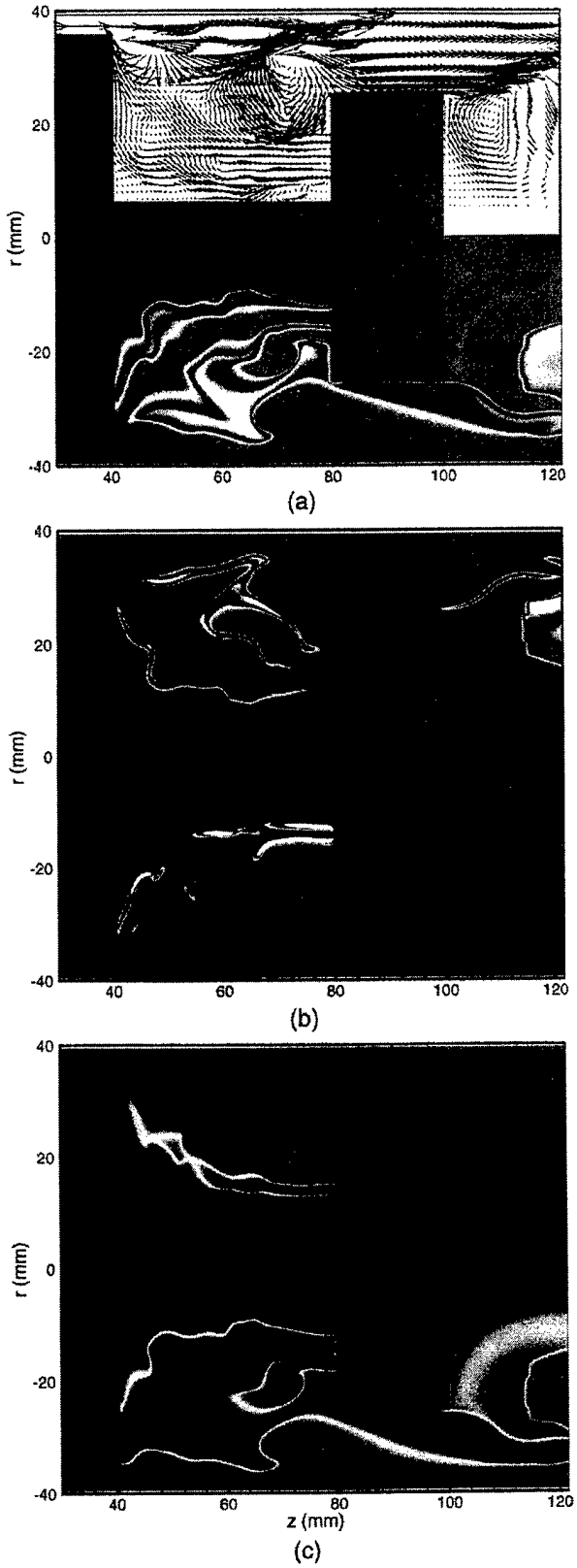

Fig. 11. Prediction using detailed-chemistry model. Flowfield at $t = t_0 + 1$ ms. (a) Velocity and temperature; (b) OH and scalar dissipation rate; (c) Fuel and oxygen.

4.1.5 Pulse Detonation Waves

One of the primary concerns in the design of pulse detonation engines (PDEs) is successful transmission of the detonation wave from a narrow predetonation chamber to a large main chamber. This problem was investigated and the results reported in a paper entitled "Numerical Studies on Cellular Detonation Wave Subjected to Sudden Expansion" (see pp. 982-985).

Presented at the 17th International Colloquium on the Dynamics of Explosions and Reactive Systems, Heidelberg, Germany, July 25-30, 1999. PUBLISHED WITH PERMISSION

Numerical Studies on Cellular Detonation Wave Subjected to Sudden Expansion

V. R. Katta*, L. P. Chin*, F. Schauer

Propulsion Directorate
Air Force Research Laboratory
Wright Patterson Air Force Base, OHIO

*Innovative Scientific Solutions, Inc.
e-mail: vrkatta@snake.appl.wpafb.af.mil
Tel: (937) 255-8781; Fax: (937) 255-3139

Abstract

One of the primary concerns in the design of PDEs is that a successful transmission of detonation wave from a narrow pre-detonation chamber to a large main chamber. This problem is investigated in the present paper by simulating the fate of a two-dimensional detonation wave when it is subjected to a sudden expansion. It is found that the reflection of transverse waves at the walls and their collision within the chamber are critical in sustaining a detonation wave in a wider channel. Results obtained for both successful and unsuccessful transitions are presented and the role of transverse waves is discussed.

Introduction

Pulse Detonation Engines (PDEs) operate at a higher thermal efficiency than the conventional constant pressure combustion engines. PDEs also provide a very high specific impulse thrust at operating frequencies of a few hundred Hz. They can be designed without the use of any rotating machinery or valves in the flow path. However, the design and operation of the PDEs is complicated by the unsteady, high-speed, pulsed combustion. In order to reduce the deflagration-to-detonation transition time, it is generally accepted that the combustible mixture in the main chamber needs to be ignited using detonation wave that was generated in a much-smaller, pre-detonation chamber. One of the primary concerns in the design of PDEs is that a successful transmission of detonation wave from pre-detonation chamber to main chamber. This problem is investigated in the present paper using numerical techniques.

The detailed cellular structure of gaseous detonations has been studied using experimental techniques in 1960's. However, only in the late 70's Taki and Fujiwara [1] and later Oran et al. [2] were able to simulate the cellular detonation structure for the two-dimensional case numerically. The cellular structure was established in their numerical computations by subjecting a one-dimensional ZND (Zeldovich, von Neumann, and Doring) wave to a large perturbation (by providing inhomogeneous region with different chemical properties). Once disturbed, the two-dimensional cellular structure develops naturally and it was found that the cell size is independent of the strength and the number of perturbations. In other words, cells can be newly generated when fewer than initial perturbations are provided, and if more than the stable number of cells are generated initially from the perturbations, some will get attenuated and eventually vanish to give the same stable number of cells. Thus, the number of cells in a cellular detonation wave is a consequence of the chemistry of the problem which is characterized by the reaction zone length scale for the ZND wave. The cell size is also found to be independent of the channel width, suggesting that doubling the channel width gives twice the number of cells across the width of the channel.

An important concern in using cellular detonation wave as a source for the burning of the reactants stems from the stability of the cellular detonation wave. Experimentally it was found that the stability of the detonation wave increases with tube diameter. In other words, the stability of a detonation propagating in a tube where the diameter is one cell size (λ) is not the same as a detonation with 13 cells propagating in a tube whose diameter is 13λ. The latter is found to be extremely stable even to large perturbations. For example, a sudden increase in the tube diameter will not quench the detonation, if $d > 13\lambda$. On the other hand, propagation of a one-cell detonation in a tube with $d \sim \lambda$ is found to be in the limiting conditions. As shown by St-Cloud et al. [3] and Moen et al. [4], a finite perturbation may lead to complete destruction of such detonations. Therefore, a small but sudden increase in tube diameter may result in a deflagration wave. In the present paper the stability of the detonation wave is investigated by numerically simulating the expansion of detonation having different number of cells.

The governing equations used are of the Euler type with exothermic chemical reactions. They can be expressed in the following form

$$\frac{\partial q}{\partial \tau}+\frac{\partial E}{\partial x}+\frac{\partial F}{\partial y}+H=0. \qquad (1)$$

Above equation represents conservation equations for mass, momentum, energy and the two progress variables depends on the variable (ρ, ρu, ρv, e, $\rho\beta$, and $\rho\alpha$) used as q.

The gas mixture considered here is a stoichiometric hydrogen-oxygen fuel diluted with Ar/He by 70%. This mixture is known to generate a well-behaving detonation. The hydrogen-oxygen reactions are represented by the Korobeinikov model consisting of two-step reaction mechanism; 1) a non-exothermic irreversible induction reaction where the progress variable (α) changes from 1 to 0, and 2) an exothermic reversible recombination reaction with its progress variable (β) changing from 1 to β_{eq}. This two-step reaction model has been successfully applied in the past to address two-dimensional unsteady detonation problems [1,5]. The Chapman-Jouguet (C-J) Mach number of the premixed gas mixture considered is 4.8. A grid system that moves at an uniform velocity of C-J value is used.

The present simulation used an explicit 2nd-order MacCormack predictor-corrector technique with 4th-order FCT (Flux Corrected Transport) scheme for capturing the shock waves accurately. All the calculations were started from a plain ZND detonation wave. A stable multi-dimensional detonation wave was generated by placing a few exothermic spots just upstream of the leading shock front. These exothermic spots perturbed the plane C-J wave and developed transverse waves. Once the propagation of detonation became stable it was then subjected to a sudden expansion having different area ratios. By using different size main chambers, studies on the survivability of detonation in the expansion environment were performed. The grids are constructed with $\Delta x=\Delta y=2L^*/9$. Here, L^* is the induction length--a characteristic distance related to the unburnt gas mixture.

Results and Discussion

Calculations were initially made for a channel width of $9L^*$. A stably propagating detonation having two transverse waves was established after ~1000 time steps. The interaction between the transverse and detonation waves results in a triple-shock structure and thereby a cellular detonation front. As the detonation propagates, these transverse waves travel toward the walls and reflect back when they interact with the walls. The structure of the detonation front propagating in the $9L^*$ channel is shown in Fig. 1 at three instants. The iso-pressure plots shown in Figs. 1(a), 1(b), and 1(c) visualize the motion of the two triple shock structures between the lower and upper walls. Note that the grid system is moving at Chapman-Jouguet velocity and the detonation front is always located in the same region with a small amount of fluctuations resulting from the deviation in local propagation velocity. The wave velocities obtained at upper and lower walls and at the mid section are plotted in Fig. 2. This shows that the reflection of a triple shock from the wall and the interaction between two triple shocks resulting in similarly enhanced combustion (increased propagation velocity) locally. However, the average non-dimensional propagation velocity is 4.96, which is close to the C-J velocity for the mixture considered.

Calculations were continued further on this detonation by suddenly increasing the channel width to $18L^*$. Results in the form of iso-pressure plots are shown in Fig. 3 at six different instants during the expansion process. It is clear that the detonation has transmitted successfully into a $18L^*$-wide channel from a $9L^*$-wide one. The entire transmission took about 100 μs and another 75 μs to establish a regular cellular structure in the $18L^*$-wide channel that is appropriate for that size. Note from Figs. 3(b) and 3(c) that while the detonation wave tends to dissipate in the larger tube, the propagation of higher-energy, triple-shock intersection points tends to strengthen the detonation. After a few passes of these intersection points on the detonation wave front, the latter establishes into a self-sustained wave with three triple-shock intersections.

The velocity modulation at the detonation wave front in the bottom, mid and top sections during the transition period are shown in Fig. 4 and those for the stable detonation in the larger tube are shown in Fig. 5. The higher-than-usual jumps in velocity in Fig. 4 indicate the formation of super-energy detonations. The smaller jumps in velocity at the tube mid section in Fig. 5 suggest that triple-shock points are not interacting at that location due to the odd number of cells. Similar calculations performed for main chambers > $18L^*$ could not yield successful transmission for detonation wave. An example of such unsuccessful transmission is shown in Figs. 6 and 7. In this calculation the channel size was suddenly increased from $9L^*$ to $20L^*$. As evident from Fig. 6(c), the reflection of transverse waves near the walls could not produce detonation wave and as a result the combustion waves further weakened as they propagated back into the channel.

References

[1] S. Taki, and T. Fujiwara, AIAA J. 16, 73 (1978).

[2] E. S. Oran, T. R. Young, J. P. Boris, J. M. Picone, and D. H. Edwards, Ninteenth Symposium (International) on Combustion, P. 573, The Combustion Institute, PA, 1982.

[3] J. P. Saint-Cloud, C. Guerraud, C. Brochet, and N. Manson, Astronautica Acta., 17, 487 (1972).

[4] I. O. Moen, M. Donato, R. Knystautas, and J. H. Lee, Eighteenth Symposium (International) on Combustion, p. 1615, The Combustion Institute.

[5] K. V. Reddy, T. Fujiwara, and J. H. Lee, Memoirs of the Faculty of Engineering, Nagoya University, Vol. 40, No. 1, 1988.

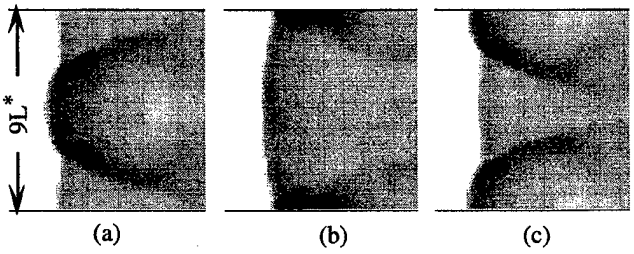

Fig. 1. Structure of detonation wave in a 9L*-wide channel at (a) t_0 μs, (b) t_0+1.6 μs, and (c) t_0+3.2 μs.

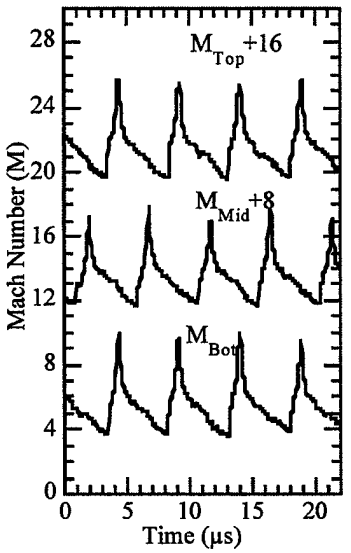

Fig. 2. Propagation velocity at different locations for 9L*-wide channel.

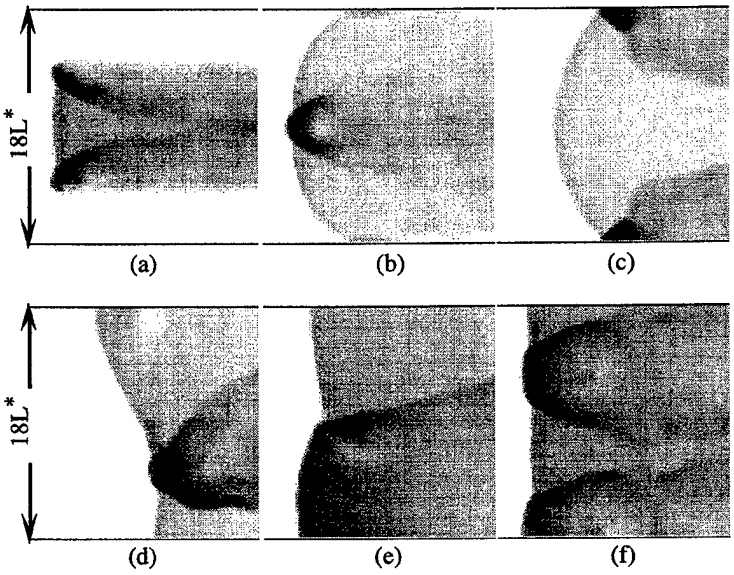

Fig. 3. Transmission of detonation wave from 9L*-wide to 18L*-wide channel. (a) 0, (b) 2.6, (c) 5.2, (d) 13, (e) 36, and (f) 175 μs.

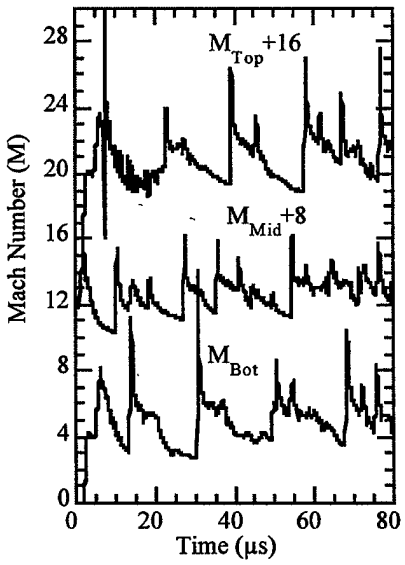

Fig. 4. Detonation propagation velocity at different locations during sudden expansion.

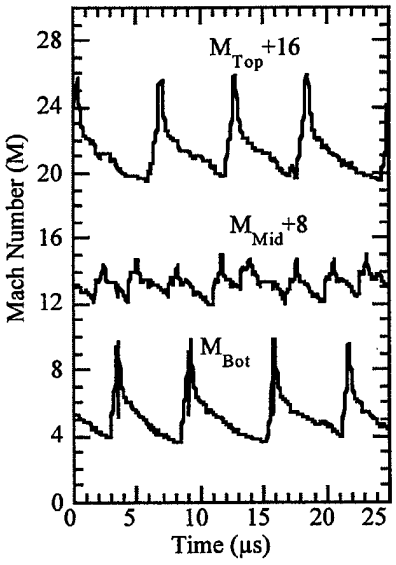

Fig. 5. Detonation propagation velocity at different locations for a 18L*-wide channel.

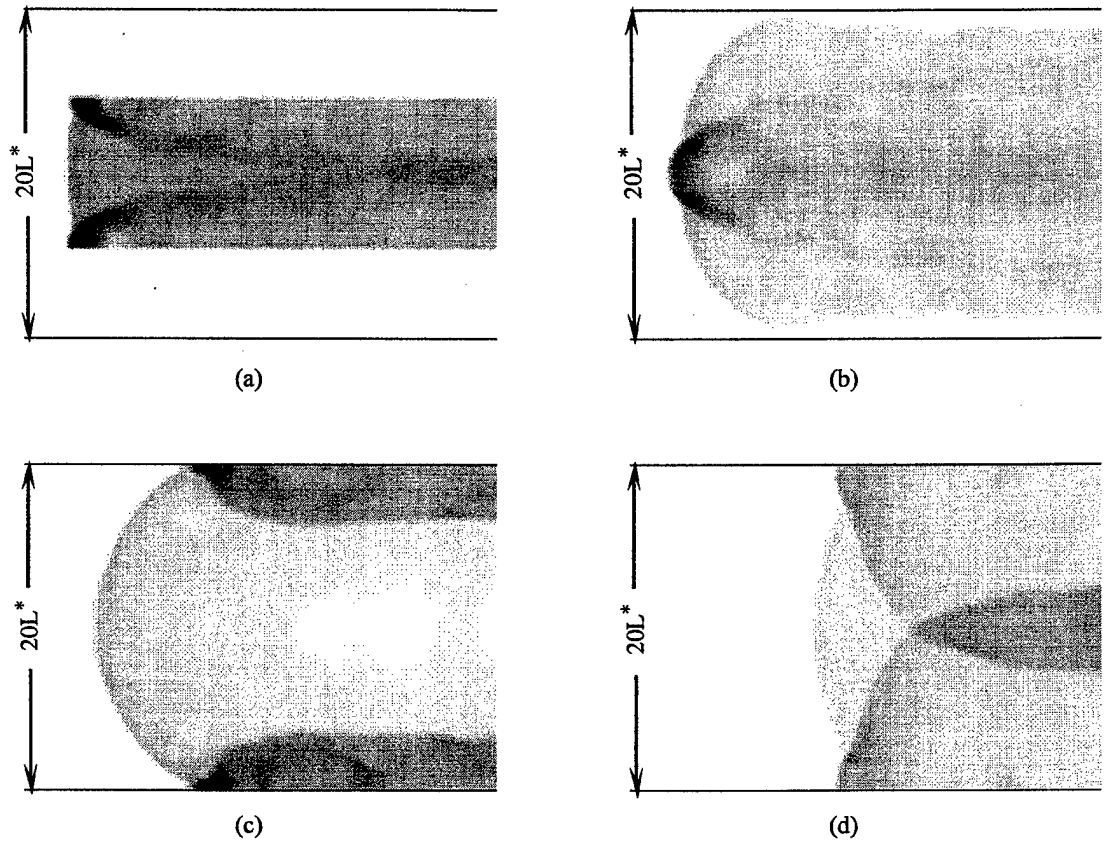

Fig. 6. Transmission of detonation wave from $9L^*$-wide to $20L^*$-wide channel. (a) 0 μs, (b) 2.8 μs, (c) 6.2 μs, (d) 11 μs. After 8 μs, detonation failed in the larger channel.

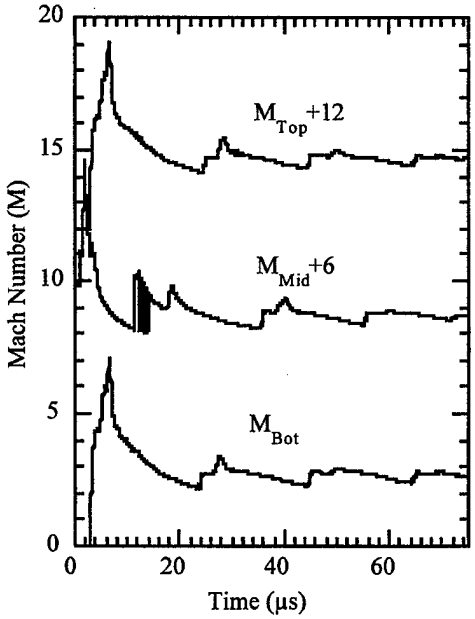

Fig. 7. Propagation velocity at different locations in $20L^*$-wide channel during sudden expansion.

4.1.6 Droplet and Two-Phase Flows

The maximum-entropy principle was used to model the size and velocity distribution of droplets generated by the disintegration of a cylindrical liquid jet; the results are reported in the paper entitled "Comparisons Between Experiments and Predictions Based on Maximum Entropy for the Breakup of a Cylindrical Liquid Jet" (see pp. 987-1004). The publication entitled "A Numerical Study of Droplet-Vortex Interactions in a Evaporating Spray" (see pp. 1005-1019) documents the results of a time-dependent axisymmetric numerical simulation of a n-heptane evaporating spray; also reported is an investigation into the droplet-vortex interactions that determine the structural and dynamic characteristics of a spray jet flow. Numerical simulations of droplet-vortex interactions in a heated jet are discussed in the publication entitled "Unsteady Spray Behavior in a Heated Jet Shear Layer: Droplet-Vortex Interactions" (see pp. 1020-1040). A numerical model based on the finite-volume approach was developed to study the evaporation process of interactive droplets and is discussed in the paper entitled "Numerical Modeling of Interactions Between Evaporating Droplets" (see pp. 1041-1051). The results of a direct numerical simulation of a droplet-laden swirling jet and the effects of swirl and two-phase momentum coupling on the jet dynamics and structural characteristics are reported in the publication entitled "Momentum Coupling Effects in a Two-Phase Swirling Jet" (see pp. 1052-1064). A numerical model based on the finite-volume approach was developed to study the evaporation and combustion process of interactive droplets; this study is documented in the paper entitled "Numerical Modeling of Interactive Burning Droplets" (see pp. 1065-1072). The dynamics and vaporization of both pure and multicomponent fuel droplets in a laminar-flow field are discussed in the paper entitled "Experimental Study of Pure and Multicomponent Fuel Droplet Evaporation in a Heated Air Flow" (see pp. 1073-1093). A droplet-laden swirling jet was numerically simulated, and the effects of swirl and two-phase momentum coupling on the jet dynamics and structural characteristics were assessed; the results are reported in the paper entitled "On the Dynamics of a Two-Phase, Nonevaporating Swirling Jet" (see pp. 1094-1114). A numerical model featuring the use of a composite grid system was developed and used to study the transport phenomena of liquid droplets in combustion systems. The results are discussed in the publication entitled "Numerical Modeling of Droplets in a Composite Grid System" (see pp. 1115-1121). A numerical study of the collision between two liquid droplets is documented in the paper entitled "Numerical Modeling of Collision Between Two Droplets" (see pp. 1122-1131).

Atomization and Sprays, vol. 5, pp. 603–620, 1995

COMPARISONS BETWEEN EXPERIMENTS AND PREDICTIONS BASED ON MAXIMUM ENTROPY FOR THE BREAKUP OF A CYLINDRICAL LIQUID JET

L. P. Chin
Systems Research Laboratories, Inc.

P. C. Hsing and R. S. Tankin
Northwestern University, Evanston, Illinois, USA

T. Jackson
Wright Patterson Air Force Base, Ohio, USA

A motion analyzer was used to measure the size and velocity distributions of droplets generated by the disintegration of a cylindrical liquid jet. The breakup of the liquid jet under consideration contains satellite droplets interspersed among the primary droplets, thus resulting in a bimodal distribution in size. The integrated velocity distribution of droplets is not Gaussian. The maximum entropy principle is used to model this phenomenon. Agreement between the model and the measurements is reasonably good.

INTRODUCTION

The process of producing droplets by the breakup of a cylindrical liquid jet is commonly called Rayleigh breakup [1, 2]. The use of a stimulated mechanism (forcing function) has been widely employed to obtain uniform droplets; this can be represented by $\delta(D - D_0)\ \delta(U - U_0)$, a coupled delta function where D_0 denotes uniform droplet size and U_0 denotes uniform droplet velocity. Such droplets are essential in calibrating spray sizing instruments and in studying the fundamental aspects of spray evaporation and combustion. In general, a stream of droplets having uniform size is difficult to achieve without external stimulation, even when experiments are carefully conducted in a vibration-isolated environment. Such a jet, as a result of nonlinear instability, frequently has a propensity to produce relatively small "satellite" droplets interspersed among the main large droplets [3]. The existence and behavior of these satellite droplets depends on the initial flow conditions and the physical properties of the liquid jet.

The maximum entropy principle has been used successfully to study the droplet size and velocity distributions for nonstimulated cylindrical water jets without satellite droplets [4]. Unforced disturbances and complicated nonlinear breakup mechanisms produce a stream of droplets that deviates from the ideal (deterministic) uniform distributions in size

This work was supported in part by the Air Force Office of Scientific Research under contract F49620-92-J-0389. The authors would like to thank Prof. Xiango Li of the University of Victoria in Canada for his valuable comments.

Copyright © 1995 by Begell House, Inc.

PUBLISHED WITH PERMISSION

NOMENCLATURE

A_e	area of prolate spheroid	k	nondimensional wave number
A_s	area of sphere	N	normalized droplet number
B	12/We	P_{ij}	joint probability
$\overline{C_{+1}}$	constant associated with constraint of primary (prolate spheroid) drops	S	information entropy
		S_m	mass source term
$\overline{C_{-1}}$	constant associated with constraint of satellite (spherical) drops	S_{mv}	momentum source term
		S_{ke}	kinetic energy source term
D	diameter of droplet	S_{se}	surface energy source term
$\overline{D}$	nondimensional droplet diameter (D/D_{30})	$\overline{U}$	nondimensional velocity (U/U_{jet})
D_c	diameter of liquid column near breakup	U_{jet}	velocity of liquid column at nozzle exit
D_{jet}	diameter of nozzle exit	We	Weber number $\left(\rho U_{jet}^2 D_{30}/\sigma\right)$
D_1	mean diameter of satellite droplets		
D_2	mean diameter of primary droplets	$\alpha_0, \alpha_1, \ldots, \alpha_6$	Lagrangian multipliers
D_{30}	mass mean diameter of droplets	λ	Wavelength of instabilities in liquid column
D_{32}	sauter mean diameter		

and velocity. The present study extends the use of the maximum entropy principle to a stream of primary and satellite droplets whose size and velocity distributions are not deterministic and thus are described by probability distribution functions.

The concept of information entropy was developed by Shannon [5], and Jaynes [6] later extended this concept to the well-known method of maximum entropy formalism. This formalism can be applied to problems that involve probability, i.e., where insufficient information is available to obtain exact solutions. Tribus [7] showed that the concepts of heat and temperature in thermodynamics could be defined through the formalism of maximum entropy. The maximum entropy formalism asserts that the least prejudiced (biased) or most appropriate probability distribution is the one that maximizes Shannon's entropy—subject to the given constraints imposed on a physical probabilistic system (or process). The maximum entropy formalism can be applied to a system (or process) about which the available knowledge or information is limited and insufficient to permit predictions that are certain to be correct by a conventional deterministic approach.

Although there is no way, at present, of proving the maximum entropy principle, its physical meaning can be understood (or interpreted) from the thermodynamic point of view by the fact that both entropies, one defined by Shannon and the other defined in classic thermodynamics, are equivalent. The second law of thermodynamics dictates that the entropy of an isolated system always increases for any natural processes. When the entropy of the system reaches its maximum value, the system is in thermodynamic equilibrium. Therefore, the probability distribution derived from the maximum entropy principle can be interpreted as the probability distribution for the system that reaches local equilibrium under given conditions (constraints). Since the equilibrium state is unique for a given set of conditions, the probability distribution corresponding to an equilibrium state is also unique.

In addition to applying the maximum entropy principle to the breakup of a cylindrical jet, the maximum entropy principle also has been used to model the spray from a pressure atomizer, and a skewed monomodal size distribution was derived [8–12]. The predicted

size distributions as well as the velocity distributions agreed with the experimental measurements [4, 8, 11, 12]. The experimental results reported in these earlier articles were obtained using a phase Doppler particle analyzer (PDPA). In a recent article by van der Geld and Vermeer [13], a size distribution function of a spray having satellite drops was derived using maximum entropy formalism. In their derivation, however, the size distribution for the primary droplets is assumed to be Gaussian. Maximum entropy theory was used to obtain the size distribution for the satellite drops; the final distribution is a composite distribution. In the study presented here, no assumption was made a priori with regard to either the primary or satellite droplet distributions. A single probability distribution function, not a composite type, was obtained that incorporates both primary and satellite drops.

The goal of this article is to examine a flow system having a strong bimodal size distribution. Rayleigh breakup of a cylindrical liquid jet with satellite droplets is an ideal candidate. This is essentially a simple spray, which, however, has complex size and velocity distributions. Stimulating the flow (piezoelectrically, acoustically, etc.) can produce very reproducible flows having a bimodal size distribution that incorporates essentially two delta functions—one for the primary drops and another for the satellite drops. These flows have been studied by conventional deterministic approaches—linear or nonlinear stability analyses [14–18]. However, a Rayleigh liquid jet that is not externally stimulated produces droplets that vary in size and velocity and thus are described by probability distribution functions that are amenable to the maximum entropy approach used in this study.

EXPERIMENT

Background

The experimental setup used in this study is similar to that described by Chin et al. [4]. In that setup, the nozzle assembly had an orifice that was 50 μm in diameter. The 50 μm orifice was formed in a bimetal nozzle plate by the fabrication technique called electroforming [19]. By adjusting the flow rate (air pressure) and observing the breakup with a microscope, one can locate a range of flow rates where satellite drops have occurred. However, when attempting to use the PDPA, three problems became apparent.

1. The satellite drop is usually captured by either the succeeding or preceding primary (large) drop within several wavelengths downstream of the breakup plane. Which primary drop captures the satellite drop depends on where the ligament separation occurs first—on the fore side or the aft side of the primary drop [3]. In the meantime, the effect of aerodynamic drag on a satellite drop is greater than that on a primary drop, which results in coalescence of the satellite drop and the primary drop—even if the ligament separation from the fore and aft primary drops occurs simultaneously. Because of the wide probe area of the PDPA ($\sim 10^{-2}$ cm^2), the measurement must be made within the first few wavelengths after the breakup plane of the liquid jet; otherwise the close proximity of the primary droplet interferes with the measurement of the satellite droplet.
2. Because the breakup plane fluctuates more than several wavelengths, the PDPA normally "sees" the cylindrical column of liquid (upstream of breakup) or the

large droplets without the satellites (too far downstream of breakup, where coalescence has occurred or is about to occur). This became obvious when we examined printouts obtained from an ICCD camera focused through a microscope on the breakup region.

3. The PDPA size measurements are based on the assumption that the droplets are spherical, which is not the case—particularly with regard to the primary (large) droplets. They oscillate between different modes ("ellipsoidal"-like shapes).

In the present study, the experimental setup has been modified to overcome the difficulties described above. Microscopic photography was used instead of PDPA to measure the droplet size and droplet velocity.

Nozzle Assembly

A schematic diagram of the apparatus used to study the evolution of droplets is illustrated in Fig. 1. A compressed-air supply forces the water from a reservoir through a filter to the nozzle assembly. The nozzle assembly, which is positioned vertically with the fluid exiting downward, has an inner diameter of about 2.54 cm. Inside the nozzle assembly are three fine stainless steel screens; above these screens are several layers of glass beads that are 0.47 cm in diameter. Thus nonuniformity and rotation of the liquid flow are removed. The orifice in the nozzle assembly consists of a sapphire orifice with a 0.08-cm hole. The flow is accurately controlled by a needle valve placed between the pressure source and the pressurized water tank, and a ball valve placed upstream of the water filter. The operating pressure drop across the nozzle assembly for this test was 7.6 kPa, yielding a volumetric flow rate of 2 ml/s. The volumetric flow rate was measured by weighing the total mass of water collected over a selected interval of time.

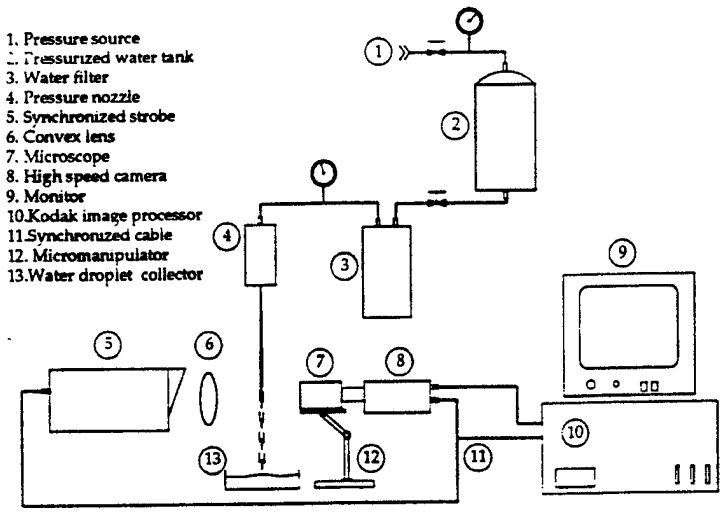

Fig. 1 Schematic drawing of the droplet generator setup.

Image Analysis System

A Kodak image analyzer was used to take pictures of the water droplets. The water issues from the nozzle assembly as a liquid column. This liquid column breaks up into droplets about 10 cm downstream from the orifice. The motion analyzer was set up about 10 cm downstream of the orifice to record the droplet formation in the vicinity of the breakup region. A strobe light having a very short pulse duration (less than a microsecond) was used to provide illumination of the droplets. The strobe flash is of sufficiently short exposure time to provide images of the droplets with little distortion due to droplet motion—which is particularly important for measuring the size of the satellite droplets. To increase the intensity of the strobe light at the test section, a convex lens was used to focus the strobe light to a circle about 2.54 cm in diameter at the plane of the droplets. The illuminating strobe light and the image camera were both triggered by a synchronized signal from the image processor. The images "seen" by the camera were enlarged 10-fold by a microscope. The strobe light, which back-lighted the droplets, was slightly offset from the line of sight.

As stated earlier, measurements must be made on droplets near the breakup region, otherwise many of the satellite drops may have coalesced with primary (large) drops. Due to the influence of inherent instabilities from various sources, the breakup plane is not fixed in space and was found to fluctuate about ±1.5 cm. This fluctuation was more than the view area seen through the microscope. Thus, some of the images had only a cylindrical column of water with no droplets (the image is upstream of the breakup plane), whereas some of the other images have satellite droplets on the verge of coalescing with the primary drop. Possibly some satellite drops may have already coalesced with primary drops and we missed counting them. In the experiment, a total of 1017 primary droplets and 877 satellite droplets were counted and analyzed. Thus, the measured number ratio of primary droplets to satellite droplets at breakup is 1.16.

Results and Analysis

Figure 2 shows the images taken at a framing rate of 1500 pictures per second. In these images the droplets are traveling from left to right. Both primary and satellite droplets appear. In Fig. 2*a*, no satellite drop is seen between droplets labeled "b" and "c" in the first frame nor between "e" and "d" of the third frame. In Fig. 2*b*, the satellite drop between droplets "b" and "c" in the first frame is about to coalesce with droplet "b" in the second frame. There are some instances where there are two satellite drops between the two primary drops.

The satellite drops are nearly spherical in shape; on the other hand, the primary drops are relatively large in size, but are far from spherical. It was necessary to characterize the drop sizes by an effective diameter. It was assumed that all the droplets are ellipsoidal in shape (either prolate or oblate spheriods), with their axes of symmetry along the flow direction (vertical in experiments and horizontal in images shown in Fig. 2). By measuring the major and minor axes of the droplet, the volume of the droplet was calculated. The diameter of a sphere with an equivalent volume was obtained and its diameter was defined as the effective diameter for the droplet. The accuracy of the measurements of the major and minor axes for an individual drop is ±22.5 μm.The standard deviation of the mean was computed from 50 such measurements on a typical satellite drop and primary drop—the values were 2.2 μm

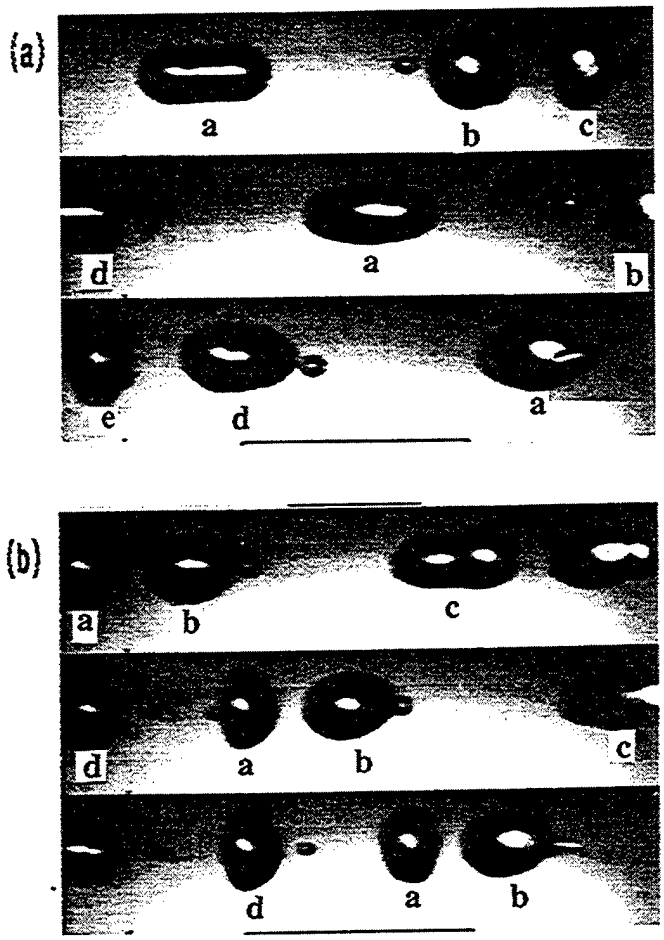

Fig. 2 Typical images taken with the Ektapro motion analyzer 10 cm from the nozzle.

(mean diameter is 0.32 mm) for the satellite drop and 3.5 μm (mean diameter is 1.35 mm) for the primary drop. Thus the measured effective diameters of the droplets are a good representation of the droplet sizes. There may be some question concerning their accuracy, but they do not have to be any more accurate because the effective diameters are nondimensionalized with the mass mean diameter (D_{30}), and D_{30} is computed based on the measured effective diameters. As a further verification of the measured diameters of the nonspherical primary drops, measurements were made far downstream (approximately 50 cm from the nozzle). At this location (see Fig. 3), the primary drops are round and their diameters (equal to effective diameters) can be measured directly (the increase in volume due to coalescence with a satellite drop is negligible). Although there may be coalescence between some primary drops at 50 cm from the nozzle, the diameters at the peak of the distribution curves in both cases (at 10 and 50 cm from the nozzle) agree at 1.37 mm.

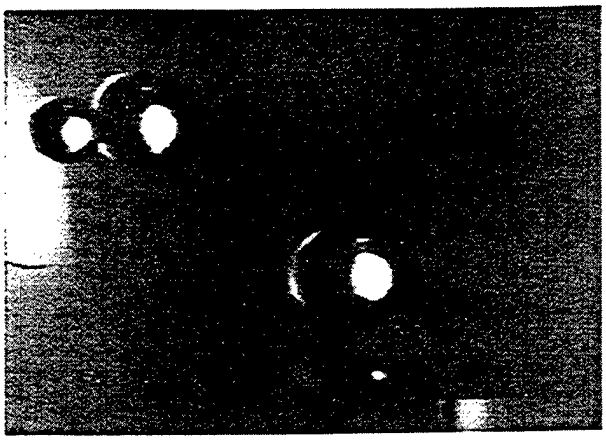

Fig. 3 Typical image taken with the Ektapro motion analyzer 50 cm from the nozzle.

The measured droplet size distribution is shown in Fig. 4. There are two peaks, one for the satellite droplets and the other for the primary droplets. The amplitude of the peak for the primary droplets is slightly larger than that for the satellite droplets. As mentioned earlier, a few satellite drops may not have been counted because of coalescence prior to the time of the images under consideration. Using the measured effective diameters, D_{30} was

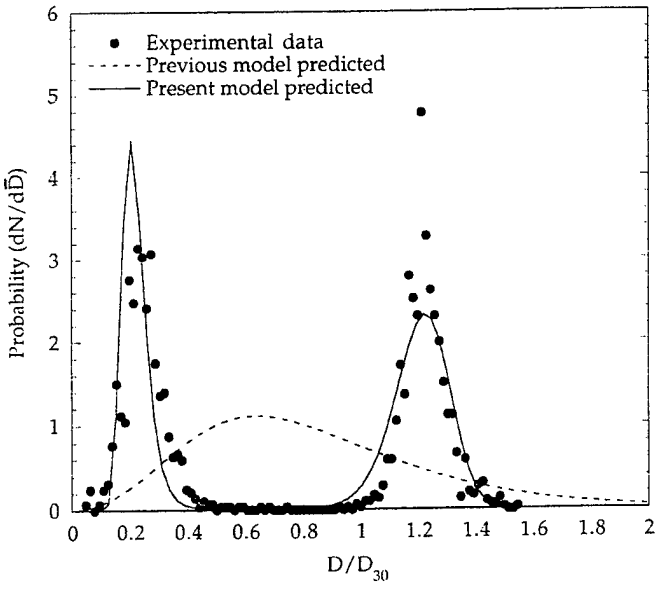

Fig. 4 Comparison between experimental and predicted droplet size distributions.

calculated to be 1.1 mm. From recorded images similar to those shown in Fig. 2, the velocities of the droplets at the breakup plane were measured. The mean velocity of the droplets at the breakup region was found to be 4.15 m/s. An experimentally measured velocity distribution will be presented later and compared with the predicted velocity distribution function.

In order to compare the drop size measurements with data in the literature, it is necessary to determine the nondimensional wave number, $k = \pi D_c/\lambda$. λ, the wavelength, was measured from data such as that shown in Fig. 5. λ equals 3.5 mm and D_c (the diameter of the liquid column near breakup) equals 0.79 mm; thus, k equals 0.71. This agrees well with the wave number at maximum growth rate ($k = 0.698$) under unforced Rayleigh breakup condition. Figure 6 is a plot showing data presented by Lefrance [18] and by Rutland and Jameson [17]. On this plot the theoretically predicted drops sizes (primary and satellite) from [18] are also presented, and these are seen as solid and dashed curves. Two data points obtained from our measurements are marked by triangles in Fig. 6, and they are found to agree with the data in [18] and [17]. This agreement further enhances confidence in our experimental data.

THEORETICAL MODEL

The maximum entropy principle is applied from one local equilibrium state (at the nozzle exit) to another local equilibrium state (where the droplets are formed) and does not become involved with the details of the liquid column instability characteristics such as the random onset and selective growth of undulations, the breakup mechanisms, the ligament formation between two primary drops, their final breakup into satellite droplets, etc. These processes are just the physical mechanisms required for the natural occurrence of the transition from one equilibrium state (at the nozzle exit) to another (where the droplets are formed). (The droplets that are formed are oscillating and thus not strictly in equilibrium. However, the energy due to the oscillations is small compared to the translational kinetic

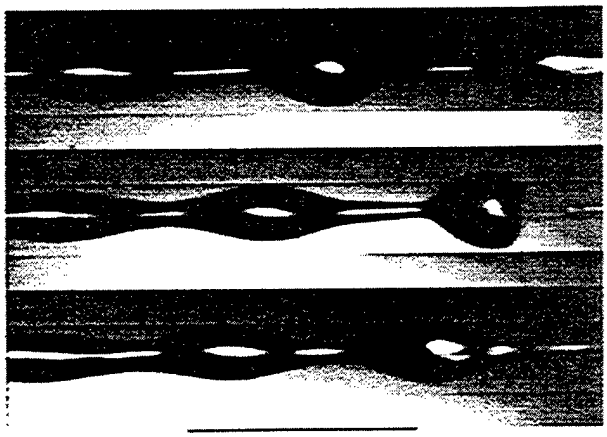

Fig. 5 Typical image of the surface of the cylindrical jet prior to breakup.

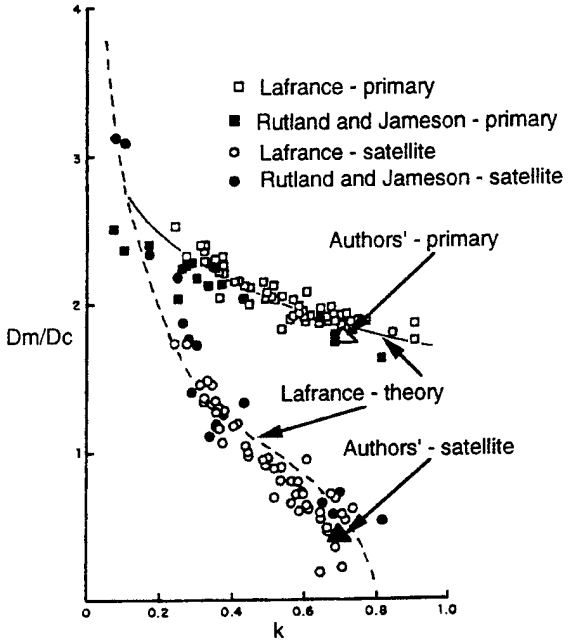

Fig. 6 Comparison of wave-number and results obtained in present experiments and those of Lafrance [18] and Rutland and Jameson [17].

energy. Therefore we modeled this problem as a quasi-equilibrium process—that is, the oscillating drops are infinitesmally near equilibrium.) The detailed physical processes of the transition plays no role in the maximum entropy approach, which only takes into account, from a statistical point of view, the macroscopic average quantities constraining an indeterminate process. In maximum entropy formalism, the transition from one local equilibrium state to another is linked through physical laws such as conservation of mass, momentum, and energy. We do not imply that the maximum entropy approach will replace the conventional deterministic approach; whenever possible, the deterministic approach should be used. However, for a stochastic process such as the one under consideration, the experimental results are represented by a probability distribution function, for which a deterministic approach is not appropriate. For this problem, the maximum entropy approach may prove useful.

Detailed formulation and derivation of the maximum entropy principle, as presented here, have been published [4, 8, 20]. However, there is one significant modification for the model presented here. The previously presented model is derived based on the assumption that the droplets are spherical. In the present study, the satellite drops in most instances are nearly spherical; however, the primary (large) drops are far from spherical. Their actual shapes, which vary from frame to frame, are complicated and difficult, if not impossible, to describe mathematically. To account for these nonspherical shapes, two new constraints are introduced—one related to the surface/volume ratio of small droplets and the other related to the nonsphericity of large droplets.

1. Since the small drops (satellite) are nearly spherical, the area/volume ratio of a satellite drop is equal to $6/D$ (where D is the diameter of the droplet). Therefore, it was assumed in this model that the mean area/volume ratio for the group of small satellite droplets varies inversely with $\overline{D}$ (D/D_{30}). This constraint is dominated by small droplets ($\overline{D} \ll 1$).
2. It is known that the surface-to-volume ratio for a sphere is smaller than that of any other shape having the same volume. From the examination of experimental data, it is observed that the larger the drops, the greater is the deviation from spherical shape. A mathematical model for large droplets based on experimental observations can be established by describing the large droplet as a prolate spheroid having a major axis a and a minor axis b. The surface area for a prolate spheroid (A_e) is greater than the surface area of a sphere (A_s) having the same volume. The greater the ratio of the major axis to the minor axis, the greater is the ratio A_e/A_s. If we assume that the ratio between the major axis and the minor axis follows this relationship, $a/b = \delta D_{eq}^{\beta}$, as the droplet size increases, then it is found that the ratio A_e/A_s is proportional to D_{eq} as shown in Fig. 7. D_{eq} is defined as the diameter of a sphere having the same volume as the prolate spheroid. The proportionality between A_e/A_s and D_{eq} depends on the values of δ and β, which indicate the degree of deviation for the shape of droplet from a sphere. It is clearly seen in Fig. 7 that the curves are approximately linear with D_{eq}. Therefore, as a second constraint, we assumed that A_e/A_s varies linearly with $\overline{D}$ ($\overline{D} = D_{eq}/D_{30}$). This constraint is dominated by large (primary) droplets.

A schematic drawing for the breakup of a liquid jet and its control volume is shown in Fig. 8. The control volume begins at the orifice and extends several (wavelengths

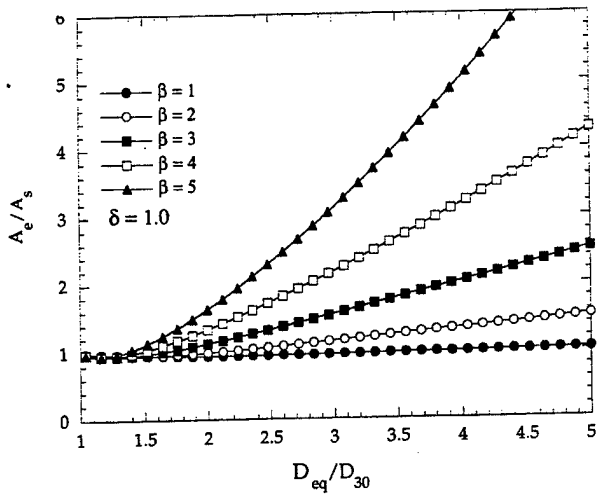

Fig. 7 A plot of A_e/A_s versus D_{eq}, where A_e is the area of a prolate spheroid, A_s is the area of a sphere having the same volume, a and b are the major and minor axes of the spheroid, and $a/b = \delta D_{eq}^{\beta}$.

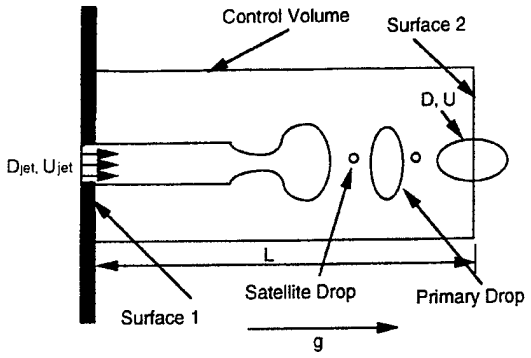

Fig. 8 Schematic drawing of the control volume chosen in this study to model the breakup of a liquid jet into droplets.

downstream of breakup. The liquid jet that enters the control volume through surface 1 has a diameter D_{jet}, and velocity U_{jet}. The droplets that emerge from the control volume through surface 2 have diameter D and velocity U. Because of the existence of individual droplets crossing surface 2, the mass, momentum, and energy leaving the control volume are not constant in time. Not only are there variations in diameter and velocity within the primary and satellite droplets, but at some instances the primary drop crosses surface 2 (as in Fig. 8) and at other instances the satellite drop crosses surface 2. Thus there are changes of these quantities (mass, momentum, kinetic energy flux, and surface energy flux) within the control volume in time. To maintain steady-state formulation, the conservation equations employed here will be derived using a time-averaged base.

Constraints Selected in Maximum Entropy Formulation

The entropy defined by Shannon [5] is expressed in the form

$$S = -K\sum_i \sum_j P_{ij} \ln\left(P_{ij}\right) \tag{1}$$

where S is called the information entropy, K is a constant, and P_{ij} is the relative frequency or joint probability of the occurrence of certain realizations (or results). The goal is to find the joint probability distribution, P_{ij}, that is realized with the greatest probability. Hence it is required that S is an extreme under whatever constraints are imposed in the physical system considered. Similar to the constraints used in the previous study for a liquid cylindrical jet [4] without satellite droplets, the balance of mass flux, momentum flux, and energy fluxes between the nozzle exit and the liquid breakup plane (in Fig. 8) can be expressed as follows:

Mass flux:
$$\frac{\pi}{6}\rho \dot{n} \sum\sum P_{ij} D_i^3 = \dot{m} + S_m = \frac{\pi}{4}\rho D_{jet}^2 U_{jet} + S_m \tag{2}$$

Momentum flux:
$$\frac{\pi}{6}\rho \dot{n} \sum\sum P_{ij} D_i^3 U_j = \dot{m} U_{jet} + S_{mv} = \frac{\pi}{4}\rho D_{jet}^2 U_{jet}^2 + S_{mv} \tag{3}$$

Kinetic energy flux: $$\frac{\pi}{12}\rho\dot{n}\sum\sum P_{ij}\,D_i^3\,U_j^2 = \frac{1}{2}\dot{m}U_{\text{jet}}^2 + S_{ke} = \frac{\pi}{8}\rho D_{\text{jet}}^2\,U_{\text{jet}}^3 + S_{ke} \tag{4}$$

Surface energy flux: $$\pi\sigma\dot{n}\sum\sum P_{ij}\,D_i^2 = \pi\rho D_{\text{jet}}U_{\text{jet}} + S_{se} \tag{5}$$

In these constraints, P_{ij} represents the joint probability of finding a droplet having diameter D_i and velocity U_j; D_{jet} and U_{jet} are the diameter of the nozzle exit and the mean liquid velocity leaving the nozzle exit; ρ and σ are the density and the surface tension of the liquid at room temperature; $\dot{n}$ is the number of droplets produced per unit time. The source terms, S_m, S_{mv}, S_{ke}, and S_{se}, account for the transport effects of mass, momentum, and energy between the two phases (liquid and gas) in the region of continuous liquid jet column. In addition, the sum of probability equals 1; that is, $\sum\sum P_{ij} = 1$.

The two new constraints mentioned above can be expressed as follows:

Spherical droplets: $$\dot{n}\sum\sum P_{ij}\left(\frac{A}{V}\right)_i \propto \dot{n}\sum\sum P_{ij}D_i^{-1} = \dot{n}\,C_{-1}\,D_{30}^{-1} \tag{6}$$

Nonspherical droplets: $$\dot{n}\sum\sum P_{ij}\left(\frac{A_e}{V_s}\right)_i \propto \dot{n}\sum\sum P_{ij}D_i^{+1} = \dot{n}\,C_{+1}\,D_{30}^{+1} \tag{7}$$

D_{30} (mass mean diameter) and U_{jet} (initial mean liquid velocity) are chosen to nondimensionalize the size ($\overline{D} = D/D_{30}$) and velocity ($\overline{U} = U/U_{\text{jet}}$) of the droplets, respectively. Thus, the constraint of normalization can be expressed in integral form as $\iint f\,d\overline{D}\,d\overline{U} = 1$.

Since the droplets are assumed to be produced in a saturated air environment, there is no mass flux loss or gain during the breakup process, and, the mass flow rate at surface 1 and surface 2 are equal on a time-averaged basis ($S_m = 0$). The constraints defined in Eqs. (2)–(7) have the following integral form:

$$\iint f\overline{D}^3\,d\overline{D}\,d\overline{U} = 1 \tag{8}$$

$$\iint f\overline{D}^3\overline{U}\,d\overline{D}\,d\overline{U} = 1 + \overline{S}_{mv} \tag{9}$$

$$\iint f\overline{D}^3\overline{U}^2\,d\overline{D}\,d\overline{U} = 1 + \overline{S}_{\text{ke}} \tag{10}$$

$$B\iint f\overline{D}^2\,d\overline{D}\,d\overline{U} = 2B/3\overline{D}_{\text{jet}} + \overline{S}_{\text{se}} \tag{11}$$

$$\iint \left(f/\overline{D}\right)d\overline{D}\,d\overline{U} = C_{-1} \tag{12}$$

$$\iint f\overline{D}\, d\overline{D}\, d\overline{U} = C_{+1} \tag{13}$$

Here, $B = 12/\mathrm{We}$ and $\mathrm{We} = \rho U_{\mathrm{jet}}^2 D_{30}/\sigma$ in Eq. (11). f is the continuous joint probability density function (PDF) of P_{ij}. By maximizing Shannon's entropy (S) subject to the above constraints [Eqs. (8)–(13)], f will have the following form:

$$f = 3\overline{D}^2 \exp\left(-\alpha_0 - \alpha_1\overline{D}^3 - \alpha_2\overline{D}^3\overline{U} - \alpha_3\overline{D}^3\overline{U}^2 - \alpha_4 B\overline{D}^2 - \alpha_5\overline{D}^{+1} - \alpha_6\overline{D}^{-1}\right) \tag{14}$$

Further discussion of the constraint given in Eq. (12) is necessary because this constraint is similar to one used by Sellens [11]. However, the physical motivation is entirely different. In Sellen's formulation this constraint is introduced to reduce his PDF at small droplet sizes—otherwise the PDF does not go to zero as droplet sizes go to zero. In our formulation, the PDF goes to zero as droplet sizes go to zero without this constraint [Eq. (12)]. The two new constraints introduced in this model account for the sphericity of the small satellite drops [Eq. (12)] and the nonsphericity of the large primary drops [Eq. (13)].

Estimates of Source Terms and Constants: $\overline{S}_{mv}$, $\overline{S}_{\mathrm{ke}}$, $\overline{S}_{\mathrm{se}}$, C_{-1}, and C_{+1}

In order to predict the droplet size distribution from a liquid cylindrical jet, the quantities on the right-hand side of the constraints [Eqs. (8)–(13)] are required to be known. Similar to the procedure used in the previous studies [4, 8], the source terms and the two constants C_{-1} and C_{+1} are estimated based on some measured mean droplet data, such as mass mean diameter (D_{30}), Sauter mean diameter (D_{32}), mean velocity (U_m), etc. The following source terms were obtained (explanation will follow): $\overline{S}_{mv} = 0.037$, $\overline{S}_{\mathrm{ke}} = 0.08$, $\overline{S}_{\mathrm{se}} = 0.041$, $C_{-1} = 2.23$ and $C_{+1} = 0.76$.

The values of $\overline{S}_{mv}$ and $\overline{S}_{\mathrm{ke}}$ were obtained from the measurements of U_{jet} and U_m. Using the control volume shown in Fig. 8, and knowing $\dot{m}$ and the velocities into and out of the control volume ($U_{\mathrm{jet}} = 4.0$ m/s and $U_m = 4.15$ m/s), $\overline{S}_{mv}$ and $\overline{S}_{\mathrm{ke}}$ were computed. They were found to be 0.037 and 0.08, respectively. Since total energy must be conserved for the sum of kinetic energy, surface energy, and potential energy ($2\,gh/U_{\mathrm{jet}}^2 = 0.12$), $\overline{S}_{\mathrm{se}}$ is determined to be about 0.04.

There are two ways of evaluating C_{-1} and C_{+1}.

1. C_{-1} and C_{+1} can be estimated from measured values of D_{30} and D_{32}. In this case, D_{30} and D_{32} were found to be 1.10 and 1.33 mm, respectively. If one assumes that the number of satellite drops equals the number of primary drops, then

$$D_{30} \approx \left(\frac{D_1^3 + D_2^3}{2}\right)^{1/3} \tag{15}$$

$$D_{32} \approx \frac{D_1^3 + D_2^3}{D_1^2 + D_2^2} \tag{16}$$

where D_1 is the mean diameter of the satellite drops, and D_2 is the mean diameter of the primary drops. Solving Eqs. (15) and (16) for D_1 and D_2 yields $D_1 = 0.30$ mm and $D_2 = 1.37$ mm. Because

$$C_{-1} = \left(\frac{1}{D_1} + \frac{1}{D_2}\right) \times \frac{D_{30}}{2} \tag{17}$$

$$C_{+1} = \frac{D_1 + D_2}{D_{30}/2} \tag{18}$$

Eq. (17) yields $C_{-1} = 2.23$ and Eq. (18) yields $C_{+1} = 0.76$. In summary, to evaluate the constraints using this method, the following measurements are required: D_{32}, D_{30}, U_{jet}, U_m, and breakup length, h (where the measurements were made).

2. Equations (12) and (13) are used to calculate C_{-1} and C_{+1} directly from experimental measurements on individual droplets. This yields $C_{-1} = 2.49$ and $C_{+1} = 0.77$. The resulting distribution is essentially the same as that shown in Fig. 4.

It is very important to emphasize that the procedure described above is not merely a curve-fitting technique. Although the continuous joint probability distribution function [Eq. (14)] has seven constants (Lagrange multipliers $\alpha_0 - \alpha_6$), it was derived from a well-established statistical method in terms of a set of physical constraints. These constants cannot be chosen freely, but are solved according to the seven constraints imposed. If a pure curve-fitting method (e.g, least-squares method) is used to calculate the seven constants based on direct experimental measurements, the resulting distribution function will not be guaranteed to satisfy all the constraints [normalization and Eqs. (8)–(13)] required physically.

Domain of Integration

In this section we will respond to a point raised by van der Geld and Vermeer [13] regarding the sensitivity of the predicted size distribution function to the domain of integration. The limits of integration chosen to predict the droplet distributions are important only when the resulting probabilities do not approach zero near the integration limits. For the domain of droplet size, the upper limit should be chosen such that the PDF approaches zero at the limit of integration. The results presented in Figs. 7 and 8 of [13] clearly show several distributions that increase exponentially near the upper limit of integration. This, of course, is not physically reasonable. If we obtained such a result, which we did not, it would not be accepted as a correctly predicted distribution. The reasons for predicting such unrealistic distributions are twofold: (1) The spray quantities [right-hand sides of Eqs. (9)–(13)] in the set of constraints are not prescribed appropriately, that is, unreasonable estimates are made of the spray quantities; (2) an incomplete set of constraints are imposed, thus resulting in a distribution of improper functional form. In our opinion, it is not appropriate to justify the sensitivity of integration domains based on results (as presented in [13]) that were obtained using either unreasonable estimates of the spray quantities or an incomplete set of constraints. For the present model, if the predicted

droplet size distribution is physically reasonable (as in the case presented in this article as well as those in [4] and [8]), then the integration limits will not have an effect on the results.

In the integration domain for droplet velocity, the effect of integration limits appears only for small droplets ($\overline{D} \ll 1$), because the amplitude of velocity PDF for small droplet sizes approaches zero at both velocity limits very slowly. As a result, the velocity distribution for small droplets is much wider than that for large droplets (see Fig. 8*a* in [8]). To minimize the influence of the velocity domain, one can expand the velocity domain further such that the PDF becomes sufficiently small near the limits (an infinite velocity domain is ideal, but computationally impossible). It is important to emphasize, however, that the velocity domain has very little influence on the droplet size distribution as long as the domain is sufficiently large. The sensitivity of the predicted PDF on the integration domain as presented by van der Weld and Vermeer has not been observed by us.

RESULTS AND DISCUSSION

Once the source terms and constants in the constraints are determined, the droplet size distribution is obtained by integrating Eq. (14) over $\overline{U}$. This yields

$$\frac{dN}{d\overline{D}} = \frac{3}{2}\sqrt{\frac{\pi\overline{D}}{\alpha_3}}\,\theta\left(\overline{D},\overline{U}\right)\exp\left[-\alpha_0 - \left(\alpha_1 - \frac{\alpha_2^2}{4\alpha_3}\right)\overline{D}^3 - \alpha_4 B\overline{D}^2 - \alpha_5\overline{D}^{+1} - \alpha_6\overline{D}^{-1}\right] \quad (19)$$

where $\theta\left(\overline{D},\overline{U}\right) = \text{erf}\left(X_{\max}\right) - \text{erf}\left(X_{\min}\right)$ and erf(X) is the error function of X:

$$X_{\max} = \left(\overline{U}_{\max} + \frac{\alpha_2}{2\alpha_3}\right)\sqrt{\alpha_3\overline{D}^3} \qquad X_{\min} = \left(\overline{U}_{\min} + \frac{\alpha_2}{2\alpha_3}\right)\sqrt{\alpha_3\overline{D}^3} \quad (20)$$

Here, N is the normalized droplet number, and $\overline{U}_{\max}$ and $\overline{U}_{\min}$ are the integration limits.

The solid line in Fig. 4 shows the predicted size distribution from Eq. (19), where the values of the source terms, C_{-1}, and C_{+1} listed above, are used. One can see that there is reasonably good agreement between the experimental size distribution and the computed size distribution. A predicted size distribution having the same source terms without constraints C_{-1}, and C_{+1} is also shown in Fig. 4. This plot is not bimodal and does not agree with the experimental data. Thus, to obtain a bimodal size distribution for Rayleigh breakup of a cylindrical jet using the maximum entropy principle, one must introduce additional constraints such as C_{-1}, and C_{+1} in our model.

In Fig. 9 are plots of the experimental and computed velocity distributions obtained from the probability density function [Eq. (14)]. Again, it is seen that there is reasonably good agreement between experimental and computed velocity distributions. It should be noted that the velocity distribution for both the experimental and computed curves are broad at the base and merge rather abruptly into a rather narrow distribution that is not a Gaussian shape. To further explain this non-Gaussian shape, the joint probability distribution function, $f\left(\overline{D},\overline{U}\right)$, is plotted in Fig. 10. The velocity distributions for the satellite drops and the primary drops are Gaussian individually, but the integrated velocity distribution is a non-Gaussian distribution. Figure 10 shows that the satellite drops have a much

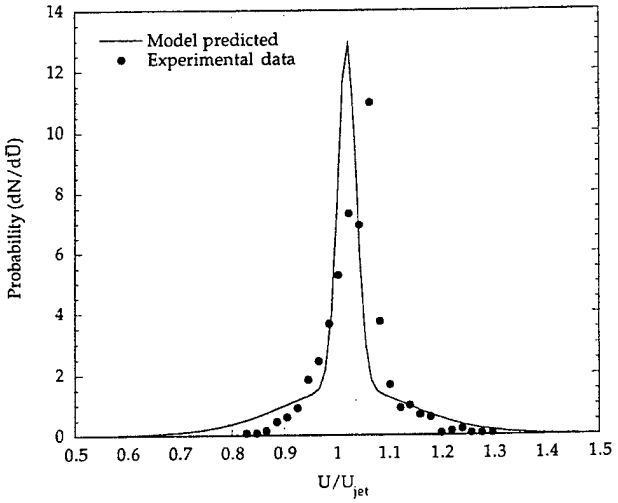

Fig. 9 Comparison between experimental data and predicted droplet velocity distribution.

broader velocity distribution than the primary drops. Physically, one would expect a broader velocity distribution for the satellite drops because their velocity variance depends to a large extent on where the ligament separation first occurs—on the fore side of the primary drop (giving the satellite a higher velocity) or on the aft side of the primary drop

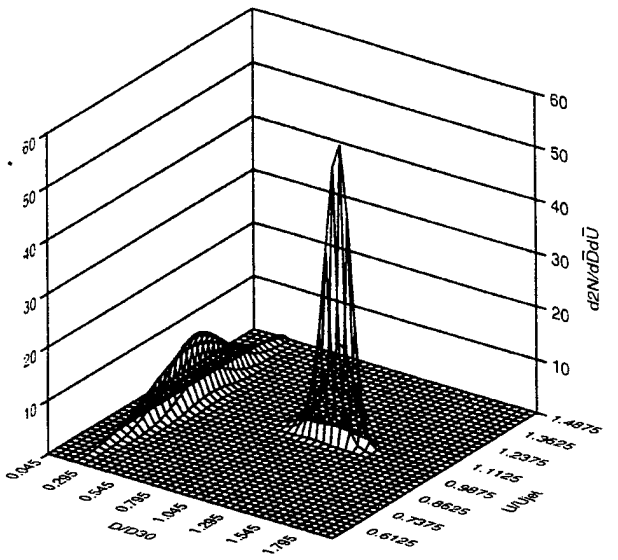

Fig. 10 Three-dimensional plot of predicted joint probability distribution function.

(giving the satellite a lower velocity). Thus, the maximum entropy solution predicts a velocity distribution that accounts for the effect of ligament separation without specifically considering this in the formulation of the problem. This illustrates the point that the detailed physical processes involving the transition from one equilibrium state to another equilibrium state play no role in the maximum entropy approach.

A question arises: What would happen if the constraints involving nonsphericity (C_{-1} and C_{+1}) were introduced to formulate a pressure atomizer experiment [8] where the measured size distribution is not bimodal? Figure 11 shows the predicted droplet size distribution (labeled Model A) presented in [8] without the constraints C_{-1} and C_{+1}. The curve labeled Model B is a plot where $C_{-1} = 2.10$ and $C_{+1} = 0.73$ (the other constraints in both models are kept the same). The values of C_{-1} and C_{+1} were obtained by evaluating Eqs. (12) and (13) from the measurement data for the pressure atomizer. Even though C_{-1} and C_{+1} were introduced, there is no bimodal size distribution (Model B)—it remains skewed monomodal. Thus the introduction of the constraints C_{-1} and C_{+1} does not necessarily result in a bimodal size distribution. A bimodal size distribution depends on the other constraints (involving conservation of mass, momentum, surface energy, and kinetic energy) as well.

Rayleigh breakup of a cylindrical liquid jet without satellites was also examined [4]. This system results in a distribution that is uniform in size and velocity. The values of C_{-1} and C_{+1} obtained from experimental data are 1^+ and 1^-, respectively. Using $C_{-1} = 1.04$ and $C_{+1} = 0.98$, the resulting droplet size (and velocity) is uniform—not exhibiting any bimodal shape.

In summary, the occurence of a bimodal size distribution depends on the entire set of constraints imposed, not just the introduction of C_{-1} and C_{+1}.

CONCLUSIONS

A model based on the maximum entropy formulation has been derived for a system experiencing Rayleigh jet breakup with satellite droplets. The agreement between theory

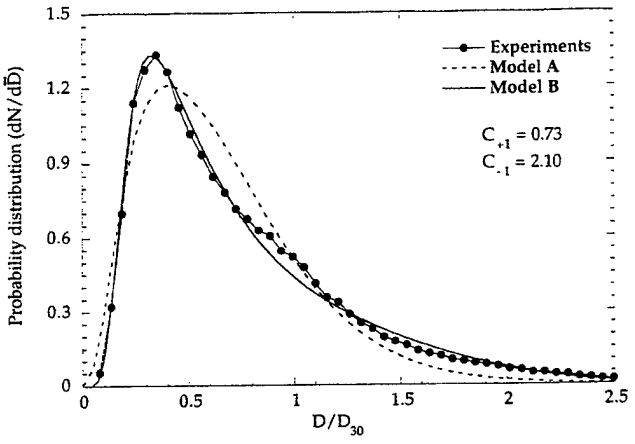

Fig. 11 Plot of computed and measured droplet size distribution from a pressurized atomizer.

and experiment is reasonably good. Both the computed velocity and the size distributions agree with the measured distributions. In order to obtain a bimodal size distribution function, it was necessary to modify the previous model [4] to account for the nonsphericity of the large droplets. Two new constraints as expressed in Eqs. (12) and (13) were introduced. The integrated velocity distributions from both the experiments and the model were not Gaussian. In conclusion, the maximum entropy model is very robust for predicting complicated droplet size and velocity distributions of sprays under a variety of flow conditions.

REFERENCES

1. L. Rayleigh, On the Instability of Jets, *Proc. London Math. Soc.*, vol. 10, 1879.
2. L. Rayleigh, Further Observations upon Liquid Jets, *Proc. R. Soc. London*, vol. 34, 1882.
3. D. B. Bogy, Drop Formation in a Circular Liquid Jet, *Annu. Rev. Fluid Mech.*, vol. 11, 1979.
4. L. P. Chin, P. G. LaRose, R. S. Tankin, T. Jackson, J. Stutrud, and G. Switzer, Droplet Distributions from the Breakup of a Cylindrical Liquid Jet, *Phys. Fluids A*, vol. 3, no. 8, 1991.
5. C. E. Shannon, A Mathematical Theory of Communication, *Bell System Tech. J.*, vol. 27, 1948; Also in D. Slepiom (ed.), *Key Papers in the Development of Information Theory*, IEEE Press, New York, NY, 1974.
6. E. T. Jaynes, Information Theory and Statistical Mechanics, *Phys. Rev.*, vol. 106, vol. 108, 1957.
7. M. Tribus, *Thermostatics and Thermodynamics*, Van Nostrand, New York, NY, 1961.
8. X. Li, L. P. Chin, R. S. Tankin, T. Jackson, J. Stutrud, and G. Switzer, Comparison between Experiments and Predictions Based on Maximum Entropy for Sprays from a Pressure Atomizer, *Combustion and Flame*, vol., 86, 1990.
9. R. W. Sellens and T. A. Brzustowski, A Prediction of Drop Size Distribution in a Spray from First Principles, *Atomization and Spray Technol.*, vol. 1, pp. 89–102, 1985.
10. R. W. Sellens and T. A. Brzustowski, A Simplified Prediction of Droplet Velocity Distributions in a Spray, *Combustion and Flame*, vol. 65, pp. 273–279, 1986.
11. R. W. Sellens, Prediction of the Droplet Size and Velocity Distribution in a Spray Based on the Maximum Entropy Formalism, *Particle Particle Syst. Charact.*, vol. 6, pp. 17–27, 1989.
12. R. W. Sellens, *Atomization and Sprays*, vol. 3, pp. 2910–310, 1993.
13. C. W. M. van der Geld and H. Vermeer, Prediction of Droplet Size Distributions in Sprays Using the Maximum Entropy Formalism: The Effect of Satellite Formation, *Int. J. Multiphase Flow*, vol. 20, pp. 363–381, 1994.
14. M. C. Yuen, Nonlinear Capillary Instability of a Liquid Jet, *J. Fluid Mech.*, vol. 33, p. 151, 1968.
15. E. F. Goedde and M. C. Yuen, Experiments on Liquid Jet Instability, *J. Fluid Mech.*, vol. 40, p. 495, 1970.
16. A. H. Nayfeh, Nonlinear Stability of a Liquid Jet, *Phys. Fluids*, vol. 13, p. 841, 1970.
17. D. F. Rutland and G. J. Jameson, Theoretical Prediction of the Size of Drops Formed in the Breakup of Capillary Jets, *Chem. Eng. Sci.*, vol. 25, p. 1689, 1970.
18. P. Lafrance, Nonlinear Breakup of a Laminar Jet, *Phys. Fluids*, vol. 17, p. 1913, 1974.
19. J. L. Dressler, Two-Dimensional, High Flow, Precisely Controlled Monodispersed Drop Source, Final Report, Wright Laboratory, WL-TR-2049, 1993.
20. X. Li and R.S. Tankin, Droplet Size Distribution: A Derivation of a Nukiyama-Tanasawa Type Distribution Function, *Combustion Sci. and Technol.*, vol. 57, p. 65, 1987.

Pergamon
REPRINTED WITH PERMISSION
FROM ELSEVIER SCIENCE LTD 0017-9310(95)00324-X

Int. J. Heat Mass Transfer. Vol. 39, No. 11, pp. 2205–2219, 1996
Copyright © 1996 Elsevier Science Ltd
Printed in Great Britain. All rights reserved
0017-9310/96 $15.00+0.00

A numerical study of droplet–vortex interactions in an evaporating spray

T. W. PARK† and S. K. AGGARWAL‡
Department of Mechanical Engineering, University of Illinois at Chicago, Chicago, IL 60607, U.S.A.

and

V. R. KATTA§
System Research Laboratory, Inc., Dayton, OH 45440, U.S.A.

(*Received* 23 *March* 1995 *and in final form* 28 *August* 1995)

Abstract—In this paper, we present the time-dependent axisymmetric numerical simulation of a n-heptane evaporating spray, and investigate the droplet–vortex interactions which determine the structural and dynamic characteristics of a spray jet flow. The spray is formed between a droplet-laden heated nitrogen jet and a coflowing air stream. A detailed, multidimensional, two-phase algorithm is developed for the simulation. Monodisperse spray is introduced into the large vortex structures that are generated by the buoyancy-induced hydrodynamic instability of the heated jet. Results focus on the two-way interactions between vortical structures and droplets, and the dynamics of both non-evaporating and evaporating sprays. The vortex structures cause droplets to disperse radially outward, and this in turn determines the fuel vapor distribution and also modifies the vortex dynamics. Thus, the dynamics and structural characteristics of evaporating sprays are strongly influenced by the two-way transient interactions. The effects of initial droplet size, injection location, and liquid-to-gas mass loading ratio on these interactions are investigated. These studies indicate that the effect of dispersed phase on gas phase is negligible for mass loading ratio less than 0.5. At higher mass loading ratios, the dispersed phase modifies the dynamics of vortex structures but not the time-average behavior for non-evaporating spray, while for evaporating spray it influences both the dynamics and the time-averaged behavior. It is also found that the spray injection characteristics have strong influence on the processes of droplet–vortex interactions. Copyright © 1996 Elsevier Science Ltd.

INTRODUCTION

Large-scale, coherent vortical structures have been found to exist in a variety of shear flows including those involving combustion and multiple phases [1–4]. In two-phase shear flows involving solid particles or liquid droplets, the transient interactions between dispersed phase and large vortical structures are expected to play a central role in determining the dynamics and structural characteristics of these flows. The transient interactions pertain to the effect of large vortical structures on the behavior of droplets/particles, and the influence of droplets on the dynamics of large vortical structures. These two effects coupled in a nonlinear manner; the vortex structures determine the droplet dispersion and gasification behavior, which in turn affects the local environment surrounding each droplet and thereby the dynamics of the two-phase system under consideration. Several numerical [5, 6] and experimental [7–10] studies in recent years have focused on the one-way coupling, examining the influence of large eddies on the dynamics of droplets/particles injected into a shear flow. These studies show that the effect of large structures on particle motion is characterized by the ratio of particle response time to characteristic time of structures. This ratio is defined as the Stokes number (St). When the particle response time is of the same order of magnitude as the vortex time scale, $St \sim O(1)$, particles can disperse significantly more than the fluid particles, the enhanced dispersion being attributed to the centrifugal action of vortices. For small Stokes number, $St \ll 1.0$, particles behave similar to the fluid particles, while for large Stokes number, particles remain largely unaffected by the vortices. More recent works [11, 12] on particle-laden flows have examined the effect of external forcing on the particle dispersion behavior. A general observation from these studies [11, 12] is that the dynamics of vortex structures, and thereby the dispersion behavior of particles in a shear layer can be manipulated by a subharmonic forcing of the shear layer.

Particle-laden shear flows in practical applications

† Currently at Wright Laboratory, Aero Propulsion and Power Directorate, Wright-Patterson Air Force Base, OH 45433, U.S.A., as a National Research Council Research Associate.
‡ Author to whom correspondence should be addressed.
§ Present address: Innovative Scientific Solutions, Inc., Dayton, OH 45430, U.S.A.

NOMENCLATURE

C_p	specific heat
d_o	initial droplet diameter
D	vapor/air binary diffusion coefficient
g	acceleration of gravity
h_{fs}	enthalpy of fuel vapor at droplet surface
$l_{k,eff}$	effective latent heat, or the heat transferred from gas phase to droplet
$\dot{m}_k$	droplet vaporization rate
M	ratio of the liquid fuel mass flow rate to the nitrogen mass flow rate
M_k	mass of each group of droplets
n_k	number of droplets in each group
p	pressure
r	radial distance
t	time
T	temperature
u	axial velocity
v	radial velocity
Y	mass fraction
z	axial distance.

Greek symbols

μ	dynamic viscosity
λ	thermal conductivity
ρ	density.

Subscripts

f	fuel vapor
g	gas-phase
k	droplet characteristic
l	liquid-phase
o	oxygen
s	surface.

involve two-way, nonlinear interactions between the continuous and dispersed phases. Previous studies cited above focus mainly on the one-way interactions, i.e. on characterizing the effect of vortex structures on droplet motion and dispersion behavior. The effects of dispersed phase on vortex dynamics, and subsequently on fuel vapor distribution and flame behavior remain largely unexplored. In this paper, we report a numerical study of two-way droplet–vortex interactions in an unsteady evaporating spray. The spray is formed between a droplet-laden heated nitrogen jet and a coflowing air stream. The jet velocity and temperature are considered in a range where the large vortical structures are generated due to the buoyancy-induced hydrodynamic instability rather than the shear-induced Kelvin–Helmholtz instability. The vaporization characteristics of n-heptane fuel spray under the influence of two-way droplet–vortex interactions are investigated. The additional complexities due to chemical reactions and heat release are avoided so as to focus on the dynamics of two-way interactions. A non-evaporating spray is also analyzed in order to distinguish the interactions involving only momentum transfer between the phases from those involving mass, momentum, and energy transfer. Results are presented that highlight the dynamics as well as the time-averaged structure of these sprays.

PHYSICAL MODEL

The evaporating spray investigated in the present study is shown schematically in Fig. 1. It consists of a central fuel jet which is a two-phase mixture of gaseous nitrogen and liquid fuel droplets and a low-speed coannulus air flow. The central jet is heated primarily to enhance the fuel evaporation; however, in the present studies, it also plays a key role for the formation of buoyancy induced vortical structures. Numerical studies on the two-way interactions between the vor-

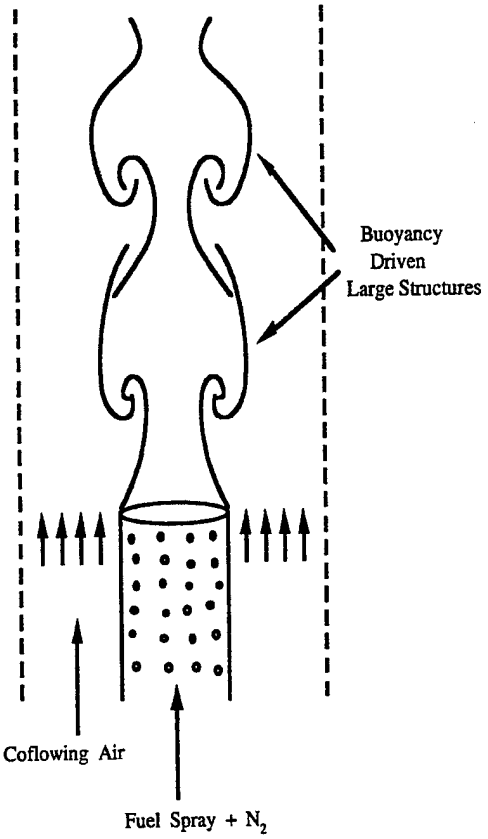

Fig. 1. A schematic of evaporating spray jet at 1 g.

Table 1. Transport coefficients and source terms appearing in governing equations

Equations	Φ	Γ^Φ	S_g^Φ	S_l^Φ
Continuity	1	0	0	$\sum_k n_k \dot{m}_k$
Axial momentum	u	μ	$-\frac{\partial p}{\partial z}+(\rho_o-\rho)g+\frac{\partial}{\partial z}\left(\mu\frac{\partial u}{\partial z}\right)+\frac{\partial}{\partial r}\left(\mu\frac{\partial v}{\partial z}\right)+\frac{\mu}{r}\frac{\partial v}{\partial z}-\frac{2}{3}\left\{\frac{\partial}{\partial z}\left(\mu\frac{\partial u}{\partial z}\right)+\frac{\partial}{\partial z}\left(\mu\frac{\partial v}{\partial r}\right)+\frac{\partial}{\partial z}\left(\mu\frac{v}{r}\right)\right\}$	$\sum_k\left(n_k\dot{m}_k u_k-n_k M_k\frac{du_k}{dt}\right)$
Radial momentum	v	μ	$-\frac{\partial p}{\partial r}+\frac{\partial}{\partial z}\left(\mu\frac{\partial u}{\partial r}\right)+\frac{\partial}{\partial r}\left(\mu\frac{\partial v}{\partial r}\right)+\frac{\mu}{r}\frac{\partial v}{\partial r}-2\mu\frac{v}{r^2}-\frac{2}{3}\left\{\frac{\partial}{\partial r}\left(\mu\frac{\partial u}{\partial z}\right)+\frac{\partial}{\partial r}\left(\mu\frac{\partial v}{\partial r}\right)+\frac{\partial}{\partial r}\left(\mu\frac{v}{r}\right)\right\}$	$\sum_k\left(n_k\dot{m}_k v_k-n_k M_k\frac{dv_k}{dt}\right)$
Mass fraction of fuel	Y_f	ρD_f	0	$\sum_k n_k\dot{m}_k$
Mass fraction of oxygen	Y_o	ρD_o	0	0
Energy	T	λ/C_p	0	$\sum_k n_k\dot{m}_k(h_{fs}-l_{k,eff})$

tex structures and the evaporating droplets are conducted by solving the unsteady, axisymmetric gas-phase equations that include the droplet source terms, and the appropriate droplet equations.

The unsteady, axisymmetric governing equations in cylindrical (z, r) coordinate system for a droplet-laden heated jet are

$$\frac{\partial(\rho\Phi)}{\partial t}+\frac{\partial(\rho u\Phi)}{\partial z}+\frac{\partial(\rho v\Phi)}{\partial r}=\frac{\partial}{\partial z}\left(\Gamma^\Phi\frac{\partial\Phi}{\partial z}\right)+\frac{\partial}{\partial r}\left(\Gamma^\Phi\frac{\partial\Phi}{\partial r}\right)-\frac{\rho v\Phi}{r}+\frac{\Gamma^\Phi}{r}\frac{\partial\Phi}{\partial r}+S_g^\Phi+S_l^\Phi. \quad (1)$$

The general form of equation (1) represents the continuity, momentum, species, or energy conservation equation depending on the variable used for Φ. Table 1 gives the transport coefficients Γ^Φ and the source terms S_g^Φ and S_l^Φ that appear in the governing equations. In this table, μ, λ and C_p represent the viscosity, the thermal conductivity and the specific heat, respectively. They are considered functions of temperature and species concentration.

The effect of dispersed phase on gas-phase properties is incorporated through the source/sink terms (S_l^Φ), representing the exchange of mass, momentum, and energy between the gas and liquid phases. In order to evaluate these terms, it is necessary to establish droplet trajectories, size and temperature histories. The Lagrangian approach is employed to solve the liquid-phase governing equations for the dynamics and vaporization history of each droplet group. The spray is characterized by a discrete number of droplet groups, distinguished by their injection location, initial size and time of injection. A droplet group in a Lagrangian treatment represents a characteristic containing a finite number of droplets. Since an axisymmetric configuration is analyzed, the liquid properties are implicitly averaged in the azimuthal direction and the number of droplets associated with each characteristic represents droplets uniformly distributed in an annual ring. The equations governing the variation of position, velocity, and size for each droplet group and other expressions are available in ref. [13]. A comprehensive vaporization model is employed to calculate the instantaneous droplet size and surface temperature along the trajectory of each group. The model includes the effects of variable thermophysical properties, non-unity Lewis number in the gas film outside the droplet, the effect of Stefan flow on the heat and mass transfer between the droplet and the gas, and the effect of transient liquid heating. The variable thermophysical properties are calculated at reference film temperature and concentrations, obtained by using the 1/3 rule, except for the gas density which is calculated at the free stream value [14]. The Wilke rule [15] is used to calculate the dynamic viscosity and thermal conductivity of the gas film. The liquid fuel (n-C_7H_{16}) properties are collected from the various sources and approximated as a function of the temperature [13]. The effect of transient liquid heating is incorporated by using the finite-conductivity model [16]. This model is deemed satisfactory in the present study, since the maximum droplet Reynolds number during droplet lifetime is less than ten and thus the effect of internal circulation is expected to be negligible. For the same reason, the effects of gas-phase convection on the heat and mass transport are represented by the Ranz–Marshall correlation [16].

SOLUTION PROCEDURE

The numerical solution of the unsteady two-phase equations employs an implicit algorithm for solving the gas-phase equations, and an explicit Runge–Kutta procedure for the liquid-phase equations. The finite-

difference forms of the momentum equations are obtained using an implicit QUICKEST scheme [17], while those of the species and energy equations are obtained using a hybrid scheme of Spalding [18]. A "finite control volume" approach with a staggered, non-uniform grid system is utilized. Body force term due to gravitational field is included in the axial momentum equation for gas-phase and the droplet motion equation for liquid-phase. An iterative ADI (Alternative Direction Implicit) technique is used for solving the resulting sets of algebraic equations. A stable numerical integration procedure is achieved by coupling the species and energy equations through the source terms (cf. Table 1). At every time step, the pressure field is calculated by solving the pressure Poisson equations simultaneously and utilizing the LU (Lower and Upper diagonal) matrix decomposition technique. It should be noted that the pressure Poisson equations consider the effect of mass transfer from the liquid phase to the gas phase, represented by a source term in the gas-phase mass continuity equation.

The liquid-phase equations are advanced in time by a second-order accurate Runge–Kutta method. Since the gas-phase solution employs an implicit procedure, the temporal step size used for integrating the liquid-phase equations is smaller than that for gas-phase equations. An automatic procedure is implemented in order to select an optimum liquid-phase time step. The procedure involves calculating the characteristic thermal response time, velocity response time and vaporization time for each droplet group, and then selecting the temporal step size as a fraction (one-hundredth) of the smallest of these time scales. A detailed examination of the various time scales, based on numerical experiments, revealed that the temporal step size is determined by either the thermal response time or the velocity response time of a given droplet group. The number of subcycles for advancing the liquid-phase solution for each gas-phase cycle typically varies from two to ten, depending upon the droplet size.

The procedure to advance the two-phase solution over one gas-phase time step is as follows. Using the known gas-phase properties, the liquid-phase equations are solved over a specified number of liquid-phase subcycles. A third-order accurate Lagrangian polynomial method is used for interpolating the gas-phase properties from the non-uniform fixed grid to the droplet characteristic location. It should be noted that the interpolation scheme for the gas-phase velocities u and v is based on their respective grid cells because of the use of a staggered grid in gas-phase calculation. The droplet properties are updated after every liquid-phase subcycle. Also, during each subcycle, the liquid-phase source terms appearing in the gas-phase equations are calculated at the characteristic location, and then distributed to the surrounding gas-phase grid points. These source terms are added at each gas-phase grid points during one gas-phase time step and then used in the implicit solution of the gas-phase equations.

RESULTS

The jet diameter of the vertically mounted evaporating spray considered in the present study is 2.54 cm. The jet velocities for the central fuel and coannular air streams are 1.0 and 0.2 m s^{-1}, respectively. Flat velocity profiles are used as the inflow conditions. Temperature chosen for the fuel jet is 1200 K while that of the surrounding annulus air is 294 K. Calculations are made for a physical domain having dimensions of 15 and 40 cm in the radial and axial direction, respectively. It should be noted that the physical domain used in the calculations is much larger than the domain of interest (3×20 cm) and hence, the results are not influenced by the computational boundaries. Results reported in the present paper are obtained using a grid system having 151 and 61 points in the axial and radial directions, respectively. Grid lines are clustered near the shear layer to resolve the steep gradients of the dependent variables. Calculations are advanced in time utilizing a low CFL number of 0.2. In an earlier study [13], it was found that the results obtained on a 151×61 mesh system (with grid spacings similar to the ones used in the present investigation) and using a CFL number less than 0.5 are grid independent and time accurate.

Numerical experiments are conducted by injecting different groups of droplets into the fuel stream to examine the changes in the flow structure due to the two-way nonlinear, two-phase interactions. The injection process consists of introducing a group of monodisperse droplets at a given instant of time. The number of droplets in each group depends on the mass loading (ratio of the liquid fuel mass flow rate to the nitrogen mass flow rate), initial droplet size, and injection time interval. As a base case for the spray calculations reported in this work, a monodisperse n-heptane spray with an initial diameter of 200 μm and mass loading of unity is considered. At a mass loading of unity, the volume occupied by liquid phase is about three orders of magnitude smaller than that of the gas-phase volume due to the high density of the liquid fuel and hence, the dilute-spray assumption is still valid. At higher mass loading, however, the assumption would become increasingly more questionable. For this reason, the mass loading of unity is the highest loading considered in the present study. The droplets are injected continuously into the jet shear layer from a radial location of 1.25 cm. A time difference of 1.428 ms ($=9\,\Delta t_{gas}$) is used between two consecutive injections for all the spray calculations reported in this work. This time interval was determined based on the constraint that the spatial separation between two successive droplet groups is large enough for neglecting the interaction between the droplets. This yields the number of droplets in each group to be 76. Three different droplet injection intervals are chosen to examine their effect on the time-averaged temperature and axial velocity profiles in the flow field. Figure 2 shows the time-averaged axial profiles of

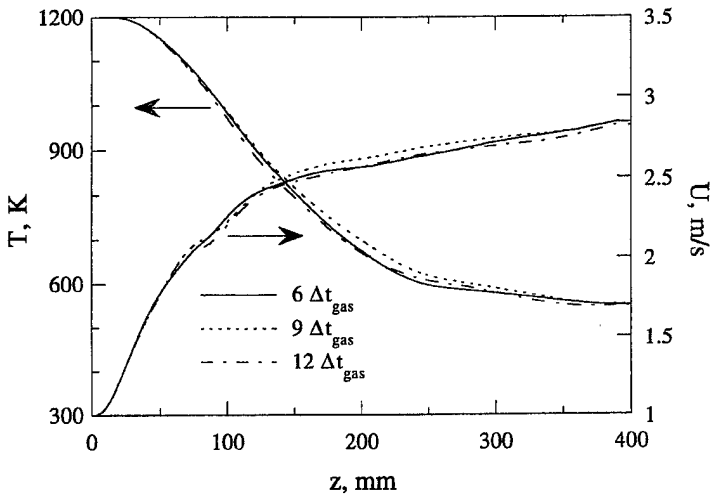

Fig. 2. Effect of droplet interval on the time-averaged temperature and axial velocity profiles of 200-μm evaporating spray with mass loading value of $M = 1.0$.

temperature and axial velocity for the three cases. As expected, the average temperature decreases along the jet axis due to gas-phase heat transport processes and cooling caused by the dispersed phase. The average axial velocity, however, increases in the axial direction due to buoyant acceleration. The important observation is that the gas-phase calculations are not sensitive to the droplet injection interval used for the base case.

The effect of dispersed phase on the dynamics of vortex structures and heated jet is portrayed in Figs. 3 and 4. Calculations are initially made without injecting droplets into the fuel stream. The shear layer between the 1200-K nitrogen jet and the cold annulus air flow became unsteady with the development of large-scale vortices. Iso-temperature contours of this heated jet are shown in Fig. 3(a). It is important to note that these vortical structures are generated without using any external forcing, and their dynamics is found to be highly periodic. The role of gravity on the

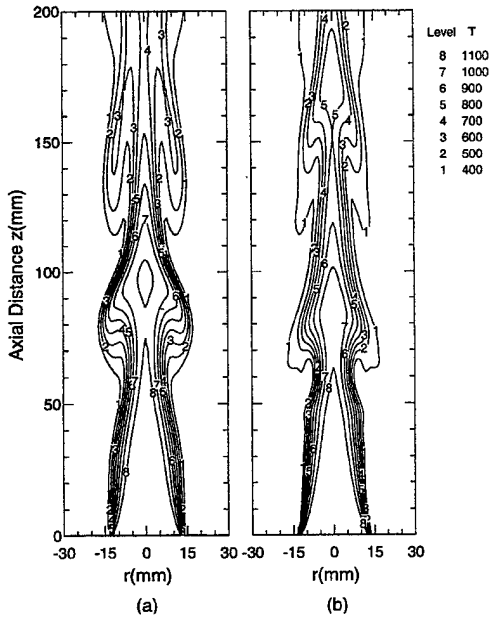

Fig. 3. Instantaneous iso-temperature contours for the heated jet: (a) without fuel spray; (b) with fuel spray.

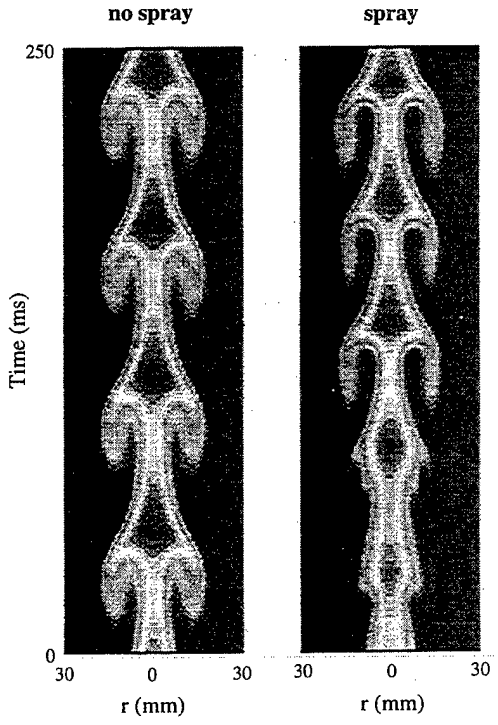

Fig. 4. Time evolution of temperature contours at axial location of 10 cm above the inlet for the cases of Fig. 3.

dynamics of the heated jet was confirmed by performing numerical experiments. When the gravitational term in the axial momentum was set equal to zero, the simulation yielded a steady laminar jet flow. This observation is in contrast with that made for heated jet flows at higher Reynolds number, in which Kelvin–Helmholtz instabilities develop independent of the assumption made for gravitational force. Most of the experimental studies on heated jets [19, 20] were focused on the higher Reynolds-number flow and did not provide insight on buoyancy-induced instabilities. However, the latter ones were extensively investigated experimentally in jet diffusion flames [21, 22] and helium jets [23]. The numerical studies [24, 25] performed on these flames and helium jet flows using the code discussed in the present study predicted the growth of buoyancy-induced instabilities very accurately.

Instantaneous iso-temperature contours for the case with fuel spray [plotted in Fig. 3(b)] are compared with the ones obtained without introducing fuel spray in Fig. 3(a). All the droplet source terms (Table 1) are incorporated in the gas-phase equations for the simulation with fuel spray. For both the cases, the buoyancy-induced vortex structures shown in Fig. 3 appear naturally without any external forcing. It is apparent from the figure that the injection of 200-μm droplets into the shear layer weakened the vortical structures and decreased the spreading of the heated jet. The weakening of vortical structures is probably caused by the cooling effect of the dispersed plane, while the decrease in the spreading rate may be expected due to fact that the addition of fuel spray to the nitrogen gas increases the jet momentum. Figure 3 further indicates that the jet oscillations are highly coherent for the gaseous (no spray) case and somewhat less coherent for the spray case. Since the presence of liquid phase modifies the spectral characteristics or the dominant instability frequency, an attempt was made to phase-lock the instantaneous images for the two cases. Consequently, the temperature contour plots in Fig. 3 for the gaseous and spray cases represent the results that are obtained at slightly different times from the start of the respective calculation.

The dynamics of vortex structures is examined by plotting the time evolution of temperature contours in Fig. 4. Temperature data along the radial location at an axial location of 10 cm above the jet exit for the gaseous and spray cases are recorded over a time period of 250 ms and shown in this figure. Again, an attempt was made to phase-lock the images for the gaseous and spray case. It can be seen from Fig. 4(a) that the vortex structures in the case of gaseous jet are highly coherent and periodic. With the addition of fuel spray the dynamics of jet has become aperiodic and the vortex crossing frequency (obtained by counting the number of vortices in a fixed time interval) has increased by about 30%. This can be confirmed by performing the spectral analysis at different axial locations in the shear layer. Temperature data were recorded at different locations during more than 10 vortex crossing times (4096 Δt_{gas}). Figure 5 clearly shows that the dominant frequency for the spray case is increased to 20.5 Hz which is about 30% higher compared to the frequency observed for the gaseous jet case. In addition, the deterioration in coherency can be seen for the spray case. The increase in frequency for the spray case is resulting from the momentum transfer between the liquid drops and the gaseous flow. The fuel drops are injected into the gaseous jet shear layer at the same velocity as that of the local gas velocity which yields higher momentum to the fuel drops. As the gaseous flow and drops convect downstream, the higher momentum of the latter transfer to the former which, in turn, increases the local gas velocity. As a result, the crossing frequency of the vortices in the shear layer, which is proportional to the local gas velocity, also increases. The increase in frequency is observed for both non-evaporating and evaporating sprays, implying again that this is primarily a momentum-transfer effect. It is also interesting to note that no vortex merging is observed for these two cases.

Effect of liquid mass loading

The structural changes noted in a buoyancy driven heated jet with the addition of fuel spray are resulting from (1) liquid mass loading, (2) droplet evaporation and (3) the two-way interaction between vortices and droplets. To further understand the impact of the above individual parameters, numerical experiments are performed by changing the liquid mass loading, evaporation characteristics, spray injection location and droplet size.

The instantaneous iso-temperature contours for five different mass loading values ($M = 0$, 0.125, 0.25, 0.5 and 1.0) for a non-evaporating spray are shown in Fig. 6. Again, the images shown in Fig. 6 are phase locked. Liquid mass flow rate is controlled by changing the number of droplets in each injected group. As the droplets are assumed to be non-evaporating in this case, only the source terms in the momentum equation (cf. Table 1) are considered in the gas-phase equations. In other words, only the momenta are exchanged in this two-phase flow calculation. The single-phase gaseous flow shown in Fig. 3(a) may be approximated as a non-evaporating spray in the limiting case of $M = 0$ [Fig. 6(a)]. It seems that the structural characteristics of low mass loading cases like $M = 0.125$ and 0.25 are similar to that of single-phase flow even though the vortex-crossing frequencies in these flows are somewhat different. The time history plots of the dynamic heated jets for different mass loading values are shown in Fig. 7. This plot clearly shows the changes in the sizes of the vortex structures and their crossing frequency for different cases. It may be observed from Fig. 7 that as the mass loading ratio is increased, the crossing frequency of vortex structures is also increasing. At higher mass loading

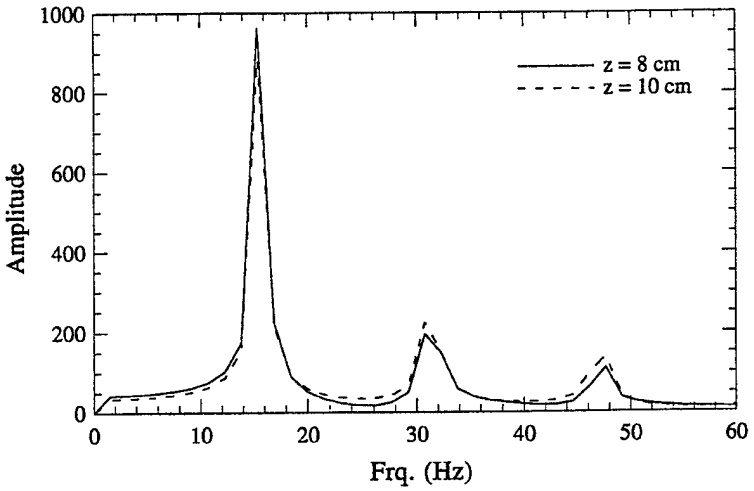

(a)

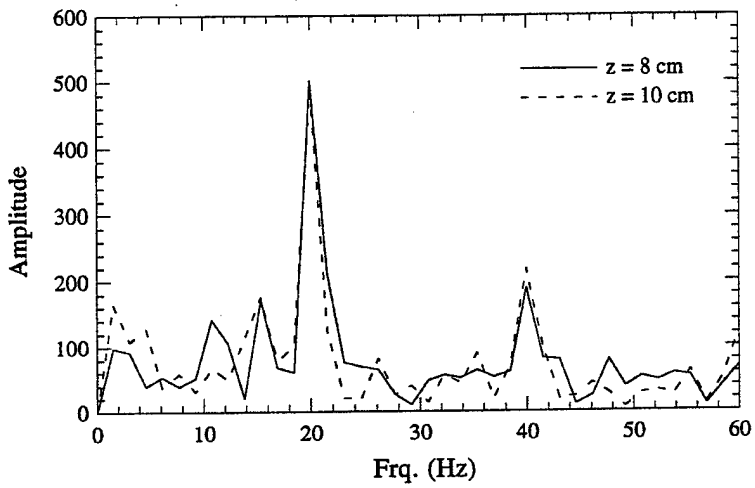

(b)

Fig. 5. Frequency spectra obtained from temperature data recorded within the shear layer at two different axial locations.

values ($M = 0.5$ and 1.0), the structural characteristics seem to change more significantly.

The effect of mass loading in an evaporating spray is depicted in Fig. 8 by plotting the phase-locked instantaneous temperature contours for the three different mass loading values ($M = 0.25, 0.5$ and 1.0). The gas-phase governing equations for this case include all the source/sink terms due to the exchange of mass, momentum and energy due to droplet dynamics and vaporization. Structure of the heated jet seems to change more significantly with the addition of evaporating spray compared to that of a non-evaporating one. Figure 9 shows the time evolution of temperature contours at $z = 7.5$ cm for the three cases shown in Fig. 8. It is interesting to compare the structures of high mass loading values ($M = 0.5$ and 1.0) for the evaporating (Fig. 9) and non-evaporating (Fig. 7) cases. The development of vortical structures for evaporating spray is more periodic than that observed in the corresponding non-evaporating cases. This is probably due to the fact that for the evaporating case the effect of momentum coupling between the phases is reduced due to droplet vaporization.

The effect of dispersed phase on the time-averaged gas-phase properties for both non-evaporating and evaporating sprays with different mass loading values is portrayed in Fig. 10. The time period used in obtaining the average values was at least 10 vortex periods. In addition, it was verified that the average values

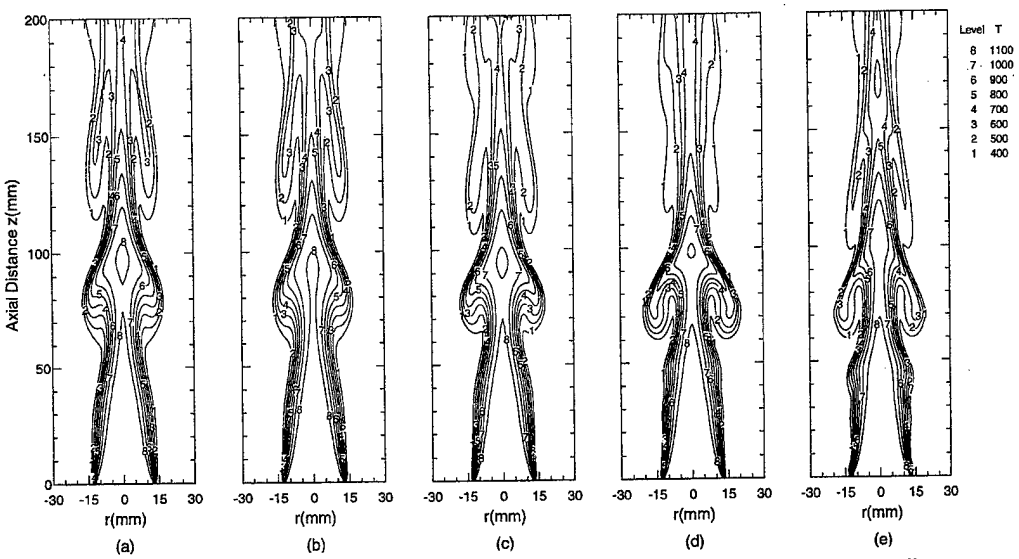

Fig. 6. Instantaneous iso-temperature contours for a 200-μm non-evaporating spray jet with five different mass loading values; (a) $M = 0$, (b) $M = 0.125$, (c) $M = 0.25$, (d) $M = 0.5$ and (e) $M = 1.0$.

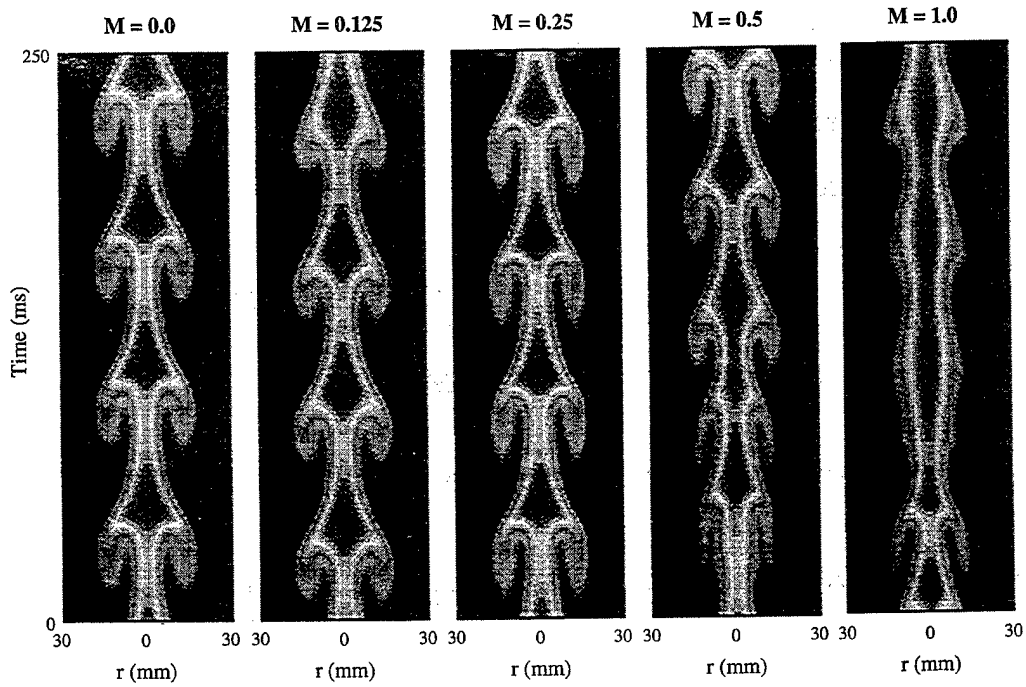

Fig. 7. Time evolution of temperature contours at axial location of 10 cm above inlet for the cases of Fig. 6.

shown in Fig. 10 were independent of this time period. An important observation is that the dispersed phase does not have any discernible influence on the time-averaged properties of non-evaporating spray jet. This is especially interesting in view of the fact that the vortex dynamics for the non-evaporation spray case is modified by the presence of the dispersed phase. As expected, the average gas-phase properties of evaporating spray are significantly affected by the dispersed phase. The average gas temperature decreases along the jet axis due to the cooling caused by droplet vaporization. The decrease in gas temperature reduces the magnitude of buoyant acceleration, resulting in a lowering of average gas velocity compared to that for

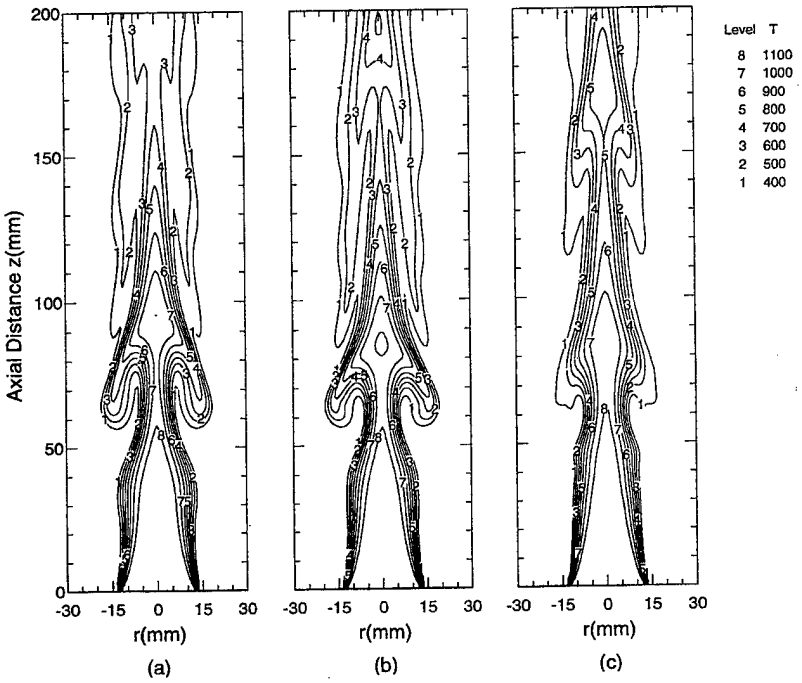

Fig. 8. Instantaneous iso-temperature contours for a 200-μm evaporating spray jet with three different mass loading values; (a) $M = 0.25$, (b) $M = 0.5$ and (c) $M = 1.0$.

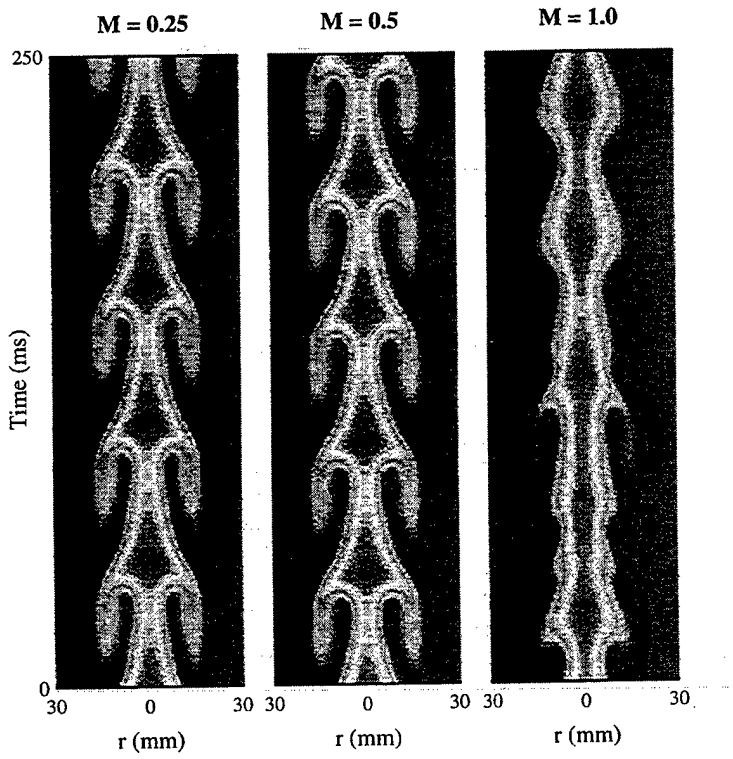

Fig. 9. Time evolution of temperature contours at a location of 7.5 cm above the inlet for the cases of Fig. 8.

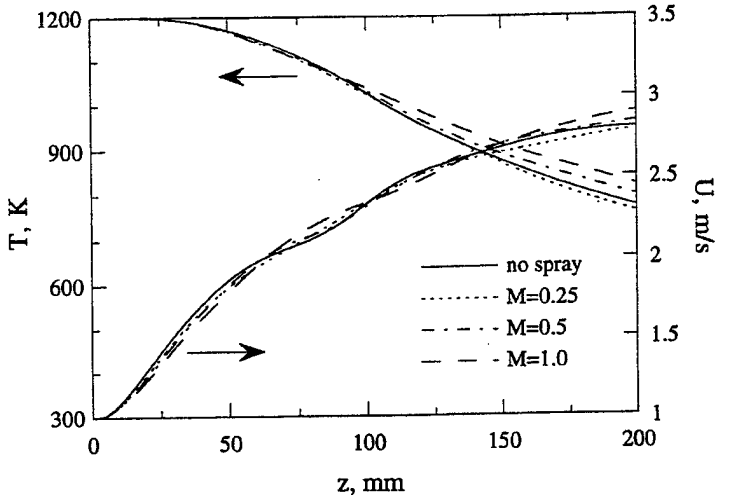

(a)

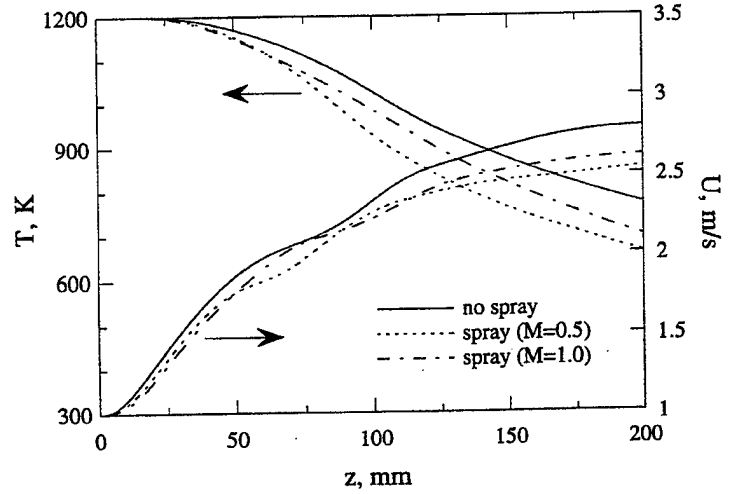

(b)

Fig. 10. Time-averaged axial profiles of gas temperature and axial velocity for (a) non-evaporating and (b) evaporating sprays with different liquid-to-gas loading ratios.

the gaseous case. Note that a reduction in the buoyant acceleration makes the vortex structures weaker as mentioned earlier.

Effect of injection characteristics

The effect of initial droplet distribution on the structural characteristics and dynamics of evaporating spray jet is studied by changing the injection characteristics. The mass loading ratio and droplet diameter are fixed at 1.0 and 200 μm, respectively. The instantaneous temperature contours for three cases having different droplet injection locations are shown in Fig. 11. The three distributions of injection locations used are as follows: (1) $r_k = 1.25$ cm, one injection location, (2) $r_k = 0.625$ and 1.25 cm, two injection locations and (3) $r_k = 0.25$, 0.50, 0.75, 1.00 and 1.25 cm, five injection locations. The mass loading ratio is kept constant by using a different number of droplets in each group for different cases. It is seen that the characteristics of the core region near the nozzle exit are quite different for the three cases due to different droplet injection processes. The use of more injection locations apparently leads to a dynamic heated spray jet with well-organized vortical structures [Fig. 11(c)]. It is known that the vaporization of a liquid droplet absorbs thermal energy and hence reduces the local temperature. This is evident in Figs. 11(b) and (c). In the former figure a valley in the temperature contours

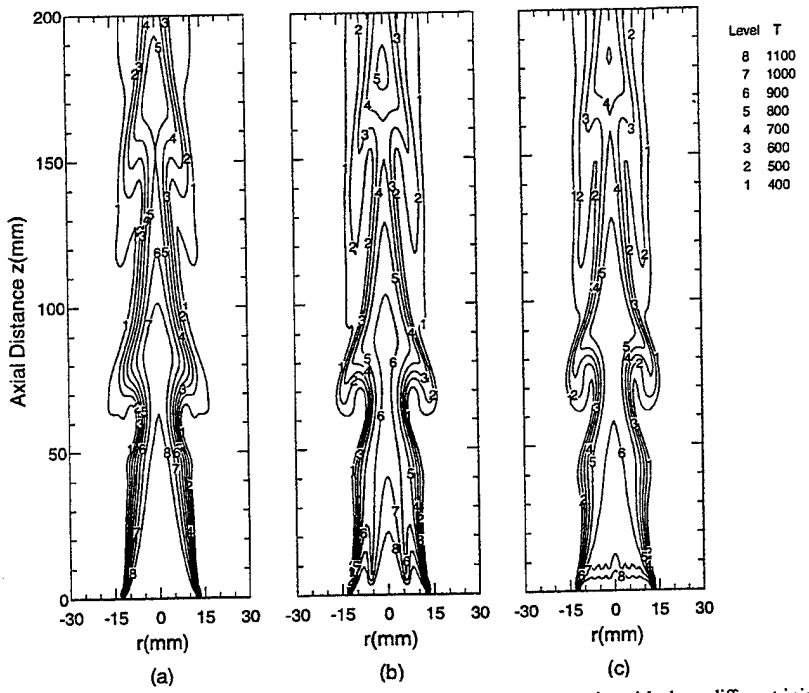

Fig. 11. Instantaneous iso-temperature contours for an evaporating spray jet with three different injection distributions; (a) $r_k = 1.25$ cm, one injection location, (b) $r_k = 0.625$ and 1.25 cm, two injection locations, (c) $r_k = 0.25$, 0.5, 0.75, 1.0 and 1.25 cm, five injection locations.

developed in the downstream region of the inner injection location (i.e. $r_k = 0.625$ cm) as the injected droplet vaporized. However, in the latter figure, the choice of more injection locations reduced the entire jet temperature uniformly leading to near flat contours for 1000 and 1100 K [contours 7 and 8 in Fig. 11(c)]. The time evolution of temperature contours at an axial location of 7.5 cm for the above three cases is plotted in Fig. 12. It clearly shows that the vortex structures are well organized and highly periodic similar to that of a single-phase flow (Fig. 3a) when the number of injection locations is increased. However, the vortex passage frequency for the spray case is different from that for the single-phase jet.

Effect of droplet size

In order to examine the effect of initial droplet size on the processes of droplet-vortex interactions, three different spray cases with initial droplet diameters of 200, 100 and 50 μm are considered. A constant mass loading ratio of $M = 1.0$ is maintained by increasing the number of droplets in each group as its initial size is decreased, and the droplets are injected in the shear layer ($r_k = 1.25$ cm). Results are portrayed in Fig. 13 in the form of snap shots of the flow field. For each case, instantaneous iso-temperature contours and velocity vectors are plotted on the left-hand and right-hand sides of the symmetric jet, respectively. It is quite evident from Fig. 13 that the initial droplet size has a strong influence on the dynamic and structural characteristics of the evaporating spray. For all three cases shown in the figure, there is a reduction in gas temperature due to the vaporization of liquid fuel. However, as the initial droplet size decreases, there is increasingly pronounced cooling in the initial part of the jet caused by droplet vaporization, which affects both the shape and the dynamics of vortex structures. This can be seen more clearly in Fig. 14 which shows the time evolution of vortical structures for the three cases. In fact, when the initial droplet size is sufficiently small ($d_o = 50$ μm), the jet temperature downstream of $z = 6$ cm is reduced to less than 500 K, and vortex structures seem to be destroyed. This drastic reduction in gas temperature is caused by the increased total liquid-phase surface area and entrainment of colder fluid into the jet interior. The latter is due to the vortex merging process and subsequent enlargement of vortex structures for the 50-μm spray case. Note that the vortex merging which occurs at an axial location between $z = 2.5$ and 5 cm is not shown in the figures (although there is some evidence of it in Fig. 13). However, the enlargement of vortex structures for the 50-μm spray can be clearly seen in Fig. 14. The vortex-merging process enhances the entrainment of colder fluid, which further reduces the gas temperature and weakens the vortex structures drastically. Figure 15 shows the effect of initial droplet size on the time-averaged axial profiles of temperature and axial velocity. The drastic reduction in gas temperature caused by droplet vaporization and entrainment of colder fluid, and the subsequent destruction of vortex structures can be clearly seen in this figure. Thus the

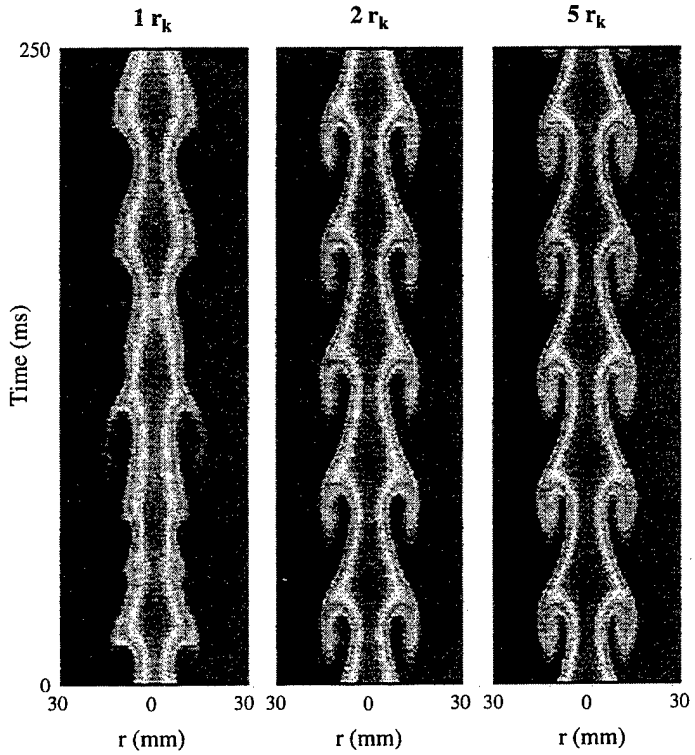

Fig. 12. Time evolution of temperature contours at axial location of 7.5 cm above inlet for the cases of Fig. 10.

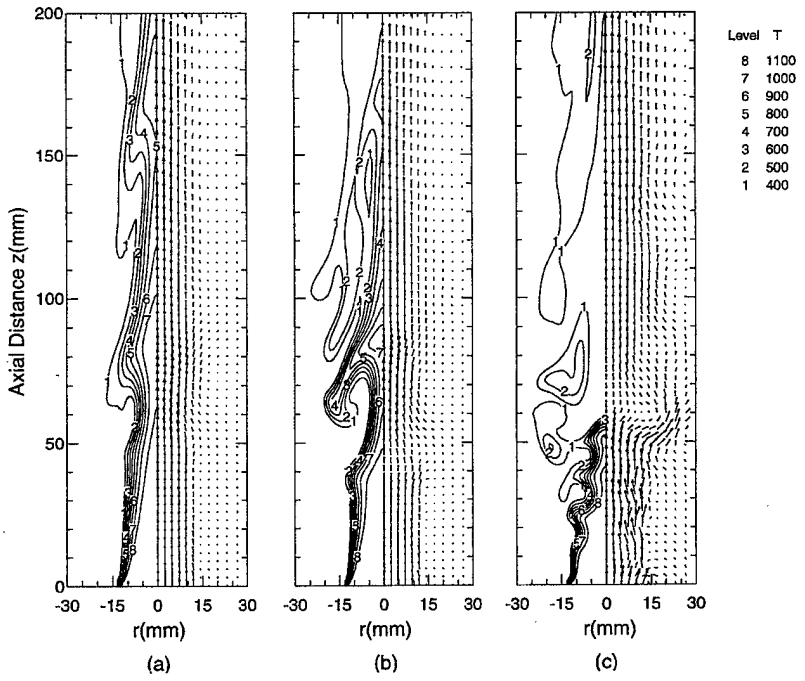

Fig. 13. Simultaneous snapshots of iso-temperature contours and velocity vectors for an evaporating spray for three different initial droplet diameters; (a) $d_o = 200$ μm, (b) $d_o = 100$ μm and (c) $d_o = 50$ μm.

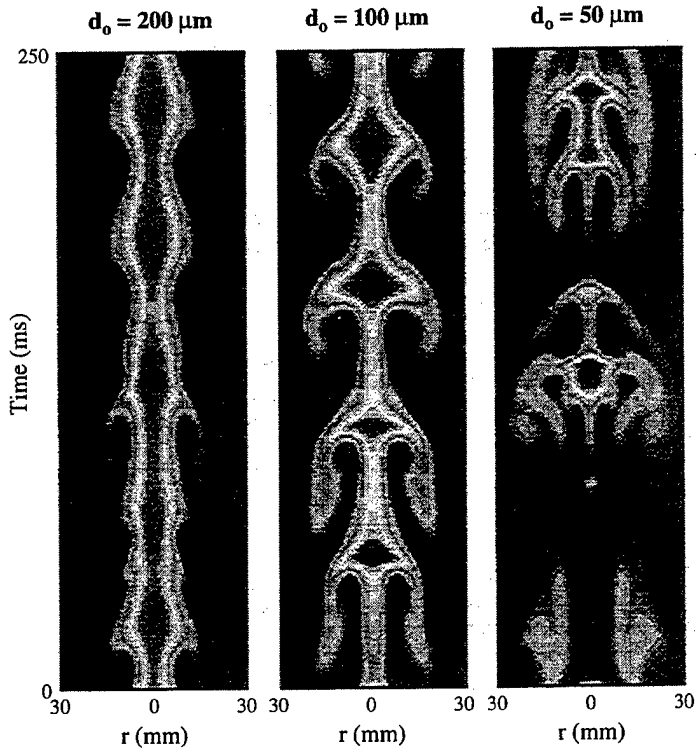

Fig. 14. Time evolution of temperature contours at a location of 7.5 cm above the inlet for the cases of Fig. 12.

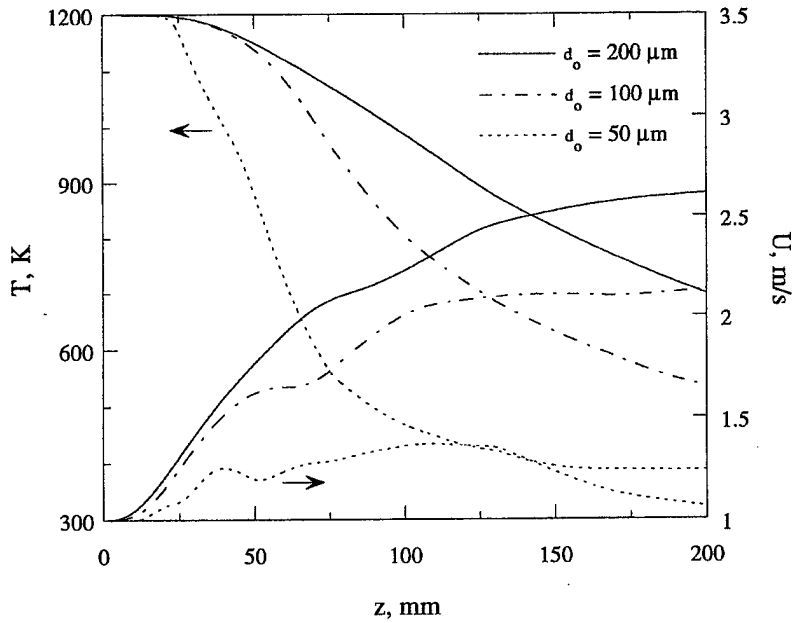

Fig. 15. Time-averaged axial profiles of gas temperature and axial velocity for an evaporating spray with three different initial droplet diameters and $M = 1.0$.

two-way nonlinear interactions seem to become stronger due to fast vaporization of 50-μm spray.

CONCLUSIONS

In this paper, we have investigated the dynamics of two-way droplet-vortex interactions and their influence on the structure of an evaporating spray. A low-speed spray formed (jet Reynolds number based on a jet temperature of 1200 K and velocity of 1.0 m s^{-1} is 154) between a droplet-laden heated nitrogen jet and a coflowing air stream has been simulated. Gravity has been used to generate large-scale vortical structures in the jet shear layer. The density difference between the heated fluid and the cold coflowing fluid gives rise to buoyant acceleration causing vortical structures to appear without any external perturbation. Liquid fuel (n-heptane) droplets are introduced into the vortex structures, and processes of droplet–vortex interactions are studied numerically by developing a time-accurate, multidimensional, two-phase algorithm. The effect of dispersed phase is incorporated through the source/sink terms in the gas-phase governing equations, representing the exchange of mass, momentum, and energy between the gas and liquid phases.

Snapshots and time evolution plots of vortex structures have been employed to analyze the effect of dispersed phase on their dynamics and time-averaged behavior under different mass loadings for both non-evaporating and evaporating sprays. The vortex structures cause droplets to disperse radially outward, and this in turn determines the fuel vapor distribution and also modifies the vortex dynamics. Thus, the dynamics and structural characteristics of the evaporating spray are strongly influenced by these interactions. The effects of initial droplet size, injection location, and liquid-to-gas mass loading ratio on the droplet–vortex interaction have been investigated by performing numerical experiments.

For both non-evaporating and evaporating sprays, the effect of dispersed phase on vortex dynamics is found to be negligible for mass loading ratio (M) less than 0.5. However, at higher loading ratios, depending upon the droplet injection characteristics, the vortex dynamics as well as the spray jet behavior may be strongly influenced by the dispersed phase. For a non-evaporating spray, the dispersed phase modifies the dynamics of vortex structures but not the time-average behavior, while it modifies both the dynamics and time-averaged behavior for an evaporating spray. For example, for 200-μm spray at $M = 1.0$ and with droplets injected into the shear layer, the vortex passage frequency is increased by about 30% and the vortex structures become weaker and less coherent compared to the gaseous jet case. This has important implications in spray applications such as gas turbine and ramjet combustors, especially when the system performance is strongly linked to some underlying unsteady phenomenon. Results also indicate that the initial droplet size has a strong influence on the two-way interactions. Due to spray vaporization, gas temperature in the jet interior decreases, which modifies the vortex dynamics and consequently the droplet dynamics and vaporization. In fact, for 50-μm spray at $M = 1.0$, the vortex dynamics is drastically modified and a vortex pairing phenomenon is observed. The latter results in a much larger entrainment of colder fluid causing a subsequent destruction of vortex structures. Thus the spray injection characteristics have strong influence on the processes of droplet–vortex interactions.

Acknowledgements—This work was funded by the AFOSR under Grant F49620-93-1-0400 monitored by Dr Julian M. Tishkoff. Many fruitful discussions with Dr W. M. Roquemore at Wright-Patterson Air Force Base are greatly appreciated. Computations were performed on Cray C-90 at the Pittsburgh Supercomputing Center.

REFERENCES

1. G. L. Brown and A. Roshko, Density effects and large scales in the developing mixing layer, *J. Fluid Mech.* **64,** 775–816 (1974).
2. A. J. Yule, Large scale structure in the mixing layer of a round jet, *J. Fluid Mech.* **89,** 413–432 (1978).
3. V. R. Katta, L. P. Goss and W. M. Roquemore, Effect of nonunity Lewis number and finite-rate chemistry on the dynamics of a hydrogen–air jet diffusion flame, *Combust. Flame* **96,** 60–74 (1994).
4. E. K. Longmire and J. K. Eaton, Structure of a particle-laden round jet, *J. Fluid Mech.* **236,** 217–257 (1992).
5. J. N. Chung and T. R. Troutt, Simulation of particle dispersion in an axisymmetric jet, *J. Fluid Mech.* **186,** 199–222 (1988).
6. D. Hansell, I. M. Kennedy and W. Kollmann, A simulation of particle dispersion in a turbulent jet, *Int. J. Multiphase Flow* **18,** 559–576 (1992).
7. B. J. Lazaro and J. C. Lasheras, Particle dispersion in the developing free shear layer—I. Unforced flow, *J. Fluid Mech.* **235,** 143–178 (1992).
8. B. J. Lazaro and J. C. Lasheras, Particle dispersion in the developing free shear layer—II. Forced flow, *J. Fluid Mech.* **235,** 179–221 (1992).
9. M. Samimy and S. K. Lele, Motion of particles with inertia in a compressible free layer, *Phys. Fluids* **A3,** 1915–1923 (1991).
10. K. Hishida, A. Ando and M. Maeda, Experiments on particle dispersion in a turbulent mixing layer, *Int. J. Multiphase Flow* **18,** 181–194 (1992).
11. J. Uthuppan, S. K. Aggarwal, F. F. Grinstein and K. Kailasanath, Particle dispersion in a transitional axisymmetric jet: a numerical simulation, *AIAA J.* **32,** 2004–2014 (1994).
12. S. K. Aggarwal, Relationship between stokes number and intrinsic frequencies in particle laden flows, *AIAA J.* **32,** 1322–1325 (1994).
13. T. W. Park, S. K. Aggarwal and V. R. Katta, Gravity effects on the dynamics of evaporating droplets in a heated jet, *AIAA J. Propulsion Power* **11,** 519–528 (1995).
14. B. Abramzon and W. A. Sirignano, Droplet vaporization model for spray combustion calculations, *Int. J. Heat Mass Transfer* **32,** 1605–1618 (1989).
15. D. K. Edwards, V. E. Denny and A. F. Mills, *Transfer Processes: An Introduction to Diffusion, Convection and Radiation* (2nd Edn). McGraw-Hill, New York (1979).
16. S. K. Aggarwal, A. Tong and W. A. Sirignano, A comparison of vaporization models for spray calculation, *AIAA J.* **22,** 1448–1457 (1984).
17. B. P. Leonard, A stable and accurate convective mod-

elling procedure based on quadratic upstream interpolation, *Comput. Meth. Appl. Mech. Engng* **19,** 59–98 (1979).
18. D. B. Spalding, A novel finite difference formulation for difference expressions involving both first and second derivatives, *Int. J. Numer. Meth. Engng* **4,** 551–559 (1972).
19. P. A. Monkewitz and K. D. Sohn, Absolute instability in hot jets, *AIAA J.* **26,** (8), 911–916 (1988).
20. S. Ragu and P. A. Monkewitz, The bifurcation of a hot round jet to limit-cycle oscillations, *Phys. Fluids A* **3,** 501–503 (1991).
21. L.-D. Chen, J. P. Seaba, W. M. Roquemore and L. P. Gross, Buoyant diffusion flames, *Proceedings Twenty-Second International Symposium on Combustion*, pp. 677–684. The Combustion Institute, Pittsburgh, PA (1988).
22. H. Eickhoff and A. Winandy, Visualization of vortex formation in jet diffusion flames, *Combust. Flame* **60** (1), 99–101 (1985).
23. T. Yuan, D. Durox and E. Villermaux, An analog study for flame flickering, *Expts Fluids* **17** (5), 337–349 (1994).
24. R. W. Davis, E. F. Moore, W. M. Roquemore, L.-D. Chen, V. Vilimpoc and L. P. Goss, Preliminary results of a numerical–experimental study of the dynamic structure of a buoyant jet diffusion flame, *Combust. Flame* **83** (3/4), 263–270 (1991).
25. V. R. Katta, L. P. Goss and W. M. Roquemore, Numerical investigations of transitional H_2/N_2 jet diffusion flames, *AIAA J.* **32,** 84–94 (1994).

PUBLISHED WITH PERMISSION
Combust. Sci. Tech., 1996, Vols. 113–114, pp. 429–449
Reprints available directly from the publisher
Photocopying permitted by license only

Copyright Ownership - Taylor & Francis Ltd.
© 1996 OPA (Overseas Publishers Association)
Amsterdam B.V. Published in The Netherlands under
license by Gordon and Breach Science Publishers SA
Printed in Malaysia

Unsteady Spray Behavior in a Heated Jet Shear Layer: Droplet-Vortex Interactions

S. K. AGGARWAL, T. W. PARK and V. R. KATTA *Department of Mechanical Engineering University of Illinois at Chicago, Chicago, IL 60607*
Innovative Scientific Solutions, Inc. Dayton, OH 45430

(Received March 1, 1996)

Abstract—Processes of droplet-vortex interactions have been studied numerically in a dynamic evaporating spray. The spray is formed between a droplet-laden heated nitrogen jet and a coflowing air stream. The jet velocity and temperature have been considered in a range, where large-scale vortex structures develop due to convective Kelvin-Helmholtz instability of the jet shear layer. Numerical simulations of the heated jet without droplets show the presence of organized vortex structures and their pairing interaction. The fundamental frequency of these structures scale with the jet diameter and velocity, yielding a Strouhal number of 0.36. Results concerning droplet dispersion indicate that 1) the dispersion of intermediate-sized droplets is enhanced due to their interaction with vortex rings during the vortex-pairing process, 2) a second Stokes number based on a droplet transit time can be used to characterize the dispersion of larger droplets, and 3) the evaporation during droplet-vortex interaction modifies dispersion significantly.

Results on the dynamics of two-way coupled system indicate that for a non-evaporating spray at a mass loading of unity, the dynamics of shear layer and vortex rings are strongly influenced by the dispersed phase. The locations of shear-layer rollup, vortex formation and pairing are shifted downstream, and their respective frequencies are reduced compared to those for the one-way coupled system. In addition, it is demonstrated that the shear-layer stability can be modulated by changing the droplet injection characteristics. For an evaporating spray, the effect of two-way coupling is more complex compared to that for a non-evaporating spray. In general, the shear-layer dynamics becomes much less organized compared to the one-way coupled system.

INTRODUCTION

Large-scale, coherent vortical structures have been found to exist in a variety of shear flows including those involving combustion (Katta *et al.* 1994) and multiphase flows (Chung and Trout 1988; Longmire and Eaton 1992). In two-phase shear flows involving solid particles or liquid droplets, the transient interactions between dispersed phase and large vortical structures are expected to play a central role in determining the dynamics and structural characteristics of these flows. These transient interactions are strongly coupled and non-linear, and pertain to the effect of large vortical structures on droplet dispersion and gasification; which, in turn, affect the local environment near each droplet and thereby the dynamics of two-phase system under consideration. In reacting sprays, the flame dynamics and pollutant formation are expected to be strongly influenced by these interactions. A fundamental understanding of such interactions is also relevant for devising passive and active control strategies for improving the combustor performance. Many recent studies,

both numerical (Chung and Trout 1988; Uthuppan *et al.* 1994) and experimental (Longmire and Eaton 1992; Lazaro and Lasheras 1992; Hishida *et al.* 1992), have focussed on one-way coupling, characterizing the effect of vortex structures on droplet dispersion. The two-way coupling or the effects of dispersed phase on vortex dynamics, and subsequently on fuel vapor distribution and flame behavior, remain largely unexplored. In addition, the role of droplet vaporization in the dispersion process has not been investigated in previous studies.

In this paper, we report a numerical study of two-way droplet-vortex interactions in a dynamic evaporating spray. The spray is formed between a droplet-laden heated nitrogen jet and a coflowing air stream. The overall objective is to study the fundamental processes of spray diffusion flames in laminar and transitional regimes in the presence of large vortical structures. In the present study, however, the physical model is simplified by considering a heated jet issuing into a coflowing air stream, so that the complexities due to chemical reactions can be avoided. The jet velocity and temperature are considered in a range, where large-scale vortex structures develop due to convective Kelvin-Helmholtz instability of the jet shear layer (Huerre and Monkewitz 1985). In a separate study (Park 1996), we investigated the interactions of droplets with buoyancy-induced vortex structures resulting from a global instability. The dynamics of vortex structures and droplet-vortex interactions in a convectively unstable shear flow are significantly different from those associated with global instability, and are examined in the present paper. In the first part, the dispersion behavior of both non-evaporating and evaporating droplets is investigated. The objective is to examine the effect of droplet evaporation on the dispersion process. Several previous studies cited above have shown that the presence of large-scale vortex structures leads to a size-dependent dispersion behavior, such that the droplets with a response time on the order of a relevant vortex time exhibit the maximum dispersion. In many applications, especially those involving spray combustion, the size of a droplet may change significantly during its interaction with a vortex, i.e. the droplet lifetime may be of the same order of magnitude as the droplet-vortex interaction time. It is therefore relevant to investigate the effect of size change on droplet dispersion. In the second part of this study, we examine the processes of two-way interactions for both non-evaporating and evaporating droplets, and make an attempt to gain an understanding of the effects caused by momentum coupling as well as mass and energy coupling between the phases.

THE PHYSICAL-NUMERICAL MODEL

The physical system simulated in the present study is shown schematically in Figure 1. It consists of a central jet which is a two-phase mixture of gaseous nitrogen and liquid fuel (*n*-heptane) droplets and a low-speed annular air flow. The jet at a velocity of 5.0 m/s and temperature of 1200 K is issuing into a coflow which is at velocity of 0.2 m/s and temperature of 294 K. The central jet is heated primarily to enhance the fuel evaporation. The jet diameter (D) is 2.54 cm. The Reynolds number based on velocity, density and viscosity of the heated jet is 790, and the Richardson number, $Ri = gD(\rho_0 - \rho_j)/(U_j^2 \cdot \rho_j)$, is 0.031. Here U_j and ρ_j are the jet velocity and

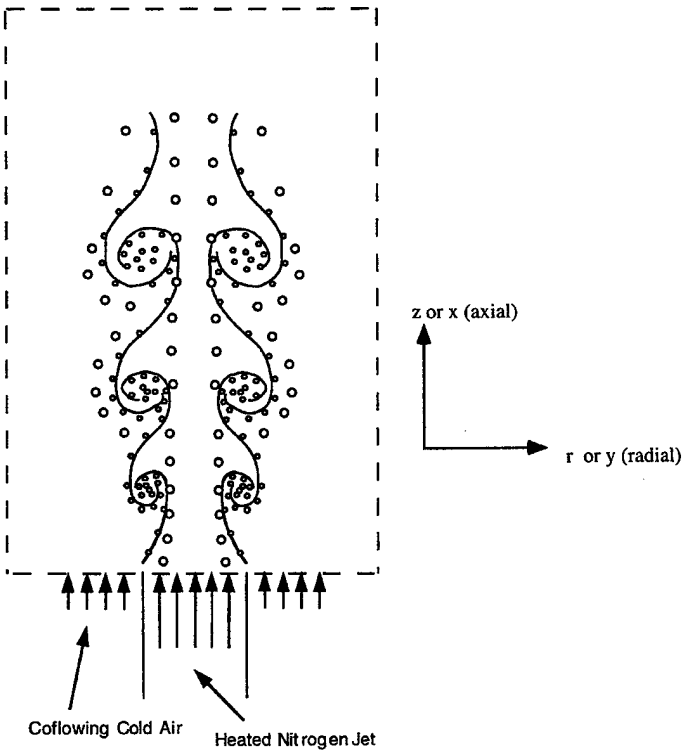

FIGURE 1 A schematic of droplet-laden heated nitrogen jet in a cold annular air flow.

density, ρ_0 the ambient density, and g the gravitational acceleration. Note that a small Richardson number $Ri = 0.031$ implies that the effect of buoyant convection is small compared to the inertial acceleration, and jet-shear-layer instability is primarily of the Kelvin-Helmholtz type. The numerical model is based on the solution of time-dependent, two-phase equations in an axisymmetric geometry. The unsteady, axisymmetric governing equations in cylindrical (z, r) coordinate system for a droplet-laden heated jet are

$$\frac{\partial(\rho\Phi)}{\partial t}+\frac{\partial(\rho u\Phi)}{\partial z}+\frac{\partial(\rho v\Phi)}{\partial r}=\frac{\partial}{\partial z}\left(\Gamma^{\Phi}\frac{\partial\Phi}{\partial z}\right)+\frac{\partial}{\partial r}\left(\Gamma^{\Phi}\frac{\partial\Phi}{\partial r}\right)-\frac{\rho v\Phi}{r}+\frac{\Gamma^{\Phi}}{r}\frac{\partial\Phi}{\partial r}+S_g^{\Phi}+S_\ell^{\Phi}. \quad (1)$$

The general form of Eq. (l) represents the continuity, momentum, species, or energy conservation equation depending on the variable used for Φ. Table I gives the transport coefficients Γ^{Φ} and the source terms S_g^{Φ} and S_ℓ^{Φ} that appear in the governing equations. In this table, μ, λ, and C_p represent the viscosity, the thermal conductivity, and the specific heat, respectively. They are considered functions of temperature and species concentration.

TABLE I

Transport coefficients and source terms appearing in governing equations

Equations	Φ	Γ_g^Φ	S_g^Φ	S_ℓ^Φ
Continuity	1	0	0	$\sum_k n_k \dot{m}_k$
Axial momentum	u	μ	$-\frac{\partial p}{\partial z}+(\rho_0-\rho)g+\frac{\partial}{\partial z}\left(\mu\frac{\partial u}{\partial z}\right)+\frac{\partial}{\partial r}\left(\mu\frac{\partial v}{\partial z}\right)+\frac{\mu}{r}\frac{\partial v}{\partial z}$ $-\frac{2}{3}\left\{\frac{\partial}{\partial z}\left(\mu\frac{\partial u}{\partial z}\right)+\frac{\partial}{\partial z}\left(\mu\frac{\partial v}{\partial r}\right)+\frac{\partial}{\partial z}\left(\mu\frac{v}{r}\right)\right\}$	$\sum_k\left(n_k\dot{m}_k u_k - n_k M_k\frac{du_k}{dt}\right)$
Radial momentum	v	μ	$-\frac{\partial p}{\partial r}+\frac{\partial}{\partial z}\left(\mu\frac{\partial u}{\partial r}\right)+\frac{\partial}{\partial r}\left(\mu\frac{\partial v}{\partial r}\right)+\frac{\mu}{r}\frac{\partial v}{\partial r}-2\mu\frac{v}{r^2}$ $-\frac{2}{3}\left\{\frac{\partial}{\partial r}\left(\mu\frac{\partial u}{\partial z}\right)+\frac{\partial}{\partial r}\left(\mu\frac{\partial v}{\partial r}\right)+\frac{\partial}{\partial r}\left(\mu\frac{v}{r}\right)\right\}$	$\sum_k\left(n_k\dot{m}_k v_k - n_k M_k\frac{dv_k}{dt}\right)$
Mass fraction of fuel	Y_f	ρD_f	0	$\sum_k n_k \dot{m}_k$
Mass fraction	Y_0	ρD_0	0	0
Energy	T	λ/C_p	0	$\sum_k n_k \dot{m}_k (h_{fs} - \ell'_{k,eff})$

The effect of dispersed phase on gas-phase properties is incorporated through the source/sink terms (S_ℓ^Φ) representing the exchange of mass, momentum, and energy between the gas and liquid phases. In order to evaluate these terms, it is necessary to establish droplet trajectories, size and temperature histories. The Lagrangian approach is employed to solve the liquid-phase governing equations for the dynamics and vaporization history of each droplet group. The spray is characterized by a discrete number of droplet groups, distinguished by their injection location, initial size, and time of injection. A droplet group in a Lagrangian treatment represent a characteristic group containing a finite number of droplets. Since an axisymmetric configuration is analyzed, the liquid properties are implicitly averaged in the azimuthal direction and the number of droplets associated with each characteristic group represents droplets uniformly distributed in an annular ring. The equations governing the variation of position, velocity, and size for each droplet group and other expressions are provided in an earlier paper (Park *et al.* 1995). A comprehensive vaporization model is employed to calculate the instantaneous droplet size and surface temperature along the trajectory of each group. The model includes the effects of variable thermophysical properties, non-unity Lewis number in the gas film outside the droplet, the effect of Stefan flow on the heat and mass transfer between the droplet and the gas, and the effect of transient liquid heating. The variable thermophysical properties are calculated at reference film temperature and concentrations, obtained by using the 1/3 rule, except for the gas density which is calculated at the free stream value (Abramzon and Sirignano 1989). The Wilke rule

(Edwards *et al.* 1979) is used to calculate the dynamic viscosity and thermal conductivity of the gas film. The liquid fuel (n-C_7H_{16}) properties are collected from various sources and approximated as a function of the temperature (Park *et al.* 1995). The effect of transient liquid heating is incorporated by using the finite-conductivity model (Aggarwal 1984).

An implicit algorithm is employed to solve the unsteady gas-phase equations. The governing equations are integrated by using a "finite control volume" approach with a staggered, non-uniform grid system.The finite-difference forms of the momentum, energy, and species-densities equations are obtained using an implicit QUICKEST scheme (Leonard 1979). An iterative ADI (Alternative Direction Implicit) technique is used for solving the resulting sets of algebraic equations. At every time step, the pressure field is calculated by solving the pressure Poisson equations at all grid points simultaneously and utilizing the LU (Lower and Upper diagonal) matrix decomposition technique. Grid lines are clustered near the shear layer to resolve the steep gradients of the dependent variables. Boundaries of the computational domain are shifted sufficiently to minimize the propagation of disturbances into region of interest. The computational domain in the radial and axial directions is 15 cm and 40 cm respectively. Thus, the boundary in the radial direction is 5.9 nozzle diameters away from the axis of symmetry and the out-flow boundary in the axial direction is 15.7 nozzle diameters away from the nozzle exit. In our earlier studies it was found that these distances are more than sufficient to avoid the boundary influences on the region of interest (2 and 7 nozzle diameters in the radial and axial directions, respectively). The flow variables at the outflow boundary are obtained using an extrapolation procedure with weighted zero and first-order terms. The main criterion used in selecting the weighting functions is that the vortices crossing this outflow boundary should leave smoothly without being distorted.

The liquid-phase equations governing the position, velocity, and size of each droplet are advanced in time by a second-order accurate Runge-Kutta method. Since the gas-phase solution employs an implicit procedure, the temporal step size used for integrating the liquid-phase equations is usually smaller than that for gas-phase equations. An automatic procedure is implemented in order to select an optimum liquid-phase time step. The procedure to advance the two-phase solution over one gas-phase time step is as follows. Using the known gas-phase properties, the liquid-phase equations are solved over a specified number of liquid-phase subcycles. A third-order accurate Lagrangian polynomial method is used for interpolating the gasphase properties from the non-uniform fixed grid to the droplet characteristic location. It should be noted that the interpolation scheme for the gas-phase velocities u and v is based on their respective grid cells because of the use of a staggered grid in gas-phase calculation. The droplet properties are updated after every liquid-phase subcycle. Also, during each subcycle, the liquid-phase source terms appearing in the gas-phase equations are calculated at the characteristic location, and then distributed to the surrounding gas-phase grid points. These source terms are added at each gasphase grid points during one gas-phase time step and then used in the implicit solution of the gas-phase equations. Additional details can be found in an earlier paper (Park *et al.* 1995).

RESULTS

The dynamics of heated jet was first studied under normal-gravity and zero-gravity conditions without injecting droplets in the flow. The objective was to assess if gravity had any influence on the jet instability for the low Richardson number ($Ri = 0.031$) condition used in this, paper. Numerical experiments were also performed to validate the numerical model and examine the stability characteristics of the jet shear layer.

Numerical validation studies employed three different grids, namely 151×61, 201×71, and 301×91, and three different temporal step sizes corresponding to CFL numbers of 0.1, 0.2 and 0.4. Note that CFL (Courant-Friedrichs-Lewis) number is merely used here to control the temporal step size, and does not imply any significance pertaining to numerical stability. In all the cases, a non-uniform grid was employed with grid lines clustered near the shear layer to resolve the steep gradients of the dependent variables. This implies that the additional grid points in the 201×71 grid are placed near the shear layer, thus effectively reducing the grid density for the 201×71 grid by about fifty percent compared to the 151×61 grid. Results for the two different grid sizes and two CFL numbers are presented by plotting the time-history of axial velocity in the shear layer. Figure 2 indicates that the results are reasonably independent of the grid size and temporal step size used in the simulations. Figures 2a and 2c indicate the presence of well-organized, periodic Kelvin-Helmholtz vortex rings, while Figure 2b indicates the occurrence of a vortex-pairing interaction. The spatial development of vortex rings and their pairing interaction are depicted in Figure 3, which shows the instantaneous iso-temperature contours in the jet shear layer under normal- and zerogravity conditions. Toroidal vortex rings roll up periodically downstream of the nozzle exit due to the Kelvin-Helmholtz instability. No artificial (external) excitation is used to generate these vortices and it is believed that the noise in the calculations is providing the needed perturbation in the shear layer. It is interesting to note that even at a low Richardson number of 0.031, the vortex structures are influenced by gravity. However, the effect is small, and can be attributed to the buoyant acceleration of the low-speed annular fluid as it gets heated in the jet thermal layer. Moreover, the shear-layer rollup and large-scale vortex dynamics are essentially governed by the Kelvin Helmholtz instability. For example, the dominant frequencies corresponding to shear layer rollup and vortex-pairing interaction remain the same whether gravity is included in the simulations or not.

Figure 3 indicates a pairing interaction starting at an axial location $z = 40$ mm as the vortices convect downstream. The dominant frequencies obtained from the fast Fourier transform of axial velocity are 70 and 35 Hz corresponding to the roll up and merging frequencies respectively. Assuming the initial momentum thickness of jet shear layer between one to two radial grid spacing, we obtain the instability Strouhal number between 0.0112–0.0224, a range which encompasses the experimental range 0.0125–0.0155 reported in the literature (Hussain and Hussain 1983). Also, according to the experimental study of Subbarao and Cantwell (1992), the jet instability frequency scales with the inertial time scale at small *Ri*. This yields a Strouhal number of 0.36 in the present case, which also agrees with the reported

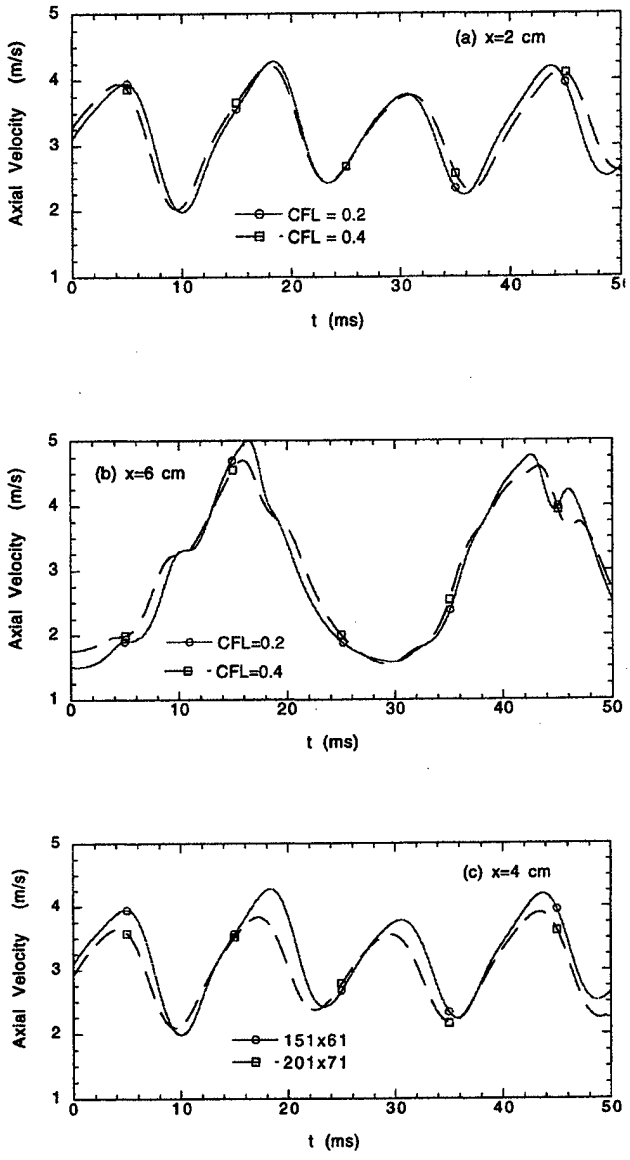

FIGURE 2 Time-history plot of axial velocity in the jet shear layer at three axial locations ((a) $x = 2$ cm, (b) $x = 6$ cm, and (c) $x = 4$ cm); effects of temporal step size and grid size.

experimental range of 0.25–0.5. The spectral analysis also indicates that the amplitude of subharmonic frequency (35 Hz) peaks at $x = 80$ mm, implying the occurrence of vortex merging at his location. This is confirmed by the iso-temperature plots in Figure 3.

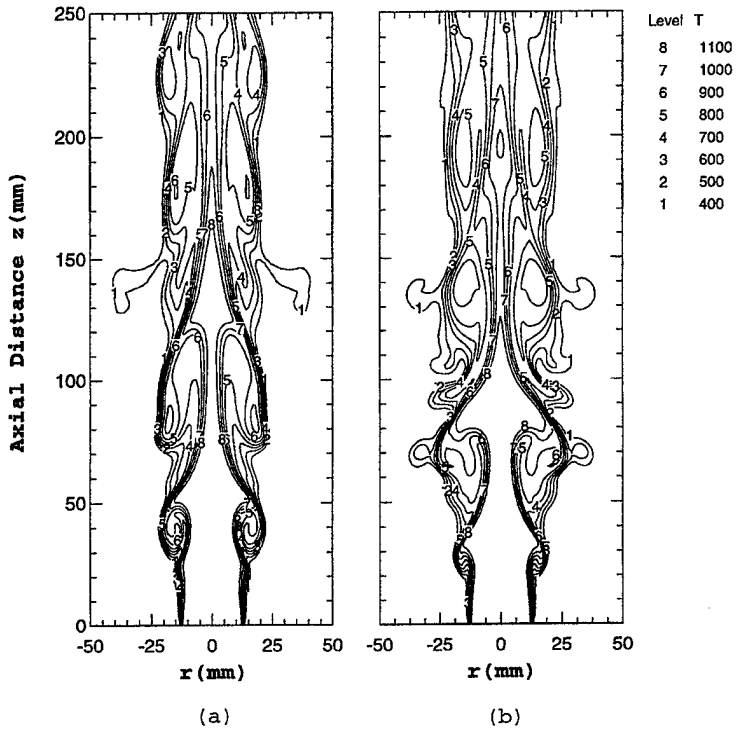

FIGURE 3 Instantaneous temperature contours for the heated nitrogen jet at (a) normal gravity and (b) zero gravity.

ONE-WAY INTERACTIONS

Results depicting the effect of large-scale structures on the dispersion of non-evaporating and evaporating droplets are summarized in Figure 4. For these results, the source terms S_ℓ^Φ representing the effects of dispersed phase on the gas phase (see Table I.) are identically set to zero. The instantaneous iso-temperature contours and droplet locations are plotted for both non-evaporating and evaporating droplets for four different droplet sizes. The red color in iso-temperature contours corresponds to a temperature of 1200 K while the purple corresponds to a value of 294 K, representing the temperature of coflowing stream. In order to examine the effect of vortex rings on droplet dispersion, instantaneous locations of non-evaporating and evaporating droplets are plotted on the left-hand and right-hand sides of the symmetric jet, respectively. Color representing the size of the droplet changes from red to blue as it evaporates from the initial size (at the instant of injection) to the size of a gas particle, which is taken as 10 μm or one-tenth of the initial size whichever is smaller. Since the droplets on the right-hand side of the jet represent non-evaporating ones, the color of the droplets remains red. Quantitative results on dispersion for both non-evaporating and evaporating droplets are depicted in Figure 5, which

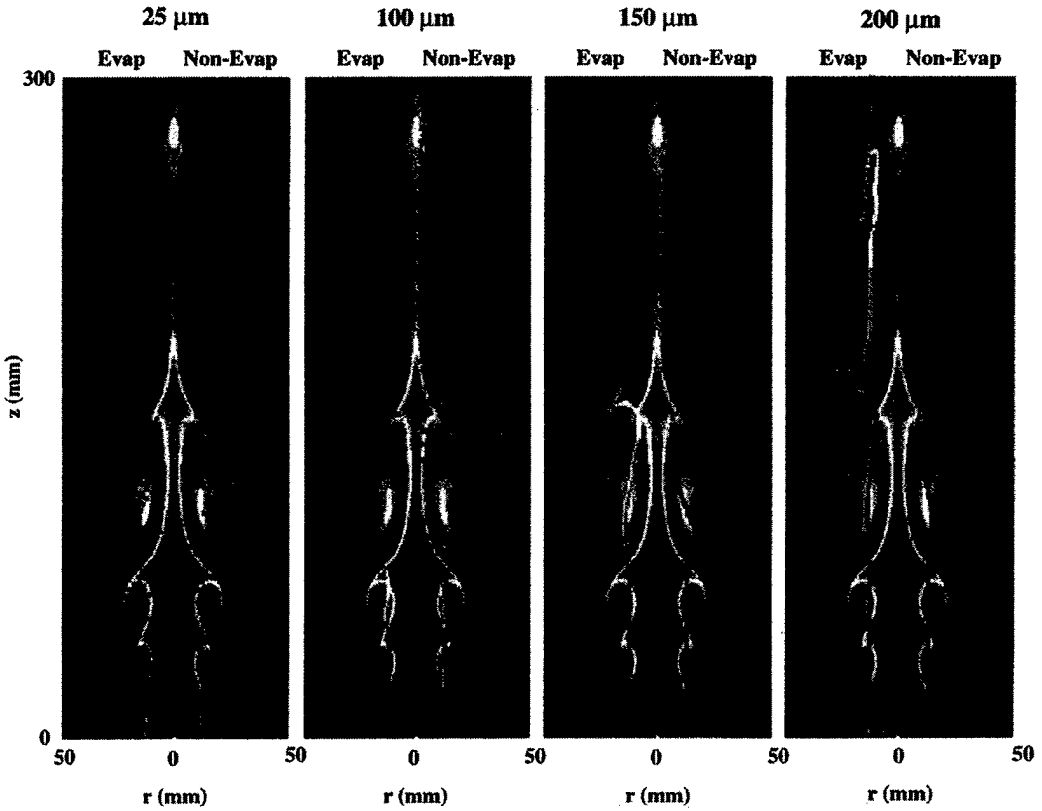

FIGURE 4 Simultaneous snapshots of the flow (iso-temperature contours) and droplets (solid squares) of different sizes; in each individual snapshot locations of the evaporating and non-evaporating droplets are plotted on the left-hand and right-hand sides of the symmetric jet, respectively. For iso-temperature contours, the red and purple colors represent the highest (1200 K) and the lowest (294 K) temperatures respectively.

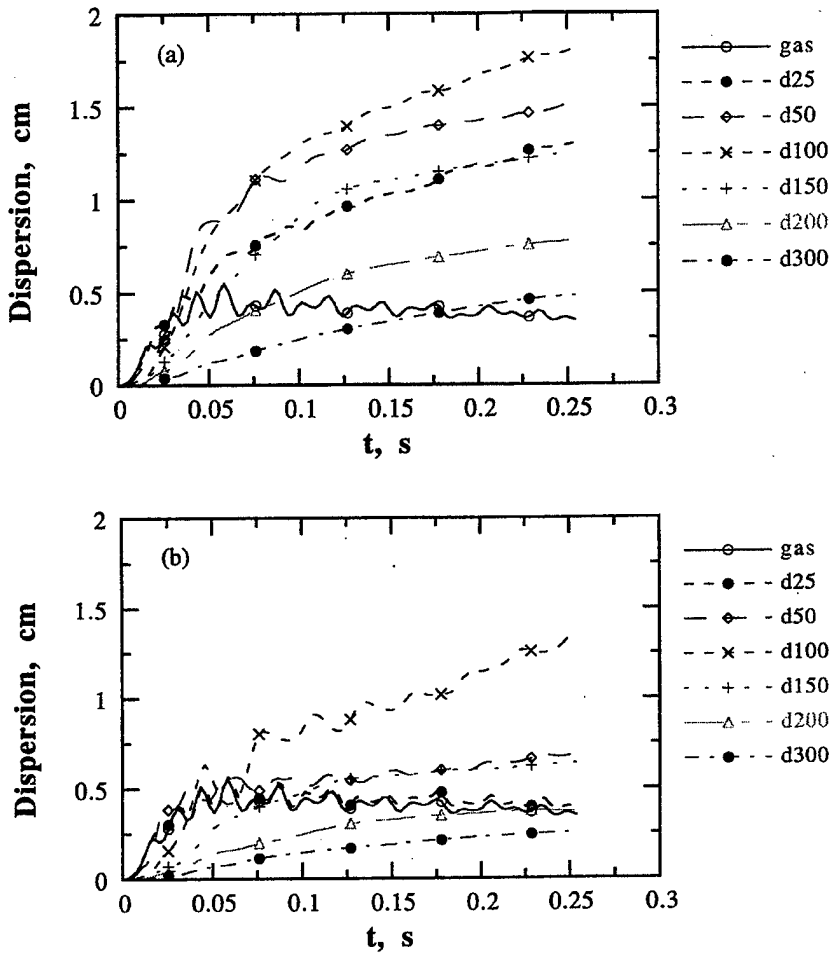

FIGURE 5 Dispersion function plotted as a function of time for (a) non-evaporating, and (b)-evaporating droplets injected at a radial location of 1.27 cm.

shows the variation of dispersion function with time for different-size droplets. The dispersion function is defined as the rms (root mean squared) lateral displacement of droplets from the initial radial injection location:

$$D(t, N) = \left[\frac{\{\sum_{i=1}^{N}(r_i(t) - r_{i0})^2\}}{N}\right]^{1/2} \tag{2}$$

where r_i the radial location of droplet i at time t, r_{i0} the radial injection location of the same droplet at nozzle exit, and N is the total number of droplets in the flow field at time t. Results in Figure 5 indicate a typical size-selective dispersion process

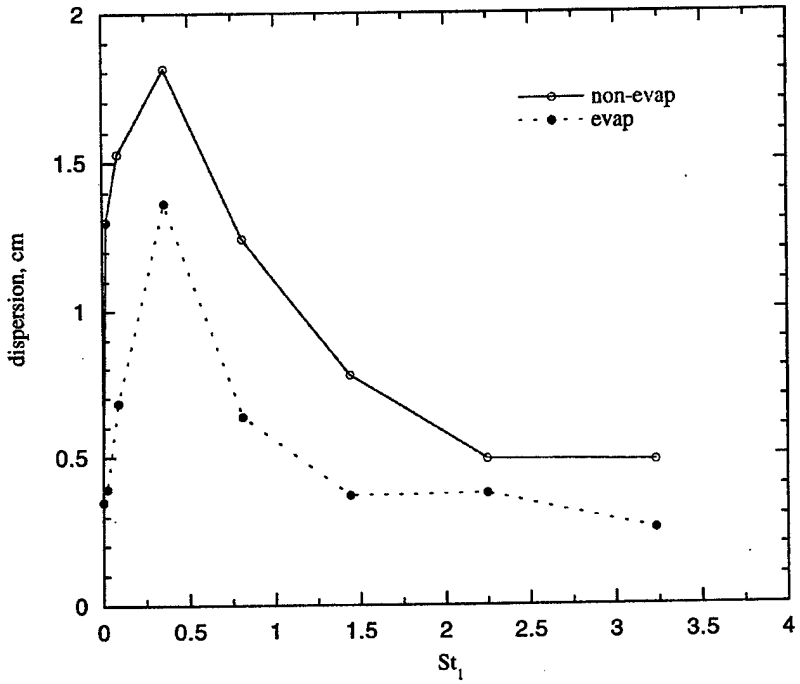

FIGURE 6 Dispersion function versus Stokes number for non-evaporating and evaporating droplets.

whereby the intermediate-sized droplets (100 μm in the present study) exhibit the maximum dispersion. Since the effect of vortex structures on non-evaporating droplets is often characterized by the Stokes number defined as the ratio of droplet response time (t_p) to a characteristic flow time (t_f), we show the variation of dispersion function with Stokes number (St_1) for both non-evaporating and evaporating droplets in Figure 6. The value of t_f is based on the first subharmonic or vortex-merging frequency, since the detailed visualization of flow field and droplet locations indicates that droplet dispersion is influenced more strongly by the vortex-merging process.

Important observations from Figure 6 are that the dispersion of intermediate-sized droplets is enhanced due to their interaction with vortex rings, that the pairing interaction is most responsible for this dispersion enhancement, and that droplet evaporation during the transient droplet-vortex interaction modifies dispersion significantly. These observations can be explained by the instantaneous snapshots given in Figure 4. For the non-evaporating case, it can be seen that the intermediate-sized droplets exhibit higher dispersion, as these droplets are centrifuged out during the vortex-pairing interaction. The larger-sized droplets disperse less as their motion is not much affected by the pairing interaction. These droplets can be dispersed, however, by the merged vortices further downstream, provided their transit time is

comparable to their aerodynamic response time. For example, 150-μm and 200-μm droplets are dispersed following their interaction with the second (merged) and third vortex respectively. This suggests that droplet transit time may also be an important parameter in addition to the flow time, in characterizing the dispersion of larger droplets. Following Hardalupas *et al.* (1992), we define a second Stokes number (St_2) or a droplet transit Stokes number as the ratio of droplet transit time to its response time. Using this Stokes number, we are able to explain the dispersion of larger-sized droplets. The transit time for 150-μm droplets is 36 ms (based on a injection velocity of 5.0 m/s and second vortex location of 18 cm) yielding $St_2 = 0.64$. Similar calculation yields $St_2 = 0.86$ for 200-μm droplets.

Another important observation from Figures 4 and 6 is that the dispersion of evaporating and non-evaporating droplets in a dynamically evolving flow are quite different. Since the effect of vaporization is to reduce the droplet response time and thus reduce the Stokes number St_1, one would expect that the plot of dispersion function versus St_1 should shift uniformly to the left of that for the non-evaporating case. However, the dynamic nature of droplet-vortex interaction alters this expected behavior. As noted earlier, small- and medium-sized non-evaporating droplets exhibit higher dispersion due to their interaction with vortex rings during the vortex-pairing process, while the dispersion of larger-sized droplets is due to their interaction with vortices after the pairing process. The evaporation during droplet-vortex interaction modifies this behavior significantly. The small- and medium-sized droplets vaporize completely prior to or during their interaction with vortex rings, and consequently their dispersion is similar to that of tracer particles. The larger-sized evaporating droplets on the other hand are not affected significantly by the pairing vortices. Their dispersion is determined by their interaction with vortices following the pairing interaction. Due to evaporation, however, their dispersion is reduced compared to that of non-evaporating droplets since the degree of centrifuging decreases with the decrease in droplet size. Consequently, the effect of vaporization is to reduce droplet dispersion over the entire droplet size range, as indicated in Figure 6.

TWO-WAY INTERACTIONS

Both non-evaporating and evaporating sprays are analyzed in order to distinguish the two-way interactions involving only momentum transfer between the phases from those involving mass, momentum, and energy transfer. Calculations are initially made without injecting droplets into the fuel stream. As discussed earlier, the shear layer between the 1200-K nitrogen jet and the cold annulus air flow becomes unsteady with the development of large-scale vortices. The gasphase simulation is started at $t = 0$, and the droplet injection is started at $t = 0.16$ s. During this time, the initial flow transients are convected out of the computational domain, and the vortex rings attained a periodic structure. Droplets are injected into the jet shear layer every $10\Delta t_{gas}$, where $\Delta t_{gas} = 0.03176$ ms, from a radial location of 1.25 cm. This time interval yields an average droplet spacing which is about 16 times the droplet diameter, and can be considered as sufficiently large so as to neglect interaction

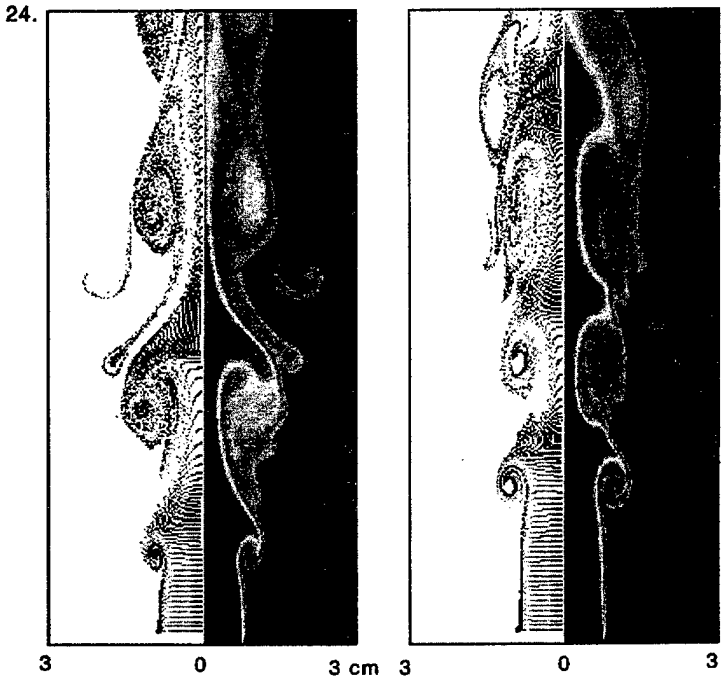

FIGURE 7 Snapshots of flow field for a non-evaporating spray with (a) one-way interaction, and (b) two-way interaction.

between the droplets. The number of droplets with each injection depends on the droplet mass loading (ratio of droplet mass flow rate to nitrogen mass flow rate in the jet), initial droplet size, and injection time interval. In the present study, a monodisperse *n*-heptane spray with an initial diameter of $d_p = 100$ μm and mass loading of unity is considered. Note that $d_p = 100$ μm corresponds to a Stokes number on the order of unity, and exhibits the maximum dispersion in the present case. It is also important to note that at a mass loading of unity, the volume occupied by liquid phase is about three orders of magnitude smaller than that of the gasphase volume, and the dilute-spray assumption is still valid. The initial diameter $d_p = 100$ μm and mass loading of unity yields the number of droplets in each injection as 673, which is equivalent to having 673 equally distributed azimuthal injection locations.

Extensive flow visualization was used to gain a qualitative understanding of the effect of dispersed phase on large-scale vortex structures. One representative result is depicted in Figure 7, which compares snapshots of the flow field for a non-evaporating spray with one-way and two-way interactions respectively. In each snapshot, we plot instantaneous iso-temperature contours on the right, and streaklines on the left. Important observation is that the momentum coupling has a significant influence on

the dynamics of vortex structures. For the two-way coupled system, the locations of shear layer rollup and vortex pairing are shifted downstream compared to the one-way coupled system. More detailed flow visualization for the two cases indicated that for the two-way coupled system, the vortex structures are stronger, though less coherent, and entrain more lowspeed (colder) fluid compared to those for the one-way coupled system. We will discuss this aspect further when quantitative results are presented for the two-way coupled system.

Figure 8 shows simultaneous snapshots of the flow and droplets for three different cases; one-way coupled system in Figure 8b and two-way coupled evaporating and non-evaporating sprays in Figures 8a and 8c respectively. For the non-evaporating case, due to the delayed vortex formation and pairing interaction, the occurrence of significant droplet dispersion is also moved farther downstream compared to the one-way coupled system. Figure 8 also indicates that the effect of dispersed phase on

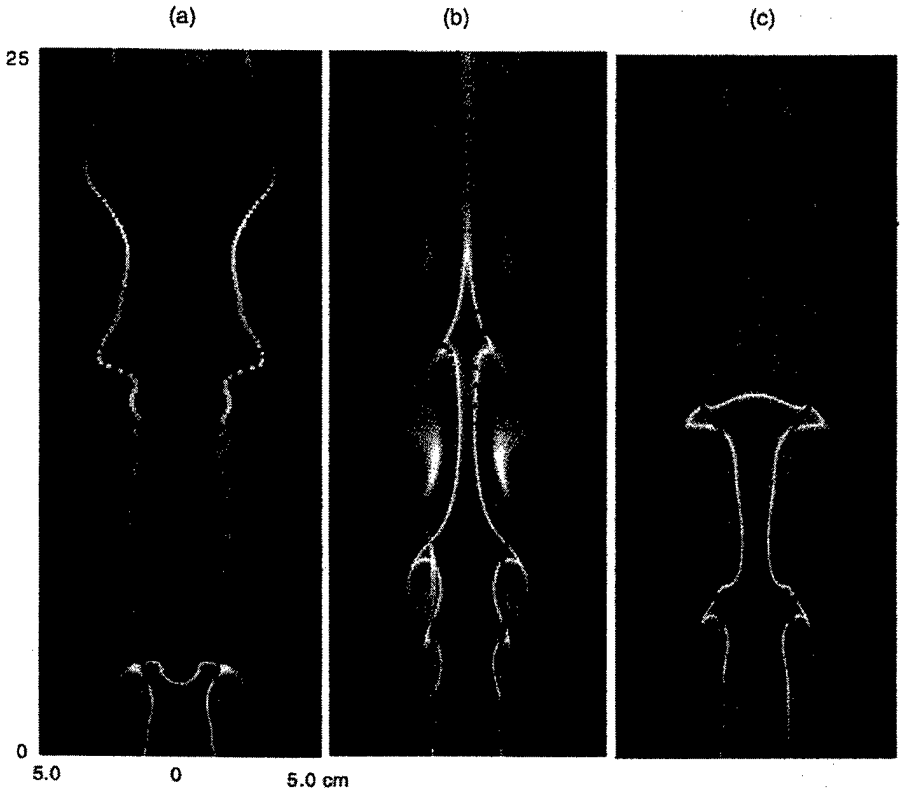

FIGURE 8 Simultaneous snapshots of the flow and droplets for (a) evaporating spray with two-way interaction, (b) spray with one-way interaction and (c) non-evaporating spray with two-way interaction. For iso-temperature contours, the red and purple colors represent the highest (1200 K) and the lowest (294 K) temperatures respectively.

the vortex structures is more significant for the evaporating case compared to the non-evaporating one. This can be attributed to the added effects of mass and energy transfer between the phases for the evaporating case. Based on a detailed visualization of the two-phase flow field for the evaporating case, the effect of dispersed phase on the temporally and spatially developing shear layer can described as follows. As the droplets are injected into the shear layer, the rollup location initially shifts downstream from 3 cm to 5 cm, similar to the non-evaporating case. However, as the droplet evaporation becomes significant, the addition of fuel vapor with density three times that of nitrogen strongly affects the vortex formation process. In addition, the jet cooling caused by droplet heating and vaporization increases the mixture density, which further modifies shear layer dynamics. Due to these two effects, the rollup location moves upstream to about 2 cm from the nozzle exit, the vortex becomes stronger and pinches the jet more strongly compared to that for the one-way coupled system. The subsequent processes, which normally involves the convection of vortices and pairing interactions for the one-way coupled system, become much less organized for the evaporating case. In general, the pairing interactions are much less frequent and coherent, and the vortices are strongly stretched as they convect downstream. In addition, the shear layer rollup becomes less organized, with the rollup location oscillating between 2 and 5 cm from the nozzle exit.

The loss of coherency in shear layer dynamics for the two-way coupled system is better illustrated by plotting the time history of axial velocity for the three cases. As indicated in Figure 9, for the one-way coupled system, the processes of shear layer rollup and vortex formation are well organized with a frequency of 70 Hz. For the two-way coupled system, however, the shear layer dynamics is much less organized, especially for the evaporating spray. This is further indicated by the Fourier transform of axial velocity shown in Figure 10. With one-way interaction, both the shear layer rollup and the vortex pairing are highly organized with frequencies of 70 and 35 Hz respectively. For the non-evaporating spray with two-way momentum coupling, the rollup and vortex-pairing frequencies are reduced to 54 and 27 Hz respectively, and the vortices are not as organized as in the one-way coupled system. For the evaporating spray with two-way coupling, the dynamics represents a much less organized behavior without any well-defined frequency.

For the non-evaporating case discussed above, the two-way coupling modifies the shear layer dynamics such that the vortex formation and pairing occur at a downstream location, and their frequencies are reduced compared to those for the one-way coupled system. In order to examine the momentum-coupling effect further, we ran additional simulations and studied the effect of droplet injection velocity on the gas-phase dynamics. The time-averaged structure of the shear layer for different droplet injection velocities is depicted in Figure 11. The axial profiles of time-averaged gas-phase velocity indicate that the axial velocity is smaller for the two-way coupled system with $U_p = 5.0$ m/s (the base case discussed) compared to that for the one-way coupled system, indicating greater entertainment of the cold fluid. For this case, the droplets are injected at the jet velocity, i.e. the gas phase and droplets initially have the same velocity. However, as the shear layer develops spatially, the gas-phase velocity decreases in the shear layer. Since droplets now have higher velocity than the gas phase, there is momentum transfer from dispersed phase to gas

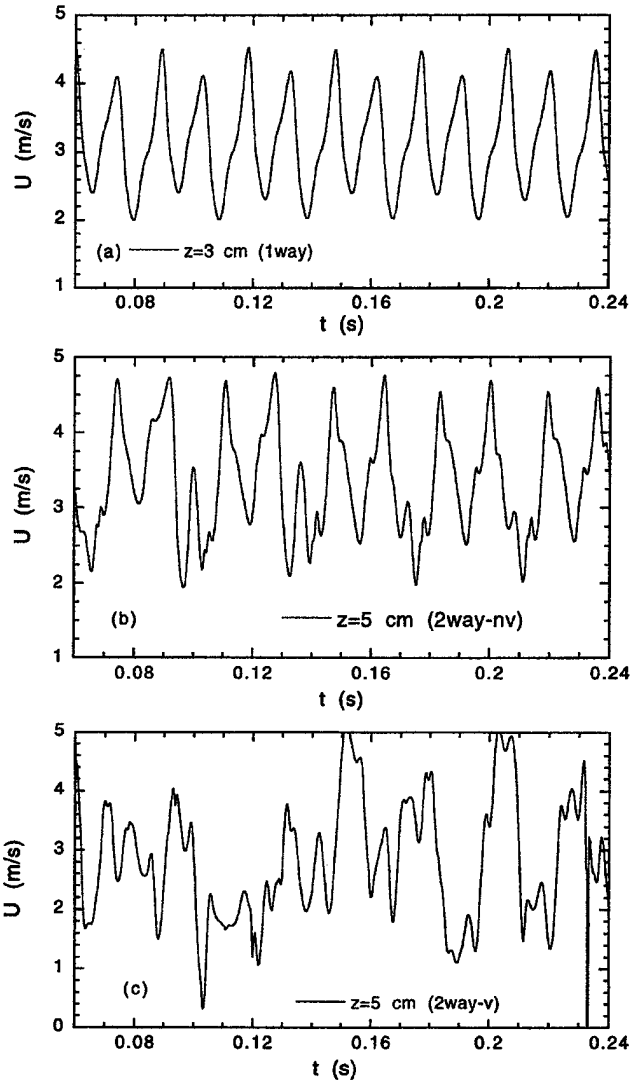

FIGURE 9 Time history of gas-phase axial velocity in the shear layer for (a) one-way interaction, (b) non-evaporating spray with two-way interaction, and (c) evaporating spray with two-way interaction.

phase, which is indicated by the fact that the gas-phase velocity is initially higher for the two-way coupled system with $U_p = 5.0$ m/s compared to that for the one-way coupled system, Figure 11a. This increases the magnitude of vorticity in the shear layer, and thus strengthens the vortex structures. However, if the droplets are injected at a velocity smaller than the jet velocity, the momentum transfer occurs in the reverse direction, reducing vorticity magnitude in the shear layer. Consequently, as

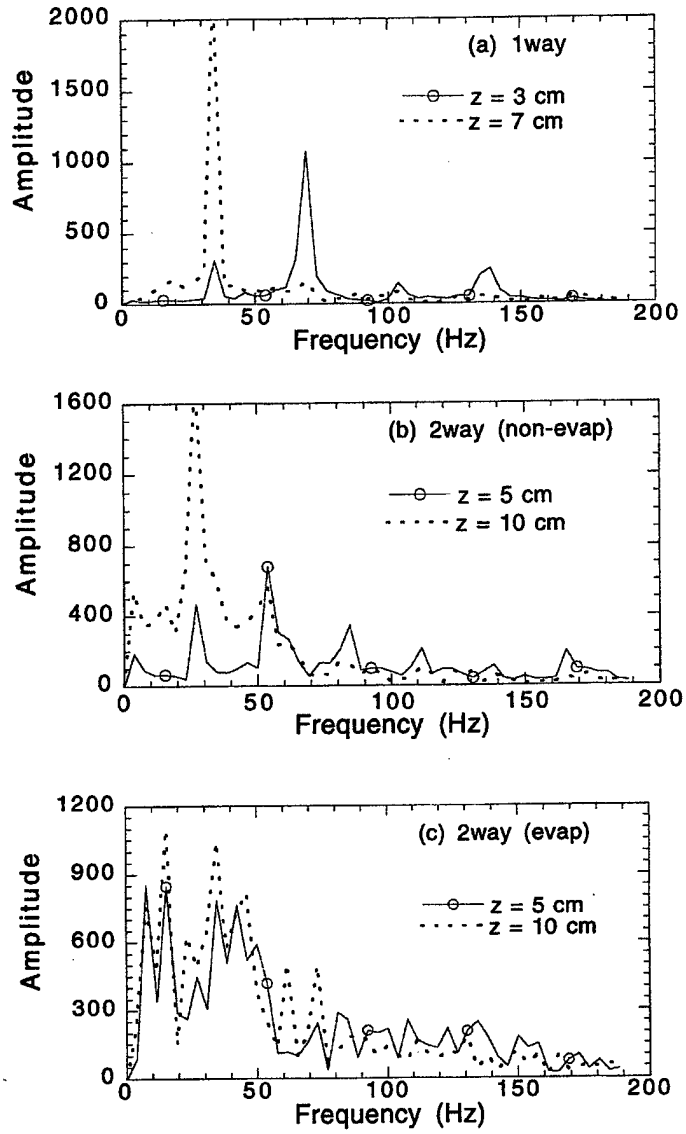

FIGURE 10 Frequency spectrum of axial gas velocity for (a) one-way interaction, (b) two-way non-evaporating spray, and (c) two-way evaporating spray.

the droplet injection velocity is decreased compared to the jet velocity, the shear layer stability is enhanced, and entrainment of the colder fluid is reduced. The axial profiles of gasphase temperature shown in Figure 11b are consistent with those of gas-phase velocity. For the two-way case with $U_p = 5.0$ m/s, the gas temperature

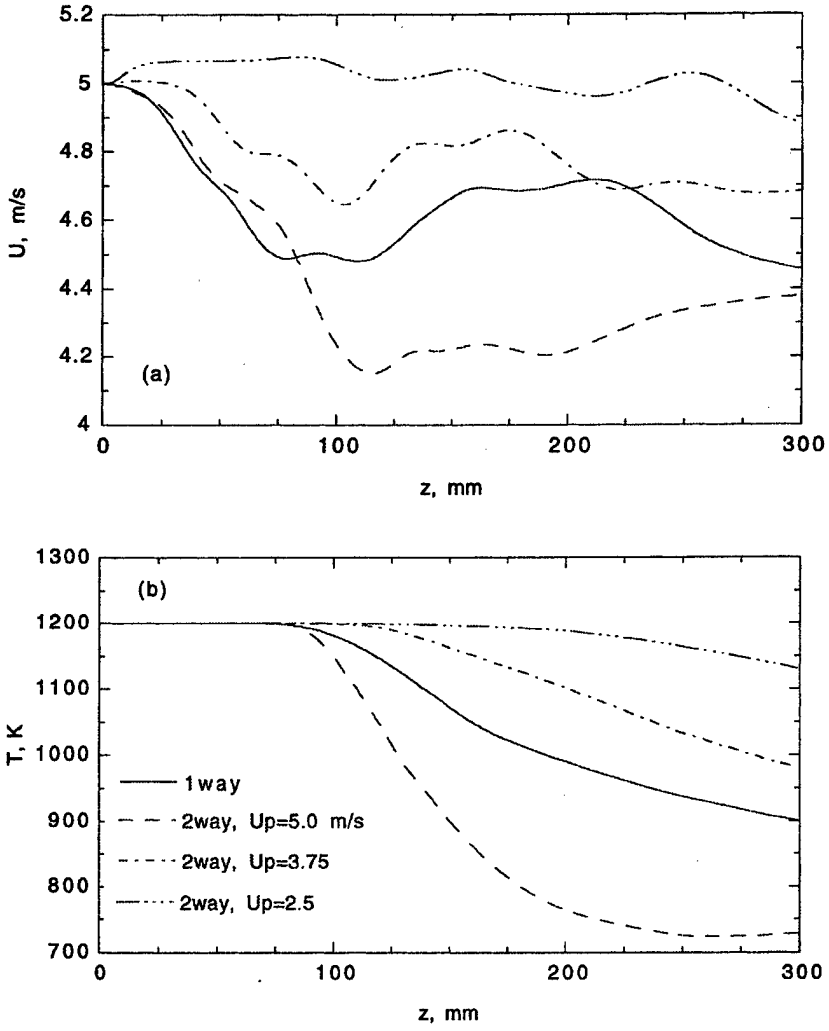

FIGURE 11 Axial profiles of time-averaged gas velocity and temperature for four different cases.

decreases faster compared to that for the one-way case, indicating greater entrainment of colder fluid in the shear layer for the former. However, as the droplet injection velocity is reduced, the shear layer becomes more stable, as indicated by a slower rate of decrease of gas temperature for $U_p = 3.75$ m/s and 2.5 m/s. The increased shear layer stability was also confirmed by employing detailed visualization of the temporally and spatially developing shear layer for different droplet injection velocities. Another confirmation is provided in Figure 12, which shows the

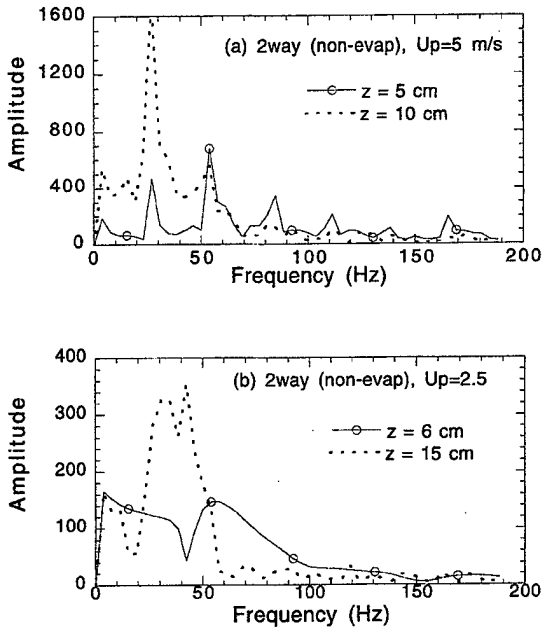

FIGURE 12 Frequency spectrum of axial gas velocity for a two-way coupled non-evaporating spray with (a) droplet injection velocity $U_p = 5.0$ m/s, and (b) $U_p = 2.5$ m/s.

Fourier spectrum of gas-phase axial velocity for two different droplet velocities. For $U_p = 2.5$ m/s, the shear layer stability is significantly enhanced with a formation of a weak vortex far downstream ($z = 15$ cm), as indicated by the significantly reduced amplitude and the absence of a dominant frequency for this case. Thus, the important observation is that at a liquid mass loading of unity, the dispersed phase has a strong effect on the stability and dynamic characteristic of jet shear layer, and this effect can be modulated by changing the droplet injection characteristics.

CONCLUSIONS

In this paper, we have investigated the effect of droplet evaporation on dispersion, and the dynamics of two-way droplet-vortex interactions and their influence on the structure of both non-evaporating and evaporating sprays. A spray formed between a droplet-laden heated nitrogen jet and a coflowing air stream has been simulated. The jet velocity and temperature have been considered in a range, where large-scale vortex structures develop due to the convective Kelvin-Helmholtz instability of the jet shear layer. Liquid fuel (*n*-heptane) droplets are introduced into the vortex structures, and processes of droplet-vortex interactions have been studied numerically by employing a third-order time-accurate, multidimensional, two-phase algorithm. The

effect of dispersed phase is incorporated through the source/sink terms in the gas-phase governing equations, representing the exchange of mass, momentum, and energy between the gas and liquid phases. Numerical results have been shown to be independent of the grid and temporal step size used in the simulation. In addition, simulation of the jet shear layer without droplets reproduced the large-scale features that have been observed in laboratory experiments and previous numerical simulations. For example, the simulation yields a Strouhal number of 0.36, based on the fundamental frequency of large-scale structures, which is within the reported experimentally range of $0.25 - 0.5$. Detailed flow visualization has been employed to gain further understanding of the dispersion of evaporating droplets, and the effect of dispersed phase on the dynamics and time-averaged structure of the shear layer.

Results for the one-way coupled system indicate that the dispersion of intermediate-sized droplets is enhanced due to their interaction with vortex rings during the vortex-pairing process, that the dispersion enhancement can be characterized by a Stokes number based on the vortex-pairing frequency, that a second Stokes number based on a droplet transit time can be used to characterize the dispersion of larger droplets, and that the evaporation during droplet-vortex interaction has a significant influence on dispersion. Results on the dynamics of two-way coupled system indicate that for a non-evaporating spray at a mass loading of unity, the dynamics of shear layer and vortex rings are strongly influenced by the dispersed phase. The locations of shear layer rollup, vortex formation and pairing are shifted downstream, and their frequencies are reduced compared to those for the one-way coupled system. In addition, it is demonstrated that the shear layer stability can be modulated by changing the droplet injection characteristics. This has important implication for the dynamic behavior of two-phase flow systems, such as gas turbine combustors and liquid propellant rocket engines. For an evaporating spray, the effect of two-way coupling is much more complex compared to that for a non-evaporating spray. In general, the dynamics of shear layer and vortex structures for a two-way coupled evaporating spray become much less organized compared to the one-way coupled system.

ACKNOWLEDGEMENTS

This work was funded by the AFOSR under Grant F49620-93-1-0400 monitored by Dr. Julian M. Tishkoff. Computations were performed on Cray C-90 at the Pittsburgh Supercomputing Center. Correspondence should be directed to S.K. Aggarwal.E-mail Suresh K. Aggarwal@uic.Edu

REFERENCES

Abramzon, B. and Sirignano, W. A. (1989). *Int. J. Heat Mass Transfer*, **32**, 1605–1618.

Aggarwal, S. K., Tong, A. and Sirignano, W. A. (1984). A Comparison of Vaporization Models for Spray Calculation. *AIAA Journal*, **22**, 1448–1457.

Chung, J. N. and Troutt, T. R. (1988). Simulation of Particle Dispersion in an Axisymmetric Jet. *J. of Fluid Mech.*, **186**, 199–222.

Hardalupas, Y., Taylor, A. M. K. P. and Whitelaw, J. H. (1992). Particle dispersion in a vertical round sudden-expansion flow. *Phil. Trans. R. Soc. Lond. A.*, **341**, 411–442.

Hishida K., Ando, A. and Maeda, M. (1992). Experiments on Particle Dispersion in a Turbulent Mixing Layer. *International Journal of Multiphase Flow*, **18**, 181–194.

Huerre, P. and Monkewitz, P.A. (1985). Absolute and Convective Instabilities in Free Shear Layers. *J. Fluid Mech.*, **159**, 151–168.

Hussain, Z.D. and Hussain, A.K.M.F. (1983). Natural Instability of Free Shear Layers. *AIAA Journal* **21**, 1512–1517.

Katta, V.R., Goss, L.P. and Roquemore, W.M. (1994). *Combustion and Flame*, Vol. **96**, pp. 60–74.

Lazaro, B.J. and Lasheras, J.C. (1992). Particle Dispersion in the Developing Free Shear Layer, Part 2-Forced Flow. *J. Fluid Mech.*, **235**, 179–221.

Leonard, B.P. (1979). A Stable and Accurate Convective Modelling Procedure Based on Quadratic Upstream Interpolation. *Comput. Methods in Applied Mechanics and Eng.*, **19**, 59–98.

Longmire, E.K. and Eaton, J.K. (1992). Structure of a Particle-Laden Round Jet. *J. Fluid Mech.*, **236**, 217–257.

Park, T.W., Aggarwal, S.K. and Katta, V.R. (1995). Gravity Effects on the Dynamics of Evaporating Droplets in a Heated Jet. *J. of Propulsion and Power*, 11, 519–528.

Park, T.W., Aggarwal, S.K. and Katta, V.R. (1996). A Numerical Study Of Droplet-Vortex Interactions In an Evaporating Spray, *Int. J. of Heat & Mass Transfer*, To appear.

Subbarao, E.R. and Cantwell, B.J. (1992). Investigation of a coflowing buoyant jet - experiments on the effect of Reynolds number and Richardson number. *J. of Fluid Mech.*, **245**, 69–90.

Uthuppan, J., Aggarwal S.K., Grinstein, F.F. and Kailasanath, K. (1994). Particle Dispersion in a Transitional Axisymmetric Jet: A Numerical Simulation. *AIAA Journal*, **32**, 2004–2014.

AIAA 97-0130

NUMERICAL MODELING OF INTERACTIONS BETWEEN EVAPORATING DROPLETS

Long P. Chin

Innovative Scientific Solutions, Inc.
3845 Woodhurst Court
Beavercreek, OH 45430-1658

35th Aerospace Sciences Meeting & Exhibit
January 6-10, 1997 / Reno, NV

For permission to copy or republish, contact the American Institute of Aeronautics and Astronautics
1801 Alexander Bell Drive, Suite 500, Reston, VA 22091

Numerical Modeling of Interactions between Evaporating Droplets

Long P. Chin
Innovative Scientific Solutions, Inc.
3845 Woodhurst Court
Beavercreek, OH 45430-1658

ABSTRACT

A numerical model based on the finite-volume approach has been developed to study the evaporation process of interactive droplets. The concept of "level set" using a distance function was incorporated to identify and trace the interfaces between two phases. The split velocities employed in an ALE (Arbitrary Lagrangian-Eulerian) grid system were used to ensure the mass conservation of droplets during the calculations. The model has been verified by comparing the time history of droplet volume with the results from the d^2-law and related empirical formulations for a single droplet in a hot-air stream. The model simulations show that the droplet is evaporating 10-40% faster than predicted from theories. Head-on collisions between two equal-sized round N-heptane droplets under various flow conditions are modeled to demonstrate the capabilities of the present numerical model.

INTRODUCTION

In most combustion systems, the evaporation process of spray is an important mechanism affecting the combustion efficiency and pollutant emission of the system. Depending on the specific requirements of each combustion system, various fuel-injection schemes are used to achieve the desired evaporation. For example, in a prevaporizing system, the spray is injected into the heated air stream where the droplets almost completely evaporate before reaching the flame. Because the spray injected upstream contains a large number of droplets having different sizes, temperatures, and velocities, the interactions among these droplets play an important role in determining the characteristics and performance of combustion downstream.

Copyright © 1997 by Long P. Chin. Published by the American Institute of Aeronautics and Astronautics, Inc. with permission

The evaporation theory of a single droplet has been intensively studied over the past several decades. The classical droplet model is well known, having been described and discussed at length in the literature (see, e.g., Refs. 1-3). However, many fundamental aspects of the evaporation mechanism for a group of droplets still are not well understood because the topological changes in the droplet geometry resulting from the interaction among droplets significantly complicate the transient processes of momentum, heat, and mass transport between the liquid and vapor phases.

In this paper, a numerical model based on an Eulerian-type finite-volume scheme is presented for studying the evaporation and combustion processes of droplets having various sizes, velocities, and temperatures. This model is an extension of the previous model [4] developed for predicting the dynamic interaction of two colliding droplets under isothermal conditions. In addition to the governing equations solved in the previous model, the energy and species equations have been solved in the present model to take into account the heat and mass transfer of the droplets.

The purpose of the present study is to demonstrate the capabilities of this numerical method in modeling the complicated transient dynamics involved in the evaporation process of interactive droplets. The detailed mathematical formulation and numerical schemes will be described in the next section. Following this, the model will be verified by simulating the evaporation for a single round droplet in a flowing air stream, which has been extensively described in the literature. Finally, the modeling of head-on collisions between two droplets in a hot-air flows will be presented to illustrate the complex evaporation phenomena.

MATHEMATICAL FORMULATION

(I) Governing equations

For the system modeled, the fluids of both phases (gaseous and liquid) can be treated mathematically as a single fluid having two significantly different properties

separated by an interface that is infinitesimally thin. The governing equations for the defined one-fluid system can be expressed as follows:

Continuity equation : $$\frac{1}{\rho}\frac{D\rho}{Dt} = -\beta\frac{DT}{Dt} = -\nabla\cdot\vec{u} \quad (1)$$

Momentum equation :

$$\rho\frac{D\vec{u}}{Dt} = -\nabla p + Re^{-1}\nabla\cdot\mu(\nabla\vec{u} + \nabla\vec{u}^T) + Fr^{-1}\rho\vec{g} + We^{-1}\int_s \sigma\kappa\delta(\vec{x}-\vec{x}_s)\vec{n}dA \quad (2)$$

Energy equation :

$$\rho\frac{DH}{Dt} + We^{-1}\rho\frac{D}{Dt}\left[\frac{1}{\rho}\int_s e_\sigma\delta(\vec{x}-\vec{x}_s)dA\right] = Re^{-1}\Phi - Fr^{-1}Sc^{-1}Re^{-1}\rho\vec{g}\cdot\sum_{k=1}^{N} D_k\nabla Y_k + Pr^{-1}Re^{-1}\nabla\cdot\left[\sum_{k=1}^{N}\rho D_k(Le^{-1} - \frac{\lambda}{\rho c_p D_k})H_k\nabla Y_k\right] + Pr^{-1}Re^{-1}\nabla\cdot\left[\frac{\lambda}{c_p}\nabla H\right] - \hat{h}_v^o\int_s \dot{\omega}_v\delta(\vec{x}-\vec{x}_s)dA$$

where $H(T) = \int_{T_o}^{T} c_p dT$ (3)

Species equation:

$$\rho\frac{DY_v}{Dt} = \nabla\cdot\rho Y_v\vec{V}_v + \int_s \delta(\vec{x}-\vec{x}_s)\dot{\omega}_v dA \quad (4)$$

All of the variables in these equations are normalized; and the non-dimensional parameters *Re, Pr, Sc, Fr, We,* and *Le* represent Reynolds, Prandtl, Schmidt, Frondle, Weber, and Lewis numbers, respectively. The integral terms represent the transport of mass, momentum, and energy exerted only on the interfaces (denoted by $\vec{x}_s$). The variables required to solve in Eqs. (1)-(4) are $\vec{u}$, the velocity vector; p, the pressure; T, the temperature; and Y_v, the vapor concentration of the droplet. The thermophysical properties ρ, μ, c_p, λ, D_k, and β denote density, viscosity, specific heat, thermal conductivity, the molecular-diffusion coefficient of species k, and the thermal expansion coefficient, respectively. The variables and properties defined on the gas-liquid interface are σ, the surface tension; e_σ, the surface energy; K, the curvature of interface; $\dot{\omega}_v$ the mass evaporation rate per unit area; and h_v^o, the latent heat of fuel at reference temperature T_o. It is important to include e_σ in the energy equation to prevent violation of the second law of thermodynamics for an evaporation system [5]. e_σ is related to σ by a surface constitutive relation. The evaporation rate at the interface, $\dot{\omega}_v$, is determined by applying chemical-equilibrium conditions while solving the species equation.

(II) "Level Set" approach

In solving these equations numerically, difficulties arise because of the locality of surface transports in momentum, energy, and evaporation that appear as the integral terms in the governing equations. The "Level Set" approach proposed by Sussman et al. [6] was adopted to reformulate these local quantities in such a way that they can be properly and smoothly re-distributed over a region having finite thickness. If ϕ is defined as a function that measures the normal distance from the interface, the surface integral terms in Eqs. (2)-(4) can be rearranged as follows:

$$\int_s \sigma\kappa\delta(\vec{x}-\vec{x}_s)\vec{n}dA \Rightarrow \sigma\kappa(\phi)\bar{\delta}(\phi)\nabla\phi$$

$$\int_s e_\sigma\delta(\vec{x}-\vec{x}_s)dA \Rightarrow e_\sigma(\phi)\bar{\delta}(\phi)$$

$$\int_s \dot{\omega}_v\delta(\vec{x}-\vec{x}_s)dA \Rightarrow \dot{\omega}_v(\phi)\bar{\delta}(\phi)$$

The distance function is assumed to be positive in the liquid phase and negative in the gaseous phase. All of the surface variables and properties have a value of zero outside the interface region defined by ϕ. For tracking the interface movement due to flow convection and droplet evaporation, the function ϕ is solved using the following equation:

$$\frac{\partial\phi}{\partial t} + \vec{u}\cdot\nabla\phi = \frac{\Delta\phi(\dot{\omega}_v)}{\Delta t} \quad (5)$$

where $\Delta\phi(\dot{\omega}_v)/\Delta t$ is the change rate of ϕ as the result of evaporation. If the volume fraction of the liquid phase within the finite interface region (with a thickness of 2α) is assumed to be $V_l = \frac{1}{2}\left[1 - sin(\frac{\pi\phi}{2\alpha})\right]$, then $\Delta\phi(\dot{\omega}_v)/\Delta t$ can be derived from

$$\dot{\omega}_v = \rho_l \frac{dV_l}{dt} = -\frac{\rho_l}{4}\frac{\pi}{\alpha}\cos\left(\frac{\pi\phi}{2\alpha}\right)\frac{\Delta\phi(\dot{\omega}_v)}{\Delta t}$$
$$\Rightarrow \frac{\Delta\phi(\dot{\omega}_v)}{\Delta t} = -4\left[\frac{\dot{\omega}_v}{\rho_l}\frac{\alpha}{\pi}\right] \Big/ \cos\left[\frac{\pi\phi}{2\alpha}\right] \qquad (6)$$

where ρ_l is the liquid density which is assumed to be constant for this formulation.

(III) Numerical schemes

The numerical scheme chosen for this study is a finite-volume method based on the ALE (Arbitrary Lagrangian-Eulerian) grid system. By coupling this scheme and the concept of split velocity [7], the parasite currents resulting from the locality of the surface force are minimized to prevent instability and also to ensure the mass conservation of droplets. An accurate accounting of the surface-tension term of Eq. (2) for this numerical method required modification of the formulation for the split velocity to incorporate the surface force with the pressure force. Figure 1 illustrates the concept of using split velocity in this numerical method. The velocity nodes are located at the corners of the grid, and the remaining field variables are located at the center of the cell. The split velocities on four sides of each velocity-node point were used to satisfy the continuity equation, which is crucial in avoiding the mass loss of droplets due to numerical inaccuracy. With the use of split velocities, the continuity equation is satisfied if the summation of all the split velocities surrounding a single scalar cell is equal to zero. That is,

$$\left[(u^n_{i+1,j} + u^s_{i+1,j+1}) - (u^n_{i,j} + u^s_{i,j+1})\right]\Delta y + \left[(v^e_{i,j+1} + v^w_{i+1,j+1}) - (v^e_{i,j} + v^w_{i+1,j})\right]\Delta x = 0 \qquad (7)$$

In the mean time, these split velocities are used to discretize the interface tracking equation [Eq. (5)] to ensure the mass conservation of the liquid phase.

A second-order upwind scheme was applied to discretize the convective term in Eq. (2) for eliminating excess numerical diffusion. Because of the large density gradient across the interface between the droplet and the surrounding gases, a fully multi-grid method coupled with a MSIP (Modified Strongly Implicit Procedure) iteration scheme was implemented.

MODELING DEMONSTRATION

(I) Single droplet evaporation

The numerical model was tested by simulating the evaporation of a single spherical N-heptane droplet injected into a hot air stream in the direction opposite to that of the flow. The droplet has a diameter of 40 μm and a temperature of 300 K initially is moving from right to left with a velocity of 1 m/s. Three different velocities of the air stream (1, 3, and 6 m/s) at a temperature of 1200 K were simulated. The corresponding Reynolds and Weber numbers of the droplet for these cases are Re = 4.2, 8.5, 15.0 and We = 0.0065, 0.026, 0.08, respectively. The surface tension for the N-heptane/air mixture is obtained from the temperature-dependent relationship : σ = 0.128 - 0.00018T. Figures 2-4 show the simulation results for all three flow conditions in terms of vapor concentrations, temperature distributions, and velocity vectors. It can be clearly seen in Fig. 2 that the droplet volume is decreasing at various rates for different flow conditions. In general, the contours of vapor concentration are very similar for all three cases, except in the regions surrounding the droplet surface during the initial short build-up stage [see Fig. 2(a)]. The initial heat-up process of the droplet is shown in the temperature contours of Fig. 3. The boiling temperature of N-heptane at 1 atm is about 371 K. The energy-transfer mode within the droplet is dominated by conduction at the early stage (e.g., Figs. (a)-(c) for Re = 4.2; Figs. (a), (b) for Re = 8.5; and Fig. (a) for Re = 15). As the internal circulation increases, convection gradually begins to dominate. At the end of this heating period, the temperature of the droplet becomes nearly uniform--a few degrees lower than the boiling temperature (371 K). The circulating motion of the liquid inside the droplet, induced by the shear stress from the surrounding higher air flow, is clearly shown in Fig. 4.

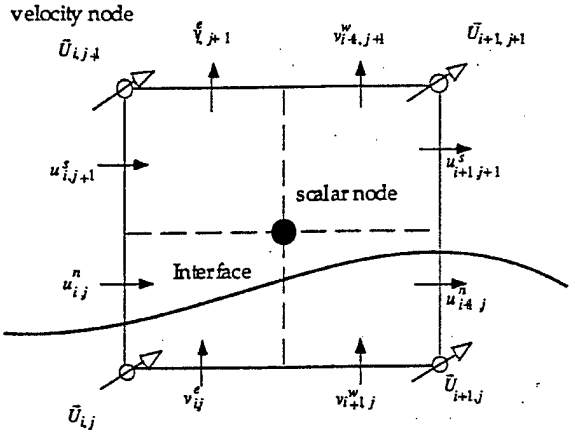

Figure 1 Schematic illustration of ALE formulation with split velocities

For comparing the modeling results with theories, the volume reduction of the droplet was plotted as a function of evaporation time (in ms) for all three flow

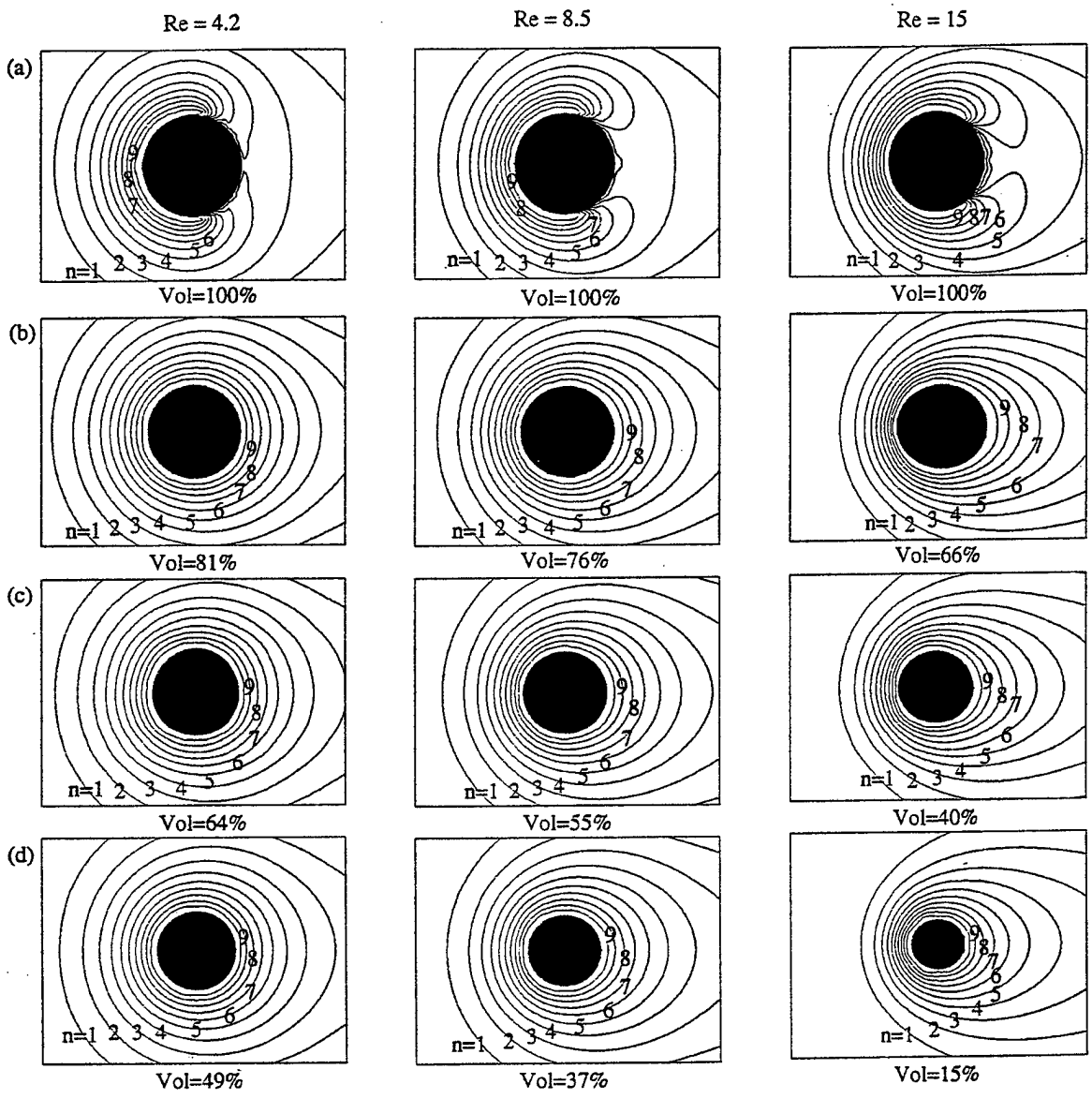

Figure 2. Concentration coutours of fuel vapor for three air-velocity conditions at (a) t= 0.02; (b) t=0.45; (c); t=0.85; (d) t=1.25 ms. The contour value is calculated from Y = 0.01 + 0.1(n-1)

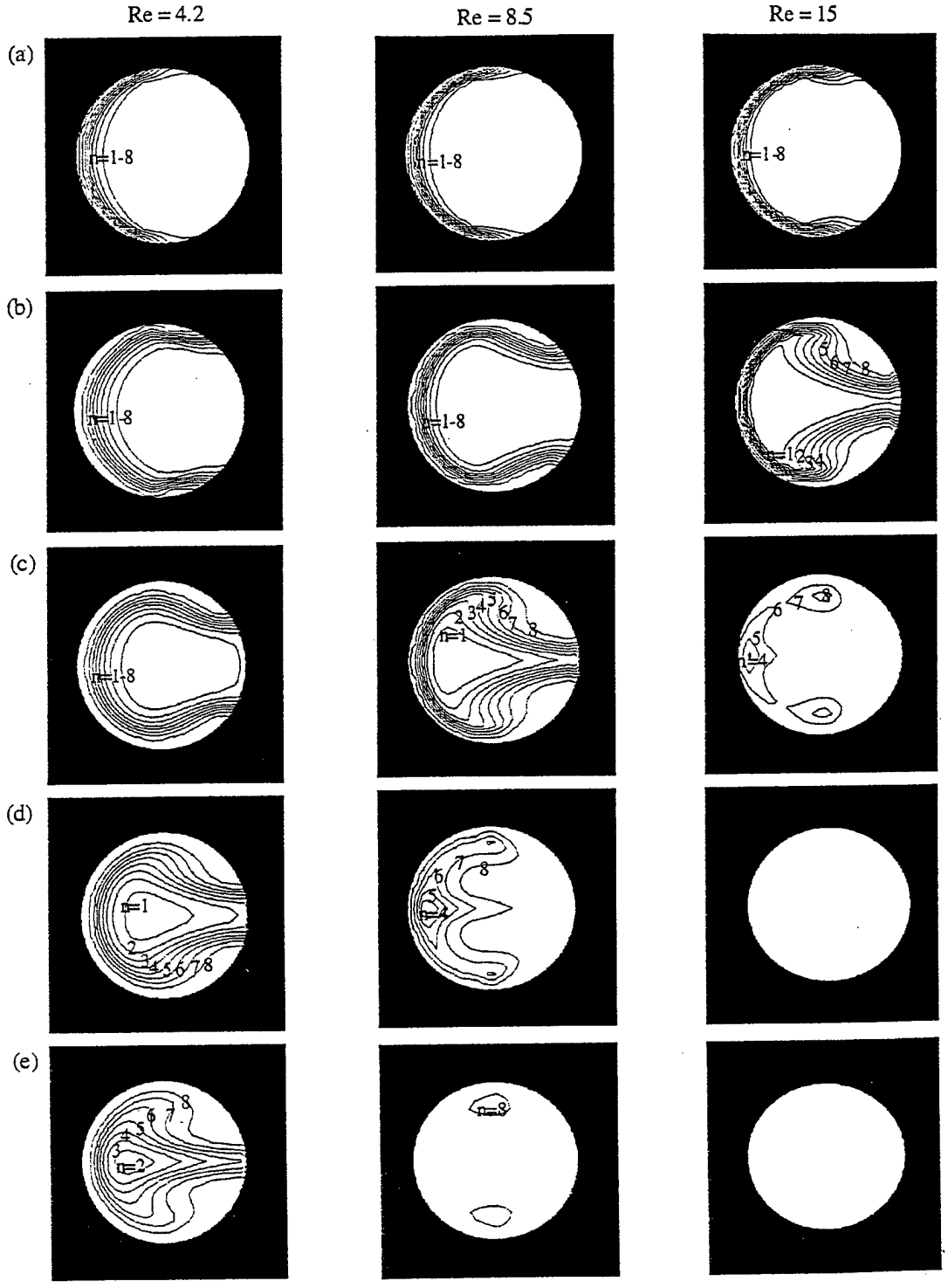

Figure 3. Temperature contours inside the droplet for three air-velocity conditions at (a) t=0.01; (b) t=0.06; (c) t=0.12; (d) t=0.18; (e) t=0.24 ms. The contour value is calculated from T = 300 + 100 (n-1) (K)

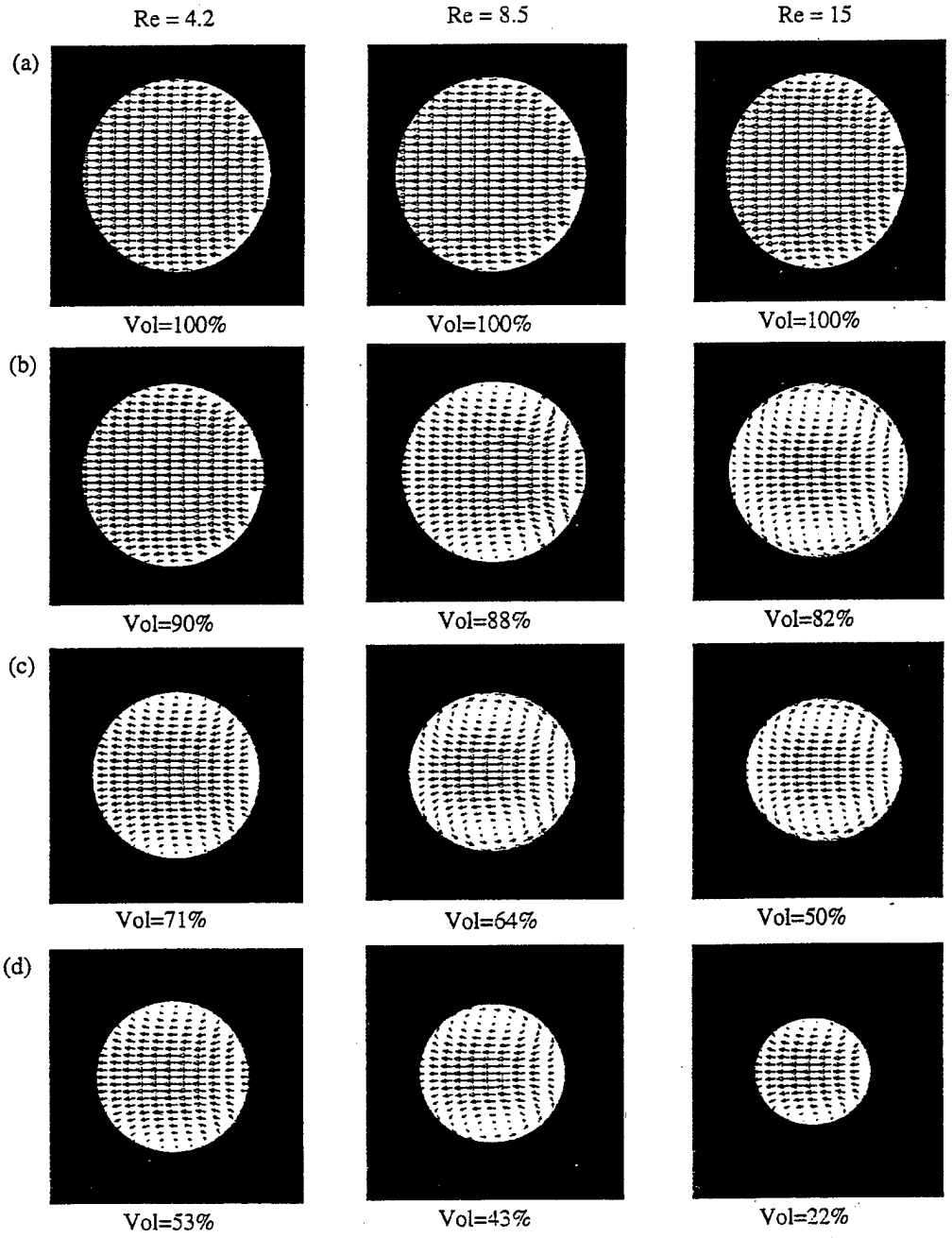

Figure 4. Velocity vectors inside the droplet for three air-velocity conditions at (a) t=0.01; (b) t=0.22; (c) t=0.67; and (d) t=1.12 ms.

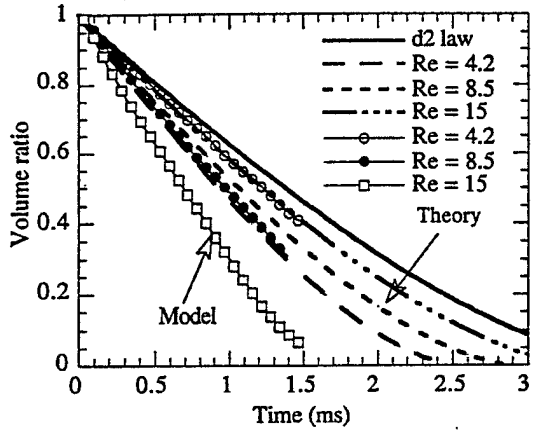

Figure 5. Volume history of evaporating droplet (normalized by its initial value) for different air velocities

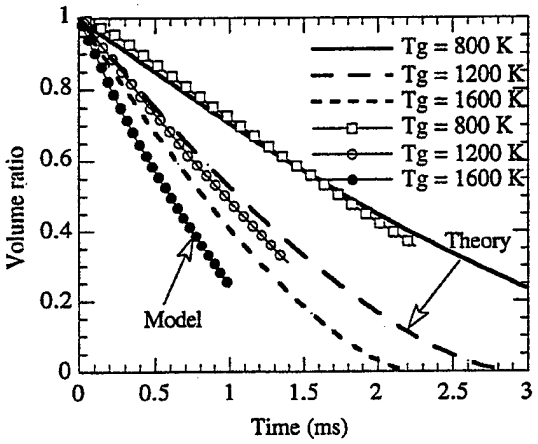

Figure 6. Volume history of evaporating droplet (normalized by its initial value) for different air temperatures

conditions. In Fig. 5 the solid line is the volume history derived from the traditional d^2 law; and the three dashed lines represent the theoretical predictions, taking into account the correction for convection. The effect of convective heat transfer is described by the Nusselt-number dependence on the Reynolds and Prandtl numbers. The empirical relationship used in the present study is $Nu = 2 + 0.6\,Re^{1/2}\,Pr^{1/3}$. The comparisons show that the evaporation rates are ~ 10-40% higher from modeling than those predicted from theories. Since the theories chosen in the study were derived based on numerous assumptions, a more rigorous verification of this numerical model is required. Similar comparisons were also made for the three different air-temperature

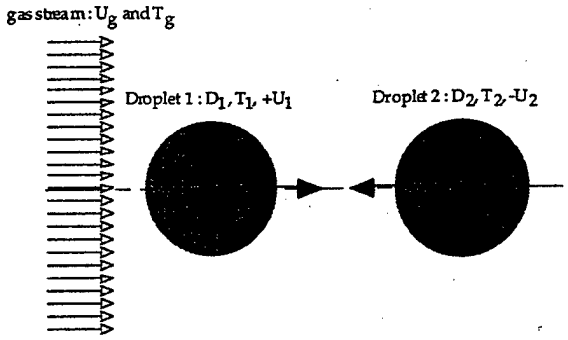

Figure 7. Schematic diagram of model for collision between two droplets

conditions (800, 1200, and 1600 K) shown in Fig. 6 with the air velocity being fixed at 3 m/s. As seen in Fig. 5, the model predicts higher evaporation rates than the theory.

(II) Evaporation from two colliding droplets

The advantage of the present model is the capability to model the evaporation process of droplets having complicated geometrical interactions. To demonstrate this, a series of simulations were made for the head-on collision between two droplets in a hot flowing air stream. Three different relative collision velocities were chosen--1, 5 and 8 m/s. Figure 7 illustrates the modeled system in which the two droplets can be of different size, velocity, and temperature. The air stream is kept constant at a velocity of 8 m/s and a temperature of 1200 K. The numerical model of droplet collision under isothermal conditions has been verified against experiments in a previous study [4] and the agreement is fairly good. Figure 8 shows the concentration distributions of fuel vapor in the early stage of collision, where the droplet mass evaporated is < 2%. Depending on the relative momentum between droplets, two different modes of collision can be observed (coalescence and separation). Figure 9 shows the temperature contours within the droplets; and the heat-up period is short compared to the lifetime of a droplet.

CONCLUSIONS

A numerical method based on the finite-volume scheme was introduced for modeling evaporation phenomena among interactive liquid droplets. This model applied the concepts of "level set" and "split velocity" to resolve the complicated topological

variations of the droplet surfaces and also to ensure that the volume loss of droplets due to numerical inaccuracy would be within the allowed tolerance. The simulation results from evaporation of a single droplet were used to verify the present model by comparing the time history of volume reduction with theoretical predictions. Head-on collisions between two round droplets in a hot air-stream were also simulated to illustrate the capability of the present model in predicting the distributions of fuel vapor surrounding the droplets and the temperature fields inside the droplets.

ACKNOWLEDGMENTS

This work was supported by the U. S. Air Force under Contract F33615-95-C-2507. The author would like to thank Dr. Mel Roquemore and Dr. Vish Katta for their comments on this work. Special thanks to Ms. Marian Whitaker for editing this paper.

REFERENCE

1. Law, C. K., "Recent Advances in Droplet Vaporization and Combustion," *Prog. Energy Combust. Sci.*, Vol. 8, pp. 171-201 (1982).

2. Faeth, G. M., "Evaporation and Combustion of Sprays," *Prog. Energy Combust. Sci.*, Vol. 9, pp. 1-76 (1983)

3. Sirignano, W. A., "Fuel Droplet Vaporization and Spray Combustion Theory," *Prog. Energy Combust. Sci.*, Vol. 9, pp. 291-322 (1983).

4. Chin, L. P., "A Numerical Study of Collision Behavior between Droplets," Presented at the 1996 Central States Section Meeting of the Combustion Institute, May 5-7, 1996, St. Louis, MO.

5. Welch, S. W. J., "Local Simulation of Two-Phase Flows Including Interface Tracking with Mass Transfer," *J. Comput. Phys.*, Vol. 121, pp. 142-154 (1995).

6. Sussman, M., Smereka, P., and Osher, S., "A Level Set Approach for Computing Solutions to Incompressible Two-Phase Flow," *J. Comput. Phys.*, Vol. 114, pp. 146-159 (1994).

7. Hwang, Y.-H., "Arbitrary Domain Velocity Analyses for the Incompressible Navier-Stokes Equations," *J. Comput. Phys.*, Vol. 110, pp. 134-149 (1994).

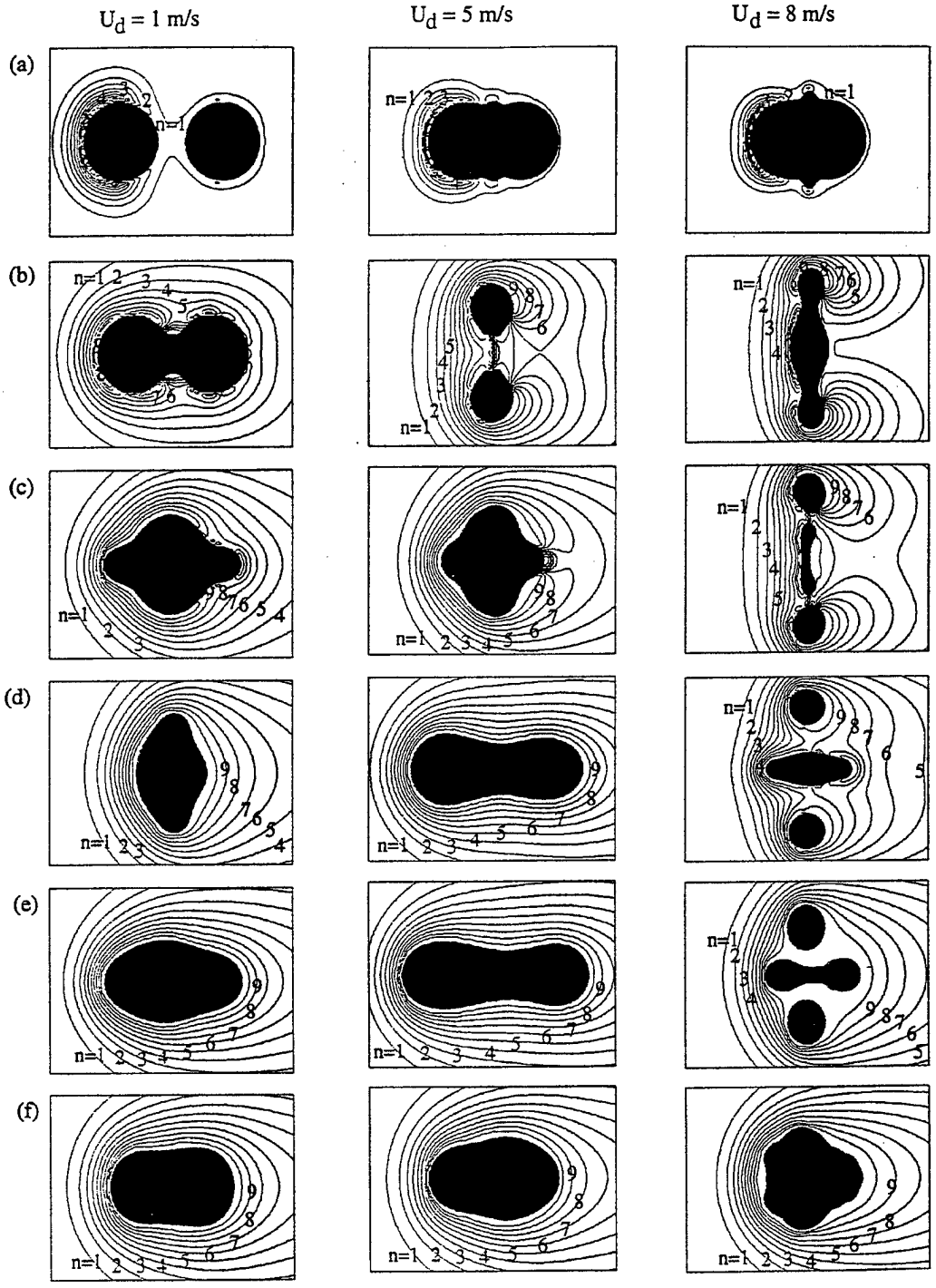

Figure 8. Concentration contours of fuel vapor for three relative collision velocities at (a) t=0.01; (b) t=0.04; (c) t=0.07; (d) t=0.10; (e) t=0.13; (f) t=0.16 ms. The contour value is calculated from Y = 0.01 + 0.1 (n-1)

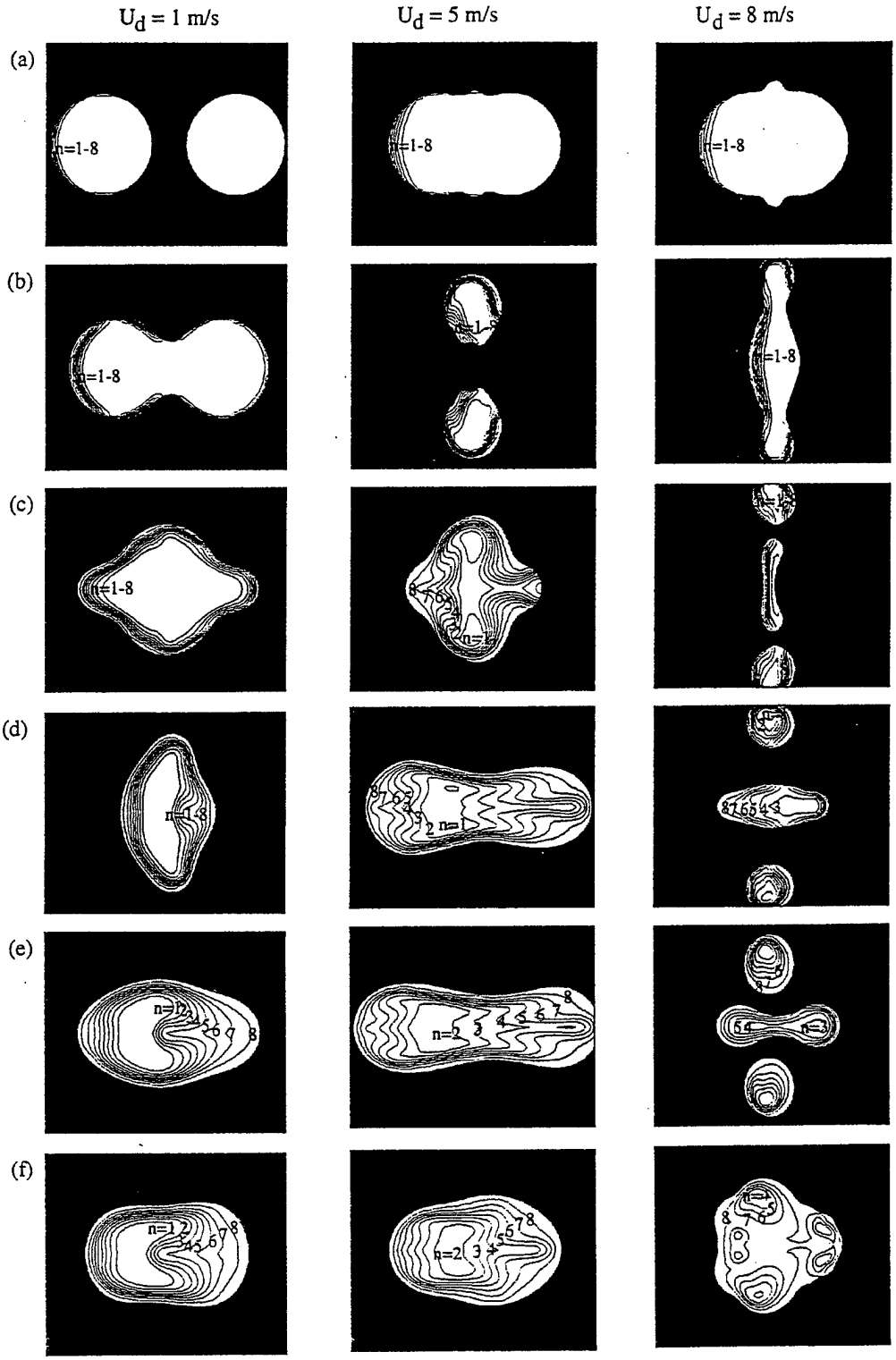

Figure 9. Temperature contours inside droplets for three relative collision velocities at (a) t=0.01; (b) t=0.04; (c) t=0.07; (d) t=0.10; (e) t=0.13; (f) t=0.16 ms. The contour value is calculated from T = 300 + 100 (n-1) (K)

AIAA 97-0128

Momentum Coupling Effects in a Two-Phase Swirling Jet

T. W. Park
Wright Laboratory
Wright-Patterson AFB, OH

S. K. Aggarwal
University of Illinois at Chicago
Chicago, IL

V. R. Katta
Innovative Scientific Solutions, Inc.
Dayton, OH

35th Aerospace Sciences Meeting & Exhibit
January 6-10, 1997 / Reno, NV

For permission to copy or republish, contact the American Institute of Aeronautics and Astronautics 1801 Alexander Bell Drive, Suite 500, Reston, VA 22091

MOMENTUM COUPLING EFFECTS IN A TWO-PHASE SWIRLING JET

T. W. Park*
Wright Laboratory
Wright-Patterson Air Force Base, OH 45433-7103

S. K. Aggarwal**
University of Illinois at Chicago
Chicago, IL 60607

and

V. R. Katta†
Innovative Scientific Solutions, Inc.
Dayton, OH 45430

Abstract

In this paper, we present direct numerical simulation of a droplet-laden swirling jet, and examine the effects of swirl and two-phase momentum coupling on the jet dynamics and structural characteristics. A time-dependent, multidimensional, two-phase algorithm is developed for the simulation. Results for the single-phase swirling jet at a Reynolds number of 800 indicate that the dynamics of large scale structures is strongly affected by the degree of swirl imparted to the incoming flow. For low and intermediate swirl intensities, the vortex rings rollup closer to the nozzle exit, their frequency increases, and pairing interactions become progressively stronger as the swirl number is increased. For a strongly swirling jet, the presence of a central stagnant zone and recirculation bubble cause a dramatic increases in the jet spreading angle, and this has a very dramatic effect on vortex dynamics. Results for the two-phase swirling jet indicate that for a mass loading ratio of unity, the jet dynamic and time-averaged behavior are strongly affected by both the interphase momentum coupling and swirl intensity.

Introduction

Swirling jet flows are utilized in a wide range of applications. By imparting swirl to the incoming flow, the structure of both nonreacting and reacting flows can be changed in a dramatic manner [1]. The structure of swirling jet, for example, is strongly affected by the degree of swirl, characterized by a swirl number (S) which is defined as the ratio of axial flux of swirl or azimuthal momentum to that of axial momentum. For a weakly swirling nonreacting jet ($S < 0.4$), the jet growth, entrainment and decay are enhanced progressively as S is increased. For a corresponding strongly swirling jet ($S > 0.5$), the behavior changes more dramatically due to the formation of a recirculation bubble. In combustion applications, the recirculation bubble perhaps represents the most significant and useful effect of swirl, as it plays a central role in flame stabilization and enhanced combustor performance.

Extensive research efforts have been expended in understanding and characterizing the effects of swirl in nonreacting and reacting flows [1-3]. A commonly used configuration in both experimental and computational studies involves a confined or free swirling jet. Most of these studies, however, deal with the time-averaged behavior of swirling jets. The transient aspects, particularly those associated with large-scale vortex structures, have not been examined, although these structures have been shown to have a dominant effect on the near jet flow dynamics of non-swirling jets. Numerous experimental and numerical studies [4-5] have shown that toroidal vortex rings form periodically in the near field of round jets and convect downstream. These axisymmetric structures roll around due to the inhomogeneous flow field, and may also undergo pairing interactions, depending on the flow conditions, such as initial disturbance level and other experimental conditions. In addition, their dynamics can be modified significantly by external forcing [6]. There are also other mechanisms that can modify their temporal and spatial growth characteristics. These include acoustic (pressure) fluctuations [7], which can modify the dominant frequency associated with large scale structures, compressibility effects [8], and density variations caused by a variation in temperature or molecular weight [9]. Yet another mechanism that may alter the dynamic of large scale structures pertains to the effect of swirl, which induces a body force in the radial momentum equation, and an adverse pressure gradient in the axial direction. For weakly swirling jets, the axial adverse pressure gradient caused by swirl can modify the processes of vortex rollup and pairing interactions. For strongly swirling jets, the jet spreading and recirculation zone created by the swirl effect can have a more dramatic effect on the dynamics of vortex rings. To our knowledge, these aspects dealing with the dynamic interactions between large scale structures and swirl, and those between large structures and droplets in a swirling shear flow, have not been investigated in previous studies.

In this paper, we present a numerical simulation of a droplet-laden swirling jet. The major objective of this study is to investigate the dynamics of large scale structures under different swirl conditions, and their interactions with the droplets injected in the shear layer

* NRC Research Associate, Member AIAA.
** Professor, Associate Fellow AIAA.
† Senior Engineer, Member AIAA.
Copyright © by the American Institute of Aeronautics and Astronics, Inc., 1997. All rights reserved.

REPRINTED WITH PERMISSION

of an axisymmetric swirling jet. A direct numerical solver without any turbulence or subgrid model is employed. The simulation first examines the dynamics of vortex rings and their interactions with the swirling flow field in a transitional heated jet. Then, a droplet-laden swirling jet is simulated in order to examine the effects of two-phase momentum coupling on the jet dynamics and structural behavior. The jet Reynolds number based on a jet velocity of 5.0 m/s, diameter of 25.4 mm, and kinematic viscosity of heated jet fluid is 800. In our earlier study [10], the dynamics of a nonswirling two-phase jet was investigated, and it was shown that the shear layer stability and vortex dynamics can be modified significantly by controlling the droplet injection characteristics. The present study extends that work to a swirling two-phase jet, and examines the effects of both swirl and two-phase momentum coupling on its dynamic and time-averaged structure.

Physical-Numerical Model

A cartoon of the two-phase swirling jet investigated in the present study is shown in Fig. 1. It consists of a central swirling jet which is a two-phase mixture of air and liquid fuel (n-heptane) droplets and a low-speed annular air flow. The jet at axial velocity of 5.0 m/s and temperature of 1200 K is issuing into a coflow with a velocity of 0.2 m/s without swirl and temperature of 294 K. Note that the use of high jet temperature is based on the consideration that we plan to investigate an evaporating spray in a subsequent study. In the present study, a nonevaporating spray is simulated in order to examine the effects of two-phase momentum coupling in the near region of a swirling jet. The jet-shear-layer instability is primarily of the Kelvin-Helmholtz type [10].

The numerical model is based on solving the time-dependent, two-phase equations in an axisymmetric geometry. The unsteady, axisymmetric governing equations in cylindrical (z, r) coordinates for a droplet-laden swirling jet are

$$\frac{\partial(\rho\Phi)}{\partial t}+\frac{\partial(\rho u\Phi)}{\partial z}+\frac{\partial(\rho v\Phi)}{\partial r}= \frac{\partial}{\partial z}\left(\Gamma^{\Phi}\frac{\partial\Phi}{\partial r}\right)+\frac{\partial}{\partial r}\left(\Gamma^{\Phi}\frac{\partial\Phi}{\partial z}\right)- \frac{\rho v\Phi}{r}+\frac{\Gamma^{\Phi}}{r}\frac{\partial\Phi}{\partial r}+S_g^{\Phi}+S_\ell^{\Phi}. \quad (1)$$

The general form of Eq. (1) represents the continuity, three momentum, and energy conservation equations depending on the variable used for Φ. The transport coefficients Γ^{Φ} and the source terms S_g^{Φ} and S_ℓ^{Φ} that appear in the governing equations are listed in Table 1. Note that the equations in Table 1 correspond to an evaporating two-phase flow. For the present study, which simulates a non-evaporating two-phase flow, the species equations are not considered, and droplet vaporization rate ($\dot{m}_k$) is taken identically equal to zero. The transport coefficients Γ^{Φ} and source terms contain the fluid properties such as viscosity (μ), thermal conductivity (λ), and specific heat (C_p). They are considered functions of temperature and species concentration.

The effect of dispersed phase on gas-phase properties is incorporated through the source/sink terms (S_ℓ^{Φ}), representing the exchange of momentum between the gas and dispersed phases. In order to evaluate these terms, it is necessary to establish droplet trajectories. The Lagrangian approach is employed to solve the liquid-phase governing equations for the dynamics of each droplet group. The spray is characterized by a discrete number of droplet groups, distinguished by their injection location, initial size, and time of injection. A droplet group in a Lagrangian treatment represents a characteristic group containing a finite number of droplets. Since an axisymmetric configuration is analyzed, the liquid properties are implicitly averaged in the azimuthal direction and the number of droplets associated with each characteristic group represents droplets uniformly distributed in an annular ring. The equations governing the variation of position and velocity of each droplet are as follows:

$$\frac{dx_k}{dt}=u_k \quad (2)$$

$$\frac{dy_k}{dt}=v_k$$

$$\frac{du_k}{dt}=\frac{3C_D\rho_g}{4d_k\rho_k}\left|u_g-u_k\right|\left(u_g-u_k\right)+\left(\frac{\rho_g}{\rho_k}-1\right)g \quad (3)$$

$$\frac{dv_k}{dt}=\frac{3C_D\rho_g}{4d_k\rho_k}\left|v_g-v_k\right|\left(v_g-v_k\right)+\frac{w_k^2}{y_k}$$

$$\frac{dw_k}{dt}=\frac{3C_D\rho_g}{4d_k\rho_k}\left|w_g-w_k\right|\left(w_g-w_k\right)-\frac{v_kw_k}{y_k}$$

where

$$C_D=\frac{24}{\mathrm{Re}_k}\left(1+\frac{\mathrm{Re}_k^{2/3}}{6}\right) \quad (4)$$

$$\mathrm{Re}_k=\frac{\rho_g\left\{\left(u_g-u_k\right)^2+\left(v_g-v_k\right)^2+\left(w_g-w_k\right)^2\right\}^{1/2}d_k}{\mu_g} \quad (5)$$

The numerical solution of the unsteady two-phase equations employs an implicit algorithm for solving the gas-phase equations, and an explicit Runge-Kutta procedure for the liquid-phase equations. The finite-difference forms of the momentum equations are obtained

using an implicit QUICKEST scheme [11], while those of energy equations are obtained using an hybrid scheme of upwind and central differencing [12]. A "finite control volume" approach with a nonuniform staggered-grid system is utilized. An orthogonal grid having expanding cell sizes in both the axial and the radial direction is employed. An iterative ADI (Alternative Direction Implicit) technique is used for solving the resulting sets of algebraic equations. At every time step, the pressure field is calculated by solving all the pressure Poisson equations simultaneously and utilizing the LU (Lower and Upper diagonal) matrix decomposition technique.

Axisymmetric calculations are made on a physical domain of 400 x 150 mm utilizing a 151 x 61 nonuniform grid system. The computational domain is bounded by the axis of symmetry and an outflow boundary in the radial direction and by the inflow and another outflow boundary in the axial direction. The outer boundaries in the z and r directions are located sufficiently far from the nozzle exit (16 nozzle diameters) and the axis of symmetry (6 nozzle diameters), respectively, to minimize the propagation of boundary-induced disturbances into the region of interest (7 and 2 nozzle diameters in the axial and radial directions, respectively). A flat profile for axial velocity and a linear profile for swirl velocity (swirl velocity being a linearly increasing function of radius) are used at the inflow boundary. A zero-gradient boundary condition with an extrapolation procedure with weighted zero- and first-order terms is used to estimate the flow variables at the outflow boundary. The weighting functions are selected using the trial-and-error approach, and the main criterion used is that the vortices crossing the outflow boundary leave smoothly without being distorted. For the given flow conditions, a steady-state solution was first obtained by neglecting the unsteady terms in the governing equations. Then, the unsteady two-phase swirling jet simulations were performed using the previously obtained steady-state solution as the initial flow condition.

The liquid-phase equations governing the position of each droplet group are advanced in time by a second-order accurate Runge-Kutta method. Since the gas-phase solution employs an implicit procedure, the temporal step size used for integrating the liquid-phase equations is usually smaller than that for gas-phase equations. An automatic procedure is implemented in order to select an optimum liquid-phase time step. The procedure to advance the two-phase solution over one gas-phase time step is as follows. Using the known gas-phase properties, the liquid-phase equations are solved over the specified number of liquid-phase subcycles. A third-order accurate Lagrangian polynomial method is used for interpolating the gas-phase properties from the nonuniform fixed grid to the droplet characteristic location. It should be noted that the interpolation scheme for the gas-phase velocities u and v is based on their respective grid cells because of the use of a staggered grid in gas-phase calculation. The droplet properties are updated after every liquid-phase subcycle. Also, during each subcycle, the liquid-phase source terms appearing in the gas-phase equations are calculated at the characteristic location, and then distributed to the surrounding gas-phase grid points. These source terms are added at each gas-phase grid points during one gas-phase time step and then used in the implicit solution of the gas-phase equations.

Numerical validation studies for both single-phase and two-phase jets, as well as for low-speed diffusion flames, employing different grids and temporal step sizes have been reported previously [10, 13]. Some additional results showing grid independence are depicted in Fig. 2. The time-history of gas velocity computed for two different grid sizes, 151x61 and 226x91 for non-swirling and swirling jets is plotted in figs 2a and 2b, while the profiles of time-averaged velocity along the jet axis for three different swirl numbers are plotted in Fig. 2c. Since a non-uniform grid is employed with grid lines clustered near the shear layer to resolve the steep gradients of the dependent variables, additional grid points in the 226x91 grid are placed near the shear layer, thus effectively reducing the grid density for this grid by nearly hundred percent compared to the 151x61 grid. The time-history plots of gas velocity clearly depicts the highly periodic nature of jet vortex rings associated with the Kelvin-Helmholtz instability. For the non-swirling jet, the Strouhal number associated with this instability obtained from the fast Fourier transform of axial velocity is 0.33, which agrees with the reported experimental range of 0.25-0.5. The aspects pertaining to the dynamic and time-averaged jet behavior for different swirl numbers are discussed in the next section. Important observation here is that the 151x61 grid is able to capture the periodic behavior, including frequency and phase of the vortex structures, as well as the time-averaged structure of both non-swirling and swirling jets.

Results and Discussion

First, we examine the dynamics of single-phase swirling jets at different swirl numbers (S). The objective is to understand and characterize the dynamic interactions between swirl and large scale structures, and the effects of these interactions on the jet behavior. Since the jet dynamics and structural characteristics are strongly influenced by the presence of both swirl and large scale structures, it is of interest to examine how the vortex dynamics is affected by swirl, and how the distribution of swirl and its decay rate are modified by vortex structures. The latter effect is important since the swirl decay rate determines the pressure distribution, and thereby the jet gross behavior, especially the onset, location and extent of the recirculation bubble at high swirl numbers. The above interactions are examined by employing flow visualization (snapshots of the flow field), as well as the instantaneous and time-averaged properties.

Figure 3 shows some representatives snapshots of the flow field for different swirl numbers. In each snapshot, we plot instantaneous iso-temperature contours on the right, and streaklines on the left. Simulations for the nonswirling jet indicate the presence of well-organized vortex rings. Toroidal vortex rings roll up periodically near z = 4 cm (z/D = 1.6) from the nozzle exit, convect downstream, and undergo a weak pairing interaction near

z=16 cm. The snapshot for S=0 clearly indicates a vortex rollup occurring near z = 4 cm, and a pairing interaction near z = 16 cm. These results were confirmed by the fast Fourier transform of axial velocity recorded at several axial locations, shown in Fig. 4, which yields dominant frequencies of 64 and 32 Hz corresponding to the roll up and merging frequencies respectively. Results for S = 0.375, Fig. 3, indicate a more dramatic effect of swirl on the dynamics of large scale structures. First of all, the vortex rollup location is shifted upstream and frequency is increased from 64 to 75 Hz compared to the nonswirling case. Second, the vortex pairing becomes a prominent feature of shear layer dynamics in the near jet region, which, we speculate, is caused by the adverse pressure gradient effect of swirl. Since, the pressure increases along the center line for the swirling case, the center-line velocity for the swirling jet decays faster compared to that for the nonswirling jet. This is indicated clearly in Fig. 5a, which shows the variation of time-averaged gas velocity along the center line for different swirl numbers. As a result, the leading toroidal vortex is slowed down, causing a well-organized pairing interaction to occur near z = 7 cm. The faster decay of center-line velocity also causes the occurrence of second vortex pairing near z=12 cm. The processes of shear layer rollup and pairing interactions for S=0.375 are clearly depicted in Fig. 3. The corresponding frequencies, obtained from the fast Fourier transform of axial velocity and displayed in Fig. 4, are 74, 37, and 19 Hz respectively. The occurrence of multiple vortex pairings in a swirling jet has an important implication with regard to the effect of swirl-vortex interaction on the jet development and entrainment. Since the presence of multiple vortex pairings is known to enhance shear layer growth and entrainment, the numerical results indicate that the addition of swirl modifies vortex dynamics in a way which further enhances the beneficial effects of swirl.

As the swirl intensity is increased, the above effects become progressively stronger. The increased swirl strength promotes greater jet spreading, mixedness, and reduction of the potential core. In addition, the vortex rollup occurs earlier (more upstream), and the convecting toroidal vortex slows down considerably, as it moves radially outward (due to jet spreading) and the center-line velocity decays more rapidly. Consequently, with increased swirl, vortex pairings occur earlier and with greater intensity, further promoting shear layer growth and entrainment. For S = 0.5, as noted in Fig. 3, the locations of vortex rollup, and first and second pairing interactions are approximately at z = 2, 5, and 8 cm respectively, compared with the corresponding values of 3, 7, and 10 cm for S = 0.375. In addition, the corresponding frequencies are higher and a third pairing interaction is observed for S = 0.5; see Fig. 4. The above observations are also confirmed by the axial profiles of time-averaged gas velocity and temperature shown in Fig. 5. As S is increased, the centerline temperature decreases more rapidly, indicating a pronounced increase in the shear layer growth and entrainment of colder fluid into the hot jet. This is a significant result in that the overall effect of swirl-vortex interaction at low to intermediate swirl intensities (S < 0.5) is to augment the effect of each. Note that both the addition of swirl and the presence of large vortex structures are known to enhance shear layer growth and entrainment. Our results indicate that an increase in swirl intensity promotes multiple vortex pairings, which further enhances shear layer growth and entrainment, i.e. large structures augment the effect of swirl and vice versa.

A more dramatic effect occurs as the swirl number exceed 0.5, which represents the onset of recirculation bubble in the jet flow. For S > 0.5, a stagnant region develops near the center line due to the reverse flow caused by adverse pressure gradient, and a toroidal recirculation bubble appears. Both the central stagnation region and recirculation bubble can be seen clearly from the time-averaged velocity vector plots in Fig. 6. Also notable in this figure is the presence of a secondary recirculation zone for S = 0.75, located just below the primary recirculation bubble. The stagnation region and reverse flow are also quite evident in the time-averaged axial velocity profile for S = 0.75 given in Fig. 5. In addition, as noted in Fig. 6, the jet shear layer for S = 0.75 is shifted significantly outward in the radial direction, and exhibits a highly dynamic structure. It is interesting to note that while at subcritical swirl numbers (S < 0.5), toroidal vortices are an intrinsic part of jet dynamics, their existence becomes less obvious at supercritical swirl numbers (S > 0.5). Thus, an important issue to be addressed here pertains to the existence and nature of large scale structures for strongly swirling jets, and whether the transient jet behavior can be attributed to these structures. One may argue that these structures get destroyed due to the rapid decay of shear and increased mixing in a strongly swirling jet. Based on an extensive visualization of the swirling jet dynamics for S = 0.75, we speculate that large vortex structures are still present, though their behavior is markedly different from those for the weakly and moderately swirling jets (S < 0.5). The vortex structures for S = 0.75 are shifted outward in the radial direction and do not look like the Kelvin-Helmholtz vortex rings that are typically observed in a transitional jet. However, a series of snapshots (not shown) indicates that they do exhibit the processes of rollup and pairing interactions, though in a significantly less organized manner. The snapshots further indicate that a pair of counter-rotating toroidal vortices (an outer Kelvin-Helmholtz type vortex rotating clockwise and an inner vortex rotating counter-clockwise; the latter may be due to the presence of central stagnation region) is generated periodically. As these vortices convect downstream, they grow in size, and the outer structure roll around the inner structure since the latter is in a nearly stagnant region. In addition, both outer and inner vortices undergo pairing interactions with other (trailing) outer and inner vortices respectively. We also speculate, based on the flow visualization and time-averaged velocity vector plots shown in Fig. 6, that the size and location of recirculation bubble is determined by these dynamic swirl-vortex interactions, and not by the adverse pressure gradient (swirl effect) alone. In other words, due to the effect of swirl, the outer vortex is shifted outward in the radial direction, and its subsequent dynamics as well as that of inner vortex are determined

by the swirling flow field. These vortices in turn play a major part in determining the location of recirculation zone; it appears that the recirculation zone is established at a location where the outer vortex structure is pulled in radially.

Two-Phase Momentum Coupling Effects

We now examine the effects of two-phase momentum coupling on the dynamics and time-averaged characteristics of a droplet-laden swirling jet. Droplets of a given size are injected from the nozzle rim, and their motion is followed by integrating Eqs. (2-3) using a second-order Runge-Kutta scheme. At low mass loadings, the effect of droplets on the jet dynamics is negligible, although their motion and concentration field are strongly influenced by the rotating toroidal vortices. As the dispersed-phase mass loading is increased, the effects due to the exchange of mass, momentum, and energy between the phases become increasingly important. In the present study, a nonevaporating two-phase jet is considered in order to isolate momentum coupling effects from those due to mass and energy coupling. These effects depend on several parameters, including liquid-to-air mass loading ratio and injection characteristics such as initial droplet size, location, and velocity. For the present study, we consider mass loading of unity and initial droplet diameter of 100 μm, with the droplets injected in the shear layer with axial velocity same as the jet velocity, and zero radial and azimuthal velocities. Note that the choice of droplet diameter is based on the consideration that it yields a Stokes number of near unity for the nonswirling jet. The Stokes number here is defined as the ratio of droplet response time to a characteristic flow time, the latter based on the dominant vortex frequency. Several experimental and numerical studies [14-17] have shown that the interaction of large structures with droplets is maximized near a Stokes number of unity.

Flow visualization is used to assess qualitatively the effects of dispersed phase on the dynamics of large scale structures under different swirl conditions. In the following discussion, case A refers to single-phase jets, while B refers to two-phase jets. Figure 7 depicts representative snapshots of the flow field for different swirl numbers. Comparison of the snapshots, for nonswirling (S = 0) single-phase and two-phase jets, given in Figs. 3 and 7 respectively, indicates that the vortex rollup location, dynamics, and pairing interactions are strongly modified due to momentum coupling. In addition, it is observed that for the two-phase jet (case B), the vortex structures are stronger and entrain more low-speed (colder) fluid compared to those for the single-phase jet (case A). The comparison of snapshots for swirling jets also indicates a significant modification of vortex dynamics due to the momentum coupling effect. For low to moderate swirl numbers (S < 0.5), the vortex pairing is a prominent feature of jet dynamics for case A, while it is not observed for case B. For the strong swirl case (S = 0.75), an important effect of two-phase momentum coupling is a drastic reduction in the size of recirculation bubble, even though the central stagnation region still exists. This can be seen more clearly in terms of time-averaged velocity vector plots in Fig. 11. The effect of momentum coupling on the time-averaged structure is discussed in the following section.

The above observations are confirmed by obtaining the spectral and time-averaged properties for the two cases. Figure 8 shows the time history of gas-phase axial velocity for single-phase and two-phase jets at different swirl numbers. Results of the fast Fourier transform of these axial-velocity histories are depicted in Figs. 4 and 9. As discussed earlier, for single-phase jets with low to moderate swirl numbers (S < 0.5), the processes of shear layer roll-up and vortex formation are well organized. In addition, the roll-up frequency increases and pairing interactions become more prominent as the swirl number is increased. These results are quite evident in Fig. 4; the roll-up frequencies are 64, 72, and 80 Hz for S = 0, 0.375, and 0.5 respectively. Also noteworthy in Fig. 4 are the first and second pairing interactions at frequencies of 36 and 18 Hz respectively for S = 0.375, and at 40 and 20 Hz respectively for S =0.5. In contrast, for the corresponding two-phase jets (case B), the shear layer dynamics is less organized, and the roll-up frequency decreases and becomes independent of the swirl number. As indicated in Figs. 8 and 9, the roll-up frequency is 50 Hz for S = 0, 0.375, and 0.5. Another important observation from Fig. 9 is the absence of pairing interactions for case B, which is also evident in Fig. 7. This is attributable to the fact that the interphase momentum coupling modifies the distribution of swirl intensity in the axial direction, resulting in a decrease of adverse pressure gradient and jet spreading angle. As noted earlier, the adverse pressure gradient caused by swirl is responsible for the enhanced vortex pairings in single-phase jets. For corresponding two-phase jets, there is a transfer of azimuthal momentum from the gas phase to droplets, which reduces swirl intensity near the nozzle. Further downstream, however, the momentum is transferred from droplets to gas phase, increasing the gas-phase swirl intensity. The resulting redistribution of swirl intensity reduces the adverse pressure gradient for the two-phase jet. This was confirmed by plotting the time-averaged azimuthal velocity contours (not shown) and axial velocity vectors, shown in Fig. 11. As a consequence, the vortex pairing, which is prominent feature of moderately swirling (S < 0.5) single-phase jets, is not observed for corresponding two-phase jets.

Momentum-Coupling Effect on the Time-Averaged Jet Structure

The effect of two-phase momentum coupling on the time-averaged jet behavior is depicted in Figs. 10 and 11. In Fig. 10, the time-averaged axial gas velocity and temperature are plotted along the jet center line, while Fig. 11 shows the time-averaged velocity vectors for different swirl numbers. The important observations from these results is that at a mass loading of unity, the dispersed phase significantly modifies the time-averaged structure of the jet shear layer, and the degree of modifications depends on the swirl intensity. For the non-swirling jet (S = 0), as the shear layer develops, the

gas-phase velocity decreases along the center line. Since the droplets are injected at the jet velocity, they now have higher velocity than the gas phase resulting in a transfer of momentum from the dispersed phase to gas phase. This seems to enhance the shear layer instability resulting in enhanced mixing and entrainment of colder fluid, as evidenced by a faster decay of centerline temperature and velocity for the two-phase jet compared to those for the single-phase jet. This effect is modified significantly by the introduction of swirl. As noted earlier, the addition of swirl (S = 0.375) to a single-phase jet causes a faster decay of the centerline velocity (compared to a non-swirling jet), resulting in vortex pairing. This leads to enhanced mixing and entrainment of colder fluid into the shear layer; note a sharp increase in the rate of decrease of centerline velocity near an axial location of 120 mm for the single-phase jet. For the corresponding two-phase jet, the transfer of azimuthal momentum from the gas phase to droplets reduces the swirl intensity near the nozzle. This initially ($z < 120$ mm) causes a faster decay of centerline velocity for the two-phase jet compared to that for the single-phase jet. Further downstream, however, the direction of azimuthal momentum transfer is reversed, resulting in a slower decay of centerline velocity for the two-phase jet. In addition, the absence of vortex pairing for two-phase jet further reduces the rate of decay of centerline velocity. Consequently, the centerline velocity of two-phase jet becomes higher than that of single-phase jet for $z > 120$ mm. The absence of vortex pairing also results in reduced mixing and entrainment for the two-phase jet. Consequently, as indicated in Fig 10b, the centerline temperature decreases less rapidly for the two-phase jet.

The above effects become progressively stronger as the swirl number is increased. For S = 0.5, as shown in Fig. 10a, the centerline velocity of single-phase jet first decreases quite rapidly due to the combined effects of shear layer growth, adverse pressure gradient, and vortex pairings, and then ($z > 100$ mm) increases due to the transfer of axial momentum in the radial direction; see also Fig. 6. For the corresponding two-phase jet, the centerline velocity decreases much less rapidly, again due to the reduced pressure gradient and the absence of vortex pairings. The centerline temperature also decreases slowly for the two-phase jet, again implying reduced mixing and entrainment due to the momentum coupling effect. Another effect of momentum coupling is seen from the comparison of time-averaged velocity vectors for single-phase and two-phase jets given in Figs. 6 and 11 respectively. The comparison of these figures show that due to the momentum transfer from droplets to gas phase in the jet shear layer, the jet width is decreased and the potential core is lengthened for the swirling two-phase jet. The effect becomes more distinguishable for S = 0.5 and 0.75, where the momentum coupling generates a curtain (or envelope) type of high-velocity narrow region inside the shear layer. An important consequence of this high-velocity curtain is the near disappearance of the stagnation region for swirling two-phase jet for S = 0.5, and that of recirculation bubble for S = 0.75. The presence of a large recirculation bubble is perhaps the most distinguishing feature of a strongly swirling (S = 0.75) single-phase jet; see Figs. 3 and 6. For the corresponding two-phase jet, our results indicate that the recirculation bubble becomes nearly non-existent, even though the central stagnation and reverse flow regions still exist inside the high-velocity curtain. The disappearance of recirculation bubble for the strongly swirl case may be attributed to the momentum coupling effect, i.e., the transfer of various momentum components between the phases. Initially, there is a transfer of swirl momentum from the gas phase to dispersed phase, causing swirling intensity to decrease much more rapidly for two-phase jet (case B) compared to that for single-phase jet (case A). At some downstream location, however, the direction of azimuthal momentum transfer reverses, since droplets have higher momentum there. Secondly, the jet spreading rate is reduced for case B due to the radial momentum transfer from the gas phase to dispersed phase. In addition, there is a reverse transfer of axial momentum, i.e., from the dispersed phase to gas phase, since the gas-phase axial velocity decreases more rapidly that of dispersed phase, generating the high-velocity curtain mentioned earlier. All of these effects, i.e., reduced entrainment, more rapid decay of swirl velocity initially, and increase of gas velocity, lead to a near disappearance of the recirculation bubble for the strongly swirling two-phase jet. Consequently, for strongly swirling jets (S > 0.5), the jet spreading angle, shear layer growth and entrainment are reduced significantly due to the effect of interphase momentum coupling.

Conclusions

In this paper, we have investigated the effects of swirl and two-phase momentum coupling on the dynamics and structural behavior of a droplet-laden swirling jet. A direct numerical solver based on an Eulerian-Lagrangian formulation, but without any turbulence or subgrid model, has been employed to simulate the transient behavior of a transitional swirling jet. Detailed flow visualization based on numerical simulation has been used to examine the dynamics of large scale structures and their interactions with the droplets in weakly and strongly swirling jet shear layers. In addition, the effects of swirl and dispersed phase on the time-averaged jet structure have been characterized. Important observations are as follows.

Results for single-phase swirling jets indicate that the dynamics of large scale structures is strongly affected by the degree of swirl imparted to the incoming jet. For low and intermediate swirl intensities, the vortex rings rollup closer to the nozzle exit, their frequency increases, and pairing interactions become progressively stronger as the swirl number is increased. For example, there is one weak vortex merging near z/D = 6 for the nonswirling jet, and two vortex mergings near z/D = 3 and 5 for S=0.375, while for S = 0.5, the vortex mergings become stronger and occur near z/D = 2 and 3 respectively. Consequently, the interaction of vortex rings with the swirling flow field gives rise to a mechanism, which seems to be responsible for the enhanced shear layer growth and entrainment, and has not been observed in

previous studies. This may be an important result, with the implication that the addition of moderate swirl to a transitional jet modifies its vortex dynamics in a way that further enhances the beneficial effects of both swirl and vortex structures on shear layer growth. For a strongly swirling jet, the presence of a central stagnant zone and recirculation bubble causes a drastic increase in the jet spreading angle, and this has a rather dramatic effect on vortex dynamics. Detailed visualization of the shear layer dynamics indicates that as the shear layer is shifted radially outward, a pair of counter-rotating toroidal vortices is generated periodically, and the eventual shear layer structure, including the location of recirculation bubble, is determined by the dynamic interactions of these structures with the stagnant zone and recirculation bubble.

Results for the two-phase swirling jet indicate that at a mass loading ratio of unity, the jet dynamics and structural characteristics are strongly modified by the interphase momentum coupling. Depending upon the amount of swirl imparted to the jet, the momentum coupling can cause varied and in some cases dramatic effects on the dynamic and time-averaged jet structure. For a nonswirling jet, the momentum coupling alters the dynamics of large vortex structures, modifying their rollup location and frequency, and causing enhanced mixing and entrainment of colder fluid into the shear layer. In contrast, for weakly and moderately swirling jets, the momentum coupling reduces the amount of adverse pressure gradient, and suppress the vortex pairing interactions. These effects are caused by the redistribution of gas-phase axial, radial, and swirl momentum components due to the dispersed phase, and lead to significantly reduced shear layer growth, mixing and entrainment rates for two-phase jets compared to those for single-phase jets. In addition, the correlation between vortex frequency and swirl number is modified due to momentum coupling. For example, the dominant vortex frequency of single-phase jets increases with increasing swirl number, while that of two-phase jets appears to be independent of S.

At high swirl numbers (S > 0.5), the effects of momentum coupling on the jet structure appears to be even more dramatic compared to those at moderate swirl numbers. Results for S = 0.75 indicate that momentum coupling can significantly modify the rate of decay of swirl intensity, and increase the gas axial momentum in the jet shear layer, leading to a dramatic reduction in the size of recirculation bubble. This could potentially neutralize the most beneficial effects of swirl in recirculating hot products for enhanced mixing, and establishing a low velocity region for flame stability.

Acknowledgement

The first author acknowledges the National Research Council and Air Force Wright Laboratory for sponsoring him on the Postdoctoral Fellowship Program. This work was in part funded by the AFOSR under Grant F49620-93-1-0400 monitored by Dr. Julian M. Tishkoff. Many fruitful discussions with Dr. W. M. Roquemore at Wright-Patterson Air Force Base are greatly appreciated.

Nomenclature

C_D	droplet drag coefficient
C_p	specific heat
D	binary diffusion coefficient
g	gravitational acceleration
h_{fs}	enthalpy of fuel vapor at droplet surface
H	enthalpy
$\ell_{k,eff}$	effective latent heat, or the heat transferred from gas phase to droplet
$\dot{m}_k$	droplet vaporization rate
M_k	mass of each group of droplets
n_k	number of droplets in each group
p	pressure
r	radial distance
Re_k	droplet Reynolds number
S	swirl number
S_g^Φ	gas-phase source term for dependent variable Φ
S_ℓ^Φ	liquid-phase source term for dependent variable Φ
t	time
T	temperature
u, v, w	axial, radial, and swirl velocity components
Y	mass fraction
z	axial distance

Greek Symbols

Γ^Φ	transport coefficient in Eq. (1)
μ	dynamic viscosity
λ	thermal conductivity
ρ	density
Φ	dependent variable of Eq. (1)

Subscripts

f	fuel vapor
g	gas-phase
i	species
k	droplet characteristic

References

1. Lilly, D. G., "Swirling Flows in Combustion: A Review," AIAA Journal, Vol. 15, No. 8, pp. 1063-1078, 1977.
2. Ribeiro, M.M. and Whitelaw, J. H., "Coaxial Jets With and Without Swirl," Journal of Fluid Mechanics, Vol. 96, pp. 769-795, 1980.
3. Leschziner, M. A. and Rodi, W., "Computation of Strongly Swirling Axisymmetric Jets," AIAA Journal, Vol. 22, No. 12, pp. 1742-1747, 1984.
4. Crow, S. C. and Champagne, F. H., "Orderly Structure in Jet Dynamics," Journal of Fluid Mechanics, Vol. 48, pp. 547-591, 1971.
5. Yule, A. J., "Large-Scale Structure in the Mixing Layer of a Round Jet," Journal of Fluid Mechanics, Vol. 89, Part 3, pp. 413-432, 1978.

6. Reynolds, W. C. and Bouchard, E. E., "The Effect of Forcing on the Mixing Region of a Circular Jet," Unsteady Turbulent Shear Layer Flows, Springer, New York, pp. 401-411, 1981.
7. Kailasanath, K., Gardner, J. H., Boris, J. P., and Oran, E. S., "Acoustic-Vortex Interactions and Low-Frequency Oscillations in Axisymmetric Combustors," Journal of Propulsion and Power, Vol. 5, No. 2, pp. 24-36, 1989.
8. Shau, Y. R., Dolling, D. S., and Choi, K. Y., "Organized Structure in a Compressible Turbulent Shear Layer," AIAA Journal, Vol. 31, No. 8, pp. 1398-1405, 1993.
9. Subbarao, E. R. and Cantwell, B. J., "Investigation of a Coflowing Buoyant Jet-Experiments on the Effect of Reynolds Number and Richardson Number," Journal of Fluid Mechanics, Vol. 245, pp. 69-90, 1992.
10. Aggarwal, S. K., Park, T. W., and Katta, V. R., "Unsteady Spray Behavior in a Heated Jet Shear Layer: Droplet-Vortex Interactions," Combustion Science and Technology, Vols. 113-114, pp. 429-449, 1996.
11. Leonard, B. P., "A Stable and Accurate Convective Modeling Procedure Based on Quadratic Upstream Interpolation," Computer Methods in Applied Mech. and Engineering, Vol. 19, pp. 59-98, 1979.
12. Spalding, D. B., "A Novel Finite Difference Formulation for Difference Expressions Involving Both First and Second Derivatives," International Journal for Numerical Methods in Engineering, Vol. 4 , pp. 551-559, 1972.
13. Katta, V. R., Goss, L. P., and Roquemore, W. M., "Effect of Nonunity Lewis Number and Finite-Rate Chemistry on the Dynamics of a Hydrogen-Air Jet Diffusion Flames," Combustion and Flame, Vol. 96, Nos. 1/2, pp. 60-74, 1994.
14. Park, T. W., Aggarwal, S. K., and Katta, V. R., "A Numerical Study of Droplet-Vortex Interactions in an Evaporating Spray," International Journal of Heat and Mass Transfer, Vol. 39, No. 6, pp. 741-754, 1996.
15. Chung, J. N. and Troutt, T. R., "Simulation of Particle Dispersion in an Axisymmetric Jet," Journal of Fluid Mechanics, Vol. 186, pp. 199-222, 1988.
16. Longmire, E. K. and Eaton, J. K., "Structure of a Particle-Laden Round Jet," Journal of Fluid Mechanics, Vol. 236, pp. 217-257, 1992.
17. Uthuppan, J., Aggarwal, S. K., Grinstein F. F., and Kailasanath, K., "Particle Dispersion in a Transitional Axisymmetric Jet: A Numerical Simulation," AIAA Journal, Vol. 32, pp. 2004-2014, 1994.

Table 1: Transport coefficients and source terms appearing in governing equations

Equations	Φ	Γ^{Φ}	S_i^{Φ}	S_t^{Φ}
Continuity	1	0	0	$\sum_k n_k \dot{m}_k$
Axial momentum	u	μ	$-\frac{\partial p}{\partial z}+(\rho_0-\rho)g+\frac{\partial}{\partial z}\left(\mu\frac{\partial u}{\partial z}\right)+\frac{\partial}{\partial r}\left(\mu\frac{\partial v}{\partial z}\right)+\frac{\mu}{r}\frac{\partial v}{\partial z}$ $-\frac{2}{3}\left[\frac{\partial}{\partial z}\left(\mu\frac{\partial u}{\partial z}\right)+\frac{\partial}{\partial z}\left(\mu\frac{\partial v}{\partial r}\right)+\frac{\partial}{\partial z}\left(\mu\frac{v}{r}\right)\right]$	$\sum_k\left(n_k\dot{m}_k u_k - n_k M_k\frac{du_k}{dt}\right)$
Radial momentum	v	μ	$-\frac{\partial p}{\partial r}+\frac{\partial}{\partial z}\left(\mu\frac{\partial u}{\partial r}\right)+\frac{\partial}{\partial r}\left(\mu\frac{\partial v}{\partial r}\right)+\frac{\mu}{r}\frac{\partial v}{\partial r}-2\mu\frac{v}{r^2}$ $+\rho\frac{w^2}{r}-\frac{2}{3}\left[\frac{\partial}{\partial r}\left(\mu\frac{\partial u}{\partial z}\right)+\frac{\partial}{\partial r}\left(\mu\frac{\partial v}{\partial r}\right)+\frac{\partial}{\partial r}\left(\mu\frac{v}{r}\right)\right]$	$\sum_k\left(n_k\dot{m}_k v_k - n_k M_k\frac{dv_k}{dt}\right)$
Swirl momentum	w	μ	$-\left(\frac{\mu}{r^2}+\rho\frac{v}{r}+\frac{1}{r}\frac{\partial\mu}{\partial r}\right)w$	$\sum_k\left(n_k\dot{m}_k w_k - n_k M_k\frac{dw_k}{dt}\right)$
Mass fraction of fuel	Y_f	ρD_{f-N_2}	0	$\sum_k n_k\dot{m}_k$
Mass fraction of other species	Y_i $(i=1-N_s,\ i\neq f)$	ρD_{i-N_2}	0	0
Energy	H	$\frac{\lambda}{C_p}$	0	$\sum_k n_k\dot{m}_k\left(h_{fs}-\ell_{k,ref}\right)$

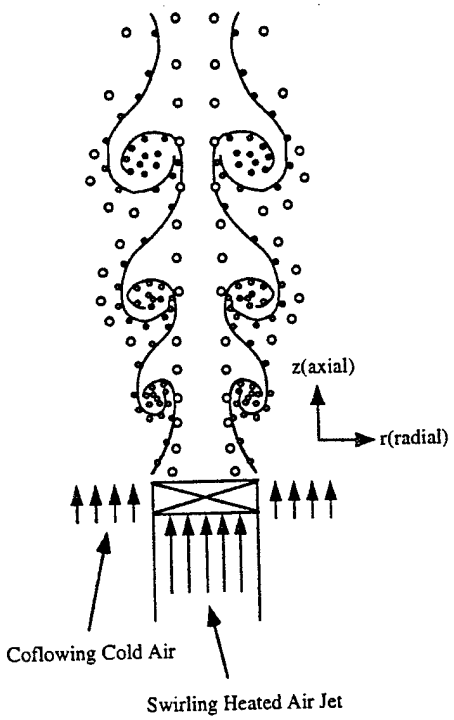

Fig. 1. Schematic of a droplet-laden swirling jet.

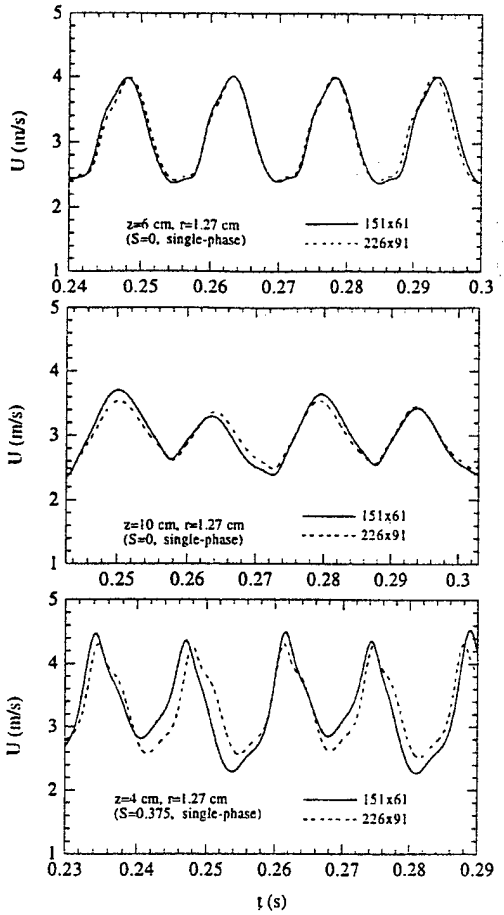

Fig. 2. Time-history plots of center-line gas velocity (figs. a and b) and axial profiles of time-averaged center-line gas velocity (fig. c) for non-swirling and swirling (S = 0.375) jets obtained by using two different grid sizes.

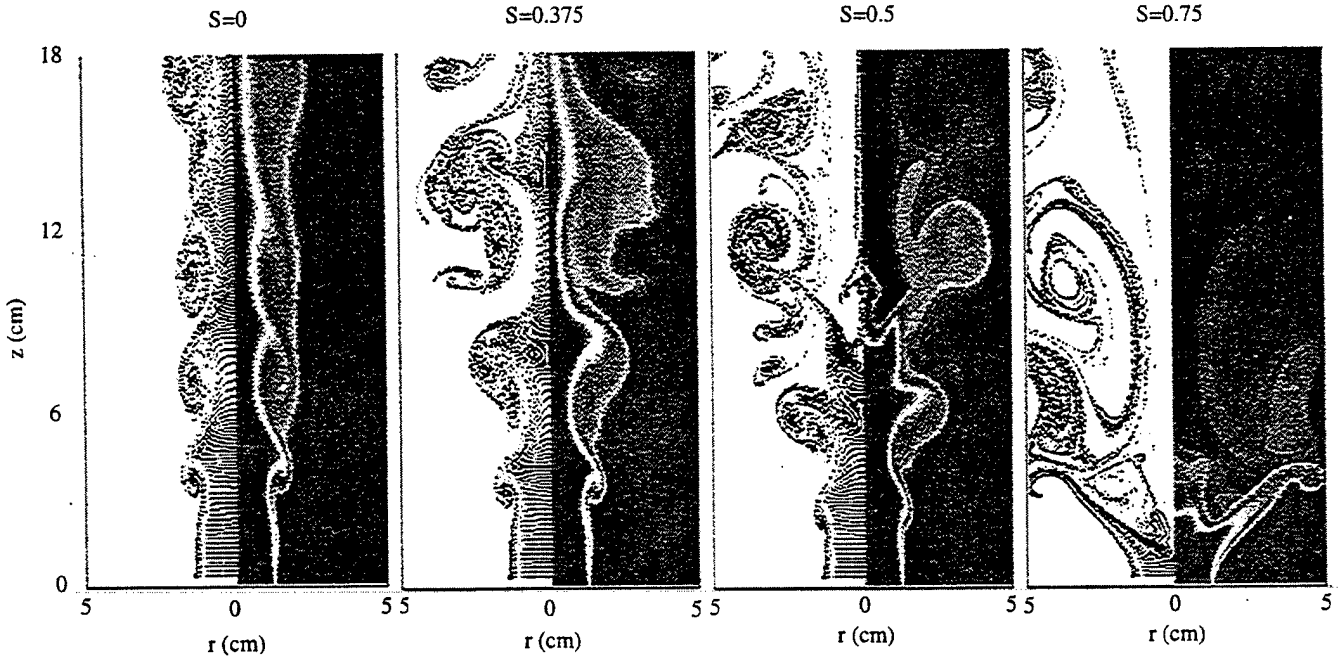

Fig. 3. Snapshots of the flow field for a swirling jet without droplets for four different swirl numbers. In each snapshot, iso-temperature contours are plotted on the right-hand side of the symmetric jet, and streaklines on the left. For iso-temperature contours, the red and purple colors represent the highest (1200 K) and the lowest (294 K) temperatures respectively

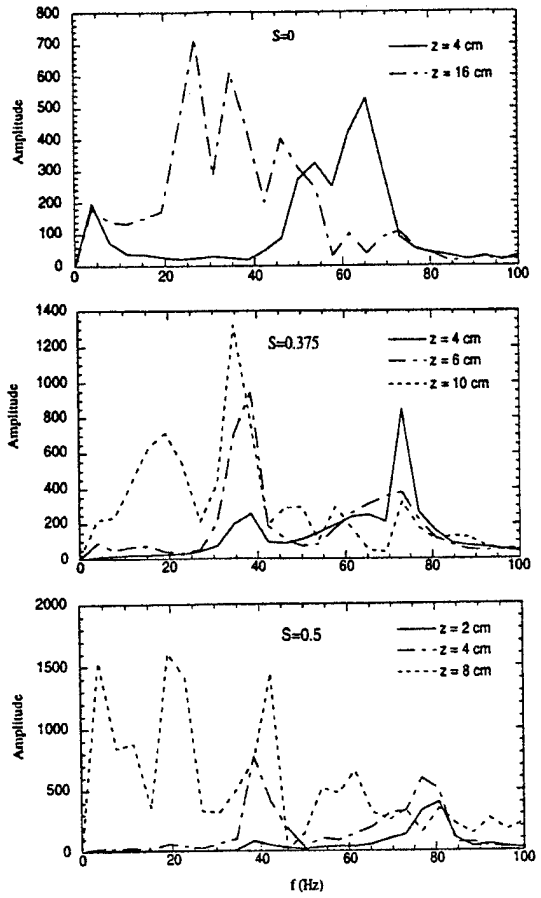

Fig. 4. Frequency spectra of axial gas velocity for a swirling jet without droplets for different swirl numbers.

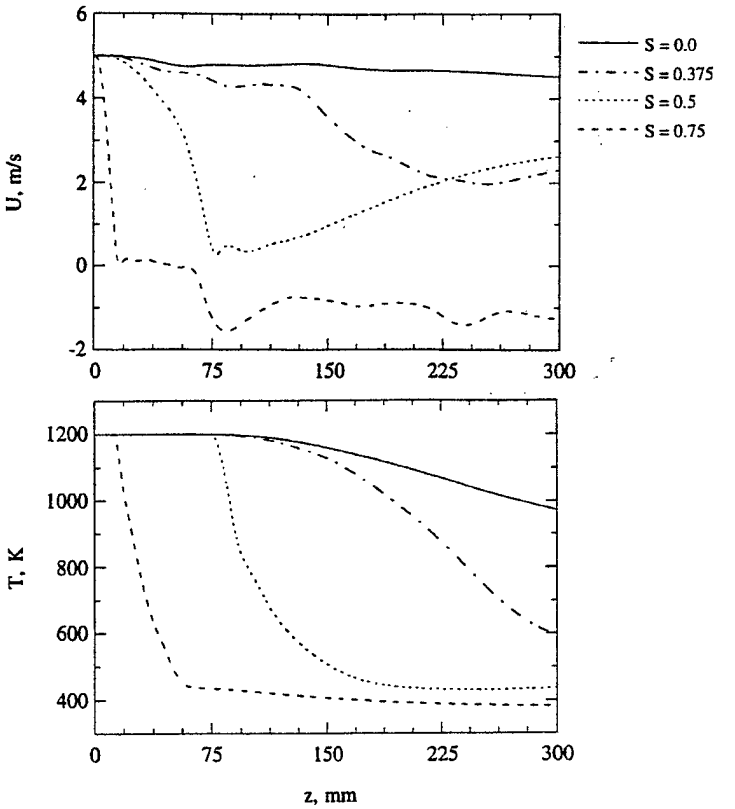

Fig. 5. Axial profiles of time-averaged gas velocity and temperature for a swirling jet without droplets for different swirl numbers.

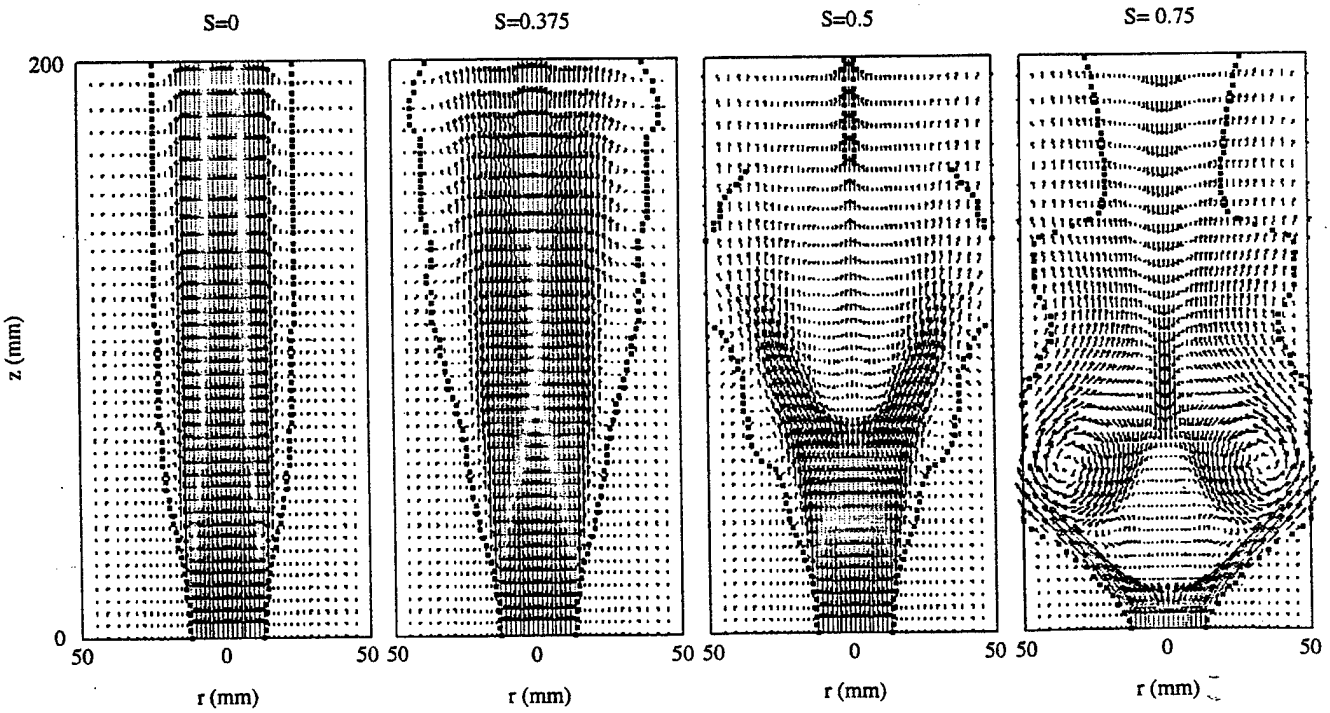

Fig. 6. Time-averaged velocity vector plots for a swirling jet without droplets for different swirl numbers.

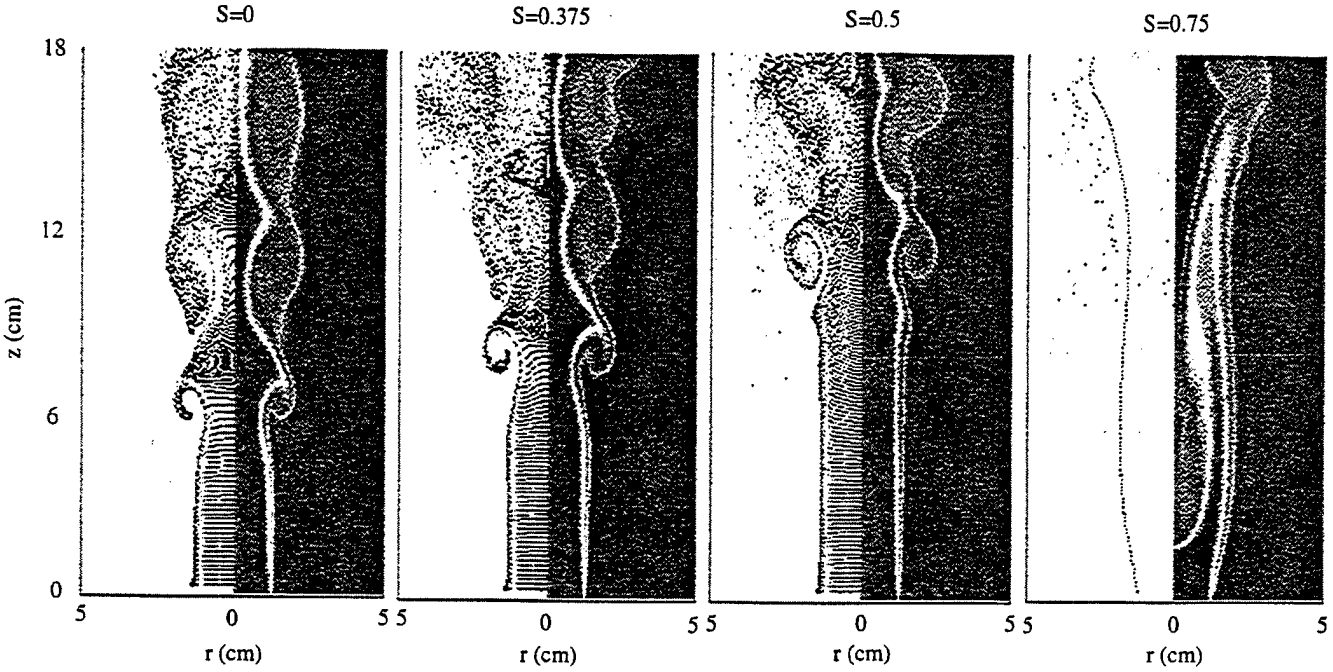

Fig. 7. Snapshots of the flow field for a swirling jet with droplets. In each snapshot, iso-temperature contours are plotted on the right-hand side of the symmetric jet, and streaklines on the left. For iso-temperature contours, the red and purple colors represent the highest (1200 K) and the lowest (294 K) temperatures respectively.

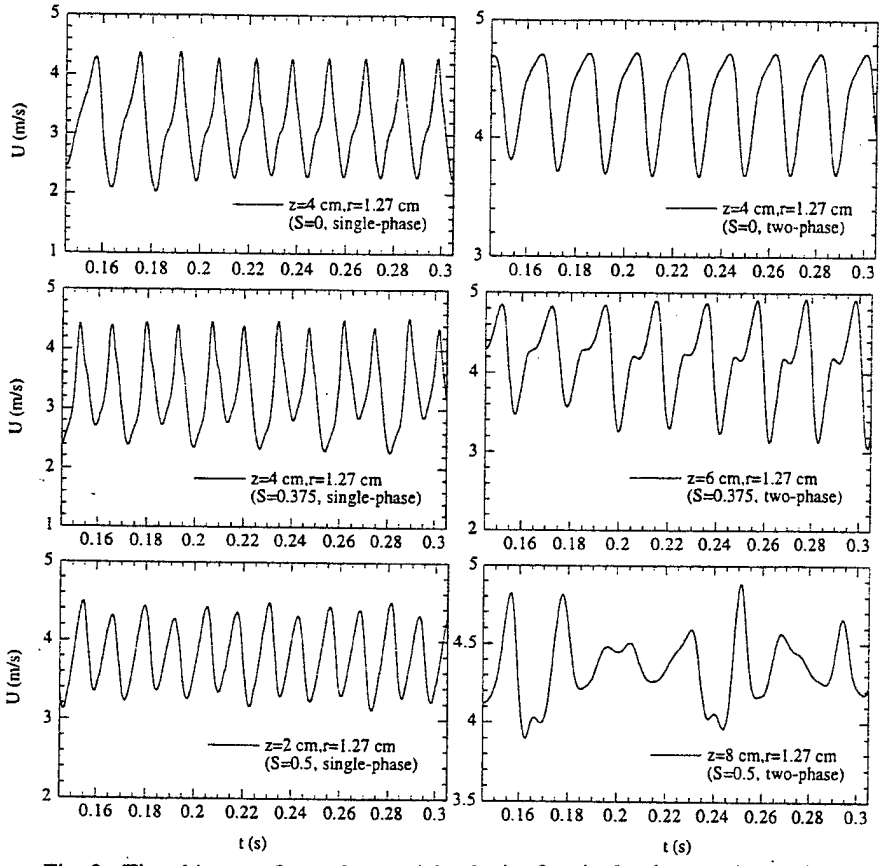

Fig. 8. Time history of gas-phase axial velocity for single-phase and two-phase jets with different swirl numbers.

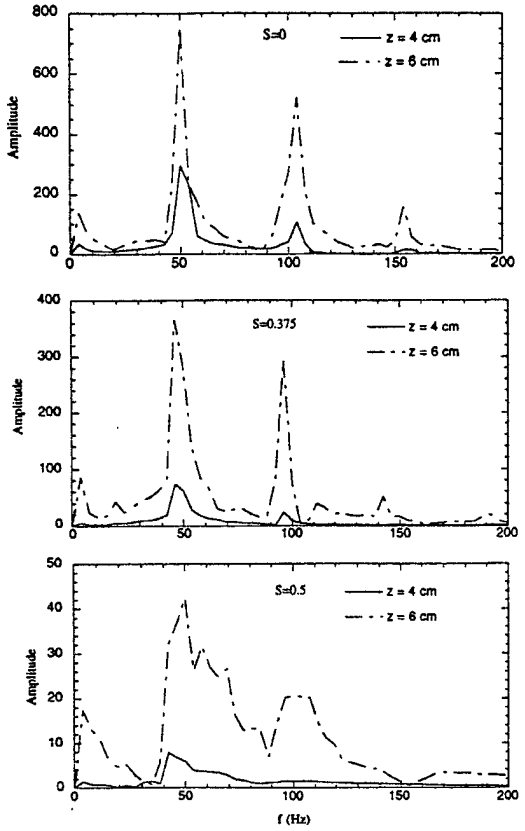

Fig. 9. Frequency spectra of axial gas velocity for a swirling jet with droplets for different swirl numbers.

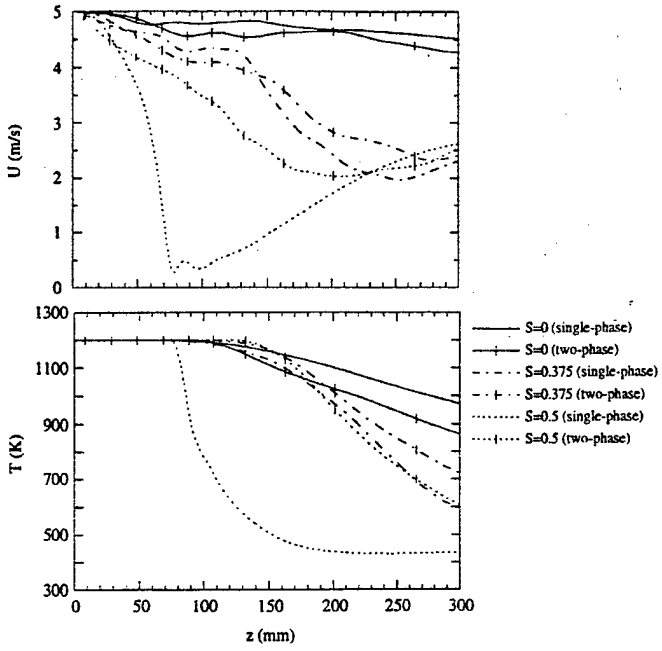

Fig. 10. Axial profiles of time-averaged gas velocity and temperature for a swirling jet without and with two-way momentum coupling for different swirl numbers.

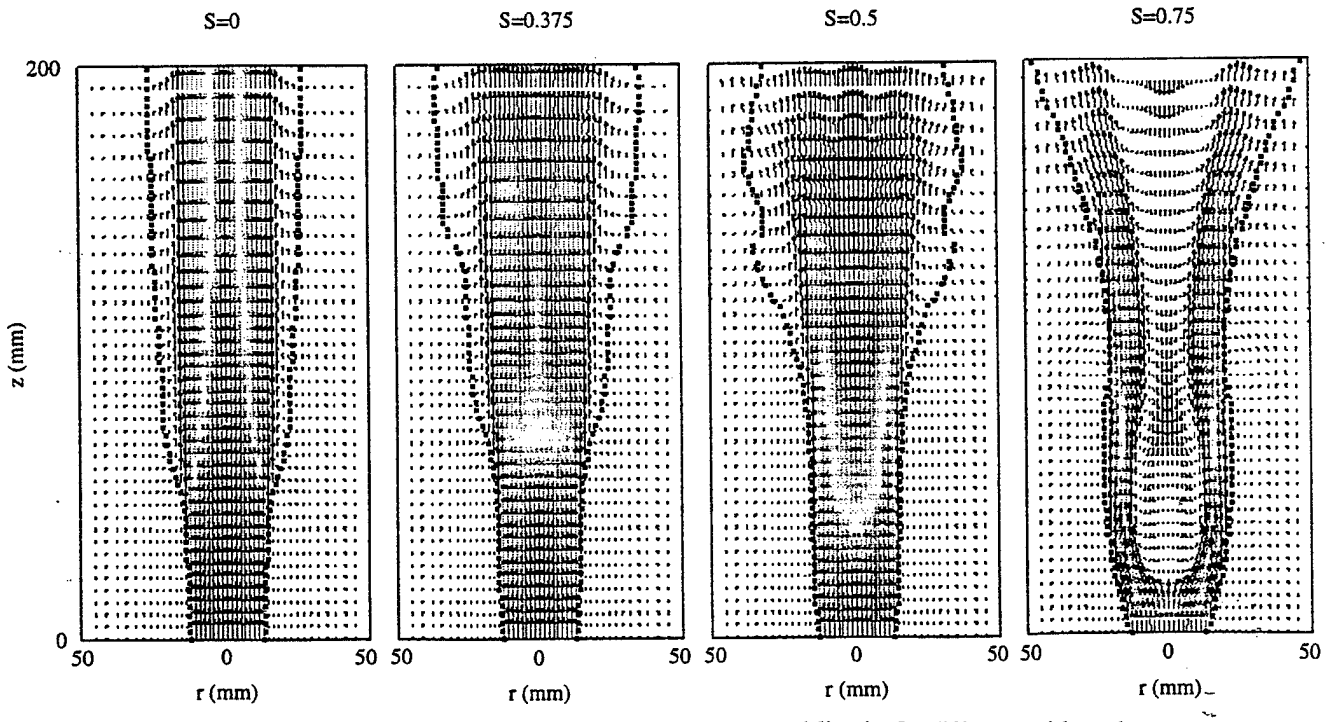

Fig. 11. Time-averaged velocity vector plots for a two-phase swirling jet for different swirl numbers.

AIAA 97-2703

NUMERICAL MODELING OF INTERACTIVE BURNING DROPLETS

Long P. Chin

Innovative Scientific Solutions, Inc.
2786 Indian Ripple Road
Dayton, OH 45440-3638

33rd AIAA/ASME/SAE/ASEEJoint Propulsion Conference & Exhibit

July 6 - 9, 1997 / Seattle, WA

For permission to copy or republish, contact the American Institute of Aeronautics and Astronautics
1801 Alexander Bell Drive, Suite 500, Reston, VA 22091

NUMERICAL MODELING OF INTERACTIVE BURNING DROPLETS

Long P. Chin
Innovative Scientific Solutions, Inc.
2786 Indian Ripple Road
Dayton, OH 45440-3638

ABSTRACT

A numerical model based on the finite-volume approach has been developed to study the evaporation and combustion process of interactive droplets. The "level set" approach of a defined distance function was incorporated to identify and trace the interfaces between two phases. Split velocities employed in an ALE (Arbitrary Lagrangian-Eulerian) grid system were used to ensure the mass conservation of droplets throughout the calculations. For verifying this model, calculated histories in surface-area reduction of single burning droplet were compared with the measurements from the experiments of Hara, Okajima and Kumagai in both stagnant and convected environments under zero-gravity condition. The agreement for both cases is reasonably good. Similar comparison was also made for the combustion of an array of three n-heptane droplets to examine the effects of interaction among droplets on evaporation rates.

INTRODUCTION

In most combustion systems, the evaporation process of spray is an important mechanism affecting the efficiency and pollutant emission of the system. Depending on the specific requirements of each combustion system, various fuel-injection schemes are used to achieve the desired evaporation and combustion. In a typical gas-turbine engine, the spray is injected into an air stream to form a nearly stoichiometric mixture of reactants in a two-phase flow. Since the fuel and air are not extensively premixed before burning, the flame has the characteristics of a diffusion flame, in which mixing of fuel and oxygen strongly influence the rate of reaction and evaporation. In addition, the spray injected upstream contains a large number of droplets with different sizes, temperatures, and velocities, thus the interactions among these droplets make the processes of mixing, evaporation, and combustion surrounding the droplets much more complex.

The evaporation theory of a single burning droplet has been intensively studied over the past several decades. The classical droplet model is well known, having been described and discussed at length in the literature (see, e.g., Refs. 1-3). However, many fundamental aspects of the evaporation mechanism affected by combustion for a group of droplets still are not well understood because the topological changes in the droplet geometry resulting from the interaction among droplets significantly complicate the transient processes of momentum, heat, and mass transport between the liquid and vapor phases.

In this paper, a numerical model based on an Eulerian-type finite-volume scheme is presented for studying the evaporation and combustion processes of droplets having various sizes, velocities, and temperatures. This model is an extension of the previous model [4] developed for predicting the dynamic interaction of two colliding droplets under isothermal conditions. In addition to the governing equations solved in the previous model, the energy and species equations have been solved in the present model to take into account the heat and mass transfer of the droplets and surrounding gases.

The purpose of the present study is to verify the numerical model against several experimental results under various conditions. The histories of surface-area reduction of droplets reported in the experiments will be used for comparisons with model simulations. Three cases are investigated in the following order: (1) A stagnant droplet burning at zero-gravity environment; (2) A moving droplet burning at zero-gravity condition; and (3) Three-droplet array burning with various spacing in a low pressure-rich oxygen environment.

Copyright © 1997 by Long P. Chin. Published by the American Institute of Aeronautics and Astronautics, Inc. with permission

MATHEMATICAL FORMULATION

(I) Governing equations

For the two-phase flow system modeled, the fluids of both phases (gaseous and liquid) will be treated mathematically as a single fluid having two significantly different properties separated by an interface that is infinitesimally thin. The governing equations for the defined one-fluid system can be expressed as follows:

Continuity equation:

$$\frac{1}{\rho}\frac{D\rho}{Dt} = -\beta\frac{DT}{Dt} = -\nabla\cdot\vec{u} \tag{1}$$

Momentum equation:

$$\begin{aligned}\rho\frac{D\vec{u}}{Dt} &= -\nabla p + Re^{-1}\nabla\cdot\mu\left(\nabla\vec{u}+\nabla\vec{u}^{T}\right)+Fr^{-1}\rho\vec{g}\\ &+We^{-1}\int_{s}-\frac{\partial\sigma}{\partial T}[I-\vec{n}\vec{n}]\delta(\vec{x}-\vec{x}_s)\cdot\nabla T dA\\ &+We^{-1}\int_{s}\sigma\kappa\delta(\vec{x}-\vec{x}_s)\vec{n}dA\end{aligned} \tag{2}$$

Energy equation:

$$\begin{aligned}&\rho\frac{DH}{Dt}+We^{-1}\rho\frac{D}{Dt}\left[\frac{1}{\rho}\int_{s}e_\sigma\delta(\vec{x}-\vec{x}_s)dA\right]\\ &=Re^{-1}\Phi+Pr^{-1}Re^{-1}\nabla\cdot\left[\frac{\lambda}{c_p}\nabla H\right]\\ &+Pr^{-1}Re^{-1}\nabla\cdot\left[\sum_{k=1}^{N}\rho D_k(Le^{-1}-\frac{\lambda}{\rho c_p D_k})H_k\nabla Y_k\right]\\ &-Fr^{-1}Sc^{-1}Re^{-1}\rho\vec{g}\cdot\sum_{k=1}^{N}D_k\nabla Y_k\\ &-h_v^o\int_{s}\dot{\omega}_v\delta(\vec{x}-\vec{x}_s)dA-h_{f,k}^o\sum_{k}\dot{\omega}_k\end{aligned} \tag{3}$$

where $H(T)=\int_{T_o}^{T}c_p dT$

Species equation:

$$\rho\frac{DY_k}{Dt}=\nabla\cdot(\rho D_k\nabla Y_k)+\dot{\omega}_k+\int_{s}\dot{\omega}_v\delta(\vec{x}-\vec{x}_s)dA \tag{4}$$

All of the variables in these equations are normalized; and the non-dimensional parameters Re, Pr, Sc, Fr, We, and Le represent Reynolds, Prandtl, Schmidt, Frondle, Weber, and Lewis numbers, respectively. The integral terms represent the transport of mass, momentum, and energy exerted only on the interfaces (denoted by $\vec{x}_s$). The variables required to solve in Eqs. (1)-(4) are $\vec{u}$, the velocity vector; p, the pressure; T, the temperature; and Y_k, the species concentration. The thermophysical properties ρ, μ, c_p, λ, D_k, and β denote density, viscosity, specific heat, thermal conductivity, the molecular-diffusion coefficient of species k, and the thermal expansion coefficient, respectively. The variables and properties defined on the gas-liquid interface are σ, the surface tension; e_σ, the surface energy; κ, the curvature of interface; $\dot{\omega}_v$ the mass evaporation rate of droplet; and h_v^o, the latent heat of evaporation at reference temperature T_o. It is important to include e_σ in the energy equation to prevent violation of the second law of thermodynamics for an evaporation system [5]. e_σ is related to σ by a surface constitutive relation. The evaporation rate at the interface, $\dot{\omega}_v$, is determined by applying chemical-equilibrium conditions while solving the species equation. The one-step simplified reaction mechanism given by Westbrook [6] for the oxidation of Hydrocarbon fuels will be used to provide the calculation of $\dot{\omega}_k$.

(II) "Level Set" approach

In solving these equations numerically, difficulties arise because of the locality of surface transports in momentum, energy, and evaporation that appear as the integral terms in the governing equations. The "Level Set" approach introduced by Sussman et al. [7] was adopted to reformulate these local quantities in such a way that they can be properly and smoothly re-distributed over a region having finite thickness. If ϕ is defined as a function that measures the normal distance from the interface, the surface integral terms in Eqs. (2)-(4) can be rearranged as follows:

$$\int_{s}\sigma\kappa\delta(\vec{x}-\vec{x}_s)\vec{n}dA\Rightarrow\sigma\kappa(\phi)\overline{\delta}(\phi)\nabla\phi$$

$$\int_{s}e_\sigma\delta(\vec{x}-\vec{x}_s)dA\Rightarrow e_\sigma(\phi)\overline{\delta}(\phi)$$

$$\int_{s}\dot{\omega}_v\delta(\vec{x}-\vec{x}_s)dA\Rightarrow\dot{\omega}_v(\phi)\overline{\delta}(\phi)$$

The distance function is assumed to be positive in the liquid phase and negative in the gaseous phase. All

of the surface variables and properties have a value of zero outside the interface region defined by ϕ. For tracking the interface movement due to flow convection and droplet evaporation, the function ϕ is solved using the following equation:

$$\frac{\partial \phi}{\partial t} + \vec{u} \cdot \nabla \phi = \frac{\delta \phi(\dot{\omega}_v)}{\delta t} \tag{5}$$

where $\delta\phi(\dot{\omega}_v)/\delta t$ is the change rate of ϕ as the result of evaporation. If the volume fraction of the liquid phase within the finite interface region (having a thickness of 2α) is assumed to be $V_l = 0.5[1 - sin(\pi\phi/2\alpha)]$, then $\delta\phi(\dot{\omega}_v)/\delta t$ can be derived from

$$\begin{aligned} \dot{\omega}_v &= -\frac{\rho_l}{4}\frac{\pi}{\alpha} cos\left(\frac{\pi\phi}{2\alpha}\right)\frac{\delta\phi(\dot{\omega}_v)}{\delta t} \\ \Rightarrow \frac{\delta\phi(\dot{\omega}_v)}{\delta t} &= -4\left[\frac{\dot{\omega}_v}{\rho_l}\frac{\alpha}{\pi}\right] \Big/ cos\left[\frac{\pi\phi}{2\alpha}\right] \end{aligned} \tag{6}$$

where ρ_l is the liquid density which is assumed to be constant for this formulation.

(III) Numerical schemes

The numerical scheme chosen for this study is a finite-volume method based on the ALE (Arbitrary Lagrangian-Eulerian) grid system. By coupling this scheme and the concept of split velocity [8], the parasite currents resulting from the locality of the surface force are minimized to prevent instability and also to ensure the mass conservation of droplets. An accurate accounting of the surface-tension term of Eq. (2) for this numerical method required modification of the formulation for the split velocity to incorporate the surface force with the pressure force. Figure 1 illustrates the concept of using split velocity in this numerical method. The velocity nodes are located at the corners of the grid, and the remaining variables are defined at the center of the cell (scalar node). The split velocities on four sides of each velocity-node point were used to satisfy the continuity equation, which is crucial in avoiding the mass loss of droplets due to numerical inaccuracy. In the mean time, these split velocities are used to discretize the interface tracking equation, Eq. 5, to ensure the mass conservation of the liquid phase.

With the implementation of split velocity in this model, the surface-force term in Eq. 2 needs to be re-arranged to couple with pressure-force term for the purpose of reducing the effects of "parasite currents."

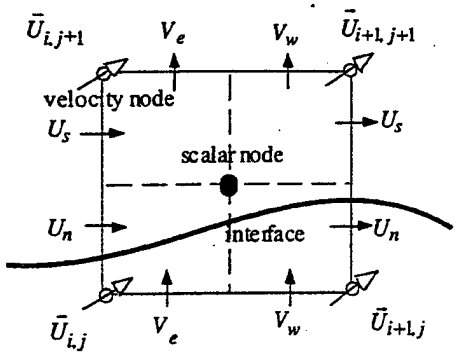

Figure 1 Schematic illustration of ALE formulation with split velocities

$$\begin{aligned} &-\nabla p + \sigma\kappa(\phi)\bar{\delta}(\phi)\nabla\phi \\ &= -\nabla p + \sigma\kappa(\phi)\nabla H(\phi) \\ &= -\nabla[p - \sigma\kappa(\phi)H(\phi)] - \sigma H(\phi)\nabla\kappa(\phi) \\ &= -\nabla\hat{p} - \sigma H(\phi)\nabla\kappa(\phi) \end{aligned} \tag{7}$$

where $H(\phi)$ is the Heaviside function derived from the delta function. Note that the newly defined pressure $\hat{p}$ will be solved instead of normal pressure p.

A second-order upwind scheme was applied to discretize the convective term in Eq. (2) for eliminating excess numerical diffusion. Because of the large density gradient across the interface between the droplet and the surrounding gases, a fully multi-grid method coupled with a MSIP (Modified Strongly Implicit Procedure) iteration scheme was implemented.

MODEL VALIDATION AND RESULTS DISCUSSION

(I) Combustion of single n-heptane droplet under stagnant and zero-gravity conditions:

The experiments conducted by Hara and Kumagai [9] are chosen to verify the numerical model in predicting the burning rate of single droplet in stagnant environment under zero-gravity condition. In their experiments, a n-heptane droplet with a diameter of 380 μm was ignited to record the variations of squared droplet diameter (D^2), flame diameter (D_f), and flame/droplet diameter ratio (D_f/D) in time. The data are re-plotted in Fig. 2 along with the simulation

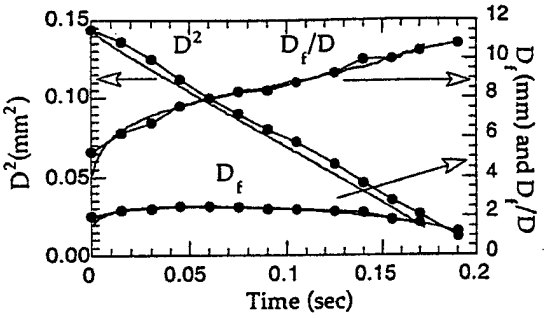

Figure 2 Variations of droplet surface-area, flame diameter, and flame/droplet diameter ratio in time for the burning of single n-heptane droplet under stagnant and zero-gravity conditions

results. Because the droplet volume (instead of droplet surface area) was obtained at every time-step during the calculations, the surface area of droplet was estimated by assuming that the droplet is maintaining spherical in shape at all times. Thus, $D^2 \propto V^{2/3}$. The results presented in Fig. 2 show the agreement between measurements and simulations is very good. The evaporation constant K is roughly 0.71 for both experiment and model.

(II) Combustion of single n-heptane droplet in a constant flowing air stream under zero-gravity conditions:

The numerical model is further verified by simulating the combustion of single spherical n-heptane droplet in a flowing air stream with a speed of 20 cm/s under zero-gravity condition. The data collected in the experiments of Okajima and Kumagai [10] are compared with simulation results. Figure 3 presents the illustration of flame structure surrounding droplet along with defined comparison parameters. Plot of numerical simulation at a specific instance is also shown on the bottom for comparison with illustration drawing on the top. The contours in Fig. 3(b) indicate the temperature field. The droplet having a diameter of 1.3 mm and a temperature of 300 K initially faces the air stream flowing from the left to the right with a velocity of 20 cm/s. In Fig. 3(a) H_1 and H_2 denote the upstream and downstream heights of flame, respectively, and 2W, the diameter of flame on the vertical section through the center of the droplet. Figure 4 shows the comparison between experimental and computational results in terms of squared droplet diameter (D^2) and three flame parameters (H_1, H_2 and $2W$) defined above verse time. It is clearly shown that the $D^2 - t$ relationship is precisely linear throughout the lifetime of droplet in

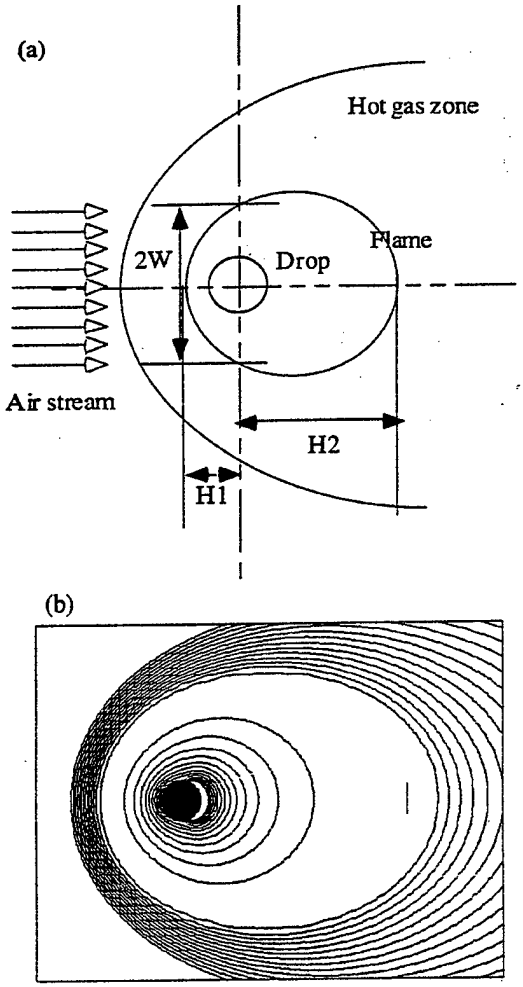

Figure 3 Illustration of burning droplet within a flowing air stream. (a) Schematic illustration; (b) Temperature contours from model simulation.

both experiments and simulations. It is also noted that the gap of D^2 between experiment and model is due to that the measured value of D^2 at t=0 from experiment is approximately 10 % less than the exact value of 1.69 mm^2 for a droplet with an initial diameter of 1.3 mm. This indicates that the droplet has burned out about 15 % of its original mass before beginning the measurements.

(III) Combustion of three-droplet array with equal spacing

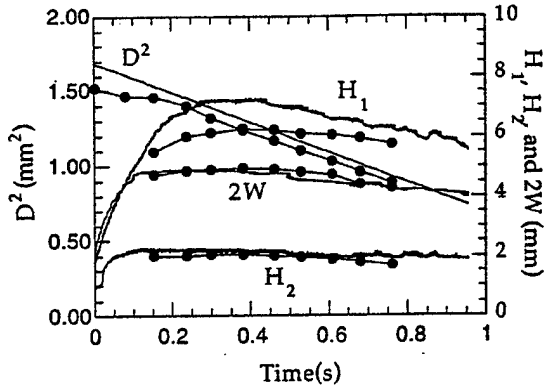

Figure 4 Comparison of squared droplet diameter and three defined flame diameters verse time between experiments and simulations.

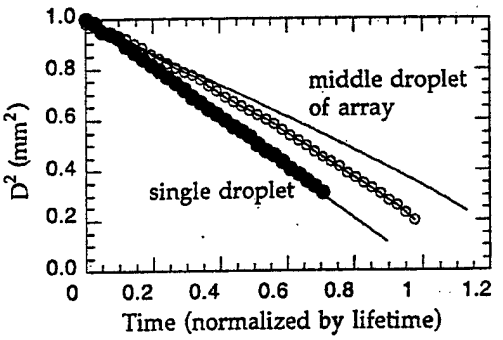

Figure 5 Comparison of temporal variations of droplet surface area between a single droplet and the middle droplet of a three-droplet array

In the experiments of Miyasaka and Law [11], the combustion of three-droplet arrays with equal spacing was performed to investigate the effects of interaction among droplets on the evaporation constants. In order to minimize buoyancy, experiments were conducted in a low-pressure and oxygen-rich environment. The low-pressure condition of experiments imposes a difficulty in numerical modeling for performing the calculations that can carry out the entire lifetime of a burning droplet array, mainly because that much larger volume of oxygen (or air) is needed to support the combustion of droplets under such condition (low pressure) compared to that required under normal atmosphere condition. For example, the volume of air required to support the completed stoichiometric combustion of a n-heptane droplet at 90 mm Hg pressure is approximately 10^5 times of the volume in droplet. This volume ratio generates, in numerical model, a computational domain (in spherical coordinate) which has a radius at least 100 (2x50) times larger than the radius of the droplet. Obviously, this costs tremendous computer time and memory. Therefore, for the present study, numerical modeling will be performed under normal atmosphere conditions with the same oxygen content in the surroundings, and the results will be presented and discussed qualitatively only.

In Fig. 7, the sequences of calculated temperature distributions in time are shown for the combustion of a three-droplet array at various spacing. The initial diameter of all the droplets is 1 mm and the spacing between the middle droplet and the side droplet is (a) L=1.25; (b) L=2.5; and (c) L=5 mm, respectively. The contours in all the frames in Fig. 7 represent temperature distributions ranging from 1500 to 3500 K. The comparison between experiments and simulations for L = 2.5 mm is presented in Fig. 5 by showing the variations of squared droplet diameters verse time. Because of the difference of pressure condition between experiments and model, the time axis in Fig. 5 was normalized based on the lifetime of droplet at each condition. The trend of bending over for the middle droplet observed in experiments is also successfully predicted from the numerical model. In Fig. 6, the plots of squared droplet diameters against time (normalized by the lifetime of single droplet) at three different spacing from numerical simulations are shown; and the characteristic of bending over is less significant when the droplets are further apart. Also the evaporation rate of the side droplet is faster than that of the middle droplet, mainly because the middle droplet is competing for oxygen with two side droplets rather than just one (the middle droplet) for the side droplet.

CONCLUSIONS

A numerical method based on the finite-volume scheme was introduced for modeling combustion and evaporation phenomena among interactive liquid droplets. This model applied the concepts of "level set" and "split velocity" to resolve the complicated topological variations of the droplet surfaces and also to ensure that the mass loss of droplets due to numerical inaccuracy would be within the allowed tolerance. Numerical simulations for the burning of single droplet under stagnant and flowing conditions were used to verify the present model by comparing the temporal variations of squared droplet diameters and flame heights with experimental measurements. Modeling for the combustion of three-droplet array with equal spacing was performed to study the influence of interaction

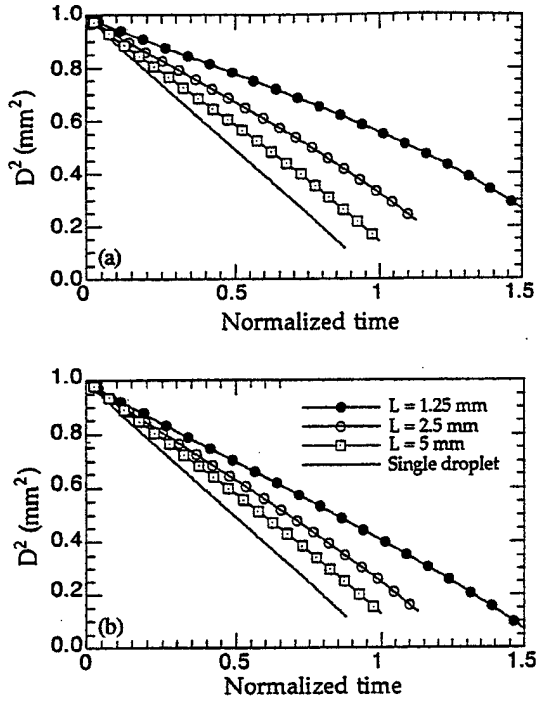

Figure 6 Effects of droplet spacing on the reduction of droplet surface area. (a) Middle droplet of the three-droplet array; (b) Side droplet of the three-droplet array.

among droplets on evaporation characteristics of individual droplets. The trend of bending over of the evaporation curves is also successfully predicted from the model.

ACKNOWLEDGMENTS

This work was supported by the U. S. Air Force under Contract F33615-95-C-2507. The author would like to thank Dr. Mel Roquemore and Dr. Vish Katta for their comments on this work.

REFERENCE

1. Law, C. K., "Recent Advances in Droplet Vaporization and Combustion," *Prog. Energy Combust. Sci.*, Vol. 8, pp. 171-201 (1982).

2. Faeth, G. M., "Evaporation and Combustion of Sprays," *Prog. Energy Combust. Sci.*, Vol. 9, pp. 1-76 (1983)

3. Sirignano, W. A., "Fuel Droplet Vaporization and Spray Combustion Theory," *Prog. Energy Combust. Sci.*, Vol. 9, pp. 291-322 (1983).

4. Chin, L. P., "A Numerical Study of Collision Behavior between Droplets," Presented at the 1996 Central States Section Meeting of the Combustion Institute, May 5-7, 1996, St. Louis, MO.

5. Welch, S. W. J., "Local Simulation of Two-Phase Flows Including Interface Tracking with Mass Transfer," *J. Comput. Phys.*, Vol. 121, pp. 142-154 (1995).

6. Westbrook, C. K., "Simplified Reaction Mechanisms for the Oxidation of Hydrocarbon Fuels in Flames," *Combust. Sci. Technol.*, Vol. 27, pp. 31-43 (1981).

7. Sussman, M., Smereka, P., and Osher, S., "A Level Set Approach for Computing Solutions to Incompressible Two-Phase Flow," *J. Comput. Phys.*, Vol. 114, pp. 146-159 (1994).

8. Hwang, Y.-H., "Arbitrary Domain Velocity Analyses for the Incompressible Navier-Stokes Equations," *J. Comput. Phys.*, Vol. 110, pp. 134-149 (1994).

9. Hara, A. and Kumagai, "The Effect of Initial Diameter on Free Droplet Combustion with Spherical Flame," *Twenty-Fifth Symposium (International) on Combustion*, The Combustion Institute, Pittsburgh, pp. 423-430 (1994).

10. Okajima, S. and Kumagai, "Experimental Studies on Combustion of Fuel Droplets in Flowing Air under Zero- and High-Gravity Conditions," *Nineteenth Symposium (International) on Combustion*, The Combustion Institute, Pittsburgh, pp. 1021-1027 (1982).

11. Miyasaka, K. and Law, C. K., "Combustion of Strongly-Interacting Linear Droplet Arrays," *Eighteenth Symposium (International) on Combustion*, The Combustion Institute, Pittsburgh, pp. 283-292 (1981).

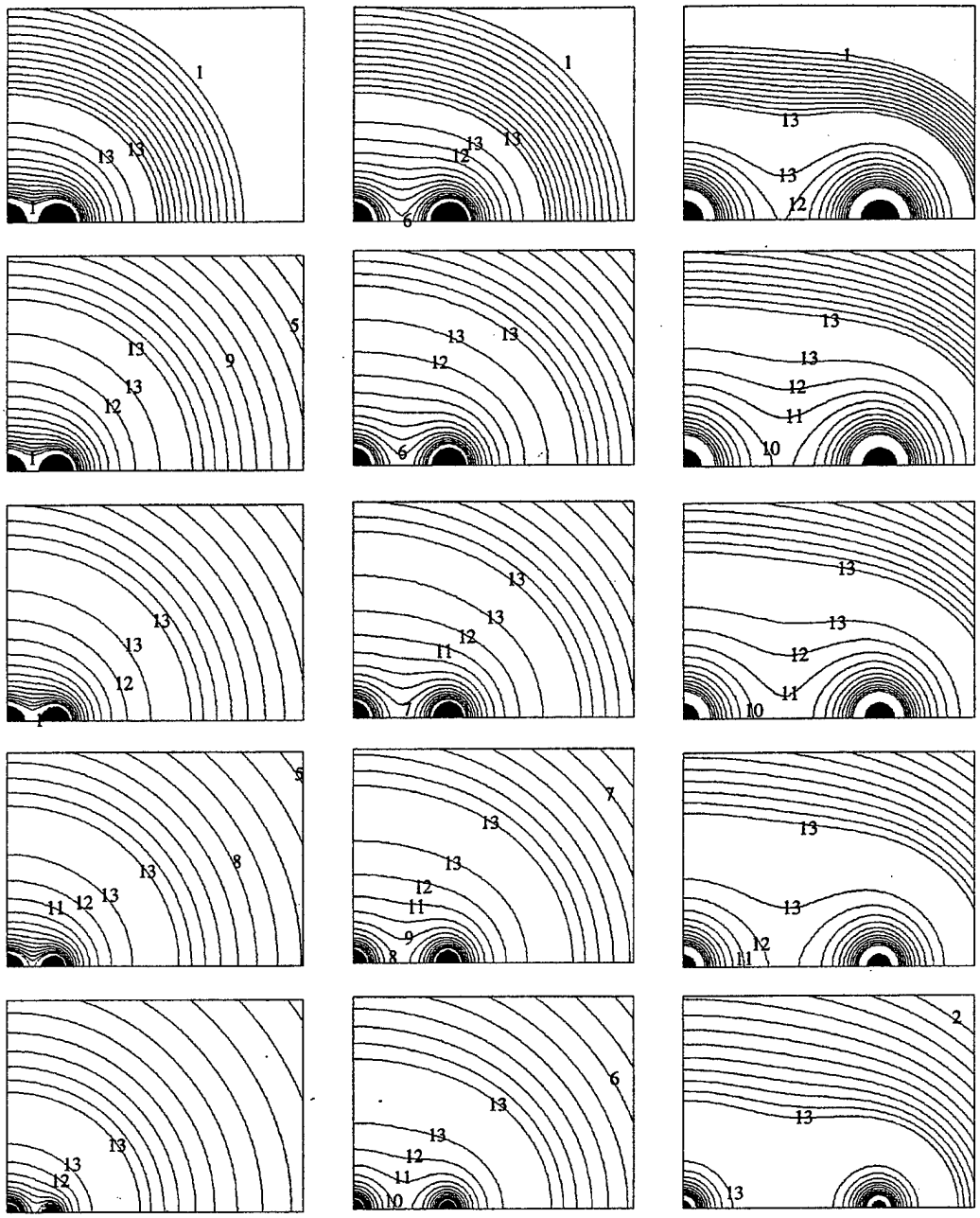

(a) L = 1.25 mm (b) L = 2.5 mm (c) L = 5 mm

Figure 7. Calculated temperature fields for the combustion of three-droplet array at three different spacing: (a) L=1.25 mm; (b) L=2.5 mm; and (c) L=5 mm. Time interval between frames is 0.24 t (normalized) and T = 1500+170(n-1) K

Atomization and Sprays, vol. 7, pp. 317–337, 1997

EXPERIMENTAL STUDY OF PURE AND MULTICOMPONENT FUEL DROPLET EVAPORATION IN A HEATED AIR FLOW

G. Chen and S. K. Aggarwal
Department of Mechanical Engineering, The University of Illinois at Chicago, Chicago, Illinois, USA

T. A. Jackson and G. L. Switzer
Wright Patterson Air Force Base, Ohio, USA

The dynamics and vaporization of both pure and multicomponent fuel droplets in a laminar-flow field are investigated. Extensive data are obtained on the velocity and size history of a fuel droplet injected into a well-characterized hot laminar flow. Fuels considered are n-hexane, n-decane, and a bicomponent mixture of equal amounts of hexane and decane. The droplet velocity and size histories are measured by phase Doppler particle analyzer, and compared with the predictions from three different liquid-phase models, the infinite-diffusion, diffusion-limit, and thin-skin models. Predicted results generally show good agreement with measured data. For the conditions of this study, it is shown that the use of a solid-sphere, steady-state drag law adequately reproduces the measured velocity history for small to moderate droplet accelerations, provided the variable-property effects are included in the model. However, the quasi-steady drag equation is not able to capture either the large deceleration experienced by the droplet near the injection location, nor the measured inflection point, where the droplet acceleration changes sign, underscoring the importance of unsteady effects on droplet motion. The comparison of vaporization history indicates that, under relatively low-temperature conditions, the predictions of both the infinite-diffusion and the diffusion-limit models are in close agreement with experiments. However, the thin-skin model overpredicts the vaporization rate, and shows significant differences with experiments, especially for less volatile (n-decane) and multicomponent fuel droplets. The comparison also indicates that the thermophysical properties of the gas film surrounding the droplet should be calculated accurately; in particular, the effect of fuel vapor should be considered.

INTRODUCTION

The gasification behavior of a liquid droplet provides a fundamental input for the modeling of many spray systems, since the collective gasification of individual droplets intimately influences the bulk spray vaporization and combustion. The basic droplet combustion model was formulated in the 1950s by Godsave [1] and Spalding [2] for an isolated pure-component droplet burning in a stagnant, oxidizing environment. This model was termed the d^2 law because it predicts that the square of the droplet diameter decreases linearly with time. Since then this model has been studied extensively, both experimentally and theoretically. These studies have been reviewed by Williams [3], Faeth [4], and Law [5]. The key assumptions in the basic model are that the droplet and gas flow are in dynamic equilibrium (zero slip velocity), the droplet heating time is negligible compared to its lifetime, the droplet surface temperature is a constant, and the thermophysical properties

PUBLISHED WITH PERMISSION
Copyright © 1997 by Begell House, Inc.

NOMENCLATURE

C_D	droplet drag coefficient
C_p	specific heat
D	mass diffusivity
D_0	initial droplet diameter
g	acceleration of gravity
$\overline{H}$	H/L
$\hat{H}$	nondimensional heat transferred from gas phase to droplet per unit mass of fuel vaporized
L	latent heat of vaporization
Le	liquid Lewis number
$\hat{m}$	nondimensional vaporization rate [Eq. 1]
P	pressure, atm
r_s	droplet radius
$\bar{r}$	radial location inside the droplet, normalized by the instantaneous droplet size
R	universal gas constant
Re	droplet Reynolds number
Sc	Schmidt number
t	time
T	temperature
T_{ib}	boiling temperature of ith component
$\hat{T}$	nondimensional temperature
T_0	initial droplet temperature
V_d	droplet velocity
V_g	gas velocity
W	molecular weight
X	mole fraction
Y	mass fraction
Z	axial location
α	thermal diffusivity
λ	thermal conductivity
μ	dynamic viscosity
ρ	density

Subscripts

f	fuel
∞	ambient
s	droplet surface
i	ith liquid fuel component
l	liquid

of the gas film surrounding the droplet are constant. More detailed studies reported by Law [5] and Aggarwal et al. [6] have considered the effects of relaxing these restrictions of the basic model. In particular, they have considered the effects of transient liquid-phase heating on the droplet vaporization rate, and proposed three different models with varying degrees of complexity to include transient heating in the d^2 model. The three models have been termed the infinite-conductivity or rapid-mixing model, the conduction-limit model, and the vortex model.

The recent increase in the utilization of synthetic and derived fuels, and the realization that most liquid fuels are mixtures of many components, has spurred interest in studying the vaporization of multicomponent liquid fuel droplets. Theoretical analysis of the multicomponent droplet presents several complexities absent in a similar analysis of the single-component droplet. First, the phase-change process at the multicomponent fuel droplet surface and the transport of fuel vapor mixture in the gas phase need to be properly described. Second, the evaporation process is inherently time-varying due to the continuous change in the composition and temperature of the droplet as vaporization proceeds. Third, because of the extremely slow rate of liquid-phase mass diffusion as compared with those of liquid-phase heat diffusion, gas-phase heat and mass diffusion, and droplet surface regression, the liquid-phase mass diffusion together with the volatility differentials become crucial factors in determining the gasification behavior of multicomponent fuel droplets.

Landis and Mills [7] investigated the vaporization of a bicomponent fuel droplet in a stagnant atmosphere. A quasi-steady gas-phase model was used, and the equations

governing the unsteady mass and heat diffusion within the droplet were solved numerically. This model is commonly known as the diffusion-limit model. Law [8] proposed a model for multicomponent droplet vaporization which neglects the effects of concentration gradients in the liquid phase and assumes that the composition and temperature within the droplet are spatially uniform but time-varying. The model predicts that the gasification process will be similar to batch distillation in that the sequence of gasification is controlled only by the volatility differentials among the different components. However, Sirignano [9] showed that even in the limit of high vortex strength, the internal liquid circulation can only reduce the characteristic length scale for diffusion by a factor of 3. In general, for droplets evaporating in a high-temperature environment, the predictions using the diffusion-limit model showed significant differences from those based on the rapid-mixing or infinite-diffusion model. In order to account for the effect of internal liquid circulation on the vaporization of a multicomponent droplet, Tong and Sirignano [10] extended their single-component vortex model to multicomponent fuels. Abramzon and Sirignano [11] proposed an effective diffusivity model for the liquid-phase processes inside the droplet, and an extended film model to account for the gas-phase convective effect on vaporization.

An interesting feature of diffusion-dominated droplet gasification is the possible attainment of approximately steady-state temperature and concentration profiles within the droplet, which then leads to correspondingly steady-state gasification rate and average droplet composition. Based on this concept, Law and Law [12] formulated a d^2-law model for multicomponent droplet vaporization and combustion. Experimental results obtained for an alcohol–alkane binary droplet confirmed the d^2-law behavior and the compositional dependence of the burning rate constant.

As indicated above, the literature on the behavior of an evaporating/burning droplet is extensive. However, most of these studies deal with droplet combustion or evaporation under high-temperature conditions, when the time scale associated with the rate of change of droplet size is small compared with that of the transient liquid-phase processes. Not much information is available on the behavior of evaporating droplets in a relatively low-temperature environment. In many applications—for example, the intake manifold of port-injected gasoline engines and gas turbine combustors using prevaporized fuel—the droplets encounter an environment where the mixture temperature is relatively low, typically below the boiling temperatures of the constituent fuels but above room temperature. Under such conditions, the possibility of an envelope flame is precluded and the droplet gasification rate is low. The droplet heatup time may not be negligibly small compared to its lifetime, and the liquid-phase transient processes may still be important. The literature review also indicates that a complete experimental data set, which can be used for the validation of theoretical models, on both the dynamics and the evaporation of a droplet, especially for multicomponent fuel droplets, in a well-characterized laminar flow is generally not available.

The present study is motivated by the above considerations. An experimental-theoretical investigation of the dynamics and evaporation of a fuel droplet is conducted. The major objective is to provide a complete set of measurements for the velocity and vaporization history of pure and multicomponent fuel droplets in a well-characterized, heated, laminar flow. The experimental data set includes the gas-phase properties, such as velocity and temperature along the droplet trajectory, as well as the droplet velocity and size history along its trajectory. Special care was taken to keep the flow field as simple as possible, and to control the initial droplet properties, such as temperature, diameter, and

injection frequency, as much as possible. For example, the flow field was established with only axial gradients of temperature and velocity, and the droplet traveled with only axial velocity. In the experiments, a stream of droplets is injected in a hot laminar flow and the droplet size and velocity along its trajectory are measured. The measurements are compared with the predictions of three droplet vaporization models. In the predictions, the variable thermophysical properties of the gas film outside the droplet as well as the liquid-phase properties are calculated in a comprehensive manner. The present study is important because past research on droplet vaporization has not reported any results for the conditions considered in the present work. As discussed above, such conditions are relevant in many practical applications. In addition, the study may be relevant to the understanding and modeling of the processes in nondilute sprays, where the gas temperature and vaporization rate are relatively low.

EXPERIMENT FACILITY

The test configuration has been designed for injecting fuel droplets in a well-controlled, laminar heated flow field with only axial gradients of temperature and velocity. It consists of heating elements, inlet flow conditioning equipment, a droplet-on-demand injection system, and a confined test section as shown in Fig. 1. The chamber contains, in series, a sintered metal diffusing element, a fine mesh screen, two resistance heating elements, a second fine mesh screen, and a flow-straightening honeycomb. At the end of this section the flow had been evenly distributed, heated to 400 K, and decelerated to a velocity of 0.16 m/s. This air then enters a circular-to-square transition section leading to the test section. In this transition the flow is accelerated to a mean velocity of 1 m/s. The mean and root-mean-square (rms) velocity profiles at the test section inlet are illustrated in Fig. 2. Note the very low values of the rms, indicating turbulence intensities of less than 3%. These measurements were made with a hot-wire anemometer and confirmed with phase Doppler particle analyzer (PDPA) measurements. Figure 2 also shows the inlet air temperature profiles (orthogonal to each other and both through the center of the test section). These measurements were taken with microthermocouple (Chromel-Alumel, 0.13-mm diameter lead joined to form a measurement bead approximately 0.25 mm in diameter).

The test section is 8.9×8.9 cm and 45.0 cm long, constructed of four Pyrex panels. The flow is driven vertically upward. Droplets are injected in the center of this section. Figure 3 is an illustration of the test section along with a photo of a stream of droplets illuminated with a sheet of laser light. Optical measurements of droplet diameter and local velocity are made along the flow axis by the PDPA. For this experiment the test chamber assembly is positioned, relative to fixed measurement volumes, by an x-y-z precision traversing table. The PDPA is an interferometric droplet sizing device. It sizes single droplets by measuring the radius of curvature of the droplet. Several publications, including those of Bachalo [13] and Jackson and Samuelsen (14], describe its features and the accuracy with which it determines droplet size. For this effort a single-component system was used.

The most critical component of the experimental setup is the droplet-on-demand generator. The study of the droplet vaporization behavior for various fuels requires a generator which can inject droplets axially into a flow of heated air without perturbing the velocity or temperature uniformity of the flow. Single monosized droplets are required

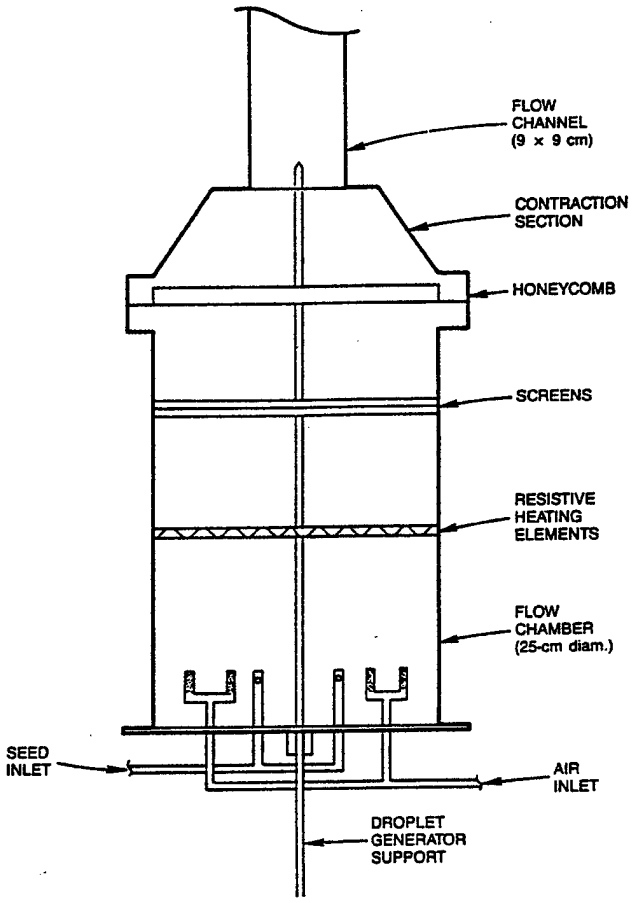

Fig. 1 Schematic diagram of flow chamber employed for droplet vaporization studies.

having diameters in the range 50–100 μm, each droplet having identical velocity and trajectory. An essential characteristic of the system is its long-term stability. Several designs were tested before deciding on the final configuration for the droplet-on-demand generator, as shown in Fig. 4. Its operation is based on a piezoelectric (PZT) cylinder 0.7 mm ID × 1.3 mm OD × 19 mm in length. A voltage pulse applied between the inner and outer surfaces of the PZT causes the cylinder to contract radially. This contraction creates a pressure pulse which forces liquid in the cylinder through a glass nozzle whose aperture diameter is approximately equal to that of the desired droplet. The most critical aspect of this generator design is the shape and quality of the nozzle, which is formed by melting and polishing glass capillary tubing. An important aspect of generator operation is the thermal isolation required over the 60-cm length of the droplet-generator support, shown in Fig. 4, from the heated air flow to prevent prevaporization of the fuel. This isolation is provided by a water-cooled sheath which also serves as a support for the generator.

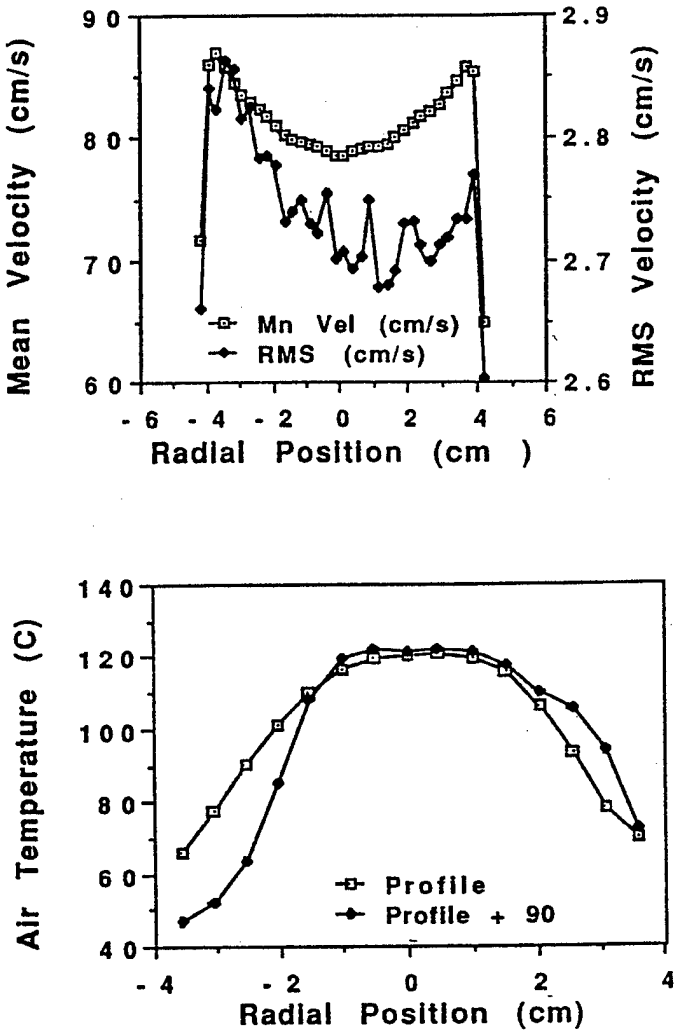

Fig. 2 Air velocity and temperature profiles.

Several operational parameters have been identified which have major influence on successful generator performance, the most sensitive of these being PZT drive-voltage amplitude, pulse width, pulse-repetition frequency, and liquid pressure. The liquid viscosity, PZT temperature, and rise and fall times of the PZT pulse also affect generator performance, but to a lesser extent. Proper generator operation requires a delicate balance among these parameters. Development efforts during this study resulted in a compact, versatile, and reliable technique for production of single droplets and introduction of these droplets into a well-controlled hot air flow. The droplet-on-demand generator has produced droplets using water, hexane, and decane as the working fluids. Through precise control of the operational parameters, several discrete diameters in the range of 40–90 μm can be

stably generated from a single 65-μm nozzle aperture. Droplet-generation frequencies range from one droplet up to a stream of droplets at 1 kHz, with adjustable exit velocities varying between 0.2 and 10 m/s.

Several data sets have been obtained by using the above generator facility. Fuels considered are hexane, decane, and a bicomponent fuel with equal amounts of hexane and decane. For each set, the droplet size and velocity are measured along its trajectory. The local gas velocity and temperature profiles are also measured. The latter information along with the initial droplet size and velocity are used in the predictions. Note that the gas-phase turbulence level has been maintained sufficiently low so that the hot air flow can be considered essentially laminar. The experimental data are employed to validate several theoretical dynamics and vaporization models, which are described next.

THEORETICAL MODEL

The theoretical model involves the calculation of velocity, size, and surface properties of an evaporating droplet along its trajectory in a laminar hot air flow. The time-dependent Lagrangian equations for the droplet position, velocity, and size are solved numerically.

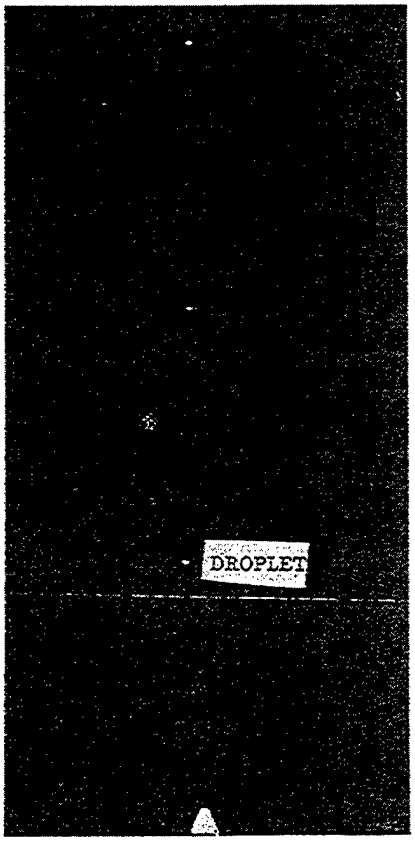

Fig. 3 Generation of 55-μm droplets at 10-Hz rate.

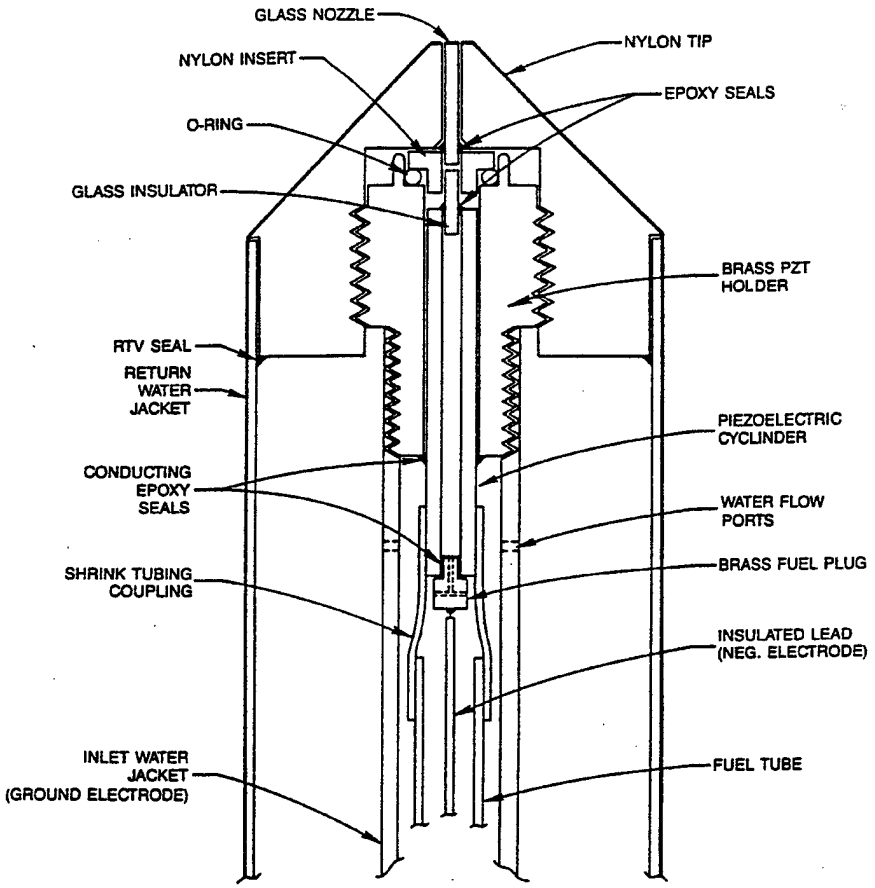

Fig. 4 Schematic diagram of water-cooled droplet-on-demand generator.

Droplet Evaporation

As discussed by Law [5], the gas-phase transient time is much smaller than the characteristic time for the liquid-phase processes in most circumstances under subcritical conditions. Consequently, the gas-phase processes can be considered as quasi-steady and the equations can be solved analytically for the nondimensional mass evaporation rate $\hat{m}$, the fractional mass evaporation rate ε_i, and the effective latent heat $\hat{H}$ as

$$\hat{m} = \ln\left(1 + \frac{Y_{fs} - Y_{f\infty}}{1 - Y_{fs}}\right) \tag{1}$$

$$\varepsilon_i = \frac{\hat{m}_i}{\hat{m}} = Y_{fs} + (1 - Y_{fs})\,\frac{Y_{fis} - Y_{fi\infty}}{Y_{fs} - Y_{f\infty}} \tag{2}$$

$$\hat{H} = \frac{(1 - Y_{fs})(\hat{T}_\infty - \hat{T}_s)}{Y_{fs} - Y_{f\infty}} \tag{3}$$

At any given time instant, with known droplet surface temperare T_s and liquid-phase species mole fraction X_{il}, the gas-phase species mass fractions at the droplet surface, Y_{fis}, can be obtained by means of Raoult's law,

$$X_{is} = X_{il} X_{0i} \tag{4}$$

where X_{0i} is the equilibrium vapor mole fraction for the pure liquid i and is given by the Clausius-Clapeyron relation,

$$X_{0i} = \left(\frac{1}{P}\right) \exp\left\{\frac{L_i W_i}{R\left[(T_{ib})^{-1} - (T_s)^{-1}\right]}\right\} \tag{5}$$

Finally, X_{is}, is related to Y_{is}, through

$$Y_{is} = \frac{X_{is} W_i}{\left(1 - \sum_{i=1}^{n} X_{is}\right) + \sum_{i=1}^{n} X_{is} W_i} \tag{6}$$

where W_i is the ratio of the molecular weight of the ith vaporizing species to an average molecular weight of all the noncondensable inert species at the droplet surface. As indicated above, the liquid-phase transient processes appear through the variables X_{il} and T_s. To examine their influence, three liquid-phase models considered are the infinite-diffusion, diffusion-limit, and thin-skin models. The first two models have been described by Tong and Sirignano [10]. The implicit assumption in the infinite-diffusion model is that the internal circulation is so fast that the droplet temperature and composition are maintained spatially uniform, though still temporally varying. The volatile components are continuously brought to the droplet surface, where they are preferentially vaporized. The vaporization process is expected to resemble that of batch distillation. The temporal variations of droplet composition and temperature are determined from the overall mass and energy conservation equations. In the diffusion-limit model, the transient heat and mass transport in the liquid are assumed to be governed by the unsteady heat and mass diffusion equations. Since the droplet is vaporizing, the diffusion field has a moving boundary. For the convenience of calculation, a transformation is used to cast the moving-boundary problem into a fixed one.

The thin-skin model is based on the assumption of high liquid Lewis number and high droplet evaporation rate. Under these conditions, we may assume that the droplet surface temperature and its concentration distributions remain constant at T_s and X_{il} $(\hat{r})$, respectively. This is the extension of single-component d^2 law to the multicomponent case. The temperature assumption implies that it is unnecessary to study transient liquid-phase processes. Then the effective latent heat is equal to the actual latent heat and the constant concentration profiles are given by

$$\frac{1}{\bar{r}^2}\frac{d}{d\bar{r}}\left(\bar{r}^2\frac{dY_{il}}{d\bar{r}}\right) = \mathrm{Le}_l K\hat{m}\bar{r}\frac{dY_{il}}{d\bar{r}} \tag{7}$$

The solution of Eq. (7) is

$$Y_{il}(\bar{r},T_s) = Y_{il0}\left\{1 + \left[\frac{1/x_i}{\sum_{j=1}^{n} Y_{jl0}/x_j} - 1\right]\exp\left[-C_k m/\mathrm{Le}_l(1-\bar{r})\right]\right\} \tag{8}$$

The only unknown parameter, T_s, can be found by solving Eq. (3). For additional details, the reader is referred to Chen [15].

Convective Effects

Mostly semiempirical approaches have been employed to include the effects of gas-phase convection on the droplet dynamics and vaporization rate. At higher Reynolds numbers, a typical form of the Ranz-Marshall correlation [16] is frequently adopted. However, heat transfer measurements by Yuge [17] considered corrections due to natural convection at low Reynolds number, and found that the following correlation gives a better fit to his experimental data:

$$\frac{\hat{m}_{\mathrm{conv}}}{\hat{m}} = 1 + 0.27\ \mathrm{Re}^{1/2}\,\mathrm{Sc}^{1/3} \tag{9}$$

Based on Frossling and Ranz-Marshall correlations, Agoston et al. [18] developed another correlation,

$$\frac{\hat{m}_{\mathrm{conv}}}{\hat{m}} = 1 + 0.24\ \mathrm{Re}^{1/2} \tag{10}$$

The comparison of predicted and experimental results indicates that Eq. (10) provides a better correlation for the present case. It is important to mention that more advanced models have been proposed in recent years; for example, Peng and Aggarwal [19]. However, we have included only those that are deemed directly relevant to the present study.

The relative gas velocity also produces a drag force. At any time t, the droplet velocity and location along its trajectory can be found from the following equations:

$$\rho_l r_s^3\frac{dV_d}{dt} = \frac{3}{8}r_s^2\rho_\infty|V_\infty - V_d|(V_\infty - V_d)C_D - gr_s^3(\rho_l - \rho_\infty) \tag{11}$$

$$\frac{dZ_d}{dt} = V_d \tag{12}$$

where C_D is the drag coefficient and is correlated to the Reynolds number [20] by

$$C_D = 27\ \mathrm{Re}^{0.84} \tag{13}$$

Effects of Variable Properties

The classical study of droplet vaporization and combustion assumes that the latent heat, specific heat, thermal conductivity, product ρD are constants, and that the Lewis number $\mathrm{Le} = (\lambda/C_p \rho D)$ is unity. These assumptions have been used by many theoretical studies. In reality, these properties are strong functions of both temperature and species concentrations. To consider these effects, a reference-state scheme proposed by Law and Williams [21], which differs from the usual one-third rule, is used in the present study. A comprehensive procedure is then employed to obtain the thermophysical properties at the reference film temperature and concentrations. The method of calculating mixture properties is discussed by Chen [15]. Another important property is the latent heat L_i. In the present study, the ambient temperature is relatively low, so the droplet surface temperature is much lower than the boiling temperature. In such cases , it is incorrect to use a constant L_i at the boiling temperature. Here, a modified Watson relation [22] is used for the correlation,

$$L_i = L_i^0 \left(\frac{1 - T_{r2}}{1 - T_{r1}} \right)^{n + \beta(1 - T_r)} \tag{14}$$

where the parameter β is determined from experiments.

RESULTS AND DISCUSSION

Several experimental data sets for *n*-hexane, *n*-decane, and bicomponent fuel droplets injected into a prescribed hot air flow are provided in Tables 1–3. In each table, the droplet size and velocity history along its trajectory are given. The corresponding air

Table 1 Measured Droplet Size and Velocity History for *n*-Decane Fuel[a]

Axial location	Set 1		Set 2		Set 3	
Z (mm)	D (μm)	V_d (m/s)	D (μm)	V_d (m/s)	D (μm)	V_d (m/s)
1	59.36	1.10	58.00	0.99	55.91	1.10
2	58.38	0.96				
4	58.48	0.68				
8	58.21	0.36				
10	58.09	0.31	58.06	0.32	56.61	0.20
20	56.08	0.38	56.48	0.42	56.31	0.24
30	53.89	0.47	55.00	0.50	55.41	0.27
40	52.18	0.54	52.36	0.57	55.12	0.30
50	49.39	0.60	50.11	0.61	55.34	0.32
60	46.37	0.65	46.56	0.67	55.03	0.33
70	43.57	0.69	43.75	0.71	55.44	0.35

[a] Set 1 and 2 are for heated air flow, while for set 3, air is at 300 K.

Table 2 Measured Droplet Size and Velocity History for *n*-Hexane Fuel

Axial location	Set 1		Set 2		Set 3	
Z (mm)	D (μm)	V_d (m/s)	D (μm)	V_d (m/s)	D (μm)	V_d (m/s)
1	61.20	1.12	64.57	1.15	63.13	1.36
10	58.31	0.37	53.15	0.39	61.60	0.59
20	46.15	0.42	42.80	0.44	59.80	0.27
30	37.78	0.54	35.80	0.55	52.00	0.29
40	26.48	0.62	32.27	0.76	49.90	0.32
50	16.05	0.71	24.59	0.81	47.19	0.34
60	6.35	0.74	6.96	0.76	45.01	0.36

velocity and temperature are provided in Table 4. These data are used for the validation of several droplet dynamics and vaporization models. For the predictions, a second-order Runge-Kutta scheme with variable time step, controlled by the rate of change of the droplet diameter, is used to integrate Eqs. (11)–(12). Results for the pure fuel droplets are shown in Figs. 5 and 6, whereas those for the multicomponent case are given in Figs. 7–9. As noted in the figures, we have not included error bars with experimental data. Our estimate indicated uncertainties of 5% in velocity data, 5–7% in size, and 3–5% in temperature.

Single-Component Case

Figure 5 shows the predicted and experimental droplet velocities along their trajectories for both hexane and decane droplets. The measured gas velocity is also shown in the figure. The droplet velocity, which is much higher than the gas velocity at the injection point, relaxes rapidly to an equilibrium value and then follows the variation of gas velocity along the trajectory. While the overall agreement between the predicted and experimental values is reasonably good, the comparison underscores the deficiency of the standard (steady-state) drag equation to capture the large deceleration experienced by the droplet near the injection location. In addition, the steady drag equation is not able to reproduce the measured inflection point, where the droplet acceleration changes sign. This implies that the effect of droplet relative acceleration (see Peng and Aggarwal [23]) is important

Table 3 Measured Droplet Size and Velocity History for Bicomponent Hexane–Decane (50/50) Fuel

Axial location	Set 1		Set 2		Set 3	
Z (mm)	D (μm)	V_d (m/s)	D (μm)	V_d (m/s)	D (μm)	V_d (m/s)
1	68.95	1.13	68.17	1.02	67.56	1.02
10	62.82	0.23	63.65	0.31	64.33	0.24
20	56.29	0.33	57.45	0.32	61.92	0.21
30	55.71	0.44	55.61	0.43	60.37	0.25
40	54.36	0.51	53.98	0.50	56.97	0.29
50	49.15	0.59	51.11	0.57	55.70	0.31
60	47.05	0.63	48.17	0.62	55.17	0.33

Table 4 Air Velocity and Temperature along the Droplet Trajectory

Z (mm)	V (m/s)	T (K)
1	0.39	371
3	0.12	373
5	0.21	371
10	0.35	375
20	0.58	382
30	0.72	389
50	0.93	398
70	1.04	404
90	1.08	409

in this region. For small to moderate droplet accelerations, however, the standard drag correlation seems to work well, provided the properties of the gas film surrounding the droplet are calculated accurately.

Figure 6 shows the variation of the droplet diameter squared obtained experimentally and predicted by the thin-skin, diffusion limit, and infinite diffusion models. Note that several data sets were obtained to assess the repeatability of data, although only one is shown in the figure; other data sets are provided in Tables 1–3. The overall agreement between predictions and experiments is quite good. For hexane, the calculated values are not very sensitive to the models. For decane, however, some sensitivity to the models is indicated, where the diffusion-limit and infinite-diffusion models show better agreement with the experimental data compared to the thin-skin model. These results can be explained by following the droplet surface temperature history [15]. For hexane, the boiling temperature is relatively low, and the evaporation proceeds at a relatively fast rate. However, the latent heat needed for phase change is more than the heat transferred from the gas phase to the droplet surface. Consequently, the surface temperature will decrease until the heat needed for evaporation is provided by the heat transferred from the ambient. Therefore, the wet-bulb temperature is below the initial droplet temperature. The liquid-phase transient time is very short, and all three models predict almost the same surface temperature; therefore, the droplet size variation is not sensitive to the models. For decane, however, the wet-bulb temperature is relatively high and the droplet transient heating becomes important. As a result, the vaporization behavior is sensitive to the models. Initially, the evaporation rate is very low and the amount of heat needed for evaporation is higher than the heat transferred to the droplet surface. Consequently, the droplet temperature keeps increasing until it reaches an equilibrium temperature. Because the thin-skin model neglects the initial transient droplet heating, the droplet vaporizes faster than for the other two models. Thus, the important observation is that the difference between the models is more significant for heavier fuels which have higher boiling temperature and, thus, a longer transient heating period.

Another important observation is that the predictions of the diffusion-limit and infinite-diffusion models are almost the same. Since the ambient temperature is relatively low, the temperature gradient between the droplet surface and environment is small. Thus the rate of heat transport to the surface is not much faster than the rate of heat transport within the droplet for the diffusion-limit model. Consequently, these two models predict

almost the same surface temperature and, hence, the same vaporization rate. However, for higher ambient temperatures, the rate of heat transfer to the droplet surface will be higher, and the difference between these two models will become apparent [15].

Multicomponent Case

The multicomponent case is more complex because of the existence of slow liquid-phase diffusion. An incorrect prediction of liquid surface composition will cause a significant difference in the predicted droplet diameter history. Figure 7 shows the variation of the diameter squared along the trajectory of a hexane/decane droplet with initial mass fraction of each being 0.5. It is interesting to note that the experimental data indicates a batch-distillation

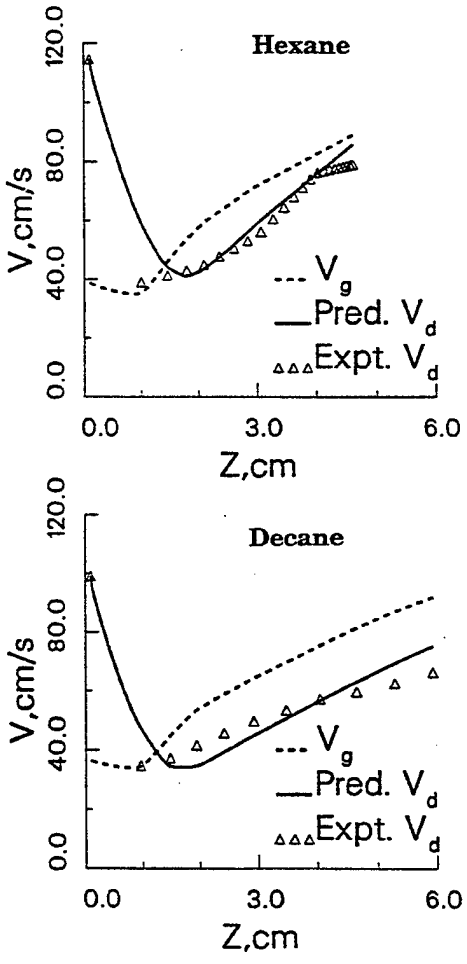

Fig. 5 Comparison of predicted and experimental droplet velocities along the trajectory.

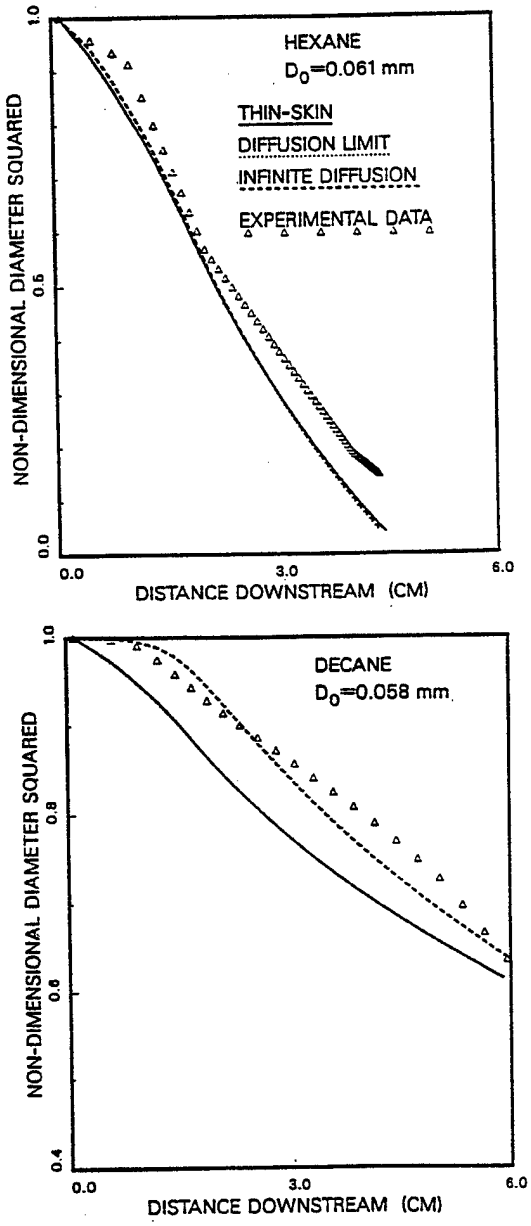

Fig. 6 Diameter squared along the trajectory for a fuel droplet.

type of behavior, which is better simulated by the infinite-diffusion model. This means that the assumption of a spatially uniform liquid temperature and composition may be a good approximation for the present case. This is due to the slow rate of vaporization at relatively

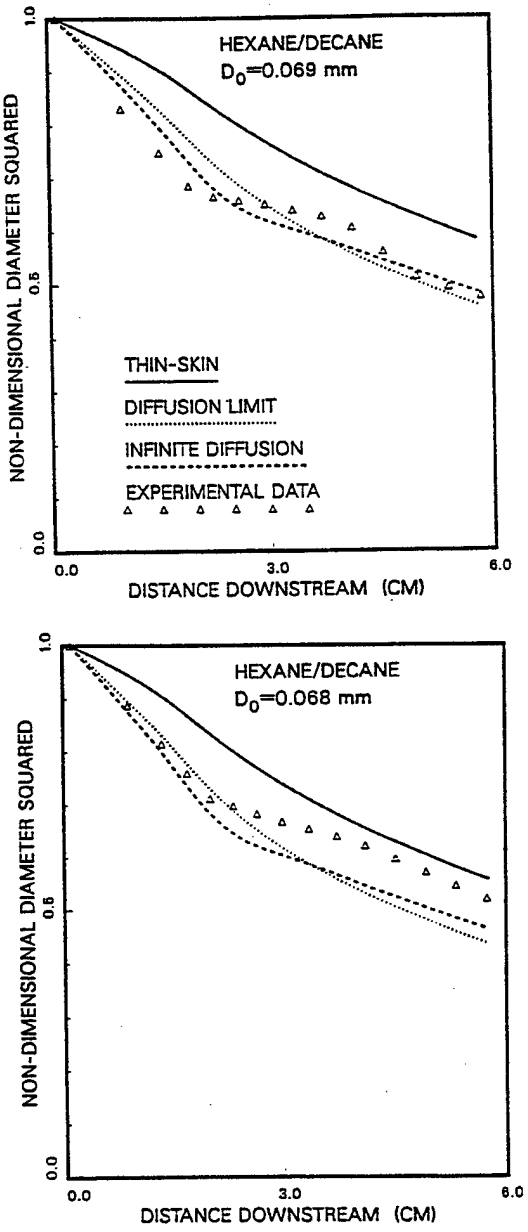

Fig. 7 Diameter squared along the trajectory for a multicomponent fuel droplet.

low environment temperature, which makes the droplet evaporation time ($R^2/4\beta$) comparable to the mass diffusion time (R^2/D) and heat conduction time (R^2/α). Here, R represents the initial droplet radius, β a characteristic vaporization rate constant, D the mass diffusivity, and α the thermal diffusivity. It is also noteworthy that the differences between this model and the diffusion-limit model are not significant. The thin-skin model does not show as good an agreement as the other two models. This is due largely to the excessively slow rate of evaporation and long liquid transient time causing the assumption of constant temperature and composition profiles to deviate from the real situation.

Figure 8 shows the variation of the surface mass fraction of liquid hexane as well as the surface temperature along the droplet trajectory. Significant disagreements exist among the three models. For the thin-skin model, the surface concentration and temperature, by definition, have constant values, while for the diffusion-limit model, the surface concentration initially decreases much faster than that for infinite-diffusion model and then levels off at almost a constant value. For the infinite-diffusion model, the surface mass fraction of hexane decreases steadily due to the preferential vaporization of more volatile species, whereas the surface temperature initially has a constant value given by the wet-bulb temperature of the hexane component. It then continues to increase slowly as the wet-bulb temperature increases following the change in the liquid surface composition. Finally, it approaches the wet-bulb temperature of decane. There is a transition region between the two inflection points of the curve which corresponds to the depletion of the hexane component.

The differences in the surface temperature and liquid concentrations cause differences in the predictions of surface vapor concentrations. It is observed, though not shown here, that the liquid concentration has a more dominant effect on the surface vapor concentration. As a result, the diffusion-limit model underpredicts the vaporization rate compared to the infinite-diffusion model. Note that this behavior is observed for low ambient temperatures. At relatively high ambient temperatures, the behavior is significantly different [5].

Figure 9 shows the sensitivity of predictions to the method of calculating reference properties for the variable-property effects. Method 1 considers only the effect of temperature, while methods 2 and 3 consider the effects of both mixture temperature and composition. For methods 1 and 2, the commonly used one-third rule is employed, while method 3 [21] uses a different averaging rule for calculating the reference values. An important observation is that method 1, which considers only the variable temperature effect, shows significant differences from the experimental results, especially later in the lifetime when the heavier fuel (decane) begins to vaporize. The difference between methods 2 and 3, which consider the variable temperature and fuel vapor effects, is negligible. Method 3 has been used for calculating the variable thermo-transport properties in the present study.

CONCLUSIONS

The vaporization behavior of a fuel droplet in a laminar hot air flow has been studied experimentally and theoretically. Pure as well as multicomponent fuels have been considered. Several experimental data sets are provided in a form such that other researchers can easily use them for model validation. Numerical results predicted by three vaporization models have been compared with experimental data. Important conclusions are as follows.

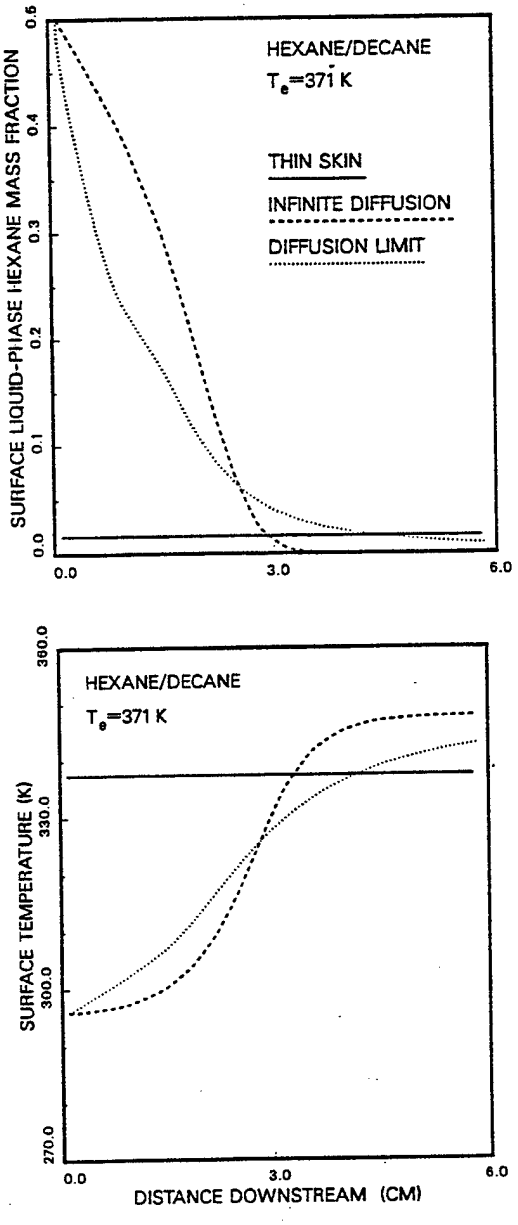

Fig. 8 Liquid hexane mass fraction and temperature at the droplet surface along the trajectory.

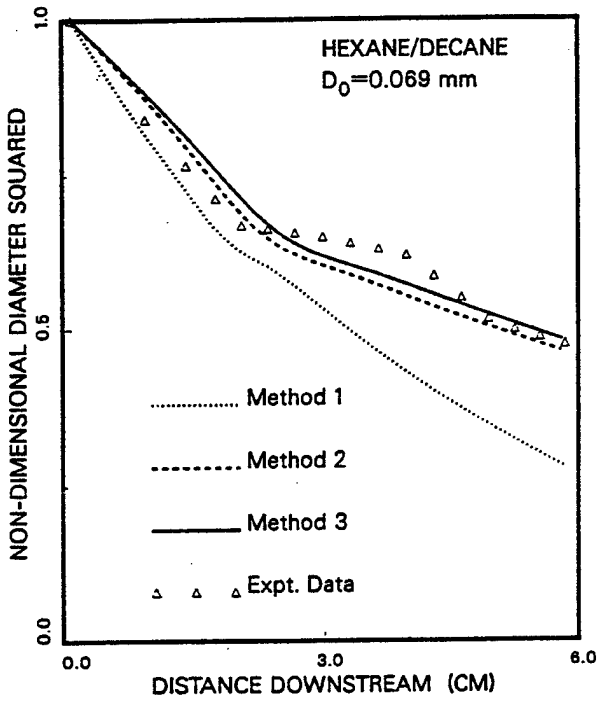

Fig. 9 Comparison of droplet size squared along the trajectory with different methods of calculating thermophysical properties.

1. While the overall agreement between the predicted and experimental velocity histories is reasonably good, the comparison underscores the deficiency of the standard (steady-state) drag equation to capture the large deceleration experienced by the droplet near the injection location. In addition, the steady drag equation is not able to reproduce the measured inflection point, where the droplet acceleration changes sign. This implies that the effect of droplet relative acceleration (see Peng and Aggarwal [23]) is important in this region. For small to moderate droplet accelerations, however, the standard drag correlation seems to work well, provided the properties of the gas film surrounding the droplet are calculated accurately.
2. The vaporization behavior of a hexane fuel droplet is not sensitive to the vaporization models. For less volatile fuels such as decane, however, the vaporization behavior shows some degree of sensitivity to the models. The thin-skin model is less accurate. The other two models show excellent agreement with experimental data. The difference between the infinite-diffusion and diffusion-limit models becomes more significant at higher environment temperatures.
3. The vaporization behavior of a multicomponent fuel droplet is better simulated by the infinite-diffusion model for a relatively low-temperature case. However, the difference between the infinite-diffusion and diffusion-limit models is not very

significant. The thin-skin model shows significant deviation from the experimental values.

4. The variable property effects are important for an accurate prediction of droplet velocity and size. Not only the effect of temperature but also that of fuel vapor should be considered for calculating the thermophysical properties of the gas film surrounding the droplet. For the low-environment-temperature case, the accurate prediction of the latent heat of fuel also becomes important.

To conclude, the present study illustrates that for relatively low ambient temperatures, both the infinite-diffusion and diffusion-limit methods can accurately predict the vaporization of pure as well as multicomponant fuel droplets. However, it is important to include the effects of variable thermophysical properties of the gas film outside the droplet as well as of the liquid-phase properties in a comprehensive manner. The present study also indicates the need for measuring the surface properties of the multicomponent fuel droplet. In particular, the measurement of the time history of surface temperature and species concentrations is recommended.

REFERENCES

1. G. A. E. Godsave, Studies of the Combustion of Drops in a Fuel Spray—The Burning of Single Drops of Fuel. *Fourth Symp. (Int.) on Combusion,* pp. 818–830, Williams & Wilkins, Baltimore, MD, 1953.
2. D. B. Spalding, The Combustion of Liquid Fuels, *Fourth Symp. (Int.) on Combustion,* pp. 847–864, Williams & Wilkins, Baltimore, MD, 1953.
3. A. Williams, Combustion of Droplets of Liquid Fuels: A Review, *Combustion and Flame,* vol. 21, pp. 1–31, 1973
4. G. M. Faeth, Evaporation and Combustion of Sprays, *Progr. Energy Combustion Sci.,* vol. 3, pp. 1–76, 1977.
5. C. K. Law, Recent Advances in Droplet Vaporization and Combustion, *Progr. Energy Combustion Sci.,* vol. 8, pp. 171–201, 1982.
6. S. K. Aggarwal, A. Tong, and W. A. Sirignano, A Comparison of Vaporization Models in Spray Calculation, *AIAA J.,* vol. 22, pp. 1448–1457, 1984.
7. R. B. Landis and A. F. Mills, Effects of Internal Resistance on the Vaporization of Binary Droplets, Fifth Int. Heat Transfer Conf., Tokyo, Japan, Paper B7-9, 1974.
8. C. K. Law, Multicomponent Droplet Combustion with Rapid Mixing, *Combustion and Flame,* vol. 26, pp. 219–233, 1976.
9. W. A. Sirignano, Theory of Multicomponent Fuel Droplet Vaporization, *Arch. Thermodynam. Combustion,* vol. 9, pp. 231–251, 1979.
10. A. Y. Tong and W. A. Sirignano, Multicomponent Droplet Vaporization in a High Temperature Gas, *Combustion and Flame,* vol. 66, pp. 221–235, 1986.
11. B. Abramzon and W. A. Sirignano, *Int. J. Heat Mass Transfer,* Vol. 32, pp. 1605–1618, 1989.
12. C. K. Law and H. K. Law, A d^2-Law for Multicomponent Droplet Vaporization and Combustion, *AIAA J.,* vol. 20, pp. 522–527, 1982.
13. W. D. Bachalo, Methods of Measuring the Size and Velocity of Spheres by Dual-Beam Light-Scatter Interferometer, *Appl. Opt.,* vol. 19, pp. 363–370, 1980.
14. T. A. Jackson and G. S. Samuelsen, Droplet Sizing Interferometry: A Comparison of the Visibility and Phase/Doppler Techniques, *Appl. Opt.,* vol. 26, pp. 2134–2137, 1987.
15. G. Chen, Vaporization Behavior of Pure and Multicomponent Fuel Droplets in a Hot Air Stream, M.S. thesis, The University of Illinois at Chicago, 1989.

16. W. E. Ranz and W. R. Marshall, Evaporation from Drops, *Chem. Eng. Progr.*, vol. 48, pp. 141–146, 173–180, 1952.
17. T. Yuge, Droplet Evaporation under Natural Convection, *Trans. ASME*, ser. C, vol. 82, pp. 214–221, 1960.
18. G. A. Agoston, H. Wise, and W. A. Rosser, Dynamic Factors Affecting the Combustion of Liquid Spheres, *Sixth Symp. (Int.) on Combustion*, Reinhold, NY, pp. 708–717, 1957.
19. F. Peng and S. K. Aggarwal, A Review of Droplet Dynamics and Vaporization Modeling for Engineering Calculations, *ASME J. Eng. Gas Turbines Power*, vol. 117, pp. 453–461, 1995.
20. R. D. Ingebo, Drag Coefficients for Droplets and Solid Spheres in Clouds Accelerating in Airstreams, NACA Technical Note 3762, 1956.
21. C. K. Law and F. A. Williams, Kinetics and Convection in the Combustion of Alkane Droplets, *Combustion and Flame*, vol. 19, pp. 393–405, 1972.
22. R. C. Reid, J. M. Prausnitz, and T. K. Sherwood, *The Properties of Gases and Liquids*, 3rd ed., McGraw-Hill, New York, NY, 1977.
23. F. Peng and S. K. Aggarwal, Droplet Motion under the Influence of Flow Nonuniformity and Relative Acceleration, *Atomization and Sprays*, vol. 6, pp. 42–65, 1996.

Pergamon

Int. J. Multiphase Flow Vol. 24, No. 2, pp. 295–317, 1998
© 1998 Elsevier Science Ltd. All rights reserved
Printed in Great Britain
0301-9322/98 $19.00 + 0.00

PII: S0301-9322(97)00045-1

REPRINTED WITH PERMISSION
FROM ELSEVIER SCIENCE LTD

ON THE DYNAMICS OF A TWO-PHASE, NONEVAPORATING SWIRLING JET

T. W. PARK[1], V. R. KATTA†[1] and S. K. AGGARWAL[2]‡

[1]Wright-Patterson Air Force Base, OH 45430, U.S.A.
[2]Department of Mechanical Engineering, University of Illinois at Chicago, Chicago, IL 60607, U.S.A.

(Received 1 August 1996; in revised form 23 May 1997)

Abstract—In this paper, we present direct numerical simulation of a droplet-laden swirling jet, and examine the effects of swirl and two-phase momentum coupling on the jet dynamics and structural characteristics. A time-dependent, multi-dimensional, two-phase algorithm is developed for the simulation. Results for the single-phase swirling jet at a Reynolds number of 800 indicate that the dynamics of large-scale structures are strongly affected by the degree of swirl imparted to the incoming flow. For low and intermediate swirl intensities, the vortex rings roll up closer to the nozzle exit, their frequency increases, and pairing interactions become progressively stronger as the swirl number (S) is increased. Thus, the addition of swirl to a transitional jet appears to modify its vortex dynamics in a way that enhances the beneficial effects of both swirl and vortex structures on the shear layer growth and entrainment. For a strongly swirling jet, the presence of a central stagnant zone and recirculation bubble causes a dramatic increases in the jet spreading angle, and this has a very dramatic effect on vortex dynamics. Based on a detailed visualization of the dynamic structure, we speculate that vortex structures in turn play an important role in determining the location and size of recirculation bubble. Results for the two-phase swirling jet indicate that for a mass loading ratio of unity, the jet dynamic and time-averaged behavior are strongly affected by both the interphase momentum coupling and swirl intensity. For a nonswirling two-phase jet, the momentum coupling modifies the dynamics of large vortex structures, including their roll-up location and frequency, which leads to enhanced mixing and entrainment of colder fluid into the shear layer. In contrast, for weakly and moderately swirling two-phase jets ($S < 0.5$), the momentum coupling reduces the shear layer growth, as well as mixing and entrainment rate. As the swirl number is increased, the effect becomes progressively stronger, manifested by the reduced rate of decay of gas velocity and temperature along the jet axis. In addition, the relation between roll-up frequency and swirl is modified in that the frequency increases with S for a single-phase jet, while it becomes independent of S for the corresponding two-phase jet. Consequently, the vortex pairing interactions, which are responsible for enhanced mixing and entrainment for single-phase swirling jets, are suppressed for two-phase jets. For strongly swirling two-phase jets ($S > 0.5$), the effect of momentum coupling becomes even more dramatic. Results for $S = 0.75$ indicate a drastic reduction in the size of the recirculation bubble for the two-phase jet. © 1998 Elsevier Science Ltd. All rights reserved

Key Words: two-phase flow, swirling jet, large-scale structures, transient behavior

1. INTRODUCTION

Swirling jet flows are utilized in a wide range of applications. By imparting swirl to the incoming flow, the structure of both nonreacting and reacting flows can be changed in a dramatic manner (Lilley 1977). The structure of swirling jet, for example, is strongly affected by the degree of swirl, characterized by a swirl number (S) which is defined as the ratio of axial flux of swirl or azimuthal momentum to that of axial momentum. For a weakly swirling nonreacting jet ($S < 0.4$), the jet growth, entrainment and decay are enhanced progressively as S is increased. For a corresponding strongly swirling jet ($S > 0.5$), the behavior changes more dramatically due to the formation of a recirculation bubble. In combustion applications, the recirculation bubble perhaps represents the most significant and useful effect of swirl, as it plays a central role in flame stabilization and enhanced combustor performance.

†Present address: Innovative Scientific Solutions, Inc., Dayton, OH 45430, U.S.A.
‡To whom all correspondence should be addressed. Phone: (312) 996-2235; fax: (312) 413-0447; e-mail: ska@uic.edu.

Extensive research efforts have been expended in understanding and characterizing the effects of swirl in nonreacting and reacting flows (Lilley 1977; Ribeiro and Whitelaw 1980; Leschziner and Rodi 1984). A commonly used configuration in both experimental and computational studies involves a confined or free swirling jet. Most of these studies, however, deal with the time-averaged behavior of swirling single-phase (Leschziner and Rodi 1984; Dellenbach *et al.* 1988; Durst and Wennerberg 1991) and two-phase jets (Sommerfeld and Qui 1993). The transient aspects, particularly those associated with large-scale vortex structures, have not been examined, although these structures have been shown to have a dominant effect on the near jet flow dynamics of non-swirling jets. Numerous experimental and numerical studies (Crow and Champagne 1971; Yule 1978) have shown that toroidal vortex rings form periodically in the near field of round jets and convect downstream. These axisymmetric structures roll around due to the inhomogeneous flow field, and may also undergo pairing interactions, depending on the flow conditions, such as initial disturbance level and other experimental conditions. In addition, their dynamics can be modified significantly by external forcing (Reynolds and Bouchard 1981). There are also other mechanisms that can modify their temporal and spatial growth characteristics. These include acoustic (pressure) fluctuations (Kailasanath *et al.* 1989), which can modify the dominant frequency associated with large scale structures, compressibility effects (Shau *et al.* 1993), and density variations caused by a variation in temperature or molecular weight (Subbarao and Cantwell 1992). Yet another mechanism that may alter the dynamics of large-scale structures pertains to the effect of swirl, which induces a body force in the radial momentum equation, and an adverse pressure gradient in the axial direction. For weakly swirling jets, the axial adverse pressure gradient caused by swirl can modify the processes of vortex roll-up and pairing interactions. For strongly swirling jets, the jet spreading and recirculation zone created by the swirl effect can have a more dramatic effect on the dynamics of vortex rings. To our knowledge, these aspects dealing with the dynamic interactions between large scale structures and swirl, and those between large structures and droplets in a swirling shear flow, have not been investigated in previous studies.

In this paper, we present a numerical simulation of a droplet-laden swirling jet. The major objective of this study is to investigate the dynamics of large-scale structures under different swirl conditions, and their interactions with the droplets injected in the shear layer of an axisymmetric swirling jet. A direct numerical solver without any turbulence or subgrid model is employed. The simulation first examines the dynamics of vortex rings and their interactions with the swirling flow field in a transitional heated jet. Then, a droplet-laden swirling jet is simulated in order to examine the effects of two-phase momentum coupling on the jet dynamics and structural behavior. The jet Reynolds number based on a jet velocity of 5.0 m/s, diameter 25.4 mm, and kinematic viscosity of heated jet fluid is 800. In our earlier study (Aggarwal *et al.* 1996), the dynamics of a nonswirling two-phase jet were investigated, and it was shown that the shear layer stability and vortex dynamics can be modified significantly by controlling the droplet injection characteristics. The present study extends that work to a swirling two-phase jet, and examines the effects of both swirl and two-phase momentum coupling on its dynamic and time-averaged structure.

2. PHYSICAL- NUMERICAL MODEL

A cartoon of the two-phase swirling jet investigated in the present study is shown in figure 1. It consists of a central swirling jet which is a two-phase mixture of air and liquid fuel (n-heptane) droplets and a low-speed annular air flow. The jet at axial velocity of 5.0 m/s and temperature of 1200 K is issuing into a co-flow with a velocity of 0.2 m/s without swirl and temperature of 294 K. Note that the use of high jet temperature is based on the consideration that we plan to investigate an evaporating spray in a subsequent study. In the present study, a nonevaporating spray is simulated in order to examine the effects of two-phase momentum coupling in the near region of a swirling jet. The jet–shear-layer instability is primarily of the Kelvin–Helmholtz type (Aggarwal *et al.* 1996).

The numerical model is based on solving the time-dependent, two-phase equations in an axisymmetric geometry. The unsteady, axisymmetric governing equations in cylindrical (z, r)

coordinates for a droplet-laden swirling jet are:

$$\frac{\partial(\rho\Phi)}{\partial t}+\frac{\partial(\rho u\Phi)}{\partial z}+\frac{\partial(\rho v\Phi)}{\partial r}=\frac{\partial}{\partial z}\left(\Gamma^{\Phi}\frac{\partial\Phi}{\partial r}\right)+\frac{\partial}{\partial r}\left(\Gamma^{\Phi}\frac{\partial\Phi}{\partial z}\right)-\frac{\rho v\Phi}{r}+\frac{\Gamma^{\Phi}}{r}\frac{\partial\Phi}{\partial r}+S_G^{\Phi}+S_L^{\Phi}. \quad [1]$$

The general form of [1] represents the continuity, three momentum, and energy conservation equations depending on the variable used for Φ. The transport coefficients Γ^{Φ} and the source terms S_G^{Φ} and S_L^{Φ} that appear in the governing equations are listed in table 1. Note that the equations in table 1 correspond to an evaporating two-phase flow. For the present study, which simulates a nonevaporating two-phase flow, the species equations are not considered, and droplet vaporization rate ($\dot{m}_k$) is taken identically equal to zero. The transport coefficients Γ^{Φ} and source terms contain the fluid properties such as viscosity (μ), thermal conductivity (λ), and specific heat (C_p). They are considered functions of temperature and species concentration.

The effect of dispersed phase on gas-phase properties is incorporated through the source/sink terms (S_L^{Φ}), representing the exchange of momentum between the gas and dispersed phases. In order to evaluate these terms, it is necessary to establish droplet trajectories. The Lagrangian approach is employed to solve the liquid-phase governing equations for the dynamics of each droplet group. The spray is characterized by a discrete number of droplet groups, distinguished by their injection location, initial size, and time of injection. A droplet group in a Lagrangian treatment represents a characteristic group containing a finite number of droplets. Since an axisymmetric configuration is analyzed, the liquid properties are implicitly averaged in the azimuthal direction and the number of droplets associated with each characteristic group represents droplets uniformly distributed in an annular ring. The equations governing the variation of position and velocity of each droplet are as follows:

$$\frac{dz_k}{dt}=u_k$$

$$\frac{dy_k}{dt}=v_k \quad [2]$$

$$\frac{du_k}{dt}=\frac{3C_D\rho_G}{4d_k\rho_k}|u-u_k|(u-u_k)+\left(\frac{\rho_G}{\rho_k}-1\right)g$$

$$\frac{dv_k}{dt}=\frac{3C_D\rho_G}{4d_k\rho_k}|v-v_k|(v-v_k)+\frac{w_k^2}{y_k} \quad [3]$$

$$\frac{dw_k}{dt}=\frac{3C_D\rho_G}{4d_k\rho_k}|w-w_k|(w-w_k)-\frac{v_kw_k}{y_k}$$

where

$$C_D=\frac{24}{\mathrm{Re}_k}\left(1+\frac{\mathrm{Re}_k^{2/3}}{6}\right) \quad [4]$$

$$\mathrm{Re}_k=\frac{\rho_G\{(u-u_k)^2+(v-v_k)^2+(w-w_k)^2\}^{1/2}d_k}{\mu_G}. \quad [5]$$

In the above equations, z_k and y_k are, respectively, the instantaneous axial and radial locations of a droplet group, while u_k, v_k, and w_k are, respectively, its axial, radial, and azimuthal velocity components. Further, d_k, ρ_k, and Re_k are, respectively, the droplet size, material density and Reynolds number, whereas ρ_G and μ_G are the gas density and viscosity, respectively. In the present simulation, we consider nonevaporating n-heptane droplets. In a subsequent study, we plan to extend the analysis to evaporating droplets. The density of n-heptane fuel is assumed to be 649.4 kg/m^3, which yields a value of more than 100 for the ratio of droplet density to gas density, with the latter value based on an average gas temperature of 750 K. This sufficiently large density ratio allows us to neglect the Basset force, pressure gradient and other contri-

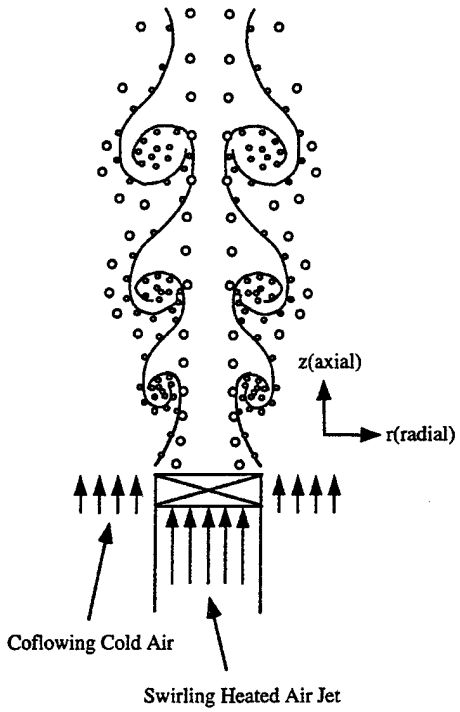

Figure 1. Schematic of a droplet-laden swirling jet..

butions from flow non-uniformities, and consider only the quasi-steady drag and gravity forces in [3].

The numerical solution of the unsteady two-phase equations employs an implicit algorithm for solving the gas-phase equations, and an explicit Runge–Kutta procedure for the liquid-phase equations. The finite-difference forms of the momentum equations are obtained using an implicit QUICKEST scheme (Leonard 1979), while those of energy equations are obtained using a hybrid scheme of upwind and central differencing (Spalding 1972). A 'finite control volume' approach with a nonuniform staggered-grid system is utilized. An orthogonal grid having expanding cell sizes in both the axial and the radial direction is employed. An iterative ADI (Alternative Direction Implicit) technique is used for solving the resulting sets of algebraic equations. At every time step, the pressure field is calculated by solving all the pressure Poisson equations simultaneously and utilizing the LU (lower and upper diagonal) matrix decomposition technique.

Axisymmetric calculations are made on a physical domain of $400 \times 150\,\text{mm}^2$ utilizing a 151×61 nonuniform grid system. The computational domain is bounded by the axis of symmetry and an outflow boundary in the radial direction and by the inflow and another outflow boundary in the axial direction. The outer boundaries in the z and r directions are located sufficiently far from the nozzle exit (16 nozzle diameters) and the axis of symmetry (six nozzle diameters), respectively, to minimize the propagation of boundary-induced disturbances into the region of interest (seven and two nozzle diameters in the axial and radial directions, respectively). A flat profile for axial velocity and a linear profile for swirl velocity (swirl velocity being a linearly increasing function of radius) are used at the inflow boundary. It is important to mention that, for a given swirl number, one can employ different swirl velocity profiles at the inflow boundary, and this may affect the jet development. However, a linear velocity profile provides a good approximation to the real situation, and has often been used in computational studies (Ribeiro and Whitelaw 1980; Leschziner and Rodi 1984). A zero-gradient boundary condition with an extrapolation procedure with weighted zero- and first-order terms is used to estimate the flow variables at the outflow boundary. The weighting functions are selected using

Table 1. Transport coefficients and source terms appearing in gas-phase governing equations

Equations	Φ	Γ^{Φ}	S_G^{Φ}	S_T^{Φ}
Continuity	1	0	0	$\sum_k n_k \dot{m}_k$
Axial momentum	u	μ	$-\frac{\partial p}{\partial z}+(\rho_0-\rho)g+\frac{\partial}{\partial z}\left(\mu\frac{\partial u}{\partial z}\right)+\frac{\partial}{\partial r}\left(\mu\frac{\partial v}{\partial z}\right)+\frac{\mu}{r}\frac{\partial v}{\partial z}-\frac{2}{3}\left[\frac{\partial}{\partial z}\left(\mu\frac{\partial u}{\partial z}\right)+\frac{\partial}{\partial z}\left(\mu\frac{\partial v}{\partial r}\right)+\frac{\partial}{\partial z}\left(\mu\frac{v}{r}\right)\right]$	$\sum_k\left(n_k\dot{m}_k u_k - n_k M_k\frac{\mathrm{d}u_k}{\mathrm{d}t}\right)$
Radial momentum	v	μ	$-\frac{\partial p}{\partial r}+\frac{\partial}{\partial z}\left(\mu\frac{\partial u}{\partial r}\right)+\frac{\partial}{\partial r}\left(\mu\frac{\partial v}{\partial r}\right)+\frac{\mu}{r}\frac{\partial v}{\partial r}-2\mu\frac{v}{r^2}+\rho\frac{w^2}{r}-\frac{2}{3}\left[\frac{\partial}{\partial r}\left(\mu\frac{\partial u}{\partial z}\right)+\frac{\partial}{\partial r}\left(\mu\frac{\partial v}{\partial r}\right)+\frac{\partial}{\partial r}\left(\mu\frac{v}{r}\right)\right]$	$\sum_k\left(n_k\dot{m}_k v_k - n_k M_k\frac{\mathrm{d}v_k}{\mathrm{d}t}\right)$
Swirl momentum	w	μ	$-\left(\frac{\mu}{r^2}+\rho\frac{v}{r}+\frac{1}{r}\frac{\partial\mu}{\partial r}\right)w$	$\sum_k\left(n_k\dot{m}_k w_k - n_k M_k\frac{\mathrm{d}w_k}{\mathrm{d}t}\right)$
Mass fraction of fuel	Y_f	ρD_{f-N_2}	0	$\sum_k n_k\dot{m}_k$
Mass fraction of other species	Y_i (i = 1-N_s, $i\neq f$)	ρD_{i-N_2}	0	0
Energy	H	$\frac{\lambda}{C_p}$	0	$\sum_k n_k\dot{m}_k(h_{fs}-l_{k,\mathrm{eff}})$

the trial-and-error approach, and the main criterion used is that the vortices crossing the outflow boundary leave smoothly without being distorted. For the given flow conditions, a steady-state solution was first obtained by neglecting the unsteady terms in the governing equations. Then, the unsteady two-phase swirling jet simulations were performed using the previously obtained steady-state solution as the initial flow condition.

The liquid-phase equations governing the position of each droplet group are advanced in time by a second-order accurate Runge-Kutta method. Since the gas-phase solution employs an implicit procedure, the temporal step size used for integrating the liquid-phase equations is usually smaller than that for gas-phase equations. An automatic procedure is implemented in order to select an optimum liquid-phase time step. The procedure to advance the two-phase solution over one gas-phase time step is as follows. Using the known gas-phase properties, the liquid-phase equations are solved over the specified number of liquid-phase subcycles. A third-order accurate Lagrangian polynomial method is used for interpolating the gas-phase properties from the nonuniform fixed grid to the droplet characteristic location. It should be noted that the interpolation scheme for the gas-phase velocities (u, v and w) is based on their respective grid cells because of the use of a staggered grid in gas-phase calculation. The droplet properties are updated after every liquid-phase subcycle. Also, during each subcycle, the liquid-phase source terms appearing in the gas-phase equations are calculated at the characteristic location, and then distributed to the surrounding gas-phase grid points. These source terms are added at each gas-phase grid points during one gas-phase time step and then used in the implicit solution of the gas-phase equations. It is also important to note that the integration of droplet equations [3] in cylindrical coordinates require special care near the axis of symmetry, where a specular boundary condition is imposed. This implies that, as a droplet approaches the left boundary, it is replaced by another droplet entering the domain at the reflected angle.

Numerical validation studies for both single-phase and two-phase jets, as well as for low-speed diffusion flames, employing different grids and temporal step sizes have been reported previously (Aggarwal *et al.* 1996; Katta *et al.* 1994). Some additional results showing grid independence are depicted in figure 2. The time-history of gas velocity computed for two different grid sizes, 151×61 and 226×91 for nonswirling and swirling jets is plotted in figure 2(a) and 2(b), while the profiles of time-averaged velocity along the jet axis for three different swirl numbers are plotted in figure 2(c). Since a nonuniform grid is employed with grid lines clustered near the shear layer to resolve the steep gradients of the dependent variables, additional grid points in the 226×91 grid are placed near the shear layer, thus effectively reducing the grid density for this grid by nearly 100% compared to the 151×61 grid. The time-history plots of gas velocity clearly depict the highly periodic nature of jet vortex rings associated with the Kelvin–Helmholtz instability. For the nonswirling jet, the Strouhal number associated with this instability obtained from the fast Fourier transform of axial velocity is 0.33, which agrees with the reported experimental range of 0.25–0.5 (Hussain and Hussain 1983). The aspects pertaining to the dynamic and time-averaged jet behavior for different swirl numbers are discussed in the next section. An important observation here is that the 151×61 grid is able to capture the periodic behavior, including the frequency and phase of vortex structures, as well as the time-averaged structure of both nonswirling and swirling jets.

3. RESULTS

The swirl number is defined as

$$S = \frac{1}{r_0} \frac{\int_0^{r_0} uwr^2 \, dr}{\int_0^{r_0} u^2 r \, dr} \qquad [6]$$

where r_o is the radial extent of computational domain, r is the radial coordinate, and u and w are, respectively, the gas axial and azimuthal velocity components. This definition treats S as a function of axial distance. Thus, at the inflow boundary r_0 becomes equal to the jet radius.

First, we examine the dynamics of single-phase swirling jets at different swirl numbers (S). The objective is to understand and characterize the dynamic interactions between swirl and

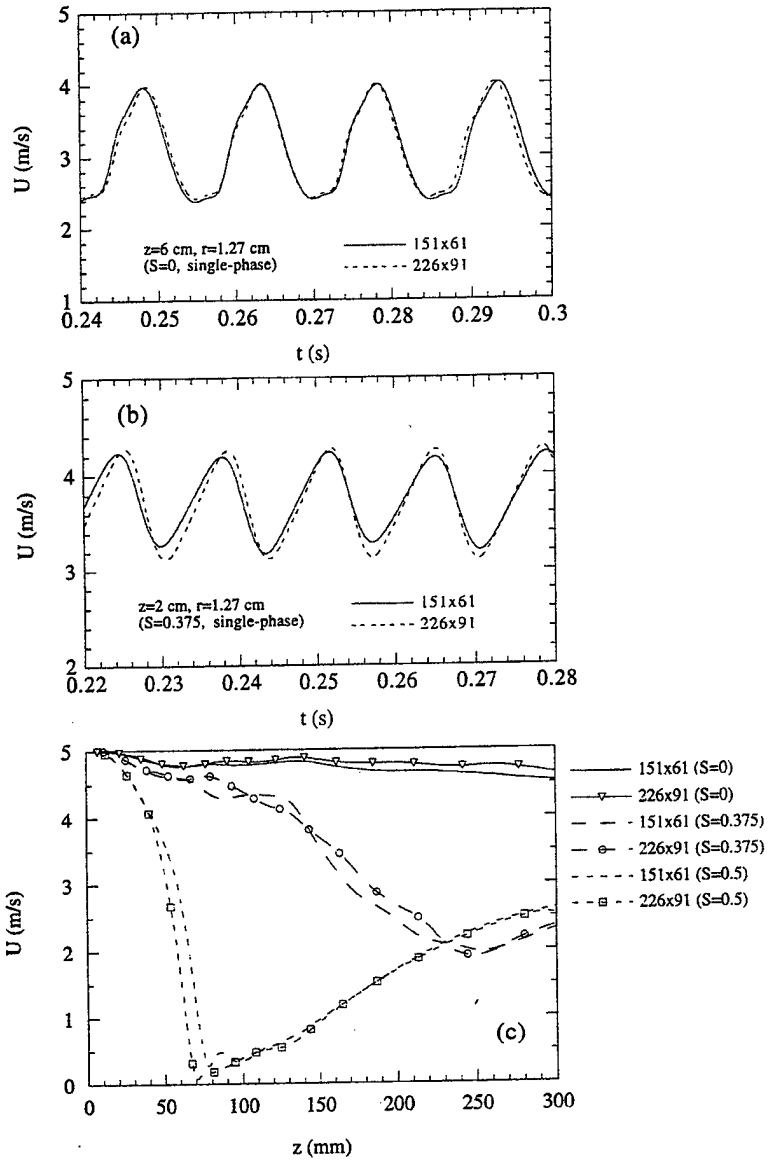

Figure 2. Time-history plots of centerline gas velocity (a and b) and axial profiles of time-averaged centerline gas velocity (c) for nonswirling and swirling (swirl number $S = 0.375$) jets obtained by using two different grid sizes..

large-scale structures, and the effects of these interactions on the jet behavior. Since the jet dynamics and structural characteristics are strongly influenced by the presence of both swirl and large scale structures, it is of interest to examine how the vortex dynamics are affected by swirl, and how the distribution of swirl and its decay rate are modified by vortex structures. The latter effect is important since the swirl decay rate determines the pressure distribution, and thereby the jet gross behavior, especially the onset, location and extent of the recirculation bubble at high swirl numbers. The above interactions are examined by employing flow visualization (snapshots of the flow field), as well as the instantaneous and time-averaged properties.

Figure 3 shows some representative snapshots of the flow field for different swirl numbers. In each snapshot, we plot instantaneous iso-temperature contours on the right, and streaklines on the left. Simulations for the nonswirling jet indicate the presence of well-organized vortex rings. Toroidal vortex rings roll up periodically near $z = 4$ cm ($z/D = 1.6$) from the nozzle exit,

convect downstream, and undergo a weak pairing interaction near $z = 16$ cm. The snapshot for $S = 0$ clearly indicates a vortex roll-up occurring near $z = 4$ cm, and a pairing interaction near $z = 16$ cm. These results were confirmed by the fast Fourier transform of axial velocity recorded at several axial locations, shown in figure 4(a), which yields dominant frequencies of 64 and 32 Hz corresponding to the roll-up and merging frequencies, respectively. Results for $S = 0.375$, figure 3, indicate a more dramatic effect of swirl on the dynamics of large scale structures. First of all, the vortex roll-up location is shifted upstream and the frequency is increased from 64 to 75 Hz compared to the nonswirling case. Second, the vortex pairing becomes a prominent feature of shear layer dynamics in the near jet region, which, we speculate, is caused by the adverse pressure gradient effect of swirl. Since, the pressure increases along the centerline for the swirling case, the centerline velocity for the swirling jet decays faster compared to that for the nonswirling jet. This is indicated clearly in figure 5(a), which shows the variation of time-averaged gas velocity along the centerline for different swirl numbers. As a result, the leading toroidal vortex is slowed down, causing a well-organized pairing interaction to occur near $z = 7$ cm. The faster decay of centerline velocity also causes the occurrence of second vortex pairing near $z = 12$ cm. The processes of shear layer roll-up and pairing interactions for $S = 0.375$ are clearly depicted in figure 3. The corresponding frequencies, obtained from the fast Fourier transform of axial velocity and displayed in figure 4(b), are 74, 37, and 19 Hz, respectively. The occurrence of multiple vortex pairings in a swirling jet has an important implication with regard to the effect of swirl–vortex interaction on the jet development and entrainment. Since the presence of multiple vortex pairings is known to enhance shear layer growth and entrainment, the numerical results indicate that the addition of swirl modifies vortex dynamics in a way which further enhances the beneficial effects of swirl.

As the swirl intensity is increased, the above effects become progressively stronger. The increased swirl strength promotes greater jet spreading, mixedness, and reduction of the potential core. In addition, the vortex roll-up occurs earlier (more upstream), and the convecting toroidal vortex slows down considerably, as it moves radially outward (due to jet spreading) and the centerline velocity decays more rapidly. Consequently, with increased swirl, vortex pairings occur earlier and with greater intensity, further promoting shear layer growth and entrainment. For $S = 0.5$, as noted in figure 3, the locations of vortex roll-up and first and second pairing interactions are at approximately $z = 2$, 5, and 8 cm, respectively, compared with the corresponding values of 3, 7, and 10 cm for $S = 0.375$. In addition, the corresponding frequencies are higher and a third pairing interaction is observed for $S = 0.5$; see figure 4(c). The above observations are also confirmed by the axial profiles of time-averaged gas velocity and temperature shown in figure 5. As S is increased, the centerline temperature decreases more rapidly, indicating a pronounced increase in the shear layer growth and entrainment of colder fluid into the hot jet. This is a significant result in that the overall effect of swirl–vortex interaction at low to intermediate swirl intensities ($S < 0.5$) is to augment the effect of each. Note that both the addition of swirl and the presence of large vortex structures are known to enhance shear layer growth and entrainment. Our results indicate that an increase in swirl intensity promotes multiple vortex pairings, which further enhances shear layer growth and entrainment, i.e. large structures augment the effect of swirl and *vice versa*.

A more dramatic effect occurs as the swirl number exceeds 0.5, which represents the onset of recirculation bubble in the jet flow. For $S > 0.5$, a stagnant region develops near the centerline due to the reverse flow caused by adverse pressure gradient, and a toroidal recirculation bubble appears. Both the central stagnation region and recirculation bubble can clearly be seen from the time-averaged velocity vector plots in figure 6. Also notable in this figure is the presence of a secondary recirculation zone for $S = 0.75$, located just upstream of the primary recirculation bubble. The stagnation region and reverse flow are also quite evident in the time-averaged axial velocity profile for $S = 0.75$ given in figure 5. In addition, as noted in figure 6, the jet shear layer for $S = 0.75$ is shifted significantly outward in the radial direction, and exhibits a highly dynamic structure. It is interesting to note that, while at subcritical swirl numbers ($S < 0.5$) toroidal vortices are an intrinsic part of jet dynamics, their existence becomes less obvious at supercritical swirl numbers ($S > 0.5$). Thus, an important issue to be addressed here pertains to the existence and nature of large scale structures for strongly swirling jets, and whether the tran-

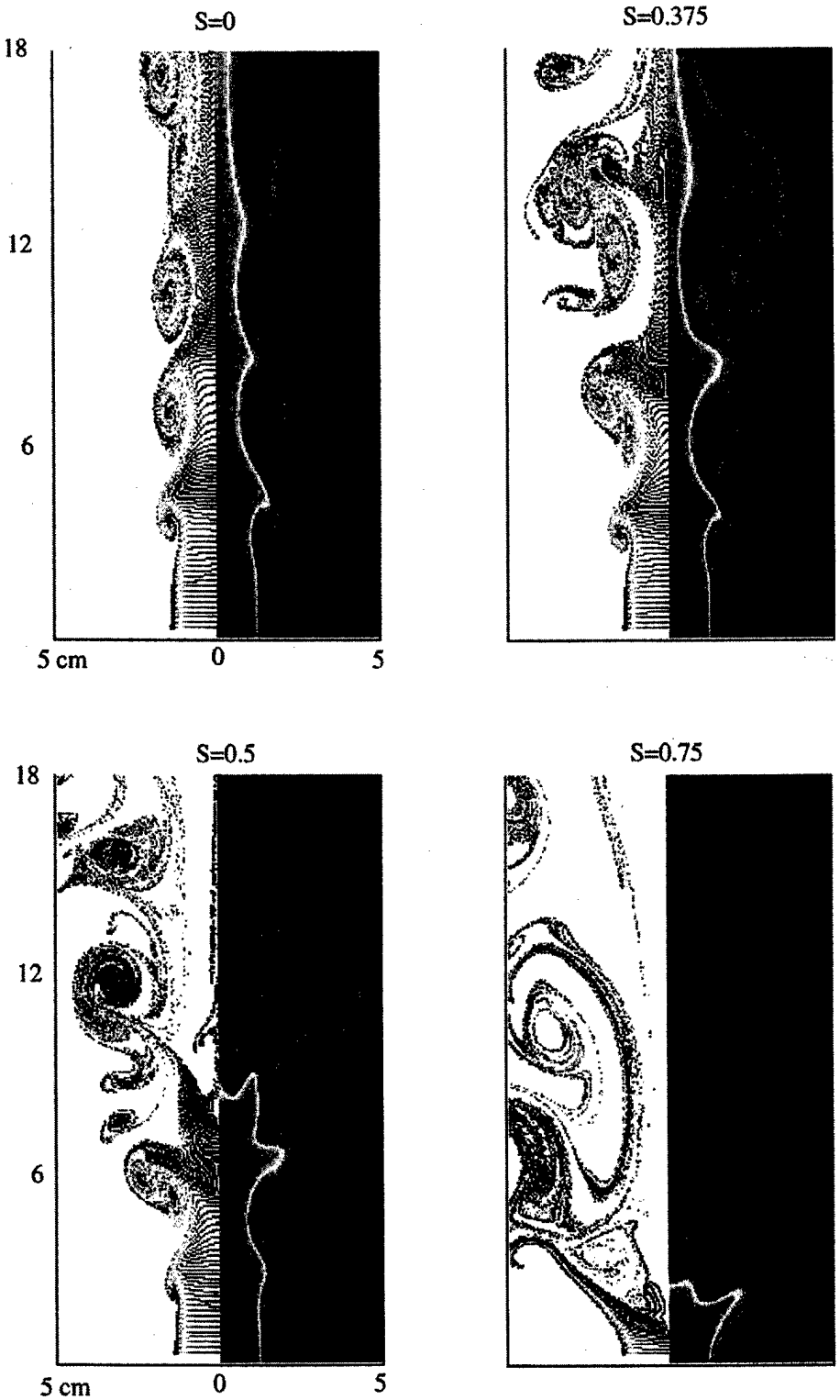

Figure 3. Snapshots of the flow field for a swirling jet without droplets for four different swirl numbers. In each snapshot, iso-temperature contours are plotted on the right-hand side of the symmetric jet, and streaklines on the left. For iso-temperature contours, the red and purple colors represent the highest (1200 K) and the lowest (294 K) temperatures, respectively. The times of the snapshots are 0.21, 0.24, 0.25, 0.2 s for S = 0, 0.375, 0.5, and 0.75, respectively..

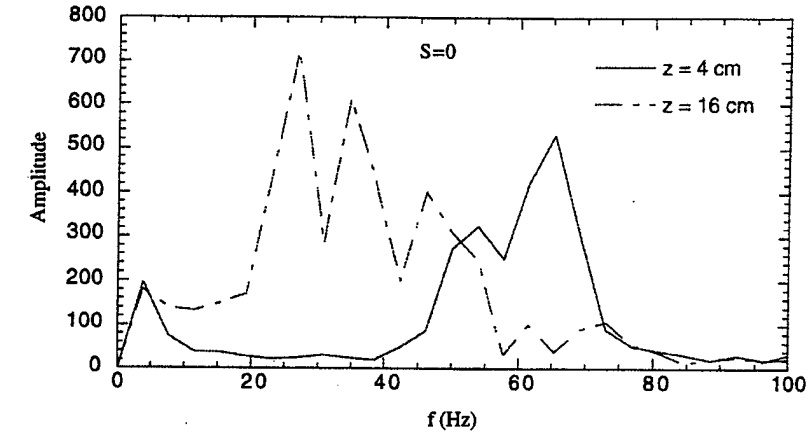

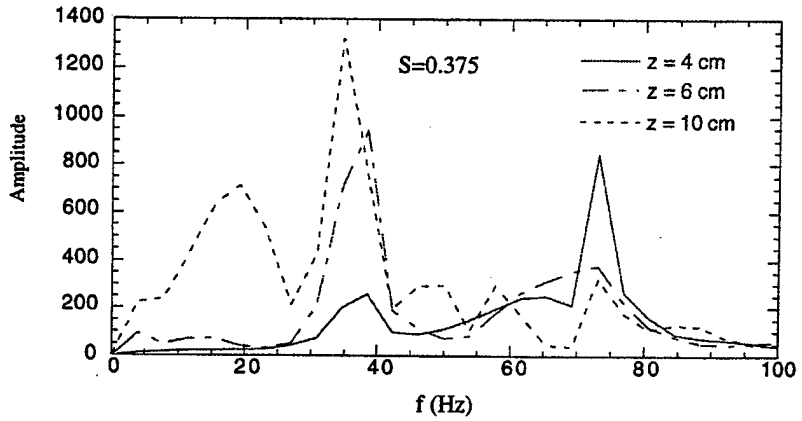

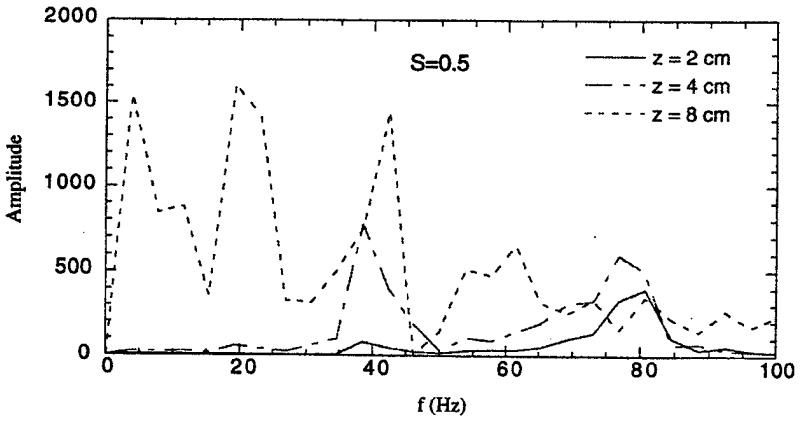

Figure 4. Frequency spectra of axial gas velocity for a swirling jet without droplets for different swirl numbers..

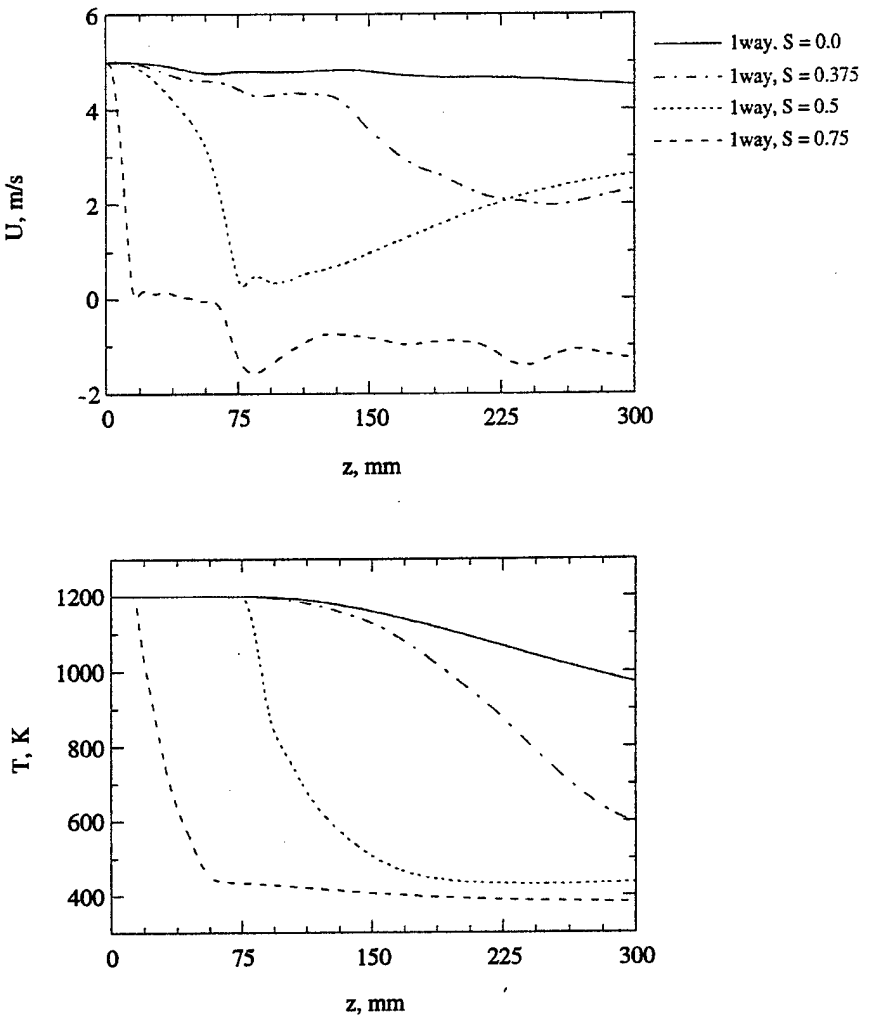

Figure 5. Axial profiles of time-averaged gas velocity and temperature for a swirling jet without droplets for different swirl numbers..

sient jet behavior can be attributed to these structures. One may argue that these structures get destroyed due to the rapid decay of shear and increased mixing in a strongly swirling jet. Based on an extensive visualization of the swirling jet dynamics for $S = 0.75$, we speculate that large vortex structures are still present, though their behavior is markedly different from those for the weakly and moderately swirling jets ($S < 0.5$). The vortex structures for $S = 0.75$ are shifted outward in the radial direction and do not look like the Kelvin–Helmholtz vortex rings that are typically observed in a transitional jet. However, a series of snapshots (not shown) indicated that they do exhibit the processes of roll-up and pairing interactions, though in a significantly less organized manner. The snapshots further indicate that a pair of counter-rotating toroidal vortices (an outer Kelvin–Helmholtz type vortex rotating clockwise and an inner vortex rotating counter-clockwise; the latter may be due to the presence of central stagnation region) is generated periodically. As these vortices convect downstream, they grow in size, and the outer structure rolls around the inner structure since the latter is in a nearly stagnant region. In addition, both outer and inner vortices undergo pairing interactions with other (trailing) outer and inner vortices, respectively. We also speculate, based on the flow visualization and time-averaged velocity vector plots shown in figure 6, that the size and location of recirculation bubble is deter-

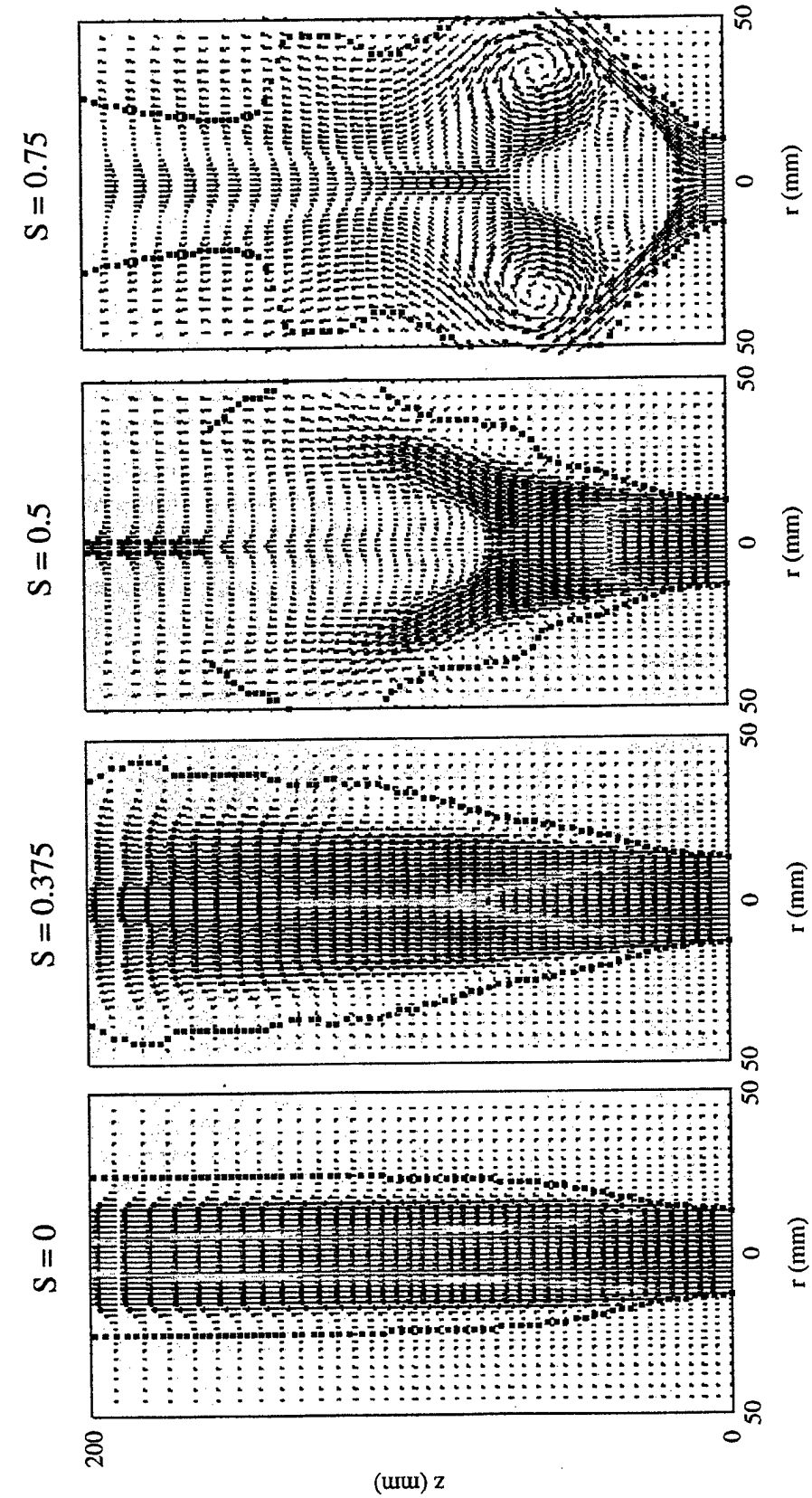

Figure 6. Time-averaged velocity vector plots for a swirling jet without droplets for different swirl numbers..

mined by these dynamic swirl–vortex interactions, and not by the adverse pressure gradient (swirl effect) alone. In other words, due to the effect of swirl, the outer vortex is shifted outward in the radial direction, and its subsequent dynamics as well as those of the inner vortex are determined by the swirling flow field. These vortices in turn play a major part in determining the location of recirculation zone; it appears that the recirculation zone is established at a location where the outer vortex structure is pulled in radially.

3.1. *Two-phase momentum coupling effects*

We now examine the effects of two-phase momentum coupling on the dynamics and time-averaged characteristics of a droplet-laden swirling jet. Droplets of a given size are injected from the nozzle rim, and their motion is followed by integrating [2] and [3] using a second-order Runge–Kutta scheme. At low mass loadings, the effect of droplets on the jet dynamics is negligible, although their motion and concentration field are strongly influenced by the rotating toroidal vortices. As the dispersed-phase mass loading is increased, the effects due to the exchange of mass, momentum, and energy between the phases become increasingly important. In the present study, a nonevaporating two-phase jet is considered in order to isolate momentum coupling effects from those due to mass and energy coupling. These effects depend on several parameters, including liquid-to-air mass loading ratio and injection characteristics such as initial droplet size, location, and velocity. For the present study, we consider mass loading of unity† and initial droplet diameter of 100 μm, with the droplets injected in the shear layer with axial velocity the same as the jet velocity, and zero radial and azimuthal velocities. Note that the choice of droplet diameter is based on the consideration that it yields a Stokes number of near unity for the nonswirling jet. The Stokes number here is defined as the ratio of droplet response time to a characteristic flow time, the latter based on the dominant vortex frequency. Several experimental (Longmire and Eaton 1992) and numerical studies (Chung and Troutt 1988; Uthuppan *et al.* 1994; Park *et al.* 1996) have shown that the interaction of large structures with droplets is maximized near a Stokes number of unity.

Flow visualization is used to assess qualitatively the effects of dispersed phase on the dynamics of large-scale structures under different swirl conditions. In the following discussion, case A refers to single-phase jets, while case B refers to two-phase jets. Figure 7 depicts representative snapshots of the flow field for different swirl numbers. For these results, a droplet group is introduced every tenth computational time step, and the computations are performed for a total of 10,000 time steps. Thus, there are 1000 droplet groups for the two-phase results shown in figure 7. Comparison of the snapshots, for nonswirling ($S = 0$) single-phase and two-phase jets, given in figures 3 and 7, respectively, indicates that the vortex roll-up location, dynamics, and pairing interactions are strongly modified due to momentum coupling. In addition, it is observed that for the two-phase jet (case B), the vortex structures are stronger and entrain more low-speed (colder) fluid compared to those for the single-phase jet (case A). The comparison of snapshots for swirling jets also indicates a significant modification of vortex dynamics due to the momentum coupling effect. For low to moderate swirl numbers ($S < 0.5$), the vortex pairing is a prominent feature of jet dynamics for case A, while it is not observed for case B. For the strong swirl case ($S = 0.75$), an important effect of two-phase momentum coupling is a drastic reduction in the size of recirculation bubble, even though the central stagnation region still exists. This can be seen more clearly in terms of time-averaged velocity vector plots in figure 11. The effect of momentum coupling on the time-averaged structure is discussed in the following section.

The above observations are confirmed by obtaining the spectral and time-averaged properties for the two cases. Figure 8 shows the time-history of gas-phase axial velocity for single-phase and two-phase jets at different swirl numbers. Results of the fast Fourier transform of these axial-velocity histories are depicted in figures 4 and 9. As discussed earlier, for single-phase jets with low to moderate swirl numbers ($S < 0.5$), processes of shear layer roll-up and vortex formation are well organized. In addition, the roll-up frequency increases and pairing interactions

†In an earlier study (Aggarwal *et al.* 1996) it was shown that at unity mass loading, two-phase momentum coupling has a significance influence on the jet dynamics and structural characteristics.

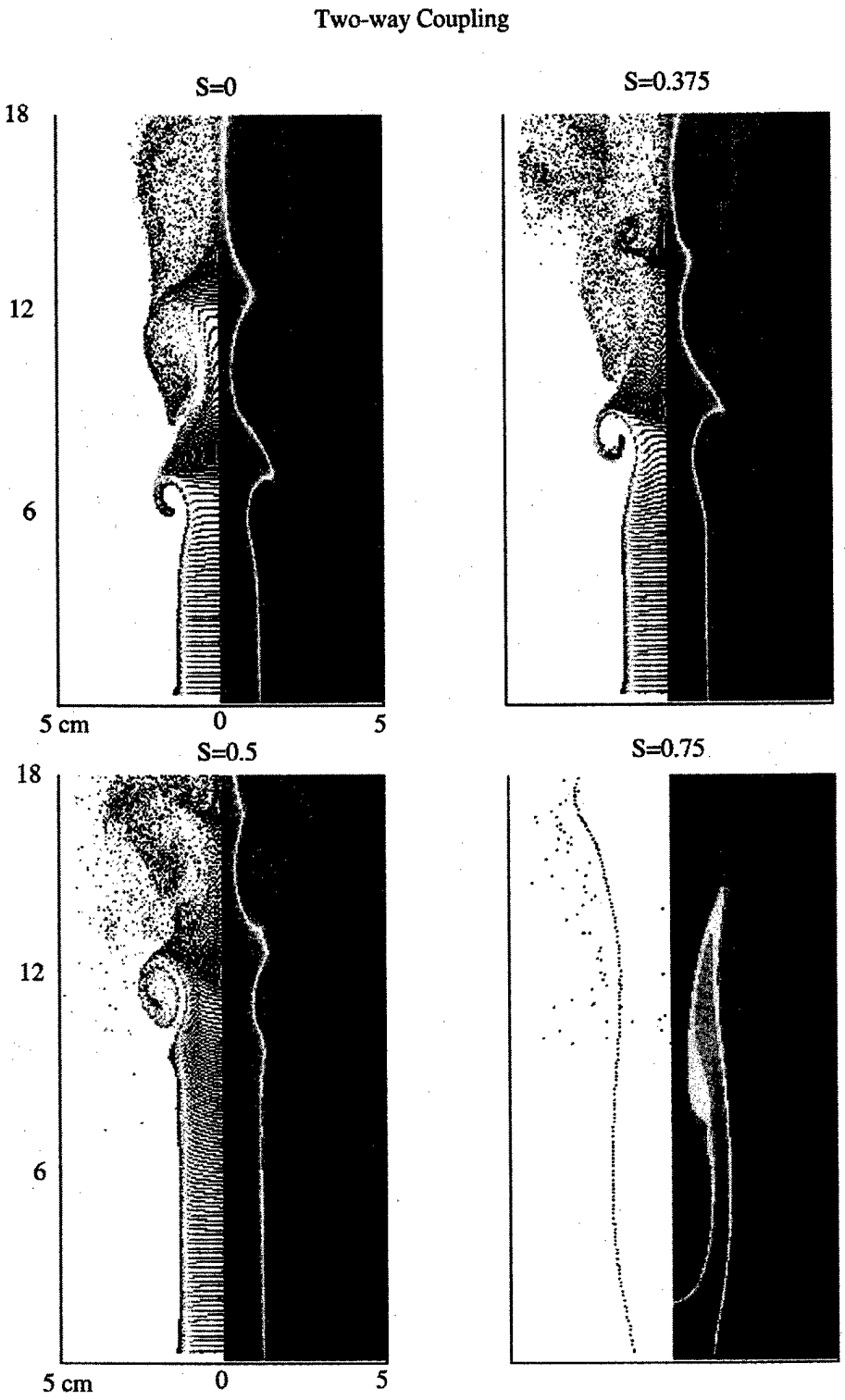

Figure 7. Snapshots of the flow field for a swirling jet with droplets. In each snapshot, iso-temperature contours are plotted on the right-hand side of the symmetric jet, and streaklines on the left. For iso-temperature contours, the red and purple colors represent the highest (1200 K) and the lowest (294 K) temperatures, respectively..

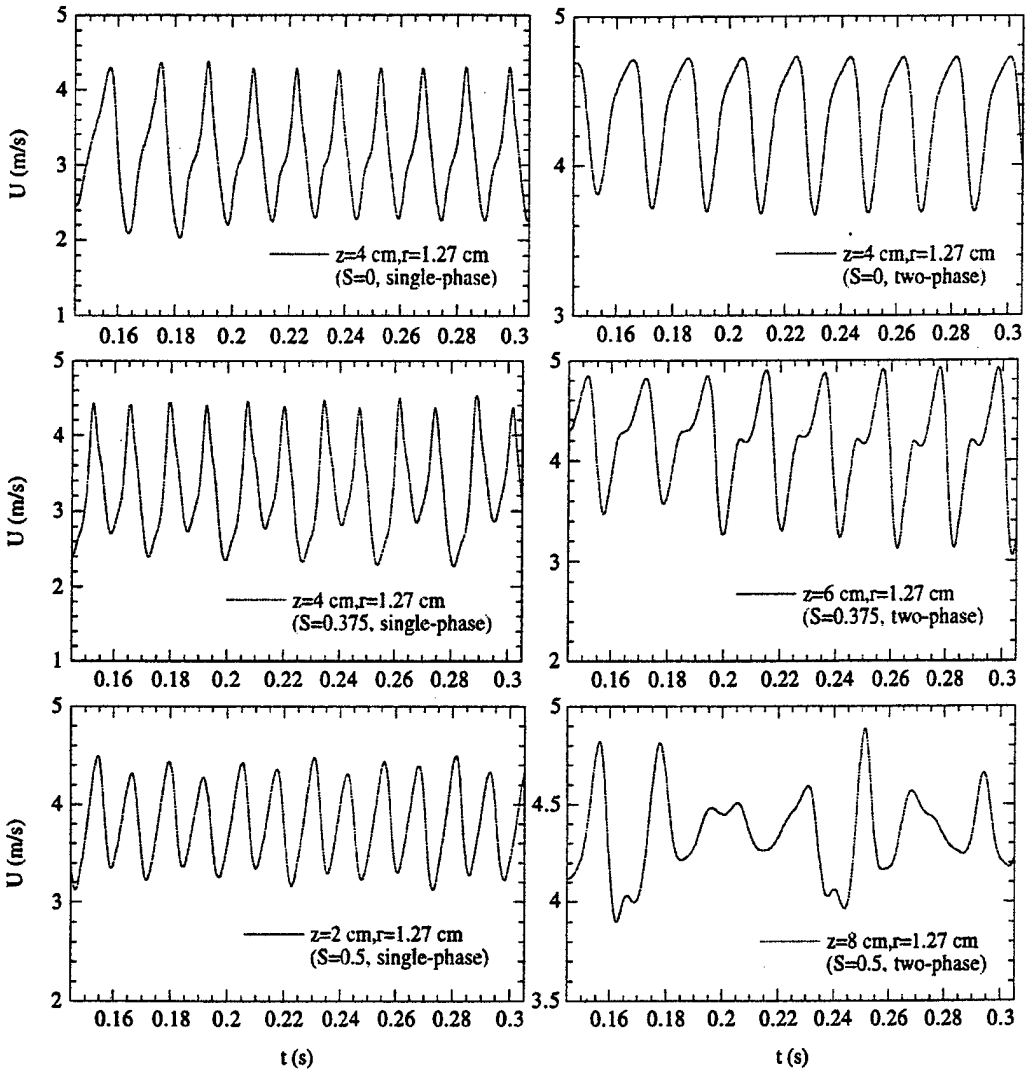

Figure 8. Time history of gas-phase axial velocity for single-phase and two-phase jets with different swirl numbers..

become more prominent as the swirl number is increased. These results are quite evident in figure 4; the roll-up frequencies are 64, 72, and 80 Hz for $S = 0$, 0.375, and 0.5, respectively. Also noteworthy in figure 4 are the first and second pairing interactions at frequencies of 36 and 18 Hz respectively, for $S = 0.375$, and at 40 and 20 Hz respectively, for $S = 0.5$. In contrast, for the corresponding two-phase jets (case B), the shear layer dynamics are relatively less organized, and the roll-up frequency decreases and becomes independent of the swirl number. As indicated in figures 8 and 9, the roll-up frequency is 50 Hz for $S = 0$, 0.375, and 0.5. Another important observation from figure 9 is the absence of pairing interactions for case B, which is also evident in figure 7. This is attributable to the fact that the interphase momentum coupling modifies the distribution of swirl intensity in the axial direction, resulting in a decrease of adverse pressure gradient and jet spreading angle. As noted earlier, the adverse pressure gradient caused by swirl is responsible for the enhanced vortex pairings in single-phase jets. For corresponding two-phase jets, there is a transfer of azimuthal momentum from the gas phase to the droplets, which reduces swirl intensity near the nozzle. Further downstream, however, the momentum is trans-

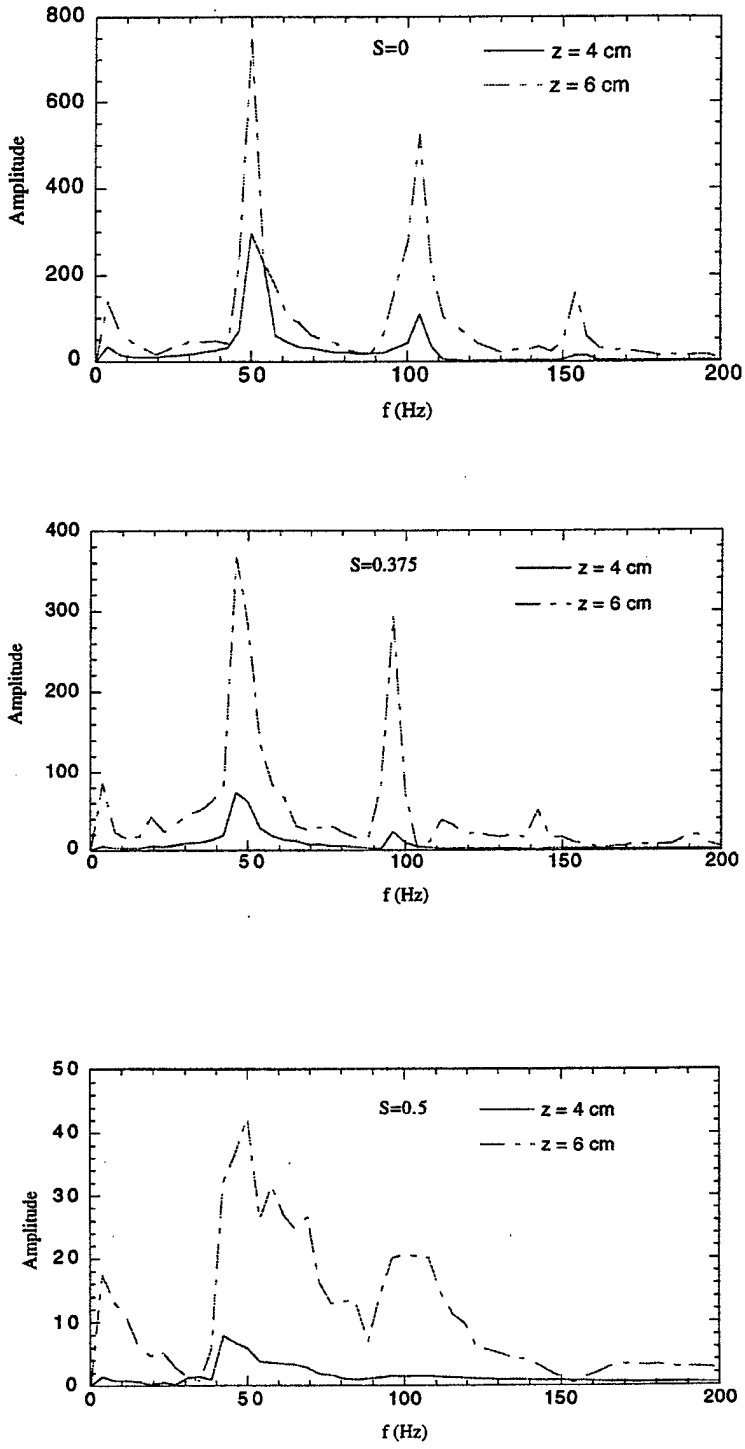

Figure 9. Frequency spectra of axial gas velocity for a swirling jet with droplets for different swirl numbers..

ferred from droplets to gas phase, increasing the gas-phase swirl intensity. The resulting redistribution of swirl intensity reduces the adverse pressure gradient for the two-phase jet. This was confirmed by plotting the time-averaged azimuthal velocity contours (not shown) and axial velocity vectors, shown in figure 11. As a consequence, the vortex pairing, which is prominent feature of moderately swirling ($S < 0.5$) single-phase jets, is not observed for corresponding two-phase jets.

3.2. *Momentum coupling effect on the time-averaged jet structure*

The effect of two-phase momentum coupling on the time-averaged jet behavior is depicted in figures 10 and 11. In figure 10, the time-averaged axial gas velocity and temperature are plotted along the jet centerline, while figure 11 shows the time-averaged velocity vectors for different swirl numbers. The important observation from these results is that, at a mass loading of unity, the dispersed phase significantly modifies the time-averaged structure of the jet shear layer, and

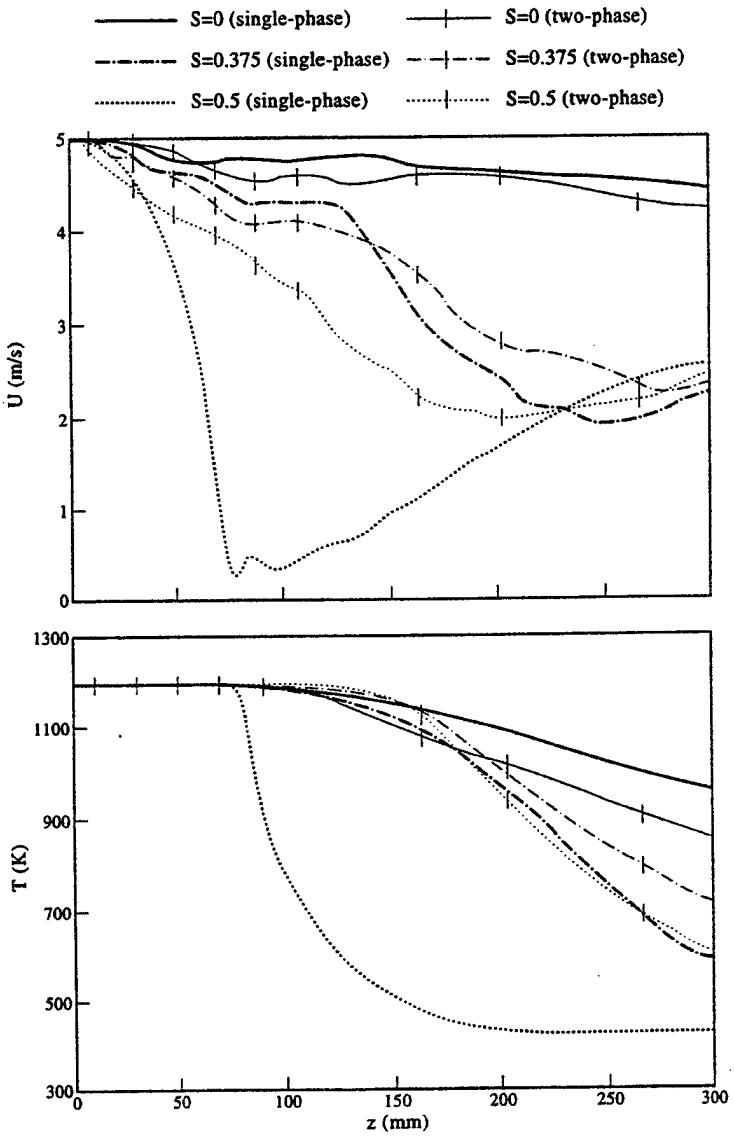

Figure 10. Axial profiles of time-averaged gas velocity and temperature for a swirling jet without and with two-way momentum coupling for different swirl numbers..

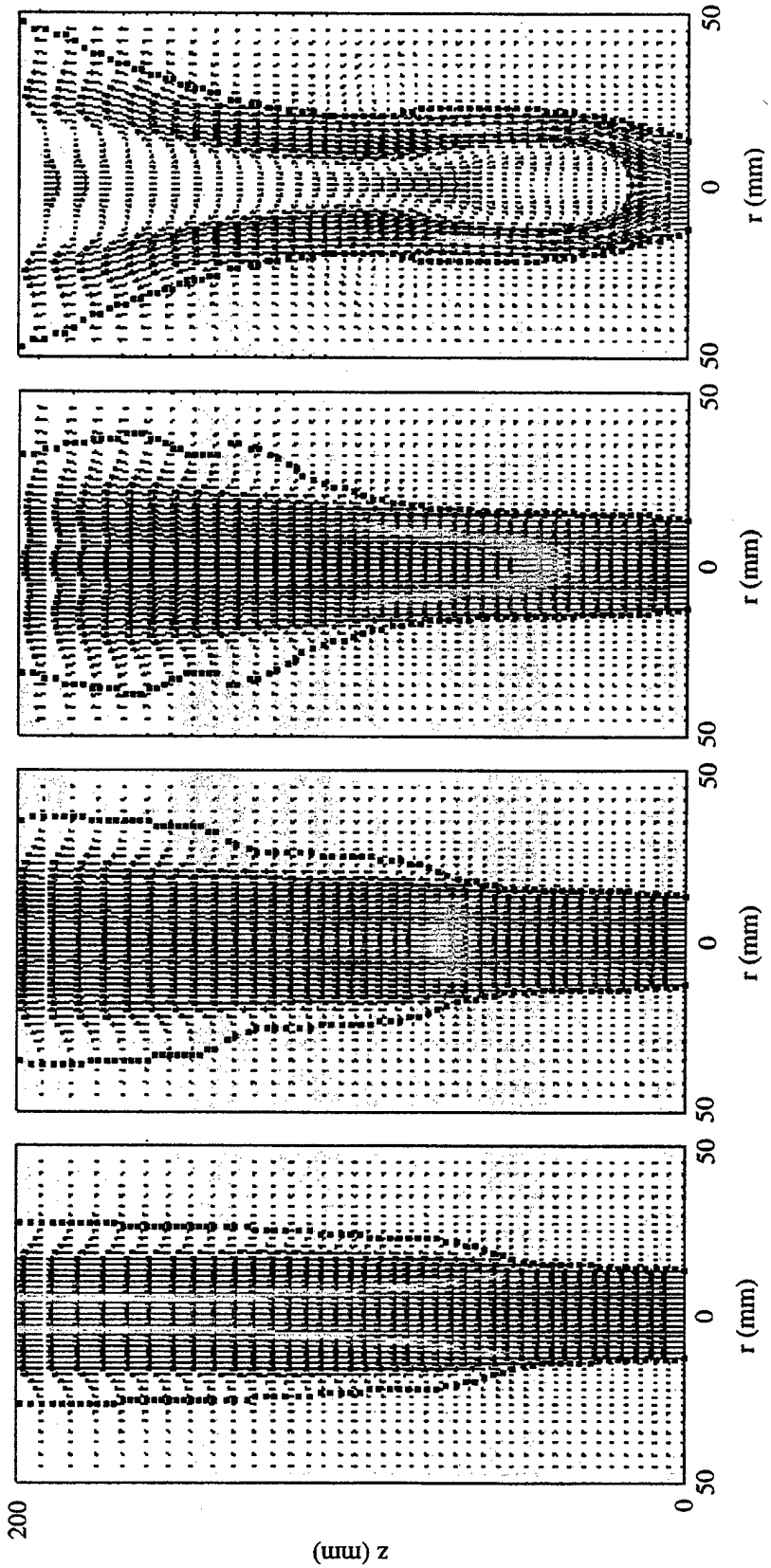

Figure 11. Time-averaged velocity vector plots for a two-phase swirling jet for different swirl numbers..

the degree of modification depends on the swirl intensity. For the nonswirling jet ($S = 0$), as the shear layer develops, the gas-phase velocity decreases along the centerline. Since the droplets are injected at the jet velocity, they now have higher velocity than the gas phase, resulting in a transfer of momentum from the dispersed phase to the gas phase. This seems to enhance the shear layer instability, resulting in enhanced mixing and entrainment of colder fluid, as evidenced by a faster decay of centerline temperature and velocity for the two-phase jet compared to those for the single-phase jet. This effect is modified significantly by the introduction of swirl. As noted earlier, the addition of swirl ($S = 0.375$) to a single-phase jet causes a faster decay of the centerline velocity (compared to a nonswirling jet), resulting in vortex pairing. This leads to enhanced mixing and entrainment of colder fluid into the shear layer; note a sharp increase in the rate of decrease of centerline velocity near an axial location of 120 mm for the single-phase jet. For the corresponding two-phase jet, the transfer of azimuthal momentum from the gas phase to droplets reduces the swirl intensity near the nozzle. This initially ($z < 120$ mm) causes a faster decay of centerline velocity for the two-phase jet compared to that for the single-phase jet. Further downstream, however, the direction of azimuthal momentum transfer is reversed, resulting in a slower decay of centerline velocity for the two-phase jet. In addition, the absence of vortex pairing for two-phase jet further reduces the rate of decay of centerline velocity. Consequently, the centerline velocity of two-phase jet becomes higher than that of single-phase jet for $z > 120$ mm. The absence of vortex pairing also results in reduced mixing and entrainment for the two-phase jet. Consequently, as indicated in figure 10(b), the centerline temperature decreases less rapidly for the two-phase jet.

The above effects become progressively stronger as the swirl number is increased. For $S = 0.5$, as shown in figure 10(a), the centerline velocity of single-phase jet first decreases quite rapidly due to the combined effects of shear layer growth, adverse pressure gradient, and vortex pairings, and then ($z > 100$ mm) increases due to the transfer of axial momentum in the radial direction; see also figure 6. For the corresponding two-phase jet, the centerline velocity decreases much less rapidly, again due to the reduced pressure gradient and the absence of vortex pairings. The centerline temperature also decreases slowly for the two-phase jet, again implying reduced mixing and entrainment due to the momentum coupling effect. Another effect of momentum coupling is seen from the comparison of time-averaged velocity vectors for single-phase and two-phase jets given in figures 6 and 11, respectively. The comparison of these figures shows that, due to the momentum transfer from droplets to gas phase in the jet shear layer, the jet width is decreased and the potential core is lengthened for the swirling two-phase jet. The effect becomes more distinguishable for $S = 0.5$ and 0.75, where the momentum coupling generates a curtain (or envelope) of high-velocity narrow region inside the shear layer. An important consequence of this high-velocity curtain is the near disappearance of the stagnation region for swirling two-phase jet for $S = 0.5$, and that of recirculation bubble for $S = 0.75$. The presence of a large recirculation bubble is perhaps the most distinguishing feature of a strongly swirling ($S = 0.75$) single-phase jet; see figures 3 and 6. For the corresponding two-phase jet, our results indicate that the recirculation bubble becomes nearly non-existent, even though the central stagnation and reverse flow regions still exist inside the high-velocity curtain. The disappearance of recirculation bubble for the strongly swirling case may be attributed to the momentum coupling effect, i.e. the transfer of various momentum components between the phases. Initially, there is a transfer of swirl momentum from the gas phase to dispersed phase, causing swirling intensity to decrease much more rapidly for two-phase jet (case B) compared to that for single-phase jet (case A). At some downstream location, however, the direction of azimuthal momentum transfer reverses, since droplets have higher momentum there. Secondly, the jet spreading rate is reduced for case B due to the radial momentum transfer from the gas phase to the dispersed phase. In addition, there is a reverse transfer of axial momentum, i.e. from the dispersed phase to gas phase, since the gas-phase axial velocity decreases more rapidly than that of dispersed phase, generating the high-velocity curtain mentioned earlier. All of these effects, i.e. reduced entrainment, more rapid decay of swirl velocity initially, and increase of gas velocity, lead to a near disappearance of the recirculation bubble for the strongly swirling two-phase jet. Consequently, for strongly swirling jets ($S > 0.5$), the jet spreading angle, shear layer

growth and entrainment are reduced significantly due to the effect of interphase momentum coupling.

4. CONCLUSIONS

In this paper, we have investigated the effects of swirl and two-phase momentum coupling on the dynamics and structural behavior of a droplet-laden swirling jet. A direct numerical solver based on an Eulerian–Lagrangian formulation, but without any turbulence or subgrid model, has been employed to simulate the transient behavior of a transitional swirling jet. Numerical results have been shown to be grid-independent both in terms of the global predictions and the detailed spatio-temporal profiles of relevant gas-phase profiles at different swirl numbers. In addition, the predicted Strouhal number associated with the large-scale structures for the non-swirling jet has been shown to be in agreement with the available experimental data. Then, a detailed flow visualization based on numerical simulation has been used to examine the dynamics of large scale structures and their interactions with the droplets in weakly and strongly swirling jet shear layers. In addition, the effects of swirl and dispersed phase on the time-averaged jet structure have been characterized. Important observations are as follows.

Results for single-phase swirling jets indicate that the dynamics of large scale structures are strongly affected by the degree of swirl imparted to the incoming jet. For low and intermediate swirl intensities, the vortex rings roll up closer to the nozzle exit, their frequency increases, and pairing interactions become progressively stronger as the swirl number is increased. For example, there is one weak vortex merging near $z/D = 6$ for the nonswirling jet, and two vortex mergings near $z/D = 3$ and 5 for $S = 0.375$, while for $S = 0.5$ the vortex mergings become stronger and occur near $z/D = 2$ and 3, respectively. Consequently, the interaction of vortex rings with the swirling flow field gives rise to a mechanism, which seems to be responsible for the enhanced shear layer growth and entrainment, and has not been observed in previous studies. This may be an important result, with the implication that the addition of moderate swirl to a transitional jet modifies its vortex dynamics in a way that further enhances the beneficial effects of both swirl and vortex structures on shear layer growth. For a strongly swirling jet, the presence of a central stagnant zone and recirculation bubble causes a drastic increase in the jet spreading angle, and this has a rather dramatic effect on vortex dynamics. Detailed visualization of the shear layer dynamics indicates that, as the shear layer is shifted radially outward, a pair of counter-rotating toroidal vortices is generated periodically, and the eventual shear layer structure, including the location of recirculation bubble, is determined by the dynamic interactions of these structures with the stagnant zone and recirculation bubble.

Results for the two-phase swirling jet indicate that at a mass loading ratio of unity, the jet dynamics and structural characteristics are strongly modified by the interphase momentum coupling. Depending upon the amount of swirl imparted to the jet, the momentum coupling can cause varied and in some cases dramatic effects on the dynamic and time-averaged jet structure. For a nonswirling jet, the momentum coupling alters the dynamics of large vortex structures, modifying their roll-up location and frequency, and causing enhanced mixing and entrainment of colder fluid into the shear layer. In contrast, for weakly and moderately swirling jets, the momentum coupling reduces the amount of adverse pressure gradient, and suppresses the vortex pairing interactions. These effects are caused by the redistribution of gas-phase axial, radial, and swirl momentum components due to the dispersed phase, and lead to significantly reduced shear layer growth, mixing and entrainment rates for two-phase jets compared to those for single-phase jets. In addition, the correlation between vortex frequency and swirl number is modified due to momentum coupling. For example, the dominant vortex frequency of single-phase jets increases with increasing swirl number, while that of two-phase jets appears to be independent of S.

At high swirl numbers ($S > 0.5$), the effects of momentum coupling on the jet structure appears to be even more dramatic compared to those at moderate swirl numbers. Results for $S = 0.75$ indicate that momentum coupling can significantly modify the rate of decay of swirl

intensity, and increase the gas axial momentum in the jet shear layer, leading to a dramatic reduction in the size of recirculation bubble.

Acknowledgements—This work was funded in part by the AFOSR under Grant F49620-93-1-0400 monitored by Dr. Julian M. Tishkoff. One of the authors (T.W.P.) was supported by the NRC Fellowship. Computations were performed on the Cray C-90 at the Pittsburgh Supercomputing Center.

REFERENCES

Aggarwal, S. K., Park, T. W. and Katta, V. R. (1996) Unsteady spray behavior in a heated jet shear layer: droplet–vortex interactions. *Combustion Science and Technology* **113,** 429–450.

Chung, J. N. and Troutt, T. R. (1988) Simulation of particle dispersion in an axisymmetric jet. *J. Fluid Mech.* **186,** 199–222.

Crow, S. C. and Champagne, F. H. (1971) Orderly structure in jet dynamics. *J. Fluid Mech.* **48,** 547–591.

Dellenbach, P. A., Metzger, D. E. and Neitzel, G. P. (1988) Measurements in turbulent swirling flow through an abrupt axisymmetric expansion. *AIAA J.* **26,** 669–681.

Durst, F. and Wennerberg, D. (1991) Numerical aspects on calculation of confined swirling flows with internal circulation, computation of strongly swirling axisymmetric jets. *Int. J. Numr. Meth. Fluids* **12,** 203–224.

Hussain, Z. D. and Hussain, A. K. M. F. (1983) Natural instability of free shear layers. *AIAA J.* **21,** 1512–1517.

Kailasanath, K., Gardner, J. H., Boris, J. P. and Oran, E. S. (1989) Acoustic–vortex interactions and low-frequency oscillations in axisymmetric combustors. *J. Propulsion and Power* **5,** 24–36.

Katta, V. R., Goss, L. P. and Roquemore, W. M. (1994) . *Combustion and Flame* **96,** 60–74.

Leonard, B. P. (1979) A stable and accurate convective modelling procedure based on quadratic upstream interpolation. *Comput. Meth. Appl. Mech. Eng.* **19,** 59–98.

Leschziner, M. A. and Rodi, W. (1984) Computation of strongly swirling axisymmetric jets. *AIAA J.* **22,** 1742–1747.

Lilley, D. G. (1977) Swirling flows in combustion: A review. *AIAA J.* **15,** 1063–1078.

Longmire, E. K. and Eaton, J. K. (1992) Structure of a particle-laden Round Jet. *J. Fluid Mech.* **236,** 217–257.

Park, T. W., Aggarwal, S. K. and Katta, V. R. (1996) A numerical study of droplet–vortex interactions in an evaporating spray. *Int. J. Heat Mass Transfer* **39,** 741–754.

Ribeiro, M. M. and Whitelaw, J. H. (1980) Coaxial jets with and without swirl. *J. Fluid Mech.* **96,** 769–795.

Reynolds, W. C. and Bouchard, E. E. (1981) *The Effect of Forcing on the Mixing Region of a Circular Jet, Unsteady Turbulent Shear Layer Flows.* Springer, New York, pp. 401–411.

Shau, Y. R., Dolling, D. S. and Choi, K. Y. (1993) Organized structure in a compressible turbulent shear layer. *AIAA J.* **31,** 1398–1405.

Sommerfeld, M. and Qui, H.-H. (1993) Characterization of particle-laden, confined swirling flows by phase-doppler anemometry and numerical calculation. *Int. J. Multiphase Flow* **19,** 1093–1127.

Spalding, D. B. (1972) A novel finite difference formulation for difference expressions involving both first and second derivatives. *Int. J. Num. Methods Eng.* **4,** 551–559.

Subbarao, E. R. and Cantwell, B. J. (1992) Investigation of a coflowing buoyant jet–experiments on the effect of Reynolds number and Richardson number. *J. Fluid Mech.* **245,** 69–90.

Uthuppan, J., Aggarwal, S. K., Grinstein, F. F. and Kailasanath, K. (1994) Particle dispersion in a transitional axisymmetric jet: A numerical simulation. *AIAA J.* **32,** 2004–2014.

Yule, A. J. (1978) Large-scale structure in the mixing layer of a round jet. *J. Fluid Mech.* **89,** 413–432.

AIAA 99-0212

NUMERICAL MODELING OF DROPLETS IN A COMPOSITE GRID SYSTEM

Long P. Chin

Air Force Research Laboratory
Wright-Patterson AFB
Dayton, OH 45433-7103

37th AIAA Aerospace Sciences Meeting and Exhibit
January 11-14, 1999 / Reno, NV

For permission to copy or republish, contact the American Institute of Aeronautics and Astronautics 1801 Alexander Bell Drive, Suite 500, Reston, VA 20191

Numerical Modeling of Droplets in a Composite Grid System

Long P. Chin*
Air Force Research Laboratory
Wright-Patterson AFB, Dayton, OH 45433-7103

ABSTRACT

A numerical model featuring the use of a composite grid system has been developed for studying the transport phenomena of liquid droplets in combustion systems. The composite grid system consists of 1) Eulerian-type volume grids, which are fixed in space and time, for tracking the movement of droplet surfaces and 2) adaptive Lagrangian-type surface grids, which vary in space and time, for handling the mass and heat-transport processes at the interfaces. The scheme of "Level Set" implemented in the model not only provides a systematic mathematical representation of droplet surfaces controlled by the underlying flow fields but also properly redistributes the highly concentrated surface force (due to surface tension) within a thin finite region. Several examples presented to demonstrate the present model involve the processes of head-on collision between two droplets under three different flow conditions (isothermal, evaporating-only, and combusting). The result of two types of collision (coalescent and bouncing) are discussed, along with the distributions of flow variables at the droplet surfaces.

INTRODUCTION

In combustion systems, the way a spray burns depends on the specific goal. In efforts to develop a useful tool for modeling complicated spray phenomena, each method of burning poses a different problem. In a prevaporizing system, the spray is injected into the heated air stream where the droplets almost completely evaporate before reaching the flame. Because the spray injected upstream of the system contains a large number of droplets having different sizes, temperatures, and velocities, the interaction among these droplets plays an important role in determining the characteristics and performance of combustion downstream.

Copyright © 1999 by Long P. Chin. Published by the American Institute of Aeronautics and Astronautics, Inc. with permission

* AIAA member, Innovative Scientific Solutions, Inc.

In the past, the numerical methods for solving two-phase droplet problems basically have been placed in two different categories-- Eulerian-type [e.g., Ref. 1] and Lagrangian-type [e.g., Ref. 2] approaches, depending mainly on the characteristics of the grid structures for representing the interfaces between the two phases. In the Eulerian approach, all computational grids are fixed in space at all times, and a mathematical function in terms of the volume grids is defined to represent the topology of the interfaces numerically. Since in the Eulerian approach the grid nodes do not always coincide with the droplet interfaces, the local transport phenomena that occur at the interfaces are very difficult to evaluate numerically by the surrounding volume-averaged flow variables alone. The local characteristics of the surface transport loss significantly through the averaging process. On the other hand, in the Lagrangian approach, the computational grids are always defined at the droplet interfaces to avoid the smoothing problem of the local properties by averaging. However, the changes of grid locations in space and time impose a difficult and tedious task in attempts to track these grids accurately, particularly when interface coalescence among droplets occurs during collision. The numerical difficulty for each approach mentioned above can be avoided by combining the two types of structures into a single composite grid. With the usual volume grids fixed in space and time, a new set of additional grids (surface grids) are superimposed to provide a clearer outline on the topology of the droplet surfaces. The primary function of the fixed volume grids will be used to trace the movement of droplets; and the superimposed surface grids will be utilized when the calculations of local transports on mass and energy are desired.

The mathematical formulations of the present model and the proposed composite-grid structure will be explained in the next section. Several examples based on this new model will also be presented including simulation results and distributions of flow variables along the surface grids that outline the droplet interfaces.

MATHEMATICAL FORMULATION

Governing Equations

For the droplet system modeled, the fluids of both phases (gaseous and liquid) will be treated as a single fluid having two significantly different properties separated by an interface that is infinitesimally thin. The governing equations for the defined one-fluid system can be expressed as follows:
Continuity equation:

$$\frac{1}{\rho}\frac{D\rho}{Dt} = -\beta\frac{DT}{Dt} = -\nabla\cdot\vec{u} \tag{1}$$

Momentum equation:

$$\rho\frac{D\vec{u}}{Dt} = -\nabla p + Re^{-1}\nabla\cdot\mu\left(\nabla\vec{u} + \nabla\vec{u}^{T}\right) + Fr^{-1}\rho\vec{g} + We^{-1}\int_{s}\sigma\kappa\delta(\vec{x}-\vec{x}_s)\vec{n}dA \tag{2}$$

Energy equation:

$$\rho\frac{DH}{Dt} + We^{-1}\rho\frac{D}{Dt}\left[\frac{1}{\rho}\int_{s} e_\sigma\delta(\vec{x}-\vec{x}_s)dA\right] = Pr^{-1}Re^{-1}\nabla\cdot\left[\frac{l}{c_p}\nabla H\right] + Re^{-1}\Phi + Pr^{-1}Re^{-1}\nabla\cdot\left[\sum_{k=1}^{N}\rho D_k\left(Le^{-1} - \frac{\lambda}{\rho c_p D_k}\right)H_k\nabla Y_k\right] - h_v^o\int_{s}\omega_v\delta(\vec{x}-\vec{x}_s)dA - h_{f,k}^o\sum_{k}\omega_k - Fr^{-1}Sc^{-1}Re^{-1}\rho\vec{g}\cdot\sum_{k=1}^{N}D_k\nabla Y_k$$

$$\text{where}\quad H(T) = \int_{T_o}^{T} c_p dT \tag{3}$$

Species equation:

$$\rho\frac{DY_k}{Dt} = \nabla\cdot(\rho D_k\nabla Y_k) + \omega_k + \int_{s}\omega_v\delta(\vec{x}-\vec{x}_s)dA \tag{4}$$

The variables in these equations are normalized; and the non-dimensional parameters Re, Pr, Sc, Fr, We, and Le represent Reynolds, Prandtl, Schmidt, Frondle, Weber, and Lewis numbers, respectively. The integral terms represent the transport of mass, momentum, and energy exerted only on the interfaces (denoted by $\vec{x}_s$). The flow variables required to solve Eqs. (1) - (4) are $\vec{u}$ (the velocity vector), p (the pressure), T (the temperature) and Y_k (the species concentration). The thermophysical properties ρ, μ, c_p, λ, D_k, and β denote density, viscosity, specific heat, thermal conductivity, the molecular-diffusion coefficient of species k, and the thermal expansion coefficient, respectively. The variables and properties defined on the gas-liquid interface are σ (the surface tension), e_σ (the surface energy), K (the curvature of interface) ω_v (the mass evaporation rate of the droplet) and h_v^o (the latent heat of the evaporation at reference temperature). It is important to include e_σ in the energy equation to prevent violation of the second law of thermodynamics in evaporation systems [3]. e_σ is related to σ by a surface constitutive relationship. The evaporation rate at the interface, ω_v, is determined by applying chemical-equilibrium conditions while solving the species equation. The one step simplified reaction mechanism given by Westbrook [4] for the oxidation of Hydrocarbon fuels will be used to provide the calculation of ω_k.

"Level Set" Approach

In solving these equations numerically, difficulties arise because of the locality of surface transports (momentum, energy, and mass) that appear as the integral terms in the governing equations. The "Level Set" approach developed by Sussman et al. [5] was adopted to reformulate these local quantities in such a way that they can be properly and smoothly redistributed over a region having finite thickness. If ϕ is defined as a function that measures the normal distance from the interface, the surface integral terms in Eqs. (2)-(4) can be rearranged as follows:

$$\int_{s}\sigma\kappa\delta(\vec{x}-\vec{x}_s)\vec{n}dA = \sigma\kappa(\phi)\bar{\delta}(\phi)\nabla\phi$$

$$\int_{s}\sigma\kappa[\delta(\vec{x}-\vec{x}_s)\vec{n}\cdot\vec{u}]dA = \sigma\kappa(\phi)\bar{\delta}(\phi)(\nabla\phi\cdot\vec{u})$$

$$\int_{s}\delta(\vec{x}-\vec{x}_s)\omega_k dA = \bar{\delta}(\phi)\overline{\omega_k}(\phi)$$

The distance function is assumed to be positive in the liquid phase and negative in the gaseous phase. All of the surface variables and properties have a value of zero outside the interface region defined by ϕ. For tracking the interface movement due to flow convection and droplet evaporation, the function ϕ is solved using the following equation:

$$\frac{\partial\phi}{\partial t} + \vec{u}\cdot\nabla\phi = \frac{\delta\phi(\omega_v)}{\delta t} \tag{5}$$

where $\delta\phi(\omega_v)/\delta t$ is the change rate of ϕ as a result of evaporation.

Numerical Schemes

The numerical scheme chosen for this study is a finite-volume method based on the ALE (Arbitrary Lagrangian-Eulerian) grid system. By coupling this scheme and the concept of split velocity [6], the parasite currents resulting from the locality of the surface force are minimized to prevent instability and also to ensure the mass conservation of droplets. An accurate accounting of the surface-tension term of Eq. (2) for this numerical method required modification of the formulation for the split velocity to incorporate the surface force with the pressure force. Figure 1 illustrates the concept of using split velocity in this numerical method. The pressure and the distance function of ϕ are defined at the center of the cell; and the remaining variables (including velocity vector and the other scalar variables) are defined at the corners of the cell. The split velocities on four sides of each velocity node were used to satisfy the continuity equation, which is crucial in avoiding the mass loss of droplet due to numerical inaccuracy. In the mean time, these split velocities are used to discretize the interface-tracking equation [Eq. (5)] to ensure the mass conservation.

With the implementation of split velocity in this model, the surface-force term in Eq. (2) must be rearranged to couple with the pressure-force term for the purpose of reducing the effects of "parasite currents." The procedure is expressed as follows:

$$\begin{aligned} &-\nabla p+\sigma\kappa(\phi)\bar{\delta}(\phi)\nabla\phi \\ &=-\nabla p+\sigma\kappa(\phi)\nabla H(\phi) \\ &=-\nabla[p-\sigma\kappa(\phi)H(\phi)]-\sigma H(\phi)\nabla\kappa(\phi) \\ &=-\nabla\hat{p}-\sigma H(\phi)\nabla\kappa(\phi) \end{aligned} \tag{6}$$

Where $H(\phi)$ is the Heavside function derived from the delta function. Note that the newly defined pressure $\hat{p}$ will be solved instead of the normal pressure p. A second-order upwind scheme was applied to discretize the convection term in Eq. (2) for eliminating excess numerical diffusion. Because of the large density gradient across the interface in a two-phase system, a fully multigrid method coupled with a MSIP (Modified Strongly Implicit Procedure) iteration technique was employed to solve the pressure field efficiently.

Structure of Composite Grid

Once the distance function ϕ is determined from Eq. (5), the adaptive surface grids can be constructed by finding the locations (by extrapolation) along the cell boundaries where the value of ϕ is zero (see Fig. 2).

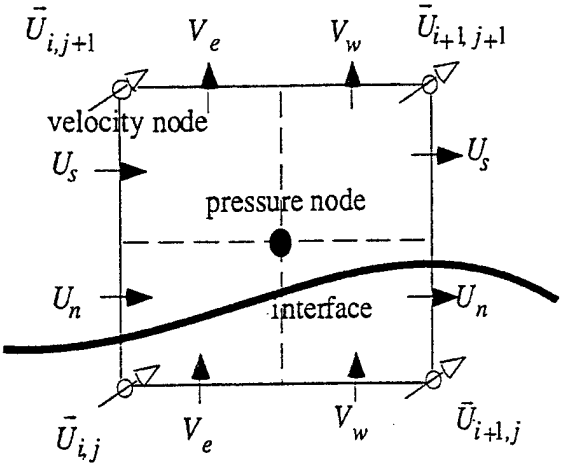

Figure 1. Schematic illustration of ALE formulation with split velocity.

For the grids shown in Fig. 2, the lines connecting two velocity nodes are defined as the primary boundaries; and the lines connecting two pressure nodes are defined as the auxiliary boundaries. The surface grids on both primary and auxiliary boundaries are selected to achieve more accurate representation of the droplet surfaces. The primary surface grids (a, c, e, and f in Fig. 2) on the primary boundaries will be designated as part of the computational grids during solution of the transport equations [Eqs. (3)-(4)]; but the flow variables of the auxiliary surface grids (b and d in Fig. 2) on the auxiliary boundaries will be evaluated through extrapolation from two neighboring surface (primary or auxiliary) grids. The surface matching boundary conditions (energy and mass balance) were applied only to the primary surface grids. Since the neighboring nodes around a primary surface grid are not orthogonal to each other, coordinate transformation was performed to derive the following generalized formulations for mass and energy balances at the primary surface grids:

Energy balance: $q_{n,g}-q_{n,l}=h_v^o\omega_v$.

Mass balance: $\omega_v=\omega_v Y_{fs}-D_f\left(\partial Y_{fs}/\partial n\right)$

where $q_{n,g}$ is the normal heat flux of the gaseous phase at the interface; $q_{n,l}$, the normal heat flux of the liquid phase at the interface; and Y_{fs} is the fuel concentration at the interface.

MODELING RESULTS

The numerical model based on the composite-grid system will be demonstrated by presenting simulation

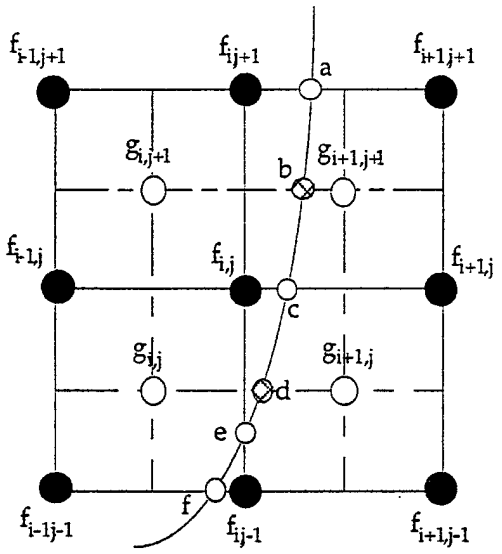

Figure 2. Structure of composite grids

results for coalescent and bouncing droplets (Figs. 3 and 4), which involve head-on collision between two identical droplets under three different flow conditions (isothermal, evaporating-only and combusting). For bouncing droplets (see Fig. 3), interface coalescence never occurs, and the two droplets bounce back in opposite direction after collision. For coalescent droplets (see Fig. 4), the two droplet interfaces coalesce at a certain time when the clearance between two droplets reaches a critical value and eventually merge and become a singe droplet after collision. Readers who are interested in the numerical study of collision dynamics between droplets can refer to Ref. 7. For both cases, the two droplets initially have a diameter of 0.3 mm. The incoming velocity of the droplet is 0.32 m/s in the bouncing case and 0.62 m/s in the coalescent case. Three different surrounding flow conditions are presented (1) isothermal (room temperature at 300 K); (2): evaporating-only (hot surrounding air is at a temperature of 1000 K); and (3): combusting condition. In both figures, the contours shown in (2) and (3) are temperature distributions, with the range being from 300 to 1000 K in (2) and 300 to 2200 K in (3). Basically, the collision dynamics under three different flow conditions are almost identical, but the coalescence or the bouncing timing may differ somewhat.

CONCLUSIONS

A numerical method based on the finite-volume scheme coupled with the composite-grid system was introduced for modeling complicated dynamics and transport phenomena in two-phase spray systems. The model applies the concept of "level set" and "split velocity" to resolve the topological variations of the droplet surfaces and also to ensure that the mass loss of droplets due to numerical inaccuracy is minimal. In the mean time, the composite grid coupled with the additional surface grids provides accurate information on the orientation of the droplet surface, which is critical in determining the correct transport fluxes of mass and heat across the interfaces. This study of droplet collisions was conducted to illustrate the application of the present model under various flowing conditions.

ACKNOWLEDGMENT

This work was supported by the U. S. Air Force under Contract F33615-95-C-2507. The author would like to thank Dr. Katta for his comments on this work. Special thanks to Ms. Marian Whitaker for editing this paper.

REFERENCE

1. Brackbill, J. U., Kothe, D. B. and Zemach, C., "A Continuum Method for Modeling Surface Tension," *J. Comput. Phys.*, Vol. 100, pp. 335-354 (1992).
2. Fyfe, D. E., Oran, E. S. and Fritts, M. J., "Surface Tension and Viscosity with Lagrangian Hydrodynamics on a Triangular Mesh," *J. Comput. Phys.*, Vol. 76, pp. 349-384 (1988).
3. Welch, S. W. J., "Local Simulation of Two-Phase Flows Including Interface Tracking with Mass Transfer," *J. Comput. Phys.*, Vol. 121, pp. 142-154 (1995).
4. Westbrook, C. K., "Simplified Reaction Mechanisms for the Oxidation of Hydrocarbon Fuels in Flames," *Combust. Sci. Technol.*, Vol. 27, pp. 31-43 (1981).
5. Sussman, M., Smereka, P. and Osher, S., "A Level Set Approach for Computing Solutions to Incompressible Two-Phase Flow," *J. Comput. Phys.*, Vol. 114, pp. 146-159 (1994).
6. Hwang, Y.-H., "Arbitrary Domain Velocity Analyses for the Incompressible Navier-Stokes Equations," *J. Comput. Phys.*, Vol. 110, pp. 134-149 (1994).
7. Chin, L. P., "A Numerical Study of Collision Behavior between Droplets," Presented at the 1996 Central States Section Meeting of the Combustion Institute, May 5-7, 1996, St. Louis, MO.

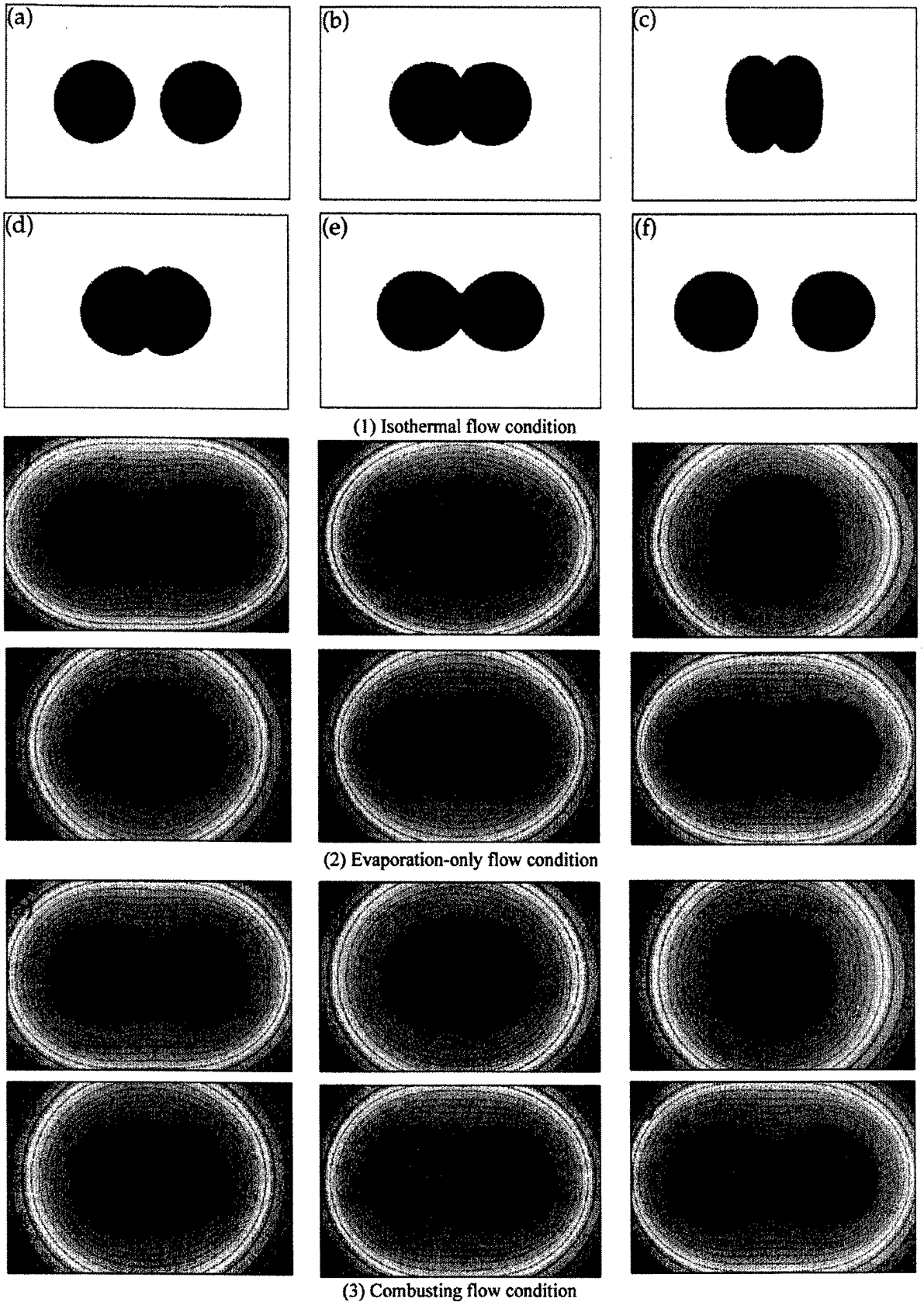

Figure 3. Sequences of simulations for droplet collision at a relative velocity of 0.64 m/s; t= (a) 0; (b) 0.26; (c) 0.52; (d) 0.78; (e) 1.04; (f) 1.30 ms.

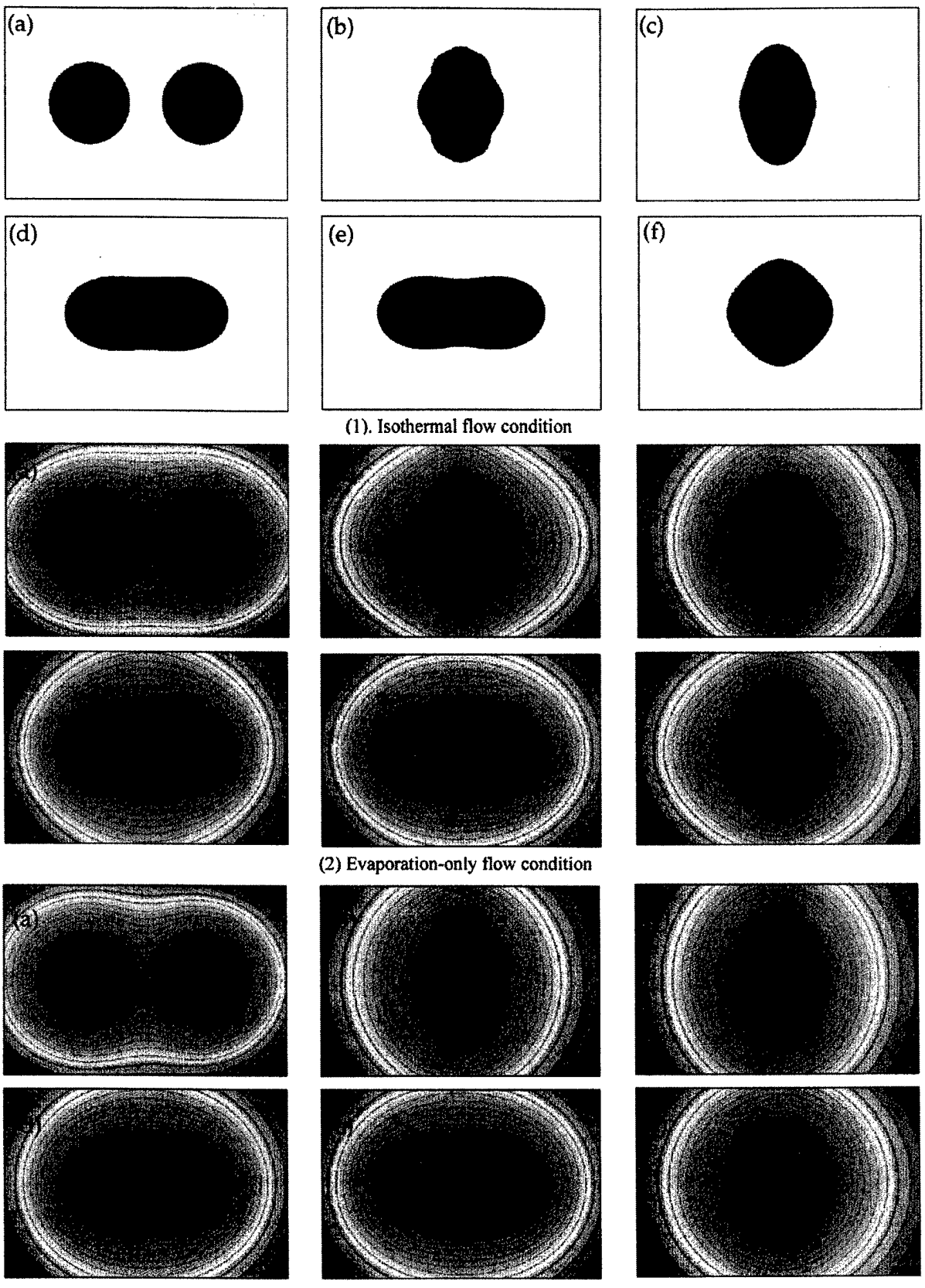

Figure 4. Sequences of simulations for droplet collision at a relative velocity of 1.24 m/s; t= (a) 0; (b) 0.34; (c) 0.68; (d) 1.02; (e) 1.36; (f) 1.70 ms.

AIAA 99-3319

NUMERICAL MODELING OF COLLISION BETWEEN TWO DROPLETS

Long P. Chin

Air Force Research Laboratory
Wright-Patterson AFB
Dayton, OH 45433-7103

14th Computational Fluid Dynamics Conference

28 June - 1 July, 1999 / Norfolk, VA

For permission to copy or republish, contact the American Institute of Aeronautics and Astronautics 1801 Alexander Bell Drive, Suite 500, Reston, VA 20191

NUMERICAL MODELING OF COLLISION BETWEEN TWO DROPLETS

Long P. Chin*
Air Force Research Laboratory
Wright-Patterson AFB, Dayton, OH 45433-7103

ABSTRACT

The collision between two liquid droplets (head-on and off-center) has been studied numerically. The technique of "Level Set", which identifies the interfaces between two phases, was applied to solve the fluid motion both inside and outside the droplets based on a 3-D finite volume scheme incorporated with the ALE grid system. The various modes of collision results observed in the experiments by Jiang et al. [1] are correctly predicted in a wide range of droplet Weber number (*We*) and Reynolds number (*Re*). To simulate the dynamics of droplet collision properly, a predetermined time for interface coalescence is required to be accurately implemented in the numerical process and is found to have significant impact on the collision results. The collision dynamics is further studied by examining the energy balance and mode shift (between kinetic energy, surface energy, viscous dissipation, and works by surface force) during the entire period of collision.

INTRODUCTION

Droplet dynamics in various spray systems is an interesting and important research topic in the field of combustion modeling. Because of the dense nature of the droplet ensemble in the region downstream of the nozzle injectors, strong interactions between droplets prior to combustion are expected to modify the distributions of droplets with regard to size, velocity, and number density significantly. To obtain detailed information to aid the understanding of the physical processes involved in droplet interactions, a simple and fundamental study was conducted on the collision behavior of two spherical droplets.

In the past, numerous experiments have been conducted to study the dynamics of droplet collision in various ranges of size and velocity [1-4]. From these experiments some generalized collision outcomes have been observed and categorized. A study by Jiang, Umemura and Law [1] reported that four different modes resulting from the collision between equal-sized hydrocarbon droplets are identified for either head-on or off-center arrangement. Depending on the Weber number (*We*) and impact parameter (*B*), the collision results between droplets could be bouncing, coalescence, separation or shattering. However, in the same range of study, only two modes were observed for the water droplets.

When two droplets approach each other prior to impact, a thin fluid layer with high pressure is established between them. This thin fluid layer provides a resistance to keep the interfaces of two droplets separate for a period of time without merging. However, when the thickness of this thin fluid layer between droplets reaches below a critical value that is within the range of the intermolecular forces of the fluid [1], the two droplets may coalesce to form a single droplet. The determination of when or whether this critical clearance value can be reached under different flow conditions become very critical for deciding the dynamic characteristics of droplet collision.

The phenomenon of critical clearance between colliding droplets imposes a very difficult problem for the numerical modeling because the critical clearance value (in the order of 10^2 *A*) of coalescence is much smaller than the resolution employed for the most numerical schemes used today. It will be impossible to resolve the fluid structures within this thin layer numerically. To simplify this problem in the modeling, the thin fluid layer can be treated in two different ways depending on the type of numerical scheme applied to track the interfaces. For the Lagrangian type approach in which the interfaces of two droplets are always separate, the thin fluid layer will be removed at a prescribed time if the coalescence collision is expected [5,6]. On the other hand, if the Eulerian type approach is chosen, in which the interfaces of two droplets

Copyright © 1999 by Long P. Chin. Published by the American Institute of Aeronautics and Astronautics, Inc. with permission

* AIAA member, Innovative Scientific Solutions, Inc.

automatically merge whenever they are within the distance imposed by the numerical resolution, a thin fluid layer with a prescribed thickness will be inserted artificially until it is removed at later time [7-9].

In the present study, the second approach (Eulerian type) will be used to model the head-on collision between two equal-sized hydrocarbon droplets for all four modes observed in the experiments [1]. The detailed numerical method will be described in the next section. The modeling results and the comparisons between 2-D axisymmetric and three-dimensional will be presented in the following section. The effects of the timing to release the thin fluid layer between droplets on the collision outcome also will be thoroughly discussed along with the energy balance.

NUMERICAL METHOD

The numerical model used for simulating the droplet collision in the present study is a "Level Set" approach for the incompressible two phase flow developed by Sussman, Smereka and Osher [8]. In this model, the interface between the two fluids is described as the zero level set of a smooth function, which is defined as the distance from the interface. The flow field in the two-phase single-fluid system is calculated by solving the 3-D Navier-Stokes equation (in Cartesian Coordinates) in the following form:

$$\frac{\partial u}{\partial x}+\frac{\partial v}{\partial y}+\frac{\partial w}{\partial z}=0 \tag{1}$$

$$\rho\frac{Du}{Dt}=\left[\nabla\cdot\mu\nabla u+\frac{\partial}{\partial x}\mu\frac{\partial u}{\partial x}+\frac{\partial}{\partial y}\mu\frac{\partial v}{\partial x}+\frac{\partial}{\partial z}\mu\frac{\partial w}{\partial x}\right]-\frac{\partial p}{\partial x}+g_x+\sigma\kappa(\phi)\delta(\phi)\frac{\partial\phi}{\partial x} \tag{2}$$

$$\rho\frac{Dv}{Dt}=\left[\nabla\cdot\mu\nabla v+\frac{\partial}{\partial x}\mu\frac{\partial u}{\partial y}+\frac{\partial}{\partial y}\mu\frac{\partial v}{\partial y}+\frac{\partial}{\partial z}\mu\frac{\partial w}{\partial y}\right]-\frac{\partial p}{\partial y}+g_y+\sigma\kappa(\phi)\delta(\phi)\frac{\partial\phi}{\partial y} \tag{3}$$

$$\rho\frac{Dw}{Dt}=\left[\nabla\cdot\mu\nabla v+\frac{\partial}{\partial x}\mu\frac{\partial u}{\partial z}+\frac{\partial}{\partial y}\mu\frac{\partial v}{\partial z}+\frac{\partial}{\partial z}\mu\frac{\partial w}{\partial z}\right]-\frac{\partial p}{\partial z}+g_z+\sigma\kappa(\phi)\delta(\phi)\frac{\partial\phi}{\partial z} \tag{4}$$

In Eqns. (1)-(4), ρ,μ,σ,κ, are density, viscosity, surface tension and surface curvature, respectively, $\delta(\phi)$ is a three-dimensional delta function. To avoid smoothing the sharpness of droplet properties at the interface by excessive numerical diffusion, the defined "distance" function (ϕ, which is linear across the interface) is solved according to the following propagation equation in an incompressible fluid system:

$$\frac{\partial\phi}{\partial t}+\vec{u}\cdot\nabla\phi=0 \tag{5}$$

To solve equations (1) to (4), the finite volume scheme in an ALE (Arbitrary Lagrangian-Eulerian) grid developed by Hwang [10] was used. The concept of split velocity was employed to eliminate the pressure wiggle problem. To account for the surface tension term in Eqns.(2-4), the formulation for the split velocity is modified to incorporate the surface force with pressure force [10]. A second order upwind scheme was applied to discretize the convective term in Eqns. (2-4) for eliminating excess numerical diffusion. To solve the pressure field, a fully multi-grid method [12] coupled with MSIP (Modified Strongly Implicit Procedure) iteration scheme [13] was implemented.

The distance function, ϕ, defined in this model is required to maintain the correct distance from the interface at all times after each calculation step to avoid producing irregular interface. This can be achieved easily by solving the following problem to steady state

$$\frac{\partial\phi}{\partial t}=S(\phi_o)(1-\sqrt{\nabla\cdot\nabla\phi}) \tag{6}$$

where S is the sign function depending on the value of ϕ_o. The distance function remains unchanged at the interface during the calculations.

The energy modes that play important roles in droplet dynamics include kinetic energy, surface energy, viscous dissipation. pressure work and surface work. The mathematical expression in the present numerical modeling for above five energy terms can be written as follows:

$$E_{k.e.} = \sum \frac{1}{2}(u^2 + v^2 + w^2)\Delta V$$

$$E_{s.e.} = \sigma \sum \delta(\phi)\Delta V$$

$$E_{v.d.} = 2\sum \mu[u_x^2 + v_y^2 + w_z^2]\Delta V + \sum \mu[(u_y + v_x)^2 + (u_z + w_x)^2 + (v_z + w_y)^2]\Delta V$$

$$E_{p.w.} = \sum (\nabla p \cdot \vec{u})\Delta V$$

$$E_{s.w.} = \sigma \sum (\kappa \vec{n} \cdot \vec{u})\delta(\phi)\Delta V$$

Where ΔV is the volume of one computational cell and $\vec{n}$ the unit normal to the droplet surface.

NUMERICAL RESULTS

Four sets of simulations were performed for the conditions corresponding to the head-on collision experiments conducted by Jiang et al. [1]. In each case both 2-D axisymmetric and three dimensional simulations were performed for comparison. Since the comparison between experiments and axisymmetric simulations has been made in previous study [14], the experimental results will not be shown in the present study and comparison will only be focused on the effects of three-dimensional structures. Initially, two equal-sized spherical hydrocarbon droplets (0.30 mm in diameter) are placed 0.1 mm apart. The density and viscosity of liquid are 730.0 kg/m^3 and $0.95\times10^{-3} N\cdot s/m^2$, respectively. The surface tension between air and the working liquid is 2.45×10^{-2}N/m. The initial velocity of both droplets is chosen identical to those produced in experiments. The four velocity conditions are (I) 0.07 m/s, (II) 0.32 m/s, (III) 0.62 m/s and (IV) 1.15 m/s. Since the effect of surrounding air on the droplets is very small, in the simulations the droplets were started to be uniformly moving along the collision axis (line connected between two droplet centers). The droplet Reynolds number and Weber number (Re/We) for these four chosen velocities are 32/0.17, 147/3.7, 286/13.8, 530/47.6, respectively. Figure 1 shows the simulation results (2-D axisymmetric on the left and 3-D on the right) for all four cases. The collision phenomenon for each mode is explained as follows:

(I) V=0.07 m/s: Since the impact velocity for this condition is very small, the interfaces of droplets were observed to coalesce immediately after initial contact and form a single larger droplet (see the frame at 0.30 ms). When the two droplets merge, they will remain coalesced and oscillating with decayed amplitude comparable to that theory predicted [13].

(II) V=0.32 m/s: When the impact momentum between droplets increases, the collision is sufficiently energetic that substantial droplet deformation occurs. However the two droplet interfaces do not coalesce during the whole collision process and eventually bounce away from each other at later stage. This result indicates that the thin fluid layer between droplets will not reach below the critical clearance at all times and keep two interfaces apart. To simulate the bouncing droplets, a thin fluid layer (air) is inserted artificially between two droplets whenever they are in contact within the distance of a half grid.

(III) V=0.62 m/s and (IV) V=1.15 m/s: Under these two velocity conditions, the process of interface coalescence observed from the experiments is not clear and to be more complicated than two previous modes. The information regarding the timing of interface coalescence strongly depend on the collision parameters such as *Re* and *We* of the droplets. Unlike the phenomena seen in previous two conditions (I and II) in which the interface coalescence either occurs right at the instance when two droplets make contact (I) or never occur (II), for conditions (III) and (IV) the two droplets are remained separate during initial period of contact until the momentum of droplets is sufficiently high that the thin fluid layer is forced to be removed. To model these two modes numerically, an approximate time of interface coalescence needs to be determined in advance based on the observations from experiments. For both simulations presented in Fig. 1, the pre-determined coalescence time is at t= 0.13 ms for (III) and t=0.08 ms for (IV). In condition (III), for example, the coalescence occurs between the second (0.09 ms) and the third frame (0.18 ms). The main difference between (III) and (IV) is the production of satellite drops at higher velocity condition. At condition (IV), the collision impact is so strong that the surface tension of the coalesced liquid is not sufficient to hold the liquid in a closed surface. The contraction of coalesced droplet (see the frame at t=1.26 ms) splits the single droplet into two. The instability of ligament produced during the contraction period is the source for generating the satellite drops.

As evidenced by the simulations presented above, the timing for releasing the thin fluid layer between droplets has significant impact on the collision results. A significant difference on the collision dynamics can be observed if the forced coalescence timing is released from the numerical modeling for cases (III) and (IV). In Fig. 2, the sequence on the left presents the calculations without using the forced coalescence timing and the sequence on the right is the same results shown in Fig 1(III) with the frames chosen at different times. Without forcing the numerical coalescence, it is clearly seen that droplet merge

much earlier [see Fig. 2(a) at t=0.06 ms] compared to that in forced simulations [Fig. 2(b) at t=0.13 ms].

To further study the dynamics of droplet collision, five energy modes defined earlier are estimated for all four velocity cases. The energy balance and mode shift verse time are presented in Fig. 3. The energy for all five modes are normalized by the initial surface energy which is independent of droplet velocity. During the whole period of collision. the energy conservation can be identified based on the summations of several energy modes. Two of these summations discussed in the present study are the sum of kinetic energy, surface energy, viscous dissipation and pressure work ($E_1 = E_{k.e.} + E_{s.e.} + E_{v.d.} + E_{p.w.}$) and the sum of kinetic energy, viscous dissipation, surface and pressure works ($E_2 = E_{k.e.} + E_{s.w.} + E_{v.d.} + E_{p.w.}$). It's interesting to note that the second energy sum (E_2) always maintains constant throughout the whole process, but the first energy sum (E_1) only will be totally conserved if the droplets are either in bouncing mode [Fig. 3(a)] or making quick coalescence after the contact [Fig. 3(b)]. The sharp drop of the first energy sum (E_1) in Figs. 3(c) and 3(b) are caused by the merge of two interfaces into one while the coalescence is occurring.

To model the coalescence phenomena between droplet in the present model, a critical clearance need to be defined in order for the two surfaces to merge at the proper time. Because the interface carrier used in the "level set" scheme is a distance function (ϕ), it will be a natural candidate for an indication that shows how far the two droplet is apart during the collision process. Fig. 4 shows the progress of function ϕ in time when two droplets approach to each other at a speed of 0.90 m/s. Based on the size of defined surface thickness, α, the maximum value ϕ can reach is one α without coalescence. In order to find the proper critical clearance for coalescence, a set of simulations (by varying the Weber number) were performed to examine the characteristics of maximally allowed clearance by forcing the droplets never merged. Figure 5 is the plot showing the maximum value of ϕ reached along the contact line without coalescence. It is interesting to note that the characteristic of the curve in Fig. 5 is similar to that observed in the experiments in terms of the outcomes of collision. By intersecting the curve with a horizontal straight line (constant ϕ), the droplet collision in numerical modeling will result from coalescence, bouncing, then to coalescence again as the Weber number increases as long as the straight cut through two points of the curve. If the straight line is chosen to be places below the curve then no bouncing will be found. On the other hand if the straight line is place above 0.5α, the first region of coalescence will not be seen in simulations. Based on this information a empirical formula is derived to define the critical clearance for the present model.

$$\delta = \delta_o P^c \tag{7}$$

where δ_o is the critical clearance at 1 atm and c is a constant (>0). Basically, δ_o, a function of numerical resolution, is primarily determined by the properties of liquid droplet; and the constant c is affected by the gas properties.

CONCLUSIONS

The dynamics of head-on collision between two equal-sized droplets was studied numerically using the concept of "Level Set.". The simulation results from the 2-D axisymmetric modeling is extremely accurate for low to moderate velocity range. However, the 3-D modeling will be a useful tool if the study of off-center or high-speed droplet collision is desired. A preset time of releasing the fluid layer between droplets under some conditions is imposed in the model to conduct the interface coalesced properly. A simple empirical formula has been derived for the critical clearance by using the characteristics of the scheme of "level set." In the future to develop a theoretical sub-model, which can describe the coalescence physics rigorously and is suitable to be implemented in the numerical scheme, will be helpful in the study of collision dynamics under much more complication conditions.

ACKNOWLEDGMENTS

This work was supported by the U. S. Air Force under Contract F33615-95-C-2507. The author would like to thank Dr. Mel Roquemore and Dr. Vish Katta for their comments on this work. Special thanks to Ms. Whitaker for editing this paper

REFERENCE

1. Jiang, Y. J., Umemura, A. and Law, C. K., "An experimental investigation on the collision behavior of hydrocarbon droplets," *J. Fluid Mech.*, Vol. 234, pp. 171-190 (1992)

2. Adam, J. R., Lindblad, N. R. and Hendricks, C. D., "The collision, coalescence, and disruption of water droplets, *J. Appl. Phys.*, Vol. 49, pp. 5173-5180 (1968)

3. Bradley, S. G. and Stow, C. D., "Collisions between liquid drops," *Phil Trans. R. Soc. Lond.* A Vol. 287, pp. 635-678 (1978)

4. Ashgriz, N. and Poo, J. Y., "Coalescence and separation in binary collisions of liquid drops *J. Fluid Mech.*, Vol. 221, pp. 183-204 (1990)
5. Unverdi, S. O. and Tryggvason, G., "A front-tracking method for viscous, incompressible, Multi-fluid flows," *J. Compt. Phys.*, Vol. 100, pp. 25-37 (1992)
6. Nobari, M. R., Jan, Y.-J. and Tryggvason, G., "Head-on collision of drops -- a numerical investigation," *Phys. Fluids*, Vol. 8, No.1, pp. 29-42 (1996)
7. Brackbill, J. U., Kothe, D. B. and Zemach, C., "A continuum method for modeling surface tension," *J. Compt. Phys.*, Vol. 100, pp. 335-354 (1992)
8. Sussman, M., Smereka, P. Osher, S., "A level set approach for computing solutions to incompressible two-phase flow," *J. Compt. Phys.*, Vol. 114, p. 146-159 (1994)
9. Lafaurie, B, Nardone, C, Scardovelli, R., Zaleski, S. and Zanetti, G., "Modeling Merging and Fragmentation in Multiphase Flows with SURFER," *J. Compt. Phys.*, Vol. 113, pp. 134-147 (1994)
10. Hwang, Y.-H., "Arbitrary Domain Velocity Analyses for the Incompressible Navier-Stokes Equations," *J. Compt. Phys.*, Vol. 110, pp. 134-149 (1994)
11. Press, W. H. and Teukolsky, A., "Multigrid methods for boundary value problems I and II," *Computers in Physics*, Sep/Oct (1991)
12. Schneider, G. E., and Zedan, M., "A Modified Strongly Implicit Procedure for the numerical solution of field problems, "*J. Compt. Phys.*, Vol. 4, pp. 1-19 (1981)
13. Becker, E. Hiller, W. J. and Kowalewski, T. A., "Nonlinear dynamics of viscous droplets," *J. Fluid Mech.*, Vol. 258, pp. 191-216 (1994).
14. Chin, L. P., "A Numerical Study of Collision Behavior between Droplets," Presented at the 1996 Central States Section Meeting of the Combustion Institute, May 5-7, 1996, St. Louis, MO.

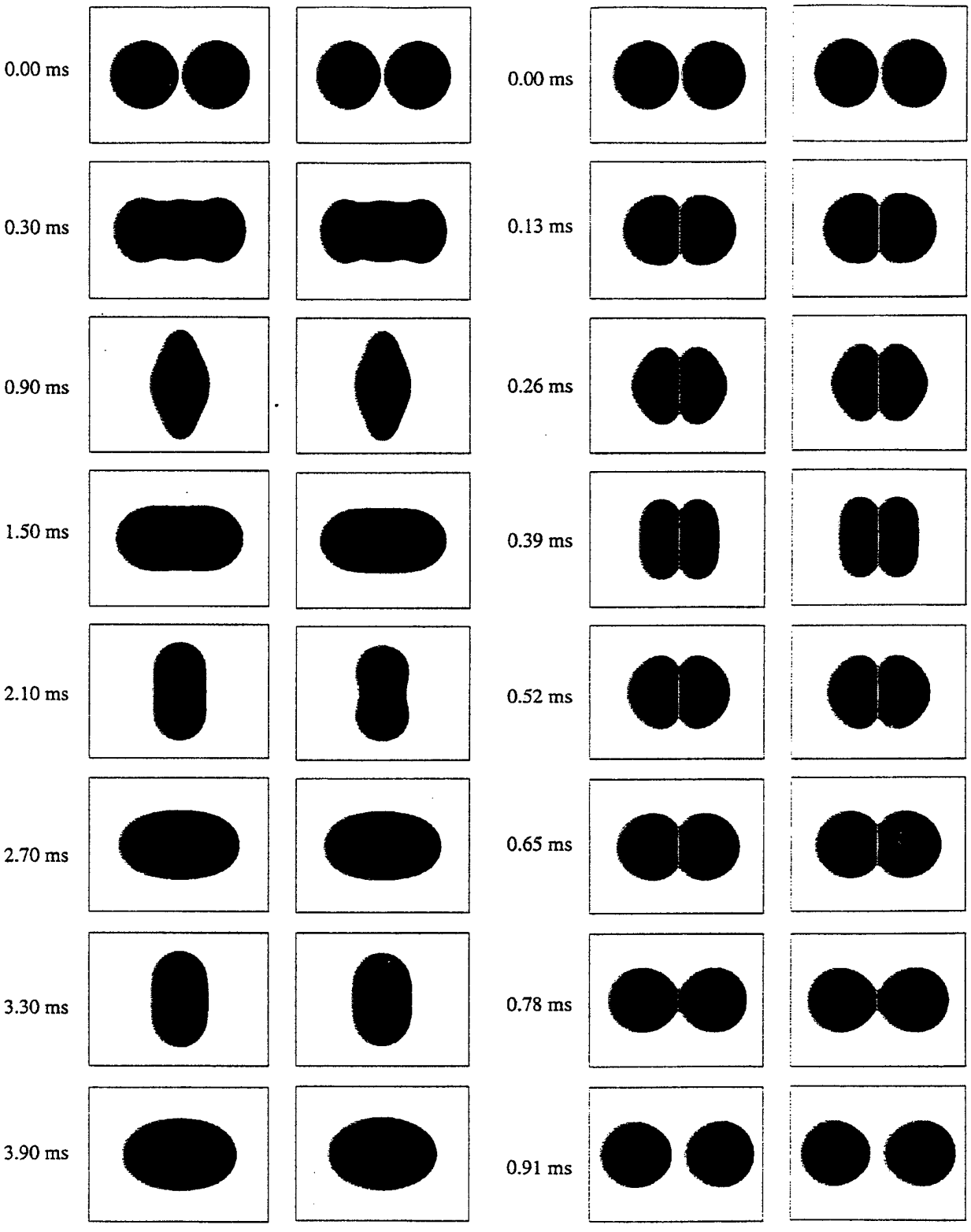

Figure 1. Sequences of head-on collision for four different modes : (I) V=0.07 m/s; (II) V=0.32 m/s; (III) V=0.62 m/s; (IV) V=1.15 m/s. For each conditions axiymmetric simulations are shown on the left column and 3-D simulations are shown on the right column

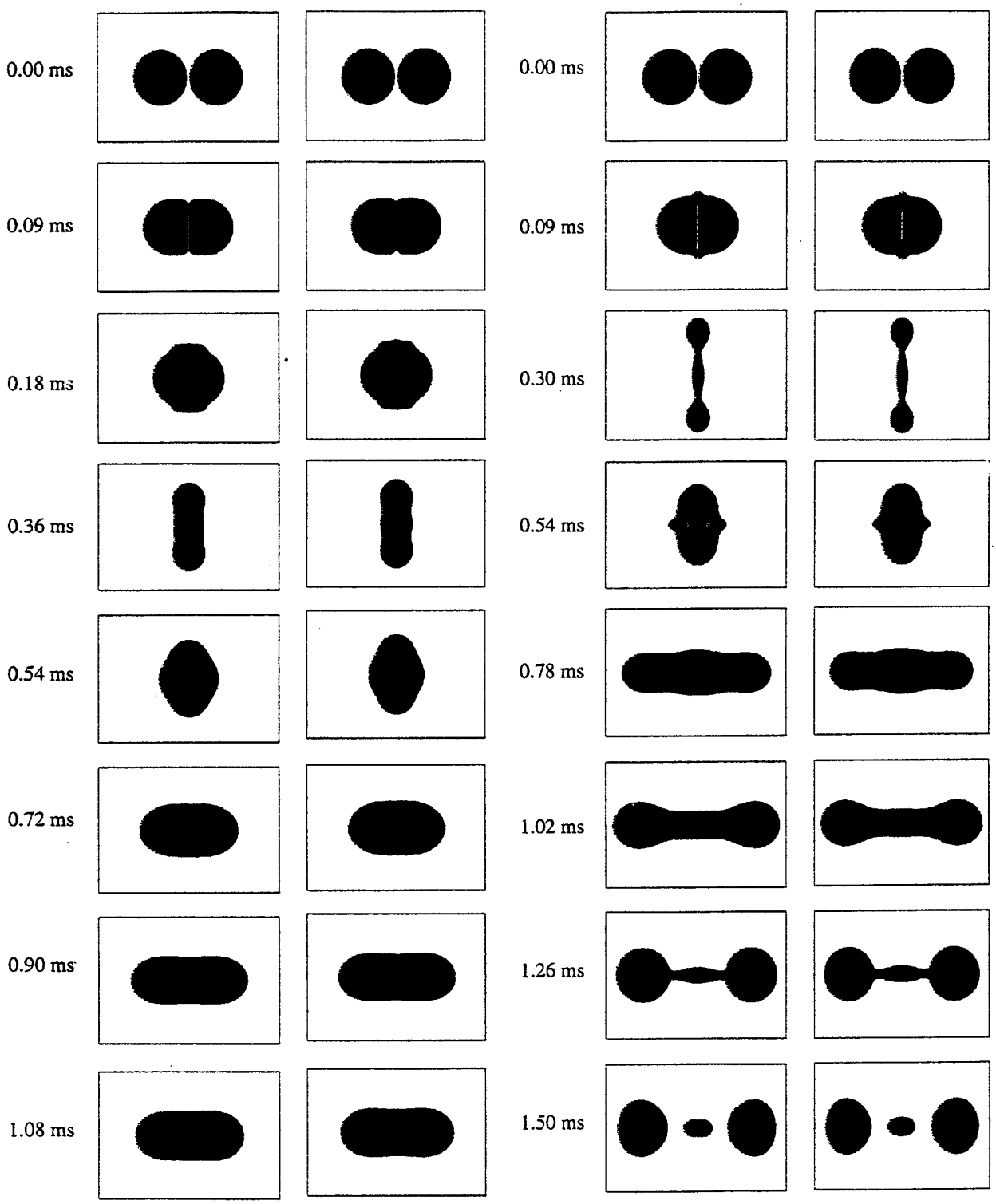

(III) : V= 0.62 m/s

(IV): V= 1.15 m/s

Caption see last page

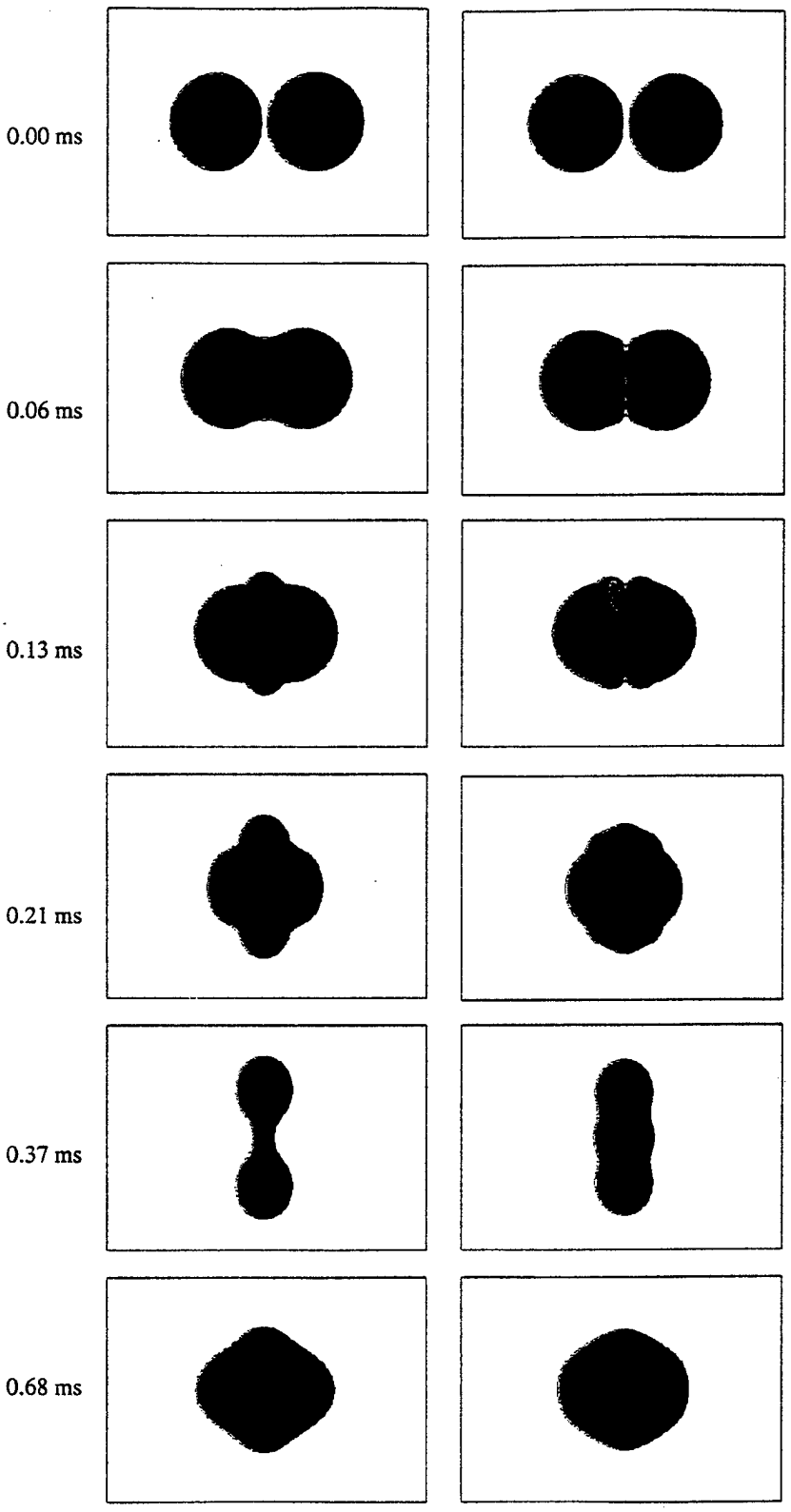

(a) Unforced coalescense (b) Forced coalescense

Figure 2. Comparison of droplet collision at V= 0.62 m/s. (a) Unforced coalescence (b) Force coalescence

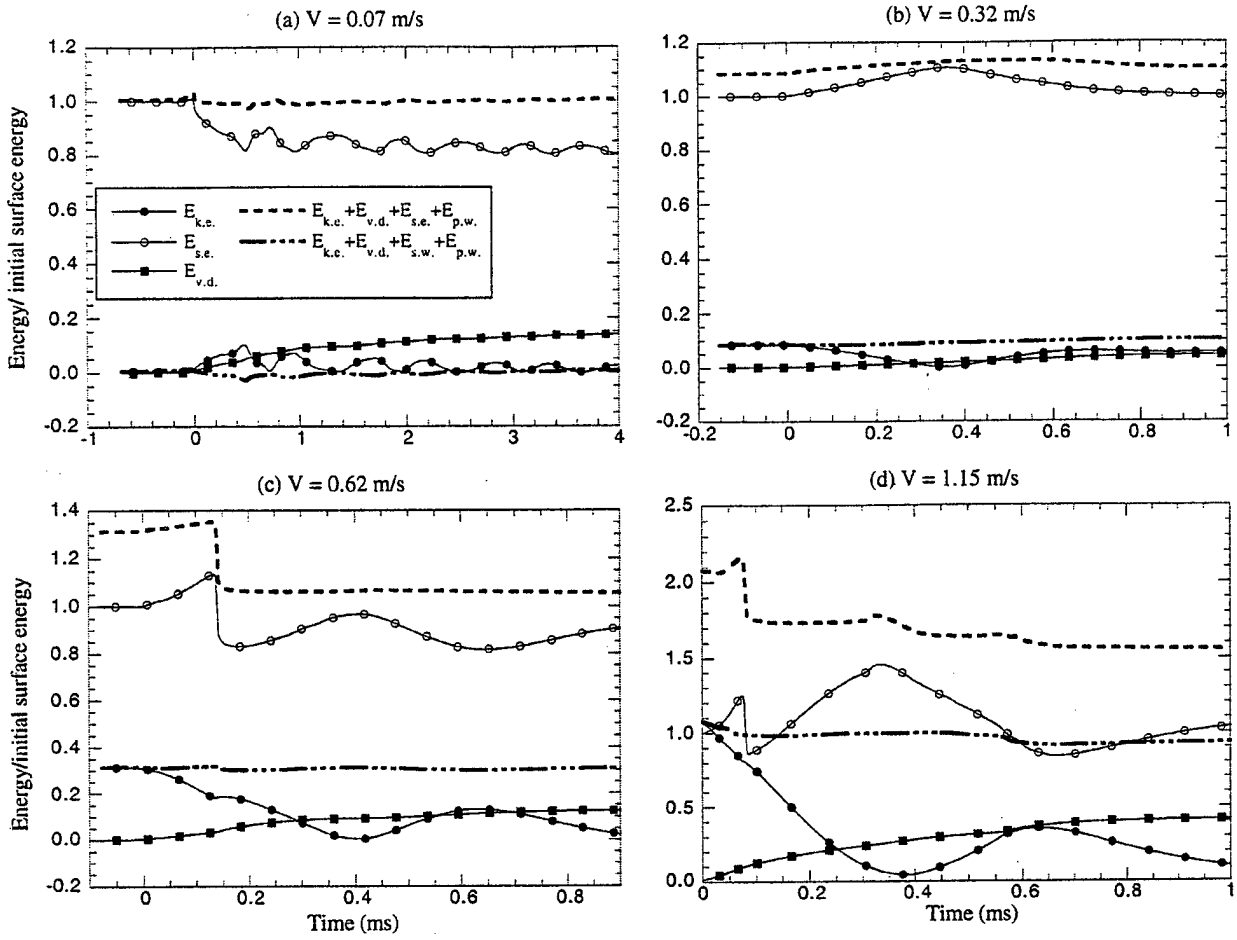

Figure 3. Histories of various energy modes for all four flow conditions. (a) V=0.07; (b) V=0.32; (c) V=0.62; (d) V=1.15 m/s

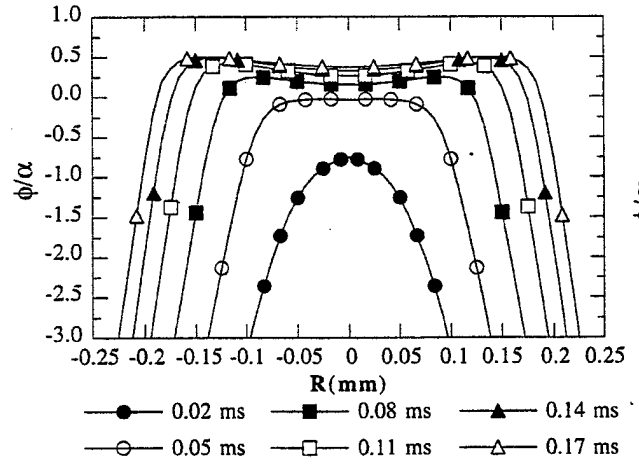

Figure 4. Distribution of the distance function along the contact line (normalized by the interface thickness)

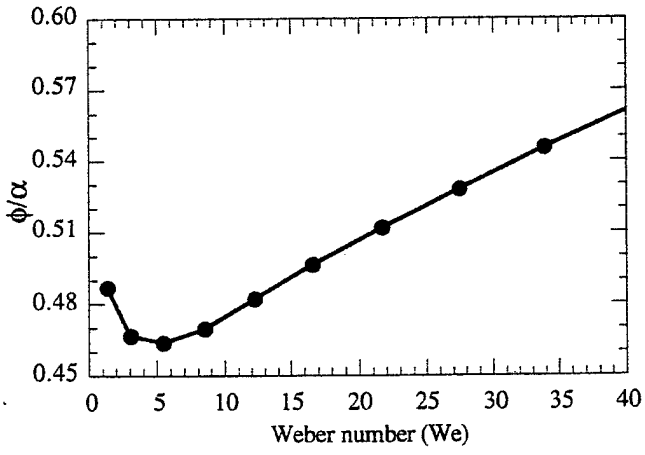

Figure 5. Maximally allowed clearance for various Weber numbers

4.2 MODELING OF FUEL THERMAL STABILITY

4.2.1 Overview

The thermal stability of jet fuels results from a complex set of chemical reactions, and the deposition process is further complicated by physical mechanisms such as agglomeration and solvation. Although a vast amount of experimental data has been obtained by several research groups, the specific mechanisms responsible for thermal degradation of fuels and the consequent deposit-formation process are still largely unknown. This results primarily from the fact that the fluid and the heat transfer that influence the deposition process vary significantly from experiment to experiment. The CFDC models are thought to be useful for correlating the data obtained from a number of experiments and, thereby, exploring this large database to aid the understanding of the deposition phenomenon. The success of this approach depends on the accuracy of the global-chemistry models used in the CFDC codes. The results of applying CFDC codes to guide the study of fuel thermal stability are discussed below.

4.2.2 Fuel Thermal Stability

The results of using a chemical-kinetics model employing global reactions to simulate fuel deposition under specific flow conditions are reported in the paper entitled "Global Kinetic Modeling of Aviation Fuel Fouling in Cooled Regions in a Flowing System." This paper was co-authored by J. S. Ervin, T. F. Williams (both of the University of Dayton Research Institute), and V. R. Katta and published in Industrial and Engineering Chemistry Research, Vol. 35, pp. 4028-4036 (1996). A nine-step global-chemistry model was developed to predict quantities such as oxygen consumption, surface deposits, hydroperoxides, and bulk insolubles. This new model is discussed in the paper entitled "Modeling of Deposition Process in Liquid Fuels" (see pp. 1133-1145). The results of a numerical and experimental study on pyrolysis and pyrolytic deposition of Norpar-13 under high-pressure and low-temperature conditions are reported in the paper entitled "Modeling of Pyrolysis and Pyrolytic Deposition of Norpar-13 under Supercritical Conditions" (see pp. 1146-1149). A three-step global model was developed to describe the thermal cracking of Norpar-13 under supercritical and near-critical conditions; this model is described in the paper entitled "Thermal Cracking of Norpar-13 under Near-Critical and Supercritical Conditions" (see pp. 1150-1158). The nine-step global-chemistry model was found to improve the accuracy of predicting quantities such as oxygen consumption, surface deposits, hydroperoxides, and bulk insolubles. A comparison of experimental and numerical results with the nine-step global-chemistry model is documented in the publication entitled "Modeling of Deposition Process in Liquid Fuels" (see pp. 1159-1195).

AIAA 97-3040

Modeling of Deposition Process in Liquid Fuels

V. R. Katta and E. G. Jones
Innovative Scientific Solutions, Inc
Dayton, OH

W. M. Roquemore
Wright Laboratory
Wright-Patterson AFB, OH

33rd AIAA/ASME/SAE/ASEEJoint Propulsion Conference & Exhibit
July 6 - 9, 1997 / Seattle, WA

For permission to copy or republish, contact the American Institute of Aeronautics and Astronautics 1801 Alexander Bell Drive, Suite 500, Reston, VA 22091

Modeling of Deposition Process in Liquid Fuels

Viswanath R. Katta* and E. Grant Jones+
Innovative Scientific Solutions, Inc.
2786 Indian Ripple Road
Dayton, OH 45440-3638

and

W. M. Roquemore++
Wright Laboratory
Wright-Patterson Air Force Base, OH 45433-7103

Abstract:

The thermal stability of jet fuels results from a complex set of chemical reactions, and the deposition process is further complicated by physical mechanisms such as agglomeration and solvation. Although a vast amount of experimental data has been obtained by several researchers, the specific mechanisms responsible for thermal degradation of fuels and the consequent deposit-formation process are still largely unknown. This is primarily due to the fact that the fluid flow and the heat transfer which influence the deposition process vary significantly from experiment to experiment. It is thought that Computational Fluid Dynamics with Chemistry (CFDC) models can be used to correlate the data obtained from a number of experiments and, thereby, explore this large data base to aid the understanding of the deposition phenomenon. The success of this approach depends on the accuracy of the global-chemistry models used in the CFDC codes. Recent experiments on blended fuel prepared by mixing a hydrotreated fuel with a non-hydrotreated one suggest that the thermal stability of the blend cannot be linearly extrapolated from the thermal-stability characteristics of the neat fuels. The global-chemistry models developed previously are found to be insufficient for the simultaneous prediction of deposition and oxidation rates associated with the blended fuel; however, a nine-step model recently developed appears to yield qualitatively correct results. The rate expressions for the bulk-fuel reactions in this model are modified to take into account antioxidant behavior in jet fuels. The modified nine-step global-chemistry model not only improves the accuracies in predicting quantities such as oxygen consumption and surface deposits but also provides additional capabilities for predicting quantities such as hydroperoxides and bulk insolubles.

Introduction:

Before fuel in an aircraft is burned in the combustion chamber, it is used to cool several engine and airframe components as well as electronic equipment. The bulk-fuel temperature and the high wall temperature of these components lead to degradation of the fuel (i.e., chemical decomposition of fuel resulting in the formation of gums and solids that cause fouling of fuel nozzles and heat exchangers). Several laboratory experiments of the flowing[1,2] and static[3] type have been designed to study the thermal stability of jet fuel. Temperature is usually treated as an effective parameter[4] for correlating experimentally obtained data and fuel behavior in aircraft. Recent studies[5,6] have indicated strong involvement of certain species such as dissolved oxygen and hydroperoxides in the fouling process. In order to extend the findings derived from these laboratory experiments to real aircraft fuel systems, a thorough understanding of the experimental data is needed. However, since high temperatures are normally used to accelerate the experiments performed in studies on fuel thermal stability, often there is no correlation between the results of the different laboratory experiments and no knowledge of how the results are related to the thermal decomposition of the fuel in aircraft fuel-system components. Recently a general theoretical framework was established by integrating the Computational Fluid Dynamics conservation equations with global-chemistry models for the investigation of thermal-decomposition mechanisms.[7] The resulting Computational-Fluid-Dynamics-with-Chemistry (CFDC) models offer potential for predicting fuel behavior in an engine component based on knowledge gained from laboratory experiments. The success of this approach depends on the development of a universal global-chemistry model that can be calibrated for a given fuel by laboratory experiments and the ability of the model to predict deposition over a wide range of flow and temperature conditions for any fuel-system component.

Significant progress has been made in the use of CFD models to predict fluid and thermal characteristics in the complex geometries of practical systems. On the other hand, developments in the chemistry modeling of thermal deposition have been hindered by the lack of fundamental understanding of the complex fuel-degradation processes. Recent studies have shown the usefulness of the CFDC approach with simple global-chemistry models for predicting fuel thermal stability under different conditions in heated-tube experiments[8,9,10] and in complicated geometries.[11] These

* Senior Engineer, Member AIAA
+ Senior Chemist
++Senior Scientist, Member AIAA
This paper declared a work of the U. S. Government and is not subjected to copyright protection in the United States.

successes offer a hope that the CFDC models will become useful tools for research as well as fuel-system component design.

This paper describes several global-chemistry models that have recently been developed and their relationship to the current understanding on semi-detailed chemistry for jet-fuel thermal stability. Also testing of the most recently developed nine-step global-chemistry model for its ability to predict the thermal-stability characteristics of blended fuels obtained by mixing hydrotreated and non-hydrotreated Jet-A fuels. Finally, details are given on modifications proposed and implemented into the nine-step global-chemistry model not only for improving accuracies in predicting quantities such as oxygen consumption and surface deposits but also for predicting additional quantities such as hydroperoxides and bulk insolubles.

Background:

The susceptibility of hydrocarbon fuel to thermal degradation is usually referred to as thermal instability and is believed to result from a set of complex chemical reactions. Even though the detailed chemical reactions that result in fuel deposits are poorly understood, it is well recognized that the thermal instability of a hydrocarbon fuel depends on many factors such as fuel type, temperature, pressure and the material in contact with the fuel.[1,5,12,13,14] The effect of these factors on deposition has been investigated experimentally under both the static and flowing conditions. Several researchers have reported[6,15,16,17] that the reaction is usually initiated by liquid-phase oxidation of the fuel, which is promoted by dissolved oxygen. The early investigations of Taylor,[13,14] which provide the major source of reliable information on fouling of hydrocarbon fuels, suggest that the principal class of fouling reactions is auto-oxidation polymerization which is propagated by a free-radical chain-reaction mechanism in which dissolved molecular oxygen plays a crucial role. Common impurities such as compounds of sulfur, nitrogen, and dissolved metals play a role by either accelerating the reactions or affecting the solubility of the degradation products. On the other hand, at high temperatures (> 750 K), the deposition reaction is characterized by the pyrolysis of hydrocarbon molecules and the scission of hydrocarbon. The general free-radical mechanism agreed upon by several researchers and outlined by Jones et al.[18] is given bellow.

Initiation:

$RH + O_2 \longrightarrow R^{\bullet}$ (1a)

$ROOH \longrightarrow RO^{\bullet} + {}^{\bullet}OH$ (1b)

Propagation:

$R^{\bullet} + O_2 \longrightarrow ROO^{\bullet}$ (1c)

$ROO^{\bullet} + RH \longrightarrow ROOH + R^{\bullet}$ (1d)

Termination:

$ROO^{\bullet} + ROO^{\bullet} \longrightarrow$ non-radical products (1e)

$ROOH + R'S \longrightarrow$ gums, solids (1f)

Here, RH and R'S represent hydrocarbon fuel and a peroxide-decomposing sulfur compound, respectively; $R^{\bullet}$, $RO^{\bullet}$, and $ROO^{\bullet}$ represent alkyl, alkoxy and peroxy radicals, respectively; and ROOH represents hydroperoxides.

Studying the rates of oxidation and gum formation in different fuels, Mayo and Lan[19] found that some fuels oxidize faster when initiators such as t-BU_2O_2 are added. Based on these studies they proposed that gum formation is initiated with coupling of two alkyl peroxyl radicals in the chain termination of oxidation. It is now generally thought that fuel-degradation products such as soluble gums, insoluble gums, and solids are formed by termination steps in the above oxidation mechanism.

The reaction paths (1a)-(1f) describe the oxidation and deposition processes globally; in fact, each of these steps represents several elementary reaction steps. As discussed by Zabarnick,[20] no generally accepted rate parameters exist for the pseudo-global reactions (1a)-(1f). Even though a detailed description of autoxidation and thermal degradation of hydrocarbon fuel may be formulated by conducting a study on several fuels over a wide range of conditions, the above-described general mechanism yields valuable insights for developing global-chemistry models for the thermal stability of fuels.

Global Models for Thermal Stability:

Early deposition models were primarily based on the assumption that the quantity of carbon deposited on metal walls is proportional to the amount of heat transferred up to that time (or temperature). These models are basically obtained by representing the mechanism (1a)-(1f) using the global reaction

Fuel ---> Deposits (2a)

The deposition rate is given by

$$\frac{dD}{dt} = \alpha A_{2a} e^{\left(\frac{-E_{2a}}{RT}\right)} \qquad (2b)$$

Here, D represents deposits on a metal surface, and α is a constant which may be a function of velocity. Because of the over simplifications used, these models mask the physical and chemical structures of the deposition process; however, they are still found to be useful as engineering tools.[21]

Two-Step Global Model:

A two-step kinetic reaction mechanism was postulated and successfully applied to a number of heated-tube experiments by Giovanetti and Szetela.[16] By representing the oxygenated species (hydroperoxides, alcohols, ketones,

and carbon monoxide) formed during thermal stressing of the fuel as intermediary precursor (P) to the deposits (D), they postulated the following two-step reaction mechanism:

$$\text{Fuel} + O_2 \text{ ---> Fuel} + P \quad (3a)$$
$$\text{Fuel} + P \text{ ---> Fuel} + D \quad (3b)$$

The reaction rates are given by

$$RR_{3a} = [O_2] A_{3a} e^{\left(\frac{-E_{3a}}{RT}\right)} \quad (3c)$$

$$RR_{3b} = [P] A_{3b} e^{\left(\frac{-E_{3b}}{RT}\right)} \quad (3d)$$

In comparison with the mechanism given by Eqs. (1a)-(1f), the first reaction step (3a) of the Giovanetti and Szetela mechanism may be considered the propagation step and the second one (3b), the termination step. This simplification is valid only when the concentrations of R$^\bullet$ and ROO$^\bullet$ are significant. Usually, non-hydrotreated aircraft fuels contain some types of antioxidants which tend to control the concentrations of R$^\bullet$ and ROO$^\bullet$ through the termination step (1f).

In addition to the limitations of the above two-step global mechanism in modeling various fuels, the model has two major drawbacks: 1) It does not take into account mass-transfer effects; 2) It does not have possible precursor-decomposition reactions which are relevant at high temperatures. The experiments of Marteney and Spadaccini[1] and Taylor[14] indicate that at higher temperatures (> 645 K), the deposition rate decreases suddenly. This sudden decrease may be due to possible mass-transfer resistance at higher temperatures and/or precursor decomposition. Marteney and Spadaccini[1] also studied the effect of fuel velocity on deposition rate and found that the reactions become mixing (or transport) limited at elevated temperatures. Clark and Thomas[22] also found that deposition may be dominated by physical transport or a chemical-reaction process, and the relative importance of these factors is fuel dependent.

Three-Step Global Model:

In an attempt to improve deposition modeling by incorporating mass-transfer effects and the precursor-decomposition process, Deshpande et al.[23] proposed the following three-step global mechanism.

$$\text{Fuel} + O_2 \text{ ---> Fuel} + P \quad (4a)$$
$$\text{Fuel} + P \text{ ---> Fuel} + D \quad (4b)$$
$$\text{Fuel} + P \text{ ---> Fuel} + CO_2 \quad (4c)$$

It is assumed that reactions (4a) and (4c) occur in the bulk and that reaction (4b) occurs on the wall surface. As a result, the reaction rate (RR_{4c}) for Eq. (4b) is calculated using the concentration of precursor on the wall surface. The time rates of change of the active species are given by

$$\frac{d[O_2]}{dt} = -RR_{4a} \quad (4d)$$

$$\frac{d[P]}{dt} = RR_{4a} - RR_{4c} - R_m \quad (4e)$$

$$\frac{d[D]}{dt} = RR_{4b} \quad (4f)$$

Here, the mass-transfer rate, R_m is given by

$$R_m = K_m s ([P]-[P]_s)$$

where K_m is the mass-transfer coefficient, s is surface area, and $[P]_s$ is the concentration of precursor at the wall which is calculated from molecular diffusion of bulk precursor.

The limited comparisons of predictions and available experimental data[23] have indicated that the results obtained with the three-step model are only marginally improved over the predictions made by Giovanetti and Szetela[16] using their two-step model. However, the significant improvement in deposition modeling made by Deshpande et al.[23] through the incorporation of mass-transfer effects and the precursor-decomposition process may be recognized when results for oxygen consumption and deposit formation are compared simultaneously. Equations (3a) and (3b) require that at any time during the reaction, the sum of the concentrations of oxygen, precursor, and deposit must be constant and equal to the initial concentration of oxygen (assuming that the initial concentrations of precursor and deposit species are negligible). Because of this constraint on species concentration, Giovanetti and Szetela[16] were forced to use an initial concentration of oxygen of only 16% of the value for air-saturated fuel in order to match the predicted and measured maximum deposition rates. This anomaly between initial oxygen concentration and peak deposition rate was resolved in the three-step model since only a fraction of the generated precursor transforms into deposition; the rest either remains in the fuel (because of mass-transfer effect) or is converted into solubles [through Eq. (4c)].

The success with the three-step global model is limited, in part, by the one-dimensional analysis which Deshpande et al.[23] used for the prediction of heated-tube experiments in which large gradients for temperature and, hence, species concentrations exist across the tube. Recognizing the barrier to the development of thermal-stability models imposed by fluid-dynamics simplifications, Roquemore et al.[7] proposed a general theoretical framework by integrating the Computational Fluid Dynamics (CFD) conservation equations with global-thermal-stability models. Krazinski et al.[8] implemented such a framework for studying deposition process in heated-tube experiments by incorporating a three-

step deposition model in a steady-state two-dimensional CFD code.

The three-step model that Krazinski et al.[8] used is identical to the three-step model [Eqs. (4a)-(4c)] described previously. Krazinski et al.[8] assumed that the precursor generated in the bulk fuel is transported to the wall through convection and diffusion, adheres to the wall, and then transforms into deposits. The last two processes were represented globally with a wall reaction such as Eq. (4b). The CFDC approach for predicting thermal stability of fuels was further extended by Katta and Roquemore[9,24] for the prediction of real-time deposition process in a heated tube and by Chin and Katta[11] for the prediction of deposition in complex geometries such as aircraft fuel nozzles. The three-step model of Krazinski et al.[8] used in all these investigations was found to yield reasonable predictions for a variety of flow and thermal conditions.

Nine-Step Global Model:

Recent experimental efforts of Jones et al.,[18] Heneghan et al.,[25] Hardy,[26] and Kauffman et al.[27] suggest that 1) the rate of autoxidation in the majority of fuels is nearly independent of dissolved-oxygen concentration, 2) the deposit-forming precursor is generated through chemical reactions involving hydroperoxides but not directly from reactions involving molecular oxygen, and 3) fuels which oxidize rapidly tend to form more gums and less solids or deposits. The semi-detailed thermal-stability model [Eqs. (1a)-(1f)] described earlier accounts for all of these observations, whereas the two- or three-step global models developed for the prediction of deposition are not capable of addressing these issues.

A new nine-step thermal-stability model has been proposed by Katta et al.[28] for the simultaneous prediction of autoxidation and deposit formation in different flowing systems. The model was formulated based on observations made during static flask and dynamic tube experiments and consists of both bulk-phase and wall reactions. The six bulk reactions used in this model are as follows:

$$O_2 + \text{Fuel} \longrightarrow \text{ROOH} \quad (5a)$$
$$\text{ROOH} + \text{Fuel} \longrightarrow \text{Solubles} \quad (5b)$$
$$\text{ROOH} + F_s \longrightarrow P \quad (5c)$$
$$P + \text{Fuel} \longrightarrow \text{Solubles} \quad (5d)$$
$$\text{ROOH} + \text{Fuel} \longrightarrow D_{bulk} \quad (5e)$$
$$D_{bulk} + \text{Fuel} \longrightarrow 2\,D_{bulk} \quad (5f)$$

In this global model the species ROOH represents either ROOH or ROO˙. The first step (5a) of the nine-step model represents the propagation step in the general formulation [i.e., Eq. (1b)], the second, third, and fifth steps represent the termination reactions (1e) and (1f); the fourth step is the precursor-removing reaction; and finally, the agglomeration of bulk particles is represented chemically with the sixth step. F_s [or R'S in Eq. (1f)], a non-depleting sulfur compound present in the fuel which usually promotes the deposition process. This model closely follows the general formulation, except that it has no initiation and propagation reactions for controlling the autoxidation process. It was assumed that if the oxygen consumption in a fuel is described by Eq. (5a), then by choosing the appropriate activation energy and pre-exponential factor, the above six bulk reactions can represent the thermal stability of hydrocarbon fuels. The specific reaction rates for the six reactions are obtained assuming that the reactions are elementary in nature (i.e., based on the reactant concentrations). However, for fitting the autocatalysis-type oxidation behavior of the aviation fuels, the reaction rate for Eq. (5a) is made independent of oxygen concentration (i.e., zeroth-order reaction).

In addition to the six bulk reactions (5a)-(5f), three wall reactions were also used in the above model to describe the entrainment and sticking processes of O_2, P, and D_{bulk} – which, eventually transform to surface deposits after attaching to the walls. The nine-step model, in general, yielded very good predictions for surface deposits under significantly different flow and heating conditions. Some of the comparisons between model predictions and experimental data are given in References 10,11,28. Even though the model predicts the concentration distributions for ROOH and D_{bulk}, these distributions do not compare well with the experimental data due, in part, to the insufficient representation of production and destruction mechanisms for intermediate species such as ROOH and D_{bulk} in the nine-step model.

Results and Discussion:

Thermal Stability of Fuel Blends:

The fuel in advanced aircraft will be subjected to a more hostile environment from a temperature viewpoint since these aircraft will generate increased heat loads. To avoid the problems associated with the thermal decomposition of fuel at these expected elevated temperatures, researchers are increasingly concentrating on the development of methods of mitigating fuel-fouling processes. A fundamental method of quantitatively improving the thermal-stability characteristics of a lesser-quality fuel is to introduce additives which may be cost effective compared to refining techniques. An obvious extension of this approach is to consider the potential impact on thermal stability of a fuel mixture obtained by blending two fuels having drastically different thermal-stability characteristics. Recent studies conducted on fuel mixtures include the work of Zabarnick et al.,[29] Balster et al.,[30] and Jones et al.[31]

For the modeling of thermal stability of a jet fuel in a flowing system, the global-chemistry models described previously must be calibrated specifically for that fuel. This is mainly because of the lack of fundamental data such as concentrations of constituent species in that fuel. When two

fuels are blended, then the constituent species in that mixture can be obtained by a linear combination of constituent species of individual species. This suggests that the global-chemistry model of a mixture can be derived from the calibrated global-chemistry models of the individual species. Of course, the success of this approach depends on the accuracy of the model used. In other words, the accuracy of a global-chemistry model in describing the thermal-stability characteristics of a fuel may be tested by predicting the characteristics of a blended fuel using the models calibrated for the individual fuels.

Jones et al.[31] found that the thermal-stability characteristics of a mixture obtained by blending POSF-2827 and POSF-2747 Jet-A fuels could be improved only if the percentage of the former fuel in the mixture is significantly low. These two fuels were previously studied[32] individually with regard to thermal-stability behavior. It is known that the hydrotreated Jet-A fuel (POSF 2747) belongs to a class of highly stable fuels, and the dissolved oxygen in this fuel will be consumed rapidly (typically, in about 3 min. at 185 K) when the fuel is heated and at the same time will generate very few deposits. On the other hand, POSF-2827 is a straight-run (non-hydrotreated) Jet-A fuel containing significant amounts of sulfur compounds as impurities. Investigations on this fuel revealed that the dissolved oxygen is consumed very slowly when the fuel is heated (for example, 13 min. at 185 K) and, at the same time, significant amounts of bulk and surface deposits are generated. This inverse behavior between oxygen consumption rate and deposition rate in jet fuels was found by several investigators, and a comprehensive report based on a number of fuels was prepared by Hardy et al.[26]

The experimental data obtained by Jones et al.[31] for two fuels (POSF-2827 and POSF-2747) and for different mixtures of these fuels are shown in Figs. 1 and 2. These measurements were made using the experimental rig known as NIFTR (Near-Isothermal Flowing Test Rig). The details of the rig, the measuring techniques employed, and the data-reduction procedures used are described elsewhere.[18,30] The experiments conducted to obtain the data shown in Figs. 1 and 2 employed a constant temperature of 185 K. Figure 1 shows the consumption of dissolved oxygen; Figure 2 shows the surface-deposition rate with stress duration. It is important to note that the stress duration for the oxygen-consumption data is varied by changing the residence time (flow rate) in a fixed-length heated tube, whereas the stress duration in Fig. 2 represents the location of the fuel element moving at a constant velocity (flow rate). In the absence of surface reactions, these two times should represent the same under isothermal conditions. Since the thermal-deposition process is significantly affected by the surface reactions, the stress time obtained with constant velocity may not represent the events recorded at the same stress time obtained by varying the velocity. For this reason, calculations were made using a CFDC code known as "foul2d" for the individual experiments. A brief description of the code is given bellow [details are given in Ref. (9)]:

Fluid motion inside the tubular test section is assumed to be axisymmetric and bounded by the fuel-deposit interface. The time-dependent Navier-Stokes equations along with the turbulent-energy, species-conservation, and enthalpy equations are solved in the x-r cylindrical coordinate system. The transport properties along with the

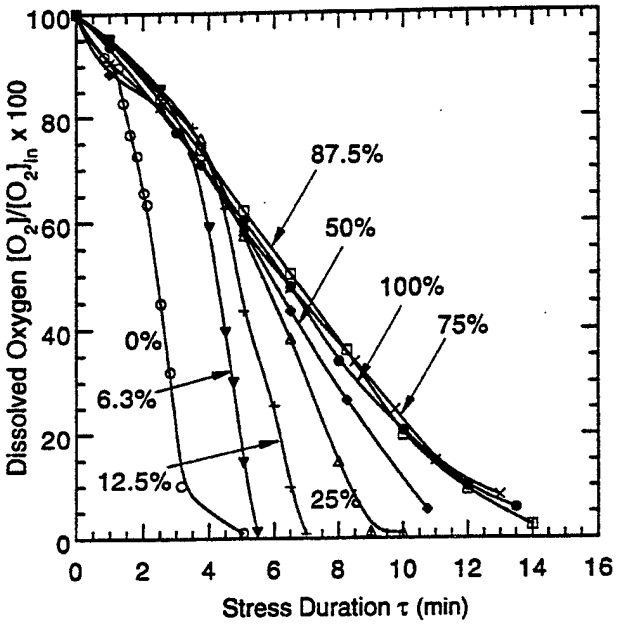

Fig. 1. Measured oxygen consumption in POSF-2827 and POSF-2747 blends.

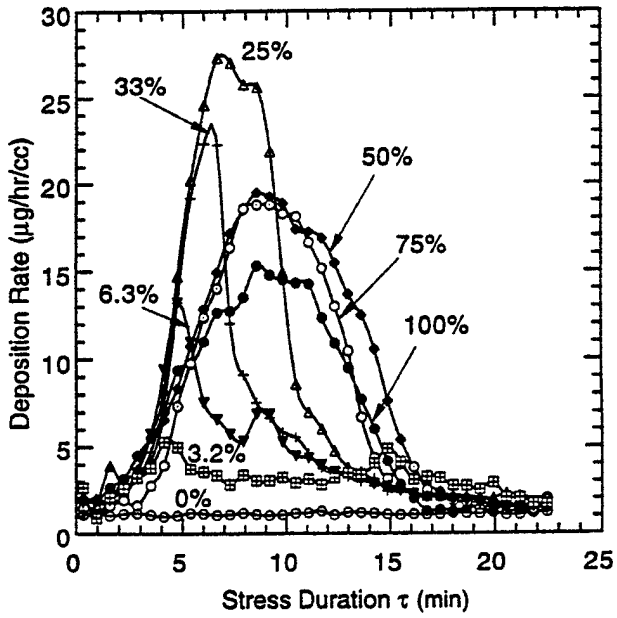

Fig. 2. Measured surface deposition rate in POSF-2827 and POSF-2747 blends.

enthalpy and density at a given temperature are obtained from the curve fits developed for Jet-A fuel. The governing equations are discretized utilizing a hybrid scheme[33] which is a second-order central-differencing scheme everywhere but changes to a first-order upwind scheme when the local Peclet number becomes greater than two. An implicit approach is employed to advance the calculations using a large time-step. This allows the calculations to be performed for real times ranging from minutes to thousands of hours. For the turbulent-flow calculations, wall functions have been used to determine the variations of the flow variables near the fuel-deposit interface.

Predictions for the thermal-stability of the blended fuels were made using the nine-step global chemistry model described previously. The calibration parameters in this model are 1) the activation energy and the pre-exponential factor for the autoxidation reaction (5a) and 2) the concentration of F_s which represents the amount of sulfur compounds present in fuel. Using the experimental data obtained for the neat POSF-2827 and POSF-2747 fuels, the global nine-step models were calibrated. The rate constants obtained for the autoxidation of POSF-2827 are $A_{5a} = 4.4 \times 10^{13}$ mole/m^3/s and $E_{5a} = 32{,}000$ cal/mole/K, and the concentration of F_s was found to be 100 ppm. Similarly, the calibration parameters obtained for POSF-2747 are $A_{5a} = 2.0 \times 10^{14}$ mole/m^3/s, $E_{5a} = 32{,}000$ cal/mole/K, and $F_s = 1.2$ ppm. Once the models for the neat fuel are calibrated then the global-chemistry model for a mixture of these two neat fuels is obtained by weight averaging of the pre-exponential and F_s values (note that the activation energies are the same). The weighting factors were determined from the mass fractions of POSF-2827 and POSF-2747 fuels in the blend.

Results obtained in the form of oxygen consumption and surface deposition for the two neat fuels and three blends are shown in Figs. 3 and 4, respectively. Here, the percentage number indicates the amount of POSF-2827 present in the blend. The neat POSF-2747 fuel is referred to as 0% blend. As expected, the model predicted that the oxygen-consumption rates for the blended fuels fall between the rates obtained for the two neat fuels. In general, as the oxygen consumption rate increases with dilution of POSF-2827, the location of the peak deposition rate shifts toward shorter stress times. Interestingly, the magnitude of the peak deposition rate initially increased for a dilution of up to 50% and then decreased with further dilution. The predictions for oxygen consumption (Fig. 3) and deposition (Fig. 4) obtained with the nine-step global-chemistry model qualitatively agree with the respective experimental data in Figs. 1 and 2. The measured oxygen-consumption rate for the blended fuels falls in between the rates obtained for the two neat fuels, and the peak deposition rate initially increases with dilution of POSF-2827. However, a critical comparison of predictions and measurements reveals some important deficiencies of the nine-step thermal-stability model.

The experimental data in Fig. 1 suggest that when POSF-2747 is added to POSF-2827, the rate of consumption of dissolved oxygen does not change significantly for dilution of up to 75% but then increases nearly exponentially with further dilution. Jones et al.[31] attributed this behavior to excess amounts of antioxidants present in the straight-run POSF-2827 fuel. Antioxidants in a fuel are known to tie-up the free radicals that are necessary

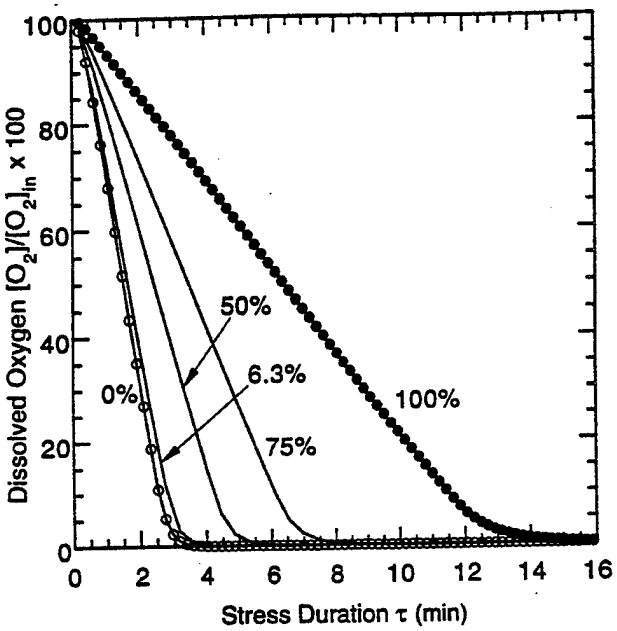

Fig. 3. Oxygen consumption in POSF-2827 and POSF-2747 blends predicted using nine-step global-chemistry

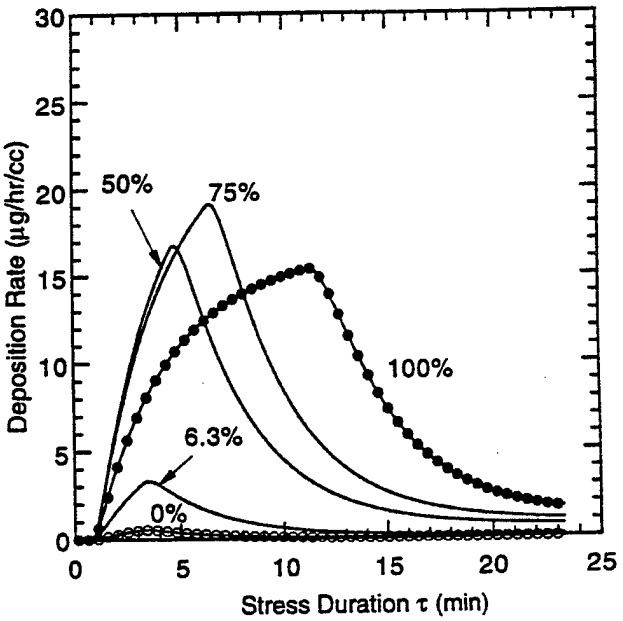

Fig. 4. Surface deposition rate in POSF-2827 and POSF-2747 blends predicted using nine-step global-chemistry model.

for the autoxidation process. Usually small amounts of antioxidants are sufficient to affect the autoxidation process. On the other hand, the negligible amount of antioxidants present in the hydrotreated POSF-2747 fuel does not influence the autoxidation process and, hence, dissolved oxygen is consumed rapidly in this neat fuel. When POSF-2827 is diluted with antioxidant-free POSF-2747, the effective concentration of antioxidant appears to decrease exponentially with dilution. On the other hand, since the autoxidation reaction (5a) used in the nine-step global model is not a direct function of antioxidant concentration (it needs to be calibrated for a given fuel), the autoxidation in blended fuels decreases exponentially with contamination of POSF-2747 fuel by POSF-2827 fuel. Note that in the model, the blended fuels are treated as linear combinations of the two neat fuels with respect to every constituent species.

Since the oxygen consumption in the blended fuel was not altered significantly for dilution of up to 75% (with respect to POSF-2827), the location of the peak deposition rate in the experiments (Fig. 2) did not move significantly from that of the neat POSF-2827. For the other blends having more diluted POSF-2827, the peak-deposition-rate location followed the oxygen-consumption rate and shifted exponentially toward shorter stress times. The peak deposition rate for all blends having at least 6.3% POSF-2827 is higher than that for the neat POSF-2827 . This higher deposition rate is attributed to the higher steady-state concentrations of hydroperoxides which mainly buildup when the oxygen consumption is delayed by antioxidants. The termination reaction (1f) is thought to be the main pathway responsible for deposition in jet fuels. The precursor-formation reaction (5c) in the nine-step global-chemistry model represents this termination process; hence, the predicted peak deposition rate increases when the neat POSF-2827 is diluted up to ~40% with POSF-2747. However, the amount of increase is much smaller than that obtained in the experiments. This could be due, in part, to the difficulty in predicting oxygen-consumption rates for the blended fuels.

Modified Nine-Step Model:

A close look at the semi-detailed, thermal-stability model [Eqs. (1a)-(1f)] suggests that the termination of hydroperoxides due to sulfur compounds (R'S) affects the propagation as well as the termination reactions. On the other hand, F_s in the nine-step model influences only the termination of hydroperoxides, having no bearing on the autoxidation reaction (5a) and, hence, on the production of hydroperoxides. Recently, Ervin et al.[34] incorporated the autoxidation mechanism described by Zabarnick[20] into the "foul2d" code and demonstrated that the rate of consumption of oxygen in the fuel can be controlled by varying the concentration of antioxidant or sulfur compounds. This mechanism consists of 17 bulk-phase reactions for the autoxidation process alone. When this mechanism is combined with the insoluble-formation and wall reactions to obtain a comprehensive description for the thermal stability of fuel, the resulting model (still a global one) could become very complicated and the number of "unknowns" in the model could make the calibration procedure using the limited data a near-impossible task. Further research must be performed to determine the rate constants from the first principles for at least some of the reactions involved in this model. Therefore, even though such comprehensive models could be extremely useful in understanding specific processes such the antioxidant behavior in fuels, incorporation of these models into the global-chemistry models for fuel thermal stability may not be possible in the near future. As an alternative approach, some of the problems associated with the nine-step model in predicting the blended-fuel characteristics can be overcome by making F_s in the model influencing all the reactions directly or indirectly. This can easily be done by treating the six reactions (5a)-(5f) as global reactions (i.e., reaction rate could be a function of reactants as well as other species). The proposed modifications for the rate expressions of the six reactions (5a)-5(f) are as follow:

$$k_{5a} = \left[\frac{1}{F_s}\right]^{0.4} A_{5a} e^{\left(\frac{-E_{5a}}{RT}\right)} \tag{5g}$$

$$k_{5b} = [F_s]^{0.4}[ROOH] A_{5b} e^{\left(\frac{-E_{5b}}{RT}\right)} \tag{5h}$$

$$k_{5c} = [F_s][ROOH] A_{5c} e^{\left(\frac{-E_{5c}}{RT}\right)} \tag{5i}$$

$$k_{5d} = \left[\frac{[O_2]_{in} - [O_2]}{[O_2]_{in}}\right][P] A_{5d} e^{\left(\frac{-E_{5d}}{RT}\right)} \tag{5j}$$

$$k_{5e} = [F_s][ROOH] A_{5e} e^{\left(\frac{-E_{5e}}{RT}\right)} \tag{5k}$$

$$k_{5f} = [D_{bulk}]^{0.4} A_{5f} e^{\left(\frac{-E_{5f}}{RT}\right)} \tag{5l}$$

Here, $[O_2]_{in}$ represents the initial concentration of dissolved oxygen present in the fuel and F_s, the equivalent concentration of sulfur compounds and antioxidants. According to the new rate expression (5g) for the autoxidation reaction (5a), the rate of consumption of oxygen decreases as the concentration of F_s increases. A hydrotreated fuel with a very low value of F_s depletes the dissolved oxygen rapidly. However, the modification incorporated to the rate expression for reaction (5a) affects the production of ROOH as well. The semi-detailed model for thermal stability suggests that the rate of oxygen consumption in the fuel is controlled by the steady-state concentration of ROOH which is modified by the presence of antioxidants and sulfur compounds. Therefore, the rapid buildup of ROOH with decreasing F_s in the modified nine-step model is controlled by accelerating the conversion of

ROOH into solubles using Eq. (5h). The rate expression (5i) is the same as the one used in the original model.

Several experiments have shown that the rate of surface deposition decreases to a near-zero value as the oxygen in the fuel is completely consumed which means that certain products generated during the oxidation of fuel tend to remove the deposit-forming precursor. This effect is integrated into the nine-step global model by making the rate expression (5j) for the precursor-destruction reaction proportional to the amount of oxygen depleted. The production of bulk particles in the modified nine-step model is also set proportional to the concentration F_s, and their agglomeration is limited by replacing power 1 with 0.4 in Eq. (5l).

The modified nine-step model is used to predict the thermal-stability characteristics of the blended fuels. The activation energy and pre-exponential factors for the six bulk-phase and three wall reactions used were the same as those calibrated for the neat POSF-2827 fuel and F_s in this fuel was fixed at 100 ppm. The neat fuel POSF-2747 is treated mathematically in the same way as the POSF-2827 fuel except that the concentration of F_s is only 1.2 ppm. Therefore, only one set of rate constants was used for the simulation of thermal-stability characteristics of two neat fuels and their blends.

The oxygen-consumption and surface-deposition rates in different mixtures of POSF-2827 and POSF-2747 fuels are shown in Figs. 5 and 6, respectively. As the neat POSF-2827 is diluted with the hydrotreated POSF-2747 fuel, the oxygen-consumption rate increases slightly for dilution up to 75% and then increases rapidly with further dilution. These consumption rates agree very well with those obtained in the experiments (Fig. 1). Following oxygen consumption, the location of the peak deposition rate in Fig. 6 for the blends also shifts toward shorter stress times--initially slowly and then more rapidly with POSF-2747 dilution. The mixture of 25% POSF-2827 and 75% POSF-2747 yields the highest deposition rate of ~ 27 mg/hr/cc. The peak deposition rates for different blends and neat fuels correspond well to those measured by Jones et al.[31]

The modified-nine-step model was developed to predict the concentrations of bulk deposits in stressed fuel along with oxygen-consumption and surface-deposition rates. Bulk deposits in the experiments are usually measured by placing a sub-micron-size filter in the fuel passage. Jones et al.[31] collected the bulk deposits in different blended fuels of POSF-2827 and POSF-2747 by placing a sub-micron-size filter in the fuel stream immediately downstream of the heated-tube test section. Therefore, the calculated concentrations of bulk deposits present in the fuel at the end of the heated-tube section were obtained for different fuel blends in the present simulations and plotted in Fig. 7 along with the total amount of surface deposits. The latter was obtained by integrating the area under each curve shown in Fig. 6. The corresponding data obtained from the experiments[31] are shown in Fig. 8. As the POSF-2827 fuel is mixed with POSF-2747, both the bulk and surface deposits (or insolubles) increase for dilution up to 25% with respect to the former fuel. While the neat POSF-2827 fuel yields more surface deposits than bulk deposits, the former gradually decreases with POSF-2747 dilution, whereas the latter gradually increases. Calculations showed that when the dilution level is increased to 50%, bulk insolubles exceed those collected on the surface. As dilution is

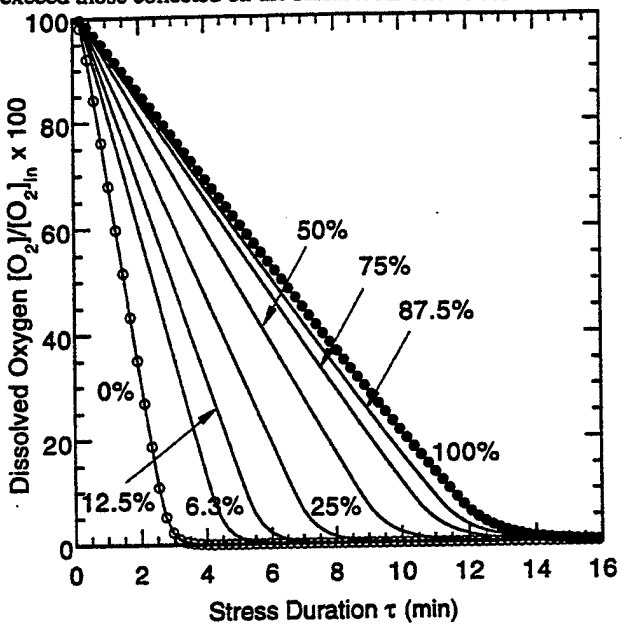

Fig. 5. Oxygen consumption in POSF-2827 and POSF-2747 blends predicted using modified nine-step global-chemistry model.

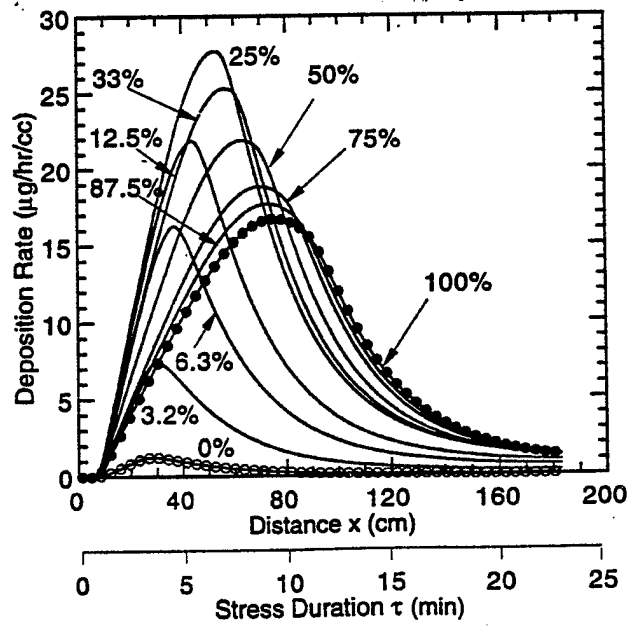

Fig. 6. Surface deposition rate in POSF-2827 and POSF-2747 blends predicted using modified nine-step global-chemistry model.

increased beyond the 25% level, both the surface and bulk deposits decrease rapidly, and a very small amount of deposits is predicted for neat POSF-2747 fuel. Similar trends in bulk and surface deposits with respect to dilution of POSF-2827 with POSF-2747 were observed in the experiments of Jones et al.[31] As shown in Figs. 7 and 8, good agreement between the predictions and experimental data was obtained.

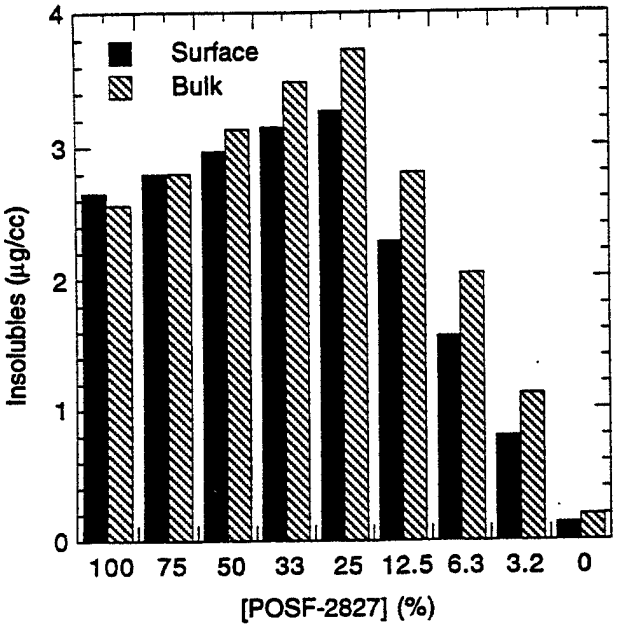

Fig. 7. Predicted total amount of surface and bulk deposits in POSF-2827 and POSF-2747 blends.

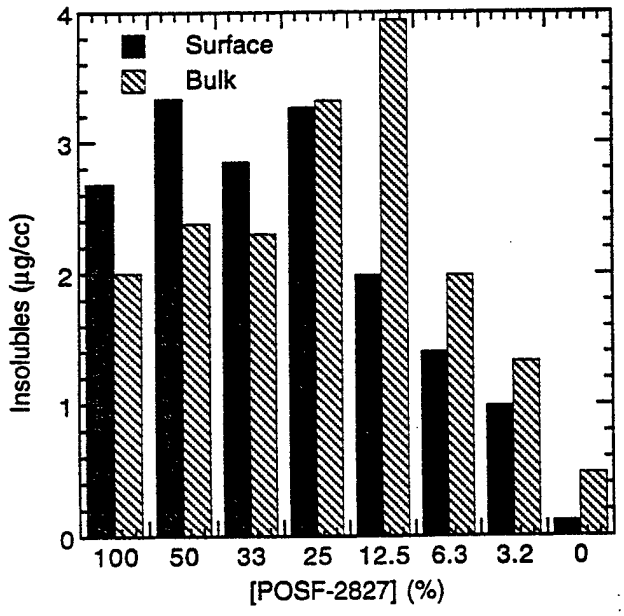

Fig. 8. Total quantity of surface and bulk deposits formed in POSF-2827 and POSF-2747 blends.

The calculated and measured[31] hydroperoxide concentrations for different fuel blends are shown in Figs. 9 and 10, respectively. In general, the concentration of ROOH decreases with the contamination of POSF-2747 with POSF-2827. The low concentration of sulfur compounds in the hydrotreated fuel is responsible for the build-up of ROOH. In contrast, the high concentration of Fs in the straight-run fuel (POSF-2827) is consuming most of the

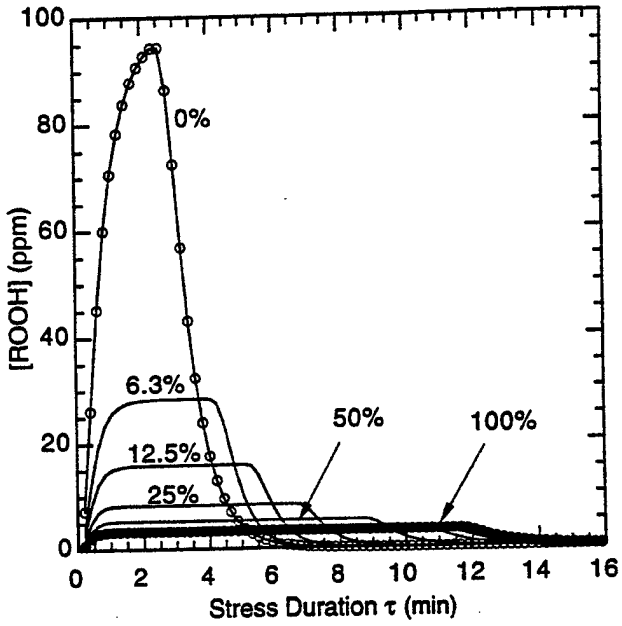

Fig. 9. Predicted hydroperoxides in POSF-2827 and POSF-2747 blends.

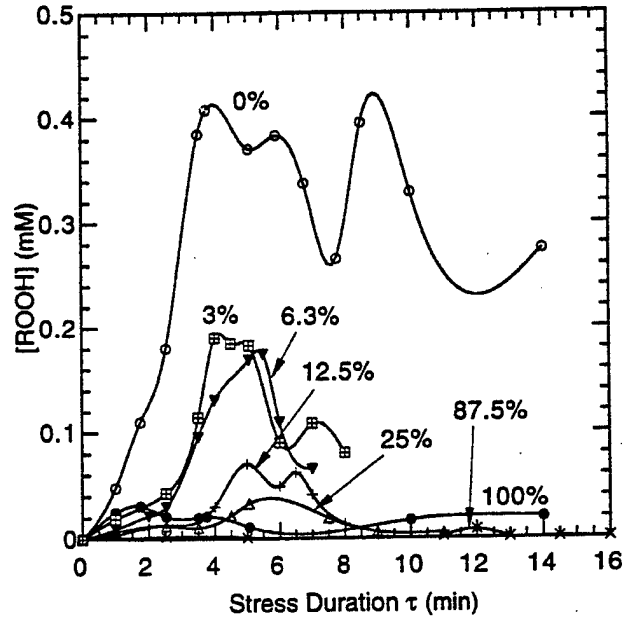

Fig. 10. Measured hydroperoxides in POSF-2827 and POSF-2747 blends.

hydroperoxides formed during the autoxidation process. In neat POSF-2747 the concentration of ROOH has increased rapidly with stress duration, reaching a maximum value at about 3 min. The qualitative agreement between the predicted and measured concentrations for ROOH seems reasonable, especially considering the fact that a significant amount of uncertainty exists in the measurements for ROOH. The major discrepancy can be noted from the data obtained for neat POSF-2747 in Figs. 9 and 10. While calculations yielded rapid consumption of ROOH after a maximum at ~ 3 min, the experiments showed a steady concentration at all times after 3 min of stressing. Interestingly, even in the blended fuel having nearly 93.3% POSF-2747 (i.e., 6.3% of POSF-2827), hydroperoxide depletion began soon after the maximum was reached. To understanding the observed peculiar behavior of neat POSF-2747, further investigations will be required.

The bulk deposits shown in Fig. 7 were obtained at the end of the heated-tube section, and the surface deposits shown in Figs. 6 and 7 were obtained at the tube surface. A majority of these surface deposits are resulting from the transport of precursor (P) in the bulk fuel to the walls. The distributions of bulk precursor and deposits in the heated tube are shown in Figs. 11 and 12, respectively. The bulk precursor concentrations closely follow the surface-deposition rates shown in Fig. 6 for these isothermal conditions. Also, the identical shapes of the plots in Figs. 6 and 11 suggest that the fraction of precursor lost to the walls during the deposition process is quite insignificant. Most of the precursor is converted to solubles through reaction (5d). As seen in Fig. 12, the concentration of bulk deposits has increased almost linearly and then reaches a constant value. The agglomeration process seems very slow at this temperature of 185 K.

Figure 13 shows the distribution of velocity, temperature, and concentration of O_2, ROOH, P, and D_{bulk} within the test-section for the neat POSF-2827 case. At this low flow rate of 0.25 cc/min, the flow became as a fully developed laminar one and most of the flow is under isothermal conditions. Oxygen [Fig. 13(c)] is consumed gradually, and oxygen-free fuel is established in the second half of the test-section. During the autoxidation process, the concentration of ROOH remained nearly constant, as seen in Fig. 13(d). The modified nine-step model simulates steady-state concentrations for ROOH--very similar to the semi-detailed oxidation-model predictions. Interestingly, even though the fuel in the test-section is under isothermal conditions, the concentrations of different species are not uniform within the tube cross section because of the small heating zone at the entrance of the test-section. Among the species considered, the bulk particles show the most significant variation across the tube cross section.

Summary and Conclusions:

Although vast amount of experimental data has been obtained by several researchers, the exact mechanisms governing thermal degradation of fuels and the consequent deposit-formation process are still largely unknown, primarily because the fluid flow and heat transfer which

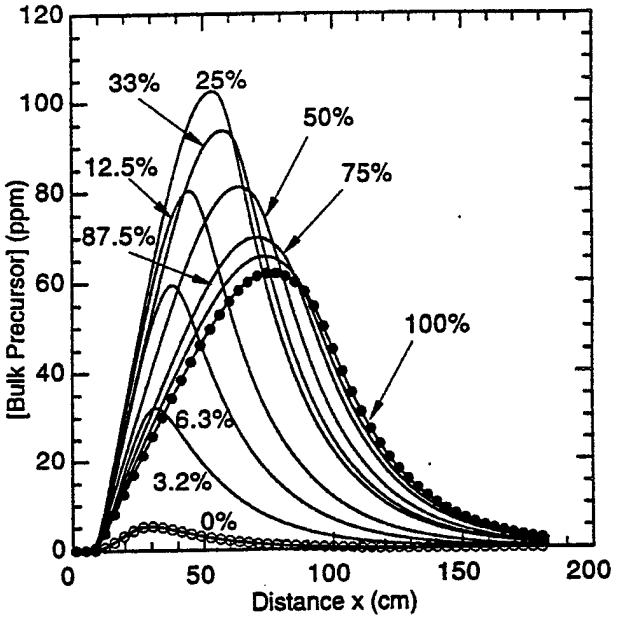

Fig. 11. Predicted concentrations of precursor in bulk fuel as POSF-2827 and POSF-2747 blended fuel passes through the heated tube.

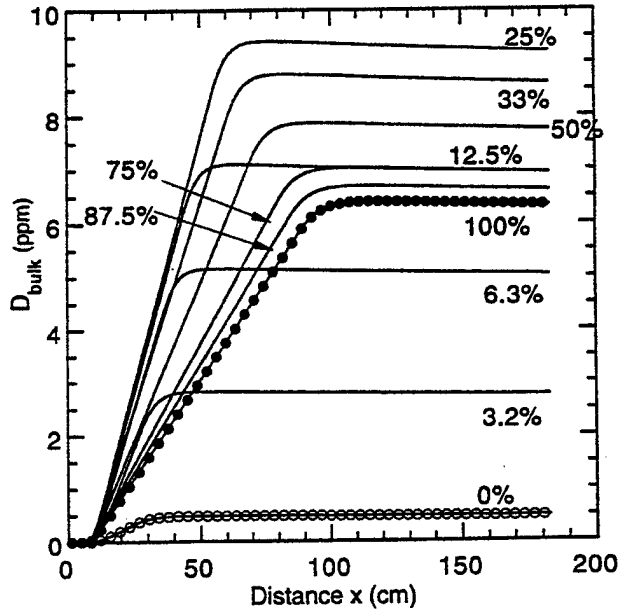

Fig. 12. Predicted concentrations of solids in bulk fuel (Dbulk) as POSF-2827 and POSF-2747 blended fuel passes through the heated tube.

influence the deposition process vary significantly from experiment to experiment. It is thought that CFDC models can be used to correlate the data obtained from various experiments and, thereby, explore the large data base in attempts to understand the deposition phenomenon. The success of this approach depends on the accuracy of the global-chemistry models used in the CFDC codes. Different global-chemistry models that are developed recently have been described in this paper as well as their relationship with respect to current understanding on the semi-detailed chemistry for jet-fuel thermal stability.

Recent experiments on blended fuels prepared by mixing hydrotreated fuel with a non-hydrotreated fuel suggest that the thermal stability of the blend cannot be linearly extrapolated from the thermal-stability characteristics of the neat fuels. Calculations were performed using the CFDC code known as "foul2d" for the prediction of the thermal-stability behavior of fuel blends. The global-chemistry models developed previously were found to be insufficient for simultaneous prediction of the deposition and oxidation rates associated with the blend fuels. However, the recently developed nine-step model appears to yield qualitatively correct results. The rate expressions for the bulk-fuel reactions in the nine-step model were modified to incorporate antioxidant behavior in jet fuels. The modified nine-step global-chemistry model not only improves the accuracies in predicting quantities such as oxygen consumption and surface deposits but also provides additional capabilities for predicting quantities such as hydroperoxides and bulk insolubles.

Acknowledgments:

This work was supported, in part, by Air Force Contract F33615-95-C-2507 and the Air Force Office of Scientific Research. The authors would like to thank Mrs. Marian Whitaker for editorial assistance.

References:

1. Marteney, P. J., and Spadaccini, L. J., "Thermal Decomposition of Aircraft Fuels," ASME Journal of Engineering for Gas Turbines and Power, Vol. 108, October 1986, pp. 648-653.
2. Ballal, D. R., Byrd, R. J., Heneghan, S. P., Martel, C. R., Williams, T. F., and Zabarnick, S., "Combustion and Heat Transfer Studies Utilizing Advanced Diagnostics: Fuels Research," Wright Laboratory Technical Report WL-TR-92-2112, Nov. 1992, Wright-Patterson AFB, OH.
3. Jones, E. G., and Balster, W. J., "Application of a Sulphur-Doped System to the Study of Thermal Oxidation of Jet Fuels," ASME Paper 92-GT-122, Presented at the International Gas Turbine and Aeroengine Congress and Exposition, Cologne, Germany, June 1-4, 1992.
4. Epstein, N., "Fouling of Heat Exchangers," in Heat Exchangers Sourcebook, Ed., Pale, J. W., Hemisphere Publishing Co., Washington, D.C.
5. ANON: CRC Literature Survey on Thermal Oxidation Stability of Jet Fuel. CRC Report No. 590, Coordination Research Council, Inc., Atlanta, GA, April 1979.
6. Hazlett, R. N., Progress Report on Advanced Hydrocarbon Fuel Development, Naval Research Laboratory, March 1975; Also Ind. Eng. Chem., Product Res. Div., Vol. 16, No. 2, pp. 171-177, 1977.
7. Roquemore, W. M., Pearce, J. A., Harrison, W. E. III, Krazinski, J. L., and Vanka, S. P., "Fouling in Jet Fuels: A new Approach," Presented at 198th National ACS Meeting, Symposium Structure on Future Jet Fuels II, Miami Beach, FL, September 10-5, 1989.
8. Krazinski, J. L., Vanka, S. P., Pearce, J. A., and Roquemore, W. M., "A Computational Fluid Dynamics and Chemistry Model for Jet Fuel Thermal Stability," Journal of Engineering for Gas Turbines and Power, Vol. 114, Jan. 1992, pp. 104-110.
9. Katta, V. R., and Roquemore, W. M., "Numerical Method for Simulating Fluid-Dynamic and Heat-Transfer Changes in Jet-Engine Injector Feed-Arm due to Fouling," Journal of Thermophysics and Heat Transfer, Vol. 7, No. 4, Oct.-Dec., 1993, pp. 651-660
10. Zhou, N., and Krishnan, A., "Calibration of a Global Mechanism for Jet Fuel Deposition," AIAA Paper 96-3238, AIAA, Reston, VA, 1996.
11. Chin, L. P., and Katta, V. R., "Numerical Modeling of Deposition in Fuel-Injection Nozzles," AIAA Paper 95-0497, AIAA, Reston, VA, 1995.
12. Marteney, P. J., "Thermal Decomposition of JP-5 in Long Duration Tests," United Technologies Research Center Report No. R88-957403-23, Prepared for the U.S. NAVY under Contract No. N00140-83-C-9119.N, 1988.
13. Taylor, W. F., "Kinetics of Deposit Formation from Hydrocarbon Fuels at High Temperature: General Features of the Process," Ind. Eng. Chem., Prod. Res. Devl., Vol. 6, pp. 258-262, 1967.
14. Taylor, W. F., "Catalysis in Liquid Phase Autoxidation. II. Kinetics of the Poly (Tetrafluoroethylene)-Catalyzed Oxidation of Tetralin," J. Phy. Chem., Vol. 74, pp. 2250-2256, 1970.
15. Kendall, D. R., Houlbrook, G., Clark. R. H., Bullock, S. P., and Lewis, C., "The Thermal Degradation of Aviation Fuels in Jet Engine Injector Feed-Arms: Part 1 - Results from a Full-Scale Rig," Presented at the 30th International Gas Turbine Congress, Tokyo, Oct. 1987.
16. Giovanetti, A. J., and Szetela, E. J., "Long Term Deposit Formation in Aviation Turbine Fuel at Elevated Temperature," AIAA Paper 86-0525, AIAA, New York, NY, 1986.
17. Fodor, G. E., Energy and Fuel, Vol. 2, p. 729, 1988.
18. Jones, E. G., Balster, W. J., and Anderson, S. D., "Formation of Insolubles in Jet Fuels: Effects of Oxygen," Preprints Symposia-Structure of Jet Fuels III, Division of Petroleum Chemistry, American Chemical Society, Washington, D. C., Vol. 37, No. 2, p. 393
19. Mayo, F. R., and Lan, B. Y., Ind. Eng. Chem. Res. Vol. 25, p. 333, 1986.
20. Zabarnick, S., "Chemical Kinetics Modeling of Jet Fuel Autoxidation and Antioxidant Chemistry," To be published in Fuels, 1993.

21. Chin, J. S., and Lefebvre, A. H., "Influence of Flow Conditions on Deposits from Heated Hydrocarbon Fuels," ASME Paper 92-GT-114, Presented at the International Gas Turbine and Aeroengine Congress and Exposition, Cologne, Germany, June 1-4, 1992.
22. Clark, R. H., and Thomas, L., "An Investigation of the Physical and Chemical Factors Affecting the Performance of Fuels in the JFTOT," Presented at the SAE Aerospace Technology Conf. and Exposition, Anaheim, CA, 1988.
23. Deshpande, G. V., Michael, A. S., Solomon, P. R., and Malhotra, R., "Modeling of the Thermal Stability of Aviation Fuels'" Presented at the 198th ACS National Meeting, Symposium on the Chemical Aspects of Hypersonic Propulsion, Miami, FL, 1989.
24. Katta, V. Reddy, and Roquemore, W. M., "A Time-Dependent Model with Global Chemical for Decomposition and Deposition of Aircraft Fuels," Symposium on the Stability and Oxidation Chemistry of Middle Distillate Fuels, Division of Fuel and Petroleum Chemistry, ACS, Washington, Aug. 26031, 1990.
25. Heneghan, S. P., and Zabarnick, S., "Oxidation of Jet Fuels and the Formation of Deposits," Fuel, 1994, Vol. 73, p. 35.
26. Hardy, D. R., Beal, E. J., and Burnett, J. C., Proceedings of the 4th International Conference on Stability and Handling of Liquid Fuels, US Department of Energy, Washington, D.C., 1991, p. 260.
27. Kauffman, R. E., University of Dayton Research Institute, Ohio, Private communications, 1993.
28. Katta, V. R., Jones, E. G., and Roquemore, W. M., "Development of Global-Chemistry Model for Jet-Fuel Thermal Stability Based on Observations from Static and Flowing Experiments," AGARD-CP-536, Paper No. 19, Sep., 1993.
29. Zabarnick, S., "Chemical Kinetic Modeling of Antioxidant Chemistry for Jet Fuel Applications," Submitted to Ind. Eng. Chem. Res.
30. Balster, L. J., Balster, W. J., and Jones, E. G., "Thermal Stability of Jet-Fuel/Paraffin Blends," Ind. Eng. Chem. Res., Vol. 10, p. 1176, 1996.
31. Jones, E. G., Balster, L. J., and Balster, W. J., "Thermal Stability of Jet-A Fuel Blends," Energ. Fuels, Vol. 10, p. 509, 1996.
32. Edwards, T., Anderson S. D., Pearce, J. A., and Harrison, W. E., "High Temperature Thermally Stable JP Fuels--An Overview," AIAA 92-0683, Presented at 30th Aerospace Sciences Meeting and Exhibit, Jan. 6-9, 1992, Reno, NV.
33. Spalding, D. B., "A Novel Finite Difference Formulation for Difference Expressions Involving Both First and Second Derivatives," Int. J. for Num. Meth. in Eng., Vol. 4, 1972, pp. 551-559.
34. Ervin, J. S., Zabarnick, S., and Williams, T. F., "Modeling of Jet Fuel Oxidation at Low Temperatures," AIAA Paper, Presented at 35th AIAA Aerospace Sciences Meeting, Reno, NV, Jan. 6-10, 1997.

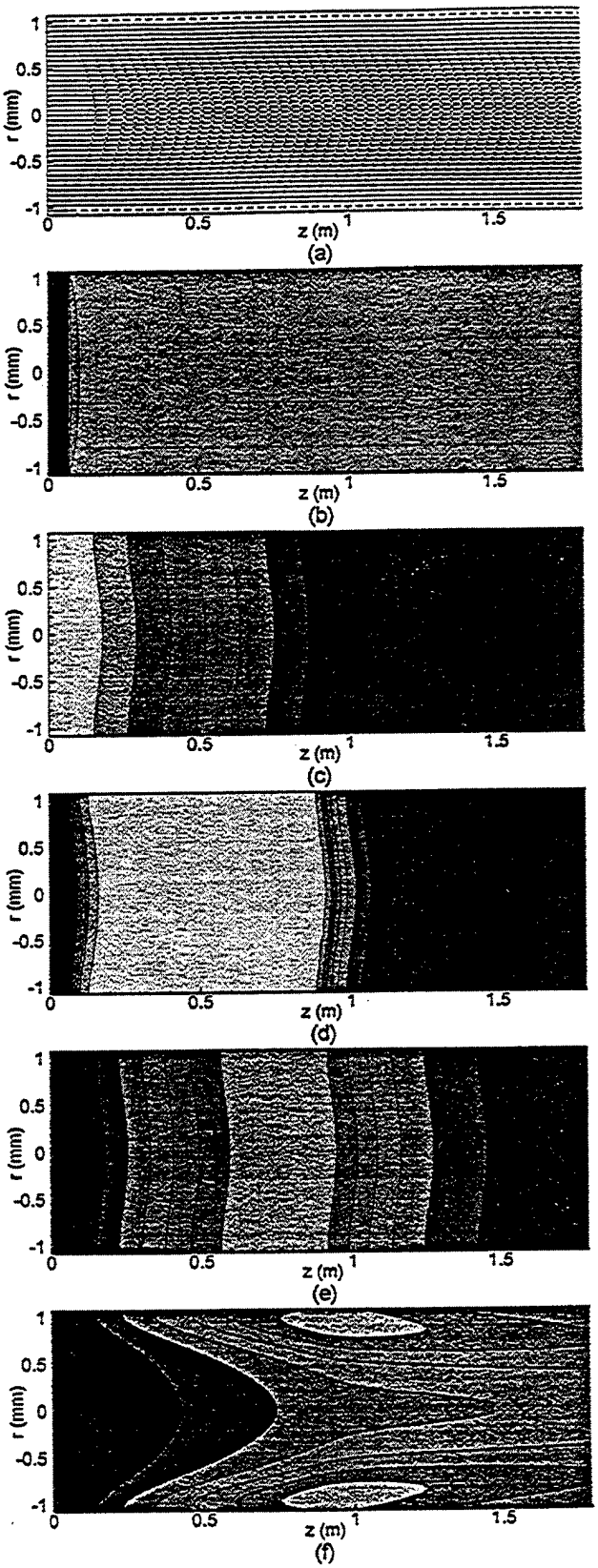

Fig. 13. Distributions of (a) velocity, (b) temperature, (c) remaining dissolved oxygen, hydroperoxides, (d) precursor, and (e) Dbulk particles.

Preprints of Symposia - ACS, Division of Petroleum Chemistry 43(3), 390 (July 1998).

Symposium on Structure of Jet Fuels V
Presented Before the Division of Petroleum Chemistry, Inc.
216th National Meeting, American Chemical Society
Boston, MA, August 23-27, 1998

Modeling of Pyrolysis and Pyrolytic Deposition of Norpar-13 under Supercritical Conditions

Jyh-Cherng Sheu, Ning Zhou and Anantha Krishnan
CFD Research Corporation
215 Wynn Drive
Huntsville, AL 35805

A. Grant Jones and Viswanath R. Katta
Innovative Scientific Solution, Inc.
2786 Indian Ripple Road
Dayton, OH 45440

INTRODUCTION

Studies on the pyrolysis and coke formation of hydrocarbon fuels have continued for several decades. Most of these studies were performed at low pressure (atmospheric) and high temperature (> 600°C) conditions due to the requirements of petroleum industry. A typical fuel system in aircraft is operated at high pressure (between 3.4 and 6.9 MPa) and relatively low temperature (< 600°C) conditions (1). Only limited studies were done under such environments (2-4). But those have focused on the investigation of fuel pyrolysis, without addressing the issue of coke formation.

The pyrolysis of hydrocarbon fuels in fuel lines is accompanied by coke deposits. Earlier efforts on the modeling of coke formation in aviation fuels were concentrated at a lower temperature range (< 400°C). The deposits formed at such temperature range are mainly autoxidative. Therefore, the deposition mechanisms developed in earlier studies (5, 6) can not be used to simulate the jet fuel deposition under pyrolytic conditions. A few studies were conducted in the modeling of pyrolytic deposition for hydrocarbon fuels (7-11). But the models developed by these authors are for use in the petroleum industry (i.e., low pressure and high temperature conditions). Direct use of these models in predicting the pyrolytic deposition of aviation fuels may not be suitable. To authors knowledge, models for describing the pyrolytic deposition of aviation fuels are yet to be developed.

In the present study, pyrolysis and pyrolytic deposition of Norpar-13 under high pressure and relatively low temperature (<600°C) conditions are investigated both experimentally and numerically. This article emphasizes the modeling work. Thermal cracking of Norpar-13 is described by a one-step global model, and pyrolytic deposition is described as a zero-order surface reaction. The cracking and deposition models are implemented in a multi-dimensional CFD code (CFD-ACE) to simulate the heat/mass transfer of Norpar-13 under supercritical conditions. The simulated wall temperature and deposition rate are found to be consistent with experimental results.

EXPERIMENTAL

Norpar-13 flows in an upward direction through Silcosteel passivated tubing (12) (0.125 in o.d. and 0.085 in i.d). at room temperature and 1000 psia (> critical pressure of Norpar-13). The tube is painted with a flat-black high-temperature paint to maintain a constant emissivity. The tube is electrically heated by passing a high current through the length of the tube. The test duration for each run is 6 hours. Several fuel flow rates (ranging from 10 to 30 ml/min), bulk fuel temperatures at tube exit (ranging from 570 to 600°C), and tube lengths (24, 42, and 60 in) are tested. Wall temperatures are measured using an optical pyrometer, cracked gas products collected at tube exit are analyzed using gas chromatography (GC), and the quantity of deposits on the wall surface is determined using standard surface carbon burn-off technique (13).

Numerical

Pyrolysis Model

Based on our measurements, the distribution of cracked gas products are similar for the ranges of temperature and flow rate tested. This observation implies that the thermal cracking of Norpar-13 under the conditions examined can be approximated as a one-step global reaction, i.e.,

Norpar-13 → β Products 1)

Only gas composition are considered for the cracked products in Eq. 1). The composition of gas products is obtained from measurements. After knowing the product composition, the coefficient β is determined based on the mass conservation of the cracking reaction. According to Yu and Eser (4), supercritical thermal cracking of n-alkanes or mixtures of n-alkanes can be represented by a first-order, Arrenenius-type kinetic. Because Norpar-13 is a mixture of n-alkanes, the cracking rate of Eq. 1) is expressed as:

$$-d[\text{Norpar-13}]/dt = k\,[\text{Norpar-13}] \quad \text{and} \quad k = Ae(-E/R_uT) \qquad 2)$$

where k is the rate constant, A the pre-exponential factor, E the activation energy, R_u the universal gas constant, and T the reaction temperature. The rate constant k in Eq. 2) is estimated by linear combination of the rate constants for the thermal cracking of pure compounds (4). The calculated pre-exponential factor A and activation energy E are 3.64×10^{15} (kmole/m^3s) and 63 (kcal/mole), respectively.

Deposition Model

Pyrolytic deposition is believed to be closely related to fuel pyrolysis. Therefore, it is difficult to develop a deposition model without knowing the details of pyrolysis. However, our experimental results suggest that pyrolytic deposition can be well represented as a unique function of wall temperature (see Figure 1). This observation implies that 1) the surface reactions along the wall, not the pyrolytic reactions in the bulk flow region, dominate the formation of pyrolytic deposits, and 2) conversion of Norpar-13 does not play an important role in affecting coke formation. Based on these two arguments, a zero-order, surface-reaction model is proposed to describe the pyrolytic deposition of Norpar-13, i.e.,

Norpar-13 → Deposits 3)

and the reactions rate is expressed as

$$R = A_w e(-E_w/R_u T_w) \qquad 4)$$

where R is the reaction rate, A_w the pre-exponential factor, E_w the activation energy, and T_w the wall temperature. A_w and E_w are determined by fitting the experimental data shown in Figure 1. The best fitted values for A_w and E_w are 2.0×10^{16} (μg/cm^2h) and 60 (kcal/mole), respectively (see Figure 1).

Numerical Method

The thermal cracking model described above is incorporated in CFD-ACE, a commercial CFD software developed by CFD Research Corporation. Numerical simulation of Norpar-13 pyrolysis in a flowing system is then performed using the modified CFD-ACE code. In the simulation, fluid motion in the tube is assumed to be axisymmetric and in steady-state. The fluid properties of the mixture (i.e., mixture of Norpar-13 and cracked products) are estimated using SUPERTRAPP (14). For the thermal boundary conditions, uniform and constant heat flux is applied along the tube wall. The heating power used in the simulation is 10% lower than the experimental value to account for the heat loss from the connection between clip holder and fuel

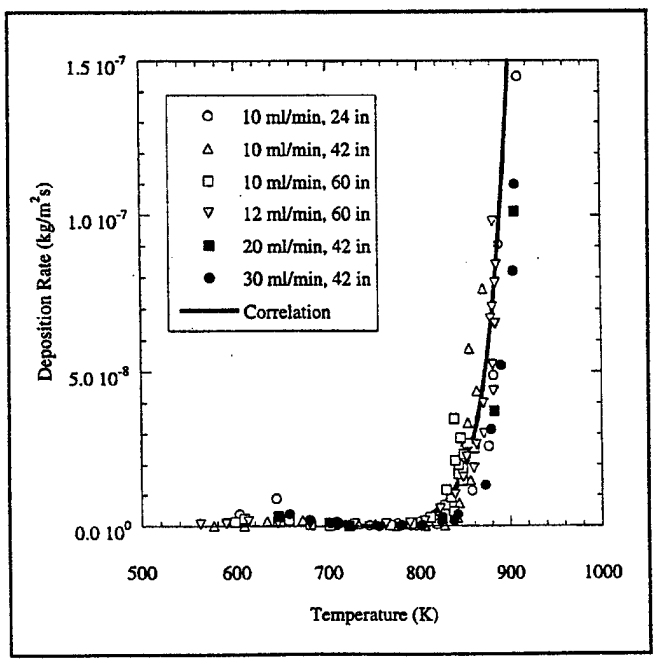

Figure 1. Deposition Rate as function of wall temperature.

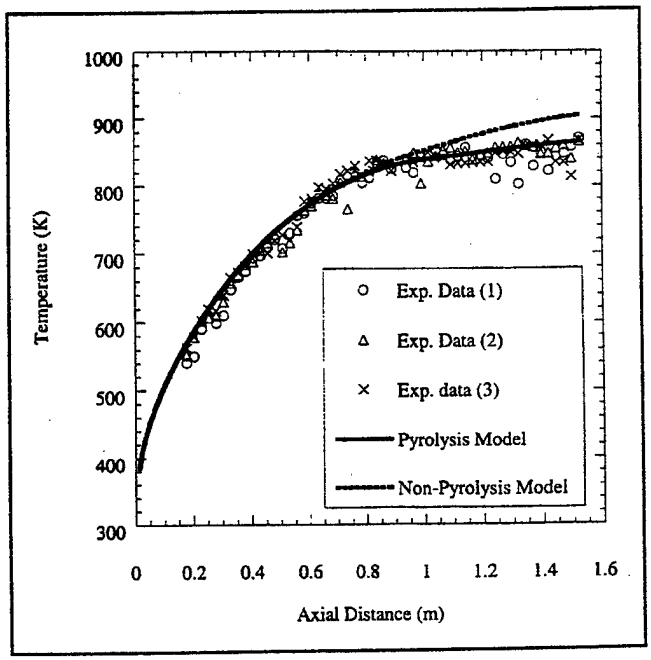

Figure 2. Axial distributions of wall temperature predicted under the conditions of 10 ml/min, 654 W, and 60 in.

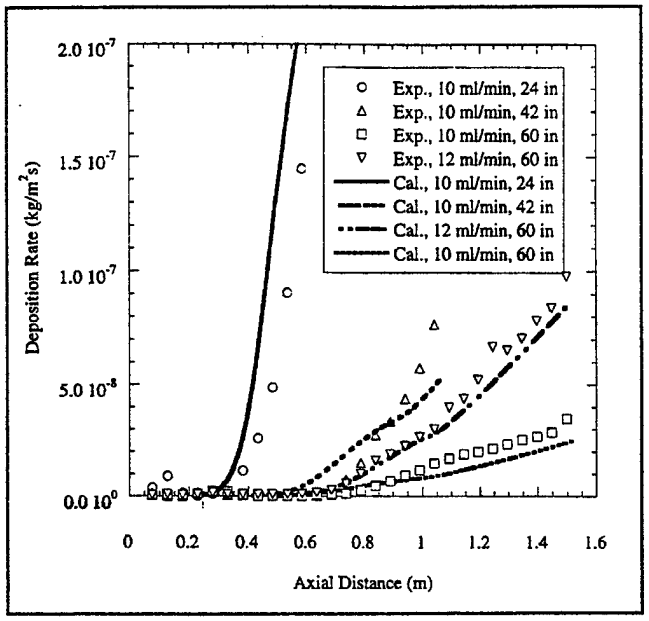

Figure 3. Comparison of predicted deposition rates and experimental results (inlet flow rate: 10 and 12 ml/min, bulk exit temperature: 570-580°C).

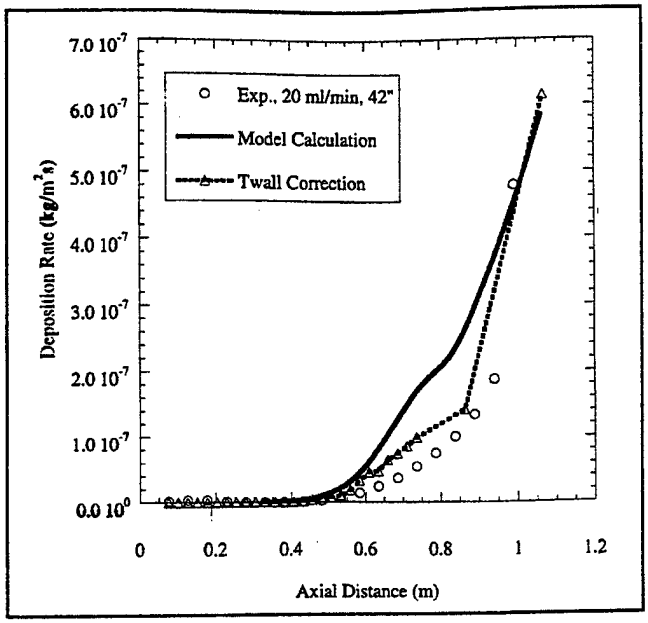

Figure 4. Comparison of predicted deposition rates and experimental results (inlet flow rate: 20 ml/min, bulk exit temperature: 595°C).

tube. Because the wall temperature considered in the studies can be as high as 900 K, radiation and convection heat loss can not be neglected. The heat loss from radiation is estimated by the Stefan-Boltzmann law and that from convection is estimated by Newton's law of cooling.

RESULTS AND DISCUSSION

Validation of Pyrolysis Model

The Norpar-13 pyrolysis model is validated using experimental data measured using a 60-in tube at an inlet flow rate of 10 ml/min and heating power of 654 W. Figure 2 shows the predicted axial distribution of wall temperature (solid line in the figure). The three sets of experimental data in the figure represent the measured temperatures at different times during the experiment. As illustrated in Figure 2, the predicted wall temperature compares well with experiment data. The calculated wall temperatures at other flow rates ,bulk temperatures, and tube lengths are also consistent with experimental data (not shown).

Endothermic Effect

Aviation fuel is used as primary cooling source for removing excess heat generated in military and commercial aircraft. It is thus important to examine the endothermic performance of Norpar-13 pyrolysis under high pressure conditions. This task is performed by comparing the wall temperatures predicted using the numerical models with and without considering pyrolytic reactions. The results are illustrated in Figure 2. In the upstream region (i.e., from tube inlet to axial distance of 0.8 m), measurements as well as two simulation results show that wall temperature increases along the axial direction. The wall temperature distributions predicted by both models agree well with experimental data. The results of this comparison suggest that the endothermic effect of Norpar-13 pyrolysis in the upstream region is negligible because the fuel temperature is too low. In the downstream region (i.e., from axial distance of 0.8 m to tube outlet), measurements and two simulation results show that the increase of wall temperature falls as axial distance increases. But the flattening trend of wall temperature predicted by non-pyrolysis model is not as significant as that predicted by pyrolysis model. The comparison in downstream region suggest that the flattening trend predicted by non-pyrolysis model is due to the radiation and convection heat loss, and the difference between the temperature predicted by pyrolysis model and experimental data results from the endothermic effect of pyrolytic reactions.

Pyrolytic Deposition

The proposed zero-order deposition model for Norpar-13 pyrolysis is tested against several sets of experimental data. The test conditions include 10 and 12 ml/min of inlet flow rates, 570-580°C of bulk exit temperature, and 24, 42, and 60 inches of tube lengths. To calculate the deposition rate, the wall temperature value is obtained from the calculation using the one-step pyrolysis model. Figure 3 shows the predicted deposition-rate distributions as well as experimental data. For all the conditions examined, the predicted deposition rates match

well with experimental data not only qualitatively but quantitatively.

The test of zero-order deposition model is also performed at higher flow rate (20 ml/min) and temperature (595°C of bulk exit temperature) conditions. The test results are plotted in Figure 4. The predicted deposition rates again quantitatively agree well with experimental data. But the predicted axial location where the deposits increase exponentially is observed to occur earlier than experimental data (see Figure 4). The difference between predictions and measurements may not result from the inadequacy of deposition model. Instead, it may result from the difference in predicted wall temperature and measurements. This can be confirmed by examining the deposition-rate distribution calculated directly using the measured wall temperature. As illustrated in Figure 4, the predicted axial location now compares well with experimental data. The test results suggest that wall temperature plays an essential role in affecting the formation of pyrolytic deposition. The results also imply that for the ranges of flow rate and temperature studied, the effects of bulk fuel temperature and fuel conversion on pyrolytic deposition can be neglected.

CONCLUSIONS

A one-step global model is proposed to describe the pyrolysis of Norpar-13 under high pressure conditions. The proposed model is validated using the experimental data obtained at different flow rates, bulk fuel temperatures, and tube lengths. For the conditions examined, the model predictions agree well with measurements. The endothermic effect of Norpar-13 pyrolysis is examined by modifying the radiation and convection heat loss in the calculations. From our predictions, the flattening trend of wall temperature distribution (as observed in the downstream region of fuel tube) is due to combined effects of heat loss and Norpar-13 pyrolysis.

The coke deposits resulted from Norpar-13 pyrolysis is described by a zero-order, surface-reaction model. The model is tested at different flow rates and temperatures. The test results indicate that wall temperature plays an essential role in affecting the formation of pyrolytic deposition. For the conditions tested, the pyrolytic deposition rate is found to be well represented as a unique function of wall temperature.

ACKNOWLEDGMENTS

This work is supported by an AF contract (# F33615-96-C-2619) monitored by Mr. Edwin Corporan. The experimental efforts of Mr. Walt J. Balster (ISSI) and Ms. Lori M. Balster (ISSI) are acknowledged.

LITERATURE CITED

(1) Edwards, T., and Zabarnick, S., Ind. Eng. Chem. Res., 32, 3117 (1993).

(2) Khorasheh, F., and Murray, R. G., Ind. Eng. Chem. Res., 32, 1853 (1993).

(3) Yu, J., and Eser, S., Ind. Eng. Chem. Res., 36, 574 (1997).

(4) Yu, J., and Eser, S., Ind. Eng. Chem. Res., 36, 585 (1997).

(5) Katta, V. R., Jones, E. G., and Roquemore,. W. M., Development of Global-Chemistry Model for Jet-Fuel Thermal Stability Based on Observation from Static and Flowing Experiments, AGARD-CP-536, Paper No. 19, Sep., 1992.

(6) Katta, V. R., and Roquemore, W. M., Modeling of Deposition Process in Liquid Fuels, AIAA Paper 97-3040, AIAA, Reston, VA, 1997.

(7) Kumar, P. and Kunzru, D., 63, 598 (1985).

(8) Mandal, T. K., and Kunzru, D., Ind. Eng. Chem. Process Des. Dev., 25, 794 (1985).

(9) Kopinke, F. D., Zimmermann, G., and Nowak, S., Carbon, 26, 117 (1988).

(10) Kopinke, F. D., Zimmermann, G., Reyniers, G., and Froment, F., Ind. Eng. Chem. Res., 32, 56 (1993).

(11) Kopinke, F. D., Zimmermann, G., Reyniers, G., and Froment, F., Ind. Eng. Chem. Res., 32, 2620 (1993).

(12) Restek Corporation, Bellefonte, PA.

(13) Jones, E. G., and Balster, W. J., Energy and Fuel, 7, 963 (1993).

(14) Ely , J. F., and Huber, M. L., NIST Thermophysical Properties of Hydrocarbon Mixtures Database (SUPERTRAPP), V.1.0 Users Guide, July 1992.

AIAA 98-3758

Thermal Cracking of Norpar-13 Fuel under near-critical and Supercritical Conditions

Jyh-Cherng Sheu, Ning Zhou, and Anantha Krishnan
CFD Research Corporation
215 Wynn Drive
Huntsville, AL 35805

E. Grant Jones and Viswanath R. Katta
Innovative Scientific Solutions, Inc.
2766 Indian Ripple Road
Dayton, OH 45440-3638

34th AIAA/ASME/SAE/ASEE
Joint Propulsion Conference & Exhibit
July 13-15, 1998 / Cleveland, OH

For permission to copy or republish, contact the American Institute of Aeronautics and Astronautics
1801 Alexander Bell Drive, Suite 500, Reston, VA 20191 REPRINTED WITH PERMISSION

Thermal Cracking of Norpar-13 under Near-Critical and Supercritical Conditions

Jyh-Cherng Sheu, Ning Zhou*, and Anantha Krishnan
CFD Research Corporation
215 Wynn Drive
Huntsville, AL 35805

and

E. Grant Jones and Viswanath R. Katta**
Innovative Scientific Solutions, Inc.
2766 Indian Ripple Road
Dayton, OH 45440-3638

Abstract:

A three-step global model is developed to describe the thermal cracking of Norpar-13 under supercritical and near-critical conditions. This cracking model is incorporated into a multi-dimensional Computational Fluid Dynamics (CFD) code to simulate the heat/mass transfer and thermal cracking of Norpar-13 in flow systems. The proposed model is tested against the experimental data measured at different temperatures and residence times. Agreement is obtained when comparing the simulations results with measurements. The endothermic effect of Norpar-13 thermal cracking is analyzed using the validated cracking model. The results show that the energy absorbed by the cracking reactions has importance consequence in reducing the fuel and wall temperature although it only accounts for a small portion of total input power.

Introduction:

Aviation fuel is used as primary cooling source for removing excess heat generated in military and commercial aircraft. The amount of excess heat that fuel can absorb is limited by fuel temperature. Due to thermal stability problems, the bulk fuel temperature in aircraft fuel system is restricted to 436 K [1]. In the future the fuel system will be operating at much higher temperature conditions (for example, 800 K) because of the requirements of increased thermal loads. At such high-temperature environments, thermal cracking and pyrolytic deposition of fuel occur. Thermal cracking is an endothermic process that increases the fuel cooling capacity. But pyrolytic deposition causes serious problems in fuel systems. It is believed that the deposit formation is closely related to fuel thermal cracking. Therefore, better understanding of the thermal cracking mechanisms for jet fuels is important in order to utilize the endothermic features of thermal cracking reactions.

Studies on the thermal cracking of hydrocarbon fuels have continued for several decades. Most of these studies were conducted under low-pressure (atmospheric) conditions due to the requirements of petroleum industry. Typical fuel system in aircraft is operated under supercritical or near-critical (between 3.4 and 6.9 MPa) pressure conditions [2]. The mechanisms of fuel thermal cracking under low-pressure conditions may be different from those under high-pressure conditions. Only a few studies were done under high-pressure environments [3-6]. But those have focused on the investigation of thermal cracking mechanisms for normal alkanes. Thermal cracking mechanisms for jet fuels under high-pressure conditions are yet to be developed.

To date, the thermal cracking chemistry of hydrocarbon fuels (under both low-pressure and high-pressure conditions) is still unclear. Consequentially, development of detailed kinetic models for fuel thermal cracking is impossible. Alternatives such as global chemistry models have been used to describe fuel thermal cracking. One method for developing the global kinetic model is the lumping technique. The lumping method have been employed in the petroleum industry to develop kinetic models for the (thermal and catalytic) cracking of practical fuels [7-10]. According to this method, species are lumped into one group and treated as a pseudo component as the dynamic behavior of these species is independent of the species composition [11].

In the present study, a three-step global model is proposed to describe the thermal cracking of Norpar-13 under high-pressure conditions. This cracking model is developed based on the lumping method that divides the Norpar-13/products mixture into Norpar-13, cracked n-alkane liquids, cracked 1-alkene liquids, and cracked gases. The cracking model is implemented in a multi-dimensional CFD code (CFD-ACE) to simulate the heat/mass transfer and thermal cracking of Norpar-13 under near-critical and supercritical conditions. This model is tested against experimental data measured at

* Project Engineer, Member AIAA
\+ Principal Engineer, Member AIAA
++ Senior Engineer, Member AIAA

various temperatures and residence times. The simulated results for all test conditions are found to be consistent with experimental results. Based on these simulation results, the endothermic effect of Norpar-13 thermal cracking and the relative importance of the cracking reactions are analyzed.

Experimental Method:

Norpar-13 flows in an upward direction through Silcosteel passivated tubing [12] (3.175 mm o.d. and 2.159 mm i.d) at room temperature and 1000 psia (> critical pressure of Norpar-13). The tube is electrically heated by passing a high current through the length of the tube. The test duration for each run is 6 hours. Test conditions with fuel flow rate from 10 to 30 ml/min, bulk exit temperature from 843 to 873 K, and three tube lengths (0.6, 1.1, and 1.5 m) are considered in the experiments. Wall temperatures are measured using an optical pyrometer, cracked gas and liquid products collected at tube exit are analyzed using gas chromatography (GC), and the quantity of deposits on the wall surface is determined using standard surface carbon burn-off techniques [13].

For pure compounds like dodecane or hexadecane, fuel conversion is usually determined as the fraction of the disappearance of parent fuel. But for hydrocarbon mixtures like gas oils or jet fuels, this definition is not practical. To quantify the cracking level of jet fuels, conversion is measured based on the liquid volume change, i.e.,

$$\text{Conversion} = 1 - \frac{V(\text{liquid})_{exit}}{V(\text{Norpar13})_{inlet}}$$

according to the definition used by Edwards and Anderson [14]. In the above equation, $V(\text{Norpar13})_{inlet}$ is the volume of Norpar-13 inlet fed, and $V(\text{liquid})_{exit}$ the volume of liquid mixture collected at tube exit.

Kinetic Modeling:

A three-step model for Norpar-13 thermal cracking under high-pressure conditions is developed using the lumped kinetic approach. The Norpar-13/product mixture is first lumped into parent fuel (Norpar-13), cracked liquids, and cracked gases. The cracking model is described as

Norpar-13 → α Gases (1)
Norpar-13 → β Liquids (2)
Liquids → γ Gases (3)

Norpar-13 in Eq. (1), based on our analysis, is made up of 0.7 wt% undecane, 15.0% dodecane, 51.3% tridecane, 32.3% tetradecane, and 0.7% pentadecane. The composition of cracked gases in Eq. (1) is adopted from the experimental data measured at 12 ml/min of flow rate and 855 K of bulk exit temperature (see Table 1). From our experimental observation, the compositions of cracked gases collected at different temperatures and residence times are similar. Therefore, the composition of the cracked gases is treated as constant in the model. The major components of cracked liquids in Eq. (2), based on our experimental analysis, are n-alkanes and 1-alkenes. From this observation, the model assumes the liquid products are composed of n-C_mH_{2m+2} and 1-C_mH_{2m} ($6 < m < 10$). The model also assumes that the 1-alkenes in the liquid products are not further cracked into gas species. The above assumption is based on the argument that 1-alkenes are more likely to form 2-alkenes through isomerization reactions or to form heavier hydrocarbon through alkylation reactions. According to the descriptions above, Eqs.(2) and (3) are modified as

Norpar-13 → β (n-alkanes + 1-alkenes) (4)
n-alkanes → γ Gases (5)

The compositions of n-alkanes and 1-alkenes in Eqs. (4) and (5) are adopted from the experimental data measure at 10 ml/min of flow rate and 853 K of bulk exit temperature (see Tables 2 and 3). After knowing the compositions of gas and liquid products, the coefficient α, β, and γ in Eqs. (1), (4), and (5) are determined based on the mass conservation of each cracking reaction.

The reaction rates of Eqs. (1), (4) and(5) are assumed to follow the first-order, Arrhenius-type kinetics, i.e.,

$$-d[\text{Norpar-13}]/dt = k_1[\text{Norpar-13}]$$
$$-d[\text{Norpar-13}]/dt = k_4[\text{Norpar-13}]$$
$$-d[\text{n-alkanes}]/dt = k_5[\text{n-alkanes}]$$

and

$$k_1 = A_1 e^{(-E_1/R_uT)}$$
$$k_4 = A_4 e^{(-E_4/R_uT)}$$
$$k_5 = A_5 e^{(-E_5/R_uT)} \quad (6)$$

where k_i ($i = 1, 4$, and 5) is the rate constant, A_i the pre-exponential factor, E_i the activation energy, R_u the universal gas constant, and T the reaction temperature. The rate constants k_1 and k_4 are estimated by linear combination of the rate constants for the thermal cracking of pure compounds. The cracking rates of the pure compounds are adopted from the correlation of Yu and Eser [15]. The calculated pre-exponential factors and activation energies are

$$A_1 = A_4 = 3.64 \times 10^{15}\ (1/s)$$

and

$E_1 = E_4 = 63$ (kcal/mole)

The linear combination method; however, can not be used to estimate the rate constant k_5 due to the lack of information on the cracking rate of n-C_6H_{14} and n-C_7H_{16} under high-pressure conditions. The kinetic correlation in [15] is only good for the range n-$C_{10}H_{22}$ - n-$C_{14}H_{30}$, and extendible to the range n-C_8H_{18} - $C_{16}H_{34}$. For simplicity, k_5 in the current model is approximated as the rate constant of n-C_8H_{18} thermal cracking. Using the correlation in [15], A_5 and E_5 are calculated as 5.34×10^{11} (1/s) and 52.4 (kcal/mole), respectively.

Table 1. Composition of gas products from Norpar-13 thermal cracking

Compound	Chemical Formula	Vol. %
hydrogen	H_2	1.99
methane	CH_4	10.64
ethylene	C_2H_4	12.81
ethane	C_2H_6	16.47
propylene	C_3H_6	18.19
propane	C_3H_8	13.73
1-butene	C_4H_8	13.85
n-butane	C_4H_{10}	1.86
unidentified	C_5^*	10.46

* The unidentified C_5^* is assumed to be 1-pentene in the model

Table 2 Composition of n-alkanes liquid products from Norpar-13 thermal cracking

Compound	Chemical Formula	Vol. %
n-hexane	C_6H_{14}	34.95
n-heptane	C_7H_{16}	25.48
n-octane	C_8H_{18}	16.46
n-nonane	C_9H_{20}	13.56
n-decane	$C_{10}H_{22}$	9.55

Table 3 Composition of 1-alkenes liquid products from Norpar-13 thermal cracking

Compound	Chemical Formula	Vol. %
1-hexene	C_6H_{12}	31.43
1-heptene	C_7H_{14}	24.16
1-octene	C_8H_{16}	18.60
1-nonene	C_9H_{18}	14.15
1-decene	$C_{10}H_{20}$	11.66

Numerical Method:

The thermal cracking model described above is incorporated in CFD-ACE, a commercial computational fluid dynamics software developed by CFD Research Corporation. Numerical simulations of Norpar-13 thermal cracking in flow systems are then performed using the modified CFD-ACE code. In the simulation, fluid motion in the tube is assumed to be axisymmetric and in steady-state. The flow is assumed to be turbulent, and is simulated using the standard k-e model. The fluid properties of the Norpar-13/product mixture are estimated using SUPERTRAPP [16]. For the thermal boundary conditions, uniform and constant heat flux is applied along the tube wall. The heating power used in the simulation is 10-15 % lower than experimental value to account for the heat loss from the connection between electrical terminal and fuel tube. Because the wall temperature considered in the studies can be as high as 950 K, radiation and convection heat loss can not be neglected. The heat loss from radiation is estimated by the Stefan-Boltzmann law and that from convection by Newton's law of cooling, i.e.,

$$q_{loss} = q_{conv} + q_{rad} = h(T_{wall} - T_\infty) + \varepsilon\sigma(T_{wall}^4 - T_\infty^4) \qquad (7)$$

where q_{loss} represents the total heat loss, q_{rad} the radiative heat loss, q_{conv} the convective heat loss, T_{wall} the wall temperature, T_∞ the surrounding temperature, σ the Stefan-Boltzmann constant, ε the emissivity determined from experimental calibration, and h the heat transfer coefficient determined from the correlation of Churchill and Chu [17].

Results and Discussion:

Heat Loss Evaluation:

As mentioned earlier in last section, the heat loss to the environment is not negligible in the current study. Therefore it is important to know the heat loss amount during the experiment in order to correctly predict the endothermic effects of fuel thermal cracking. The amount of heat loss is determined experimentally by comparing the powers used to heat insulated and non-insulated tubes. The test is performed using a 0.6-m tube with inlet flow rate of 10 ml/min and bulk exit temperature of 843 K. The measured powers for heating insulated and non-insulated tubes are 346.2 and 463.5 W, respectively. The fraction of heat loss with respect to the input power is calculated as 25.3 %.

The evaluation of heat loss is also performed numerically by simulating the test cases described above. The non-insulated case is simulated by including both thermal cracking and heat loss models in

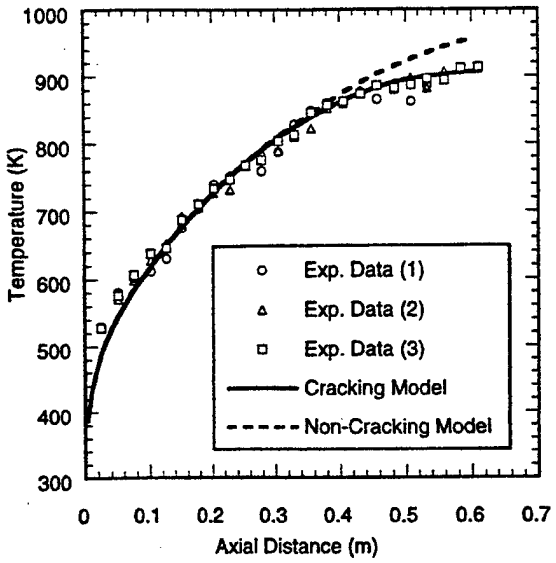

Figure 1.Axial distributions of wall temperature calculated using a 0.6-m tube with flow rate of 10 ml/min and bulk exit temperature of 847 K.

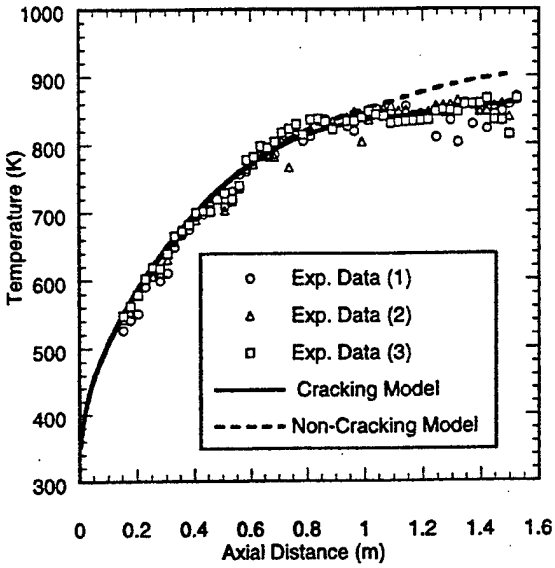

Figure 3. Axial distributions of wall temperature calculated using a 1.5-m tube with flow rate of 10 ml/min and bulk exit temperature of 848 K.

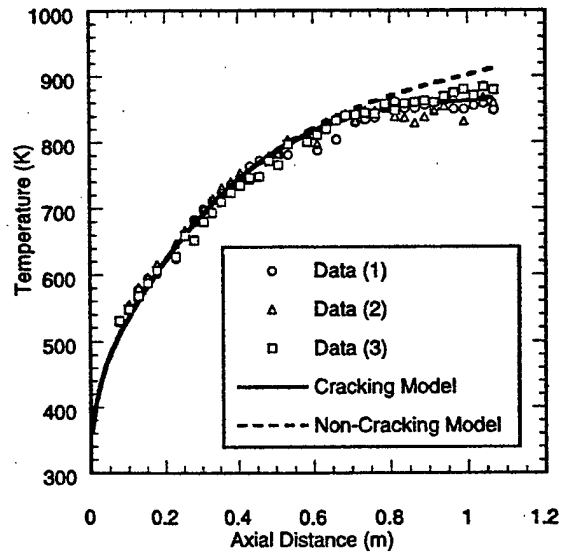

Figure 2. Axial distributions of wall temperature calculated using a 1.1-m tube with flow rate of 10 ml/min and bulk exit temperature of 847 K.

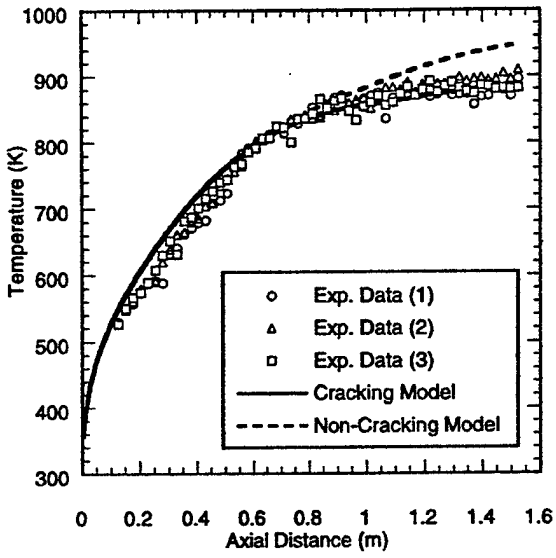

Figure 4. Axial distributions of wall temperature calculated using a 1.5-m tube with flow rate of 12 ml/min and bulk exit temperature of 855 K.

the calculation, and the insulated case is simulated by including only the thermal cracking model in the calculation. The calculated powers for heating the insulated and non-insulated tubes are 325 and 460 W, respectively, comparing favorably with the experimental values above.

Cracking Model Validation:

Six test cases with flow rate from 10 to 30 ml/min, bulk exit temperature from 847 to 871 K, and tube length from 0.6 to 1.5 m are simulated. The calculated wall temperature distributions and fuel conversions are compared with experimental data. Figures 1-6 show the

distributions of wall temperature obtained from calculations and measurements for the six test cases. In the figures, the circle, triangle, and rectangular symbols represent three sets of experimental data measured at different times during the same experiment and the solid line represents the simulation results. For all cases examined, the simulated wall temperatures match experimental data both qualitatively and quantitatively. The calculated and measured conversion values for the six test cases are listed in Table 4. Except Test Case 6, the predicted conversion values agree well with experimental data. The reason to cause the difference between the calculated and measured conversions for Test Case 6 is not clear at the current stage. It may either attribute to the limitation of current model in simulating higher flow-rate conditions, or the uncertainties of measurements.

Table 4. Measured and calculated conversion values

Test No.*	Test Conditions * (ml/min)	(K)	(m)	Conversion (%) Measurement	Calculation
1	10	847	0.6	16.0	15.0
2	10	847	1.1	15.0	15.6
3	10	848	1.5	22.0	20.5
4	12	855	1.5	33.0	29.2
5	20	868	1.1	23.0	23.0
6	30	871	1.1	10.5	18.0

* The test conditions in orders are inlet flow rate, bulk exit temperature, and tube length.

Endothermic Effect of Thermal Cracking:

The amount of heat absorbed by the thermal cracking reactions (i.e., endotherm) can be determined by analyzing the energy balance on the heated tube. Following Sobel and Spadaccini [18], the endotherm, Q_{endo}, is expressed as

$$Q_{endo} = Q_{in} - Q_{sens} - Q_{loss} \quad (8)$$

where Q_{in} represents the input heating power, Q_{loss} the heat loss, and Q_{sens} the sensible heating used to raise fuel temperature. Q_{in} is determined by measurements, and Q_{sens} and Q_{loss} are estimated based on simulation results. The values of Q_{endo}/Q_{in} and Q_{loss}/Q_{in} calculated using Eq. (8) are listed in Table 5. For the six cases examined, the calculated endotherm is significantly less than the heat loss, confirming the requirement of considering heat loss in the current study. The endotherm, although not as significant as the heat loss, has important consequence in reducing the fuel and wall temperatures. This can be demonstrated by comparing the simulation results predicted by the cracking and non-cracking models. For the six cases studied, the bulk exit temperatures predicted by the non-cracking model are 50-80 K higher than those obtained by the cracking model (see Table 6).

The endothermic effect on the wall temperature is studied by comparing the axial distributions of wall temperature predicted by both models. The simulation results for the six cases are shown in Figs 1-6. The results of Test Case 1 (see Fig. 1) are discussed as follows. In the upstream region (i.e., from tube inlet to axial distance of 0.5 m), the wall temperatures predicted by both models are almost identical. This suggests that the endothermic effect of thermal cracking reactions is negligible because the fuel temperature in this region is too low. In the downstream region (i.e., from axial distance of 0.5 m to tube exit), the wall temperature calculated by the non-cracking model becomes increasingly higher than that by the cracking model as the axial distance increases. At the tube exit, the wall temperature calculated by the non-cracking model is observed to be 52 K higher than that by the cracking model. Similar trends are also observed when comparing the simulation results for the remaining five test cases (see Figs 2-6). The predicted exit wall temperatures by the non-cracking model are 43-74 K higher than those by the cracking model for Test Cases 2-5 (see Table 6).

Table 5. Calculated endotherm for Norpar-13 thermal cracking

Test No.*	Q_{endo}/Q_{in} (%)	Q_{loss}/Q_{in} (%)
1	9.2	29.0
2	8.3	31.4
3	8.7	43.6
4	11.6	46.7
5	12.5	24.5
6	11.5	19.1

* The test conditions are the same as those in Table 4.

Table 6. Bulk and wall exit temperatures calculated by endothermic and non-endothermic models

Test No.*	Endothermic Tbulk (K)	Twall (K)	Non-Endothermic Tbulk (K)	Twall (K)
1	860	906	914	958
2	850	868	900	911
3	850	860	900	903
4	875	888	942	947
5	890	921	970	995
6	891	931	963	998

* The test conditions are the same as those in Table 4.

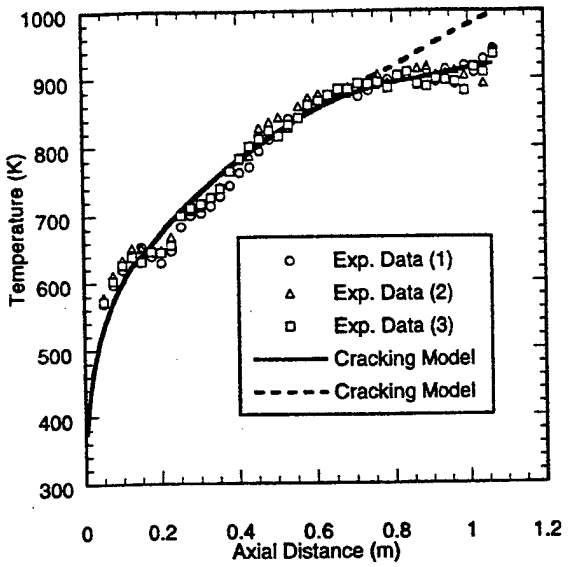

Figure 5. Axial distributions of wall temperature calculated using a 1.1-m tube with flow rate of 20 ml/min and bulk exit temperature of 868 K.

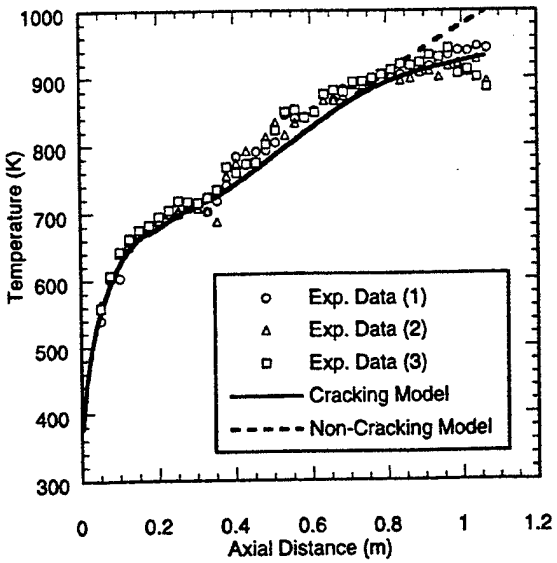

Figure 6. Axial distributions of wall temperature calculated using a 1.1-m tube with flow rate of 30 ml/min and bulk exit temperature of 871 K.

Parametric Study of Cracking Reactions:

Parametric study of the three cracking reactions is performed to examine (1) the relative importance of the primary and secondary cracking, and (2) the relative endothermic performance of the cracking (from Norpar-13) to gases and to liquids. Three cracking models are used in the parametric study. The first cracking model (denoted as Model A) considers only the first-step reaction, i.e., Eq. (1), the second model (denoted as Model B) considers the first- and second-step reactions, i.e., Eqs. (1) and (4), and the third one is the present three-step cracking model.

The relative importance of the primary and secondary cracking is studied by comparing the bulk exit temperatures calculated by Models B and the three-step cracking model. As illustrated in Table 7, the exit temperatures calculated by the two models are almost identical. This comparison suggests that the secondary cracking from n-alkanes to gases is negligible. This result is not surprising since the reaction rate of secondary cracking used in the three-step model is much smaller than those of primary cracking. As suggested by Yu and Eser [15], heavier alkanes can accelerate the cracking of lighter ones in the thermal reactions of n-alkane mixture. If this happens in our tests, re-calibration of secondary cracking rate in our model will be required.

The relative endothermic performance of the cracking to gases and to liquids is analyzed by comparing the bulk exit temperatures predicted by Models A and the three-step model. From Table 7, the bulk exit temperatures calculated by the three-step model are only 5-7 K lower than those obtained by Model A. As discussed earlier in last section, the endotherm of Norpar-13 thermal cracking results in decrease of bulk exit temperature by 50-80 K. This indicates that the cracking to liquids only has minor effect in reducing fuel temperature. Most of the endothermic effect comes from the cracking to gas products.

Table 7. Bulk exit temperatures (K) calculated by Model A, Model B[a], and the current three-step cracking model.

Test No.[b]	Model A	Model B	Three-step
1	866	860	860
2	865	850	850
3	855	850	850
4	881	875	875
5	896	890	890
6	898	891	891

a Model A includes only the first-step reaction and Model B includes the first-step and second-step reactions in the cracking model.
b The test conditions are the same as those in Table 4.

CONCLUSION:

A three-step global model is proposed to describe the thermal cracking of Norpar-13 under supercritical

and near-critical pressure conditions. The cracking model is developed based on a method that lumps the Norpar-13/product mixture into Norpar-13, cracked n-alkane in liquid phase, cracked 1-alkene in liquid phase, and cracked gases. The cracking model is incorporated into a multi-dimensional CFD code to simulate the heat/mass transfer and thermal cracking of Norpar-13 in flow systems. This model is tested against experimental data measured at different flow temperatures and residence times. The simulated temperature and conversion values agree well with experimental data.

The endothermic effect of Norpar-13 thermal cracking is studied using the validated cracking model. For the conditions studied, the calculated endotherm only absorbs about 10% of input power. The calculated endotherm, although not as significant as the heat lost to the environment, has non-negligible effect in reducing fuel and wall temperatures. Our studies show that the endotherm of Norpar-13 thermal cracking results in decreases of bulk exit and wall exit temperatures by 50-80 K and 43-74 K, respectively. The relative endothermic contributions of the cracking (from Norpar-13) to gases and the cracking to liquids are analyzed using the parametric study on the three cracking reactions. The simulation results show that most of the endothermic effect comes from the cracking to gases. The cracking to liquids only plays a minor role in increasing the fuel cooling capacity.

Acknowledgments:

This work is supported by an AF contract (# F33615-96-C-2619). The authors thank Mr. Edwin Corporan, the project monitor, for his support of this work. The authors would also like to thank Dr. Mel Roquemore and Dr. Tim Edwards of Wright Laboratory for their guidance during the course of this work.. The analysis of the cracked gas and liquid products were performed by Mr. Rich Striebich of The University of Dayton Research Institute. The experimental efforts of Mr. Walt J. Balster (ISSI) and Ms Lori M. Balster (ISSI) are acknowledged.

References:

1. Edwards, T., Roquemore, W. M., Harrison, W. E., and Anderson, S. D., "Research and Development of High Temperature Thermal Stability Fuels," AGARD 81st Symp. on Fuels and Comb. Tech., May 10 - 14, 1993, Colleferro, Italy, AGARD-CP-536, pp. 18-1 to 18-19.
2. Edwards, T., and Zabarnick, S., "Supercritical Fuel Deposition Mechanisms," Ind. Eng. Chem. Res., Vol. 32, 1993, pp. 3117-3122.
3. Fabuss, B. M., Smith, J. O., and Satterfield, C. N., "Rapid Thermal Cracking of n-Hexadecane at Elevated Pressures,"., Ind. Eng. Chem. Process Des. Dev., Vol. 1, 1962, pp. 293-299.
4. Zhou, P., and Crynes, B. L., "Thermolytic Reactions of Dodecane," Ind. Eng. Chem. Process Des. Dev., Vol. 25, 1986, pp. 508-514.
5. Khorasheh, F., and Murray, R. G., "High-Pressure Thermal Cracking of n-Hexadecane," Ind. Eng. Chem. Res., Vol. 32, 1993, pp. 1853-1863.
6. Yu, J., and Eser, S., "Thermal Decomposition of C_{10}-C_{14} Normal Alkanes in Near-Critical and Supercritical Regions: Product Distributions and Reaction Mechanisms," Ind. Eng. Chem. Res., Vol. 36, 1997, pp. 574-584.
7. Fabuss, B. M., Smith., J. O., Lait, R. I., Fabuss, M. A., and Satterfield, C. N., "Kinetics of Thermal Cracking of Paraffinic and Naphthenic Fuels at Elevated Pressures," Ind. Eng. Chem. Process Des. Dev., Vol. 3, 1964, pp. 33-37.
8. Wei, J., Kuo, J. C. W., "A Lumping Analysis in Monomolecular Reaction System," Ind. Eng. Chem. Fundam., Vol. 8, 1969, pp. 114-123.
9. Weekman, V. W., Jr., "Lumps, Models, and Kinetics in Practice," AICHE Monogr. Ser., Vol. 75, 1979.
10. Gianetto, A., Farag, H. I., Blasetti, A. P., and de Lasa, H. I., "Fluid Catalytic Cracalyst for Reformed Gasolines. Kinetic Modeling," Ind. Eng. Chem. Res., Vol. 33, 1994, pp. 3053-3062.
11. Coxson, P. G., Bischoff, K. B., "Lumping Strategy. 1. Introductory Technique and Applications of Cluster Analysis," Ind. Eng. Chem. Res., Vol. 26, 1987, pp. 1239-1248.
12. Restek Corporation, Bellefonte, PA.
13. Jones, E. G., and Balster, W. J., "Phenomenological Study of Formation of Insolubles in a Jet-A Fuel," Energy and Fuel, Vol. 7, 1993, pp. 968-977.
14. Edwards T., N., and Anderson, S. D., "Results of High Temperature JP-7 Cracking Assessment," AIAA-93-0806, Reno, NV, 1993.
15. Yu, J., and Eser, S., "Kinetics of Supercritical-Phase Thermal Decomposition of C_{10}-C_{14} Normal Alkanes and Their Mixtures," Ind. Eng. Chem. Res., Vol. 36, 1997, pp. 585-591.
16. Ely , J. F., and Huber, M. L., "NIST Thermophysical Properties of Hydrocarbon Mixtures Database (SUPERTRAPP)," V.1.0 Users' Guide, July 1992.
17. Churchill, S. W., and Chu,. H. S., "Correlating Equations for Laminar and Turbulent Free Convection from a Vertical Plate," Int. J. Heat Mass Transfer, Vol. 18, 1975, p. 1323.
18. Sobel, D. R., and Spadaccini, L. J., "Hydrocarbon Fuel Cooling Technologies for Advanced

Propulsion," ASME-95-GT-226, presented at the 40th International Gas Turbine and Aeroengine Congress and Exhibition, Houston, Texas, June 5-8, 1995.

REPRINTED WITH PERMISSION
Combust. Sci. and Tech., 1998, Vol. 139, pp. 75–111
Reprints available directly from the publisher
Photocopying permitted by license only

Copyright Ownership -
Taylor & Francis Ltd
© 1998 OPA (Overseas Publishers Association) N.V.
Published by license under
the Gordon and Breach Science
Publishers imprint.
Printed in Malaysia.

Modeling of Deposition Process in Liquid Fuels

V. R. KATTA*,†, E. G. JONES† and W. M. ROQUEMORE

Air Force Research Laboratory, Wright-Patterson Air Force Base, OH 45433-7103

(Received 9 August 1997; In final form 31 August 1998)

The thermal stability of jet fuels results from a complex set of chemical reactions, and the deposition process is further complicated by physical mechanisms such as agglomeration and solvation. Although a vast amount of experimental data has been obtained by several researchers, the specific mechanisms responsible for thermal degradation of fuels and the consequent deposit-formation process are still largely unknown. This is primarily due to the fact that the fluid flow and the heat transfer which influence the deposition process vary significantly from experiment to experiment. It is thought that Computational Fluid Dynamics with Chemistry (CFDC) models can be used to correlate the data obtained from a number of experiments and, thereby, explore this large data base to aid the understanding of the deposition phenomenon. The success of this approach depends on the accuracy of the global-chemistry models used in the CFDC codes. Recent experiments on blended fuel prepared by mixing a hydrotreated fuel with a non-hydrotreated one suggest that the thermal stability of the blend cannot be linearly extrapolated from the thermal-stability characteristics of the neat fuels. The global-chemistry models developed previously are found to be insufficient for the simultaneous prediction of deposition and oxidation rates associated with the blended fuel; however, a nine-step model developed most recently appears to yield qualitatively correct results. To improve the predictive capabilities of this model, the rate expressions for the bulk-fuel reactions are modified by taking the antioxidant behavior in jet fuels into account. The resulting modified nine-step global-chemistry model yielded the experimentally observed thermal stability characteristics for the blended fuels. Predictions made for higher flow-rate and temperature conditions also matched well with the experimental data. Overall, the modified nine-step global-chemistry model is found not only to improve the accuracy in predicting quantities such as oxygen consumption and surface deposits but also to provide additional capabilities for predicting quantities such as hydroperoxides and bulk insolubles.

Keywords: Fuels; oxidation chemistry; thermal-stability; modeling; deposition

* Corresponding author. e-mail: vrkatta@snake.appl.wpafb
† Current address: Innovative Scientific Solutions, Inc., 2766 Indian Ripple Road, Dayton, OH 45440-3638.

INTRODUCTION

Before fuel is an aircraft is burned in the combustion chamber, it is used to cool several engine and airframe components as well as electronic equipment. The bulk-fuel temperature and the high wall temperature of these components lead to degradation of the fuel (*i.e.*, chemical decomposition of fuel resulting in the formation of gums and solids that cause fouling of fuel nozzles and heat exchangers). Several laboratory experiments of the flowing (Marteney and Spadaccini, 1986; Ballal *et al.*, 1992) and static (Jones *et al.*, 1992) type have been designed to study the thermal stability of jet fuel. In order to extend the findings derived from various laboratory experiments to real aircraft fuel systems, a thorough understanding of the experimental data is needed. Temperature is usually treated as an effective parameter (Epstein, 1978) for correlating experimentally obtained data and fuel behavior in aircraft. It was also recognized (ANNON:CRC Literature Survey on Thermal Oxidation Stability of Jet Fuel, 1979; Hazlett, 1977) that certain species such as dissolved oxygen and hydroperoxides strongly influence the fouling process. However, since high temperatures and lowflow rates are normally used to accelerate the experiments, often there is no correlation between the results of the different laboratory experiments and no knowledge of how the results are related to the thermal decomposition of the fuel in aircraft fuel-system components. Recently, a general theoretical framework was established by integrating the Computational Fluid Dynamics conservation equations with global-chemistry models for the investigation of thermal-decomposition mechanisms (Roquemore *et al.*, 1989). The resulting Computational-Fluid-Dynamics-with-Chemistry (CFDC) models offer potential for predicting fuel behavior in an engine component based on knowledge gained from laboratory experiments. The success of this approach however, depends on the development of a universal global-chemistry model that can be calibrated for a given fuel using laboratory experiments and the ability of the model to predict deposition over a wide range of flow and temperature conditions for any fuel-system component.

Significant progress has been made in the use of CFD models to predict fluid and thermal characteristics in the complex geometries of practical systems. On the other hand, developments in the chemistry modeling of thermal deposition have been hindered by the lack of fundamental understanding of the complex fuel-degradation processes. However, recent studies with simple global-chemistry models have shown the usefulness of the CFDC approach for predicting fuel thermal stability under different

conditions in heated-tube experiments (Krazinski *et al.*, 1992; Katta and Roquemore, 1993; Zhou and Krishnan, 1996) and in a complicated geometries (Chin and Katta, 1995). These successes offer hope that the CFDC models will become useful tools for research as well as fuel-system component design.

This paper describes several global-chemistry models that have recently been developed and their relationship to the current understanding on semi-detailed chemistry for jet-fuel thermal stability. Also the most recently developed nine-step global-chemistry model was tested for its ability to predict the thermal-stability characteristics of blended fuels obtained by mixing hydrotreated and non-hydrotreated Jet-A fuels. Finally, details are given on modifications proposed and implemented into the nine-step global-chemistry model not only for improving accuracies in predicting quantities such as oxygen consumption and surface deposits but also for predicting additional quantities such as hydroperoxides and bulk insolubles.

BACKGROUND

The susceptibility of hydrocarbon fuel to thermal degradation is usually referred to as thermal instability and is believed to result from a set of complex chemical reactions. Even though the detailed chemical reactions that result in fuel deposits are poorly understood, it is well recognized that the thermal instability of a hydrocarbon fuel depends on many factors such as fuel type, temperature, pressure and the material in contact with the fuel (Marteney and Spadaccini, 1986; ANNON:CRC Literature Survey on Thermal Oxidation Stability of Jet Fuel, 1979; Marteney, 1988; Taylor, 1967; Taylor, 1970). The effect of these factors on deposition has been investigated experimentally under both static and flowing conditions. Several researchers have reported (Hazlett, 1977; Kendall *et al.*, 1987; Giovanetti and Szetela, 1986; Fodor *et al.*, 1988) that the reaction is usually initiated by liquid-phase oxidation of the fuel, which is promoted by dissolved oxygen. The early investigations of Taylor (1967, 1970) which provide the major source of reliable information on fouling of hydrocarbon fuels, suggest that the principal class of fouling reactions is auto-oxidation polymerization which is propagated by a free-radical chain-reaction mechanism in which dissolved molecular oxygen plays a crucial role. Common impurities such as compounds of sulfur, nitrogen, and dissolved metals play a role by either accelerating the reactions or affecting the solubility of the degradation products. On the other hand, at high

temperatures (> 750 K), the deposition reaction is characterized by the pyrolysis of hydrocarbon molecules and the scission of hydrocarbon. The general free-radical mechanism agreed upon by several researchers and outlined by Jones *et al.* (1991) is given below.

Initiation:

$$RH + O_2 \rightarrow R^\circ + {}^\circ OOH \tag{1a}$$

$$ROOH \rightarrow RO^\circ + {}^\circ OH \tag{1b}$$

Propagation:

$$R^\circ + O_2 \rightarrow ROO^\circ \tag{1c}$$

$$ROO^\circ + RH \rightarrow ROOH + R^\circ \tag{1d}$$

Termination:

$$ROO^\circ + ROO^\circ \rightarrow \text{non-radical products} \tag{1e}$$

Here, RH represents hydrocarbon fuel; R°, RO°, and ROO° represent alkyl, alkoxy and peroxy radicals, respectively; and ROOH represents hydroperoxides.

While studying the rates of oxidation and gum formation in different fuels, Mayo and Lan (1986) found that some fuels oxidize faster when initiators such as t-BU_2O_2 are added. Based on these studies they proposed that gum formation is initiated with coupling of two alkyl peroxyl radicals in the chain termination of oxidation (1e). However, it is now generally thought that fuel-degradation products such as soluble gums, insoluble gums, and solids are formed from the hydroperoxides which may be represented using the global step (Zabarnick, 1993)

$$ROOH + R'S \rightarrow \text{gums, solids} \tag{1f}$$

Here, R'S represents a peroxide-decomposing sulfur compound available in the fuel.

The reaction paths (1a)–(1f) describe the oxidation and deposition processes globally; in fact, each of these steps represents several elementary reaction steps. As discussed by Zabarnick (1993), no generally accepted rate parameters exist for the pseudo-global reactions (1a)–(1f). Even though a

detailed description of autoxidation and thermal degradation of hydrocarbon fuel may be formulated by conducting a study on several fuels over a wide range of conditions, the above-described general mechanism yields valuable insights for developing global-chemistry models for the thermal stability of fuels.

GLOBAL MODELS FOR THERMAL STABILITY

Early deposition models were primarily based on the assumption that the quantity of carbon deposited on metal walls is proportional to the amount of heat transferred up to that time (or temperature). These models are basically obtained by representing the mechanism (1a)–(1f) using the global reaction

$$\text{Fuel} \rightarrow \text{Deposits} \tag{2a}$$

The deposition rate is given by

$$\frac{dD}{dt} = \alpha A_{2a} e^{(-E_{2a}/RT)} \tag{2b}$$

Here, D represents deposits on a metal surface, and α is a constant which may be a function of velocity. Because of the over simplifications used, these models mask the physical and chemical structures of the deposition process; however, they are still found to be useful as engineering tools (Chin and Lefebvre, 1992).

Two-step Global Model

A two-step kinetic reaction mechanism was postulated and successfully applied to a number of heated-tube experiments by Giovanetti and Szetela (1986). By representing the oxygenated species (hydroperoxides, alcohols, ketones and carbon monoxide) formed during thermal stressing of the fuel as intermediary precursor (P) to the deposits (D), they formulated the following two-step reaction mechanism:

$$\text{Fuel} + O_2 \rightarrow \text{Fuel} + P \tag{3a}$$

$$\text{Fuel} + P \rightarrow \text{Fuel} + D \tag{3b}$$

The reaction rates are given by

$$RR_{3a} = [O_2]A_{3a}e^{(-E_{3a}/RT)} \tag{3c}$$

$$RR_{3b} = [P]A_{3b}e^{(-E_{3b}/RT)} \tag{3d}$$

In comparison with the mechanism given by Eqs. (1a)–(1f), the first reaction step (3a) of the Giovanetti and Szetela mechanism may be considered the propagation step and the second one (3b), the termination step. This simplification, which yields a tight coupling between the oxygen consumption and deposit formation, is valid only when the concentrations of R° and ROO° are significant. Usually, aircraft fuels contain some types of antioxidants and/or sulfur compounds which tend to control the concentrations of R° and ROO° and, thereby, develops a lag between the oxygen consumption and deposit formation.

In addition to the limitations of the above two-step global mechanism in modeling various fuels, the model has two major drawbacks: (1) It does not take into account mass-transfer effects; (2) It does not have possible precursor-decomposition reactions which are relevant at high temperatures. The experiments of Marteney and Spadaccini (1986) and Taylor (1970) indicate that at higher temperatures (> 645 K), the deposition rate decreases suddenly. This sudden decrease may be due to possible mass-transfer resistance at higher temperatures and/or precursor decomposition. Marteney and Spadaccini (1986) also studied the effect of fuel velocity on deposition rate and found that the reactions become mixing (or transport) limited at elevated temperatures. Clark and Thomas (1988) also found that deposition may be dominated by physical transport or a chemical-reaction process, and the relative importance of these factors is fuel dependent.

Three-step Global Model

In an attempt to improve deposition modeling by incorporating mass-transfer effects and the precursor-decomposition process, Deshpande *et al.* (1989) proposed the following three-step global mechanism.

$$\text{Fuel} + O_2 \rightarrow \text{Fuel} + P \tag{4a}$$

$$\text{Fuel} + P \rightarrow \text{Fuel} + D \tag{4b}$$

$$\text{Fuel} + P \rightarrow \text{Fuel} + CO_2 \tag{4c}$$

It is assumed that reactions (4a) and (4c) occur in the bulk and that reaction (4b) occurs on the wall surface. As a result, the reaction rate (RR_{4b}) for Eq. (4b) is calculated using the concentration of precursor on the wall surface. The time rates of change of the active species are given by

$$\frac{d[O_2]}{dt} = -RR_{4a} \tag{4d}$$

$$\frac{d[P]}{dt} = -RR_{4a} - RR_{4c} - R_m \tag{4e}$$

$$\frac{d[D]}{dt} = RR_{4b} \tag{4f}$$

Here, the mass-transfer rate, R_m is given by

$$R_m = K_m s([P] - [P]_s)$$

where K_m is the mass-transfer coefficient, s is surface area, and $[P]_s$ is the concentration of precursor at the wall which is calculated from molecular diffusion of bulk precursor.

The limited comparisons of predictions and available experimental data (1989) have indicated that the results obtained with the three-step model are only marginally improved over the predictions made by Giovanetti and Szetela (1986) using their two-step model. However, the significant improvement in deposition modeling made by Deshpande *et al.* (1989) through the incorporation of mass-transfer effects and the precursor-decomposition process may be recognized when results for oxygen consumption and deposit formation are compared simultaneously. Equations (3a) and (3b) require that at any time during the reaction, the sum of the concentrations of oxygen, precursor, and deposit must be constant and equal to the initial concentration of oxygen (assuming that the initial concentrations of precursor and deposit species are negligible). Because of this constraint on species concentration, Giovanetti and Szetela (1986) were forced to use an initial concentration of oxygen of only 16% of the value for air-saturated fuel in order to match the predicted and measured maximum deposition rates. This anomaly between initial oxygen concentration and peak deposition rate was resolved in the three-step model since only a fraction of the generated precursor transforms into deposition; the rest either remains in the fuel (because of mass-transfer effect) or is converted into solubles [through Eq. (4c)].

The success with the three-step global model is limited, in part, by the one-dimensional analysis which Deshpande *et al.* (1989) used for the prediction of heated-tube experiments in which large gradients for temperature and, hence, species concentrations exist across the tube. Recognizing the barrier to the development of thermal-stability models imposed by fluid-dynamics simplifications, Roquemore *et al.* (1989) proposed a general theoretical framework by integrating the Computational Fluid Dynamics (CFD) conservation equations with global-thermal-stability models. Krazinski *et al.* (1992) implemented such a framework for studying deposition processes in heated-tube experiments by incorporating a three-step deposition model in a steady-state two-dimensional CFD code.

The three-step model that Krazinski *et al.* (1992) used is identical to the three-step model [Eqs. (4a)–(4c)] described previously. Krazinski *et al.* (1992) assumed that the precursor generated in the bulk fuel is transported to the wall through convection and diffusion, adheres to the wall, and then transforms into deposits. The last two processes were represented globally with a wall reaction such as Eq. (4b). The CFDC approach for predicting thermal stability of fuels was further extended by Katta and Roquemore (1990, 1993) for the prediction of real-time deposition processes in a heated tube and by Chin and Katta (1995) for the prediction of deposition in complex geometries such as aircraft fuel nozzles. The three-step model of Krazinski *et al.* (1992) used in all these investigations was found to yield reasonable predictions for a variety of flow and thermal conditions.

Nine-step Global model

Recent experimental efforts of Jones *et al.* (1991); Heneghan *et al.* (1994); Hardy (1991) and Kauffman *et al.* (1993) suggest that (1) the rate of autoxidation in the majority of fuels is nearly independent of dissolved-oxygen concentration, (2) the deposit-forming precursor is generated through chemical reactions involving hydroperoxides but not directly from reactions involving molecular oxygen, and (3) fuels which oxidize rapidly tend to form more gums and less solids or deposits. The semi-detailed thermal-stability model [Eqs. (1a)–(1f)] described earlier accounts for all of these observations, whereas the two- or three-step global models developed for the prediction of deposition are not capable of addressing these issues.

A nine-step thermal-stability model has been proposed by Katta *et al.* (1993) for the simultaneous prediction of autoxidation and deposit formation in different flowing systems. The model was formulated based on observations made during static flask and dynamic tube experiments and

consists of both bulk-phase and wall reactions. The six bulk reactions used in this model are as follows:

$$O_2 + \text{Fuel} \rightarrow \text{ROOH} \tag{5a}$$

$$\text{ROOH} + \text{Fuel} \rightarrow \text{Solubles} \tag{5b}$$

$$\text{ROOH} + F_s \rightarrow P \tag{5c}$$

$$P + \text{Fuel} \rightarrow \text{Solubles} \tag{5d}$$

$$\text{ROOH} + \text{Fuel} \rightarrow D_{\text{bulk}} \tag{5e}$$

$$D_{\text{bulk}} + \text{Fuel} \rightarrow 2D_{\text{bulk}} \tag{5f}$$

In this global model the species ROOH represents either ROOH or ROO° in the mechanism (1a)–(1f). The first step (5a) of the nine-step model represents the initiation step in the general formulation [*i.e.*, Eq. (1b)]; the second, third and fifth steps represent the reactions (1e) and (1f); the fourth step is the precursor-removing reaction; and finally, the agglomeration of bulk particles is represented chemically with the sixth step. F_s [or R'S in Eq. (1f)] is a non-depleting sulfur compound present in the fuel which usually promotes the deposition process. This model closely follows the general formulation, except that it has no initiation and propagation reactions for controlling the autoxidation process. It was assumed that if the oxygen consumption in a fuel is described by Eq. (5a) with appropriate activation energy and pre-exponential factor, then the above six bulk reactions can represent the thermal stability of hydrocarbon fuels. The specific reaction rates for the six reactions are obtained assuming that the reactions are elementary in nature (*i.e.*, based on the reactant concentrations). However, for fitting the autocatalysis-type oxidation behavior of the aviation fuels, the reaction rate for Eq. (5a) is made independent of oxygen concentration (*i.e.*, zeroth-order reaction).

In addition to the six bulk reactions (5a)–(5f), the following three wall reactions were also used in the above model to describe the entrainment and sticking processes of O_2, P, and D_{bulk}–which, eventually transform to surface deposits (D) after attaching to the walls.

$$O_2|_{wall} \rightarrow D \tag{5g}$$

$$P|_{wall} \rightarrow D \tag{5h}$$

$$D_{bulk}|_{wall} \rightarrow D \tag{5i}$$

The nine-step model, in general, yielded good predictions for surface deposits under significantly different flow and heating conditions. Some of the comparisons between model predictions and experimental data are given in References 10, 11, 28. Even though the model predicts the concentration distributions for ROOH and D_{bulk}, these distributions do not compare well with the experimental data due, in part, to the insufficient representation of production and destruction mechanisms for these intermediate species in the nine-step model.

RESULTS AND DISCUSSION

Thermal Stability of Fuel Blends

The fuel in advanced aircraft will be subjected to a more hostile environment from a temperature viewpoint since these aircraft will generate increased heat loads. To avoid the problems associated with the thermal decomposition of fuel at these expected elevated temperatures, researchers are increasingly concentrating on the development of methods of mitigating fuel-fouling processes. A fundamental method of quantitatively improving the thermal-stability characteristics of a lesser-quality fuel is to introduce additives which may be cost effective compared to refining techniques. An obvious extension of this approach is to consider the potential impact on thermal stability of a fuel mixture obtained by blending two fuels having drastically different thermal-stability characteristics. Recent studies conducted on fuel mixtures include the work of Zabarnick *et al.* (1997); Balster *et al.* (1996) and Jones *et al.* (1996).

For the modeling of thermal stability of a jet fuel in a flowing system, the global-chemistry models described previously must be calibrated specifically for that fuel. This is mainly because of the lack of fundamental data such as concentrations of constituent species in that fuel. When two fuels are blended, then the constituent species in that mixture can be obtained by a linear combination of concentrations of individual species. This suggests that the global-chemistry model of a mixture can be derived from the

calibrated global-chemistry models of the individual fuels. Of course, the success of this approach depends on the accuracy of the model used. In other words, the accuracy of a global-chemistry model in describing the thermal-stability characteristics of a fuel may be tested by predicting the characteristics of a blended fuel using the models calibrated for the individual fuels.

Jones *et al.* (1996) found that the thermal-stability characteristics of a mixture obtained by blending POSF-2827 and POSF-2747 Jet-A fuels could be improved only if the percentage of the former fuel in the mixture were significantly low. These two fuels were previously studied (1992) individually with regard to thermal-stability behavior. It is known that the hydrotreated Jet-A fuel (POSF 2747) belongs to a class of highly stable fuels, and the dissolved oxygen in this fuel will be consumed rapidly (typically, in about 3 min. at 458 K) when the fuel is heated and at the same time the fuel will generate very few deposits. On the other hand, POSF-2827 is a straight-run (non-hydrotreated) Jet-A fuel containing significant amounts of sulfur compounds as impurities. Investigations on this fuel revealed that the dissolved oxygen is consumed very slowly when the fuel is heated (for example, 13 min. at 458 K) and, at the same time, significant amounts of bulk and surface deposits are generated. This inverse behavior between oxygen consumption rate and deposition rate in jet fuels was found by several investigators, and a comprehensive report based on a number of fuels was prepared by Hardy *et al.* (1991).

The experimental data obtained by Jones *et al.* (1996) for two fuels (POSF-2827 and POSF-2747) and for different mixtures of these fuels are shown in Figures 1 and 2. These measurements were made using the experimental rig known as NIFTR (Near-Isothermal Flowing Test Rig). The details of the rig, the measuring techniques employed, and the data-reduction procedures used are described elsewhere (Jones *et al.*, 1991; Balster *et al.*, 1996). The experiments conducted to obtain the data shown in Figures 1 and 2 employed a constant block temperature of 458 K and a stainless steel tube having 0.3175-cm o.d., 0.216-cm i.d., and 188-cm length. However, the initial 5.08 cm of the tube is not placed in the heated copper block. Figure 1 shows the consumption of dissolved oxygen; Figure 2 shows the surface-deposition rate with stress duration. It is important to note that the stress duration for the oxygen-consumption data is varied by changing the residence time (flow rate) in a fixed-length heated tube, whereas the stress duration in Figure 2 represents the location of the fuel element moving at a constant velocity (flow rate = 0.25 cc/min). Under isothermal conditions these two times should represent the same time provided the velocity

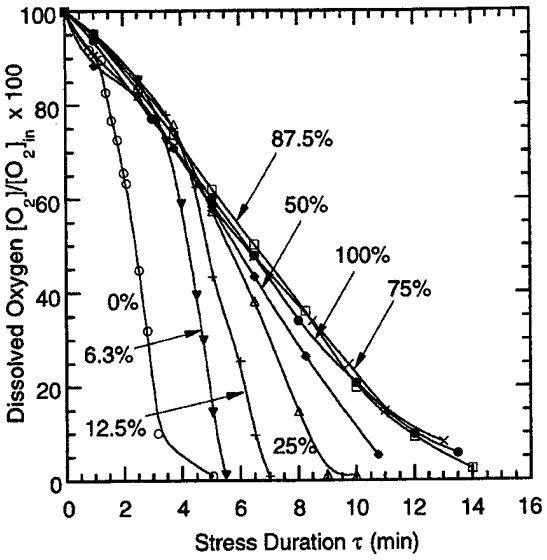

FIGURE 1 Measured oxygen consumption in POSF-2827 and POSF-2747 blends. Percentages represent amount of POSF-2827 in the mixture.

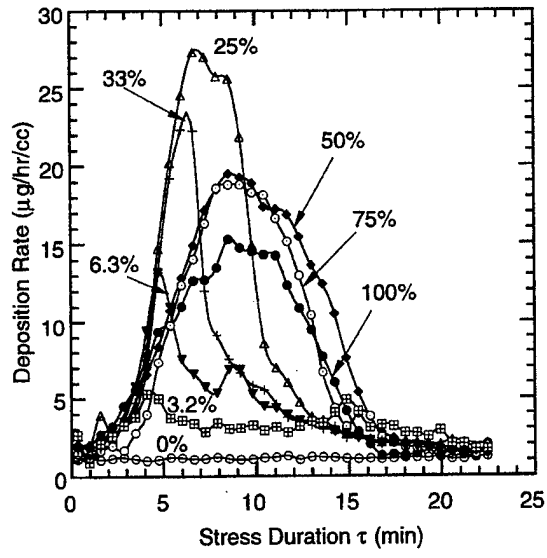

FIGURE 2 Measured surface deposition rate in POSF-2827 and POSF-2747 blends. Percentages represent amount of POSF-2827 in the mixture.

distribution across the tube is independent of flow rate. As the temperature of the fuel in NIFTR increases from room to block (458 K) value in a finite tube length, the extent of the region with non-isothermal conditions along with the velocity distribution vary with the flow rate; hence, the stress time obtained with constant flow rate may not represent the events recorded at the same stress time obtained by varying the flow rate. For this reason, calculations were made using a CFDC code known as "foul2d" for the individual experiments. A brief description of the code is given below [details are given in Ref. (9)].

Fluid motion inside the tubular test section is assumed to be axisymmetric and bounded by the fuel-deposit interface. The time-dependent Navier–Stokes equations along with the turbulent-energy, species-conservation, and enthalpy equations are solved in the x-r cylindrical coordinate system. The transport properties along with the enthalpy and density at a given temperature are obtained from the curve fits developed for Jet-A fuel. The governing equations are discretized utilizing a hybrid scheme (Spalding, 1972) which is a second-order central-differencing scheme everywhere but changes to a first-order upwind scheme when the local Peclet number becomes greater than two. An implicit approach is employed to advance the calculations using a large time-step. This allows the calculations to be performed for real times ranging from minutes to thousands of hours. For the turbulent-flow calculations, wall functions have been used to determine the variations of the flow variables near the fuel-deposit interface. The numerical accuracy and the implementation of boundary conditions were discussed in Reference 9.

Calculations were made for different blends of POSF-2827 and POSF-2747 fuels using the three-step global chemistry model developed by Krazinski *et al.* (1992) Results in the form of oxygen consumption and deposit formation with stress duration are shown in Figures 3 and 4, respectively. The calibrated pre-exponential factors and activation energies for the two neat fuels are shown in Table I. Since the activation energies for the neat fuels are the same, the pre-exponential factors for the blended fuels are obtained from those of the neat fuels using a concentration-based weighted averaging method.

A comparison between the predicted and measured thermal stability data in Figures 1–4 illustrates the difficulties associated with the three-step global-chemistry model. The oxygen-consumption reaction used in the three-step model is first order with respect to oxygen concentration. Therefore, the dissolved oxygen in the fuel decreased exponentially with time as shown in Figure 3 for all fuels, which is quite different from

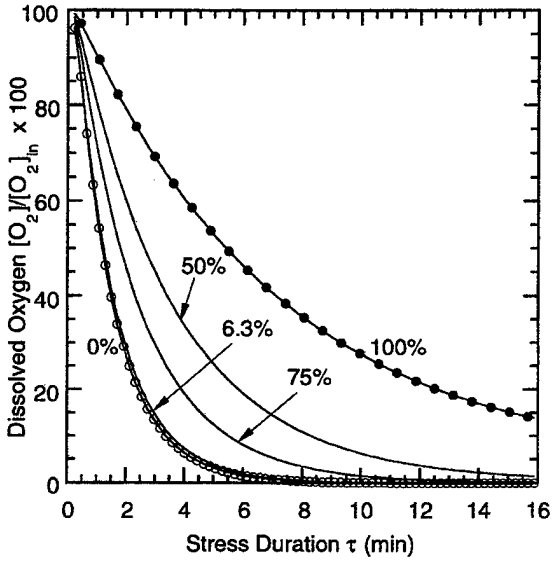

FIGURE 3 Oxygen consumption in POSF-2827 and POSF-2747 blends predicted using two-step global-chemistry model. Percentages represent amount of POSF-2827 in the mixture.

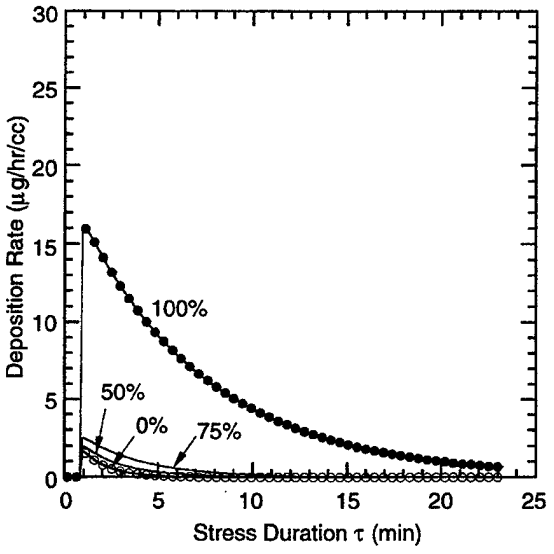

FIGURE 4 Surface deposition rate in POSF-2827 and POSF-2747 blends predicted using two-step global-chemistry model. Percentages represent amount of POSF-2827 in the mixture.

TABLE I Rate constants used for the three-step global-reaction model

Parameter	*POSF-2827*	*POSF-2747*
Activation energy for Reaction (4a)	32,000 cal/mole/K	32,000 cal/mole/K
Pre-exponential factor for Reaction (4a)	$5.22 \times 10^{12}\,s^{-1}$	$4.0 \times 10^{13}\,s^{-1}$
Activation energy for Reaction (4b)	17,000 cal/mole/K	17,000 cal/mole/K
Pre-exponential factor for Reaction (4b)	12 m/s	12 m/s
Activation energy for Reaction (4c)	30,000 cal/mole/K	30,000 cal/mole/K
Pre-exponential factor for Reaction (4c)	1.2×10^{12}	1.2×10^{12}

observations in the experiments (Fig. 1). And also, the predicted oxygen consumption rates for blended fuels decreased more slowly as the concentration of POSF-2827 was reduced, whereas the measured rates decreased more quickly. An explanation for this type of autoxidation behavior in blended fuels is given a little later in this section.

Since deposit-forming precursor in the model is directly generated during the oxidation process, the deposition rate started with a maximum value and then decreased with stress duration (note that the initial 5.08-cm tube is not heated). The models for POSF-2827 and POSF-2747 were calibrated to yield maximum deposition rates of ~ 16 and $\sim 2\,\mu g/hr/cc$, respectively. As seen from Figure 4, the predicted deposition rates for blended fuels deviate significantly from the measurements (Fig. 2). Overall, the three-step model failed to predict the peak deposition rate and its location for different blends of POSF-2827 and POSF-2747 fuels.

Predictions for the thermal-stability of the blended fuels were made using the nine-step global chemistry models described previously. The calibration parameters in this model are (1) the activation energy and the pre-exponential factor for the autoxidation reaction (5a) and (2) the concentration of F_s which represents the amount of sulfur compounds present in fuel. Using the experimental data obtained for the neat POSF-2827 and POSF-2747 fuels, the global nine-step models for these fuels were calibrated. The rate constants obtained for the autoxidation of POSF-2827 are $A_{5a} = 4.4 \times 10^{13}\,mole/m^3/s$ and $E_{5a} = 32{,}000\,cal/mole/K$, and the concentration of F_s was found to be 100 ppm. Similarly, the calibration parameters obtained for POSF-2747 are $A_{5a} = 2.0 \times 10^{14}\,mole/m^3/s$, $E_{5a} = 32{,}000\,cal/mole/K$, and $F_s = 1.2$ ppm. Once the models for the neat fuel are calibrated, then the global-chemistry model for a mixture of these two neat fuels is obtained by weight averaging the pre-exponential and F_s values of the neat fuels (note that the activation energies are the same). The weighting factors were determined from the mole fractions of POSF-2827 and POSF-2747 fuels in the blend. The rate constants for the other reactions are chosen to be the same as those used in Ref. 28.

Results obtained in the form of oxygen consumption and surface deposition for the two neat fuels and three blends are shown in Figures 5 and 6, respectively. Here, the percentage number indicates the amount of POSF-2827 present in the blend. The neat POSF-2747 fuel is referred to as 0% blend. As expected, the model predicted that the oxygen-consumption rates for the blended fuels fall between the rates obtained for the two neat fuels. In general, as the oxygen consumption rate increases with dilution of POSF-2827, the location of the peak deposition rate shifts toward shorter stress times. Interestingly, the magnitude of the peak deposition rate initially increased for a dilution of up to 50% and then decreased with further dilution. The predictions for oxygen consumption (Fig. 5) and deposition (Fig. 6) obtained with the nine-step global-chemistry model qualitatively agree with the respective experimental data in Figures 1 and 2. The measured oxygen-consumption rate for the blended fuels also falls between the rates obtained for the two neat fuels, and the peak deposition rate also initially increases with dilution of POSF-2827. However, a critical comparison of predictions and measurements reveals some important deficiencies of the nine-step thermal-stability model.

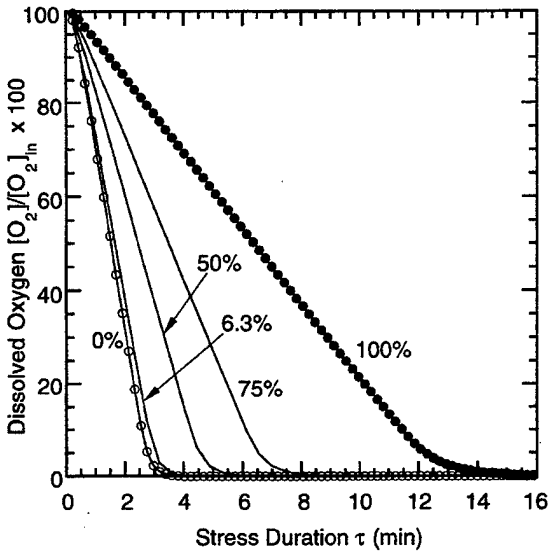

FIGURE 5 Oxygen consumption in POSF-2827 and POSF-2747 blends predicted using nine-step global-chemistry model. Percentages represent amount of POSF-2827 in the mixture.

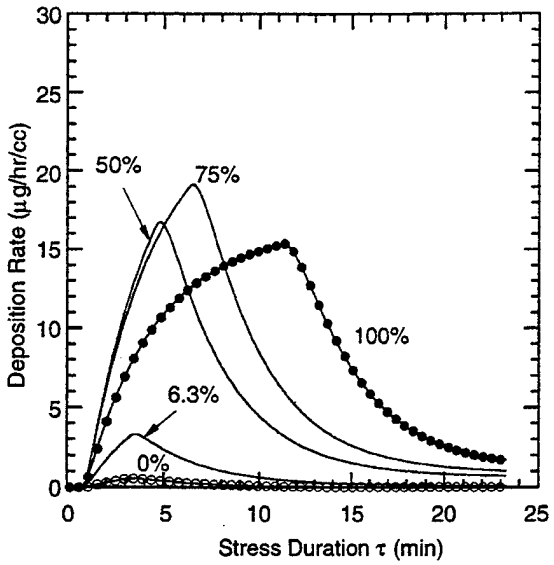

FIGURE 6 Surface deposition rate in POSF-2827 and POSF-2747 blends predicted using nine-step global-chemistry model. Percentages represent amount of POSF-2827 in the mixture.

The experimental data in Figure 1 suggest that when POSF-2747 is added to POSF-2827, the rate of consumption of dissolved oxygen does not change significantly for dilution of up to 75% but then increases more rapidly with further dilution. Jones *et al.* (1996) attributed this behavior to excess amounts of antioxidants present in the straight-run POSF-2827 fuel. Antioxidants in a fuel are known to tie-up the free radicals that are necessary for the autoxidation process. Usually small amounts of antioxidants are sufficient to affect the autoxidation process. On the other hand, the negligible amount of antioxidants present in the hydrotreated POSF-2747 fuel does not influence the autoxidation process and, hence, dissolved oxygen is consumed rapidly in this neat fuel. When POSF-2827 is diluted with antioxidant-free POSF-2747, the effective concentration of antioxidant appears to decrease more quickly with dilution. On the other hand, since the autoxidation reaction (5a) used in the nine-step global model is not a direct function of antioxidant concentration (it needs to be calibrated for a given fuel), the autoxidation rate in blended fuels decreases more slowly with contamination of POSF-2747 fuel by POSF-2827 fuel. Note that in the model, the blended fuels are treated as linear combinations of the two neat fuels with respect to every constituent species.

Since the oxygen consumption in the blended fuel was not altered significantly for dilution of up to 75% (with respect to POSF-2827), the location of the peak deposition rate in the experiments (Fig. 2) did not move significantly from that of the neat POSF-2827. For the other blends having more diluted POSF-2827, the peak-deposition-rate location followed the oxygen-consumption rate and shifted exponentially toward shorter stress times. The peak deposition rate for all blends having at least 6.3% POSF-2827 is higher than that for the neat POSF-2827. This higher deposition rate is attributed to the higher steady-state concentrations of hydroperoxides which mainly build up when the oxygen consumption is delayed by antioxidants. The peroxide-decomposition reaction (1f) is thought to be the main pathway responsible for deposition in jet fuels. The precursor-formation reaction (5c) in the nine-step global-chemistry model represents this peroxide-decomposition process; hence, the predicted peak deposition rate increases when the neat POSE-2827 is diluted up to $\sim$40% with POSF-2747. However, the amount of increase is much smaller than that obtained in the experiments. This could be due, in part, to the difficulty in predicting oxygen-consumption rates for the blended fuels.

Modified Nine-Step Model

A close look at the semi-detailed, thermal-stability model [Eqs. (1a)–(1f)] suggests that the termination of ROOH due to sulfur compounds [R′S in Eq. (1f)] reduces the rate of free-radical initiation and thereby, delays depletion of oxygen in the fuel. On the other hand, as R′S promotes the production of gums and solids, its presence in the fuel increases the deposition also. This behavior of sulfur compounds in the fuel is similar to that of antioxidants. The overall effects of antioxidant reactions due to sulfur compounds are to decrease ROOH and to increase deposition. In contrast, the dissolved metals in the fuel augment the radical initiation [Eq. (1b)] through catalytic reactions and thereby, promote deposition. The overall effects of catalytic reactions due to the dissolved metals are to increase ROOH and deposition in the fuel.

The calibration parameter F_s used in the nine-step model was designed to represent fuels having impurities such as sulfur compounds and metals. However, in the model it influences only the destruction of hydroperoxides, having no bearing on the autoxidation reaction (5a) and, hence, on the production of hydroperoxides. Recently, Ervin *et al.* (1997) incorporated the autoxidation mechanism described by Zabarnick (1993) into the "foul2d" code and demonstrated that the rate of consumption of oxygen in the fuel

can be controlled by varying the concentration of antioxidant or sulfur compounds. This mechanism consists of 17 bulk-phase reactions for the autoxidation process alone. When this mechanism is combined with the insoluble-formation and wall reactions to obtain a comprehensive description for the thermal stability of fuel, the resulting model (still a global one) could become very complicated and the number of "unknowns" in the model could make the calibration procedure using the limited data a near-impossible task. Further research must be performed to determine the rate constants from the first principles for at least some of the reactions involved in this model. Therefore, even though such comprehensive models could be extremely useful in understanding specific processes such the antioxidant behavior in fuels, incorporation of these models into the global-chemistry models for fuel thermal stability may not be possible in the near future. As an alternative approach, some of the problems associated with the nine-step model in predicting the blended-fuel characteristics can be overcome by making F_s in the model influence all the reactions directly or indirectly. This can easily be done by treating the six bulk reactions (5a)–(5f) as global reactions (*i.e.*, reaction rate could be a function of reactants as well as other species). The proposed modifications for the rate expressions of the six reactions (5a)–(5f) are as follow:

$$k_{5a} = \left[\frac{1}{F_s}\right]^{0.4} A_{5a} e^{(-E_{5a}/RT)} \tag{6a}$$

$$k_{5b} = [F_s]^{0.4}[\mathrm{ROOH}] A_{5b} e^{(-E_{5b}/RT)} \tag{6b}$$

$$k_{5c} = [F_s][\mathrm{ROOH}] A_{5c} e^{(-E_{5c}/RT)} \tag{6c}$$

$$k_{5d} = \left[\frac{[\mathrm{O_2}]_{\mathrm{in}} - [\mathrm{O_2}]}{[\mathrm{O_2}]_{\mathrm{in}}}\right]^3 [P][F_s]^{-1} A_{5d} e^{(-E_{5d}/RT)} \tag{6d}$$

$$k_{5e} = [F_s][\mathrm{ROOH}] A_{5e} e^{(-E_{5e}/RT)} \tag{6e}$$

$$k_{5f} = [D_{\mathrm{bulk}}]^{0.4} A_{5f} e^{(-E_{5f}/RT)} \tag{6f}$$

Here, $[\mathrm{O_2}]_{\mathrm{in}}$ represents the initial concentration of dissolved oxygen present in the fuel and F_s, the equivalent concentration of sulfur compounds and

antioxidants. According to the new rate expression (6a) for the autoxidation reactions (5a), the rate of consumption of oxygen decreases as the concentration of F_s increases. A hydrotreated fuel with a very low value of F_s depletes the dissolved oxygen rapidly. However, the modification incorporated to the rate expression for reaction (5a) affects the production of ROOH as well. The semi-detailed model for thermal stability suggests that the rate of oxygen consumption in the fuel is controlled by the steady-state concentration of ROOH which is modified by the presence of antioxidants and sulfur compounds. Therefore, the rapid buildup of ROOH with decreasing F_s in the modified nine-step model is controlled by accelerating the conversion of ROOH into solubles using Eq. (6b). The rate expression (6c) is the same as the one used in the original nine-step model (Katta *et al.*, 1993).

Finally, the surface-deposition rate resulting from the wall reactions (5g) through (5i) is given as

$$\frac{d[D]}{dt} = [O_2]_{wall} A_{5g} e^{(-E_{5g}/RT)} + [P]_{wall} A_{5h} e^{(-E_{5h}/RT)} + [D_{bulk}]_{wall} A_{5i} e^{(-E_{5i}/RT)} \tag{6g}$$

Note that the shear-stress factor used in the original nine-step model is not considered in this modified one to avoid the influence of possible uncertainties in estimating shear stress using different turbulence models on deposition prediction.

Several experiments have shown that the rate of surface deposition decrease to a near-zero value as the oxygen in the fuel is completely consumed which means that certain products generated during the oxidation of fuel tend to remove the deposit-forming precursor. This effect is integrated into the nine-step global model by making the rate expression (6d) for the precursor-destruction reaction proportional to the amount of oxygen depleted and inversely proportional to F_s. The production of bulk particles in the modified nine-step model is also set proportional to the concentration F_s, and their agglomeration is limited by replacing power 1 with 0.4 in Eq. (6f).

The modified nine-step model is used to predict the thermal-stability characteristics of the blended fuels. The activation energy and pre-exponential factors for the six bulk-phase and three wall reactions were calibrated for the neat POSF-2827 fuel by assuming 100 ppm of F_s present in this fuel. The rate parameters are given in Table II. The neat fuel POSF-2747 is treated mathematically in the same way (same rate constants) as the

TABLE II Rate constants used for the modified nine-step global-reaction model

Reaction	*Pre-exponential factor (A)*	*Activation energy (E)*
5a	1.16×10^{11} mole/m^3/s	32,000 cal/mole/K
5b	3.98×10^{5} s^{-1}	10,000 cal/mole/K
5c	8.0×10^{9} s^{-1}	15,000 cal/mole/K
5d	2.4×10^{10} s^{-1}	35,000 cal/mole/K
5e	1.2×10^{6} s^{-1}	10,000 cal/mole/K
5f	1.0×10^{-8} s^{-1}	0
5g	2.0×10^{-2} m/s	15,000 cal/mole/K
5h	1.4×10^{3} m/s	22,000 cal/mole/K
5i	0.5×10^{-2}	10,000 cal/mole/K

POSF-2827 fuel except that the concentration of F_s is only 1.2 ppm. Therefore, only one set of rate constants was used for simulation of the thermal-stability characteristics of two neat fuels and their blends.

The oxygen-consumption and surface-deposition rates in different mixtures of POSF-2827 and POSF-2747 fuels are shown in Figures 7 and 8, respectively. As the neat POSF-2827 is diluted with the hydrotreated POSF-2747 fuel, the oxygen-consumption rate increases slightly for dilution up to 75% and then increases rapidly with further dilution. These

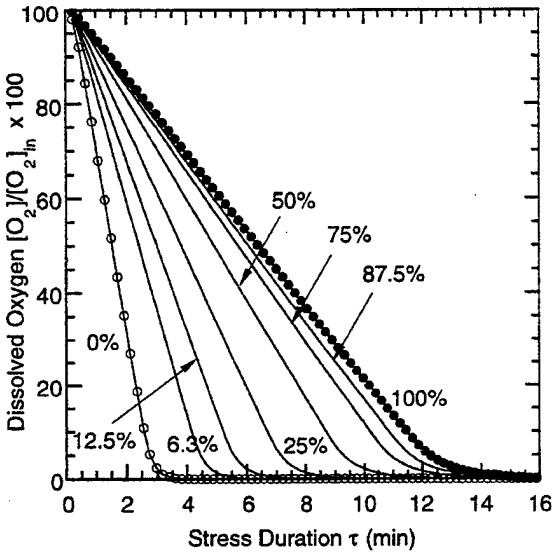

FIGURE 7 Oxygen consumption in POSF-2827 and POSF-2747 blends predicted using modified nine-step global-chemistry model. Percentages represent amount of POSF-2827 in the mixture.

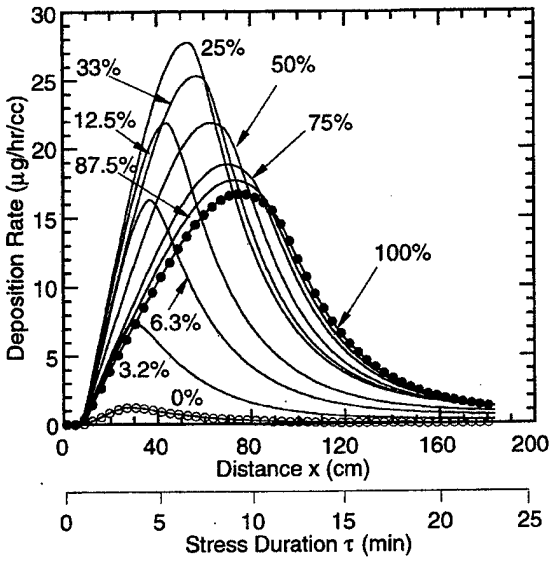

FIGURE 8 Surface deposition rate in POSF-2827 and POSF-2747 blends predicted using modified nine-step global-chemistry model. Percentages represent amount of POSF-2827 in the mixture.

consumption rates agree very well with those obtained in the experiments (Fig. 1). Following oxygen consumption, the location of the peak deposition rate in Figure 8 for the blends also shifts toward shorter stress times – initially slowly and then more rapidly with POSF-2747 dilution. The mixture of 25% POSF-2827 and 75% POSF-2747 yields the highest deposition rate of ~ 27 mg/hr/cc. The peak deposition rates for different blends and neat fuels correspond well to those measured by Jones *et al.* (1996).

The modified-nine-step model was developed to predict the concentrations of bulk deposits in stressed fuel along with oxygen-consumption and surface-deposition rates. Bulk deposits in the experiments are usually measured by placing a sub-micron-size filter in the fuel passage. Jones *et al.* (1996) collected the bulk deposits in different blended fuels of POSF-2827 and POSF-2747 by placing a sub-micron-size filter in the fuel stream immediately downstream of the heated-tube test section. Therefore, the concentrations of bulk deposits present in the fuel at the end of the heated-tube section were obtained for different fuel blends in the present simulations and plotted in Figure 9 along with the total amount of surface

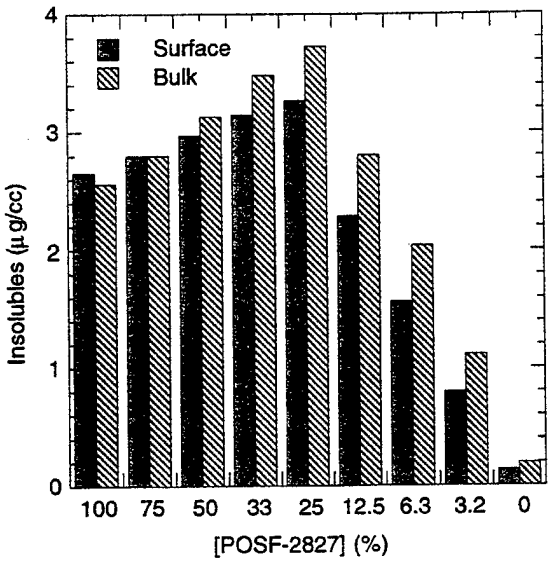

FIGURE 9 Predicted total amount of surface and bulk deposits in POSF-2827 and POSF-2747 blends.

deposits. The latter was obtained by integrating the area under each curve shown in Figure 8. The corresponding data obtained from the experiments (Jones *et al.*, 1996) are shown in Figure 10. As the POSF-2827 fuel is mixed with POSF-2747, both the bulk and surface deposits (or insolubles) increase for dilution up to 25% with respect to the former fuel. While the neat POSF-2827 fuel yields more surface deposits than bulk deposits, the former gradually decreases with POSF-2747 dilution, whereas the latter gradually increases. Calculations showed that when the dilution level is increased to 50%, bulk insolubles exceed those collected on the surface. As dilution is increased beyond the 25% level, both the surface and bulk deposits decrease rapidly, and a very small amount of deposits is predicted for neat POSF-2747 fuel. Similar trends in bulk and surface deposits with respect to dilution of POSF-2827 with POSF-2747 were observed in the experiments of Jones *et al.* (1996). As shown in Figures 9 and 10, good agreement between the predictions and experimental data was obtained.

The calculated and measured (Jones *et al.*, 1996) hydroperoxide concentrations for different fuel blends are shown in Figures 11 and 12, respectively. In general, the concentration of ROOH decreases with the contamination of POSF-2747 with POSF-2827. The low concentration of

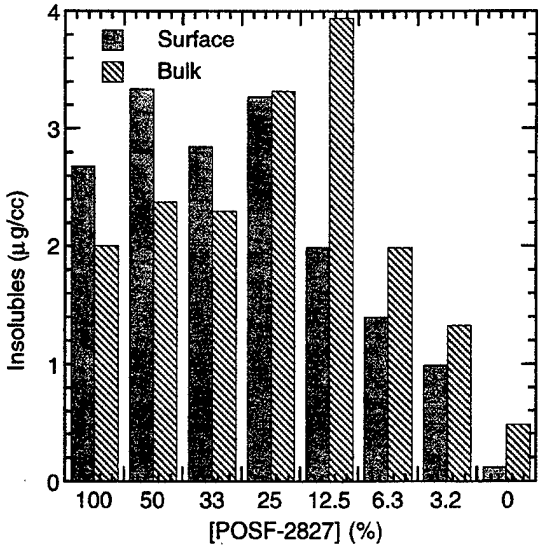

FIGURE 10 Total quantities of surface and bulk deposits measured in POSF-2827 and POSF-2747 blends.

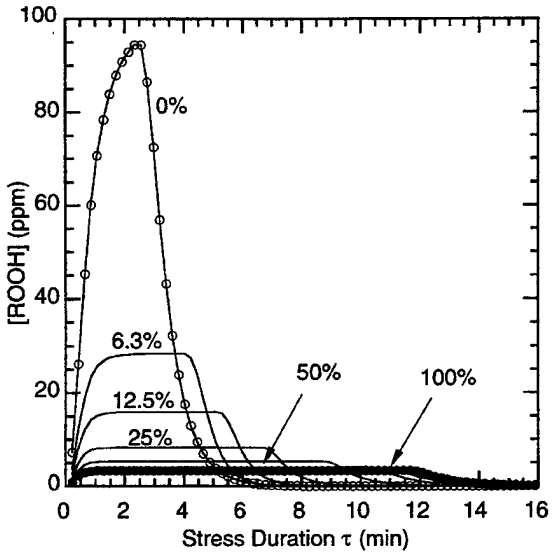

FIGURE 11 Predicted hydroperoxides in POSF-2827 and POSF-2747 blends. Percentage represent amount of POSF-2827 in the mixture.

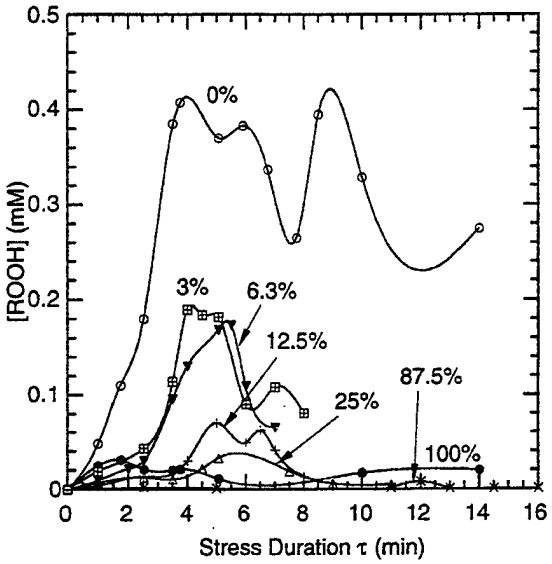

FIGURE 12 Measured hydroperoxides in POSF-2827 and POSF-2747 blends. Percentage represent amount of POSF-2827 in the mixture.

sulfur compounds in the hydrotreated fuel is responsible for the buildup of ROOH. In contrast, the high concentration of F_s in the straight-run fuel (POSF-2827) is consuming most of the hydroperoxides formed during the autoxidation process. In neat POSF-2747 the concentration of ROOH has increased rapidly with stress duration, reaching a maximum value at about 3 min. The qualitative agreement between the predicted and measured concentrations for ROOH seems reasonable, especially considering the fact that a significant amount of uncertainty exists in the measurements for ROOH. A major discrepancy can be noted from the data obtained for neat POSF-2747 in Figures 11 and 12. While calculations yielded rapid consumption of ROOH after a maximum at $\sim$3 min, the experiments showed a steady concentration at all times after 3 min of stressing. Interestingly, even in the blended fuel having nearly 93.3% POSF-2747 (*i.e.*, 6.3% of POSF-2827), hydroperoxide depletion began soon after the maximum was reached. To understanding the observed peculiar behavior of neat POSF-2747, further investigations will be required.

The bulk deposits shown in Figure 9 were obtained at the end of the heated-tube section, and the surface deposits shown in Figures 8 and 9 were obtained at the tube surface. A majority of these surface deposits result from

the transport of precursor (P) in the bulk fuel to the walls. The distributions of bulk precursor and deposits in the heated tube are shown in Figures 13 and 14, respectively. The bulk precursor concentrations closely follow the surface-deposition rates shown in Figure 8 for these isothermal conditions. Also, the identical shapes of the plots in Figures 8 and 13 suggest that the fraction of precursor lost to the walls during the deposition process is quite insignificant. Most of the precursor is converted to solubles through reaction (5d). As seen in Figure 14, the concentration of bulk deposits has increased almost linearly and then reached a constant value. The agglomeration process seems very slow at this temperature of 458 K.

Figure 15 shows the distribution of velocity, temperature, and concentration of O_2, ROOH, P, and D_{bulk} within the test-section for the neat POSF-2827 case. At this low flow rate of 0.25 cc/min, the flow became a fully developed laminar one and most of the flow is under isothermal conditions. Oxygen [Fig. 15(c)] is consumed gradually, and oxygen-free fuel is established in the second half of the test-section. During the autoxidation process, the concentration of ROOH remained nearly constant, as seen in Figure 15(d). The modified nine-step model simulates steady-state concen-

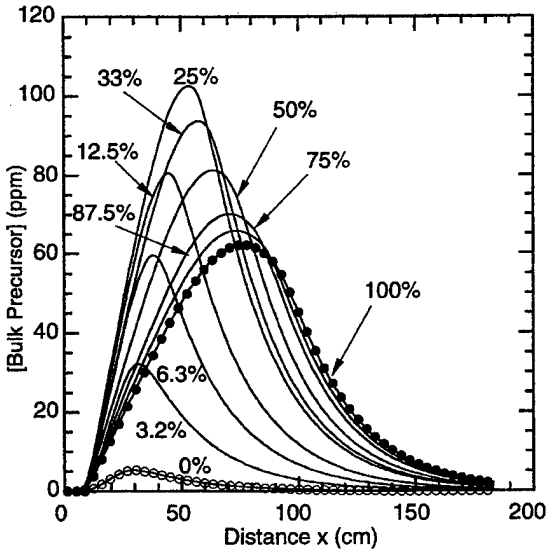

FIGURE 13 Predicted concentrations of precursor in bulk fuel as POSF-2827 and POSF-2747 blended fuel passes through the heated tube. Percentages represent amount of POSF-2827 in the mixture.

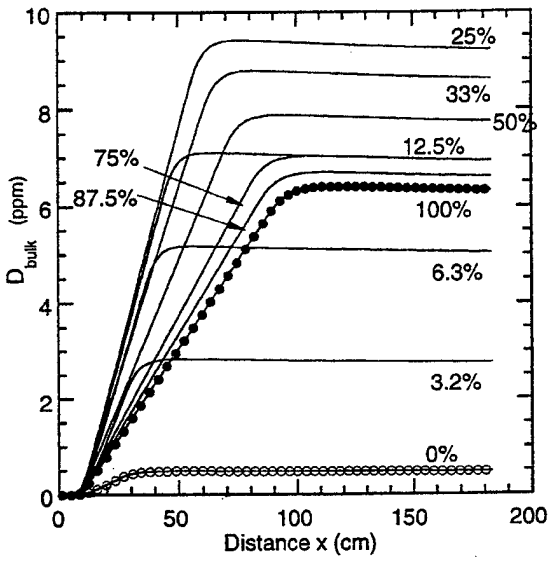

FIGURE 14 Predicted concentrations of solids in bulk fuel (D_{bulk}) as POSF-2827 and POSF-2747 blended fuel passes through the heated tube. Percentages represent amount of POSF-2827 in the mixture.

trations for ROOH—very similar to the semi-detailed oxidation-model predictions. Interestingly, even though the fuel in the test-section is under isothermal conditions, the concentrations of different species are not uniform within the tube cross section because of the small heating zone at the entrance of the test-section. Among the species considered, the bulk particles show the most significant variation across the tube cross section.

Predictions for Higher Flow-Rate Conditions

Simulations made for blended POSF-2827 and POSF-2747 fuels at 458 K and a flow rate of 0.25 cc/min suggest that the modified nine-step model for fuel thermal stability predicts the surface and bulk deposits with reasonable accuracy. These near-isothermal studies are useful for understanding and, thereby, developing global mathematical models for thermal stability. However, since most practical systems involving thermal management operate under non-isothermal and turbulent-flow conditions, the thermal-stability models developed under iso-thermal conditions should also be applicable for flows in which the temperature varies over a wide range.

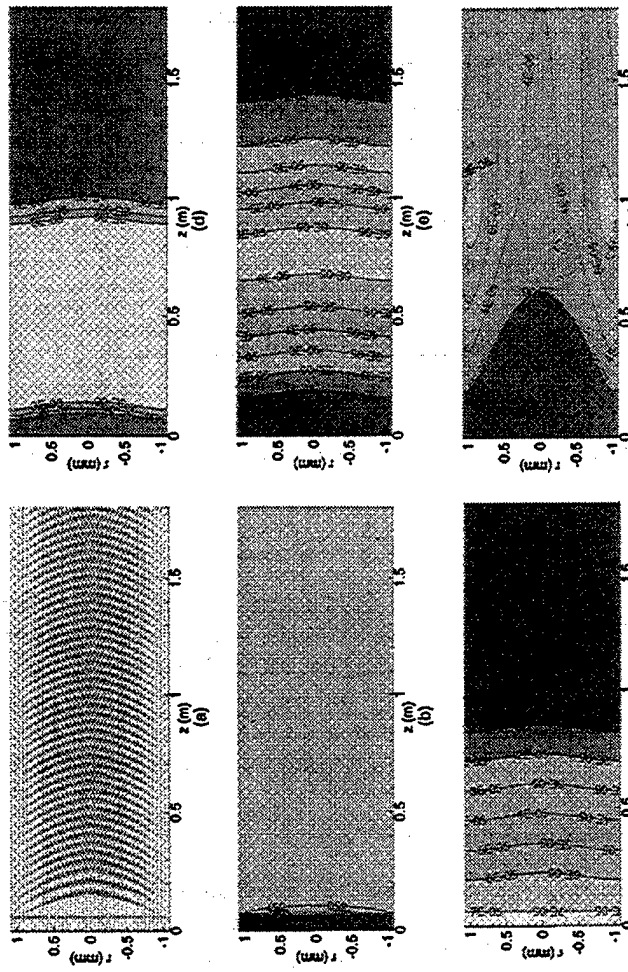

FIGURE 15 Distributions of (a) velocity, (b) temperature, (c) remaining dissolved oxygen, (d) hydroperoxides, (e) precursor, and (f) D_{bulk} particles in near-isothermal heated tube.

Recently, Jones *et al.*, extended the operating range of the NIFTR for studying the effects of additives on fuel thermal stability under non-isothermal conditions. Typical results obtained for a Jet-A fuel with JP-8 additive (designated by Wright Laboratory as POSF-3219 fuel) are shown in Figure 16. The block temperature (T_{Block}) and flow rate used in this experiment were 573 K and 16 cc/min, respectively. Calculations were made for this experiment using the modified nine-step model. The only variable in this model that must be calibrated for a given fuel is, F_s, the concentration of sulfur compounds involved in the deposition process. It is known that 1) the thermal-stability characteristics of JP-8 class POSF-3219 fuel are superior to those of the straight-run POSF-2827 fuel and 2) the total amount of sulfur present in the former fuel is only ~42% of that in the latter (321 and 763 ppm, respectively). Therefore, calculations for the heated-tube experiment with POSF-3219 fuel were performed using a value of 40 ppm (by volume) for F_s rather than the 100 ppm used for the simulations with POSF-2827 fuel.

Earlier numerical and experimental studies (Katta *et al.*, 1995) on a rig very similar to the NIFTR suggested that (1) although the flow at 16 cc/min does not represent a turbulent one based on Reynolds number, it becomes turbulent because of buoyancy and a simulation assuming turbulent flow inside the tube represents the experiment more closely and (2) the

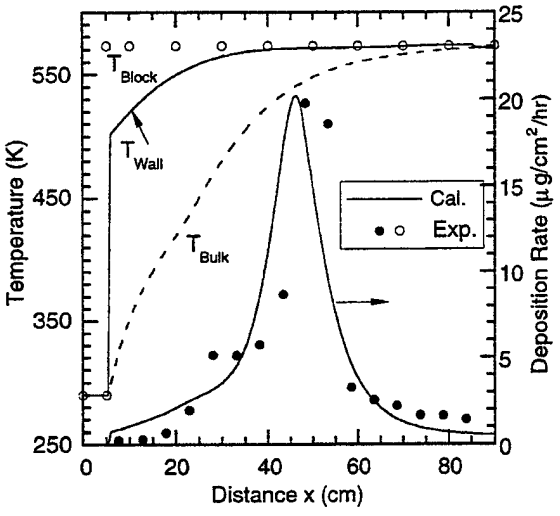

FIGURE 16 Predicted and measured surface deposition rate along tube length. Flow rate was 16 cc/min, block temperature was 573 K, and fuel used was POSF-3219.

temperature of the tube wall deviates from that of the block near the entrance. Therefore, calculations for the NIFTR experiment under non-isothermal conditions were performed assuming the flow to be turbulent and the wall-temperature (T_{wall}) distribution to be as shown in Figure 16. Predicted surface deposition rate and bulk-fuel temperature are shown by solid and broken lines, respectively. As this figure shows, a good correlation between predicted and measured deposition rates is obtained with the modified nine-step model. The measured and predicted oxygen-consumption rates at 458 K with respect to stress duration are plotted in Figure 17. As expected, calculations predict that the dissolved oxygen in POSF-3219 fuel (70 ppm by weight) will be completely consumed in about 7 min – much more rapidly than that observed in POSF-2827 fuel which has a higher concentration of sulfur compounds. Predictions for dissolved oxygen showed good correlation with measurements until the available oxygen fell below 50% of the initial value. At this level the measured data suggest that consumption of oxygen is accelerated and that all available oxygen is depleted in about 4.5 min. It is believed that this acceleration in the experiments results from increased decomposition of hydroperoxides through Reaction (1b) at the active tube walls. Usually, in deposition experiments such as those represented by Figure 16, the reactivity of the tube walls decreases as the deposits build up. As a result the oxygen-consumption rate in tubes coated with carbon is lower than that in the clean tubes. Since the data shown in Figure 17 were obtained with clean tubes, the acceleration at longer stress durations could result from surface catalysis which is not considered in the present nine-step model. Overall, the agreement obtained between predictions and experimental data for both surface deposition and oxygen consumption under non-isothermal conditions is quite reasonable.

The second case considered for the purpose of assessing the ability of the modified nine-step model in predicting fuel thermal stability under turbulent conditions is taken from the experimental work of Edwards and Krieger (1995). A Jet-A fuel (designated by Wright Laboratory as POSF-2926) was passed through a 0.32-cm-o.d, 0.14-cm-i.d, and 122-cm-long stainless steel tube placed in a furnace heated to $\sim$800 K. The flow rate used in this experiment was 102 cc/min. Because of the high flow rate and poor contact between the furnace and the tube outer wall, the thermal boundary condition along the tube outer wall was a combination of constant heat flux and constant temperature; however, for simulation purposes it is thought that a constant-heat-flux boundary condition represents this experiment more accurately than a constant-temperature boundary condition.

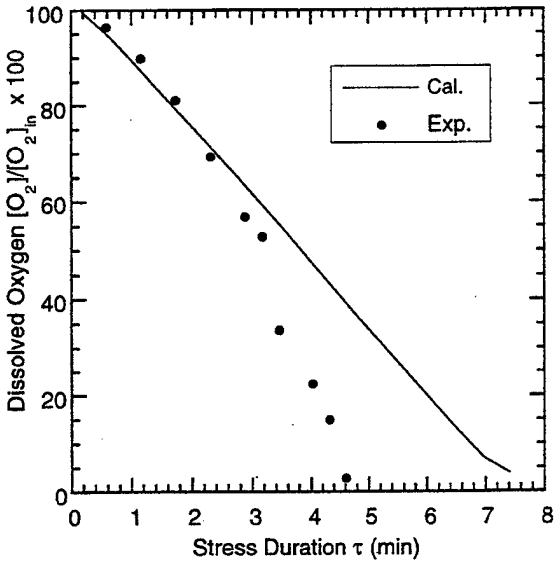

FIGURE 17 Predicted and measured oxygen consumption in POSF-3219 fuel. F_s = 40 ppm by volume.

Results obtained from the turbulent simulations for the above experiment are shown in Figure 18. Toward the exit of the tube, the tube wall (T_{wall}) begins to attain the furnace temperature. The bulk fuel temperature predicted at the exit of the tube correlates well with the measured value. Since the total sulfur present in this fuel (POSF-2926) is 524 ppm (~ 67% of that measured in POSF-2827 fuel), a value of 70 ppm (by volume) is used for F_s to simulate the thermal stability of the fuel in this experiment. The predicted and measured deposition rates are plotted in Figure 19. The predicted peak deposition rate of 250 μg/cm^2/hr, its location of 80 cm, and its fall off for tube lengths > 80 cm compare favorably with measured values. However, experiments have yielded higher deposition rates in tube sections that are < 80 cm from the entrance. This could be due, in part, to the inaccuracy in prescribing the temperature boundary condition along the tube outer wall.

The last case considered here is an experimental investigation conducted by Marteney and Spadaccini (1986) at United Technology Research Center (UTRC). They used a 244-cm-long stainless-steel tube having an inside diameter of 0.224 cm for determining the thermal stability of a copper-contaminated JP-5 fuel. The tube was directly heated by passing current

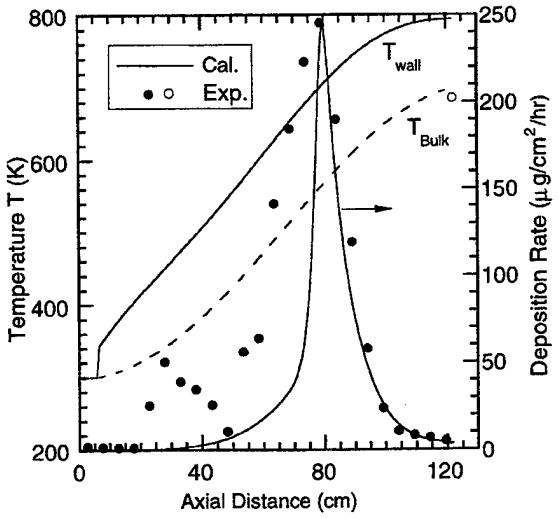

FIGURE 18 Predicted and measured surface deposition rate along tube length. Flow rate was 102 cc/min, block temperature was 800 K, and fuel used was POSF-2926.

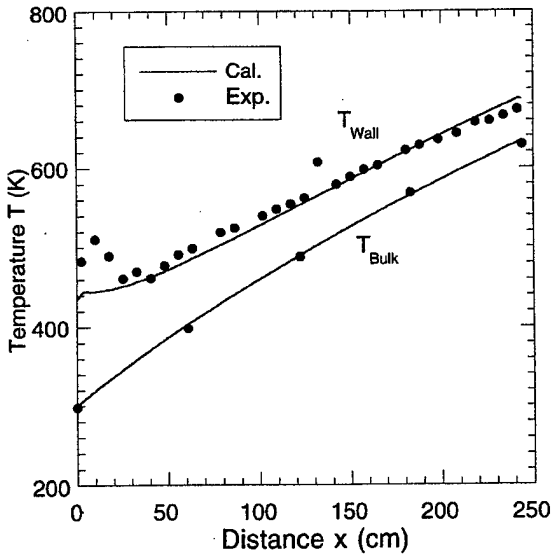

FIGURE 19 Wall and bulk-fuel temperatures along tube length obtained in UTRC's constant-heat-flux experiment. Jet A fuel at a flow rate of 502 cc/min was used.

through it which resulted in a constant-heat-flux boundary condition. A flow rate of 502 cc/min was used to generate a fully turbulent flow inside the tube. This experiment was modeled earlier by Giovanetti and Szetela (1986) using a two-step mechanism and by Krazinski *et al.* (1992) using three-step mechanism. In both of these works, this experiment was used to calibrate the rate constants of the two-step and three-step reaction mechanisms.

Calculations were made for the experiment of Marteney and Spadaccini using the modified nine-step model and "foul2d" time-dependent CFD code. The near-linear temperature profiles of the tube outer wall and bulk fuel resulting from the constant-heat-flux boundary condition are compared with the experimental data in Figure 19. The initial spike in tube-outer-wall temperature indicates the flow transition from laminar to turbulent. However, calculations did not predict this spike since they were performed assuming a turbulent flow all along the tube. The predicted and measured deposition rates are compared in Figure 20. The high peak deposition rate on the order of 1200 $\mu g/cm^2/hr$ resulted, in part, because of the copper used in the fuel to accelerate the deposition process. Since all the metals that promote deposition are treated as "F_s" in the nine-step model, a high value of 400 ppm (by volume) was chosen for F_s to simulate this copper-

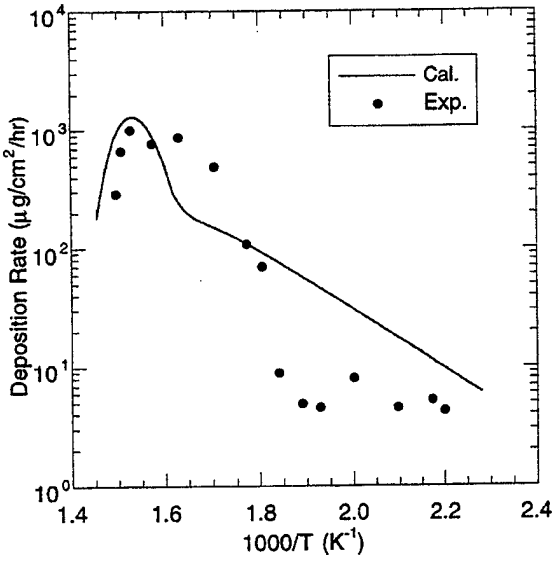

FIGURE 20 Predicted and measured surface deposition rate with respect to wall temperature in UTRC's experiment. F_s = 400 ppm by volume.

contaminated JP-5 fuel. As evident from Figure 20, the model correctly predicted the location and magnitude for the peak deposition rate. However, as also observed in the previous case (Fig. 17), the model predictions appear to deviate from the measurements at lower temperatures.

The modified nine-step model developed in the present study represents a "global" model for the thermal stability of the fuel, and the rate constants given in Table II are not the universal values. A fine adjustment for these rate constants may be required for each fuel to achieve a more accurate representation which requires a significant amount of controlled experimental data just for calibration purposes. On the other hand, the significant advancement in the modeling of fuel thermal stability achieved with the modified nine-step model is the use of a single variable "F_s" that must be calibrated for a given fuel. Calculations made with POSF-2827, POSF-2747, POSF-3219, and POSF-2926 fuels suggest that the value of "F_s" in a given fuel can be obtained by measuring the total amount of sulfur present in the fuel.

SUMMARY AND CONCLUSIONS

Although a vast amount of experimental data has been obtained by several researchers, the specific mechanisms governing thermal degradation of fuels and the consequent deposit-formation process have yet to be identified, primarily because the fluid flow and heat transfer which influence the deposition process vary significantly from experiment to experiment. It is thought that CFDC models will be useful in correlating the data obtained from various experiments and, thereby, exploring the large data base in attempts to understand the deposition phenomenon. The success of this approach depends on the accuracy of the global-chemistry models used in the CFDC codes. Different recently developed global-chemistry models have been described in this paper as well as their relationship to current understanding on the semi-detailed chemistry for jet-fuel thermal stability.

Recent experiments on blended fuels prepared by mixing hydrotreated fuel with a non-hydrotreated fuel suggest that the thermal stability of the blend cannot be linearly extrapolated from the thermal-stability characteristics of the neat fuels. Calculations were performed using the CFDC code known as "foul2d" for the prediction of the thermal-stability behavior of fuel blends. The global-chemistry models developed previously were found to be insufficient for simultaneous prediction of the deposition and oxidation rates associated with the blend fuels. However, the recently developed nine-step model appears to yield qualitatively correct results. The

rate expressions for the bulk-fuel reactions in the nine-step model were modified to incorporate antioxidant behavior in jet fuels. These modifications yielded results that are in good agreement with the experimental data. Predictions made for higher flow-rate and temperature conditions also showed good correlation with the experimental data. Overall, the modified nine-step global-chemistry model has been found not only to improve the accuracy in predicting quantities such as oxygen consumption and surface deposits but also to provide additional capabilities for predicting quantities such as hydroperoxides and bulk insolubles.

Acknowledgements

This work was supported, in part, by Air Force Contract F33615-95-C-2507 and the Air Force Office of Scientific Research. The authors would like to thank Mrs. Marian Whitaker for editorial assistance and Dr. J. C. Sheu for testing the models using CFDRC's ACE code.

References

ANON: CRC Literature Survey on Thermal Oxidation Stability of Jet Fuel (1979) CRC Report No. 590, Coordination Research Council, Inc., Atlanta, GA, April.

Ballal, D. R., Byrd, R. J., Heneghan, S. P., Martel, C. R., Williams, T. F. and Zabarnick, S. (1992) Combustion and Heat Transfer Studies Utilizing Advanced Diagnostics: Fuels Research, Wright Laboratory Technical Report WL-TR-92-2112, Nov. 1992, Wright-Patterson AFB, OH.

Balster, L. J., Blaster, W. J. and Jones, E. G. (1996) Thermal Stability of Jet-Fuel/Paraffin Blends, *Ind. Eng. Chem. Res.*, **10**, 1176.

Clark, R. H. and Thomas, L. (1988) "An investigation of the Physical and Chemical Factors Affecting the Performance of Fuels in the JFTOT", *Presented at the SAE Aerospace Technology Conf. and Exposition*, Anaheim, CA.

Chin, J. S. and Lefebvre, A. H. (1992) Influence of Flow Conditions on Deposits from Heated Hydrocarbon Fuels, ASME Paper 92-GT-114, *Presented at the International Gas Turbine and Aeroengine Congress and Exposition*, Cologne, Germany, June 1–4.

Chin, L. P. and Katta, V. R. (1995) *Numerical Modeling of Deposition in Fuel-Injection Nozzles*, AIAA Paper 95-0497, AIAA, Reston, VA.

Deshpande, G. V., Micheal, A. S., Solomon, P. R. and Malhotra, R. (1989) Modeling of the Thermal Stability of Aviation Fuels, *Presented at the 198th ACS National Meeting, Symposium on the Chemical Aspects of Hypersonic Propulsion*, Miami, FL.

Edwards, T., Anderson, S. D., Pearce, J. A. and Harrison, W. E. (1992) High Temperature Thermally Stable JP Fuels–An Overview, AIAA 92-0683, *Presented at 30th Aerospace Sciences Meeting and Exhibit*, Jan. 6–9, Reno. NV.

Edwards, T. and Krieger, J. (1995) The Thermal Stability of Fuels at 480°C (900 F). Effect of Test Time, Flow Rate, and Additives, Paper No. 95-GT-68, *Presented at the International Gas Turbine and Aeroengine Congress and Expo.*, Houston, TX, June 5–8.

Epstein, N. (1978) Fouling of Heat Exchanges, *in Heat Exchangers Sourcebook*, Ed., Pale, J. W., Hemisphere Publishing Co., Washington, D.C., pp. 235–253.

Ervin, J. S., Zabarnick, S. and Williams, T. F. (1997) Modeling of Jet Fuel Oxidation at Low Temperatures, AIAA Paper, *Presented at 35th AIAA Aerospace Sciences Meeting*, Reno, NV, Jan. 6–10.

Fodor, G. E., Naegeli, D. W. and Kohl, K. B. (1988) Peroxide Formation in Jet Fuels, *Energy and Fuel*, **2**, 729.

Giovanetti, A. J. and Szetela, E. J. (1986) Long Term Deposit Formation in Aviation Turbine Fuel at Elevated Temperature, AIAA Paper 86-0525, *24th Aerospace Sciences Meeting*, Reno, NV, Jan. 12–17.

Hardy, D. R., Beal, E. J. and Burnett, J. C. (1991) *Proceedings of the 4th International Conference on Stability and Handling of Liquid Fuels*, US Department of Energy, Washington, D.C., 1991, p. 260.

Hazlett, R. N. (1975) Progress Report on Advanced Hydrocarbon Fuel Development, Naval Research Laboratory, March 1977; Also *Ind. Eng. Chem.*, Product Res. Div., **16**, 171.

Heneghan, S. P. and Zabarnick, S. (1994) Oxidation of Jet Fuels and the Formation of Deposits, *Fuel*, **73**, 35.

Jones, E. G. and Balster, W. J. (1992) Application of a Sulphur-Doped System to the Study of Thermal Oxidation of Jet Fuels, ASME Paper 92-GT-122, *Presented at the International Gas Turbine and Aeroengine Congress and Exposition*, Cologne, Germany, June 1–4.

Jones, E. G., Balster, W. J. and Anderson, S. D., "Formation of Insolubles in Jet Fuels: Effects of Oxygen", Preprints Symposia-Structure of Jet Fuels III, Division of Petroleum Chemistry, *American Chemical Society*, Washington, D.C., Vol. 37, No. 2, pp. 393–402.

Jones, E. G., Balster, L. J. and Balster, W. J. (1996) Thermal Stability of Jet-A Fuel Blends", *Energy and Fuels*, **10**, 509.

Kauffman, R. E. (1993) University of Dayton Research Institute, Ohio, Private communications.

Katta, V. Reddy and Roquemore, W. M. (1990) A Time-Dependent Model with Global Chemical for Decomposition and Deposition of Aircraft Fuels, *Symposium on the Stability and Oxidation Chemistry of Middle Distillate Fuels*, Division of Fuel and Petroleum Chemistry, ACS, Washington, Aug. 26–31.

Katta, V. R., Jones, E. G. and Roquemore, W. M. (1993) "Development of Global-Chemistry Model for Jet-Fuel Thermal Stability Based on Observations from Static and Flowing Experiments", AGARD-CP-536, Paper No. 19, September.

Katta, V. R. and Roquemore, W. M. (1993) Numerical Method for Simulating Fluid-Dynamic and Heat-Transfer Changes in Jet-Engine Injector Feed-Arm due to Fouling, *Journal of Thermophysics and Heat Transfer*, **7**, 651.

Katta, V. R., Blust, J., Williams, T. F. and Martel, C. R. (1995) Role of Buoyancy in Fuel-Thermal Stability Studies, *Journal of Thermophysics and Heat Transfer*, **9**, 159.

Kendall, D. R., Houlbrook, G., Clark, R. H., Bullock, S. P. and Lewis, C. (1987) The Thermal Degradation of Aviation Fuels in Jet Engine Injector Feed-Arms: Part 1–Results from a Full-Scale Rig, *Presented at the 30th International Gas Turbine Congress*, Tokyo, October.

Krazinski, J. L., Vanka, S. P., Pearce, J. A. and Roquemore, W. M. (1992) A Computational Fluid Dynamics and Chemistry Model for Jet Fuel Thermal Stability, *Journal of Engineering for Gas Turbines and Power*, **114**, 104.

Marteney, P. J. and Spadaccini, L. J. (1986) Thermal Decomposition of Aircraft Fuels, *ASME Journal of Engineering for Gas Turbines and Power*, **108**, 648.

Marteney, P. J. (1988) Thermal Decomposition of JP-5 in Long Duration Tests, United Technologies Research Center Report No. R88-957403-23, Prepared for the U.S. NAVY under Contract No. N00140-83-C-9119.N.

Mayo, F. R. and Lan, B. Y. (1986) *Ind. Eng. Chem. Res.*, **25**, 333.

Roquemore, W. M., Pearce, J. A., Harrison, W. E. III, Krazinski, J. L. and Vanka, S. P. (1989) Fouling in Jet Fuels: A New Approach, *Presented at 198th National ACS Meeting*, Symposium Structure on Future Jet Fuels II, Miami Beach, FL, September 10–15.

Spalding, D. B. (1972) A Novel Finite Difference Formulation for Difference Expressions Involving Both First and Second Derivatives, *International Journal for Numerical Methods in Engineering*, **4**, 551.

Taylor, W. F. (1967) Kinetics of Deposit Formation from Hydrocarbon Fuels at High Temperature: General Features of the Process, *Ind. Eng. Chem.*, Prod. Res. Devl., **6**, 258.

Taylor, W. F. (1970) Catalysis in Liquid Phase Autoxidation. II. Kinetics of the Poly (Tetrafluoroethylene)-Catalyzed Oxidation of Tetralin. *J. Phy. Chem.*, **74**, 2250.

Zabarnick, S. (1993) "Chemical Kinetics Modeling of Jet Fuel Autoxidation and Antioxidant Chemistry", *Ind. Eng. Chem. Res.*, **32**, 1012.
Zabarnick, S. (1997) "Chemical Kinetics Modeling of Antioxidant Chemistry for Jet Fuel Applications", Submitted to *Ind. Eng. Chem. Res.*
Zhou, N. and Krishnan, A. (1996) Calibration of a Global Mechanism for Jet Fuel Deposition, AIAA Paper 96-3238, AIAA, Reston, VA.

APPENDIX

Publications, Presentations, and Patents

[Papers preceded by an asterisk (*) are included in the text of this report.]

"Titanium:Sapphire-Based Laser Sources for Two-Photon Fluorescence Spectroscopy," K. D. Grinstead, F. E. Lytle, W. L. Weaver, and J. R. Gord, Presented at the 22nd Annual Conference of the Federation of Analytical Chemistry and Spectroscopy Societies, 15-20 October 1995, Cincinnati, OH.

"Ultrafast Pump-Probe Studies of Rotational Diffusion in Supercritical Fluids," J. R. Gord, W. L. Weaver, E. Niemeyer, and F. V. Bright, Presented at the 22nd Annual Conference of the Federation of Analytical Chemistry and Spectroscopy Societies, 15-20 October 1995, Cincinnati, OH.

"Quantitation of Dissolved Oxygen Concentration, Particle Size, and Surface Mass Deposition Rate in Thermally Stressed Aviation Fuel," W. L. Weaver, V. Vilimpoc, S. W. Buckner, and J. R. Gord, Presented at the 22nd Annual Conference of the Federation of Analytical Chemistry and Spectroscopy Societies, 15-20 October 1995, Cincinnati, OH.

"Time-Correlated Single-Photon Counting Investigations of the Effects of Temperature, Solvent, and Excitation Energy on the Fluorescence Lifetime of Adamantyl Diazirine," J. S. Buterbaugh, J. P. Toscano, W. L. Weaver, J. R. Gord, T. L. Gustafson, and M. S. Platz, Presented at the 22nd Annual Conference of the Federation of Analytical Chemistry and Spectroscopy Societies, 15-20 October 1995, Cincinnati, OH.

"Particle Image Velocimetry (PIV) for Research in Fluid Processes and Flow Measurement at NIST," S. P. Gogineni, Invited presentation to the National Institute of Standards and Technology, 18 October 1995, Gaithersburg, MD.

* "The Structure of a Dynamic Nonpremixed H_2-Air Flame," C. D. Carter, R. D. Gould, L. P. Goss, V. R. Katta, and K. Y. Hsu, Presented at the Fall Meeting of the Western States Section of the Combustion Institute, 30-31 October 1995, Stanford, CA, and published as Paper No. WSS/CI 95F-222.

"Bi-Modal Size Distributions Predicted by Maximum Entropy are Compared with Experiments in Sprays," L. P. Chin, G. Switzer, R. S. Tankin, T. Jackson, and J. Stutrud, Combust. Sci. Technol. 109 (1-6), 35 (November 1995).

* "Comparisons Between Experiments and Predictions Based on Maximum Entropy for the Breakup of a Cylindrical Liquid Jet," L. P. Chin, R. S. Tankin, and T. Jackson, Atomization Sprays 5, 603 (November/December 1995).

* "Simultaneous Measurement of Particle Size, Mass Rate of Deposition, and Oxygen Concentration in Thermally Stressed Jet Fuel," V. Vilimpoc, B. Sarka, W. L. Weaver, and J. R. Gord, Presented at the 1995 International Mechanical Engineering Congress and Exposition, 12-17 November 1995, San Francisco, CA.

"Fluorescence Imaging of Droplet Internal Fluid Motion," J. M. Hartings, G. L. Switzer, K.-Y. Hsu, and J. R. Gord, Poster presented at the 13th Annual Picture Gallery of Fluid Motion in conjunction with the 48th Annual Meeting of the Division of Fluid Dynamics of the American Physical Society, 19-21 November 1995, Irvine, CA.

"Dispersion of Particles During Vortex-Wall Interaction," V. R. Katta, T. W. Park, and W. M. Roquemore, Poster presented at the 13th Annual Picture Gallery of Fluid Motion in conjunction with the 48th Annual Meeting of the Division of Fluid Dynamics of the American Physical Society, 19-21 November 1995, Irvine, CA.

"Vortex-Flame Interactions in Opposing-Jet Diffusion Flame," V. R. Katta and W. M. Roquemore, Poster presented at the 13th Annual Picture Gallery of Fluid Motion in conjunction with the 48th Annual Meeting of the Division of Fluid Dynamics of the American Physical Society, 19-21 November 1995, Irvine, CA.

"High Free Stream Turbulence Influence on Turbine Film Cooling Flows," S. P. Gogineni, R. B. Rivir, D. J. Pestian, and L. P. Goss, Poster presented at the 13th Annual Picture Gallery of Fluid Motion in conjunction with the 48th Annual Meeting of the Division of Fluid Dynamics of the American Physical Society, 19-21 November 1995, Irvine, CA. Of the 50 posters presented, this was one of six selected to receive an award.

"Two-Color PIV Employing a Color CCD Camera," S. Gogineni, D. Trump, and L. Goss, Presented at the 48th Annual Meeting of the Division of Fluid Dynamics of the American Physical Society, 19-21 November 1995, Irvine, CA; abstract published in Bull. APS 40(12), 1950 (1995).

"Local Quenching in Methane Jet Diffusion Flame," V. R. Katta and W. M. Roquemore, Presented at the 48th Annual Meeting of the Division of Fluid Dynamics of the American Physical Society, 19-21 November 1995, Irvine, CA; abstract published in Bull. APS 40(12), 2014 (1995).

"Influence of Combustion Air Jets in the Formation of Gas Turbine Emissions," M. Roquemore, D. Shouse, S. Gogineni, and G. Sturgess, Presented at the 48th Annual Meeting of the Division of Fluid Dynamics of the American Physical Society, 19-21 November 1995, Irvine, CA; abstract published in Bull. APS 40(12), 1979 (1995).

"Effect of High Free Stream Turbulence on Flat Plate Film Cooling Flows," D. Pestian, S. Gogineni, D. Trump, and R. Rivir, Presented at the 48th Annual Meeting of the Division of Fluid Dynamics of the American Physical Society, 19-21 November 1995, Irvine, CA; abstract published in Bull. APS 40(12), 2035 (1995).

* "The Role of Transverse Air Jets in the Formation of Gas Turbine Emissions," D. Shouse, C. Frayne, J. Stutrud, S. Gogineni, and G. J. Sturgess, Presented at the AIAA 34th Aerospace Sciences Meeting and Exhibit, 15-18 January 1996, Reno, NV, and published as AIAA Paper No. 96-0705. This paper was nominated for the "Best of Session" award.

"PIV Measurements of Flat Plate Film Cooling Flows with High Free Stream Turbulence," S. P. Gogineni, R. B. Rivir, D. J. Pestian, and L. P. Goss, Presented at the AIAA 34th Aerospace Sciences Meeting and Exhibit, 15-18 January 1996, Reno, NV, and published as AIAA Paper No. 96-0617.

* "Numerical Experiments on the Local Extinction of Jet Diffusion Flames," F. Takahashi and V. R. Katta, Presented at the AIAA 34th Aerospace Sciences Meeting and Exhibit, 15-18 January 1996, Reno, NV, and published as AIAA Paper No. 96-0521.

"Application of JFA-5 as an Anti-Fouling Additive in a Jet-A Fuel," E. G. Jones, W. J. Balster, and L. P. Goss, Ind. Eng. Chem. Res. 35(3), 837 (March 1996).

"Investigation of a Premixed Jet Flame at Near-Blowout Limit," V. R. Katta and W. M. Roquemore, Presented at the Society for Industrial and Applied Mathematics 6th International Conference on Numerical Combustion, 4-6 March 1996, New Orleans, LA; published in Proceedings, pp. 93-94.

"Vortex Interactions in Jet in a Cross Flow," S. P. Gogineni, Presented at the Windows-on-Science Vortex-Flame Interactions Colloquium, 11-14 March 1996, Wright-Patterson AFB, OH.

* "Use of MDA, BHT, and Dispersant Singly and in Combination as Jet-Fuel Additives," W. J. Balster, L. M. Balster, and E. G. Jones, Presented at the American Chemical Society National Meeting, 24-28 March 1996, New Orleans, LA; published in Prepr.-Am. Chem. Soc., Div. Pet. Chem. 41(2), 446 (March 1996).

"Autoxidation of POSF-2827 Jet Fuel," J. M. Pickard and E. G. Jones, Presented at the American Chemical Society National Meeting, 24-28 March 1996, New Orleans, LA; published in Prepr.-Am. Chem. Soc., Div. Pet. Chem. 41(2), 474 (March 1996).

"Quantification of Thermal Stability of Blended Fuels," L. M. Balster, W. J. Balster, and E. G. Jones, Presented at the American Chemical Society National Meeting, 24-28 March 1996, New Orleans, LA; published in Prepr.-Am. Chem. Soc., Div. Pet. Chem. 41(2), 464 (March 1996).

"Vortex/Boundary-Layer Interactions in a Wall Jet," S. P. Gogineni, Presented at the 22nd Annual Mini-Symposium on Aerospace Science and Technology, 28 March 1996, Dayton, OH. This paper received the "Best of Session" Award.

* "Unsteady Spray Behavior in a Heated Jet Shear Layer: Droplet-Vortex Interactions," S. K. Aggarwal, T. W. Park, and V. R. Katta, Combust. Sci. Technol. 113/114, 429 (March-May 1996).

"Thermal Stability of Jet-A Fuel Blends," E. G. Jones, L. M. Balster, and W. J. Balster, Energy Fuels 10(2), 509 (April 1996).

* "Study of Flame Stability in a Step Swirl Combustor," M. D. Durbin, D. Vangsness, D. R. Ballal, and V. R. Katta, Trans. ASME: J. Eng. Gas Turb. Power 118, 308 (April 1996).

* "Surface Fouling in Aviation Fuels: An Isothermal Chemical Study," E. G. Jones, W. J. Balster, and J. R. Pickard, Trans. ASME: J. Eng. Gas Turb. Power 118, 287 (April 1996).

"Effectiveness of Fuel Additives Used Singly and in Combination," E. G. Jones, Presented at the Coordinating Research Council Meeting of the Oxidation Stability of Gas Turbine Fuels Group of the CRC-Aviation Fuel, Lubricant, and Equipment Research Committee, 23 - 24 April 1996 Alexandria, VA.

"Recent Progress in Pressure Sensitive Paint Development for Turbomachinery," K. Sabroske, Presented at the UTECA (United Technologies Engineering Coordination Activities) '96, 7th Annual UTC Engineering Conference and Technology Expo, 30 April - 2 May 1996, Cromwell, CT.

"Autoxidation of Aviation Fuels in Heated Tubes: Surface Effects," E. G. Jones, L. M. Balster, and W. J. Balster, Energy Fuels 10(3), 831 (May 1996).

* "An Experimental and Numerical Investigation on Local Extinction in Jet Diffusion Flames," K.-Y. Hsu, V. R. Katta, and W. M. Roquemore, Presented at the 1996 Technical Meeting of the Central States Section of the Combustion Institute, 5-7 May 1996, St. Louis, MO; published in Combustion Fundamentals and Applications (The Combustion Institute, Pittsburgh, PA, 1996), pp. 437-442.

* "Extinction in Methane-Air Counterflow Diffusion Flame--A Direct Numerical Study," V. R. Katta and W. M. Roquemore, Presented at the 1996 Technical Meeting of the Central States Section of the Combustion Institute, 5-7 May 1996, St. Louis, MO; published in Combustion Fundamentals and Applications (The Combustion Institute, Pittsburgh, PA, 1996), pp. 449-454.

"A Numerical Study on the Collisional Behavior of Droplets," L. P. Chin, Presented at the 1996 Technical Meeting of the Central States Section of the Combustion Institute, 5-7 May 1996, St. Louis, MO; published in Combustion Fundamentals and Applications (The Combustion Institute, Pittsburgh, PA, 1996), pp. 330-335.

"A Numerical Study of the Stability of Methane Jet Diffusion Flames," F. Takahashi and V. R. Katta, Presented at the 1996 Technical Meeting of the Central States Section of the Combustion Institute, 5-7 May 1996, St. Louis, MO; published in Combustion Fundamentals and Applications (The Combustion Institute, Pittsburgh, PA, 1996), pp. 263-268.

"Experimental and Numerical Studies on the Flow Structures in a Simulated Twin-Jet Airblast Atomizer," P. C. Hsing, R. S. Tankin, and L. P. Chin, Presented at the 1996 Technical Meeting of the Central States Section of the Combustion Institute, 5-7 May 1996, St. Louis, MO; published in Combustion Fundamentals and Applications (The Combustion Institute, Pittsburgh, PA, 1996), pp. 344-349.

"Momentum Coupling Effects in a Two-Phase Swirling Jet," T. W. Park, S. K. Aggarwal, and V. R. Katta, Presented at the 1996 Technical Meeting of the Central States Section of the Combustion Institute, 5-7 May 1996, St. Louis, MO; published in Combustion Fundamentals and Applications (The Combustion Institute, Pittsburgh, PA, 1996), pp. 350-355.

"Vortex-Flame Interactions in Hydrogen Jet Diffusion Flames: An Experimental and Computational Investigation," R. D. Hancock, F. R. Schauer, R. P. Lucht, V. R. Katta, and K-Y. Hsu, Presented at the 1996 Technical Meeting of the Central States Section of the Combustion Institute, 5-7 May 1996, St. Louis, MO; published in Combustion Fundamentals and Applications (The Combustion Institute, Pittsburgh, PA, 1996), pp. 425-430.

"On Flame-Vortex Dynamics in an Inverse Diffusion Flame Combustor," Z. Hsu, S. K. Aggarwal, V. R. Katta, and I. K. Puri, Presented at the 1996 Technical Meeting of the Central States Section of the Combustion Institute, 5-7 May 1996, St. Louis, MO; published in Combustion Fundamentals and Applications (The Combustion Institute, Pittsburgh, PA, 1996), pp. 431-436.

"Thermal Diffusion and the Nonunity Lewis Number Effects in Hydrogen Jet Diffusion Flames," F. R. Schauer, R. D. Hancock, R. P. Lucht, and V. R. Katta, Presented at the 1996 Technical Meeting of the Central States Section of the Combustion Institute, 5-7 May 1996, St. Louis, MO; published in Combustion Fundamentals and Applications (The Combustion Institute, Pittsburgh, PA, 1996), pp. 97-102.

"Possible Combustor Design Trends for Future Aircraft Gas Turbine Engines," G. J Sturgess, Invited presentation at the AGARD Workshop on Active Combustion Control for Propulsion Systems/Propulsion and Energetics Panel 87th Symposium on Service Life of Solid Propellant Systems, 6-10 May 1996, Athens, Greece.

"PIV Technology for Turbine Applications," S. Gogineni, Presented at the AFOSR Annual Review, 7 May 1996, Aero Propulsion and Power Directorate, Wright-Patterson AFB, OH,

"Study of Trapped-Vortex Concepts for Aerodynamic Drag Reduction," V. R. Katta and W. M. Roquemore, Presented at the 1st AFOSR Conference on Dynamic Motion CFD, 3-5 June 1996, New Brunswick, NJ; published in Proceedings of the 1st AFOSR Conference on Dynamic Motion CFD (L. Sakell and D. D. Knight, Eds.) (Rutgers University, New Brunswick, NJ, 1996), pp. 379-381.

"Combustion/Turbulence Interaction: A Bridge Between Theory and Application," G. J. Sturgess, Presented at the AFOSR/ARO Contractors' Meeting, 3-7 June 1996, Virginia Beach, VA.

"Assessment of the Effectiveness of a Metal Deactivator as Jet Fuel Additive," L. M. Balster, W. J. Balster, and E. G. Jones, Poster presented at the American Chemical Society 28th Central Regional Meeting, Chemistry in the 90's and Beyond, 9-12 June 1996, Dayton, OH.

"Techniques to Characterize the Thermal-Oxidation Stability of Jet Fuels and the Effects of Additives," V. Vilimpoc, B. Sarka, W. L. Weaver, J. R. Gord, and S. Anderson, Reviewed paper, Presented at the 41st ASME Gas Turbine and Aeroengine Congress/Users Symposium and Exposition, 10-13 June 1996, Birmingham, England; published as ASME Paper No. 96-GT-44.

"Evaluation of the Effectiveness of a Metal Deactivator and Other Additives in Reducing Insolubles in Aviation Fuels," E. G. Jones, W. J. Balster, and L. M. Balster, Reviewed paper, Presented at the 41st ASME Gas Turbine and Aeroengine Congress/Users Symposium and Exposition, 10-13 June 1996, Birmingham, England; published as ASME Paper No. 96-GT-204.

"PIV Measurements of Periodically Forced Flat Plate Film Cooling Flows with High Free Stream Turbulence," S. Gogineni, D. Trump, D. Pestian, and R. Rivir, Reviewed paper, Presented at the 41st ASME Gas Turbine and Aeroengine Congress/Users Symposium and Exposition, 10-13 June 1996, Birmingham, England; published as ASME Paper No. 96-GT-236.

"Recent Progress in Pressure Sensitive Paint Development for Turbomachinery," K. Sabroske, Presented at the AEDC Propulsion Instrumentation Working Group Team Meeting, 18-20 June 1996, Tullahoma, TN.

* "A Numerical Study of Droplet-Vortex Interactions in an Evaporating Spray," T. W. Park, S. K. Aggarwal, and V. R. Katta, Int. J. Heat Mass Transfer 39(11), 2205 (July 1996).

* "Emissions and Operability Trades in the Primary Zones of Gas Turbine Combustors," G. Sturgess, S. P. Gogineni, D. Shouse, C. Frayne, and J. Stutrud, Presented at the 32nd AIAA/ASME/SAE/ASEE Joint Propulsion Conference, 1-3 July 1996, Lake Buena Vista, FL, and published as AIAA Paper No. 96-2758.

* "A Hybrid Model for Calculating Lean Blow-outs in Practical Combustors," G. J. Sturgess and D. Shouse, Presented at the 32nd AIAA/ASME/SAE/ASEE Joint Propulsion Conference, 1-3 July 1996, Lake Buena Vista, FL, and published as AIAA Paper No. 96-3125.

* "Numerical Studies on Trapped-Vortex Combustor," V. R. Katta and W. M. Roquemore, Presented at the 32nd AIAA/ASME/SAE/ASEE Joint Propulsion Conference, 1-3 July 1996, Lake Buena Vista, FL, and published as AIAA Paper No. 96-2660.

"High-Resolution Digital Two-Color PIV (D2CPIV) and Its Applications to High-Freestream Turbulent Flows," S. P. Gogineni, D. Trump, L. Goss, R. Rivir, and D. Pestian, Reviewed paper, Presented at the 8th International Symposium on Applications of Laser Techniques to Fluid Mechanics, 8-11 July 1996, Lisbon, Portugal; published in Proceedings, Vol. I, pp. 18.2.1 - 18.2.8.

"Optical Pressure and Temperature Measurements Based on Fluorescence Quenching," J. R. Gord, D. C. Rabe, D. Car, C. E. Baird, L. P. Goss, K. P. Sabroske, and K. D. Grinstead, Presented at the 38th Rocky Mountain Conference on Analytical Chemistry, 21-26 July 1996, Denver, CO.

* "Thermal Diffusion Effects and Vortex-Flame Interactions in Hydrogen Jet Diffusion Flames," R. D. Hancock, F. R. Schauer, R. P. Lucht, V. R. Katta, and K-Y. Hsu, Reviewed paper, Presented at the 26th International Symposium on Combustion, 28 July - 5 August 1996, Naples, Italy; published in Twenty-Sixth Symposium (International) on Combustion (The Combustion Institute, Pittsburgh, PA, 1996), pp. 1087-1093.

* "Unsteady Extinction Mechanisms of Diffusion Flames," F. Takahashi and V. R. Katta, Reviewed paper, Presented at the 26th International Symposium on Combustion, 28 July - 5 August 1996, Naples, Italy; published in Twenty-Sixth Symposium (International) on Combustion (The Combustion Institute, Pittsburgh, PA, 1996), pp. 1151-1160.

"The Role of Transverse Air Jets in the Formation of Gas Turbine Emissions," D. Shouse, C. Frayne, J. Stutrud, S. Gogineni, and G. J. Sturgess, Submitted in August 1996 to the Journal of Propulsion and Power.

"Influence of Combustion Air Jets on Primary Zone Characteristics for Gas Turbine Combustors," S. P. Gogineni, D. Shouse, C. Frayne, J. Stutrud, and G. Sturgess, Submitted in August 1996 to the Journal of Propulsion and Power (in revision).

"Recent Progress in Pressure Sensitive Paint Development for Turbomachinery," K. Sabroske, Presented at the Air Force Institute of Technology, 26 August 1996, Wright-Patterson Air Force Base, OH.

"High Free Stream Turbulence Influence on Turbine Film Cooling Flows," S. P. Gogineni, R. B. Rivir, D. J. Pestian, and L. P. Goss, Phys. Fluids. 8(9), S4 (September 1996)

"Emissions and Operability Trades in the Primary Zones of Gas Turbine Combustors," G. Sturgess, S. Gogineni, D. Shouse, C. Frayne, and J. Stutrud, Submitted in September 1996 to AIAA Journal of Propulsion and Power (in revision).

"PIV Technology for Simulated Turbine Film Cooling Flows," S. Gogineni, R. Rivir, L. P. Goss, and D. Pestian, Presented at the 6th International Symposium on Flow Modelling and Turbulence Measurements, 8-10 September 1996, Tallahassee, FL; published in Flow Modeling and Turbulence Measurements VI (C-J. Chen, C. Shih, J. Lienau, and R. J. Kung, Eds.) (Balkema, Rotterdam, 1996), pp. 193-200.

"Possible Combustor Design Trends for Future Gas Turbine Engines," G. J. Sturgess, Invited presentation at the IHPTET (Integrated High Performance Turbine Engine Technology) Air Force Turbine Engine Technology Symposium, 9-12 September 1996, Dayton, OH.

"Kinetics of the Autoxidation of a Jet-A Fuel," J. M. Pickard and E. G. Jones, Energy Fuels 10(5), 1074 (September/October 1996).

"Numerical Studies on Trapped Vortex Concepts for Stable Combustion," V. R. Katta and W. M. Roquemore, Reviewed paper, Presented at the ASME Turbo Asia '96 Congress and Exposition, 5-7 November 1996, Jakarta, Indonesia; published as ASME Paper No. 96-TA-19.

* "Combustor Design Trends for Aircraft Gas Turbine Engines," G. J. Sturgess, Reviewed paper, Presented at the ASME Turbo Asia '96 Congress and Exposition, 5-7 November 1996, Jakarta, Indonesia; published as ASME Paper No. 96-TA-29.

"Development of Holographic PIV for Flame Studies," S. Gogineni, J. Estevadeordal, L. Goss, and H. Meng, Presented at the 49th Annual Meeting of the American Physical Society, Division of Fluid Dynamics, 24-26 November 1996, Syracuse, NY; Bull. APS 41(9), 1833 (1996).

"Global Kinetic Modeling of Aviation Fuel Fouling in Cooled Regions in a Flowing System," J. S. Ervin, T. F. Williams, and V. R. Katta, Ind. Eng. Chem. Res. 35, 4028 (November 1996).

"3D Visualization of Vortex-Ring and Bag-Shaped Instabilities Using Holography," J. Estevadeordal, S. P. Gogineni, L. P. Goss, H. Meng, and W. M. Roquemore, Poster presented at the 14th Annual Picture Gallery of Fluid Motion in conjunction with the 49th Annual Meeting of the American Physical Society, Division of Fluid Dynamics, 24-26 November 1996, Syracuse, NY. Of the 35 posters presented, this was one of six selected to receive an award.

"Large Eddy Simulation (LES) of Jet in Cross Flow and Comparison with Experimental Results," B. V. Kiel and S. Gogineni, Presented at the 49th Annual Meeting of the American Physical Society, Division of Fluid Dynamics, 24-26 November 1996, Syracuse, NY; Bull. APS 41(9), 1729 (1996).

"Thermal Stability of Jet-Fuel/Paraffin Blends," L. M. Balster, W. J. Balster, and E. G. Jones, Energy Fuels 10(6), 1176 (November/December 1996).

* "Simulation of Local Quenching in a Methane-Air Jet Diffusion Flame," V. R. Katta and W. M. Roquemore, Presented at the 1996 Technical Meeting of the Eastern States Section of the Combustion Institute, Chemical and Physical Processes in Combustion, 9-11 December 1996, Hilton Head, SC; published in Chemical and Physical Processes in Combustion (The Combustion Institute, Pittsburgh, PA, 1996), pp. 381-384.

"A Further Analysis of the Stabilizing Region of Methane Jet Diffusion Flames," F. Takahashi and V. R. Katta, Presented at the 1996 Technical Meeting of the Eastern States Section of the Combustion Institute, Chemical and Physical Processes in Combustion, 9-11 December 1996, Hilton Head, SC; published in Chemical and Physical Processes in Combustion (The Combustion Institute, Pittsburgh, PA, 1996), pp. 385-388.

"Characteristics of Simulated Turbine Film Cooling Flows," R. B. Rivir and S. P. Gogineni, Reviewed paper; Invited presentation to the International Congress on Fluid Dynamics and Propulsion, 29-31 December 1996, Cairo, Egypt; published in Proceedings, Vol. 1, pp. 95-107.

"A Vortex-Flame Interaction Study Using Four-Wave Mixing Techniques," F. Grische, B. Attal-Tretout, P. Bouchardy, V. R. Katta, and W. M. Roquemore, J. Nonlinear Opt. Phys. Mater. 5(3), 505 (1996).

* "Numerical Modeling of Interactions Between Evaporating Droplets," L. P. Chin, Presented at the AIAA 35th Aerospace Sciences Meeting and Exhibit, 6-10 January 1997, Reno, NV, and published as AIAA Paper No. 97-0130.

* "Influences of Airblast-Atomizing Fuel Injector Design on Primary Zone Characteristics at Blowout," G. J. Sturgess, S. Gogineni, and D. T. Shouse, Presented at the AIAA 35th Aerospace Sciences Meeting and Exhibit, 6-10 January 1997, Reno, NV, and published as AIAA Paper No. 97-0269.

"Experimental and Numerical Investigation of Transitional Plane-Wall Jet," S. Gogineni, M. Visbal, and C. Shih, Presented at the AIAA 35th Aerospace Sciences Meeting and Exhibit, 6-10 January 1997, Reno, NV, and published as AIAA Paper No. 97-0071.

* "Entrainment of Mainstream Flow in a Trapped-Vortex Combustor," G. J. Sturgess and K.-Y. Hsu, Presented at the AIAA 35th Aerospace Sciences Meeting and Exhibit, 6-10 January 1997, Reno, NV, and published as AIAA Paper No. 97-0261.

"Flame-Vortex Dynamics in an Inverse Partially Premixed Combustor: The Froude Number Effects," Z. Shu, S. K. Aggarwal, V. R. Katta, and I. K. Puri, Presented at the AIAA 35th Aerospace Sciences Meeting and Exhibit, 6-10 January 1997, Reno, NV, and published as AIAA Paper No. 97-0259.

* "Momentum Coupling Effects in a Two-Phase Swirling Jet," T. W. Park, S. K. Aggarwal, and V. R. Katta, Presented at the AIAA 35th Aerospace Sciences Meeting and Exhibit, 6-10 January 1997, Reno, NV, and published as AIAA Paper No. 97-0128.

* "A Numerical Investigation of the Stabilizing Mechanism of Methane Jet Diffusion Flames," F. Takahashi and V. R. Katta, Presented at the AIAA 35th Aerospace Sciences Meeting and Exhibit, 6-10 January 1997, Reno, NV, and published as AIAA Paper No. 97-0251.

* "Simulation of Dynamic Methane Jet Diffusion Flame Using Finite-Rate Chemistry Model," V. R. Katta and W. M. Roquemore, Presented at the AIAA 35th Aerospace Sciences Meeting and Exhibit, 6-10 January 1997, Reno, NV, and published as AIAA Paper No. 97-0904.

"Demodulating Camera System for Picosecond Pump/Probe Imaging," T. Setterson, C. Fisher, N. Middleton, M. Linne, J. Gord, G. Fiechtner, and P. Paul, Presented at the AIAA 35th Aerospace Sciences Meeting and Exhibit, 6-10 January 1997, Reno, NV, and published as AIAA Paper No. 97-0158.

"Application of Photon-Correlation Spectroscopy and Quartz-Crystal Microbalance to the Study of Thermally Stressed Jet Fuel," V. Vilimpoc and B. Sarka, Ind. Eng. Chem. Res. 36(2), 451 (February 1997).

"Pressure-Sensitive Paint," K. R. Navarra, Presented at the Air Force Science and Technology High Cycle Fatigue Program Kick-Off, 24-25 February 1997, Berkeley, CA.

* "Dynamics of Propane Jet Diffusion Flames," V. R. Katta, L. P. Goss, W. M. Roquemore, and L.-D. Chen, Invited chapter in Atlas of Visualization III (The Visualization Society of Japan, Ed.) (CRC Press, New York, 1997), Chapter 12, pp. 181-198.

"Additive Testing at ISSI," E. G. Jones, Presented at the JP-8+100 Program Review, 18-19 March 1997, Wright-Patterson Air Force Base, OH.

"Future Directions in Gas Turbines for Civil Aircraft Propulsion," G. J. Sturgess, Invited Keyote address delivered at the NASA Combustion Dynamics and Control Workshop, 15-16 April 1997, Cleveland, OH.

"Fluorescence Lifetime Measurements and Spectral Analysis of Adamantyldiazirine," J. S. Buterbaugh, J. P. Toscano, W. L. Weaver, J. R. Gord, C. M. Hadad, T. L. Gustafson, and M. S. Platz, J. Am. Chem. Soc. 119(15), 3580 (April 16, 1997).

"A Numerical Analysis of a Methane Diffusion Flame Over a Flat Plate," F. Takahashi and V. R. Katta, Presented at the Spring Technical Meeting of the Central States Section of the Combustion Institute, 27-29 April 1997, Point Clear, AL; published in Combustion Fundamentals and Applications (The Combustion Institute, Pittsburgh, PA, 1997), pp. 164-169.

"NOx Formation in a Dynamic Methane-Air Jet Diffusion Flame," V. R. Katta and W. M. Roquemore, Presented at the Spring Technical Meeting of the Central States Section of the Combustion Institute, 27-29 April 1997, Point Clear, AL; published in Combustion Fundamentals and Applications (The Combustion Institute, Pittsburgh, PA, 1997), pp. 390-394.

"A Numerical Investigation of the Flame Structure of an Unsteady Inverse Partially Premixed Flame," Z. Shu, S. K. Aggarwal, V. R. Katta, and I. K. Puri, Presented at the Spring Technical Meeting of the Central States Section of the Combustion Institute, 27-29 April 1997, Point Clear, AL; published in Combustion Fundamentals and Applications (The Combustion Institute, Pittsburgh, PA, 1997), pp. 68-73.

* "Flame Structure of Stabilization Region in a Laminar Hydrogen Jet Diffusion Flame," F. R. Schauer, S. M. Green, R. P. Lucht, R. D. Hancock, and V. R. Katta, Presented at the Spring Technical Meeting of the Central States Section of the Combustion Institute, 27-29 April 1997, Point Clear, AL; published in Combustion Fundamentals and Applications (The Combustion Institute, Pittsburgh, PA, 1997), pp. 170-175.

"Structures of Laminar Partially Premixed and Diffusion Flames in a Co-Flow Configuration," Z. Shu, S. K. Aggarwal, I. K. Puri, and V. R. Katta, Presented at the Spring Technical Meeting of the Central States Section of the Combustion Institute, 27-29 April 1997, Point Clear, AL.

"Development of Trapped-Vortex Combustor," K.-Y. Hsu and W. M. Roquemore, Invited Graduate Seminar, University of Iowa, Department of Mechanical Engineering, 1 May 1997, Iowa City, Iowa.

"Development of the Pressure-Sensitive-Paint Technique for Advanced Turbomachinery Applications," K. N. Navarra, M. S. Thesis, Virginia Polytechnic Institute and State University, 9 May 1997, Blacksburg, VA.

"Development of the Pressure-Sensitive-Paint Technique for Advanced Turbomachinery Applications," K. N. Navarra, Presented at the Fifth Pressure Sensitive Paint Workshop, 14-16 May 1997, Arnold Air Force Base, TN.

"Development of the Pressure-Sensitive-Paint Technique for Advanced Turbomachinery Applications," K. N. Navarra, Presented at the 23rd Turbine Test Facility Working Group Meeting, 20 May 1997, Cincinnati, OH.

"Trends in Gas Turbine Engine Design with Emphasis on Combustion," G. J. Sturgess, Invited seminar at the University of California-Davis, 29 May 1997, Sacramento, CA.

"Impact of Additives on the Autoxidation of a Thermally Stable Aviation Fuel," E. G. Jones and L. M. Balster, Energy Fuels 11(3), 610 (May/June 1997).

* "Experimental Study of Pure and Multicomponent Fuel Droplet Evaporation in a Heated Air Flow," G. Chen, S. K. Aggarwal, T. A. Jackson, and G. L Switzer, Atomiz. Sprays 7, 317 (May-June 1997).

* "Experimental Investigation of the Unsteady Structure of a Transitional Plane Wall Jet," S. P. Gogineni and C. Shih, Exp. Fluids 23, 121 (June 1997).

"Effects of Temperature on Formation of Insolubles in Aviation Fuels," W. J. Balster and E. G. Jones, Presented at the 42nd ASME Gas Turbine and Aeroengine Congress, 2-5 June 1997, Orlando, FL; published as ASME Paper No. 97-GT-218.

"Investigation of Holographic Visualization and Holographic PIV Techniques for Fluid Flows and Flames," J. Estevadeordal, H. Meng, S. Gogineni, L. Goss, D. Trump, and B. Sarka, Presented at the ASME Fluids Engineering Division Summer Meeting on Experimental and Numerical Flow Visualization and Laser Anemometry, 22-26 June 1997, Vancouver, B. C., Canada; published as ASME Paper No. FEDSM97-3093.

"Digital Two-Color PIV and Flow-Visualization Studies for Complex Supersonic Flows," S. Gogineni, L. Goss, D. Glawe, R. Bowersox, and R. Wier, Presented at the ASME Fluids Engineering Division Summer Meeting on Experimental and Numerical Flow Visualization and Laser Anemometry, 22-26 June 1997, Vancouver, B.C., Canada; published as ASME Paper No. FEDSM97-3092.

"A Numerical Study of a Methane Diffusion Flame Over a Flat Surface," F. Takahashi and V. R. Katta, Presented at the Second international Symposium on Scale Modeling (ISSM-II), 23-27 June 1997, Lexington, KY.

"Hybrid Modeling for Emissions and Stability," G. J. Sturgess, Invited seminar at General Electric Corporate R&D Center, 25 June 1997, Schenectady, NY.

* "Assessment of an Abbreviated Jet-A/JP-5/JP-8 Reaction Mechanism for Modeling Gas Turbine Engine Gaseous Emissions," G. J. Sturgess, Presented at the 33rd AIAA/ ASME/SAE/ASEE Joint Propulsion Conference and Exhibit, 6-9 July 1997, Seattle, WA, and published as AIAA Paper No. 97-2709.

* "Numerical Modeling of Interactive Burning Droplets," L. P. Chin, Presented at the 33rd AIAA/ASME/SAE/ASEE Joint Propulsion Conference and Exhibit, 6-9 July 1997, Seattle, WA, and published as AIAA Paper No. 97-2703.

* "Emissions Characteristics of Liquid Hydrocarbons in a Well Stirred Reactor," J. W. Blust, D. R. Ballal, and G. J. Sturgess, Presented at the 33rd AIAA/ASME/SAE/ASEE Joint Propulsion Conference and Exhibit, 6-9 July 1997, Seattle, WA, and published as AIAA Paper No. 97-2710.

"Study on Trapped-Vortex Combustor--Effect of Injection on Dynamics of Non-Reacting and Reacting Flows in a Cavity," V. R. Katta and W. M. Roquemore, Presented at the 33rd AIAA/ASME/SAE/ASEE Joint Propulsion Conference and Exhibit, 6-9 July 1997, Seattle, WA, and published as AIAA Paper No. 97-3256.

* "Modeling of Deposition Process in Liquid Fuels," V. R. Katta, E. G. Jones, and W. M. Roquemore, Presented at the 33rd AIAA/ASME/SAE/ASEE Joint Propulsion Conference and Exhibit, 6-9 July 1997, Seattle, WA, and published as AIAA Paper No. 97-3040.

"Picosecond Pump/Probe Measurement of Absolute CH Concentrations," M. Linne, T. Settersen, J. Gord, and G. Fiechtner, Poster presented at the 1997 Gordon Research Conference on the Physics and Chemistry of Laser Diagnostics in Combustion, 6-11 July 1997, Plymouth, NH.

"Holographic Flow Visualization as a Tool for Studying 3D Coherent Structures and Instabilities," H. Meng, J. Estevadeordal, S. Gogineni, L. Goss, and W. M. Roquemore, Presented at the Second International Workshop on PIV '97 - Fukui, 8-11 July 1997, Fukui, Japan; published in Proceedings of the Second International Workshop on PIV '97 - Fukui (T. Kobayashi and F. Yamamoto, Eds.) (The Visualization Society of Japan, 1997), pp. 27-34; selected as a high-quality paper with permanent value to be published in Journal of Visualization.

"3D Flow Visualization of Coherent Structures, Instabilities, and Vortex-Flame Interactions Using Holography," J. Estevadeordal, H. Meng, S. Gogineni, and L. Goss, Presented at the 1997 JSME Centennial Grand Congress, 13-16 July 1997, Tokyo, Japan.

"Continuing Development of Luminescence Techniques for Characterizing Aviation Fuels," J. R. Gord, M. R. Rabe, K. D. Grinstead, and W. L. Weaver, Presented at the 39th Annual Rocky Mountain Conference on Analytical Chemistry, 3-7 August 1997, Denver, CO.

"Development of Sol-Gel-Derived Pressure Sensitive Coatings for Lifetime-Based Imaging," J. D. Jordan, F. V. Bright, L. P. Goss, W. L. Weaver, K. D. Grinstead, J. R. Gord, and M. R. Gruber, Presented at the 39th Annual Rocky Mountain Conference on Analytical Chemistry, 3-7 August 1997, Denver, CO.

"Aerodynamic Pressure and Temperature Measurement Through Fluorescence Lifetime Imaging," K. D. Grinstead, L. P. Goss, D. D. Trump, and J. R. Gord, Presented at the 39th Annual Rocky Mountain Conference on Analytical Chemistry, 3-7 August 1997, Denver, CO.

* "Active Combustion Control for Propulsion Systems," K. Schadow, V. Yang, F. Culick, T. Rosfjord, G. Sturgess, and B. Zinn, AGARD Report No. AGARD-R-820 (Advisory Group for Aerospace R&D, Neuilly-sur-Seine, France, September 1997) (report prepared at the request of the Propulsion and Energetics Panel of AGARD on papers presented at the AGARD Workshop on Active Combustion Control for Propulsion Systems/PEP 87th Symposium on Service Life of Solid Propellant Systems, 6-9 May 1996, Athens, Greece).

"3D Visualization of Vortex-Ring and Bag-Shaped Instabilities Using Holography," J. Estevadeordal, S. P. Gogineni, L. P. Goss, H. Meng, and W. M. Roquemore, Phys. Fluids 9(9), S5 (September 1997).

* "Investigation of Jet Diffusion Flames Using Holographic Flow Visualization (HFV) and Holographic PIV (HPIV) Techniques," S. Gogineni, J. Estevadeordal, H. Meng, and L. Goss, Presented at the 7th International Conference on Laser Anemometry Advances and Applications, 8-11 September 1997, Karlsruhe, Germany; published in Laser Anemometry Advances and Applications (B. Ruck, A. Leder, and D. Dopheide, Eds.) (German Association for Laser Anemometry, 1997), pp. 203-210.

"Direct Numerical Simulation of Unsteady Non-Reacting Flows in a Trapped-Vortex Combustor," V. R. Katta and W. M. Roquemore, Presented at the 7th International Symposium on Computational Fluid Dynamics, 15-19 September 1997, Beijing, China; published in Proceedings of the Seventh International Symposium on Computational Fluid Dynamics (F. G. Zhuang, Ed.) (International Academic Publishers, Beijing, China, 1997), pp. 791-796.

"Loading Analysis of Wrap-Around Fin Missiles Using Pressure-Sensitive Paint," T. McIntyre, L. P. Goss, D. D. Trump, and R. D. W. Bowersox, Presented at the 17th International Congress on Instrumentation in Aerospace Simulation Facilities (ICIASF), Naval Post Graduate School, 29 September - 2 October 1997, Monterey, CA.

"Split-Film Anemometry and CFD Study of a Jet in Cross-Flow," B. V. Kiel, Master's thesis submitted in October 1997 to Colorado State University, Ft. Collins, CO.

* "Evaluation of the Effectiveness of a Metal Deactivator and Other Additives in Reducing Insolubles in Aviation Fuels," E. G. Jones, W. J. Balster, and L. M. Balster, Trans. ASME, J. Eng. Gas Turb. Power 119, 830 (October 1997).

"Impact of Fuel Recirculation on Thermal Stability," E. G. Jones, W. J. Balster, and L. M. Balster, Presented at the 6th International Conference on Stability and Handling of Liquid Fuels, 13-17 October 1997, Vancouver, B.C., Canada; published in Proceedings of the 6th International Conference on Stability and Handling of Liquid Fuels, Vol. 1 (H. N. Giles, Ed.) (U. S. Department of Energy, Washington, D. C., 1998), pp. 201-210.

"Liquid-Phase Oxidation Kinetics for a Paraffin Blend," J. M. Pickard and E. G. Jones, Poster presented at the 6th International Conference on Stability and Handling of Liquid Fuels, 13-17 October 1997, Vancouver, B.C., Canada; published in Proceedings of the 6th International Conference on Stability and Handling of Liquid Fuels, Vol. 2 (H. N. Giles, Ed.) (U. S. Department of Energy, Washington, D. C., 1998), pp. 975-983.

"The Measurement of Antioxidant Performance in Aviation Turbine Fuel Using the Quartz Crystal Microbalance and Near Isothermal Flowing Test Rig," S. Zabarnick, M. S. Mick, E. G. Jones, L. M. Balster, and S. D. Anderson, Poster presented at the 6th International Conference on Stability and Handling of Liquid Fuels, 13-17 October 1997, Vancouver, B.C., Canada; abstract published in Proceedings of the 6th International Conference on Stability and Handling of Liquid Fuels, Vol. 2 (H. N. Giles, Ed.) (U. S. Department of Energy, Washington, D. C., 1998), p. 989.

"Overview of ACC R&D in Aeroengine Gas Turbines," G. J. Sturgess, Invited presentation at the Second AGARD Workshop on Active Combustion Control for Propulsion Systems, 16-18 October 1997, Von Karman Institute, Brussels, Belgium.

"Phase-Resolved PIV and DNS Investigation of a Translational Plane Wall Jet," S. Gogineni, Invited Seminar at the Aerodynamics Institute, 20 October 1997, Aachen, Germany.

- "The Unsteady Structure of Simulated Turbine Film Cooling Flows from PIV," R. Rivir, S. Gogineni, L. Goss, and D. J. Pestian, Paper No. 47 presented at the AGARD Propulsion and Energetics Panel Symposium on Advanced Non-Intrusive Instrumentation for Propulsion Engines, 20-24 October 1997, Brussels, Belgium; published in AGARD-CP-598 (AGARD, Neuilly-sur-Seine, France, May 1998), pp. 47-1 – 47-13.

* "Optical Measurements of Surface Pressure and Temperature in Turbomachinery," K. Navarra, L. Goss, J. Jordan, D. Rabe, J. Gord, and D. Car, Paper No. 18 presented at the AGARD Propulsion and Energetics Panel Symposium on Advanced Non-Intrusive Instrumentation for Propulsion Engines, 20-24 October 1997, Brussels; published in AGARD-CP-598 (AGARD, Neuilly-sur-Seine, France, May 1998), pp. 18-1 – 18-13.

"Aviation Fuel Recirculation and Surface Fouling," E. G. Jones, W. J. Balster, and L. M. Balster, Energy Fuels 11(6), 1303-1308 (November/December 1997).

"Catalysis of Jet-A Fuel Autoxidation by Fe_2O_3," J. M. Pickard and E. G. Jones, Energy Fuels 11(6), 1232-1236 (November/December 1997).

"Optical Diagnostics Development: Getting to Know Your Flow," W. L. Weaver, Invited presentation to the Chemistry Department, Wittenberg University, 4 November 1997, Springfield, OH.

"Investigation of Fluid Flows Using Two-Color Digital Particle Image Velocimetry (DPIV) and Holographic (3D) Flow-Visualization (HFV) Techniques," S. P. Gogineni, Invited seminar to the Iowa Institute of Hydraulic Research, University of Iowa, 7 November 1997, Iowa City, IA.

"Why Active Combustion Control?" G. J. Sturgess, Invited presentation at the JANNAF Combustion Subcommittee Technology Awareness Seminar on Active Combustion Control (ACC) in Propulsion Systems, 12 November 1997, Cleveland, OH.

"Numerical Study of Two-Phase Flow Field in a Simplified Swirl Cup Combustor," T. W. Park, V. R. Katta, W. M. Roquemore, and S. K. Aggarwal, Presented at the 1997 ASME International Mechanical Engineering Congress and Exposition (IMEC&E), Symposium on Dispersed Flows in Combustion, Incineration, and Propulsion Systems, 16-21 November 1997, Dallas, TX; published in Proceedings ASME Fluids Engineering Division ASME 1997, FED-Vol. 244, pp. 215-223.

"Flame-Vortex Interactions in a Forced Counterflow Burner," I. Vihinen, J. R. Gord, J. M. Donbar, R. D. Hancock, W. M. Roquemore, G. J. Fiechtner, C. D. Carter, K. D. Grinstead, V. R. Katta, and J. C. Rolon, Poster presented at the ASME Heat Transfer Gallery Competition in conjunction with the 1997 ASME International Mechanical Engineering Congress and Exposition (IMEC&E), Symposium on Dispersed Flows in Combustion, Incineration, and Propulsion Systems, 16-21 November 1997, Dallas, TX. Of the 30-40 entrants, this poster was one of eight to be selected for an award and publication in ASME Journal of Heat Transfer.

"Phase-Resolved DPIV Investigation of Vortex-Flame Interactions in Hydrogen Jet Diffusion Flames," S. Gogineni, R. Hancock, F. Schauer, and R. Lucht, Presented at the 50th Annual Meeting of the American Physical Society, Division of Fluid Dynamics, 23-25 November 1997, San Francisco, CA.

"Visualization of Non-Circular, Coaxial Nozzle Flow Structure," J. W. Bitting, D. E. Nikitopoulos, S. P. Gogineni, and E. J. Gutmark, Presented at the 50th Annual Meeting of the American Physical Society, Division of Fluid Dynamics, 23-25 November 1997, San Francisco, CA.

"Flow Structure of Coaxial Jets," J. Bitting, D. Nikitopoulos, S. Gogineni, and M. Roquemore, Poster presented at the 50th Annual Meeting of the American Physical Society, Division of Fluid Dynamics, 23-25 November 1997, San Francisco, CA.

"Flame-Vortex Interactions in a Forced Counterflow Burner," I. Vihinen, J. R. Gord, J. M. Donbar, R. D. Hancock, W. M. Roquemore, G. J. Fiechtner, C. D. Carter, K. D. Grinstead, V. R. Katta, and J. C. Rolon, Poster presented at the 50th Annual Meeting of the American Physical Society, Division of Fluid Dynamics, 23-25 November 1997, San Francisco, CA.

"A Numerical Investigation of the Flame Structure of an Unsteady Inverse Partially Premixed Flame," Z. Shu, S. K. Aggarwal, V. R. Katta, and I. K. Puri, Combust. Flame 111, 296 (December 1997).

"Flame-Vortex Dynamics in an Inverse Partially Premixed Combustor: The Froude Number Effects," Z. Shu, S. K. Aggarwal, V. R. Katta, and I. K. Puri, Combust. Flame 111, 276 (December 1997).

"PIV and DNS Investigation on a Transitional Plane Wall Jet," S. Gogineni, M. Visbal, and D. Gaitonde, Presented at the Seventh Asian Congress of Fluid Mechanics, 8-12 December 1997, Chennai (Madras), India; published in Proceedings, pp. 223-226.

"Instantaneous Structure of Jet in a Cross Flow," S. Gogineni and L. Goss, Presented at the Seventh Asian Congress of Fluid Mechanics, 8-12 December 1997, Chennai (Madras), India; published in Proceedings, pp. 227-230.

* "Numerical Studies on Trapped-Vortex Concepts for Stable Combustion," V. R. Katta and W. M. Roquemore, J. Eng. Gas Turb. Power 120, 60 (January 1998).

* "Structure of a Compressible Boundary Layer Over a Curved Wall," R. C. Wier, R. D. W. Bowersox, D. D. Glawe, and S. P. Gogineni, Presented at the AIAA 36th Aerospace Sciences Meeting and Exhibit, 12-15 January 1998, Reno, NV, and published as AIAA Paper No. 98-0621.

* "NOx in Methane-Air Jet Diffusion Flames," V. R. Katta and W. M. Roquemore, Presented at the AIAA 36th Aerospace Sciences Meeting and Exhibit, 12-15 January 1998, Reno, NV, and published as AIAA Paper No. 98-0155.

* "Developments in Picosecond Pump/Probe Diagnostics," M. Linne, T. Settersen, J. Gord, and G. Fiechtner, Invited review paper presented at the AIAA 36th Aerospace Sciences Meeting and Exhibit, 12-15 January 1998, Reno, NV, and published as AIAA Paper No. 98-0306.

* "Characteristics of a Trapped-Vortex Combustor," K.-Y. Hsu, L. P. Goss, and W. M. Roquemore, AIAA J. Propul. Power 14(1), 57 (January-February 1998).

"Recent Developments in Optical Surface Pressure Measurements," K. R. Navarra, J. D. Jordan, D. D. Trump, and W. A. Stange, Presented at the 3rd National Turbine Engine High Cycle Fatigue (HCF) Conference, 2-5 February 1998, San Antonio, TX.

* "On the Dynamics of a Two-Phase, Nonevaporating Swirling Jet," T. W. Park, V. R. Katta, S. K. Aggarwal, Int. J. Multiphase Flow 24, 295 (March-April 1998).

"Manipulation of a Jet in a Cross Flow," S. P. Gogineni, L. P. Goss, and W. M. Roquemore, Experim. Therm. Fluid Sci. 16, 209 (March 1998),

"Experiments on the Structure of Turbulent $CO/H_2/N_2$ Jet Flames," R. S. Barlow, G. J. Fiechtner, C. D. Carter, and J.-Y. Chen, Presented at the 1998 Spring Technical Meeting of the Western States Section of the Combustion Institute, 23-24 March 1998, Berkeley, CA; published as Paper No. WSS/CI 98S-58.

"Comparison of CO Measurements by Raman Scattering and Two-Photon LIF in Laminar and Turbulent Methane Flames," R. S. Barlow, J. H. Frank, and J. G. Fiechtner, Presented at the 1998 Spring Technical Meeting of the Western States Section of the Combustion Institute, 23-24 March 1998, Berkeley, CA; published as Paper No. WSS/CI 98S-19.

"Autoxidation of Aviation Fuel Blends," L. M. Balster and E. G. Jones, Presented at the 215th ACS National Meeting, 29 Mar - 2 April 1998, Dallas, TX, and published in Prepr. Symp. - ACS, Div. Fuel Chem. 43(1), 49 (1998).

"Autoxidation of Diluted Aviation Fuels," E. G. Jones and L. M. Balster, Presented at the 215th ACS National Meeting, 29 Mar - 2 April 1998, Dallas, TX, and published in Prepr. Symp. - ACS, Div. Fuel Chem. 43(1), 44 (1998).

"Liquid-Phase Oxidation Kinetics of Aviation Fuels," E. G. Jones and J. M. Pickard, Presented at the 215th ACS National Meeting, 29 Mar - 2 April 1998, Dallas, TX, and published in Prepr. Symp. - ACS, Div. Fuel Chem. 43(1), 53 (1998).

* "Jet Fuel System Icing Inhibitors: Synthesis and Stability," G. W. Mushrush, E. J. Beal, D. R. Hardy, W. M. Stalick, S. Basu, D. Grosjean, and J. Cummings, Presented at the 215th ACS National Meeting, 29 Mar - 2 April 1998, Dallas, TX, and published in Prepr. Symp. - ACS, Div. Fuel Chem. 43(1), 60 (1998).

* "Effects of Temperature on Formation of Insolubles in Aviation Fuels," W. J. Balster and E. G. Jones, J. Eng. Gas Turb. Power 120, 289 (April 1998).

"Holographic Flow Visualization (HFV) for Complex Fluid Flows," S. P. Gogineni, J. Estevadeordal, and H. Meng, Presented at the Twenty-Third Annual Mini-Symposium on Aerospace Science and Technology, 3 April 1998, Dayton, OH.

"Experimental Studies of Aerodynamic Fan Spray Fuel Injectors for a Trapped-Vortex Combustor," I. Vihinen, R. Hancock, A. Johnson, F. Sun, B. Kiel, G. Switzer, and S. Gogineni, Presented at the Twenty-Third Annual Mini-Symposium on Aerospace Science and Technology, 3 April 1998, Dayton, OH; selected as Best Presentation in Session 5A – Fuel Atomization and Mixing.

"Vortex-Flame Interactions Part I: Vortex Characterization by Two-Color PIV and Acetone PLIF," J. R. Gord, J. M. Donbar, G. J. Fiechtner, and C. D. Carter, Presented at the Twenty-Third Annual Mini-Symposium on Aerospace Science and Technology, 3 April 1998, Dayton, OH.

"Vortex-Flame Interactions Part II: Extinction Studies by OH PLIF," G. J. Fiechtner, C. D. Carter, J. R. Gord, and J. M. Donbar, Presented at the Twenty-Third Annual Mini-Symposium on Aerospace Science and Technology, 3 April 1998, Dayton, OH.

* "Study on Trapped-Vortex Combustor--Effect of Injection on Flow Dynamics," V. R. Katta and W. M. Roquemore, J. Propul. Power 14, 273 (May/June 1998).

"High-Frequency Pressure-Sensitive Paints for Turbomachinery Applications," J. D. Jordan, D. D. Trump, B. Sarka, K. R. Navarra, W. L. Weaver, and L. P. Goss, Presented at the 44th International Instrumentation Symposium, 3-7 May 1998, Reno, NV, and published in Proceedings of the 44th International Instrumentation Symposium (Instrument Society of America, Research Triangle Park, NC, 1998), pp. 110-119.

"Laser-Based Visualization of Vortex-Flame Interactions in a Forced Counterflow Burner," J. R. Gord, J. M. Donbar, R. D. Hancock, I. Vihinen, W. M. Roquemore, G. J. Fiechtner C. D. Carter, K. D. Grinstead, Jr., and J. C. Rolon, Poster presented at the Annual Poster Session of the Society for Applied Spectroscopy (Ohio Valley Section), 22 May 1998, Columbus, OH.

"Investigation of Complex Fluid Flows Using Particle Imaging Velocimetry (PIV) and Holographic (3D) Flow Visualization (HFV) Techniques," S. P Gogineni, Invited seminar, Mechanical Engineering Department, Wright State University, 29 May 1998, Fairborn, OH.

"DPIV Investigation of Vortex-Flame Interactions in Hydrogen Jet Diffusion Flames," S. Gogineni, F. Schauer, R. Hancock, and R. Lucht, Presented at the Central States Section Meeting of the Combustion Institute, 31 May–2 June 1998, Lexington, KY, and published in Combustion Fundamentals and Applications (The Combustion Institute, Pittsburgh, PA, 1998), pp. 267-272.

"Vortical Structures in a Two-Dimensional Bluff-Body Burner," L. P. Chin, Presented at the Central States Section Meeting of the Combustion Institute, 31 May–2 June 1998, Lexington, KY, and published in Combustion Fundamentals and Applications (The Combustion Institute, Pittsburgh, PA, 1998), pp. 363-368.

"Calculation of Premixed Methane-Air Flames Using Detailed Chemical Kinetics," V. R. Katta and W. M. Roquemore, Presented at the Central States Section Meeting of the Combustion Institute, 31 May–2 June 1998, Lexington, KY, and published in Combustion Fundamentals and Applications (The Combustion Institute, Pittsburgh, PA, 1998), pp. 134-139.

"An Experimental and Numerical Investigation of the Structure of Steady Two-Dimensional Partially Premixed Methane-Air Flames," Z. Shu, B. J. Krass, C. W. Choi, S. K. Aggarwal, V. R. Katta, and I. K. Puri, Presented at the Central States Section Meeting of the Combustion Institute, 31 May–2 June 1998, Lexington, KY, and published in Combustion Fundamentals and Applications (The Combustion Institute, Pittsburgh, PA, 1998), pp. 374-378.

"Gravitational Effects on the Structure of Steady Two-Dimensional Partially Premixed Methane-Air Flames," Z. Shu, B. J. Krass, C. W. Choi, S. K. Aggarwal, V. R. Katta, and I. K. Puri, Presented at the Central States Section Meeting of the Combustion Institute, 31 May–2 June 1998, Lexington, KY, and published in Combustion Fundamentals and Applications (The Combustion Institute, Pittsburgh, PA, 1998), pp. 369-373.

"Open Forum - Future Trends in Gas Turbine Systems," G. J. Sturgess, Invited presentation at the Active Control of Gas Turbine Workshop on Goals and Technologies for Tomorrow's Gas Turbines, 15-16 June 1998, Atlanta, GA. Dr. Sturgess was Moderator of Session V: Panel Discussion and Laboratories Tour.

"Direct Numerical Simulation of a Forced Transitional Plane Wall Jet," M. Visbal, G-C. Zha, D. Gaitonde, and S. Gogineni, Presented at the AIAA 29th Fluid Dynamics Conference, 15-18 June 1998, Albuquerque, NM; published as AIAA Paper No. 98-2643.

* "Structure of Square Coaxial Nozzle Flows," J. W. Bitting, D. E. Nikitopoulos, E. J. Gutmark, and S. P. Gogineni, Presented at the AIAA 29th Fluid Dynamics Conference, 15-18 June 1998, Albuquerque, NM; published as AIAA Paper No. 98-2917.

* "Vortex-Flame Interactions in Hydrogen Jet Diffusion Flames: A DPIV and DNS Investigation," F. Schauer, R. Hancock, and S. Gogineni, Presented at the 1998 ASME Fluids Engineering Division Summer Meeting, 21-25 June 1998, Washington, D. C., and published as ASME Paper No. FEDSM98-5253.

"Visualization and Two-Color DPIV Measurements of Flows in Circular and Square Coaxial Nozzles," J. W. Bittting, D. E. Nikitopoulos, E. J. Gutmark, and S. Gogineni, Presented at the 1998 ASME Fluids Engineering Division Summer Meeting, 21-25 June 1998, Washington, D. C., and published as ASME Paper No. FEDSM98-5255.

"Instantaneous and Mean Compositional Structure of Bluff-Body-Stabilized Nonpremixed Flames," B. B. Dally, A. R. Masri, R. S. Barlow, and G. J. Fiechtner, Comb. Flame 114, 119 (June/July 1998).

* "Holographic Flow Visualization as a Tool for Studying Three-Dimensional Coherent Structures and Instabilities," H. Meng, J. Estevadeordal, S. Gogineni, L. Goss, and W. Roquemore, J. Visualization 1(2), 133 (July 1998).

"Flame-Vortex Interactions in a Nonpremixed H_2/N_2/Air Counterflow Burner," G. J. Fiechtner, C. D. Carter, J. R. Gord, K. D. Grinstead, W. M. Roquemore, and J. C. Rolon, Presented at the 34th AIAA/ASME/SAE/ASEE Joint Propulsion Conference and Exhibit, 13-15 July 1998, Cleveland, OH, and published as AIAA Paper No. 98-3770.

* "Simulation of Unsteady Flows in an Axisymmetric Research Combustor Using Detailed-Chemical Kinetics," V. R. Katta and W. M. Roquemore, Presented at the 34th AIAA/ASME/SAE/ASEE Joint Propulsion Conference and Exhibit, 13-15 July 1998, Cleveland, OH, and published as AIAA Paper No. 98-3766.

* "Thermal Cracking of Norpar-13 Fuel under Near-Critical and Supercritical Conditions," J.-C. Sheu, N. Zhou, A. Krishnan, E. G. Jones, and V. R. Katta, Presented at the 34th AIAA/ASME/SAE/ASEE Joint Propulsion Conference and Exhibit, 13-15 July 1998, Cleveland, OH, and published as AIAA Paper No. 98-3758.

"PIV and OH LIF Imaging of Flame-Vortex Interactions in an Opposed-Jet Burner," J. R. Gord, J. M. Donbar, G. J. Fiechtner, C. D. Carter, and J. C. Rolon, Presented at the Ninth International Symposium on Applications of Laser Techniques to Fluid Mechanics, 13-16 July 1998, Lisbon, Portugal.

"Thoughts on Combustion Difficulties and Operability Issues Associated with High Altitude Missions," G. J. Sturgess, Invited Presentation to the Air Force Research Laboratory Joint Air Force/Industry Workshop on Ignition and Combustion at High-Altitude Conditions, 22 July 1998, Wright-Patterson Air Force Base, OH.

"Ignition Diagnostics," J. R. Gord, D. T. Shouse, R. D. Hancock, C. Tyler, G. J. Fiechtner, K. D. Grinstead, Jr., J. Fues, M. Cochran, and F. Grigsby, Presented at the Air Force Research Laboratory Joint Air Force/Industry Workshop on Ignition and Combustion at High-Altitude Conditions, 22 July 1998, Wright-Patterson Air Force Base, OH.

"Ignition Modeling," V. R. Katta, Presented at the Air Force Research Laboratory Joint Air Force/Industry Workshop on Ignition and Combustion at High-Altitude Conditions, Presented at the Air Force Research Laboratory Joint Air Force/Industry Workshop on Ignition and Combustion at High-Altitude Conditions, 22 July 1998, Wright-Patterson Air Force Base, OH.

"Asynchronous Optical Sampling with Modelocked Ti:Sapphire Lasers," K. D. Grinstead, Jr., G. J. Fiechtner, J. R. Gord, and C. E. Bunker, Presented at the 40th Rocky Mountain Conference on Analytical Chemistry, 26-31 July 1998, Denver, CO.

"Characterizing Aviation Fuels at high Temperature and Pressure," J. R. Gord, C. E. Bunker, and K. D. Grinstead, Jr., Presented at the 40th Rocky Mountain Conference on Analytical Chemistry, 26-31 July 1998, Denver, CO.

"Mode-Locked Picosecond Laser-Based Diagnostics and Novel Sensors for Turbulence Measurement," T. Settersten, C. Fisher, N. Middleton, M. Linne, J. Gord, and G. J. Fiechtner, Presented at the Third International Workshop on Measurement and Computation of Turbulent Nonpremixed Flames, 30 July - 2 August 1998, Boulder, CO.

"Flame-Vortex Interactions in a Forced Counterflow Burner," I. Vihinen, J. R. Gord, J. M. Donbar, R. D. Hancock, W. M. Roquemore, G. J. Fiechtner, C. D. Carter, K. D. Grinstead, V. R. Katta, and J. C. Rolon, ASME J. Heat Trans. 120, 540 (August 1998).

* "An Account of Fuel Air Unmixedness Effects on NOx Generation in Gas Turbine Combustors," G J. Sturgess, Paper No. IECEC-98-353 presented at the 33rd Intersociety Engineering Conference on Energy Conversion (IECEC), 2-6 August 1998, Colorado Springs, CO.

* "Interaction of a Vortex with a Flat Flame Formed Between Opposing Jets of Hydrogen and Air," V. R. Katta, C. D. Carter, G. J. Fiechtner, W. M. Roquemore, J. R. Gord, and J. C. Rolon, Publication No. 4F01 presented at the Twenty-Seventh International Symposium on Combustion, 2-7 August 1998, Boulder, CO, and published in Twenty-Seventh Symposium (International) on Combustion (The Combustion Institute, Pittsburgh, PA, 1998), pp. 587-594.

* "An Experimental and Numerical Investigation of the Sturcture of Steady Two-Dimensional Partially Premixed Methane-Air Flames," Z. Shu, B. J. Krass, C. W. Choi, S. K. Aggarwal, V. R. Katta, and I. K. Puri, Presented at the Twenty-Seventh International Symposium on Combustion, 2-7 August 1998, Boulder, CO, and published in Twenty-Seventh Symposium (International) on Combustion (The Combustion Institute, Pittsburgh, PA, 1998), pp. 625-632.

* "Attachment Mechanisms of Diffusion Flames," F. Takahashi, W. J. Schmoll, and V. R. Katta, Presented at the Twenty-Seventh International Symposium on Combustion, 2-7 August 1998, Boulder, CO, and published in Twenty-Seventh Symposium (International) on Combustion (The Combustion Institute, Pittsburgh, PA, 1998), pp. 675-684.

"Experimental Study of the Annular Extinction of a Laminar Nonpremixed H_2/N_2/Air Flame in an Opposed Jet Burner," G. J. Fiechtner, C. D. Carter, J. R Gord, J. M. Donbar, R. D. Hancock, and J. C. Rolon, Poster No. W2DO2 presented at the Work-in-Progress Poster Session, Twenty-Seventh International Symposium on Combustion, 2-7 August 1998, Boulder, CO.

"Developments in Picosecond Pump/Probe Diagnostics," T. Settersten, M. Linne, J. Gord, and G. J. Fiechtner, Poster presented at the Work-in-Progress Poster Session, Twenty-Seventh International Symposium on Combustion, 2-7 August 1998, Boulder, CO.

* "Local Extinction in an Unsteady Methane-Air Jet Diffusion Flame," V. R. Katta, K.-Y. Hsu, and W. M. Roquemore, Publication No. 5A03 presented at the Twenty-Seventh International Symposium on Combustion, 2-7 August 1998, Boulder, CO, and published in Twenty-Seventh Symposium (International) on Combustion (The Combustion Institute, Pittsburgh, PA, 1998), pp. 1121-1129.

"Effects of Pre-Stressing on the Autoxidation of Aviation Fuel," E. G. Jones, L. M. Balster, and W. J Balster, Presented at the 216th National Meeting of the American Chemical Society, 23-27 August 1998, Boston, MA, and published in Prepr. Symp.-ACS, Div. Pet. Chem. 43(3), 346 (July 1998).

* "Modeling of Pyrolysis and Pyrolytic Deposition of Norpar-13 under Supercritical Conditions," J.-C. Sheu, N. Zhou, A. Krishnan, E. G. Jones, and V. R. Katta, Presented at the 216th National Meeting of the American Chemical Society, 23-27 August 1998, Boston, MA, and published in Prepr. Symp.-ACS, Div. Pet. Chem. 43(3), 390 (July 1998).

* "Spectroscopic Investigations of High-Temperature, High-Pressure Model Aviation Fuels," C. E. Bunker J. R. Gord, and K. D. Grinstead, Presented at the 216th National Meeting of the American Chemical Society, 23-27 August 1998, Boston, MA, and published in Prepr. Symp.-ACS, Div. Pet. Chem. 43(3), 467 (July 1998).

"Autoxidation of Neat and Blended Aviation Fuels," E. G. Jones, L. M. Balster, and W. J. Balster, Energy Fuels 12(5), 990 (September/October 1998).

"Visualization of Vortex-Flame Interactions in a Counterflow Diffusion Flame," I. Vihinen, J. R. Gord, J. M. Donbar, G. J Fiechtner, C. D. Carter, and J. C. Rolon, Presented at the 8th International Symposium on Flow Visualization, 1-4 September 1998, Sorrento, Italy, and published in Proceedings (available on CD-ROM).

"High-Frequency Pressure-Sensitive Paints," J. D. Jordan, A. N. Watkins, D. D. Trump, B. Sarka, W. L. Weaver, L. P. Goss, K. R. Navarra, and W. A. Stange, Invited presentation at the 1998 Turbine Engine Technology Symposium, 14-17 September 1998, Dayton, OH.

"Dynamic Behavior of Injection Scheme for Combustor Line Jets," B. Kiel and S. Gogineni, Presented at the 1998 Turbine Engine Technology Symposium, 14-17 September 1998, Dayton, OH.

"Ultrastable Blue-LED Illumination Sources for PSP Applications," J. D. Jordan, A. N. Watkins, D. D. Trump, W. L. Weaver, L. P. Goss, G. A. Dale, and G. Clinehens, Invited presentation at the HCF Instrumentation Action Team Meeting, 18 September 1998, Dayton, OH.

"Two-Color Digital PIV Employing a Single CCD Camera," S. Gogineni, L. Goss, D. Pestian, and R. Rivir, Exp. Fluids 25(4), 320 (October 1998).

"Visualization and Two-Color Measurements of Flows in Circular and Square Coaxial Nozzles," D. Nikitopoulos, J. Bitting, E. Gutmark, and S. P. Gogineni, Submitted in October 1998 to Experiments in Fluids.

"PSP Data Analysis: From Calibration to Visualization," W. L. Weaver, J. D. Jordan, G. A. Dale, and K. R. Navarra, Presented at the 1998 PSP Workshop, 2-9 October 1998, Seattle, WA.

"Sol-Gel-Based Coatings: A Universal PSP Platform," J. D. Jordan, A. N. Watkins, W. L. Weaver, D. D. Trump. L. P. Goss, J. H. Bell, G. A. Dale, and K. R. Navarra, Presented at the 1998 PSP Workshop, 2-9 October 1998, Seattle, WA.

"Picosecond Laser-Based Combustion Diagnostics," M. Linne, T. Settersten, C. Fisher, N. Middleton, and G. Fiechtner, Invited paper presented at the 1998 Federation of Analytical Chemistry and Spectroscopy Societies (FACSS) Meeting, 11-16 October 1998, Austin, TX.

"A Modelocked Ti:Sapphire Based Asynchronous Optical Sampler for Ultrafast Pump-Probe Experiments," J. R. Gord, K. D. Grinstead, Jr., G. J. Fiechtner, and C. E. Bunker, Presented at the 1998 Federation of Analytical Chemistry and Spectroscopy Societies (FACSS) Meeting, 11-16 October 1998, Austin, TX.

"Ultrafast Laser Studies of Chemical Dynamics in Supercritical Fluids," C. E. Bunker, K. D. Grinstead, Jr., and J. R. Gord, Presented at the 1998 Federation of Analytical Chemistry and Spectroscopy Societies (FACSS) Meeting, 11-16 October 1998, Austin, TX.

* "Combustion Characteristics of a Trapped Vortex Combustor," G. J. Sturgess and K-Y. Hsu, Paper No. 44, Presented at the Applied Vehicle Technology Panel Symposium on Gas Turbine Engine Combustion, Emissions, and Alternative Fuels, 12-16 October 1998, Lisbon, Portugal, and published in Gas Turbine Engine Combustion Emissions and Alternative Fuels, NATO Research and Technology Organization (RTO) Meeting Proceedings 14 (North Atlantic Treaty Organization, Neuilly-sur-Seine, France, June 1999), pp. 44-1 – 44-13.

"Optical Diagnostics Applied to a Jet Diffusion Flame," F. Grisch, B. Attal-Tretout, P. Bouchardy, V. R. Katta, and W. M Roquemore, Paper No. 17, Presented at the Applied Vehicle Technology Panel Symposium on Gas Turbine Engine Combustion, Emissions, and Alternative Fuels, 12-16 October 1998, Lisbon, Portugal, and published in Gas Turbine Engine Combustion Emissions and Alternative Fuels, NATO Research and Technology Organization (RTO) Meeting Proceedings 14 (North Atlantic Treaty Organization, Neuilly-sur-Seine, France, June 1999), pp. 17-1 – 17-9.

* "Dynamic Interactions of a Flame and an Isolated Vortex," G. J. Fiechtner, C. D. Carter, K. D. Grinstead, Jr., J. R. Gord, J. M. Donbar, and J. C. Rolon, Presented at the Fall Technical Meeting of the Western States Section of the Combustion Institute, 26-27 October 1998, Seattle, WA, and published as Paper No. 98-F10.

* "Simulation of Dynamic Methane Jet Diffusion Flames Using Finite Rate Chemistry Models," V. R. Katta and W. M. Roquemore, AIAA J. 36(11), 2044 (November 1998).

"Understanding Dynamic Flames Using Numerical and Experimental Techniques," V. R. Katta, Invited seminar to be given at Yale University, 11 November 1998, New Haven, CT.

"A Study of Square and Circular Coaxial Jet Flows," D. E. Nikitopoulos, J. W. Bitting, E. J. Gutmark, and S. Gogineni, Presented at the 51st Annual Meeting of the American Physical Society, Division of Fluid Dynamics, 22-24 November 1998, Philadelphia, PA.

"3D DNS and PIV Investigation of Forced Transitional Plane Wall Jet," M. Visbal, D. Gaitonde, and S Gogineni, Presented at the 51st Annual Meeting of the American Physical Society, Division of Fluid Dynamics, 22-24 November 1998, Philadelphia, PA.

"Double-Helix Instability in a Forced Wall Jet," M. Visbal, D. Gaitonde, and S. Gogineni, Poster presented at the 16th Annual Picture Gallery of Fluid Motion held in conjunction with the 51st Annual Meeting of the American Physical Society, Division of Fluid Dynamics, 22-24 November 1998, Philadelphia, PA. Of the 37 posters presented, this was one of five selected to receive an award and be published in the September 1999 issue of Physics of Fluids. The poster was displayed at the APS 1999 Centennial Meeting, which will be held 20-26 March 1999 in Atlanta, GA.

"Liquid-Phase Oxidation Kinetics: Paraffin Blends," J. M. Pickard and E. G. Jones, Energy Fuels 12(6), 1241 (November/December 1998).

* "Effects of Mach Number on Supersonic Wrap Around Fin Aerodynamics," T. C McIntyre, R. D. W. Bowersox, and L. P. Goss, J. Spacecr. Rockets 35(6), 742 (November-December 1998).

* "Modeling of Deposition Process in Liquid Fuels," V. R. Katta, E. G. Jones, and W. M. Roquemore, Combust. Sci. Technol. 139, 75 (November/December 1998).

* "Role of Flow Visualization in the Development of UNICORN," W. M. Roquemore and V. R. Katta, Keynote lecture given at the International Conference on Optical Technology and Image Processing in Fluid, Thermal, and Combustion Flow, 6-10 December 1998, Yokohama, Japan, and published as Paper No. KL310.

"Experimental and Computational Visualization of Vortex-Flame Interactions in an Opposed-Jet Burner," J. R. Gord, J. M. Donbar, G. J. Fiechtner, C. D. Carter, V. R. Katta, and J. C. Rolon, Paper No. AB082 presented at the International Conference on Optical Technology and Image Processing in Fluid, Thermal, and Combustion Flow, 6-10 December 1998, Yokohama, Japan.

"Experimental Investigation of Supersonic Wrap-Around Fin Aerodynamic Mach Number Effects," T. C. McIntyre, R. D. W. Bowersox, and L. P. Goss, Presented at the AIAA 37th Aerospace Sciences Meeting and Exhibit, 11-14 January 1999, Reno, NV, and published as AIAA Paper No. 99-0991.

* "Characteristics of Combustion Instability Associated with Trapped-Vortex Burner," K.-Y. Hsu, C. D. Carter, V. R. Katta, and W. M. Roquemore, Presented at the AIAA 37th Aerospace Sciences Meeting and Exhibit, 11-14 January 1999, Reno, NV, and published as AIAA Paper No. 99-0488.

* "Sol-Gel-Based Pressure-Sensitive Paint Development," J. D. Jordan, A. N. Watkins, W. L. Weaver, G. A. Dale, and K. R. Navarra, Presented at the AIAA 37th Aerospace Sciences Meeting and Exhibit, 11-14 January 1999, Reno, NV, and published as AIAA Paper No. 99-0566.

* "Phase Sensitive Imaging in Flows," C W. Fisher, M A. Linne, N. T. Middleton, G. Fiechtner, and J. R. Gord, Presented at the AIAA 37th Aerospace Sciences Meeting and Exhibit, 11-14 January 1999, Reno, NV, and published as AIAA Paper No. 99-0771.

* "Data Analysis Methods for the Development and Deployment of Pressure-Sensitive Paints," W. L. Weaver J. D. Jordan, G. A. Dale, and K. R. Navarra, Presented at the AIAA 37th Aerospace Sciences Meeting and Exhibit, 11-14 January 1999, Reno, NV, and published as AIAA Paper No. 99-0565.

* "Regimes of Interaction between a Nonpremixed Hydrogen-Air Flame and an Isolated Vortex," G. J. Fiechtner, C. D. Carter, V. R. Katta, J R. Gord, J. M. Donbar, and J. C. Rolon, Presented at the AIAA 37th Aerospace Sciences Meeting and Exhibit, 11-14 January 1999, Reno, NV, and published as AIAA Paper No. 99-0320.

* "Numerical Modeling of Droplets in a Composite Grid System," L. P. Chin, Presented at the AIAA 37th Aerospace Sciences Meeting and Exhibit, 11-14 January 1999, Reno, NV, and published as AIAA Paper No. 99-0212.

"Investigation of Complex Fluid Flows Using PIV and HFV Techniques," S. P. Gogineni, Invited seminar at the Department of Mechanical Engineering, Louisiana State University, 12 February 1999, Baton Rouge, LA.

"Asynchronous Optical Sampling for Ultrafast Pump-Probe Studies," K. D. Grinstead, Jr., G. J. Fiechtner, J. R. Gord, and C. E. Bunker, Paper No. 483 presented at the Pittsburgh Conference on Analytical Chemistry, 7-12 March 1999, Orlando, FL.

"Spectroscopic Characterization of High-Temperature Aviation Fuels," J. R. Gord, C. E. Bunker, and K. D. Grinstead, Jr., Paper No. 1074 presented at the Pittsburgh Conference on Analytical Chemistry, 7-12 March 1999, Orlando, FL.

"Laser-Based Visualization of Vortex-Flame Interactions," K. D. Grinstead, Jr., G. J. Fiechtner, C. D. Carter, J. R. Gord, P. H. Renard, and J. C. Rolon, Paper No. 1076 presented at the Pittsburgh Conference on Analytical Chemistry, 7-12 March 1999, Orlando, FL.

"Determination of Water in Aviation Fuel," D. E. Hirt, J. R. Gord, C. E. Bunker, and K. D. Grinstead, Jr., Paper No. 1529 presented at the Pittsburgh Conference on Analytical Chemistry, 7-12 March 1999, Orlando, FL.

"An Overview of PIV and HPIV," S. P. Gogineni, Invited seminar at the University of Central Florida, 10 March 1999, Orlando, FL.

"Numerical Modeling of Droplet-Flame Interaction," L. P. Chin and V. R. Katta, Presented at the First Joint Technical Meeting of the U. S. Sections of the Combustion Institute, Chemical and Physical Processes in Combustion, 14-17 March 1999, Washington, DC.

"Experimental Studies of Vortex-Flame Interactions in an Opposed-Jet Burner," G. J. Fiechtner, P.-H. Renard, C. D. Carter, J. R. Gord, J. M. Donbar, and J. C. Rolon, Presented at the First Joint Technical Meeting of the U. S. Sections of the Combustion Institute, Chemical and Physical Processes in Combustion, 14-17 March 1999, Washington, DC.

"In-House Research and Development of a Pulse Detonation Engine," R. A. Anthenien, F. R. Schauer, J. S. Stutrud, C. W. Frayne, R. P. Bradley, L. P. Chin, and V. R. Katta, Presented at the First Joint Technical Meeting of the U. S. Sections of the Combustion Institute, Chemical and Physical Processes in Combustion, 14-17 March 1999, Washington, DC.

* "A Role of Chemical Kinetics in the Simulation of the Reaction Kernel of Methane Jet Diffusion Flames," F. Takahashi and V. R. Katta, Presented at the 5th ASME/JSME Joint Thermal Engineering Conference, 15-19 March 1999, San Diego, CA, and published as Paper No. AJTE99-6190.

* "Fuel Effects on Lean Blowout and Emissions from a Well-Stirred Reactor," J. W. Blust, D. R. Ballal, and G. J Sturgess, J. Propul. Power 15(2), 216 (March-April 1999).

"Ultrafast Imaging of a Gas Turbine Spark Igniter," K. D. Grinstead, Jr., G. J. Fiechtner, J. R. Gord, C. Tyler, M. Cochran, and J. R. Frus, Presented at the 24th Dayton-Cincinnati Aerospace Science Symposium, 9 April 1999, Dayton, OH.

"Continuing Studies of Vortex-Flame Interactions," J. R. Gord, G. J. Fiechtner, K. D. Grinstead, Jr., C. D. Carter, P. H. Renard, and J. C. Rolon, Presented at the 24th Dayton-Cincinnati Aerospace Science Symposium, 9 April 1999, Dayton, OH. Received award for Best Paper in Session on Vortex Flows.

"A Facility for Basic Research Studies of Fire-Suppression Dynamics," J. R. Gord, G. J. Fiechtner, and K. D. Grinstead, Jr., Presented at the 24th Dayton-Cincinnati Aerospace Science Symposium, 9 April 1999, Dayton, OH.

"Quantitative Measurements of CO Concentrations in Laminar and Turbulent Flames Using Two-Photon Laser-Induced Fluorescence," G. J. Fiechtner, C. D. Carter, and R. S. Barlow, Presented at the 24th Dayton-Cincinnati Aerospace Science Symposium, 9 April 1999, Dayton, OH.

"Development of an Advanced Imaging System," G. J. Fiechtner, J. R. Gord, C. W. Fisher, M. A. Linne, and N. T. Middleton, Presented at the 24th Dayton-Cincinnati Aerospace Science Symposium, 9 April 1999, Dayton, OH. Received award for Best Paper in Instrumentation Session.

"Vortex Branching and Spanwise Instabilities in a Forced Walljet," M. R. Visbal, Gaitonde, and S. P. Gogineni, Presented at the 24th Dayton-Cincinnati Aerospace Science Symposium, 9 April 1999, Dayton, OH.

"LIF Nitric Oxide Measurements in Driven Jet Diffusion Flames," R. Hancock, F. Schauer, R. P. Lucht, T. R. Meyer, and V. R. Katta, Presented at the 24th Dayton-Cincinnati Aerospace Science Symposium, 9 April 1999, Dayton, OH.

"Flow Structure of Coaxial Jets," S. P. Gogineni, J. W. Bitting, D. E. Nikitoupolos, and W. M. Roquemore, Poster presented at the 24th Dayton-Cincinnati Aerospace Science Symposium, 9 April 1999, Dayton, OH.

"Experimental Studies of a Macrolaminate Fuel Injector for a Trapped Vortex Combustor," I. Vihinen D. Shouse, A. Johnson, M. Benjamin, P. Laing, and G. Switzer, Presented at the 24th Dayton-Cincinnati Aerospace Science Symposium, 9 April 1999, Dayton, OH.

"Effects of Recirculation on Aviation Fuels: A Simulation," L. M. Balster, W. J. Balster, and E. G. Jones, Presented at the 24th Dayton-Cincinnati Aerospace Science Symposium, 9 April 1999, Dayton, OH.

"Flame-Vortex Interactions in a Driven Diffusion Flame," K. Y. Hsu, W. M. Roquemore, V. R. Katta, L. P. Goss, and D. D. Trump, Poster presented at the Art in the Science Competition held in conjunction with the 24th Dayton-Cincinnati Aerospace Science Symposium, 9 April 1999, Dayton, OH. Received the Prof. Britton Choice Award.

"A Visualization of the Convergence of Phase-Doppler Particle Analyzer Beams in a Three-Dimensional Cone Spray," I. Vihinen, G. Switzer, A. Johnson, and D. Shouse, Poster presented at the Art in the Science Competition held in conjunction with the 24th Dayton-Cincinnati Aerospace Science Symposium, 9 April 1999, Dayton, OH.

"Combustion Dynamics - What Degree of Physical Understanding is Necessary," G. J. Sturgess, Keynote address at the Advanced Gas Turbine Systems Research Combustion Workshop VI, 18-21 April 1999, Blacksburg, VA.

"High-Frequency Pressure-Sensitive Paints for Turbomachinery Applications," J. D. Jordan, A. N. Watkins, W. L. Weaver, D. D. Trump, B. Sarka, L. P. Goss, and K. R. Navarra, Presented at the 45th International Instrumentation Symposium, 2-6 May 1999, Albuquerque, NM.

"Density Matrix and Rate Equation Analyses for Picosecond Pump/Probe Combustion Diagnostics," T. Settersten, M. Linne, J. Gord, G. Fiechtner, AIAA J. 37(6), 723 (June 1999).

"Research Needs for Air Quality Compliance: Diesels, Turbines, and Ordnance – Turbines," G. J. Sturgess, W. M. Roquemore, R. D. Hancock, I. Vihinen, J. R. Gord, and R. Mantz, Invited report for the Workshop on Research Needs for Air Quality Compliance - Diesels, Turbines, and Ordnance, 2-3 June 1999, Linthicum, MD.

* "Extended Liquid-Phase Oxidation of Aviation Fuels," L. M. Balster, W. J. Balster, and E. G. Jones, Paper No. 99-GT-55, Presented at the 44th ASME International Gas Turbine and Aeroengine Technical Congress, Exposition, and Users Symposium, 7-10 June 1999, Indianapolis, IN.

"Pressure-Sensitive-Paint Measurements in a Large-Scale Commercial-Engine Test Stand," J. D. Jordan, A. N. Watkins, J. C. P. N. Davis, W. L. Weaver, G. A. Dale, K. R. Navarra, J. R. Urban, W. E. Devoid, and R. A. Strange, Presented at the 18th International Congress on Instrumentation in Aerospace Simulation Facilities, 14-17 June 1999, Toulouse, France.

* "Stability-Limit Predictions of Methane Jet Diffusion Flames," F. Takahashi and V. Katta, Presented at the 35th AIAA/ASME/SAE/ASEE Joint Propulsion Conference and Exhibit, 20-23 June 1999, Los Angeles, CA, and published as AIAA Paper No. 99-2781.

* "Numerical Modeling of Collision between Two Droplets," L. P. Chin, Presented at the 14th AIAA Computational Fluid Dynamics Conference, 28 June - 1 July 1999, Norfolk, VA, and published as AIAA Paper 99-3319.

"Phase-Resolved PIV Measurements in a Translational Plane Wall Jet: A Numerical Comparison," S. P. Gogineni, M. Visbal, and C. Shih, Exp. Fluids 27(2), 126 (July 1999).

* "Gravity Effects on Steady Two-Dimensional Partially Premixed Methane-Air Flames," Z. Shu, C. W. Choi, S. K. Aggarwal, V. R. Katta, and I. K. Puri, Comb. Flame 118, 91 (July 1999).

"Autoxidation of Dilute Jet-Fuel Blends," E. G. Jones and L. M. Balster, Energy Fuels 13(4), 796 (July/August 1999).

"Analysis of Flow Transition in an Acoustically Excited Wall Jet," S. Gogineni, M. Visbal, D. Gaitonde, and C. Shih, Presented at the 3rd ASME/JSME Joint Fluids Engineering Conference and FED Annual Summer Meeting/Exhibition, 18-22 July 1999, San Francisco, CA, and published as Paper No. FEDSM99-6959.

* "Application of Imaging Techniques to the Study of Vortex-Flame Interactions," G. J. Fiechtner, P. H. Renard, J. R. Gord, K. D. Grinstead, Jr., C. D. Carter, and J. C. Rolon, Presented at the Optical Methods and Data Processing in Heat and Fluid Flow Conference (SPIE International Symposium on Optical Science, Engineering, and Instrumentation), 18-23 July 1999, Denver, CO, and published as Paper No. 3783-03.

* "Imaging Strategies for the Study of Gas Turbine Spark Ignition," J. R. Gord, C. Tyler, K. D. Grinstead, Jr., G. J. Fiechtner, M. J. Cochran, and J. R. Frus, Presented at the Optical Methods and Data Processing in Heat and Fluid Flow Conference (SPIE International Symposium on Optical Science, Engineering, and Instrumentation), 18-23 July 1999, Denver, CO.

* "Numerical Studies on Cellular Detonation Wave Subjected to Sudden Expansion," V. R. Katta, L. P. Chin, and F. Schauer, Presented at the 17th International Colloquium on the Dynamics of Explosions and Reactive Systems, 25-30 July 1999, Heidelberg, Germany.

"Studying the Solvent-Dependent Spectroscopy of IR-125 through Asynchronous Optical Sampling," C. E. Bunker, J. R. Gord, K. D. Grinstead, Jr., and G. J. Fiechtner, Presented at the 41st Rocky Mountain Conference on Analytical Chemistry, 1-5 August 1999, Denver, CO.

"Capturing Gas Turbine Spark Ignition through Utrafast Imaging," K. D. Grinstead, Jr., G. J. Fiechtner, J. R. Gord, C. Tyler, M. Cochran, and J. R. Frus, Presented at the 41st Rocky Mountain Conference on Analytical Chemistry, 1-5 August 1999, Denver, CO.

"Optical Diagnostic Techniques for Characterizing Vortex-Flame Interactions," J. R. Gord, G. J. Fiechtner, K. D. Grinstead, Jr., C. D. Carter, P. H. Renard, and J. C. Rolon, Presented at the 41st Rocky Mountain Conference on Analytical Chemistry, 1-5 August 1999, Denver, CO.

* "AFRL In-House Pulse Detonation Engine Research Program," F. R. Schauer, J. S. Stutrud, R. A. Anthenien, R. P. Bradley, L. P. Chin, and V. R. Katta, Presented at the 12th ONR Propulsion Meeting, 4-6 August 1999, Salt Lake City, UT, and published in Proceedings (G. D. Roy and S. L. Anderson, Eds.)

"Quantitative Measurements of CO Concentrations in Laminar and Turbulent Flames Using Two-Photon Laser-Induced Fluorescence," G. J. Fiechtner, C. D. Carter, and R S. Barlow, Paper No. HTD99-298 presented at the 33rd Joint ASME, AIChE, ANS, and AIAA 1999 National Heat Transfer Conference, 15-17 August 1999, Albuquerque, NM.

"Characterizing the Interaction of a Vortex with a Laminar Opposed-Jet Flame," J. R. Gord, G. J. Fiechtner, P. H. Renard, C. D. Carter, and J. C. Rolon, Paper No. HTD99-295 presented at the 33rd Joint ASME, AIChE, ANS, and AIAA 1999 National Heat Transfer Conference, 15-17 August 1999, Albuquerque, NM.

* "Dilution Method for Estimating Concentration of Primary Antioxidants in Lubricants," E. G. Jones and L. M. Balster, Presented at the 218th National Meeting of the American Chemical Society, 22-26 August 1999, New Orleans, LA, and published in Prepr. Symp.-ACS, Div. Pet. Chem. 44(3), 305 (July 1999).

* "Effect of Pressure on Supercritical Pyrolysis of n-Paraffins," E. G. Jones, L. M. Baster, W. J. Balster, and R. C. Striebich, Presented at the 218th National Meeting of the American Chemical Society, 22-26 August 1999, New Orleans, LA, and published in Prepr. Symp.-ACS, Div. Pet. Chem. 44(3), 394 (July 1999).

"Thermal Stability and Autoxidation of Jet Fuels Measured at 185 °C," E. G. Jones, L. M. Balster, and W. J. Balster, Presented at the 218th National Meeting of the American Chemical Society, 22-26 August 1999, New Orleans, LA, and published in Prepr. Symp.-ACS, Div. Pet. Chem. 44(3), 382 (July 1999).

* "Optical Method for Quantitating Dissolved Oxygen in Fuel," J. R. Gord, S. W. Buckner, W. L. Weaver, and K. D. Grinstead, Jr., U. S. Patent No. 5,919,710 issued 6 July 1999.

"Double-Helix Instability in a Forced Wall Jet," M. Visbal, D. Gaitonde, and S. Gogineni, Phys. Fluids 11(9), 57 (September 1999).

* "Quantitative Visualization of Flowfields Using Two-Color PIV," S. Gogineni, L. Goss, G. Fiechtner, C. Carter, F. Schauer, J. Gord, and J. Donbar, Poster and paper presented at the 3rd International Workshop on Particle Image Velocimetry, 16-18 September 1999, Santa Barbara, CA. Dr. Gogineni Chaired the Session on PIV Applications II.

* "Vortex Injection of Noble Gases in an Opposed-Jet Burner," G. J. Fiechtner, J. R. Gord, C. D. Carter, K. D. Grinstead, Jr., V. R. Katta, P.-H. Renard, and J. C. Rolon, Presented at the Fall Technical Meeting of the Eastern States Section of the Combustion Institute, 11-13 October 1999, Raleigh, NC.

* "Ultrafast Imaging of a Gas Turbine Spark Igniter," J. R. Gord, G. J. Fiechtner, K. D. Grinstead, Jr., M. J. Cochran, and J. R. Frus, Presented at the Fall Technical Meeting of the Eastern States Section of the Combustion Institute, 11-13 October 1999, Raleigh, NC.

* "Development of a Research Pulse Detonation Engine," F. R. Schauer, J. S. Stutrud, R. A. Anthenien, R. P. Bradley, L. P. Chin, and V. R. Katta, Invited paper presented at the JANNAF Combustion Subcommittee, Air Breathing Subcommittee, and Propulsion Systems Hazards Subcommittee Joint Meeting, 18-22 October 1999, Cocoa Beach, FL.

"Vortex-Initiated Chemical Reactions in Combusting Flowfields," K. D. Grinstead, Jr., G. J. Fiechtner, C. D. Carter, J. R. Gord, P.-H. Renard, and J. C. Rolon, Presented at the Federation of Analytical Chemistry and Spectroscopy Societies (FACSS) Annual Meeting in conjunction with the 45th International Conference on Analytical Sciences and Spectroscopy (ICASS), 24-29 October 1999, Vancouver, Canada.

"Continuing Development, Characterization, and Application of an Asynchronous Optical Sampler," K. D. Grinstead, Jr., G. J. Fiechtner, C. E. Bunker, D. K. Phelps, and J. R. Gord, Presented at the Federation of Analytical Chemistry and Spectroscopy Societies (FACSS) Annual Meeting in Conjunction with the 45th International Conference on Analytical Sciences and Spectroscopy (ICASS), 24-29 October 1999, Vancouver, Canada.

"A Study of Flame-Vortex Interactions in the Rolon Burner," G. J. Fiechtner, Invited Seminar at Purdue University, Department of Mechanical Engineering, 2 November 1999, West Lafayette, IN.

"Studying Vortex-Flame Interactions with Laser-Based Visualization," K. D. Grinstead, Jr., G. J. Fiechtner, C. D. Carter, J. R. Gord, P.-H. Renard, and J. C. Rolon, Presented at the Eastern Analytical Symposium and Exposition, 14-19 November 1999, Somerset, NJ.

"Effects of Diffusion Shaped Holes on Turbine Film Cooling Performance," S. Gogineni, J. Estevadeordal, M. Chyu, and T. I.-P. Shih, Presented at the 52nd Meeting of the American Physical Society, Division of Fluid Dynamics, 21-23 November 1999, New Orleans, LA.

"Measurements of Turbulent Flow Structure in Supersonic Curved Wall Boundary Layers," R. D. W. Bowersox, R. C. Wier, D. D. Glawe, and S. Gogineni, J. Propul. 16(1), 153 (January 2000).

"Comparisons between Circular and Square Coaxial Jet Flows," D. E. Nikotopoulos, J. W. Bitting, and S. Gogineni, Presented at the 38th AIAA Aerospace Sciences Meeting and Exhibit, 10-13 January 2000, Reno, NV, and published as AIAA Paper No. 2000-0661.

* "Visualization and DPIV Measurements of Non-Circular Coaxial Jet Flows," S. Gogineni, J. W. Bitting, and D. E. Nikitopoulos, Presented at the 38th AIAA Aerospace Sciences Meeting and Exhibit, 10-13 January 2000, Reno, NV, and published as AIAA Paper No. 2000-0660.

* "Injection of Single and Multiple Vortices in an Opposed-Jet Burner," G. J. Fiechtner, P.-H. Renard, C. D. Carter, J. R. Gord, and J. C. Rolon, J. Visualization 2(3-4), 331 (January/February 2000).

* "Role of Flow Visualization in the Development of UNICORN," W. M. Roquemore and V. R. Katta, J. Visualization 2(3-4), 257 (January/February 2000).

* "Experiments on the Scalar Structure of Turbulent $CO/H_2/N_2$ Jet Flames," R. S. Barlow, G. J. Fiechtner, C. D. Carter, and J.-Y. Chen, Comb. Flame 120, 549 (March 2000).

"Calculation of Methane Flames in the Presence of Fire Suppressing Agent," V. R. Katta and W. M. Roquemore, Presented at the Eighth International Conference on Numerical Combustion, 5-8 March 2000, Amelia Island, FL.

"An Asynchronous Optical Sampler for Studying Ultrafast Solvent Dynamics," J. R. Gord, C. E. Bunker, K. D. Grinstead, Jr., and G. J. Fiechtner, Presented at the Annual Poster Session 2000, Dayton Section of the American Chemical Society and Ohio Valley Section of the Society for Applied Spectroscopy, 8 March 2000, Dayton, OH.

"Dual-Pump Coherent Anti-Stokes Raman Spectroscopy for Combustion-Efficiency Measurements," G. J. Fiechtner, C. D. Carter, R. P. Lucht, P. M. Danehy, R. L. Farrow, and J. R. Gord, Presented at the Annual Poster Session 2000, Dayton Section of the American Chemical Society and the Ohio Valley Section of the Society for Applied Spectroscopy, 8 March 2000, Dayton, OH.

"Characterizing Vortex-Flame Interactions with Laser-Based Diagnostics," J. R. Gord, G. J. Fiechtner, K. D. Grinstead, Jr., C. D. Carter, P.-H. Renard, and J. C. Rolon, Presented at the Annual Poster Session 2000, Dayton Section of the American Chemical Society and the Ohio Valley Section of the Society for Applied Spectroscopy, 8 March 2000, Dayton, OH.

"High-Speed Schlieren Imaging of a Unison Spark Igniter," J. R. Gord, G. J. Fiechtner, K. D. Grinstead, Jr., M. J. Cochran, and J. R. Frus, Presented at the Annual Poster Session 2000, Dayton Section of the American Chemical Society and the Ohio Valley Section of the Society for Applied Spectroscopy, 8 March 2000, Dayton, OH.

"Interline-Transfer CCD for Lifetime-Based Pressure-Sensitive-Paint Measurements," L. P. Goss, G. J. Fiechtner, J. R. Gord, T. F. Drouillard, C. W. Fisher, M. A. Linne, and N. T. Middleton, Presented at the 25th Annual Dayton-Cincinnati Aerospace Science Symposium, 30 March 2000, Dayton, OH.

"Vortex-Based Ingiter for Advanced Propulsion Applications," G. L. Switzer, G. J Fiechtner, and J. R. Gord, Presented at the 25th Annual Dayton-Cincinnati Aerospace Science Symposium, 30 March 2000, Dayton, OH.

"Megahertz-Framing Rate Images of a Gas Turbine Spark Igniter," J. R. Gord, G. J. Fiechtner, K. D. Grinstead, Jr., M. J. Cochran, and J. R. Frus, Presented at the 25th Annual Dayton-Cincinnati Aerospace Science Symposium, 30 March 2000, Dayton, OH.

"Optical Parametric Oscillator for Mid-Infrared Combustion Measurements," J. R. Gord, G. E. Tietz, A. Henderson, P. Roper, R. Mead, and G. J. Fiechtner, Presented at the 25th Annual Dayton-Cincinnati Aerospace Science Symposium, 30 March 2000, Dayton, OH.

"Exhaust Gas Analysis by Dual-Pump Coherent Anti-Stokes Raman Spectroscopy," G. J. Fiechtner, C. D. Carter, R. P. Lucht, P. M. Danehy, R. L. Farrow, and J. R. Gord, Presented at the 25th Annual Dayton-Cincinnati Aerospace Science Symposium, 30 March 2000, Dayton, OH. Received Best Paper Award in Fuels and Combustion.

"Influence of CHF_3 on Unsteady Buoyant Jet Diffusion Flame," V. R. Katta and W. M. Roquemore, Presented at the 2000 Technical Meeting of the Central States Section of the Combustion Institute, 16-18 April 2000, Indianapolis, IN, and published in Combustion Fundamentals and Applications (The Combustion Institute, Pittsburgh, PA, 2000), pp. 427-432.

"Absorption and the Dimensionless Overlap Integral for Two-Photon Excitation," G. J. Fiechtner and J. R. Gord, Accepted in May 2000 for publication in the Journal of Quantum Spectroscopy and Radiation Transfer.

* "Chemical Kinetic Structure of the Reaction Kernel of Methane Jet Diffusion Flames," F. Takahashi and V. R. Katta, Comb. Sci. Technol. 155, 243 (May 2000).

"Interaction of a Synthetic Hindered-Phenol with Natural Fuel Antioxidants in the Autoxidation of Paraffins," E. G. Jones and L. M. Balster, Energy Fuels 14(3), 640 (May-June 2000).

"Vortex-Flame Interactions: Experimental Observation of an Annular Local Extinction," G. J. Fiechtner, C. D. Carter, J. R. Gord, P.-H. Renard, D. Thevenin, and J. C. Rolon, Submitted in June 2000 to Combustion and Flame.

* "Influence of Ceramic-Matrix-Composite Wall Plates on Combustor Performance," V. R. Katta, R. Anthenien, R. Mantz, W. M. Roquemore, R. A. Brockman, R. John, L. P. Zawada, T. A. Parthasarathy, and R. Kerans, Presented at the 36th AIAA/ASME/SAE/ ASEE Joint Propulsion Conference and Exhibit, 17-19 July 2000, Huntsville, AL, and published as AIAA Paper No. 2000-3351.

"Rotational Anisotropy Decay in Supercritical Fluids and Liquid Solvents: Investigating Phase Transitions," C. E. Bunker and J. R. Gord, Presented at the 42nd Rocky Mountain Conference on Analytical Chemistry, 30 July - 3 August 2000, Denver, CO.

"Density-Dependent Spectral Shifts of Pyrene in Supercritical Fuels," D. K. Phelps, C. E. Bunker, and J. R. Gord, Presented at the 42nd Rocky Mountain Conference on Analytical Chemistry, 30 July - 3 August 2000, Denver, CO.

"Lifetime Imaging with an Interline-Transfer CCD Camera for Pressure-Sensitive-Paint Applications," J. R. Gord, L. P. Goss, G. J. Fiechtner, T. F. Drouillard, C. W. Fisher, M. A. Linne, and N. T. Middleton, Presented at the 42nd Rocky Mountain Conference on Analytical Chemistry, 30 July - 3 August 2000, Denver, CO.

"New Spectral Sources for Studying Combustion and Fuels," J. R. Gord, G. J. Fiechtner, M. S. Brown, A. Henderson, P. Roper, R. Mead, J. V. Rudd, D. Zimdars, and M. Warmuth, Presented at the 42nd Rocky Mountain Conference on Analytical Chemistry, 30 July - 3 August 2000, Denver, CO.

* "Experimental and Numerical Investigation of the Structures of Two-Dimensional Partially Premixed Methane-Air Flames," V. R. Katta, L. Brenez, and J. C. Rolon, Presented at the 28th International Symposium on Combustion, 30 July - 4 August 2000, Edinburgh, Scotland, and be published in Proceedings of the Combustion Institute 28 (2000).

* "Response of a Hydrogen-Air Opposing-Jet Diffusion Flame to Different Types of Perturbations," V. R. Katta and W. M. Roquemore, Presented at the 28th International Symposium on Combustion, 30 July - 4 August 2000, Edinburgh, Scotland, and be published in Proceedings of the Combustion Institute 28 (2000).

* "A Reaction Kernel Hypothesis for the Stability Limit of Methane Jet Diffusion Flames," F. Takahashi and V. R. Katta, Presented at the 28th International Symposium on Combustion, 30 July - 4 August 2000, Edinburgh, Scotland, and published in Proceedings of the Combustion Institute 28 (2000).

* "Regimes of Nonpremixed Flame/Vortex Interactions," D. Thevenin, P.-H. Renard, G. J. Fiechtner, J. R. Gord, and J. C. Rolon, Presented at the 28th International Symposium on Combustion, 30 July - 4 August 2000, Edinburgh, Scotland, and published in Proceedings of the Combustion Institute 28 (2000).

"AFRL's In-House Pulse Detonation Engine Program," F. Schauer, J. Stutrud, and R. Bradley, Invited presentation at the 13th ONR Propulsion Meeting, 10-12 August 2000, Minneapolis, MN.

"Modeling and Measurement of the Interaction of Starting Jets and Flames," G. J. Fiechtner, V. R. Katta, C. D. Carter, J. R. Gord, W. M. Roquemore, and J. C. Rolon, Selected for publication as frontispiece in J. Visualization 3(2) (September 2000).

"Visualization of Vortex-Shedding and Blade Synchronization in a Transonic Compressor," J. Estevadeordal, S. Gogineni, L. Goss, W. Copenhaver, and S. Gorrell, Selected for publication as frontispiece in J. Visualization 3(2) (September 2000).

* "A Numerical and Experimental Study of the Structure of a Diffusion Flame Established in a Laminar Boundary Layer along a Vertical Porous Plate," F. Takahashi, V. R. Katta, M. Nagamori, T. Ueda, and M. Takeuchi, Presented at the Third International Symposium on Scale Modeling, 10-13 September 2000, Nagoya, Japan, and published in the Conference Proceedings.

"Increasing the Sensitivity of Second-Harmonic-Detected Two-Photon-Excited Molecular Fluorescence," K. D. Grinstead, J. R. Gord, W. L. Weaver, and F. E. Lytle, To be submitted to Applied Spectroscopy.